

PROGRAMA OFICIAL DE POSGRADO EN
TECNOLOGÍAS DE LA INFORMACIÓN Y LA COMUNICACIÓN

Departamento de Química Analítica
Departamento de Teoría de la Señal, Telemática y Comunicaciones

UNIVERSIDAD DE GRANADA



TESIS DOCTORAL

ESTUDIO DE MÉTODOS PARA LA ESTIMACIÓN DEL
TIEMPO DE VIDA DE LUMINISCENCIA EN FASES SENSORAS
ÓPTICAS: DESARROLLO, IMPLEMENTACIÓN Y
EVALUACIÓN DE UN BANCO DE PRUEBAS DE
LABORATORIO PARA LA CARACTERIZACIÓN DE FASES
SENSORAS ÓPTICAS DE DIVERSO TIPO

Realizada por:

Ing. Santiago Medina Rodríguez

Dirigida por:

Dr. D. Alberto Fernández Gutiérrez

Dr. D. Ángel de la Torre Vega

Dr. D. Jorge Fernando Fernández Sánchez

Editor: Editorial de la Universidad de Granada
Autor: Santiago Medina Rodríguez
D.L.: GR 1866-2014
ISBN: 978-84-9083-050-5

OFFICIAL GRADUATE PROGRAM IN
INFORMATION TECHNOLOGY AND COMMUNICATION

Department of Analytical Chemistry
Department of Signal Theory, Telematics and Communications

UNIVERSITY OF GRANADA



PH.D. THESIS DISSERTATION

STUDY OF METHODS FOR ESTIMATING LUMINESCENCE
LIFETIME IN OPTICAL SENSING PHASES: DEVELOPMENT,
IMPLEMENTATION AND EVALUATION OF A LABORATORY
TEST BENCH FOR THE CHARACTERISATION OF OPTICAL
SENSING PHASES OF DIFFERENT TYPES

Written by:

Eng. Santiago Medina Rodríguez

Supervised by:

Dr. D. Alberto Fernández Gutiérrez

Dr. D. Ángel de la Torre Vega

Dr. D. Jorge Fernando Fernández Sánchez

El doctorando D. Santiago Medina Rodríguez y los directores de la tesis Dr. D. Alberto Fernández Gutiérrez, Catedrático de Universidad adscrito al Departamento de Química Analítica de la Universidad de Granada, Dr. D. Ángel de la Torre Vega, Profesor Titular de Universidad adscrito al Departamento de Teoría de la Señal, Telemática y Comunicaciones de la Universidad de Granada y Dr. D. Jorge Fernando Fernández Sánchez, Profesor Titular de Universidad adscrito al Departamento de Química Analítica de la Universidad de Granada,

GARANTIZAMOS AL FIRMAR ESTA TESIS DOCTORAL

que el trabajo ha sido realizado por el doctorando bajo la dirección de los directores de la tesis y hasta donde nuestro conocimiento alcanza, en la realización del trabajo se han respetado los derechos de otros autores a ser citados, cuando se han utilizado sus resultados o publicaciones.

Granada, a 5 de febrero de 2014

LOS DIRECTORES DE LA TESIS:

Prof. Dr. D. Alberto Fernández Gutiérrez
Catedrático del Departamento de Química Analítica de la UGR

Prof. Dr. D. Ángel de la Torre Vega
Profesor Titular del Departamento de Teoría de la Señal, Telemática y Comunicaciones de la UGR

Prof. Dr. D. Jorge Fernando Fernández Sánchez
Profesor Titular del Departamento de Química Analítica de la UGR

EL DOCTORANDO:

D. Santiago Medina Rodríguez
Ingeniero de Telecomunicaciones



UNIVERSIDAD DE GRANADA

*Departamento de Química Analítica “Profesor Fermín Capitán García”
Campus Universitario Fuentenueva 18071 Granada, España*

El Prof. Dr. D. Alberto Fernández Gutiérrez, Catedrático del Departamento de Química Analítica “Profesor Fermín Capitán” de la Facultad de Ciencias, y Director del Grupo de Investigación FQM-297 “Control Analítico, Bioquímico y Alimentario” de la Universidad de Granada,

CERTIFICA QUE:

El trabajo que se presenta en esta tesis doctoral con el título: “ESTUDIO DE MÉTODOS PARA LA ESTIMACIÓN DEL TIEMPO DE VIDA DE LUMINISCENCIA EN FASES SENSORAS ÓPTICAS. DESARROLLO, IMPLEMENTACIÓN Y EVALUACIÓN DE UN BANCO DE PRUEBAS DE LABORATORIO PARA LA CARACTERIZACIÓN DE FASES SENSORAS ÓPTICAS DE DIVERSO TIPO”, que ha sido realizado bajo mi dirección y la de los Profesores Dr. D. Ángel de la Torre Vega y Dr. D. Jorge F. Fernández Sánchez, reúne todos los requisitos legales, académicos y científicos para hacer que el doctorando D. Santiago Medina Rodríguez pueda optar al grado de Doctor Internacional en Ingeniería de Telecomunicaciones. Esta Tesis ha sido realizada en los laboratorios que el grupo FQM-297 tiene en el Departamento de Química Analítica y también, parcialmente, en el Institute of Robotics and Intelligent Systems (IRIS) del Swiss Federal Institute of Technology (ETH) de Zurich (Suiza) y en los del Departamento de Teoría de la Señal, Telemática y Comunicaciones, con colaboraciones de la School of Chemistry de la Universidad de Birmingham y del Departamento de Ingeniería Eléctrica y Electrónica de la Universidad Pública de Navarra.

Y para que así conste, expido y firmo el presente certificado en Granada a 5 de febrero de 2014:

Prof. Dr. D. Alberto Fernández Gutiérrez
Catedrático del Departamento de Química Analítica de la UGR

Esta tesis doctoral ha sido realizada gracias a una beca predoctoral FPI asignada a un Proyecto de Investigación del Ministerio de Economía y Competitividad (Ref. Beca: BES-2009-026919; Proyecto: CTQ2011-25316), y a la financiación con cargo a fondos del grupo FQM-297 “Control Analítico, Bioquímico y Alimentario” del Plan Andaluz de Investigación de la Junta de Andalucía, procedentes de diferentes contratos, proyectos y subvenciones de la Administración Central y Autonómica del Estado y del Plan Propio de Investigación de la Universidad de Granada.

Agradecimientos

TRAS cuatro años de intenso trabajo, ¡por fin tengo la Tesis! Durante este tiempo he tenido la gran suerte de poder conocer a mucha gente extraordinaria que me ha ayudado mucho en los momentos más difíciles, y gracias a la cual he podido culminar esta Tesis. A todos ellos, muchísimas gracias por vuestra generosidad y compañerismo.

La travesía no ha sido fácil, qué duda cabe, y más aún cuando decides realizar la Tesis en un campo de investigación relativamente alejado de tu perfil académico. No obstante, el reto de tener que trabajar con personas de áreas muy distintas (como los químicos o los ingenieros químicos) me ha enriquecido mucho, y la verdad es que estoy encantado de haber podido vivir esa experiencia. Quisiera agradecer a todos mis compañeros y amigos del grupo de investigación FQM-297 del Departamento de Química Analítica de la UGR su ayuda incondicional y su compañerismo. Gracias a: Elena, Rocío, María, Adil, Pachy, Antonio Luis, Ángel, Tere, Mari Carmen, Esther, Paulina, Marta, Paco, Alegría, etc., a todos los compañeros del CIDAF y también al resto de compañeros de otros grupos a los que he tenido la suerte de conocer durante estos años. De todos ellos, me gustaría hacer una excepción con aquellos con los que he podido colaborar estrechamente: a Paulina le tengo que agradecer su infinita generosidad y lo mucho que me ayudó en mis inicios (te recordaré siempre Pauli, y sirvan estas líneas para expresarte mi más profunda admiración por tu constancia, paciencia e inigualable talla humana); a Paco quisiera agradecerle su amistad, su franqueza y su enorme apoyo científico y humano en todos estos años (gracias por tu amistad sincera, por apoyarme en los momentos de debilidad, por tu trabajo, por tu hospitalidad y por haberme dado la oportunidad de conocer tu fantástica tierra (Logroño) y a tu extraordinaria familia; nunca lo olvidaré); y finalmente, tengo que acordarme de Marta para agradecerse prácticamente todo (tú has sido mi más estrecha colaboradora en estos cuatro años, en los cuales he tenido el enorme privilegio de poder trabajar contigo “codo con codo” para intentar sacar adelante todo aquello que nos proponíamos); te agradezco tu infinita paciencia (por aguantarme todos los días), tu generoso esfuerzo por intentar entender mis razonamientos y cabezonerías, y sobre todo, quisiera agradecerte tu sincera amistad y el estar siempre ahí para ayudarme y apoyarme en todo lo que podía. Gracias infinitas ‘Sate’, gran parte de los éxitos de esta Tesis son tanto tuyos como míos (bien lo sabes); te recordaré siempre como la gran compañera y amiga que has sido, por todo lo que me has ayudado y por lo mucho que he podido aprender trabajando a tu lado; sirvan pues estas letrillas para expresarte mi más profunda admiración, cariño y agradecimiento por todo ello.

A Alegría tengo que dedicarle forzosamente un agradecimiento muy especial, porque sin duda alguna se lo merece con creces. Ale, sinceramente he de decirte que jamás conocí a nadie que reuniera tantísimas virtudes como tú reúnes. Tu infinita generosidad y entrega a los demás, tu extraordinario sentido del humor incluso en las situaciones más estresantes, tu simpatía y cercanía, tu campechanía, tu humildad, tu optimismo y profesionalidad, te hacen, sin duda alguna, única en tu especie, y lo que es mejor, eres capaz de contagiar toda esa ‘alegría’ a todo aquel que te rodea. Eres, sin duda, un ejemplo a seguir en lo profesional y en lo personal, y en mi opinión, eres el auténtico faro del grupo de toda la Facultad de Ciencias!. Para mí siempre serás un referente y un espejo en el que mirarme. Mil gracias por todo Ale, siempre estaré en deuda contigo por lo mucho que me has ayudado en todo este tiempo, por tus bromas, por tus risas, por esas sobremesas, en fin . . . sirvan estas palabras para agradecerte todo eso y para decirte que siempre te recordaré con muchísimo cariño.

Por otro lado, también quisiera agradecer a mis compañeros del Departamento de TSTC su amistad y compañerismo en todos estos años, y muy especialmente a mis compañeros y amigos del CITIC: a Rafa, José María, Alberto, Rosa, Rita, Fernando, Álex, Miguel, Pablo, Joaquín, Povedano, Plata, Leo, Roberto, etc. Al igual que antes, me gustaría hacer una excepción con dos de ellos: Rafa y José María. A vosotros dos os quiero agradecer los diez años que llevamos juntos (Carrera, Máster y Tesis) y los inolvidables momentos que hemos podido compartir en todo este tiempo. Espero seguir contando con vuestra valiosa amistad, y quisiera emplear estas líneas para expresaros mi más profunda admiración, respeto y cariño. Gracias por ser como sois, nunca os olvidaré!.

También quisiera acordarme de todos mis compañeros y amigos del colegio del Ave María Casa Madre. Gracias a: Elena, Marta, Violeta, Iván, Tania, Azucena, Claudio, Salva . . . y a todos esos magníficos profesores que tuve la suerte de tener y que me enseñaron las bases de todo lo que sé y de lo que soy.

Agradezco también el apoyo de mis tres directores de Tesis: Prof. Dr. Alberto Fernández Gutiérrez, Prof. Dr. Ángel de la Torre Vega y el Prof. Dr. Jorge F. Fernández Sánchez, quienes me dieron la oportunidad de iniciarme en el mundo de la investigación. Les quiero dar las gracias por depositar su confianza en mí, por proporcionarme los medios necesarios para poder realizar mi trabajo, por su infinita paciencia y comprensión, y por ofrecerme su ayuda, conocimiento y experiencia sin reservas.

Por último, quisiera acordarme de todos mis amigos, familiares y conocidos de mi barrio de siempre, el Sacromonte. Y por supuesto, quisiera acordarme muy especialmente de mis padres, Antonio y Serafina, por educarme y protegerme durante tantos años, y por haberme dado la oportunidad de formarme en lo que he querido. Finalmente, quisiera terminar esta lista de agradecimientos acordándome de mi hermano gemelo Carlos, al cual agradezco estos 28 años de convivencia fraternal, y en quien encuentro, sin duda alguna, mi mejor y más valioso apoyo. Gracias brother!

*A mis padres, Antonio y Serafina
A mi hermano gemelo, Carlos*

*Caminante, son tus huellas
el camino, y nada más;
caminante, no hay camino,
se hace camino al andar.*

*Al andar se hace camino,
y al volver la vista atrás
se ve la senda que nunca
se ha de volver a pisar.*

*Caminante, no hay camino,
sino estelas en la mar...*

(“Cantares” XXIX, Antonio Machado (1875-1939))

Objetivos

EL objetivo principal de esta memoria es el desarrollo, implementación y evaluación de un banco de pruebas de laboratorio para la caracterización y evaluación de una amplia variedad de fases sensoras ópticas, usando para ello medidas de intensidad de luminiscencia y medidas de tiempo de vida en el dominio de la frecuencia. Asimismo, este banco de pruebas debe proporcionar la plataforma necesaria para el desarrollo de múltiples aplicaciones potenciales en el ámbito de los sensores químicos de naturaleza óptica, permitiendo no solo la caracterización y evaluación de nuevos materiales con propiedades luminiscentes, sino también el análisis, diseño, desarrollo, implementación y evaluación de nuevos sistemas de medida e instrumentos que hagan uso de estos materiales. Para conseguirlo, se fijaron los siguientes objetivos parciales:

- Profundizar en el conocimiento de los sensores químicos de naturaleza óptica con propiedades fotoluminiscentes, estudiando su configuración y su principio de funcionamiento, así como las principales técnicas de medida empleadas para su caracterización. Asimismo, también se pretende profundizar en el conocimiento de la instrumentación empleada en el desarrollo de sensores ópticos luminiscentes, y recabar información acerca de los principales sistemas de medida propuestos en la literatura.
- Desarrollar e implementar un sistema de medida sencillo que permita la caracterización y evaluación de fases sensoras ópticas usando medidas de intensidad de luminiscencia (las más simples). Este primer diseño del banco de pruebas sentará las bases de futuras implementaciones y permitirá progresar en el conocimiento tanto de las fases sensoras ópticas como de la instrumentación necesaria para su caracterización y evaluación.
- Extender la funcionalidad del sistema de medida para permitir la caracterización y evaluación de las fases sensoras ópticas mediante medidas de tiempo de vida de luminiscencia en el dominio de la frecuencia. Tras desarrollar e implementar dicho sistema de medida se tratará de evaluar su respuesta mediante la caracterización y evaluación de diversas fases sensoras. Este sistema permitirá profundizar en el conocimiento de las medidas de tiempo de vida en el dominio de la frecuencia, así como conocer los principios básicos de funcionamiento de la instrumentación empleada para este fin, sirviendo de base para el diseño, desarrollo, implementación y evaluación de futuros sistemas de medida con alguna aplicación práctica.
- Desarrollar nuevos métodos de medida de modulación de fase que permitan abaratar los

costes de la instrumentación habitualmente empleada en este tipo de sistemas, mejorar su sensibilidad analítica, o simplemente hacer posible su miniaturización y portabilidad, así como testar su fiabilidad y robustez en diferentes escenarios de medida (condiciones de bajo nivel de iluminación o alto nivel de ruido) y llevar a cabo su implementación en sistemas reales de medida para comprobar su aplicabilidad en el desarrollo de sensores ópticos.

- Proponer nuevos métodos de modulación de fase basados en técnicas avanzadas de procesamiento digital de señales que permitan: (1) mejorar la sensibilidad analítica en aplicaciones de espectroscopía de luminiscencia, y (2) obtener una descripción analítica más completa de sistemas luminiscentes.
- Finalmente, se pretende profundizar en el estudio de los modelos clásicos de calibración descritos para los sensores ópticos luminiscentes, proponiendo y evaluando nuevos modelos de calibración que sean sencillos y, a ser posible, más escalables que los actuales.

Objectives

THE main objective of this Doctoral Thesis is the development, implementation and evaluation of a laboratory test bench to characterise and evaluate a wide variety of optical sensor phases, using luminescence intensity measurements and lifetime measurements in the frequency domain. Also, this test bench should provide the platform required to develop multiple potential applications in the field of optical chemical sensors, not only allowing the characterisation and evaluation of new luminescence materials, but also the analysis, design, development, implementation and evaluation of new measurement systems and instruments that make use of these materials. To achieve this, the following sub-objectives have been established:

- Improving knowledge of optical chemical sensors with photoluminescent properties, studying their configuration and working principle and the main measurement techniques used for their characterisation. Furthermore, this Thesis also intends to improve knowledge of the instrumentation used in the development of luminescent optical sensors and to gather information about the main measurement systems proposed in the literature.
- Developing and implementing a simple measurement system that allows for the characterisation and of optical sensing phases using luminescence intensity measurements (the simplest). This first design of tests will provide the basis for future implementations and allow progress in the knowledge of both the optical sensor phases and the instrumentation required for characterisation and evaluation.
- Extending the functionality of the measuring system to allow for the characterisation and evaluation of optical sensor phases using luminescence lifetime measurements in the frequency domain. After developing and implementing such a measurement system, we will try to evaluate its response through characterisation and evaluation of various sensing phases. This system will allow for better understanding of lifetime measurements in the frequency domain, as well as learning the basic principles of operation of the instrumentation used for this purpose, providing a basis for the design, development, implementation and evaluation of future measurement systems with some practical application.
- Developing new methods for measuring phase-modulation lifetime allowing lower costs for instrumentation commonly used in such systems, improving analytical sensitivity,

or simply enabling miniaturisation and portability, as well as testing reliability and robustness in different measurement scenarios (under low levels of lighting or high noise levels) and carrying out their implementation in real measurement systems to test applicability to the development of optical sensors.

- Suggesting new phase modulation methods based on advanced digital signal processing techniques enabling: (1) improvement of analytical sensitivity in luminescence spectroscopy applications, and (2) a more complete analytical description of the photoluminescent systems.
- Finally, the Thesis aims to go deeper into the study of classic calibration models described for luminescent optical sensors, proposing and evaluating new calibration models that are simple and, if possible, more scalable than the current ones.

Resumen

ESTA memoria presenta los resultados obtenidos durante la realización de la Tesis Doctoral titulada: *“Estudio de métodos para la estimación del tiempo de vida de luminiscencia en fases sensoras ópticas. Desarrollo, implementación y evaluación de un banco de pruebas de laboratorio para la caracterización de fases sensoras ópticas de diverso tipo”*.

La memoria ha sido dividida en dos partes principales: la introducción y la parte experimental.

La **introducción** recoge algunos de los conceptos y generalidades más importantes de los sensores químicos, mostrando especial interés en los sensores químicos de naturaleza óptica, objeto de estudio de la presente memoria. En el primer apartado se lleva a cabo una descripción general de los sensores químicos (definición y componentes más importantes), seguida de una clasificación general de los mismos. Acto seguido, se resume la importancia y actualidad de los sensores químicos, destacando algunos de sus campos de aplicación más relevantes. En el segundo apartado se profundiza en los conceptos y generalidades de los sensores químicos de naturaleza óptica, explicándose algunos de sus parámetros descriptivos más importantes y llevando a cabo una clasificación general de los mismos. El tercer apartado se centra en la descripción de los sensores ópticos luminiscentes para el control de oxígeno, al ser éstos los mayoritariamente utilizados en la parte experimental de esta memoria. En primer lugar, se muestra una visión general de la importancia de la determinación de oxígeno en diferentes campos de la Ciencia y la Tecnología, así como las principales técnicas existentes para realizar dicha determinación. En segundo lugar se proporciona una información más detallada sobre la determinación de oxígeno por el fenómeno de la atenuación de la luminiscencia. Para ello, se describen tanto los fundamentos del fenómeno de la luminiscencia molecular como los diferentes métodos existentes para su detección, haciendo especial énfasis en la descripción de los dos métodos luminiscentes predominantes: los métodos basados en la medida de la intensidad de la luminiscencia y los basados en la medida del tiempo de vida de luminiscencia. Dentro de éstos últimos se describen los dos métodos de medida principales: aquellos basados en el dominio del tiempo (métodos de luz pulsada) y los basados en el dominio de la frecuencia (métodos de modulación de fase). En el cuarto y último apartado de la introducción se realiza una revisión general de la instrumentación empleada para llevar a cabo medidas de fluorescencia y fosforescencia. Asimismo, hay tres apéndices que complementan esta información y tratan aspectos relacionados con sistemas de inyección de flujo (**Apéndice 1**), sensores ópticos tipo sonda (optodos) (**Apéndice 2**) y elementos que componen un sensor

óptico luminiscente para la determinación de oxígeno (**Apéndice 3**).

La segunda parte de la memoria, denominada **parte experimental**, recoge los resultados obtenidos durante la realización de la presente Tesis Doctoral y la discusión de los mismos. Esta parte ha sido dividida en siete capítulos, cuyo contenido se describe a continuación.

El **Capítulo 1** proporciona una descripción general del banco de pruebas de laboratorio desarrollado. En primer lugar, se describen sus características más sobresalientes, analizando sus principales componentes instrumentales y sus diversas configuraciones de medida, ya sea para la adquisición de medidas de intensidad o de tiempos de vida de luminiscencia en el dominio de la frecuencia. Asimismo, también se muestra una visión general de las distintas etapas del proceso de desarrollo del sistema, desde sus primeras versiones hasta su versión final, mencionando las principales dificultades encontradas y las soluciones aportadas. Parte de los conocimientos necesarios para llevar a cabo el desarrollo final del sistema de medida propuesto fueron adquiridos en el *Institute of Robotics and Intelligent Systems* (IRIS) del *Swiss Federal Institute of Technology* de Zúrich (ETH Zúrich, Suiza).

El **Capítulo 2** se centra en el desarrollo y caracterización de una fase sensora óptica para la determinación de dióxido de carbono (CO_2) tanto en muestras acuosas como gaseosas. La fase sensora se basa en un co-polímero lineal funcionalizado con un indicador luminiscente de pH y un agente de transferencia de fase (hidróxido de tetraoctil amonio (TONOH)). En este trabajo se optimizó tanto la composición de la fase sensora como las condiciones de medida, usando para ello un espectrofluorímetro comercial. Asimismo, también se determinaron sus características analíticas, demostrando una alta sensibilidad y selectividad tanto en muestras acuosas como gaseosas. Por último, para demostrar la versatilidad de la fase sensora propuesta, se desarrolló un sensor de fibra óptica basado en medidas de intensidad, obteniendo un intervalo dinámico lineal razonable y un buen límite de detección.

El **Capítulo 3** versa sobre la utilización de medidas de desplazamiento de fase para el desarrollo de fases sensoras ópticas capaces de detectar concentraciones muy bajas de oxígeno. Este trabajo fue desarrollado en colaboración con la *School of Chemistry* de la Universidad de Birmingham (Edgbaston, Inglaterra). En total se caracterizaron cuatro fases sensoras formadas por cuatro compuestos organometálicos (uno de platino (PtTFPP) y tres de iridio (N969, N1008 y EB146)) depositados sobre un soporte nanoestructurado de óxido hidróxido de aluminio (AP200/19). Para llevar a cabo la caracterización de las fases sensoras se determinaron sus propiedades espectroscópicas (espectros de excitación y de emisión), sus tiempos de respuesta (t_{95}) y sus curvas de calibración para diferentes intervalos de concentración de oxígeno (0-1 % de O_2 y 0-10 % de O_2). Las medidas fueron realizadas utilizando un instrumento comercial (un detector de fase-fija (*Lock-In Amplifier*, LIA)). Las fases sensoras mostraron una excelente sensibilidad a bajas y ultra-bajas concentraciones de oxígeno (0-10 % de O_2 y 0-1 % de O_2 respectivamente), siendo especialmente significativa la sensibilidad obtenida para la membrana PtTFPP-AP200/19. Esta fase sensora resultó ser unas 62 veces más sensible que cuando se deposita el compuesto en una membrana clásica de poliestireno y unas 8 veces más sensible que cuando se deposita en partículas de sílice. Por otro lado, también se llevaron a cabo estudios de fotoestabilidad, demostrándose que las medidas de desfase son significativamente más robustas a la fotodegradación de las fases sensoras que las medidas basadas en intensidad (factor de modulación). Finalmente, también se demostró que las membranas no se veían afectadas por la humedad, y que presentaban una completa reversibilidad y una

larga estabilidad a largo plazo (más de 12 meses).

En el **Capítulo 4** se desarrolla un optosensor sencillo y versátil para la determinación de oxígeno basado en un método de modulación de fase multifrecuencia (llamado método I/Q multifrecuencia). Este método permite calcular el desfase introducido por la fase sensora (el cual varía con la concentración de O_2) a varias frecuencias de modulación, usando para ello una única medida (una señal multifrecuencia consistente en una combinación lineal de varias funciones sinusoidales de distinta frecuencia). El método propuesto se basa en los principios de la detección en cuadratura y puede ser completamente implementado en un procesador digital de señales (DSP). Así, en este capítulo, se discuten los aspectos teóricos del método I/Q así como los detalles técnicos del sistema de medida. La respuesta del sistema de medida fue evaluada mediante la caracterización y evaluación de una fase sensora óptica sensible a oxígeno (PtTFPP inmovilizado en una membrana polimérica permeable al oxígeno). Además, estos resultados fueron comparados satisfactoriamente con aquellos obtenidos por un sistema de medida de referencia basado en un detector de fase comercial (LIA) y usando la misma fase sensora en todos los casos. El sistema propuesto obtuvo una incertidumbre inferior a 0.2 kPa en la determinación de la presión parcial de oxígeno en el intervalo de concentraciones de 0-20 kPa.

En el **Capítulo 5** se evalúa la respuesta del método I/Q (descrito en el Capítulo 4) para distintas condiciones de ruido. Para ello, se llevó a cabo un conjunto de pruebas experimentales usando señales sinusoidales analógicas de frecuencia fija, 1 segundo de duración, fases aleatorias conocidas entre 0 y -180° y diferentes niveles de ruido blanco gaussiano aditivo (AWGN) (intervalo de SNRs entre -18 y 36 dB). Estas señales analógicas fueron generadas numéricamente en un ordenador (usando Matlab) y convertidas posteriormente al dominio analógico mediante un conversor D/A de una tarjeta de adquisición de datos. Las medidas de desfase obtenidas con el método I/Q usando estas señales fueron comparadas con las obtenidas por un equipo de medida de referencia (un LIA comercial), obteniéndose resultados muy similares en ambos casos. Además, la respuesta del método I/Q también fue evaluada en un sistema real de medida para demostrar su aplicabilidad. Para ello, se usó el sistema de medida de oxígeno descrito en el Capítulo 4 y se evaluó el método I/Q bajo diferentes condiciones de iluminación. Esto se consiguió variando la amplitud de la señal de excitación entre 22 y 1000 mV, de manera que se obtuvieron señales de emisión de diferente intensidad óptica (valores de amplitud más bajos de la señal de excitación se tradujeron en señales de emisión menos intensas, esto es, con menor nivel de SNR). De nuevo, estos resultados fueron comparados con los obtenidos por un sistema de medida convencional basado en un LIA comercial, obteniéndose resultados similares. Dichos resultados demostraron la robustez del método I/Q frente al ruido y su eficiencia computacional, confirmando que la detección en cuadratura es una técnica ideal para la determinación exacta de la fase de una señal sinusoidal incluso en presencia de niveles de ruido elevados (muy bajos niveles de SNR).

En el **Capítulo 6** se describe un nuevo método de modulación de fase multifrecuencia para espectroscopía de luminiscencia. El método propone el uso de una señal de excitación rectangular con un ciclo de trabajo corto para: (1) mejorar la sensibilidad analítica en la determinación de la concentración, y (2) obtener una información más completa del sistema luminiscente analizado. El método se basa en un algoritmo sencillo que combina la información multifrecuencia proporcionada por los diferentes armónicos de la señal rectangular, el cual puede ser implementado fácilmente en instrumentos de fotoluminiscencia existentes

simplemente cambiando la forma de onda de la señal usada para modular la fuente de luz de excitación (una señal rectangular de ciclo corto en lugar de una señal sinusoidal), e implementado (en software) el algoritmo de procesamiento digital de señal apropiado después del transductor. Estas afirmaciones se han demostrado usando un optodo de oxígeno basado en una fase sensora conocida (una porfirina de Pt(II) inmovilizada en poliestireno). Los resultados experimentales demostraron que el método propuesto permite disminuir la raíz cuadrada del error cuadrático medio (RMSE) en la determinación analítica (de 0.1035 a 0.0053 kPa a 0.5 kPa de O₂ y de 1.1087 a 0.1209 kPa a 20 kPa de O₂) cuando éste es comparado con un método de modulación de fase convencional basado en una fuente de excitación modulada sinusoidalmente (en igualdad de condiciones de potencia luminosa). Este trabajo se realizó en colaboración con el Departamento de Ingeniería Eléctrica y Electrónica de la Universidad Pública de Navarra.

Por último, en el **Capítulo 7** se propone un nuevo modelo de calibración para sensores ópticos fotoluminiscentes y se compara con los modelos clásicos propuestos en la literatura (modelos de Stern-Volmer, Lehrer y Demas). Este nuevo modelo puede ser considerado como una variante del modelo de Stern-Volmer y proporciona un buen compromiso entre el número de parámetros y la exactitud del ajuste, en comparación con otros modelos clásicos de similar complejidad (es decir, con el mismo número de parámetros). Además, en este capítulo se demuestra también la importancia del criterio de optimización usado para la calibración del modelo. Para ello, se presentan los resultados obtenidos para 25 experimentos reales, donde intervienen 7 fases sensoras ópticas sensibles a oxígeno diferentes (PtTFPP-PS, N969-AP200/19, EB146-AP200/19, PtTFPP-AP200/19, N1008-AP200/19, EB146-PS0X, N1008-PS0X), 3 señales analíticas diferentes (intensidad de luminiscencia, tiempo de vida determinado a partir del desplazamiento de fase y tiempo de vida determinado a partir del factor de modulación) y 3 instrumentos de medida distintos (un espectrómetro de luminiscencia, un detector de fase-fija (LIA) y un sistema de medida basado en el método I/Q (descrito en los Capítulos 4, 5 y 6)). En este capítulo también se proporcionan todos los detalles necesarios para la implementación de los diferentes procedimientos de calibración, así como el código fuente (compatible con Matlab y Octave) que realiza la calibración para cada modelo y criterio.

Summary

THIS report presents the results obtained during the Doctoral Thesis entitled: “Study of methods for estimating luminescence lifetime in optical sensing phases. Development, implementation and evaluation of a laboratory test bench for the characterisation of optical sensing phases of different types”.

The report has been divided into two main sections: the introduction and the experimental section.

The **introduction** includes some of the most important concepts and generalities of the chemical sensors, showing particular interest in chemical optical sensors, under consideration herein. The first section includes an overview of chemical sensors (definition and major components), followed by a general classification of them. It then summarises the importance and relevance of chemical sensors, highlighting some of the most relevant application fields. The second section delves into the concepts and generalities of optical chemical sensors, explaining some of their most important descriptive parameters and carrying out a general classification thereof. The third section focuses on the description of the luminescent optical sensors for monitoring oxygen, these being mainly used in the experimental section of this Thesis. Firstly, an overview of the importance of the determination of oxygen in different science and technological fields and the main techniques existing for making such a determination are shown. Secondly, more detailed information on the determination of oxygen through the phenomenon of luminescence quenching is provided. For this, both the basics of the phenomenon of molecular luminescence as well as the different methods for their detection are described, with particular emphasis on the description of the two dominant luminescent methods: the methods based on the measurement of luminescence intensity and those based on the measurement of luminescence lifetime. The latter includes two principal measurement methods: those based on time domain (pulsed light methods) and those based on frequency domain (phase modulation methods). In the fourth and final section of the introduction there is an overview of the instrumentation used in analytical chemistry to carry out fluorescence and phosphorescence measurements. Additionally, there are three appendices which supplement the information and address some aspects related to flow injection systems (**Appendix 1**), optical fibre sensors (optodes) (**Appendix 2**) and elements that comprise a luminescent optical sensor for the determination of oxygen (**Appendix 3**).

The second section of the report, entitled the experimental section, shows the results obtained during the performance of this Doctoral Thesis and the discussion thereof. This

section is divided into seven chapters, the contents of which are listed below.

Chapter 1 provides an overview of the laboratory test bench developed. Firstly, their salient features are described, analysing their main components and their various instrumental configurations, either to acquire luminescence lifetime or intensity measurements in the frequency domain. Also, an overview of the different stages of the system's development process is also shown, from its early versions to the final version, mentioning the main difficulties encountered and the solutions selected. Part of the knowledge necessary to carry out the final development of the proposed measurement system was acquired from the *Institute of Robotics and Intelligent Systems* (IRIS) of the *Swiss Federal Institute of Technology Zurich* (ETH Zurich, Switzerland).

Chapter 2 focuses on the development and characterisation of an optical sensing phase for determining carbon dioxide (CO_2) in both aqueous and gaseous media. The sensing phase is based on a functionalised linear co-polymer with a pH luminescence indicator and a phase transfer agent (tetraoctyl ammonium hydroxide (TONOH)). In this work we optimised both the composition of the sensing phase and the measurement conditions using a commercial spectrofluorometer. We also determined their chemical properties, showing high sensitivity and selectivity in both aqueous and gaseous media. Finally, to demonstrate the versatility of the proposed sensing phase, a fibre optical sensor was developed based on intensity measurements, obtaining a reasonable linear dynamic range and a good detection limit.

Chapter 3 deals with the use of phase shift measurements to develop optical sensors capable of detecting very low concentrations of oxygen. This work was developed in collaboration with the *School of Chemistry* at the University of Birmingham (Edgbaston, England). A total of four phases consisting of four sensing phases using organometallic compounds (one platinum (PtTFPP) and three iridium (N969, N1008 and EB146)) immobilised on an aluminium oxide hydroxide nanostructured support (AP200/19) were characterised. To perform characterisation of the sensing phases their spectroscopic properties (excitation and emission spectra), response times (t_{95}) and calibration curves for various concentration ranges of oxygen (0-1% O_2 and 0-10% O_2) were determined. The measurements were taken using a commercial lock-in amplifier instrument (LIA). The sensing phases showed excellent sensitivity at low and ultra-low oxygen concentrations (0-10% O_2 and 0-1% O_2 respectively), the sensitivity obtained for the PtTFPP-AP200/19 membrane being particularly significant. This sensing phase proved to be 62 times more sensitive than when the compound is placed in a conventional polystyrene membrane, and about 8 times more sensitive than when deposited on silica particles. In addition, photostability studies were also conducted, showing that the phase shift measurements are significantly more resistant to the photodegradation of the sensing phases than measurements based on intensity (modulation factor). Finally, it was also shown that the membranes were not affected by humidity, and presented complete reversibility and long-term stability (over 12 months).

In **Chapter 4** a simple and versatile optosensor was developed for oxygen determination based on a multi-frequency phase modulation method (called the I/Q multi-frequency method). This method allows for calculation of the phase shift introduced by the sensing phase (which varies with the concentration of O_2) at various modulation frequencies, using a single measurement for this (a multi-frequency signal consisting of a linear combination of multiple sinusoidal functions of different frequency). The method proposed is based on the

principles of quadrature detection and can be fully implemented in a digital signal processor (DSP). Thus, in this chapter, the theoretical aspects of the I/Q method as well as the technical details of the measurement system are discussed. The response of the measurement system was evaluated through characterisation and evaluation of an optical oxygen-sensitive sensing phase (PtTFPP immobilized into an oxygen-permeable polymer membrane). Additionally, these results were successfully compared with those obtained using a reference measurement system based on a commercial lock-in amplifier (LIA), and using the same sensing phase in all cases. The proposed system obtained an accuracy of below 0.2 kPa in determination of the partial pressure of oxygen in the concentration range of 0-20 kPa.

In **Chapter 5** the response of the I/Q method is evaluated (as described in Chapter 4) for different noise conditions. For this purpose, a series of experimental tests were performed using fixed-frequency analog sinusoidal signals, 1 second in length, known random phases between 0 and -180° and different levels of Additive White Gaussian Noise (AWGN) (SNRs interval between -18 and 36 dB). These analog signals were generated on a computer digitally (using Matlab) and then converted to the analog domain using a D/A converter from a data acquisition card. Phase shift measurements obtained with the I/Q method using these signals were compared with those obtained by a reference measurement equipment (a commercial LIA) give very similar results in both cases. Additionally, the response of the I/Q method was also tested in an actual measurement system to demonstrate applicability. For this, the oxygen measuring system described in Chapter 4 was used and the I/Q method evaluated under different lighting conditions. This was achieved by varying the amplitude of the excitation signal between 22 and 1000 mV, so that emission signals with different optical intensities were obtained (lower amplitude values of the excitation signal resulted in less intense emission signals, that is, with lower SNR). Again, these results were compared with those obtained using a conventional measurement system based on a commercial LIA, yielding similar results. These results demonstrate the robustness of the I/Q method against noise and its computational efficiency, confirming that quadrature detection is an ideal technique for accurate determination of the phase of a sinusoidal signal in the presence of high noise levels (very low SNR levels).

In **Chapter 6** a new method for multi-frequency phase modulation luminescence spectroscopy is described. The proposed method uses a rectangular excitation signal with a short duty cycle to: (1) improve the analytical sensitivity in the determination of the concentration, and (2) to obtain more complete information on the luminescent system analysed. The method is based on a simple algorithm which combines multi-frequency information provided by the different harmonics of the rectangular signal, and which can be easily implemented in existing photoluminescence instruments simply by changing the waveform of the signal used to modulate the source of excitation light (a rectangular short cycle signal rather than a sinusoidal signal), and implementing (in software) the appropriate digital signal processing algorithm after the transducer. These claims have been proven using an oxygen optode using a well-known sensing phase (a porphyrin of Pt(II) immobilised in polystyrene). The experimental results demonstrate that the proposed method reduces the root mean square error (RMSE) in the analytical determination of oxygen (from 0.1035 to 0.0053 kPa to 0.5 kPa O_2 and from 1.1087 to 0.1209 kPa to 20 kPa O_2) when it is compared with a conventional phase-modulation method based on a sinusoidally modulated excitation source (under equal luminous power conditions). This work was carried out in collaboration with the Department

of Electrical and Electronic Engineering at the Public University of Navarra.

Finally, **Chapter 7** proposes a new calibration model for photoluminescent optical sensors and compares it to the classical models proposed in the literature (Stern-Volmer, Lehrer and Demas models). This new model can be considered as a variant of the Stern-Volmer model and provides a good compromise between the number of parameters and accuracy of the adjustment, in comparison with other classic models of similar complexity (i.e., with the same number of parameters). In addition, this chapter also demonstrates the importance of the optimisation criterion used for model calibration. To do this, the results for 25 real experiments were obtained, with 7 optical oxygen-sensitive sensing phases (PtTFPP-PS, N969-AP200/19, EB146-AP200/19, PtTFPP-AP200/19, N1008-AP200/19, EB146-PS0X, N1008-PS0X), 3 different analytical signals (intensity of luminescence, lifetime determined from the phase shift and lifetime given from the modulation factor) and 3 different measuring instruments (a luminescence spectrometer, a Lock-in Amplifier (LIA) and a measurement system based on the I/Q method (described in Chapters 4, 5 and 6)). This chapter also covers all the details necessary for the implementation of the different calibration procedures, as well as the source code (compatible with Matlab and Octave) to perform calibration for each model and criterion.

Contenido

Introducción	1
0.1 Sensores químicos: concepto y generalidades	1
0.1.1 Definición y componentes de un sensor químico	2
0.1.2 Clasificación de los sensores químicos	4
0.1.3 Importancia y actualidad de los sensores químicos	7
0.2 Sensores químicos de naturaleza óptica	10
0.2.1 Generalidades de los sensores ópticos	10
0.2.2 Parámetros descriptivos de los sensores ópticos	10
0.2.3 Clasificación de los sensores ópticos	13
0.2.4 Fases sensoras y mecanismos de reconocimiento óptico	16
0.3 Sensores ópticos luminiscentes para el control de oxígeno	18
0.3.1 La importancia del oxígeno	18
0.3.1.1 El oxígeno en el metabolismo celular	19
0.3.1.2 El oxígeno en el sector médico y clínico: hipoxia e hiperoxia en los tejidos	19
0.3.1.3 El oxígeno en el sector alimentario	20
0.3.1.4 El papel del oxígeno en aplicaciones industriales y tecnológicas	21
0.3.1.5 El oxígeno disuelto y el ambiente	22
0.3.1.6 El oxígeno en botánica	22
0.3.2 Métodos generales de determinación de oxígeno	23

0.3.2.1	Análisis gravimétrico	23
0.3.2.2	Detección manométrica	23
0.3.2.3	Cromatografía de gases	23
0.3.2.4	Valoración Química (Método de Winkler)	24
0.3.2.5	Métodos electroquímicos (Electrodo de Clark)	24
0.3.2.6	Resonancia paramagnética electrónica (EPR)	27
0.3.2.7	Métodos ópticos	27
0.3.3	Determinación de oxígeno por atenuación de la luminiscencia	28
0.3.3.1	El fenómeno luminiscente	28
0.3.3.2	Atenuación de la luminiscencia por el oxígeno molecular	31
0.3.3.3	Medidas de intensidad de la luminiscencia	38
0.3.3.4	Medidas de tiempo de vida de la luminiscencia	41
0.4	Instrumentación empleada en sensores ópticos	50
0.4.1	Fuentes de excitación	51
0.4.1.1	Lámparas convencionales	51
0.4.1.2	Lámparas pulsantes	51
0.4.1.3	Diodos fotoemisivos (LEDs)	52
0.4.1.4	Láseres	56
0.4.2	Selectores de longitud de onda	58
0.4.2.1	Filtros ópticos	58
0.4.2.2	Monocromadores	60
0.4.3	Fibras ópticas	62
0.4.3.1	Análisis de la propagación en fibras ópticas mediante óptica geométrica	63
0.4.3.2	Fibras ópticas en fosforescencia	67
0.4.4	Detectores y sistemas detectores	68
0.4.4.1	Fototubos y tubos fotomultiplicadores	68
0.4.4.2	Contador de fotones	69
0.4.4.3	Detectores multicanal	71

0.4.5	Instrumentación comercial	72
	Referencias	77
1	Arquitectura del banco de pruebas de laboratorio	115
1.1	Motivación para el desarrollo del banco de pruebas	115
1.2	Arquitectura del banco de pruebas de laboratorio	117
1.3	Antecedentes del banco de pruebas propuesto	128
2	A new highly sensitive and versatile optical sensing film for controlling CO₂ in gaseous and aqueous media	135
2.1	Introduction	137
2.2	Experimental details	138
2.2.1	Chemical reagents and materials	138
2.2.2	Preparation and characterization of sensing films	139
2.2.3	Measurement setup	139
2.3	Results and discussion	140
2.3.1	Optical properties of CO ₂ -sensing films	140
2.3.2	Optimization of the composition of the sensing film	142
2.3.3	Analytical performances	143
2.3.4	Reliability and response time	144
2.3.5	Effect of flow rate and interference study	146
2.3.6	Photo and thermostability study	146
2.3.7	Implementation in an optical fiber sensor	147
2.4	Conclusions	149
	References	149
	ESI	152
3	High performance optical sensing nanocomposites for low and ultra-low oxygen concentrations using phase-shift measurements	159
3.1	Introduction	161
3.2	Experimental details	163

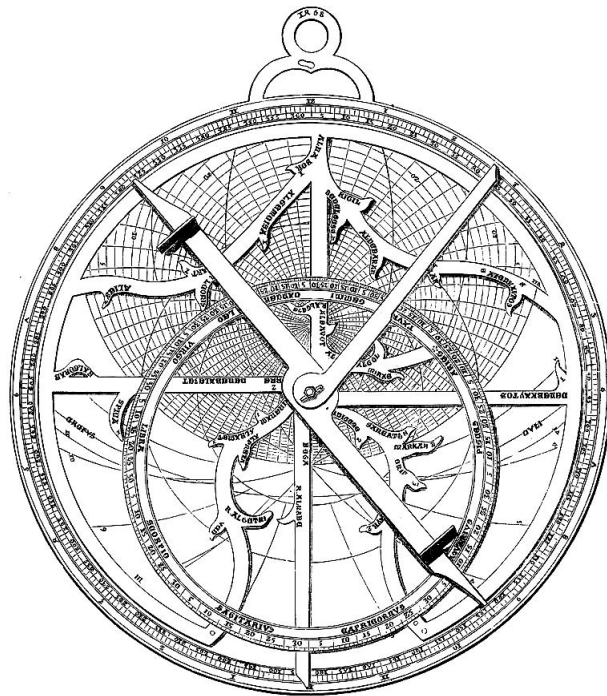
3.2.1	Materials and chemicals	163
3.2.2	Preparation of the oxygen-sensing films	164
3.2.3	Instruments and methods	164
3.3	Results and discussion	164
3.3.1	Photophysical properties of the nanocomposites	164
3.3.2	Selection of the modulation frequency	165
3.3.3	Oxygen-sensitive properties	167
3.3.4	Reversibility, response times, stability and the effect of humidity . . .	172
3.4	Conclusions	177
	References	178
	ESI	182
4	An open and low-cost optical-fiber measurement system for the optical detection of oxygen using a multifrequency phase-resolved method	223
4.1	Introduction	225
4.2	Measurement method theory	227
4.2.1	In-phase and quadrature sinusoidal components	227
4.2.2	Signal processing in the measurement system	228
4.2.3	Multifrequency phase estimation	229
4.3	Experimental	230
4.3.1	Materials used for the synthesis of the oxygen sensing film	230
4.3.2	Measurement system (experimental setup)	230
4.3.3	Preparation of the sensing film	233
4.3.4	Characterization of the sensing film	233
4.4	Results and discussion	233
4.4.1	Spectroscopic behavior of the sensing film	234
4.4.2	Performance of the proposed measurement method	234
4.4.3	Analytical characterization of the sensing film	234
4.4.4	Evaluation of the system response for oxygen sensing	239
4.5	Conclusions	241

References	243
ESI	247
5 Evaluation of a simple PC-based quadrature detection method at very low SNR for luminescence spectroscopy	261
5.1 Introduction	263
5.2 Theory	264
5.2.1 Standard digital lock-in detection (LIA)	264
5.2.2 Proposed phase measuring technique (I/Q method)	265
5.3 Experimental	267
5.3.1 Materials and chemicals	267
5.3.2 Preparation of the oxygen-sensitive film	267
5.3.3 Evaluation of the I/Q method using numerically generated signals	267
5.3.4 Measurement system	268
5.3.5 Characterization and test of the oxygen-sensitive film	270
5.4 Results and discussion	270
5.4.1 Validation of the I/Q method using analog signals	270
5.4.2 Response of the phase measuring system during a real-world application (oxygen sensor)	271
5.5 Conclusions	274
References	275
ESI	278
6 A novel multifrequency phase-modulation method using rectangular-wave signals for improving the analytical sensitivity in luminescence spectroscopy	289
6.1 Introduction	291
6.2 Theory: Multifrequency luminescence response using rectangular-wave signals	293
6.3 Experimental	295
6.3.1 Chemicals and reagents	295
6.3.2 Preparation of the sensing fibre	296

6.3.3	Measurement system	296
6.3.4	Implementation of rectangular-wave modulated excitation in phase-modulation methods	297
6.4	Results and discussion	299
6.4.1	Estimation of the apparent lifetimes and calibration	299
6.4.2	Evaluation of the accuracy of the proposed method	301
6.5	Conclusions	304
	References	304
	ESI	307
7	On the calibration of chemical sensors based on photoluminescence: Selecting the appropriate model and criterion	331
7.1	Introduction	333
7.2	Theory	335
7.2.1	Reference models included in the study	335
7.2.2	Proposed polynomial-exponent (PE) model	335
7.2.3	Sensitivity and response at null concentration	336
7.2.4	Optimization criteria for model calibration	336
7.2.5	Calibration formulas for different models and criteria	338
7.2.5.1	Generic calibration procedure	338
7.2.5.2	Stern-Volmer model using criterion (a)	338
7.2.5.3	Stern-Volmer model using criteria (b) and (c)	339
7.2.5.4	Lehrer model using criterion (a)	339
7.2.5.5	Lehrer model using criteria (b) and (c)	339
7.2.5.6	Demas model using criterion (a)	340
7.2.5.7	Demas model using criteria (b) and (c)	340
7.2.5.8	Polynomial-exponent model using criteria (b) and (c)	341
7.2.5.9	Polynomial-exponent model using criterion (a)	341
7.3	Experimental	342
7.4	Results and discussion	343

7.4.1	Calibration results	343
7.4.2	Evaluation of models	345
7.4.3	Complexity of the model and over-fitting	346
7.4.4	Comparison of different calibration criteria	347
7.5	Conclusions	348
	References	349
	ESI	351
	Conclusiones	445
	Conclusions	449
	Apéndice I: Sensores ópticos en sistemas de análisis en flujo	455
	Apéndice II: Sensores ópticos tipo sonda (Optodos)	459
	Apéndice III: Sensores ópticos luminiscentes para el control de oxígeno	469
	Apéndice IV: Lista de publicaciones y contribuciones a congresos	485

PARTE I:
INTRODUCCIÓN



Introducción

EN las dos últimas décadas se han producido importantes avances en el ámbito de las tecnologías dedicadas al desarrollo de nuevos procedimientos de análisis en el área de la Química Analítica. En este sentido, el acoplamiento de sistemas (bio)químicos a transductores de tipo electroquímico u óptico ha dado lugar al desarrollo y consolidación de una nueva rama de la Química Analítica: los “*sensores químicos*”. Esta nueva rama de la Química Analítica atraviesa las fronteras de las disciplinas tradicionales, ejerciendo hoy día una profunda influencia sobre los procedimientos analíticos actuales. En la actualidad, el ámbito de la investigación y desarrollo de los sensores químicos se extiende más allá de los dominios de la Química, llegando a ser una vasta rama multidisciplinar capaz de aunar áreas de conocimiento tan diversas como la Electrónica, la Nanotecnología o la Teoría de la Señal.

0.1 Sensores químicos: concepto y generalidades

La elección de la técnica de medida a emplear en cada problema analítico depende en gran medida del analito y de la matriz en que se encuentre. Las técnicas analíticas tradicionales empleadas hasta la fecha implican, en la mayoría de los casos, la necesidad de recoger la muestra y analizarla en el laboratorio, lo cual supone una complicación añadida, ya que deben de seguirse unos estrictos protocolos de toma de muestra y almacenamiento (con el consiguiente riesgo de contaminación que ello conlleva). Por otro lado, al tener que analizar las muestras en el laboratorio se estaría alterando el entorno natural de la muestra, lo cual puede conducir a alteraciones del propio analito. Todo ello justifica la necesidad actual de buscar nuevas tecnologías analíticas capaces de desarrollar métodos de análisis económicos, con instrumentación sencilla (preferiblemente portátil), y que permitan dar solución a los problemas ya mencionados, es decir, el análisis *‘in situ’* y, a ser posible, en tiempo real [1].

Dentro de esta línea, la tecnología de los sensores químicos ofrece un potencial analítico elevado [2]. No obstante, cabe señalar que el desarrollo de sensores químicos no es un fenómeno reciente; así, baste recordar que desde hace ya algunos años se vienen empleando sistemas sensores como el electrodo de *Clark* o el de pH en medidas de rutina para el control de determinadas especies (concentración de oxígeno y de protones, respectivamente). Sin

embargo, es cierto que en los últimos años se ha producido un crecimiento exponencial de la investigación en el campo de los sensores químicos, debido tanto a la mejora de la tecnología de los materiales empleados en su desarrollo, como a la demanda de métodos analíticos capaces de hacer determinaciones rápidas, *'in situ'* y con un coste operativo muy reducido [1].

0.1.1 Definición y componentes de un sensor químico

La aportación de una definición exacta y universal de *sensor químico* resulta complicada, debido a la gran diversidad de sistemas que se consideran hoy día como “*sensores*”. Una de las definiciones más aceptadas parece ser la propuesta por Janata y Bezegh [3], que definen un “*sensor químico*” como “*un dispositivo capaz de transformar (transducir) la magnitud de un fenómeno cuya cuantificación resulta de interés, y que generalmente es el objeto de la medida (p. ej., la concentración de una especie química), en una señal física medible, proporcionando información química de su entorno*”.

También es posible encontrar en la literatura definiciones más concretas de sensor químico. Así, Roe *et al.* [4] lo definen como “*un dispositivo capaz de detectar y/o cuantificar en tiempo real una especie química en un medio complejo (muestra de interés) a través de una interacción química selectiva*”. Por otro lado, la IUPAC (International Union of Pure and Applied Chemistry) propone una definición según la cual, “*un sensor químico es un dispositivo que transforma la información química, variando desde la concentración de un componente específico de la muestra hasta el análisis total de su composición, en una señal analítica útil*” [5]. La información química puede ser originada a través de una reacción química del analito o de una propiedad física del sistema investigado. Además, el sensor puede incluir elementos que posean las siguientes funciones: toma de muestra, transporte de muestra y procesamiento de la señal y/o datos [5].

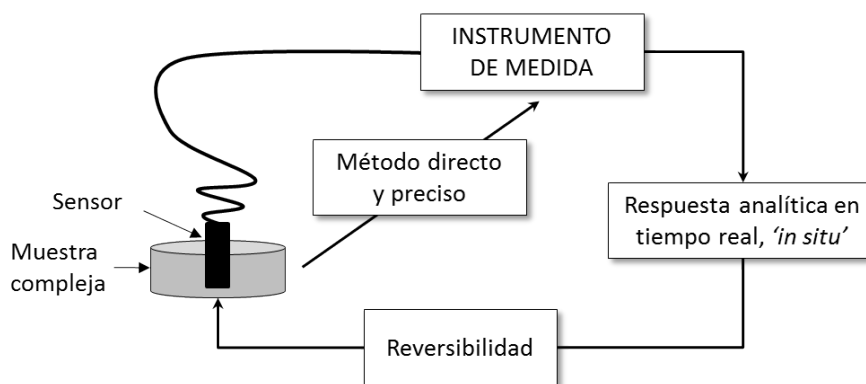


Figura 1: Características analíticas básicas de un sensor químico [6].

Idealmente, un sensor químico debe operar de manera continua y reversible directamente en la matriz de la muestra, y tener la capacidad de proporcionar información sobre la distribución espacial y temporal de una especie molecular o iónica en tiempo real [1, 7–9] (Figura 1). Otras características importantes que debería tener un sensor ideal son las de ser portátil, barato, fácil de usar y requerir un mantenimiento mínimo [7]. El ejemplo más

típico de un sensor químico es el electrodo de pH, el cual cumple con todos los requisitos necesarios para ser considerado un sensor ideal, ya que ofrece medidas rápidas, reversibles y no destructivas de la actividad del ion hidrógeno (sin ser afectado en la mayoría de los casos por la matriz de la muestra); se trata del sensor más ampliamente utilizado no solo en Química Analítica sino también en otras muchas áreas de la ciencia y la tecnología [1, 9]. Sin embargo, en la práctica, son muy pocos los sensores que cumplen estrictamente con todas las especificaciones anteriores, por lo que es frecuente que muchos autores consideren también como sensores algunos diseños que no son capaces de medir de forma continua la concentración de ciertas especies o que solo permiten una determinación [10, 11]. En otras ocasiones también puede ocurrir que el sensor no sea lo suficientemente selectivo; en cuyo caso suele resultar conveniente la incorporación de alguna técnica simple de pretratamiento de muestra en línea con la detección para separar el analito de interés de las especies interferentes presentes en la muestra. Así pues, en línea con lo que acabamos de mencionar, cabe señalar que muchos de los sensores descritos en la literatura carecen de la sensibilidad, la selectividad y la precisión necesarias para garantizar una buena respuesta analítica, por lo que en este caso la operación en tiempo real y/o *in situ* carece de valor. Por todo ello, las definiciones de sensor dadas anteriormente han de ser consideradas exclusivamente en términos ideales. Así pues, en sentido amplio, podemos acabar definiendo un sensor como cualquier dispositivo de uso sencillo que sea para los instrumentos de medida lo que los sentidos son para los seres vivos [1], es decir, un sistema que proporciona una determinada respuesta a un estímulo exterior; respuesta que posteriormente es analizada y procesada por el resto de elementos del sensor.

En general, un sensor químico sensible a una especie química concreta consta básicamente de tres partes [5, 12, 13] (véase la Figura 2):

- En primer lugar podemos diferenciar la *fase sensora* o *zona de reconocimiento* del sensor, que es donde se produce la interacción selectiva con el analito de interés. Esta interacción produce un cambio en alguna propiedad física o química del sistema (transferencia de electrones, vibración, absorbancia, luminiscencia, índice de refracción, conductividad, cambio de masa, etc.) cuya magnitud estará relacionada con la concentración de la especie a determinar. Así pues, esta interacción entre el analito de interés y la fase sensora constituye la primera etapa del proceso de transducción del sensor.
- A continuación podemos encontrar un elemento *transductor*, que es el encargado de transformar las propiedades fisicoquímicas de la fase sensora en una señal analítica medible (generalmente una señal de naturaleza eléctrica). El transductor por sí mismo no muestra selectividad al analito de interés.
- Por último, la señal eléctrica generada por el transductor llega a un *sistema electrónico*, donde tiene lugar el acondicionamiento de la señal y el posterior procesamiento de los datos. Dicho sistema electrónico suele estar integrado dentro del sensor en dispositivos comerciales, de modo que la magnitud de la señal analítica obtenida tras el procesamiento puede ser relacionada con la concentración de analito a través de una curva de calibrado realizada previamente.

Así pues, en resumen, en la zona de reconocimiento (o fase sensora) la información química relativa al analito se transforma en una información física, información que es recogida por

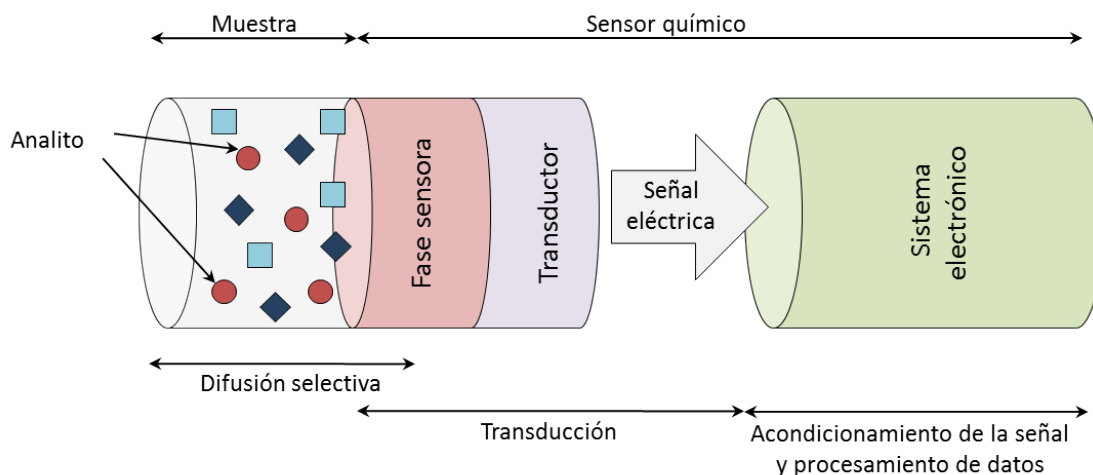


Figura 2: Componentes básicos de un sensor químico [14].

un transductor apropiado que la transforma en una señal analítica medible. Esta señal es procesada adecuadamente y transformada en la información deseada.

0.1.2 Clasificación de los sensores químicos

La gran variedad de sensores (bio)químicos desarrollados hasta la fecha ha hecho necesario llevar a cabo una sistematización de los mismos. Dicha clasificación puede hacerse atendiendo a diferentes criterios, tales como el tipo de transductor, la naturaleza de las muestras a analizar, la reversibilidad de la fase sensora, etc., dando lugar a una amplia variedad de clasificaciones [2, 5, 6, 8, 9, 15]. Una de estas clasificaciones es recogida en el trabajo de Varcárcel y Luque [8] (véase la Figura 3).

A continuación pasaremos a describir brevemente algunos de los criterios más utilizados en la clasificación de los sensores (bio)químicos:

- Atendiendo al tipo de reconocimiento, los sensores pueden clasificarse en sensores *químicos* o *bioquímicos*. Cuando la etapa de reconocimiento se produce mediante un elemento sensible biológico (por ejemplo un anticuerpo, una célula, una enzima, etc.), el dispositivo resultante se conoce como *biosensor*. Así pues, la diferencia entre un *sensor químico* y un *biosensor* reside básicamente en la distinta naturaleza de la reacción (química o biológica) empleada para llevar a cabo el reconocimiento del analito.
- Los (bio)sensores químicos también pueden ser clasificados como *activos* o *pasivos* dependiendo de si se produce o no una reacción (bio)química en la zona de reconocimiento. Los sensores pasivos se basan simplemente en la medida directa de una propiedad fisicoquímica del analito (sin que tenga lugar una reacción química entre el analito y la fase sensora), por lo que suelen ser los más fáciles de realizar, operan de forma similar a los sensores activos y además tienen la ventaja añadida de poseer una completa reversibilidad; es por ello que suelen ser los más utilizados en la mayoría de las aplicaciones industriales [8, 15].

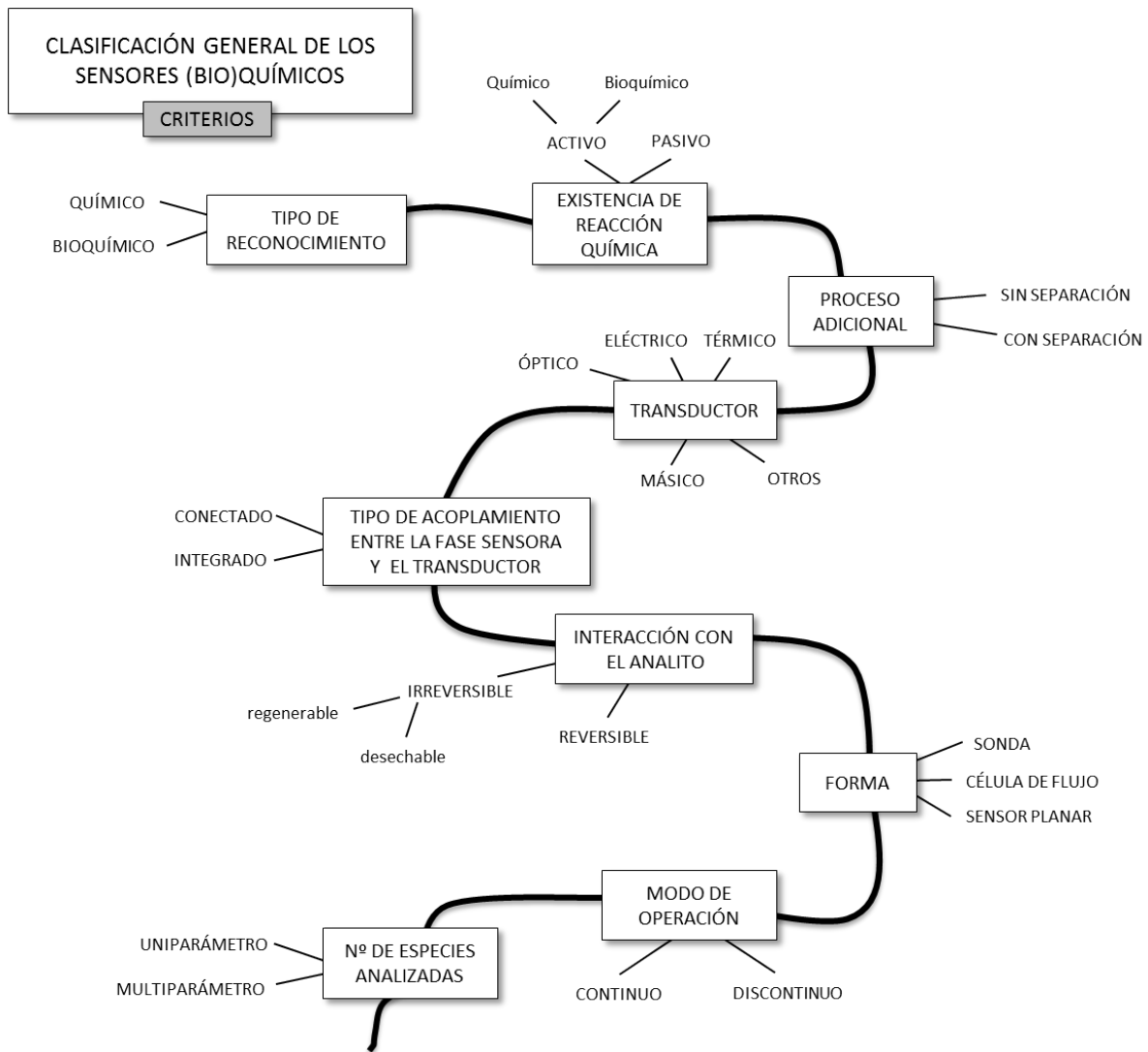


Figura 3: Clasificación general de los sensores (bio)químicos atendiendo a diferentes criterios [8].

- Algunos (bio)sensores requieren de un *proceso de separación* previo a la reacción (bio)química y a la detección. Habitualmente se trata de un proceso de adsorción y detección simultánea o, alternativamente, procesos de difusión de gases, diálisis o extracción líquido-líquido en presencia o ausencia de una reacción (bio)química [15].
- Otra clasificación de los (bio)sensores establece tres categorías en función del tipo de acoplamiento entre el elemento de reconocimiento y el transductor. Estos dos elementos esenciales pueden estar *conectados* (p. ej., mediante un cable o una fibra óptica), *no conectados* (cuando se hallan separados una cierta distancia) o bien estar *integrados* en un único elemento.
- En función de la naturaleza de la interacción medible (interacción con el analito), los (bio)sensores pueden clasificarse en *reversibles* o *irreversibles*. Se denominan *reversibles* aquellos sensores en los que no se produce un consumo de la fase sensora durante su interacción con el analito. Este tipo de (bio)sensores responden tanto a altas como a

bajas concentraciones de analito y proporcionan una respuesta nula en ausencia del mismo. Por su parte, se consideran como *irreversibles* aquellos sensores en los que sí existe un consumo de la fase sensora. A su vez, estos últimos pueden ser clasificados como *regenerables* y *desechables*. Los primeros son aquellos que presentan una respuesta similar a la de un sensor *reversible*, pero con la diferencia de que no operan de forma continua, ya que requieren de una etapa de regeneración de la fase sensora para poder ser utilizados de nuevo. Por su parte, los (bio)sensores *desechables* únicamente responden a incrementos de la concentración del analito, saturándose con facilidad, por lo que su uso suele quedar limitado a una única medida.

- Según la forma externa o configuración del (bio)sensor, podemos distinguir entre: (bio)sensores *tipo sonda*, *tipo microchip* y *tipo célula de flujo*. En el primer caso (sensores *tipo sonda*), la fase sensora está localizada en el extremo del terminal sensible (*p. ej.*, un electrodo o una fibra óptica), que a su vez se encuentra en contacto directo con la muestra. En el caso de los (bio)sensores de *tipo microchip*, el elemento sensor se halla sobre una superficie plana, superficie sobre la que se depositan unas gotas de la muestra. Finalmente, en los (bio)sensores *tipo célula de flujo*, la muestra es aspirada (o inyectada) y transferida a una célula de flujo donde se sitúa la fase sensora. Su principal característica reside en que la fase sensora se encuentra ubicada en el sistema de detección y, por lo tanto, los procesos de reacción y detección son simultáneos.
- Por otro lado, atendiendo al modo de operación, los (bio)sensores químicos pueden trabajar en modo *discontinuo* (o *discreto*) o en modo *continuo* (medidas de flujo).
- Los (bio)sensores químicos también pueden ser clasificados en función del número de analitos que son capaces de determinar en una misma muestra. Así, la mayoría de los (bio)sensores químicos responden a la concentración de una única especie (*uniparamétricos*), pero también existen otros capaces de determinar simultáneamente la presencia de varios analitos (*multiparamétricos*). Entre estos últimos podemos distinguir dos tipos: aquellos que incorporan un elemento de reconocimiento específico para cada analito; y aquellos que hacen uso de un único elemento de reconocimiento (conectado o integrado a un transductor capaz de realizar el análisis multianalítico) [15].
- Finalmente, una clasificación general, aunque muy práctica, consiste en considerar la naturaleza de la señal física que se genera y mide, es decir, atendiendo al tipo de transductor empleado para detectar los cambios fisicoquímicos que tienen lugar en el sistema sensor en presencia del analito de interés [8, 15]. La Figura 4 muestra algunos de los principales tipos de sistemas de transducción empleados en la fabricación de (bio)sensores químicos.
 - *Electroquímicos*: miden cambios en alguna propiedad eléctrica del sistema (potencial, intensidad de corriente, conductividad, etc.), la cual es función de la concentración del analito. Así pues, existen sensores electroquímicos de tipo amperométrico, conductimétrico, impedimétrico, potenciométrico, ISFET (transistor de efecto campo sensible a iones), etc.
 - *Ópticos*: responden a cambios en alguna propiedad óptica del sistema (absorbancia, reflectancia (UV, NIR, IR), transmitancia, luminiscencia, etc.) relacionada con la concentración de la especie a determinar.

- *Térmicos*: cuantifican calores de reacción o cambios en la temperatura del sistema originados durante la reacción de reconocimiento.
- *Piezoeléctricos*: miden cambios de masa, viscosidad, etc.
- También se han desarrollado, aunque en menor medida, algunos sensores que utilizan otros tipos de detección menos comunes, tales como los sensores de ondas acústicas de superficie y los magnéticos (estos últimos basados en medidas de paramagnetismo).

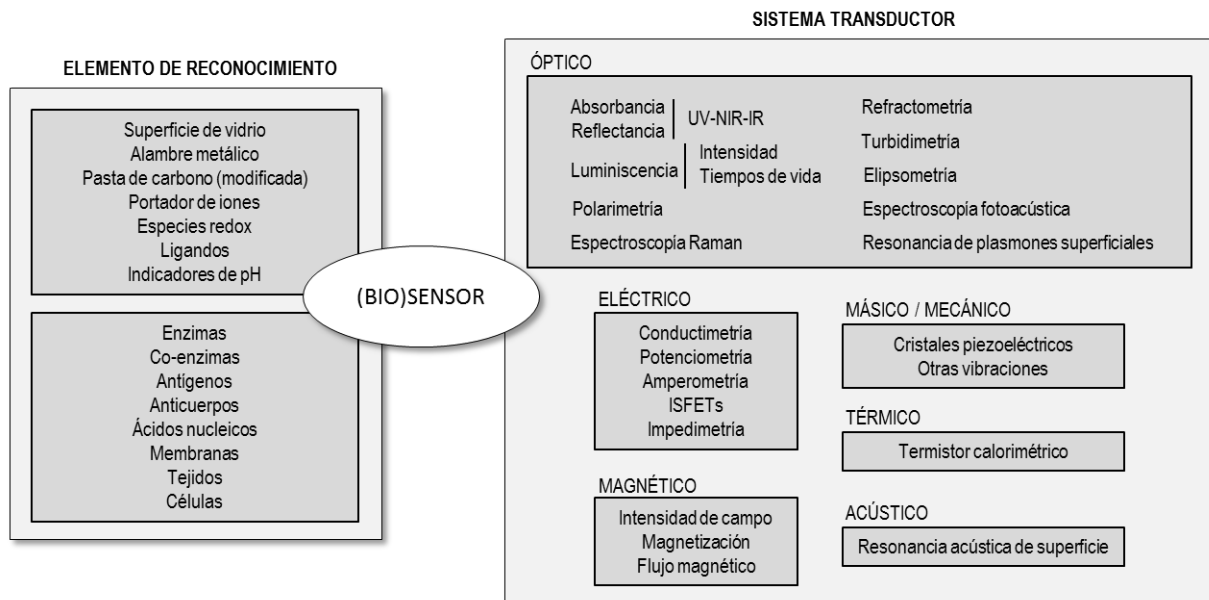


Figura 4: Principales tipos de sistemas de transducción empleados en la fabricación de (bio)sensores químicos [8, 15].

0.1.3 Importancia y actualidad de los sensores químicos

En las dos últimas décadas, el desarrollo de sensores químicos ha experimentado un creciente interés en campos tan diversos como el de las ciencias de la salud, el ambiental, el industrial, el biotecnológico, la domótica, etc.

En el campo de la Química Analítica Clínica [16–21], la posibilidad de miniaturización de los sensores ha proporcionado resultados muy satisfactorios, llegando a desarrollarse dispositivos muy económicos (desechables o reutilizables) que pueden ser separados del módulo principal. Asimismo, debido a su carácter miniaturizable y a su capacidad de medida continua e *‘in situ’*, cada vez son más las investigaciones orientadas al desarrollo de sensores ópticos con aplicaciones médicas [22, 23].

En el campo del control ambiental [24–28], el empleo de sensores químicos constituye una herramienta muy útil en la identificación y cuantificación de contaminantes de forma remota y continua, proporcionando información muy valiosa a la hora de llevar a cabo una estrategia

adecuada para remediar los efectos de la contaminación en áreas contaminadas o en zonas con desechos peligrosos para la vida.

También, la demanda de la automatización de los procesos industriales [29–32] ha experimentado un importante crecimiento en los últimos años, ya que la medida de determinados parámetros químicos es esencial para el seguimiento y control de muchos procesos (bio)químicos. Además, la disponibilidad de sensores químicos en los procesos industriales ha permitido el empleo de métodos de análisis *on line*.

Los llamados “paquetes inteligentes” (*Smart Packaging*) [33, 34] surgen como respuesta a la creciente demanda de calidad en productos alimentarios, cada vez con menos conservantes, con requerimientos legales más estrictos, y todo ello en un mercado más globalizado y preocupado por la seguridad alimentaria [35, 36]. Los paquetes inteligentes se definen como sistemas que controlan las condiciones de los alimentos empaquetados, proporcionando información sobre la calidad de estos alimentos durante su periodo de transporte y/o almacenaje [37]. En este sentido, el desarrollo de sistemas sensores que determinen la calidad de los alimentos en términos de frescura, oxidación o deterioro microbiano, se ha convertido en un objetivo prioritario en la industria alimentaria [38, 39], teniendo especial aplicación en sistemas de trazabilidad y Análisis de Peligros y Puntos Críticos de Control (APPCC) [34].

Las características de los sensores químicos más demandadas por la industria son el precio, la robustez, la estabilidad con el tiempo y/o con la temperatura, y la biocompatibilidad en procesos biotecnológicos. En el campo biotecnológico, por ejemplo, los sensores ópticos [22, 40, 41] han despertado un gran interés en los últimos años, debido a que se trata de dispositivos no invasivos (o mínimamente invasivos), que no destruyen la muestra, y que, por consiguiente, podrían mejorar notablemente la respuesta de los dispositivos actuales. Fundamentalmente, puede decirse que la aplicación estrella de los sensores ópticos en procesos biotecnológicos es el control de oxígeno en cultivos celulares [42], así como directamente en el interior de las células [43], habiendo ya algunos prototipos para el uso de estos sensores en el tratamiento temprano contra el cáncer [44] o en la detección precoz de enfermedades oculares relacionadas con la hipoxia retiniana [22].

Finalmente, otro campo donde los sensores químicos presentan una gran aplicabilidad es el de la domótica. Cada vez más, la sociedad demanda un mayor número de sistemas inteligentes (o domóticos) en los hogares y en los recintos públicos, así como el disponer de dispositivos pequeños y automáticos que mejoren, sin un gran coste adicional, su calidad de vida. En este sentido, los sensores ópticos tienen mucho que decir, ya que son fácilmente miniaturizables y tremendamente versátiles para una gran cantidad de aplicaciones (*p. ej.*, control de la calidad del aire, sensores tipo alarma para detectar posibles contaminantes y/o fugas de gases nocivos para la salud [45], etc.).

La utilización de sensores químicos en todos estos campos de aplicación puede proporcionar resultados cuantitativos o semicuantitativos rápidos en la propia matriz de la muestra, es decir, *in situ*, reduciéndose así los costes de transporte y de material de laboratorio, ya que se minimiza considerablemente el número de muestras requeridas en comparación con las que serían necesarias para su análisis en el laboratorio (empleando métodos analíticos clásicos para su determinación). Además, la posibilidad de obtener medidas en tiempo real, hace que estos dispositivos sean especialmente adecuados para aquellas situaciones en las que la mues-

tra no se pueda llevar fácilmente al laboratorio (por motivos de peligrosidad, degradación, etc.), o bien para el análisis de rutina. Los sensores químicos permiten realizar tres tipos de análisis aplicables al control analítico, los cuales, en función de las necesidades, se clasifican en: control continuo en línea en tiempo real (monitorización), control de alarma regular y control ocasional discreto o al azar [25].

Se puede considerar que el objetivo final de un sensor químico es su comercialización y venta, y para ello, sus características analíticas de robustez, selectividad, sensibilidad, linealidad, ausencia de efectos de matriz, etc., deben ser lo suficientemente elevadas para poder competir con los métodos analíticos tradicionales empleados en los laboratorios. Simultáneamente, sus características de portabilidad, miniaturización y facilidad de uso son también muy importantes para su éxito comercial final.

Tras varias décadas de investigación en el desarrollo de sensores químicos, los esfuerzos realizados en universidades e institutos de investigación han dado como resultado una amplia variedad de sistemas sensores, aunque solo una pequeña parte de ellos ha llegado finalmente a comercializarse. Varios son los obstáculos que dificultan su comercialización. En primer lugar, las características analíticas de sensibilidad, intervalo lineal, reproducibilidad, estabilidad, etc., demostradas para estos sensores a nivel de laboratorio, son a menudo insuficientes para satisfacer las necesidades de los usuarios. Además, incluso cuando se logren valores óptimos en el laboratorio, estas características analíticas se verán reducidas drásticamente durante el proceso de desarrollo y producción en serie de un sensor. Por lo tanto, es muy importante el estudio de nuevas fases sensoras cuyas características permitan dar una respuesta satisfactoria a las demandas exigidas por la sociedad, y que posean características fisicoquímicas simples que permitan el uso de tecnologías ya desarrolladas tanto como sea posible.

El segundo lugar, la necesidad desarrollar sistemas integrados y de interfases limita en cierta medida su comercialización. En el concepto de un sensor comercial, es necesario cuidar en detalle el diseño de los prototipos, ya que éstos deben ser intuitivos y fáciles de usar por usuarios no experimentados. Es decir, es necesario llevar a cabo el desarrollo de dispositivos simples, robustos, que necesiten un mantenimiento mínimo y que aporten la información justa y precisa que demanda la sociedad. Por último, el tercer gran obstáculo concierne a la competitividad del mercado. La comercialización de los sensores químicos se torna difícil o imposible si no se definen las verdaderas ventajas que éstos tienen sobre sus competidores, basados en tecnologías ya desarrolladas y ampliamente probadas.

Por todo ello, es necesario seguir investigando en este campo, e invertir tiempo, dinero y esfuerzo en acercar las características de los sensores químicos desarrollados en los laboratorios a las necesidades de la industria y/o la sociedad, demostrando sus ventajas frente a los dispositivos imperantes.

0.2 Sensores químicos de naturaleza óptica

0.2.1 Generalidades de los sensores ópticos

Los sensores ópticos son un tipo particular de sensores químicos en los que la interacción del analito de interés con la fase sensora produce un cambio en alguna propiedad óptica del sistema (transmitancia, transfectancia, reflexión interna atenuada, índice de refracción, luminiscencia, etc.), cuya magnitud será proporcional a la concentración del analito. En el caso de los sensores ópticos, esta transducción es de carácter físico (cambio en las propiedades espectroscópicas de la fase sensora), si bien este cambio puede estar asociado a una reacción química (p. ej., caso típico de los sensores enzimáticos con transducción de oxígeno [14]). De una manera más concreta, un sensor óptico también podría definirse como “*un dispositivo pequeño capaz de responder de forma selectiva y sensible a la presencia de un determinado analito, dando como resultado una información óptica*” [46].

La importancia y el potencial de los sensores ópticos ha ido creciendo progresivamente en las últimas décadas. Los primeros trabajos publicados en la literatura sobre sensores químicos se enfocaron desde una perspectiva electroquímica (sensores potenciométricos y amperométricos). Sin embargo, el gran avance experimentado en los últimos años tanto en la tecnología de fabricación de detectores ópticos y fibras ópticas como en el desarrollo de nuevos métodos óptico-espectroscópicos, y las enormes posibilidades que éstos ofrecen, han dado lugar al desarrollo de nuevas líneas de investigación en el campo de los sensores ópticos con detección óptico-espectroscópica [1, 47–51].

La espectroscopía de emisión luminiscente ha desarrollado métodos analíticos de elevada selectividad, sensibilidad y versatilidad, mientras que la industria de las telecomunicaciones ha logrado la comercialización de fibras ópticas de bajo coste que permiten la transmisión de luz a largas distancias. Además, la fabricación de nuevas fuentes de radiación baratas como los láseres y los diodos emisores de luz (LEDs, *Light-Emitting Diodes*) permiten excitar la muestra en prácticamente todo el intervalo de longitudes de onda del espectro electromagnético UV-visible. Asimismo, también se han desarrollado fotodetectores de elevada sensibilidad y bajo coste, como es el caso de los fotodiodos y las cámaras CCD (*Charge-Coupled Device*), así como una amplia variedad de componentes ópticos de reducidas dimensiones y bajo coste (filtros ópticos, colimadores, divisores de haz, etc.). Finalmente, la disponibilidad de circuitos integrados de bajo coste y elevada capacidad de cómputo y memoria (p. ej., microcontroladores, microprocesadores, procesadores digitales de señales (DSPs), etc.) y los avances en computación (p. ej., redes neuronales [52], técnicas avanzadas de procesamiento de señal, etc.), han permitido el desarrollo de sensores ópticos de pequeño tamaño, bajo coste, bajo consumo, portátiles y de elevadas prestaciones analíticas [53, 54], ya sea para el análisis y/o control de parámetros de interés químico [54–56], ambiental [53, 57–59], clínico [20, 22, 60, 61], industrial [62, 63], biotecnológico [64, 65], alimentario [66], etc.

0.2.2 Parámetros descriptivos de los sensores ópticos

Algunos de los principales parámetros que definen el comportamiento de un sensor óptico son la sensibilidad, la selectividad, el tiempo de respuesta, la reproducibilidad o el tiempo de vida

útil del sensor. A continuación se enumeran algunos de los parámetros más importantes usados con frecuencia para describir la respuesta de un sensor óptico [52, 67] (véase la Figura 5):

- **Linealidad:** Máxima desviación de la curva de calibración respecto a una línea recta especificada. Consiste en estimar el coeficiente de correlación lineal (R^2) entre las dos variables X e Y (la concentración de analito y la señal analítica, respectivamente). Dicho coeficiente es calculado normalmente mediante un método de mínimos cuadrados (*Least Squares Method*, LSM).
- **Sensibilidad:** Según la IUPAC, la sensibilidad se define como el cociente entre la señal analítica medida (Y) y la concentración de analito (X). Cuando trabajamos con curvas de calibrado, la sensibilidad es la pendiente de la curva a una concentración dada ($\Delta y/\Delta x$). En caso de ser una recta, coincide con la pendiente de la misma. Se trata de uno de los principales parámetros que definen la respuesta de un sensor.
- **Intervalo:** Valores máximo y mínimo para las variables de entrada y salida del sensor.
- **Intervalo dinámico lineal:** Es el intervalo de concentraciones (valores máximo y mínimo) donde existe una relación lineal entre éstas y las señales analíticas. En este intervalo, los valores deben presentar un nivel aceptable de precisión y exactitud, con lo cual, no pueden ser inferiores al límite de cuantificación (LOQ).
- **Resolución:** Se define como la mínima variación en la concentración (X) que es necesaria para producir un cambio en la señal analítica (Y) (o dicho de otro modo, es la mínima diferencia o incremento de concentración que puede ser detectado de forma fiable por el instrumento de medida).

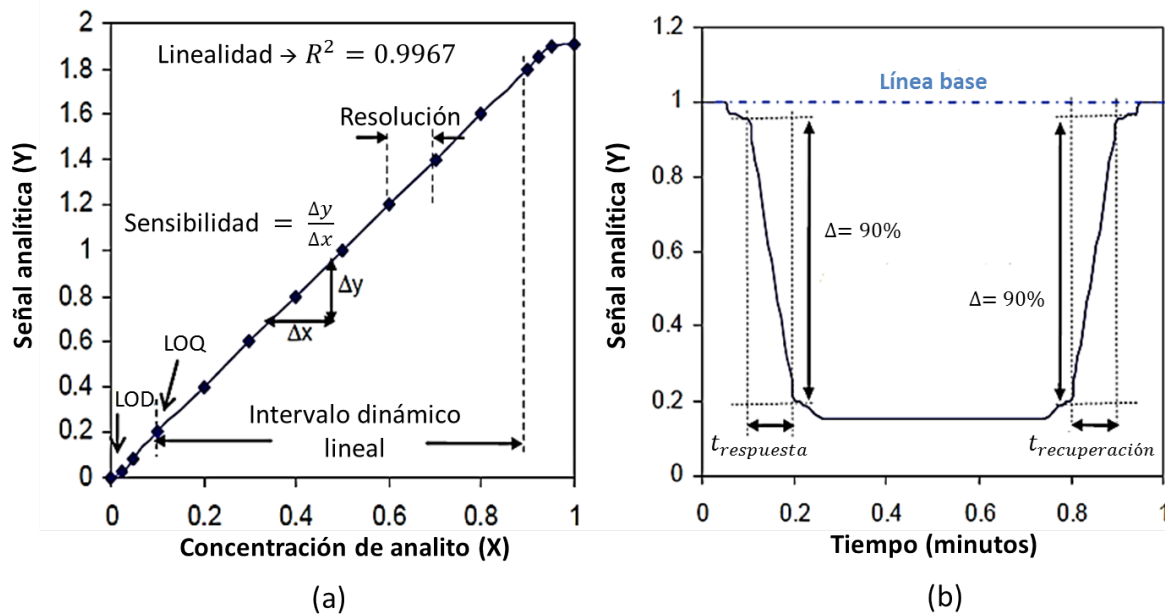


Figura 5: (a) Ejemplo típico de una curva de calibración de un sensor donde se muestra la relación entre la señal analítica (Y) y la concentración de analito (X); en ella también se muestran algunos de los principales parámetros comúnmente usados para describir el comportamiento de un sensor. (b) Ejemplo típico de la respuesta temporal de un sensor donde se indican los tiempos de respuesta y recuperación al 90% [52].

- **Exactitud:** Expresa la desviación (o error relativo) de la lectura de un sistema de medida respecto a una entrada conocida. Por tanto, este parámetro da cuenta de la proximidad entre el valor medido por el instrumento y el valor real.
- **Precisión:** Es el grado de concordancia entre réplicas de una misma medida (es decir, es la capacidad de medida de un instrumento para proporcionar la misma lectura cuando se realizan repetidas mediciones de la misma magnitud bajo idénticas condiciones). La precisión está relacionada con la varianza de un conjunto de medidas, e implica la similitud entre lecturas sucesivas, aunque no necesariamente cercanas al valor verdadero (la precisión es una condición necesaria pero no suficiente para la exactitud de las medidas). La precisión está definida por dos parámetros: la repetibilidad y la reproducibilidad.
- **Repetibilidad:** Es la capacidad de reproducir una lectura con una precisión dada cuando un conjunto de mediciones de la misma magnitud es llevado a cabo por el mismo operario, usando el mismo equipo de medida, la misma muestra, el mismo método analítico, en el mismo laboratorio y en intervalos de tiempo cortos. La repetibilidad viene dada por la desviación estándar de un conjunto de medidas.
- **Reproducibilidad:** Tiene el mismo sentido que la repetibilidad, excepto que se utiliza cuando se toman medidas de la misma magnitud bajo condiciones diferentes (las medidas son realizadas por distintos operarios, con distintos equipos de medida o fases sensoras, en laboratorios diferentes y/o en intervalos de tiempo largos).
- **Línea base:** Es el nivel de la señal analítica (Y) tomado como referencia en condiciones de inactividad o reposo. En el caso de los sensores químicos, la línea base se define como el nivel de la señal analítica obtenido tras un blanco (muestra con una concentración nula del analito a determinar).
- **Límite de detección (*Limit of detection*, LOD):** Es la menor cantidad de una magnitud cuya señal puede ser distinguida de la del ruido. En el caso de los sensores químicos, se trata de la mínima concentración de analito que es posible detectar con el instrumento de medida (sensor). Según la IUPAC, el LOD se define como la concentración de analito que proporciona una señal analítica igual a la del blanco más tres veces la desviación estándar del blanco [68].
- **Límite de cuantificación o determinación (*Limit of quantification*, LOQ):** Es la mínima concentración de analito que es posible detectar con el sensor de forma cuantitativamente precisa y exacta (es decir, el LOQ toma un valor mayor que el LOD y establece un límite de detección por encima del cual el sensor opera en el intervalo dinámico lineal de forma precisa y exacta). Según la IUPAC, el LOQ se define como la concentración de analito que proporciona una señal analítica igual a la del blanco más diez veces la desviación estándar del blanco [68].
- **Tiempos de respuesta y recuperación:** Es el tiempo que tarda la señal analítica del sensor en alcanzar un valor estacionario cuando se produce un cambio (o transitorio) en la concentración del analito. Así, el tiempo de respuesta del sensor se define como el tiempo que tarda la señal analítica (Y) en pasar del 10 % al 90 % de su variación total cuando se produce dicho cambio en la concentración, mientras que el tiempo de recuperación se define como el tiempo que tarda la señal analítica del sensor en pasar del 90 % al 10 % de su variación total (tiempo de recuperación de la línea base).

- **Correlación cruzada:** Estima la influencia de diversos parámetros externos sobre la medida, como por ejemplo, la temperatura, la humedad, la luz parásita, etc., parámetros que se supone no serán registrados durante la medida.
- **Selectividad:** Se define como la capacidad del sensor para identificar únicamente al analito de interés, mostrando una baja correlación cruzada a otros analitos (interferentes) que pudieran estar presentes en la muestra.
- **Vida útil:** Se define como el periodo de tiempo estimado en el que un sensor puede continuar funcionando correctamente (dentro de unos límites predeterminados). Normalmente se estima en horas de trabajo. En el caso de los sensores químicos, el tiempo de vida útil está fuertemente ligado a la estabilidad de la fase sensora. De este modo, depende fundamentalmente de las características del reactivo indicador y del método de inmovilización seleccionado. En algunos casos, los reactivos inmovilizados pueden experimentar degradaciones fotoquímicas o térmicas, o bien ser alterados por las disoluciones empleadas para su regeneración. Un problema que afecta drásticamente a la estabilidad de los sensores luminiscentes es la fotodegradación del luminóforo, mientras que en el caso de los sensores enzimáticos o irreversibles, el tiempo de vida útil dependerá de la velocidad de desactivación de la enzima o de consumición y/o degradación del reactivo. Para la determinación de este parámetro es necesario estudiar las condiciones de conservación más drásticas para el sensor.
- **Robustez:** Es la inercia que presenta un método analítico (o un equipo de medida) a modificar su señal analítica cuando tienen lugar pequeños cambios en las condiciones ambientales u operativas, que se consideran las variables que gobiernan el experimento de medida. Para el estudio de la robustez, estas condiciones son modificadas ligeramente, siguiendo un determinado diseño experimental, y se comprueba su influencia sobre la señal analítica. Con ello, se puede concluir qué variables son las más significativas a la hora de realizar las medidas y, por tanto, cuáles de ellas deberían requerir un mejor control.

0.2.3 Clasificación de los sensores ópticos

A medida que la ciencia ha ido desarrollando nuevos sensores ópticos para la determinación de especies químicas, las clasificaciones propuestas para estos sensores se han ido modificando y diversificando. Así, atendiendo a las distintas propiedades de estos sensores se han propuesto diferentes clasificaciones [1, 69]:

- 1) *Según la naturaleza y el fenómeno óptico medido*, se puede hablar de sensores de absorbancia, de reflectancia, de dispersión Raman, de transferencia de energía, de luminiscencia (fluorescentes, fosforescentes, quimioluminiscentes), etc.

En los sensores de absorbancia, la relación existente entre la intensidad de la luz incidente y la luz reflejada es directamente proporcional a la concentración del analito a determinar. Estos sensores suelen caracterizarse por su sencillez y robustez, pero también por su escasa selectividad.

Por su parte, los procesos fotoluminiscentes resultan particularmente atractivos para el desarrollo de sensores ópticos, ya que la radiación detectada (emisión) puede ser diferen-

ciada de la radiación incidente (excitación) por su longitud de onda. Además, dan lugar a sistemas sensores altamente sensibles, que permiten determinar niveles muy bajos de concentración de analito. Estas características hacen especialmente adecuado el uso de dichas técnicas fotoluminiscentes como método de detección en el desarrollo de sensores químicos de naturaleza óptica.

De las dos técnicas analíticas derivadas del fenómeno fotoluminiscente, la fluorimetría y la fosforimetría, la fluorimetría ha sido tradicionalmente la técnica empleada en el desarrollo de sensores ópticos luminiscentes [51]. Sin embargo, cabe señalar que el número de sensores fosforescentes a temperatura ambiente es mucho menor que el de los sensores fluorescentes [70]. Esto se debe fundamentalmente al escaso número de moléculas disponibles capaces de desarrollar fosforescencia. No obstante, en los últimos años la fosforescencia ha cobrado una gran importancia como método de detección, debido a las múltiples ventajas que presenta sobre la fluorescencia en el desarrollo de sensores ópticos [71]: (1) permite desarrollar una instrumentación sencilla, empleando componentes electrónicos de bajo coste que permitan la medida de tiempos de vida de fosforescencia (todo ello permitido por los largos tiempos de vida del estado triplete), (2) debido a que las posibles interferencias procedentes de emisiones residuales fluorescentes de la propia muestra o de la luz dispersa pueden ser evitadas o minimizadas (usando un tiempo de demora adecuado tras la excitación con fuentes pulsadas), es posible obtener relaciones señal/ruido elevadas, (3) la gran separación existente entre las longitudes de onda de excitación y de emisión fosforescente (banda de *Stokes*) hace que la discriminación entre ellas sea mucho más fácil, permitiendo el uso de selectores de longitud de onda de bajo coste (p. ej., filtros ópticos), (4) permite obtener sistemas sensores más selectivos, ya que la fosforescencia es un fenómeno menos común en la naturaleza que el de la fluorescencia. Sin embargo, la fosforescencia también presenta algunos inconvenientes tales como: (1) la escasez de moléculas luminiscentes que exhiban una emisión fosforescente a temperatura ambiente, y (2) la necesidad, en la mayoría de los casos, de desoxigenar las muestras para poder medir la emisión fosforescente del analito, ya que el oxígeno es un atenuador muy eficaz de la fosforescencia [70, 72, 73].

2) *Según la configuración externa del sensor*, los sensores ópticos se clasifican en cuatro grandes grupos atendiendo a la posición de la fase sensora: (1) ubicada en el interior de una celda de flujo, (2) depositada sobre una guía de onda, (3) depositada directamente sobre el detector, y (4) no conectada con el detector [8, 14, 22, 71, 74]. La Figura 6 muestra un esquema de dicha clasificación. A continuación se describen las características más importantes de cada uno de ellos:

- *Sensores tipo célula de flujo (optosensores)*. En este tipo de sensores la fase sensora se encuentra empaquetada en una celda de flujo. El término optosensor fue introducido por Ruzicka y Hansen [75] para definir un nuevo principio de detección en análisis por inyección de flujo (*Flow Injection Analysis*, FIA), basado en el cambio de las propiedades ópticas de una superficie activa situada en el paso de un flujo.

La celda de flujo con la fase sensora puede estar situada en el compartimento de muestra del propio equipo de medida, dando lugar a un *optosensor convencional*, o en el exterior del mismo (*optosensor no convencional*). En este último caso, a veces es preciso el uso de fibras ópticas para transportar la luz de excitación hasta la fase sensora y/o para guiar la luz de emisión hacia el instrumento de medida (transductor) [71]. Una información más completa sobre estos sensores puede ser consultada en el Apéndice I de esta memoria.

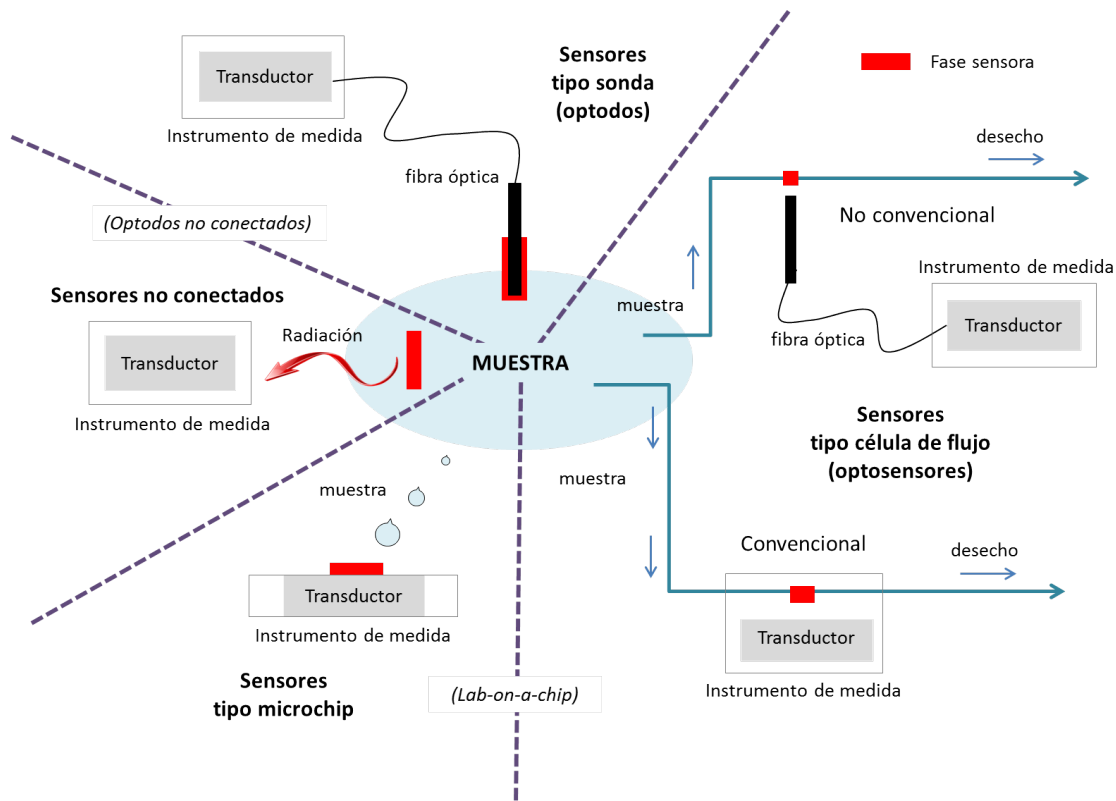


Figura 6: Clasificación de los sensores ópticos en función de la posición de la fase sensora respecto a la matriz medida (muestra) y el transductor [14, 71].

- *Sensores tipo sonda (optodos)*. Estos sensores están constituidos por una fase ópticamente activa situada en una guía de onda, normalmente de geometría cilíndrica (fibra óptica) [76, 77, 77, 78], aunque también existen otras de geometría plana (véase la Figura 7). Tradicionalmente estos sensores han recibido el nombre de *optodos* [79] (del griego “óptico” y “camino”), aunque también se les suele denominar a veces como *optodos* (del inglés “optical electrode”) [80]. Una información más completa sobre estos sensores puede ser consultada en el Apéndice II de esta memoria.
- *Sensores tipo microchip*. En ellos, la fase sensora se encuentra inmovilizada directamente sobre el transductor (o sobre un soporte inerte unido físicamente al transductor), el cual se halla integrado en un microchip que posee todos los componentes necesarios para realizar la medida (fuente de excitación, detector, filtros ópticos, etc.) [81–86]. La aparición de este tipo de sensores ha aumentado las posibilidades de miniaturización (véase la Figura 8), dando lugar a equipos de medida muy compactos y de una gran versatilidad [13, 53, 87–91].
- *Sensores no conectados*. Es el caso de aquellas configuraciones en las que la zona de reconocimiento no está conectada con la zona de medida y, por tanto, la detección se lleva a cabo a una cierta distancia de separación. Éste es el caso de sensores ópticos para la determinación de oxígeno en líquido ocular [22].

No obstante, esta clasificación no es cerrada, y podrían hacerse infinidad de ellas atendiendo a otros muchos aspectos de los sensores ópticos [92–94]. En otras ocasiones, en cambio, resulta difícil discernir entre un tipo de sensor u otro, como es el caso de los mi-

cosistemas de flujo (μ FIA) integrados en un chip (*Lab-on-a-chip*) [95], los cuales podrían ser considerados como una configuración híbrida entre un sensor de tipo microchip y un optosensor convencional.

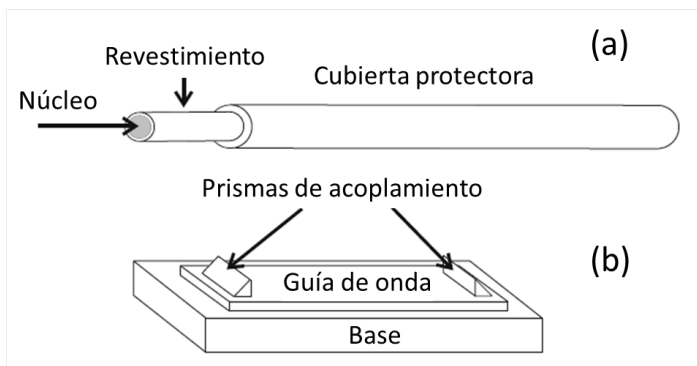


Figura 7: Diferentes tipos de guías de onda ópticas: (a) de geometría cilíndrica (fibra óptica), (b) de geometría plana [96].

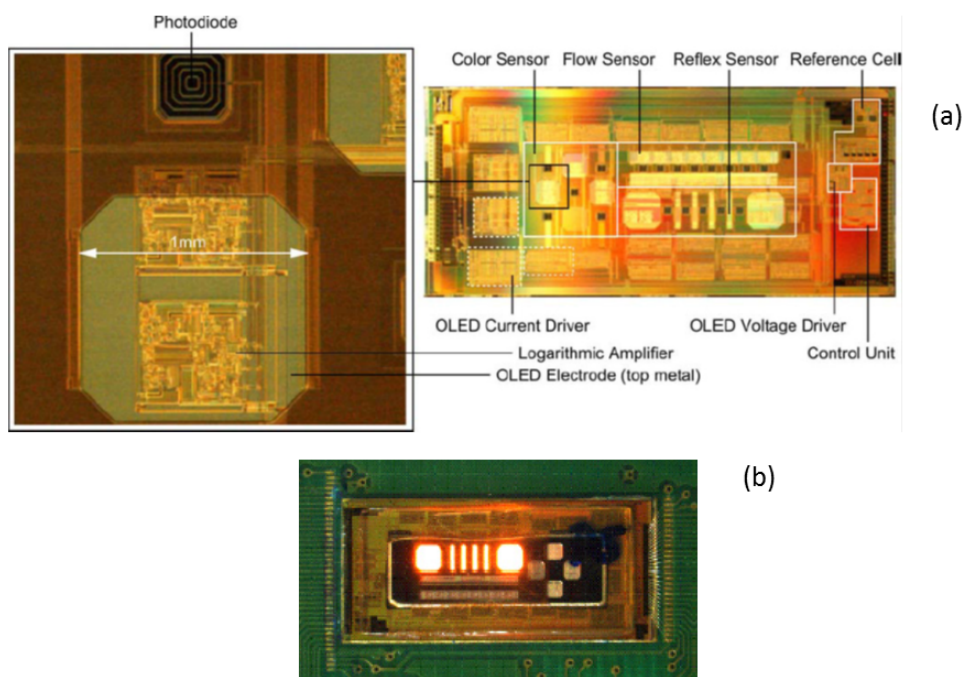


Figura 8: Imágenes de un sensor de tipo microchip (*Application-Specific Integrated Circuit, ASIC*) que incluye tanto dispositivos emisores de luz como fotodetectores (integrados en un mismo chip de silicio), así como otros sensores [91]. (a) Detalle de un diodo OLED de dicho chip fabricado con circuitos integrados. (b) Detalle general del chip implementado sobre una placa de circuito impreso.

0.2.4 Fases sensoras y mecanismos de reconocimiento óptico

Todos los sensores ópticos tienen un elemento esencial en común para que pueda tener lugar el reconocimiento y la detección del analito de interés: la *fase sensora* o *zona de reconocimiento óptico*. Dicha fase sensora está constituida generalmente por un reactivo indicador

inmovilizado sobre un soporte sólido [1]. El empleo de estos soportes sólidos, ya sean orgánicos (polímeros y copolímeros) o inorgánicos (p. ej., sílice), confieren a la fase sensora una serie de ventajas importantes, como son: una mayor estabilidad de los reactivos, sensibilidad, selectividad o incluso una mayor velocidad de reacción, siendo su coste de fabricación y adquisición generalmente moderado [1, 97]. Estas cualidades hacen de los soportes sólidos una herramienta ampliamente utilizada en la preparación de fases sensoras [1, 70, 98].

La fase sensora puede ser una membrana polimérica en la que pueden ser solubilizados diferentes reactivos que interaccionen con el analito de interés (produciendo un cambio en las propiedades ópticas de la misma [73, 99]), membranas nanoestructuradas formadas por un óxido metálico o un sol-gel en el que se inmovilice un reactivo que actúe de la misma forma que en el caso anterior [25, 73, 100, 101], nano/micropartículas orgánicas/inorgánicas o híbridas [102] (partículas magnéticas con un núcleo magnético (Fe_3O_4) recubierto con una capa polimérica o nano/microfibras [103, 104]) que incorporen el reactivo en su superficie, una resina polimérica entrecruzada en la que los analitos se adsorban en su superficie (preconcentrándose y produciendo una variación en las propiedades ópticas de la fase sensora) [105], o un polímero de impronta molecular (MIP, del inglés *Molecularly Imprinted Polymer*) en cualquiera de sus diversos formatos (micro/nanopartículas esféricas, micro/nanofibras o membranas poliméricas de impronta molecular) [106, 107], en el que se hayan generado huecos específicos para el analito de interés [70]. Una mayor información sobre fases sensoras ópticas sensibles a oxígeno puede ser consultada en el Apéndice III de esta memoria.

El mecanismo de reconocimiento óptico va a depender, por tanto, del tipo de fase sensora que se diseñe. Así, los principales mecanismos de reconocimiento de los sensores ópticos son los siguientes [70, 98]:

- 1) *Mecanismo de coextracción o cambio iónico*: La fase sensora contiene un ionóforo (que interacciona con el analito), un cromoionóforo (cuyas propiedades ópticas serán sensibles al cambio de una propiedad química de la membrana, por ejemplo el pH) y, en el caso de un cambio de carga en la membrana debido a la entrada o salida de especies cargadas, un aditivo aniónico lipofílico (encargado de mantener la electroneutralidad dentro de la membrana). La interacción del analito de interés con el ionóforo provoca un cambio en una propiedad química de la membrana, por ejemplo, la entrada de iones H^+ (coextracción) que modifican el pH de la membrana, o la cesión de iones H^+ del ionóforo al cromoionóforo (cambio iónico), que al igual que en el caso anterior, produce un cambio en el pH de la membrana. Esta variación de pH induce un cambio en las propiedades ópticas del cromoionóforo, cambio que se relaciona con la concentración del analito de interés. Por tanto, se trata de un mecanismo de reconocimiento indirecto.
- 2) *Mecanismo catalítico/enzimático*: La fase sensora contiene un catalizador (o enzima) inmovilizado, que en presencia del analito de interés, cataliza una reacción donde se genera una nueva sustancia que produce un cambio en las propiedades ópticas de la misma. Este cambio puede ser un aumento o una disminución de la propiedad óptica medida, por ejemplo, la aparición de luminiscencia, siendo ésta proporcional a la concentración del analito.
- 3) *Mecanismo de interacción directa analito-cromoionóforo*: La fase sensora contiene un cromoionóforo, que tras interaccionar con el analito de interés (interacción física o química),

cambia alguna de sus propiedades ópticas. Esta variación puede ser un aumento o una disminución de dicha propiedad, como por ejemplo, una atenuación de la luminiscencia molecular proporcional a la concentración del analito.

- 4) *Mecanismo de interacción directa analito-soporte*: La fase sensora, que no contiene ningún aditivo ópticamente activo, interacciona con el analito que se retiene por interacciones físicas y/o químicas, preconcentrándose y produciendo una variación en las propiedades ópticas de la fase sensora, variación que será proporcional a la concentración del analito. Éste es el caso de las fases sensoras basadas en resinas poliméricas entrecruzadas o en polímeros de impronta molecular.

0.3 Sensores ópticos luminiscentes para el control de oxígeno

0.3.1 La importancia del oxígeno

El oxígeno es uno de los elementos más abundantes de la Tierra (incluyendo el agua, la corteza terrestre y la atmósfera), y está presente tanto como constituyente de moléculas en la corteza terrestre y océanos, como en su forma molecular más frecuente: el O_2 . A temperatura ambiente, el oxígeno molecular o dióxígeno es un gas incoloro e inodoro formado por moléculas de dos átomos de oxígeno [14].

El oxígeno molecular es el segundo gas atmosférico más abundante en la Tierra después del nitrógeno, encontrándose con un porcentaje del 20.95 % en volumen. La principal fuente de oxígeno atmosférico son las bacterias fotosintéticas, las algas y las plantas durante el proceso de la fotosíntesis, a partir del dióxido de carbono (CO_2), el agua y la luz. Pero además, el oxígeno también es incorporado a la atmósfera mediante la fotólisis de las moléculas de monóxido de nitrógeno (NO) y vapor de agua presentes en la atmósfera, y está presente en océanos, mares y ríos como oxígeno disuelto, siendo un elemento esencial para la vida de los seres acuáticos, tanto animales como vegetales [108].

El descubrimiento del oxígeno se asigna al farmacéutico sueco Carl Wilhelm Scheele (1742-1786) en 1771, ya que fue el primer científico capaz de aislarlo, pero su trabajo no obtuvo un reconocimiento inmediato y en ocasiones se atribuye al clérigo británico Joseph Priestley (1733-1804), quien lo descubrió independientemente el 1 de agosto de 1774. El químico francés Antoine Lavoisier (1743-1794) también reconocía la importancia del oxígeno, demostrando que la combustión es un proceso en el que se produce la combinación de una sustancia con oxígeno, y que a su vez éste juega un papel muy importante en la respiración de las plantas y los animales. Hasta entonces el oxígeno era denominado con el término de “*flogisto*”, y fue Lavoisier quien acuñó por primera vez el término de “*oxígeno*”, con la idea errónea de que todos los ácidos contenían este tipo de gas (de la raíz griega ‘*oxus geinomais*’, generador de ácido) [109].

En 1877 Louis-Paul Cailletet (1832-1913) y Raoul Pictet (1846-1929) consiguieron licuar el oxígeno por primera vez, aunque la producción industrial no comenzó hasta 1902 gracias al proceso de licuación del aire propuesto por Carl von Linde (1842-1934). Hasta 1961 el oxígeno fue usado como elemento de referencia para la asignación de masas atómicas relativas, cuando fue sustituido por el carbono 12 [108].

En cualquiera de los casos, el oxígeno molecular es fundamental para la vida y su concentración en la Tierra es el resultado de un balance bioquímico y fisiológico entre los animales que lo consumen y las plantas que lo generan a través de la fotosíntesis. Así, el O_2 interviene en reacciones biológicas de diferente escala molecular, desde seres microscópicos como las bacterias, hasta seres macroscópicos, ya sea en la respiración celular o en la fotosíntesis.

0.3.1.1 El oxígeno en el metabolismo celular

El análisis de las poblaciones de células, su viabilidad y el metabolismo celular, juegan un papel muy importante en la biología celular moderna, la medicina y la biotecnología [110]. El principal objetivo de la respiración celular es generar energía en forma de ATP (del inglés *adenosine triphosphate*), donde por cada dos moléculas de ATP se consume una molécula de oxígeno [111, 112].

Por tanto, una adecuada presencia de O_2 es importante para el crecimiento y desarrollo de las células, lo que lo convierte en un metabolito clave tanto en células aeróbicas como en organismos mayores. Así, la concentración de O_2 es un marcador muy útil del estado metabólico y de salud de las células, y proporciona información sobre su respuesta frente a estímulos externos e internos [113]. Así, por ejemplo, se puede correlacionar el suministro de oxígeno con el desarrollo de un tejido (en términos de su composición bioquímica, apariencia y propiedades), tratándose de un parámetro necesario para la optimización de los sistemas de cultivo [114–116].

0.3.1.2 El oxígeno en el sector médico y clínico: hipoxia e hiperoxia en los tejidos

La importancia del oxígeno para las células hace que el suministro y la difusión de oxígeno en los tejidos sea indispensable para la vida. La hipoxia resulta como consecuencia de un balance negativo entre la demanda de oxígeno de los tejidos y la capacidad del sistema vascular para suministrarlo. Diversas patologías como la diabetes, la inflamación o el cáncer pueden afectar de forma negativa a la oxigenación de los tejidos [117].

La hipoxia se encuentra presente en desórdenes vasculares, inflamaciones agudas o crónicas [118] y en el crecimiento de tumores malignos, donde se relaciona con un crecimiento agresivo del tumor, un mayor riesgo de metástasis o incluso con una mayor resistencia del tumor a la radio y la quimioterapia [119–121].

Una disminución del aporte de oxígeno en el tejido durante un trasplante puede producir daños irreparables o incluso la pérdida del órgano trasplantado. Los tejidos, y en especial el tejido muscular, son muy sensibles a la isquemia producida por la pérdida transitoria del riego sanguíneo durante el trasplante [122].

El suministro inadecuado de oxígeno en los tejidos del cuerpo humano también se relaciona con la aparición de cierto tipo de enfermedades, como por ejemplo, las oculares [123]. En otras situaciones, la determinación de oxígeno también puede resultar útil para determinar la viabilidad de los fetos [124]. Así, por ejemplo, tanto condiciones de hipoxia como de hiperoxia durante el desarrollo fetal pueden provocar lesiones importantes durante el desarrollo cerebral

del bebé [125]. De hecho, un exceso de oxígeno puede provocar la muerte de tejidos debido al estrés oxidativo y la formación de especies reactivas (ROS, de sus siglas en inglés *Reactive Oxygen Species*) [126, 127]. Estos radicales libres intervienen en el envejecimiento celular y en la estabilidad oxidativa y pueden tener influencia en enfermedades neurodegenerativas [128]. Otro ejemplo de los daños producidos por la hiperoxia se encuentra en muchas enfermedades crónicas como la arterioesclerosis o las enfermedades pulmonares [129]. Los problemas debidos a la toxicidad del oxígeno pueden aparecer en pacientes sometidos a terapias hiperbáricas con oxígeno [130], en bebés prematuros [131, 132], o incluso en submarinistas [133].

Debido a los graves daños que las situaciones de hipoxia e hiperoxia pueden producir en los pacientes, el control de oxígeno es también hoy en día indispensable en las unidades de cuidados intensivos de los hospitales y durante la anestesia [134]. Pero además, en el sector médico y clínico, diversos tipos de reacciones enzimáticas, monitorizadas a través del consumo o producción de oxígeno, pueden servir para la determinación de otros analitos de gran interés. Un ejemplo de ello es la determinación de glucosa, la cual se ha convertido en una de las áreas con mayor aplicación de la Química Analítica. La cuantificación de glucosa supone casi un 40 % de todos los análisis de sangre realizados en los laboratorios clínicos [135], y además tiene una gran aplicación en biotecnología y en la producción y procesado de diferentes tipos de alimentos.

0.3.1.3 El oxígeno en el sector alimentario

La influencia de la disponibilidad de oxígeno sobre el crecimiento bacteriano también influye en la cinética de las fermentaciones que se llevan a cabo en biorreactores. Estas reacciones ocurren normalmente en un medio acuoso, donde la solubilidad del oxígeno es baja y donde los microorganismos lo consumen rápidamente, por lo que la inyección controlada de oxígeno, bien sea a través de técnicas de aireación o de producción de oxígeno *in situ*, hace que su monitorización sea muy importante [136]. Además, el estudio de la tasa de transferencia de oxígeno (*Oxygen Transfer Rate*, OTR) [136] de los diferentes cultivos también puede ayudar a optimizar los procesos, conocer mejor el comportamiento del crecimiento bacteriano, o contribuir en el escalado de biorreactores [137, 138].

Las enzimas también son muy usadas en la industria alimentaria, tanto para el control del procesado de los alimentos (control de la temperatura mediante la termoestabilidad de enzimas), como para la determinación de sus constituyentes (proteínas, vitaminas, etc.), o incluso para determinar la calidad de los alimentos (detección de insecticidas y bacterias que puedan estar presentes en la muestra, o de subproductos provenientes de la degradación de los alimentos) [76]. Muchas de estas enzimas producen o consumen oxígeno como resultado de las reacciones que catalizan. La aplicación del control de oxígeno con el uso de enzimas también permite analizar otros parámetros, como el contenido de etanol en bebidas alcohólicas [139].

La presencia de oxígeno, junto con otros factores como la temperatura, puede alterar el sabor de determinados alimentos, como el que ocurre, por ejemplo, durante la etapa de maceración de la cerveza [140] debido a la oxidación de los lípidos. Así, los sensores para la determinación de oxígeno disuelto pueden servir para determinar el grado de descomposición de los alimentos en controles de calidad [141].

La transferencia de oxígeno a través de la comida influye en el valor nutricional, las características organolépticas y la maduración de los alimentos, frutas y verduras [142], especialmente en alimentos envasados. Del mismo modo que el oxígeno interviene durante el procesado de los alimentos, la estabilidad oxidativa de los compuestos lipídicos es fundamental para determinar las condiciones de almacenamiento, donde el control del oxígeno presente es importante [143, 144]. Del mismo modo, su concentración también es vital en envases al vacío o con atmósferas modificadas (MAP, *Modified Atmosphere Package*) para garantizar la frescura y conservación de los alimentos [145–148].

0.3.1.4 El papel del oxígeno en aplicaciones industriales y tecnológicas

El oxígeno, al ser un gas altamente reactivo, oxida una gran cantidad de elementos, lo cual hace que tenga una gran aplicación en la industria [108]. En 2004 el oxígeno fue el cuarto producto químico más producido en Estados Unidos y el primero en Europa, con 19539 y 13672 millones de metros cúbicos respectivamente [149]. Como dato anecdótico, cabe señalar que en la primera misión espacial del programa *Apollo* de la NASA (*National Aeronautics and Space Administration*) en 1969 (alunizaje del *Apollo 11*), se consumieron alrededor de 1270 m³ de oxígeno líquido para oxidar unas 550 toneladas de combustible [108]. Pero además, en la actualidad, la detección de trazas de oxígeno en el combustible de hidrógeno usado por los vehículos espaciales [150], así como la detección de posibles filtraciones o fugas en los tanques de almacenamiento, son aspectos muy importantes a controlar por razones económicas y de seguridad [151].

Del mismo modo, la determinación de oxígeno también puede servir para evitar la emisión de sustancias perjudiciales para el medio ambiente y/o para mejorar el rendimiento de los motores en la industria automovilística mediante un control de la relación aire/fuel [152].

La detección de oxígeno también puede ser útil para monitorizar la presión del aire a lo largo del tiempo en diferentes superficies (mediante el uso de pinturas sensibles a la presión (*Pressure-Sensitive Paints*, PSP)), lo cual resulta de gran utilidad en la mecánica de fluidos y en estudios aerodinámicos, como por ejemplo, el diseño de vehículos espaciales [153], la optimización de rotores [154, 155] o en diversas aplicaciones tecnológicas [156].

Además, en la industria metalúrgica, la formación de oxígeno en los electrodos durante procesos de electrodeposición (*Oxygen Evolution Reaction*, OER), es también un parámetro muy importante que se relaciona con la resistencia del material a la corrosión. Su determinación, además, permite controlar ciertas propiedades de los materiales [157], tales como su estructura y sus propiedades ópticas [158].

El oxígeno no solo es importante para el control de procesos industriales donde se consume o se produzca este gas (*p. ej.*, en procesos de combustión [159, 160] o en fermentaciones anaerobias tales como la producción de biogás [161], etc.), sino que también tiene un papel destacado en sistemas de seguridad de plantas químicas y petroquímicas (*p. ej.*, en el control de posibles explosiones) o en plantas de residuos peligrosos [162, 163].

Por otro lado, el control de oxígeno disuelto permite evitar los posibles procesos de corrosión en instalaciones de calderas de vapor o sistemas refrigerantes que se pueden producir debido al poder oxidante del oxígeno [164, 165]. La presencia de ciertos niveles de oxígeno

en las aguas en estos sistemas, no solo puede dañar la instalación, sino que además puede suponer un riesgo importante en determinados casos (p. ej., si restos de óxido llegaran a un reactor nuclear).

0.3.1.5 El oxígeno disuelto y el ambiente

La concentración de oxígeno disuelto es uno de los parámetros más importantes a considerar en la calidad de las aguas. La concentración de oxígeno disuelto depende de la temperatura y la profundidad, y suele ser de unos 8 ppm (a 1 atm de presión y 20 °C de temperatura). Así, el O₂ es esencial para los organismos marinos, lo cuales requieren diferentes cantidades de oxígeno para su metabolismo [166]. Gracias a este oxígeno, los microorganismos aeróbicos son capaces de eliminar los contaminantes del medio. Sin embargo, si la cantidad de contaminantes es alta, esto puede producir una reducción significativa de los niveles de oxígeno, afectando negativamente a los organismos acuáticos [167]. Por la misma razón, es interesante monitorizar el oxígeno en piscifactorías para lograr una reproducción óptima de las especies y evitar su mortalidad debido a un suministro inadecuado de O₂.

Por otro lado, el control de las propiedades fisicoquímicas y microbiológicas en aguas potables es fundamental para proteger a los consumidores. En la mayoría de los países desarrollados existe una legislación sobre las aguas potables, donde se establecen los niveles máximos de elementos tóxicos admitidos en el agua de consumo. En este sentido, la cantidad de oxígeno disuelto es un indicador muy importante de la calidad del agua, pues indica su nivel de contaminación. Así, la medida de la demanda biológica de oxígeno (DBO) y la demanda química de oxígeno (DQO) son parámetros frecuentemente utilizados para la caracterización de la calidad de las aguas. El primero, proporciona información sobre la cantidad de oxígeno requerida para la biodegradación de la materia orgánica presente en el agua, a través de la actividad metabólica de los microorganismos que la digieren. Por otro lado, la DQO corresponde a una oxidación química de las sustancias oxidables presentes en el agua, por lo que también proporciona información sobre la materia inorgánica no biodegradable [167], permitiendo en cualquier caso un mejor control sobre el tratamiento de las aguas residuales [168, 169].

0.3.1.6 El oxígeno en botánica

Teniendo en cuenta que la ruptura de las moléculas de agua durante la fotosíntesis conlleva la formación de oxígeno, su determinación también resulta de interés en el campo de la botánica [170, 171]. Al contrario que los animales, las plantas no tienen un sistema de suministro de oxígeno en sus tejidos, por lo que la concentración de este gas depende del balance entre el consumo celular y su producción vía fotosíntesis [172]. Además, la permeabilidad del tejido de las plantas tanto al oxígeno como al monóxido de carbono es un factor muy importante en su desarrollo y crecimiento [173], mientras que una correcta aireación de las raíces es un factor clave en el crecimiento de vegetales y plantas [174].

0.3.2 Métodos generales de determinación de oxígeno

En este apartado se describirán de forma general los métodos de determinación de oxígeno más comunes encontrados en la bibliografía, comentando en cada caso sus ventajas e inconvenientes, así como su campo de aplicación. La Tabla 1 recoge un resumen de estos métodos y sus características.

0.3.2.1 Análisis gravimétrico

Este método permite evaluar el oxígeno adsorbido por una muestra determinada, simplemente mediante diferencia de pesada. Para realizar este tipo de análisis hace falta una microbalanza de precisión para monitorizar el aumento o disminución de peso. Aunque este instrumento de medida es sencillo, debe estar aislado herméticamente para que la muestra pueda ser desgasificada antes de comenzar el análisis, y también para controlar perfectamente las condiciones de temperatura y humedad. Se trata pues de una técnica global, que no permite conocer la concentración de oxígeno localmente. Además, cuando la concentración de oxígeno es muy baja, las variaciones de masa detectadas debidas a elementos volátiles (entre ellos el vapor de agua) no pueden ser diferenciadas del oxígeno [175]. Esta técnica ha sido especialmente usada para la determinación de la estabilidad oxidativa de ciertos alimentos [176] y para la determinación de la constante de difusión e isotermas de adsorción de materiales. Aunque hoy en día existen balanzas de gran precisión, la gravimetría ha sido sustituida por otras técnicas más avanzadas, tales como las electroquímicas o las ópticas [14].

0.3.2.2 Detección manométrica

Este tipo de análisis se basa en la cuantificación de oxígeno mediante el cambio de presión de un sistema. De este modo, la diferencia entre las presiones de entrada y salida del sistema se puede relacionar con la cantidad de oxígeno consumida por los microorganismos o adsorbida en una determinada muestra. Las diferentes variantes de este principio son esencialmente usadas para evaluar tasas metabólicas a partir de la estimación de un consumo de oxígeno [177–179], aunque también pueden usarse para conocer la solubilidad del oxígeno y la capacidad antioxidante de determinados alimentos [175].

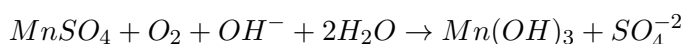
0.3.2.3 Cromatografía de gases

La cromatografía de gases es una técnica muy eficaz para la determinación de oxígeno gaseoso, el cual se separa del resto de gases mediante el uso de columnas de diferentes tipos. El detector acoplado al cromatógrafo de gases suele ser de conductividad térmica [168, 180, 181], aunque también es posible el uso de otros detectores [182, 183].

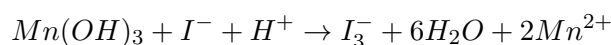
El uso de esta técnica está orientado principalmente a la determinación de oxígeno en muestras gaseosas, ya que su principal desventaja en matrices sólidas o acuosas es que requiere recoger “la atmósfera” que rodea a la muestra analizada y conducirla hasta el cromatógrafo, lo cual puede perturbar el equilibrio de la muestra [14].

0.3.2.4 Valoración Química (Método de Winkler)

El método más antiguo para la determinación de oxígeno disuelto es la valoración colorimétrica o método de Winkler, y aún hoy sigue siendo el procedimiento volumétrico más exacto y fiable para analizar oxígeno disuelto en agua. Este método requiere la fijación del oxígeno disuelto en forma de hidróxido de manganeso mediante la adición de un exceso de $Mn(II)$ y una base fuerte, que producirán la aparición de un precipitado marrón de $Mn(OH)_3$:



La posterior adición de iones yoduro en un medio ácido, permite la reducción del $Mn(III)$ a $Mn(II)$ a costa de la oxidación del ión yoduro (I^-) a triyoduro (I_3^-), en una concentración proporcional a la concentración inicial de oxígeno disuelto [14]:



Por tanto, la valoración del triyoduro formado con un patrón de tiosulfato sódico, permite determinar la concentración de oxígeno. El punto final de la valoración se puede detectar tanto visualmente, utilizando almidón como indicador, o bien mediante técnicas potenciométricas o espectroscópicas, las cuales permiten una automatización más sencilla [184–187].

En general, el método de Winkler es usado a menudo como método de referencia para la calibración de otros instrumentos que miden oxígeno, aunque únicamente puede ser aplicado a muestras líquidas, y siempre y cuando se garantice que no se pierde ni se introduce oxígeno durante las diferentes etapas del proceso. Además, la muestra debe estar libre de otros compuestos que puedan reducir u oxidar el yoduro [188]. Debido a que el análisis produce la destrucción de la muestra de agua, la determinación de oxígeno mediante este método está especialmente dirigida a volúmenes grandes de muestra [14].

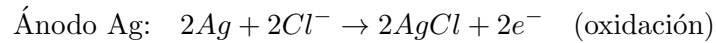
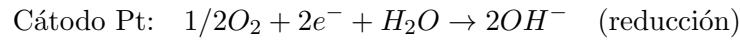
0.3.2.5 Métodos electroquímicos (Electrodo de Clark)

Los métodos electroquímicos se basan en el uso de un electrolito para reducir al oxígeno y crear una corriente eléctrica entre dos electrodos, la cual se relaciona con la concentración de oxígeno.

En función del parámetro electroquímico medido que contiene la información, los sensores electroquímicos para oxígeno se pueden agrupar como: *potenciométricos*, si lo que se mide es una diferencia de potencial, *amperométricos*, si lo que se detecta es una corriente eléctrica, o *conductimétricos*, si el parámetro medido es una conductividad [13, 189].

Por su importancia y robustez, nos centraremos en el electrodo de Clark [190]. El electrodo de Clark es un método estándar ampliamente utilizado en la industria para la determinación de oxígeno. Se trata de un dispositivo amperométrico polarográfico compuesto por un electrodo de platino (que sirve como cátodo) y un electrodo de plata (que sirve como ánodo), ambos sumergidos en un electrolito de KCl . El sistema se separa del medio a estudiar por una membrana de teflón permeable al O_2 (véase la Figura 9), siendo ésta su principal diferencia con respecto a otros sensores amperométricos [13]. Al aplicar un potencial de polarización a los electrodos, el oxígeno llega al sensor mediante difusión a través de la membrana permeable

que separa la muestra y el electrolito, y se reduce en la superficie del cátodo, dando lugar a una corriente eléctrica medible que se relaciona con la concentración de oxígeno presente en la muestra. Las reacciones químicas que tienen lugar en los electrodos son:



La magnitud de la corriente medida vendrá determinada por el espesor de la membrana, la velocidad de difusión del O_2 a través de la membrana y el tamaño del cátodo. Sin embargo, como se puede deducir de las reacciones, el electrodo de Clark también presenta una serie de desventajas tales como [175, 191]: (1) consume oxígeno, por lo que la utilización de este electrodo para llevar a cabo medidas de oxígeno en aguas estancadas (entre otras aplicaciones), puede provocar un empobrecimiento de su nivel de oxígeno en la zona próxima a la membrana, dando así lugar a derivas en la señal; (2) la obstrucción del ánodo con el tiempo debido al cloruro de plata formado; (3) se requiere una agitación continua de la muestra debido al uso de una membrana permeable, por lo que la difusión de oxígeno puede ser lenta, resultando en tiempos de respuesta largos; (4) baja estabilidad a largo plazo, debido a que es necesario reemplazar con cierta frecuencia el electrolito que utiliza el electrodo (el uso del electrolito durante varios días puede dar lugar a derivas en la señal, debido al consumo del electrolito); (5) la respuesta del electrodo, especialmente cuando se miden señales de bajo nivel, puede verse seriamente afectada por la presencia en el medio de determinadas especies fácilmente reducibles, tales como el SH_2 , algunas proteínas y diversos compuestos orgánicos; (6) tiene serios problemas de esterilización; (7) presenta peligro de electroshock.

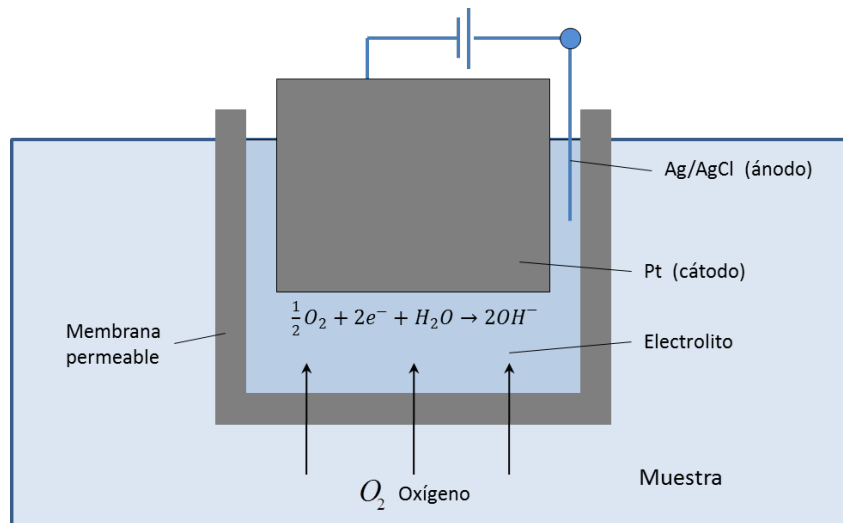


Figura 9: Esquema de un electrodo de Clark.

Tabla 1: Comparación entre los principales métodos de determinación de oxígeno [14]. G: gas, L: líquido, S: sólido.

Método	Gravimétrico	Manométrico	Cromatografía de gases	Winkler	Electrodo Clark	EPR	Óptico luminiscente
Parámetro estimado	Masa	Presión	Área de pico/ Intensidad	Moles	Corriente	Anchura de pico/ Intensidad	Disminución intensidad/ Tiempo de vida
Medio de medida	L/S	L/S	G/L/S	L	G/L/S	G/L/S	G/L/S
Contacto con la muestra	No	No	No	Destructivo	Invasivo	No	Invasivo
Necesidad de calibración	No	Sí	Sí	No	Sí	Sí	Sí
Reversible	No	No	Sí	No	Sí	Sí	Sí
Consumo de oxígeno	No	No	Sí	Sí	Sí	No	No
Tiempo de medida	Horas	Horas	Minutos	Minutos	Segundos	Minutos	Segundos
Tipo de media	Global	Global	Global	Global	Local/Global	Distribución O ₂	Local/Global/ Distribución O ₂
Miniaturización	No	Sí	No	No	Sí	No	Sí
Medida <i>'in situ'</i>	No	No	No	No	Sí	No	Sí
Aplicación típica	Adsorción de O ₂ en alimentos	Tasas metabólicas en organismos	O ₂ en muestras gaseosas	O ₂ disuelto en aguas	Variada	Imágenes tejidos	Variada
Referencia	[175]	[192]	[182]	[188]	[191]	[121, 193]	[87]

A pesar de estas desventajas, la detección de oxígeno mediante el electrodo de Clark ha sido y es ampliamente usada en numerosos campos de la ciencia y la tecnología debido a su robustez y flexibilidad. Además, varios de los problemas mencionados anteriormente ya han podido ser solucionados parcialmente mediante modificaciones del diseño original, y en la actualidad, diversas variantes adaptadas a diferentes ambientes han sido y están siendo desarrolladas para detectar oxígeno bajo diferentes configuraciones, incluyendo el uso de microelectrodos [111, 112, 139, 141, 148, 169, 171, 174, 194].

0.3.2.6 Resonancia paramagnética electrónica (EPR)

Uno de los métodos más utilizados para la determinación de oxígeno es la resonancia paramagnética electrónica (RPE de sus siglas en español, o más conocido como EPR, del inglés *Electron Paramagnetic Resonance*) [191]. La EPR es análoga a las técnicas de resonancia magnética nuclear (*Nuclear Magnetic Resonance*, NMR), pero en lugar de la excitación del núcleo atómico, la interacción se produce con el espín de los electrones. La mayoría de las moléculas tienen sus electrones apareados, por lo que esta técnica ofrece una gran especificidad, teniendo en cuenta los electrones desapareados que posee el oxígeno [14]. Debido a las características no invasivas de este tipo de métodos [121], se han usado principalmente para obtener imágenes de alta resolución de la distribución de oxígeno en tejidos celulares [120, 121, 193].

Además, también se puede hacer uso de las técnicas de RMN para obtener imágenes de resonancia magnética nuclear (*Magnetic Resonance Imaging*, MRI) y detectar situaciones de hipoxia en tejidos, ya sea haciendo uso de biomarcadores de hipoxia, sondas fluoradas, o mediante las propiedades de la desoxihemoglobina [121, 193, 195].

0.3.2.7 Métodos ópticos

Sensores fotométricos: La absorción por parte de las moléculas de oxígeno ocurre en el infrarrojo cercano (IR cercano), en torno a 760 nm, donde no se conocen interferencias de otros gases. Esta característica permite detectar este gas mediante la medida de la absorbancia [14]. Para ello es necesario un láser a la longitud de onda adecuada, de modo que a medida que aumenta la concentración de oxígeno presente en la muestra, la intensidad de luz del láser que llega al detector es menor, pues parte de ella es absorbida por las moléculas de oxígeno. La mayoría de las aplicaciones de espectrometría de absorción de diodo láser son de carácter industrial [162] o médico [196, 197].

Sensores luminiscentes: Los sensores ópticos basados en la atenuación de la luminiscencia han tenido un gran desarrollo y aplicación en los últimos años, y actualmente son el método óptico de detección de oxígeno más ampliamente usado junto con los métodos polarográficos [50, 87, 198]. Estos sensores se basan en la disminución de la luminiscencia de una molécula orgánica en presencia de oxígeno, de modo que esta atenuación puede relacionarse con la concentración de oxígeno presente en el medio. En la Figura 10 se esquematiza el proceso de la atenuación de la luminiscencia producido por el oxígeno. El primero en observar que el oxígeno podía atenuar la fluorescencia de ciertos compuestos luminiscentes fue Hans Kautsky

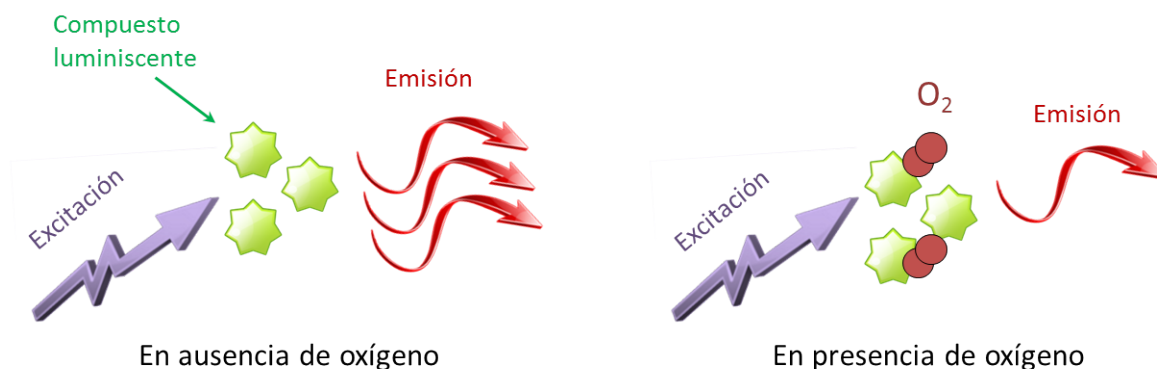


Figura 10: Proceso esquemático simplificado de la atenuación de la luminiscencia de un compuesto luminiscente ante la presencia de oxígeno [14].

en 1939 [199]. Sin embargo, se tardaron más de 25 años en desarrollar el primer sensor óptico de medida de oxígeno [200].

La principal ventaja de estos sensores frente al electrodo de Clark es que no consumen oxígeno. Los sensores ópticos ofrecen una gran selectividad comparada con otros sensores químicos [1, 14, 98]. Además, permiten el uso de fibras ópticas para unir la zona de análisis con los dispositivos de medida [50], lo cual permite realizar medidas remotas, incluso en ambientes potencialmente peligrosos (como zonas radiactivas o atmósferas explosivas). Asimismo, al ser un proceso reversible, dichos sensores permiten monitorizar la concentración de oxígeno a lo largo del tiempo [73].

0.3.3 Determinación de oxígeno por atenuación de la luminiscencia

Todas las técnicas ópticas de análisis químico se basan en la interacción de la radiación electromagnética con la materia: absorbancia, luminiscencia, reflectancia difusa, dispersión Raman, onda evanescente, etc. De todas ellas, la espectroscopía de luminiscencia molecular ha sido, desde muy antiguo, una de las técnicas analíticas más usadas, teniendo un considerable desarrollo a través de los años gracias a sus propiedades fundamentales de sensibilidad y selectividad [1, 51].

Los sensores de luminiscencia molecular se basan en la información obtenida a partir de los espectros de emisión de moléculas que han sido previamente excitadas. Dicha emisión luminiscente puede proceder del analito de interés o bien de una molécula indicadora sensible a éste (como es el caso de los sensores ópticos luminiscentes para la determinación de oxígeno). Así pues, en este apartado se describirá el fenómeno de la luminiscencia molecular, así como su utilidad para la determinación de oxígeno molecular. Finalmente, se describirán algunos de los principales métodos luminiscentes para la determinación de oxígeno.

0.3.3.1 El fenómeno luminiscente

La luminiscencia molecular es una rama de la espectroscopía de emisión en la que intervienen, fundamentalmente, los estados electrónicos de una molécula. Por tanto, las técnicas luminis-

centes son aquellas en las que existe una interacción entre la radiación electromagnética y la materia, existiendo procesos de absorción y/o emisión de dicha radiación. Concretamente, dentro del nombre de este colectivo pueden distinguirse tres tipos de fenómenos luminiscentes relacionados entre sí: fluorescencia, fosforescencia y quimioluminiscencia. Estos tres fenómenos están basados en la emisión de radiación electromagnética tras la formación de una especie excitada, ya sea mediante una reacción química (quimioluminiscencia) o mediante la absorción de fotones (fluorescencia y fosforescencia).

La fluorescencia y la fosforescencia se diferencian básicamente en las transiciones electrónicas que tienen lugar en el proceso de emisión de la radiación electromagnética, y que confieren a cada fenómeno unas características determinadas. Así, si la molécula se desactiva desde el primer estado singlete excitado al estado fundamental emitiendo un fotón, esta transición se denomina fluorescencia, mientras que si por el contrario el electrón pasa al primer estado triplete excitado, produciéndose un cambio en la multiplicidad de espín, y posteriormente la molécula pasa al estado fundamental emitiendo un fotón, esta transición se denomina fosforescencia. Esta última transición está prohibida por las reglas de selección y se caracteriza por su larga duración ($10^{-6} - 10^2$ s), mientras que la fluorescencia ocurre en tiempos más cortos ($10^{-11} - 10^{-7}$ s). Esto hace que las medidas de fosforescencia sean más sensibles que las de fluorescencia, ya que la concentración de desactivador necesaria para alcanzar la misma eficiencia de desactivación que en la fluorescencia es unas $10^3 - 10^5$ veces inferior, debido a los largos tiempos de vida de la emisión fosforescente [71]. Además, como los niveles de energía implicados en uno y otro proceso son diferentes, la fosforescencia suele presentarse en longitudes de onda mayores que la fluorescencia [51].

Todo proceso fotoluminiscente comienza con la absorción de luz (A), como resultado de la interacción del campo electromagnético de la luz excitatriz con los electrones débilmente asociados de la molécula a excitar, lo que provoca que la energía sea cedida por campo electromagnético de la luz a la molécula, alterándose la distribución electrónica de la misma. La intensidad de luz absorbida viene dada por la Ley de Lambert-Beer (ecuación (2)):

$$\log \left(\frac{I}{I_0} \right) = \varepsilon b C \quad \Leftrightarrow \quad I = I_0 10^{-\varepsilon b C} \quad (1)$$

$$I_a = I_0 - I = I_0 \left(1 - 10^{-\varepsilon b C} \right) \quad (2)$$

donde I_a es la intensidad de la luz absorbida, I_0 e I son respectivamente las intensidades de la luz incidente y transmitida, ε es la absorptividad molar (la cual representa la probabilidad de absorción de cada especie molecular), C es la concentración molar de la sustancia absorbente y b es el espesor (en centímetros) de la muestra atravesada por el haz de luz.

Las transiciones electrónicas que tienen lugar y que explican el fenómeno luminiscente se pueden representar mediante el diagrama de Jablonski (Figura 11), donde se muestran gráficamente las diferentes transiciones radiantes y no radiantes en una molécula después de su excitación a un estado singlete.

Cada estado electrónico molecular tiene varios estados vibracionales asociados, y se cumple que, a temperatura ambiente, casi todas las moléculas se encuentran en el estado vibracional más bajo del estado electrónico fundamental S_0 . Tras excitar la molécula con una radiación

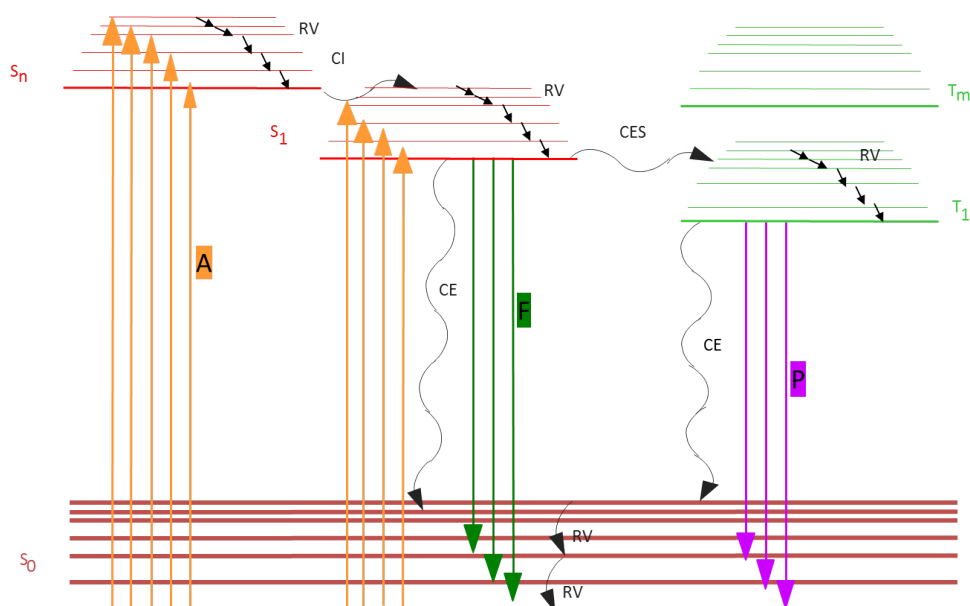


Figura 11: Diagrama de Jablonski. S_0 : estado singlete fundamental; S_n : estado singlete excitado de mayor energía; S_1 : estado singlete excitado de menor energía; T_1 : estado triplete excitado de menor energía; RV : relajación vibracional; CI : conversión interna; CE : conversión externa; CES : cruzamiento entre sistemas; A : absorción; F : fluorescencia; P : fosforescencia.

electromagnética de la región ultravioleta (UV) o visible (vis) del espectro, ésta es promovida a un determinado estado vibracional de un estado electrónico excitado ($S_0 \rightarrow S_n$). La pérdida del exceso de energía vibracional y electrónica en la molécula ocurre inmediatamente, y esta energía es absorbida por moléculas en fase condensada (moléculas del disolvente que se encuentran en constante colisión con el soluto excitado). Este proceso de desactivación térmica se llama *relajación vibracional* (RV) cuando la molécula pierde la energía vibracional dentro de un estado electrónico dado, S_n , hasta alcanzar el nivel vibracional más bajo de dicho estado, o *conversión interna* (CI) cuando la molécula sufre una transición sin radiación desde un estado electrónico superior al estado electrónico excitado de la misma multiplicidad de espín pero de menor energía ($S_n \rightarrow S_{n-1}$). Por tanto, puede decirse que los procesos de RV y de CI son los encargados de desactivar la molécula excitada hasta el nivel vibracional más bajo del estado singlete excitado de menor energía ($S_n \rightarrow S_1$), sin que ello conlleve la emisión de luz. Este proceso se lleva a cabo en un periodo de tiempo de 10^{-14} a 10^{-12} s.

Muchas moléculas regresan de nuevo al estado electrónico fundamental por desactivación térmica ($S_1 \rightarrow S_0$), proceso denominado como *conversión externa* (CE). Sin embargo, en algunas moléculas, concretamente aquellas con una estructura molecular rígida, el retorno desde el estado excitado singlete de menor energía al estado electrónico fundamental por CE está desfavorecido (debido a bajas probabilidades o a una duración excesiva de dicho proceso). En estas moléculas, el retorno al estado electrónico fundamental ocurre por mecanismos más lentos. Uno de estos mecanismos implica la emisión directa de radiación UV-vis, cuyas frecuencias y longitudes de onda vienen dadas por la diferencia de energía entre el estado excitado singlete de menor energía y el estado electrónico fundamental. La transición radiativa entre estos dos estados se llama *fluorescencia* (F) y ocurre entre 10^{-11} y 10^{-7} s después de la excitación inicial. El hecho de que el estado electrónico fundamental de la molécula tenga varios niveles vibracionales provoca que su fluorescencia no ocurra a una única longitud de

onda. De hecho, la fluorescencia se manifiesta sobre un amplio intervalo de longitudes de onda, las cuales corresponden a varias transiciones vibracionales que son componentes de una única transición electrónica.

Existe otro mecanismo por el cual una molécula se puede desactivar desde su estado singlete excitado de menor energía, y que, normalmente, ocurre al mismo tiempo que la fluorescencia. Este mecanismo implica el *cruzamiento entre sistemas (CES)*, y tiene lugar cuando se produce la transición de la molécula desde el estado singlete excitado más bajo a un cierto nivel vibracional del estado triplete excitado ($S_1 \rightarrow T_n$). El CES está acompañado por un cambio en el momento angular de espín, lo cual viola la ley de conservación del momento angular. El hecho de que esto ocurra es un millón de veces menos probable (más lento) que la CE (cambio de estado singlete a singlete). El CES ocurre a una velocidad comparable a la de fluorescencia, por lo tanto, compite con ella por la desactivación del estado singlete más bajo. Las moléculas que se desactivan por medio del CES llegarán por RV al nivel vibracional más bajo del estado triplete excitado de menor energía (T_1). Desde este estado, las moléculas pueden pasar al estado fundamental ($T_1 \rightarrow S_0$) con o sin emisión de radiación. Si lo hacen mediante un proceso radiante (emisión de fotones), esta emisión se denomina *fosforescencia (P)*, la cual también está prohibida y se caracteriza por su larga duración (desde 10^{-6} a 10^2 s).

0.3.3.2 Atenuación de la luminiscencia por el oxígeno molecular

A la hora de desarrollar un sensor óptico basado en medidas de luminiscencia es posible diferenciar tres casos: (1) el analito es un luminóforo, (2) el reactivo indicador presenta propiedades luminiscentes que varían como resultado de la interacción de éste, en el estado fundamental, con el analito, y (3) la emisión luminiscente del reactivo varía debido a la interacción de éste, en el estado excitado, con el analito [15], como es el caso de la detección de oxígeno [14].

Así pues, se define como atenuación o “*quenching*” de la luminiscencia a cualquier proceso que disminuya la fluorescencia o fosforescencia de una molécula luminiscente. Durante estos fenómenos de atenuación de los estados singlete y triplete por parte del oxígeno en su estado fundamental, $^3\Sigma_g O_2$, se generan, respectivamente, los estados excitados del oxígeno $^1\Sigma_g O_2^+$ y $^1\Delta_g O_2$ [201]. Los mecanismos fisicoquímicos por los cuales el oxígeno desactiva o atenúa estos procesos luminiscentes, y la relación del estado excitado de estas moléculas sobre la producción de oxígeno singlete, han sido ampliamente estudiados en la literatura [201–204]. Una comprensión más profunda de este proceso requiere tener en cuenta una gran variedad de procesos fotofísicos relacionados con el oxígeno [201].

En general, los procesos que pueden producir una atenuación de la luminiscencia son [51, 205]: (1) reacciones en el estado excitado (transferencia oxidativa o reductiva de electrones), (2) transferencias de energía por resonancia (*Fluorescence Resonance Energy Transfer*, FRET), (3) atenuación estática (*Static Quenching*, SQ), (4) atenuación colisional o dinámica (*Dynamic Quenching*, DQ) [14].

La atenuación de la luminiscencia por los procesos citados resulta en una disipación de la energía del luminóforo en forma de calor y no en forma lumínica. Para que esto tenga

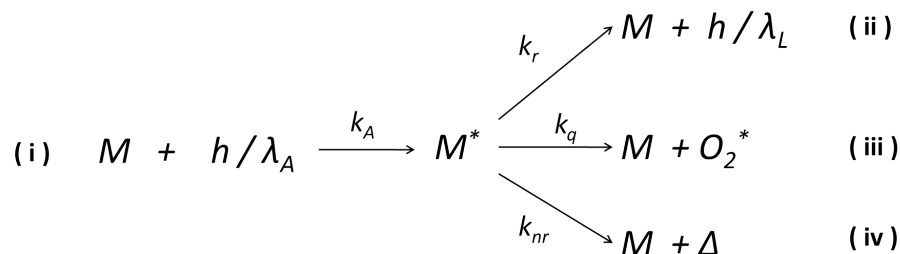


Figura 12: Representación de las reacciones implicadas en la excitación y emisión de un indicador. (i) Absorción de luz y excitación del luminóforo; (ii) Desactivación luminiscente; (iii) Desactivación por el oxígeno; (iv) Desactivación no radiativa.

lugar, es necesario un contacto molecular entre el luminóforo y el atenuador. La principal diferencia entre los distintos procesos de atenuación radica en la naturaleza del contacto entre dichas moléculas: en el caso de FRET, existe una transferencia de energía entre un donador (luminóforo) y un aceptor (atenuador) que se realiza a largas distancias. En cambio, la SQ y DQ son procesos de corto alcance ($< 2 \text{ \AA}$). En la SQ, el contacto entre el luminóforo y el atenuador (oxígeno) se debe a la formación de un compuesto. En cambio, la DQ implica un choque entre ambas moléculas, de ahí que en algunas ocasiones se denomine también “desactivación colisional”. Dado que la SQ implica que la atenuación ocurre cuando el oxígeno forma un compuesto con el indicador, el decaimiento de la luminiscencia tiene lugar sin necesidad de que exista una difusión. En cambio, la DQ está gobernada por la difusión del oxígeno en el medio donde se encuentra el luminóforo, lo cual es necesario para que se produzca la colisión entre las moléculas [14].

El oxígeno es uno de los desactivadores dinámicos de la luminiscencia más eficaces, y de ahí que la detección de oxígeno mediante este método haya experimentado un importante crecimiento en los últimos años [87, 206]. En la Figura 12 se muestran los procesos involucrados en la excitación y emisión de un indicador, donde pueden coexistir hasta cuatro tipos reacciones: absorción, desactivación luminiscente, desactivación por el oxígeno y desactivación térmica [14]. M y M^* es el luminóforo en su estado fundamental y excitado respectivamente, O_2 es el atenuador, λ_A y λ_L son las longitudes de onda de absorción y emisión respectivamente, y Δ es el término de energía por desactivación no radiativa. Las constantes involucradas en cada proceso se definen a continuación, las cuales usaremos también para describir y entender una serie de parámetros relacionados con la luminiscencia.

El tiempo de vida (τ) del estado excitado se define como el tiempo medio que la molécula pasa en su estado excitado antes de volver al estado fundamental por cualquiera de los mecanismos de desactivación citados en los procesos (ii) y (iv) [51]. El tiempo de vida engloba tanto a procesos radiativos como no radiativos, y en general se define sin tener en cuenta los procesos de desactivación (iii):

$$\tau = \frac{1}{k_{nr} + k_r} \quad (3)$$

donde k_r es la constante de la emisión radiativa del luminóforo, y k_{nr} es la constante de los procesos no radiativos.

Del mismo modo, el tiempo de vida de un luminóforo en ausencia de procesos no radiativos, es decir, cuando toda su energía se desactiva en forma lumínica según el proceso (ii), se

denomina tiempo de vida natural o intrínseco (τ_n), y es igual a:

$$\tau_n = \frac{1}{k_r} \quad (4)$$

Por otro lado, se puede definir el rendimiento cuántico (*Quantum Yield*, QY) de la luminiscencia como la relación entre el número de fotones absorbidos y el número de fotones emitidos en ausencia de atenuador:

$$QY = \frac{\text{fotones emitidos}}{\text{fotones absorbidos}} = \frac{k_r}{k_A} = \frac{k_r}{k_r + k_{nr}} \quad (5)$$

donde k_A es la constante del proceso de absorción de fotones. Esta definición nos permite calcular el tiempo de vida natural a partir del rendimiento cuántico y el tiempo de vida (ecuaciones (3),(4),(5)), como:

$$\tau_n = \frac{\tau}{QY} \quad (6)$$

Debido a los procesos no radiativos, τ_n es normalmente mayor que τ [14, 51]. Sin embargo, si la constante de los procesos no radiativos es mucho menor que la constante de la emisión radiativa ($k_{nr} \ll k_r$), el rendimiento cuántico será muy cercano a la unidad. En este caso tendremos una luminiscencia muy efectiva, donde todos los fotones absorbidos son reemitidos en forma de luz, y por tanto, el tiempo de vida del luminóforo será íntegramente su tiempo de vida natural.

Una forma de diferenciar la SQ de la DQ es precisamente mediante el tiempo de vida medio de la luminiscencia, ya que para la desactivación estática, donde existe una interacción continua entre el atenuador y el luminóforo, no se produce ningún cambio en el tiempo de vida medio, sino únicamente una disminución de la población de luminóforos [14, 70]. Sin embargo, en la DQ, aquellos luminóforos que tardan más en emitir tienen más probabilidad de ser atenuados por una colisión con el oxígeno, y como resultado, el tiempo de vida medio de la población disminuye.

Por otro lado, debido a que la DQ depende de un proceso de difusión, se verá afectada por cualquier efecto que varíe el coeficiente de difusión del atenuador en el material, lo que también puede servir para diferenciar la DQ de la SQ. Así, un aumento de la temperatura produce un aumento del coeficiente de difusión y, por tanto, un aumento de la DQ. Asimismo, un aumento de la temperatura produce una disminución de la estabilidad del compuesto luminóforo-atenuador, lo que provoca una disminución de la SQ. Por otro lado, un aumento de la viscosidad produce una disminución del coeficiente de difusión, lo que provoca una disminución de la DQ, mientras que la SQ, normalmente, no se ve afectada [14, 70].

Demas y Carraway no encontraron evidencias de atenuación estática en el uso de sensores ópticos para la determinación de oxígeno [207, 208]. En cualquier caso, como ya se ha mencionado, la desactivación estática ocurre cuando el luminóforo y el atenuador forman un compuesto en su estado fundamental, el cual no es luminiscente, por lo que las medidas de tiempo de vida no se verán afectadas [14, 209].

La ecuación de Stern-Volmer

El tiempo de vida de luminiscencia permite la resolución de una gran cantidad de problemas analíticos gracias a su relación con la concentración de oxígeno (analito). Normalmente se utiliza el subíndice “0” para indicar el valor del tiempo de vida en ausencia de oxígeno (τ_0), que viene dado por la siguiente expresión:

$$\tau_0 = \frac{1}{k_{nr} + k_r} \quad (7)$$

mientras que en presencia de atenuador $[O_2]$, contemplando los procesos (ii), (iii) y (iv) (véase la Figura 12), sería de la forma:

$$\tau = \frac{1}{k_{nr} + k_r + k_q[O_2]} \quad (8)$$

donde k_q es la constante de desactivación bimolecular. Dividiendo las expresiones (7) y (8) se obtiene:

$$\frac{\tau_0}{\tau} = 1 + \frac{k_q[O_2]}{k_{nr} + k_r} = 1 + k_q \tau_0 [O_2] \Rightarrow \frac{\tau_0}{\tau} = 1 + k_{SV}[O_2] \quad (9)$$

La ecuación (9) es conocida como la ecuación de Stern-Volmer, y relaciona los cambios producidos en el tiempo de vida del estado excitado (τ) con la concentración de oxígeno ($[O_2]$) mediante la constante de Stern-Volmer (k_{SV}). Aunque esta cinética fue desarrollada para procesos en disolución, su aplicación también es válida para procesos en fase sólida [14].

De un modo similar, también es posible relacionar la intensidad de la luminiscencia con la concentración de oxígeno. Cuando no existe oxígeno en el medio, la variación de la concentración de moléculas del estado excitado ($[M^*]_0$) a lo largo del tiempo vendrá dada por las constantes de desactivación de los procesos radiativos y no radiativos:

$$-\frac{d[M^*]_0}{dt} = k_A[M]_0 - k_{nr}[M^*]_0 - k_r[M^*]_0 \quad (10)$$

mientras que en presencia de oxígeno habrá que considerar también la constante de atenuación k_q , de modo que:

$$-\frac{d[M^*]}{dt} = k_A[M] - k_{nr}[M^*] - k_r[M^*] - k_q[M^*][O_2] \quad (11)$$

Una vez alcanzado el equilibrio, la concentración de moléculas del estado excitado se mantendrá constante, ya sea en ausencia o en presencia de oxígeno, pudiéndose aplicar entonces la aproximación del estado estacionario:

$$\frac{d[M^*]_0}{dt} = 0 \quad \frac{d[M^*]}{dt} = 0 \quad (12)$$

Así pues, a partir de las expresiones anteriores (10), (11) y (12), es posible despejar la concentración de moléculas del estado excitado en ausencia de oxígeno ($[M^*]_0$) y en presencia de oxígeno ($[M^*]$):

$$k_{nr}[M^*]_0 + k_r[M^*]_0 = k_A[M]_0 \Rightarrow [M^*]_0 = \frac{k_A[M]_0}{k_{nr} + k_r} \quad (13)$$

$$k_{nr}[M^*] + k_r[M^*] + k_q[M^*][O_2] = k_A[M] \Rightarrow [M^*] = \frac{k_A[M]}{k_{nr} + k_r + k_q[O_2]} \quad (14)$$

Teniendo en cuenta que la intensidad de la luminiscencia (I) es proporcional al número de moléculas que emiten en el estado excitado, dividiendo las expresiones (13) y (14), se obtiene:

$$\begin{aligned} \frac{I_0}{I} &= \frac{\alpha [M^*]_0}{\alpha [M^*]} = \frac{k_{nr} + k_r + k_q[O_2]}{k_{nr} + k_r} = 1 + \frac{k_q[O_2]}{k_{nr} + k_r} \Rightarrow \\ &\Rightarrow \frac{I_0}{I} = 1 + k_q \tau_0 [O_2] = 1 + k_{SV}[O_2] \end{aligned} \quad (15)$$

donde I_0 e I son las intensidades de emisión en ausencia y presencia de desactivador respectivamente, $[O_2]$ es la concentración del desactivador (oxígeno) y k_{SV} es la denominada constante de Stern-Volmer (que representa la sensibilidad). La ecuación de Stern-Volmer (15) es la encargada de relacionar la concentración de atenuador $[O_2]$ con la intensidad de luminiscencia (I) [51]. Por último, cabe destacar que las ecuaciones (9) y (15) solo serán equivalentes cuando el decaimiento de la luminiscencia sea monoexponencial, lo que en la práctica casi nunca ocurre [51].

Desviaciones de la ecuación de Stern-Volmer

En principio, la ecuación de Stern-Volmer ((9)) puede usarse para conocer la concentración de oxígeno o de cualquier otro atenuador ([Q]). Sin embargo, debido a que un gran número de moléculas pueden actuar como atenuadores de la luminiscencia (iones metálicos, oxidantes, reductores, surfactantes, proteínas, etc.) [51], para la detección de oxígeno es necesario que el luminóforo o molécula indicadora se encuentre aislada de los posibles interferentes, normalmente mediante el uso de membranas permeables al oxígeno [205, 206, 210]. La principal desventaja del uso de soportes sólidos es que añaden un cierto grado de heterogeneidad, lo que se manifiesta en desviaciones de la linealidad de la ecuación de Stern-Volmer debidas a decaimientos multiexponenciales o no exponenciales del tiempo de vida y/o de la intensidad luminiscente [14, 51, 70].

Estas desviaciones se pueden explicar en base a modelos que suponen que, dentro de un mismo sistema, existen sitios o ambientes donde el luminóforo presenta un diferente comportamiento hacia el oxígeno, siendo el modelo de dos sitios el más simple [211]. Algunos de estos modelos consideran que la desviación de la ecuación de Stern-Volmer es debida a una difusión no homogénea del oxígeno dentro de la fase que soporta al indicador [208]. Por ejemplo, en soportes de naturaleza polimérica, la teoría de adsorción dual (*dual mode sorption theory*) postula la existencia de dos tipos de sitios dentro del soporte con diferente dependencia de la presión parcial de oxígeno: uno de ellos donde la penetración de oxígeno sigue la ley de Henry, y otro donde el oxígeno se adsorbe siguiendo la isoterma de Langmuir [209].

En cualquier caso, estos modelos simplemente tratan de dar una explicación matemática a un proceso de naturaleza fisicoquímica, sin que ello implique que sean ciertos. Probablemente, las desviaciones de la linealidad respondan a una mezcla de muchos factores. Otros modelos de ajuste que no contemplan parámetros físicos se basan en distribuciones Gaussianas, exponenciales, Gamma, Lorentz, Max-Boltzmann, etc., pero todos ellos suelen presentar una mayor complejidad computacional y un peor ajuste que el modelo de sitios múltiples o multiestado [51, 212].

En el modelo multiestado, la interpretación matemática de este fenómeno puede hacerse considerando cada ambiente como una fracción del total de sitios en los que puede estar localizado el luminóforo, de modo que en cada uno de ellos el luminóforo se atenúa siguiendo la ecuación de Stern-Volmer, con su constante correspondiente [211]:

$$\frac{\tau_0}{\tau} = \frac{I_0}{I} = \left(\sum_{i=1}^m \frac{x_i}{1 + k_{SVi}[Q]} \right)^{-1} \quad (16)$$

donde m es el número de ambientes diferentes, k_{SVi} es la constante de Stern-Volmer asociada a cada ambiente, $[Q]$ es la concentración de atenuador (oxígeno en este caso) y x_i es la fracción del total de sitios con la que contribuye cada ambiente, donde $\sum x_i = 1$.

Por norma general, los modelos de dos ambientes ($m = 2$) suelen proporcionar un buen ajuste de los datos experimentales [73, 99]. Estos modelos fueron propuestos por Demas [213] y Lehrer [214] y se describen a continuación:

Modelo de Demas: en cada uno de los dos ambientes el luminóforo está expuesto de forma diferente al atenuador, y por tanto, las constantes k_{SV1} y k_{SV2} toman valores distintos pero mayores que cero:

$$\frac{\tau_0}{\tau} = \frac{I_0}{I} = \left(\frac{x_1}{1 + k_{SV1}[Q]} + \frac{x_2}{1 + k_{SV2}[Q]} \right)^{-1} \quad (17)$$

Modelo de Lehrer: hay dos ambientes diferentes, pero en este caso se considera que el luminóforo localizado en uno de los ambientes no se ve afectado por el atenuador, y por tanto, $k_{SV2} = 0$:

$$\frac{\tau_0}{\tau} = \frac{I_0}{I} = \left(\frac{x_1}{1 + k_{SV1}[Q]} + (1 - x_1) \right)^{-1} \quad (18)$$

La sensibilidad en los sensores luminiscentes

Para conocer cuáles son los parámetros que tienen una influencia sobre la sensibilidad, se puede considerar la ecuación de Stern-Volmer (ecuación (9) o (15)) y relacionarla con una serie de parámetros fisicoquímicos [209, 215]. Así pues, en procesos de atenuación dinámica (o gobernados por procesos de difusión), la constante bimolecular de la atenuación (k_q) se puede relacionar mediante la ecuación (19) con la eficiencia del atenuador, es decir, con la proporción de colisiones que atenúan efectivamente (α), y con la constante de accesibilidad del luminóforo al atenuador (k_{dif}) [51]:

$$k_q = \alpha k_{dif} \quad (19)$$

donde $\alpha = 1$ para compuestos fluorescentes, mientras que para compuestos fosforescentes esta probabilidad queda reducida a 1/9, debido a que la fosforescencia implica transiciones prohibidas [216]. k_{dif} es la constante bimolecular de difusión dada por la ecuación de Smoluchowski [217]:

$$k_{dif} = \frac{4\pi RND}{1000} \quad (20)$$

donde R es el radio colisional, N el número de Avogadro, y D es la suma de los coeficientes de difusión del atenuador y del luminóforo. En procesos controlados por la difusión del atenuador,

$D \approx D_{O_2}$. Por tanto, teniendo en cuenta las ecuaciones (19) y (20), se obtiene que la constante bimolecular de atenuación (k_q) es igual a:

$$k_q = \alpha \frac{4}{1000} \pi R D_{O_2} \quad (21)$$

En interfaces en equilibrio [14], la concentración de oxígeno [O_2] es proporcional a la presión parcial de oxígeno (p_{O_2}), según la Ley de Henry:

$$[O_2] = S_{O_2} p_{O_2} \quad (22)$$

donde S_{O_2} es la constante de solubilidad del oxígeno en el medio. Sustituyendo las ecuaciones (21) y (22) en la ecuación de Stern-Volmer (15):

$$\frac{I_0}{I} = 1 + k_{SV} [O_2] = 1 + \tau_0 k_q [O_2] = 1 + \tau_0 \alpha \frac{4}{1000} \pi R D_{O_2} S_{O_2} p_{O_2} \quad (23)$$

A partir de esta expresión, la constante de Stern-Volmer (k_{SV}) puede ser expresada como:

$$k_{SV} = \tau_0 \alpha \frac{4}{1000} \pi R D_{O_2} S_{O_2} \quad (24)$$

Por otro lado, haciendo uso de la ecuación de Stokes-Einstein [217], el coeficiente de difusión del oxígeno en disolución (D_{O_2}) puede ser calculado como:

$$D_{O_2} = \frac{kT}{6 \pi \eta R} \quad (25)$$

donde k es la constante de Boltzman, η la viscosidad del disolvente y T la temperatura. Así pues, analizando de la ecuaciones (24) y (25) se puede decir que la constante de Stern-volmer (y por ende, la sensibilidad de una fase sensora), es proporcional a:

$$k_{SV} \propto \tau_0 \frac{T}{\eta} S_{O_2} \quad (26)$$

A partir de la ecuación (26) se pueden deducir los factores que influyen sobre la sensibilidad (k_{SV}) de los sensores ópticos, los cuales vienen determinados tanto por las propiedades del luminóforo (tiempo de vida τ_0) como por las propiedades del medio que lo rodea (viscosidad η y solubilidad del oxígeno en el medio S_{O_2}), así como por la temperatura T . A continuación se detalla la influencia de cada uno de estos parámetros sobre la sensibilidad [14]:

- *Tiempo de vida luminóforo* (τ_0): Como ya se ha comentado, tiempos de vida largos suelen dar lugar a valores de sensibilidad más altos, ya que las moléculas del luminóforo permanecen durante más tiempo en el estado excitado, y por tanto, tienen una mayor probabilidad de ser desactivadas mediante colisiones con el oxígeno. No obstante, para un luminóforo con un tiempo de vida dado, también habrá que tener en cuenta otros procesos que pueden influir sobre su respuesta, tales como la autoatenuación (debida a la agregación del compuesto por problemas de solubilidad), procesos de transferencia de carga con otras moléculas, etc.

- *Temperatura (T)*: Como se observa en la ecuación (26), la k_{SV} es directamente proporcional a la temperatura. Esto es debido a que, a temperaturas más altas, el coeficiente de difusión del oxígeno en el medio que rodea al indicador también aumenta (ecuación (25)), favoreciéndose así el contacto entre el atenuador (oxígeno) y el indicador. Sin embargo, hay que tener en cuenta que los procesos luminiscentes se ven menos favorecidos a temperaturas altas (debido a la desactivación no radiativa (térmica) de la luminiscencia [213]).
- *Viscosidad (η)*: Como se deduce de la ecuación de Stokes-Einstein (25), la influencia de la viscosidad tiene un importante efecto sobre el coeficiente de difusión del oxígeno en el medio. Esto hace que al aumentar la viscosidad del medio también disminuya la sensibilidad, pues indirectamente se está variando la difusión del oxígeno en el medio, al reducir la movilidad de las moléculas.
- *Solubilidad a oxígeno (S_{O_2})*: La solubilidad del oxígeno en el medio es importante cuando el indicador se encuentra en disolventes de diferente naturaleza; por ejemplo, la solubilidad del oxígeno en disolventes orgánicos es mayor que en agua, y a su vez, la solubilidad en agua es 100 veces mayor que en la mayoría de las matrices rígidas [215].

0.3.3.3 Medidas de intensidad de la luminiscencia

En este tipo de medidas el compuesto luminiscente es excitado con una fuente de luz adecuada (uniforme y constante en el tiempo), registrándose de forma continua su intensidad de emisión a una determinada longitud de onda (véase la Figura 13). Aunque la emisión de luminiscencia se produce en todas las direcciones, el detector se sitúa normalmente en un ángulo de 90° con respecto a la fuente de luz. De este modo se evita que una gran parte de la luz de excitación pueda llegar al detector junto con la emisión, lo cual podría producir errores significativos en la medida de la intensidad de emisión. Una medida de intensidad será, por tanto, un valor promedio de la intensidad de emisión que presenta el compuesto luminiscente a una determinada longitud de onda y bajo ciertas condiciones experimentales. Si dicha intensidad de emisión es directamente proporcional a la intensidad de la luz de excitación, y asumiendo un decaimiento monoexponencial de la luminiscencia a lo largo del tiempo, $I(t) = I_0 e^{-t/\tau}$, entonces integrando en un tiempo infinito se obtiene que:

$$I = \int_0^{\infty} I_0 e^{-t/\tau} dt = I_0 \tau \quad (27)$$

El valor de I_0 depende de la concentración de luminóforo presente en la muestra y de los parámetros instrumentales, y se puede considerar constante bajo ciertas condiciones. Sin embargo, en la práctica, la mayoría de las muestras reales presentarán curvas de decaimiento algo más complejas, como por ejemplo de tipo multiexponencial, donde la curva de decaimiento vendrá dada por la suma pesada de diferentes términos exponenciales, y por tanto, la intensidad de emisión registrada en función del tiempo será de la forma: $I(t) = \sum_j \alpha_j e^{-t/\tau_j}$, donde τ_j es el tiempo de vida de cada uno de los decaimientos monoexponenciales y α_j el peso asociado a cada uno de ellos, donde $\sum_j \alpha_j = 1$. En cualquier caso, en las medidas de intensidad directas se puede decir que la intensidad de emisión registrada en estado estacionario es proporcional al tiempo de vida del compuesto luminiscente (ecuación (27)), cualquiera que sea la forma de su decaimiento [51]. Así, si la intensidad luminiscente del luminóforo

es atenuada en presencia de oxígeno, el tiempo de vida (τ) tomará valores más cortos, de forma que la intensidad de emisión registrada será menor. Un ejemplo se puede observar en las Figuras 13 y 14. En la Figura 13 se muestran los espectros de emisión de un compuesto luminiscente registrados a diferentes concentraciones de oxígeno entre 0% y 10%. Como puede observarse, la magnitud de la intensidad luminiscente a la longitud de onda señalada ($\lambda_{em} = 617 \text{ nm}$) es menor para las concentraciones de oxígeno más altas (fenómeno de la atenuación (o *quenching*) de la luminiscencia por el oxígeno molecular). En la Figura 14 se muestra la variación de la intensidad de emisión de dicho compuesto con la concentración de oxígeno. Como puede observarse, las medidas de intensidad son bastantes estables para una concentración dada, y diferentes para cada concentración de oxígeno. Así pues, las medidas de intensidad promedio obtenidas para cada concentración de oxígeno pueden ser relacionadas de forma directa con la concentración de oxígeno mediante la ecuación de Stern-Volmer (15) [51].

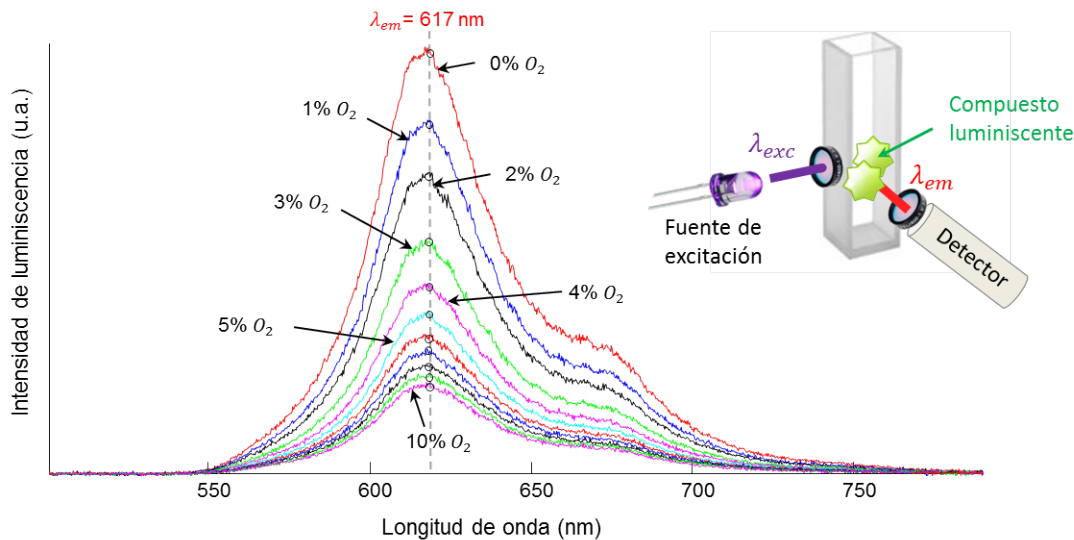


Figura 13: Espectros de emisión de un compuesto luminiscente a diferentes concentraciones de oxígeno entre 0% y 10%.

Las medidas de intensidad son relativamente simples y precisas en el laboratorio [51, 73, 78, 218], sin embargo, presentan algunas desventajas en aplicaciones reales, ya que son muy sensibles a una serie de factores tales como [219]: fluctuaciones de intensidad de la fuente de excitación, pérdidas de luz en el camino óptico (atenuación introducida por los filtros ópticos, lentes y otros componentes ópticos del sistema), derivas de los dispositivos optoelectrónicos, calidad de las superficies ópticas, concentración, lixiviación y/o fotodegradación del luminóforo, distancia de separación y orientación entre la fase sensora y el detector, etc.

Esta serie de factores influyen en la precisión de las medidas de intensidad registradas por el detector, pudiendo variar de una muestra a otra, lo que obliga a tener un especial cuidado con las condiciones de medida (posición de la fase sensora, parámetros instrumentales, etc.) y a realizar recalibraciones periódicas [220]. Además, otra desventaja de las medidas de intensidad es que suelen requerir el uso de una instrumentación cara y voluminosa [219, 221] (como es el caso de los espectrómetros de luminiscencia usados en la mayoría de los laboratorios

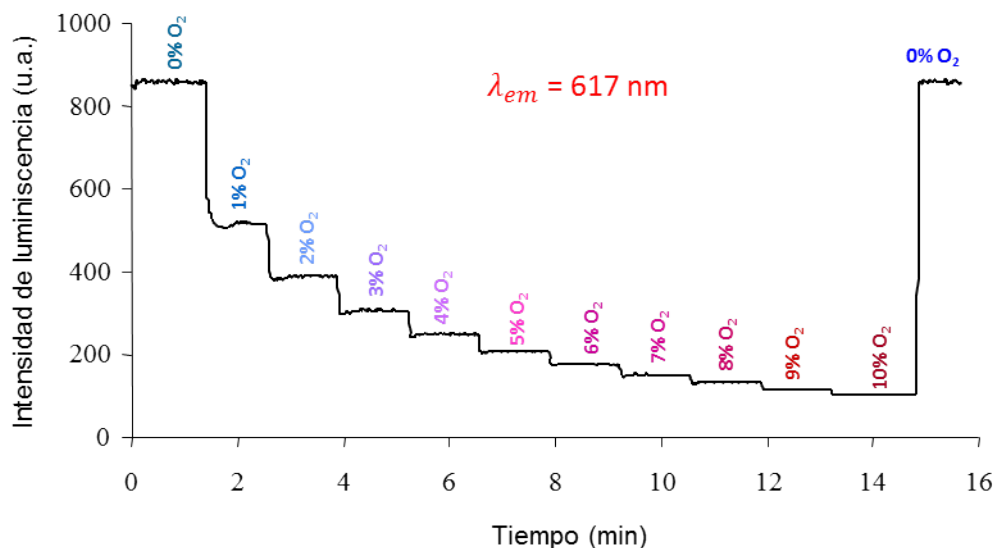


Figura 14: Variación de la intensidad de luminiscencia en función de la concentración de oxígeno.

[73]), o bien de equipos de medida portátiles igualmente caros y específicos (tales como los espectrofotómetros de fibra óptica [78] y las cámaras CCD [92]). No obstante, hay que destacar la importante presencia de estos instrumentos en laboratorios de medida avanzados, ya que suelen resultar muy útiles para llevar a cabo la caracterización espectroscópica de una amplia variedad de especies luminiscentes [73], así como para realizar calibraciones rápidas y sencillas de diversas fases sensoras [78]. Esto ha hecho que su uso nunca haya desaparecido y que se hayan desarrollado nuevos métodos de medida basados en medidas de intensidad que sean menos sensibles a todos esos factores externos (extrínsecos a la fase sensora). Tal es el caso de los métodos relativos, los cuales basan su funcionamiento en el uso de una referencia interna [222, 223]. Esta referencia es una molécula luminiscente no sensible al atenuador (oxígeno) coinmovilizada junto al indicador, o bien un luminóforo que presenta dos longitudes de onda de emisión, siendo solo una de ellas sensible al oxígeno [222, 224]. De este modo, el espectro de emisión presentará una región espectral no atenuada por el oxígeno (generalmente asociada a la fluorescencia), y otra región espectral sí atenuada por el oxígeno (generalmente asociada a la fosforescencia), tal como se observa en la Figura 15, lo cual permite obtener medidas de intensidad relativas mucho más robustas que las medidas de intensidad directas a una única longitud de onda.

Otro tipo de medidas relativas menos desarrolladas son las basadas en la detección de la polarización de la luminiscencia, donde, en lugar de usar una relación de intensidades a diferentes longitudes de onda, la medida relativa se consigue entre las componentes verticales y horizontales de una emisión polarizada [224]. Este método se basa en las propiedades de anisotropía de la emisión luminiscente [51, 224, 225] y pueden ser usadas en sistemas viscosos y con concentraciones de indicador mayores que las medidas de intensidad directas.

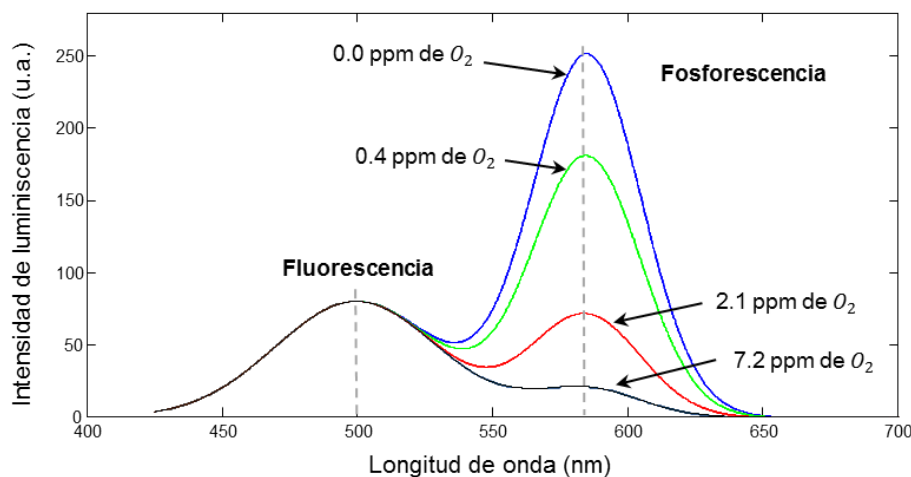


Figura 15: Medidas de intensidad relativas donde se observan dos regiones espectrales: una de ellas no afectada por el oxígeno (asociada a la fluorescencia) y otra de ellas sí afectada por el oxígeno (asociada a la fosforescencia) [222].

0.3.3.4 Medidas de tiempo de vida de la luminiscencia

Muchos de los problemas asociados a las medidas de intensidad directas pueden ser minimizados mediante la medida del tiempo de vida de luminiscencia [51, 226, 227]. El tiempo de vida, a diferencia de la intensidad, es una propiedad intrínseca del luminóforo, y por tanto es virtualmente independiente de muchas de las perturbaciones externas que sí afectan a las medidas de intensidad directas. Así, por ejemplo, el tiempo de vida es independiente de la concentración del luminóforo (la variación de la concentración del indicador por fotodescomposición o lixiviación no afecta a la medida del tiempo de vida), y en general tampoco se ve afectado por las posibles fluctuaciones de intensidad de la fuente de excitación, las interferencias de la luz ambiente o las derivas instrumentales del detector. Esto permite la determinación del tiempo de vida en escenarios o situaciones de medida difíciles (condiciones de baja SNR), tales como las medidas de campo [23], dispositivos de pequeño tamaño [22], etc. Por todo ello, las medidas de tiempo de vida (también llamadas de tiempo resuelto [51]) son a menudo las preferidas para el desarrollo de sensores ópticos luminiscentes robustos y fiables [51, 220, 227–229].

En la actualidad, las medidas de tiempo de vida son ampliamente usadas en espectroscopía de luminiscencia, especialmente para el estudio de macromoléculas biológicas, y cada vez más, para el análisis de imágenes celulares [51]. Además de las ventajas mencionadas anteriormente, otra característica destacable de las medidas de tiempo de vida es que contienen una mayor información que las medidas de estado estacionario (medidas de intensidad). Por ejemplo, considere el caso de una proteína que contiene dos residuos de triptófano, cada uno de ellos con un tiempo de vida distinto. Debido al solapamiento espectral de la absorción y la emisión, normalmente no será posible distinguir la emisión de los dos residuos usando medidas de estado estacionario (medidas de intensidad). Sin embargo, los datos de tiempo resuelto (o de tiempo de vida) pueden revelar dos tiempos de decaimiento diferentes, que pueden ser usados para resolver los espectros de emisión y las intensidades relativas de los dos residuos

de triptófano. Estas medidas de tiempo de vida pueden ayudar a entender cómo los residuos de triptófano presentes en la proteína se ven afectados por las interacciones con su sustrato u otras macromoléculas [51]. Existen otros muchos ejemplos donde las medidas de tiempo de vida resultan ventajosas frente a las medidas de estado estacionario, tales como: la distinción entre la atenuación dinámica y estática, la determinación de la eficiencia en procesos de transferencia de energía por resonancia (*Resonance Energy Transfer*, RET), el análisis 2D y 3D de imágenes celulares mediante microscopía de tiempo de vida de imágenes fluorescentes (*Fluorescence Lifetime Imaging Microscopy*, FLIM) [51, 92], etc.

Actualmente, los dos métodos predominantes para la medida del tiempo de vida son: los métodos basados en el dominio del tiempo (*Time-domain*, TD) y los métodos basados en el dominio de la frecuencia (*Frequency-domain*, FD) [51]. Antes de proceder con la descripción de estos dos métodos, analizaremos el significado del tiempo de vida o el tiempo de decaimiento de la luminiscencia.

Significado del tiempo de vida o tiempo de decaimiento de la luminiscencia

Antes de profundizar más en las medidas de tiempo de vida, es importante conocer cuál es el significado del tiempo de vida τ . Supongamos que disponemos de una muestra que contiene un determinado luminóforo y que ésta es excitada con un pulso de luz infinitamente estrecho (idealmente una función delta de Dirac δ). Esta excitación de la muestra dará como resultado una población inicial (n_0) de luminóforos en el estado excitado, la cual decaerá con una constante $\Gamma + k_{nr}$ según la siguiente expresión:

$$\frac{dn(t)}{dt} = (\Gamma + k_{nr})n(t) \quad (28)$$

donde $n(t)$ es el número de moléculas excitadas en un tiempo t posterior a la excitación, Γ es la constante de decaimiento radiativa y k_{nr} es la constante de decaimiento no radiativa. La emisión es un proceso aleatorio, de manera que cada luminóforo excitado tendrá la misma probabilidad de emitir en un periodo de tiempo dado. Esto resulta en un decaimiento exponencial de la población del moléculas del estado excitado, $n(t) = n_0 e^{-t/\tau}$ [51]. Sin embargo, en un experimento luminiscente no observaremos el número de moléculas excitadas, sino la intensidad de la luminiscencia, la cual va a ser proporcional a $n(t)$. Por lo tanto, la ecuación (28) también puede ser escrita en términos de la intensidad de la luminiscencia en función del tiempo $I(t)$. La integración de la ecuación (28), tras sustituir el número de moléculas $n(t)$ por la intensidad $I(t)$, da como resultado la expresión típica de un simple decaimiento exponencial:

$$I(t) = I_0 e^{-t/\tau} \quad (29)$$

donde I_0 es la intensidad inicial en un tiempo cero. El tiempo de vida τ es el inverso de la constante de decaimiento total, $\tau = (\Gamma + k_{nr})^{-1}$. En general, el inverso del tiempo de vida es la suma de las constantes que despueblan el estado excitado. El tiempo de vida de la luminiscencia puede ser determinado a partir de la pendiente de la gráfica del $\log I(t)$ versus t , o comúnmente ajustando los datos de intensidad con modelos de decaimiento apropiados [51].

El tiempo de vida τ se define como la cantidad de tiempo promedio que un luminóforo permanece en el estado excitado después de la excitación. Éste puede ser visto como el cálculo

del tiempo promedio en el estado excitado $\langle t \rangle$, cuyo valor se obtiene promediando t sobre el decaimiento de la intensidad del luminóforo:

$$\langle t \rangle = \frac{\int_0^{\infty} t I(t) dt}{\int_0^{\infty} I(t) dt} = \frac{\int_0^{\infty} t I_0 e^{-t/\tau} dt}{\int_0^{\infty} I_0 e^{-t/\tau} dt} \quad (30)$$

El denominador es igual a τ , mientras que la integración por partes del numerador da como resultado un valor igual a τ^2 . Por tanto, para un decaimiento exponencial simple, se cumple que el tiempo promedio que permanece un luminóforo en el estado excitado es igual al tiempo de vida [51]:

$$\langle t \rangle = \tau \quad (31)$$

Es importante destacar que la ecuación (31) no será cierta para modelos de decaimiento más complejos, tales como decaimientos multiexponenciales o no exponenciales. Por ejemplo, para el caso de una muestra que contenga una mezcla de luminóforos, la curva de decaimiento total de la luminiscencia se ajustará típicamente a un modelo multiexponencial:

$$I(t) = \sum_j \alpha_j e^{-t/\tau_j} \quad (32)$$

donde α_j representa la fracción de cada luminóforo en la cinética de desactivación registrada. Este mismo planteamiento es aplicable a sistemas heterogéneos que contienen un único indicador luminiscente en diferentes sitios, siendo entonces α_j la fracción de moléculas del compuesto luminiscente en cada sitio (donde $\sum_j \alpha_j$ se normaliza a la unidad). Para este tipo de sistemas multiexponenciales, el tiempo de vida promedio $\langle \tau \rangle$ vendrá dado por:

$$\langle t \rangle = \frac{\int_0^{\infty} t I(t) dt}{\int_0^{\infty} I(t) dt} = \frac{\sum_j \alpha_j \tau_j^2}{\sum_j \alpha_j \tau_j} \quad (33)$$

El valor del tiempo de vida promedio siempre podrá ser calculado a partir de la ecuación (30), independientemente del modelo de decaimiento considerado. Sin embargo, hay que tener en cuenta que el tiempo de vida promedio puede ser el resultado una función compleja de parámetros que describan el verdadero decaimiento de la intensidad de la luminiscencia. Por este motivo, debe tenerse mucho cuidado a la hora de realizar interpretaciones sobre el tiempo de vida promedio. Otro concepto importante es que el tiempo de vida es un promedio estadístico, y que los luminóforos emiten aleatoriamente durante todo el tiempo del decaimiento, por tanto, no todos ellos emitirán en un tiempo de retardo igual al del tiempo de vida. Así, dada una población numerosa de luminóforos, unos cuantos de ellos emitirán rápidamente después de la excitación, mientras que otros lo harán en tiempos mayores al del tiempo de vida. Esta distribución temporal de los fotones emitidos es el decaimiento de la intensidad de la luminiscencia [51].

Medidas de tiempo de vida en el dominio del tiempo

En las medidas de tiempo de vida en el dominio del tiempo (o de luz pulsada) la muestra se excita con un pulso de luz muy estrecho (véase la Figura 16), registrándose el decaimiento de la intensidad de luminiscencia en función del tiempo $I(t)$, que en el caso más simple sigue un decaimiento monoexponencial [51]. El ancho del pulso debe ser lo más estrecho posible

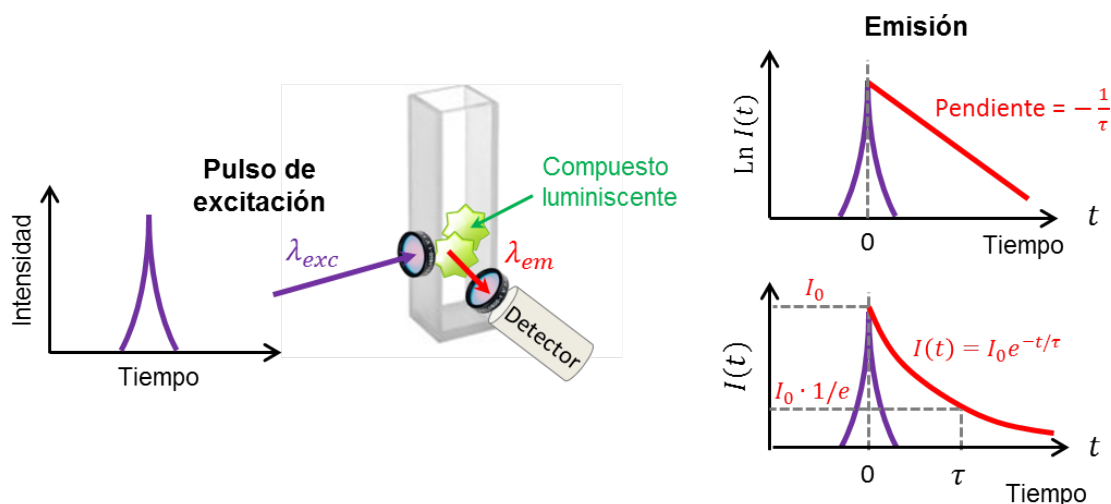


Figura 16: Medidas de tiempo de vida en el dominio del tiempo (o de luz pulsada) [51].

(idealmente una delta de Dirac), y preferiblemente mucho más corto que el tiempo de vida τ de la muestra [51]. La Figura 17 muestra los diferentes parámetros de tiempo que presenta un pulso de luz estrecho utilizado en medidas de tiempo de vida en el dominio del tiempo.

El tiempo de vida puede obtenerse fácilmente a partir de la pendiente de la gráfica del $\log I(t)$ versus t , o a partir del tiempo en el cual la intensidad de la luminiscencia decae a un $1/e$ de la intensidad inicial a $t = 0$ (I_0) (véase la Figura 16). Esto quiere decir que aproximadamente el 63% de las moléculas excitadas habrán emitido en un tiempo $t < \tau$, mientras que el 27% restante lo hará para $t > \tau$. La falta de linealidad de la gráfica del $\log I(t)$ versus t puede indicar la existencia de varios procesos luminiscentes en la muestra (debidos a la presencia de diferentes luminóforos, o de uno solo inmovilizado en un sistema heterogéneo con diferentes entornos), pudiendo ser el decaimiento total de la intensidad de luminiscencia de tipo multiexponencial o no exponencial [51, 230].

La presencia de un atenuador como el oxígeno producirá cambios en el tiempo de vida promedio del estado excitado del compuesto luminiscente, de manera que dichos cambios en el tiempo de vida podrán ser relacionados con la concentración de atenuador (oxígeno) mediante la ecuación de Stern-Volmer (ecuación (9)), (en el caso simple de un decaimiento monoexponencial de la luminiscencia).

Los tiempos de vida típicos de los compuestos fluorescentes varían entre 2–20 ns, mientras que los tiempos de vida de los compuestos fosforescentes son relativamente mayores, del orden de $1 \mu\text{s}$ –10 s [14]. Debido a que en este tipo de medidas es preciso registrar la variación de la intensidad de la luminiscencia a lo largo del tiempo (tras excitar la muestra con un pulso de luz estrecho), generalmente se requiere el uso de detectores de alta velocidad [51, 231], especialmente si nos encontramos ante procesos fluorescentes [51]. Por ello, en los últimos años ha habido un considerable interés por la búsqueda de nuevos indicadores luminiscentes con tiempos de vida relativamente largos (del orden de μs o mayores) [73, 232–235], de forma que se puedan reducir los costes y la complejidad de los dispositivos de medida empleados [51, 219, 222]. Pese a esto, los métodos de medida en el dominio del tiempo son ideales para eliminar las interferencias (luminiscencia de fondo y dispersión de la luz [51, 231, 236]), y

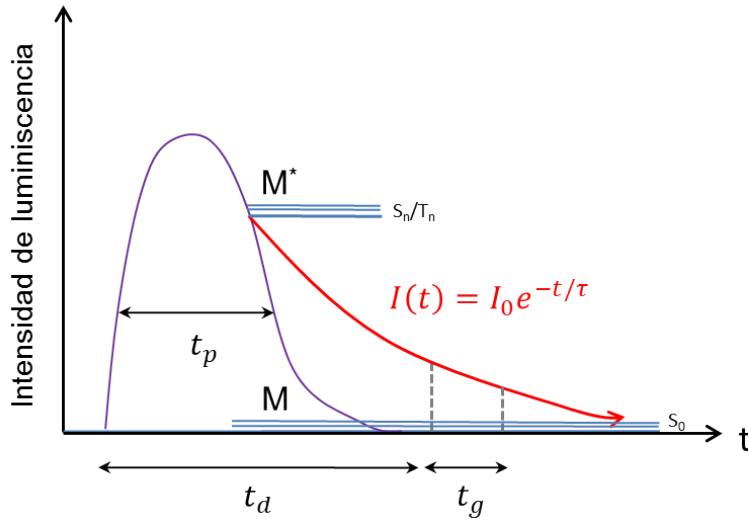


Figura 17: Parámetros de un pulso de luz utilizado en medidas de tiempo de vida en el dominio del tiempo: t_p es el tiempo medio que tarda el pulso de la lámpara, t_d es el tiempo de demora (“delay time”) y t_g es el tiempo de medida (“gate time”) durante el cual se registra la intensidad de la luminiscencia en función del tiempo $I(t)$.

en los últimos años ha habido un gran desarrollo en la instrumentación para este tipo de medidas, haciéndose en general más simple y barata [51, 223].

En los últimos años se han propuesto diferentes métodos o variantes de medida para la determinación del tiempo de vida en el dominio del tiempo [51, 92], como por ejemplo, el método de determinación rápida de tiempos de vida (*Rapid Lifetime Determination Method*, RLD) [92, 237], donde el tiempo de vida es calculado en dos instantes temporales diferentes de la curva de decaimiento, permitiendo así una monitorización de oxígeno autoreferenciada [92, 238]. Otra posibilidad es la obtención de imágenes de fluorescencia (FLIM) haciendo uso del método de conteo de fotones individuales correlacionados con el tiempo (*Time-Correlated Single-Photon Counting*, TCSPC) [51, 92, 239]. Este último método es quizá uno de los más utilizados en la actualidad, y consiste en excitar la muestra luminiscente con un pulso de luz muy estrecho (del orden de picosegundos o femtosegundos), registrando posteriormente la emisión luminiscente. En el método TCSPC se ajustan las condiciones de medida para detectar a lo sumo un único fotón de la emisión por cada pulso de excitación. De hecho, la tasa típica de detección suele ser de 1 fotón por cada 100 pulsos de excitación. En este método se mide la diferencia de tiempo entre el pulso de excitación y el fotón observado (para un número muy elevado de repeticiones), y se almacena en un histograma. El eje- x de dicho histograma son las diferencias de tiempos medidas y el eje- y el número de fotones detectados para esas diferencias de tiempos. Cuando la tasa de detección de fotones es mucho menor a 1 fotón por pulso, el histograma representa la forma de onda del decaimiento [51].

Medidas de tiempo de vida en el dominio de la frecuencia

Los métodos basados en el dominio de la frecuencia no suelen requerir de una instrumentación tan compleja y costosa como la de los métodos basados en el dominio del tiempo [51, 219–221], lo que ha fomentado su uso y desarrollo en los últimos años, convirtiéndolos en los métodos de medida preferidos para el desarrollo de sistemas sensores baratos, sencillos,

portables y fiables [51, 219]. En estas medidas, la muestra se excita con una fuente de luz modulada en intensidad (generalmente una señal periódica de determinada frecuencia con forma de onda sinusoidal o cuadrada) [51] (véase la Figura 18), la cual produce una emisión luminiscente modulada de la misma frecuencia. Sin embargo, debido al tiempo de vida intrínseco de la molécula indicadora (cuyo valor varía en función de la concentración de oxígeno), la señal de emisión no será idéntica a la de excitación, mostrando un cierto retraso temporal y un cambio de amplitud con respecto a ésta (véase la Figura 18). El retraso temporal es medido como un desplazamiento de fase (φ_ω) entre las señales de excitación y emisión, donde ω es la frecuencia de modulación en rad/s ($\omega = 2\pi f$). El tiempo de vida finito del estado excitado también produce una disminución de la amplitud pico-a-pico de la emisión modulada con respecto a la amplitud pico-a-pico de la excitación modulada (tomada como referencia) [51, 229]. Dicha relación de amplitudes entre las señales de excitación y emisión es lo que se conoce como factor de modulación (m_ω) (véase la Figura 18 para más detalles).

El desplazamiento de fase φ_ω y el factor de modulación m_ω de la emisión modulada dependen de los valores relativos del tiempo de vida y la frecuencia de modulación (a medida que aumenta la frecuencia de modulación f (en Hz), φ_ω aumenta, mientras que m_ω disminuye). La dependencia de la fase φ y el factor de modulación m con la frecuencia de modulación se usa a menudo para obtener alguna información sobre la forma del decaimiento de la intensidad de la muestra, para posteriormente interpretar dicha información en términos de características moleculares de la muestra. Por tanto, en los métodos basados en el dominio de la frecuencia es habitual la medida de φ_ω y m_ω en un intervalo amplio de frecuencias de modulación, para obtener así lo que se denomina como la respuesta en frecuencia de la muestra. A medida que aumenta la frecuencia de modulación, la fase φ_ω se incrementa desde 0 a 90° (siendo éste el máximo valor de fase que puede obtenerse para el caso de decaimientos exponenciales o multiexponenciales, independientemente de la frecuencia de modulación) [51]. Por su parte, el factor de modulación m_ω disminuye desde 1.0 hasta 0 a medida que se incrementa la frecuencia de modulación (m_ω tomará un valor cero cuando la frecuencia de modulación f sea mucho mayor que la tasa de emisión de la muestra ($f \gg 1/\tau$)) [51]. La forma de la respuesta en frecuencia vendrá determinada por el número “decaimientos” observados en la muestra. Si el decaimiento de la luminiscencia responde a una función exponencial simple, la respuesta en frecuencia es simple, y en este caso puede usarse la fase φ_ω y/o el factor de modulación m_ω obtenidos a cualquier frecuencia para calcular el tiempo de vida promedio de la muestra. Para un decaimiento exponencial simple, la fase y el factor de modulación pueden ser relacionados con el tiempo de vida (τ) mediante las siguientes ecuaciones [51]:

$$\tan(\varphi_\omega) = \omega\tau = 2\pi f\tau \quad (34)$$

$$m_\omega = (1 + \omega^2\tau^2)^{-1/2} \quad (35)$$

Estas ecuaciones pueden ser obtenidas por diferentes vías [51, 240–242]. El enfoque más simple se basa en el uso de las ecuaciones cinéticas [240, 241], y supone que la excitación es una fuente de luz modulada sinusoidalmente (véase la Figura 18):

$$L(t) = a + b\text{sen}(\omega t) \quad (36)$$

donde $b/a = m_L$ es la modulación de la luz incidente. La emisión luminiscente presenta la misma frecuencia que la excitación, pero diferente fase y modulación. Así pues, la población

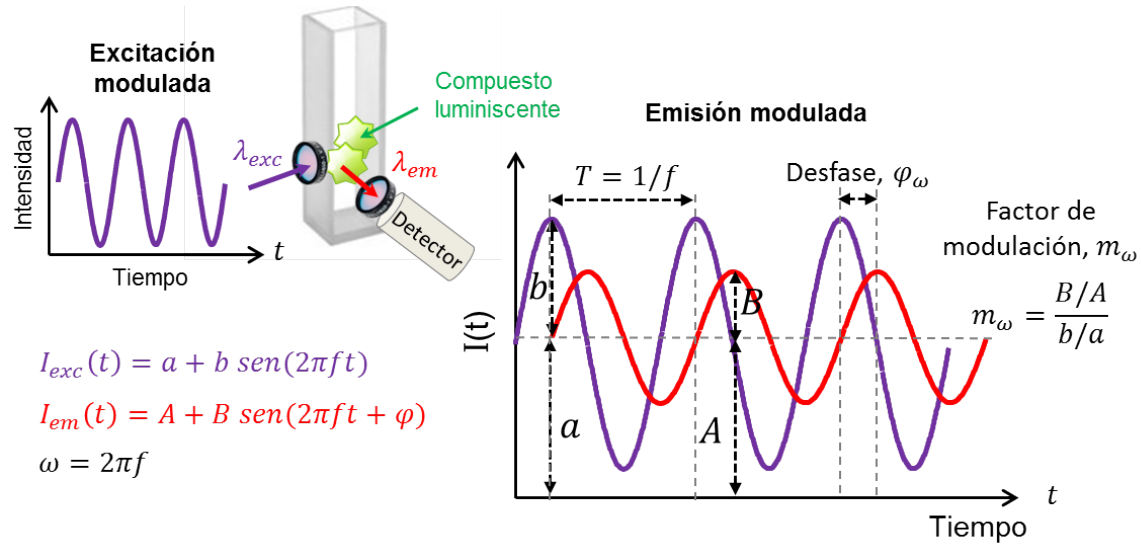


Figura 18: Medidas de tiempo de vida en el dominio de la frecuencia (o de modulación de fase) [51].

de moléculas en el estado excitado puede ser expresada de la forma:

$$N(t) = A + B \text{sen}(\omega t - \varphi) \quad (37)$$

donde dicha expresión permite relacionar la población de moléculas en el estado excitado $N(t)$ con el desplazamiento de fase (φ) y el factor de modulación (m) de la emisión modulada. La intensidad $I(t)$ en cualquier instante de tiempo es proporcional al número de moléculas en el estado excitado $N(t)$. Por tanto, suponiendo un decaimiento monoexponencial de la intensidad de luminiscencia (tras excitar la muestra con un pulso de luz (función δ)):

$$I(t) = I_0 e^{-t/\tau} \quad (38)$$

la ecuación diferencial que describe la variación temporal de la población de moléculas en el estado excitado vendrá dada por:

$$\frac{dI(t)}{dt} = -\frac{1}{\tau} I(t) + L(t) \quad (39)$$

Sustituyendo la ecuación (37) dentro de la ecuación (39) se obtiene:

$$\omega B \cos(\omega t - \varphi) = -\frac{1}{\tau} [A + B \text{sen}(\omega t - \varphi)] + a + b \text{sen}(\omega t) \quad (40)$$

Esta ecuación será válida para cualquier valor tiempo t . La relación entre los valores de a , b , A y B y el tiempo de vida de luminiscencia τ puede obtenerse mediante el desarrollo de las funciones seno y coseno, e igualando los términos constantes y los términos en $\text{sen}(\omega t)$ y $\text{cos}(\omega t)$. Esto proporciona las siguientes expresiones:

$$a - (1/\tau)A = 0 \quad (41)$$

$$\omega \cos(\varphi) - (1/\tau) \text{sen}(\varphi) = 0 \quad (42)$$

$$\omega \operatorname{sen}(\varphi) + (1/\tau) \cos(\varphi) = b/B \quad (43)$$

A partir de la ecuación (42) se obtiene la relación entre el tiempo de vida y el desplazamiento de fase (mostrada en la ecuación (34)):

$$\frac{\operatorname{sen}(\varphi)}{\cos(\varphi)} = \tan(\varphi) = \omega \tau_\varphi \quad (44)$$

Elevando al cuadrado las ecuaciones (42) y (43) y sumándolas, se obtiene:

$$[\omega^2 + (1/\tau)^2] = (b/B)^2 \quad (45)$$

Finalmente, teniendo en cuenta que $A = a\tau$ [ecuación (41)], se obtiene que:

$$m = \frac{B/A}{b/a} = [1 + \omega^2 \tau_m^2]^{-1/2} \quad (46)$$

donde dicha expresión muestra la relación entre el tiempo de vida y el factor de modulación (mostrada en la ecuación (35)).

Una forma alternativa de obtener las ecuaciones (34) y (35) es mediante la integral de convolución [243]. La expresión de la intensidad en función del tiempo $I(t)$ viene dada por la convolución de la función de excitación (ecuación (36)) con la función impulso-respuesta (ecuación (38)):

$$I(t) = \int_0^\infty L(t') + I(t - t') dt' \quad (47)$$

Sustituyendo las ecuaciones (36) y (38) en la ecuación (47) se obtiene:

$$I(t) = I_0 \int_0^\infty e^{-t'/\tau} |a + b \cos(\omega t - \omega t')| dt' \quad (48)$$

Estas integrales pueden ser calculadas recordando las siguientes identidades:

$$\cos(x - y) = \cos(x) \cos(y) + \operatorname{sen}(x) \operatorname{sen}(y) \quad (49)$$

$$\int_0^\infty e^{-kx} \operatorname{sen}(mx) dx = \frac{m}{k^2 + m^2} \quad (50)$$

$$\int_0^\infty e^{-kx} \cos(mx) dx = \frac{a}{k^2 + m^2} \quad (51)$$

Usando estas identidades se obtiene:

$$\int_0^\infty e^{-t'/\tau} \cos(\omega(t - t')) dt' = \quad (52)$$

$$= \frac{\tau}{\sqrt{1 + \omega^2 \tau^2}} \left\{ \frac{\cos(\omega t)}{\sqrt{1 + \omega^2 \tau^2}} + \frac{\omega t \operatorname{sen}(\omega t)}{\sqrt{1 + \omega^2 \tau^2}} \right\} = \frac{\tau}{\sqrt{1 + \omega^2 \tau^2}} \cos(\omega t - \varphi) \quad (53)$$

donde la ecuación (53) ha sido obtenida usando las expresiones:

$$\cos(\varphi) = (1 + \omega^2 \tau^2)^{-1/2} \quad (54)$$

$$\tan(\varphi) = \frac{\text{sen}(\varphi)}{\text{cos}(\varphi)} \quad (55)$$

Por tanto, la función de la intensidad $I(t)$ vendrá dada por:

$$I(t) = I_0 \tau \left\{ a + \frac{b}{\sqrt{1 + \omega^2 \tau^2}} \cos(\omega t - \varphi) \right\} \quad (56)$$

Esta expresión muestra que la emisión modulada está multiplicada por un factor $(1/\sqrt{1 + \omega^2 \tau^2})$ y desfasada un ángulo φ con respecto a la señal de excitación [51].

Como puede deducirse de las ecuaciones (34) y (35), tanto el desplazamiento de fase φ_ω como el factor de modulación m_ω pueden ser usados para calcular el tiempo de vida de la muestra a una frecuencia de modulación fija [51, 229]. No obstante, en la práctica, la medida del desfase suele ser más utilizada que la del factor de modulación [229], ya que ésta última, al igual que sucede con las medidas de intensidad directas, es más sensible a factores externos tales como: fluctuaciones de intensidad de la fuente de excitación, interferencias de la luz ambiental, fotodegradación del compuesto, atenuación de la señal en el camino óptico, etc. Los tiempos de vida calculados a partir de datos de φ_ω o m_ω obtenidos a una simple frecuencia, suelen ser denominados generalmente como tiempos de vida “aparentes” y vienen dados por [51]:

$$\tau_\varphi^{ap} = \frac{1}{\omega} \tan(\varphi_\omega) \quad (57)$$

$$\tau_m^{ap} = \frac{1}{\omega} \left[\frac{1}{m_\omega^2} - 1 \right]^{1/2} \quad (58)$$

Estos valores de tiempo de vida aparentes (τ_φ^{ap}) y (τ_m^{ap}) solo serán iguales si el decaimiento de la intensidad de la muestra responde a un modelo exponencial simple, en cuyo caso se cumple que [51]:

$$\tau_\varphi^{ap} = \tau_m^{ap} = \tau \quad (59)$$

Para el caso de decaimientos multiexponenciales o no exponenciales (frecuentes en la mayoría de las muestras de interés), los tiempos de vida aparentes determinados a partir del desfase serán más cortos que los tiempos de vida aparentes determinados a partir del factor de modulación ($\tau_\varphi^{ap} < \tau_m^{ap}$). Además, (τ_φ^{ap}) y (τ_m^{ap}) tomarán valores más pequeños a frecuencias de modulación más altas. Así pues, puede decirse que los tiempos de vida aparentes (τ_φ^{ap}) y (τ_m^{ap}) dependen de las condiciones experimentales, esto es, del método de medida usado (desfase o factor de modulación) y de la frecuencia de modulación. Por tanto, generalmente será difícil interpretar estos valores aparentes en términos de las características moleculares de la muestra. Además, tampoco se miden realmente tiempos de vida aparentes, ya que éstos valores son estimados indirectamente a partir de otras cantidades medibles, como son en este caso los valores de desfase y del factor de modulación [51].

0.4 Instrumentación empleada en sensores ópticos

Hoy en día se pueden encontrar en la literatura numerosas referencias relativas a la instrumentación empleada en análisis químico para llevar a cabo medidas de fluorescencia y fosforescencia [51, 244–250].

En general, la adquisición de datos luminiscentes requiere el uso de una serie de componentes básicos que aparecen representados en la Figura 19: una fuente de radiación para la excitación, un selector de longitudes de onda de excitación, un compartimento para la muestra, un dispositivo para seleccionar la longitud de onda de emisión y un sistema de detección. Concretamente, para medir señales fosforescentes, es necesario distinguirlas de las señales fluorescentes y, por ello, se requiere también en este caso el uso de un obturador rotatorio (normalmente llamado fosforoscopia) o una lámpara pulsante provista de un sistema de “*detector puerta*” (del inglés, *gate detector*) [244].

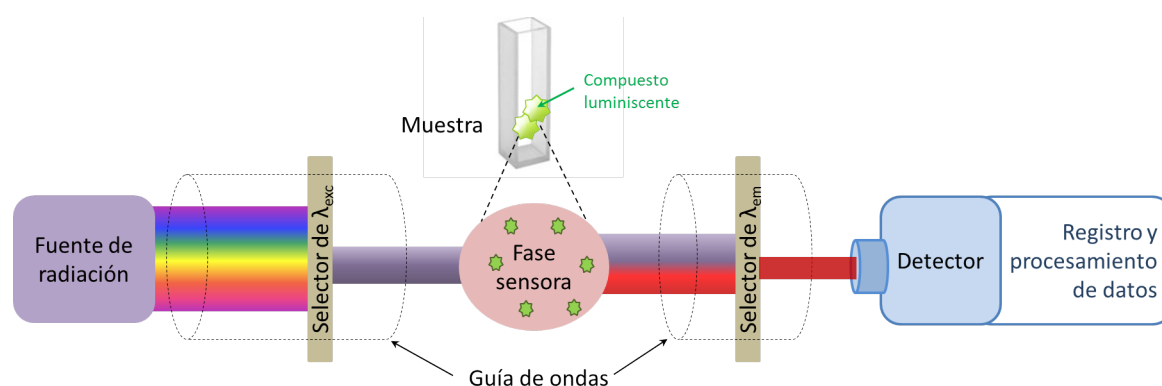


Figura 19: Componentes básicos de la instrumentación empleada para llevar a cabo medidas de luminiscencia. La línea de puntos indica la posibilidad de utilizar una guía de onda para conducir el haz de luz. λ_{exc} y λ_{em} son las longitudes de onda de excitación y emisión de la fase sensora respectivamente [14].

En la mayoría de los luminómetros comerciales y de investigación, algunos de los componentes empleados coinciden con los usados en los espectrofotómetros de ultravioleta-visible y, aunque hay algunas similitudes en el diseño instrumental de ambos, también existen importantes diferencias en su diseño debido, sobre todo, a que la intensidad de luz incidente sobre el detector es mucho más baja para medidas luminiscentes que para medidas fotométricas [251]. Esto se debe a que: (1) las medidas luminiscentes analíticas normalmente se hacen con bajas absorciones ($A < 0.05$), (2) la fracción de luz emitida que incide en el sistema de detección es bastante pequeña, (3) la observación se produce en una pequeña porción de la cubeta de muestra (o de la fase sensora), y (4) los rendimientos cuánticos de fluorescencia y fosforescencia son considerablemente inferiores a la unidad [244].

Por todo ello, la instrumentación luminiscente está diseñada para maximizar la capacidad de detección de la señal óptica, con el objetivo de obtener una relación señal-ruido lo más alta posible. En este apartado se van a abordar los componentes básicos de un espectrofosforímetro, destacando las aportaciones más recientes recogidas en la bibliografía, así como sus aspectos positivos y negativos en el diseño instrumental de equipos.

0.4.1 Fuentes de excitación

0.4.1.1 Lámparas convencionales

Hoy día, las fuentes de excitación más usadas en instrumentación luminiscente para la medida de fluorescencia son: la lámpara de arco de xenón (lámpara de descarga de gas) y la lámpara de mercurio de alta presión, aunque prácticamente no se usan para llevar a cabo medidas de fosforescencia. De las dos lámparas, la de arco de xenón (Figura 20(a)) es la que se ha usado y se usa con mayor frecuencia debido a su emisión continua en la zona del ultravioleta-visible [245], mientras que la lámpara de mercurio de alta presión (Figura 20(b)) se utiliza cuando las especies luminiscentes pueden excitarse con una de las líneas de emisión del mercurio [244].

Otro tipo de lámparas convencionales que también se han usado en el diseño de espectroluminómetros son las lámparas incandescentes (de wolframio y wolframio/halógeno) y las lámparas de vapor de mercurio de baja presión [252, 253]. Las primeras son baratas y estables y no requieren complicadas fuentes de alimentación, si bien presentan la desventaja de su limitado intervalo de longitudes de onda de emisión disponible (en la zona del visible). Las lámparas de vapor de mercurio de baja presión se han usado, con alguna extensión, en análisis luminiscente, ya que tampoco requieren una sofisticada fuente de alimentación y también son muy estables, si bien presentan la limitación de emitir en líneas específicas. Este tipo de lámparas se usan también como fuentes para calibrar los monocromadores [244].

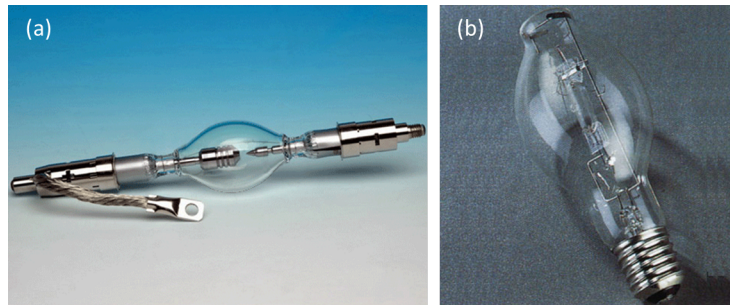


Figura 20: Lámparas convencionales: (a) lámpara de arco de xenón, (b) lámpara de mercurio de alta presión.

0.4.1.2 Lámparas pulsantes

Actualmente, las lámparas pulsantes son las fuentes más usadas en instrumentación para medidas de fosforescencia, pues al emitir pulsos, permiten que se puedan distinguir las señales de fosforescencia y fluorescencia sin la necesidad de usar un fosforoscopio. Además, ofrecen una construcción más compacta y un menor calentamiento que las lámparas continuas, proporcionan una mayor intensidad de luz, emiten en todas las regiones del espectro UV-Vis-IR y presentan una mayor estabilidad del arco (lo que se traduce en una mayor durabilidad de la lámpara) [244].

Aunque es posible encontrar en la bibliografía la descripción de alguna lámpara pulsante de estroncio 90 [254], sin duda las lámparas más usadas son las de xenón [255–257] (Figura 21). Las lámparas de pulsos están formadas por una bombilla compacta rellena de xenón de alta

pureza a una elevada presión y su distribución espectral varía en función del material con el cual se construye la ventana de la lámpara. Esta ventana se localiza en la parte superior de la bombilla y puede ser de sílice sintética, de vidrio UV o de borosilicato. El interior de la lámpara consta de un electrodo principal con excelente emisión de electrones y varias sondas denominadas sondas desencadenantes. Además, están provistas de un espejo que refleja eficientemente la luz emitida para aumentar su poder luminoso. La descarga de la lámpara de pulsos se crea aplicando un voltaje determinado entre el cátodo y el ánodo, apareciendo de esta forma una diferencia de potencial entre ambos electrodos. Esta diferencia hace que se carguen paulatinamente las sondas desencadenantes hasta que descargan su energía en forma de luz [244].



Figura 21: Lámparas comerciales de pulsos [244].

La duración y anchura del pulso depende de la capacitancia del condensador de la fuente de alimentación principal, de la longitud del cable de conexión al alimentador y del voltaje empleado. La duración del pulso también depende de la distancia entre el ánodo y el cátodo. La intensidad del pulso producido por la lámpara es inversamente proporcional a la distancia entre los electrodos, variando también con la temperatura, ya que la eficacia del pulso varía con la presión del gas. Para conseguir un buen funcionamiento de una lámpara de pulsos, hay que mantenerla encendida al menos durante 10 minutos para que alcance el máximo de emisión y se establezca su intensidad. Las lámparas de pulsos requieren voltajes altos (entre 5 y 7 kV por pulso), por lo que se genera ruido electromagnético que es necesario contrarrestar en los instrumentos usados para medidas de precisión. El ruido es generado por la lámpara, la conexión al alimentador de corriente, el cable y la fuente de alimentación; por consiguiente, para minimizarlo es necesario que tanto la lámpara como la conexión al alimentador de corriente se introduzcan en una caja metálica, que la conexión al alimentador sea a través de un cable apantallado y que la fuente de alimentación esté conectada a tierra.

Para que las lámparas se puedan usar en medidas de fosforescencia, deben poseer una intensidad uniforme con el tiempo. Así, puesto que la intensidad luminosa es directamente proporcional a la corriente proporcionada por la fuente de alimentación, se precisa la utilización de un estabilizador de corriente [244].

0.4.1.3 Diodos fotoemisivos (LEDs)

Los diodos fotoemisivos, también llamados diodos de emisión de luz, son más conocidos por sus siglas inglesas LED (*“Light Emission Diode”*). Aunque parecen bombillas diminutas

(véase la Figura 22(a)), son realmente muy diferentes a éstas tanto en su fabricación como en la forma en la que producen la luz, y son fuentes de luz muy fiables que, en función de su configuración, pueden resultar muy útiles para diferentes aplicaciones [244].

Un diodo es un simple y pequeño dispositivo electrónico de dos terminales que permite la circulación de la corriente eléctrica a través de él en un solo sentido. Los LEDs son un tipo especial de diodos, formados básicamente por cuatro componentes: una estructura de plomo, una unión positivo-negativa o unión $p-n$ (que generalmente está fabricada con galio combinado con arsénico, fósforo, aluminio o indio), contactos metálicos para las conexiones y todos estos componentes encapsulados en una base epoxy. La base epoxy que reviste los componentes electrónicos del diodo LED es una resina sólida cristalina irrompible que los hace muy resistentes, y por tanto, favorece la longevidad de los LEDs, posibilitando una duración de 10 años o más funcionando continuamente [244]. Las configuraciones posibles a la hora de implementar un LED son diversas, y aunque en esencia el LED es una unión pn polarizada en directa, es posible mejorar sus características mediante el empleo de heteroestructuras. En general, son tres los tipos de estructuras que suelen emplearse: LED de emisión superficial, LED de emisión lateral y LED superluminiscente [258].

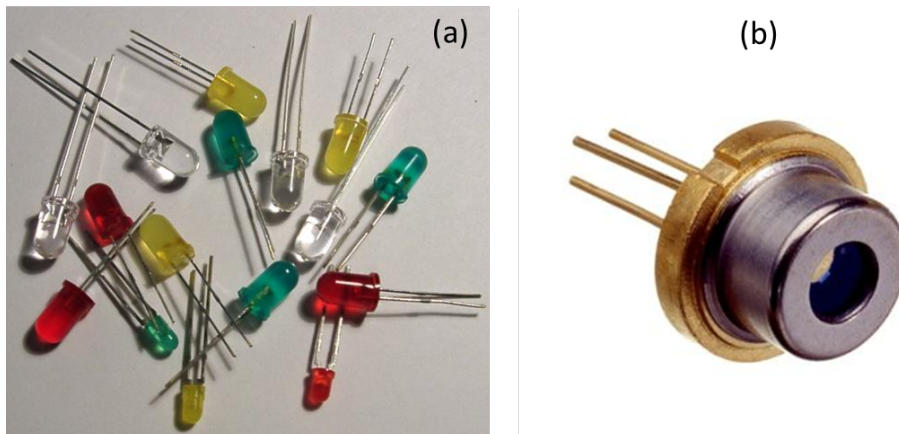


Figura 22: (a) Diodos emisores de luz (LEDs); (b) Diodo láser.

En corriente continua (CC) o polarización directa, todos los diodos emiten cierta cantidad de radiación cuando los pares electrón-hueco se recombinan; es decir, cuando los electrones “caen” desde la banda de conducción (de mayor energía) a la banda de valencia (de menor energía) emitiendo fotones en el proceso. Este efecto es llamado electroluminiscencia, y el color de la luz (correspondiente a la energía del fotón) dependerá de la altura de la banda prohibida (diferencias de energía entre las bandas de conducción y valencia), es decir, de los materiales empleados. Los diodos convencionales, de silicio o germanio, emiten radiación infrarroja muy alejada del espectro visible. Sin embargo, con materiales especiales pueden conseguirse longitudes de onda visibles [259, 260] (véase la Figura 23). El primer LED que emitía en el espectro visible fue desarrollado por el ingeniero Nick Holonyak (de la *General Electric Company*) en 1962.

La calidad de los LEDs y, por tanto, la cantidad de luz que emiten, no solo depende de las características intrínsecas del propio LED, sino también de la electrónica que lo controla

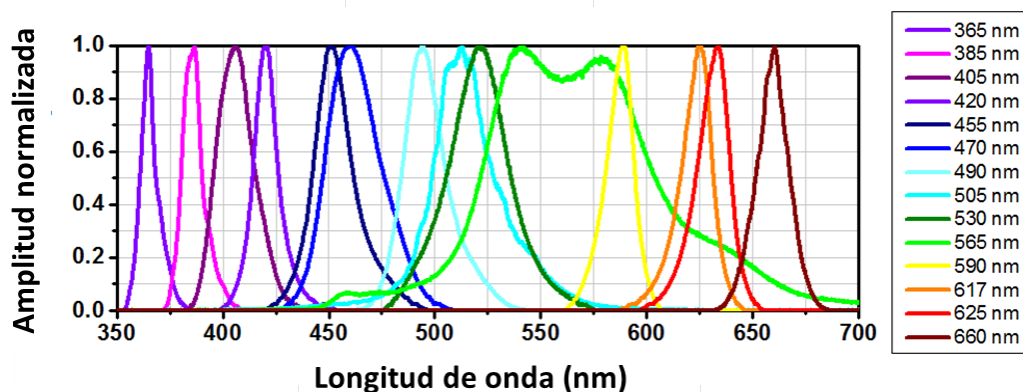


Figura 23: Espectros de emisión de diodos emisores de luz (LEDs).

(circuitos denominados como *LED drivers* en inglés). Para obtener una buena intensidad luminosa (expresada generalmente en milicandelas (mcd)) debe escogerse bien la corriente que atraviesa el LED (véase la Figura 24). Como puede observarse, la relación entre la intensidad luminosa del LED y la corriente inyectada, es aproximadamente lineal (siempre y cuando ésta última se mantenga por debajo de un determinado valor). Para ello, hay que tener en cuenta que el voltaje de operación de un LED va desde 1.8 V hasta 3.8 V aproximadamente (lo que está relacionado con el material de fabricación y el color de la luz que emite), y la gama de intensidades de corriente que puede circular por él varía en función del voltaje aplicado (Ley de Ohm: $V_{LED} = I_{LED} R$). Los valores típicos de corriente directa de polarización de un LED estándar están comprendidos entre los 10 y los 40 mA.

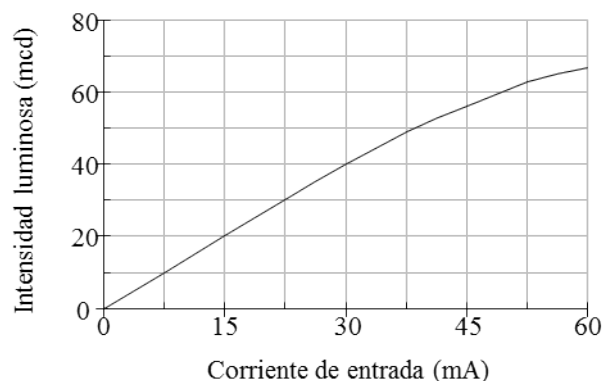


Figura 24: Dependencia de la intensidad lumínica de un LED con la intensidad de corriente.

Por lo general, el área de emisión de los LEDs (sustrato semiconductor) es muy pequeña (menor a 1 mm^2), por lo que tienen una intensidad de luz y un patrón de radiación limitados comparados con las demás fuentes. Un parámetro característico de los LEDs (aparte de la luminosidad) es el ángulo de visión, que se define generalmente como el desplazamiento angular desde la perpendicular donde la potencia de emisión del LED disminuye a la mitad. Según la aplicación que se le vaya a dar al LED se necesitarán distintos ángulos de visión, así son típicos LEDs con 4, 6, 8, 16, 24, 30, 45, 60 y hasta 90 grados de visión. Generalmente, el ángulo de visión está determinado por el radio de curvatura del reflector del LED y,

principalmente, por el radio de curvatura del encapsulado. Por supuesto, cuanto más pequeño sea el ángulo de visión (y a igual sustrato semiconductor) mayor será la potencia de emisión y viceversa.

Pese a estas limitaciones, las excelentes características de los LEDs superan con creces estas posibles desventajas: su disponibilidad para todas las longitudes de onda del espectro visible (rojos, naranjas, amarillos, verdes, turquesas, azules, violetas), e incluso blancos (básicamente LEDs azules dopados con un fosforóforo), la posibilidad de usar un array de LEDs de diferentes colores para conseguir un intervalo más amplio de longitudes de onda [260], su larga vida de operación (10 años o más), su bajo consumo de energía (los LEDs blancos, azules o turquesas únicamente consumen de un 5 a un 10 % de la energía que usarían las lámparas convencionales, mientras que los rojos, amarillos y verdes consumen aproximadamente un 1 %), su amplio intervalo de temperaturas de trabajo (desde -40 a 85 °C), su pequeño tamaño (que permite acercar el LED a la muestra y también la miniaturización de los dispositivos de medida), etc. Además, siempre será posible el uso de filtros ópticos en aquellos casos en los que se requiera definir mejor la longitud de onda del LED (esto es, limitar su espectro de emisión a un intervalo muy estrecho de longitudes de onda) [51]. Por otro lado, a diferencia de las lámparas de xenón, los LEDs apenas emiten radiación infrarroja, por lo que no requieren el uso de filtros de calor. Este hecho es muy importante, ya que la temperatura suele jugar un papel muy significativo en la mayoría de los procesos luminiscentes [51].

También se están realizando grandes esfuerzos para desarrollar LEDs blancos de alto brillo, los cuales ya se usan en linternas LEDs y en los faros de muchos automóviles. Hoy en día se están desarrollando y empezando a comercializar LEDs con prestaciones muy superiores a las de hace unos años, y con un futuro muy prometedor en diversos campos, incluso en aplicaciones generales de iluminación. Como ejemplo, se puede destacar que la compañía *Nichia Corporation* ha desarrollado LEDs de luz blanca con una eficiencia luminosa de 150 lm/W, utilizando para ello una corriente de polarización directa de 20 miliamperios (mA). Esta eficiencia, comparada con otras fuentes de luz únicamente en términos de rendimiento, es aproximadamente 1.7 veces superior a la de una lámpara fluorescente con prestaciones de color altas (90 lm/W) y aproximadamente 11.5 veces la de una lámpara incandescente (13 lm/W). Su eficiencia es incluso más alta que la de una lámpara de vapor de sodio de alta presión (132 lm/W), que está considerada como una de las fuentes de luz más eficientes [261].

Por todo lo comentado, los LEDs constituyen actualmente una fuente de luz barata, sencilla, eficiente y cómoda que permite excitar un compuesto químico a una determinada longitud de onda. Además, a diferencia de las lámparas de arco o las lámparas incandescentes, la intensidad luminiscente de los LEDs puede ser pulsada o modulada. Algunos LEDs, por ejemplo, permiten ser modulados en amplitud hasta los 100 MHz [262–264], lo que los convierte en una excelente alternativa a las costosas lámparas de arco moduladas [264]. Esto hace pensar que un futuro muy próximo los LEDs (y los diodos láser) serán las fuentes de luz dominantes en la instrumentación de modulación de fase y de luz pulsada de bajo coste.

Estos dispositivos son de uso reciente para el desarrollo de métodos en Química Analítica. En 1996, Hartmann y Ziegler [265] usaron una matriz de 8 LEDs conectados en serie (controlados por un generador de funciones que pulsaba la luz de los LEDs) como fuente de excitación alternativa a los láseres en el desarrollo de un sensor óptico de oxígeno. En 1997, Liao *et al.* [266] usaron un LED pulsado como fuente de excitación en el desarrollo de un

sensor de temperatura y de concentración de oxígeno, mientras que Hartmann *et al.* [267] demostraron que los diodos fotoemisivos son capaces de reemplazar a las costosas fuentes láser en los instrumentos de medida de tiempos de vida, usando una matriz de 8 LEDs como fuente de excitación en el sensor de oxígeno que propusieron.

En 1998, Holst *et al.* [255] emplearon un LED azul de luz pulsada como fuente de excitación barata y alternativa a los láseres en el diseño de un nuevo sistema modular de adquisición de imágenes de tiempos de vida de luminiscencia. Un año más tarde, Rieser *et al.* [256] utilizaron una matriz de LEDs como posible fuente de excitación en el nuevo espectrómetro de luminiscencia que diseñaron para llevar a cabo medidas de fosforescencia.

En el año 2000, Liebsch *et al.* [268] usaron una matriz de LEDs pulsados como fuente de excitación en el desarrollo de un sensor óptico de oxígeno, pH, dióxido de carbono y temperatura. Kostov *et al.* [269] usaron un LED azul en su sistema de detección de oxígeno, y Trinkel *et al.* [270] propusieron otro sensor modular de pequeñas dimensiones para la detección de trazas de oxígeno usando diodos fotoemisivos como fuentes de excitación. En los últimos años se han propuesto una amplia variedad de sistemas sensores en el ámbito de la Química Analítica y la Química Clínica en los que se usan LEDs como fuentes de excitación [22, 23, 99, 219, 228, 262, 264, 271, 272].

Además de los LEDs, existen otros diodos fotoemisivos que usan compuestos orgánicos en su fabricación, los llamados diodos fotoemisivos orgánicos y conocidos por sus siglas en inglés “*Organic Light Emitting Diodes*” (OLEDs). En los últimos años se han estudiado y fabricado diferentes tipos de moléculas y polímeros [273, 274] que son útiles en el desarrollo de OLEDs. Se han investigado algunos conceptos estructurales de estas fuentes y algunos materiales fosforescentes para obtener OLEDs de alta eficiencia de luminiscencia [275–280].

0.4.1.4 Láseres

Los primeros estudios espectrométricos luminiscentes con excitación láser se llevaron a cabo en fluorimetría [281–286]. No obstante, la excitación con luz láser cada vez se está aplicando más a la fosforimetría [256, 287–291].

Aunque probablemente los láseres convencionales no desplazarán a las lámparas de pulsos en el análisis de rutina en un futuro inmediato, éstos presentan grandes ventajas como su elevada intensidad, alto grado de monocromaticidad y elevada coherencia espacial. Además, los láseres pulsantes generan pulsos de luz muy cortos y son buenas fuentes para medidas de tiempos de vida [51, 244]. No obstante, en las últimas décadas se ha producido un espectacular avance en la tecnología de fabricación de dispositivos láser, siendo un claro ejemplo de ello los diodos láser (LD, de las siglas en inglés *Laser-Diode*), los cuales son dispositivos semiconductores similares a los LEDs pero que bajo las condiciones adecuadas emiten luz láser.

En los diodos láser, para favorecer la emisión estimulada y la generación de luz láser, el cristal semiconductor del diodo puede tener la forma de una lámina delgada con un lado totalmente reflectante y otro parcialmente reflectante (aunque muy reflectante también), lográndose así una unión *pn* de grandes dimensiones con las caras exteriores perfectamente paralelas y reflectantes. Es importante aclarar que las dimensiones de la unión *pn* guardan

una estrecha relación con la longitud de onda a emitir. Este conjunto forma una guía de onda similar a un resonador de tipo Fabry-Perot. En ella, los fotones emitidos en la dirección adecuada se reflejarán repetidamente en dichas caras reflectantes (en una totalmente y en la otra solo parcialmente), lo que ayuda a su vez a la emisión de más fotones estimulados dentro del material semiconductor y, por consiguiente, a que se amplifique la luz (mientras dure el bombeo derivado de la circulación de corriente por el diodo). Parte de estos fotones saldrán del diodo láser a través de la cara parcialmente transparente (la que es únicamente reflectante de forma parcial). Este proceso da lugar a que el diodo emita luz de tipo láser, que al ser coherente en su mayor parte (debido a la emisión estimulada), posee una gran pureza espectral [258]. Así pues, los LDs (véase la Figura 22(b)) son muy eficientes y fiables, tienen tiempos medios de vida muy largos, son económicos, permiten la modulación directa de la radiación emitida (pudiéndose modular a varios GHz), su volumen y peso son pequeños, el umbral de corriente que necesitan para funcionar es relativamente bajo, su consumo de energía es reducido (comparado con otras fuentes de luz), el ancho de banda de su espectro de emisión es angosto y están disponibles en el intervalo de longitudes de onda de 405 a 1500 nm. Todas estas ventajas hacen pensar que un futuro no muy lejano los LDs serán las fuentes de luz dominantes en la instrumentación de luz pulsada de bajo coste [51].

En cuanto a sus inconvenientes, los más significativos son debidos a la fuerte dependencia de su comportamiento con los valores de la corriente inyectada y la temperatura en la zona activa. Esto hace que necesiten una electrónica de control mucho más compleja que la de los LEDs, para controlar y mantener constante tanto la temperatura en la zona activa como la potencia óptica de salida del dispositivo.

Ya en 1981, Wright *et al.* [284] compararon la capacidad teórica de una lámpara de arco de xenón y un láser como fuentes de excitación en fluorimetría y, posteriormente, Lytle [285] extendió la comparación a varios aspectos de la fluorescencia molecular de disoluciones. En general, un láser es más eficiente que una lámpara de arco de xenón, ya que la anchura de la línea de emisión de la fuente láser es habitualmente más estrecha que la anchura de la absorción, y todos los fotones que inciden sobre la muestra tienen la posibilidad de ser absorbidos [244]. Por ejemplo, un láser de onda-continua puede generar 1 W a una longitud de onda de 555 nm ($\approx 2.5 \times 10^{18}$ fotones s^{-1}), que pueden ser absorbidos por la disolución de muestra [285]. Usando las mismas condiciones que con la lámpara de xenón, la disolución fluorescente tendría una concentración de 2.3×10^{-20} M [244].

La mayoría de los láseres usados para excitación luminiscente son de nitrógeno (337.1 nm), de argón ionizado (ya sea de 488.0 nm o de 514.5 nm) y de colorantes [244].

Boutilier y Winefordner [292, 293] estudiaron el efecto del átomo pesado externo en fosforimetría a baja temperatura, a tiempo resuelto y con excitación láser. Las conclusiones más importantes de estos estudios, fueron las siguientes: (1) El láser pulsante de nitrógeno es una excelente fuente de excitación para fosforóforos que tengan una absorptividad molar del orden de 10 a una longitud de onda de 337 nm. Esto es debido a la alta energía de la fuente y a la excelente reproducibilidad del láser pulsante de nitrógeno; (2) El láser pulsante de colorantes necesita un sistema para compensar las variaciones del pulso, la composición del colorante y las desviaciones del cristal de doble frecuencia para que se pueda usar en fosforimetría con una finalidad analítica.

Más recientemente, Yang *et al.* [287] propusieron un nuevo método para la determinación en tiempo real de reacciones de formación de compuestos antígeno-anticuerpo mediante anisotropía de fosforescencia, diseñando un nuevo fosforímetro consistente en un láser pulsante de Nd:YAG de doble frecuencia como fuente de excitación, un doble canal en forma de T como sistema de detección, un digitalizador y un microprocesador para el tratamiento de datos. Alcalá *et al.* [288, 289] usaron un láser pulsante de Ne-He como fuente de excitación para el desarrollo de un sensor de temperatura basado en el cambio del tiempo de vida de fosforescencia de un cristal de alejandrita o de rubí entre 15 y 45 °C, con una precisión de 0.2 °C y 0.1 °C, respectivamente. Campiglia *et al.* [290] propusieron un nuevo método de análisis mediante fosforescencia inducida por láser, a temperatura ambiente en superficie sólida para hidrocarburos aromáticos policíclicos, usando como fuente de excitación un láser de nitrógeno a 337 nm, obteniendo límites de detección del orden de los nanogramos y aplicándolo a la determinación de éstos en muestras sólidas. Estos mismos autores [291, 294] utilizaron un láser de He-Cd en el desarrollo del primer espectrómetro de imágenes para fosforescencia a temperatura ambiente en superficie sólida. Hedaya *et al.* [295] usaron un láser de nitrógeno para la determinación de uranio mediante un análisis cinético de fosforescencia. Por último, en 1999, Rieser *et al.* [256] propusieron un nuevo instrumento de medida de fosforescencia equipado con un láser infrarrojo de 850 nm.

0.4.2 Selectores de longitud de onda

Su empleo sirve para aislar (o acotar) la banda de excitación perteneciente a una fuente luminosa, especialmente si ésta presenta un intervalo de emisión muy ancho, y también para discriminar la señal óptica de interés analítico (generada en el sensor óptico) de la luz interferente que habitualmente la acompaña (emisión Raman y dispersión Rayleigh principalmente). La necesidad del empleo de selectores de longitud de onda en el sistema óptico depende en gran parte del tipo de medida en el que se fundamenta el instrumento de medida desarrollado. Así, éste puede no requerir ningún tipo de selector de longitud de onda (medidas de quimioluminiscencia), emplear uno situado generalmente antes del detector (medidas de absorbancia y reflectancia), o bien, necesitar dos sistemas de selección de longitud de onda, uno en el canal de excitación y otro en el de emisión (medidas de luminiscencia). A la hora de elegir el selector de longitud de onda más adecuado, han de tenerse en cuenta aspectos como el coste, la resolución espectral y el propósito del análisis.

Los componentes ópticos usados para la selección de la longitud de onda en trabajos luminiscentes son prácticamente los mismos que los usados en análisis por absorción ultravioleta-visible. En la bibliografía puede encontrarse una gran cantidad de información acerca de las propiedades y características de los componentes ópticos usados en análisis luminiscente y por absorción [51, 244, 252, 296]. Por tal motivo, en las próximas dos secciones sobre filtros y monocromadores, únicamente se dará una visión global de estos dos dispositivos de selección de longitudes de onda.

0.4.2.1 Filtros ópticos

Los filtros son el sistema más sencillo de selección de longitudes de onda de excitación y de emisión. Sin embargo, éstos se han usado más para medidas de fluorescencia que para las de

fosforescencia. Normalmente, la fluorescencia se mide en disolución a temperatura ambiente, siendo la fosforescencia bastante débil en estas condiciones [244]. Los filtros se pueden usar para medir fosforescencia, pero además de éstos es imprescindible el uso de otros sistemas adicionales en la instrumentación para minimizar la interferencia de la radiación dispersa y la emisión fluorescente. En la Figura 19 se puede ver la localización de los selectores de longitudes de onda en un instrumento luminiscente.

En general, los filtros se catalogan por la longitud de onda a la cual se obtiene la transmisión máxima y por su ancho de banda efectivo. Los filtros pueden seleccionar anchos de banda muy estrechos (< 1 nm) o muy anchos (≈ 100 nm) con una transmisión de pico de hasta un 90%. La Figura 25 muestra las características de transmisión de filtros comunes de *absorción* y de *interferencia* [244] (véase también la Figura 26(a) y (b)). Los primeros se basan en la absorción de luz en ciertas zonas del espectro electromagnético, transmitiendo únicamente determinadas bandas del espectro. Éstos están fabricados a partir de vidrios coloreados montados en una estructura de soporte, o bien a partir de colorantes suspendidos en gelatina (colocados entre dos placas de vidrio). Este tipo de filtros suelen tener anchos de banda efectivos de 50 a 250 nm, por lo que presentan picos de transmitancia más bajos que los filtros de interferencia. Dependiendo del intervalo de longitudes de onda que dejen pasar sin filtrar, se clasifican en: (a) filtros *paso-banda*, los cuales dejan pasar una determinada banda del espectro electromagnético, filtrando todas aquellas longitudes de onda que quedan fuera de esta banda, (b) filtros de *corte* (*cutt-off*), los cuales dejan pasar todo el rango de longitudes de onda que queda por encima (filtros *de paso largo*) o por debajo (filtros *de paso corto*) de un determinado valor umbral, denominado como longitud de onda de corte. Otro tipo de filtros ópticos son los llamados de filtros de *densidad neutra*, que se limitan a atenuar la luz uniformemente en todo el rango espectral.

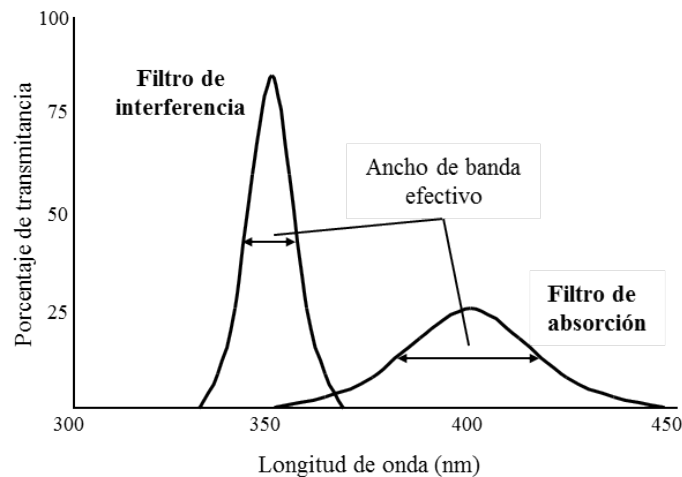


Figura 25: Anchura de banda efectiva para dos tipos de filtros: de absorción y de interferencia [244].

Por su parte, los filtros de *interferencia* o *dicroicos* (del griego *dikroos*, dos colores), a diferencia de los filtros de absorción mencionados anteriormente, reflejan parte de la luz que incide sobre ellos. Un filtro dicroico o interferencial está formado por una lámina transparente que posee un recubrimiento reflectante en una de sus superficies, el cual refleja la luz que se desea filtrar. De este modo, se consigue separar la luz en dos haces cromáticos diferentes

mediante el principio de interferencia. Estos filtros son generalmente mucho más caros que los filtros de absorción, pero también presentan unas características muy superiores (filtrado mucho más selectivo y eficaz, con anchos de banda efectivos de 5 a 20 nm). Este tipo de filtros se fabrican depositando capas de sustancias reflectantes sobre un sustrato, generalmente vidrio. Variando el número y grosor de estas capas puede ajustarse con mucha precisión la longitud de onda de corte del filtro y el ancho de banda deseado, siguiendo los principios del interferómetro de Fabry-Perot [258].

Ambos filtros (de absorción y de interferencia) pueden usarse como selectores de longitud de onda y se han empleado en muchas aplicaciones luminiscentes. Así, Guilbault [252] da una lista detallada de filtros usados en trabajos luminiscentes y Fister *et al.* [297] emplean filtros de interferencia en el diseño de un sensor óptico de temperatura. En los últimos años se han empezado a utilizar también filtros acústico-ópticos sintonizables, siendo Campiglia *et al.* [291, 294] quienes los aplicaron por primera vez su en un espectrómetro de imágenes para fosforescencia a temperatura ambiente en superficie sólida.

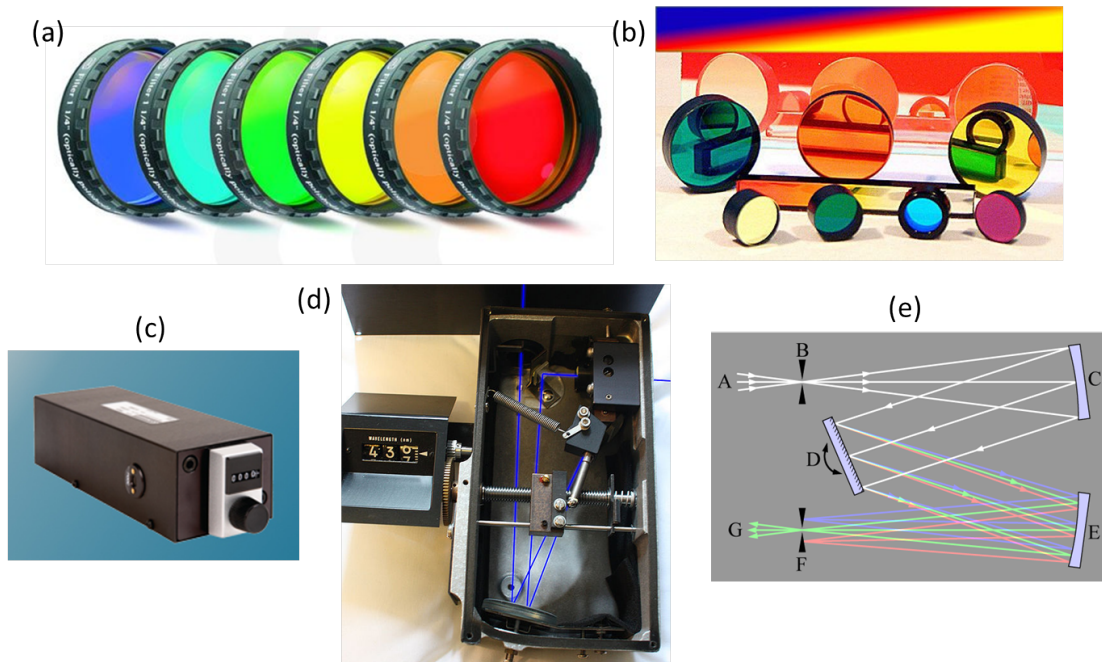


Figura 26: Imágenes de selectores de longitud de onda. (a) filtros ópticos de colores (absorbancia); (b) filtros ópticos de interferencia (reflectancia); (c) imagen de un monocromador comercial; (d) distribución interna de los componentes ópticos de un monocromador de Fastie-Ebert (similar al monocromador de Czerny-Turner pero con un espejo común colimador/focalizador); (e) diagrama de un monocromador de Czerny-Turner.

0.4.2.2 Monocromadores

Los filtros ópticos son la elección más idónea cuando se pretende construir un sistema sencillo y barato. En cambio, para aquellas aplicaciones en las que se requiera una selección muy precisa de la longitud de onda, el uso de monocromadores (véase la Figura 26(c)) constituye la única solución. Los monocromadores están especialmente diseñados para realizar barridos

espectrales en aquellos sistemas en los que sea imprescindible poder seleccionar, de forma continua y en un rango amplio, la longitud de onda exacta de la radiación electromagnética procedente de la fuente de radiación o de la fase sensora. Estos dispositivos constan de una *rendija de entrada* de luz, una *lente* o *espejo colimador* que produce un haz de luz paralelo a la radiación, un *prisma* o *red de difracción* que descompone la luz en sus diferentes componentes espectrales, y un *elemento focalizador* (espejo cóncavo) que conduce la radiación imagen hasta el denominado plano focal, donde se encuentra situada la rendija de salida, encargada de aislar la banda espectral deseada.

Los prismas no son muy utilizados en instrumentos luminiscentes, ya que presentan una gran dispersión en la zona del ultravioleta, mientras que en las redes de difracción, la dispersión varía sólo ligeramente con la longitud de onda y resultan más baratas que los prismas. Otras ventajas destacables de las redes de difracción son la de ofrecer una resolución uniforme y una dispersión lineal a todas las longitudes de onda y la de posibilitar que hasta un 50 % de la radiación incidente se pueda difractar dentro del primer orden con una red pulimentada [244]. Su mayor desventaja, en cambio, es que se obtienen espectros de varios órdenes de magnitud. Una manera de minimizar este problema es el uso de filtros en el paso óptico. Por ejemplo, para observar la línea espectral de 600 nm sin interferencia de la línea espectral de segundo orden de 300 nm, se puede usar un filtro óptico que elimine la radiación por debajo de 400 nm [252].

Las redes de difracción pulimentadas son las más usadas en los instrumentos de luminiscencia. Las ranuras de la redes están aluminizadas y tienen la pendiente precisa para difractar la máxima cantidad de radiación para un determinado ángulo. Por ejemplo, si la red ha sido pulida para 450 nm, su máximo de salida será a 450 nm. La eficacia de la red disminuirá tanto más cuanto más se distancie la longitud de onda del valor para el que se pulimentó. Los montajes más comunes para monocromadores en los luminómetros comerciales son dos: el montaje Fastie-Ebert (Figura 26(d)) y el montaje Czerny-Turner (Figura 26(e)) [245]. En estos montajes, la red de difracción va girando para cambiar la longitud de onda de salida, mientras que el ángulo entre el rayo incidente y el difractado permanece constante. La Figura 26(e) muestra el diagrama de un monocromador de Czerny-Turner. El haz de luz incidente es focalizado sobre la rendija de entrada (B) y colimado por un espejo cóncavo (C). Este haz de rayos colimados (o paralelos) es difractado por una red de difracción giratoria (D). La luz dispersada (descompuesta en sus diferentes componentes cromáticas) es focalizada por un segundo espejo (E) sobre la rendija de salida (F). Cada componente de longitud de onda es focalizada en un punto diferente de la rendija de salida (F). La longitud de onda que finalmente se transmite a la salida (G), depende del ángulo de rotación de la red de difracción (D).

Cuando se coloca un detector en la rendija de salida del monocromador y se gira la red de difracción, de forma que una de las líneas emergentes se recoja en la rendija de salida, la salida del detector presenta la forma de una curva gaussiana [244]. La anchura de la banda efectiva de un monocromador depende de la dispersión del prisma o de la red de difracción empleada, de la distancia focal, así como de la anchura de las rendijas de entrada y salida. Un monocromador de alta calidad tendrá un ancho de banda efectivo de unas pocas décimas de nanómetro en la región del ultravioleta-visible. El ancho de banda efectivo de un monocromador adecuado para la mayoría de las aplicaciones cuantitativas es de 1 a 20 nm. Usualmente hay una disyuntiva entre la intensidad de luz que lo atraviesa y el poder de

resolución de un monocromador, ya que una disminución del ancho de las rendijas aumenta la resolución, pero a costa de disminuir la intensidad de la señal [245]. Muchos monocromadores vienen equipados con mecanismos de ajuste de rendijas que permiten cierto control sobre el ancho de banda efectivo. Una rendija estrecha reduce el ancho de banda efectivo, pero disminuye también la potencia del rayo emergente. Por tanto, un ancho de banda mínimo que sea práctico puede estar limitado por la sensibilidad del detector [244]. Actualmente, las *redes holográficas* están adquiriendo cada vez mayor importancia, ya que permiten rechazar entre 10 y 100 veces más la luz difusa que las redes de difracción convencionales.

0.4.3 Fibras ópticas

Es imposible comprender el rápido desarrollo sufrido por los sistemas de comunicaciones ópticas durante los últimos treinta años sin tener en cuenta el desarrollo experimentado en la tecnología y en los componentes que los sustentan. De los componentes empleados en sistemas de comunicaciones ópticas, la fibra óptica ha sido el que más rápido se ha desarrollado. Solo pasaron cuatro años desde la propuesta de Kao y Hockman (1966) de usar la fibra como medio de transmisión, hasta la obtención de un portador con pérdidas “aceptables” en la “primera ventana” (20 dB/Km), desarrollado por los ingenieros Kapron, Keck y Maurer de la compañía *Corning Glass*. Los siguientes pasos en la evolución de la fibra óptica fueron vertiginosos. Grandes compañías (*Bell Labs, Phillips Research, Corning Glass, Sumimoto-NTT*, etc.) comenzaron a invertir importantes sumas de dinero para obtener métodos de fabricación cada vez más refinados, con los que reducir hasta niveles insignificantes la presencia de cationes metálicos y radicales OH^- en el material de sílice que compone el núcleo de la fibra. Estas impurezas eran las responsables de las enormes pérdidas que presentaban las primeras fibras. Así, a finales de los años setenta ya se habían obtenido fibras con valores de pérdidas muy próximos al mínimo teórico impuesto por el denominado *scattering de Rayleigh* (2 dB/Km a 850 nm, 0.5 dB/Km a 1300 nm y 0.2 dB/Km a 1550 nm). En la Figura 27 se muestra esquemáticamente la curva de atenuación típica de una fibra óptica con las tres ventanas de transmisión más empleadas en la actualidad.

La fibra óptica es, en esencia, una guía de onda dieléctrica cilíndrica compuesta por un cilindro interior (núcleo) y una corona cilíndrica externa (revestimiento), tal y como se muestra en la Figura 28(a). También, y aunque no es esencial, suele recubrirse la fibra con una vaina o funda externa (recubrimiento), generalmente plástica, que proporciona a la fibra protección mecánica y térmica. Sin entrar en mayor profundidad, es necesario que el índice de refracción del material que compone el núcleo de la fibra óptica (n_1) sea superior al del material que compone el revestimiento (n_2) para que la energía luminosa inyectada en la fibra se propague de forma guiada a través del núcleo, sin escapar por el revestimiento. Esta propagación puede describirse a partir de una serie de rayos de luz (denominados *modos de propagación*) que sufren sucesivas reflexiones al incidir sobre la superficie de separación entre el núcleo y el revestimiento, tal y como se muestra en la Figura 28(b).

Los dos mecanismos que limitan las prestaciones de la fibra óptica como medio de transmisión son [258]: la *atenuación* o pérdida de la potencia de la señal y la *dispersión*; mecanismo que provoca el ensanchamiento temporal de los pulsos transmitidos por la fibra y que limita la máxima velocidad de transmisión digital que puede soportar la fibra para evitar la

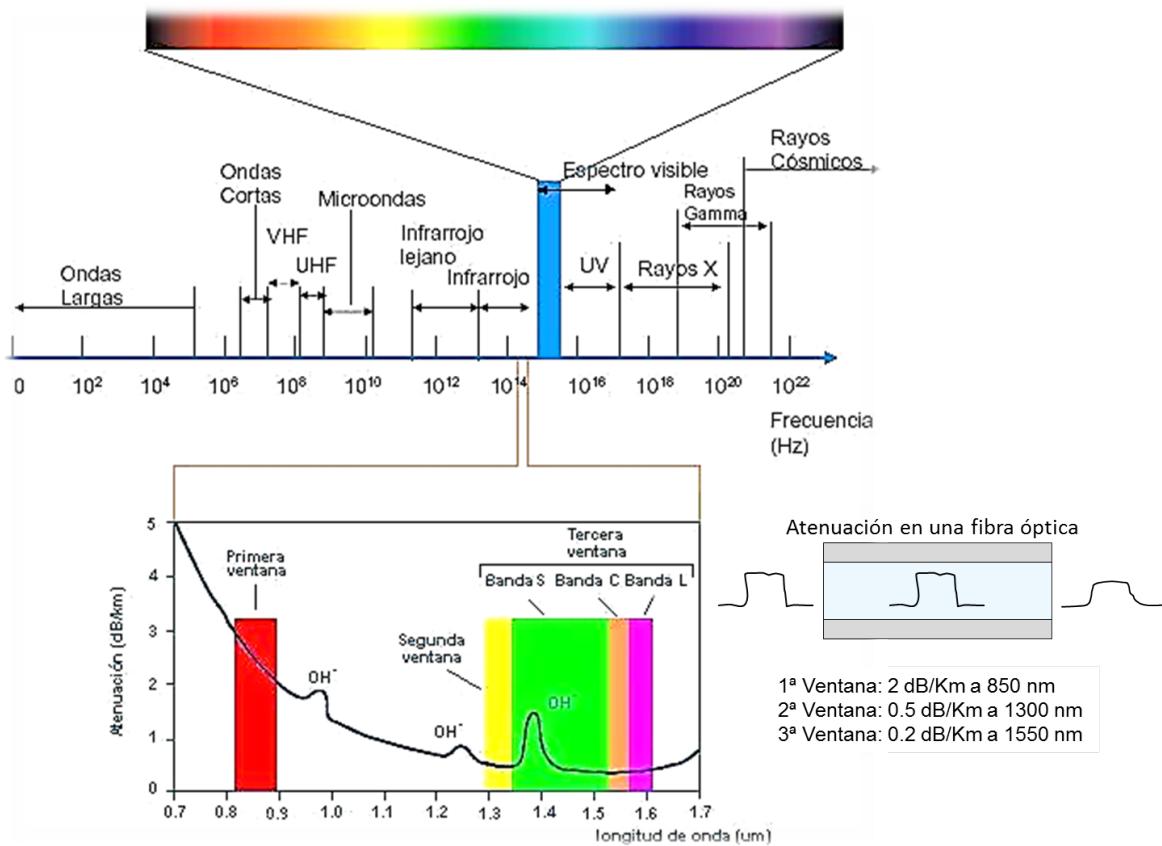


Figura 27: Concepto de atenuaci3n en una fibra 3ptica. Curva de atenuaci3n en funci3n de la longitud de onda en una fibra 3ptica.

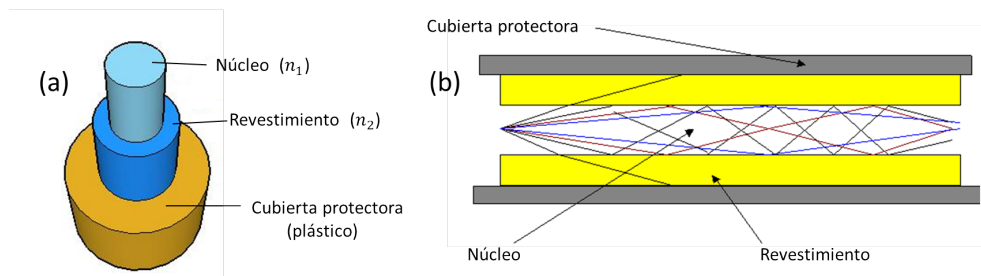


Figura 28: (a) Partes de una fibra 3ptica; (b) Mecanismo de la propagaci3n de rayos en una fibra 3ptica.

interferencia entre s3mbolos [258].

0.4.3.1 An3lisis de la propagaci3n en fibras 3pticas mediante 3ptica geom3trica

La forma m3s adecuada de analizar la propagaci3n en cualquier gui3 de onda en general, y en la fibra en particular, es a trav3s de las ecuaciones de Maxwell y la Teor3a Electromagn3tica. Este an3lisis es muy preciso, pero en la mayor3a de los casos resulta bastante tedioso, no siendo siempre f3cil extraer los conceptos f3sicos que de 3l se derivan. En el caso que nos ocupa, al tratar con se3ales 3pticas cuya longitud de onda est3 comprendida entre 0.6 μm

y $1.7 \mu\text{m}$, ésta será (casi) siempre muy inferior a las dimensiones transversales del núcleo y el revestimiento, por lo que es posible emplear una aproximación conocida como Teoría de Rayos u Óptica Geométrica, cuyas ecuaciones se obtienen a partir de las de Maxwell en el caso límite de que la longitud de onda de las señales tienda a cero ($\lambda \rightarrow 0$). Este caso presenta la particularidad de que la trayectoria descrita por la luz en su propagación a través de los diferentes medios viene descrita por medio de rayos [258]. La aproximación de la Óptica Geométrica permite la comprensión y fácil asimilación de los conceptos de reflexión total interna y del guiado de señales en una fibra óptica. Por ello, realizaremos el análisis de la propagación en fibras ópticas mediante esta aproximación.

En su forma más general, una fibra óptica está compuesta por un núcleo cilíndrico de material dieléctrico de radio a , rodeado de un revestimiento también de material dieléctrico de radio exterior b , tal y como se muestra en la Figura 29. En determinadas condiciones, dicha estructura se comporta como una guía de onda dieléctrica, permitiendo la propagación de señales confinadas dentro de su núcleo sin que sean radiadas al exterior. La propagación de señales a través de la fibra óptica se realiza en la dirección z . El plano transversal a la dirección de propagación viene caracterizado a través de las coordenadas (x, y) o (r, θ) , según convenga utilizar coordenadas cartesianas o cilíndricas (aunque en el caso de las fibras ópticas, al ser su geometría cilíndrica, parece más adecuado el empleo de coordenadas cilíndricas; existen, sin embargo, otro tipo de guías de onda, las planas, para las que resulta más adecuado el empleo de coordenadas cartesianas). La relación entre dichas coordenadas queda explícita en la parte derecha de la Figura 29.

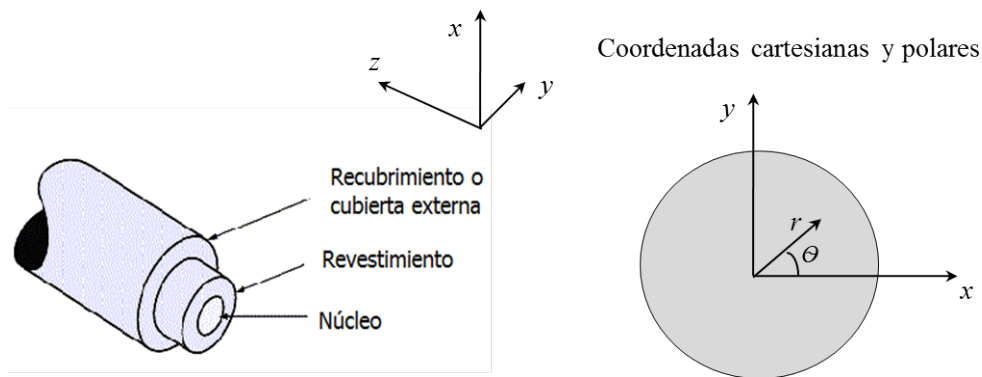


Figura 29: Geometría de una fibra óptica y relación entre coordenadas cartesianas y cilíndricas.

Los materiales dieléctricos que componen el núcleo y el revestimiento de la fibra son compuestos formados generalmente por vidrio de sílice (SiO_2) y una serie de dopantes tales como germanio, fósforo y boro, los cuales vienen caracterizados por sendos índices de refracción, diferentes entre sí, y que indican la densidad óptica en ambas zonas. El índice de refracción del revestimiento, n_2 , suele ser, en la mayoría de los casos, constante con la coordenada radial r a lo largo del revestimiento, mientras que el índice de refracción del núcleo puede ser constante o variable con dicha coordenada, por lo que usaremos el símbolo $n_1(r)$ para caracterizar dicho índice de refracción. Atendiendo a la variación del índice de refracción del núcleo con la coordenada radial, las fibras se pueden clasificar en dos tipos. Si el índice de refracción del núcleo es constante con r , entonces la fibra es denominada de *salto de índice*, debido a que el índice de refracción, al mantenerse constante en el núcleo y en el revestimiento, sufre una

transición brusca o “salto” en la interfase entre ambas regiones, que viene caracterizada por la ecuación $r = a$. Al ser constante el índice de refracción en el núcleo, se emplea el símbolo n_1 desprovisto de su dependencia radial para caracterizarlo. El segundo tipo de fibras ópticas son aquellas en las que el índice de refracción del núcleo varía suavemente y de forma decreciente con la coordenada radial, desde un valor máximo $n_1(0)$ en su eje ($r = 0$), hasta un valor de $n_2 = n_1(a)$ en la interfase de separación entre el núcleo y el revestimiento ($r = a$). Estas fibras se denominan de *índice gradual* y en ellas no se produce discontinuidad de índice en la transición del núcleo al revestimiento. En la Figura 30 se muestra la sección transversal y el perfil de índices (variación del índice de refracción con la coordenada radial) para ambos tipos de fibras. Puede observarse que el índice de refracción en el núcleo es superior al del revestimiento. Este hecho, que se justificará a continuación, es esencial para que la fibra óptica se comporte como una guía de onda de luz.

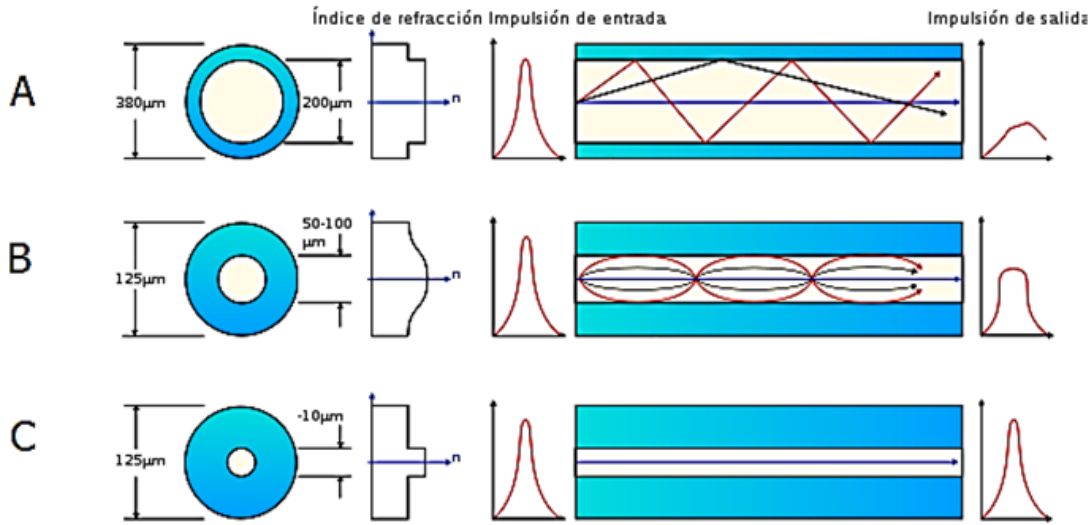


Figura 30: Perfiles de índice, secciones transversales y trayectorias típicas de propagación de rayos en diferentes tipos de fibras ópticas. (A) Fibra multimodo de salto de índice; (B) Fibra multimodo de índice gradual; (C) Fibra monomodo de salto de índice.

La propagación de rayos en una fibra óptica de salto de índice puede ser estudiada a partir de la *ley de Snell* (refracción de luz en la interfase de separación entre dos medios dieléctricos con distinto índice de refracción). En la Figura 31 se ilustra dicha ley, así como el principio de reflexión total interna [258]. Refiriéndonos a la Figura 31(a), en ella podemos observar el paso de un rayo de luz de un medio dieléctrico de índice de refracción n_1 , a otro medio dieléctrico de índice de refracción n_2 . La ley de Snell relaciona los ángulos que forman los rayos incidente y transmitido con la normal a la superficie de separación entre ambos medios:

$$n_1 \operatorname{sen}\theta_1 = n_2 \operatorname{sen}\theta_2 \quad (60)$$

Como puede observarse en la Figura 31(a), al atravesar el rayo incidente la interfase de separación entre los dos medios dieléctricos, éste sufre un cambio en su dirección de propagación. El efecto visual es como si el rayo se “partiese”, de ahí el empleo del término refracción para identificar a este fenómeno. Si el medio donde se origina el rayo incidente posee un índice

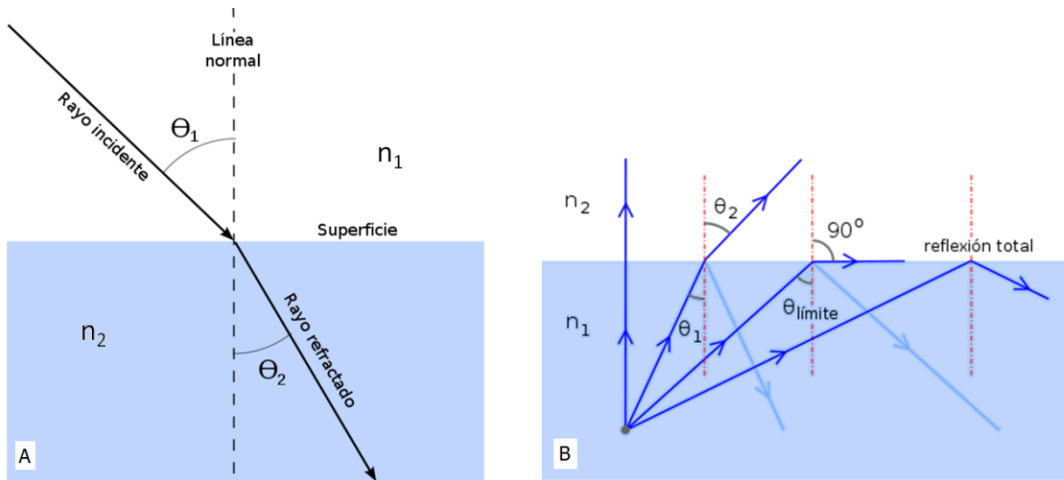


Figura 31: Ilustración de la ley de Snell y del concepto de reflexión total interna.

de refracción superior al del medio al que se transmite, $n_1 > n_2$, entonces, según la ley de Snell, $\theta_1 < \theta_2$, es decir, que el rayo transmitido se “aleja” de la normal a la superficie de separación entre ambos medios. Para un determinado ángulo de incidencia $\theta_1 = \theta_c$, denominado *ángulo crítico o límite*, se verifica que $\theta_2 = \pi/2$, tal y como puede observarse en la figura Figura 31(b). Para ángulos de incidencia superiores al crítico, es decir, para $\theta_1 > \theta_c$, no existirá rayo transmitido, debido a que el rayo incidente se reflejará totalmente en la superficie de separación entre ambos medios, formando un ángulo con la normal igual al de incidencia ($\theta_{1,r} = \theta_1$). Este fenómeno se conoce como *reflexión total interna* y es la base en la que se sustenta el proceso de propagación de luz en una fibra óptica. El valor del ángulo crítico puede calcularse directamente a partir de la ecuación (60), sin más que recordar que $\theta_2 = \pi/2 \rightarrow \text{sen}\theta_2 = 1$, por lo que:

$$\theta_c = \arcsen \frac{n_2}{n_1} \quad (61)$$

En la Figura 32 se muestra el corte longitudinal de una fibra óptica de salto de índice y las trayectorias internas de un rayo guiado y otro no guiado. Para comprender el fenómeno de guiado de rayos en la fibra basta con suponer que la superficie de separación entre el núcleo y el revestimiento es como la superficie de separación entre los dos dieléctricos que acabamos de estudiar. Si el rayo incide sobre dicha superficie de separación (núcleo-revestimiento) formando un ángulo con su normal superior al ángulo crítico (θ_c), éste se reflejará completamente, dirigiéndose a la interfase de separación inferior, donde por consideraciones de simetría también se reflejará completamente. En consecuencia, dicho rayo se propaga a través de la fibra al ser confinado en su núcleo por las sucesivas reflexiones totales que sufre cada vez que llega a la superficie de separación con el revestimiento. Por el contrario, si el rayo no forma un ángulo superior al crítico con la normal a la superficie de separación núcleo-revestimiento, parte de éste se reflejará hacia el núcleo y otra parte se transmitirá al revestimiento, de manera que tras pocas reflexiones, toda su energía se habrá transmitido al exterior, por lo que no será guiado a través de la fibra.

Dado que la luz se inyecta a la fibra desde un medio externo, tal y como se muestra en la Figura 32, resulta conveniente obtener la condición de reflexión total interna de un rayo en función del ángulo que éste forma con el eje z de propagación, al ser inyectado en la

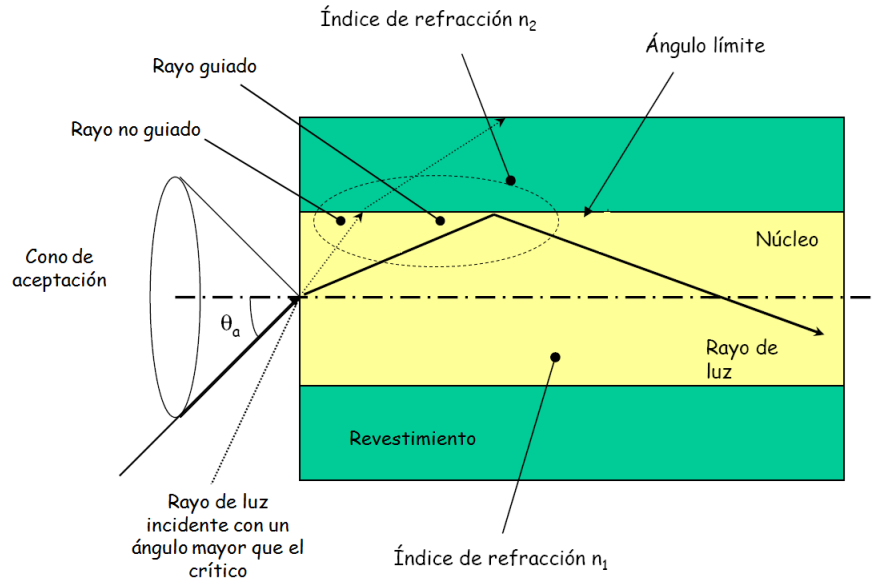


Figura 32: Guiado de rayos en una fibra óptica. Cono de aceptación de luz.

fibra. Para ello utilizaremos el diagrama de la Figura 32. En ella se aprecia la existencia de dos interfases entre dieléctricos. La interfase núcleo-revestimiento, anteriormente citada, y la interfase medio externo-núcleo. Para esta última, la ley de Snell es de la forma:

$$n_0 \operatorname{sen} \theta_a = n_1 \operatorname{sen} \theta_1 = n_1 \operatorname{cos} \theta_c \quad (62)$$

Cuando $\theta_1 < \theta_c$, entonces se cumple que:

$$\operatorname{cos} \theta_c = \sqrt{1 - (n_2/n_1)^2} \quad (63)$$

y la condición de reflexión total interna o de guiado de rayos, referida a su ángulo de entrada con el eje z , es de la forma:

$$n_0 \operatorname{sen} \theta_a \leq n_0 \operatorname{sen} \alpha_{in} = \sqrt{n_1^2 - n_2^2} \quad (64)$$

donde α_{in} es el denominado ángulo máximo de aceptación, y define un cono de revolución alrededor del eje z , de forma que todo rayo que incida sobre la fibra dentro de él será guiado por la fibra. La ecuación (64) permite definir un parámetro que es de gran importancia a la hora de caracterizar una fibra óptica. Dicho parámetro se conoce como *Apertura Numérica* de la fibra o AN , y viene definido por:

$$AN = \sqrt{n_1^2 - n_2^2} = n_1 \sqrt{2\Delta} \quad (65)$$

donde $\Delta = (n_1^2 - n_2^2)/2n_1^2$ es la diferencia relativa entre índices de refracción del núcleo y del revestimiento.

0.4.3.2 Fibras ópticas en fosforescencia

Los materiales empleados en la fabricación de fibras ópticas dependen, en parte, del tipo de radiación que se pretende transmitir. Así, las fibras de núcleo de sílice fundida o de cuarzo,

transmiten luz en el ultravioleta y en el visible (190-1300 nm), mientras que las de vidrio o plástico, más económicas, lo hacen solo en el visible (450-700 nm). El recubrimiento de la fibra se fabrica siempre con materiales resistentes al medio externo donde vaya a operar. Las fibras ópticas de cuarzo son resistentes a medios fuertemente ácidos o moderadamente alcalinos, si bien sufren el ataque del ácido fluorhídrico y de las bases fuertes ($\text{pH} > 13$). La máxima temperatura a la que se puede trabajar con la mayoría de las fibras ópticas está limitada por la resistencia del material que constituye la envoltura protectora y suele ser de unos $125\text{ }^\circ\text{C}$. Para trabajar en el IR, exceptuando el NIR, se utilizan fibras de sílice fundida especial (de fluoruro de zirconio o vidrios de calcogenuro). Las fibras líquidas funcionan de forma similar a las fibras ópticas sólidas, pero están formadas por tubos rellenos de un fluido transparente en cuyos extremos se sitúan sendas placas pulidas de gel de sílice. En general, estas fibras transmiten en el intervalo de 270-720 nm. Los sistemas que usan fibras ópticas, como los optodos, requieren acopladores ópticos que eviten las pérdidas de luz desde que ésta sale de la fuente hasta que llega al detector óptico. Para ello, se utilizan normalmente lentes de vidrio o cuarzo para focalizar la radiación luminosa [258, 298].

El desarrollo experimentado por la tecnología de fibras ópticas a lo largo de los últimos años, ha propiciado un crecimiento espectacular en la preparación de sensores de fibra óptica. Así, desde que Carroll y Hieftje [299] idearon un nuevo instrumento para medir intensidad y tiempo de vida de fosforescencia a baja temperatura usando fibras ópticas como guías de luz, y comprobaran su utilidad, versatilidad y ventajas frente a la instrumentación convencional, son muchos los instrumentos y sensores que se han desarrollado y que utilizan fibras ópticas. Así, actualmente se dispone de sensores de oxígeno [266, 300–303], temperatura [266, 288, 289], de pesticidas [257, 304], de europio [78], para la determinación de cocaína y benzoilecgonina [305], etc., en los que se usan fibras ópticas para transportar la radiación tanto de excitación como de emisión fluorescente o fosforescente [244].

0.4.4 Detectores y sistemas detectores

La selección del detector óptico adecuado será siempre un compromiso entre la sensibilidad requerida para el sistema y los factores económicos. Idealmente, un detector debe poseer una alta sensibilidad en un intervalo amplio de longitudes de onda, rápidos tiempos de respuesta y una señal de salida mínima en ausencia de iluminación externa (corriente de oscuridad).

0.4.4.1 Fototubos y tubos fotomultiplicadores

Los fototubos son sistemas de detección que constan de un cátodo semicilíndrico y un ánodo de filamento encerrados herméticamente en un recipiente transparente, en el que se ha hecho el vacío. La Figura 33 muestra la forma de un fototubo y su circuito complementario. Estos dispositivos independientes no se solían usar como sistemas de detección en los espectroluminómetros comerciales, sin embargo, en los últimos años, debido a la miniaturización, simplificación y abaratamiento de los sistemas de medida, se ha llegado a sustituir el tubo fotomultiplicador (PMT, *photomultiplier tube*) por un simple fototubo. Así, Kostov *et al.* [269] desarrollaron un sensor óptico tipo sonda que usaba como sistema de detección un fototubo.

Los tubos fotomultiplicadores son los detectores más usados tanto en fluorescencia como

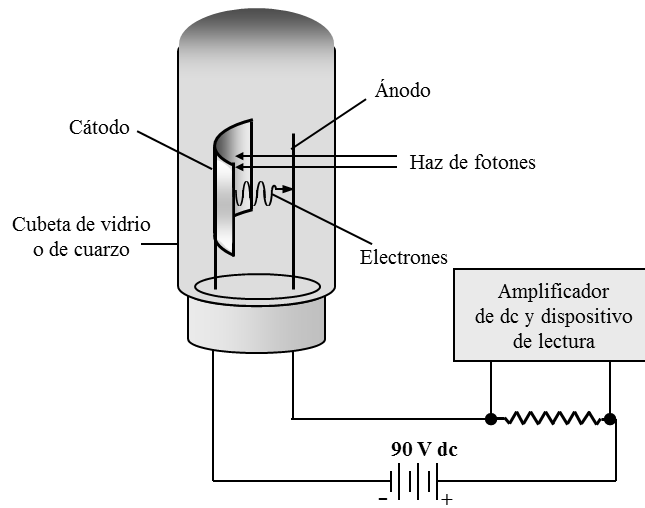


Figura 33: Fototubo y su circuito complementario [244].

en fosforescencia. Este tipo de detectores, que se muestran en la Figura 34, son una versión sofisticada de un fototubo, pero mucho más sensibles. Además del cátodo fotoemisor, el PMT contiene una serie de electrodos llamados dínodos, cada uno de los cuales está sometido a un potencial 50-100 V más positivo que el precedente. El cátodo está recubierto por una superficie fotoemisora como la utilizada en los fototubos. Los dínodos están recubiertos por una fina capa de BeO o $CsSb$ que desprende varios electrones cuando es bombardeada con electrones de alta energía. Cada dínodo está configurado para enfocar los electrones emitidos hacia el dínodo siguiente. La radiación que llega al fotocátodo provoca la emisión de electrones primarios (fotoelectrones), que son acelerados por un campo eléctrico hasta el primer dínodo. Al incidir sobre él, cada fotoelectrón origina la emisión de varios electrones adicionales; éstos a su vez son acelerados hasta el dínodo siguiente y así sucesivamente. Finalmente, la corriente generada se recoge en el ánodo. Los tubos fotomultiplicadores contienen 9 ó 10 dínodos, los cuales originan hasta 10^6 electrones por cada fotoelectrón generado en el cátodo. Esta alta amplificación interna permite que puedan ser detectadas potencias ópticas muy bajas sin necesidad de una amplia amplificación externa. El sistema se caracteriza por su respuesta rápida y elevada sensibilidad (la cual varía con la longitud de onda). Los tubos PMTs son muy sensibles a la radiación ultravioleta/visible y sus tiempos de respuesta son extremadamente rápidos (en torno a 10^{-8} s, lo cual es suficientemente rápido para todas las medidas, incluso para las medidas de luminiscencia basadas en tiempos de decaimiento [51]). Generalmente, la sensibilidad de estos detectores está limitada por su corriente de oscuridad, debida fundamentalmente a la emisión térmica, la cual puede ser minimizada fácilmente mediante enfriamiento [51]. Estos sistemas se utilizan para medir radiaciones ópticas de muy baja potencia, ya que una luz intensa genera un daño irreversible en la superficie fotoeléctrica, razón por la cual se alojan convenientemente en compartimentos herméticamente cerrados.

0.4.4.2 Contador de fotones

Los contadores de fotones se emplean para la medida de bajas intensidades de luz. En un contador de fotones, los pulsos de los fotoelectrones en el ánodo del tubo fotomultiplicador

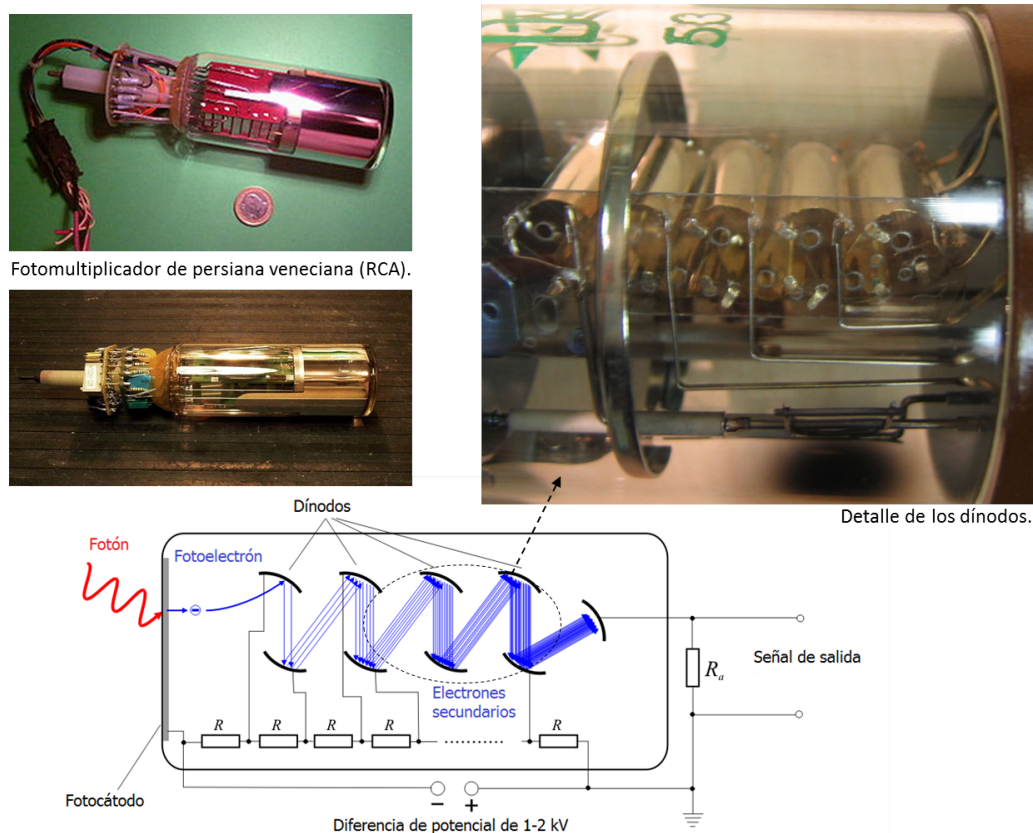


Figura 34: Tubo fotomultiplicador (PMT). Detalle de funcionamiento de un tubo fotomultiplicador (PMT).

se contabilizan con un contador electrónico de alta velocidad. Como media, cada pulso de fotoelectrón contiene L electrones con una carga total de eL culombios. Asumiendo que L tiene un valor aproximado de 10^6 , la carga resultante es suficientemente grande para causar un pulso de voltaje apreciable en el fototubo. Por cada fotoelectrón que llega al fototubo se produce un pulso. Así pues, la relación pulso/número de cuentas es proporcional al nivel de luz. Esto implica que la sensibilidad del cátodo es constante. Los pulsos están generalmente en torno a varios milivoltios, y pueden ser amplificados mediante el empleo de un amplificador de corriente alterna de banda ancha y contados por contadores electrónicos [51, 244].

Los contadores de fotones presentan como ventajas más importantes las siguientes: tienen una menor deriva que los sistemas analógicos, detectan niveles muy bajos de luz, se pueden usar tiempos de conteo largos para acumular las cuentas totales, se pueden discriminar varios tipos de ruido con respecto a otros detectores, y las lecturas digitales son fáciles de realizar y pueden ser acopladas directamente a unidades de procesamiento (p. ej., ordenadores personales). Como desventaja hay que citar que la ganancia del tubo fotomultiplicador no puede ser variada cambiando el voltaje aplicado. También, los contadores de fotones tienen un intervalo de intensidades limitado (zona en la que la relación de conteo es lineal). Generalmente, estos detectores no se pueden usar con niveles altos de señal. Por ejemplo, para estar dentro del intervalo lineal, la anchura de las rendijas debe ser ajustada, o bien la intensidad de fluorescencia debe ser regulada empleando filtros. Además, la relación señal-ruido puede llegar a ser insatisfactoria para relaciones inferiores a 10.000 fotones por segundo [51].

Varios sistemas contadores de fotones desarrollados para su empleo en fluorescencia pueden ser adaptados al análisis de fosforescencia. Franklin *et al.* [306] describieron un contador de fotones relativamente simple y barato que puede ser conectado a tubos fotomultiplicadores. Jameson *et al.* [307] discutieron la construcción y desarrollo de un espectrofluorímetro con un detector contador de fotones. Koester y Dowben [308] emplearon un espectrofluorímetro usando como detector un contador de fotones en el rango de los subnanosegundos y como fuente de excitación un láser de colorantes sintonizable, actuando de forma síncrona. Darland *et al.* [309] describieron un método para calcular la eficiencia relativa de los experimentos de conteo de pulsos. Meade [310] revisó los aspectos prácticos del conteo de fotones, teniendo en cuenta problemas asociados con la optimización del detector, el amplificador y el discriminador. También se discutieron diferentes tipos de configuraciones de conteo que se encuentran en equipos disponibles comercialmente [51]. En la actualidad, los detectores contadores de fotones son ampliamente usados en estudios de cálculo de tiempos de vida de fluorescencia (fluorescencia de tiempo resuelto), aunque a veces también se usan en instrumentos capaces de medir fosforescencia [311–313].

0.4.4.3 Detectores multicanal

El uso de los detectores multicanal en espectrometría de luminiscencia comienza en la década de los ochenta y aún continúa en desarrollo en la actualidad. Los modernos detectores multicanal constan de una serie de pequeños elementos fotoeléctricos en un único chip semiconductor, que contiene los circuitos electrónicos que hacen posible la determinación de la señal eléctrica ya sea secuencialmente o simultáneamente [296]. La mayor ventaja de los detectores multicanal es su potencialidad en las medidas luminiscentes. Así, el tiempo requerido para N detectores observando simultáneamente N canales para obtener una relación señal/ruido dada, es un factor N veces menor que el requerido para un detector sencillo observando secuencialmente N canales [244]. Normalmente toda la ventaja del multicanal nunca se alcanza debido a que no se llega a las condiciones ideales [51, 283, 314].

Existen diferentes tipos de detectores de imagen comercialmente disponibles [315–318] y en la actualidad son cuatro los detectores multicanales más empleados en la construcción de instrumentos espectroscópicos comerciales: los fotodiodos en serie (PDA, *photodiode array*), los tubos vidicon (*silicon intensifier target (SIT) vidicon tube*) y los dispositivos de transferencia de carga (CID (*charge injection device*) y CCD (*charge coupled device*)) [51, 283, 296, 319]. En la Figura 35 se muestra un ejemplo de cada uno de estos detectores. Los detectores de CCD (dispositivos de carga acoplada) son cada vez más usados como sistemas de detección en instrumentos comerciales [51]. Estos dispositivos ofrecen la ventaja de una mayor sensibilidad para bajos niveles de luz, y además, debido a que permiten la obtención de imágenes 2D, se han usado en sensores sensibles a más de un componente [268], en aplicaciones bioquímicas [320, 321] y para obtener distribuciones espaciales de uno o varios compuestos químicos [255, 267, 322, 323].

Las cámaras CCD se están utilizando cada vez más en el diseño de sensores de fibra óptica. Así existen en la bibliografía sensores de oxígeno [94, 265, 300], de pesticidas [257, 304] y de hidrocarburos aromáticos policíclicos [324] que usan este sistema de detección para recoger la emisión luminiscente. Además, ya hay diseñados varios luminómetros que incorporan una cámara CCD como sistema de detección [256, 291, 294].

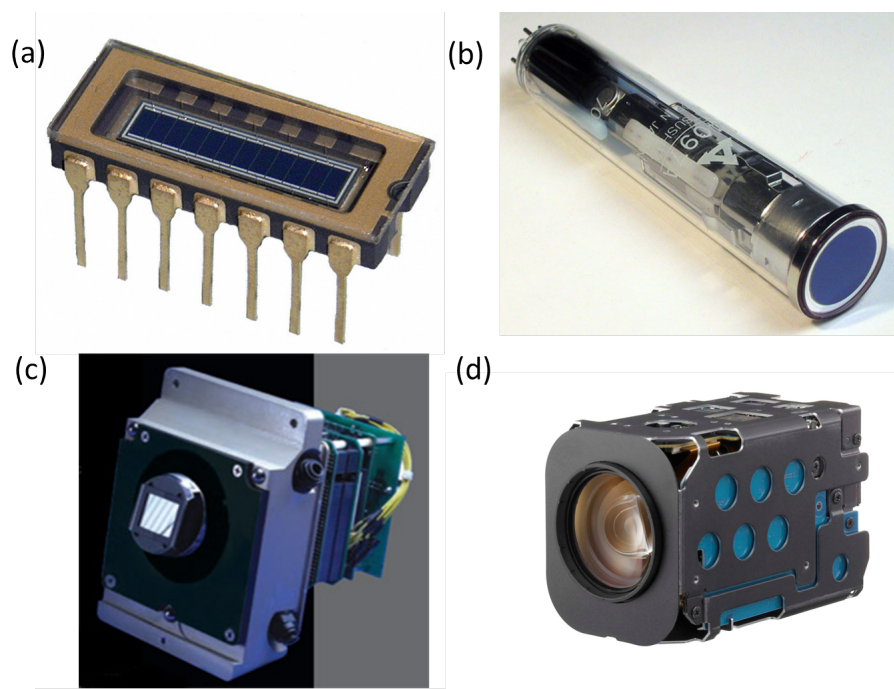


Figura 35: Fotografías de detectores multicanal. (a) fotodiodo en serie (PDA); (b) tubo vidicon (SIT); (c) dispositivo de inyección de carga (CID); (d) cámara CCD.

0.4.5 Instrumentación comercial

Los primeros fosforímetros de tiempo resuelto que se usaron en aplicaciones analíticas disponían de una fuente pulsante de xenón [325]; posteriormente se introdujo la fuente láser en estos equipos [291–295] y los detectores multicanal [256, 326]. Más tarde, se establecieron las bases teóricas y los desarrollos instrumentales para la utilización de los fosforímetros de tiempo resuelto en la resolución de sistemas multicomponentes [327–329].

Hoy día, la mayoría de los instrumentos comerciales son fosforímetros de tiempo de resuelto, y usan la misma base teórica y prácticamente la misma instrumentación que esos primeros fosforímetros, aunque ahora están asistidos por potentes ordenadores para llevar a cabo complejas operaciones y facilitar el tratamiento de las señales. Actualmente existen diversas posibilidades comerciales a la hora de adquirir un instrumento para llevar a cabo medidas de fosforescencia. De forma general, suelen ser instrumentos desarrollados para llevar a cabo medidas de fluorescencia que disponen de un accesorio para fosforescencia o llevan acoplada una lámpara pulsante de xenón de gran potencia (habitualmente de 150 W). Otra posibilidad, aunque menos frecuente, es la de emplear un sistema de hélice rotatoria en el haz de excitación y un detector de pulsos [51, 244].

Existen varias empresas comerciales que distribuyen equipos de luminiscencia aptos para llevar a cabo medidas de fosforescencia. Repasando la bibliografía se puede encontrar que los más ampliamente utilizados son los espectrómetros de la casa Perkin-Elmer, seguidos de los Aminco-Bowman, aunque existen otras muchas posibilidades [51, 244]. Algunos de los equipos más frecuentes que pueden ser encontrados en la literatura son: el espectrómetro

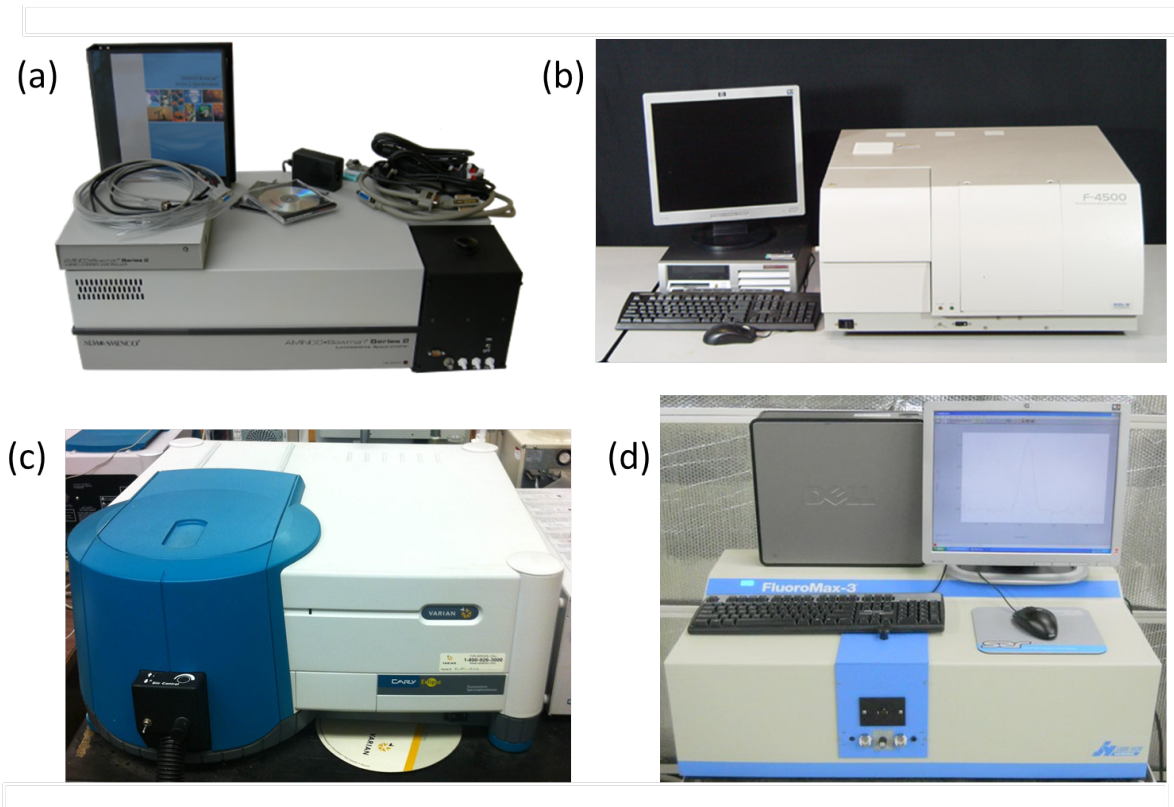


Figura 36: Equipos de luminiscencia comerciales aptos para llevar a cabo medidas de fosforescencia. (a) espectrómetro de luminiscencia Aminco-Bowman Series 2; (b) espectrómetro de luminiscencia Hitachi Instruments F-4500; (c) espectrofotómetro de fluorescencia Varian Cary Eclipse; (d) espectrofluorímetro Jobin-Yvon modelo Spex Fluoromax-3.

de luminiscencia Perkin-Elmer LS50B, espectrómetro de luminiscencia Aminco-Bowman Series 2, espectrómetro de luminiscencia Hitachi Instruments F-4500, espectrofotofluorímetro Quantamaster modelo C-61, espectrofotómetro de fluorescencia Varian Cary Eclipse, espectrofluorímetros Jobin-Yvon (modelos Spex Fluoromax-3 y Spex Fluorog-3) y el espectrómetro de tiempos de vida de fluorescencia FL900. En la Figura 36 se muestran las fotografías de algunos de estos equipos.

Por otro lado, en los últimos años también se han producido grandes avances en la instrumentación de modulación de fase (fluorimetría/fosforimetría en el dominio de la frecuencia). Antes de 1983, la fluorimetría en el dominio de la frecuencia ya permitía la determinación de tiempos de vida de luminiscencia, pero todavía no era capaz de resolver decaimientos de intensidad complejos. Esta limitación se debía fundamentalmente a que solo se disponía de fluorímetros de modulación de fase capaces de trabajar a una, dos o tres frecuencias de modulación fijas. La correcta caracterización de un decaimiento complejo requiere la adquisición de medidas en un intervalo amplio de frecuencias de modulación que permitan barrer la respuesta en frecuencia de la muestra. Antes de 1983, ya se habían desarrollado algunos instrumentos de medida de frecuencia variable, sin embargo, éstos eran generalmente poco prácticos y estaban limitados por los errores sistemáticos. El primer instrumento útil capaz de realizar un barrido de frecuencias fue descrito a mediados de la década de 1980 [330, 331].

Estos instrumentos permitían la medida de la fase y la modulación desde 1 a 200 MHz [331]. Estos primeros diseños fueron la base de los instrumentos de medida actuales. Hoy en día, la fluorimetría/fosforimetría en el dominio de la frecuencia es ampliamente usada en numerosos campos de aplicación [264, 332–336], existiendo una amplia variedad de instrumentos disponibles comercialmente [264]. Los fluorímetros de modulación de fase más avanzados permiten trabajar con frecuencias de modulación de hasta 10 GHz [51], y suelen ser usados habitualmente para el estudio de muestras complejas que presentan decaimientos de intensidad multiexponenciales o no exponenciales (debidos a procesos de transferencia de energía por resonancia, relajación de las moléculas del disolvente, atenuación dinámica, etc.) [51].

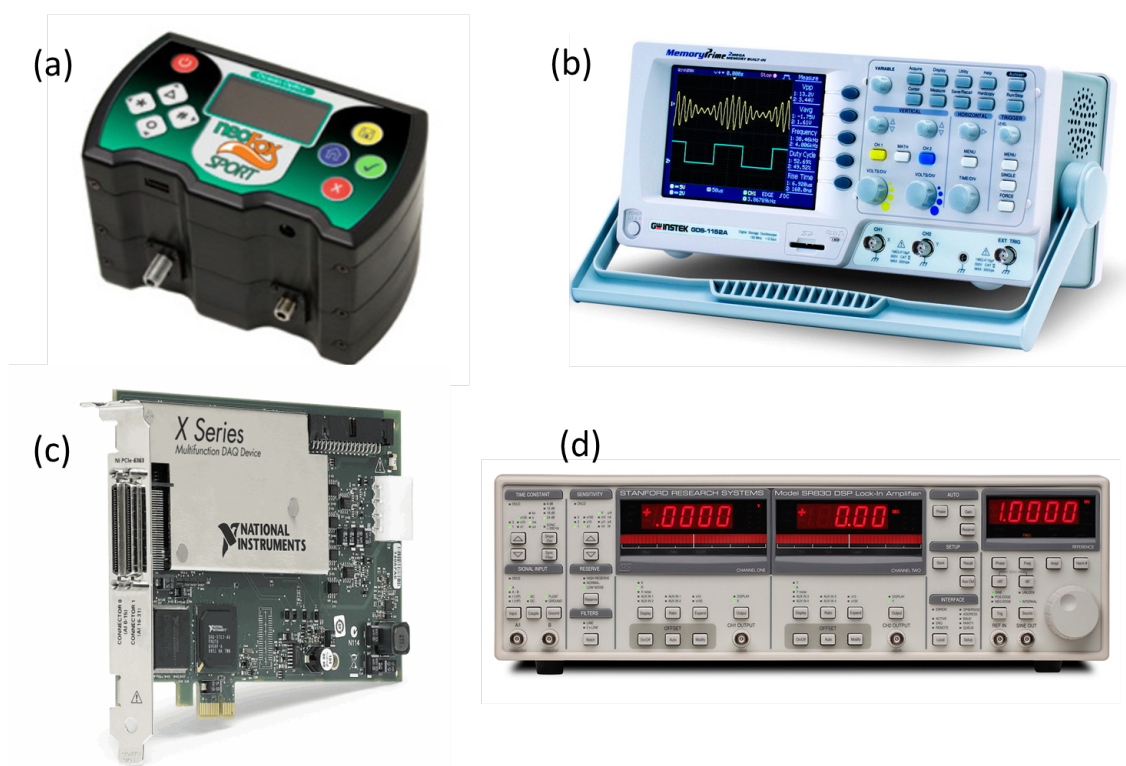


Figura 37: Instrumentación empleada en fosforimetría de modulación de fase (dominio de la frecuencia). (a) sensor comercial *NeoFox Sport* de Ocean Optics para la medida de oxígeno usando medidas de fase; (b) osciloscopio digital; (c) tarjeta de adquisición de datos AD/DA; (d) detector de fase-fija (*lock-in amplifier*, LIA).

El coste de estos instrumentos de medida se incrementa exponencialmente con la frecuencia de operación (intervalo de frecuencias de modulación que son capaces de barrer), por lo que su uso suele quedar limitado casi exclusivamente al ámbito de los laboratorios de investigación. Una fracción muy importante del coste total de estos equipos reside en la fuente de luz y/o en la óptica de modulación [51]. No obstante, la disponibilidad actual de fuentes de luz simples y baratas, como es el caso de los LEDs y los diodos láser [51], y de fibras ópticas para el guiado de la luz de excitación/emisión hacia/desde la muestra, ha permitido la miniaturización y el abaratamiento de estos equipos de medida. Un ejemplo de ello es el sensor comercial *NeoFox Sport* desarrollado por la compañía Ocean Optic Sensors para la medida de oxígeno y basado en medidas de fase (véase la Figura 37(a)). Finalmente, cabe destacar que

las medidas basadas en la técnica de modulación de fase (dominio de la frecuencia) también pueden ser obtenidas usando instrumentación de medida de propósito general, tales como osciloscopios digitales (Figura 37(b)), tarjetas de adquisición de datos AD/DA (Figura 37(c)), detectores de fase-fija (*lock-in amplifiers*, LIAs)(Figura 37(d)), ordenadores personales, etc. Dicha instrumentación suele estar disponible en la mayoría de los laboratorios de medida, ya que se usa para otras muchas tareas, lo que supone un importante ahorro económico, y también permite que dichos sistemas de medida de modulación de fase puedan ser adaptados fácilmente a una amplia variedad de escenarios y aplicaciones [22, 51, 99, 219, 228], proporcionándoles una gran versatilidad.

Así pues, podemos acabar concluyendo que la Química Analítica actual evoluciona de forma divergente siguiendo dos grandes líneas. Por un lado, se pretende conseguir equipos complejos de gran potencia y fiabilidad para el análisis de multitud de compuestos, mientras que por otro lado se pretende desarrollar sensores simples y selectivos para la resolución de problemas analíticos concretos. Por esto, la instrumentación empleada en luminiscencia evoluciona y continuará evolucionando en ambos sentidos, por una parte desarrollando complejos sistemas para acoplar la metodología luminiscente como técnica de detección de los potentes sistemas separativos de análisis, y por otra, posibilitando cada vez más, instrumentos portátiles sencillos para la medida de luminiscencia “in situ”.

Referencias

- [1] J. Rodríguez-Fernández, *Sensores ópticos de compuestos volátiles de azufre para el diagnóstico de halitosis oral*. PhD thesis, Departamento de Química Física y Analítica, Universidad de Oviedo (España), 2001.
- [2] J. Janata, M. Josowicz, P. Vanýsek, and D. M. DeVaney, "Chemical Sensors," *Analytical Chemistry*, vol. 70, no. 12, pp. 179R–208R, 1998.
- [3] J. Janata and A. Bezegh, "Chemical Sensors," *Analytical Chemistry*, vol. 60, pp. 62R–74R, 1988.
- [4] J. N. Roe, F. C. Szoka, and A. S. Verkman, "Fiber optic sensor for the detection of potassium using fluorescence energy-transfer," *Analyst*, vol. 115, pp. 353–358, 1990.
- [5] S. Hulanicki, A. Glab and F. Ingman, "Chemical Sensors: Definition and clasification," *Pure and Applied Chemistry*, vol. 63, pp. 1247–1250, 1991.
- [6] M. N. Velasco-García, *Sensores (bio)químicos ópticos para especies de interés clínico y medioambiental en medios no acuosos*. PhD thesis, Departamento de Química Física y Analítica, Universidad de Oviedo (España), 1997.
- [7] R. Badía, *Sensores químicos luminiscentes para el control de especies contaminantes en aguas*. PhD thesis, Departamento de Química Física y Analítica, Universidad de Oviedo (España), 1997.
- [8] M. Valcárcel and M. D. Luque de Castro, "Flow-through (bio)chemical sensors—Plenary lecture," *Analyst*, vol. 118, pp. 593–600, 1993.
- [9] N. Bustamante-Álvarez, *Sensores de temperatura, pH y detergentes para control medioambiental con un prototipo que utiliza fibra óptica y luminiscencia con resolución de fase*. PhD thesis, Departamento de Química Orgánica, Universidad Complutense de Madrid (España), 2001.
- [10] M. F. Choi and P. Hawkins, "The development of optical chemical sensors for the detection of volatile compounds from spoiled hams," *Sensors and Actuators B: Chemical*, vol. 39, pp. 390–394, 1997.

- [11] S. J. Hawkins, N. M. Ratcliffe, and A. Sagastizabal, "The use of thin silver films for the detection of low concentrations of hydrogen sulphide," *Analytica Chimica Acta*, vol. 359, pp. 125–132, 1998.
- [12] T. Edmonds, *Chemical Sensors*. London, UK: Blackie, 1988.
- [13] J. Janata, *Principles of Chemical Sensors*. New York, USA: Springer, 2 ed., 2010.
- [14] M. Marín-Suárez, *Desarrollo de nuevas fases sensoras ópticas para el control de oxígeno molecular con aplicaciones biotecnológicas, industriales y clínicas*. PhD thesis, Departamento de Química Analítica, Universidad de Granada (España), 2012.
- [15] M. D. Marazuela-Lamata, *Diseño, caracterización y aplicación analítica de (bio)-sensores de fibra óptica para la determinación de CO₂, O₂ y metabolitos de interés clínico*. PhD thesis, Departamento de Química Analítica, Universidad Complutense de Madrid (España), 1997.
- [16] C. Kolle, W. Gruber, W. Trettnak, K. Biebernik, C. Dolezal, F. Reininger, and P. O'Leary, "Fast optochemical sensor for continuous monitoring of oxygen in breath-gas analysis," *Sensors and Actuators B: Chemical*, vol. 38, pp. 141–149, 1997.
- [17] A. Elamari, N. Gisin, J. L. Munoz, S. Poitry, M. Tsacopoulos, and H. Zbinden, "Photon-counting optical-fiber sensor for the detection of ammonia in neurochemical applications," *Sensors and Actuators B: Chemical*, vol. 38, pp. 183–188, 1997.
- [18] P. W. Barone, R. S. Parker, and M. S. Strano, "In vivo fluorescence detection of glucose using a single-walled carbon nanotube optical sensor: Design, fluorophore properties, advantages, and disadvantages," *Analytical Chemistry*, vol. 77, pp. 7556–7562, 2005.
- [19] S. DuBois, S. Eng, R. Bhattacharya, S. Rulyak, T. Hubbard, D. Putnam, and D. Kearney, "Breath ammonia testing for diagnosis of hepatic encephalopathy," *Digestive Diseases and Sciences*, vol. 50, pp. 1780–1784, 2005.
- [20] K. Billingsley, M. K. Balaconis, J. M. Dubach, N. Zhang, E. Lim, K. P. Francis, and H. A. Clark, "Fluorescent nano-optodes for glucose detection," *Analytical Chemistry*, vol. 82, pp. 3707–3713, 2010.
- [21] A. Fercher, S. M. Borisov, A. V. Zhdanov, I. Klimant, and D. B. Papkovsky, "Intracellular O₂ sensing probe based on cell-penetrating phosphorescent nanoparticles," *ACS Nano*, vol. 5, pp. 5499–5508, 2011.
- [22] O. Ergeneman, G. Chatzipirpiridis, J. Pokki, M. Marín-Suárez, G. A. Sotiriou, S. Medina-Rodríguez, J. F. Fernández-Sánchez, A. Fernández-Gutiérrez, S. Pané, and B. J. Nelson, "In Vitro Oxygen Sensing Using Intraocular Microrobots," *IEEE Transactions on Biomedical Engineering*, vol. 59, no. 11, pp. 3104–3109, 2012.
- [23] G. A. Holst, T. Köster, E. Voges, and D. W. Lübbers, "FLOX—an oxygen-flux-measuring system using a phase-modulation method to evaluate the oxygen-dependent fluorescence lifetime," *Sensors and Actuators B: Chemical*, vol. 29, no. 1-3, pp. 231–239, 1995.
- [24] K. R. Rogers and J. N. Lin, "Biosensors for environmental monitoring," *Biosensors and Bioelectronics*, vol. 7, pp. 317–321, 1992.

- [25] J. F. Fernández-Sánchez, *Desarrollo de optosensores fluorescentes para la determinación de principios activos farmacológicos y contaminantes ambientales en muestras reales*. PhD thesis, Departamento de Química Analítica, Universidad de Granada (España), 2003.
- [26] Z. Yanaz, H. Filik, and R. Apak, “Development of an optical fibre reflectance sensor for lead detection based on immobilised arsenazo III,” *Sensors and Actuators B: Chemical*, vol. 147, pp. 15–22, 2010.
- [27] B. Nuriman-Kuswandi and W. Verboom, “Optical fiber chemical sensing of Hg(II) ions in aqueous samples using a microfluidic device containing a selective tripodal chromoionophore-PVC film,” *Sensors and Actuators B: Chemical*, vol. 157, pp. 438–443, 2011.
- [28] J. Richardson, A. Drake, C. Lazo-Miller, J. Hand, T. Morgan, and I. Lagadic, “Lead detection in environmental water sample using an organoclay film-based attenuated total reflectance sensor,” *Sensors and Actuators B: Chemical*, vol. 158, pp. 271–277, 2011.
- [29] W. Bourgeois, G. Gardey, M. Servieres, and R. M. Stuetz, “A chemical sensor array based system for protecting wastewater treatment plants,” *Sensors and Actuators B: Chemical*, vol. 91, pp. 109–116, 2003.
- [30] S. Beutel and S. Henkel, “In situ sensor techniques in modern bioprocess monitoring,” *Applied Microbiology and Biotechnology*, vol. 91, pp. 1493–1505, 2011.
- [31] M. Yasin, S. W. Harun, C. F. Tan, S. W. Phang, and H. Ahmad, “Fiber optic chemical sensor using fiber coupler probe based on intensity modulation for alcohol detection,” *Microwave and Optical Technology Letters*, vol. 53, pp. 1935–1938, 2011.
- [32] C. L. Yuana, C. P. Chang, and Y. Song, “Hazardous industrial gases identified using a novel polymer/MWNT composite resistance sensor array,” *Materials Science and Engineering B: Advanced Functional Solid-State Materials*, vol. 176, pp. 821–829, 2011.
- [33] A. R. De Jong, H. Boumans, T. Slaghek, J. Van Veen, R. Rijk, and M. Van Zandvoort, “Active and intelligent packaging for food: Is it the future?,” *Food Additives and Contaminants*, vol. 22, pp. 975–979, 2005.
- [34] K. L. Yam, P. T. Takhistov, and J. Miltz, “Intelligent packaging: Concepts and applications,” *Journal of Food Science*, vol. 70, pp. R1–R10, 2005.
- [35] T. V. Duncan, “Applications of nanotechnology in food packaging and food safety: barrier materials, antimicrobials and sensors,” *Journal of Colloid and Interface Science*, vol. 363, pp. 1–24, 2011.
- [36] D. Restuccia, U. G. Spizzirri, O. I. Parisi, G. Cirillo, M. Curcio, F. Iemma, F. Puoci, G. Vinci, and N. Picci, “New EU regulation aspects and global market of active and intelligent packaging for food industry applications,” *Food Control*, vol. 21, pp. 1425–1435, 2010.

- [37] C. Wanihsuksombat, V. Hongtrakul, and P. Suppakul, "Development and characterization of a prototype of a lactic acid-based time-temperature indicator for monitoring food product quality," *Journal of Food Engineering*, vol. 100, pp. 427–434, 2011.
- [38] A. Alimelli, G. Pennazza, M. Santonico, R. Paolesse, D. Filippini, A. D'Amico, I. Lundstrom, and C. Di Natale, "Fish freshness detection by a computer screen photoassisted based gas sensor array," *Analytica Chimica Acta*, vol. 582, pp. 320–328, 2007.
- [39] L. Gil, J. M. Barat, D. Baigts, R. Martínez-Manez, J. Soto, E. García-Breijo, M. C. Aristoy, F. Toldra, and E. Llobet, "Monitoring of physical-chemical and microbiological changes in fresh pork meat under cold storage by means of a potentiometric electronic tongue," *Food Chemistry*, vol. 126, pp. 1261–1268, 2011.
- [40] P. C. Thomas, M. Halter, A. Tona, S. R. Raghavan, A. L. Plant, and S. P. Forry, "A noninvasive thin film sensor for monitoring oxygen tension during in vitro cell culture," *Analytical Chemistry*, vol. 81, pp. 9239–9246, 2009.
- [41] T. S. Myllyla, A. Abou Elseoud, H. S. S. Sorvoja, R. A. Myllyla, J. M. Harja, J. Nikkinen, O. Tervonen, and V. Kiviniemi, "Fibre optic sensor for non-invasive monitoring of blood pressure during MRI scanning," *Journal of Biophotonics*, vol. 4, pp. 98–107, 2011.
- [42] M. Naciri, D. Kuystermans, and M. Al-Rubeai, "Monitoring pH and dissolved oxygen in mammalian cell culture using optical sensors," *Cytotechnology*, vol. 57, pp. 245–250, 2008.
- [43] D. Sud and M. A. Mycek, "Calibration and validation of an optical sensor for intracellular oxygen measurements," *Journal of Biomedical Optics*, vol. 14, 2009. doi:10.1117/1.3116714.
- [44] H. Y. Zhu, P. S. Dale, C. W. Caldwell, and X. D. Fan, "Rapid and label-free detection of breast cancer biomarker CA15-3 in clinical human serum samples with optofluidic ring resonator sensors," *Analytical Chemistry*, vol. 81, pp. 9858–9865, 2009.
- [45] D. Thomazy, S. So, A. Kosterev, R. Lewicki, L. Dong, A. A. Sani, and F. K. Tittel, "Low-power laser-based carbon monoxide sensor for fire and post-fire detection using a compact Herriott multipass cell," *In Quantum Sensing and Nanophotonic Devices VII*, vol. 7608; Razeghi M., Sudharasan R., Brown G.J., Eds., 2010.
- [46] I. Oehme and O. Wolfbeis, "Optical sensors for determination of heavy metal ions," *Mikrochimica Acta*, vol. 126, pp. 177–192, 1997.
- [47] D. J. Monk and D. R. Walt, "Optical fiber-based biosensors," *Analytical and Bioanalytical Chemistry*, vol. 379, pp. 931–945, 2004.
- [48] A. Leung, P. M. Shankar, and R. Mutharasan, "A review of fiber-optic biosensors," *Sensors and Actuators B: Chemical*, vol. 125, pp. 688–703, 2007.
- [49] G. Orellana and D. Haigh, "New trends in fiber-optic chemical and biological sensors," *Current Analytical Chemistry*, vol. 4, pp. 273–295, 2008.

- [50] O. S. Wolfbeis, B. M. Weidgans, F. Baldini, A. N. Chester, J. Homola, and S. Martellucci, *Fiber Optic Chemical Sensors and Biosensors: A View Back Optical Chemical Sensors*, vol. 224 of *NATO Science Series*, pp. 17–44. Springer Netherlands, 2006.
- [51] J. R. Lakowicz, *Principles of Fluorescence Spectroscopy*. New York: Kluwer Academic, 2nd ed., 1999.
- [52] C. Elosúa-Aguado, *Contribution to the development of optical fibre sensors to detect volatile organic compounds and their potential application in opto-electronic noses*. PhD thesis, Department of Electric and Electronic Engineering, Universidad Pública de Navarra (España), 2010.
- [53] A. Martínez-Olmos, I. M. Pérez de Vargas-Sansalvador, A. J. Palma, J. Banqueri, M. D. Fernández-Ramos, and L. F. Capitán-Vallvey, “Multisensor probe for soil monitoring,” *Sensors and Actuators B: Chemical*, vol. 160, pp. 52–58, 2011.
- [54] A. Martínez-Olmos, S. Capel-Cuevas, N. López-Ruiz, A. J. Palma, I. de Orbe, and L. F. Capitán-Vallvey, “Sensor array-based optical portable instrument for determination of pH,” *Sensors and Actuators B: Chemical*, vol. 156, pp. 840–848, 2011.
- [55] J. Goicoechea, C. R. Zamarreño, I. R. Matias, and F. J. Arregui, “Optical fiber pH sensors based on layer-by-layer electrostatic self-assembled neutral red,” *Sensors and Actuators B: Chemical*, vol. 132, pp. 305–311, 2008.
- [56] V. M. Chauhan, G. R. Burnett, and J. W. Aylott, “Dual-fluorophore ratiometric pH nanosensor with tuneable pK(a) and extended dynamic range,” *Analyst*, vol. 136, pp. 1799–1801, 2011.
- [57] K. Alizadeh, R. Parooi, P. Hashemi, B. Rezaei, and M. R. Ganjali, “A new Schiff’s base ligand immobilized agarose membrane optical sensor for selective monitoring of mercury ion,” *Journal of Hazardous Materials*, vol. 186, pp. 1794–1800, 2011.
- [58] G. G. Huang, C. J. Lee, B. C. Tsai, J. Yang, M. Sathiyendiran, and K. L. Lu, “Gondola-shaped tetra-rhenium metallacycles modified evanescent wave infrared chemical sensors for selective determination of volatile organic compounds,” *Talanta*, vol. 85, pp. 63–69, 2011.
- [59] F. Long, C. Gao, H. C. Shi, M. He, A. N. Zhu, A. M. Klibanov, and A. Z. Gu, “Reusable evanescent wave DNA biosensor for rapid, highly sensitive, and selective detection of mercury ions,” *Biosensors and Bioelectronics*, vol. 26, pp. 4018–4023, 2011.
- [60] L. I. B. Silva, A. C. Freitas, T. A. P. Rocha-Santos, M. E. Pereira, and A. C. Duarte, “Breath analysis by optical fiber sensor for the determination of exhaled organic compounds with a view to diagnostics,” *Talanta*, vol. 83, pp. 1586–1594, 2011.
- [61] J. P. Phillips, R. M. Langford, S. H. Chang, P. A. Kyriacou, and D. P. Jones, “Photoplethysmographic measurements from the esophagus using a new fiber-optic reflectance sensor,” *Journal of Biomedical Optics*, vol. 16, 2011. doi: 10.1117/1.3598858.
- [62] R. Kato, K. Kide, T. Hattori, A. Wakahara, and M. Yamaguchi, “Detection of moisture in oil using evanescent absorption from sapphire optical waveguide coated with co-doped silica film,” *Analytical Letters*, vol. 44, pp. 577–584, 2011.

- [63] A. R. Sadrolhosseini, M. M. Moxsin, W. M. M. Yunus, and Z. A. Talib, "Application of surface plasmon resonance sensor in detection of water in palm-oil-based biodiesel and biodiesel blend," *Sensors and Materials*, vol. 23, pp. 315–324, 2011.
- [64] D. Wildeboer, P. Jiang, R. G. Price, S. Yu, F. Jeganathan, and R. A. Abuknesha, "Use of antibody-hapten complexes attached to optical sensor surfaces as a substrate for proteases: Real-time biosensing of protease activity," *Talanta*, vol. 81, pp. 68–75, 2010.
- [65] E. Moczko, M. Cauchi, C. Turner, I. Meglinski, and S. Piletsky, "Optical assay for biotechnology and clinical diagnosis," *IEEE Transactions on Biomedical Engineering*, vol. 58, pp. 2154–2160, 2011.
- [66] D. Álvarez, M. Castillo, Y. L. Xiong, and F. A. Payne, "Prediction of beef meat emulsion quality with apparent light backscatter extinction," *Food Research International*, vol. 43, pp. 1260–1266, 2010.
- [67] W. R. Habel, *Reliable Use of Fiber Optic Sensors. In Encyclopedia of Structural Health Monitoring*. John Wiley & Sons ISBN-10: 0-470-05822-6, ISBN-13: 978-0-470-05822-0, Edition January 2009.
- [68] IUPAC, "Nomenclature, symbols, units and their usage in spectro-chemical analysis-ii: Data interpretation.," *Spectrochimica Acta, Part B: Atomic Spectroscopy*, vol. 33B, pp. 242–248, 1978.
- [69] M. D. Luque de Castro and M. Valcárcel, "Flow-through (bio)chemical sensors in environmental analysis," *Techniques and Instrumentation in Analytical Chemistry*, vol. 17, pp. 111–163, 1995.
- [70] A. L. Medina-Castillo, *Nuevas estrategias para la síntesis y caracterización de fases sensoras ópticas nanoestructuradas*. PhD thesis, Departamento de Química Analítica, Universidad de Granada (España), 2011.
- [71] J. M. Costa-Fernández and A. Sanz-Medel, *Fosforescencia molecular analítica: una aproximación práctica*. Editorial Universidad de Granada, España, 2001. A. Fernández-Gutiérrez and S. G. Schulman (Eds.).
- [72] A. F. Faria, R. A. Mignone, M. A. Montenegro, A. Z. Mercadante, and C. D. Borsarelli, "Characterization and singlet oxygen quenching capacity of spray-dried microcapsules of edible biopolymers containing antioxidant molecules," *Journal of Agricultural and Food Chemistry*, vol. 58, pp. 8004–8011, 2010.
- [73] M. Marín Suárez del Toro, J. F. Fernández-Sánchez, E. Baranoff, M. K. Nazeeruddin, M. Graetzel, and A. Fernández-Gutiérrez, "Novel luminescent Ir(III) dyes for developing highly sensitive oxygen sensing films," *Talanta*, vol. 82, pp. 620–626, 2010.
- [74] J. N. Anker, Y. E. Koo, and R. Kopelman, "Magnetically controlled sensor swarms," *Sensors and Actuators B: Chemical*, vol. 121, pp. 83–92, 2007.
- [75] J. Ruzicka and E. H. Hansen, "Optosensing at active surfaces: a new detection principle in flow injection analysis," *Analytica Chimica Acta*, vol. 173, pp. 3–21, 1985.

- [76] Y. Wang, S. Meng, Y. Song, W. Zhong, J. Jiang, S. Chen, and C. Bai, "Fluorescence optical fibre sensor provides accurate continuous oxygen detection in rabbit model with acute lung injury," *Respirology*, vol. 15, pp. 99–106, 2010.
- [77] K. Tsukada, S. Sakai, K. Hase, and H. Minamitani, "Development of catheter-type optical oxygen sensor and applications to bioinstrumentation," *Biosensors and Bioelectronics*, vol. 18, pp. 1439–1445, 2003.
- [78] F. J. Sainz-Gonzalo, C. Elosua, J. F. Fernández-Sánchez, C. Popovici, I. Fernández, F. L. Ortiz, F. J. Arregui, I. R. Matias, and A. Fernández-Gutiérrez, "A novel luminescent optical fibre probe based on immobilized tridentate bis(phosphinic amide)-phosphine oxide for europium(III) ion aqueous detection in situ," *Sensors and Actuators B: Chemical*, vol. 173, pp. 254–261, 2012.
- [79] G. Boisde, "Les capteurs chimiques à fibres optiques. Réalités et perspectives. Chemical optical-fiber sensors: realities and prospects," *Entropie*, vol. 26, pp. 28–42, 1990.
- [80] U. E. Spichiger-Keller, *Optical Sensors, Optodes. In Chemical Sensors and Biosensors for Medical and Biological Applications*. John Wiley & Sons, 2008.
- [81] Y. Takabayashi, M. Uemoto, K. Aoki, T. Odake, and T. Korenaga, "Development and optimization of a lab-on-a-chip device for the measurement of trace nitrogen dioxide gas in the atmosphere," *Analyst*, vol. 131, pp. 573–578, 2006.
- [82] K. Schult, A. Katerkamp, D. Trau, F. Grawe, K. Cammann, and M. Meusel, "Disposable optical sensor chip for medical diagnostics: New ways in bioanalysis," *Analytical Chemistry*, vol. 71, pp. 5430–5435, 1999.
- [83] B. Kuswandi, Nuriman, J. Huskens, and W. Verboom, "Optical sensing systems for microfluidic devices: A review," *Analytica Chimica Acta*, vol. 601, pp. 141–155, 2007.
- [84] A. S. Watts, A. A. Urbas, E. Moschou, V. G. Gavalas, J. V. Zoval, M. Madou, and L. G. Bachas, "Centrifugal microfluidics with integrated sensing microdome optodes for multiion detection," *Analytical Chemistry*, vol. 79, pp. 8046–8054, 2007.
- [85] S. Ramírez-García, M. Baeza, M. O'Toole, Y. Wu, J. Lalor, G. G. Wallace, and D. Diamond, "Towards the development of a fully integrated polymeric microfluidic platform for environmental analysis," *Talanta*, vol. 77, pp. 463–467, 2008.
- [86] E. Verpoorte, "Focus Chip vision-optics for microchips," *Lab on a Chip*, vol. 3, pp. 42N–52N, 2003.
- [87] D. B. Papkovsky, K. S. Chandan, and L. S. Gregg, *Methods in Optical Oxygen Sensing: Protocols and Critical Analyses. In Methods in Enzymology*, vol. 381. Academic Press, 2004.
- [88] I. Pérez de Vargas-Sansalvador, A. Martínez-Olmos, A. Palma, M. Fernández-Ramos, and L. Capitán-Vallvey, "Compact optical instrument for simultaneous determination of oxygen and carbon dioxide," *Microchimica Acta*, vol. 172, pp. 455–464, 2011.
- [89] O. Geschke, H. Klank, and P. Telleman, *Microsystem Engineering of Lab-on-a-chip Devices*. John Wiley & Sons, 2004.

- [90] A. Ríos, A. Escarpa, and S. Bartolomé, *Miniaturization of Analytical Systems: Principles, Designs and Applications*. John Wiley & Sons, 2009.
- [91] S. Reckziegel, D. Kreye, T. Puegner, C. Grillberger, M. Toerker, and U. Vogel, “Op-toelectronic chips integrate emitters and sensors,” *SPIE Digital Library*, 2008. doi: 10.1117/2.1200806.1151.
- [92] M. Schäferling, “The Art of Fluorescence Imaging with Chemical Sensors,” *Angewandte Chemie International*, vol. 51, pp. 3532–3554, 2012.
- [93] J. P. Fischer and K. Koop-Jakobsen, “The multi fiber optode (MuFO): A novel system for simultaneous analysis of multiple fiber optic oxygen sensors,” *Sensors and Actuators B: Chemical*, vol. 168, pp. 354–359, 2012.
- [94] N. López-Ruiz, A. Martínez-Olmos, I. M. Pérez de Vargas-Sansalvador, M. D. Fernández-Ramos, M. A. Carvajal, L. F. Capitán-Vallvey, and A. J. Palma, “Determination of O₂ using colour sensing from image processing with mobile devices,” *Sensors and Actuators B: Chemical*, vol. 171–172, pp. 938–945, 2012.
- [95] M. Miró and E. H. Hansen, “Recent advances and future prospects of mesofluidic Lab-on-a-Valve platforms in analytical sciences: A critical review,” *Analytica Chimica Acta*, vol. 750, pp. 3–15, 2012.
- [96] P. Gründler, *Chemical Sensors: An Introduction for Scientists and Engineers*. Springer-Verlag, 2007.
- [97] R. J. Hurtubise, “Solid-surface luminescence spectrometry,” *Analytical Chemistry*, vol. 61, pp. 889A–895A, 1989.
- [98] F. Sainz-Gonzalo, *Desarrollo de fases sensoras ópticas para el control de la calidad de aguas y vinos*. PhD thesis, Departamento de Química Analítica, Universidad de Granada (España), 2012.
- [99] M. Marín-Suárez, S. Medina-Rodríguez, O. Ergeneman, S. Pané, J. F. Fernández-Sánchez, B. J. Nelson, and A. Fernández-Gutiérrez, “Electrophoretic deposition as a new approach to produce optical sensing films adaptable to microdevices,” *Nanoscale*, 2013. doi: 10.1039/C3NR03336H.
- [100] J. F. Fernández-Sánchez, R. Cannas, S. Spichiger, R. Steiger, and U. E. Spichiger-Keller, “Novel nanostructured materials to develop oxygen-sensitive films for optical sensors,” *Analytica Chimica Acta*, vol. 566, pp. 271–282, 2006.
- [101] J. F. Fernández-Sánchez, R. Cannas, S. Spichiger, R. Steiger, and U. E. Spichiger-Keller, “Optical CO₂-sensing layers for clinical application based on pH-sensitive indicators incorporated into nanoscopic metal-oxide supports,” *Sensors and Actuators B: Chemical*, vol. 128, pp. 145–153, 2007.
- [102] S. M. Borisov, T. Mayr, G. Mistlberger, K. Waich, K. Koren, P. Chojnacki, and I. Klimant, “Precipitation as a simple and versatile method for preparation of optical nanochemosensors,” *Talanta*, vol. 79, pp. 1322–1330, 2009.

- [103] J. E. Díaz, A. Barrero, M. Márquez, A. Fernández-Nieves, and I. G. Loscertales, "Absorption properties of microgel-PVP composite nanofibers made by electrospinning," *Macromolecular Rapid Communications*, vol. 31, pp. 183–189, 2010.
- [104] S. Pelfrey, T. Cantu, M. R. Papantonakis, D. L. Simonson, R. A. McGill, and J. Macosay, "Microscopic and spectroscopic studies of thermally enhanced electrospun PMMA micro- and nanofibers," *Polymer Chemistry*, vol. 1, pp. 866–869, 2010.
- [105] A. Salinas-Castillo, J. F. Fernández-Sánchez, A. Segura-Carretero, and A. Fernández-Gutiérrez, "Solid-surface phosphorescence characterization of polycyclic aromatic hydrocarbons and selective determination of benzo(a)pyrene in water samples," *Analytica Chimica Acta*, vol. 550, pp. 53–60, 2005.
- [106] I. Sánchez-Barragán, K. Karim, J. M. Costa-Fernández, S. A. Piletsky, and A. Sanz-Medel, "A molecularly imprinted polymer for carbaryl determination in water," *Sensors and Actuators B: Chemical*, vol. 123, pp. 798–804, 2007.
- [107] I. Sánchez-Barragán, J. M. Costa-Fernández, A. Pereiro, R.; Sanz-Medel, A. Salinas, A.; Segura, A. Fernández-Gutiérrez, A. Ballesteros, and J. M. González, "Molecularly imprinted polymers based on iodinated monomers for selective room-temperature phosphorescence optosensing of fluoranthene in water," *Analytical Chemistry*, vol. 77, pp. 7005–7011, 2005.
- [108] N. N. Greenwood and A. Earnshaw, *Chemistry of the Elements*. Elsevier, 2 ed., 1997.
- [109] L. N. Magner, *A History of the Life Sciences*. Marcel-Dekker Inc.: New York - Basel, 3 ed., 2005.
- [110] J. Alderman, J. Hynes, S. M. Floyd, J. Krüger, R. O'Connor, and D. B. Papkovsky, "A low-volume platform for cell-respirometric screening based on quenched-luminescence oxygen sensing," *Biosensors and Bioelectronics*, vol. 19, pp. 1529–1535, 2004.
- [111] E. Thedinga, A. Kob, H. Holst, A. Keuer, S. Drechsler, R. Niendorf, W. Baumann, I. Freund, M. Lehmann, and R. Ehret, "Online monitoring of cell metabolism for studying pharmacodynamic effects," *Toxicology and Applied Pharmacology*, vol. 220, pp. 33–44, 2007.
- [112] Z. Li and B. H. Graham, *Measurement of Mitochondrial Oxygen Consumption Using a Clark Electrode*. In *Mitochondrial Disorder*, vol. 837. Springer New York, 2012.
- [113] F. C. O'Mahony, C. O'Donovan, J. Hynes, T. Moore, J. Davenport, and D. B. Papkovsky, "Optical oxygen microrespirometry as a platform for environmental toxicology and animal model studies," *Environmental Science & Technology*, vol. 39, pp. 5010–5014, 2005.
- [114] K. Kellner, G. Liebsch, I. Klimant, O. S. Wolfbeis, T. Blunk, M. B. Schulz, and A. Göpferich, "Determination of oxygen gradients in engineered tissue using a fluorescent sensor," *Biotechnology and Bioengineering*, vol. 80, pp. 73–83, 2002.
- [115] S. W. O'Driscoll, J. S. Fitzsimmons, and C. N. Commisso, "Role of oxygen tension during cartilage formation by periosteum," *Journal of Orthopaedic Research*, vol. 15, pp. 682–687, 1997.

- [116] M. Radisic, J. Malda, E. Epping, W. Geng, R. Langer, and G. Vunjak-Novakovic, "Oxygen gradients correlate with cell density and cell viability in engineered cardiac tissue," *Biotechnology and Bioengineering*, vol. 93, pp. 332–343, 2006.
- [117] A. Carreau, B. E. Hafny-Rahbi, A. Matejuk, C. Grillon, and C. Kieda, "Why is the partial oxygen pressure of human tissues a crucial parameter? Small molecules and hypoxia," *Journal of Cellular and Molecular Medicine*, vol. 15, pp. 1239–1253, 2011.
- [118] J. Kiss, J. Kirchberg, and M. Schneider, "Molecular oxygen sensing: implications for visceral surgery," *Langenbeck's Archives of Surgery*, vol. 397, pp. 603–610, 2012.
- [119] M. Brahim-Horn, J. Chiche, and J. Pouysségur, "Hypoxia and cancer," *Journal of Molecular Medicine*, vol. 85, pp. 1301–1307, 2007.
- [120] M. Elas, K. H. Ahn, A. Parasca, E. D. Barth, D. Lee, C. Haney, and H. J. Halpern, "Electron paramagnetic resonance oxygen images correlate spatially and quantitatively with oxylite oxygen measurements," *Clinical Cancer Research*, vol. 12, pp. 4209–4217, 2006.
- [121] J. Pacheco-Torres, P. López-Larrubia, P. Ballesteros, and S. Cerdán, "Imaging tumor hypoxia by magnetic resonance methods," *NMR in Biomedicine*, vol. 24, pp. 1–16, 2010.
- [122] A. Dragu, C. Taeger, R. Buchholz, B. Sommerfeld, H. Hübner, T. Birkholz, J. Kleinmann, F. Münch, R. Horch, and K. Präbst, "Online oxygen measurements in ex vivo perfused muscle tissue in a porcine model using dynamic quenching methods," *Archives of Orthopaedic and Trauma Surgery*, vol. 132, pp. 655–661, 2011.
- [123] C. A. K. Lange, P. Stavrakas, U. F. O. Luhmann, D. J. de Silva, R. R. Ali, Z. J. Gregor, and J. W. B. Bainbridge, "Intraocular oxygen distribution in advanced proliferative diabetic retinopathy," *American Journal of Ophthalmology*, vol. 152, pp. 406–412, 2011.
- [124] A. Macnab, B. Shadgan, P. Janssen, and D. Rurak, "Fetal oxygenation measurement using wireless near infrared spectroscopy," *Proceedings of the Society of Photo-Optical Instrumentation - SPIE*, vol. 8229, p. 822902, 2012.
- [125] T. Heldt, F. M. Kashif, M. Sulemanji, H. M. O'Leary, A. J. Du Plessis, and G. C. Vergheze, "Continuous quantitative monitoring of cerebral oxygen metabolism in neonates by ventilator-gated analysis of NIRS recordings," *Acta Neurochirurgica Supplementum*, vol. 114, pp. 177–180, 2012.
- [126] M. A. Acosta, P. Ymele-Leki, Y. V. Kostov, and J. B. Leach, "Fluorescent microparticles for sensing cell microenvironment oxygen levels within 3D scaffolds," *Biomaterials*, vol. 30, pp. 3068–3074, 2009.
- [127] R. E. Ross, "Age-specific decrease in aerobic efficiency associated with increase in oxygen free radical production in *Drosophila melanogaster*," *Journal of Insect Physiology*, vol. 46, pp. 1477–1480, 2000.
- [128] V. Bunik, J. Schloss, J. Pinto, G. Gibson, and A. Cooper, "Enzyme-catalyzed side reactions with molecular oxygen may contribute to cell signaling and neurodegenerative diseases," *Neurochemical Research*, vol. 32, pp. 871–891, 2007.

- [129] K. Grinnell, H. Duong, J. Newton, S. Rounds, G. Choudhary, and E. O. Harrington, "Heterogeneity in apoptotic responses of microvascular endothelial cells to oxidative stress," *Journal of Cellular Physiology*, vol. 227, pp. 1899–1910, 2012.
- [130] C. Dennog, A. Hartmann, G. Frey, and G. Speit, "Detection of DNA damage after hyperbaric oxygen (HBO) therapy," *Mutagenesis*, vol. 11, pp. 605–609, 1996.
- [131] O. D. Saugstad, "Oxygen toxicity in the neonatal period," *Acta Paediatrica*, vol. 79, pp. 881–892, 1990.
- [132] B. Weinberger, D. L. Laskin, D. E. Heck, and J. D. Laskin, "Oxygen toxicity in premature infants," *Toxicology and Applied Pharmacology*, vol. 181, pp. 60–67, 2002.
- [133] P. Wilmshurst, "ABC of oxygen: diving and oxygen," *BMJ Journal*, vol. 317, pp. 996–999, 1998.
- [134] N. Gopal-Mandal, "Measurement of gas concentrations: oxygen, carbon dioxide, nitrogen, nitrous oxide and volatile anaesthetic agents," *Anaesthesia & Intensive Care Medicine*, vol. 9, pp. 559–563, 2008.
- [135] M.-S. Steiner, A. Duerkop, and O. S. Wolfbeis, "Optical methods for sensing glucose," *Chemical Society Reviews*, vol. 40, pp. 4805–4839, 2011.
- [136] S. Suresh, V. C. Srivastava, and I. M. Mishra, "Techniques for oxygen transfer measurement in bioreactors: a review," *Journal of Chemical Technology & Biotechnology*, vol. 84, pp. 1091–1103, 2009.
- [137] C. Peña, C. P. Peter, J. Büchs, and E. Galindo, "Evolution of the specific power consumption and oxygen transfer rate in alginate-producing cultures of *Azotobacter vinelandii* conducted in shake flasks," *Biochemical Engineering Journal*, vol. 36, pp. 73–80, 2007.
- [138] X. Ge and G. Rao, "Real-time monitoring of shake flask fermentation and off gas using triple disposable noninvasive optical sensors," *Biotechnology Progress*, vol. 28, pp. 872–877, 2012.
- [139] A. M. Pisoschi, A. Pop, A. I. Serban, and G. P. Negulescu, "Ethanol determination by an amperometric bienzyme sensor based on a Clark-type transducer," *Journal of Electroanalytical Chemistry*, vol. 671, pp. 85–91, 2012.
- [140] M. J. Arts, C. Grun, R. L. de Jong, H. P. Voss, A. Bast, M. J. Mueller, and G. R. Haenen, "Oxidative Degradation of Lipids during Mashing," *Journal of Agricultural and Food Chemistry*, vol. 55, pp. 7010–7014, 2007.
- [141] M. Numata, N. Funazaki, S. Ito, Y. Asano, and Y. Yano, "Flow-injection analysis for hypoxanthine in meat with dissolved oxygen detector and enzyme reactor," *Talanta*, vol. 43, pp. 2053–2059, 1996.
- [142] C. Pénicaud, S. Guilbert, S. Peyron, N. Gontard, and V. Guillard, "Oxygen transfer in foods using oxygen luminescence sensors: Influence of oxygen partial pressure and food nature and composition," *Food Chemistry*, vol. 123, pp. 1275–1281, 2012.

- [143] S. F. O’Keefe and O. A. Pike, *Food Analysis*. Springer: Dordrecht Heidelberg London New York, 2010.
- [144] P. Lopes, C. Saucier, P. L. Teissedre, and Y. Glories, “Main routes of oxygen ingress through different closures into wine bottles,” *Journal of Agricultural and Food Chemistry*, vol. 55, pp. 5167–5170, 2007.
- [145] F. C. O’Mahony, T. C. O’Riordan, N. Papkovskaia, J. P. Kerry, and D. B. Papkovsky, “Non-destructive assessment of oxygen levels in industrial modified atmosphere packaged cheddar cheese,” *Food Control*, vol. 17, pp. 286–292, 2006.
- [146] M. Smiddy, M. Fitzgerald, J. P. Kerry, D. B. Papkovsky, C. K. O’ Sullivan, and G. G. Guilbault, “Use of oxygen sensors to non-destructively measure the oxygen content in modified atmosphere and vacuum packed beef: impact of oxygen content on lipid oxidation,” *Meat Science*, vol. 61, pp. 285–290, 2002.
- [147] R. C. Soliva-Fortuny and O. Martín-Belloso, “New advances in extending the shelf-life of fresh-cut fruits: a review,” *Trends in Food Science & Technology*, vol. 14, pp. 341–353, 2003.
- [148] J. Lammertyn, N. Scheerlinck, B. E. Verlinden, W. Schotsmans, and B. M. Nicolä, “Simultaneous determination of oxygen diffusivity and respiration in pear skin and tissue,” *Postharvest Biology and Technology*, vol. 23, pp. 93–104, 2001.
- [149] “Facts & Figures for the Chemical Industry,” *Chemical & Engineering News*, vol. 83, p. 41, 2005.
- [150] M. M. Tripathi, K. E. Eseller, F. Y. Yueh, and J. P. Singh, “An optical sensor for multi-species impurity monitoring in hydrogen fuel,” *Sensors and Actuators B: Chemical*, vol. 171-172, pp. 416–422, 2012.
- [151] M. Beshay, S. Garon, D. Ruíz, and L. U. Kempen, “Intrinsically safe oxygen and hydrogen optical leak detector,” in *Proceedings of SPIE, the International Society for Optical Engineering*, 2011.
- [152] T. Takeuchi, “Oxygen sensors,” *Sensors and Actuators B: Chemical*, vol. 14, pp. 109–124, 1988.
- [153] L. Yang, H. Zare-Behtash, E. Erdem, and K. Kontis, “Investigation of the double ramp in hypersonic flow using luminescent measurement systems,” *Experimental Thermal and Fluid Science*, vol. 40, pp. 50–56, 2012.
- [154] T. J. Juliano, K. J. Disotell, J. W. Gregory, J. Crafton, and S. Fonov, “Motion-deblurred, fast-response pressure-sensitive paint on a rotor in forward flight,” *Measurement Science and Technology*, vol. 23, p. 045303, 2012.
- [155] C. Han, J. Ren, and H. Jiang, “Multi-parameter influence on combined-hole film cooling system,” *International Journal of Heat and Mass Transfer*, vol. 55, pp. 4232–4240, 2012.
- [156] T. Kameya, Y. Matsuda, H. Yamaguchi, Y. Egami, and T. Niimi, “Pressure-sensitive paint measurement on co-rotating disks in a hard disk drive,” *Optics and Lasers in Engineering*, vol. 50, pp. 82–86, 2012.

- [157] Y. Li, L. X. Jiang, X. J. Lv, Y. Q. Lai, H. L. Zhang, J. Li, and Y. X. Liu, "Oxygen evolution and corrosion behaviors of co-deposited Pb/Pb-MnO₂ composite anode for electrowinning of nonferrous metals," *Hydrometallurgy*, vol. 109, pp. 252–257, 2011.
- [158] N. B. Hasan, A. J. Haider, and M. A. Al-Amar, "Effect of oxygen pressure on the structural, morphology and optical properties of nanocrystalline TiO₂ thin films prepared by pulsed laser deposition," *European Journal of Scientific Research*, vol. 69, pp. 520–526, 2012.
- [159] A. A. Santos, L. Goldstein, and C. A. Ferrari, "An experiment on the effect of oxygen content and air velocity on soot formation in acetylene laminar diffusion flame produced in a burner with a parallel annular coaxial oxidizer flow," *International Communications in Heat and Mass Transfer*, vol. 36, pp. 445–450, 2009.
- [160] G. Särner, U. Göransson, J. Lindén, M. Richter, and M. Aldén, "Using oxygen-quenched pressure-sensitive paint for oxygen concentration measurements in low-temperature combustion environments," *Measurement Science and Technology*, vol. 19, p. 085307, 2008.
- [161] P. Brglez, A. Holobar, A. Pivec, N. Belsak, and M. Kolar, "Determination of oxygen by means of a biogas and gas-interference study using an optical tris (4,7-diphenyl-1,10-phenanthroline) ruthenium(II) dichloride complex sensor," *Acta Chimica Slovenica*, vol. 59, pp. 50–58, 2012.
- [162] I. Linnerud, P. Kaspersen, and T. Jaeger, "Gas monitoring in the process industry using diode laser spectroscopy," *Applied Physics B: Lasers and Optics*, vol. 67, pp. 297–305, 1998.
- [163] Y. Nakamura, D. Ito, T. Yokoyama, S. Okazaki, H. Nakagawa, and T. Arai, "Development of a fiber-optic oxygen sensor for long-term corrosion monitoring of radioactive-waste repository," *Sensor Letters*, vol. 6, pp. 951–955, 2008.
- [164] V. Makarenko, S. Shatilo, K. Gumerskii, and V. Belyaev, "Effect of oxygen and hydrogen sulfide on carbon dioxide corrosion of welded structures of oil and gas installations," *Chemical and Petroleum Engineering*, vol. 36, pp. 125–130, 2000.
- [165] B. Liu, D. Wu, Q. L. Sun, W. Y. Zheng, J. D. Lu, G. X. Lin, and X. M. Li, "Maintenance of water-cooled generator stator coils during outage," *Corrosion Science and Protection Technology*, vol. 21, pp. 305–307, 2009.
- [166] J. F. Gouin, F. Baros, D. Birot, and J. C. André, "A fibre-optic oxygen sensor for oceanography," *Sensors and Actuators B: Chemical*, vol. 39, pp. 401–406, 1997.
- [167] R. Ballance, *Field Testing Methods. In Water Quality Monitoring*. E & FN Spon: London, 1 ed., 1996.
- [168] J. Mu, F. Zhang, X. Zhu, and X. Dong, "A gas chromatography method established for oxygen transfer efficiency measurement," *Journal of Environmental Sciences*, vol. 21, pp. S146–S148, 2009.

- [169] Y. Plekhanova, A. Reshetilov, T. Manolov, and L. Taranova, "Biosensor monitoring of microbial treatment of wastewater from nonylphenol polyethoxylates under flow-through conditions," *Applied Biochemistry and Microbiology*, vol. 47, pp. 846–851, 2011.
- [170] G. Renger and B. Hanssum, "Oxygen detection in biological systems," *Photosynthesis Research*, vol. 102, pp. 487–498, 2009.
- [171] J. Woelfel, K. Sorensen, M. Warkentin, S. Forster, and A. Oren, "Oxygen evolution in a hypersaline crust: in situ photosynthesis quantification by microelectrode profiling and use of planar optode spots in incubation chambers," *Aquatic Microbial Ecology*, vol. 56, pp. 263–273, 2009.
- [172] E. Schmäzlin, J. T. Van Dongen, I. Klimant, B. Marmodée, M. Steup, J. Fisahn, P. Geigenberger, and H. G. Löhmannsröben, "An optical multifrequency phase-modulation method using microbeads for measuring intracellular oxygen concentrations in plants," *Biophysical Journal*, vol. 89, pp. 1339–1345, 2005.
- [173] V. Liddiard and J. Carman, "Simulating in ovulo osmotic potentials and O₂ tensions normalize growth and pigmentation of immature cotton embryos," *Plant Cell, Tissue and Organ Culture*, vol. 102, pp. 1–8, 2010.
- [174] S. Shimamura, R. Yamamoto, T. Nakamura, S. Shimada, and S. Komatsu, "Stem hypertrophic lenticels and secondary aerenchyma enable oxygen transport to roots of soybean in flooded soil," *Annals of Botany*, vol. 106, pp. 277–284, 2010.
- [175] C. Pénicaud, S. Peyron, N. Gontard, and V. Guillard, "Oxygen quantification methods and application to the determination of oxygen diffusion and solubility coefficients in food," *Food Reviews International*, vol. 28, pp. 113–145, 2012.
- [176] J. A. García-Mesa, M. D. L. de Castro, and M. Valcárcel, "Determination of the oxidative stability of olive oil by use of a robotic station," *Talanta*, vol. 40, pp. 1595–1600, 1993.
- [177] W. De Vries, W. M. C. Van Wijck-Kapteijn, and A. H. Stouthamer, "Influence of oxygen on growth, cytochrome synthesis and fermentation pattern in propionic acid bacteria," *Journal of General Microbiology*, vol. 71, pp. 515–524, 1972.
- [178] W. A. Van Voorhies, R. G. Melvin, J. W. O. Ballard, and J. B. Williams, "Validation of manometric microrespirometers for measuring oxygen consumption in small arthropods," *Journal of Insect Physiology*, vol. 54, pp. 1132–1137, 2008.
- [179] K. Roppola, T. Kuokkanen, J. Rämö, H. Prokkola, and J. Ruotsalainen, "Characterisation of organic fractions of pulp and paper mill wastewater with a manometric respirometric biochemical oxygen demand method and automatic chemical oxygen demand analyses," *Chemical Speciation and Bioavailability*, vol. 21, pp. 121–130, 2009.
- [180] H. Zenz and H. Katinger, "A gas-chromatographic method for the determination of oxygen uptake in aerated cultures," *Antonie van Leeuwenhoek*, vol. 37, pp. 289–295, 1971.

- [181] T. Hirata, T. Nishiyama, H. Sato, Y. Ishikawa, T. Shina, and T. Ishitani, "A fast gas chromatographic method for the separation of nitrogen, oxygen, carbon dioxide and argon and Its application to In-package modified atmosphere," *Journal of Packaging Science and Technology*, vol. 2, pp. 15–23, 1993.
- [182] M. J. van Rensburg, *Analysis of trace amounts of oxygen, carbon monoxide and carbon dioxide in nitrogen using gas chromatography*. PhD thesis, Department of Chemistry, University of Pretoria (South Africa), 2007.
- [183] N. J. Driscoll, M. Duffy, and S. Pappas, "Determination of water and oxygen at low ppm levels by GC/far-FUV detection," *American Laboratory*, pp. 68–71, 1988.
- [184] C. H. Culberson and S. Huang, "Automated amperometric oxygen titration," *Deep Sea Research Part A. Oceanographic Research Papers*, vol. 34, pp. 875–880, 1987.
- [185] W. Granéli and E. Granéli, "Automatic potentiometric determination of dissolved oxygen," *Marine Biology*, vol. 108, pp. 341–348, 1991.
- [186] P. Sahoo, R. Ananthanarayanan, N. Malathi, M. P. Rajiniganth, N. Murali, and P. Swaminathan, "Pulsating potentiometric titration technique for assay of dissolved oxygen in water at trace level," *Analytica Chimica Acta*, vol. 669, pp. 17–24, 2010.
- [187] T. Martz, Y. Takeshita, R. Rolph, and P. Bresnahan, "Tracer monitored titrations: measurement of dissolved oxygen," *Analytical Chemistry*, vol. 84, pp. 290–296, 2012.
- [188] J. H. Carpenter, "The accuracy of the Winkler method for dissolved oxygen analysis," *American Society of Limnology and Oceanography*, vol. 10, pp. 135–140, 1965.
- [189] J. R. Stetter and J. Li, "Amperometric gas sensors: a review," *Chemical Reviews*, vol. 108, pp. 352–366, 2008.
- [190] L. Clark, R. Wolf, D. Granger, and Z. Taylor, "Continuous recording of blood oxygen tensions by polarography," *Journal of Applied Physiology*, vol. 6, pp. 189–193, 1953.
- [191] L. A. Pouvreau, M. J. Strampraad, S. V. Berloo, J. H. Kattenberg, S. de Vries, and K. P. Robert, *NO, N₂O, and O₂ Reaction Kinetics: Scope and Limitations of the Clark Electrode*. In *Methods in Enzymology*, vol. 436. Academic Press, 2008.
- [192] J. M. Vanderkooi, M. Erecinska, and I. A. Silver, "Oxygen in mammalian tissue: methods of measurement and affinities of various reactions," *American Journal of Physiology - Cell Physiology*, vol. 260, pp. C1131–C1150, 1991.
- [193] R. Ahmad and P. Kuppusamy, "Theory, instrumentation, and applications of electron paramagnetic resonance oximetry," *Chemical Reviews*, vol. 110, pp. 3212–3236, 2010.
- [194] H. N. Rasmussen and U. F. Rasmussen, "Oxygen solubilities of media used in electrochemical respiration measurements," *Analytical Biochemistry*, vol. 319, pp. 105–113, 2003.

- [195] M. C. Krishna, S. English, K. Yamada, J. Yoo, R. Murugesan, N. Devasahayam, J. A. Cook, K. Golman, J. H. Ardenkjaer-Larsen, S. Subramanian, and J. B. Mitchell, "Overhauser enhanced magnetic resonance imaging for tumor oximetry: Coregistration of tumor anatomy and tissue oxygen concentration," *Proceedings of the National Academy of Sciences*, vol. 99, pp. 2216–2221, 2002.
- [196] B. Cummings, M. L. Hamilton, L. Ciaffoni, T. R. Pragnell, R. Peverall, G. A. D. Ritchie, G. Hancock, and P. A. Robbins, "Laser-based absorption spectroscopy as a technique for rapid in-line analysis of respired gas concentrations of O₂ and CO₂," *Journal of Applied Physiology*, vol. 111, pp. 303–307, 2011.
- [197] P. Lundin, E. K. Svanberg, L. Cocola, M. Lewander, S. Andersson-Engels, J. Jahr, V. Fellman, K. Svanberg, and S. Svanberg, "Non-invasive gas monitoring in newborn infants using diode laser absorption spectroscopy: a case study," in *Optical Diagnostics and Sensing XII: Toward Point-of-Care Diagnostics; and Design and Performance Validation of Phantoms Used in Conjunction with Optical Measurement of Tissue IV*, pp. 822903–11, SPIE: San Francisco, California, USA, 2012.
- [198] W. Rudolf-Seitz, "Chemical sensors based on fiber optics," *Analytical Chemistry*, vol. 56 (A16), 1984.
- [199] H. Kautsky, "Quenching of luminescence by oxygen," *Transactions of the Faraday Society*, vol. 35, pp. 216–219, 1939.
- [200] I. Bergman, "Rapid-response atmospheric oxygen monitor based on fluorescence quenching," *Nature*, vol. 218, p. 396, 1968.
- [201] C. Schweitzer and R. Schmidt, "Physical mechanisms of generation and deactivation of singlet oxygen," *Chemical Reviews*, vol. 103, pp. 1685–1758, 2003.
- [202] C. G. Hübner, A. Renn, I. Renge, and U. P. Wild, "Direct observation of the triplet lifetime quenching of single dye molecules by molecular oxygen," *Journal of Chemical Physics*, vol. 115, pp. 9619–9623, 2001.
- [203] M. C. DeRosa and R. J. Crutchley, "Photosensitized singlet oxygen and its applications," *Coordination Chemistry Reviews*, vol. 233–234, pp. 351–371, 2002.
- [204] F. Wilkinson, D. J. McGarvey, and A. F. Olea, "Excited triplet state interactions with molecular oxygen: influence of charge transfer on the bimolecular quenching rate constants and the yields of singlet oxygen ($O_2^* \ ^1\Delta_g$) for substituted naphthalenes in various solvents," *The Journal of Physical Chemistry*, vol. 98, pp. 3762–3769, 1994.
- [205] J. N. Demas and B. A. DeGraff, "Applications of luminescent transition platinum group metal complexes to sensor technology and molecular probes," *Coordination Chemistry Reviews*, vol. 211, pp. 317–351, 2001.
- [206] O. S. Wolfbeis, "Materials for fluorescence-based optical chemical sensors," *Journal of Materials Chemistry*, vol. 15, pp. 2657–2669, 2005.
- [207] E. R. Carraway, J. N. Demas, and B. A. DeGraff, "Luminescence quenching mechanism for microheterogeneous systems," *Analytical Chemistry*, vol. 63, pp. 332–336, 1991.

- [208] J. N. Demas, B. A. Degraff, and W. Xu, "Modeling of luminescence quenching-based sensors: comparison of multisite and nonlinear gas solubility models," *Analytical Chemistry*, vol. 67, pp. 1377–1380, 1995.
- [209] X. Lu and M. A. Winnik, "Luminescence quenching in polymer/filler nanocomposite films used in oxygen sensors," *Chemistry of Materials*, vol. 13, pp. 3449–3463, 2001.
- [210] Y. Amao, "Probes and polymers for optical sensing of oxygen," *Microchimica Acta*, vol. 143, pp. 1–12, 2003.
- [211] E. R. Carraway, J. N. Demas, B. A. DeGraff, and J. R. Bacon, "Photophysics and photochemistry of oxygen sensors based on luminescent transition-metal complexes," *Analytical Chemistry*, vol. 63, pp. 337–342, 1991.
- [212] A. Mills, "Response characteristics of optical sensors for oxygen: a model based on a distribution in tau and kq," *Analyst*, vol. 124, pp. 1309–1314, 1999.
- [213] J. Demas and B. DeGraff, "Luminescence-based sensors: microheterogeneous and temperature effects," *Sensors and Actuators B: Chemical*, vol. 11, pp. 35–41, 1993.
- [214] S. Lehrer, "Solute perturbation of protein fluorescence. Quenching of the tryptophyl fluorescence of model compounds and of lysozyme by iodide ion," *Biochemistry*, vol. 10, pp. 3254–3263, 1971.
- [215] A. Mills, "Controlling the sensitivity of optical oxygen sensors," *Sensors and Actuators B: Chemical*, vol. 51, pp. 60–68, 1998.
- [216] O. L. Gijzeman, F. Kaufman, and G. Porter, "Oxygen quenching of aromatic triplet states in solution. Part 1," *Journal of the Chemical Society, Faraday Transactions 2: Molecular and Chemical Physics*, vol. 69, pp. 708–720, 1973.
- [217] M. Arik, N. Celebi, and Y. Onganer, "Fluorescence quenching of fluorescein with molecular oxygen in solution," *Journal of Photochemistry and Photobiology A: Chemistry*, vol. 170, pp. 105–111, 2005.
- [218] C. McDonagh, B. D. MacCraith, and A. K. McEvoy, "Tailoring of sol-gel films for optical sensing of oxygen in gas and aqueous phase," *Analytical Chemistry*, vol. 70, pp. 45–50, 1998.
- [219] W. Trettnak, C. Kolle, F. Reininger, C. Dolezal, and P. O'Leary, "Miniaturized luminescence lifetime-based oxygen sensor instrumentation utilizing a phase modulation technique," *Sensors and Actuators B: Chemical*, vol. 36, pp. 506–512, 1996.
- [220] C. McDonagh, C. Kolle, A. K. McEvoy, D. L. Dowling, A. A. Cafolla, S. J. Cullen, and B. D. MacCraith, "Phase fluorometric dissolved oxygen sensor," *Sensors and Actuators B: Chemical*, vol. 74, pp. 124–130, 2001.
- [221] G. O'Keeffe, B. D. MacCraith, A. K. McEvoy, C. M. McDonagh, and J. F. McGilp, "Development of a LED-based phase fluorimetric oxygen sensor using evanescent wave excitation of a sol-gel immobilized dye," *Sensors and Actuators B: Chemical*, vol. 29, pp. 226–230, 1995.

- [222] H. Hochreiner, I. Sánchez-Barragán, J. M. Costa-Fernández, and A. Sanz-Medel, “Dual emission probe for luminescence oxygen sensing: a critical comparison between intensity, lifetime and ratiometric measurements,” *Talanta*, vol. 66, pp. 611–618, 2005.
- [223] R. B. Thompson and J. R. Lakowicz, “Fiber optic pH sensor based on phase fluorescence lifetimes,” *Analytical Chemistry*, vol. 65, pp. 853–856, 1993.
- [224] Y. Kostov and G. Rao, “Ratio measurements in oxygen determinations: wavelength ratiometry, lifetime discrimination, and polarization detection,” *Sensors and Actuators B: Chemical*, vol. 90, pp. 139–142, 2003.
- [225] X. D. Wang, H. X. Chen, Y. Zhao, X. Chen, and X. R. Wang, “Optical oxygen sensors move towards colorimetric determination,” *TrAC Trends in Analytical Chemistry*, vol. 29, pp. 319–338, 2010.
- [226] P. Hartmann, M. J. P. Leiner, and M. E. Lippitsch, “Response characteristics of luminescent oxygen sensors,” *Sensors and Actuators B: Chemical*, vol. 29, pp. 251–257, 1995.
- [227] H. Szmajcinski and J. Lakowicz, *Lifetime-Based Sensing: Topic in Fluorescence Spectroscopy*. Springer, US, 2002.
- [228] M. Valledor, J. Campo, I. Sánchez-Barragán, J. Costa-Fernández, J. Álvarez, and A. Sanz-Medel, “Determination of phosphorescence lifetimes in the presence of high background signals using phase-shift measurements,” *Sensors and Actuators B: Chemical*, vol. 113, pp. 249–258, 2006.
- [229] D. Andrzejewski, I. Klimant, and H. Podbielska, “Method for lifetime-based chemical sensing using the demodulation of the luminescence signal,” *Sensors and Actuators B: Chemical*, vol. 84, pp. 160–166, 2002.
- [230] M. E. Lippitsch and S. Draxler, “Luminescence decay-time-based optical sensors: principles and problems,” *Sensors and Actuators B: Chemical*, vol. 11, pp. 97–101, 1993.
- [231] H. M. Rowe, S. P. Chan, J. N. Demas, and B. A. DeGraff, “Elimination of fluorescence and scattering backgrounds in luminescence lifetime measurements using gated-phase fluorometry,” *Analytical Chemistry*, vol. 74, pp. 4821–4827, 2002.
- [232] Y. Amao, K. Asai, I. Okura, H. Shinohara, and H. Nishide, “Platinum porphyrin embedded in poly(1-trimethylsilyl-1-propyne) film as an optical sensor for trace analysis of oxygen,” *Analyst*, vol. 125, pp. 1911–1914, 2000.
- [233] S. M. Borisov, G. Zenkl, and I. Klimant, “Phosphorescent platinum(II) and palladium(II) complexes with azatetrabenzoporphyrins: A new red laser diode-compatible indicators for optical oxygen sensing,” *ACS Applied Materials and Interfaces*, vol. 2, pp. 366–374, 2010.
- [234] S. M. Borisov, P. Lehner, and I. Klimant, “Novel optical trace oxygen sensors based on platinum(II) and palladium(II) complexes with 5,10,15,20-meso-tetrakis-(2,3,4,5,6-pentafluorophenyl)-porphyrin covalently immobilized on silica-gel particles,” *Analytica Chimica Acta*, vol. 690, pp. 108–115, 2011.

- [235] S. M. Borisov and I. Klimant, "Ultrabright oxygen optodes based on cyclometalated iridium(III) coumarin complexes," *Analytical Chemistry*, vol. 79, pp. 7501–7509, 2007.
- [236] D. M. Jenkins, C. Zhu, and W. W. Su, "A simple hybrid circuit for direct determination of fluorescence lifetimes," *Applied Engineering in Agriculture*, vol. 24, pp. 259–263, 2008.
- [237] S. P. Chan, Z. J. Fuller, J. N. Demas, and B. A. DeGraff, "Optimized gating scheme for rapid lifetime determinations of single-exponential luminescence lifetimes," *Analytical Chemistry*, vol. 73, pp. 4486–4490, 2001.
- [238] C. Lochmann, T. Häupl, and J. Beuthan, "Luminescence lifetime determination for oxygen imaging in human tissue," *Laser Physics Letters*, vol. 5, pp. 151–155, 2008.
- [239] W. Becker, A. Bergmann, M. A. Hink, K. König, K. Benndorf, and C. Biskup, "Fluorescence lifetime imaging by time-correlated single-photon counting," *Microscopy Research and Technique*, vol. 63, pp. 58–66, 2004.
- [240] R. D. Spencer and G. Weber, "Measurement of subnanosecond fluorescence lifetimes with a cross-correlation phase fluorometer," *Annals of the New York Academy of Sciences*, vol. 158, pp. 361–376, 1969.
- [241] D. M. Jameson, E. Gratton, and R. D. Hall, "The measurement and analysis of heterogeneous emissions by multifrequency phase and modulation fluorometry," *Applied Spectroscopy Reviews*, vol. 20, pp. 55–106, 1984.
- [242] W. R. Ware, *Transient luminescence measurements. In Creation and detection of the excited state*. Marcel Dekker, New York, 1971.
- [243] P. Herman, B. P. Maliwal, H. J. Lin, and J. R. Lakowicz, "Frequency domain fluorescence microscopy with the LED as a light source," *Journal of Microscopy*, vol. 203, pp. 176–181, 2001.
- [244] A. Fernández-Gutiérrez and S. G. Schulman, *Fosforescencia Molecular Analítica: Una Aproximación Práctica*, vol. 1. Editorial Universidad de Granada, España, 2001.
- [245] R. J. Hurtubise, G. D. Christian, and J. B. Callis, *Trace Analysis: Spectroscopic Methods for Molecules*. Wiley InterScience, New York, 1986.
- [246] T. Vo-Dinh, *Room-temperature Phosphorimetry for Chemical Analysis*. Wiley InterScience, New York, 1984.
- [247] R. J. Hurtubise, *Solid-surface Luminescence Analysis*. Marcel Dekker, New York, 1981.
- [248] G. W. Ewing, *Analytical Instrumentation Handbook*. Marcel Dekker, New York, 2 ed., 1997.
- [249] D. A. Skoog, F. J. Holler, and T. A. Nieman, *Principios de Análisis Instrumental*. Mc-Graw Hill, Madrid, 5 ed., 2000.
- [250] H. Günzler and A. Williams, *Handbook of Analytical Techniques*. Wiley-VCH, 1 ed., 2001.

- [251] W. R. Seitz, P. Elving, E. J. Meehan, and I. M. Kolthoff, *Treatise on Analytical Chemistry*. Wiley, New York, 2 ed., 1981.
- [252] G. G. Guilbault, *Practical Fluorescence: Theory, Methods and Techniques*. Marcel Dekker, New York, 1973.
- [253] S. G. Schulman, *Fluorescence and Phosphorescence Spectroscopy: Physicochemical Principles and Practices*. Pergamon Press, Elmsford, 1977.
- [254] S. E. Hobbs and G. M. Hieftje, "Scintillator-based nanosecond light-source for time-resolved fluorimetry," *Applied Spectroscopy*, vol. 49, pp. 15–19, 1995.
- [255] G. Holst, O. Khol, I. Klimant, B. König, M. Kuhl, and T. Richter, "A modular luminescence lifetime imaging-system for mapping oxygen distribution in biological samples," *Sensors and Actuators B: Chemical*, vol. 51, pp. 163–170, 1998.
- [256] U. Rieser, J. Habermann, and G. A. Wagner, "Luminescence dating: a new high sensitivity TL/OSL emission spectrometer," *Quaternary Geochronology*, vol. 18, pp. 311–315, 1999.
- [257] A. Ghauch, "Determination of carbaryl and biphenyl through optical fiber ccd-assisted flash lamp induced room temperature phosphorescence," *Fresenius Journal of Analytical Chemistry*, vol. 367, pp. 545–550, 2000.
- [258] J. Capmany, F. J. Fraile-Peláez, and J. Martí, *Fundamentos de Comunicaciones Ópticas*. Síntesis S.A, Madrid, 1998.
- [259] S. Landgraf, "Use of ultrabright LEDs for the determination of static and time-resolved fluorescence information of liquid and solid crude oil samples," *Journal of Biochemical and Biophysical Methods*, vol. 61, pp. 125–134, 2004.
- [260] S. J. Hart and R. D. JiJi, "Light emitting diode excitation emission matrix fluorescence spectroscopy," *Analyst*, vol. 127, pp. 1643–1699, 2002.
- [261] S. Ookubo, "Nichia unveils white led with 150 lm/w luminous efficiency," *Tech-On!*, 2006.
- [262] J. Sipior, G. M. Carter, J. R. Lakowicz, and G. Rao, "Blue light-emitting diode demonstrated as an ultraviolet excitation source for nanosecond phase-modulation fluorescence lifetime measurements," *Review of Scientific Instruments*, vol. 68, pp. 2666–2670, 1997.
- [263] S. Fantini, M. A. Franceschini, J. B. Fishkin, B. Barbieri, and E. Gratton, "Quantitative determination of the absorption spectra of chromophores in strongly scattering media: a light-emitting diode based technique," *Applied Optics*, vol. 33, pp. 5204–5213, 1994.
- [264] J. R. Lakowicz and I. Gryczynski, *Frequency-domain fluorescence spectroscopy. In Topics in fluorescence spectroscopy*, vol. 1. Plenum Press, New York, 1991.
- [265] P. Hartmann and W. Ziegler, "Lifetime imaging of luminescent oxygen sensors based on all-solid-state technology," *Analytical Chemistry*, vol. 68, pp. 4512–4514, 1996.

- [266] S. C. Liao, Z. Xu, J. A. Izatt, and J. R. Alcala, "Real-time frequency domain temperature and oxygen concentration sensor with a single optical fiber," *IEEE Transactions on Biomedical Engineering*, vol. 44, pp. 1114–1121, 1997.
- [267] P. Hartmann, W. Ziegler, G. Holst, and D. W. Lübbers, "Oxygen flux fluorescence lifetime imaging," *Sensors and Actuators B: Chemical*, vol. 38, pp. 110–115, 1997.
- [268] G. Liebsch, I. Klimant, B. Frank, G. Holst, and O. S. Wolfbeis, "Luminescence lifetime imaging of oxygen, pH, and carbon dioxide distribution using optical sensors," *Applied Spectroscopy*, vol. 54, pp. 548–559, 2000.
- [269] Y. Kostov, K. A. van Houten, P. Harms, R. S. Pilato, and G. Rao, "Unique oxygen analyzer combining a dual emission probe and a low-cost solid-state ratiometric fluorometer," *Applied Spectroscopy*, vol. 54, pp. 864–868, 2000.
- [270] M. Trinkel, W. Trettnak, and C. Kolle, "Oxygen trace analysis utilising a miniaturised luminescence lifetime-based sensor instrumentation," *Química Analítica*, vol. 19, pp. 112–117, 2000.
- [271] H. Szmacinski and Q. Chang, "Micro- and sub-nanosecond lifetime measurements using a UV light-emitting diode," *Journal of Applied Spectroscopy*, vol. 54, pp. 106–109, 2000.
- [272] A. Pasic, H. Koehler, I. Klimant, and L. Schaupp, "Miniaturized fiber-optic hybrid sensor for continuous glucose monitoring in subcutaneous tissue," *Sensors and Actuators B: Chemical*, vol. 122, pp. 60–68, 2007.
- [273] Y. Hamada, T. Sano, K. Shibata, and K. Kuroki, "Influence of the emission site on the running durability of organic electroluminescent devices," *Japanese Journal of Applied Physics*, vol. 34, pp. L824–L826, 1995.
- [274] J. Shi and C. W. Tang, "Doped organic electroluminescent devices with improved stability," *Applied Physics Letters*, vol. 70, pp. 1665–1667, 1997.
- [275] T. Wakimoto, Y. Fukuda, K. Nagayama, A. Yokoi, H. Nakada, and M. Tsuchida, "Organic EL cells using alkaline metal-compounds as electron injection materials," *IEEE Transactions on Electron Devices*, vol. 44, pp. 1245–1248, 1997.
- [276] M. A. Baldo, D. F. O'Brien, Y. You, A. Shoutstikov, S. Sibley, M. E. Thompson, and S. R. Forrest, "Highly efficient phosphorescent emission from organic electroluminescent devices," *Nature*, vol. 395, pp. 151–154, 1998.
- [277] Y. Fukuda, S. Miyaguchi, S. Ishizuka, T. Wakimoto, J. Fumaki, H. Kubota, T. Watanabe, H. Ochi, T. Sakamoto, M. Tsuchida, I. Ohshita, H. Nakada, and T. Tohma, "Organic LED full color passive-matrix display," *SID Symposium Digest of Technical Papers*, vol. 30, pp. 430–433, 1999.
- [278] M. A. Baldo, S. Lamansky, P. E. Burrows, M. E. Tompson, and S. R. Forrest, "Very high-emitting devices based on electrophosphorescence," *Applied Physics Letters*, vol. 75, pp. 4–6, 1999.

- [279] T. Tsutsui, M. J. Yang, M. Yahiro, K. Nakamura, T. Watanabe, T. Tsuji, Y. Fukuda, T. Wakimoto, and S. Miyaguchi, "High quantum efficiency in organic light-emitting devices with iridium-complex as a triplet emissive center," *Japanese Journal of Applied Physics*, vol. 38, pp. L1502–L1504, 1999.
- [280] T. Watanabe, K. Nakamura, S. Kawami, Y. Fukuda, T. Tsuji, T. Wakimoto, S. Miyaguchi, M. Yahiro, M. J. Yang, and T. Tsutsui, "Optimization of emitting efficiency in organic LED cells using Ir complex," *Synthetic Metals*, vol. 122, pp. 203–207, 2001.
- [281] G. M. Hieftje, J. C. Travis, and F. E. Lytle, *Lasers in Chemical Analysis*. Humana Press, Clifton, NJ, 1981.
- [282] N. Omenetto and J. D. Winefordner, "Lasers in analytical spectroscopy," *Critical Reviews in Analytical Chemistry*, vol. 13, pp. 59–115, 1981.
- [283] J. H. Richardson and E. L. Wehry, *Modern Fluorescence Spectroscopy*. Plenum Press, New York, 1981.
- [284] J. C. Wright, G. M. Hieftje, J. C. Travis, and F. E. Lytle, *Lasers in Chemical Analysis*. Humana Press, Clifton, 1981.
- [285] F. E. Lytle, "Laser-excited molecular fluorescence of solutions," *Journal of Chemical Education*, vol. 59, pp. 915–920, 1982.
- [286] E. G. Piepmeiner, *Analytical Applications of Lasers*. Wiley-InterScience, New York, 1986.
- [287] L. Q. Yang, D. Mcstay, A. J. Rogers, and P. J. Quinn, "A novel dual-channel phosphorimeter for studies of antigen-antibody complexes," *Measurement Science and Technology*, vol. 5, pp. 1096–1104, 1994.
- [288] J. R. Alcala, S. C. Liao, and J. Zheng, "Real-time frequency-domain fibreoptic temperature sensor," *IEEE Transactions on Biomedical Engineering*, vol. 42, pp. 471–476, 1996.
- [289] J. R. Alcala, S. C. Liao, and J. Zheng, "Real-time frequency-domain fibreoptic temperature sensor using ruby crystals," *Medical Engineering and Physics*, vol. 18, pp. 51–56, 1996.
- [290] A. D. Campiglia, D. M. Hueber, and T. VoDinh, "Analysis of polycyclic aromatic compounds in soil samples using laser-induced phosphorimetry," *Polycyclic Aromatic Compounds*, vol. 8, pp. 117–128, 1996.
- [291] A. D. Campiglia, F. Moreau, D. M. Hueber, and T. VoDinh, "Phosphorescence imaging system using an acoustic-optic filter-based charge-coupled device," *Analytica Chimica Acta*, vol. 351, pp. 229–239, 1997.
- [292] G. D. Boutilier and J. D. Winefordner, "External heavy atom effect on detection limits and lifetime of phosphorescence in time resolved laser excited," *Analytical Chemistry*, vol. 51, pp. 1384–1391, 1979.

- [293] G. D. Boutilier and J. D. Winefordner, "Influence of type and concentration of external heavy atoms upon phosphorescence lifetimes," *Analytical Chemistry*, vol. 51, pp. 1391–1399, 1979.
- [294] A. D. Campiglia, D. M. Hueber, F. Moreau, and T. VoDinh, "Phosphorescence imaging system using an acoustic-optic tunable filter and a charge-coupled device," *Analytica Chimica Acta*, vol. 346, pp. 361–372, 1997.
- [295] M. A. Hedaya, H. P. Brikenfeld, and R. L. Kathren, "A sensitive method for the determination of uranium in biological samples utilizing kinetic phosphorescence analysis (KPA)," *Journal of Pharmaceutical and Biomedical Analysis*, vol. 15, pp. 1157–1165, 1997.
- [296] J. D. Ingle and S. R. Crouch, *Spectrochemical Analysis*. Prentice Hall, Englewood Cliffs, NJ, 1988.
- [297] J. C. Fister, D. Rank, and J. M. Harris, "Delayed fluorescence optical thermometry," *Analytical Chemistry*, vol. 67, pp. 4269–4275, 1995.
- [298] C. Yeh, *Handbook of Fiber Optics. Theory and Applications*. New York: Academic Press, 1990.
- [299] M. K. Carroll and G. M. Hieftje, "New fiber-optic based instrumentation for the measurement of low-temperature phosphorescence intensities and lifetimes," *Applied Spectroscopy*, vol. 46, pp. 126–130, 1992.
- [300] J. Díaz-García, J. M. Costa-Fernández, N. Bordel-García, and A. Sanz-Medel, "Room-temperature phosphorescence fiber-optic instrumentation for simultaneous multiposition analysis of dissolved oxygen," *Analytica Chimica Acta*, vol. 429, pp. 55–64, 2001.
- [301] J. C. Rodríguez, M. A. García, M. G. Vega, and F. J. Ferrero, "Measurement of low oxygen concentration by phosphorescence lifetime using optical fibers," *IEEE Transactions on Instrumentation and Measurement*, vol. 48, pp. 949–955, 1999.
- [302] D. B. Papkovsky, T. O'Riordan, and A. Soini, "Phosphorescent porphyrin probes in biosensor and sensitive bioassays," *Biochemical Society Transactions*, vol. 25, pp. 74–77, 2000.
- [303] J. M. Costa-Fernández, N. Bordel, J. C. Campo, F. J. Ferrero, M. A. Pérez, and A. Sanz-Medel, "Portable fibre optic oxygen sensor based on room-temperature phosphorescence lifetime," *Mikrochimica Acta*, vol. 134, pp. 145–152, 2000.
- [304] A. Ghauch, J. Rima, A. Charef, and M. Martinbouyer, "Use of an imaging spectrograph system with a fiber optical sensor and a 2-dimensional cooled CCD detector for solid-surface room-temperature phosphorescence of pesticides," *Analytical Letters*, vol. 33, pp. 709–728, 2000.
- [305] A. D. Campiglia and T. VoDinh, "Rapid screening method for cocaine and benzoylecgonine in saliva samples," *Analytica Chimica Acta*, vol. 372, pp. 349–355, 1998.

- [306] M. L. Franklin, G. Horlick, and H. V. Malmstadt, "Basic and practical consideration in utilising photon counting for quantitative spectrochemical methods," *Analytical Chemistry*, vol. 41, pp. 2–10, 1969.
- [307] D. M. Jameson, R. D. Spencer, and G. Weber, "Construction and performance of a scanning, photon-counting spectrofluorometer," *Review of Scientific Instruments*, vol. 47, pp. 1034–1038, 1976.
- [308] V. J. Koester and D. R. M., "Subnanosecond single photon counting fluorescence spectroscopy using synchronously pumped tunable dye laser excitation," *Review of Scientific Instruments*, vol. 49, pp. 1186–1191, 1978.
- [309] E. J. Darland, G. E. Leroi, and C. G. Enke, "Maximum efficiency pulse counting in computerized instrumentation," *Analytical Chemistry*, vol. 52, pp. 714–723, 1980.
- [310] M. L. Meade, "Instrumentation aspects of photon-counting applied to photometry," *Journal of Physics E: Scientific Instruments*, vol. 14, pp. 909–918, 1981.
- [311] T. Salthammer, H. Dreeskamp, D. J. Birch, and R. E. Imhof, "Fluorescence quenching of perylene by Co^{2+} ions via energy-transfer in viscous and non-viscous media," *Journal of Photochemistry and Photobiology A: Chemistry*, vol. 55, pp. 53–62, 1990.
- [312] M. Komfort, B. Rohne, H. Dreeskamp, and M. Zander, "Exciplex formation between polycyclic aromatic-compounds and Ag^+ ions," *Journal of Photochemistry and Photobiology A: Chemistry*, vol. 71, pp. 39–43, 1993.
- [313] O. Ohta, A. Kato, and R. Kato, "Temperature variation of phosphorescence decay in NaNO_2 crystals: spin-lattice relaxation of the triplet state in NO^{2-} ," *Journal of the Physical Society of Japan*, vol. 65, pp. 318–324, 1996.
- [314] G. D. Christian, J. B. Callis, E. R. Davidson, and E. L. Wehry, *Modern Fluorescence Spectroscopy*. Plenum Press, New York, 1981.
- [315] Y. Talmi, "Applicability of TV-Type multichannel detector to spectroscopy," *Analytical Chemistry*, vol. 47, pp. 658A–670A, 1975.
- [316] A. Talmi, D. C. Baker, J. R. Jadamec, and W. A. Saner, "Fluorescence spectrometry with optoelectronic image detectors," *Analytical Chemistry*, vol. 50, pp. 936A–952A, 1978.
- [317] Y. Talmi, "Spectrophotometry and spectrofluorometry with the self-scanned photodiode array," *Applied Spectroscopy*, vol. 36, pp. 1–18, 1982.
- [318] Y. Talmi, *Multichannel Image Detectors*. ACS Symposium Series, American Chemical Society, Washington, DC, 1983.
- [319] D. A. Skoog and J. J. Leary, *Principles of Instrumental Analysis/Solution Manual*. Saunders College Publishing Co., 4 ed., 1992.
- [320] M. J. Lim, W. F. Patton, M. F. López, K. H. Spofford, N. Shojaee, and D. Shepro, "A luminescent europium complex for the sensitive detection of proteins and nucleic-acids immobilized on membrane support," *Analytical Biochemistry*, vol. 245, pp. 184–195, 1997.

- [321] H. J. Tanke, R. R. Dehaas, C. Sagner, M. Ganser, and R. P. Vangijlswijk, "Use of platinum coproporphyrin and delayed luminescence imaging to extend the nuclear of target fish karyotyping," *Cytometry*, vol. 33, pp. 453–459, 1998.
- [322] W. L. Rumsey, M. Pawlowski, N. Lejevardi, and D. F. Wilson, "Oxygen-prepressure distribution in the heart in-vivo and evaluation of the isochemic border zone," *American Journal of Physiology*, vol. 266, pp. H1676–H1680, 1994.
- [323] S. A. Vinogrov, L. W. Lo, W. T. Jenkins, S. M. Evans, C. Koch, and D. F. Wilson, "Noninvasive imaging of the distribution in oxygen in tissue in-vivo using near-infrared phosphors," *Biophysical Journal*, vol. 70, pp. 1609–1617, 1996.
- [324] A. Ghauch, J. Rima, C. Fachinger, J. Suptil, and M. Martin-Bouyer, "Room temperature phosphorescence analyses of polycyclic aromatic hydrocarbons using an imaging sensing system combined with a bifurcated optical fiber and a cooled charge coupled device detector," *Talanta*, vol. 51, pp. 807–816, 2000.
- [325] K. F. Harbaugh, C. M. O'Donnell, and J. D. Winefordner, "Pulsed source time resolved phosphorimetry for the quantitative and qualitative analysis of drug," *Analytical Chemistry*, vol. 46, pp. 1206–1209, 1974.
- [326] D. E. Goeringer and H. C. Pardue, "Time-resolved phosphorescence spectrometry with a silicon intensified target vidicon and regression analysis methods," *Analytical Chemistry*, vol. 51, pp. 1054–1060, 1979.
- [327] K. Nithipatikom and B. D. Pollard, "An instrument for determining single and multiple room-temperature phosphorescence lifetimes," *Applied Spectroscopy*, vol. 39, pp. 109–115, 1985.
- [328] C. N. Ho and I. M. Warner, "Multidimensional phosphorimetry," *TrAC Trends in Analytical Chemistry*, vol. 1, pp. 159–163, 1982.
- [329] D. W. Johnson, J. B. Callis, and G. D. Christian, "Rapid scanning fluorescence spectroscopy," *Analytical Chemistry*, vol. 49, pp. 747A–757A, 1977.
- [330] E. Gratton and M. Limkeman, "A continuously variable frequency cross-correlation phase fluorometer with picosecond resolution," *Biophysical Journal*, vol. 44, pp. 315–324, 1983.
- [331] J. R. Lakowicz and B. P. Maliwal, "Construction and performance of a variable-frequency phase-modulation fluorometer," *Biophysical Chemistry*, vol. 21, pp. 61–78, 1985.
- [332] E. Gratton, "The measurement and analysis of heterogeneous emissions by multifrequency phase and modulation fluorometry," *Applied Spectroscopy Reviews*, vol. 20, pp. 55–106, 1984.
- [333] E. Gratton, D. M. Jameson, and R. D. Hall, "Multifrequency phase and modulation fluorometry," *Annual Review of Biophysics and Bioengineering*, vol. 13, pp. 105–124, 1984.

- [334] F. V. Bright, T. A. Betts, and K. S. Litwiler, "Advances in multifrequency phase and modulation fluorescence analysis," *Analytical Chemistry*, vol. 21, pp. 389–405, 1990.
- [335] J. R. Lakowicz, "Frequency-domain fluorometry for resolution of time-dependent fluorescence emission," *Spectroscopy*, vol. 1, pp. 28–37, 1985.
- [336] E. Rabinovich, M. O'Brien, B. Srinivasan, S. Elliott, X. C. Long, and K. J. Ravinder, "A compact, LED-based phase fluorimeter-detection system for chemical and biosensor arrays," *Proceedings of SPIE —The International Society for Optical Engineering*, vol. 3258, pp. 2–10, 1998.
- [337] M. Valcárcel and M. D. Luque de Castro, "Integration of reaction (retention) and spectroscopic detection in continuous-flow systems. Invited lecture," *Analyst*, vol. 115, pp. 699–703, 1990.
- [338] A. Ruíz-Medina and E. J. Llorent-Martínez, "Recent progress of flow-through optosensing in clinical and pharmaceutical analysis," *Journal of Pharmaceutical and Biomedical Analysis*, vol. 53, pp. 250–261, 2010.
- [339] E. J. Llorent-Martínez, P. Ortega-Barrales, M. L. Fernández-de Córdova, and A. Ruíz-Medina, "Trends in flow-based analytical methods applied to pesticide detection: A review," *Analytica Chimica Acta*, vol. 684, pp. 30–39, 2011.
- [340] M. Valcárcel and M. D. Luque de Castro, *Flow-through (Bio)Chemical Sensors*. Elsevier, 1994.
- [341] A. Sanz-Medel, "Solid surface photoluminescence and flow analysis: a happy marriage," *Analytica Chimica Acta*, vol. 283, pp. 367–378, 1993.
- [342] M. D. Luque de Castro and M. Valcárcel, "Integration of separation and detection in continuous-flow systems," *Trac-Trends in Analytical Chemistry*, vol. 10, pp. 114–121, 1991.
- [343] J. F. Van Staden, A. E. Joubert, and H. R. Van Vliet, "Flow-injection determination of nitrate in natural-waters with copper-cadmium and copperized cadmium tubes in the reaction manifold system," *Fresenius Zeitschrift Fur Analytische Chemie*, vol. 325, pp. 150–152, 1986.
- [344] J. Ruz, F. Lázaro, and M. D. Luque de Castro, "Immobilized enzymes in flow-injection analysis—present and trends," *Journal of Automatic Chemistry*, vol. 10, pp. 15–19, 1988.
- [345] E. H. Hansen, "Flow-injection enzymatic assays," *Analytica Chimica Acta*, vol. 216, pp. 257–273, 1989.
- [346] J. M. Fernández-Romero and M. D. Luque de Castro, "Flow-injection configurations for enzyme activity determination," *Chimica Oggi—Chemistry Today*, vol. 17, p. 49, 1998.
- [347] M. Valcárcel and A. Ríos, "Selectivity in analytical-chemistry," *Analisis*, vol. 18, pp. 469–475, 1990.

- [348] J. F. Fernández-Sánchez, A. Segura-Carretero, C. Cruces-Blanco, and A. Fernández-Gutiérrez, “Room-temperature luminescence optosensings based on immobilized active principles actives: Application to nafronyl and naproxen determination in pharmaceutical preparations and biological fluids,” *Analytica Chimica Acta*, vol. 462, pp. 217–224, 2002.
- [349] J. F. Fernández-Sánchez, A. Segura-Carretero, C. Cruces-Blanco, and A. Fernández-Gutiérrez, “A sensitive fluorescence optosensor for analysing propranolol in pharmaceutical preparations and a test for its control in urine in sport,” *Journal of Pharmaceutical and Biomedical Analysis*, vol. 31, pp. 859–865, 2003.
- [350] S. Casado-Terrones, J. F. Fernández-Sánchez, B. Cañabate-Díaz, A. Segura-Carretero, and A. Fernández-Gutiérrez, “A fluorescence optosensor for analyzing naphazoline in pharmaceutical preparations: Comparison with other sensors,” *Journal of Pharmaceutical and Biomedical Analysis*, vol. 38, pp. 785–789, 2005.
- [351] A. Salinas-Castillo, J. F. Fernández-Sánchez, A. Segura-Carretero, and A. Fernández-Gutiérrez, “A facile flow-through phosphorimetric sensing device for simultaneous determination of naptalam and its metabolite 1-naphthylamine,” *Analytica Chimica Acta*, vol. 522, pp. 19–24, 2004.
- [352] G. N. Piccirilli, G. M. Escandar, F. C. Cañada, I. D. Meras, and A. Muñoz de la Peña, “Flow-through photochemically induced fluorescence optosensor for the determination of linuron,” *Talanta*, vol. 77, pp. 852–857, 2008.
- [353] A. Salinas-Castillo, I. Sánchez-Barragán, J. M. Costa-Fernández, R. Pereiro, A. Ballesteros, J. M. González, A. Segura-Carretero, A. Fernández-Gutiérrez, and A. Sanz-Medel, “Iodinated molecularly imprinted polymer for room temperature phosphorescence optosensing of fluoranthene,” *Chemical Communications*, pp. 3224–3226, 2005. doi: 10.1039/B502706C.
- [354] A. Valero-Navarro, J. F. Fernández-Sánchez, A. L. Medina-Castillo, F. Fernández-Ibáñez, A. Segura-Carretero, J. M. Ibáñez, and A. Fernández-Gutiérrez, “A rapid, sensitive screening test for polycyclic aromatic hydrocarbons applied to Antarctic water,” *Chemosphere*, vol. 67, pp. 903–910, 2007.
- [355] A. Valero-Navarro, A. Salinas-Castillo, J. F. Fernández-Sánchez, A. Segura-Carretero, R. Mallavia, and A. Fernández-Gutiérrez, “The development of a MIP-optosensor for the detection of monoamine naphthalenes in drinking water,” *Biosensors and Bioelectronics*, vol. 24, pp. 2305–2311, 2009.
- [356] N. S. Kapany and N. Silbertrust, “Fibre optics spectrophotometer for in vivo oximetry,” *Nature*, vol. 204, pp. 138–142, 1964.
- [357] Y. Enson, W. A. Briscoe, M. L. Polanyi, and A. Cournand, “In vivo studies with an intravascular and intracardiac reflection oximeter,” *Journal of Applied Physiology*, vol. 17, pp. 552–558, 1962.
- [358] G. Vurek and R. Bowman, “Fiber-optic colorimeter for submicroliter samples,” *Analytical Biochemistry*, vol. 29, pp. 238–247, 1969.

- [359] H. Eysel, "Ramanstreuung polykristalliner substanzen: aufnahme mit hilfe faseloptischer querschnittswandler," *Spectrochimica Acta Part A: Molecular Spectroscopy*, vol. 27, pp. 173–177, 1971.
- [360] G. E. Walrafen, "New slitless optical fiber laser-Raman spectrometer," *Applied Spectroscopy*, vol. 29, pp. 179–185, 1975.
- [361] J. I. Peterson and S. R. Goldstein, "Fiber optic pH probe," U.S. Pat. Appl. 855384 (1977); U.S. Pat. Appl. 4200110 (1980).
- [362] J. I. Peterson and S. R. Goldstein, "Dye fixation by copolymerization," U.S. Pat. Appl. 855397 (1977); U.S. Pat. Appl. 4194877 (1980).
- [363] M. Fernández-Vallejo and M. López-Amo, "Optical fiber networks for remote fiber optic sensors," *Sensors*, vol. 12, pp. 3929–3951, 2012.
- [364] K. Toth, G. Nagy, T. T. L. Bui, J. Jeney, and S. J. Choquette, "Planar waveguide ion-selective sensors," *Analytica Chimica Acta*, vol. 353, pp. 1–10, 1997.
- [365] C. R. Lavers, K. Itoh, S. C. Wu, M. Murabayashi, I. Mauchline, G. Stewart, and T. Stout, "Planar optical waveguides for sensing applications," *Sensors and Actuators B: Chemical*, vol. 69, pp. 85–95, 2000.
- [366] A. Abdukayum, A. Yimit, M. Mahmut, and K. Itoh, "A planar optical waveguide sensor for hydrogen sulfide detection," *Sensor Letters*, vol. 5, pp. 395–397, 2007.
- [367] D. S. Bagal, A. Vijayan, R. C. Aiyer, R. N. Karekar, and M. S. Karve, "Fabrication of sucrose biosensor based on single mode planar optical waveguide using co-immobilized plant invertase and GOD," *Biosensors and Bioelectronics*, vol. 22, pp. 3072–3079, 2007.
- [368] D. Bhatta, A. A. Michel, M. Marti-Villalba, G. D. Emmerson, I. J. G. Sparrow, E. A. Perkins, M. B. McDonnell, R. W. Ely, and G. A. Cartwright, "Optical microchip array biosensor for multiplexed detection of bio-hazardous agents," *Biosensors and Bioelectronics*, vol. 30, pp. 78–86, 2011.
- [369] S. C. B. Gopinath, K. Awazu, M. Fujimaki, and P. K. R. Kumar, "Signal changes for dye-complexed biomolecular interactions on waveguide-sensor chips," *Sensors and Actuators B: Chemical*, vol. 155, pp. 239–244, 2011.
- [370] M. A. Arnold, "Fiber-Optic Chemical Sensors," *Analytical Chemistry*, vol. 64, pp. 1015A–1025A, 1992.
- [371] M. E. Collison and M. E. Meyerhoff, "Chemical sensors for bedside monitoring of critically ill patients," *Analytical Chemistry*, vol. 62, pp. 425A–437A, 1990.
- [372] S. Schulman, *Molecular Luminescence Spectroscopy: Methods and Applications*. Chemical analysis, John Wiley & Sons, 1988.
- [373] Y. Rao, C. Zhou, and T. Zhu, "A novel chirped-FBG-based F-P sensor network using SFDM/WDM," in *Optical Fiber Sensors, Sensor Networking and Multiplexing (FA6)*, Cancún, México, 2006.

- [374] G. Hudon, C. Guy, and J. Hermia, "Measurement of odor intensity by an electronic nose," *Journal of the Air and Waste Management Association*, vol. 50, pp. 1750–1758, 2000.
- [375] S. Ampuero and J. O. Bosset, "The electronic nose applied to dairy products: a review," *Sensors and Actuators B: Chemical*, vol. 94, pp. 1–12, 2003.
- [376] R. L. Plant and D. H. Burns, "Quantitative, depth-resolved imaging of oxygen concentration by phosphorescence lifetime measurement," *Applied Spectroscopy*, vol. 47, pp. 1594–1599, 1993.
- [377] P. M. Gewehr and D. T. Delpy, "Optical oxygen sensor based on phosphorescence lifetime quenching and employing a polymer immobilised metalloporphyrin probe: Part 1 - Theory and instrumentation," *Medical and Biological Engineering and Computing*, vol. 31, pp. 2–10, 1993.
- [378] C. D. McGuinness, K. Sagoo, D. McLoskey, and D. J. S. Birch, "A new sub-nanosecond LED at 280 nm: application to protein fluorescence," *Measurement Science and Technology*, vol. 15, pp. L19–L22, 2004.
- [379] O. S. Wolfbeis, "Chemical sensors-survey and trends," *Fresenius Journal of Analytical Chemistry*, vol. 337, pp. 522–527, 1990.
- [380] J. Pérez-Hernández, J. Albero, X. Correig, E. Llobet, and E. Palomares, "Multivariate calibration analysis of colorimetric mercury sensing using a molecular probe," *Analytica Chimica Acta*, vol. 633, pp. 173–180, 2009.
- [381] M. Corbalán, M. S. Millán, and M. J. Yzuel, "Color measurement in standard CIELAB coordinates using a 3CCD camera: correction for the influence of the light source," *Optical Engineering*, vol. 39, pp. 1470–1476, 2000.
- [382] T. A. Dickinson, J. White, J. S. Kauer, and D. R. Walt, "Current trends in 'artificial-nose' technology," *Trends in Biotechnology*, vol. 16, pp. 250–258, 1998.
- [383] J. White, T. A. Dickinson, D. R. Walt, and J. Kauer, "An olfactory neuronal network for vapor recognition in an artificial nose," *Biological Cybernetics*, vol. 78, pp. 245–251, 1998.
- [384] A. Zipp, "Solid-phase chemistry: Its principles and applications in clinical analysis," *Talanta*, vol. 31, pp. 863–877, 1984.
- [385] J. Lin and C. W. Brown, "Sol-gel glass as a matrix for chemical and biochemical sensing," *TrAC Trends in Analytical Chemistry*, vol. 16, pp. 200–211, 1997.
- [386] I. Klimant, F. Ruckruh, and O. Wolfbeis, "Fast response oxygen micro-optodes based on novel soluble ormosil glasses," *Mikrochimica Acta*, vol. 131, pp. 35–46, 1999.
- [387] M. A. Buttler, "Optical fiber hydrogen sensor," *Applied Physics Letters*, vol. 45, pp. 1007–1009, 1984.
- [388] E. E. Hardy, D. J. David, N. S. Kapany, and F. C. Unterleitner, "Coated optical guides for spectrophotometry of chemical reactions," *Nature*, vol. 257, p. 666, 1975.

- [389] J. M. Costa-Fernández, M. E. Díaz-García, and A. Sanz-Medel, “Sol-gel immobilized room-temperature phosphorescent metal-chelate as luminescent oxygen sensing material,” *Analytica Chimica Acta*, vol. 360, pp. 17–26, 1998.
- [390] R. E. Dessy, “Waveguides as chemical sensors,” *Analytical Chemistry*, vol. 61, pp. 1079A–1094A, 1989.
- [391] A. S. Kocincova, S. M. Borisov, C. Krause, and O. S. Wolfbeis, “Fiber-optic micro-sensors for simultaneous sensing of oxygen and pH, and of oxygen and temperature,” *Analytical Chemistry*, vol. 79, pp. 8486–8493, 2007.
- [392] P. Bhatia and B. D. Gupta, “Fabrication and characterization of a surface plasmon resonance based fiber optic urea sensor for biomedical applications,” *Sensors and Actuators B: Chemical*, vol. 161, pp. 434–438, 2012.
- [393] F. A. A. Matias and M. Tubino, “A portable fiber-optic chemical device for the quantitative determination of carbon monoxide from automobile exhaust emissions,” *Journal of the Air and Waste Management*, vol. 51, pp. 962–965, 2001.
- [394] R. S. Mahendran, L. Wang, V. R. Machavaram, S. D. Pandita, R. Chen, S. N. Kukureka, and G. F. Fernando, “Fiber-optic sensor design for chemical process and environmental monitoring,” *Optics and Lasers in Engineering*, vol. 47, pp. 1069–1076, 2009.
- [395] H. Filik, D. Aksu, R. Apak, A. Sener, and E. Kiliç, “An optical fibre reflectance sensor for p-aminophenol determination based on tetrahydroxycalix[4]arene as sensing reagent,” *Sensors and Actuators B: Chemical*, vol. 136, pp. 105–112, 2009.
- [396] Rajan, S. Chand, and B. D. Gupta, “Surface plasmon resonance based fiber-optic sensor for the detection of pesticide,” *Sensors and Actuators B: Chemical*, vol. 123, pp. 661–666, 2007.
- [397] E. Peña-Vázquez, E. Maneiro, C. Pérez-Conde, M. C. Moreno-Bondi, and E. Costas, “Microalgae fiber optic biosensors for herbicide monitoring using sol-gel technology,” *Biosensors and Bioelectronics*, vol. 24, pp. 3538–3543, 2009.
- [398] M. Consales, A. Buosciolo, A. Cutolo, G. Breglio, A. Irace, S. Buontempo, P. Petagna, M. Giordano, and A. Cusano, “Fiber optic humidity sensors for high-energy physics applications at CERN,” *Sensors and Actuators B: Chemical*, vol. 159, pp. 66–74, 2011.
- [399] L. S. Ziemer, W. M. F. Lee, S. A. Vinogradov, C. Sehgal, and D. F. Wilson, “Oxygen distribution in murine tumors: characterization using oxygen-dependent quenching of phosphorescence,” *Journal of Applied Physiology*, vol. 98, pp. 1503–1510, 2005.
- [400] R. Dmitriev and D. Papkovsky, “Optical probes and techniques for O₂ measurement in live cells and tissue,” *Cellular and Molecular Life Sciences*, vol. 69, pp. 2025–2039, 2012.
- [401] A. Sharma and O. S. Wolfbeis, “Fiberoptic oxygen sensor based on fluorescence quenching and energy transfer,” *Applied Spectroscopy*, vol. 42, pp. 1009–1011, 1988.

- [402] Y. Amao, K. Asai, and I. Okura, "A novel optical oxygen sensing based on quenching of photoexcited triplet state of C70 in polystyrene film by oxygen using time-resolved spectroscopy," *Chemistry Letters*, vol. 28, pp. 183–184, 1999.
- [403] Y. Amao, K. Asai, and I. Okura, "Fluorescence quenching oxygen sensor using an aluminum phthalocyanine-polystyrene film," *Analytica Chimica Acta*, vol. 407, pp. 41–44, 2000.
- [404] P. D. Fleischauer and P. Fleischauer, "Photoluminescence of transition metal coordination compounds," *Chemical Reviews*, vol. 70, pp. 199–230, 1970.
- [405] L. Sacksteder, J. N. Demas, and B. A. DeGraff, "Design of oxygen sensors based on quenching of luminescent metal complexes: Effect of ligand size on heterogeneity," *Analytical Chemistry*, vol. 65, pp. 3480–3483, 1993.
- [406] W. Xu, K. A. Kneas, J. N. Demas, and B. A. DeGraff, "Oxygen sensors based on luminescence quenching of metal complexes: Osmium complexes suitable for laser diode excitation," *Analytical Chemistry*, vol. 68, pp. 2605–2609, 1996.
- [407] J. N. Demas, E. W. Harris, C. M. Flynn, and D. Diemante, "Luminescent osmium(II) and iridium(III) complexes as photosensitizers," *Journal of the American Chemical Society*, vol. 97, pp. 3838–3839, 1975.
- [408] S. Jianliang, H. Ge, S. Qing, Z. Zhaohong, and G. Lei, "Nanofibers doped with a novel red-emitting Europium complex: Synthesis, characterization, photophysical property and sensing activity toward molecular oxygen," *Spectrochimica Acta Part A: Molecular and Biomolecular Spectroscopy*, vol. 91, pp. 192–197, 2012.
- [409] E. Vander-Donckt, B. Camerman, R. Herne, and R. Vandeloise, "Fibre-optic oxygen sensor based on luminescence quenching of a Pt(II) complex embedded in polymer matrices," *Sensors and Actuators B: Chemical*, vol. 32, pp. 121–127, 1996.
- [410] H. N. McMurray, P. Douglas, C. Busa, and M. S. Garley, "Oxygen quenching of tris(2,2'-bipyridine) ruthenium(II) complexes in thin organic films," *Journal of Photochemistry and Photobiology A: Chemistry*, vol. 80, pp. 283–288, 1994.
- [411] A. Mills and M. D. Thomas, "Effect of plasticizer viscosity on the sensitivity of an $[\text{Ru}(\text{bpy})_3^{2+}(\text{Ph}_4\text{B}^-)_2]$ -based optical oxygen sensor," *Analyst*, vol. 123, pp. 1135–1140, 1998.
- [412] B. H. Han, I. Manners, and M. A. Winnik, "Oxygen sensors based on mesoporous silica particles on layer-by-layer self-assembled films," *Chemistry of Materials*, vol. 17, pp. 3160–3171, 2005.
- [413] P. Hartmann, M. J. P. Leiner, and M. E. Lippitsch, "Luminescence quenching behavior of an oxygen sensor based on a Ru(II) complex dissolved in polystyrene," *Analytical Chemistry*, vol. 67, pp. 88–93, 1995.
- [414] Y. Amao, Y. Ishikawa, and I. Okura, "Green luminescent iridium(III) complex immobilized in fluoropolymer film as optical oxygen-sensing material," *Analytica Chimica Acta*, vol. 445, pp. 177–182, 2001.

- [415] G. Di Marco, M. Lanza, M. Pieruccini, and S. Campagna, "A luminescent iridium(III) cyclometallated complex immobilized in a polymeric matrix as a solid-state oxygen sensor," *Advanced Materials*, vol. 8, pp. 576–580, 1996.
- [416] A. L. Medina-Castillo, J. F. Fernández-Sánchez, C. Klein, M. K. Nazeeruddin, A. Segura-Carretero, A. Fernández-Gutiérrez, M. Graetzel, and U. E. Spichiger-Keller, "Engineering of efficient phosphorescent iridium cationic complex for developing oxygen-sensitive polymeric and nanostructured films," *Analyst*, vol. 132, pp. 929–936, 2007.
- [417] S. K. Lee and I. Okura, "Photoluminescent determination of oxygen using metalloporphyrin-polymer sensing systems," *Spectrochimica Acta – Part A: Molecular and Biomolecular Spectroscopy*, vol. 54, pp. 91–100, 1998.
- [418] G. Di Marco and M. Lanza, "Optical solid-state oxygen sensors using metalloporphyrin complexes immobilized in suitable polymeric matrices," *Sensors and Actuators B: Chemical*, vol. 63, pp. 42–48, 2000.
- [419] S. K. Lee and I. Okura, "Photostable optical oxygen sensing material: platinum tetrakis(pentafluorophenyl)porphyrin immobilized in polystyrene," *Analytical Communications*, vol. 34, pp. 185–188, 1997.
- [420] D. B. Papkovsky, G. V. Ponomarev, W. Trettnak, and P. O’Leary, "Phosphorescent complexes of porphyrin ketones: optical properties and application to oxygen sensing," *Analytical Chemistry*, vol. 67, pp. 4112–4117, 1995.
- [421] P. Hartmann and W. Trettnak, "Effects of polymer matrices on calibration functions of luminescent oxygen sensors based on porphyrin ketone complexes," *Analytical Chemistry*, vol. 68, pp. 2615–2620, 1996.
- [422] A. Juris, V. Balzani, F. Barigelletti, S. Campagna, P. Belser, and A. von Zelewsky, "Ru(II) polypyridine complexes: photophysics, photochemistry, electrochemistry, and chemiluminescence," *Coordination Chemistry Reviews*, vol. 84, pp. 85–277, 1988.
- [423] A. J. Lees, "Luminescence properties of organometallic complexes," *Chemical Reviews*, vol. 87, pp. 711–743, 1987.
- [424] A. McEvoy, C. McDonagh, and B. MacCraith, "Optimisation of sol-gel-derived silica films for optical oxygen sensing," *Journal of Sol-Gel Science and Technology*, vol. 8, pp. 1121–1125, 1997.
- [425] J. F. Fernández-Sánchez, T. Roth, R. Cannas, M. K. Nazeeruddin, S. Spichiger, M. Graetzel, and U. E. Spichiger-Keller, "Novel oxygen sensitive complexes for optical oxygen sensing," *Talanta*, vol. 71, pp. 242–250, 2007.
- [426] M. C. DeRosa, D. J. Hodgson, G. D. Enright, B. Dawson, C. E. B. Evans, and R. J. Crutchley, "Iridium luminophore complexes for unimolecular oxygen sensors," *Journal of the American Chemical Society*, vol. 126, pp. 7619–7626, 2004.
- [427] K. Koren, S. M. Borisov, R. Saf, and I. Klimant, "Strongly phosphorescent iridium(III)-porphyrins – New oxygen indicators with tuneable photophysical properties and functionalities," *European Journal of Inorganic Chemistry*, no. 10, pp. 1531–1534, 2011.

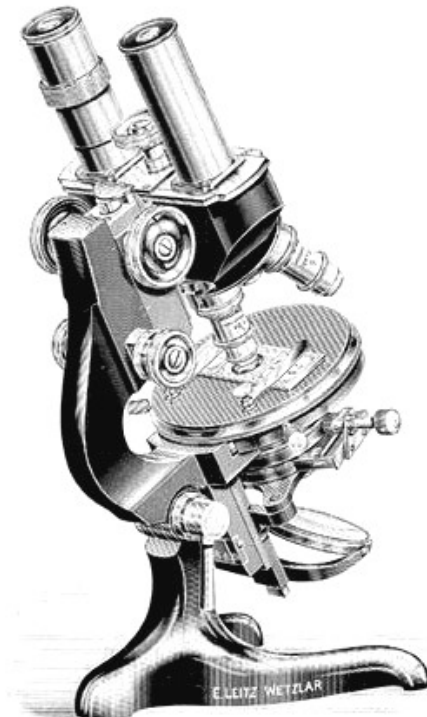
- [428] A. Ruggi, F. W. B. van Leeuwen, and A. H. Velders, "Interaction of dioxygen with the electronic excited state of Ir(III) and Ru(II) complexes: Principles and biomedical applications," *Coordination Chemistry Reviews*, vol. 255, pp. 2542–2554, 2011.
- [429] L. Flamigni, A. Barbieri, C. Sabatini, B. Ventura, and F. Barigelletti, "Photochemistry and photophysics of coordination compounds: Iridium," *Topics in Current Chemistry*, vol. 281, pp. 143–203, 2007.
- [430] H. A. Clark, S. L. R. Barker, M. Brasuel, M. T. Miller, E. Monson, S. Parus, Z. Y. Shi, A. Song, B. Thorsrud, R. Kopelman, A. Ade, W. Meixner, B. Athey, M. Hoyer, D. Hill, R. Lightle, and M. A. Philbert, "Subcellular optochemical nanobiosensors: probes encapsulated by biologically localised embedding (PEBBLEs)," *Sensors and Actuators B: Chemical*, vol. 51, pp. 12–16, 1998.
- [431] A. K. McEvoy, C. M. McDonagh, and B. D. MacCraith, "Dissolved oxygen sensor based on fluorescence quenching of oxygen-sensitive ruthenium complexes immobilized in sol-gel-derived porous silica coatings," *Analyst*, vol. 121, pp. 785–788, 1996.
- [432] C. Baleizao, S. Nagl, M. Schäferling, M. N. Berberan-Santos, and O. S. Wolfbeis, "Dual fluorescence sensor for trace oxygen and temperature with unmatched range and sensitivity," *Analytical Chemistry*, vol. 80, pp. 6449–6457, 2008.
- [433] G. Mistlberger, S. M. Borisov, and I. Klimant, "Enhancing performance in optical sensing with magnetic nanoparticles," *Sensors and Actuators B: Chemical*, vol. 139, pp. 174–180, 2009.
- [434] B. D. MacCraith, C. M. McDonagh, G. O'Keeffe, A. K. McEvoy, T. Butler, and F. R. Sheridan, "Sol-gel coatings for optical chemical sensors and biosensors," *Sensors and Actuators B: Chemical*, vol. 29, pp. 51–57, 1995.
- [435] C. S. Chu and Y. L. Lo, "Optical fiber dissolved oxygen sensor based on Pt(II) complex and core-shell silica nanoparticles incorporated with sol-gel matrix," *Sensors and Actuators B: Chemical*, vol. 151, pp. 83–89, 2010.
- [436] G. Mistlberger, A. L. Medina-Castillo, S. Borisov, T. Mayr, A. Fernández-Gutiérrez, J. F. Fernández-Sánchez, and I. Klimant, "Mini-emulsion solvent evaporation: a simple and versatile way to magnetic nanosensors," *Microchimica Acta*, vol. 172, pp. 299–308, 2011.
- [437] S. Bonacchi, D. Genovese, R. Juris, M. Montalti, L. Prodi, E. Rampazzo, and N. Zaccaroni, "Luminescent silica nanoparticles: Extending the frontiers of brightness," *Angewandte Chemie International Edition*, vol. 50, pp. 4056–4066, 2011.
- [438] A. Abdelghani, J. Chovelon, N. Jaffrezic-Renault, M. Lacroix, H. Gagnaire, C. Veillas, B. Berkova, M. Chomat, and V. Matejec, "Optical fibre sensor coated with porous silica layers for gas and chemical vapour detection," *Sensors and Actuators B: Chemical*, vol. 44, pp. 495–498, 1997.
- [439] G. Decher, "Fuzzy nanoassemblies: Toward layered polymeric multicomposites," *Science*, vol. 277, pp. 1232–1237, 1997.

- [440] C. Elosúa, C. Bariáin, I. R. Matías, F. J. Arregui, A. Luquin, and M. Laguna, “Volatile alcoholic compounds fibre optic nanosensor,” *Sensors and Actuators B: Chemical*, vol. 115, pp. 444–449, 2006.
- [441] S. M. Borisov, T. Mayr, and I. Klimant, “Poly(styrene-block-vinylpyrrolidone) beads as a versatile material for simple fabrication of optical nanosensors,” *Analytical Chemistry*, vol. 80, pp. 573–582, 2008.
- [442] W. Xu, R. C. McDonough, B. Langsdorf, J. N. Demas, and B. A. DeGraff, “Oxygen sensors based on luminescence quenching: Interactions of metal complexes with the polymer supports,” *Analytical Chemistry*, vol. 66, pp. 4133–4141, 1994.
- [443] K. Koren, S. M. Borisov, and I. Klimant, “Stable optical oxygen sensing materials based on click-coupling of fluorinated platinum(II) and palladium(II) porphyrins: A convenient way to eliminate dye migration and leaching,” *Sensors and Actuators B: Chemical*, vol. 169, pp. 173–181, 2012.
- [444] P. Douglas and K. Eaton, “Response characteristics of thin film oxygen sensors, Pt and Pd octaethylporphyrins in polymer films,” *Sensors and Actuators B: Chemical*, vol. 82, pp. 200–208, 2002.
- [445] A. Apostolidis, I. Klimant, D. Andrzejewski, and O. S. Wolfbeis, “A combinatorial approach for development of materials for optical sensing of gases,” *Journal of Combinatorial Chemistry*, vol. 6, pp. 325–331, 2004.
- [446] J. Brandrup, E. H. Immergut, and E. A. Grulke, *Polymer Handbook*. Wiley-Interscience, 2003.
- [447] I. Klimant and O. S. Wolfbeis, “Oxygen-sensitive luminescent materials based on silicone-soluble ruthenium diimine complexes,” *Analytical Chemistry*, vol. 67, pp. 3160–3166, 1995.
- [448] S. D. Herman and J. B. Christen, “Fabrication and characterization of a silicone fluorescent oxygen sensor,” in *Biomedical Circuits and Systems Conference (BioCAS)*, pp. 70–73, 2010.
- [449] F. Guillaume, K. Greden, and W. H. Smyrl, “Optical sensors for corrosion systems: I. Oxygen sensing,” *Journal of The Electrochemical Society*, vol. 155, pp. J213–J219, 2008.
- [450] Y. Ichiraku, S. A. Stern, and T. Nakagawa, “An investigation of the high gas permeability of poly (1-Trimethylsilyl-1-Propyne),” *Journal of Membrane Science*, vol. 34, pp. 5–18, 1987.
- [451] Y. Tian, B. R. Shumway, and D. R. Meldrum, “A new cross-linkable oxygen sensor covalently bonded into poly(2-hydroxyethyl methacrylate)-co-polyacrylamide thin film for dissolved oxygen sensing,” *Chemistry of Materials*, vol. 22, pp. 2069–2078, 2010.
- [452] A. Mills and M. Thomas, “Fluorescence-based thin plastic film ion-pair sensors for oxygen,” *Analyst*, vol. 122, pp. 63–68, 1997.

- [453] A. Mills and A. Lepre, "Controlling the response characteristics of luminescent porphyrin plastic film sensors for oxygen," *Analytical Chemistry*, vol. 69, pp. 4653–4659, 1997.
- [454] Y. Cao, Y. E. Lee-Koo, and R. Kopelman, "Poly(decyl methacrylate)-based fluorescent PEBBLE swarm nanosensors for measuring dissolved oxygen in biosamples," *Analyst*, vol. 129, pp. 745–750, 2004.
- [455] Y. Amao, T. Miyashita, and I. Okura, "Platinum tetrakis(pentafluorophenyl)porphyrin immobilized in polytrifluoroethylmethacrylate film as a photostable optical oxygen detection material," *Journal of Fluorine Chemistry*, vol. 107, pp. 101–106, 2001.
- [456] S. M. Borisov, C. Krause, S. Arain, and O. S. Wolfbeis, "Composite material for simultaneous and contactless luminescent sensing and imaging of oxygen and carbon dioxide," *Advanced Materials*, vol. 18, pp. 1511–1516, 2006.
- [457] T. C. O'Riordan, H. Voraberger, J. P. Kerry, and D. B. Papkovsky, "Study of migration of active components of phosphorescent oxygen sensors for food packaging applications," *Analytica Chimica Acta*, vol. 530, pp. 135–141, 2005.
- [458] M. I. J. Stich, S. Nagl, O. S. Wolfbeis, U. Henne, and M. Schaeferling, "A dual luminescent sensor material for simultaneous imaging of pressure and temperature on surfaces," *Advanced Functional Materials*, vol. 18, pp. 1399–1406, 2008.
- [459] S. Borisov, R. Seifner, and I. Klimant, "A novel planar optical sensor for simultaneous monitoring of oxygen, carbon dioxide, pH and temperature," *Analytical and Bioanalytical Chemistry*, vol. 400, pp. 2463–2474, 2011.
- [460] H. S. Voraberger, H. Kreimaier, K. Biebernik, and W. Kern, "Novel oxygen optrode withstanding autoclavation: technical solutions and performance," *Sensors and Actuators B: Chemical*, vol. 74, pp. 179–185, 2001.
- [461] D. Badocco, A. Mondin, P. Pastore, S. Voltolina, and S. Gross, "Dependence of calibration sensitivity of a polysulfone/Ru(II)-Tris(4,7-diphenyl-1,10-phenanthroline)-based oxygen optical sensor on its structural parameters," *Analytica Chimica Acta*, vol. 627, pp. 239–246, 2008.
- [462] A. Mills and F. C. Williams, "Chemical influences on the luminescence of ruthenium diimine complexes and its response to oxygen," *Thin Solid Films*, vol. 306, pp. 163–170, 1997.
- [463] K. Nagai, T. Masuda, T. Nakagawa, B. D. Freeman, and I. Pinnau, "Poly[1-(trimethylsilyl)-1-propyne] and related polymers: synthesis, properties and functions," *Progress in Polymer Science*, vol. 26, pp. 721–798, 2001.
- [464] C. A. P. Quinn, R. E. Connor, and A. Heller, "Biocompatible, glucose-permeable hydrogel for in situ coating of implantable biosensors," *Biomaterials*, vol. 18, pp. 1665–1670, 1997.
- [465] D. P. O'Neal, M. A. Meledeo, J. R. Davis, B. L. Ibey, V. A. Gant, M. V. Pishko, and G. L. Cote, "Oxygen sensor based on the fluorescence quenching of a ruthenium complex immobilized in a biocompatible Poly(Ethylene glycol) hydrogel," *Sensors Journal, IEEE*, vol. 4, pp. 728–734, 2004.

- [466] Y. Onuki, U. Bhardwaj, M.Pharm., F. Papadimitrakopoulos, and D. J. Burgess, “A review of the biocompatibility of implantable devices: Current challenges to overcome foreign body response,” *Journal of Diabetes Science and Technology*, vol. 2, pp. 1003–1015, 2008.
- [467] C. Wang, B. Yu, B. Knudsen, J. Harmon, F. Moussy, and Y. Moussy, “Synthesis and performance of novel hydrogels coatings for implantable glucose sensors,” *Biomacromolecules*, vol. 9, pp. 561–567, 2008.
- [468] X. H. Wang, H. S. Peng, H. Ding, F. T. You, S. H. Huang, F. Teng, B. Dong, and H. W. Song, “Biocompatible fluorescent core-shell nanoparticles for ratiometric oxygen sensing,” *Journal of Materials Chemistry*, vol. 22, pp. 16066–16071, 2012.
- [469] A. Y. Houde and S. A. Stern, “Permeability of ethyl cellulose to light gases. Effect of ethoxy content,” *Journal of Membrane Science*, vol. 92, pp. 95–101, 1994.
- [470] D. B. Papkovsky, G. J. Mohr, and O. S. Wolfbeis, “New polar plasticizers for luminescence-based sensors,” *Analytica Chimica Acta*, vol. 337, pp. 201–205, 1997.
- [471] B. Meier, T. Werner, I. Klimant, and O. S. Wolfbeis, “Novel oxygen sensor material based on a ruthenium bipyridyl complex encapsulated in zeolite Y: dramatic differences in the efficiency of luminescence quenching by oxygen on going from surface-adsorbed to zeolite-encapsulated fluorophores,” *Sensors and Actuators B: Chemical*, vol. 29, pp. 240–245, 1995.
- [472] X. Lu, I. Manners, and M. A. Winnik, “Polymer/silica composite films as luminescent oxygen sensors,” *Macromolecules*, vol. 34, pp. 1917–1927, 2001.
- [473] J. D. Mackenzie and E. P. Bescher, “Structures, properties and potential applications of ormosils,” *Journal of Sol-Gel Science and Technology*, vol. 13, pp. 371–377, 1998.
- [474] M. Batzill and U. Diebold, “The surface and materials science of tin oxide,” *Progress in Surface Science*, vol. 79, pp. 47–154, 2005.
- [475] H. T. Chen, S. J. Xiong, X. L. Wu, J. Zhu, J. C. Shen, and P. K. Chu, “Tin oxide nanoribbons with vacancy structures in luminescence-sensitive oxygen sensing,” *Nano Letters*, vol. 9, pp. 1926–1931, 2009.
- [476] U. Spichiger-Keller, S. Spichiger, and J. F. Fernández-Sánchez, “Metal oxide membrane with a gas-selective compound,” Patent WO2006119986 A1 (2006).
- [477] J. F. Fernández-Sánchez, T. Nezel, R. Steiger, and U. E. Spichiger-Keller, “Novel optical NO₂-selective sensor based on phthalocyaninato-iron(II) incorporated into a nanostructured matrix,” *Sensors and Actuators B: Chemical*, vol. 113, pp. 630–638, 2006.

PARTE II:
EXPERIMENTAL



Arquitectura del banco de pruebas de laboratorio

EN este apartado se describen las características más importantes del banco de pruebas desarrollado para la caracterización y evaluación de una amplia variedad de fases sensoras ópticas. En primer lugar, se describen sus características más sobresalientes, analizando sus principales componentes instrumentales y sus diversas configuraciones de medida, ya sea para la adquisición de medidas de intensidad de luminiscencia o de tiempos de vida de luminiscencia en el dominio de la frecuencia. Asimismo, también se muestra una visión general de las distintas etapas del proceso de desarrollo del sistema, desde sus primeras versiones hasta su versión final, mencionando las principales dificultades encontradas y las soluciones aportadas durante este proceso.

1.1 Motivación para el desarrollo del banco de pruebas

La instrumentación habitual de que disponen la mayoría de los laboratorios de caracterización de fases sensoras ópticas suele estar compuesta por espectrofotómetros de luminiscencia comerciales como los que se mencionan en la introducción de esta memoria, los cuales suelen usarse fundamentalmente para dos tareas: (1) para llevar a cabo la caracterización espectroscópica de las fases sensoras, esto es, la obtención de los espectros de luminiscencia de excitación y de emisión (gráficos de intensidad luminiscente frente a la longitud de onda), y (2) para realizar la caracterización analítica de las fases sensoras a una determinada longitud de onda, ya sea mediante la adquisición de medidas de intensidad o de tiempos de vida de luminiscencia en el dominio del tiempo (análisis del decaimiento temporal de la luminiscencia de la muestra tras excitar ésta con luz pulsada).

Estos instrumentos son imprescindibles para la primera tarea (caracterización espectroscópica de las fases sensoras), ya que la obtención de dichos espectros de excitación y emisión requiere generalmente de un montaje instrumental complejo compuesto por dos mo-

nocromadores, uno situado entre la fuente y la muestra (monocromador de excitación) y otro situado entre la muestra y el detector (monocromador de emisión), así como de lámparas de excitación de elevada potencia óptica y anchura espectral y detectores de elevada fotosensibilidad (generalmente PMTs). Si se mantiene el monocromador de emisión a una longitud de onda fija (generalmente la correspondiente al máximo de emisión luminiscente) y se va variando la longitud de onda de excitación, se obtiene un espectro de excitación; si se mantiene el monocromador de excitación a una longitud de onda fija (generalmente la correspondiente al máximo de excitación) y se va variando la longitud de onda de emisión, se obtiene un espectro de emisión. Estos equipos comerciales permiten realizar un barrido continuo de todo el espectro (generalmente de forma automática). En aplicaciones analíticas de luminiscencia se utiliza el espectro de emisión, pero cuando se trabaja con un espectrómetro de luminiscencia (instrumento manual adecuado para realizar medidas a una o dos longitudes de onda), suele registrarse primero el espectro de excitación a fin de confirmar la identidad de la sustancia analizada y elegir la longitud de onda de excitación óptima.

En cambio, una vez se conocen las propiedades espectroscópicas de las fases sensoras (longitudes de onda de excitación y emisión óptimas), la caracterización analítica de las mismas puede ser realizada (a priori) con una instrumentación mucho menos cara, específica y voluminosa, especialmente para el caso de las especies fosforescentes. Esto tiene una enorme importancia en el ámbito del diseño de fases sensoras ópticas orientadas al desarrollo de sensores ópticos luminiscentes, ya que éstas, en la práctica, deberán ser implementadas en dispositivos finales de medida cuyas características deberán satisfacer las exigencias del mercado para poder ser comercializados con éxito. Así pues, la caracterización analítica y la evaluación de fases sensoras ópticas implementadas en sistemas sensores “prototipo” que estén próximos a los dispositivos finales de medida se torna fundamental de cara a poder evaluar de una forma objetiva y realista las prestaciones de dichas fases sensoras en sistemas de medida reales (con alguna aplicación práctica).

En este contexto, en esta memoria de Tesis nos planteamos el desarrollo e implementación de un banco de pruebas de laboratorio modular, versátil y flexible que permita la caracterización y evaluación de una amplia variedad de fases sensoras ópticas y que pueda ser adaptado fácilmente a casi cualquier tipo de diseño experimental (sustituyendo algunos de sus componentes por otros). En este caso, el sistema desarrollado permite, al menos, la adquisición de dos tipos de medidas luminiscentes: (1) medidas de intensidad directas de la luminiscencia y (2) medidas de tiempo de vida de luminiscencia en el dominio de la frecuencia. Estas últimas medidas son más interesantes desde el punto de vista analítico, ya que proporcionan una mayor información analítica del proceso luminiscente que las medidas de intensidad estacionarias y también resultan más interesantes desde el punto de vista de la instrumentación, ya que generalmente no requieren de una instrumentación tan sofisticada como las medidas de intensidad, pudiendo emplearse para su determinación fuentes de iluminación simples y baratas como los LEDs y diversos dispositivos opto-electrónicos. Además, las medidas de tiempo de vida suelen ser más robustas a las perturbaciones externas que las medidas de intensidad, lo que las convierte en las medidas luminiscentes preferidas a la hora de desarrollar sistemas sensores ópticos fiables y robustos. Así pues, el banco de pruebas desarrollado en esta memoria se centra fundamentalmente en este tipo de medidas (tiempo de vida) por ser éstas las más prometedoras desde el punto de vista instrumental y analítico.

La mayor parte de la instrumentación disponible para la medida de tiempos de vida de

luminiscencia se basa en métodos de medida en el dominio del tiempo (usando lámparas de luz pulsadas y PMTs de respuesta rápida). Estos equipos son muy adecuados para la eliminación del ruido de fondo (luz de fondo), pero suelen ser muy caros y voluminosos, lo que los inhabilita para el desarrollo de sensores ópticos con aplicación práctica. Recientemente se han empezado a comercializar dispositivos más pequeños, versátiles y económicos para la medida de tiempos de vida usando métodos de modulación de fase (en el dominio de la frecuencia), pero generalmente estos equipos suelen estar diseñados para aplicaciones específicas, siendo difíciles de adaptar a un espectro amplio de diseños experimentales. Así pues, una de las razones que han motivado el desarrollo del banco de pruebas presentado en esta memoria ha sido la de disponer de un sistema de medida abierto y modular que permita su fácil adaptación a cualquier tipo de diseño experimental, y también, a ser posible, que permita la automatización del proceso de medida para poder abordar experimentos de caracterización y evaluación más complejos. Otra de las razones que han motivado su desarrollo ha sido su naturaleza digital, esto es, la flexibilidad para generar y procesar las señales en un ordenador, permitiendo de esta forma un control total sobre las señales, así como la posibilidad de implementar algoritmos avanzados de procesamiento de señal que permitan mejorar la precisión y la sensibilidad analítica y la funcionalidad de este tipo de sistemas.

1.2 Arquitectura del banco de pruebas de laboratorio

La arquitectura general del banco de pruebas desarrollado se muestra en el diagrama esquemático de la Figura 1.1. Dicho sistema permite la adquisición de dos tipos de medidas luminiscentes: (1) medidas de intensidad de luminiscencia y (2) medidas de tiempo de vida de luminiscencia en el dominio de la frecuencia. En este apartado describiremos los componentes instrumentales más importantes del sistema de medida propuesto (muchos de ellos comunes a ambas configuraciones de medida) así como las características particulares más relevantes de cada una de estas configuraciones.

(1) Ordenador personal (PC): El sistema de medida propuesto permite ser controlado desde un ordenador personal (Intel(R) Core(TM)2 Quad CPU Q9400 2.66 GHz, 3.24 GB RAM, Microsoft Windows XP Home Edition, versión 2002, Service Pack 2). La conexión de los diferentes equipos del sistema al PC se realiza de forma cableada a través de distintos puertos de comunicación: USB (para el espectrómetro de fibra óptica), puerto serie RS232 (para los controladores de flujo másico y el lock-in amplifier), PCI (para la tarjeta de adquisición de datos) y Ethernet (para el osciloscopio digital). El control remoto de dichos equipos desde el PC se realiza a través de un programa principal implementado en MATLAB 7.10, que permite la comunicación (envío y recepción de comandos de control y/o de datos) con los diferentes equipos del sistema. Este programa principal ejecuta a su vez un conjunto de programas específicos desarrollados para cada equipo (implementados en MATLAB y LabView 8.5). Este control centralizado de los equipos permite la completa automatización del proceso de medida, requiriendo únicamente la intervención del usuario al principio del experimento (configuración del sistema para llevar a cabo las medidas). Asimismo, la automatización del sistema también ofrece la posibilidad de programar “a la carta” procesos de medida complejos que impliquen el cambio de muchas variables instrumentales (amplios barridos de frecuencia de modulación, cambios de concentración del analito, distintos tipos de señales de excitación,

etc.) o el registro continuo de datos durante varios días de medida. La automatización también permite la monitorización del proceso de medida en todo momento (visualización de los resultados obtenidos por pantalla en tiempo real), el apagado automático de los equipos una vez finalizado el proceso de medida (característica importante para no fotodegradar innecesariamente la fase sensora, prolongar la vida del PMT, LED, etc., y reducir el consumo del sistema), así como el procesamiento y/o el correcto almacenamiento de los datos y/o de las señales en el disco duro del ordenador para su posterior análisis. Finalmente, otra de las posibilidades que ofrece el sistema de medida es el uso de herramientas de escritorio remoto (tales como TeamViewer) para controlar el PC del sistema de forma remota desde cualquier ordenador conectado a internet, visualizando no solo la pantalla del ordenador, sino también la pantalla del osciloscopio digital (en caso de que éste sea usado para la adquisición y visualización de las señales).

(2) Tarjeta de adquisición de datos AD/DA: El sistema desarrollado dispone de una tarjeta de adquisición de datos AD/DA (NI-DAQ PCIe-6363, National Instruments, www.ni.com) con 32 entradas analógicas (2 MS/s monocal, 1.25 MS/s multicanal, resolución de 16 bits, ± 10 V), 4 salidas analógicas (2.86 MS/s, resolución de 16 bits, ± 10 V), 48 líneas de E/S digital (32 temporizadas por hardware hasta 10 MHz), 4 contadores/temporizadores de 32 bits (para PWM, codificador, contar eventos y otros), disparo analógico y digital y temporización avanzada con la tecnología NI-STC3, y soporte para Windows 7/Vista/XP/2000. Además, debido a que la tarjeta de adquisición de datos PCI no permite una conectividad directa de las señales, se requiere el uso de un bloque conector (NI-BNC 2120, National Instruments) que funciona como una interfaz entre las señales del sistema de medida y la tarjeta AD/DA. Este bloque conector dispone de conectores BNC para conexiones de E/S, así como un generador de funciones y un codificador en cuadratura, entre otros elementos. La conexión entre el bloque conector y la tarjeta AD/DA se realiza mediante un cable conector (NI-PCI Bus) proporcionado por esta misma casa comercial. Las imágenes de estos elementos se muestran en la Figura 1.2.

La tarjeta AD/DA se usa para generar las señales analógicas que modulan la corriente del LED (usado como fuente de luz de excitación para la fase sensora) en el LED driver. Dichas señales analógicas son generadas a partir de las muestras de señales digitales generadas numéricamente en el ordenador usando MATLAB. Si bien es posible el uso de los generadores internos de la tarjeta (o de un generador de señales convencional) para generar estas señales analógicas (señales periódicas sinusoidales o cuadradas), resulta complejo o poco práctico la generación de señales analógicas con formas de onda algo más complicadas (tales como señales cuadradas con un ciclo de trabajo distinto de 50%). Así pues, para tener una mayor flexibilidad a la hora de generar las señales analógicas de excitación, así como un mayor control sobre sus muestras, se optó por la compra de esta tarjeta AD/DA. Además, la disponibilidad de conectores BNC en el bloque conector facilita la conexión de las señales a los distintos equipos del sistema (lock-in amplifier, LED driver, osciloscopio digital) usando cables coaxiales estándar con conectores BNC. Por otro lado, dicha tarjeta también podría ser usada para digitalizar las señales analógicas proporcionadas por el sistema de medida, así como para visualizar en tiempo real dichas señales registradas usando MATLAB (al igual que un osciloscopio digital pero con un coste inferior a éste).

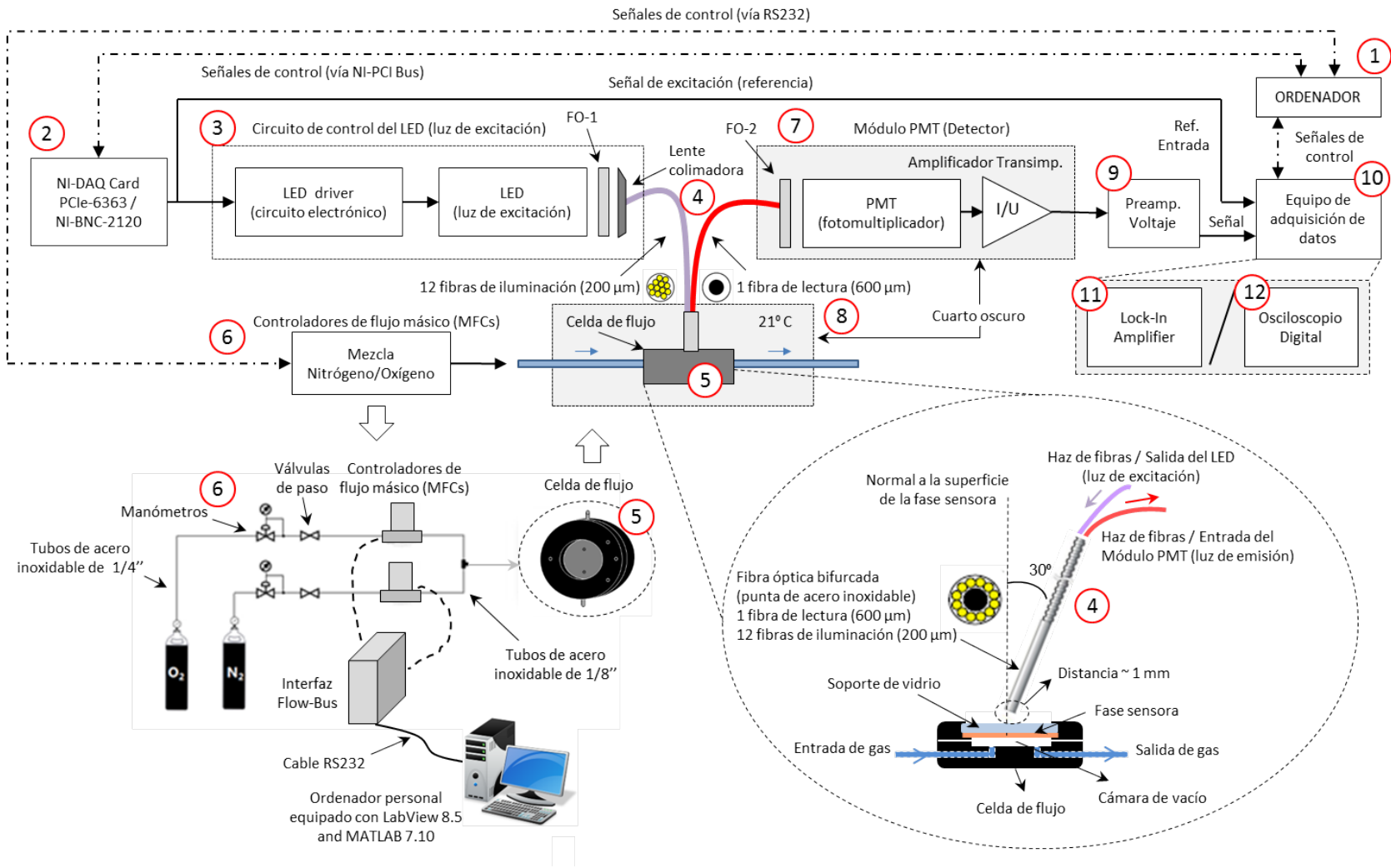


Figura 1.1: Diagrama esquemático de la arquitectura general del banco de pruebas desarrollado.

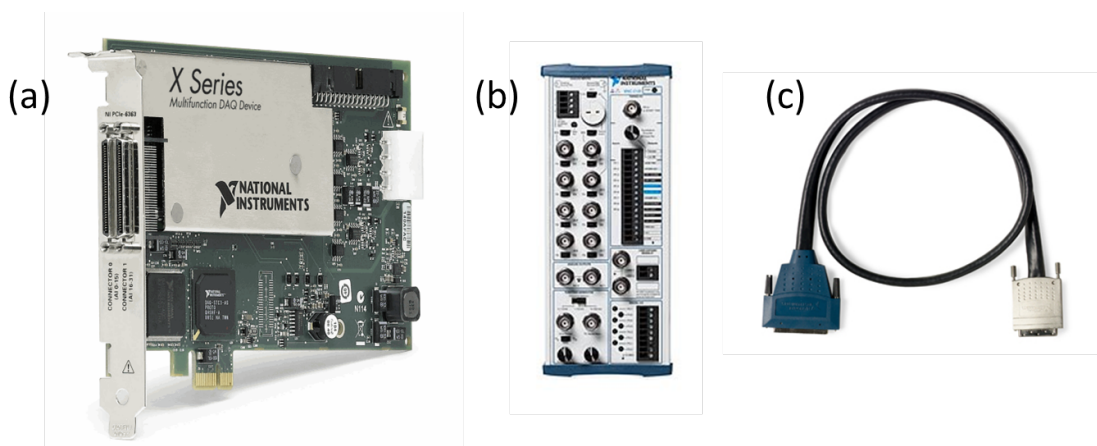


Figura 1.2: Tarjeta de adquisición de datos AD/DA y accesorios. (a) Tarjeta NI-DAQ PCIe-6363 National Instruments; (b) Bloque conector NI-BNC 2120 National Instruments; (c) Cable para la conexión tarjeta-bloque conector (NI-PCI Bus National Instruments).

(3) Circuito de control del LED (LED driver): Como puede observarse en el diagrama esquemático de la Figura 1.3(a), el circuito electrónico diseñado para controlar la corriente eléctrica que circula por el LED (LED driver) y, por tanto, su intensidad luminosa, está compuesto por componentes electrónicos sencillos tales como resistencias, condensadores, un LED estándar que indica si el circuito está siendo alimentado con un voltaje $VDD = +5\text{ V}$, un transistor bipolar NPN (BC547B) que actúa como una fuente de corriente regulada por la tensión aplicada a su base, y un LED de alto brillo (intercambiable) usado como fuente de luz de excitación para la fase sensora (generalmente se trata de un LED UV o azul). En la Figura 1.3(b) se muestran algunas fotografías del LED driver diseñado.

Su funcionamiento es simple. El LED driver dispone de dos entradas de señal (conectores BNC): una de ellas es la alimentación del circuito (tensión fija $VDD = +5\text{ V}$), la cual es suministrada por una fuente de tensión programable controlada desde el PC y la otra es una señal analógica (generada con la tarjeta AD/DA) aplicada a la base del transistor para modular la intensidad de corriente que circula por el LED y, por tanto, su intensidad luminosa. Por otro lado, cabe destacar que en el caso de trabajar con señales sinusoidales, es muy importante seleccionar adecuadamente el valor de la amplitud y el offset de la señal de modulación, de manera de que el diodo LED siempre se encuentre encendido y operando dentro de sus límites lineales de respuesta (de otro modo, la señal lumínica proporcionada por el LED no seguirá la forma de onda sinusoidal de la señal moduladora).

El diodo LED se halla encapsulado dentro de un porta-LED cilíndrico de metal (véase la Figura 1.3(b)) que encaja perfectamente dentro del cabezal metálico de una fuente LED (LS-450, Ocean Optics, www.oceanoptics.com). Dicho porta-LED es fijado a la estructura del cabezal de la fuente LED mediante un tornillo, evitando así cualquier desplazamiento de éste dentro del cabezal. Esto evita el desalineamiento óptico entre el LED y la fibra óptica y/o la variación de la distancia óptima de separación entre el LED y la lente colimadora del cabezal, lo que se traduciría en una pérdida de potencia óptica acoplada a la fibra. El cabezal de la fuente LED incorpora a su vez un filtro óptico paso-corto (FO-1, intercambiable) que elimina todas las longitudes de onda de excitación del LED superiores a la longitud de onda de corte del filtro, evitando así que éstas interfieran con el espectro de emisión de la fase sensora en el detector. También incorpora una lente colimadora/convergente cuya misión es la de colimar

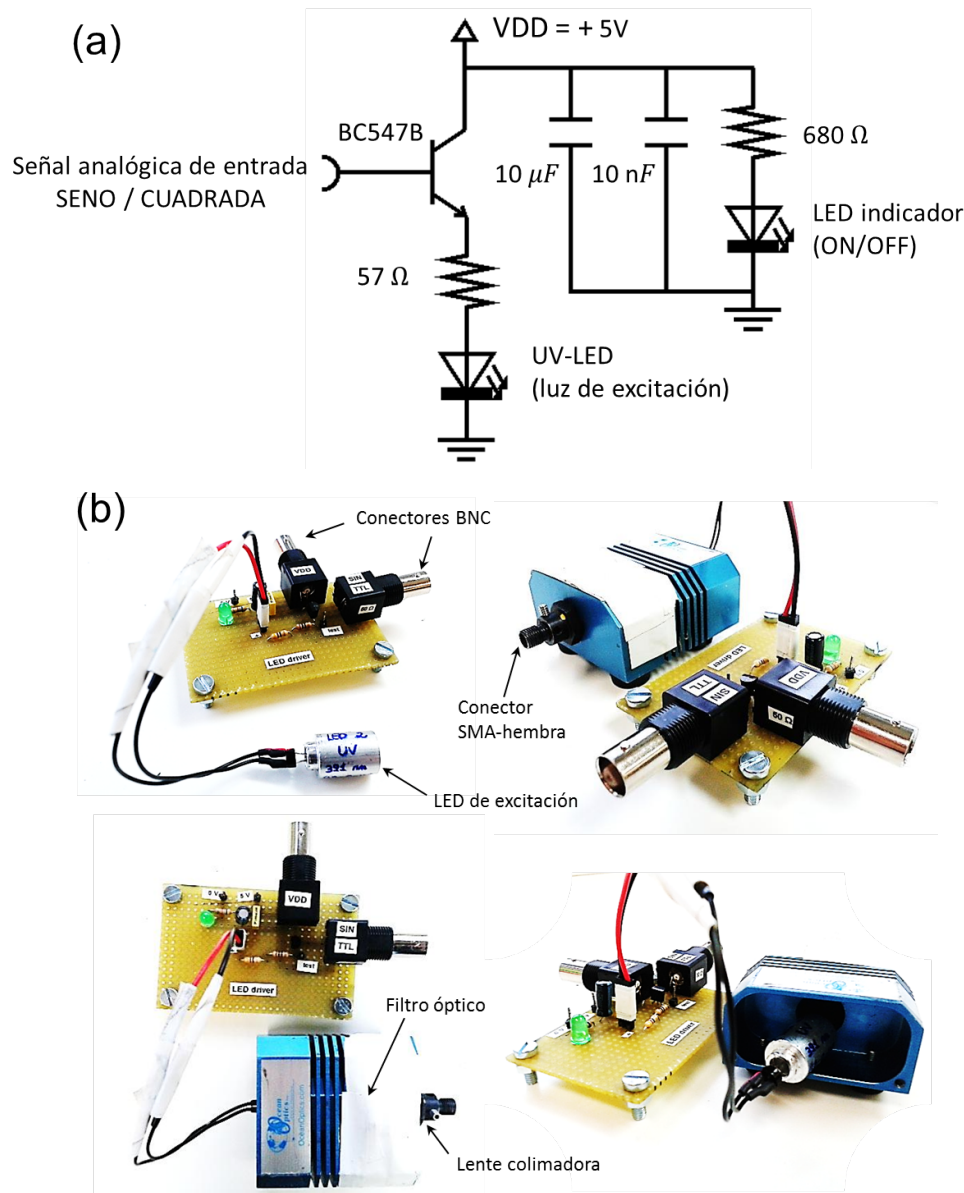


Figura 1.3: Circuito electrónico diseñado para modular la corriente del LED (LED driver) en el sistema de medida propuesto. (a) diagrama esquemático; (b) fotografías desde distintos ángulos.

(generar haces de rayos paralelos) y concentrar la luz emitida por el diodo LED, mejorando así la eficiencia del acoplamiento de potencia óptica dentro de la fibra (esto es, la cantidad de potencia óptica emitida por el LED que finalmente logra ser acoplada dentro del núcleo de la fibra). El cabezal de la fuente LED dispone a su salida de un conector SMA-hembra, donde es conectada una de las ramas de la fibra óptica bifurcada (haz de 12 fibras de $200 \mu\text{m}$ de diámetro de núcleo que conducirá la luz de excitación hasta la fase sensora).

(4) Fibra óptica bifurcada: El sistema de medida propuesto hace uso de una fibra óptica bifurcada (Avantes Inc., modelo FCR-7xx200-2, www.avantes.com, intervalo de longitudes de onda 200-800 nm (UV-vis), $AN=0.22$) para el guiado de la luz hacia/desde la fase sensora. Como puede observarse en el esquema de la Figura 1.1, la luz de excitación del LED es

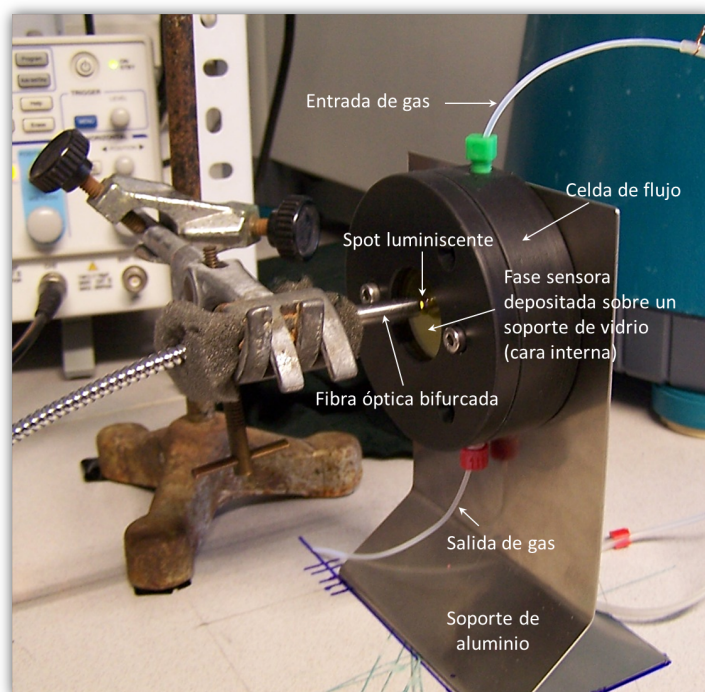


Figura 1.4: Detalle de la excitación de una fase sensora con la fibra óptica bifurcada y la formación del “spot” luminiscente.

conducida por una de las ramas de la fibra óptica (rama de color violeta; formada por un haz de 12 fibras de excitación de $200\ \mu\text{m}$ de diámetro de núcleo) hasta la superficie de la fase sensora. Dicha rama de excitación termina en una punta (o ferrule) de acero inoxidable donde las fibras de excitación del haz se distribuyen circularmente alrededor de una fibra central de lectura (rama de color rojo; formada por una única fibra de $600\ \mu\text{m}$ de diámetro de núcleo), la cual será la encargada de recoger y guiar la luz emitida por la fase sensora hasta el detector. Esta peculiar distribución de las fibras de excitación en el terminal común de la fibra óptica bifurcada no es casual, ya que permite focalizar la luz de excitación sobre una región muy pequeña de la fase sensora, dando lugar a la formación de un punto o “spot” luminiscente de unos pocos milímetros de diámetro (véase la Figura 1.4), cuya luz (de mayor longitud de onda que la excitación) será recogida por la fibra central de lectura y guiada hasta el detector. Las ramas de excitación y lectura de la fibra bifurcada terminan en conectores SMA-905. Por otro lado, tal y como se muestra en el diagrama de la Figura 1.1, en la mayoría de los casos suele ser recomendable situar el terminal de la fibra bifurcada con un cierto ángulo respecto a la normal de la fase sensora, lo cual evita que una gran parte de la luz de excitación reflejada se acople junto con la emisión en la fibra central de lectura. El uso de una fibra óptica bifurcada para el guiado de luz proporciona, sin duda, una gran flexibilidad y versatilidad al sistema de medida propuesto.

(5) Celda de flujo: En la Figura 1.5 se muestra la estructura y el detalle de funcionamiento de la celda de flujo diseñada para el sistema de medida propuesto. Ésta fue diseñada y fabricada en los talleres del Centro de Instrumentación Científica (CIC) de la Universidad de Granada, empleando como material teflón (PTFE, Politetrafluoroetileno) de color negro para evitar las reflexiones de luz y garantizar la inactividad química. La celda de flujo se

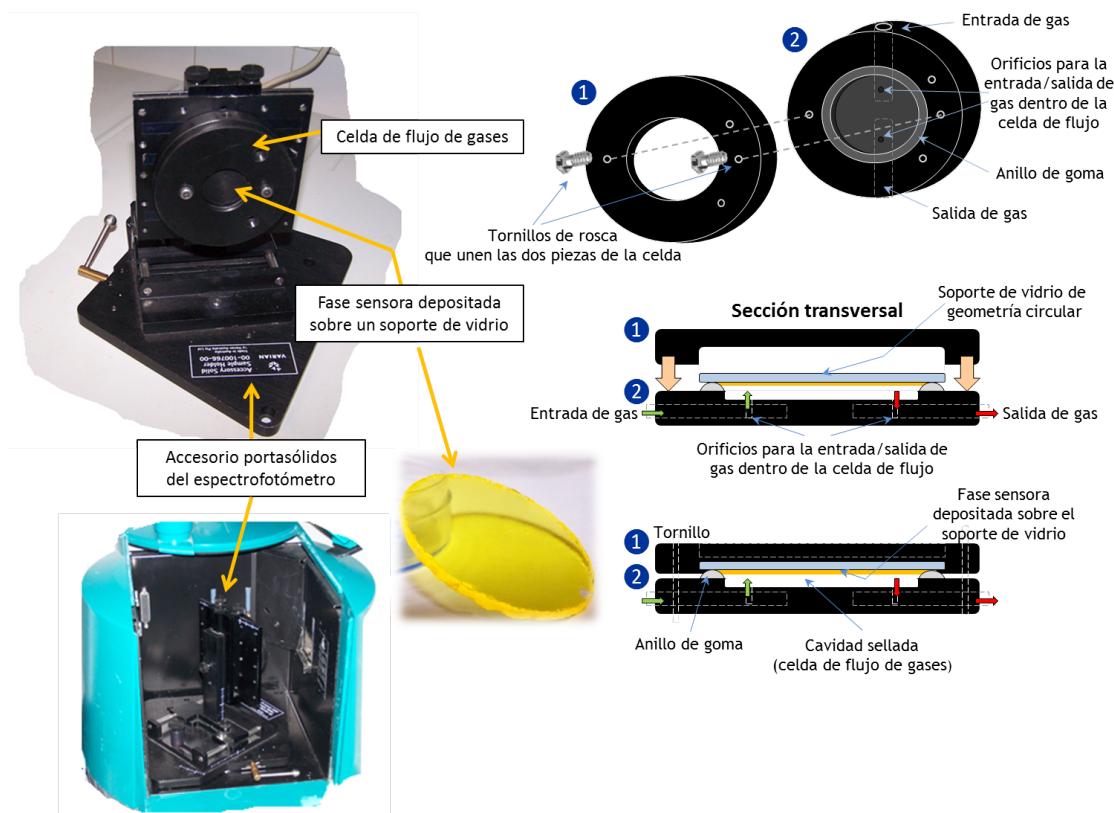


Figura 1.5: Estructura y detalle de funcionamiento de la celda de flujo diseñada.

compone de dos piezas de forma circular en medio de las cuales se coloca un soporte de vidrio (también de forma circular) donde se halla depositada la fase sensora en una de sus caras. Todo el conjunto es ensamblado con dos tornillos de rosca de la forma mostrada en la Figura 1.5. De esta forma, se crea una cámara “hermética” que encierra a la fase sensora (aislándola del exterior). La celda de flujo dispone de dos orificios estratégicamente situados para la entrada y salida de gases (o fluidos), que permiten crear un flujo homogéneo dentro de dicha cavidad. La celda de flujo no fue termostatizada, ya que fue concebida para trabajar a temperatura ambiente (generalmente 21 °C en un entorno de temperatura controlada). No obstante, para controlar y registrar la temperatura durante el proceso de medida, se hace uso de un sensor de temperatura inalámbrico (Fourtec-Fourier Technologies, MicroLite, www.fouriersystems.com) ubicado en un punto cercano a la celda de flujo. Por otro lado, tal y como se muestra en las Figuras 1.4 y 1.5, la celda de flujo puede ser fijada fácilmente a distintos soportes.

(6) Estación de gases: El laboratorio de instrumentación del Dpto. de Química Analítica de la Universidad de Granada dispone de las canalizaciones necesarias para el transporte de diferentes tipos de gases hasta los equipos del laboratorio. Estos gases son: nitrógeno (N_2), oxígeno (O_2), helio (He) y aire sintético. Asimismo también se dispone de botellas pequeñas (fácilmente transportables) de otros gases, tales como dióxido de carbono (CO_2) o dióxido de nitrógeno (NO_2). Dicha instalación también dispone de cierta instrumentación de control, como válvulas de paso, manómetros y controladores de flujo másico (dispositivos necesarios para la mezcla controlada de gases). Un esquema de la instalación del sistema de gases del laboratorio se muestra en la Figura 1.1. El sistema de gases dispone, pues, de:

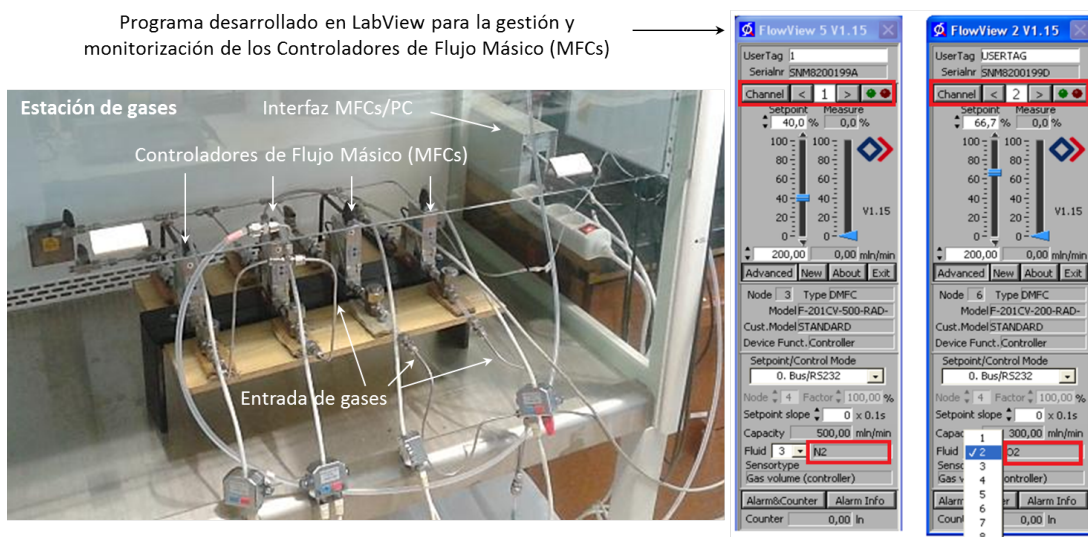


Figura 1.6: Fotografía que muestra los distintos elementos que componen la estación de gases del sistema de medida propuesto. También se muestra una imagen del programa desarrollado en LabView para monitorizar y regular en tiempo real la cantidad de flujo de gas que circula por cada uno de los MFCs.

(1) manómetros (Air Liquide, www.airliquide.com) que permiten medir y regular el flujo de gas que circula por las distintas canalizaciones del sistema, (2) válvulas de paso (Swagelok, www.swagelok.com) que permiten abrir o cerrar el flujo de gas en determinados tramos de dichas canalizaciones, (3) canalizaciones de gas realizadas con tubos de acero inoxidable de 1/4" y 1/8" (Swagelok), (4) 4 controladores de flujo másico (MFCs) (Bronkhorst High-Tech, EL-FLOW Select F-201CV, www.bronkhorst.com) con velocidades de flujo máximas de 500 (2), 300 (1) y 20 (1) ml min^{-1} respectivamente, los cuales son controlados por una unidad de control digital gestionada desde el PC (mediante un programa desarrollado en LabView que permite regular la cantidad de flujo de gas que circula por cada uno de los MFCs). En la Figura 1.6 se muestra una fotografía de la estación de gases donde pueden apreciarse estos elementos.

(7) Detector óptico (PMT): La luz emitida por la fase sensora es guiada hasta el detector óptico por una de las ramas de la fibra óptica bifurcada (rama de color rojo en la Figura 1.1). En esta figura se muestra el diagrama de bloques del módulo PMT (tubo fotomultiplicador) usado como detector óptico en el sistema de medida propuesto, y en la Figura 1.7 se muestra una fotografía real del mismo. El módulo PMT (H10723-20, Hamamatsu Photonics Japan, www.hamamatsu.com) presenta las siguientes características: ancho de banda de DC-1 MHz, intervalo de longitudes de onda de 230-920 nm (con pico de sensibilidad a 630 nm), control de ganancia ajustable, factor de conversión de corriente a voltaje de $0.1 \text{ V}/\mu\text{A}$, intervalo de temperatura -20 a 50°C , sensibilidad luminosa típica del cátodo de $500 \mu\text{A}/\text{lm}$, sensibilidad luminosa típica del ánodo de $1.0 \times 10^8 \text{ V}/\text{lm}$, voltaje de salida típico asociado a la corriente de oscuridad de 1 mV, fotocátodo de área circular de 8 mm de diámetro, dimensiones de $51.0 \times 24.0 \times 25.0 \text{ mm}$. Como puede observarse en la Figura 1.7, el módulo PMT dispone de varios accesorios adaptadores: uno de ellos es un adaptador SMA que permite la conexión de una fibra óptica al PMT; el otro es un bloque adaptador que permite colocar un filtro óptico (con un tamaño comprendido entre 8 y 14 mm diámetro) delante de la ventana de recepción del PMT. Estos filtros ópticos (FO-2) son intercambiables, y en nuestro caso disponemos

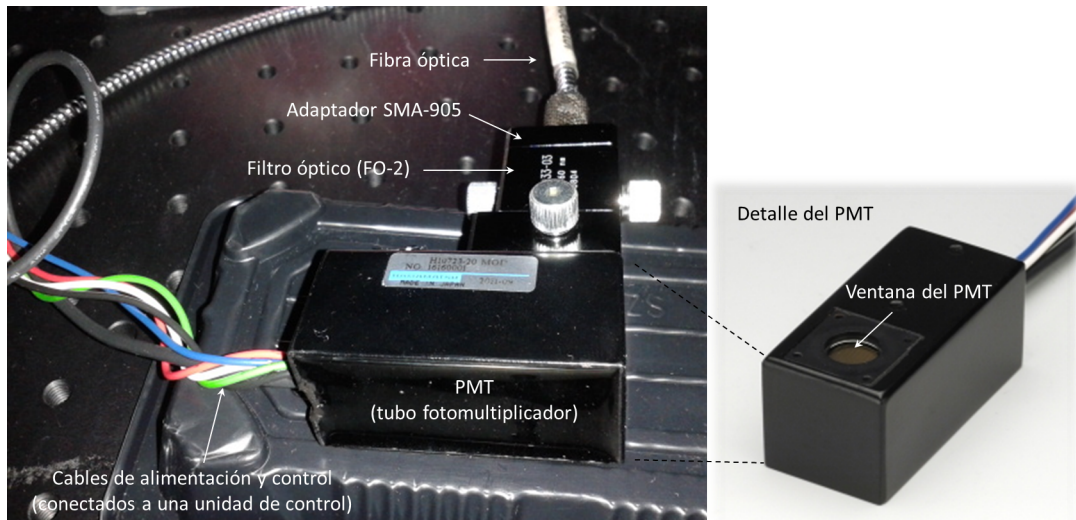


Figura 1.7: Fotografía del módulo PMT usado como detector óptico en el sistema de medida propuesto.

de dos para nuestros experimentos: un filtro óptico paso-larga ($\lambda_c = 450$ nm, NT62-975, Edmund Optics, www.edmundoptics.com) y un filtro óptico paso-banda ($\lambda_c = 630 \pm 30$ nm, A10033-03, Hamamatsu Photonics Japan).

Por otro lado, cabe mencionar que en la configuración del sistema basada en medidas de intensidad, no se hace uso del módulo PMT como detector, siendo éste reemplazado en este caso por un espectrómetro de fibra óptica comercial (Ava-Spec 2048, Avantes, www.avantes.com). En la Figura 1.8 se muestra una fotografía de este equipo. Este espectrómetro de fibra óptica está compuesto básicamente por: (1) un dispositivo monocromador que permite seleccionar de forma precisa una determinada longitud de onda, y (2) un array de fotodetectores (array-CCD de 2048 píxeles) que permite detectar la intensidad luminiscente en un amplio intervalo de longitudes de onda (200-1100 nm, esto es, en el rango UV-Vis-IR). Dicho equipo es conectado al PC del sistema de medida mediante conexión USB. En este caso, se hace uso del software (AvaSoft v.6.1) proporcionado por el fabricante del equipo, que permite la visualización y el almacenamiento de los espectros de emisión registrados por el dispositivo, así como la medida en continuo de la intensidad luminiscente a una determinada longitud de onda seleccionada previamente (entre otras funciones). Algunos de los parámetros instrumentales que pueden ser modificados con esta herramienta son: el tiempo de integración, el número de promedios del espectro visualizado o el intervalo espectral de barrido (entre otros). En la Figura 1.8 se muestra una captura de pantalla de la ventana principal de este programa. En el Capítulo 2 de esta memoria se proporcionan más detalles sobre la configuración de medida basada en medidas de intensidad.

(8) Cuarto oscuro: Para prevenir las interferencias de la luz parásita, la celda de flujo y el módulo PMT son alojados en el interior de un cuarto oscuro diseñado específicamente para estos fines (Thorlabs GmbH, modelo XE25C1, www.thorlabs.com). Dicha estructura dispone de una base de metal perforada que permite atornillar los distintos componentes del sistema a su base. Esto evita el posible desplazamiento de los componentes durante la medida, lo que redundaría en una mayor reproducibilidad de las medidas. En la Figura 1.9 se muestran varias fotografías de dicho cuarto oscuro.



Figura 1.8: Fotografía del espectrómetro de fibra óptica comercial usado para la adquisición de las medidas de intensidad de luminiscencia en el sistema de medida propuesto. También se muestra una captura de pantalla del software usado para controlar dicho equipo.



Figura 1.9: Fotografías del cuarto oscuro utilizado para alojar la celda de flujo y el módulo PMT en el sistema de medida propuesto.

(9) Etapa de acondicionamiento de señal: La señal de voltaje obtenida a la salida del módulo PMT suele ser del orden de unos pocos mV. Así pues, en la mayoría de los casos suele ser necesaria una etapa de amplificación previa de la señal antes de que ésta pueda ser aplicada al equipo de adquisición de datos. Para ello, el sistema propuesto hace uso de amplificador de voltaje de bajo ruido (véase la Figura 1.10(a)). Este amplificador (Stanford Research Systems, modelo SIM911 BJT, www.thinksrs.com) presenta las siguientes características: ruido de entrada de $1.8 \text{ nV}/\sqrt{\text{Hz}}$, bajo ruido de salida, ancho de banda de 1 MHz, ganancia seleccionable entre 1 y 100, acoplamiento AC o DC, $100 \text{ k}\Omega$ de impedancia de entrada, 85 dB de CMRR y posibilidad de control remoto. En otras ocasiones, además de la etapa de amplificación, también suele ser recomendable una etapa de filtrado para eliminar el ruido de alta frecuencia de la señal. En la Figura 1.10(b) se muestra un filtro RC pasivo paso-baja de tres etapas muy sencillo para filtrar las señales de excitación (referencia) y emisión.

(9) Equipo de adquisición de datos: Finalmente, la señal de excitación (tomada como referencia) y la señal de emisión (obtenida a la salida de la etapa de acondicionamiento) son aplicadas como entradas a un equipo de adquisición de datos, que será el encargado de digitalizar dichas señales y de procesar sus muestras para extraer de ellas la información de interés (señal analítica): en nuestro caso, el sistema de medida propuesto proporciona, para esta configuración, una medida del desfase y/o del factor de modulación entre las señales de excitación y emisión. Estos valores de desfase y de factor de modulación dependerán de la

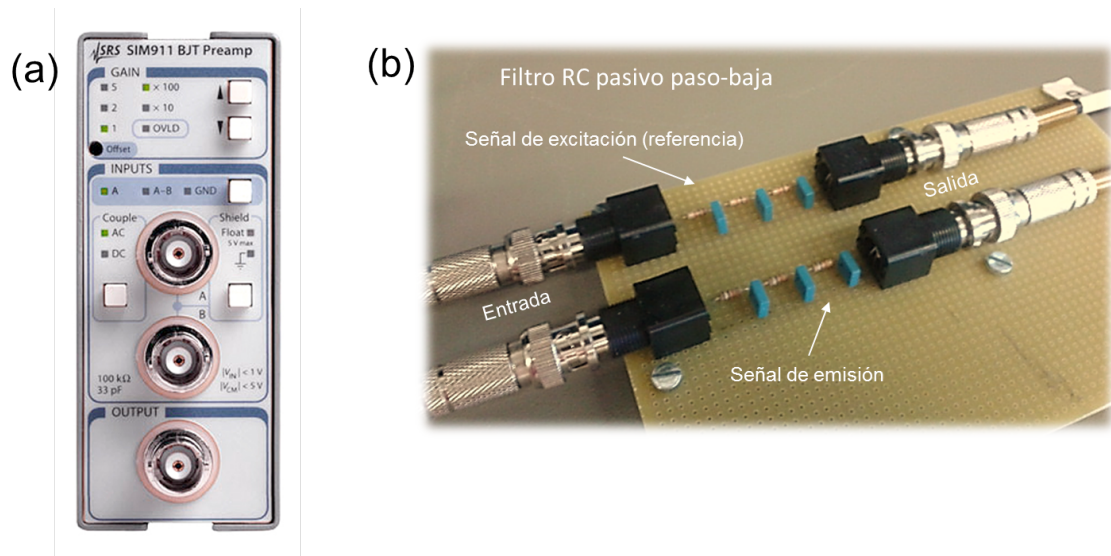


Figura 1.10: Acondicionamiento de señal en el sistema de medida propuesto. (a) amplificador de voltaje de bajo ruido; (b) filtro RC pasivo paso-baja de tres etapas.

concentración de analito presente en la celda de flujo durante la medida. Así pues, el registro de la señal analítica para un intervalo amplio de concentraciones proporcionará la curva de calibrado de la fase sensora analizada (este asunto será tratado con mayor profundidad en los próximos capítulos). Además, a partir de estos valores estimados de desfase y/o de factor de modulación, también podrán calcularse los tiempos de vida aparentes de la fase sensora analizada (usando las ecuaciones que se proporcionan en la parte de la introducción).

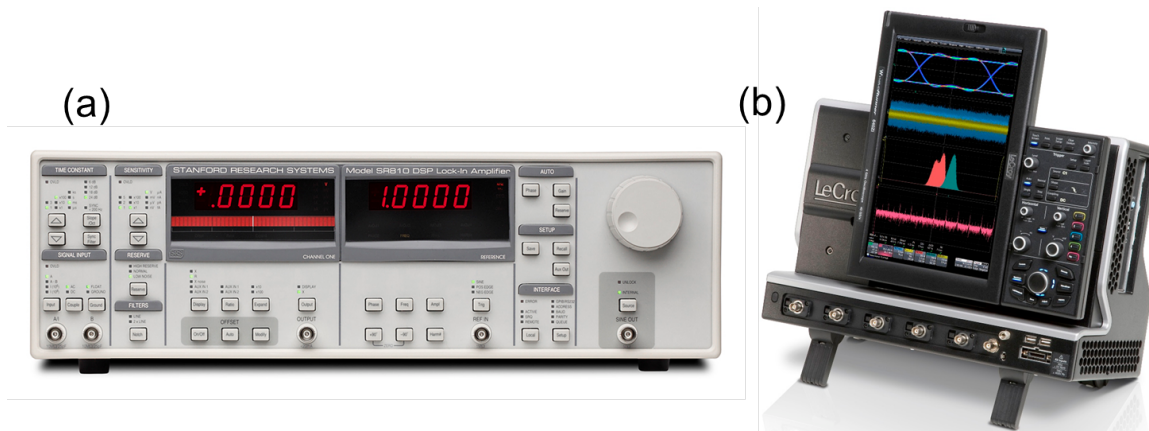


Figura 1.11: Equipos de adquisición de datos para la medida del desfase y/o del factor de modulación en el sistema de medida propuesto. (a) un detector de fase-fija comercial (*lock-in amplifier* (LIA)); (b) un osciloscopio digital conectado a un ordenador personal para el posterior procesamiento de los datos usando MATLAB.

El sistema de medida propuesto dispone de dos equipos de adquisición de datos para la medida de los valores de desfase y/o del factor de modulación: (1) un detector de fase-fija comercial (*lock-in amplifier* (LIA), Stanford Research Systems, modelo SR830), y (2) un osciloscopio digital (LeCroy, modelo WaveRunner 604Zi, www.lecroy.com) conectado a un ordenador personal para el posterior procesamiento de los datos usando MATLAB. En la

Figura 1.11 se muestra una fotografía de cada uno de ellos.

En ambas configuraciones se utiliza la señal de excitación como referencia para calcular el desplazamiento de fase y/o el factor de modulación de la señal de emisión (véase el esquema de la Figura 1.1). En el primer caso, el LIA comercial procesa internamente estas dos señales y proporciona como salida los valores de desfase y/o de factor de modulación. Estos datos son transferidos en tiempo real al ordenador del sistema de medida a través de puerto serie (véanse los Capítulos 3 y 5 para más detalles). Este equipo puede operar con señales de frecuencia fija en el intervalo de 1 mHz a 102.4 kHz y presenta una estabilidad de 5 ppm/°C, 0.01 grados de resolución de fase y constantes de tiempo ajustables en el intervalo de 10 μ s a 30 ks. En el segundo caso, el osciloscopio digital se usa para visualizar y digitalizar las señales analógicas de excitación y emisión. Las muestras de las señales adquiridas son transferidas vía Ethernet al ordenador del sistema de medida para su posterior procesamiento usando programas desarrollados en MATLAB. Los detalles del algoritmo implementado para calcular el desplazamiento de fase y/o el factor de modulación entre ambas señales pueden ser consultados en los Capítulos 4, 5 y 6 de esta memoria. El osciloscopio utilizado presenta las siguientes características: ancho de banda nominal de 400 MHz, 4 canales de entrada, resolución vertical de 8 bits, tasa de muestreo por canal de 10 GS/s usando 4 canales o de 20 GS/s usando 2 canales, tiempo de subida (10-90 %) de 875 ps, elevada tasa de transferencia de datos vía Ethernet (mínima de 320 Mb/s) y memoria de almacenamiento de 16 Mpts/canal usando 4 canales o de 32 Mpts/canal si se usan solo 2 canales.

1.3 Antecedentes del banco de pruebas propuesto

La etapa de diseño e implementación del banco de pruebas presentado en esta memoria ha supuesto un 60 % del periodo total de la Tesis, requiriendo un gran trabajo previo de documentación y de pruebas experimentales hasta llegar a desarrollar el sistema final que aquí presentamos.

En un primer momento se comenzó diseñando circuitos sencillos para modular la corriente del LED y para la etapa de la detección óptica (detección de las señales ópticas procedentes de las fases sensoras). Para ello se usaron componentes electrónicos sencillos de bajo coste (tales como LEDs, resistencias, condensadores, amplificadores operacionales de transimpedancia, transistores BJT, fotodiodos, etc.) e instrumentación de propósito general para la generación y adquisición de las señales eléctricas (tales como un generador de funciones (PROMAX, modelo GF-857, www.promax.es) (véase la Figura 1.16(3)) y un osciloscopio digital (Tenma Test Equipment, modelo 72-7240, www.farnell.com) (véase la Figura 1.16(1))). En la Figura 1.12 se muestran los diagramas esquemáticos de algunos de los primeros circuitos desarrollados para modular la corriente del LED y para la etapa de la detección óptica. En la Figura 1.15(1) y (2) se muestran algunas imágenes del circuito implementado para la etapa de la detección óptica. En este caso, el circuito dispone de una primera etapa basada en un fotodiodo en la que se lleva a cabo la conversión de la señal óptica procedente de la fase sensora (conducida hasta el detector a través de una fibra óptica) a una señal de naturaleza eléctrica (fotocorriente). A continuación dispone de un amplificador operacional que convierte la corriente generada por el fotodiodo en una señal de tensión, la cual es amplificada posteriormente por una etapa de ganancia constituida por transistores BJT (dos etapas en cascada en configuración de emisor

común). Esto permite que la señal de salida de la etapa de amplificación presente un nivel de tensión adecuado para ser visualizada en el osciloscopio digital. Para poder determinar el desfase y/o el factor de modulación de la señal de emisión con respecto a la señal de excitación (usada como referencia), ambas señales son adquiridas con el osciloscopio. Dichas señales son promediadas 256 veces (en el osciloscopio) para reducir el ruido en un factor 16 (es decir, 24 dB) y transferidas al PC del sistema para su posterior procesamiento usando MATLAB. Sin embargo, la práctica totalidad de estos diseños resultaron insuficientes para la detección de las débiles señales ópticas procedentes de las fases sensoras (debido al ruido electrónico de los componentes del sistema, las interferencias electromagnéticas, la insuficiente sensibilidad óptica de los fotodiodos utilizados para la detección óptica, el deficiente acoplamiento óptico entre de la fibra y el fotodiodo, etc.), así como el ancho de banda limitado de los componentes utilizados (que impedía analizar fases sensoras ópticas con tiempos de vida pequeños, esto es, con frecuencias de modulación óptimas mayores a 40 kHz).

Por todas estas razones, se estudió la posibilidad de adquirir un dispositivo comercial para la etapa de la detección óptica. En este caso se optó por la compra de un módulo APD (Hamamatsu Photonics Japan, modelo C10508, www.hamamatsu.com) (véase la Figura 1.13) equipado con un fotodiodo de avalancha (APD) de 1 mm de diámetro y elevada sensibilidad en el infrarrojo. Este módulo también dispone de una etapa de ganancia controlada manualmente. El intervalo de frecuencias de operación comprende desde DC hasta los 10 MHz, con una sensibilidad fotoeléctrica en dicha banda de 1.5×10^6 V/W. Además dispone a su entrada de un conector SMA-905 (hembra) para la conexión de una fibra óptica con conector tipo SMA-905 (macho); la señal de voltaje a la salida del dispositivo es entregada a través de un conector BNC (hembra), lo que facilita su conexión directa con un osciloscopio digital. Otro aspecto importante a destacar es la posibilidad de colocar un filtro óptico paso-larga delante del fotodiodo para eliminar la radiación de excitación (reflejada) de la radiación de emisión. Una descripción más detallada de este módulo se muestra en la Figura 1.13).

La adquisición de este nuevo dispositivo de detección óptica mejoró significativamente las prestaciones del sistema de medida, pudiéndose caracterizar un conjunto amplio de fases sensoras ópticas usando métodos de modulación de fase. No obstante, pese a la mejora, el módulo APD seguía sin proporcionar la sensibilidad óptica suficiente para permitir el análisis de fases sensoras ópticas con bajos rendimientos cuánticos de luminiscencia o con longitudes de onda de emisión cortas (ya que la sensibilidad del módulo APD era significativamente menor en la zona del UV). Por otro lado, el sistema de medida propuesto presentaba otras carencias importantes que dificultaban notablemente el procedimiento de caracterización y evaluación de las fases sensoras ópticas. Algunas de ellas eran: las prestaciones limitadas del osciloscopio digital usado para la visualización y la adquisición de las señales (escasa capacidad de memoria, ancho de banda limitado y una lenta transferencia de datos vía RS232 desde la memoria del osciloscopio al PC), la capacidad limitada para generar señales de excitación analógicas con forma de onda arbitraria usando el generador de funciones mencionado, la insuficiente calidad de los filtros ópticos de excitación y de emisión, etc. En la Figura 1.14 se muestra una fotografía del banco de pruebas desarrollado en esta primera fase del proceso de diseño.

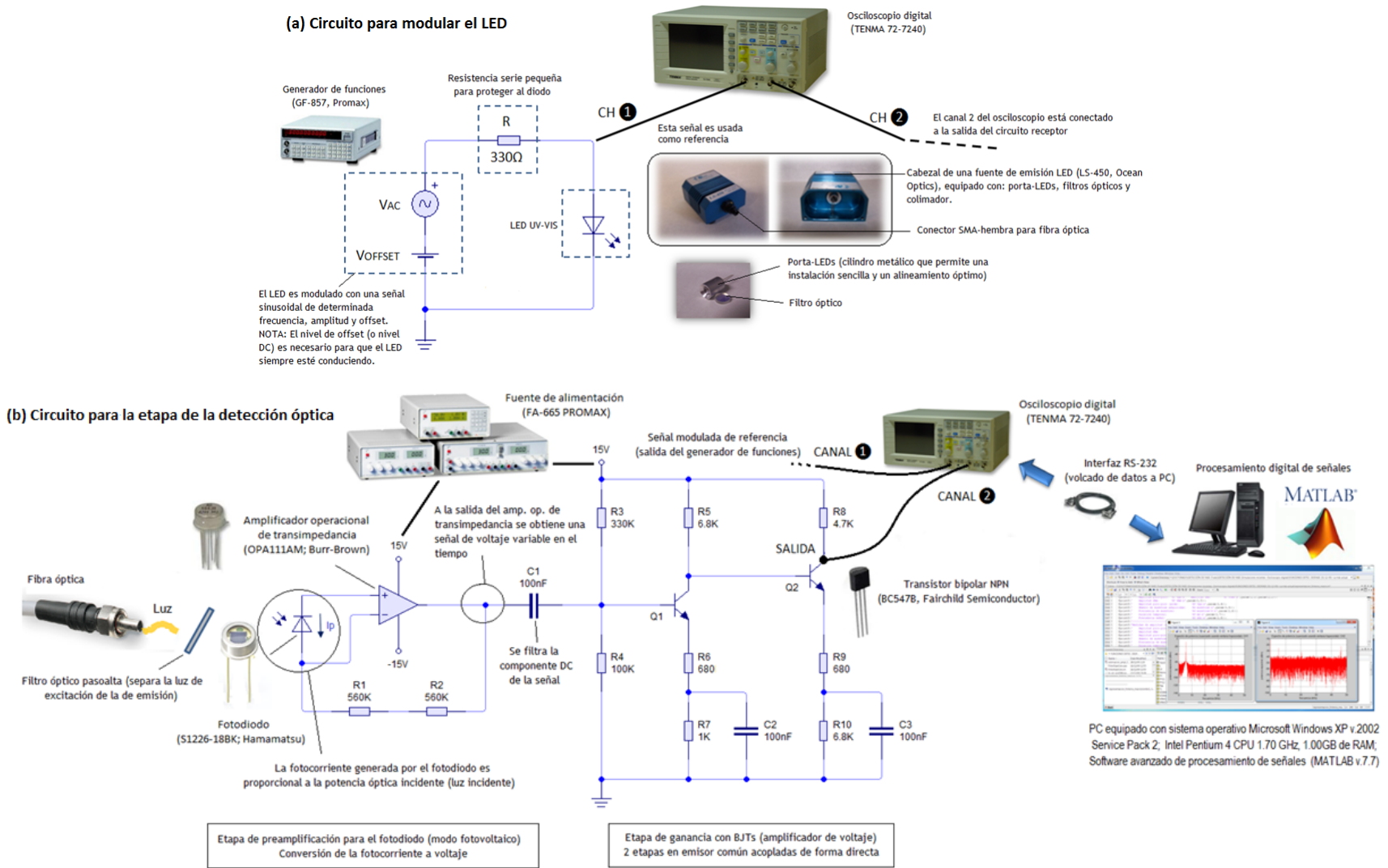


Figura 1.12: Diagramas esquemáticos de los primeros circuitos desarrollados para el sistema de medida. (a) circuito para modular la corriente del LED; (b) circuito para la etapa de la detección óptica.

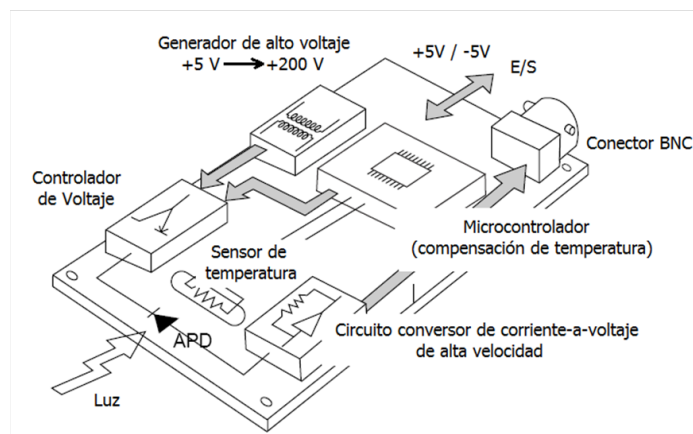
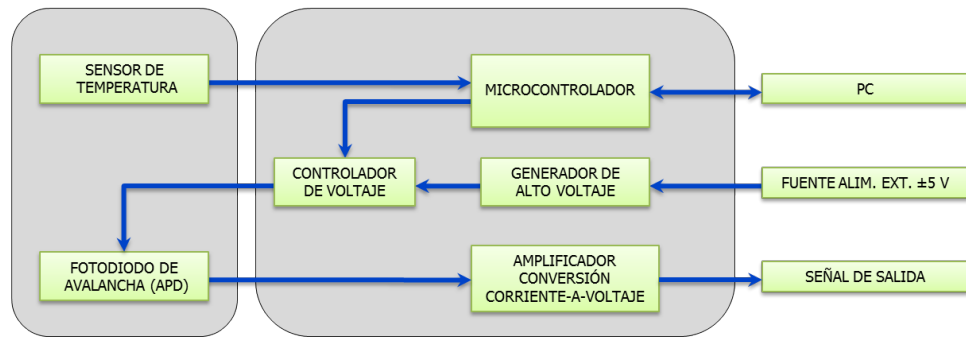
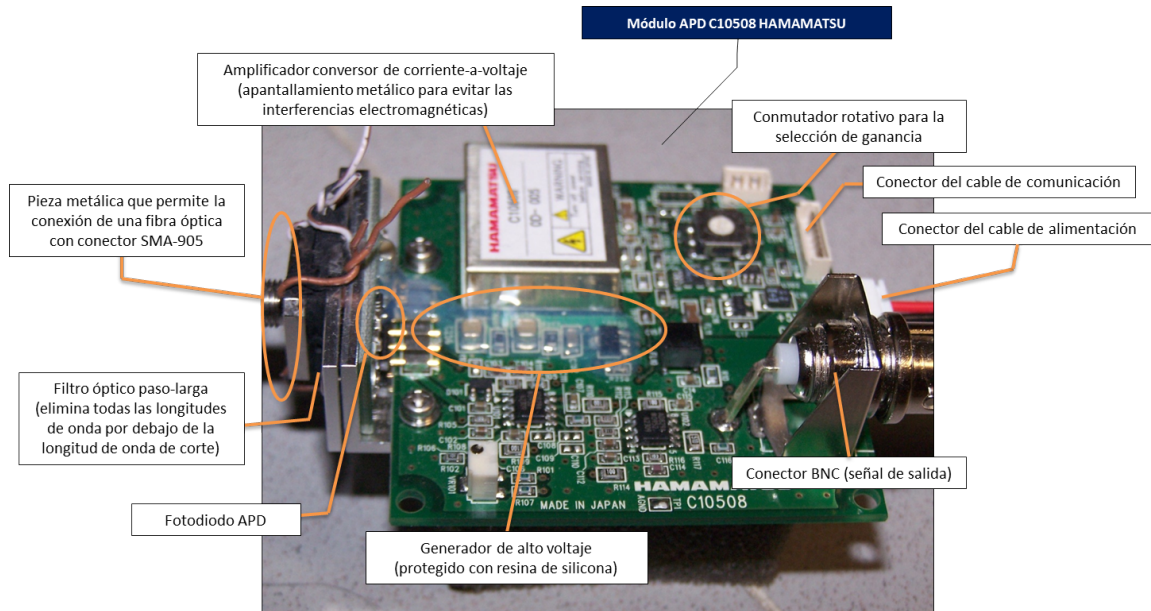


Figura 1.13: Módulo APD comercial (Hamamatsu Photonics Japan, modelo C10508) usado como detector óptico en versiones anteriores del sistema de medida.

Una vez conocidas las carencias instrumentales y experimentales se continuó perfeccionando el sistema de medida que condujo al diseño definitivo del banco de pruebas. Así, se incorporaron nuevos componentes ópticos y opto-electrónicos de mayor calidad (LEDs, fil-

tros ópticos de excitación y emisión), un tubo fotomultiplicador (PMT) como detector óptico (Hamamatsu Photonics Japan, modelo H10723-20), un equipo comercial de amplificación analógica (Stanford Research Systems, modelo SIM911 BJT), un equipo comercial para la medida de desfases (lock-in amplifier (LIA), Stanford Research Systems, modelo SR830) usado con frecuencia en la mayoría de los laboratorios y sistemas de medida descritos en la literatura (equipo de referencia), una tarjeta de adquisición de datos AD/DA para la generación de las señales analógicas (National Instruments, modelo NI-DAQ PCIe-6363) (véase la Figura 1.16(4)) y un osciloscopio digital de altas prestaciones (LeCroy, modelo WaveRunner 604Zi) (véase la Figura 1.16(2)) para la visualización y adquisición de las señales eléctricas. También se adquirió un cuarto oscuro para aislar y proteger los componentes ópticos del exterior (luz parásita, ambiental, golpes, etc.) y para poder fijar estos elementos a una base sólida. La Figura 1.15 muestra un resumen gráfico de la evolución del diseño de la etapa de detección óptica en el sistema de medida propuesto. Por su parte, la Figura 1.16 muestra los cambios realizados en la instrumentación empleada para la generación y la adquisición de las señales en el sistema de medida propuesto. Finalmente, la Figura 1.17 muestra una imagen completa del banco de pruebas final desarrollado en esta memoria de Tesis. Una vez solventados los problemas instrumentales del sistema de medida, se procedió a una mayor profundización en el apartado del procesamiento digital de las señales.

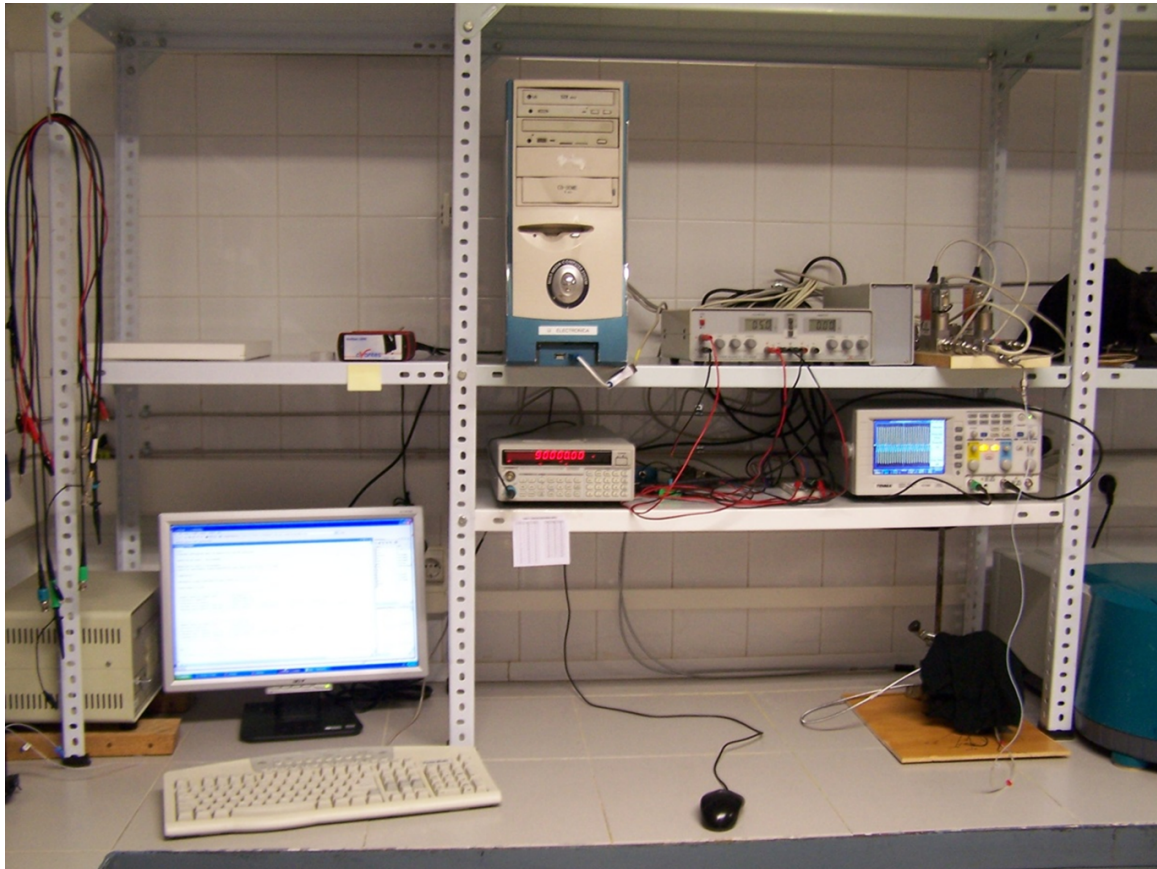


Figura 1.14: Fotografía del banco de pruebas desarrollado en las primeras fases del diseño.

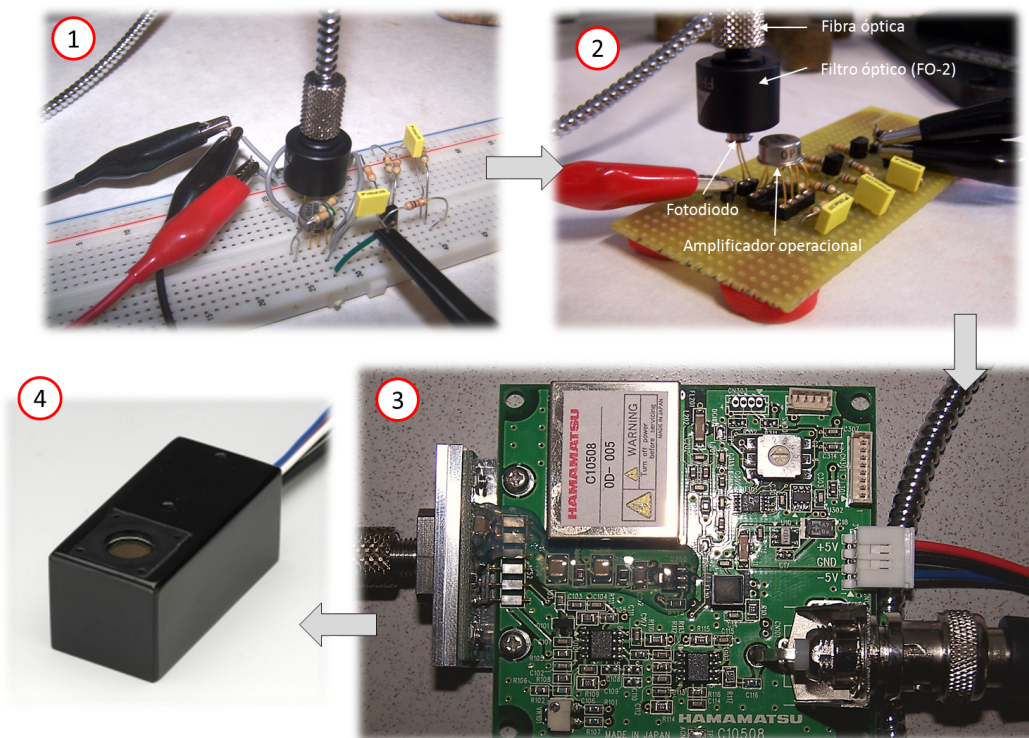


Figura 1.15: Resumen gráfico de la evolución del diseño de la etapa de detección óptica en el sistema de medida propuesto.

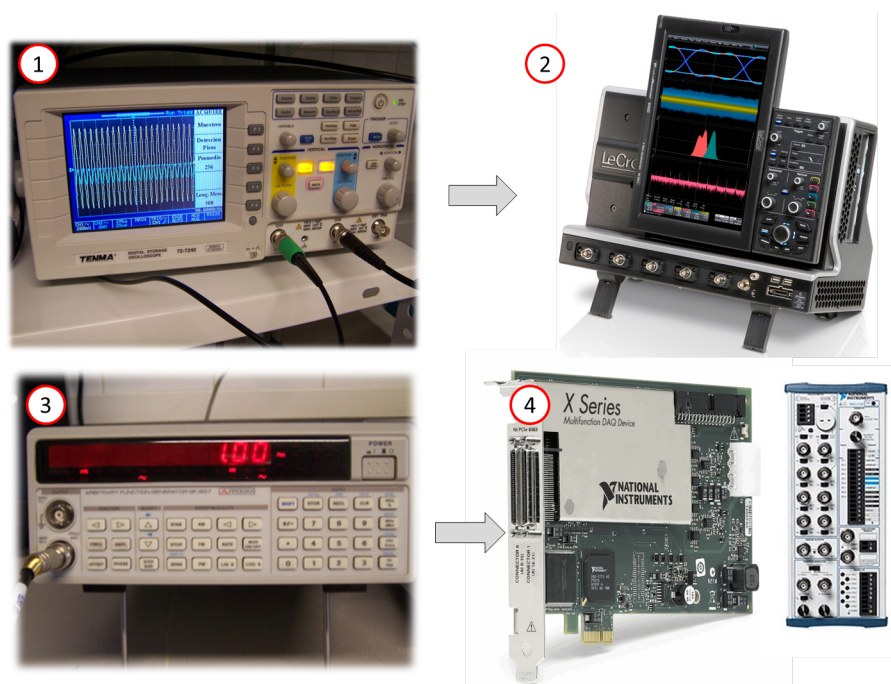


Figura 1.16: Evolución de la instrumentación empleada para la generación y la adquisición de las señales en el sistema de medida propuesto (versiones anteriores y actual).



Figura 1.17: Fotografía del banco de pruebas final presentado en esta memoria.

A new highly sensitive and versatile optical sensing film for controlling CO₂ in gaseous and aqueous media

Paulina Karem Contreras Gutiérrez^a, Santiago Medina Rodríguez^{a,b}, Antonio Luis Medina Castillo^c, Jorge Fernando Fernández Sánchez^{a,*} and Alberto Fernández Gutiérrez^a

^a*Department of Analytical Chemistry, Faculty of Sciences, University of Granada, Avda. Fuentenueva s/n, E-18071 Granada, Spain.*

^b*Department of Signal Theory, Networking and Communications, CITIC-UGR, University of Granada, C/ Periodista Rafael Gómez 2, E-18071 Granada, Spain.*

^c*NanoMyP[®], Nanomateriales y Polímeros S.L., Spin-Off Company of the UGR, BIC Building, Avda. de la Innovación 1, E-18100 Granada, Spain.*

Published in *Sensors and Actuators B: Chemical* 184 (2013) 281-287

A new highly sensitive and versatile optical sensing film for controlling CO₂ in gaseous and aqueous media

Abstract—We describe a CO₂-selective sensing film based on the incorporation of a phase-transfer agent, tetraoctylammonium hydroxide (TONOH), into a fluorescence pH-sensitive functionalized polymer. This film can be used for CO₂ determination in gaseous and aqueous media. We have investigated the effect of the concentration of TONOH, and the influence of external parameters such as flow rate, humidity and interfering gases (O₂, CO and NO₂). The sensing films respond to CO₂ concentrations in the gas phase between 7.7 and 40% CO₂ (v/v) and between 4.4 and 60% CO₂ (v/v) in aqueous media, with detection limits of 2.3 and 1.3% CO₂ (v/v), respectively. The covalent immobilization of the fluorescence pH-indicator on the polymer chains provides lower probability of aggregation and no leaching of the optical pH-sensitive dye. In addition, the developed sensing film quick response time ($t_{95} = 5$ s from 0 to 20% CO₂ (v/v) in gas phase), good opto-thermal stability and high versatility. In order to demonstrate this claim, we have developed an optical fiber sensor. It shows good analytical properties (linear dynamic range of 1.4–40% CO₂ (v/v) with a detection limit of 0.4% CO₂ (v/v).

keywords: CO₂; Luminescent polymers; Gas analysis; Water analysis; Medical application; Breath-by-breath analysis.

2.1 Introduction

CARBON dioxide is one of the most important compounds on earth. Produced by living beings, CO₂ is dangerous to them at high concentrations. Apart from environmental monitoring [1, 2] because of its role in global climate change, a variety of other applications exist where determining CO₂ concentration is essential. The quantitative detection of CO₂ is of interest to the food [3, 4], beverage [5], biotechnological [6, 7], and health [8–10] industries.

Analysis of CO₂ in gas phase is commonly accomplished by nondispersive infrared (NDIR) sensors which are an inexpensive alternative to traditional FT-IR [5]. These sensors cannot be used for analysis of aqueous CO₂, where the Severinghaus electrode is considered as standard [11, 12]. Nevertheless, this electrode, or modified versions, is expensive, bulky, susceptible to interferences and slow [13]. The use of optical sensors for quantitative CO₂ analysis offers potential advantages over other analytical methods such as, for example, electrical isolation, reduced noise interference, the possibility of miniaturization and remote sensing, and when coupled to optical fibers it provides a non-invasive monitoring system that is free from electromagnetic interferences [14]. In addition, they are often inexpensive and can be mass-produced as disposable materials [13].

Optical CO₂ sensing is normally based on the pH change due to protonation of a pH indicator when exposed to acidic CO₂ gas. This involves either a colorimetric [10, 14–18] or fluorescent [19–22] pH indicator which is incorporated, either covalently [23] or physically, in a liquid polymeric membrane [1, 14, 24, 25] or sol gel matrix [3, 13, 26–28] in the presence of a transfer agent such as tetraoctylammonium hydroxide (TONOH). Changes in the optical properties of either colorimetric or fluorescent dyes rely on the protonation of the dye counterion (D⁻) by bicarbonate ion formed by the interaction of CO₂ with the transfer agent [8, 13, 14, 21, 29].

Most of the studies utilize the colorimetric dye α -naphtholphthalein (NAF) or the luminescent dye 1-hydroxypyrene-3,6,8-trisulfonate (HPTS or pyranine) physically immobilized in polymer or sol gel matrix, respectively. The incorporation of a dye into a polymer matrix may involve some drawbacks such as aggregation and/or precipitation of the dye into the liquid membrane, and lexiviation of the pH-sensitive dye. In addition, the physical immobilization of a dye into a sol-gel matrix provides a decreasing on its sensitivity compared with its immobilization in polymeric matrices [1], and they are prone to aging caused by structural evolution of the sol-gel, which in turn severely can affect sensitivity to CO₂ [30]. Thus, the development of alternative materials is still of much interest. Hence, we propose to use a matrix which contains the pH-indicator covalently attached to the polymeric matrix. This approach maintains the advantages of the polymeric matrices and solves some of its drawbacks: avoid both the lexiviation and agglomeration of the pH-sensitive dye.

Nowadays new polymers which contain luminescent pH-sensitive dyes chemically attached to their structures are commercially available. One of them is called Polym-H7 and is supplied by nanoMyP[®]. It is perfectly compatible with aqueous media and is based on the co-polymerization of fluorescein o-acrylate (FOA), methylmethacrylate (MMA) and hydroxymethylmethacrylate (HEMA) in the presence of 3-methacryloylaminopropyl-trimethylammoniumchloride (MAPTAC) by reverse atom-transfer radical polymerization (ATPR). The pH fluorescent probe (FOA) covalently attached on the copolymer chains shows an apparent pK_a of 7.8. Polym-H7 has been tested for the development of pH-sensitive sensing films [31].

The aim of this work is to demonstrate that these kinds of copolymers can be used for developing CO₂-sensing films for gas and aqueous samples and that these sensing films can be easily implemented in a optical fiber sensor.

2.2 Experimental details

2.2.1 Chemical reagents and materials

Polym-H7 (nanoMyP[®], Spain, www.nanomyp.com) and tetraoctylammonium hydroxide (TONOH, 20% in MeOH, Fluka Chemie AG, Buchs) were used as received. Dry N₂, quality 5.5, was supplied from a 50 L bottle at 200 bar (Air Liquide). CO₂, quality 4.8, from 10 L bottle at 49.5 bar (Abello Linde), NO₂ 10 ppm and CO 1000 ppm in N₂ from 10 L bottles at 200 bar (Abello Linde) were also used.

2.2.2 Preparation and characterization of sensing films

The cocktails were prepared in sealable 4 mL flasks containing 50 mg mL⁻¹ of Polym-H7, 125 mg mL⁻¹ of TONOH and MeOH.

The sensing films were prepared by spin-coating using a Laurell spin-coater model WS-400B-6NPP/LITE (North Wales, PA, USA). 200 μ L of the cocktail was injected onto a rotating glass plate of a spinning device at 300 rpm. All the membranes were transparent and allowed visible light to pass through. The thickness of the layer was optimized for this concrete application. It should be re-optimized for other applications and/or deposition methods. The sensing films were characterized by measuring ($I_0 - I_x$) at $\lambda_{exc/em} = 480/520$ nm, with a detector voltage of 650 V and excitation and emission slit width of 5 nm where I_0 is the fluorescence emission of the film in absence of CO₂ and I_x is the luminescence emission on exposure to different percentages of CO₂. Although the excitation and emission wavelengths were quite close, problems with dispersed light were not observed due to the small width of the excitation and emission slits.

In gas analysis the concentration of CO₂ was set balancing the target analyte with N₂ and providing a gas carrier stream with a 40% relative humidity (RH) and a flow rate of 100 mL min⁻¹. The concentration of CO₂ in aqueous phase was set by bubbling an accurately controlled mixture of CO₂ and N₂ through the carrier of the FIA system.

All measurements were made in triplicate to check experimental error and all the results are expressed as the average of 3 replicas \pm error (st/\sqrt{n}), where s is the standard deviation, t is the student t , and n is the number of replicas.

2.2.3 Measurement setup

Fluorescence was measured on a Cary Eclipse luminescence spectrometer (Varian Inc.) using a specially designed flow-through cell. CO₂-sensitive films were fitted in the cell and a gas or aqueous stream was applied. Copper and stainless-steel tubing was used for the connections.

For gas analysis, dry N₂ was split into two lines before two mass-flow controllers (MFCs) Bronkhorst. One branch was humidified by guiding the N₂ over water in a 2-neck glass flask, thus avoiding the formation of water droplets. A relative humidity (RH) of up to 85% was obtained. This was monitored with a hygrometer (Rotronic, Bassersdorf) coupled after the measurement cell. The two lines of N₂ were merged to provide the desired carrier gas stream, to which additional lines could be connected. The responses of the CO₂-sensing films were normally investigated using a flow of N₂ humidified to 40% RH. The percentage of CO₂ was varied by using mass-flow controllers to balance CO₂ with humidified N₂. To investigate the effect of interference by other gases such as humidity, O₂, NO₂ and CO a constant concentration of CO₂ was mixed with different flow rates of these gases using mass-flow controllers.

For aqueous determination, a gas station was coupled with a flow injection system (FIA). The gas station consist in two MFCs (one for N₂ and other for CO₂) which bubbling an accurately controlled mixture of CO₂ and N₂ through the carrier solution of the FIA system.

A Minipuls 3 Gilson peristaltic pump (Gilson, Villiers Le Bel, France) was used for carrier delivering and flow regulation. PTFE connecting tubing (0.8 mm id) were used to connect the carrier with the flow-cell. Fig. 2.1 shows the scheme of both devices.

Both gas stations (for gas and aqueous analysis) were controlled by home-made LabVIEW programs which fully control the MFCs via RS-232. The luminescence measurements were controlled by Cary Eclipse software for Windows 95/98/NT system. For the development of the optical fiber sensor, a 470 nm blue LED (Ocean Optics, USA) was used to excite the sensing film. This LED device was installed in a LS-450 holder (Ocean Optics, USA) which is equipped with a SMA-905 connector for an optical fiber and a bandpass optical filter $\lambda_{central} = 469$ nm, BW = 35 nm (Thorlabs GmbH, model MF469-35).

A bifurcated optical fiber probe, $\frac{1}{2}$ " Industrial Fluorescence Probe (Avantes BV) was used to focus the light emitted by the LED to the sensing film and also to collect the fluorescence emission from the cell to the detector. A branch of the probe which has 12 UV/VIS fibers of 200 μm -external diameter (called the illumination branch) was connected via SMA-905 to the LS-450 holder. The other branch, which is equipped with a 600 μm -external diameter fiber (called the detection branch) was also connected via SMA-905 with the CCD spectrometer. The end of the probe consists of a stainless steel cylinder, $\frac{1}{2}$ " diameter, containing a 10 mm diameter \times 1 mm thick sapphire windows with anti-reflection coating and the 12 illuminating 200 μm -fibers round surrounding the single 600 μm -fiber which is in the middle of the tip.

The measurement cell used was specially designed for this work. It allows the use of gaseous or aqueous streams, and contains the sensing film and the end of the optical fiber probe perfectly coupled. The Fiber Optic Spectrometer AvaSpec-2048 was used as detector. It was used to record the emission fluorescence. It is based on the AvaBench-75 symmetrical Czerny-Turner design with 2048 pixel CCD Detector Array. The spectrometer has a SMA fiber-optic entrance connector, a collimating and focusing mirror and a UB (UV/VIS; 200-800 nm) diffractive grating with a blaze at 0 nm and a slit of 500 μm . Avasoft-Full software controls the spectrometer and saves the emission spectra. The software also permits the recording of 8 different time-drive functions simultaneously, thus permitting the recording of the emission intensity at 8 different wavelengths versus time simultaneously, or 7 wavelengths and a complete emission spectrum versus time, etc.

To decrease the background and increase the sensitivity, a longpass filter $\lambda = 500$ nm (Thorlabs GmbH, model FEL0500) was placed between the sensing film and the CCD-detector. Electronic Supporting Information (ESI) shows the scheme of this device (see ESI, Fig. ESI-1).

2.3 Results and discussion

2.3.1 Optical properties of CO₂-sensing films

The reaction process between the chemically attached pH-indicator and tetraoctylammonium hydroxide (TONOH) with CO₂ has been previously described by several authors [14, 16–18];

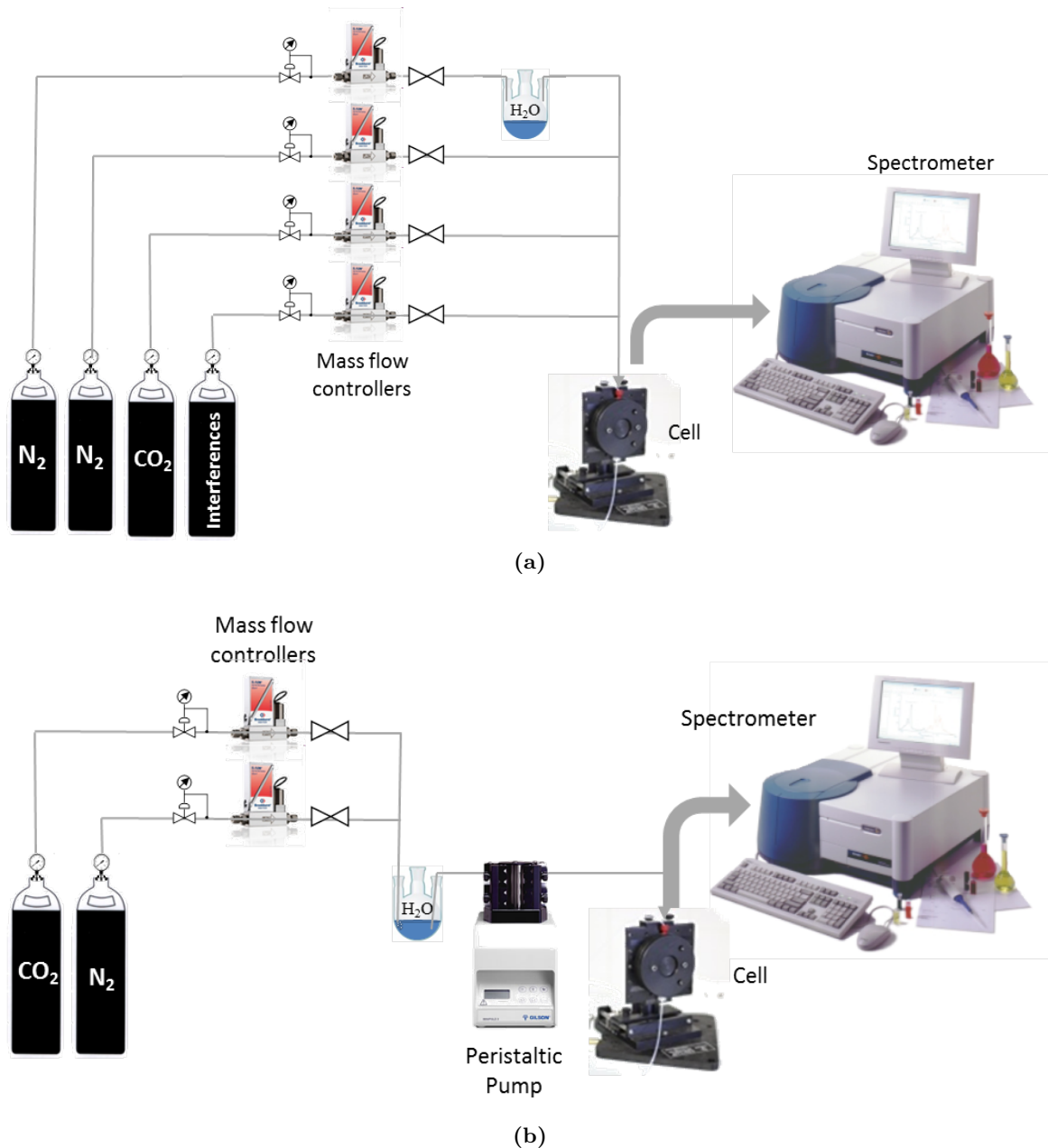


Figure 2.1: Schemes of the devices developed for (a) gas and (b) aqueous determination of CO_2 .

Scheme 2.2 shows the recognition mechanism of the proposed membrane, where P-DH is the protonated form of the chemically attached pH indicator and $\text{P-D}^- \cdot \text{TON}^+ \cdot x\text{H}_2\text{O}$ is the ion pair formed between the tetraoctylammonium cation (TON^+) and the deprotonated form of the chemically attached pH indicator (P-D^-). Because the protonated and deprotonated forms of the dyes have different fluorescence emission spectra the ratio of the concentrations of the chemically attached pH dye in its protonated and deprotonated forms can be used to determine the concentration of CO_2 .

Fig. 2.3 shows the fluorescence emission of the sensing layer in the absence and in the

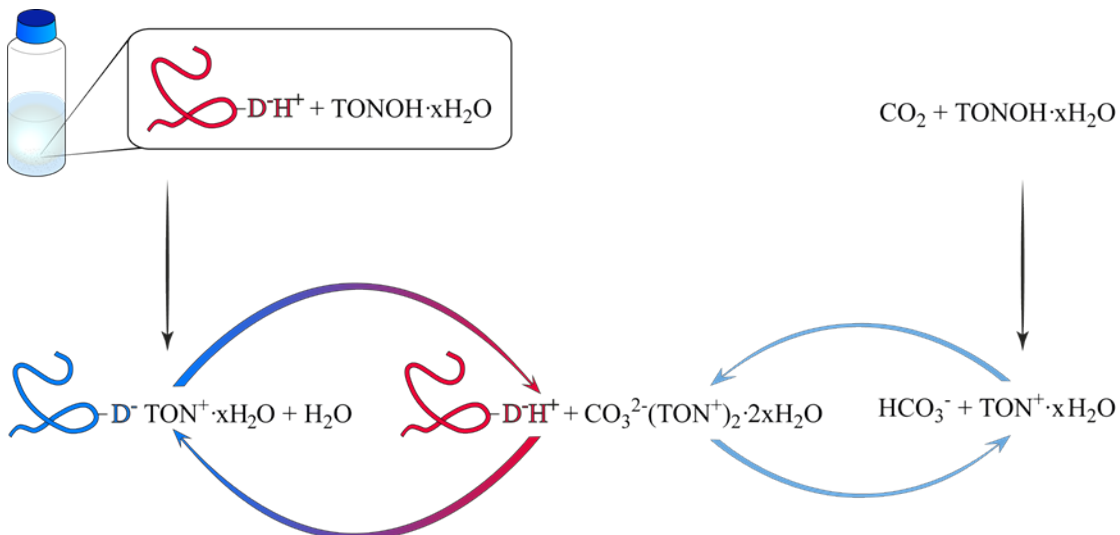
presence of CO₂ in gaseous phase and in solution when the sensing film is excited at 480 nm. In both cases, the sensing layer shows a maximum fluorescence emission at 520 nm which decreases when it is exposed to CO₂.

Comparing the luminescence properties of the sensing layer with those of the polymer [31] it is possible to conclude that no differences were found. Thus, the addition of TONOH to the polymer does not affect its luminescence properties.

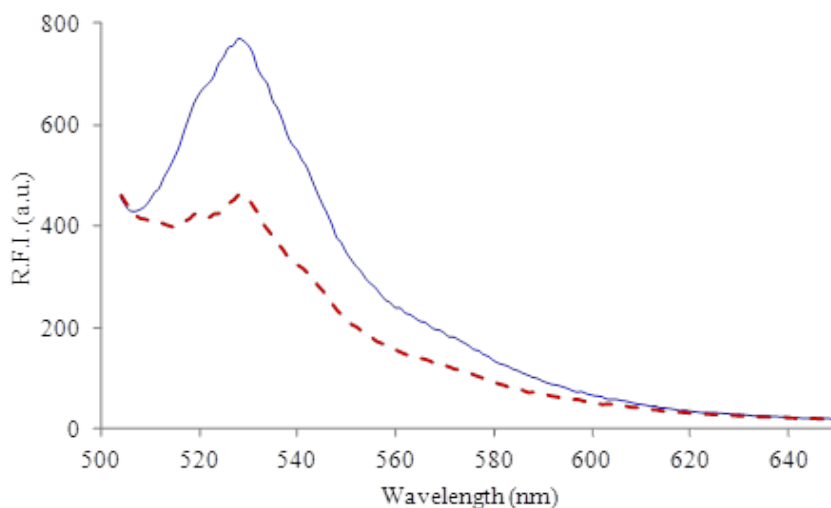
2.3.2 Optimization of the composition of the sensing film

Previous studies have demonstrated that the CO₂-sensitive dye should have a pK_a higher than 7.5 and two types of functional groups, one that can be deprotonated (e.g. a phenol) and other that can stabilize the negative charge (e.g. lactone, sulphite or diazo groups) [32]. Such molecules return to their initial structure when protonated by bicarbonate. Polym-H7 was selected because it contains a covalently bonded pH-indicator with these two functional groups (a phenol and a lactone group) and, in addition, it shows a pK_a higher than 7.5.

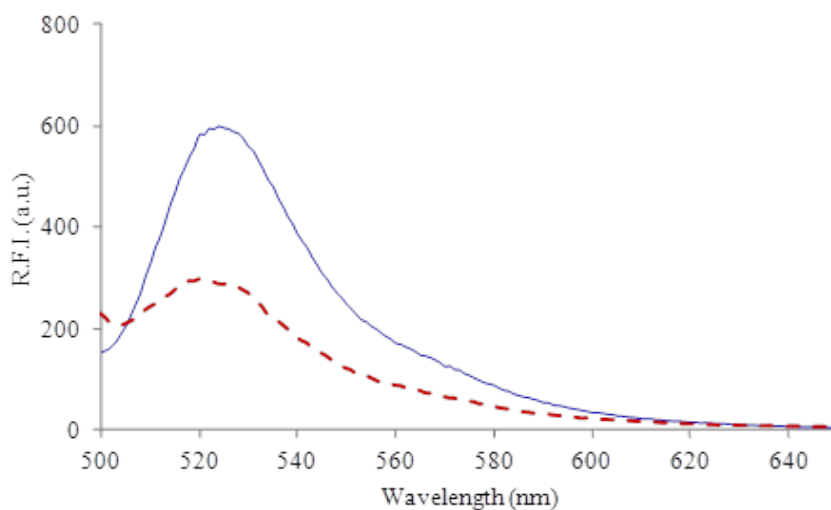
On the other hand, the recognition mechanism suggests that TONOH has to be added in excess to react with CO₂ and produce HCO₃⁻, which is the responsible for recognizing CO₂. Therefore, the effect of the concentration of TONOH has to be evaluated. Several sensing films were prepared by using a fix concentration of polymer (50 mg mL⁻¹) with different concentrations of TONOH (50, 75, 100, 125 and 150 mg mL⁻¹). The $I_0 - I_x$ signal at $\lambda_{exc/em} = 480/520$ nm (flow rate of 100 mL min⁻¹ in N₂ at 40% RH) were measured and evaluated. The experimental results conclude that an increase in the concentration of TONOH up to 125 mg mL⁻¹ resulted in a concomitant increase in $I_0 - I_x$. When the concentration of TONOH is higher than 125 mg mL⁻¹, the signal starts to decrease. Thus, 125 mg mL⁻¹ were set as the optimum TONOH concentration. ESI (see Fig. ESI-2) shows an overview of this experiment.



Scheme 2.2: Recognition mechanism.



(a)



(b)

Figure 2.3: Emission spectra of the proposed sensing layer in the absence of CO₂ (solid line) and in the presence of 100% CO₂ (dashed line) in (a) gas and (b) aqueous phases. [Polym-H7] = 50 mg mL⁻¹, [TONOH] = 125 mg mL⁻¹, λ_{exc} = 480 nm, slits width_{exc/em} = 5/5 nm, average time = 3 s, detector voltage = 650 V, RH = 40%.

2.3.3 Analytical performances

The CO₂-sensitive film was calibrated according to the recommended procedures between 0 and 50% CO₂ (v/v) in gaseous phase and between 0 and 80% CO₂ (v/v) in aqueous phase, exciting at 480 nm and collecting the emission at 520 nm (slits width_{exc/em} = 5/5 nm, average time = 3 s and detector voltage = 650 V).

Fig. 2.4 shows the variation of the sensing response at several CO₂ percentages (v/v) in

gas and aqueous phases and their respective calibration curves. Linear response functions $(I_0 - I_x) = f([CO_2])$ of between 7.7% and 40.0% CO₂ (v/v) and 4.4% and 60% CO₂ (v/v) were obtained for gas and aqueous phases, respectively. The regression equations were $I = 4.33C - 1.98$ ($r = 0.9974$) for gas phase and $I = 0.496C + 2.104$ ($r = 0.9895$) for aqueous phase, where C is the CO₂ percentage (v/v), I is the sensing response ($I_0 - I_x$ at $\lambda_{exc/em} = 480/520$ nm) and r is the correlation coefficient. All the features of the proposed sensing substrate are summarized in Table 2.1. The wide linear range, the small standard deviation and the correlation coefficient close to unity indicate very good calibration linearity. The detection and quantification limits were determined using the IUPAC method ($LOD = 3 s_b/m$; $LOQ = 10 s_b/m$), where s_b is the standard deviation for ten blank samples and m is the slope of the calibration curve.

Table 2.1: Analytical properties of the proposed CO₂-sensing film in gas and aqueous phases.

Media	Parameter	Value
Gas phase	LOD (% , v/v)	2.3
	LOQ (% , v/v)	7.7
	Linear range (% , v/v)	7.7–40.0
Aqueous phase	LOD (% , v/v)	1.3
	LOQ (% , v/v)	4.4
	Linear range (% , v/v)	4.4–60.0

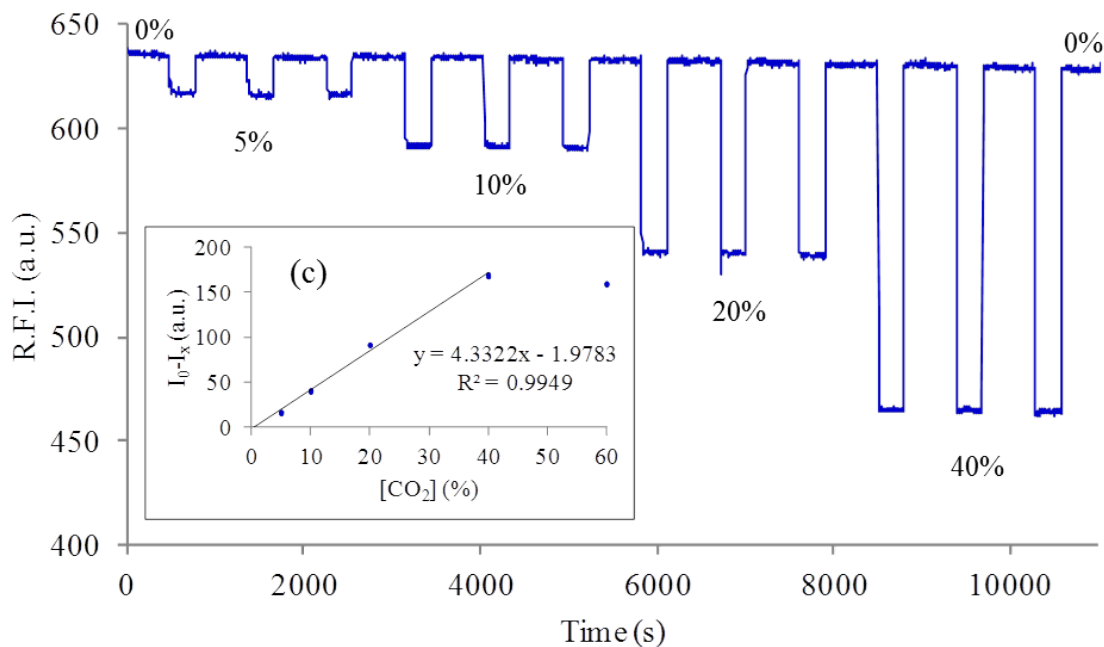
2.3.4 Reliability and response time

Fig. 2.4 shows the typical response of the sensing film with CO₂ (see Fig. 2.4a and b). It shows that the CO₂-sensitive membranes are able to monitor continuously increases and decreases in the amount of CO₂ in air and water. The CO₂-recognition chemical reaction set out in Scheme 2.2 is a reversible process.

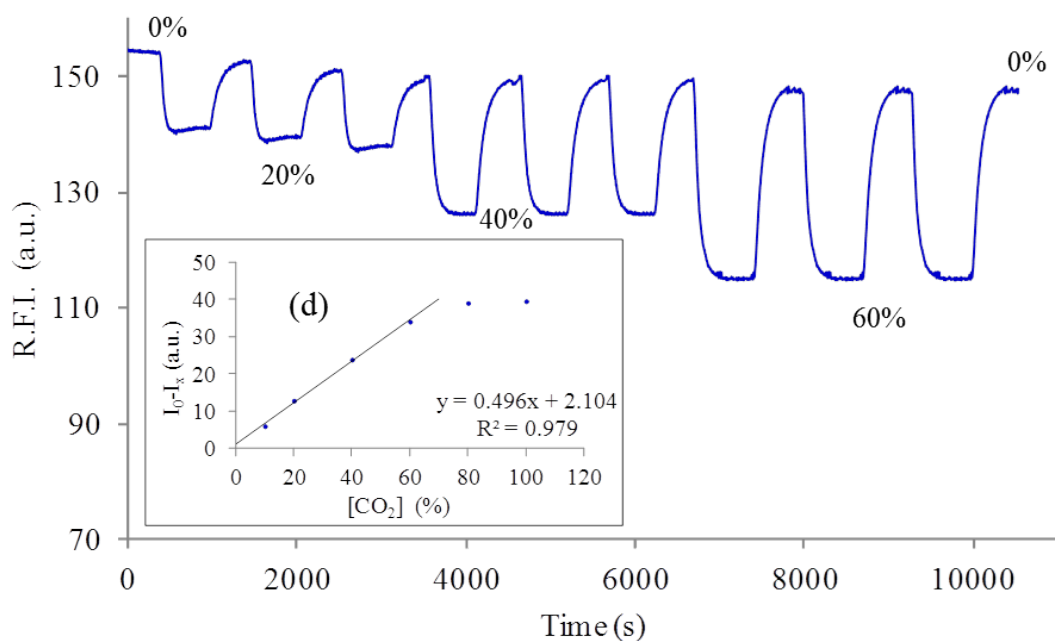
In order to demonstrate that the proposed sensing films can be reused several times several experiments were developed in gas and aqueous phases. The first one consisted on the exposition of the sensing layer to 150 cycles of 15% CO₂ (v/v) in gas phase (see ESI, Fig. ESI-3a). Each cycle consists on 600 s exposition of 100% N₂ and 300 s of 15% CO₂ (v/v). No relevant changes were observed during this experiment. It is possible to conclude that the sensing layer is stable and reproducible and can be used, at least, for 150 measurements in gas phase.

The second one consisted on the evaluation of the reproducibility in aqueous phase during 40 cycles (see ESI, Fig. ESI-3b). In addition, this study also helps to know if any of the sensing reagents could be lixiviated from the sensing film with the flow stream. It can be concluded that the sensing film is highly reproducible also in water and that the variation in the response is negligible up to 40 cycles. Therefore, pH-indicator and TONOH are quite well incorporated to the sensing membrane and none of them is lixiviated with the flow stream.

The response times of the CO₂-selective membranes were also evaluated. The t_{95} response time of the sensing film is < 5 s on going from N₂ to 20% CO₂ (v/v) and < 10 s on going



(a)



(b)

Figure 2.4: Variation of the relative fluorescence intensity (R.F.I.) of the proposed sensing film with the percentage of CO₂ (a) in gas and (b) in aqueous phases, and calibration curves (c) in gas and (d) in aqueous phases. [Polym-H7] = 50 mg mL⁻¹, [TONOH] = 125 mg mL⁻¹, $\lambda_{exc/em}$ = 480/520 nm, slits width_{exc/em} = 5/5 nm, average time = 3 s, detector voltage = 650 V, RH = 40%.

from 20% CO₂ (v/v) to N₂. In aqueous phase, the t_{95} response time of the sensing is < 30 s on going from 0 to 40% CO₂ (v/v) and < 50 s on going from 40 to 0% CO₂ (v/v). The t_{95} response time is defined as the time necessary to reach the 95% of the analytical signal.

2.3.5 Effect of flow rate and interference study

For real applications, the effect of the flow rate on $I_0 - I_x$ signal was evaluated between 25 and 200 mL min⁻¹. ESI shows the effect of the flow rate on the signal response for determining 15% CO₂ (v/v) (see Fig. ESI-4). The sensing response $I_0 - I_x$ is increasing up to 100 mL min⁻¹ while decreases for higher flow rates. Therefore, the flow rate is an important parameter to bear in mind for the use of the proposed sensing film in real applications.

To study the selectivity of the proposed film we tested the effects of humidity and several gas species such as O₂, NO₂ and CO, which might be present together with CO₂ and interfere with the results. The luminescence changes brought about by varying concentrations of the interfering gases compared to a constant concentration of CO₂ (15% CO₂ (v/v)) were investigated at a flow rate of 100 ml min⁻¹ (see ESI, Fig. ESI-5).

O₂ and CO did not interfere on the determination of CO₂ up to 35% and 200 ppm, respectively. Only the false positive induced by NO₂ might be taken into account. Concentrations of NO₂ higher than 1 ppm provide signals which are higher than the 5% of the signal obtained in the determination of 20% CO₂.

Since humidity was added to the carrier gas as a background, we investigated its effect by varying the humidity of the carrier gas and monitoring the effect of the humidity on the determination of CO₂. Only a change from 0% to 15% relative humidity produced a change in sensing response. When humidity was higher than 15% the signal remains constant. Thus, the proposed CO₂-sensitive film seems not to be affected by humidity except between 0% and 15% RH (see ESI, Fig. ESI-6).

2.3.6 Photo and thermostability study

One of the main drawbacks of optical sensing phases is their photo-thermal instability. This is mainly due to the photodegradation of the optically active compound and its precipitation/agglomeration inside the polymeric membrane, which leads to a decrease on the sensitivity [14].

As it is commented in the introduction, we proposed the chemical immobilization of the pH indicator in the polymeric backbone to prevent aggregation (precipitation). In order to demonstrate this claim, several sensing phases were prepared and stored in different environments. After that, the evolution of the signal response at 15% CO₂ (v/v) was measured and analyzed. This study will help to determine the most relevant parameter to be considered for industrial production of these optical sensing phases.

The study was conducted with 15 membranes which were stored at 5 different environments (3 replicates for each ambient) for a total of 5 months. The ambient 1 was dark and 4°C; the ambient 2 was darkness and room temperature (20°C, approx.); the ambient 3

consisted on dark and 35 °C; the ambient 4 was UV light (163 lumens) and room temperature (20 °C, approx.); and the ambient 5 was direct sunlight and room temperature (30 °C, approx.) ESI shows all the figures of this study (see Fig. ESI-7). To sum up, the sensing layer is highly stable when it is stored in the absence of light and at temperature equal or lower to 20 °C. It lost 19% of the signal up to 4 months when it was stored at room temperature and 17% when was stored at 4 °C. If it is storage in dark at 35 °C, the membrane is stable for half month approximately (17 days), losing 32% of the response at the end of the first month and maintained this sensitivity by the least 3 months.

When the membrane is exposed to UV light, it is stable for 10 days and thereafter it loses sensitivity; 50% at the end of the first month and 100% after two months. However, the analytical properties of proposed sensing film remain completely intact after 10 days of continuous UV illumination, thus it can be considered stable.

Finally, when the sensing film is exposed to sunlight and hence to heat simultaneously, it is deteriorated quite rapidly, losing 22% of its signal after 2 hours and 70% after 5 hours. However, it should be noted that thereafter the signal is maintained constant for at least 45 hours.

2.3.7 Implementation in an optical fiber sensor

Once the applicability of the proposed sensing layer for the detection and quantification of CO₂ in gaseous and aqueous phases has been demonstrated, it was implemented in an optical fiber sensor in order to further demonstrate its versatility.

For this purpose, the transducer (commercial luminescence spectrometer) was replaced by an optical fiber spectrometer and a LED as light source. To couple the excitation source and detector with the sensing film a bifurcated optical fiber probe and other optical components were used (see Fig. ESI-1). Fig. 2.5 shows the emission spectra collected with the optical fiber spectrometer in the absence and the presence of CO₂. It is possible to see that the emission at 530 nm decreased when the sensing film is exposed to CO₂. It also shows that this decreasing is proportional to the concentration of this gas.

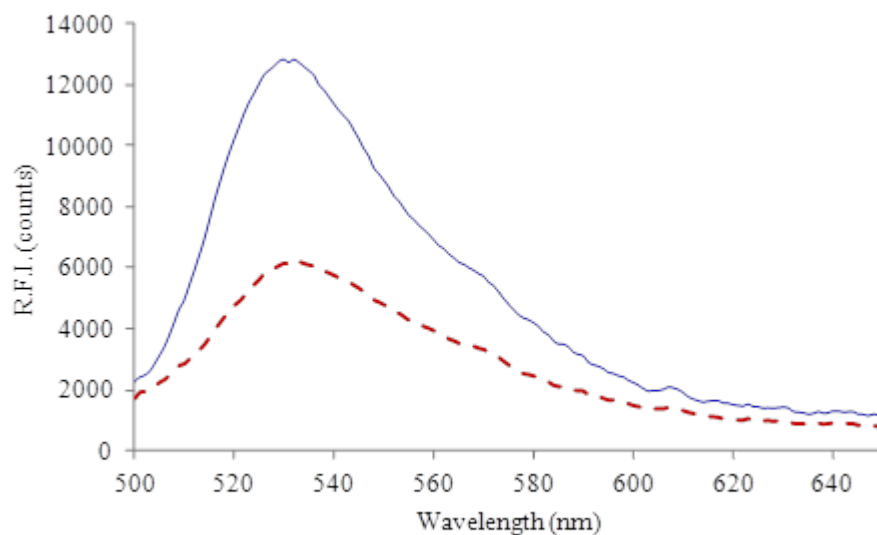
The CO₂-sensitive optical fiber sensor was calibrated according to the recommended procedures between 0 and 40% CO₂ (v/v) in gaseous phase (see Fig. 2.5b and ESI, Fig. ESI-8). Linear response function ($I_0 - I_x = f([CO_2])$) of between 0% and 40.0% CO₂ (v/v) was obtained. The regression equations were $I = 194.26C - 18.942$ ($r = 0.9965$), where C is the CO₂ percentage (v/v), I is the sensing response ($I_0 - I_x$) and r is the correlation coefficient. All the features of the proposed optical fiber sensor are summarized in Table 2.2. The wide linear range, the small standard deviation and the correlation coefficient close to unity indicate very

Table 2.2: Analytical features of the proposed CO₂-sensing optical fiber sensor in gas phase.

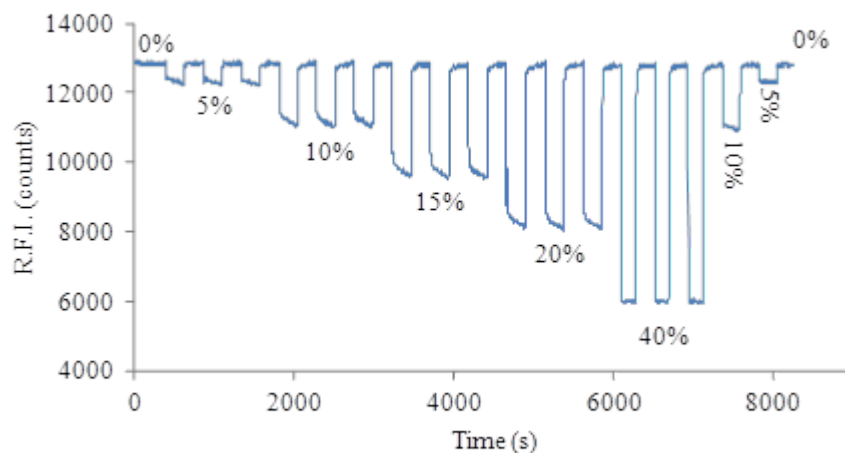
Parameter	Value
Detection limit (% v/v)	0.4
Quantification limit (% v/v)	1.4
Linear range (% v/v)	1.4–40.0

good calibration linearity. The detection and quantification limits were determined using the IUPAC method ($LOD = 3 s_b/m$; $LOQ = 10 s_b/m$), where s_b is the standard deviation for ten blank samples and m is the slope of the calibration curve.

It is possible to conclude that the developed sensing film is highly versatile and can be easily implemented on portable devices that allow the *'in situ'* determination of CO_2 at real time and, if necessary, remotely.



(a)



(b)

Figure 2.5: (a) Emission spectra obtained with the fiber optic CCD spectrometer of the proposed sensing layer in the absence of CO_2 (solid line) and in the presence of 100% CO_2 (dashed line) in gas phase; [Polym-H7] = 50 mg mL^{-1} , [TONOH] = 125 mg mL^{-1} , RH = 40%. (b) Variation of the relative fluorescence intensity (R.F.I.) observed with the optical fiber sensor with the percentage of CO_2 ; [Polym-H7] = 50 mg mL^{-1} , [TONOH] = 125 mg mL^{-1} , RH = 40%.

2.4 Conclusions

We have demonstrated that it is possible to develop a CO₂-sensing film using a copolymer which contains a luminescence pH-sensitive dye covalently attached to its structure, in the presence of tetraoctylammonium hydroxide, with many advantages over other currently used techniques.

The transparent Polym-H7-TONOH CO₂-selective films detect low percentages of CO₂ (2.3% and 1.3% (v/v) in gas and aqueous phases, respectively), are not interfered with to any significant degree by humidity, O₂, and CO; concentrations higher than 1 ppm NO₂ could interfere the CO₂ determination. The proposed sensing film also shows quick response time ($t_{95} = 5$ s from 0 to 20% CO₂ (v/v) in gas phase) and good opto-thermal stability; in darkness, it lost only the 19% of the signal up to 4 months when it was stored at 21 °C and 17% when was stored at 4 °C. In addition, the covalent immobilization of the fluorescence pH-indicator on the polymeric structure provides lower probability of aggregation and no leaching of the optical dye.

In order to demonstrate the applicability and versatility of the proposed sensing film, we have developed an optical fiber sensor. It shows good linear dynamic range of 1.4-40% CO₂ (v/v) with a very good detection limit (0.4% CO₂ (v/v)) in gas phase.

Acknowledgments

The authors gratefully acknowledge the financial support of the Spanish Ministry of Economy and Competitiveness (Projects CTQ2008-01394 and CTQ2011-25316 and Medina-Rodríguez's grant reference BES-2009-026919) and Medina-Castillo's contract PTQ-11-04904 and the Regional Government of Andalusia (Excellence Projects P07-FQM-2625 and P07-FQM-2738).

Appendix A. Supplementary data

Supplementary data associated with this article can be found in the Electronic Supporting Information (ESI).

References

- [1] S.M. Borisov, M.C. Waldhier, I. Klimant, O.S. Wolfbeis, Optical carbon dioxide sensors based on silicone-encapsulated room-temperature ionic liquids, *Chemistry of Materials* 19 (2007) 6187-6194.
- [2] A. Marsal, G. Dezanneau, A. Cornet, J.R. Morante, A new CO₂ gas sensing material, *Sensors and Actuators B: Chemical* 95 (2003) 266-270.

- [3] C. von Bültzingslöwen, A.K. McEvoy, C. McDonagh, B.D. MacCraith, I. Klimant, C. Krause, et al., Sol-gel based optical carbon dioxide sensor employing dual luminophore referencing for application in food packaging technology, *Analyst* 127 (2002) 1478-1483.
- [4] C. von Bültzingslöwen, A.K. McEvoy, C. McDonagh, B.D. MacCraith, Lifetime-based optical sensor for high-level $p\text{CO}_2$ detection employing fluorescence resonance energy transfer, *Analytica Chimica Acta* 480 (2003) 275-283.
- [5] C.D. Geddes, J.R. Lakowicz, A. Mills, S. Hodgen, Fluorescent carbon dioxide indicators, in: C.D. Geddes, J.R. Lakowicz (Eds.), *Topics in Fluorescence Spectroscopy*, Springer, US, 2005, pp. 119-161.
- [6] J.A. Ferguson, B.G. Healey, K.S. Bronk, S.M. Barnard, D.R. Walt, Simultaneous monitoring of pH, CO_2 and O_2 using an optical imaging fiber, *Analytica Chimica Acta* 340 (1997) 123-131.
- [7] X. Ge, Y. Kostov, G. Rao, Low-cost noninvasive optical CO_2 sensing system for fermentation and cell culture, *Biotechnology and Bioengineering* 89 (2005) 329-334.
- [8] A. Mills, A. Lepre, L. Wild, Breath-by-breath measurement of carbon dioxide using a plastic film optical sensor, *Sensors and Actuators B: Chemical* 39 (1997) 419-425.
- [9] R.K. Meruva, M.E. Meyerhoff, Catheter-type sensor for potentiometric monitoring of oxygen, pH and carbon dioxide, *Biosensors and Bioelectronics* 13 (1998) 201-212.
- [10] C.G. Cooney, B.C. Towe, C.R. Eyster, Optical pH, oxygen and carbon dioxide monitoring using a microdialysis approach, *Sensors and Actuators B: Chemical* 69 (2000) 183-188.
- [11] J. Severinghaus, A. Bradley, First electrodes for blood PO_2 and PCO_2 determination, *Journal of Applied Physiology* 13 (1958) 515-520.
- [12] H. Beyenal, C.C. Davis, Z. Lewandowski, An improved Severinghaus-type carbon dioxide microelectrode for use in biofilms, *Sensors and Actuators B: Chemical* 97 (2004) 202-210.
- [13] R.N. Dansby-Sparks, J. Jin, S.J. Mechery, U. Sampathkumaran, T.W. Owen, B.D. Yu, et al., Fluorescent-dye-doped sol-gel sensor for highly sensitive carbon dioxide gas detection below atmospheric concentrations, *Analytical Chemistry* 82 (2009) 593-600.
- [14] J.F. Fernández-Sánchez, R. Cannas, S. Spichiger, R. Steiger, U.E. Spichiger-Keller, Optical CO_2 -sensing layers for clinical application based on pH-sensitive indicators incorporated into nanoscopic metal-oxide supports, *Sensors and Actuators B: Chemical* 128 (2007) 145-153.
- [15] H. Segawa, E. Ohnishi, Y. Arai, K. Yoshida, Sensitivity of fiber-optic carbon dioxide sensors utilizing indicator dye, *Sensors and Actuators B: Chemical* 94 (2003) 276-281.
- [16] Y. Amao, T. Komori, Optical CO_2 sensor of the combination of colorimetric change of [alpha]-naphtholphthalein in poly(isobutyl methacrylate) and fluorescent porphyrin in polystyrene, *Talanta* 66 (2005) 976-981.
- [17] Y. Amao, N. Nakamura, Optical CO_2 sensor with the combination of colorimetric change of [alpha]-naphtholphthalein and internal reference fluorescent porphyrin dye, *Sensors and Actuators B: Chemical* 100 (2004) 347-351.

- [18] Y. Amao, N. Nakamura, An optical sensor with the combination of colorimetric change of [alpha]-naphtholphthalein and internal reference luminescent dye for CO₂ in water, *Sensors and Actuators B: Chemical* 107 (2005) 861-865.
- [19] Z. Zhujun, W.R. Seitz, A carbon dioxide sensor based on fluorescence, *Analytica Chimica Acta* 160 (1984) 305-309.
- [20] O.S. Wolfbeis, L.J. Weis, M.J.P. Leiner, W.E. Ziegler, Fiber-optic fluorosensor for oxygen and carbon dioxide, *Analytical Chemistry* 60 (1988) 2028-2030.
- [21] A. Mills, Q. Chang, Fluorescence plastic thin-film sensor for carbon dioxide, *Analyst* 118 (1993) 839-843.
- [22] M.D. Marazuela, M.C. Moreno Bondi, G. Orellana, Enhanced performance of a fibre-optic luminescence CO₂ sensor using carbonic anhydrase, *Sensors and Actuators B: Chemical* 29 (1995) 126-131.
- [23] B.H. Weigl, A. Holobar, N.V. Rodriguez, O.S. Wolfbeis, Chemically and mechanically resistant carbon dioxide optrode based on a covalently immobilized pH indicator, *Analytica Chimica Acta* 282 (1993) 335-343.
- [24] A. Mills, G.A. Skinner, Water-based colourimetric optical indicators for the detection of carbon dioxide, *Analyst* 135 (2010) 1912-1917.
- [25] A. Mills, G.A. Skinner, P. Grosshans, Intelligent pigments and plastics for CO₂ detection, *Journal of Materials Chemistry* 20 (2010) 5008-5010.
- [26] C.-S. Chu, Y.-L. Lo, Fiber-optic carbon dioxide sensor based on fluorinated xerogels doped with HPTS, *Sensors and Actuators B: Chemical* 129 (2008) 120-125.
- [27] C.-S. Chu, Y.-L. Lo, Highly sensitive and linear optical fiber carbon dioxide sensor based on sol-gel matrix doped with silica particles and HPTS, *Sensors and Actuators B: Chemical* 143 (2009) 205-210.
- [28] D. Wencel, J. Moore, N. Stevenson, C. McDonagh, Ratiometric fluorescence-based dissolved carbon dioxide sensor for use in environmental monitoring applications, *Analytical and Bioanalytical Chemistry* 398 (2010) 1899-1907.
- [29] A. Mills, Q. Chang, N. McMurray, Equilibrium studies on colorimetric plastic film sensors for carbon dioxide, *Analytical Chemistry* 64 (1992) 1383-1389.
- [30] D.A. Nivens, M.V. Schiza, S.M. Angel, Multilayer sol-gel membranes for optical sensing applications: single layer pH and dual layer CO₂ and NH₃ sensors, *Talanta* 58 (2002) 543-550.
- [31] A.L. Medina-Castillo, J.F. Fernández-Sánchez, A. Segura-Carretero, A. Fernández-Gutiérrez, Design of novel, fluorescent-tuneable, pH-sensing, water-insoluble, linear copolymers synthesized by ATRP and its application in the development of pH-sensing nanofibres made by electrospinning, *Journal of Materials Chemistry* 21 (2011) 6742-6750.
- [32] R. Cannas, G. Zhylyak, T. Nezel, U.E. Spichiger-Keller, Optical Sensors for CO₂, *Eu-roptrode VII, Madrid, Spain, 2004*, pp. Communication P-6.

Appendix A. Supplementary data

Electronic Supporting Information (ESI)

A new highly sensitive and versatile optical sensing film for controlling CO₂ in gaseous and aqueous media

Paulina Karem Contreras Gutiérrez^a, Santiago Medina Rodríguez^{a,b}, Antonio Luis Medina Castillo^c, Jorge Fernando Fernández Sánchez^{a,*} and Alberto Fernández Gutiérrez^a

^a*Department of Analytical Chemistry, Faculty of Sciences, University of Granada, Avda. Fuentenueva s/n, E-18071 Granada, Spain.*

^b*Department of Signal Theory, Networking and Communications, CITIC-UGR, University of Granada, C/ Periodista Rafael Gómez 2, E-18071 Granada, Spain.*

^c*NanoMyP[®], Nanomateriales y Polímeros S.L., Spin-Off Company of the UGR, BIC Building, Avda. de la Innovación 1, E-18100 Granada, Spain.*

List of Figures

- Fig. ESI-1. Scheme of the optical fiber sensor.
- Fig. ESI-2. Effect of TONOH.
- Fig. ESI-3. Reproducibility study.
- Fig. ESI-4. Effect of flow-rate.
- Fig. ESI-5. Interference study.
- Fig. ESI-6. Effect of humidity.
- Fig. ESI-7. Photo-thermal stability study.
- Fig. ESI-8. Calibration curve of the optical fiber sensor.

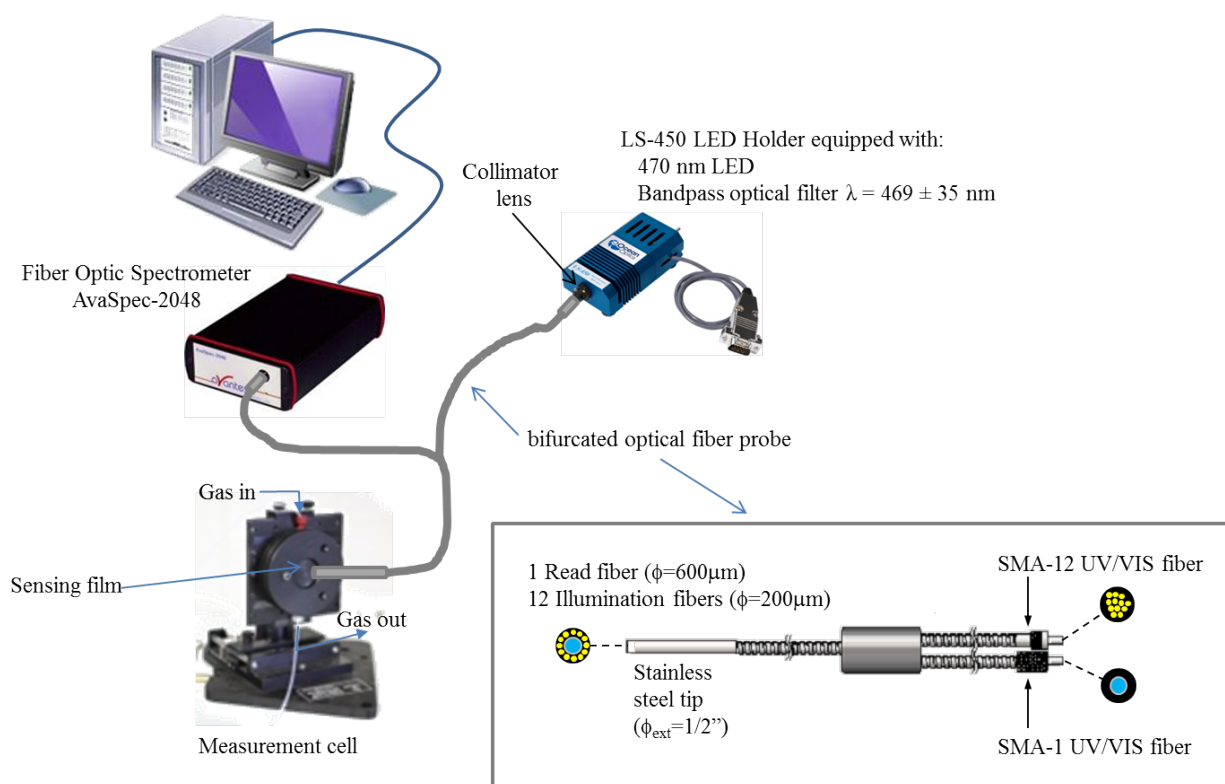


Fig. ESI-1. Scheme of the optical fiber sensor and the optical bifurcated probe.

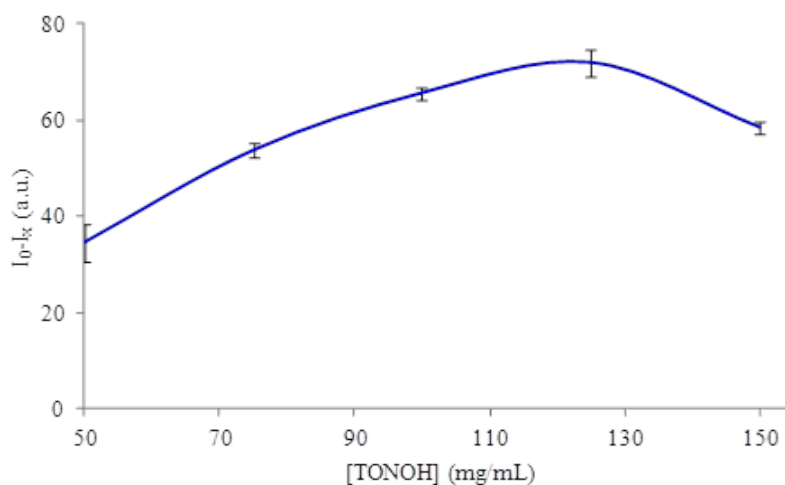


Fig. ESI-2. Effect of the TONOH concentration on the sensing response $I_0 - I_x$. [Polym-H7] = 50 mg mL⁻¹, [CO₂] = 15% (v/v), flow-rate = 100 mL min⁻¹, $\lambda_{\text{exc/em}}$ = 480/520 nm, slits width_{exc/em} = 5/5 nm, average time = 3 s, detector voltage = 650 V, RH = 40%.

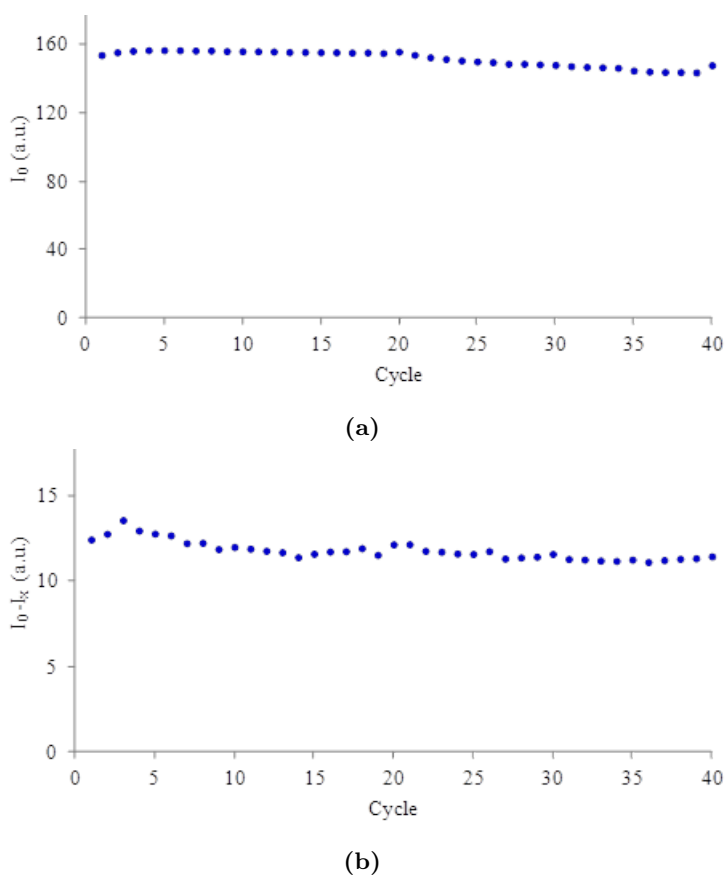


Fig. ESI-3. Variation of the I_0 and $I_0 - I_x$ during 40 cycles of determination of CO_2 in (a) gas and (b) aqueous phases, respectively. $[\text{Polym-H7}] = 50 \text{ mg mL}^{-1}$, $[\text{TONOH}] = 125 \text{ mg mL}^{-1}$, $\lambda_{exc/em} = 480/520 \text{ nm}$, slits width $_{exc/em} = 5/5 \text{ nm}$, average time = 3 s, detector voltage = 650 V, RH = 40%.

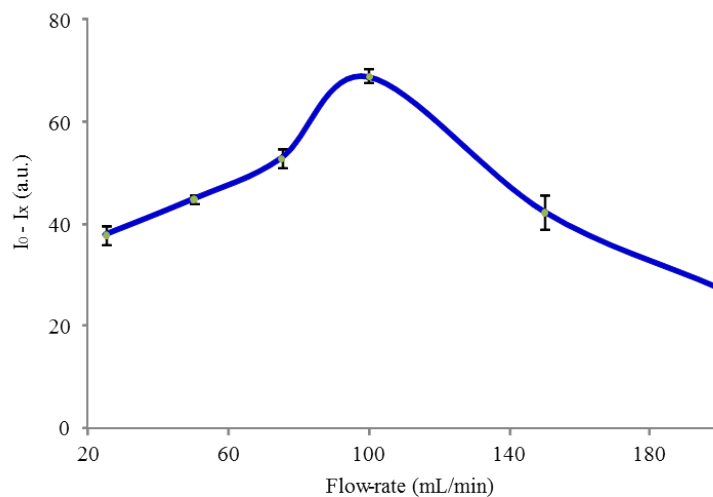


Fig. ESI-4. Effect of the flow-rate on the sensing response $I_0 - I_x$. $[\text{Polym-H7}] = 50 \text{ mg mL}^{-1}$, $[\text{TONOH}] = 125 \text{ mg mL}^{-1}$, $[\text{CO}_2] = 15\% \text{ (v/v)}$, $\lambda_{exc/em} = 480/520 \text{ nm}$, slits width $_{exc/em} = 5/5 \text{ nm}$, average time = 3 s, detector voltage = 650 V, RH = 40%.

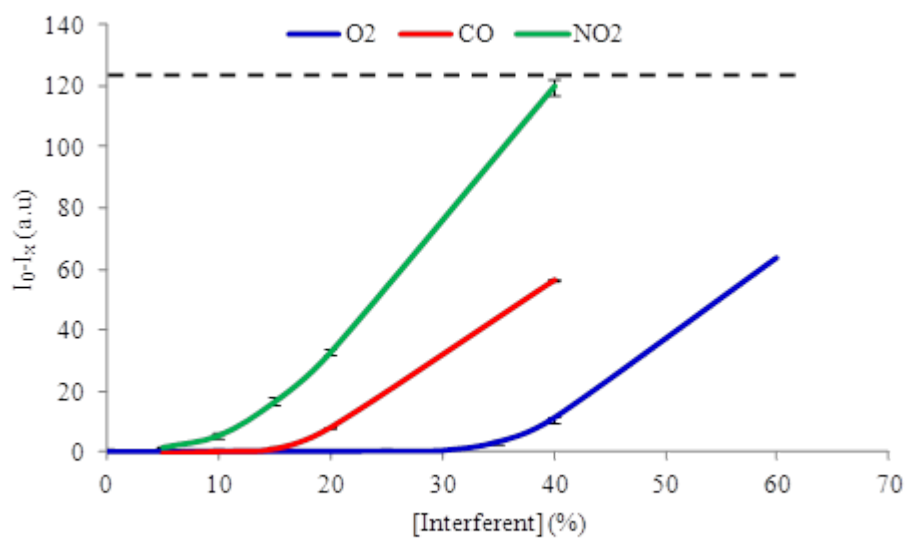


Fig. ESI-5. Effect of O₂ (blue line), CO (red line) and NO₂ (green line) on the sensing response $I_0 - I_x$ of 15% CO₂ (v/v) (dashed line). [Polym-H7] = 50 mg mL⁻¹, [TONOH] = 125 mg mL⁻¹, $\lambda_{exc/em}$ = 480/520 nm, slits width_{exc/em} = 5/5 nm, average time = 3 s, detector voltage = 650 V, RH = 40%.

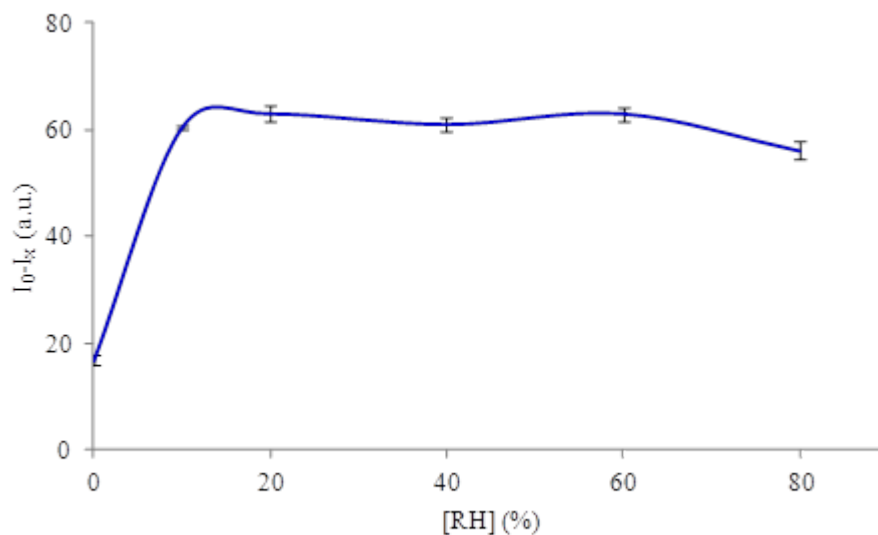


Fig. ESI-6. Effect of the relative humidity (RH, %) on the sensing response $I_0 - I_x$ of 15% CO₂ (v/v) (dashed line). [Polym-H7] = 50 mg mL⁻¹, [TONOH] = 125 mg mL⁻¹, $\lambda_{exc/em}$ = 480/520 nm, slits width_{exc/em} = 5/5 nm, average time = 3 s, detector voltage = 650 V, RH = 40%.

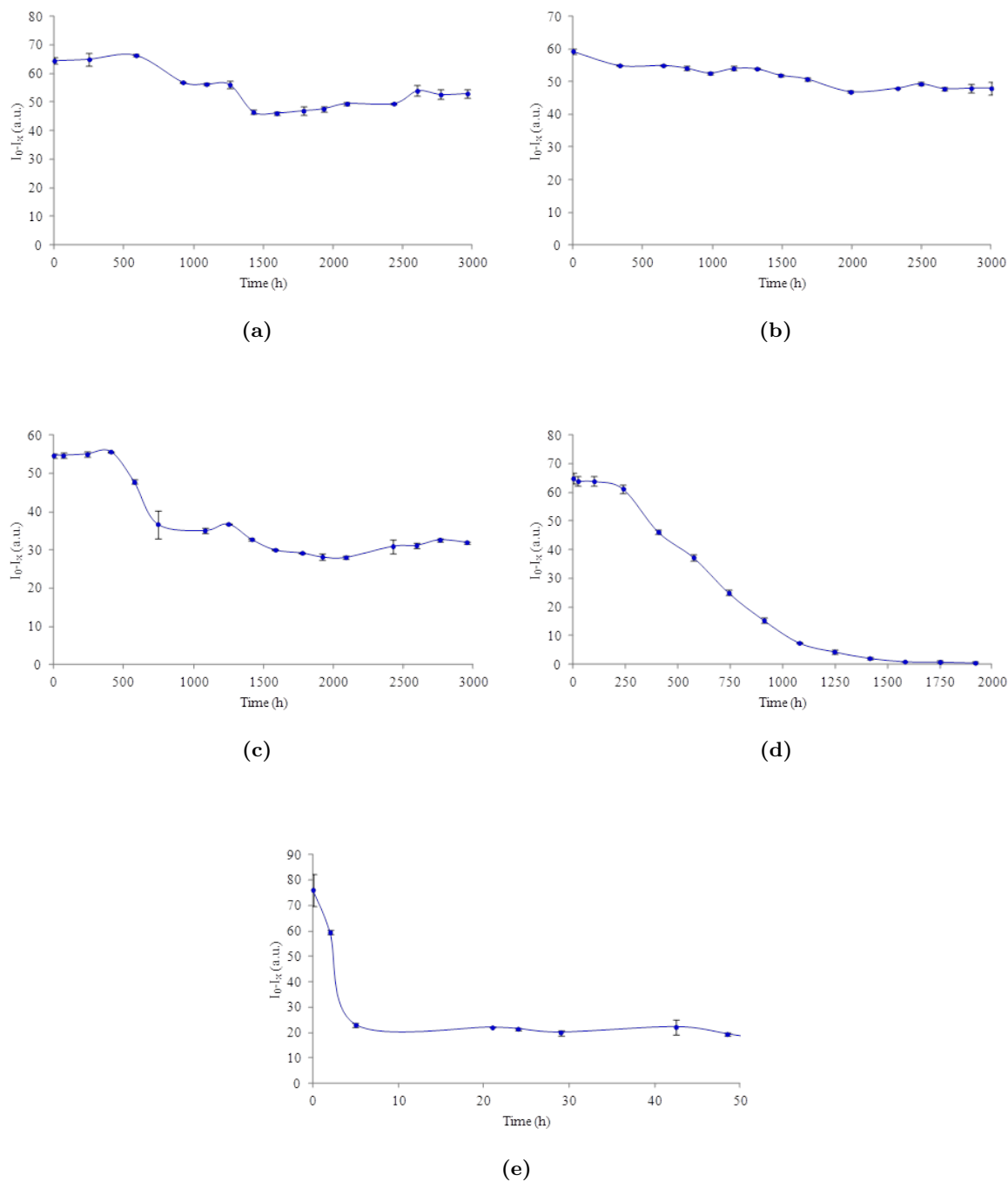


Fig. ESI-7. Stability of the sensing phase at (a) 4 °C and darkness, (b) 20 °C and darkness, (c) 35 °C and darkness, (d) 20 °C and UV-light, (e) 30 °C and sunlight. [Polym-H7] = 50 mg mL⁻¹, [TONOH] = 125 mg mL⁻¹, $\lambda_{exc/em}$ = 480/520 nm, slits width_{exc/em} = 5/5 nm, average time = 3 s, detector voltage = 650 V, RH = 40%.

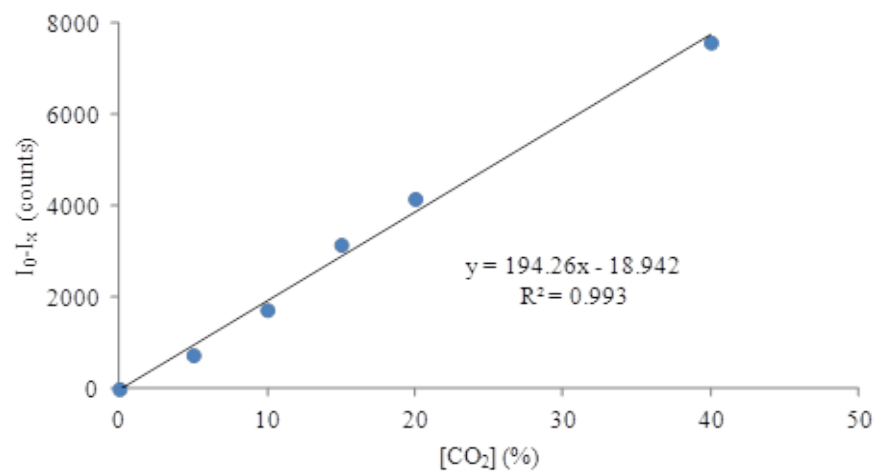


Fig. ESI-8. Calibration curve of the optical fiber sensor.

High performance optical sensing nanocomposites for low and ultra-low oxygen concentrations using phase-shift measurements

Santiago Medina Rodríguez^{a,b,*}, Marta Marín Suárez^b, Jorge Fernando Fernández Sánchez^{b,*}, Ángel de la Torre Vega^a, Etienne Baranoff^c and Alberto Fernández Gutiérrez^b

^a*Department of Signal Theory, Networking and Communications, CITIC-UGR, University of Granada, C/ Periodista Rafael Gómez 2, E-18071 Granada, Spain.*

^b*Department of Analytical Chemistry, Faculty of Sciences, University of Granada, Avda. Fuentenueva s/n, E-18071 Granada, Spain.*

^c*School of Chemistry, University of Birmingham, Edgbaston, B15 2TT, England, UK.*

Published in *Analyst* 138 (2013) 4607-4617

High performance optical sensing nanocomposites for low and ultra-low oxygen concentrations using phase-shift measurements

Abstract—The accurate and real-time measurement of low and ultra-low concentration of oxygen using non-invasive methods is a necessity for a multitude of applications, from brewing beer to developing encapsulating barriers for optoelectronic devices. Current optical methods and sensing materials often lack the necessary sensitivity, signal intensity, or stability for practical applications. In this report we present a new optical sensing nanocomposite resulting in an outstanding overall performance when combined with the phase-shift measurement method (determination of luminescence lifetime in the frequency domain). For the first time we have incorporated the standard PtTFPP dye (PtTFPP = platinum(II) 5,10,15,20-meso-tetrakis-(2,3,4,5,6-pentafluorophenyl)-porphyrin) into AP200/19, a nanostructured aluminium oxide-hydroxide solid support. This sensing film shows an excellent sensitivity between 0 and 1% O₂ ($K_{SV} = 3102 \pm 132 \text{ bar}^{-1}$) and between 0 and 10% O₂ ($K_{SV} = 2568 \pm 614 \text{ bar}^{-1}$) as well as $\Delta\tau_{0.05\%}$ ($62.53 \pm 3.66\%$), which makes it 62 times more sensitive than PtTFPP immobilized in polystyrene and also 8 times more sensitive than PtTFPP immobilized on silica beads. Furthermore, the phase-shift measurement method results in a significant improvement (about 23 times) in stability compared to the use of intensity recording methods. The film also displays full reversibility, long shelf stability (no change observed after 12 months), and it is not affected by humidity. To establish this sensing methodology and develop sensors over the full range of the visible light, we also studied three other dye-AP200/19 nanocomposites based on phosphorescent cyclometalated iridium(III) complexes.

keywords: Optical sensing; Trace oxygen; Phase-resolved; LED, Phase-shift measurement; Intelligent packaging.

3.1 Introduction

IN recent years there has been a considerable interest and tremendous research activity in the field of chemical sensing for real-time monitoring of analytes (CO₂, O₂, etc.) and properties (pH, temperature, etc.) [1, 2]. Molecular oxygen is one of the most important analytes in our environment as it is widely involved in a variety of chemical and biochemical reactions both as a reactant and as a product. Although the detection of oxygen is well known in principle, this area continues to attract sustained attention. New methods, new oxygen sensing materials, and new sensors with improved performance have been developed in the last two decades to detect oxygen in both gas and liquid phases [3–12]. Clark electrodes and Winkler titration are widely used methods to quantify oxygen. However, these two methods are both invasive

and destructive. Consequently optical sensors have gained particular interest in recent years as a non-invasive, non-destructive measurement method.

Optical sensors are particularly attractive due to the absence of electromagnetic interferences, their high sensitivity and resolution, and null oxygen consumption. In addition, the versatility of formats (planar, nanoparticles, paints, optical fibers, etc.), the possibility of miniaturization, and the suitability for 2D and 3D imaging have also encouraged their utilization [13]. They also provide a wireless readout, fast response, as well as non-invasive, real-time monitoring in remote, hazardous, or *in vivo* environments [4]. For these reasons, optical sensors have become very popular in many fields related to industry, medicine, biotechnology, and environment [8, 14–23]. However, current optical methods and sensing materials often lack the necessary sensitivity, signal intensity, or stability for practical applications. Furthermore, most of them are optimized for detecting physiological concentrations and are less suitable for low oxygen concentrations [13]. Sensing of oxygen traces is of great interest in many areas of science and technology; for example, oxygen trace sensing has become crucial in microbiology, since a variety of microorganisms grow under special conditions, from low levels of residual oxygen to anaerobic conditions [24]. Oxygen trace sensing also has special application in the control of modified atmosphere packaging (MAP), where an adequate oxygen concentration is required inside the package in order to maintain the microbiological stability of fresh-cut fruits and vegetables, by limiting aerobic respiration without inducing anaerobic processes [25]. In addition, oxygen trace control is important for avoiding discoloration, browning and softening of these products, where oxygen concentrations typically below 0.25-5 kPa are required [26–28].

The development of an oxygen-sensitive sensor requires: (1) a luminescent dye, the luminescence of which changes with the oxygen concentration; (2) a solid support in which the dye can be immobilized; (3) a signal transduction system, which correlates the luminescent changes with the oxygen concentration.

Optical oxygen sensors have previously been demonstrated with numerous luminescent dyes [3, 8, 9, 29–33]. Iridium(III) organometallic complexes have been widely used due to their high luminescence quantum yields, high photostability, long decay times (luminescence lifetimes), strong absorption bands, large Stokes' shift, fast response time and high Stern-Volmer constants [3, 29, 30, 33, 34]. Platinum(II) and palladium(II) porphyrin complexes are also very successful materials for optical sensing of low and ultra-low oxygen concentrations [13, 35–38]. In this paper, four organometallic complexes (one of Pt(II) and three of Ir(III)) have been used as oxygen-sensitive dyes.

The solid support is an important component of an oxygen sensor as it impacts the sensing ability mainly in two ways [29]: first by the permeability to oxygen, which enables fast diffusion of oxygen to the emitting molecules for quenching; second by their chemical nature, which leads to different aggregation behaviors of the dyes resulting in different accessibility of oxygen. Ideally, a matrix must be permeable to oxygen, should be structurally stable enough to withstand mechanical stress, and should increase photostability [33]. In addition, it has to prevent the leaching and migration of chemical compounds by insulation of the dyes and has to preclude the aggregation of the dye [11]. In this paper, a nanostructured inorganic (aluminium oxide-hydroxide; AlOOH) solid support has been selected due to its excellent properties for the aforementioned requirements [29, 30, 34, 39, 40].

Most optical methods for measuring the oxygen concentration are based on recording changes in emission intensity or luminescence lifetime [19, 20, 22, 41–44]. Unfortunately, while intensity measurements are relatively simple and accurate in the laboratory [30, 43, 45], they are often inadequate in real-world applications because the emission intensity is highly influenced by external perturbations [43, 46]. These difficulties can be minimized by measuring the luminescence lifetime [43, 47]. The luminescence lifetime can be measured either in the time domain (time-resolved methods) or in the frequency domain (phase-resolved methods) [4]. Although time-resolved methods are ideally suited for the elimination of the background luminescence and scattering [4], high-speed photodetectors and specific signal processing devices are required, which makes this approach rather expensive. On the other hand, frequency-domain lifetime measurement does not generally require much sophisticated instrumentation [22, 46], and allows for the use of simple and cheap light sources and electronic devices [43, 48]. Thus, a phase-resolved method is usually preferred for the design of robust and reliable sensors, and was employed in this work.

To sum up, in this work four organometallic complexes immobilized into a nanostructured AlOOH solid support have been characterized by a phase-resolved method for the determination of low and ultra-low oxygen concentrations. To the best of our knowledge, this is the first time that this type of sensing material has been characterized by luminescence lifetime in the frequency domain. In addition, it is the first time that the PtTFPP complex has been immobilized into a nanostructured AlOOH solid support. Combining the intrinsic properties of PtTFPP (long lifetime of the excited state, good stability and excellent photochemical properties), the properties that the immobilization into a nanostructured solid support provides (increase of the sensitivity to oxygen and decrease of the response time), and the phase-shift measurement method (increase in resolution and stability), we developed one of the best candidates for ultra-low oxygen-sensitive films which has good luminescence signal intensity, excellent sensitivity, complete reversibility, exceptional stability, and is not affected by humidity. Finally, the use of phosphorescent cyclometalated iridium(III) complexes with various emission wavelengths allowed us to establish this sensing methodology and develop sensors over the full range of colors of the visible spectrum.

3.2 Experimental details

3.2.1 Materials and chemicals

Platinum(II) 5,10,15,20-meso-tetrakis-(2,3,4,5,6-pentafluorophenyl)-porphyrin, named Pt-TFPP, was obtained from Frontier Scientific (<http://www.frontiersci.com>). Iridium(III) complexes [Ir(2-(2,4-difluorophenyl)pyridine)₂(4,4'-dimethylamino-2,2'-bipyridine)](PF₆), named N969, [Ir(2-(2,4-difluorophenyl)pyridine)₂(4,7-diphenyl-1,10-phenanthroline)](PF₆), named N1008, and [Ir(2-(2,4-difluoro-3-methylesterphenyl)pyridine)₂(4-(*N,N*-dimethylamino)picolinate)], named EB146, were synthesized as described in the literature [29, 30, 49]. ESI shows the chemical structure of these oxygen-sensitive dyes (see Fig. ESI-1).

The nanostructured material was prepared by Ilford Imaging Switzerland following the procedure previously published [34, 39]. It is called AP200/19, and it is based on a thin plate of polyethylene terephthalate (PET) coated with a thin layer of aluminium oxide hydroxide

(AlOOH), which provides a positively charged nanostructured film with a pore diameter of 19 nm and a total pore volume of 20 mL m^{-2} [30].

Chloroform was obtained from Fluka (<http://www.sigmaaldrich.com>), which was used as an organic solvent due to its good properties to dissolve the dyes. Nitrogen and oxygen (all of 99.999% purity) were obtained from Air Liquide (<http://www.airliquide.com>).

3.2.2 Preparation of the oxygen-sensing films

The cocktails were prepared by dissolving PtTFPP, N969, N1008 or EB146 in 2 mL of chloroform (dye concentration of 1.5 mg mL^{-1}). The cocktails were shaken on an IKA-Vibramax-VXR (IKA-Labortechnik, Staufen, Germany) until the dye was completely dissolved. The oxygen-sensitive membranes were obtained using a Laurell spin-coater (WS-400B-6NPP/LITE, Laurell Technologies, <http://www.laurell.com>, North Wales, PA, USA). 100 μL of the cocktail were injected onto the rotating metal oxide support fixed onto a spinning device at 300 rpm. AP200/19 membranes obtained after the deposition process were translucent and allowed some visible light to pass through them. Three replicas for each membrane were prepared in order to evaluate the error. All the experimental results were expressed as the average of 3 replicas \pm error ($s t / \sqrt{n}$), where s is the standard deviation, t is the Student's t , and n is the number of replicas.

3.2.3 Instruments and methods

Excitation and emission spectra were acquired on a Varian Cary-Eclipse luminescence spectrometer (Varian Inc.-Agilent Technologies, <http://www.agilent.com>, CA, USA) equipped with a Xe flash lamp (peak power equivalent to 75 kW), Czerny-Turner monochromators, and a red-sensitive photomultiplier tube (PMT) R-928 from Hamamatsu Photonics (<http://www-sales.hamamatsu.com>, Japan) with manual or automatic voltage regulator.

The control of oxygen and lifetime measurements was carried out with a homemade system (see details in the ESI). Details about the fundamentals of oxygen sensing measured by the phase-resolved method (frequency domain) and about the characterization of the oxygen-sensing films are given in the ESI.

3.3 Results and discussion

3.3.1 Photophysical properties of the nanocomposites

Four different oxygen-sensing films have been evaluated. They are based on the immobilization of one Pt(II) (PtTFPP) and three Ir(III) (N969, N1008 and EB146) oxygen-sensitive dyes into an inorganic nanostructured matrix (AP200/19).

PtTFPP was selected because it is one of the most popular and widely used oxygen-sensitive luminescent dyes for the preparation of optical oxygen sensors [44]. It is primarily

due to its excellent photostability, rapid response times, high sensitivity at low oxygen concentrations, and strong phosphorescence at room temperature (*i.e.*, high photoluminescence quantum yield) [13, 32, 50].

N969, N1008 and EB146 were selected to cover a large variety of properties, such as a wide range of emission wavelengths, high quantum yield, and an expected high sensitivity to low oxygen concentrations, according to previous studies developed by our research group [29, 30]. This range of properties make them interesting not only for controlling residual oxygen or anaerobic conditions (*i.e.*, as optical trace oxygen sensors), but also in applications that require different excitation and/or emission wavelengths and sensitivities (case of multi-parameter optical sensors) [6, 51–55].

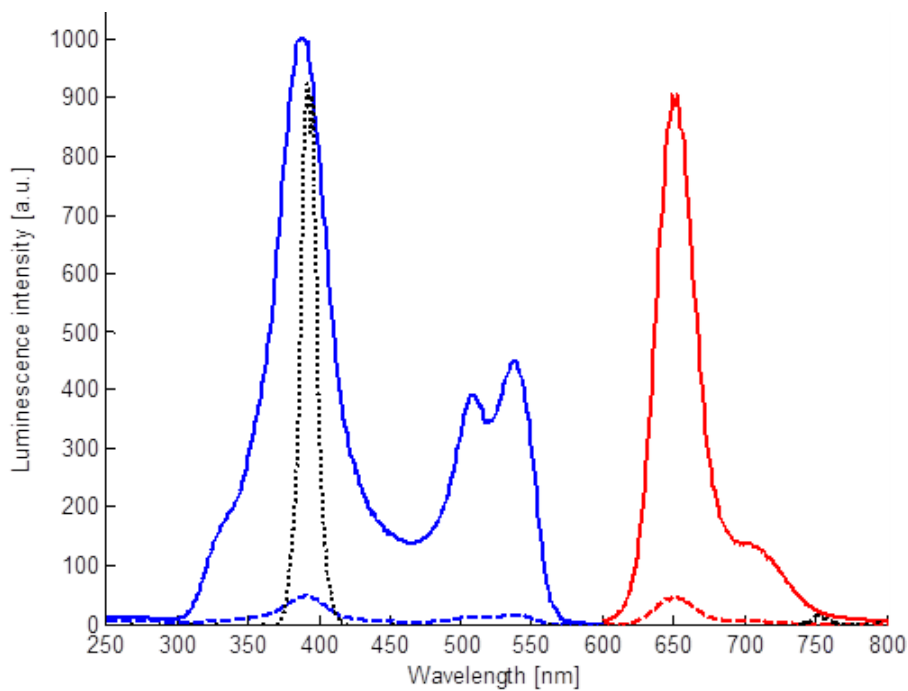
Table 3.1 shows the luminescence excitation and emission properties of the different sensing films, as well as their luminescence lifetimes in the absence of oxygen and at 21 °C. Fig. 3.1 shows the luminescence excitation and emission spectra in the absence and in the presence of oxygen (100% N₂ and 100% O₂, respectively) of PtTFPP and N969 (as a representative Ir(III) complex) immobilized into AP200/19; the spectra of the other two Ir(III) complexes are similar to those of N969 and they are shown in the ESI (see Fig. ESI-3). In all cases, the emission was clearly quenched when the sensing films were exposed to oxygen. In addition, Fig. 3.1 also shows the emission spectra of both LEDs used for exciting the dyes. The Ir(III) complexes immobilized into AP200/19 can be efficiently excited in the near ultraviolet range (320–380 nm), showing good compatibility with the selected ultraviolet 375 nm LED, and PtTFPP immobilized into AP200/19 can be excited in the Soret band (380–400), thus the selected ultraviolet 395 nm LED is optimum for the excitation of this sensing film.

The maximal luminescence excitation and emission wavelengths of PtTFPP immobilized into AP200/19 are similar to the maxima obtained for this dye incorporated into a classical polystyrene membrane [43, 51], chemically attached to silica beads [13], and in solution [56]. Thus, the incorporation of PtTFPP into AP200/19 does not affect its emission spectrum. Interestingly, the luminescence lifetime (τ_0) for PtTFPP immobilized into AP200/19 ($\simeq 97 \mu\text{s}$) is higher than the same dye dissolved in polystyrene ($\simeq 55 \mu\text{s}$) [32] and chemically immobilized in silica beads ($\simeq 71 \mu\text{s}$) [13]. It could be due to the high efficiency of incorporation into the nanopores of the nanostructured aluminum oxide which reduces the probability of radiationless excited state deactivation [34, 40].

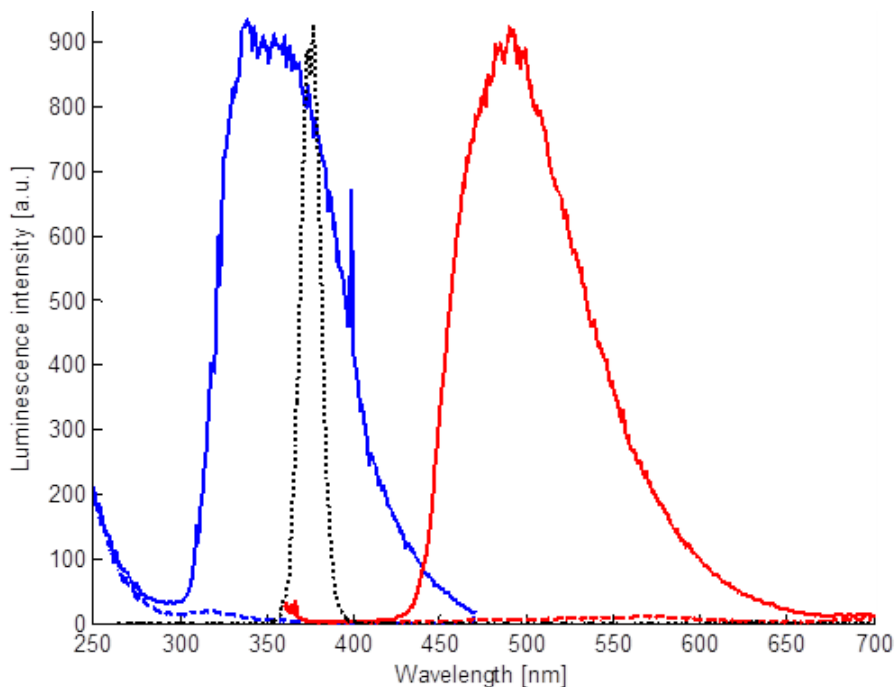
The incorporation of N969, N1008 and EB146 into AP200/19 has been previously analyzed [29, 30]. The incorporation of N969 and N1008 into the nanostructured material provides a shift in their excitation and emission wavelengths compared with those in solution. It was attributed to the ionic nature of these complexes; they are positively charged with negatively charged counterions and therefore possibly interact strongly with the positively charged metal oxide [30]. On the other hand, the immobilization of EB146 into AP200/19 does not affect its luminescence properties because it is a neutral complex [29].

3.3.2 Selection of the modulation frequency

The phase-based lifetime measurement at a fixed frequency requires the choice of an optimal modulation frequency for a given measurement range of oxygen [43, 57]. In this case,



(a) PtTFPP-AP200/19



(b) N969-AP200/19

Figure 3.1: Excitation (blue lines) and emission (red lines) spectra of the dyes in the absence (solid lines) and in the presence (dashed lines) of oxygen of (a) PtTFPP and (b) N969 immobilized into AP200/19. The black dotted line (\cdots) is the emission spectrum of the LED used to excite the sensing film. $[\text{Dye}] = 1.5 \text{ mg mL}^{-1}$, $\lambda_{exc} = 389 \text{ nm}$ for PtTFPP and 350 nm for N969, $\lambda_{em} = 650 \text{ nm}$ for PtTFPP and 490 nm for N969, $\text{slit-width}_{exc/em} = 10/10 \text{ nm}$, delay time = 0.1 ms , gate time = 5 ms , detector voltage = 440 V for PtTFPP and 590 V for N969, flow-rate 200 mL min^{-1} .

Table 3.1: Maxima luminescence excitation and emission wavelengths ($\lambda_{exc/em}$) and luminescence lifetime in the absence of oxygen (τ_0) of the dyes incorporated into AP200/19. [Dye concentration] = 1.5 mg mL⁻¹ and monochromator slit-width_{exc/em} = 10/10 nm.

Dye	λ_{exc} (nm)	λ_{em} (nm)	τ_0 (μ s)
PtTFPP	395	650	97.25 \pm 3.21
N969	350	490	3.74 \pm 0.02
N1008	340	512	8.40 \pm 0.07
EB146	335	470	1.88 \pm 0.01

measurement intervals between 0 and 1% O₂ and between 0 and 10% O₂ were chosen as the measurement ranges of interest to calibrate the oxygen-sensitive films. In order to select the most appropriate value of the modulation frequency of each sensing film at a given oxygen range, the average phase-shift differences between 0 and 1% O₂ ($|\phi_{0\%} - \phi_{1\%}|$) and between 0 and 10% O₂ ($|\phi_{0\%} - \phi_{10\%}|$) within a certain range of modulation frequencies (from 100 Hz to 98 kHz, the maximum operating frequency available for the commercial dual-phase lock-in amplifier) were determined.

A simple and powerful methodology based on a multifrequency phase-resolved method (referred to as multifrequency I/Q method and developed by our research group) [43] was used to detect the oxygen-concentration-dependent phase-shift simultaneously at multiple modulation frequencies (see ESI, Fig. ESI-4 and Table ESI-1). Multifrequency signals composed of 16 sinusoids of different frequencies were used to find the most appropriate value of the modulation frequency for each sensing film. This frequency was defined as the lowest modulation frequency giving the highest $|\phi_{0\%} - \phi_{x\%}|$. This multifrequency method significantly reduces the measurement time required to find the modulation frequency of a sensing film, providing similar results to those obtained with the well-known commercial dual-phase lock-in amplifier operating at a single frequency (see Fig. ESI-5 and Tables ESI-2 to ESI-5).

This study concludes that the most suitable modulation frequencies (in the frequency range 100 Hz - 98 kHz) for the measurement range 0-10% O₂ are 94100 Hz for the sensing films containing N969 (average phase difference of 32.97°) and EB146 (average phase difference of 28.41°), 30100 Hz for the sensing film containing N1008 (average phase difference of 24.59°) and 40100 Hz (average phase difference of 53.20°) for the sensing film containing PtTFPP. Similar modulation frequencies were obtained for the measurement range 0-1% O₂.

3.3.3 Oxygen-sensitive properties

All the membranes under study were evaluated with the setup described in Fig. ESI-2, and phase-shift measurements were obtained for several oxygen concentrations. Fig. 3.2 shows the variation of the phase shift of PtTFPP and N969 incorporated into AP200/19 when they are exposed to various concentrations of oxygen; ESI shows the phase shift variation for the other sensing films under study (see Fig. ESI-6) and the values obtained for all the measurements (see Tables ESI-6 to ESI-13). Using equation ESI-4, we determined the lifetimes and therefore the Stern-Volmer plots (τ_0/τ versus oxygen concentration) of all membranes. Fig. 3.3 shows the calibration curves and the Stern-Volmer plots of the four oxygen-sensitive films along the

fitting according to Demas model (equation ESI-2).

Table 3.2 summarizes the fitting parameters. Data in Table 3.2 show that the most sensitive sensing film is PtTFPP immobilized into AP200/19, which has K_{SV1} of 3102 bar^{-1} in the range 0-1% O_2 and K_{SV1} of 2568 bar^{-1} in the range 0-10% O_2

Table 3.2: Oxygen sensitivity of dye-AP200/19 films between 0-1% and 0-10% O_2 .

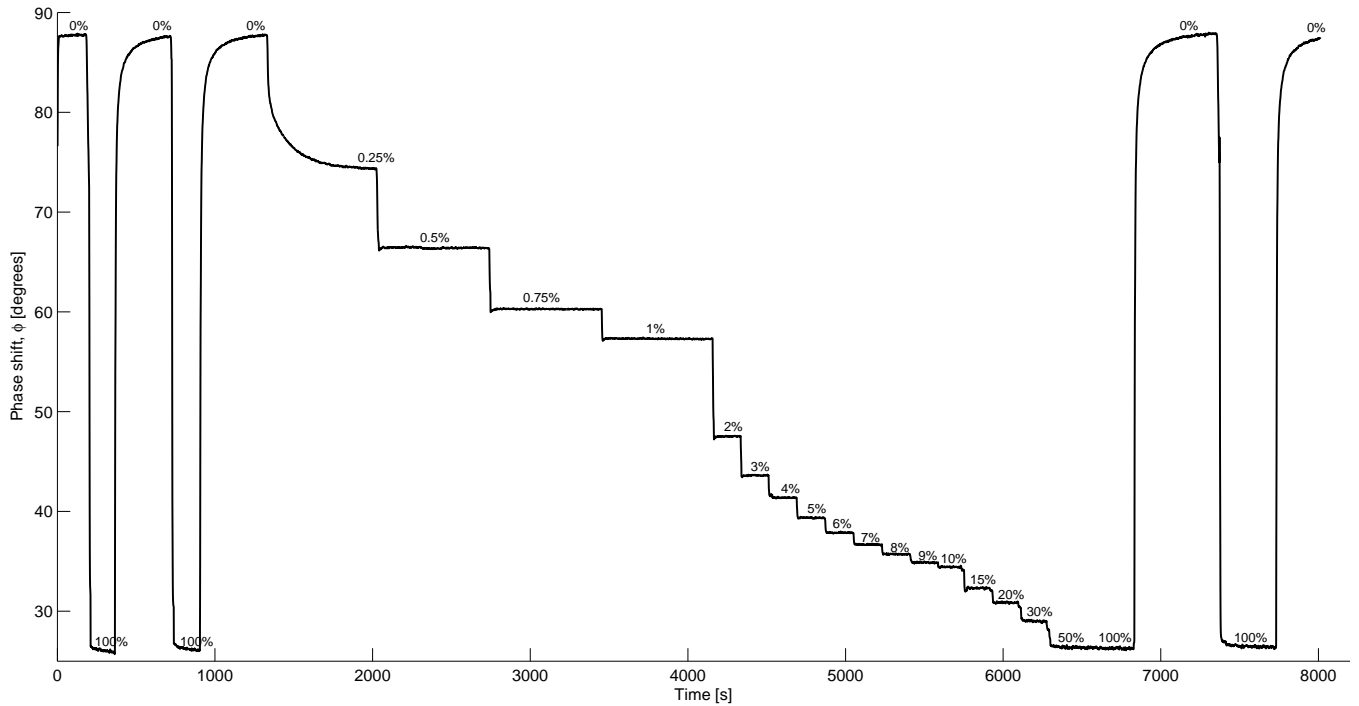
Range	Parameter	Dye ^a			
		PtTFPP	N969	N1008	EB146
0-1% O_2	$K_{SV1}(\text{bar}^{-1})$	3102 ± 132	941 ± 194	401 ± 51	289 ± 73
	x_1	0.99 ± 0.02	0.54 ± 0.05	0.26 ± 0.04	0.52 ± 0.04
	$K_{SV2}(\text{bar}^{-1})$	0.00 ± 0.00	15.19 ± 7.61	20.14 ± 3.59	7.92 ± 5.84
	x_2	0.03 ± 0.01	0.45 ± 0.05	0.73 ± 0.04	0.47 ± 0.04
	R^2	0.9988 ± 0.0016	0.9999 ± 0.0001	0.9997 ± 0.0004	0.9997 ± 0.0005
0-10% O_2	$K_{SV1}(\text{bar}^{-1})$	2568 ± 614	479 ± 72	145 ± 32	170 ± 19
	x_1	0.90 ± 0.10	0.64 ± 0.01	0.52 ± 0.01	0.64 ± 0.01
	$K_{SV2}(\text{bar}^{-1})$	1.66 ± 0.83	2.22 ± 0.44	2.35 ± 0.14	1.83 ± 0.70
	x_2	0.02 ± 0.00	0.33 ± 0.01	0.46 ± 0.01	0.33 ± 0.01
	R^2	0.9994 ± 0.0008	0.9983 ± 0.0005	0.9992 ± 0.0001	0.9985 ± 0.0009

^a[dye concentration] = 1.5 mg mL^{-1} ; the results are the average of 3 replicas $\pm st/\sqrt{n}$ ($n = 3$, $t = 4.303$ ($2P=0.05$)).

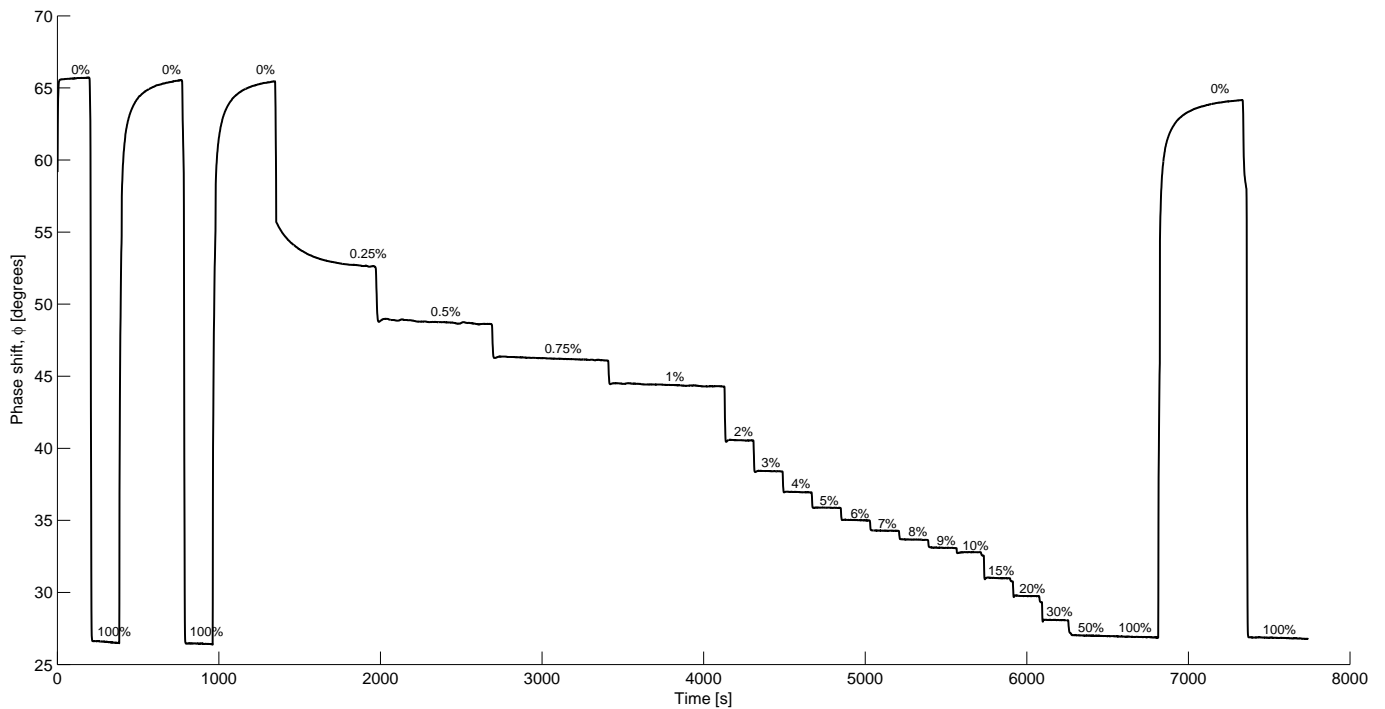
To compare with a more classical membrane for detecting O_2 , the PtTFPP was immobilized into a polystyrene (PS) support and measured with the same setup and under the same conditions (from 0 to 10% pO_2) at its optimal modulation frequency (5145 Hz) [43]. In this case, the data have to be fitted with the Lehrer model (see equation ESI-3 in the ESI). PtTFPP immobilized into PS shows the following results: $x_0 = 0.846 \pm 0.005$, $K_{SV} = 41.42 \pm 0.87 \text{ bar}^{-1}$. The incorporation of PtTFPP into AP200/19 increases its sensitivity more than 62 times referenced to PS. Furthermore, the Stern-Volmer constant between 0 and 1% O_2 of PtTFPP chemically attached to silica beads is 423 bar^{-1} and chemically attached to silica beads in silicone is 370 bar^{-1} [13]. The incorporation of PtTFPP into AP200/19 increases the sensitivity more than 8 times compared to silica beads. This interestingly increase of sensitivity has been previously described for Ru(II) and Ir(III) complexes, but is demonstrated for the first time for a Pt(II) complex.

Concerning the Ir(III) complexes immobilized into AP200/19, the highest sensitivity for low oxygen concentrations is obtained for N969. It shows a K_{SV1} of 941 bar^{-1} in the range 0-1% O_2 , which is about 23 times higher than the K_{SV1} of PtTFPP incorporated into PS and more than 2 times higher than the K_{SV1} of PtTFPP incorporated into silica beads, even when its luminescence lifetime is more than 18 times lower. Therefore, N969 incorporated into AP200/19 is an alternative of Pt(II) complex for oxygen trace sensing.

By comparing these results with other sensing membranes described in the literature [13, 32, 51], PtTFPP immobilized into AP200/19 is one of the most sensitive sensing layers developed to date. Only two oxygen-sensitive sensing films are more sensitive. The first one is based on fullerene C_{70} incorporated into ethylcellulose. It shows a K_{SV} of 70 000

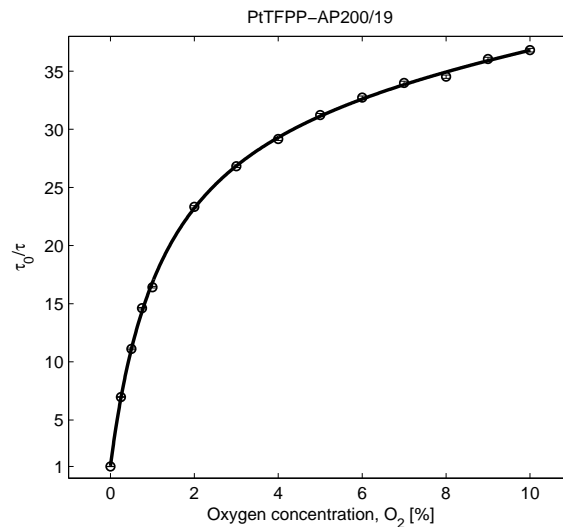
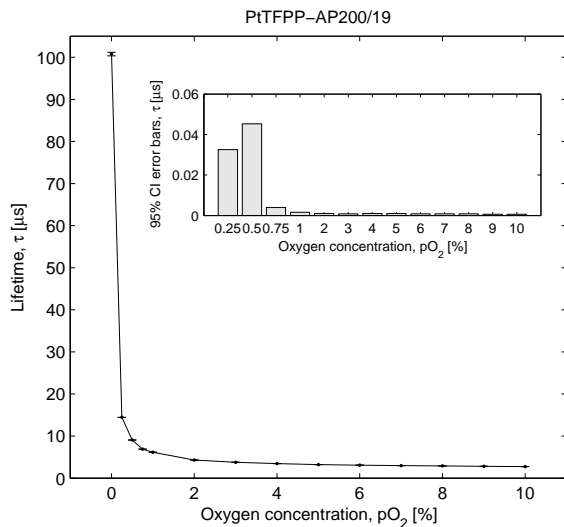


(a) PtTFPP AP200/19

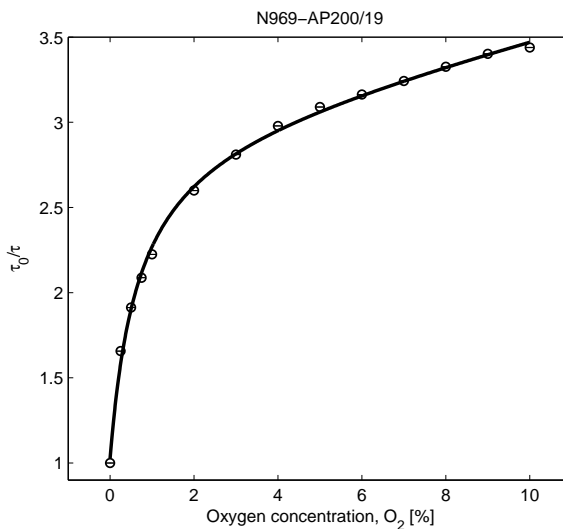
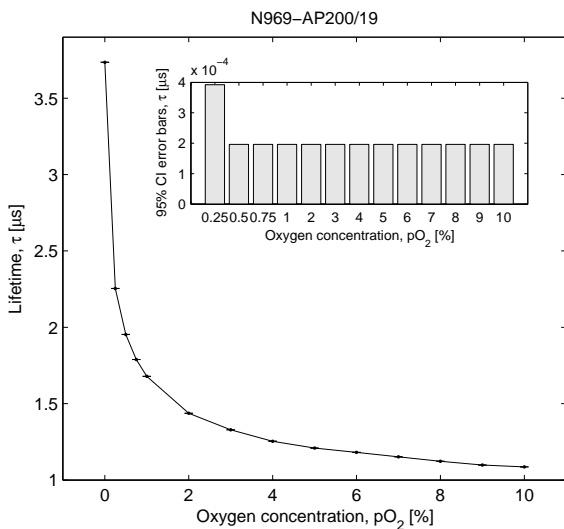


(b) N969-AP200/19

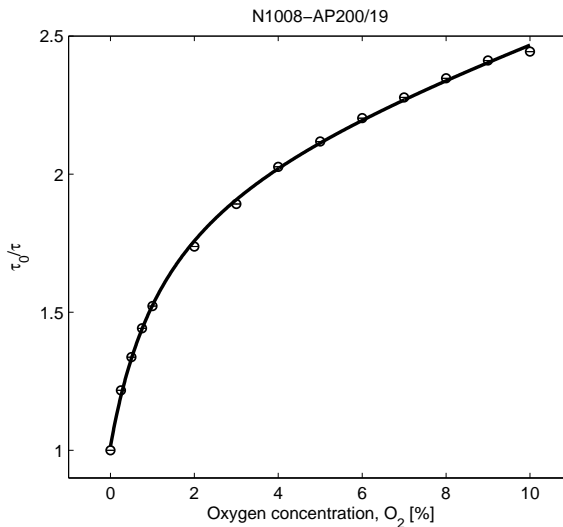
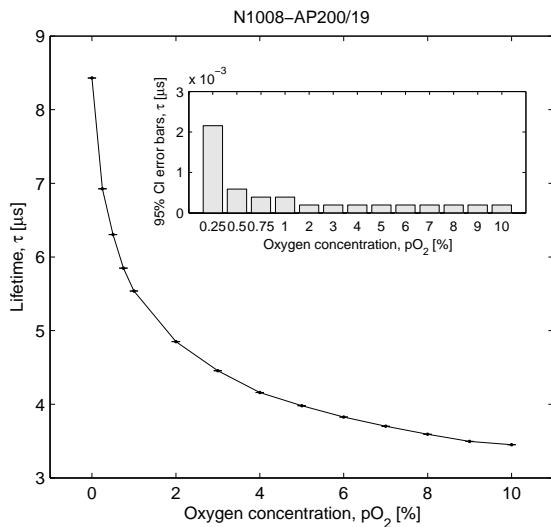
Figure 3.2: Variation of the phase shift of (a) PtTFPP and (b) N969 incorporated into AP200/19 with the oxygen concentration.



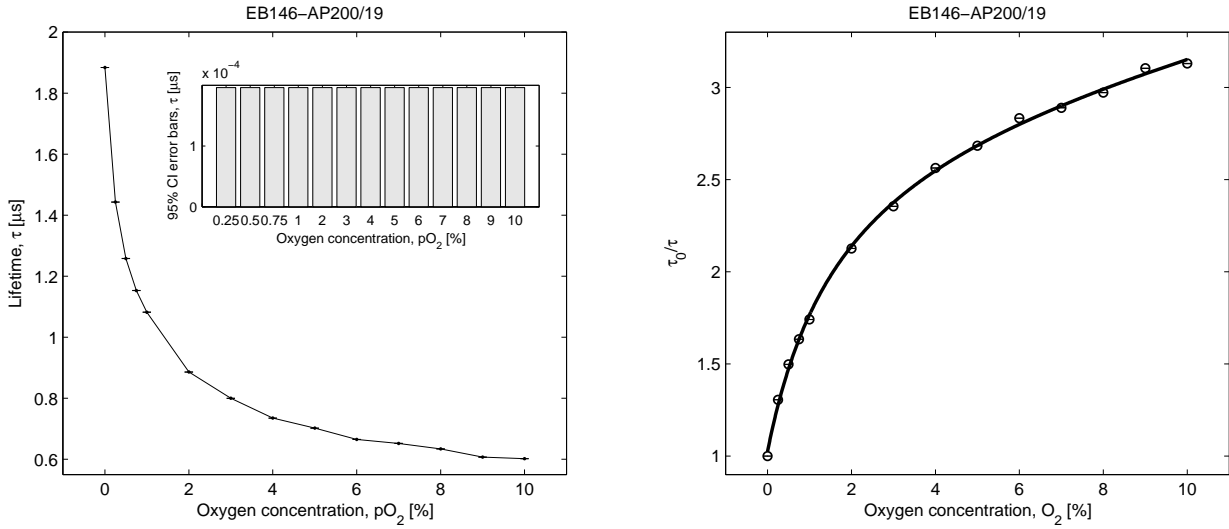
(a) PtTFPP-AP200/19



(b) N969-AP200/19



(c) N1008-AP200/19



(d) EB146-AP200/19

Figure 3.3: Calibration curves of (a) PtTFPP, (b) N969, (c) N1008 and (d) EB146 incorporated into AP200/19 at 21 °C. Left, decay time plots. Right, Stern-Volmer plots. Each point in figures represents the average value of 100 luminescence-lifetime measurements together with its error (*i.e.*, $\bar{\tau} \pm \text{error}$); where $\bar{\tau} = (1/100) \sum_{n=1}^{N=100} \tau_n$, and error bars indicate the 95% confidence intervals based on Student's t-distribution, calculated as: $\text{error (95\%)} = 1.96 s/\sqrt{N}$; with $s = \left((1/N - 1) \sum_{i=1}^{N=100} (\tau_i - \bar{\tau})^2 \right)^{1/2}$ (standard deviation of the $N=100$ luminescence-lifetime measurements).

bar^{-1} [58], 22 times higher than PtTFPP in AP200/19 from 0 to 1% O_2 , but this dye shows low luminescence brightness at RT and high temperature dependence of lifetime and sensitivity [13]. The second one consists on PdTFPP chemically immobilized in silica-beads in silicone and shows a K_{SV} of 6700 bar^{-1} from 0 to 0.1% O_2 [13], that is twice more than PtTFPP in AP200/19 from 0 to 1% O_2 ; it should be noted that the available data for PdTFPP are for a range 0-0.1% O_2 while the data obtained for PtTFPP are from 0 to 1% O_2 . The high sensitivity of PdTFPP is due to its long luminescence lifetime; therefore it is anticipated that its sensitivity would also increase if this dye is immobilized in AP200/19. On the other hand, the sensitivity of PdTFPP and PtTFPP sensing layers has low temperature dependence and both dyes are highly photostable.

In order to demonstrate that the developed sensing films can also be used for ultra-low oxygen detection the gas station was modified by replacing the pure oxygen with synthetic air (mixture of oxygen and nitrogen). With this new setup, the minimum oxygen concentration achievable is 0.05% pO_2 . ESI (see Tables ESI-14 to ESI-21) shows the phase shift and luminescence lifetime variations for all the measurements between 0 and 0.26% pO_2 and a summary of the results is shown in Fig. 3.4, which demonstrates that all the membranes can be used for detecting ultra-low oxygen concentrations.

To determine the most sensitive membrane for concentrations lower than 0.05% pO_2 , $\Delta\tau_{0.05\%}$ was determined. $\Delta\tau_{0.05\%}$ is defined as the percentage of the luminescence lifetime quenched at 0.05% oxygen and is a rough guide to the sensitivity of the optical oxygen sensing films. It was calculated according to equation (6.1):

$$\Delta\tau_{0.05\%} = \frac{\tau_0 - \tau_{0.05}}{\tau_0 - \tau_{100}} \times 100 \quad (3.1)$$

where τ_0 corresponds to the luminescence lifetime in the absence of oxygen, $\tau_{0.05}$ is the luminescence lifetime in the presence of 0.0005 bar (0.05%) oxygen and τ_{100} is the luminescence lifetime in the presence of 1 bar (100%) oxygen. It shows that PtTFPP in AP200/19 shows the highest $\Delta\tau_{0.05\%} = 62.53 \pm 3.66\%$ and therefore is the most suitable for ultra-low detection of oxygen. It means that the 62.53% of the signal of the sensing phase is quenched at 0.05% O₂. The most sensitive Ir(III) complex-based nanocomposite between 0 and 0.05% O₂ is N969 incorporated into AP200/19, which shows a $\Delta\tau_{0.05\%}$ value of $20.98 \pm 1.02\%$.

Finally, to demonstrate the usefulness of the developed sensing films, several air samples were analysed and the oxygen concentrations measured with the sensing films are compared with the real O₂ concentration in Table 3.3.

Table 3.3: Measurement capability of the developed sensing films.

Real pO ₂ ; %	Determined pO ₂ ; (relative error; %)			
	PtTFPP-AP200/19	N969-AP200/19	N1008-AP200/19	EB146-AP200/19
0.10	0.101 (1.22)	0.098 (1.67)	0.102 (2.34)	0.104 (3.46)
0.21	0.206 (1.92)	0.205 (2.52)	0.217 (3.21)	0.204 (2.70)
0.50	0.492 (1.62)	0.497 (2.43)	0.508 (3.20)	0.505 (3.67)
0.75	0.769 (2.50)	0.751 (2.07)	0.763 (2.97)	0.737 (2.67)
1	0.979 (2.07)	0.997 (1.89)	0.997 (3.13)	0.999 (2.78)
2	2.025 (1.27)	1.9652 (2.11)	1.929 (3.55)	2.053 (3.40)
5	5.025 (1.27)	5.074 (2.24)	5.039 (3.55)	5.046 (3.30)
8	7.840 (1.99)	8.100 (2.85)	8.155 (3.50)	7.751 (3.11)

3.3.4 Reversibility, response times, stability and the effect of humidity

The physico-chemical quenching reaction does not consume oxygen and therefore is a reversible process. Fig. 3.2 shows the variation of the phase-shift *versus* the partial pressure of oxygen; when the membranes are consecutively exposed to 0 and 100% O₂, the phase-shift sensing responses are completely reversible. The complete reversibility of the luminescence lifetime of the oxygen-sensitive films allows the continuous monitoring of increased and decreased pO₂ levels.

Table 3.4: Response times (t_{95}) of the dyes incorporated into AP200/19^a.

Dye	t_{95} Response time (s)	
	0-10% pO ₂	10-0% pO ₂
PtTFPP	24.5 ± 0.5	44.0 ± 0.8
N969	18.3 ± 0.4	47.3 ± 0.4
N1008	7.6 ± 0.4	20.7 ± 0.3
EB146	18.0 ± 0.4	37.9 ± 0.4

^a[dye concentration] = 1.5 mg mL⁻¹; the results are the average of 3 replicas ± st/\sqrt{n} ($n = 3$, $t = 4.303$ (2P=0.05)).

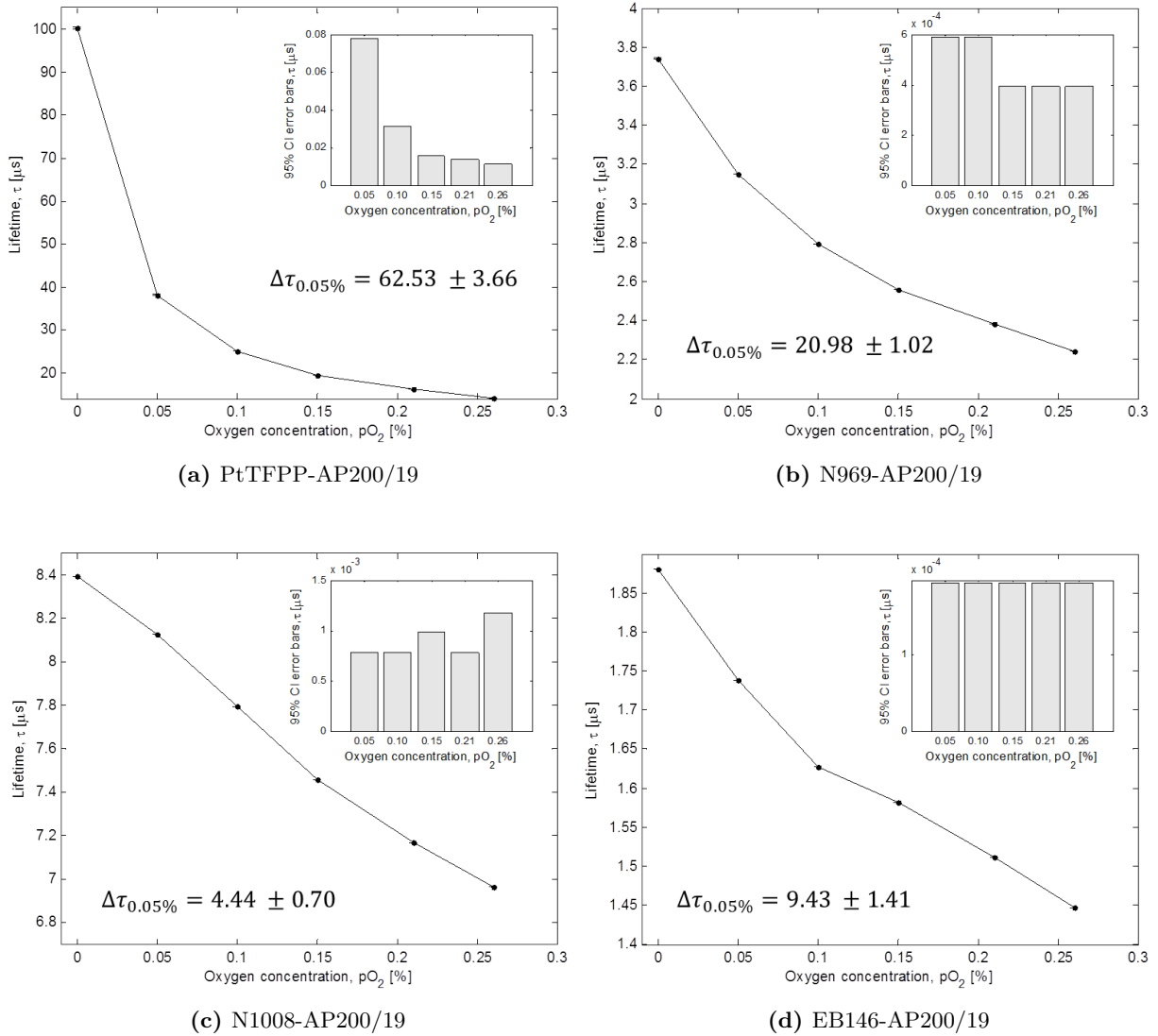


Figure 3.4: Variation of the luminescence lifetime between 0 and 0.26% $p\text{O}_2$ of (a) PtTFPP, (b) N969, (c) N1008 and (d) EB146 incorporated into AP200/19 at 21 °C, and the parameter $\Delta\tau_{0.05\%}$. Each point in figures represents the average value of 100 luminescence-lifetime measurements together with its error (*i.e.*, $\bar{\tau} \pm \text{error}$); where $\bar{\tau} = (1/100) \sum_{n=1}^{N=100} \tau_n$, and error bars indicate the 95% confidence intervals based on Student's t-distribution, calculated as: $\text{error (95\%)} = 1.96 s / \sqrt{N}$; with $s = \left((1/N - 1) \sum_{i=1}^{N=100} (\tau_i - \bar{\tau})^2 \right)^{1/2}$ (standard deviation of the $N=100$ luminescence-lifetime measurements).

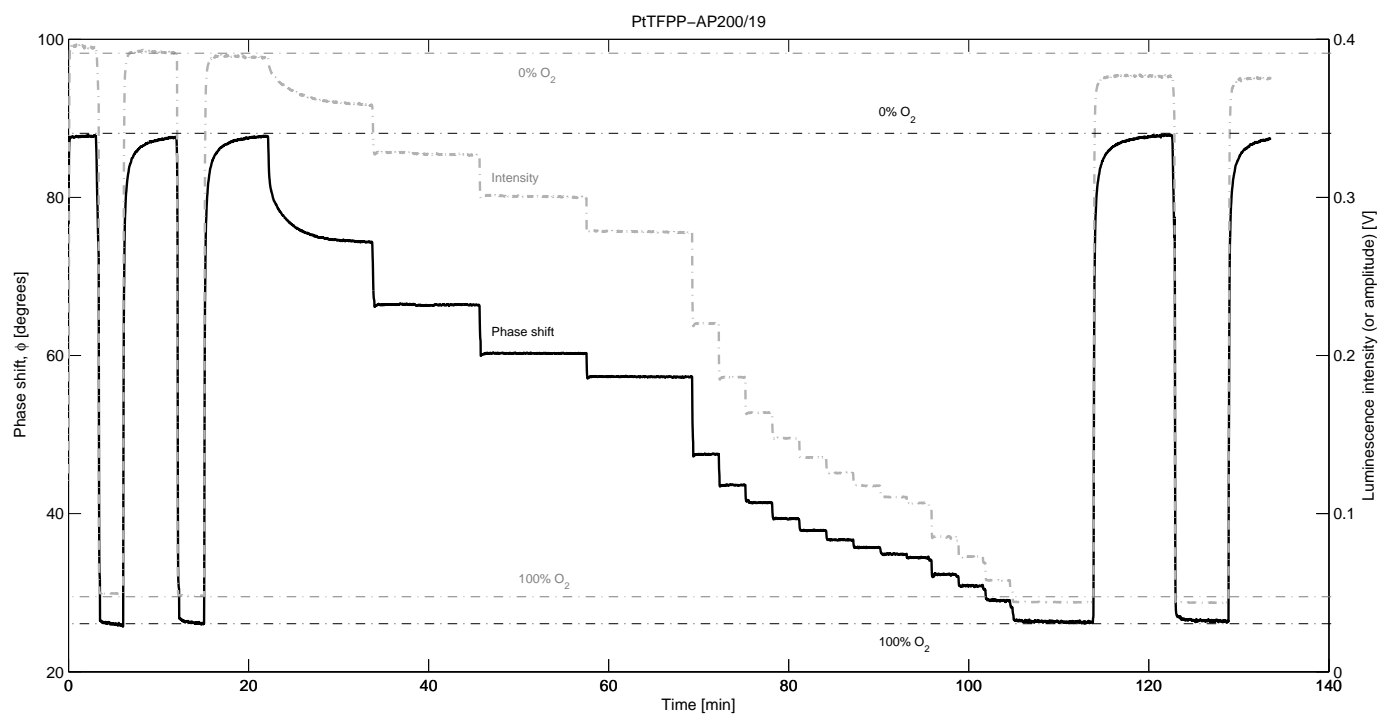
The oxygen-sensitive membranes show short response times: the t_{95} response times for all of the sensing films are shown in Table 3.4. All of them were shorter than 24 s when changing from 0 to 100 vol.% $p\text{O}_2$, and shorter than 47 s when changing from 100 to 0 vol.% $p\text{O}_2$. In comparison with other membranes, the registered response times are higher. For example, PtTFPP incorporated into PS shows a response time of 18 s when changing from 0 to 100 vol.% $p\text{O}_2$ and 60 s when changing from 100 to 0 vol.% $p\text{O}_2$ [56]; when incorporated into polytrifluoroethylmethacrylate, PtTFPP shows a response time of 5.6 s when changing from 0 to 100 vol.% $p\text{O}_2$ and 32 s when changing from 100 to 0 vol.% $p\text{O}_2$ [50]. The registered response times are in fact the response time of the system, which is the time needed by

the system to change the O₂ concentration from 0 to 100% and reverse. This claim is corroborated by the response times determined for these dyes immobilized into the same nanostructured solid support measured by intensity which were determined to be lower than 2 s when changing from 0 to 10 vol.% pO₂ and lower than 4 s when changing from 10 to 0 vol.% pO₂ [30].

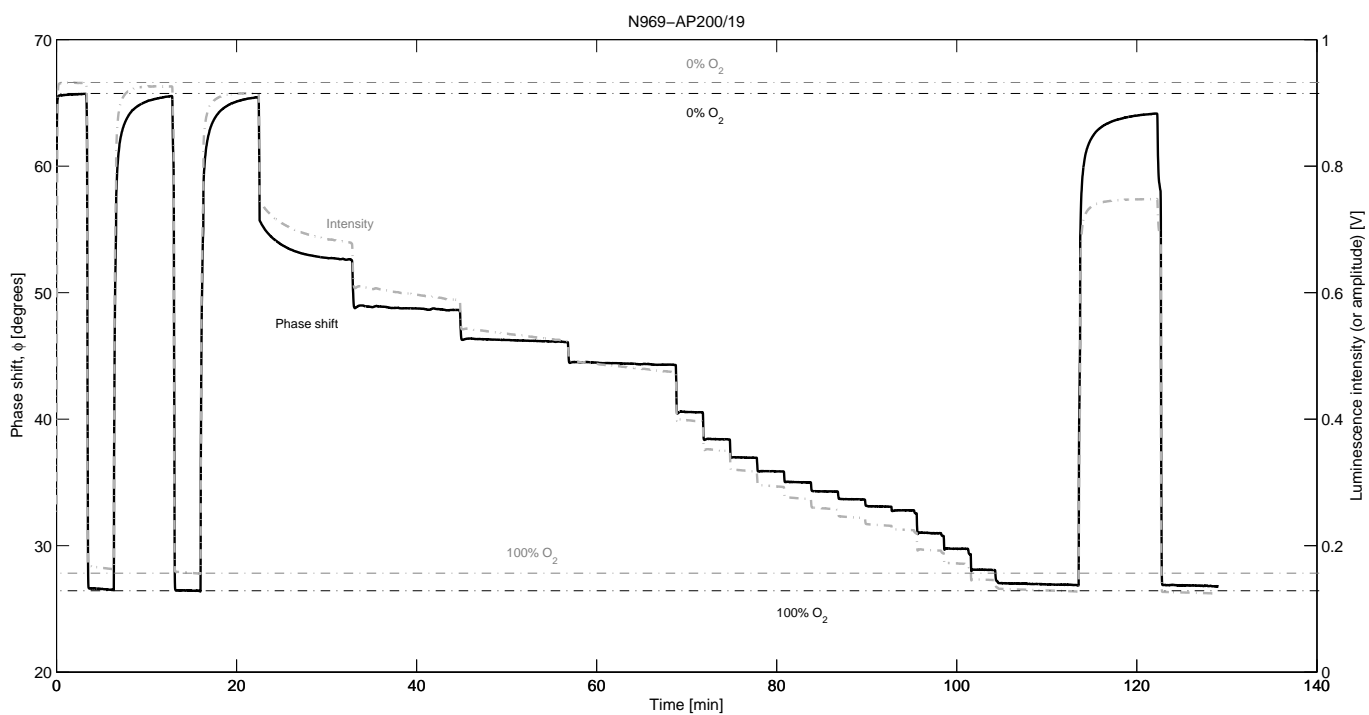
An important concern common to all optical sensors is the degradation of the sensor's quantum efficiency following prolonged sampling and continuous illumination. Thus, to evaluate the optical stability of the sensing films, they were illuminated with the LED over a period of 2 h, which corresponds to 7200 measuring points, as one second is enough to acquire a single point. The data corresponding to the variation of the phase shift and the amplitude of the emitted sinusoidal waveform were recorded for different oxygen concentrations at the same time. Amplitude is correlated with the luminescent intensity of the sensing film; therefore this parameter will determine if the lifetime measurements are more stable than the intensity ones. Fig. 3.5 shows the results for PtTFPP and N969 as examples of this study; see ESI (Fig. ESI-7) for the other sensing films. The amplitude (or intensity) of PtTFPP immobilized into AP200/19 decreases by 12.8 mV (corresponding to an error of 3.75% over the full-scale range of the sensing film) when the film is illuminated for 2 h. On the other hand, the phase shift decreases by only 0.1 degrees (corresponding to an error of 0.16% over the full-scale range of the sensing film). Similar results were obtained for the other sensing films: N1008 decreases by 46 mV (8.25% error) in amplitude and 0.89 degrees (2.67% error) in phase shift, N969 decreases by 184 mV (24.05% error) in amplitude and 1.56 degrees (3.97% error) in phase shift, and EB146 decreases by 192 mV (27.79% error) in amplitude and 1.45 degrees (4.41% error) in phase shift. Thus, the phase-based measurement of the luminescence lifetime is less affected by photobleaching than the intensity-based measurement over the two hours test period (see Fig. 3.5). This result is promising in improving the applicability and long-term stability of the optical sensing films, and thus strongly supports the selection of phase-based lifetime as the preferred sensing technique.

Since their analytical performance (K_{SV}) did not change over 12 months stored under ambient conditions and in the absence of light, the long-term stability of all the oxygen-sensitive membranes is considered to be sufficiently good for measurements in the gas phase.

Finally, these dyes have not been immobilized into a hydrophobic membrane therefore the effect of the humidity on the sensing response has to be evaluated in order to demonstrate their real capability. PtTFPP and N969 immobilized into AP200/19 have been used to determine the concentration of oxygen between 0 and 100% at several relative humidities (0, 10, 20, 40, 60 and 80% RH). ESI (see Tables ESI-22 to ESI-25) and Fig. 3.6 show the experimental results. It is possible to conclude that PtTFPP immobilized into AP200/19 is not affected by RH. On the other hand, N969 immobilized into AP200/19 is highly affected by RH as an increase of the RH results in a decrease of the sensitivity. Therefore, if N969 is used, the relative humidity of the media has to be taken into account in the calibration of the sensing film.

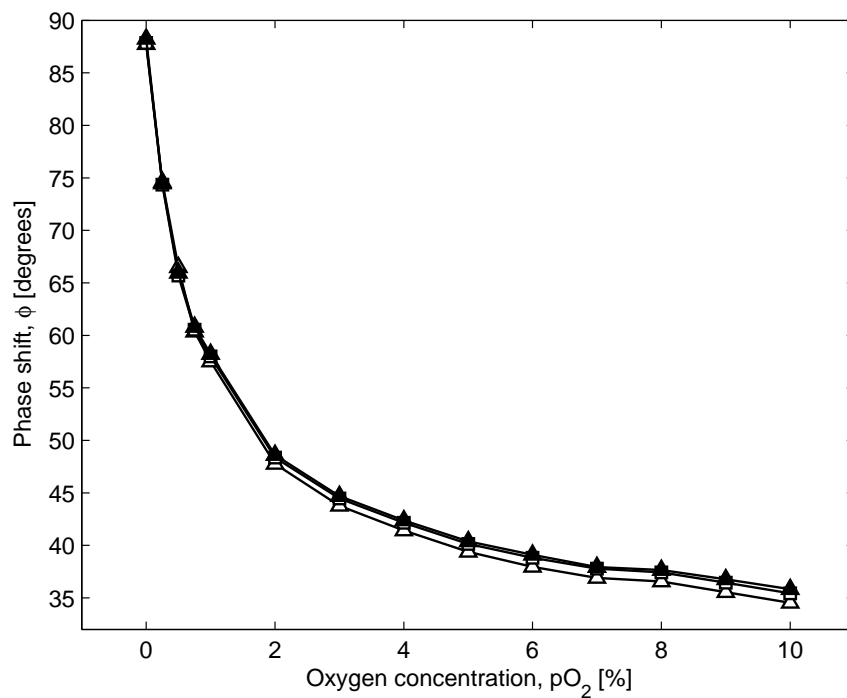


(a) PtTFPP-AP200/19

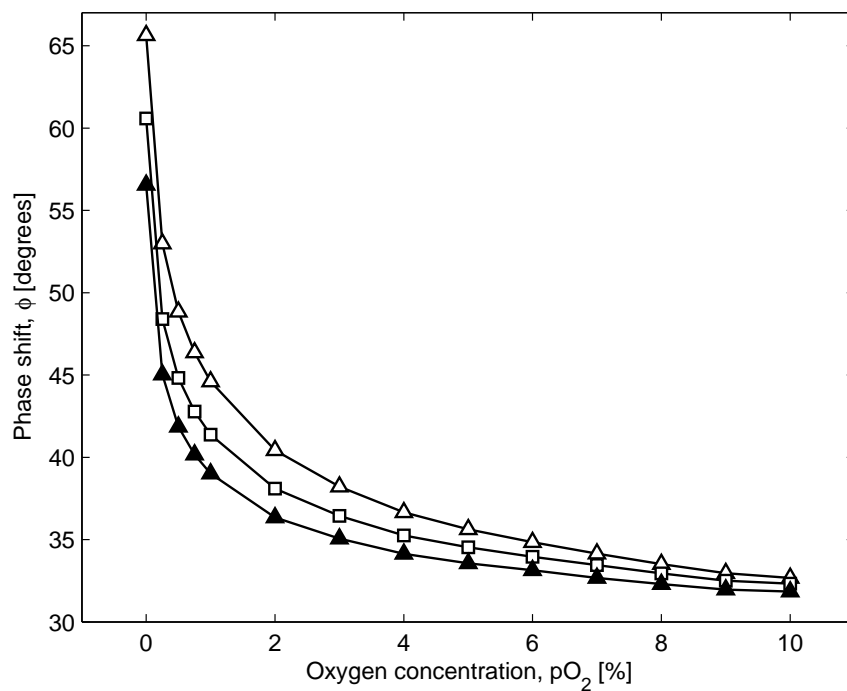


(b) N969-AP200/19

Figure 3.5: Stability of the phase shift (dark solid line) and amplitude (light dotted line) of (a) PtTFPP and (b) N969 incorporated into AP200/19 at 21 °C.



(a) PtTFPP-AP200/19



(b) N969-AP200/19

Figure 3.6: Effect of relative humidity (Δ 0% RH, \square 20% RH and \blacktriangle 80% RH) on the phase shift of (a) PtTFPP and (b) N969 incorporated into AP200/19 at 21 °C.

3.4 Conclusions

The luminescent platinum-complex PtTFPP and iridium-complexes N969, N1008 and EB146 were investigated for the optical sensing of low and ultra-low oxygen concentrations using phase-shift measurements. The organometallic complexes were incorporated into a nano-structured, metal oxide matrix and characterized under a controlled atmosphere.

To the best of our knowledge, this is the first time that a Pt(II) complex has been incorporated into AP200/19. The spectral properties of PtTFPP are not affected by the solid support but, interestingly, its luminescence lifetime increases significantly ($\tau_{0(AP200/19)} = 97 \mu\text{s}$, $\tau_{0(PS)} = 55 \mu\text{s}$ and $\tau_{0(silica\ beads)} = 71 \mu\text{s}$). This sensing film also shows the highest sensitivity, with a Stern-Volmer constant equal to $3102 \pm 132 \text{ bar}^{-1}$ in the range between 0 and 1% O₂ and $2568 \pm 614 \text{ bar}^{-1}$ in the range between 0 and 10% O₂. When compared to PtTFPP immobilized in polystyrene, the Stern-Volmer constant is over 62 times higher in the range 0-10% O₂ for PtTFPP immobilized in AP200/19. In comparison to PtTFPP immobilized on silica beads, the sensitivity of PtTFPP incorporated into AP200/19 improved more than 8 times in the range 0-1% O₂. In addition, this O₂-sensing film is not affected by humidity even though AP200/19 is not a hydrophobic membrane. Concerning the Ir(III) doped films, the most sensitive one is based on N969, which shows a Stern-Volmer constant of $941 \pm 194 \text{ bar}^{-1}$ in the range between 0 and 1% O₂ and $479 \pm 72 \text{ bar}^{-1}$ in the range between 0 and 10% O₂. Thus, N969 incorporated into AP200/19 shows a sensitivity about 23 times higher than that of PtTFPP immobilized into PS and more than 2 times higher than that of PtTFPP immobilized on silica beads. Therefore, N969 is a possible alternative to the PtTFPP complex for oxygen trace sensing with a different emitted wavelength.

In order to demonstrate that these sensing films can be used for ultra-low oxygen detection, the gas station was modified in order to decrease the amount of oxygen to 0.05%. The variation of the phase shift between 0 and 0.26% demonstrates this claim and the parameter $\Delta\tau_{0.05\%}$ shows that the most sensitive sensing film for controlling ultra-low oxygen concentrations (lower than 0.05% O₂) consists of PtTFPP incorporated into AP200/19, with a $\Delta\tau_{0.05\%}$ value of $62.53 \pm 3.66\%$. These results make this film one of the most sensitive sensing films published in the literature. It was followed by the incorporation of N969 into AP200/19 ($\Delta\tau_{0.05\%}$ value of $20.98 \pm 1.02\%$), further supporting its use as an alternative to PtTFPP with a different emitted wavelength.

The photostability study proved the high stability of the proposed sensing films and demonstrated that the phase-based measurement of the luminescence lifetime minimizes the effect of photobleaching of the optical sensing films, which significantly improves their applicability.

Finally, the oxygen-sensitive films show complete reversibility with short response times and long-term stability of more than 12 months.

Acknowledgments

The authors gratefully acknowledge the financial support from the Spanish Ministry of Economy and Competitiveness (CTQ2011-25316 and Medina-Rodríguez's grant reference BES-

2009-026919) and the Regional Government of Andalusia (Excellence projects P07-FQM-2625 and P07-FQM-2738). Also, the authors are grateful to Ilford Imaging Switzerland GmbH (Switzerland) for supplying the metal oxide membranes.

Appendix A. Supplementary data

Supplementary data associated with this article can be found in the Electronic Supporting Information (ESI): Chemical structures of the dyes, full details about the homemade oxygen sensing characterization system, fundamentals of oxygen sensing measured by the phase-resolved method (frequency domain), full details of characterization of the oxygen-sensing films, additional figures for the oxygen sensitivity of the iridium(III) complexes, and additional tables including the data measured.

References

- [1] J. Janata, M. Josowicz, P. Vanýsek and D.M. DeVaney, *Anal. Chem.*, 1998, **70**, 179R-208R.
- [2] D.B. Papkovsky and T.C. O’Riordan, *J. Fluoresc.*, 2005, **15**, 569-584.
- [3] J.F. Fernández-Sánchez, T. Roth, R. Cannas, M.K. Nazeeruddin, S. Spichiger, M. Graetzel and U.E. Spichiger-Keller, *Talanta*, 2007, **71**, 242-250.
- [4] J.R. Lakowicz, *Principles of Fluorescence Spectroscopy*, Kluwer Academic, New York, 2nd edn., 1999.
- [5] S.M. Borisov, A.S. Vasylevska, C. Krause and O.S. Wolfbeis, *Adv. Funct. Mater.*, 2006, **16**, 1536-1542.
- [6] S.M. Borisov, R. Seifner and I. Klimant, *Anal. Bioanal. Chem.*, 2011, **400**, 2463-2474.
- [7] K. Koren, S.M. Borisov, R. Saf and I. Klimant, *Eur. J. Inorg. Chem.*, 2011, 1531-1534.
- [8] Y. Amao, *Microchim. Acta*, 2003, **143**, 1-12.
- [9] O.S. Wolfbeis, *J. Mater. Chem.*, 2005, **15**, 2657-2669.
- [10] C. McDonagh, C.S. Burke and B.D. MacCraith, *Chem. Rev.*, 2008, **108**, 400-422.
- [11] O.S. Wolfbeis, *Anal. Chem.*, 2008, **80**, 4269-4283.
- [12] S.M. Mitrovski and R.G. Nuzzo, *Lab Chip*, 2005, **5**, 634-645.
- [13] S.M. Borisov, P. Lehner and I. Klimant, *Anal. Chim. Acta*, 2011, **690**, 108-115.
- [14] R. Loloee, P.A. Askeland and R.N. Ghosh, *Proceedings of IEEE Sensors*, 2007.
- [15] C.A.K. Lange, P. Stavrakas, U.F.O. Luhmann, D.J. De Silva, R.R. Ali, Z.J. Gregor and J.W.B. Bainbridge, *Am. J. Ophthalmol.*, 2011, **152**, 406-412.

- [16] A.L. Medina-Castillo, J.F. Fernández-Sánchez and A. Fernández-Gutiérrez, *Adv. Funct. Mater.*, 2011, **21**, 3488-3495.
- [17] K. Xie, X.-W. Zhang, L. Huang, Y.-T. Wang, Y. Lei, J. Rong, C.-W. Qian, Q.-L. Xie, Y.-F. Wang, A. Hong and S. Xiong, *Cytotechnology*, 2011, **63**, 345-350.
- [18] D.H. Song, H.D. Kim and K.C. Kim, *Opt. Lasers Eng.*, 2012, **50**, 74-81.
- [19] G.A. Holst, T. Köster, E. Voges and D.W. Lübbers, *Sens. Actuators, B*, 1995, **29**, 231-239.
- [20] O. Ergeneman, G. Dogangil, M.P. Kummer, J.J. Abbott, M.K. Nazeeruddin and B.J. Nelson, *IEEE Sens. J.*, 2008, **8**, 29-37.
- [21] D.E. Achatz, R.J. Meier, L.H. Fischer and O.S. Wolfbeis, *Angew. Chem., Int. Ed.*, 2011, **50**, 260-263.
- [22] W. Trettnak, C. Kolle, F. Reininger, C. Dolezal and P. O'Leary, *Sens. Actuators, B*, 1996, **36**, 506-512.
- [23] M. Tscherner, C. Konrad, A. Bizzarri, M. Suppan, M. Cajlakovic and V. Ribitsch, *IEEE Sens. J.*, 2009, 1660-1665.
- [24] F.A. Rainey and A. Oren, in *Methods in Microbiology*, ed. F.A. Rainey and A. Oren, Elsevier, 2006, vol. 35, pp. 1-25.
- [25] R.C. Soliva-Fortuny and O. Martin-Belloso, *Trends Food Sci. Technol.*, 2003, **14**, 341-353.
- [26] E.V.D.B. Vilas-Boas and A.A. Kader, *Postharvest Biol. Technol.*, 2006, **39**, 155-162.
- [27] J.R. Gorny, B. Hess-Pierce, R.A. Cifuentes and A.A. Kader, *Postharvest Biol. Technol.*, 2002, **24**, 271-278.
- [28] S.C. Fonseca, F.A.R. Oliveira, J.K. Brecht and K.V. Chau, *Postharvest Biol. Technol.*, 2005, **35**, 279-292.
- [29] M. Marín-Suárez, B.F.E. Curchod, I. Tavernelli, U. Rothlisberger, R. Scopelliti, I. Jung, D. Di Censo, M. Grätzel, J.F. Fernández-Sánchez, A. Fernández-Gutiérrez, M.K. Nazeeruddin and E. Baranoff, *Chem. Mater.*, 2012, **24**, 2330-2338.
- [30] M. Marín-Suárez del Toro, J.F. Fernández-Sánchez, E. Baranoff, M.K. Nazeeruddin, M. Grätzel and A. Fernández-Gutiérrez, *Talanta*, 2010, **82**, 620-626.
- [31] M.I.J. Stich, L.H. Fischer and O.S. Wolfbeis, *Chem. Soc. Rev.*, 2010, **39**, 3102-3114.
- [32] S.M. Borisov and I. Klimant, *Anal. Chem.*, 2007, **79**, 7501-7509.
- [33] A.L. Medina-Castillo, J.F. Fernández-Sánchez, C. Klein, M.K. Nazeeruddin, A. Segura-Carretero, A. Fernández-Gutiérrez, M. Graetzel and U.E. Spichiger-Keller, *Analyst*, 2007, **132**, 929-936.
- [34] J.F. Fernández-Sánchez, R. Cannas, S. Spichiger, R. Steiger and U.E. Spichiger-Keller, *Anal. Chim. Acta*, 2006, **566**, 271-282.

- [35] Y. Amao and I. Okura, *J. Porphyrins Phthalocyanines*, 2009, **13**, 1111-1122.
- [36] Y. Amao, K. Asai, I. Okura, H. Shinohara and H. Nishide, *Analyst*, 2000, **125**, 1911-1914.
- [37] Y. Amao, T. Miyashita and I. Okura, *Analyst*, 2000, **125**, 871-875.
- [38] Y. Amao, T. Miyashita and I. Okura, *React. Funct. Polym.*, 2001, **47**, 49-54.
- [39] J.F. Fernández-Sánchez, I. Fernández, R. Steiger, R. Beer, R. Cannas and U.E. Spichiger-Keller, *Adv. Funct. Mater.*, 2007, **17**, 1188-1198.
- [40] J.F. Fernández-Sánchez, T. Nezel, R. Steiger and U.E. Spichiger-Keller, *Sens. Actuators, B*, 2006, **113**, 630-638.
- [41] K. Tsukada, S. Sakai, K. Hase and H. Minamitani, *Biosens. Bioelectron.*, 2003, **18**, 1439-1445.
- [42] J. Dakin and B. Culshaw, *Optical Fiber Sensors: Applications, Analysis and Future Trends*, Artech House, Norwood, MA, 1997.
- [43] S. Medina-Rodríguez, A. de la Torre-Vega, J.F. Fernández-Sánchez and A. Fernández-Gutiérrez, *Sens. Actuators, B*, 2013, **176**, 1110-1120.
- [44] T.S. Yeh, C.S. Chu and Y.L. Lo, *Sens. Actuators, B*, 2006, **119**, 701-707.
- [45] M.A. Chan, J.L. Lawless, S.K. Lam and D. Lo, *Anal. Chim. Acta*, 2000, **408**, 33-37.
- [46] C. McDonagh, C. Kolle, A.K. McEvoy, D.L. Dowling, A.A. Cafolla, S.J. Cullen and B.D. MacCraith, *Sens. Actuators, B*, 2001, **74**, 124-130.
- [47] P. Hartmann, M.J.P. Leiner and M.E. Lippitsch, *Sens. Actuators, B*, 1995, **29**, 251-257.
- [48] D. Andrzejewski, I. Klimant and H. Podbielska, *Sens. Actuators, B*, 2002, **84**, 160-166.
- [49] F. De Angelis, S. Fantacci, N. Evans, C. Klein, S.M. Zakeeruddin, J.E. Moser, K. Kalyanasundaram, H.J. Bolink, M. Graetzel and M.K. Nazeeruddin, *Inorg. Chem.*, 2007, **46**, 5989-6001.
- [50] Y. Amao, T. Miyashita and I. Okura, *J. Fluorine Chem.*, 2001, **107**, 101-106.
- [51] M. Schäferling, *Angew. Chem., Int. Ed.*, 2012, **51**, 3532-3554.
- [52] A.S. Kocincova, S.M. Borisov, C. Krause and O.S. Wolfbeis, *Anal. Chem.*, 2007, **79**, 8486-8493.
- [53] R.C. Evans and P. Douglas, *ACS Appl. Mater. Interfaces*, 2009, **1**, 1023-1030.
- [54] Y. Feng, J. Cheng, L. Zhou, X. Zhou and H. Xiang, *Analyst*, 2012, **137**, 4885-4901.
- [55] X.D. Wang, H.X. Chen, Y. Zhao, X. Chen and X.R. Wang, *TrAC, Trends Anal. Chem.*, 2010, **29**, 319-338.
- [56] S.K. Lee and I. Okura, *Anal. Commun.*, 1997, **34**, 185-188.

-
- [57] V.I. Ogurtsov and D.B. Papkovsky, *Sens. Actuators, B*, 1998, **51**, 377-381.
- [58] S. Nagl, C. Baleizão, S.M. Borisov, M. Schäferling, M.N. Berberan-Santos and O.S. Wolfbeis, *Angew. Chem., Int. Ed.*, 2007, **46**, 2317-2319.

Appendix A. Supplementary data

Electronic Supporting Information (ESI)

High performance optical sensing nanocomposites for low and ultra-low oxygen concentrations using phase-shift measurements

Santiago Medina Rodríguez^{a,b,*}, Marta Marín Suárez^b, Jorge Fernando Fernández Sánchez^{b,*}, Ángel de la Torre Vega^a, Etienne Baranoff^c and Alberto Fernández Gutiérrez^b

^a*Department of Signal Theory, Networking and Communications, CITIC-UGR, University of Granada, C/ Periodista Rafael Gómez 2, E-18071 Granada, Spain.*

^b*Department of Analytical Chemistry, Faculty of Sciences, University of Granada, Avda. Fuentenueva s/n, E-18071 Granada, Spain.*

^c*School of Chemistry, University of Birmingham, Edgbaston, B15 2TT, England, UK.*

Table of Contents

- Graphical abstract of the manuscript.
- Details of the homemade system to control the oxygen concentration and for lifetime measurements.
- Fundamentals of oxygen sensing measured by the phase-resolved method (frequency domain).
- Characterization of the oxygen-sensing films.
- References ESI.

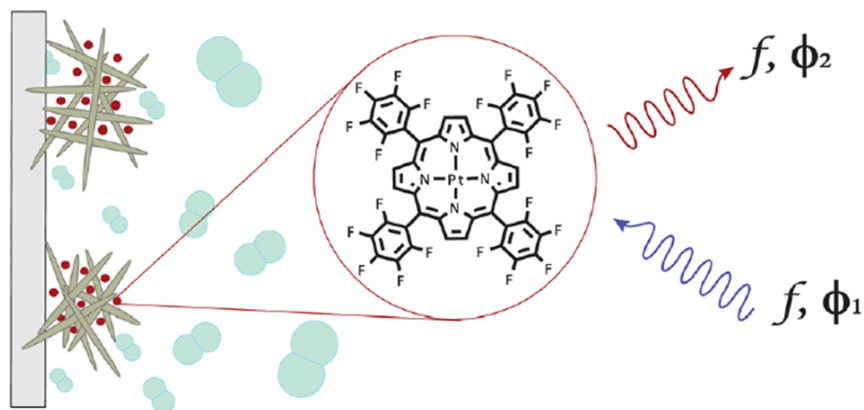
List of Figures

- Fig. ESI-1. Chemical structure of the complexes.
- Fig. ESI-2. Schematic diagrams of the designed experimental setup for phase-shift measurements and the flow cell used.
- Fig. ESI-3. Luminescence spectra of N1008 and EB146.
- Fig. ESI-4. Selection of the modulation frequency using multifrequency signals.
- Fig. ESI-5. Selection of the modulation frequency using the lock-in amplifier.
- Fig. ESI-6. Calibration of N1008 and EB146 with oxygen.

- Fig. ESI-7. Stability study.

List of Tables

- Table ESI-1. Data of the selection of the optimal modulation frequency using a multi-frequency phase-resolved method.
- Tables ESI-2 to ESI-5. Data of the selection of the optimal modulation frequency using the lock-in amplifier.
- Tables ESI-6 to ESI-12. Data of the calibrations.
- Tables ESI-13 to ESI-21. Data of the determination of ultra-low oxygen concentrations (between 0 and 0.26% pO₂).
- Tables ESI-22 to ESI-25. Data of the effect of relative humidity.



Graphical abstract of the manuscript. New optical sensing nanocomposites based on oxygen-sensitive dyes incorporated into a nanostructured metal oxide solid support resulted in an outstanding overall performance when combined with the phase-shift measurement method.

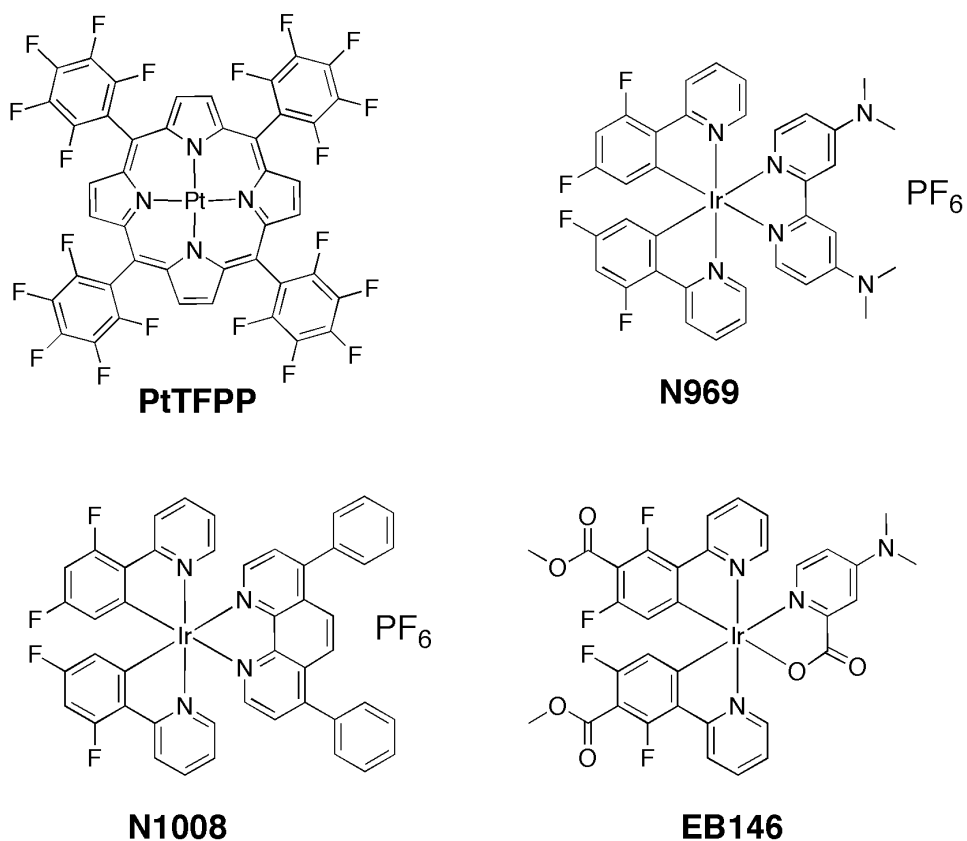


Fig. ESI-1. Chemical structure of the complexes.

PtTFPP: Platinum(II) 5,10,15,20-meso-tetrakis-(2,3,4,5,6-pentafluorophenyl)-porphyrin.

N969: [Ir(2-(2,4-difluorophenyl)pyridine)₂(4,4'-dimethylamino-2,2'-bipyridine)](PF₆).

N1008: [Ir(2-(2,4-difluorophenyl)pyridine)₂(4,7-diphenyl-1,10-phenanthroline)](PF₆).

EB146: [Ir(2-(2,4-difluoro-3-methylesterphenyl)pyridine)₂(4-(N,N-dimethylamino)picolinate)].

Details of the homemade system to control the oxygen concentration and for lifetime measurements

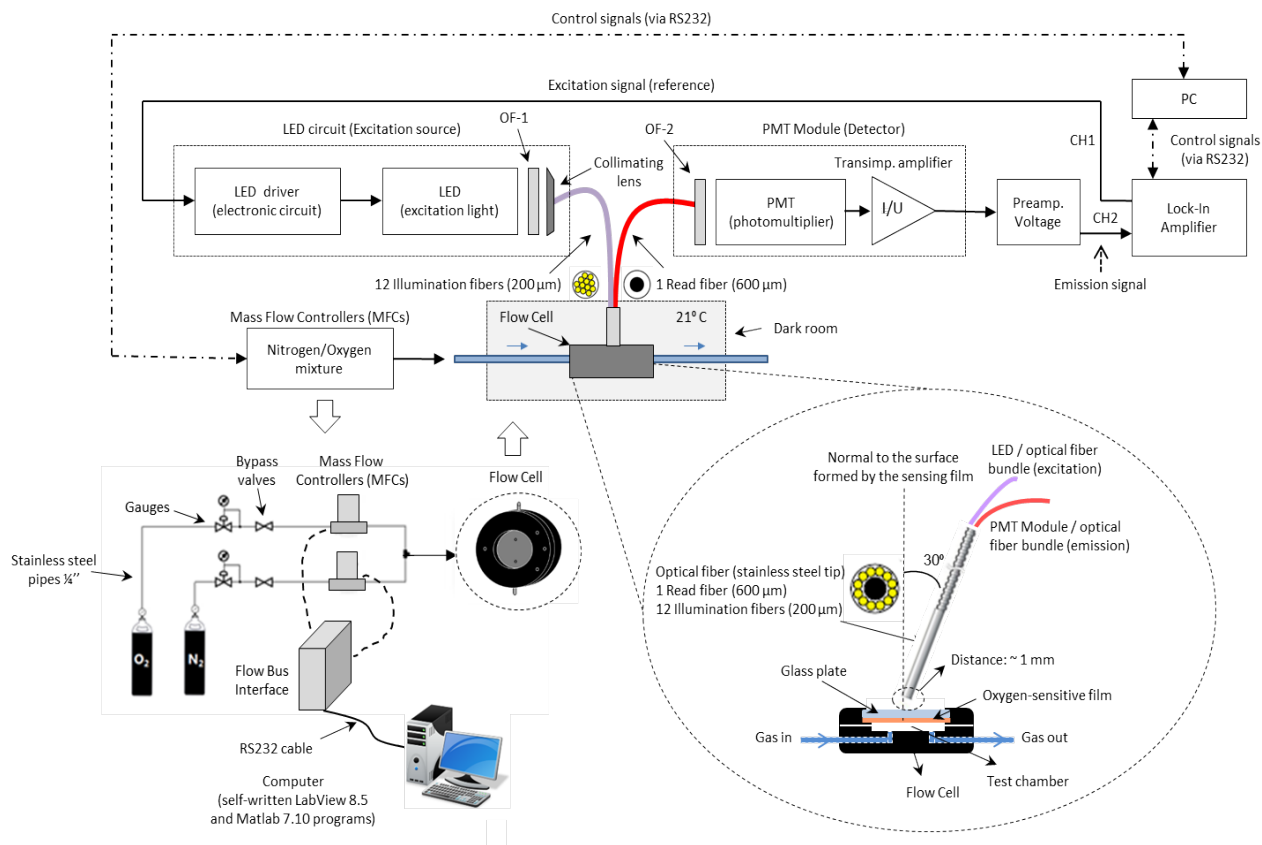


Fig. ESI-2. Schematic diagrams of the designed experimental setup for phase-shift measurements and the flow cell used.

The control of oxygen and lifetime measurements was carried out with a homemade system (see Fig.ESI-2). For it, a flow-through cell, which functions as a gas chamber, was designed in our laboratories to hold the sensing films. The flow cell was made of black PTFE to prevent stray reflections and also to assure the chemical inertness. It was not thermostated since it was to be used in a constant temperature (in this case, all measurements were performed at room temperature of 21 °C). The temperature was continuously monitored using a commercial temperature sensor (MicroLite, Fourtec-Fourier Technologies, www.fouriersystems.com) located at an external point close to the flow cell. Different mixtures of nitrogen and oxygen at a constant flow rate of 200 mL min⁻¹ were passed through the flow cell to perform the calibration of the sensing films. For gas mixing, two mass-flow controllers (MFCs) (EL-FLOW Select F-201CV, Bronkhorst High-Tech, www.bronkhorst.com, Ruurlo, Netherlands) were connected to copper and stainless steel tubing. These tubes connected the MFCs and the flow cell. The gas station was completely controlled from a PC using an ad hoc computer program developed in LabView 8.5 (www.ni.com) and MATLAB 7.10 (www.mathworks.com) software. For it, the PC was connected to a Flow-Bus Interface (Bronkhorst High-Tech) that

fully controls the MFCs via a RS-232 serial port.

For the study of the effect of relative humidity, one more MFC for nitrogen was added. Thus, nitrogen was split into two lines before two mass-flow controllers. One branch was humidified by guiding the nitrogen over water in a 2-neck glass flask, thus avoiding the formation of water droplets. A relative humidity (RH) of up to 80% was obtained. This was monitored with a hygrometer (Rotronic, Bassersdorf, www.rotronic.ch) coupled after the measurement cell. The two lines of nitrogen were merged to provide the desired carrier gas stream, to which an additional line carrying oxygen was connected.

For the study of the sensing response for concentrations lower than 0.26%, oxygen was replaced by synthetic air (21% O₂ balanced in N₂). The luminescence phase shifts were measured with a dual-phase lock-in amplifier (SR830, Stanford Research Systems, www.thinksrs.com, USA). The sensing films containing the iridium(III) complexes were excited with an ultraviolet light-emitting diode (LED) ($\lambda_{max} = 375$ nm, angle of illumination 15°, LED diameter 5 mm, luminous power 6800 μ W (max.) at 15 mA, LED Supply, www.ledsupply.com, USA) filtered through an optical bandpass filter ($\lambda_{central} = 390$ nm, MF390-18, Thorlabs GmbH, www.thorlabs.com) which was sinusoidally modulated at a frequency of 94100 Hz (in the case of N969 and EB146) or at a frequency of 30100 Hz (in the case of N1008). The sensing film containing PtTFPP was excited with an ultraviolet LED ($\lambda_{max} = 395$ nm, angle of illumination 15°, LED diameter 5 mm, luminous power 25 μ W) filtered through an optical bandpass filter ($\lambda_{central} = 390$ nm, MF390-18, Thorlabs GmbH) which was sinusoidally modulated at a frequency of 40100 Hz.

A bifurcated fiber bundle (wavelength range 200-800 nm UV-VIS, 12 illumination fibers 200 μ m core diameter, 1 read fiber 600 μ m core diameter, N.A. 0.22, FCR-7xx200-2, Avantes Inc., www.avantes.com) was used to guide the excitation light to the sensing film and to guide back the luminescence after passing an optical longpass filter ($\lambda_{cut-on} = 450$ nm, NT62-975, Edmund Optics) in the case of Ir(III) complexes, or an optical bandpass filter ($\lambda_{central} = 630$ nm, BW = 30 nm, A10033-03, Hamamatsu Photonics, www.hamamatsu.com) in the case of PtTFPP. The luminescence was detected with a photomultiplier tube (PMT) (BW = DC-1 MHz, H10723-20, Hamamatsu Photonics). The voltage signal provided by the PMT (of few tens of millivolts) was amplified with a commercial low-noise programmable voltage preamplifier (SIM911 BJT, Stanford Research Systems) before being applied to the lock-in amplifier. Both the flow cell and PMT were housed in a dark room (XE25C1, Thorlabs GmbH) to prevent interference from stray light.

Fundamentals of oxygen sensing measured by the phase-resolved method (frequency domain)

The oxygen quenching process is described by the Stern-Volmer equation (Equation ESI-1):

$$\frac{\tau_0}{\tau} = 1 + K_{SV}[O_2] \quad (\text{Equation ESI-1})$$

where τ_0 and τ are the unquenched and quenched excited state lifetimes, K_{SV} is the Stern-Volmer constant, and $[O_2]$ is the concentration of quencher (oxygen).

However, in many cases it is usual to find some deviation from linearity of the response due to the heterogeneity of the matrix where the dyes are immobilized [1]. This deviation is explained by the presence of different oxygen quenching sites within the matrix [2, 3], and therefore a multi-site model with each site having a linear behaviour can be applied. The simplest one is the two-site model proposed by Demas *et al.* [4], the so-called Demas model. This model assumes that the indicator is localized in two regions of different microenvironments, explaining the deviation from the linearity in the Stern-Volmer plot. Thus, the experimental data can be nicely fitted with the following Equation ESI-2:

$$\frac{\tau_0}{\tau} = \left[\frac{x_1}{1 + K_{SV1}[O_2]} + \frac{x_2}{1 + K_{SV2}[O_2]} \right]^{-1} \quad (\text{Equation ESI-2})$$

where x_1 and x_2 are the fractions of the total emission for each component respectively (with $x_1 + x_2 = 1$), and K_{SV1} and K_{SV2} are the Stern-Volmer quenching constants for each component.

Other two-site model was proposed by Lehrer [5], where only one of the two microenvironments is accessible to the quencher ($K_{SV2} = 0$). In this case, the experimental data can be fitted with the following Equation ESI-3:

$$\frac{\tau_0}{\tau} = \left[\frac{x_1}{1 + K_{SV}[O_2]} + (1 - x_1) \right]^{-1} \quad (\text{Equation ESI-3})$$

where x_1 denotes the fraction of the total luminophores population that the quencher is able to access, and K_{SV} is the Stern-Volmer quenching constant associated with the accessible fraction of luminophores.

In the phase-resolved method (frequency domain), the sample is excited with a sinusoidally modulated light at a fixed frequency that consequently causes a modulated luminescence emission at the identical frequency. Due to the emission lifetime of the luminescent material, the emission signal exhibits a phase-shift (*i.e.*, time delay) with respect to the excitation signal. The input excitation signal is used as a reference to establish the zero-phase position, and the lifetime is obtained indirectly by measuring the phase-shift between the excitation and emission signals [6]. If the luminescence emission is directly proportional to the intensity of the excitation light, and assuming that the luminescence decay is monoexponential, the relationship between the phase-shift, ϕ , and the emission lifetime, τ , is given by Equation ESI-3 [7, 8]:

$$\tan(\phi) = 2\pi f\tau \quad (\text{Equation ESI-4})$$

where ϕ is the phase-shift, f is the exciting light modulation frequency, and τ is the decay time (or luminescence lifetime).

Characterization of the oxygen-sensing films

Excitation and emission spectra were recorded with a Varian Cary-Eclipse luminescence spectrometer. The parameter settings for spectroscopic characterization were: slit-width_{exc/em} = 10/10 nm, delay time = 0.1 ms, gate time = 5 ms, constant flow-rate of 200 mL min⁻¹, and

detector voltage = 560 V (EB146), 550 V (N1008), 590 V (N969) and 440 V (PtTFPP). All measurements were performed in the absence (100% N₂) and in the presence (100% O₂) of oxygen and at 21 °C.

Luminescence lifetimes were determined in the frequency domain, and they were calculated indirectly with the experimental setup represented in Fig. ESI-2 by measuring the phase-shift between the excitation and emission signals (see Equation ESI-4).

A disadvantage of the phase luminometry is that the SNR (signal to noise ratio) decreases with increasing modulation frequency (*i.e.*, the amplitude of the optical signal (optical power) decreases with increasing modulation frequency of the LED), and since the phase sensitivity increases with modulation frequency [7], an optimal frequency has to be selected [9, 10]. Furthermore, the choice of the optimal modulation frequency also depends on the sensing application (*i.e.*, measurement range of interest) because the changes of the phase-shift within a certain oxygen concentrations range depend on the excitation modulation frequency [11]. One choice to achieve maximum dynamic range for measuring the phase-shift (or lifetime, see Equation ESI-4) is to adjust the modulation frequency such that the phase difference between the extremes of the oxygen measurement range is maximized [11, 12]. This strategy was used in this work to select the optimal modulation frequency for a given range of oxygen concentrations (between 0 and 1% O₂ and between 0 and 10% O₂).

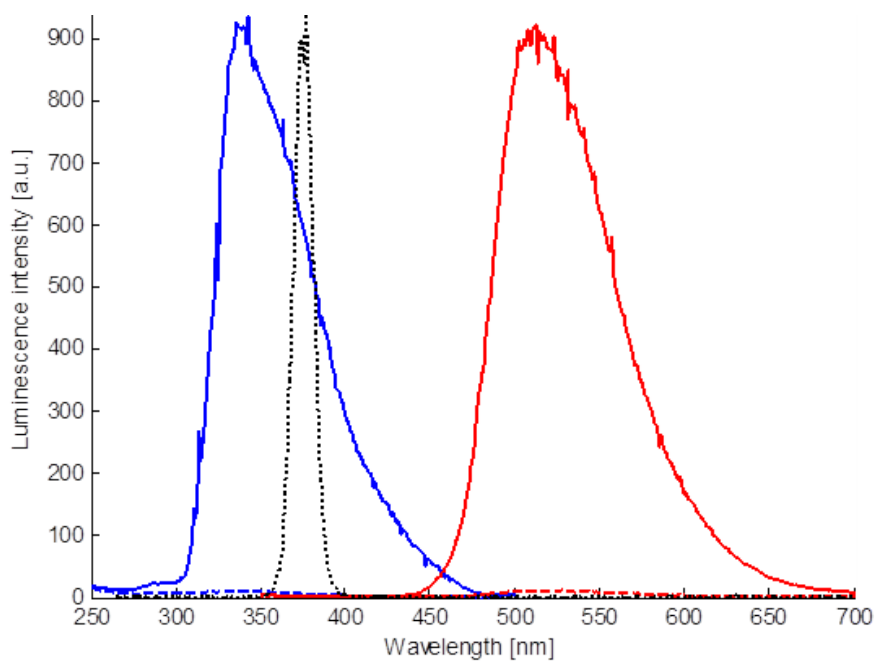
Time trace curves were used to record the luminescence phase shifts at 14 different oxygen partial pressures between 0 and 100 kPa (or 0-100 vol. % pO₂). These phase-shift measurements were used to obtain the typical calibration curves (*i.e.*, Stern-Volmer Plots (SVP)). Fitting was performed using MATLAB 7.10 software between 0 and 1 kPa (or 0-1 vol. % pO₂) and between 0 and 10 kPa (or 0-10 vol. % pO₂). Furthermore, typical response-time curves were also obtained to determine the response times of the sensing films (*i.e.*, rise and fall times to t₉₅). All measurements were done in the absence of ambient light and at 21 °C.

The oxygen concentration of the gas passing through the flow cell was calculated in real-time from the measured oxygen/nitrogen flows provided by the MFCs. A total gas flow-rate of 200 mL min⁻¹ was maintained in all gas measurements, assuming a constant environment pressure of 1000 mbar. Before starting the experiments, the MFCs were calibrated using a flow sensor.

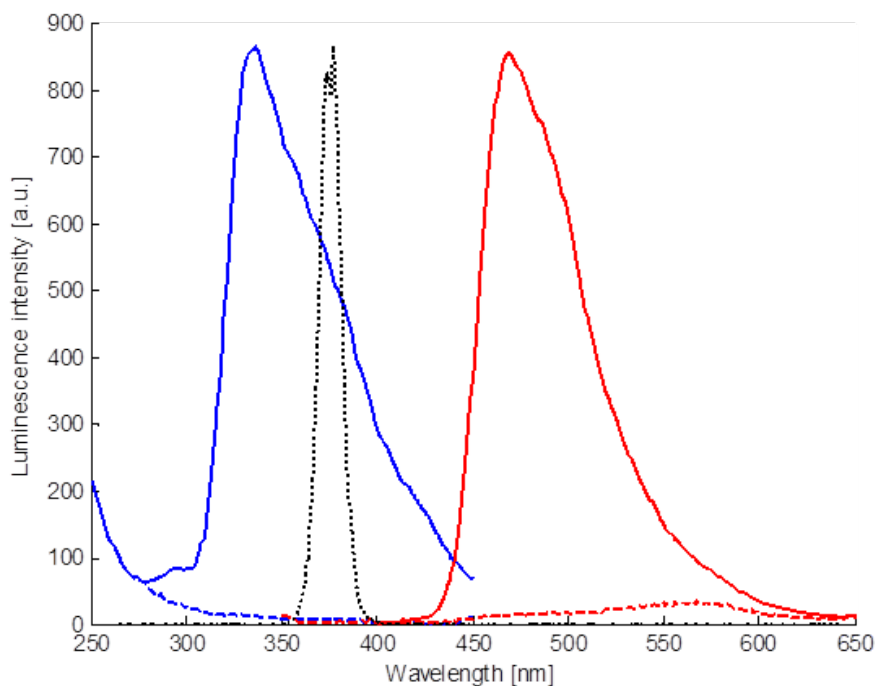
References ESI

- [1] J.F. Fernández-Sánchez, R. Cannas, S. Spichiger, R. Steiger and U.E. Spichiger-Keller, *Anal. Chim. Acta*, 2006, **566**, 271-282.
- [2] J.F. Fernández-Sánchez, T. Roth, R. Cannas, M.K. Nazeeruddin, S. Spichiger, M. Graetzel and U.E. Spichiger-Keller, *Talanta*, 2007, **71**, 242-250.
- [3] M. Marín-Suárez del Toro, J.F. Fernández-Sánchez, E. Baranoff, M.K. Nazeeruddin, M. Gräetzel and A. Fernández-Gutiérrez, *Talanta*, 2010, **82**, 620-626.
- [4] J.N. Demas and B.A. DeGraff, *Sens. Actuators, B*, 1993, **11**, 35-41.
- [5] S.S. Lehrer, *Biochemistry*, 1971, **10**, 3254-3263.

-
- [6] D. Andrzejewski, I. Klimant and H. Podbielska, *Sens. Actuators, B*, 2002, **84**, 160-166.
- [7] J.R. Lakowicz, *Principles of Fluorescence Spectroscopy*, Kluwer Academic, New York, 2nd edn., 1999.
- [8] E. Crowell and L. Geng, *Appl. Spectrosc.*, 2001, **55**, 1709-1716.
- [9] C. McDonagh, C. Kolle, A.K. McEvoy, D.L. Dowling, A.A. Cafolla, S.J. Cullen and B.D. MacCraith, *Sens. Actuators, B*, 2001, **74**, 124-130.
- [10] S. Medina-Rodríguez, A. de la Torre-Vega, J.F. Fernández-Sánchez and A. Fernández-Gutiérrez, *Sens. Actuators, B*, 2013, **176**, 1110-1120.
- [11] V.I. Ogurtsov and D.B. Papkovsky, *Sens. Actuators, B*, 1998, **51**, 377-381.
- [12] G. O’Keeffe, B.D. MacCraith, A.K. McEvoy, C.M. McDonagh and J.F. McGilp, *Sens. Actuators, B*, 1995, **29**, 226-230.

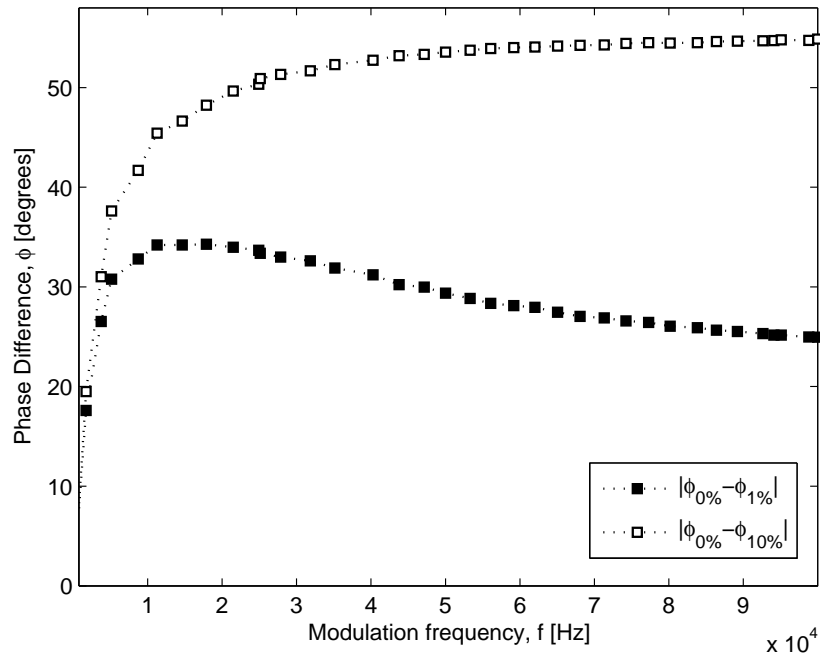


(a) N1008-AP200/19

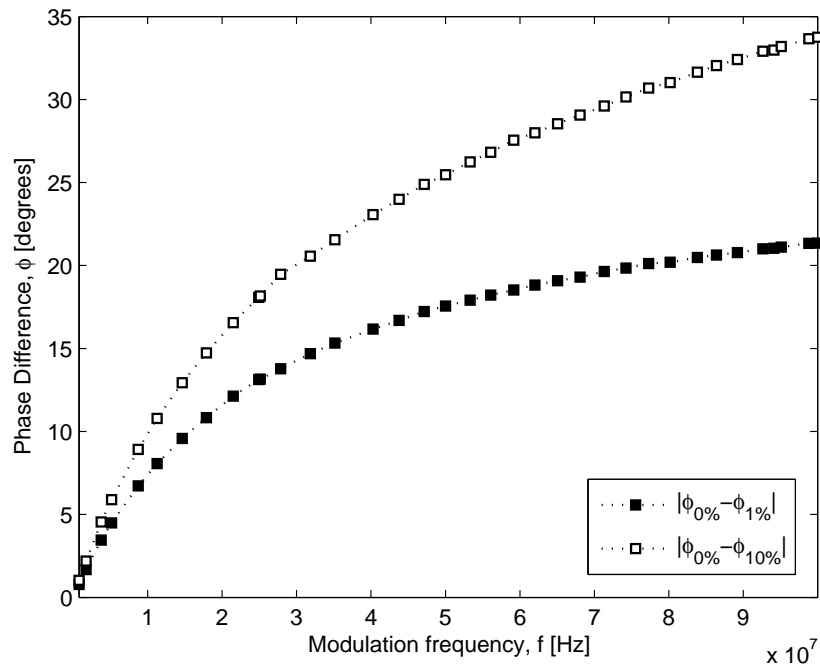


(b) EB146-AP200/19

Fig. ESI-3. Excitation (blue lines) and emission (red lines) spectra of the dyes in the absence (solid lines) and in the presence (dashed lines) of oxygen of (a) N1008 and (b) EB146 immobilized into AP200/19. The black dotted line (\cdots) is the emission spectra of the LED used to excite the sensing film. $[\text{Dye}] = 1.5 \text{ mg mL}^{-1}$, $\lambda_{exc} = 340 \text{ nm}$ for N1008 and 335 nm for EB146, $\lambda_{em} = 512 \text{ nm}$ for N1008 and 470 nm for EB146, $\text{slit-width}_{exc/em} = 10/10 \text{ nm}$, delay time = 0.1 ms , gate time = 5 ms , detector voltage = 550 V for N1008 and 560 V for EB146, flow-rate 200 mL min^{-1} .

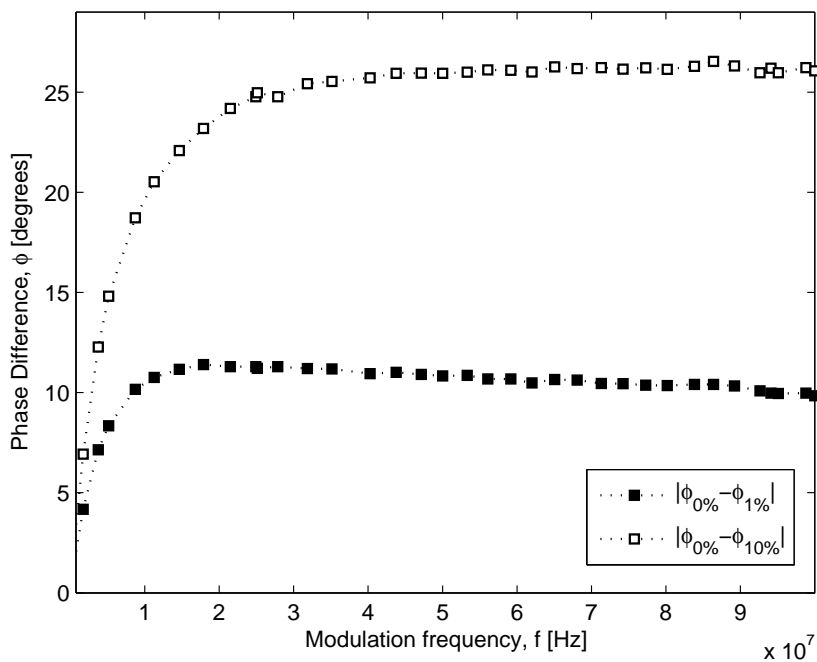


(a) PtTFPP-AP200/19

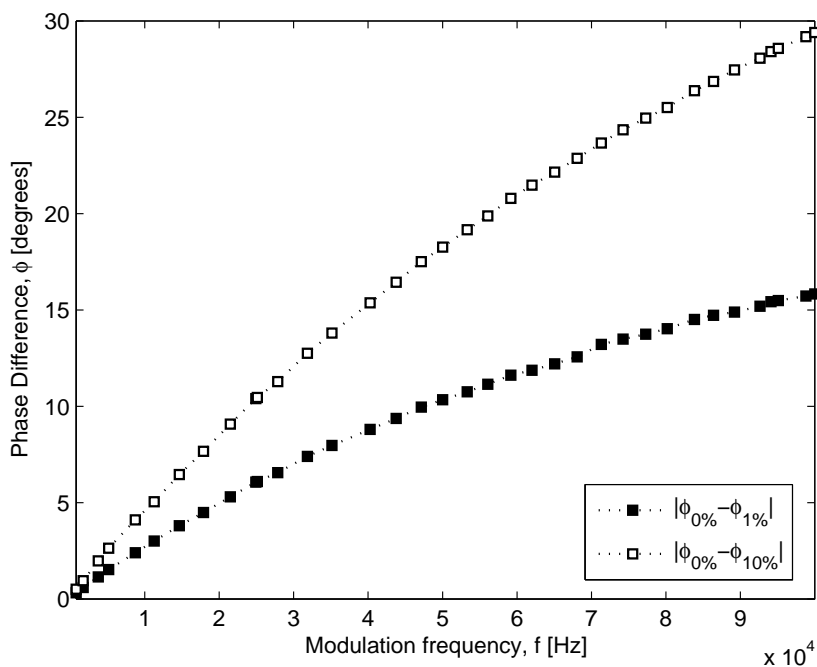


(b) N969-AP200/19

Fig. ESI-4. Effect of the modulation frequency on the phase difference at several oxygen concentrations (■ from 0 to 1% O₂ and □ from 0 to 10% O₂) for (a) PtTFPP, (b) N969, (c) N1008 and (d) EB146 incorporated into AP200/19 using a multifrequency phase-resolved method (see reference [10] of the ESI). See Table ESI-1 for the data.

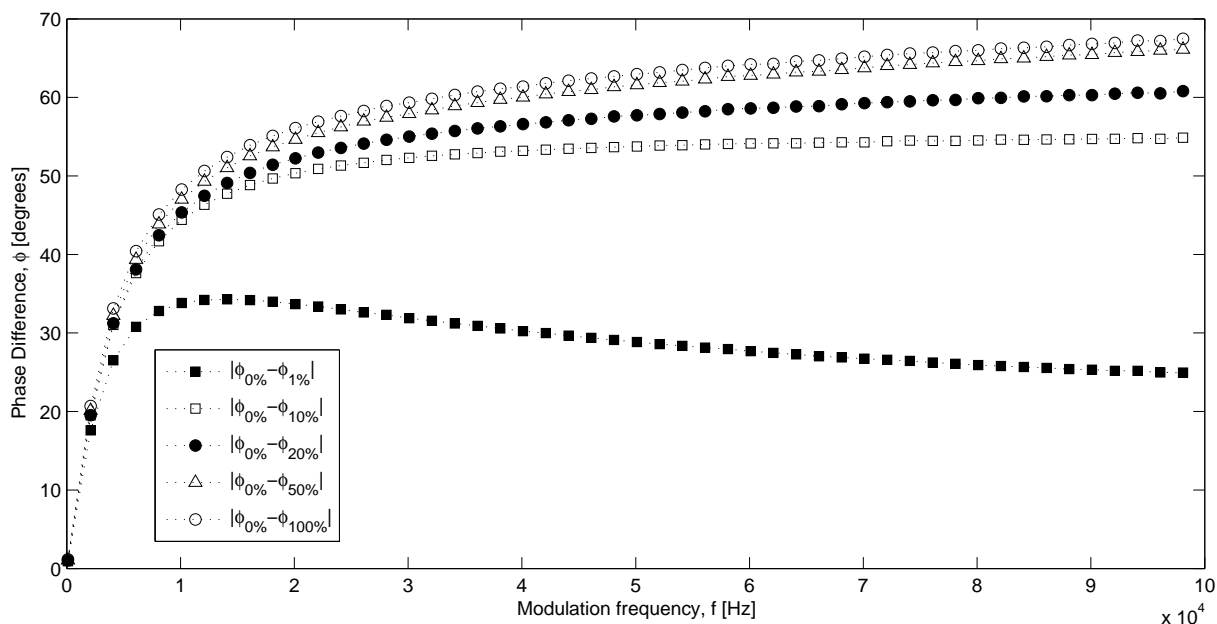


(c) N1008-AP200/19

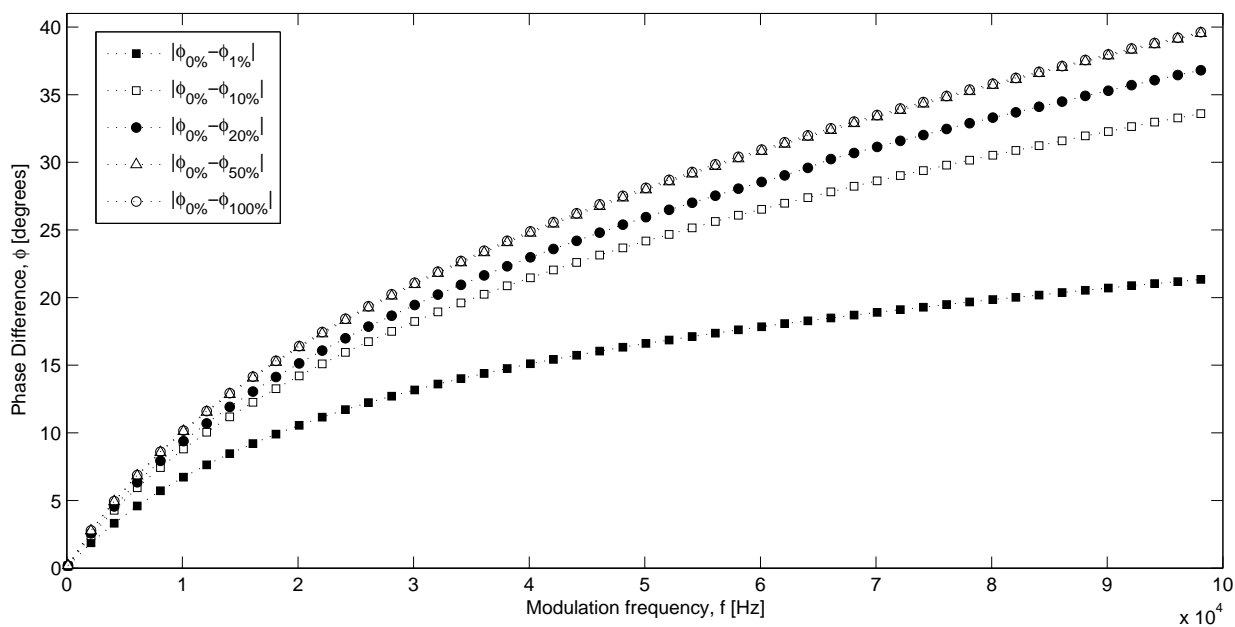


(d) EB146-AP200/19

Fig. ESI-4 (Cont.). Effect of the modulation frequency on the phase difference at several oxygen concentrations (■ from 0 to 1% O₂ and □ from 0 to 10% O₂) for (a) PtTFPP, (b) N969, (c) N1008 and (d) EB146 incorporated into AP200/19 using a multifrequency phase-resolved method (see reference [10] of the ESI). See Table ESI-1 for the data.

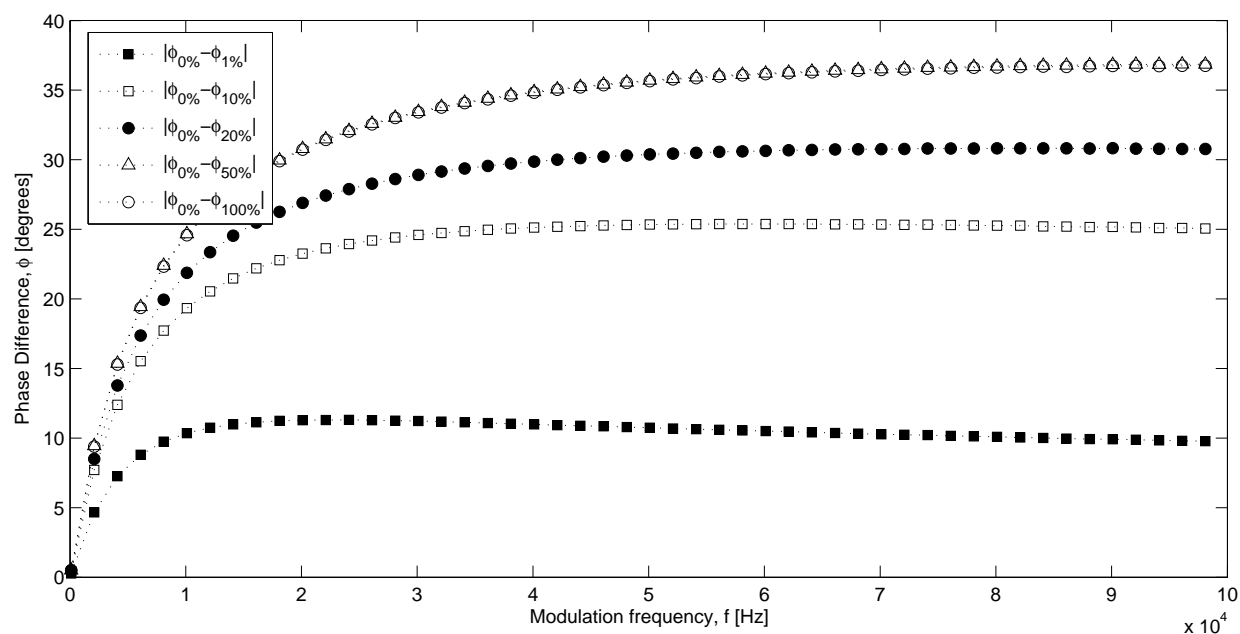


(a) PtTFPP-AP200/19

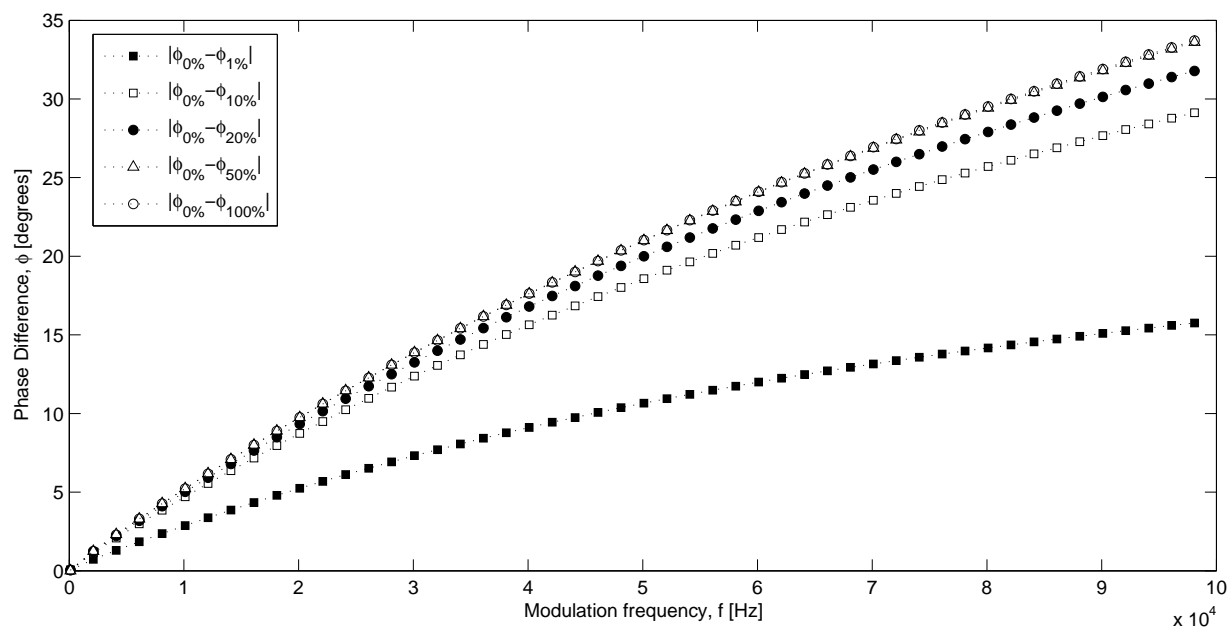


(b) N969-AP200/19

Fig. ESI-5. Effect of the modulation frequency on the phase difference at several oxygen concentrations (■ from 0 to 1% O₂, □ from 0 to 10% O₂, ● from 0 to 20% O₂, △ from 0 to 50% O₂, ○ from 0 to 100% O₂) for (a) PtTFPP, (b) N969, (c) N1008 and (d) EB146 incorporated into AP200/19 measured with the setup described in Fig. ESI-2. See Tables ESI-2 to ESI-5 for the data.

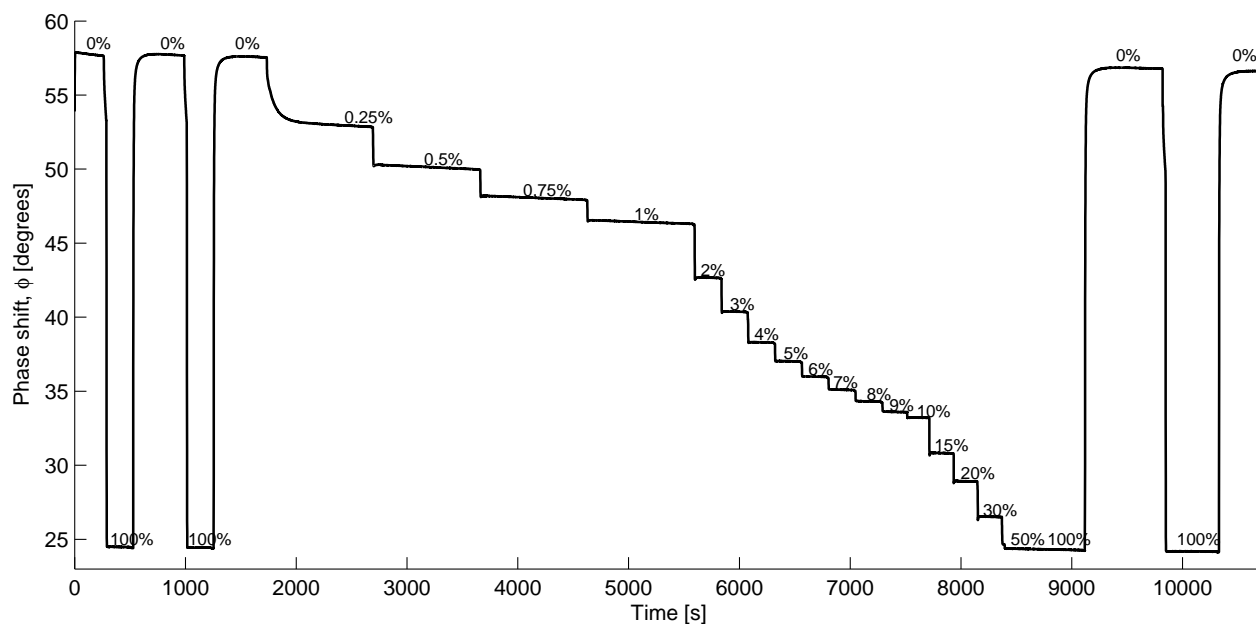


(c) N1008-AP200/19

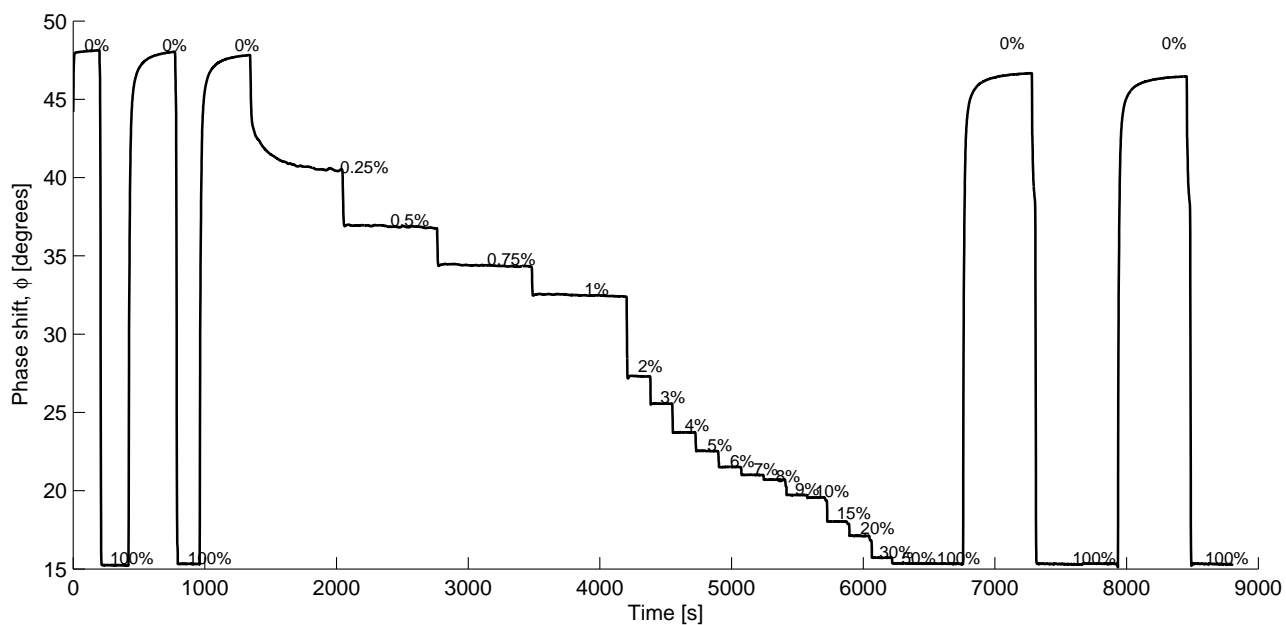


(d) EB146-AP200/19

Fig. ESI-5 (Cont.). Effect of the modulation frequency on the phase difference at several oxygen concentrations (■ from 0 to 1% O₂, □ from 0 to 10% O₂, ● from 0 to 20% O₂, △ from 0 to 50% O₂, ○ from 0 to 100% O₂) for (a) PtTFPP, (b) N969, (c) N1008 and (d) EB146 incorporated into AP200/19 measured with the setup described in Fig. ESI-2. See Tables ESI-2 to ESI-5 for the data.

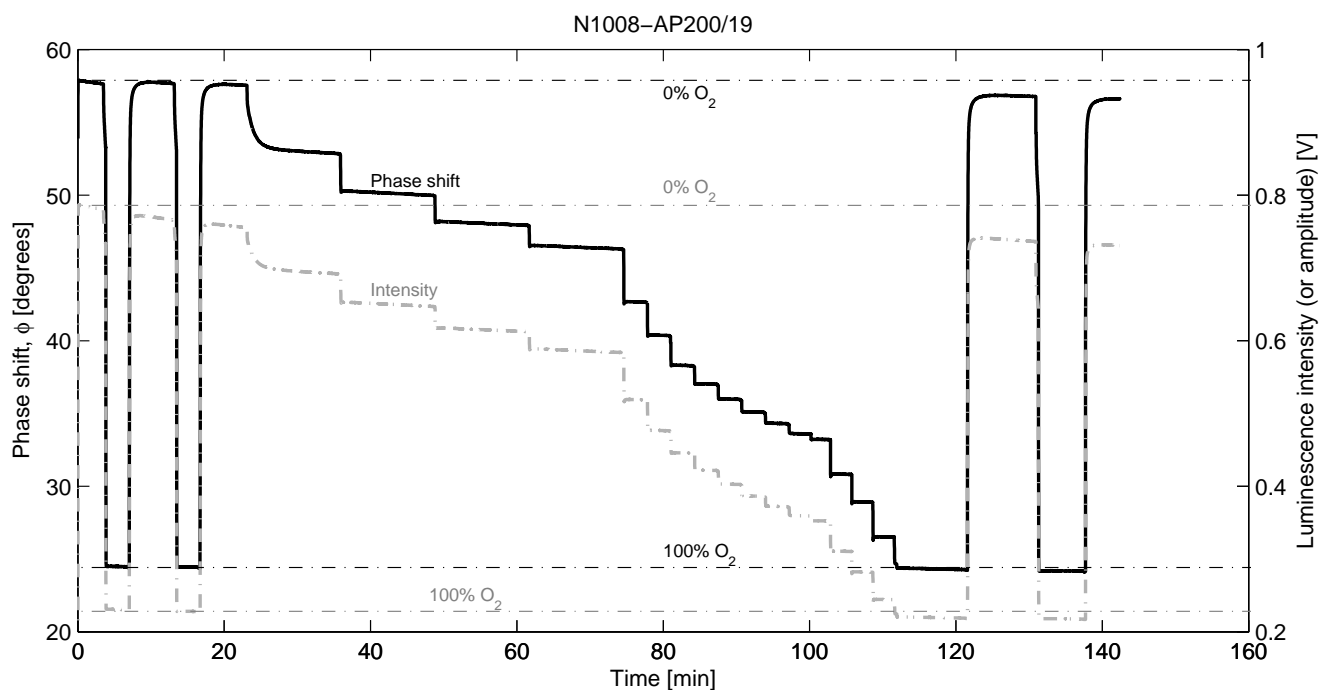


(a) N1008-AP200/19

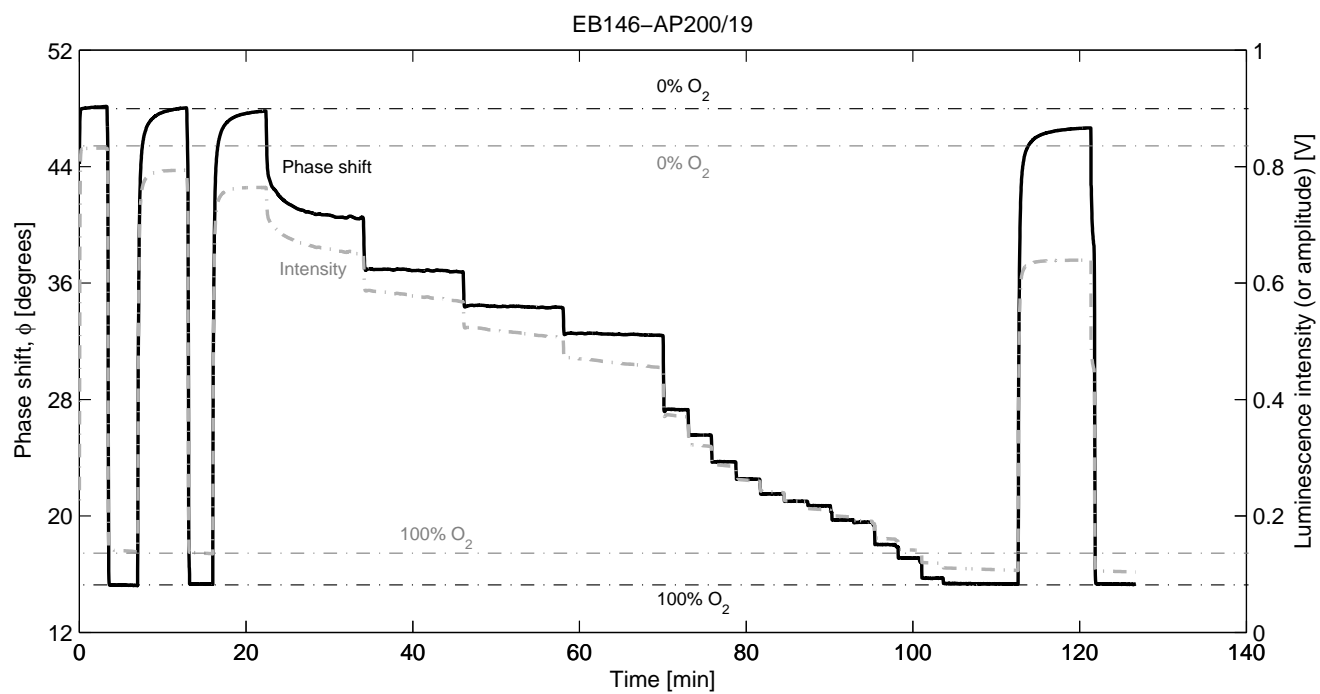


(b) EB146-AP200/19

Fig. ESI-6. Variation of the phase shift of (a) N1008 and (b) EB146 incorporated into AP200/19 with the oxygen concentration.



(a) N1008-AP200/19



(b) EB146-AP200/19

Fig. ESI-7. Stability of the phase shift (dark solid line) and amplitude (light dotted line) of (a) N1008 and (b) EB146 incorporated into AP200/19 at 21 °C.

Table ESI-1. Average phase differences ($|\phi_{0\% O_2} - \phi_{x\% O_2}|$) in degrees for several oxygen concentrations at different modulation frequencies obtained with the multifrequency phase-resolved method reported in the reference [10] of the ESI. All the values correspond to the average of 20 phase-shift measurements.

Freq. (Hz)	PtTFPP-AP200/19		N1008-AP200/19		N969-AP200/19		EB146-AP200/19	
	$ \phi_{0\%-1\% O_2} $	$ \phi_{0\%-10\% O_2} $	$ \phi_{0\%-1\% O_2} $	$ \phi_{0\%-10\% O_2} $	$ \phi_{0\%-1\% O_2} $	$ \phi_{0\%-10\% O_2} $	$ \phi_{0\%-1\% O_2} $	$ \phi_{0\%-10\% O_2} $
769	7.78	8.29	2.06	3.41	0.77	1.02	0.32	0.50
1709	17.60	19.50	4.17	6.92	1.67	2.19	0.59	0.94
3761	26.52	31.02	7.14	12.27	3.45	4.55	1.14	1.97
5145	30.77	37.62	8.34	14.80	4.48	5.89	1.52	2.63
8713	32.80	41.69	10.15	18.72	6.71	8.91	2.40	4.10
11257	34.20	45.43	10.75	20.52	8.06	10.78	3.00	5.04
14639	34.20	46.63	11.16	22.08	9.57	12.93	3.79	6.45
17881	34.27	48.23	11.39	23.18	10.82	14.72	4.48	7.66
21499	33.97	49.66	11.29	24.18	12.12	16.55	5.29	9.06
24917	33.68	50.34	11.29	24.77	13.12	18.07	6.06	10.39
25111	33.36	50.90	11.21	24.96	13.15	18.15	6.09	10.45
27847	32.99	51.32	11.29	24.77	13.77	19.46	6.55	11.27
31849	32.61	51.67	11.20	25.42	14.68	20.55	7.39	12.75
35129	31.89	52.31	11.18	25.53	15.32	21.55	7.96	13.80
40277	31.20	52.74	10.94	25.71	16.17	23.06	8.79	15.36
43777	30.23	53.20	11.01	25.93	16.69	23.98	9.36	16.43
47143	29.98	53.33	10.90	25.94	17.22	24.88	9.95	17.50
50023	29.37	53.55	10.82	25.94	17.56	25.47	10.33	18.25
53309	28.83	53.74	10.85	25.99	17.91	26.24	10.74	19.15
56087	28.35	53.91	10.68	26.11	18.21	26.82	11.14	19.87
59183	28.12	54.01	10.68	26.08	18.52	27.54	11.61	20.78
62011	27.94	54.06	10.48	26.00	18.81	27.99	11.86	21.48
65071	27.45	54.16	10.65	26.26	19.08	28.54	12.20	22.14
68071	27.03	54.24	10.62	26.17	19.30	29.06	12.56	22.86
71327	26.89	54.27	10.45	26.22	19.63	29.61	13.21	23.66
74257	26.59	54.42	10.44	26.14	19.84	30.15	13.48	24.34
77291	26.43	54.50	10.37	26.20	20.11	30.68	13.74	24.95
80191	26.06	54.46	10.34	26.13	20.19	31.02	14.02	25.50
83843	25.91	54.51	10.40	26.28	20.48	31.64	14.50	26.37
86413	25.65	54.61	10.43	26.53	20.62	32.04	14.71	26.85
89231	25.53	54.65	10.33	26.30	20.77	32.40	14.88	27.45
92647	25.31	54.69	10.08	25.96	21.01	32.91	15.18	28.06
94111	25.17	54.72	9.96	26.19	21.03	32.97	15.43	28.40
95101	25.16	54.79	9.95	25.96	21.10	33.20	15.48	28.56
98809	24.97	54.73	9.97	26.21	21.34	33.66	15.72	29.17
99991	24.95	54.86	9.83	26.06	21.34	33.75	15.83	29.39

Table ESI-2. Average phase differences ($|\phi_{0\% O_2} - \phi_{x\% O_2}|$) for several oxygen concentrations at different modulation frequencies obtained for PtTFPP immobilized into AP200/19 measured with the setup described in Fig. ESI-2. All the values correspond to the average of 100 phase-shift measurements.

Freq. (Hz)	$ \phi_{0\% O_2} - \phi_{x\% O_2} $ (degrees)					Freq. (Hz)	$ \phi_{0\% O_2} - \phi_{x\% O_2} $ (degrees)				
	$x = 1\% O_2$	$x = 10\% O_2$	$x = 20\% O_2$	$x = 50\% O_2$	$x = 100\% O_2$		$x = 1\% O_2$	$x = 10\% O_2$	$x = 20\% O_2$	$x = 50\% O_2$	$x = 100\% O_2$
100	0.953	0.952	1.019	1.070	1.173	50100	28.836	53.745	57.715	61.603	62.955
2100	17.606	19.506	19.524	20.133	20.697	52100	28.585	53.864	57.880	61.869	63.191
4100	26.527	31.028	31.236	32.232	33.129	54100	28.356	53.912	58.061	62.066	63.483
6100	30.775	37.629	38.087	39.356	40.419	56100	28.126	54.011	58.235	62.333	63.746
8100	32.803	41.691	42.438	43.860	45.081	58100	27.942	54.068	58.493	62.645	64.025
10100	33.810	44.418	45.360	47.019	48.264	60100	27.688	54.143	58.594	62.793	64.210
12100	34.206	46.339	47.479	49.301	50.636	62100	27.458	54.164	58.674	62.963	64.268
14100	34.277	47.738	49.104	51.042	52.409	64100	27.272	54.155	58.841	63.222	64.582
16100	34.178	48.844	50.381	52.545	53.917	66100	27.034	54.241	58.886	63.329	64.705
18100	33.976	49.663	51.418	53.689	55.084	68100	26.895	54.276	59.133	63.537	64.934
20100	33.685	50.346	52.238	54.651	56.099	70100	26.718	54.283	59.272	63.759	65.189
22100	33.367	50.902	52.969	55.493	56.910	72100	26.593	54.426	59.383	64.036	65.400
24100	32.999	51.327	53.561	56.232	57.625	74100	26.434	54.503	59.498	64.188	65.585
26100	32.618	51.673	54.107	56.958	58.273	76100	26.227	54.462	59.627	64.387	65.719
28100	32.301	52.040	54.601	57.451	58.906	78100	26.064	54.467	59.670	64.548	65.889
30100	31.890	52.311	55.002	57.935	59.329	80100	25.914	54.517	59.903	64.661	66.001
32100	31.552	52.556	55.387	58.403	59.817	82100	25.791	54.625	59.948	64.910	66.224
34100	31.203	52.749	55.726	58.933	60.312	84100	25.659	54.612	60.130	64.988	66.311
36100	30.894	52.922	56.042	59.325	60.740	86100	25.539	54.652	60.149	65.197	66.443
38100	30.571	53.090	56.312	59.729	61.100	88100	25.392	54.668	60.295	65.374	66.668
40100	30.232	53.207	56.603	60.020	61.362	90100	25.314	54.697	60.298	65.450	66.804
42100	29.984	53.331	56.835	60.431	61.795	92100	25.179	54.727	60.470	65.704	66.939
44100	29.662	53.454	57.098	60.727	62.118	94100	25.169	54.799	60.593	65.833	67.230
46100	29.373	53.554	57.279	60.976	62.399	96100	24.972	54.731	60.518	65.989	67.167
48100	29.106	53.672	57.575	61.355	62.677	98100	24.951	54.867	60.804	66.113	67.461

Table ESI-3. Average phase differences ($|\phi_{0\% O_2} - \phi_{x\% O_2}|$) for several oxygen concentrations at different modulation frequencies obtained for N969 immobilized into AP200/19 measured with the setup described in Fig. ESI-2. All the values correspond to the average of 100 phase-shift measurements.

Freq. (Hz)	$ \phi_{0\% O_2} - \phi_{x\% O_2} $ (degrees)					Freq. (Hz)	$ \phi_{0\% O_2} - \phi_{x\% O_2} $ (degrees)				
	$x = 1\% O_2$	$x = 10\% O_2$	$x = 20\% O_2$	$x = 50\% O_2$	$x = 100\% O_2$		$x = 1\% O_2$	$x = 10\% O_2$	$x = 20\% O_2$	$x = 50\% O_2$	$x = 100\% O_2$
100	0.135	0.168	0.181	0.189	0.183	50100	16.612	24.190	25.948	27.987	28.116
2100	1.874	2.394	2.570	2.764	2.782	52100	16.868	24.667	26.487	28.569	28.709
4100	3.321	4.272	4.565	4.925	4.950	54100	17.125	25.155	27.014	29.155	29.283
6100	4.592	5.941	6.347	6.836	6.880	56100	17.366	25.629	27.538	29.704	29.845
8100	5.718	7.439	7.936	8.553	8.605	58100	17.616	26.091	28.054	30.276	30.408
10100	6.729	8.803	9.388	10.116	10.170	60100	17.849	26.532	28.550	30.815	30.934
12100	7.636	10.047	10.700	11.536	11.605	62100	18.076	26.971	29.035	31.351	31.480
14100	8.460	11.189	11.919	12.852	12.934	64100	18.285	27.386	29.586	31.871	31.995
16100	9.213	12.260	13.057	14.069	14.158	66100	18.495	27.818	30.236	32.368	32.512
18100	9.912	13.272	14.133	15.235	15.327	68100	18.710	28.229	30.692	32.883	33.013
20100	10.561	14.210	15.133	16.319	16.415	70100	18.910	28.629	31.146	33.381	33.499
22100	11.157	15.100	16.084	17.336	17.449	72100	19.109	29.022	31.595	33.851	33.978
24100	11.714	15.951	16.995	18.325	18.434	74100	19.293	29.394	32.016	34.328	34.447
26100	12.232	16.744	17.855	19.250	19.362	76100	19.487	29.786	32.468	34.800	34.906
28100	12.711	17.502	18.663	20.128	20.242	78100	19.683	30.161	32.890	35.243	35.370
30100	13.169	18.238	19.456	20.984	21.094	80100	19.850	30.531	33.304	35.707	35.817
32100	13.605	18.941	20.222	21.809	21.919	82100	20.022	30.877	33.696	36.130	36.244
34100	14.013	19.601	20.942	22.590	22.700	84100	20.190	31.238	34.104	36.580	36.690
36100	14.391	20.248	21.635	23.335	23.458	86100	20.373	31.591	34.493	37.031	37.116
38100	14.756	20.875	22.318	24.077	24.193	88100	20.546	31.951	34.915	37.454	37.563
40100	15.107	21.468	22.972	24.773	24.890	90100	20.712	32.277	35.294	37.878	37.975
42100	15.427	22.043	23.597	25.445	25.579	92100	20.878	32.637	35.712	38.304	38.413
44100	15.733	22.602	24.201	26.112	26.235	94100	21.033	32.972	36.077	38.711	38.823
46100	16.046	23.148	24.798	26.751	26.888	96100	21.184	33.279	36.446	39.119	39.209
48100	16.328	23.678	25.391	27.384	27.517	98100	21.342	33.595	36.804	39.533	39.620

Table ESI-4. Average phase differences ($|\phi_{0\% O_2} - \phi_{x\% O_2}|$) for several oxygen concentrations at different modulation frequencies obtained for N1008 immobilized into AP200/19 measured with the setup described in Fig. ESI-2. All the values correspond to the average of 100 phase-shift measurements.

Freq. (Hz)	$ \phi_{0\% O_2} - \phi_{x\% O_2} $ (degrees)					Freq. (Hz)	$ \phi_{0\% O_2} - \phi_{x\% O_2} $ (degrees)				
	$x = 1\% O_2$	$x = 10\% O_2$	$x = 20\% O_2$	$x = 50\% O_2$	$x = 100\% O_2$		$x = 1\% O_2$	$x = 10\% O_2$	$x = 20\% O_2$	$x = 50\% O_2$	$x = 100\% O_2$
100	0.271	0.428	0.471	0.508	0.507	50100	10.747	25.343	30.383	35.707	35.649
2100	4.667	7.703	8.507	9.448	9.389	52100	10.688	25.355	30.442	35.815	35.770
4100	7.258	12.394	13.784	15.361	15.289	54100	10.640	25.368	30.498	35.930	35.868
6100	8.797	15.522	17.369	19.438	19.359	56100	10.595	25.383	30.567	36.037	35.983
8100	9.747	17.720	19.944	22.405	22.321	58100	10.543	25.384	30.603	36.118	36.066
10100	10.354	19.330	21.871	24.665	24.580	60100	10.502	25.379	30.640	36.212	36.150
12100	10.739	20.538	23.361	26.424	26.344	62100	10.463	25.382	30.676	36.277	36.228
14100	10.991	21.470	24.538	27.849	27.772	64100	10.415	25.378	30.705	36.352	36.277
16100	11.141	22.197	25.481	29.005	28.931	66100	10.366	25.361	30.737	36.414	36.355
18100	11.235	22.780	26.250	29.973	29.899	68100	10.318	25.352	30.748	36.465	36.394
20100	11.283	23.249	26.898	30.794	30.730	70100	10.276	25.343	30.766	36.526	36.455
22100	11.301	23.628	27.427	31.481	31.426	72100	10.239	25.323	30.775	36.563	36.489
24100	11.305	23.940	27.888	32.085	32.023	74100	10.215	25.331	30.812	36.622	36.548
26100	11.287	24.201	28.283	32.596	32.545	76100	10.162	25.308	30.807	36.643	36.573
28100	11.255	24.410	28.611	33.043	33.000	78100	10.124	25.280	30.809	36.684	36.611
30100	11.223	24.596	28.905	33.455	33.403	80100	10.090	25.269	30.817	36.718	36.622
32100	11.180	24.739	29.150	33.803	33.747	82100	10.043	25.261	30.824	36.750	36.662
34100	11.131	24.859	29.365	34.117	34.068	84100	10.009	25.213	30.818	36.772	36.689
36100	11.079	24.963	29.555	34.404	34.341	86100	9.965	25.197	30.822	36.782	36.672
38100	11.032	25.064	29.726	34.652	34.605	88100	9.922	25.166	30.811	36.811	36.713
40100	10.987	25.130	29.869	34.883	34.824	90100	9.911	25.168	30.830	36.830	36.738
42100	10.932	25.185	30.000	35.071	35.029	92100	9.884	25.136	30.799	36.854	36.737
44100	10.886	25.236	30.115	35.246	35.204	94100	9.833	25.098	30.781	36.844	36.731
46100	10.843	25.281	30.215	35.421	35.366	96100	9.800	25.091	30.776	36.863	36.750
48100	10.790	25.314	30.306	35.568	35.519	98100	9.779	25.057	30.770	36.859	36.748

Table ESI-5. Average phase differences ($|\phi_{0\% O_2} - \phi_{x\% O_2}|$) for several oxygen concentrations at different modulation frequencies obtained for EB146 immobilized into AP200/19 measured with the setup described in Fig. ESI-2. All the values correspond to the average of 100 phase-shift measurements.

Freq. (Hz)	$ \phi_{0\% O_2} - \phi_{x\% O_2} $ (degrees)					Freq. (Hz)	$ \phi_{0\% O_2} - \phi_{x\% O_2} $ (degrees)				
	$x = 1\% O_2$	$x = 10\% O_2$	$x = 20\% O_2$	$x = 50\% O_2$	$x = 100\% O_2$		$x = 1\% O_2$	$x = 10\% O_2$	$x = 20\% O_2$	$x = 50\% O_2$	$x = 100\% O_2$
100	0.038	0.051	0.051	0.005	0.035	50100	10.662	18.571	19.996	21.003	21.029
2100	0.727	1.140	1.211	1.244	1.241	52100	10.938	19.115	20.596	21.643	21.657
4100	1.297	2.080	2.210	2.312	2.289	54100	11.214	19.646	21.191	22.268	22.293
6100	1.842	2.982	3.176	3.297	3.304	56100	11.485	20.176	21.768	22.870	22.912
8100	2.363	3.854	4.104	4.273	4.267	58100	11.736	20.695	22.328	23.467	23.517
10100	2.871	4.709	5.019	5.236	5.220	60100	11.996	21.192	22.890	24.073	24.102
12100	3.371	5.546	5.913	6.182	6.157	62100	12.247	21.693	23.439	24.672	24.713
14100	3.857	6.365	6.788	7.082	7.088	64100	12.482	22.175	23.983	25.235	25.268
16100	4.335	7.172	7.649	8.000	7.988	66100	12.712	22.638	24.493	25.778	25.838
18100	4.793	7.961	8.499	8.896	8.883	68100	12.939	23.109	25.017	26.338	26.379
20100	5.245	8.737	9.339	9.751	9.750	70100	13.152	23.561	25.517	26.871	26.933
22100	5.686	9.491	10.147	10.619	10.608	72100	13.367	23.999	26.005	27.400	27.457
24100	6.116	10.243	10.947	11.461	11.445	74100	13.576	24.434	26.489	27.918	28.006
26100	6.517	10.963	11.733	12.273	12.270	76100	13.784	24.868	26.978	28.443	28.506
28100	6.920	11.678	12.495	13.087	13.087	78100	13.975	25.293	27.445	28.939	29.015
30100	7.316	12.379	13.254	13.883	13.873	80100	14.165	25.705	27.904	29.424	29.520
32100	7.695	13.061	13.991	14.650	14.647	82100	14.366	26.107	28.368	29.930	29.994
34100	8.065	13.735	14.711	15.413	15.415	84100	14.557	26.513	28.822	30.415	30.492
36100	8.429	14.386	15.428	16.172	16.169	86100	14.738	26.899	29.261	30.879	30.971
38100	8.777	15.025	16.124	16.892	16.907	88100	14.910	27.287	29.705	31.351	31.432
40100	9.113	15.646	16.803	17.617	17.623	90100	15.096	27.672	30.133	31.809	31.904
42100	9.443	16.254	17.470	18.313	18.338	92100	15.265	28.052	30.566	32.276	32.360
44100	9.747	16.842	18.109	19.010	18.999	94100	15.432	28.415	30.971	32.734	32.824
46100	10.064	17.438	18.764	19.694	19.690	96100	15.599	28.782	31.389	33.183	33.273
48100	10.373	18.012	19.386	20.352	20.370	98100	15.751	29.126	31.784	33.609	33.715

Table ESI-6. Phase-shift measurements for different oxygen concentrations of PtTFPP immobilized into AP200/19 in triplicate at 21 °C. Modulation frequency of 40100 Hz.

pO_2 (%)	Replica 1		Replica 2		Replica 3		Average results		$\frac{\bar{\phi}_{avg,0}}{\bar{\phi}_{avg,x}}$ ^e	Phase difference ($\bar{\phi}_{0\% pO_2} - \bar{\phi}_{x\% pO_2}$)				
	mean ^a (°)	sdev ^b (°)	mean ^a (°)	sdev ^b (°)	mean ^a (°)	sdev ^b (°)	mean ^c (°)	sdev ^d (°)		Rep. 1 ^f (°)	Rep. 2 ^f (°)	Rep. 3 ^f (°)	mean ^g (°)	sdev ^h (°)
0.00	87.743	0.047	87.593	0.049	87.645	0.050	87.660	0.076	1.000	0.000	0.000	0.000	0.000	0.000
0.25	74.635	0.168	74.492	0.095	74.258	0.059	74.462	0.190	1.176	13.108	12.901	13.387	13.132	0.243
0.50	66.347	0.535	66.150	0.033	66.548	0.037	66.348	0.198	1.320	21.396	21.243	21.097	21.245	0.149
0.75	60.076	0.074	60.475	0.047	60.091	0.035	60.214	0.226	1.454	27.667	26.918	27.553	27.380	0.403
1	57.113	0.034	57.458	0.031	57.512	0.033	57.361	0.216	1.527	30.630	29.935	30.132	30.232	0.358
2	47.420	0.034	47.698	0.036	47.769	0.030	47.629	0.184	1.839	40.323	39.695	39.875	39.964	0.323
3	43.430	0.034	43.610	0.031	43.832	0.034	43.624	0.201	2.007	44.312	43.783	43.812	43.969	0.297
4	41.044	0.045	41.272	0.044	41.516	0.044	41.277	0.235	2.122	46.699	46.121	46.129	46.316	0.331
5	39.115	0.047	39.080	0.043	39.521	0.040	39.238	0.245	2.232	48.628	48.313	48.123	48.355	0.254
6	37.811	0.043	37.587	0.046	38.053	0.030	37.817	0.232	2.316	49.932	49.806	49.592	49.776	0.172
7	36.770	0.041	36.515	0.058	37.016	0.038	36.767	0.250	2.382	50.973	50.878	50.628	50.826	0.178
8	36.334	0.042	36.233	0.044	36.687	0.046	36.418	0.238	2.405	51.409	51.159	50.957	51.175	0.226
9	35.172	0.038	35.362	0.048	35.701	0.045	35.412	0.268	2.473	52.571	52.031	51.943	52.182	0.339
10	34.602	0.037	34.447	0.046	34.108	0.053	34.386	0.252	2.547	53.141	52.946	53.536	53.207	0.300
15	32.271	0.062	32.270	0.046	32.732	0.053	32.424	0.266	2.701	55.472	55.123	54.913	55.169	0.282
20	30.711	0.057	30.977	0.054	31.264	0.053	30.984	0.276	2.827	57.031	56.416	56.381	56.609	0.366
30	28.973	0.065	29.353	0.065	29.518	0.076	29.281	0.279	2.991	58.770	58.040	58.126	58.312	0.398
50	27.339	0.053	27.552	0.074	27.854	0.076	27.581	0.258	3.175	60.404	59.841	59.790	60.012	0.340
100	26.039	0.073	26.517	0.069	26.143	0.069	26.233	0.251	3.339	61.704	60.876	61.501	61.361	0.431

^aAverage (mean) of $N = 100$ phase-shift measurements (in degrees) calculated as: $\bar{\phi} = \frac{1}{N} \sum_{n=1}^N \phi_i$

^bStandard deviation (sdev) of $N = 100$ phase-shift measurements (in degrees) calculated as: $sdev = \frac{1}{N-1} \left(\sum_{n=1}^N (\phi_i - \bar{\phi})^2 \right)^{1/2}$

^cMean of the average phase-shift values ($\bar{\phi}$, in degrees) obtained for each replica, calculated as: $\bar{\phi}_{avg} = \frac{1}{N} \sum_{n=1}^{N=3} \bar{\phi}_i$

^dStandard deviation (sdev) of the average phase-shift values ($\bar{\phi}$, in degrees) obtained for each replica, calculated as: $sdev = \frac{1}{N-1} \left(\sum_{n=1}^{N=3} (\bar{\phi}_i - \bar{\phi}_{avg})^2 \right)^{1/2}$

^eRatio between the average phase-shift values ($\bar{\phi}_{avg}$) at 0% oxygen and any oxygen concentration (*i.e.*, $\bar{\phi}_{avg}(0\% pO_2) / \bar{\phi}_{avg}(x\% pO_2)$)

^fAverage phase difference (in degrees) between the average phase-shift values ($\bar{\phi}_i$) at 0% oxygen and any oxygen concentration (*i.e.*, $\bar{\phi}_i(0\% pO_2) - \bar{\phi}_i(x\% pO_2)$)

^gAverage (mean) of the 3 average phase-difference values obtained for each replica (in degrees)

^hStandard deviation (sdev) of the 3 average phase-difference values obtained for each replica (in degrees)

Table ESI-7. Luminescence lifetime measurements for different oxygen concentrations of PtTFPP immobilized into AP200/19 in triplicate at 21 °C. Modulation frequency of 40100 Hz.

pO_2 (%)	Replica 1		Replica 2		Replica 3		Average results		$\frac{\bar{\tau}_{avg,0}}{\bar{\tau}_{avg,x}}$ ^e	Lifetime difference ($\bar{\tau}_{0\% pO_2} - \bar{\tau}_{x\% pO_2}$)				
	mean ^a (μs)	sdev ^b (μs)	mean ^a (μs)	sdev ^b (μs)	mean ^a (μs)	sdev ^b (μs)	mean ^c (μs)	sdev ^d (μs)		Rep. 1 ^f (μs)	Rep. 2 ^f (μs)	Rep. 3 ^f (μs)	mean ^g (μs)	sdev ^h (μs)
0	100.779	2.132	94.493	1.965	96.493	2.009	97.255	3.211	1.000	0.000	0.000	0.000	0.000	0.000
0.25	14.446	0.166	14.304	0.092	14.080	0.055	14.277	0.184	6.812	86.333	80.189	82.412	82.978	3.111
0.5	9.066	0.231	8.978	0.014	9.148	0.016	9.064	0.085	10.729	91.713	85.515	87.344	88.191	3.184
0.75	6.895	0.020	7.008	0.013	6.899	0.010	6.934	0.063	14.024	93.884	87.485	89.593	90.321	3.260
1	6.138	0.008	6.220	0.007	6.233	0.008	6.197	0.051	15.693	94.641	88.273	90.260	91.058	3.258
2	4.319	0.005	4.361	0.005	4.372	0.004	4.351	0.028	22.351	96.460	90.132	92.120	92.904	3.236
3	3.757	0.004	3.780	0.004	3.810	0.004	3.782	0.026	25.709	97.022	90.713	92.682	93.472	3.228
4	3.455	0.005	3.483	0.005	3.513	0.005	3.484	0.028	27.913	97.324	91.010	92.979	93.771	3.230
5	3.227	0.005	3.223	0.005	3.274	0.004	3.241	0.028	30.002	97.552	91.270	93.218	94.014	3.215
6	3.079	0.004	3.055	0.005	3.106	0.003	3.080	0.025	31.570	97.699	91.438	93.386	94.175	3.204
7	2.965	0.004	2.938	0.006	2.992	0.004	2.965	0.027	32.793	97.813	91.555	93.500	94.289	3.203
8	2.919	0.004	2.908	0.004	2.957	0.005	2.928	0.025	33.213	97.860	91.585	93.536	94.327	3.211
9	2.796	0.003	2.816	0.005	2.852	0.004	2.821	0.028	34.464	97.982	91.677	93.641	94.433	3.226
10	2.738	0.003	2.722	0.004	2.688	0.005	2.716	0.025	35.804	98.041	91.771	93.805	94.539	3.198
15	2.506	0.006	2.506	0.004	2.551	0.005	2.521	0.025	38.575	98.273	91.987	93.942	94.734	3.216
20	2.357	0.005	2.382	0.005	2.409	0.005	2.383	0.026	40.805	98.422	92.111	94.083	94.872	3.228
30	2.197	0.006	2.232	0.006	2.247	0.007	2.225	0.025	43.697	98.582	92.261	94.245	95.029	3.232
50	2.052	0.004	2.070	0.006	2.097	0.006	2.073	0.022	46.907	98.727	92.423	94.395	95.182	3.225
100	1.939	0.006	1.980	0.006	1.948	0.006	1.955	0.021	49.725	98.840	92.513	94.545	95.299	3.230

^aAverage (mean) of $N = 100$ lifetime measurements (in microseconds) calculated as: $\bar{\tau} = \frac{1}{N} \sum_{n=1}^N \tau_i$

^bStandard deviation (sdev) of $N = 100$ lifetime measurements (in microseconds) calculated as: $sdev = \frac{1}{N-1} \left(\sum_{n=1}^N (\tau_i - \bar{\tau})^2 \right)^{1/2}$

^cMean of the average lifetime values ($\bar{\tau}$, in microseconds) obtained for each replica, calculated as: $\bar{\tau}_{avg} = \frac{1}{N} \sum_{n=1}^{N=3} \bar{\tau}_i$

^dStandard deviation (sdev) of the average lifetime values ($\bar{\tau}$, in microseconds) obtained for each replica, calculated as: $sdev = \frac{1}{N-1} \left(\sum_{n=1}^{N=3} (\bar{\tau}_i - \bar{\tau}_{avg})^2 \right)^{1/2}$

^eRatio between the average lifetime values ($\bar{\tau}_{avg}$) at 0% oxygen and any oxygen concentration (*i.e.*, $\bar{\tau}_{avg}(0\% pO_2) / \bar{\tau}_{avg}(x\% pO_2)$)

^fAverage lifetime difference (in microseconds) between the average lifetime values ($\bar{\tau}_i$) at 0% oxygen and any oxygen concentration (*i.e.*,

$\bar{\tau}_i(0\% pO_2) - \bar{\tau}_i(x\% pO_2)$)

^gAverage (mean) of the 3 average lifetime-difference values obtained for each replica (in microseconds)

^hStandard deviation (sdev) of the 3 average lifetime-difference values obtained for each replica (in microseconds)

Table ESI-8. Phase-shift measurements for different oxygen concentrations of N969 immobilized into AP200/19 in triplicate at 21 °C. Modulation frequency of 94100 Hz.

pO_2 (%)	Replica 1		Replica 2		Replica 3		Average results		$\frac{\bar{\phi}_{avg,0}}{\bar{\phi}_{avg,x}}^e$	Phase difference ($\bar{\phi}_{0\% pO_2} - \bar{\phi}_{x\% pO_2}$)				
	mean ^a (°)	sdev ^b (°)	mean ^a (°)	sdev ^b (°)	mean ^a (°)	sdev ^b (°)	mean ^c (°)	sdev ^d (°)		Rep. 1 ^f (°)	Rep. 2 ^f (°)	Rep. 3 ^f (°)	mean ^g (°)	sdev ^h (°)
0	65.642	0.018	65.608	0.020	65.829	0.018	65.693	0.119	1.000	0.000	0.000	0.000	0.000	0.000
0.25	53.126	0.029	52.820	0.023	53.179	0.060	53.041	0.193	1.238	12.516	12.787	12.650	12.651	0.135
0.5	49.111	0.006	48.706	0.004	48.894	0.006	48.903	0.202	1.343	16.531	16.902	16.935	16.789	0.224
0.75	46.608	0.004	46.249	0.006	46.427	0.005	46.428	0.179	1.414	19.033	19.359	19.402	19.265	0.201
1	44.801	0.008	44.489	0.004	44.691	0.006	44.660	0.158	1.470	20.841	21.119	21.137	21.032	0.166
2	40.355	0.007	40.402	0.006	40.698	0.006	40.485	0.186	1.622	25.287	25.205	25.130	25.207	0.078
3	38.167	0.005	38.140	0.005	38.510	0.005	38.273	0.206	1.716	27.475	27.467	27.319	27.420	0.087
4	36.555	0.006	36.633	0.006	36.940	0.006	36.709	0.203	1.789	29.087	28.974	28.889	28.983	0.099
5	35.565	0.005	35.527	0.008	35.954	0.006	35.682	0.236	1.841	30.077	30.081	29.875	30.011	0.117
6	34.932	0.005	34.666	0.006	35.096	0.007	34.898	0.217	1.882	30.710	30.941	30.733	30.795	0.127
7	34.260	0.007	33.955	0.008	34.377	0.008	34.197	0.218	1.921	31.382	31.653	31.451	31.495	0.140
8	33.602	0.007	33.355	0.006	33.762	0.007	33.573	0.205	1.956	32.040	32.253	32.066	32.120	0.115
9	33.011	0.007	32.820	0.007	33.203	0.006	33.011	0.191	1.990	32.631	32.788	32.626	32.682	0.092
10	32.703	0.008	32.552	0.008	32.918	0.004	32.724	0.183	2.007	32.939	33.055	32.911	32.968	0.076
15	30.762	0.008	30.792	0.008	31.020	0.007	30.858	0.141	2.128	34.880	34.815	34.809	34.835	0.039
20	29.470	0.007	29.651	0.007	29.729	0.008	29.616	0.132	2.218	36.172	35.957	36.100	36.076	0.109
30	27.775	0.006	28.145	0.009	28.030	0.007	27.983	0.189	2.347	37.867	37.462	37.799	37.709	0.217
50	26.755	0.008	27.162	0.009	27.027	0.007	26.981	0.207	2.434	38.886	38.445	38.802	38.711	0.234
100	26.637	0.008	27.073	0.010	26.912	0.008	26.874	0.220	2.444	39.005	38.534	38.917	38.819	0.250

^aAverage (mean) of $N = 100$ phase-shift measurements (in degrees) calculated as: $\bar{\phi} = \frac{1}{N} \sum_{n=1}^N \phi_i$

^bStandard deviation (sdev) of $N = 100$ phase-shift measurements (in degrees) calculated as: $sdev = \frac{1}{N-1} \left(\sum_{n=1}^N (\phi_i - \bar{\phi})^2 \right)^{1/2}$

^cMean of the average phase-shift values ($\bar{\phi}$, in degrees) obtained for each replica, calculated as: $\bar{\phi}_{avg} = \frac{1}{N} \sum_{n=1}^{N=3} \bar{\phi}_i$

^dStandard deviation (sdev) of the average phase-shift values ($\bar{\phi}$, in degrees) obtained for each replica, calculated as: $sdev = \frac{1}{N-1} \left(\sum_{n=1}^{N=3} (\bar{\phi}_i - \bar{\phi}_{avg})^2 \right)^{1/2}$

^eRatio between the average phase-shift values ($\bar{\phi}_{avg}$) at 0% oxygen and any oxygen concentration (*i.e.*, $\bar{\phi}_{avg}(0\% pO_2) / \bar{\phi}_{avg}(x\% pO_2)$)

^fAverage phase difference (in degrees) between the average phase-shift values ($\bar{\phi}_i$) at 0% oxygen and any oxygen concentration (*i.e.*, $\bar{\phi}_i(0\% pO_2) - \bar{\phi}_i(x\% pO_2)$)

^gAverage (mean) of the 3 average phase-difference values obtained for each replica (in degrees)

^hStandard deviation (sdev) of the 3 average phase-difference values obtained for each replica (in degrees)

Table ESI-9. Luminescence lifetime measurements for different oxygen concentrations of N969 immobilized into AP200/19 in triplicate at 21 °C. Modulation frequency of 94100 Hz.

pO_2 (%)	Replica 1		Replica 2		Replica 3		Average results		$\frac{\bar{\tau}_{avg,0}}{\bar{\tau}_{avg,x}}$ ^e	Lifetime difference ($\bar{\tau}_{0\% pO_2} - \bar{\tau}_{x\% pO_2}$)				
	mean ^a (μs)	sdev ^b (μs)	mean ^a (μs)	sdev ^b (μs)	mean ^a (μs)	sdev ^b (μs)	mean ^c (μs)	sdev ^d (μs)		Rep. 1 ^f (μs)	Rep. 2 ^f (μs)	Rep. 3 ^f (μs)	mean ^g (μs)	sdev ^h (μs)
0	3.735	0.003	3.730	0.003	3.768	0.003	3.744	0.020	1.000	0.000	0.000	0.000	0.000	0.000
0.25	2.254	0.002	2.229	0.001	2.259	0.004	2.247	0.015	1.665	1.481	1.500	1.509	1.496	0.014
0.5	1.953	0.001	1.925	0.001	1.938	0.001	1.939	0.013	1.931	1.782	1.804	1.830	1.805	0.023
0.75	1.789	0.001	1.766	0.001	1.777	0.001	1.777	0.011	2.106	1.946	1.963	1.990	1.967	0.022
1	1.679	0.001	1.661	0.001	1.673	0.001	1.671	0.009	2.240	2.056	2.068	2.095	2.073	0.020
2	1.437	0.001	1.439	0.001	1.454	0.001	1.443	0.009	2.593	2.298	2.290	2.313	2.301	0.011
3	1.329	0.001	1.328	0.001	1.345	0.001	1.334	0.009	2.806	2.406	2.401	2.422	2.410	0.011
4	1.254	0.001	1.257	0.001	1.271	0.001	1.261	0.009	2.969	2.481	2.472	2.496	2.483	0.012
5	1.209	0.001	1.207	0.001	1.226	0.001	1.214	0.010	3.083	2.526	2.522	2.541	2.530	0.010
6	1.181	0.001	1.169	0.001	1.188	0.001	1.179	0.009	3.174	2.554	2.560	2.580	2.565	0.013
7	1.152	0.001	1.138	0.001	1.157	0.001	1.149	0.009	3.258	2.583	2.591	2.611	2.595	0.014
8	1.123	0.001	1.113	0.001	1.130	0.001	1.122	0.008	3.335	2.612	2.616	2.637	2.622	0.013
9	1.098	0.001	1.090	0.001	1.106	0.001	1.098	0.008	3.407	2.637	2.639	2.661	2.646	0.013
10	1.086	0.001	1.079	0.001	1.094	0.001	1.086	0.007	3.445	2.650	2.650	2.673	2.658	0.013
15	1.006	0.001	1.007	0.001	1.017	0.001	1.010	0.005	3.705	2.729	2.722	2.751	2.734	0.015
20	0.955	0.001	0.962	0.001	0.965	0.001	0.961	0.005	3.894	2.780	2.767	2.802	2.783	0.018
30	0.890	0.001	0.904	0.001	0.900	0.001	0.898	0.007	4.167	2.845	2.825	2.868	2.846	0.021
50	0.852	0.001	0.867	0.001	0.862	0.001	0.861	0.007	4.348	2.883	2.862	2.905	2.883	0.021
100	0.848	0.001	0.864	0.001	0.858	0.001	0.857	0.008	4.369	2.887	2.865	2.910	2.887	0.022

^aAverage (mean) of $N = 100$ lifetime measurements (in microseconds) calculated as: $\bar{\tau} = \frac{1}{N} \sum_{n=1}^N \tau_i$

^bStandard deviation (sdev) of $N = 100$ lifetime measurements (in microseconds) calculated as: $sdev = \frac{1}{N-1} \left(\sum_{n=1}^N (\tau_i - \bar{\tau})^2 \right)^{1/2}$

^cMean of the average lifetime values ($\bar{\tau}$, in microseconds) obtained for each replica, calculated as: $\bar{\tau}_{avg} = \frac{1}{N} \sum_{n=1}^{N=3} \bar{\tau}_i$

^dStandard deviation (sdev) of the average lifetime values ($\bar{\tau}$, in microseconds) obtained for each replica, calculated as: $sdev = \frac{1}{N-1} \left(\sum_{n=1}^{N=3} (\bar{\tau}_i - \bar{\tau}_{avg})^2 \right)^{1/2}$

^eRatio between the average lifetime values ($\bar{\tau}_{avg}$) at 0% oxygen and any oxygen concentration (*i.e.*, $\bar{\tau}_{avg}(0\% pO_2) / \bar{\tau}_{avg}(x\% pO_2)$)

^fAverage lifetime difference (in microseconds) between the average lifetime values ($\bar{\tau}_i$) at 0% oxygen and any oxygen concentration (*i.e.*,

$\bar{\tau}_i(0\% pO_2) - \bar{\tau}_i(x\% pO_2)$)

^gAverage (mean) of the 3 average lifetime-difference values obtained for each replica (in microseconds)

^hStandard deviation (sdev) of the 3 average lifetime-difference values obtained for each replica (in microseconds)

Table ESI-10. Phase-shift measurements for different oxygen concentrations of N1008 immobilized into AP200/19 in triplicate at 21 °C. Modulation frequency of 30100 Hz.

pO_2 (%)	Replica 1		Replica 2		Replica 3		Average results		$\frac{\bar{\phi}_{avg,0}}{\bar{\phi}_{avg,x}}$ ^e	Phase difference ($\bar{\phi}_{0\% pO_2} - \bar{\phi}_{x\% pO_2}$)				
	mean ^a (°)	sdev ^b (°)	mean ^a (°)	sdev ^b (°)	mean ^a (°)	sdev ^b (°)	mean ^c (°)	sdev ^d (°)		Rep. 1 ^f (°)	Rep. 2 ^f (°)	Rep. 3 ^f (°)	mean ^g (°)	sdev ^h (°)
0	57.904	0.015	58.028	0.024	57.561	0.014	57.831	0.241	1.000	0.000	0.000	0.000	0.000	0.000
0.25	52.640	0.047	53.122	0.030	52.861	0.035	52.874	0.241	1.093	5.264	4.906	4.700	4.956	0.285
0.5	50.015	0.016	50.598	0.043	50.351	0.007	50.321	0.292	1.149	7.889	7.430	7.210	7.509	0.346
0.75	47.883	0.011	48.331	0.028	48.280	0.008	48.165	0.245	1.200	10.021	9.696	9.281	9.666	0.370
1	46.326	0.010	46.772	0.016	46.726	0.008	46.608	0.245	1.240	11.578	11.255	10.835	11.223	0.372
2	42.534	0.006	43.023	0.013	42.804	0.006	42.787	0.245	1.351	15.370	15.004	14.757	15.044	0.308
3	40.121	0.004	40.616	0.011	40.262	0.003	40.333	0.255	1.433	17.783	17.411	17.299	17.498	0.253
4	38.199	0.005	38.570	0.012	38.525	0.005	38.431	0.202	1.504	19.705	19.458	19.036	19.400	0.338
5	36.970	0.005	37.410	0.010	37.002	0.004	37.127	0.245	1.557	20.934	20.618	20.559	20.704	0.201
6	35.898	0.005	36.304	0.009	35.843	0.005	36.015	0.251	1.605	22.006	21.724	21.718	21.816	0.164
7	34.992	0.006	35.361	0.008	34.855	0.005	35.069	0.262	1.649	22.912	22.666	22.706	22.762	0.131
8	34.196	0.005	34.531	0.008	34.081	0.004	34.269	0.233	1.687	23.708	23.496	23.480	23.561	0.127
9	33.474	0.004	33.875	0.009	33.381	0.005	33.577	0.262	1.722	24.430	24.153	24.180	24.254	0.152
10	33.124	0.004	33.515	0.008	33.060	0.005	33.233	0.246	1.740	24.780	24.512	24.501	24.598	0.157
15	30.629	0.004	30.993	0.006	30.559	0.004	30.727	0.233	1.882	27.275	27.035	27.002	27.104	0.148
20	28.852	0.005	29.204	0.006	28.739	0.004	28.932	0.242	1.998	29.051	28.824	28.822	28.899	0.131
30	26.332	0.006	26.787	0.007	26.231	0.005	26.450	0.296	2.186	31.572	31.241	31.330	31.381	0.171
50	24.281	0.007	24.718	0.005	24.208	0.005	24.402	0.275	2.369	33.623	33.310	33.353	33.429	0.169
100	24.241	0.006	24.734	0.007	24.317	0.006	24.431	0.265	2.367	33.663	33.294	33.244	33.400	0.228

^aAverage (mean) of $N = 100$ phase-shift measurements (in degrees) calculated as: $\bar{\phi} = \frac{1}{N} \sum_{n=1}^N \phi_i$

^bStandard deviation (sdev) of $N = 100$ phase-shift measurements (in degrees) calculated as: $sdev = \frac{1}{N-1} \left(\sum_{n=1}^N (\phi_i - \bar{\phi})^2 \right)^{1/2}$

^cMean of the average phase-shift values ($\bar{\phi}$, in degrees) obtained for each replica, calculated as: $\bar{\phi}_{avg} = \frac{1}{N} \sum_{n=1}^{N=3} \bar{\phi}_i$

^dStandard deviation (sdev) of the average phase-shift values ($\bar{\phi}$, in degrees) obtained for each replica, calculated as: $sdev = \frac{1}{N-1} \left(\sum_{n=1}^{N=3} (\bar{\phi}_i - \bar{\phi}_{avg})^2 \right)^{1/2}$

^eRatio between the average phase-shift values ($\bar{\phi}_{avg}$) at 0% oxygen and any oxygen concentration (*i.e.*, $\bar{\phi}_{avg}(0\% pO_2) / \bar{\phi}_{avg}(x\% pO_2)$)

^fAverage phase difference (in degrees) between the average phase-shift values ($\bar{\phi}_i$) at 0% oxygen and any oxygen concentration (*i.e.*, $\bar{\phi}_i(0\% pO_2) - \bar{\phi}_i(x\% pO_2)$)

^gAverage (mean) of the 3 average phase-difference values obtained for each replica (in degrees)

^hStandard deviation (sdev) of the 3 average phase-difference values obtained for each replica (in degrees)

Table ESI-11. Luminescence lifetime measurements for different oxygen concentrations of N1008 immobilized into AP200/19 in triplicate at 21 °C. Modulation frequency of 30100 Hz.

pO_2 (%)	Replica 1		Replica 2		Replica 3		Average results		$\frac{\bar{\tau}_{avg,0}}{\bar{\tau}_{avg,x}}$ ^e	Lifetime difference ($\bar{\tau}_{0\% pO_2} - \bar{\tau}_{x\% pO_2}$)				
	mean ^a (μ s)	sdev ^b (μ s)	mean ^a (μ s)	sdev ^b (μ s)	mean ^a (μ s)	sdev ^b (μ s)	mean ^c (μ s)	sdev ^d (μ s)		Rep. 1 ^f (μ s)	Rep. 2 ^f (μ s)	Rep. 3 ^f (μ s)	mean ^g (μ s)	sdev ^h (μ s)
0	8.430	0.005	8.471	0.008	8.319	0.004	8.407	0.078	1.000	0.000	0.000	0.000	0.000	0.000
0.25	6.926	0.011	7.048	0.007	6.981	0.009	6.985	0.061	1.203	1.504	1.423	1.337	1.421	0.083
0.5	6.304	0.003	6.436	0.009	6.380	0.001	6.374	0.066	1.319	2.125	2.034	1.939	2.033	0.093
0.75	5.848	0.002	5.941	0.006	5.930	0.001	5.906	0.050	1.423	2.582	2.530	2.389	2.500	0.099
1	5.538	0.002	5.625	0.003	5.616	0.001	5.593	0.047	1.503	2.892	2.846	2.703	2.813	0.098
2	4.851	0.001	4.934	0.002	4.897	0.001	4.894	0.042	1.717	3.579	3.536	3.422	3.512	0.081
3	4.456	0.001	4.534	0.001	4.478	0.001	4.489	0.040	1.872	3.974	3.936	3.841	3.917	0.068
4	4.160	0.001	4.216	0.001	4.209	0.001	4.195	0.030	2.003	4.269	4.254	4.109	4.211	0.088
5	3.980	0.001	4.044	0.001	3.984	0.001	4.003	0.035	2.100	4.450	4.427	4.334	4.404	0.061
6	3.827	0.001	3.884	0.001	3.819	0.001	3.843	0.035	2.187	4.603	4.586	4.500	4.563	0.055
7	3.701	0.001	3.752	0.001	3.682	0.001	3.712	0.036	2.264	4.729	4.718	4.637	4.695	0.050
8	3.592	0.001	3.638	0.001	3.577	0.001	3.602	0.031	2.333	4.837	4.832	4.742	4.804	0.053
9	3.496	0.001	3.549	0.001	3.484	0.001	3.510	0.035	2.395	4.934	4.921	4.835	4.897	0.053
10	3.450	0.001	3.501	0.001	3.441	0.001	3.464	0.032	2.426	4.980	4.969	4.877	4.942	0.056
15	3.130	0.001	3.176	0.001	3.122	0.001	3.143	0.029	2.674	5.299	5.295	5.197	5.264	0.057
20	2.913	0.001	2.955	0.001	2.899	0.001	2.922	0.029	2.876	5.517	5.515	5.420	5.484	0.055
30	2.617	0.001	2.669	0.001	2.605	0.001	2.630	0.034	3.195	5.813	5.801	5.714	5.776	0.054
50	2.385	0.001	2.434	0.001	2.377	0.001	2.398	0.030	3.504	6.045	6.037	5.942	6.008	0.057
100	2.380	0.001	2.435	0.001	2.389	0.001	2.402	0.029	3.500	6.049	6.035	5.930	6.005	0.065

^aAverage (mean) of $N = 100$ lifetime measurements (in microseconds) calculated as: $\bar{\tau} = \frac{1}{N} \sum_{n=1}^N \tau_i$

^bStandard deviation (sdev) of $N = 100$ lifetime measurements (in microseconds) calculated as: $sdev = \frac{1}{N-1} \left(\sum_{n=1}^N (\tau_i - \bar{\tau})^2 \right)^{1/2}$

^cMean of the average lifetime values ($\bar{\tau}$, in microseconds) obtained for each replica, calculated as: $\bar{\tau}_{avg} = \frac{1}{N} \sum_{n=1}^{N=3} \bar{\tau}_i$

^dStandard deviation (sdev) of the average lifetime values ($\bar{\tau}$, in microseconds) obtained for each replica, calculated as: $sdev = \frac{1}{N-1} \left(\sum_{n=1}^{N=3} (\bar{\tau}_i - \bar{\tau}_{avg})^2 \right)^{1/2}$

^eRatio between the average lifetime values ($\bar{\tau}_{avg}$) at 0% oxygen and any oxygen concentration (*i.e.*, $\bar{\tau}_{avg}(0\% pO_2) / \bar{\tau}_{avg}(x\% pO_2)$)

^fAverage lifetime difference (in microseconds) between the average lifetime values ($\bar{\tau}_i$) at 0% oxygen and any oxygen concentration (*i.e.*,

$\bar{\tau}_i(0\% pO_2) - \bar{\tau}_i(x\% pO_2)$)

^gAverage (mean) of the 3 average lifetime-difference values obtained for each replica (in microseconds)

^hStandard deviation (sdev) of the 3 average lifetime-difference values obtained for each replica (in microseconds)

Table ESI-12. Phase-shift measurements for different oxygen concentrations of EB146 immobilized into AP200/19 in triplicate at 21 °C. Modulation frequency of 94100 Hz.

pO_2 (%)	Replica 1		Replica 2		Replica 3		Average results		$\frac{\bar{\phi}_{avg,0}}{\bar{\phi}_{avg,x}}^e$	Phase difference ($\bar{\phi}_{0\% pO_2} - \bar{\phi}_{x\% pO_2}$)				
	mean ^a (°)	sdev ^b (°)	mean ^a (°)	sdev ^b (°)	mean ^a (°)	sdev ^b (°)	mean ^c (°)	sdev ^d (°)		Rep. 1 ^f (°)	Rep. 2 ^f (°)	Rep. 3 ^f (°)	mean ^g (°)	sdev ^h (°)
0	48.090	0.012	48.004	0.014	48.144	0.013	48.079	0.070	1.000	0.000	0.000	0.000	0.000	0.000
0.25	40.483	0.033	41.013	0.039	40.616	0.020	40.704	0.275	1.181	7.606	6.991	7.528	7.375	0.335
0.5	36.641	0.019	37.035	0.016	36.546	0.005	36.741	0.259	1.308	11.449	10.969	11.598	11.338	0.328
0.75	34.303	0.015	34.769	0.020	34.389	0.007	34.487	0.248	1.394	13.786	13.234	13.755	13.592	0.310
1	32.621	0.009	32.905	0.012	32.425	0.004	32.651	0.241	1.472	15.468	15.098	15.719	15.428	0.312
2	27.651	0.008	27.423	0.010	27.094	0.005	27.389	0.280	1.755	20.438	20.580	21.050	20.690	0.320
3	25.326	0.005	25.844	0.006	25.513	0.006	25.561	0.262	1.880	22.764	22.160	22.631	22.518	0.317
4	23.493	0.006	24.036	0.006	23.739	0.005	23.756	0.271	2.023	24.596	23.968	24.405	24.323	0.322
5	22.553	0.008	22.788	0.005	22.372	0.007	22.571	0.208	2.130	25.537	25.216	25.772	25.508	0.279
6	21.490	0.007	21.818	0.004	21.384	0.006	21.564	0.226	2.229	26.599	26.186	26.760	26.515	0.296
7	21.108	0.005	21.221	0.006	20.685	0.007	21.005	0.282	2.288	26.981	26.783	27.459	27.074	0.347
8	20.549	0.007	21.039	0.006	20.500	0.008	20.696	0.298	2.323	27.541	26.964	27.644	27.383	0.366
9	19.757	0.009	20.038	0.007	19.530	0.006	19.775	0.254	2.431	28.333	27.965	28.614	28.304	0.325
10	19.620	0.008	19.991	0.005	19.413	0.006	19.675	0.292	2.443	28.470	28.013	28.731	28.404	0.363
15	17.941	0.008	18.325	0.006	17.789	0.009	18.018	0.276	2.668	30.148	29.678	30.355	30.061	0.347
20	16.963	0.009	17.441	0.009	16.918	0.006	17.108	0.289	2.810	31.126	30.563	31.226	30.971	0.357
30	15.719	0.009	16.094	0.009	15.557	0.009	15.790	0.275	3.044	32.370	31.910	32.587	32.289	0.345
50	15.087	0.007	15.653	0.011	15.301	0.007	15.347	0.286	3.132	33.003	32.350	32.843	32.732	0.340
100	15.064	0.011	15.601	0.007	15.103	0.009	15.256	0.299	3.151	33.025	32.402	33.041	32.823	0.364

^aAverage (mean) of $N = 100$ phase-shift measurements (in degrees) calculated as: $\bar{\phi} = \frac{1}{N} \sum_{n=1}^N \phi_i$

^bStandard deviation (sdev) of $N = 100$ phase-shift measurements (in degrees) calculated as: $sdev = \frac{1}{N-1} \left(\sum_{n=1}^N (\phi_i - \bar{\phi})^2 \right)^{1/2}$

^cMean of the average phase-shift values ($\bar{\phi}$, in degrees) obtained for each replica, calculated as: $\bar{\phi}_{avg} = \frac{1}{N} \sum_{n=1}^{N=3} \bar{\phi}_i$

^dStandard deviation (sdev) of the average phase-shift values ($\bar{\phi}$, in degrees) obtained for each replica, calculated as: $sdev = \frac{1}{N-1} \left(\sum_{n=1}^{N=3} (\bar{\phi}_i - \bar{\phi}_{avg})^2 \right)^{1/2}$

^eRatio between the average phase-shift values ($\bar{\phi}_{avg}$) at 0% oxygen and any oxygen concentration (*i.e.*, $\bar{\phi}_{avg}(0\% pO_2) / \bar{\phi}_{avg}(x\% pO_2)$)

^fAverage phase difference (in degrees) between the average phase-shift values ($\bar{\phi}_i$) at 0% oxygen and any oxygen concentration (*i.e.*, $\bar{\phi}_i(0\% pO_2) - \bar{\phi}_i(x\% pO_2)$)

^gAverage (mean) of the 3 average phase-difference values obtained for each replica (in degrees)

^hStandard deviation (sdev) of the 3 average phase-difference values obtained for each replica (in degrees)

Table ESI-13. Luminescence lifetime measurements for different oxygen concentrations of EB146 immobilized into AP200/19 in triplicate at 21 °C. Modulation frequency of 94100 Hz.

pO_2 (%)	Replica 1		Replica 2		Replica 3		Average results		$\frac{\bar{\tau}_{avg,0}}{\bar{\tau}_{avg,x}}$	Lifetime difference ($\bar{\tau}_{0\% pO_2} - \bar{\tau}_{x\% pO_2}$)				
	mean ^a (μs)	sdev ^b (μs)	mean ^a (μs)	sdev ^b (μs)	mean ^a (μs)	sdev ^b (μs)	mean ^c (μs)	sdev ^d (μs)		Rep. 1 ^f (μs)	Rep. 2 ^f (μs)	Rep. 3 ^f (μs)	mean ^g (μs)	sdev ^h (μs)
0	1.884	0.001	1.878	0.001	1.888	0.001	1.883	0.004	1.000	0.000	0.000	0.000	0.000	0.000
0.25	1.443	0.001	1.471	0.002	1.450	0.001	1.455	0.014	1.294	0.440	0.407	0.437	0.428	0.018
0.5	1.258	0.001	1.276	0.001	1.253	0.001	1.262	0.011	1.491	0.626	0.602	0.634	0.621	0.016
0.75	1.153	0.001	1.174	0.001	1.157	0.001	1.161	0.010	1.621	0.730	0.704	0.730	0.721	0.014
1	1.082	0.001	1.094	0.001	1.074	0.001	1.083	0.010	1.738	0.801	0.784	0.813	0.799	0.014
2	0.886	0.001	0.877	0.001	0.865	0.001	0.876	0.010	2.149	0.998	1.001	1.022	1.007	0.013
3	0.800	0.001	0.819	0.001	0.807	0.001	0.809	0.009	2.328	1.083	1.059	1.080	1.074	0.013
4	0.735	0.001	0.754	0.001	0.743	0.001	0.744	0.009	2.530	1.149	1.124	1.144	1.139	0.013
5	0.702	0.001	0.710	0.001	0.696	0.001	0.703	0.007	2.679	1.182	1.168	1.191	1.180	0.011
6	0.665	0.001	0.677	0.001	0.662	0.001	0.668	0.007	2.818	1.218	1.201	1.225	1.215	0.012
7	0.652	0.001	0.656	0.001	0.638	0.001	0.649	0.009	2.900	1.231	1.222	1.249	1.234	0.013
8	0.634	0.001	0.650	0.001	0.632	0.001	0.639	0.010	2.947	1.250	1.228	1.255	1.244	0.014
9	0.607	0.001	0.616	0.001	0.599	0.001	0.608	0.008	3.097	1.276	1.261	1.288	1.275	0.013
10	0.602	0.001	0.615	0.001	0.596	0.001	0.604	0.009	3.114	1.281	1.263	1.291	1.278	0.014
15	0.547	0.001	0.560	0.001	0.542	0.001	0.550	0.009	3.423	1.336	1.318	1.345	1.333	0.013
20	0.515	0.001	0.531	0.001	0.514	0.001	0.520	0.009	3.618	1.368	1.347	1.373	1.363	0.013
30	0.476	0.001	0.488	0.001	0.470	0.001	0.478	0.008	3.938	1.408	1.390	1.417	1.405	0.013
50	0.456	0.001	0.473	0.001	0.462	0.001	0.464	0.009	4.057	1.428	1.404	1.425	1.419	0.012
100	0.455	0.001	0.472	0.001	0.456	0.001	0.461	0.009	4.083	1.429	1.406	1.431	1.422	0.013

^aAverage (mean) of $N = 100$ lifetime measurements (in microseconds) calculated as: $\bar{\tau} = \frac{1}{N} \sum_{n=1}^N \tau_i$

^bStandard deviation (sdev) of $N = 100$ lifetime measurements (in microseconds) calculated as: $sdev = \frac{1}{N-1} \left(\sum_{n=1}^N (\tau_i - \bar{\tau})^2 \right)^{1/2}$

^cMean of the average lifetime values ($\bar{\tau}$, in microseconds) obtained for each replica, calculated as: $\bar{\tau}_{avg} = \frac{1}{N} \sum_{n=1}^{N=3} \bar{\tau}_i$

^dStandard deviation (sdev) of the average lifetime values ($\bar{\tau}$, in microseconds) obtained for each replica, calculated as: $sdev = \frac{1}{N-1} \left(\sum_{n=1}^{N=3} (\bar{\tau}_i - \bar{\tau}_{avg})^2 \right)^{1/2}$

^eRatio between the average lifetime values ($\bar{\tau}_{avg}$) at 0% oxygen and any oxygen concentration (*i.e.*, $\bar{\tau}_{avg}(0\% pO_2) / \bar{\tau}_{avg}(x\% pO_2)$)

^fAverage lifetime difference (in microseconds) between the average lifetime values ($\bar{\tau}_i$) at 0% oxygen and any oxygen concentration (*i.e.*,

$\bar{\tau}_i(0\% pO_2) - \bar{\tau}_i(x\% pO_2)$)

^gAverage (mean) of the 3 average lifetime-difference values obtained for each replica (in microseconds)

^hStandard deviation (sdev) of the 3 average lifetime-difference values obtained for each replica (in microseconds)

Table ESI-14. Phase-shift measurements for ultra-low oxygen concentrations between 0 and 0.26% O₂ of PtTFPP immobilized into AP200/19 in triplicate at 21 °C. Modulation frequency of 40100 Hz.

pO ₂ (%)	Replica 1		Replica 2		Replica 3		Average results		$\frac{\bar{\phi}_{avg,0}}{\bar{\phi}_{avg,x}}$ ^e	Phase difference ($\bar{\phi}_{0\% pO_2} - \bar{\phi}_{x\% pO_2}$)				
	mean ^a (°)	sdev ^b (°)	mean ^a (°)	sdev ^b (°)	mean ^a (°)	sdev ^b (°)	mean ^c (°)	sdev ^d (°)		Rep. 1 ^f (°)	Rep. 2 ^f (°)	Rep. 3 ^f (°)	mean ^g (°)	sdev ^h (°)
0.00	87.736	0.075	87.614	0.069	87.892	0.085	87.747	0.139	1.000	0.000	0.000	0.000	0.000	0.000
0.05	84.068	0.086	84.114	0.077	84.086	0.079	84.089	0.023	1.043	3.668	3.500	3.806	3.658	0.153
0.10	81.013	0.070	80.954	0.061	80.873	0.065	80.946	0.070	1.084	6.723	6.660	7.019	6.800	0.191
0.15	78.427	0.054	78.461	0.060	78.563	0.049	78.483	0.070	1.118	9.309	9.153	9.329	9.263	0.096
0.21	76.241	0.066	76.408	0.062	76.367	0.061	76.338	0.087	1.149	11.495	11.206	11.525	11.408	0.176
0.26	74.322	0.066	74.425	0.057	74.493	0.063	74.413	0.086	1.179	13.414	13.189	13.399	13.334	0.125

^aAverage (mean) of $N = 100$ phase-shift measurements (in degrees) calculated as: $\bar{\phi} = \frac{1}{N} \sum_{n=1}^N \phi_i$

^bStandard deviation (sdev) of $N = 100$ phase-shift measurements (in degrees) calculated as: $sdev = \frac{1}{N-1} \left(\sum_{n=1}^N (\phi_i - \bar{\phi})^2 \right)^{1/2}$

^cMean of the average phase-shift values ($\bar{\phi}$, in degrees) obtained for each replica, calculated as: $\bar{\phi}_{avg} = \frac{1}{N} \sum_{n=1}^{N=3} \bar{\phi}_i$

^dStandard deviation (sdev) of the average phase-shift values ($\bar{\phi}$, in degrees) obtained for each replica, calculated as: $sdev = \frac{1}{N-1} \left(\sum_{n=1}^{N=3} (\bar{\phi}_i - \bar{\phi}_{avg})^2 \right)^{1/2}$

^eRatio between the average phase-shift values ($\bar{\phi}_{avg}$) at 0% oxygen and any oxygen concentration (*i.e.*, $\bar{\phi}_{avg} (0\% pO_2) / \bar{\phi}_{avg} (x\% pO_2)$)

^fAverage phase difference (in degrees) between the average phase-shift values ($\bar{\phi}_i$) at 0% oxygen and any oxygen concentration (*i.e.*, $\bar{\phi}_i (0\% pO_2) - \bar{\phi}_i (x\% pO_2)$)

^gAverage (mean) of the 3 average phase-difference values obtained for each replica (in degrees)

^hStandard deviation (sdev) of the 3 average phase-difference values obtained for each replica (in degrees)

Table ESI-15. Luminescence lifetime measurements for ultra-low oxygen concentrations between 0 and 0.26% O₂ of PtTFPP immobilized into AP200/19 in triplicate at 21 °C. Modulation frequency of 40100 Hz.

pO_2 (%)	Replica 1		Replica 2		Replica 3		Average results		$\frac{\bar{\tau}_{avg,0}}{\bar{\tau}_{avg,x}}$ ^e	Lifetime difference ($\bar{\tau}_{0\% pO_2} - \bar{\tau}_{x\% pO_2}$)				
	mean ^a (μs)	sdev ^b (μs)	mean ^a (μs)	sdev ^b (μs)	mean ^a (μs)	sdev ^b (μs)	mean ^c (μs)	sdev ^d (μs)		Rep. 1 ^f (μs)	Rep. 2 ^f (μs)	Rep. 3 ^f (μs)	mean ^g (μs)	sdev ^h (μs)
0.00	100.391	1.475	95.252	1.480	101.828	1.471	99.157	3.457	1.000	0.000	0.000	0.000	0.000	0.000
0.05	38.198	0.396	38.498	0.401	38.315	0.391	38.337	0.151	2.586	62.193	56.753	63.512	60.820	3.582
0.10	25.095	0.160	24.929	0.165	24.704	0.156	24.909	0.196	3.980	75.295	70.323	77.123	74.247	3.519
0.15	19.381	0.079	19.440	0.084	19.618	0.075	19.480	0.123	5.090	81.009	75.812	82.209	79.677	3.400
0.21	16.208	0.071	16.415	0.076	16.364	0.067	16.329	0.107	6.072	84.182	78.836	85.463	82.827	3.515
0.26	14.140	0.056	14.239	0.062	14.304	0.052	14.228	0.082	6.969	86.250	81.013	87.523	84.929	3.450

^aAverage (mean) of $N = 100$ lifetime measurements (in microseconds) calculated as: $\bar{\tau} = \frac{1}{N} \sum_{n=1}^N \tau_i$

^bStandard deviation (sdev) of $N = 100$ lifetime measurements (in microseconds) calculated as: $sdev = \frac{1}{N-1} \left(\sum_{n=1}^N (\tau_i - \bar{\tau})^2 \right)^{1/2}$

^cMean of the average lifetime values ($\bar{\tau}$, in microseconds) obtained for each replica, calculated as: $\bar{\tau}_{avg} = \frac{1}{N} \sum_{n=1}^{N=3} \bar{\tau}_i$

^dStandard deviation (sdev) of the average lifetime values ($\bar{\tau}$, in microseconds) obtained for each replica, calculated as: $sdev = \frac{1}{N-1} \left(\sum_{n=1}^{N=3} (\bar{\tau}_i - \bar{\tau}_{avg})^2 \right)^{1/2}$

^eRatio between the average lifetime values ($\bar{\tau}_{avg}$) at 0% oxygen and any oxygen concentration (*i.e.*, $\bar{\tau}_{avg}(0\% pO_2) / \bar{\tau}_{avg}(x\% pO_2)$)

^fAverage lifetime difference (in microseconds) between the average lifetime values ($\bar{\tau}_i$) at 0% oxygen and any oxygen concentration (*i.e.*, $\bar{\tau}_i(0\% pO_2) - \bar{\tau}_i(x\% pO_2)$)

^gAverage (mean) of the 3 average lifetime-difference values obtained for each replica (in microseconds)

^hStandard deviation (sdev) of the 3 average lifetime-difference values obtained for each replica (in microseconds)

Table ESI-16. Phase-shift measurements for ultra-low oxygen concentrations between 0 and 0.26% O₂ of N969 immobilized into AP200/19 in triplicate at 21 °C. Modulation frequency of 94100 Hz.

pO ₂ (%)	Replica 1		Replica 2		Replica 3		Average results		$\frac{\bar{\phi}_{avg,0}}{\bar{\phi}_{avg,x}}$ ^e	Phase difference ($\bar{\phi}_{0\% pO_2} - \bar{\phi}_{x\% pO_2}$)				
	mean ^a (°)	sdev ^b (°)	mean ^a (°)	sdev ^b (°)	mean ^a (°)	sdev ^b (°)	mean ^c (°)	sdev ^d (°)		Rep. 1 ^f (°)	Rep. 2 ^f (°)	Rep. 3 ^f (°)	mean ^g (°)	sdev ^h (°)
0.00	65.678	0.026	65.699	0.024	65.767	0.025	65.714	0.046	1.000	0.000	0.000	0.000	0.000	0.000
0.05	61.748	0.008	61.614	0.008	61.757	0.007	61.706	0.080	1.065	3.930	4.085	4.010	4.008	0.077
0.10	58.807	0.007	58.891	0.009	58.837	0.007	58.845	0.042	1.116	6.871	6.808	6.930	6.869	0.061
0.15	56.550	0.009	56.439	0.009	56.596	0.009	56.528	0.080	1.162	9.128	9.260	9.171	9.186	0.067
0.21	54.649	0.007	54.640	0.006	54.724	0.007	54.671	0.046	1.202	11.029	11.059	11.043	11.043	0.015
0.26	53.000	0.007	52.951	0.005	52.875	0.005	52.942	0.063	1.241	12.678	12.748	12.892	12.772	0.109

^aAverage (mean) of $N = 100$ phase-shift measurements (in degrees) calculated as: $\bar{\phi} = \frac{1}{N} \sum_{n=1}^N \phi_i$

^bStandard deviation (sdev) of $N = 100$ phase-shift measurements (in degrees) calculated as: $sdev = \frac{1}{N-1} \left(\sum_{n=1}^N (\phi_i - \bar{\phi})^2 \right)^{1/2}$

^cMean of the average phase-shift values ($\bar{\phi}$, in degrees) obtained for each replica, calculated as: $\bar{\phi}_{avg} = \frac{1}{N} \sum_{n=1}^{N=3} \bar{\phi}_i$

^dStandard deviation (sdev) of the average phase-shift values ($\bar{\phi}$, in degrees) obtained for each replica, calculated as: $sdev = \frac{1}{N-1} \left(\sum_{n=1}^{N=3} (\bar{\phi}_i - \bar{\phi}_{avg})^2 \right)^{1/2}$

^eRatio between the average phase-shift values ($\bar{\phi}_{avg}$) at 0% oxygen and any oxygen concentration (*i.e.*, $\bar{\phi}_{avg}(0\% pO_2) / \bar{\phi}_{avg}(x\% pO_2)$)

^fAverage phase difference (in degrees) between the average phase-shift values ($\bar{\phi}_i$) at 0% oxygen and any oxygen concentration (*i.e.*, $\bar{\phi}_i(0\% pO_2) - \bar{\phi}_i(x\% pO_2)$)

^gAverage (mean) of the 3 average phase-difference values obtained for each replica (in degrees)

^hStandard deviation (sdev) of the 3 average phase-difference values obtained for each replica (in degrees)

Table ESI-17. Luminescence lifetime measurements for ultra-low oxygen concentrations between 0 and 0.26% O₂ of N969 immobilized into AP200/19 in triplicate at 21 °C. Modulation frequency of 94100 Hz.

pO_2 (%)	Replica 1		Replica 2		Replica 3		Average results		$\frac{\bar{\tau}_{avg,0}}{\bar{\tau}_{avg,x}}$ ^e	Lifetime difference ($\bar{\tau}_{0\% pO_2} - \bar{\tau}_{x\% pO_2}$)				
	mean ^a (μs)	sdev ^b (μs)	mean ^a (μs)	sdev ^b (μs)	mean ^a (μs)	sdev ^b (μs)	mean ^c (μs)	sdev ^d (μs)		Rep. 1 ^f (μs)	Rep. 2 ^f (μs)	Rep. 3 ^f (μs)	mean ^g (μs)	sdev ^h (μs)
0.00	3.742	0.004	3.745	0.004	3.757	0.002	3.748	0.008	1.000	0.000	0.000	0.000	0.000	0.000
0.05	3.147	0.003	3.129	0.002	3.148	0.001	3.142	0.010	1.193	0.594	0.615	0.608	0.606	0.010
0.10	2.793	0.003	2.802	0.003	2.796	0.001	2.797	0.004	1.339	0.948	0.942	0.960	0.950	0.009
0.15	2.560	0.002	2.549	0.002	2.564	0.001	2.558	0.007	1.465	1.181	1.196	1.192	1.190	0.007
0.21	2.384	0.002	2.383	0.002	2.390	0.001	2.386	0.004	1.570	1.357	1.362	1.366	1.362	0.004
0.26	2.244	0.002	2.240	0.001	2.234	0.001	2.239	0.005	1.673	1.497	1.505	1.523	1.508	0.013

^aAverage (mean) of $N = 100$ lifetime measurements (in microseconds) calculated as: $\bar{\tau} = \frac{1}{N} \sum_{n=1}^N \tau_i$

^bStandard deviation (sdev) of $N = 100$ lifetime measurements (in microseconds) calculated as: $sdev = \frac{1}{N-1} \left(\sum_{n=1}^N (\tau_i - \bar{\tau})^2 \right)^{1/2}$

^cMean of the average lifetime values ($\bar{\tau}$, in microseconds) obtained for each replica, calculated as: $\bar{\tau}_{avg} = \frac{1}{N} \sum_{n=1}^{N=3} \bar{\tau}_i$

^dStandard deviation (sdev) of the average lifetime values ($\bar{\tau}$, in microseconds) obtained for each replica, calculated as: $sdev = \frac{1}{N-1} \left(\sum_{n=1}^{N=3} (\bar{\tau}_i - \bar{\tau}_{avg})^2 \right)^{1/2}$

^eRatio between the average lifetime values ($\bar{\tau}_{avg}$) at 0% oxygen and any oxygen concentration (*i.e.*, $\bar{\tau}_{avg}(0\% pO_2) / \bar{\tau}_{avg}(x\% pO_2)$)

^fAverage lifetime difference (in microseconds) between the average lifetime values ($\bar{\tau}_i$) at 0% oxygen and any oxygen concentration (*i.e.*,

$\bar{\tau}_i(0\% pO_2) - \bar{\tau}_i(x\% pO_2)$)

^gAverage (mean) of the 3 average lifetime-difference values obtained for each replica (in microseconds)

^hStandard deviation (sdev) of the 3 average lifetime-difference values obtained for each replica (in microseconds)

Table ESI-18. Phase-shift measurements for ultra-low oxygen concentrations between 0 and 0.26% O₂ of N1008 immobilized into AP200/19 in triplicate at 21 °C. Modulation frequency of 30100 Hz.

pO ₂ (%)	Replica 1		Replica 2		Replica 3		Average results		$\frac{\bar{\phi}_{avg,0}}{\bar{\phi}_{avg,x}}$ ^e	Phase difference ($\bar{\phi}_{0\% pO_2} - \bar{\phi}_{x\% pO_2}$)				
	mean ^a (°)	sdev ^b (°)	mean ^a (°)	sdev ^b (°)	mean ^a (°)	sdev ^b (°)	mean ^c (°)	sdev ^d (°)		Rep. 1 ^f (°)	Rep. 2 ^f (°)	Rep. 3 ^f (°)	mean ^g (°)	sdev ^h (°)
0.00	57.926	0.088	57.821	0.089	57.801	0.087	57.849	0.067	1.000	0.000	0.000	0.000	0.000	0.000
0.05	57.031	0.008	57.042	0.010	56.959	0.009	57.010	0.045	1.014	0.895	0.779	0.842	0.838	0.058
0.10	55.885	0.012	55.759	0.012	55.865	0.014	55.836	0.067	1.036	2.041	2.062	1.936	2.013	0.067
0.15	54.773	0.015	54.655	0.017	54.677	0.015	54.701	0.062	1.057	3.153	3.166	3.124	3.147	0.021
0.21	53.705	0.017	53.557	0.018	53.599	0.015	53.620	0.076	1.078	4.221	4.264	4.202	4.229	0.031
0.26	52.697	0.017	52.792	0.019	52.807	0.018	52.765	0.059	1.096	5.229	5.029	4.994	5.084	0.126

^aAverage (mean) of $N = 100$ phase-shift measurements (in degrees) calculated as: $\bar{\phi} = \frac{1}{N} \sum_{n=1}^N \phi_i$

^bStandard deviation (sdev) of $N = 100$ phase-shift measurements (in degrees) calculated as: $sdev = \frac{1}{N-1} \left(\sum_{n=1}^N (\phi_i - \bar{\phi})^2 \right)^{1/2}$

^cMean of the average phase-shift values ($\bar{\phi}$, in degrees) obtained for each replica, calculated as: $\bar{\phi}_{avg} = \frac{1}{N} \sum_{n=1}^{N=3} \bar{\phi}_i$

^dStandard deviation (sdev) of the average phase-shift values ($\bar{\phi}$, in degrees) obtained for each replica, calculated as: $sdev = \frac{1}{N-1} \left(\sum_{n=1}^{N=3} (\bar{\phi}_i - \bar{\phi}_{avg})^2 \right)^{1/2}$

^eRatio between the average phase-shift values ($\bar{\phi}_{avg}$) at 0% oxygen and any oxygen concentration (*i.e.*, $\bar{\phi}_{avg} (0\% pO_2) / \bar{\phi}_{avg} (x\% pO_2)$)

^fAverage phase difference (in degrees) between the average phase-shift values ($\bar{\phi}_i$) at 0% oxygen and any oxygen concentration (*i.e.*, $\bar{\phi}_i (0\% pO_2) - \bar{\phi}_i (x\% pO_2)$)

^gAverage (mean) of the 3 average phase-difference values obtained for each replica (in degrees)

^hStandard deviation (sdev) of the 3 average phase-difference values obtained for each replica (in degrees)

Table ESI-19. Luminescence lifetime measurements for ultra-low oxygen concentrations between 0 and 0.26% O₂ of N1008 immobilized into AP200/19 in triplicate at 21 °C. Modulation frequency of 30100 Hz.

pO_2 (%)	Replica 1		Replica 2		Replica 3		Average results			Lifetime difference ($\bar{\tau}_{0\% pO_2} - \bar{\tau}_{x\% pO_2}$)				
	mean ^a (μs)	sdev ^b (μs)	mean ^a (μs)	sdev ^b (μs)	mean ^a (μs)	sdev ^b (μs)	mean ^c (μs)	sdev ^d (μs)	$\frac{\bar{\tau}_{avg,0}}{\bar{\tau}_{avg,x}}$ ^e	Rep. 1 ^f (μs)	Rep. 2 ^f (μs)	Rep. 3 ^f (μs)	mean ^g (μs)	sdev ^h (μs)
0.00	8.437	0.007	8.403	0.006	8.396	0.005	8.412	0.021	1.000	0.000	0.000	0.000	0.000	0.000
0.05	8.151	0.006	8.155	0.005	8.129	0.004	8.145	0.014	1.032	0.286	0.248	0.267	0.267	0.019
0.10	7.805	0.005	7.768	0.004	7.799	0.004	7.790	0.019	1.079	0.632	0.635	0.597	0.621	0.021
0.15	7.488	0.005	7.455	0.004	7.461	0.005	7.468	0.017	1.126	0.949	0.948	0.935	0.944	0.007
0.21	7.199	0.004	7.160	0.003	7.171	0.004	7.176	0.020	1.172	1.238	1.243	1.225	1.235	0.009
0.26	6.940	0.005	6.964	0.005	6.967	0.006	6.957	0.014	1.209	1.497	1.439	1.429	1.455	0.036

^aAverage (mean) of $N = 100$ lifetime measurements (in microseconds) calculated as: $\bar{\tau} = \frac{1}{N} \sum_{n=1}^N \tau_i$

^bStandard deviation (sdev) of $N = 100$ lifetime measurements (in microseconds) calculated as: $sdev = \frac{1}{N-1} \left(\sum_{n=1}^N (\tau_i - \bar{\tau})^2 \right)^{1/2}$

^cMean of the average lifetime values ($\bar{\tau}$, in microseconds) obtained for each replica, calculated as: $\bar{\tau}_{avg} = \frac{1}{N} \sum_{n=1}^{N=3} \bar{\tau}_i$

^dStandard deviation (sdev) of the average lifetime values ($\bar{\tau}$, in microseconds) obtained for each replica, calculated as: $sdev = \frac{1}{N-1} \left(\sum_{n=1}^{N=3} (\bar{\tau}_i - \bar{\tau}_{avg})^2 \right)^{1/2}$

^eRatio between the average lifetime values ($\bar{\tau}_{avg}$) at 0% oxygen and any oxygen concentration (*i.e.*, $\bar{\tau}_{avg}(0\% pO_2) / \bar{\tau}_{avg}(x\% pO_2)$)

^fAverage lifetime difference (in microseconds) between the average lifetime values ($\bar{\tau}_i$) at 0% oxygen and any oxygen concentration (*i.e.*,

$\bar{\tau}_i(0\% pO_2) - \bar{\tau}_i(x\% pO_2)$)

^gAverage (mean) of the 3 average lifetime-difference values obtained for each replica (in microseconds)

^hStandard deviation (sdev) of the 3 average lifetime-difference values obtained for each replica (in microseconds)

Table ESI-20. Phase-shift measurements for ultra-low oxygen concentrations between 0 and 0.26% O₂ of EB146 immobilized into AP200/19 in triplicate at 21 °C. Modulation frequency of 94100 Hz.

pO ₂ (%)	Replica 1		Replica 2		Replica 3		Average results		$\frac{\bar{\phi}_{avg,0}}{\bar{\phi}_{avg,x}}$ ^e	Phase difference ($\bar{\phi}_{0\% pO_2} - \bar{\phi}_{x\% pO_2}$)				
	mean ^a (°)	sdev ^b (°)	mean ^a (°)	sdev ^b (°)	mean ^a (°)	sdev ^b (°)	mean ^c (°)	sdev ^d (°)		Rep. 1 ^f (°)	Rep. 2 ^f (°)	Rep. 3 ^f (°)	mean ^g (°)	sdev ^h (°)
0.00	48.028	0.069	47.922	0.071	47.893	0.051	47.947	0.071	1.000	0.000	0.000	0.000	0.000	0.000
0.05	45.787	0.012	45.824	0.022	45.921	0.032	45.844	0.069	1.045	2.241	2.098	1.972	2.103	0.134
0.10	43.897	0.041	43.901	0.011	43.894	0.020	43.897	0.003	1.092	4.131	4.021	3.999	4.050	0.070
0.15	43.091	0.017	42.964	0.016	43.211	0.017	43.088	0.123	1.112	4.937	4.958	4.682	4.859	0.153
0.21	41.813	0.010	41.700	0.009	41.697	0.011	41.736	0.066	1.148	6.215	6.222	6.196	6.211	0.013
0.26	40.558	0.008	40.480	0.007	40.525	0.007	40.521	0.039	1.183	7.470	7.442	7.368	7.426	0.052

^aAverage (mean) of $N = 100$ phase-shift measurements (in degrees) calculated as: $\bar{\phi} = \frac{1}{N} \sum_{n=1}^N \phi_i$

^bStandard deviation (sdev) of $N = 100$ phase-shift measurements (in degrees) calculated as: $sdev = \frac{1}{N-1} \left(\sum_{n=1}^N (\phi_i - \bar{\phi})^2 \right)^{1/2}$

^cMean of the average phase-shift values ($\bar{\phi}$, in degrees) obtained for each replica, calculated as: $\bar{\phi}_{avg} = \frac{1}{N} \sum_{n=1}^{N=3} \bar{\phi}_i$

^dStandard deviation (sdev) of the average phase-shift values ($\bar{\phi}$, in degrees) obtained for each replica, calculated as: $sdev = \frac{1}{N-1} \left(\sum_{n=1}^{N=3} (\bar{\phi}_i - \bar{\phi}_{avg})^2 \right)^{1/2}$

^eRatio between the average phase-shift values ($\bar{\phi}_{avg}$) at 0% oxygen and any oxygen concentration (*i.e.*, $\bar{\phi}_{avg} (0\% pO_2) / \bar{\phi}_{avg} (x\% pO_2)$)

^fAverage phase difference (in degrees) between the average phase-shift values ($\bar{\phi}_i$) at 0% oxygen and any oxygen concentration (*i.e.*, $\bar{\phi}_i (0\% pO_2) - \bar{\phi}_i (x\% pO_2)$)

^gAverage (mean) of the 3 average phase-difference values obtained for each replica (in degrees)

^hStandard deviation (sdev) of the 3 average phase-difference values obtained for each replica (in degrees)

Table ESI-21. Luminescence lifetime measurements for ultra-low oxygen concentrations between 0 and 0.26% O₂ of EB146 immobilized into AP200/19 in triplicate at 21 °C. Modulation frequency of 94100 Hz.

pO_2 (%)	Replica 1		Replica 2		Replica 3		Average results		$\frac{\bar{\tau}_{avg,0}}{\bar{\tau}_{avg,x}}$ ^e	Lifetime difference ($\bar{\tau}_{0\% pO_2} - \bar{\tau}_{x\% pO_2}$)				
	mean ^a (μs)	sdev ^b (μs)	mean ^a (μs)	sdev ^b (μs)	mean ^a (μs)	sdev ^b (μs)	mean ^c (μs)	sdev ^d (μs)		Rep. 1 ^f (μs)	Rep. 2 ^f (μs)	Rep. 3 ^f (μs)	mean ^g (μs)	sdev ^h (μs)
0.00	1.880	0.002	1.873	0.002	1.871	0.002	1.874	0.004	1.000	0.000	0.000	0.000	0.000	0.000
0.05	1.738	0.001	1.740	0.002	1.746	0.001	1.741	0.004	1.076	0.142	0.133	0.125	0.133	0.008
0.10	1.627	0.001	1.637	0.001	1.629	0.001	1.631	0.005	1.149	0.253	0.236	0.242	0.243	0.008
0.15	1.582	0.001	1.575	0.001	1.588	0.001	1.581	0.006	1.185	0.298	0.298	0.283	0.293	0.008
0.21	1.512	0.001	1.506	0.001	1.508	0.001	1.508	0.003	1.242	0.368	0.367	0.363	0.366	0.002
0.26	1.447	0.001	1.443	0.001	1.445	0.001	1.445	0.002	1.297	0.433	0.430	0.426	0.429	0.003

^aAverage (mean) of $N = 100$ lifetime measurements (in microseconds) calculated as: $\bar{\tau} = \frac{1}{N} \sum_{n=1}^N \tau_i$

^bStandard deviation (sdev) of $N = 100$ lifetime measurements (in microseconds) calculated as: $sdev = \frac{1}{N-1} \left(\sum_{n=1}^N (\tau_i - \bar{\tau})^2 \right)^{1/2}$

^cMean of the average lifetime values ($\bar{\tau}$, in microseconds) obtained for each replica, calculated as: $\bar{\tau}_{avg} = \frac{1}{N} \sum_{n=1}^{N=3} \bar{\tau}_i$

^dStandard deviation (sdev) of the average lifetime values ($\bar{\tau}$, in microseconds) obtained for each replica, calculated as: $sdev = \frac{1}{N-1} \left(\sum_{n=1}^{N=3} (\bar{\tau}_i - \bar{\tau}_{avg})^2 \right)^{1/2}$

^eRatio between the average lifetime values ($\bar{\tau}_{avg}$) at 0% oxygen and any oxygen concentration (*i.e.*, $\bar{\tau}_{avg}(0\% pO_2) / \bar{\tau}_{avg}(x\% pO_2)$)

^fAverage lifetime difference (in microseconds) between the average lifetime values ($\bar{\tau}_i$) at 0% oxygen and any oxygen concentration (*i.e.*,

$\bar{\tau}_i(0\% pO_2) - \bar{\tau}_i(x\% pO_2)$)

^gAverage (mean) of the 3 average lifetime-difference values obtained for each replica (in microseconds)

^hStandard deviation (sdev) of the 3 average lifetime-difference values obtained for each replica (in microseconds)

Table ESI-22. Phase-shift measurements for different oxygen concentrations and several relative humidity conditions of PtTFPP immobilized into AP200/19 at 21 °C. Modulation frequency of 40100 Hz.

pO_2 (%)	0% Humidity		10% Humidity		20% Humidity		40% Humidity		60% Humidity		80% Humidity	
	mean ^a (°)	sdev ^b (°)	mean ^a (°)	sdev ^b (°)	mean ^a (°)	sdev ^b (°)	mean ^a (°)	sdev ^b (°)	mean ^a (°)	sdev ^b (°)	mean ^a (°)	sdev ^b (°)
0.00	87.734	0.102	87.861	0.114	87.849	0.128	88.238	0.130	88.351	0.125	88.232	0.111
0.25	74.602	0.140	73.964	0.074	74.348	0.086	74.584	0.076	74.704	0.076	74.470	0.086
0.50	66.489	0.255	65.385	0.077	65.695	0.076	65.968	0.075	66.058	0.082	65.961	0.075
0.75	60.354	0.076	60.210	0.072	60.538	0.073	60.834	0.064	60.888	0.091	60.809	0.073
1	57.502	0.069	57.626	0.076	58.005	0.073	58.254	0.067	58.324	0.070	58.222	0.063
2	47.770	0.079	47.926	0.072	48.368	0.068	48.672	0.076	48.723	0.082	48.612	0.064
3	43.765	0.071	44.024	0.078	44.464	0.068	44.821	0.088	44.791	0.063	44.689	0.082
4	41.418	0.078	41.721	0.074	42.160	0.085	42.522	0.075	42.502	0.083	42.383	0.073
5	39.379	0.080	39.700	0.079	40.146	0.072	40.550	0.079	40.466	0.087	40.388	0.096
6	37.958	0.090	38.391	0.068	38.821	0.092	39.213	0.081	39.128	0.089	39.106	0.072
7	36.908	0.111	37.281	0.095	37.787	0.079	38.133	0.071	38.011	0.087	37.936	0.090
8	36.559	0.078	36.924	0.078	37.435	0.073	37.794	0.075	37.641	0.095	37.646	0.102
9	35.552	0.082	35.938	0.091	36.450	0.071	36.802	0.076	36.611	0.080	36.770	0.108
10	34.527	0.076	34.951	0.095	35.434	0.085	35.826	0.092	35.572	0.107	35.838	0.088
15	32.565	0.094	33.048	0.109	33.538	0.098	33.908	0.100	33.605	0.089	34.257	0.101
20	31.125	0.117	31.625	0.096	32.131	0.098	32.478	0.119	32.162	0.113	33.098	0.099
30	29.422	0.108	29.992	0.104	30.508	0.110	30.854	0.098	30.460	0.103	31.990	0.107
50	27.722	0.097	28.382	0.136	28.950	0.113	29.305	0.120	30.000	0.137	31.344	0.114
100	26.373	0.131	26.921	0.112	27.466	0.113	27.824	0.125	27.502	0.118	28.622	0.144

^aAverage (mean) of $N = 100$ phase-shift measurements (in degrees) calculated as: $\bar{\phi} = \frac{1}{N} \sum_{n=1}^N \phi_i$

^bStandard deviation (sdev) of $N = 100$ phase-shift measurements (in degrees) calculated as: $sdev = \frac{1}{N-1} \left(\sum_{n=1}^N (\phi_i - \bar{\phi})^2 \right)^{1/2}$

Table ESI-23. Luminescence lifetime measurements for different oxygen concentrations and several relative humidity conditions of PtTFPP immobilized into AP200/19 at 21 °C. Modulation frequency of 40100 Hz.

pO_2 (%)	0% Humidity		10% Humidity		20% Humidity		40% Humidity		60% Humidity		80% Humidity	
	mean ^a (μ s)	sdev ^b (μ s)	mean ^a (μ s)	sdev ^b (μ s)	mean ^a (μ s)	sdev ^b (μ s)	mean ^a (μ s)	sdev ^b (μ s)	mean ^a (μ s)	sdev ^b (μ s)	mean ^a (μ s)	sdev ^b (μ s)
0.00	100.315	1.207	106.273	1.437	105.714	1.238	129.085	1.339	137.933	1.428	128.647	1.677
0.25	14.411	0.013	13.808	0.023	14.165	0.015	14.394	0.019	14.512	0.011	14.282	0.014
0.50	9.123	0.017	8.663	0.005	8.788	0.005	8.901	0.005	8.938	0.005	8.898	0.005
0.75	6.973	0.005	6.933	0.005	7.026	0.005	7.111	0.004	7.127	0.006	7.104	0.005
1	6.230	0.004	6.260	0.005	6.352	0.005	6.414	0.004	6.432	0.004	6.407	0.004
2	4.372	0.005	4.396	0.005	4.465	0.004	4.513	0.005	4.521	0.005	4.503	0.004
3	3.801	0.004	3.836	0.005	3.895	0.004	3.944	0.006	3.940	0.004	3.926	0.005
4	3.501	0.005	3.538	0.005	3.593	0.005	3.639	0.005	3.637	0.005	3.622	0.005
5	3.257	0.005	3.295	0.005	3.347	0.005	3.395	0.005	3.385	0.006	3.376	0.006
6	3.096	0.006	3.144	0.004	3.193	0.006	3.238	0.005	3.228	0.006	3.226	0.005
7	2.980	0.007	3.021	0.006	3.077	0.005	3.115	0.005	3.102	0.006	3.093	0.006
8	2.943	0.005	2.982	0.005	3.038	0.005	3.078	0.005	3.061	0.006	3.061	0.007
9	2.836	0.005	2.877	0.006	2.931	0.005	2.969	0.005	2.948	0.005	2.965	0.007
10	2.730	0.005	2.774	0.006	2.824	0.005	2.865	0.006	2.838	0.007	2.866	0.006
15	2.534	0.006	2.582	0.007	2.630	0.006	2.667	0.007	2.637	0.006	2.703	0.007
20	2.396	0.008	2.444	0.006	2.492	0.006	2.526	0.008	2.495	0.007	2.587	0.006
30	2.238	0.007	2.290	0.007	2.338	0.007	2.371	0.006	2.334	0.007	2.479	0.007
50	2.085	0.006	2.144	0.009	2.195	0.007	2.227	0.008	2.291	0.009	2.417	0.007
100	1.967	0.009	2.015	0.007	2.063	0.007	2.094	0.008	2.066	0.008	2.166	0.010

^aAverage (mean) of $N = 100$ lifetime measurements (in microseconds) calculated as: $\bar{\tau} = \frac{1}{N} \sum_{n=1}^N \tau_i$

^bStandard deviation (sdev) of $N = 100$ lifetime measurements (in microseconds) calculated as: $sdev = \frac{1}{N-1} \left(\sum_{n=1}^N (\tau_i - \bar{\tau})^2 \right)^{1/2}$

Table ESI-24. Phase-shift measurements for different oxygen concentrations and several relative humidity conditions of N969 immobilized into AP200/19 at 21 °C. Modulation frequency of 94100 Hz.

pO_2 (%)	0% Humidity		10% Humidity		20% Humidity		40% Humidity		60% Humidity		80% Humidity	
	mean ^a (°)	sdev ^b (°)	mean ^a (°)	sdev ^b (°)	mean ^a (°)	sdev ^b (°)	mean ^a (°)	sdev ^b (°)	mean ^a (°)	sdev ^b (°)	mean ^a (°)	sdev ^b (°)
0.00	65.637	0.109	62.640	0.006	60.580	0.011	58.989	0.012	57.639	0.013	56.549	0.014
0.25	52.986	0.008	50.165	0.012	48.403	0.009	47.057	0.008	45.958	0.008	45.022	0.008
0.50	48.848	0.007	46.335	0.009	44.818	0.007	43.639	0.008	42.684	0.010	41.861	0.012
0.75	46.372	0.011	44.125	0.008	42.780	0.008	41.739	0.009	40.895	0.008	40.160	0.010
1	44.605	0.012	42.576	0.010	41.380	0.011	40.444	0.009	39.679	0.008	39.006	0.010
2	40.430	0.010	38.952	0.010	38.098	0.011	37.416	0.010	36.856	0.010	36.348	0.010
3	38.217	0.013	37.085	0.009	36.444	0.009	35.926	0.009	35.473	0.008	35.064	0.008
4	36.654	0.015	35.769	0.009	35.251	0.010	34.843	0.010	34.471	0.011	34.131	0.008
5	35.626	0.011	34.923	0.009	34.528	0.009	34.180	0.010	33.858	0.011	33.564	0.011
6	34.842	0.009	34.284	0.011	33.961	0.010	33.679	0.011	33.391	0.010	33.138	0.011
7	34.142	0.010	33.701	0.009	33.447	0.009	33.196	0.010	32.951	0.010	32.668	0.010
8	33.517	0.013	33.170	0.011	32.950	0.008	32.743	0.011	32.524	0.010	32.304	0.011
9	32.955	0.008	32.675	0.009	32.509	0.012	32.324	0.010	32.122	0.011	31.957	0.010
10	32.669	0.009	32.458	0.010	32.320	0.010	32.154	0.010	31.967	0.010	31.845	0.010
15	30.802	0.017	30.789	0.010	30.744	0.011	30.671	0.009	30.538	0.015	30.625	0.014
20	29.561	0.009	29.647	0.012	29.685	0.011	29.646	0.009	29.556	0.013	29.811	0.009
30	27.928	0.013	28.123	0.011	28.212	0.010	28.232	0.012	28.139	0.014	28.743	0.011
50	26.926	0.013	27.208	0.013	27.335	0.010	27.396	0.013	27.926	0.012	28.469	0.013
100	26.818	0.013	27.090	0.016	27.233	0.012	27.262	0.015	27.281	0.014	27.695	0.013

^aAverage (mean) of $N = 100$ phase-shift measurements (in degrees) calculated as: $\bar{\phi} = \frac{1}{N} \sum_{n=1}^N \phi_i$

^bStandard deviation (sdev) of $N = 100$ phase-shift measurements (in degrees) calculated as: $sdev = \frac{1}{N-1} \left(\sum_{n=1}^N (\phi_i - \bar{\phi})^2 \right)^{1/2}$

Table ESI-25. Luminescence lifetime measurements for different oxygen concentrations and several relative humidity conditions of N969 immobilized into AP200/19 at 21 °C. Modulation frequency of 94100 Hz.

pO_2 (%)	0% Humidity		10% Humidity		20% Humidity		40% Humidity		60% Humidity		80% Humidity	
	mean ^a (μs)	sdev ^b (μs)	mean ^a (μs)	sdev ^b (μs)	mean ^a (μs)	sdev ^b (μs)	mean ^a (μs)	sdev ^b (μs)	mean ^a (μs)	sdev ^b (μs)	mean ^a (μs)	sdev ^b (μs)
0.00	3.734	0.003	3.268	0.002	2.999	0.003	2.813	0.003	2.669	0.004	2.560	0.003
0.25	2.243	0.001	2.027	0.001	1.905	0.001	1.817	0.001	1.748	0.001	1.692	0.001
0.50	1.935	0.001	1.772	0.001	1.680	0.001	1.612	0.001	1.559	0.001	1.515	0.001
0.75	1.774	0.001	1.640	0.001	1.565	0.001	1.509	0.001	1.464	0.001	1.427	0.001
1	1.668	0.001	1.554	0.001	1.490	0.001	1.441	0.001	1.403	0.001	1.369	0.001
2	1.441	0.001	1.367	0.001	1.326	0.001	1.293	0.001	1.267	0.001	1.244	0.001
3	1.331	0.001	1.278	0.001	1.249	0.001	1.225	0.001	1.205	0.001	1.187	0.001
4	1.258	0.001	1.218	0.001	1.195	0.001	1.177	0.001	1.161	0.001	1.146	0.001
5	1.212	0.001	1.180	0.001	1.163	0.001	1.148	0.001	1.134	0.001	1.122	0.001
6	1.177	0.001	1.153	0.001	1.139	0.001	1.127	0.001	1.114	0.001	1.104	0.001
7	1.146	0.001	1.128	0.001	1.117	0.001	1.106	0.001	1.096	0.001	1.084	0.001
8	1.120	0.001	1.105	0.001	1.096	0.001	1.087	0.001	1.078	0.001	1.069	0.001
9	1.096	0.001	1.084	0.001	1.077	0.001	1.070	0.001	1.061	0.001	1.055	0.001
10	1.084	0.001	1.075	0.001	1.070	0.001	1.063	0.001	1.055	0.001	1.050	0.001
15	1.008	0.001	1.007	0.001	1.006	0.001	1.003	0.001	0.997	0.001	1.001	0.001
20	0.959	0.001	0.962	0.001	0.964	0.001	0.962	0.001	0.959	0.001	0.969	0.001
30	0.896	0.001	0.904	0.001	0.907	0.001	0.908	0.001	0.904	0.001	0.927	0.001
50	0.859	0.001	0.869	0.001	0.874	0.001	0.876	0.001	0.896	0.001	0.917	0.001
100	0.855	0.001	0.865	0.001	0.870	0.001	0.871	0.001	0.872	0.001	0.887	0.001

^aAverage (mean) of $N = 100$ lifetime measurements (in microseconds) calculated as: $\bar{\tau} = \frac{1}{N} \sum_{n=1}^N \tau_i$

^bStandard deviation (sdev) of $N = 100$ lifetime measurements (in microseconds) calculated as: $sdev = \frac{1}{N-1} \left(\sum_{n=1}^N (\tau_i - \bar{\tau})^2 \right)^{1/2}$

Chapter **4**

An open and low-cost optical-fiber measurement system for the optical detection of oxygen using a multifrequency phase-resolved method

Santiago Medina Rodríguez^{a,b,*}, Ángel de la Torre Vega^{a,*}, Jorge Fernando Fernández Sánchez^b and Alberto Fernández Gutiérrez^b

^a*Department of Signal Theory, Networking and Communications, CITIC-UGR, University of Granada, C/ Periodista Rafael Gómez 2, E-18071 Granada, Spain.*

^b*Department of Analytical Chemistry, Faculty of Sciences, University of Granada, Avda. Fuentenueva s/n, E-18071 Granada, Spain.*

Published in *Sensors and Actuators B: Chemical* 176 (2013) 1110-1120

An open and low-cost optical-fiber measurement system for the optical detection of oxygen using a multifrequency phase-resolved method

Abstract—In this paper we present an open and low-cost optical-fiber measurement system for the optical detection of oxygen. A multifrequency phase-resolved method is proposed as the measurement technique in order to evaluate the oxygen-concentration-dependent phase-shift (or luminescence lifetime). Such evaluation is based on the operating principles of quadrature detection (also known as I/Q method), which may be entirely performed by digital signal processing. Theoretical aspects of the proposed methodology as well as the design and construction of the measurement system are discussed in this work. The system performance is assessed by characterization and evaluation of an oxygen-sensitive film (an oxygen-sensitive luminescent dye [Pt(II) meso-Tetra(pentafluorophenyl)porphine (PtTFPP)] immobilized into an oxygen-permeable polymeric matrix). These results are compared successfully with reference measurements obtained on the same sample using a conventional experimental setup based on a commercial lock-in amplifier. In this case, a measurement accuracy of <0.2 kPa oxygen partial pressure has been obtained over the measurement range of 0–20 kPa, for short periods of continuous measurement (<2 min), and at a room temperature of 21°C .

keywords: Optical fiber; Oxygen sensor; Phase-resolved; Frequency-domain; Multifrequency; LED.

4.1 Introduction

MOLECULAR oxygen is one of the most important analytes in our environment since it is present as either a reactant or product in a vast number of chemical and biochemical processes [1–6]. Thus, the determination of oxygen is of utmost importance in many fields of science and technology [2], including biotechnology [3, 6, 7], marine science [8, 9], biology [10, 11], chemical analysis [12, 13], food industry [14–16], and in medicine [5, 17–19]. Many measurement techniques and a wide variety of oxygen sensors have been developed over the past years to detect oxygen in both gas and liquid phases [9, 12, 17, 20], and some of them have even been commercialized. However, this area continues attracting the attention of the world’s scientific community and new methods and oxygen sensors have appeared recently [21–23]. Optical sensing, based on the quenching of luminescence emitted by a luminophore sensitive to a given analyte, has become increasingly popular over the last two decades, and currently is a widely used approach for the fabrication of optical sensors [24–26]. Optical methods for the determination of dissolved or gaseous oxygen are mainly based on this principle [20],

and a variety of schemes based on the measurement of the emission intensity or luminescence lifetime have been reported in the literature in recent years [8, 17–19, 27–30].

However, while intensity measurements are relatively simple and accurate in the laboratory [31–34], they are often inadequate in real-world applications due to their dependence on the intensity of the exciting light, detector drift, degradation or leaching of the dye, light losses in the optical path, orientation and location of the sensor, concentration of the luminophore, or optical surface quality. These quantities change from sample to sample, limiting the accuracy of these measurements, and resulting in the need for frequent recalibrations [35]. These difficulties can be minimized by measuring the luminescence lifetime [36], which is an intrinsic property of the luminophore (virtually independent of the external perturbations described before). Therefore, the lifetime-based measurements are often preferred for the design of reliable and robust luminescence optical sensors [35].

The luminescence lifetime can be measured either in the time domain (time-resolved method) or in the frequency domain (phase-resolved method) [20]. Although time-resolved methods are ideally suited to eliminate background luminescence and scattering [37], high-speed photodetectors and specific signal processing devices are required, so this approach is rather expensive. Frequency-domain lifetime sensing does not generally require so sophisticated instrumentation [28, 35], and it can be measured by using simple and cheap light sources and electronic devices. That makes it the most promising method for inexpensive opto-chemical measuring systems [38].

The phase-modulation fluorometry [20, 38, 39] consists on the determination of luminescence lifetime by measuring the phase angle or modulation at a single light modulation frequency. However, in practice, the phase shift is the most commonly used parameter. This is due to the fact that the modulation is strongly affected by variable levels of background light (among many other external factors) [38]. In this method, the sample is excited with a sinusoidally modulated light at a fixed frequency, that consequently causes a modulated luminescence emission at the identical frequency. Due to the emission lifetime of the luminescent material, the emission signal exhibits a phase shift (i.e., time delay) with respect to the excitation signal. The input excitation signal is used as a reference to establish the zero-phase position, and the lifetime is obtained indirectly by measuring the phase shift between excitation and emission signals [38]. If the luminescence emission is directly proportional to the intensity of the excitation light, and assuming that the luminescence decay is monoexponential, the relationship between the phase shift, ϕ , and the emission lifetime, τ , is given by [20, 40]:

$$\tan(\phi) = 2\pi f\tau \quad (4.1)$$

where ϕ is the phase shift, f is the exciting light modulation frequency, and τ is the decay time (or lifetime). In the simplest case, the quencher concentration can be calculated from the Stern-Volmer equation [20, 38] as:

$$[O_2] = k_q^{-1}[(2\pi f)/\tan(\phi) - 1/\tau_0] \quad (4.2)$$

where τ_0 is the unquenched excited state lifetime, k_q is a diffusion-dependent bimolecular quenching constant, and $[O_2]$ is the concentration of quencher.

For determining the phase shift can be used the principle of quadrature detection [41, 42] (also known as I/Q method), which is commonly used in communication systems for efficient transmission and reception of information signals. Although some I/Q method-based oxygen measuring systems have been previously reported in literature [17, 41, 43], in most of them the signal processing is carried out by using complex analog electronic circuits built specifically for this task, or alternatively, using expensive and bulky commercial instruments such as a lock-in amplifier or a network-analyzer.

In this work, an open and low-cost optical-fiber measurement system for the optical detection of oxygen is presented. The system allows the analytical characterization and/or evaluation of a wide variety of optical oxygen-sensitive films. It uses a phase-resolved method to evaluate the oxygen-concentration-dependent phase-shift (or indirectly, the luminescence lifetime). For that end, a simple and powerful methodology conducted entirely in the digital domain (i.e., using digital signal processing techniques) has been presented. Based on the principles of I/Q method, we proposed a multifrequency phase-resolved method [44] for the simultaneous detection of the oxygen-concentration-dependent phase-shift at multiple modulation frequencies. This method significantly reduces the measurement time necessary to carry out the characterization and/or evaluation of the sensing phase, while providing a more complete and valuable information about it. The performance of the system has been assessed by the characterization and evaluation of an oxygen-sensitive film (a luminescent dye [(Pt(II) meso-Tetra(pentafluorophenyl)porphine (PtTFPP)] immobilized into an oxygen-permeable polymeric matrix).

4.2 Measurement method theory

4.2.1 In-phase and quadrature sinusoidal components

A measuring technique based on the principles of quadrature detection (I/Q method) [41, 42] was used in this work, which was relatively simple and inexpensive to be digitally implemented. This technique is well known in the field of data transmission [42] and constitutes an alternative method of describing the amplitude and the phase angle (measured with respect to a reference signal) of a sinusoidal signal. At each modulation frequency, the phase angle (ϕ) and the amplitude (A) of a sinusoidal signal can be represented as a phasor [45]. The phasor is a vector which depicts a sinusoidal signal at a given frequency. The length of the vector is proportional to the amplitude at that frequency and its direction is given by the phase angle of the sinusoidal signal with respect to the reference signal [46]. The I/Q method is merely a translation of amplitude and phase data of a sinusoidal wave from a polar coordinate system to a cartesian coordinate system. Given a sinusoidal signal of the form, $x(t) = A \cdot \cos(2\pi ft + \phi)$, where A is the amplitude, ϕ is the phase angle, and f is the frequency (where $\omega = 2\pi f$ is the angular frequency), the aim is to determine the value of ϕ . Using the trig identity, $\cos(a + b) = \cos(a) \cdot \cos(b) - \sin(a) \cdot \sin(b)$, the sinusoidal signal can be represented in terms of its in-phase ($I(t)$) and quadrature ($Q(t)$) components, according to the following equation:

$$\begin{aligned}
x(t) &= A \cdot \cos(2\pi ft + \phi) \\
&= A \cdot \cos(\phi) \cdot \cos(2\pi ft) - A \cdot \sin(\phi) \cdot \sin(2\pi ft) \\
&= \underbrace{I \cdot \cos(2\pi ft)}_{I(t)} - \underbrace{Q \cdot \sin(2\pi ft)}_{Q(t)} \tag{4.3}
\end{aligned}$$

where $I = A \cdot \cos(\phi)$ and $Q = A \cdot \sin(\phi)$. From Eq. (6.3) can be concluded that a sinusoidal signal can be expressed as the sum of a cosine function and a sine function. The component that is in phase with the original carrier (in this case, a cosine function) is referred to as the in-phase component, $I(t)$. The other component, which is always 90° ($\pi/2$ radians) out of phase, is referred to as the quadrature component, $Q(t)$. In Eq. (6.3), the terms I and Q represent the amplitudes of the in-phase and quadrature sinusoidal components, respectively. Graphically, these terms I and Q can also be interpreted as the projections of the polar coordinate sinusoidal signal on the x and y axis, respectively. Both representations (amplitude-phase and I/Q) are equivalent and contain exactly the same information but in different ways. Assuming that the value of the angular frequency ω of the sinusoidal signal is known, the terms I and Q of $x(t)$ can be estimated from the following expressions [25, 39, 45]:

$$I = \frac{\int_{t_0}^{t_1} x(t) \cos(\omega t) dt}{\sqrt{\int_{t_0}^{t_1} \cos^2(\omega t) dt}} \tag{4.4}$$

$$Q = \frac{\int_{t_0}^{t_1} x(t) \sin(\omega t) dt}{\sqrt{\int_{t_0}^{t_1} \sin^2(\omega t) dt}} \tag{4.5}$$

where $x(t)$ is the continuous-time sinusoidal signal and t_0 and t_1 are the time instants of beginning and end of the signal $x(t)$, respectively. Finally, using the relationship between polar and rectangular coordinates, the amplitude A and phase angle ϕ of the sinusoidal signal $x(t)$ can be calculated from the terms I and Q (Eqs. (6.4) and (6.5)) as follows:

$$A = \sqrt{I^2 + Q^2} \quad \phi = -\arctan(Q/I) \tag{4.6}$$

4.2.2 Signal processing in the measurement system

The objective of digital signal processing carried out by the measurement system reported in this work was the precise determination of the phase shift ϕ (or time delay) between two discrete-time sinusoidal signals of identical frequency (i.e., the excitation signal, $x_{exc}(n)$, and the emission signal, $x_{em}(n)$), even in the presence of high noise levels. The aforementioned I/Q method was used for this task by adequate adaptation of this method for use with discrete-time signals (i.e., sampled signals). Thus, for the simplest case of monofrequency signals, two discrete-time sine and cosine signals ($x_s(n)$ and $x_c(n)$, respectively) were generated and stored digitally on a computer. These signals (of identical length and frequency) were used as reference signals for further digital signal processing. The reference cosine signal, $x_c(n)$, also served as excitation signal for the modulation of the current of the LED light source

in the LED driving circuit. For it, an AD/DA board was used to convert the digital signal stored on the computer into an analog signal. Finally, the analog excitation signal, $x_{exc}(t)$, and the analog emission signal, $x_{em}(t)$, were adequately sampled and stored on a computer for subsequent digital processing. In this case, the terms I and Q for the digital signal, $x(n)$, were calculated from the following expressions:

$$I = \frac{\sum_{k=0}^{N-1} x(k)x_c(k)}{\sqrt{\sum_{k=0}^{N-1} x_c^2(k)}} = \frac{\sum_{k=0}^{N-1} x(k)\cos(2\pi(f/f_s)k)}{\sqrt{\sum_{k=0}^{N-1} \cos^2(2\pi(f/f_s)k)}} \quad (4.7)$$

$$Q = \frac{\sum_{k=0}^{N-1} x(k)x_s(k)}{\sqrt{\sum_{k=0}^{N-1} x_s^2(k)}} = \frac{\sum_{k=0}^{N-1} x(k)\sin(2\pi(f/f_s)k)}{\sqrt{\sum_{k=0}^{N-1} \sin^2(2\pi(f/f_s)k)}} \quad (4.8)$$

where $x(n) = \{x_{exc}(n), x_{em}(n)\}$ is the sampled excitation or emission signal registered by the measurement system, f is the modulation frequency (in Hz), f_s is the sampling frequency (in samples/s), and k is the index of the k th sample (with $k = 0, 1, 2, \dots, N-1$, where N is the total number of samples of the sampled signal $x(n)$). From the terms I and Q (Eqs. (6.7)-(6.8)) of $x(n)$, the amplitude A and phase angle ϕ of the digital signal were calculated as shown in Eq. (6.6). This procedure was applied separately to the sampled excitation and emission signals ($x_{exc}(n)$ and $x_{em}(n)$, respectively) in order to obtain the phase angle value of each of them measured with respect to a reference signal (sinusoidal signal stored on the computer). Finally, the subtraction of phase angle values obtained for both signals, $\phi = \phi_{exc} - \phi_{em}$, provided the phase-shift value between the excitation and emission signals. On the other hand, the phase angle value introduced by the system's electronic circuitry, considered as a constant at a fixed working frequency, was also determined. This phase value was subtracted from ϕ to obtain the sensing film specific phase-shift exclusively.

4.2.3 Multifrequency phase estimation

The method described for calculating the phase shift between two sinusoidal signals at a fixed frequency (monofrequency I/Q method, or simply, I/Q method), could also be successfully applied to multifrequency signals (multifrequency I/Q method). In this approach, the signal $x(t)$ (i.e., excitation/emission signal) was replaced by a multifrequency signal consisting of a linear combination of M sinusoidal functions with different frequencies and amplitudes:

$$x(t) = \sum_{i=1}^M A_i \cdot \cos(2\pi f_i t) \quad (4.9)$$

In this case, a reference signal (i.e., a pair of quadrature sine and cosine signals) for each frequency component, f_i , of the multifrequency signal, $x(t)$, was required. Multifrequency I/Q method consisted basically in the calculation of the terms $\{I, Q\}_i$ for each of the frequency components of $x(t)$ (see Eq. (6.9)), as shown in the following expressions:

$$I_i = \frac{\sum_{k=0}^{N-1} x(k)x_{c,i}(k)}{\sqrt{\sum_{k=0}^{N-1} x_{c,i}^2(k)}} = \frac{\sum_{k=0}^{N-1} x(k)\cos(2\pi(f_i/f_s)k)}{\sqrt{\sum_{k=0}^{N-1} \cos^2(2\pi(f_i/f_s)k)}} \quad (4.10)$$

$$Q_i = \frac{\sum_{k=0}^{N-1} x(k)x_{s,i}(k)}{\sqrt{\sum_{k=0}^{N-1} x_{s,i}^2(k)}} = \frac{\sum_{k=0}^{N-1} x(k)\sin(2\pi(f_i/f_s)k)}{\sqrt{\sum_{k=0}^{N-1} \sin^2(2\pi(f_i/f_s)k)}} \quad (4.11)$$

where the subscript ‘ i ’ denotes the i th frequency component of the multifrequency signal (with $i = 1, 2, \dots, M$), and $x(n) = \{x_{exc}(n), x_{em}(n)\}$ is the sampled version of the emission or excitation multifrequency signal registered by the measurement system. From the terms $\{I, Q\}_i$ of each frequency component, a phase angle value, ϕ_i , was obtained for each one (see Eq. (6.6)). Moreover, the phase angle value introduced by the system’s electronic circuitry in each of the working frequencies was also determined, and this value was subsequently subtracted from ϕ_i .

The main advantage of working with multifrequency signals is that they allow the simultaneous determination of the phase shift at multiple frequencies, thus providing a more complete information about the sensing film in a shorter time. Thus, for example, the use of multifrequency signals avoids the need to choose a single optimal modulation frequency for the excitation signal [20, 29, 35, 47], while allowing a more accurate measure of phase shift (i.e., greater dynamic range) over the whole oxygen measurement range.

4.3 Experimental

4.3.1 Materials used for the synthesis of the oxygen sensing film

In this work, the oxygen-sensitive luminescent dye Platinum(II) meso-tetra(pentafluorophenyl)porphine (PtTFPP; Frontier Scientific Inc., www.frontiersci.com, UT, USA) was immobilized into a transparent and oxygen-permeable polystyrene matrix (PS; Scientific Polymer Products Inc., www.scientificpolymer.com, Ontario, NY, USA). Chloroform (Sigma-Aldrich, www.sigmaaldrich.com, Química S.A., Madrid, Spain) was used as the organic solvent for the preparation of the sensing film due to its good properties to dissolve both the dye and the polymer.

4.3.2 Measurement system (experimental setup)

An optical-fiber measurement system was designed and built in this work for measuring oxygen concentration in gas phase. Fig. 4.1 shows a schematic diagram of the instrumental setup. All signal processing was performed digitally on a computer using a Matlab program developed in our laboratories.

An ultraviolet LED (Ocean Optics, model LS-450 LED-395, www.oceanoptics.com, $\lambda_{max} = 395$ nm, angle of illumination 15° , LED diameter 5 mm, luminous power $25 \mu\text{W}$ into a $600 \mu\text{m}$ optical-fiber) was used as excitation light source. A multifrequency signal digitally generated with Matlab (i.e., a linear combination of sinusoidal signals with different frequencies as shown in Eq. (6.9)) was extracted by one of the analog output channels of an AD/DA board (National Instruments, model NI PCIe-6363/NI BNC-2120, www.ni.com), and it was used to modulate the current of the LED light source in the LED driving circuit. This

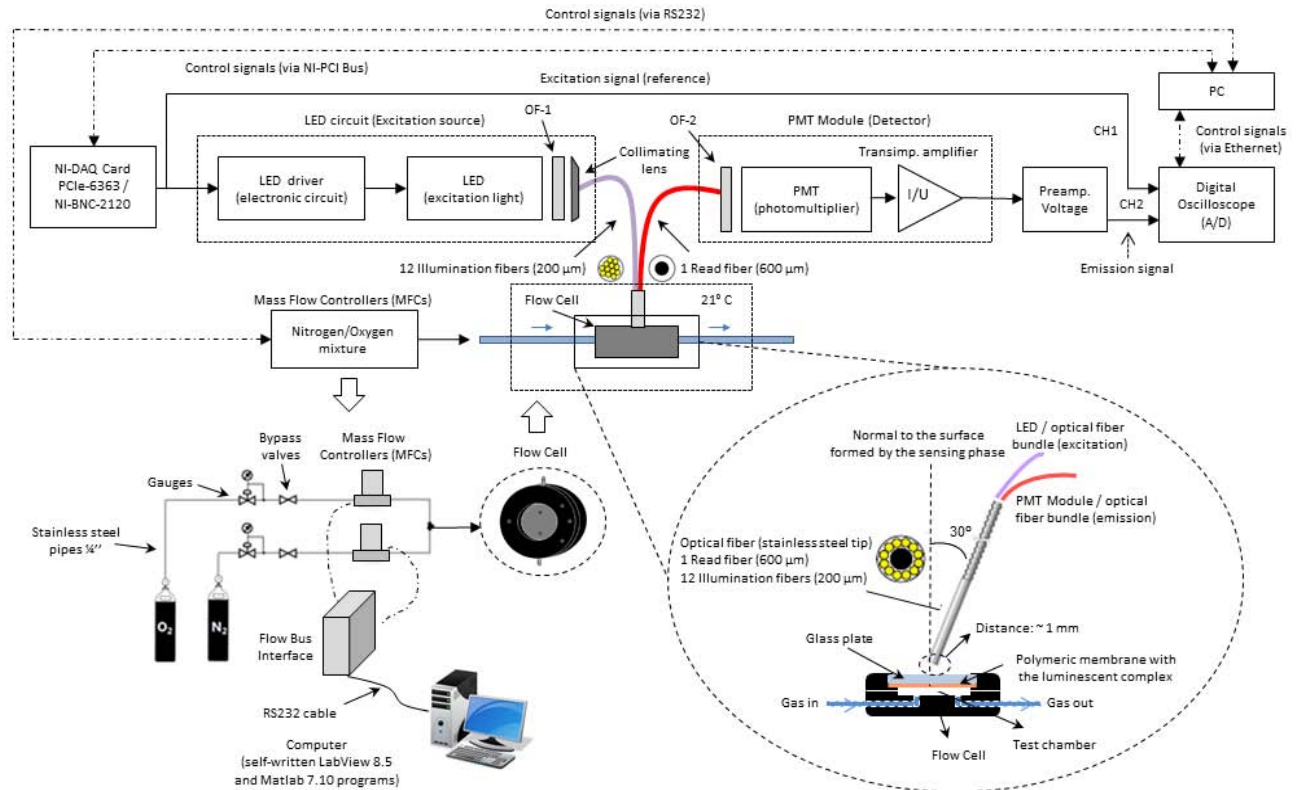


Figure 4.1: Schematic diagrams of the designed experimental setup for phase-shift measurements (based on I/Q method) and of the flow cell used.

analog excitation signal was generated by the continuous reproduction of stored signal file on the computer, thereby obtaining at the output channel a continuous-time signal. An optical band-pass filter (Thorlabs GmbH, model MF390-18, www.thorlabs.com, $\lambda_{central} = 390$ nm, $BW = 18$ nm) was placed after the UV LED to suppress undesirable wavelengths of the LED which would interfere with the luminescence signal in the detector. After the filter, the light of the LED was directly coupled into a bifurcated optical fiber bundle (Avantes Inc., model FCR-7xx200-2, www.avantes.com, wavelength range 200-800 nm (UV-VIS), 12 illumination fibers 200 μm core, 1 read fiber 600 μm core, N.A. 0.22). One of the branches of optical fiber bundle conducted the excitation light to the sensing phase, while the other was used to guide the phase-shifted luminescent emission from the sensing phase to the detector (PMT module, Hamamatsu Photonics Japan, model H10723-20, www.sales.hamamatsu.com, transimpedance 100 k Ω , BW DC-1 MHz). The emission light was previously filtered with an optical band-pass filter (Hamamatsu Photonics Japan, model A10033-03, $\lambda_{central} = 630$ nm, $BW = 60$ nm) placed before the PMT, which allowed to separate the reflected excitation light from the emission. The voltage signal provided by the PMT assembly (of few tens of millivolts) was amplified using a commercial low-noise programmable voltage preamplifier (Stanford Research Systems, model SIM911 BJT, www.thinksrs.com). Finally, both the analog excitation signal (taken as a reference) and the analog emission signal (obtained at the output of voltage preamplifier) were displayed and simultaneously digitized in real-time using a digital oscilloscope (LeCroy, model WaveRunner 604Zi, www.lecroy.com, 400 MHz, 10 GS/s, 4 Channels, 16 Mpts/Ch). The data acquisition was done at a sampling rate of 5 MS/s for signals of 1 s duration (i.e., a 5 M samples buffer was taken for each

signal). The data buffers corresponding to these two digitized signals were then transferred (via Ethernet) from the oscilloscope to a PC, where an ad hoc Matlab program was used to perform the digital signal processing (i.e., calculation of phase shift value between excitation and emission signals). The processing time of the phase estimation algorithm was less than 1 s, whereby said system can be applied for monitoring of real-time oxygen concentrations (as long as short data-acquisition times are used). Moreover, the additional phase-shift introduced by the electronic components (PMT, LED driver, voltage preamplifier, etc.) was previously evaluated for each working frequency using a reference LED (LED Supply, model L2-0-R5TH50-1, www.ledsupply.com, $\lambda_{peak} = 660$ nm, angle of illumination 50° , LED diameter 5 mm, luminous intensity 2000 mcd typ./ 20 mA) in the same spectral range of the sensing phase used. The subtraction of this phase value from the experimental results allowed to calculate the specific phase shift introduced by the sensing film exclusively.

For the gas characterization of the sensing film, the membrane was placed inside a flow-through cell designed in our laboratories (see Fig. 4.1), and different mixtures of nitrogen and oxygen gas flows were passed through the cell. The gas flow system was supplied by 50 L gas bottles at 200 bars of nitrogen and oxygen (both of 99.999% purity, obtained from Air Liquide, www.airliquide.com, Air Liquide España S.A, Llanera, Spain). The flow cell was made of black PTFE to prevent stray reflections and assure the chemical inertness. It was not thermostated, since it was considered to be used in a constant temperature environment (in this work, the temperature was kept constant at 21°C throughout the measurement time). The temperature was monitored continuously using a commercial temperature sensor (Fourtec-Fourier Technologies, model MicroLite, www.fouriersystems.com). Both the flow cell and PMT module were housed in a dark room (Thorlabs GmbH, model XE25C1) to prevent interference from stray light. For gas mixing, two mass-flow controllers (MFCs) (Bronkhorst High-Tech, model EL-FLOW Select F-201CV, www.bronkhorst.com) were used. After the MFCs, copper and stainless steel tubing were used to connect the MFCs with the flow cell. The gas system was completely controlled from a PC (via a RS232 serial port) using an ad hoc computer program developed in LabView 8.5 and Matlab 7.10.

Additionally, a conventional experimental setup based on a commercial dual-phase lock-in amplifier (Stanford Research Systems, model SR830) was used as a reference measurement system (see Fig. ESI-2 included in Electronic Supporting Information, ESI) to evaluate the response of the phase-shift measurement method proposed in this work (I/Q method). To this end, a reference oxygen sensing film was placed inside the flow cell, and a set of phase-shift measurements at different oxygen concentrations were registered with both setups. These measurements were taken using different measurement procedures, namely: (1) I/Q method here mentioned at a single frequency (in this case, an optimal modulation frequency at 5145 Hz was experimentally found for the used sensing film in a measurement range between 0% and 50% oxygen). (2) A reference system based on a commercial dual-phase lock-in amplifier as phase-sensitive detector (also using a single modulation frequency at 5145 Hz). (3) Multi-frequency I/Q method proposed herein, where a multifrequency signal consists of 4 sinusoidal components was used as the excitation signal. Furthermore, from multifrequency phase-shift measurements obtained with the measurement procedure (3), the calibration curves for the sensing film were obtained. Lastly, making use of these curves, the performance of the measurement system as an oxygen sensor was also evaluated (in terms of sensitivity and response time).

4.3.3 Preparation of the sensing film

The cocktail necessary for the elaboration of sensing film was prepared in a sealable 4 mL flask, and then was filled up to 2 mL solution volume with chloroform (dye concentration of 1.5 mg/mL; 198 mg of PS and 3 mg of PtTFPP). The cocktail was shaken on a commercial vortex mixer (Scientific Industries, model Vortex-Genie 2, www.scientificindustries.com, Bohemia, NY, USA) until all components were dissolved. Several replicas of the same membrane were obtained using a commercial spin-coater (Laurell Technologies, model WS-400B-6NPP/LITE, www.laurell.com, North Wales, PA, USA). For the preparation of the polystyrene membranes, 200 μL of cocktail were injected onto a rotating glass plate of a spinning device at 700 rpm. PtTFPP/PS membranes obtained after the deposition process were of a soft reddish color and allowed visible light to pass through them. The resulting layers showed a thickness of approximately 4 μm , mainly determined by the viscosity of the cocktail and the spin-coater rotation speed [31]. Further optimization in thickness influence will have to be carried out for the corresponding application.

4.3.4 Characterization of the sensing film

A standard protocol was used for characterizing the sensing film prepared in this work. Firstly, the spectroscopic behavior of the oxygen-sensitive film (i.e., excitation and emission spectra in the absence and in the presence of oxygen) was carried out using a commercial luminescence spectrophotometer (Varian Inc. – Agilent Technologies, model Cary Eclipse, www.home.agilent.com, CA, USA). The parameter setting for spectroscopic characterization was as follows: $\lambda_{exc} = 394$ nm, $\lambda_{em} = 650$ nm, slit-width $_{exc/em} = 10/10$ nm, detector voltage 550 V, $t_d = 0.001$ ms (delay time), $t_g = 2$ ms (gate time), and a total flow rate of 200 mL/min.

Secondly, the analytical characterization of the sensing film was performed. To this end, phase-shift measurements at different oxygen concentrations between 0 and 50% O_2 (or between 0 and 0.5 bar) were taken with the proposed measurement system using the multifrequency I/Q method. These phase-shift measurements was used to obtain the typical calibration curves for the sensing film. Furthermore, a typical response-time curve was also obtained to determine the response times of the membrane (i.e., rise and fall times to $t_{95\%}$). All measurements were done in the absence of ambient light and at 21 °C. The oxygen concentration of the gas passing through the flow cell was calculated in real-time from the measured oxygen/nitrogen flows provided by the MFCs (at a total flow rate of 200 mL/min), and assuming a constant environmental pressure of approximately 1000 mbar.

4.4 Results and discussion

PtTFPP is one of the most popular and widely used oxygen-sensitive luminescent dyes for the preparation of optical oxygen sensors [30]. It is primarily due to its good photostability and strong phosphorescence at room temperature (i.e., high photoluminescence quantum yield) [48, 49]. A polystyrene-based polymer (PS) was selected as the support matrix to immobilize the luminescent dye. Polystyrene has been widely used as a support matrix for

optical oxygen sensors [31, 49], because of its good compatibility with different dyes while providing a permeation-selective barrier to oxygen [50].

4.4.1 Spectroscopic behavior of the sensing film

The spectroscopic characterization of the oxygen-sensitive film was carried out using a luminescence spectrophotometer. The excitation and emission spectra of the sensing film in the absence and in the presence of oxygen (100% N_2 and 100% O_2 , respectively) were obtained (see Fig. ESI-3, ESI). The emission was clearly quenched when the sensing film was exposed to oxygen, and the maxima excitation and emission wavelengths were 394 and 650 nm, respectively. In this case, the sensing film showed excellent compatibility with an ultraviolet 395 nm LED (used as excitation light source). In addition, a red 660 nm LED could also be used as a reference LED to emulate the luminescent emission from the sensing film in the phase-shift determination process introduced by the system's electronic circuitry. The luminescence quantum yield of the sensing film can be found in the reference [49].

4.4.2 Performance of the proposed measurement method

A standard method was used to evaluate the response of the phase-shift measurement method proposed in this work (I/Q method). For this purpose, two different instrumental setups were used (see Section 4.3.2 for more details): (1) The phase-shift measurement system based on I/Q method (see Fig. 4.1); (2) A reference measurement system based on a commercial dual-phase lock-in amplifier (see Fig. ESI-2, ESI). The comparison of these two methods was performed using the sensing film mentioned herein, where a set of phase-shift measurements at 15 different oxygen concentrations in the range of 0-50% O_2 were measured for 4 different modulation frequencies using both setups. These results are shown in Fig. 4.2, where it can be seen that the phase-shift values obtained with both methods were very similar in all cases (maximum average absolute error $E_a (max) < 0.22^\circ$), thus demonstrating the validity of the proposed measurement method for measuring the phase shift (see Tables ESI-1 and ESI-2 in ESI for more details).

4.4.3 Analytical characterization of the sensing film

The analytical characterization of the sensing film for oxygen gas sensing was performed with the phase-shift measurement system using the multifrequency I/Q method. This method was employed to simultaneously measure the phase shift (or the lifetime) of the sensing film at multiple modulation frequencies under different oxygen concentrations. Thus, using this methodology, the optimal modulation frequency of the sensing film for a given measuring range could be quickly and easily found (based on the classical approach described in [47]). For this purpose, a multifrequency signal composed of 16 sinusoids of different frequency (in the range of 769-47153 Hz) and equal amplitude (i.e., $M = 16$, $A_i = 0.5$ V in Eq. (6.9)) was used as the excitation signal for modulating the LED light source. For each frequency component of multifrequency signal, the phase differences between 0-15% oxygen and 0-100% oxygen (extremes of the two oxygen measurement ranges considered most interesting in this

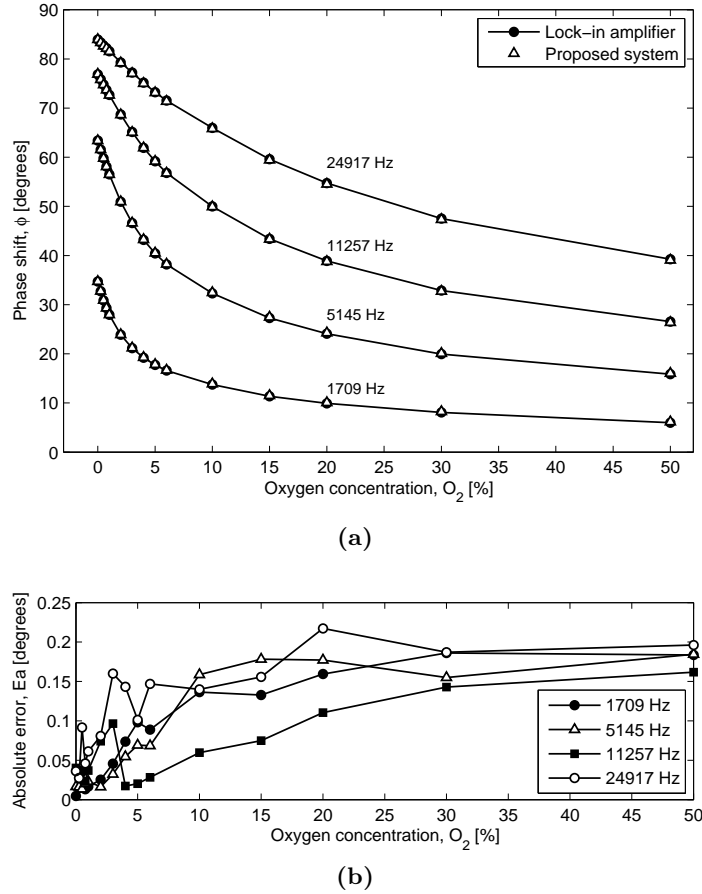


Figure 4.2: (a) Phase-shift measurements *versus* oxygen concentration for 4 different modulation frequencies using the proposed system based on I/Q method at a single frequency (\bullet), and the reference measurement system based on a commercial dual-phase lock-in amplifier (Δ). Each point in figure represents the average value of 100 phase-shift measurements. (b) Average absolute error, E_a (in degrees), calculated as: $E_a = (1/100) \sum_{n=1}^{100} |\bar{\phi}_{(set.2)} - \phi_{n(set.1)}|$, where $\bar{\phi}_{(set.2)}$ is the average phase-shift value obtained with the setup 2 (taken as a reference value) and given by: $(1/100) \sum_{n=1}^{100} \phi_{n(set.2)}$. A maximum $E_a (max) < 0.22^\circ$ was obtained at all points.

case) were calculated (see Table 4.1). In particular, as can be seen in this table, the phase-shift measurements reached a minimum value at 100% O_2 and a maximum value at 0% O_2 . The experimentally obtained phase differences between the extremes of the two considered oxygen measurement ranges were plotted as a function of modulation frequency (see Fig. ESI-4, ESI). From this plot, a maximum phase difference of 36° at 5145 Hz (between 0-15% O_2) and another of 50° at 11257 Hz (between 0-100% O_2) were found. In addition, a typical response curve (traced as a function of time) was also obtained for the sensing film at a fixed modulation frequency of 5145 Hz (selected as optimal for the measurement range of interest between 0 and 20% O_2). In this case, several cycles of phase-shift measurements were performed from the lowest concentration level (0% O_2) to the highest (100% O_2) and back to the lowest again, demonstrating the complete reversibility and stability of the sensing film as well as the excellent reproducibility of the phase-shift measurements (see Fig. ESI-5, ESI). From this curve, the response times ($t_{95\%}$) of the sensing film could be also determined, showing a fall time < 10 s (when changing from 100% N_2 to 100% O_2) and a rise time < 18 s

Table 4.1: Phase-shift measurements obtained at 16 different modulation frequencies and different oxygen concentrations (0%, 15% and 100% O_2) using the multifrequency I/Q method.

Freq. ^a (Hz)	0% O_2 ^b		15% O_2 ^b		100% O_2 ^b		0-15% O_2 ^c	0-100% O_2 ^d
	Mean (°)	Sdev (°)	Mean (°)	Sdev (°)	Mean (°)	Sdev (°)	Mean (°)	Mean (°)
769	17.681	0.029	4.953	0.106	3.009	0.143	12.727	14.671
1709	34.753	0.059	11.419	0.073	6.073	0.151	23.334	28.679
3761	56.438	0.054	23.024	0.108	14.499	0.091	33.413	41.938
5145	63.267	0.104	27.175	0.118	15.788	0.195	36.092	47.479
8713	74.361	0.045	40.185	0.171	25.602	0.097	34.175	48.758
11257	76.748	0.187	43.308	0.123	26.436	0.221	33.441	50.312
14639	80.414	0.201	50.501	0.197	31.011	0.246	29.913	49.404
17881	82.025	0.225	54.721	0.264	34.331	0.254	27.304	47.694
21499	83.297	0.241	58.512	0.205	37.666	0.298	24.784	45.631
24917	83.822	0.291	59.424	0.227	39.134	0.228	24.398	44.688
27847	84.436	0.311	62.491	0.122	41.312	0.234	21.945	43.123
31849	84.896	0.417	64.081	0.312	42.806	0.185	20.816	42.091
35129	85.015	0.421	65.501	0.434	44.486	0.279	19.513	40.528
40277	85.576	0.411	67.689	0.277	46.055	0.391	17.886	39.521
43777	86.087	0.423	68.933	0.496	47.771	0.322	17.154	38.315
47143	86.309	0.473	69.203	0.308	47.861	0.274	17.106	38.449

^aA multifrequency signal composed of 16 sinusoids with different frequencies (i.e., $M = 16$, $A_i = 0.5$ V in Eq. (6.9)) was used to find the optimal modulation frequency of the sensing film at different oxygen measurement ranges (0-15% O_2 and 0-100% O_2 , respectively).

^b20 phase-shift measurements (in degrees) were used to calculate the mean and standard deviation of all phase-shift values shown in table.

^cAverage phase difference between 0 and 15% oxygen for each modulation frequency.

^dAverage phase difference between 0 and 100% oxygen for each modulation frequency.

(when changing from 100% O_2 to 100% N_2).

Furthermore, the typical calibration curves for the sensing film (phase shift (ϕ) vs $[O_2](\%)$) were obtained using the multifrequency I/Q method (see Fig. ESI-6, ESI). A multifrequency signal formed by the summation of 4 sinusoidal functions with different frequencies was chosen as the excitation signal (see Eq. (6.9)). The frequencies selected for the signal were 1709, 5145, 11257 and 24917 Hz (two of them being the aforementioned optimal modulation frequencies for the oxygen measurement ranges of 0-15% and 0-100% O_2 , respectively, and the other two, additional frequencies above and below these). The amplitude of all sinusoidal components was set at 0.5 V. A time-domain and frequency-domain representation of the multifrequency excitation and emission signals registered by the digital oscilloscope can be observed in Figs. 4.3 and 4.4, respectively. A set of 20 phase-shift measurements (one for each frequency component of the multifrequency signal) was taken at 18 different oxygen concentrations between 0% and 50% O_2 to obtain the phase-shift calibration curves for the sensing film. The luminescence lifetimes for each frequency component were also calculated from these phase-shift measurements according to Eq. (6.1), assuming a monoexponential decay. Nevertheless, the obtained results showed that the sensing film displayed more than one decay time (see Fig. ESI-7, ESI), since different lifetimes were obtained at different modulation frequencies. Note that for the ideal case of a single-exponential decay one could use the phase angle at any frequency to calculate the lifetime [20]. Furthermore, it was also noted that higher modulation frequencies resulted in shorter lifetimes. Hence, in this case, it can be concluded that the lifetimes calculated from phase angle values (ϕ_ω), measured at a particular frequency, are only apparent values. These apparent lifetimes are the result of a complex weighting of the individual decay times and amplitudes, which depend on the experimental conditions [20] (such as the measurement method used (phase or modulation)

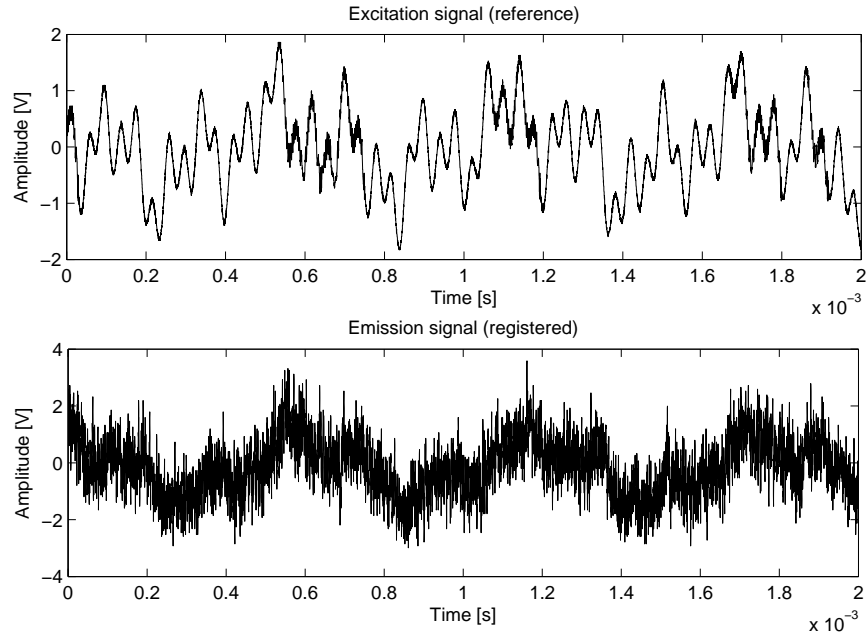


Figure 4.3: Temporal representation of a segment of the multifrequency excitation signal (top) and the multifrequency emission signal (bottom) registered simultaneously by the digital oscilloscope at a sampling rate of 5 MS/s and 0% O_2 . The temporal duration of the registered signals was 1 s. The multifrequency signal was formed by the summation of 4 sinusoidal functions with different frequencies (1709, 5145, 11257 and 24917 Hz) and equal amplitude ($M = 4$, $A_i = 0.5$ V; see Eq. (6.9)).

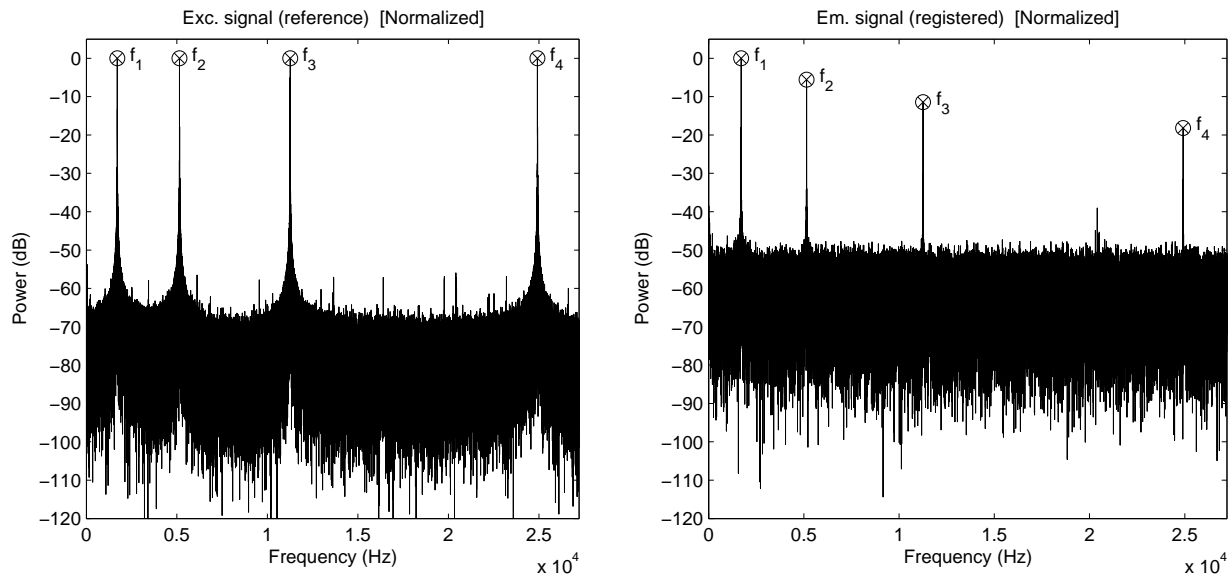


Figure 4.4: Normalized power spectrum of the multifrequency excitation signal (left) and the multifrequency emission signal (right). The length of data vectors was $N=5 \cdot 10^6$ samples. The marked peaks in the spectra correspond to the amplitudes (in dB) of the sinusoidal components of the multifrequency signal, where $f_1=1709$ Hz, $f_2=5145$ Hz, $f_3=11257$ Hz, and $f_4=24917$ Hz.

and the modulation frequency). Thus, strictly speaking, one does not actually measure apparent lifetimes. These values are simply interpretations of the measurable quantities (such

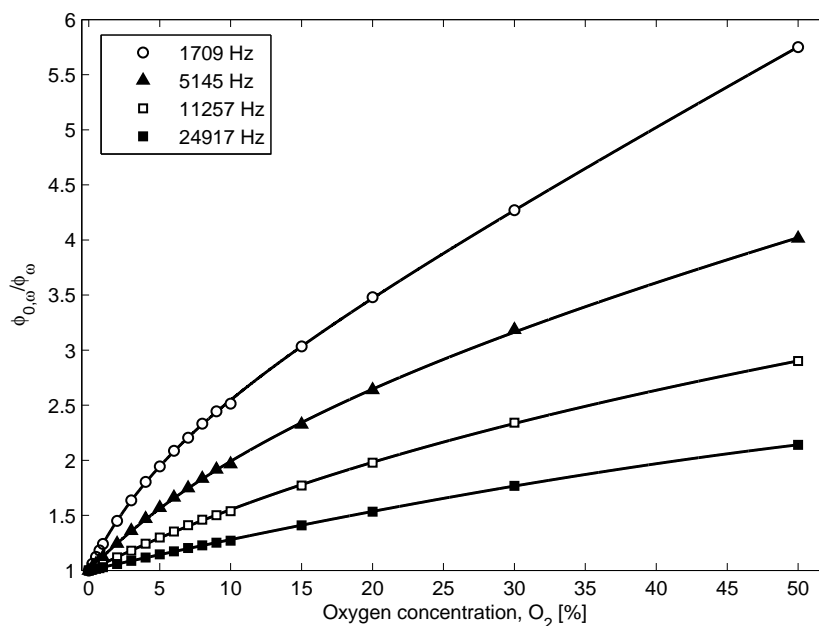


Figure 4.5: Calibration curves of normalized phase-shift versus oxygen concentration (i.e., $\phi_{0,\omega}/\phi_{\omega}$ vs. $[O_2(\%)]$) obtained from experimental data (markers in figure), where the subscript ‘0’ refers to the phase-shift value in the absence of oxygen and the subscript ‘ ω ’ to the particular frequency component of the multifrequency signal ($\omega = \{1709, 5145, 11257, 24917\}$ Hz). These phase shift-based calibration curves (solid lines in figure) were obtained individually for each frequency component of the multifrequency signal by adjusting the experimental data ($\phi_{0,\omega}/\phi_{\omega}$) to a two-site Demas model, except for the case of the calibration curve at 24917 Hz, where a Lehrer model was used to get a better fit of experimental data.

as phase and modulation values), which are often difficult to interpret in terms of molecular parameters [20]. However, although the use of apparent phase angle and modulation-based lifetimes does not seem recommendable, for a long time it has become standard practice to report these values for characterizing sensing films (i.e., lifetime values calculated from phase-shift data at a single modulation frequency).

In this work, it was considered more appropriate to work directly with the phase-shift measurements rather than with the apparent lifetime values calculated indirectly from the first. In this manner, once the average phase-shift values for each oxygen concentration and each frequency component were known, the calibration curves of normalized phase-shift versus oxygen concentration (i.e., $\phi_{0,\omega}/\phi_{\omega}$ vs. $[O_2(\%)]$) were obtained, where the subscript ‘0’ refers to the phase-shift value in the absence of oxygen and the subscript ‘ ω ’ to the particular frequency component of the multifrequency signal (i.e., modulation frequency used for the calculation of ϕ_{ω}). Fig. 4.5 shows the phase shift-based calibration curves of the sensing film, which were obtained by adjusting the experimental phase-shift data measured at each frequency ($\phi_{0,\omega}/\phi_{\omega}$) to a two-site Demas model [31, 51]. Table 4.2 summarizes the parameters obtained for these calibration curves fitted to the Demas model. The fitting of the experimental data using this model provided very good results in all cases, except for the calibration curve at 24917 Hz, where incorrect results were obtained. In this case, the Lehrer model [31, 52] was used to properly fit experimental data. The goodness-of-fit statistics for all obtained calibration curves were as follows: the sum of squares due to error (SSE) < 0.014 , root mean-square error (RMSE) < 0.01 , and $R^2 > 0.9998$.

Table 4.2: Parameters of the sensing film-calibration curves obtained by adjusting the experimental multifrequency phase-shift data to the Demas model.

Freq. (Hz)	f_1	f_2	$K_{SV1} (bar^{-1})$	$K_{SV2} (bar^{-1})$
1709	0.69 ± 0.01	0.31 ± 0.01	38.21 ± 2.87	2.43 ± 0.16
5145	0.75 ± 0.02	0.24 ± 0.03	17.25 ± 1.55	0.87 ± 0.22
11257	0.77 ± 0.04	0.22 ± 0.04	8.21 ± 0.71	0.33 ± 0.24
24917 ^a	0.82 ± 0.01	-	3.61 ± 0.08	-

^aIn this case a Lehrer model was used to properly fit experimental data.

4.4.4 Evaluation of the system response for oxygen sensing

After analytical characterization of the sensing film, some experiments were carried out to evaluate the performance of the proposed measurement system as an oxygen sensing system. For do this, the system was tested at 18 different oxygen concentrations between 0 and 50% oxygen {0, 0.25, 0.5, 0.75, 1, 2, 3, 4, 5, 6, 7, 8, 9, 10, 15, 20, 30 and 50% oxygen}, assuming a constant environmental pressure of approximately 1000 mbar, a total gas flow rate of 200 mL/min and a room temperature of 21 °C. The oxygen concentration was changed every 15 min over a period of more of 4 h, and phase-shift measurements (using the multifrequency I/Q method) were registered with the measurement system every 30 s. The multifrequency signal used as excitation signal was the same that used to obtain the calibration curves of the sensing film (see Section 4.4.3). The multifrequency phase-shift data (ϕ_ω) provided by the measurement system were then substituted into the mathematical equations obtained for the sensing film calibration curves (see Fig. 4.5 and Table 4.2). The calibration curves provided an estimation of the oxygen concentration for each frequency $[\hat{O}_{2,\omega}]$. Finally, different strategies were applied to calculate the expected value of the oxygen concentration from this multifrequency data set, and a comparison between them was reported. Some of these strategies were as follows:

- (1) $[\hat{O}_2]_{avg.}$: Average of the estimated oxygen concentration values for each of the frequency components of the multifrequency signal $[\hat{O}_{2,\omega}]$, given by:

$$[\hat{O}_2]_{avg.} = \frac{1}{4} \sum_{i=1}^{M=4} [\hat{O}_{2,\omega_i}] \quad (4.12)$$

- (2) $[\hat{O}_2]_{opt.}$: Selection of the estimated oxygen concentration value for the optimal frequency component at such oxygen concentration $[\hat{O}_{2,\omega_{opt}}]$. These optimal frequency components were previously chosen for the different oxygen measurement ranges shown in Fig. 4.2 using the following criteria: $\omega_{opt,[O_2]} = \omega_{[O_2]} \rightarrow \min\{\phi_{\omega_{[O_2]}} - \phi_{median}\}$, where $\phi_{\omega_{[O_2]}}$ is the phase-shift value for the frequency component ω at a given oxygen concentration, and ϕ_{median} is the median phase-shift value for all frequency components and concentrations. This value can be easily calculated from the data shown in Fig. 4.2 as: $\phi_{median} = \text{median}\{\phi_{min}, \phi_{max}\}$, where $\phi_{min} = \phi_{(1709 \text{ Hz}, 50\% O_2)} = 6.04^\circ$ and $\phi_{max} = \phi_{(24917 \text{ Hz}, 0\% O_2)} = 83.86^\circ$; resulting in a value of $\phi_{median} \sim 45^\circ$. Thus, the frequency components selected as optimal for the different oxygen measurement ranges were as fo-

llows: [0-0.5]% ($\omega_{opt} = 1709$ Hz), (0.5-7)% ($\omega_{opt} = 5145$ Hz), (7-20)% ($\omega_{opt} = 11257$ Hz), (20-50)% ($\omega_{opt} = 24917$ Hz).

- (3) $[\hat{O}_2]_{weig.}$: Weighed average of the estimated oxygen concentration values for each of the frequency components of the multifrequency signal $[\hat{O}_{2,\omega}]$, given by:

$$[\hat{O}_2]_{weig.} = \sum_{i=1}^{M=4} \alpha_{\omega_i} \cdot [\hat{O}_{2,\omega_i}] \quad (4.13)$$

where the normalized weighting coefficient for each frequency component, α_{ω_i} , was calculated using the following expression: $\alpha_{\omega_i} = [1/(|\hat{\phi}_{\omega_i} - \phi_{median}| + \epsilon)] / \sum_{i=1}^{M=4} \alpha_i$; where $\hat{\phi}_{\omega_i}$ is the phase-shift value measured by the measurement system for the frequency component ω_i , ϕ_{median} is the median phase-shift value previously mentioned, and ϵ is a constant of very small value (10^{-9}) to avoid division by zero errors.

- (4) $[\hat{O}_2]_{fix.}$: Selection of the estimated oxygen concentration value for the frequency component of 5145 Hz, which was selected as a fixed optimal modulation frequency for the complete measuring range between 0 and 50% oxygen (see Table 4.1).

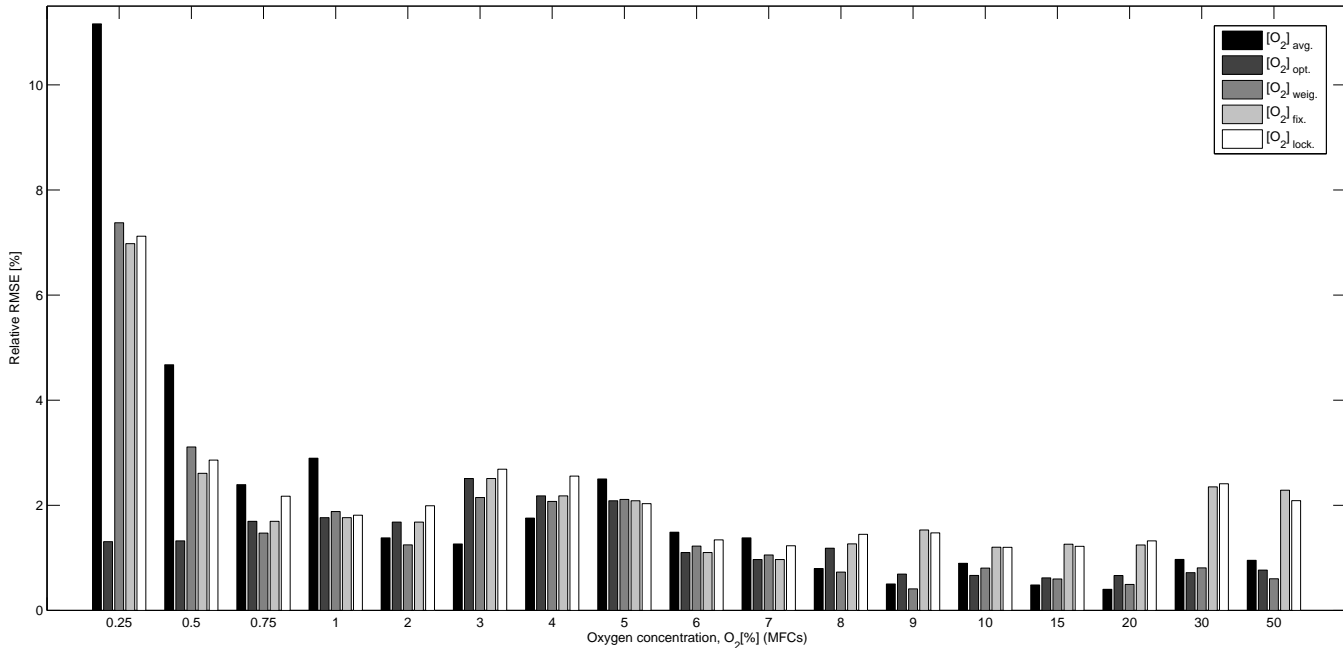


Figure 4.6: Relative root mean-square error (RRMSE(%)) for the different proposed oxygen measurement strategies at 17 different oxygen concentrations. The RRMSE values shown in figure were calculated from $N = 8$ test points (i.e., 8 estimated values of $[\hat{O}_2]$ for each strategy) by using the following expression: $RRMSE(\%) = 100 \cdot [MSE([\hat{O}_2])]^{1/2} / [O_{2,MFCs}]$; where $MSE([\hat{O}_2]) = 1/N \cdot \sum_{i=1}^N ([\hat{O}_2]_i - [O_{2,MFCs}]_i)^2$ is the mean square error of an estimator that allows to quantify the difference between values implied by an estimator ($[\hat{O}_2]$, oxygen concentration values estimated from the different strategies) and the true values of the quantity being estimated ($[O_{2,MFCs}]$, reference oxygen concentration values provided by the MFCs' control software).

The evaluation of these strategies was performed by taking a total of 8 test points (i.e., 8 values of $[\hat{O}_2]$ were estimated for each strategy) at 17 different oxygen concentrations between

Table 4.3: Relative root-mean-square error values (RRMSE) for the different oxygen measurement strategies at different oxygen measurement ranges (1-15% O_2 and 0.25-50% O_2 , respectively).

O_2 range (%)	$[\hat{O}_2]_{avg.}^a$	$[\hat{O}_2]_{opt.}^a$	$[\hat{O}_2]_{weig.}^a$	$[\hat{O}_2]_{fix.}^a$	$[\hat{O}_2]_{lock.}^a$
0.25-50	2.1111	1.2891	1.6551	2.0413	2.1738
1-15	1.3944	1.4037	1.2978	1.5947	1.7256

^aRelative root-mean-square error $RRMSE(\%)$ for an estimator $\hat{\theta}$ and N samples is given by:

$RRMSE(\%) = 100 \cdot [MSE(\hat{\theta})]^{1/2}/\theta$, where the empirical mean square error can be calculated as,

$MSE(\hat{\theta}) = 1/N \cdot \sum_{i=1}^N (\hat{\theta}_i - \theta_i)^2$, with $\hat{\theta}_i \equiv [\hat{O}_2]_i$ and $\theta_i \equiv [O_{2,MFCs}]_i$.

0.25% and 50% O_2 . From these measurements, the value of the relative root mean-square error (RRMSE(%)) for the different proposed strategies at each of assessed oxygen concentrations was calculated, and it was used as a statistic parameter to compare the response of different methods (see Fig. 4.6). It can be seen that some of the proposed strategies for estimating the expected value of the oxygen concentration based on multifrequency measurements (such as $[\hat{O}_2]_{opt.}$ and $[\hat{O}_2]_{weig.}$ strategies), showed in general a better response (i.e., lower RRMSE values) over the whole measurement range than the standard measurement method based on monofrequency measurements (i.e., a phase-resolved method at a single modulation frequency, denoted as $[\hat{O}_2]_{fix.}$ and $[\hat{O}_2]_{lock.}$ in Fig. 4.6; where $[\hat{O}_2]_{lock.}$ were measurements of $[\hat{O}_2]$ obtained from phase-shift measurements taken with the lock-in amplifier mentioned herein, at a single modulation frequency of 5145 Hz). Table 4.3 summarizes the values of RRMSE(%) obtained for the different proposed strategies considering different oxygen measurement ranges. Thus, it can be concluded that all methods showed similar RRMSE values for the measurement range of 1-15% O_2 (<1.73% in all cases), although slightly lower RRMSE values could be observed for the methods based on multifrequency measurements, such as $[\hat{O}_2]_{avg.}$ (<1.40%), $[\hat{O}_2]_{opt.}$ (<1.41%) and $[\hat{O}_2]_{weig.}$ (<1.3%). For the measurement range of 0.25-50% O_2 , a RRMSE value <2.18% was obtained in all cases, being especially interesting the response of the second strategy, $[\hat{O}_2]_{opt.}$, where a RRMSE value <1.29% was reached (in compared to the standard measurement methods, $[\hat{O}_2]_{fix.}$ and $[\hat{O}_2]_{lock.}$, with RRMSE values <2.05% and <2.18%, respectively).

The typical oxygen measurement range of the proposed measurement system was from 0 to 50% O_2 (or from 0 to 50 kPa) with a resolution <1% O_2 (or <1 kPa) over the whole measurement range. However, a higher accuracy was obtained at lower oxygen concentrations, where a measurement accuracy of <0.2% O_2 (or <0.2 kPa) was reached over the measuring range of 0-20% O_2 (or 0-20 kPa) for short periods of continuous measurement (<2 min) and at room temperature of 21 °C. The detection limit (LOD), calculated as the concentration of oxygen which produced an analytical signal three times the standard deviation of ten injections of a blank (0% oxygen in this case), was measured to be 0.01% oxygen using the measurement system and the sensing film mentioned in this work.

4.5 Conclusions

In this work, an open and low-cost optical-fiber system for measuring gaseous oxygen concentration and for characterization of optical oxygen-sensitive films was presented. It was based

on an inexpensive high-brightness LED, a signal conditioning circuit (LED driver), a photomultiplier tube (PMT), a bifurcated optical fiber, a personal computer and some general-purpose test equipment such as a digital oscilloscope and an AD/DA board. A multifrequency phase-resolved method based on the operating principles of quadrature detection (multifrequency I/Q method) was proposed to simultaneously estimate the oxygen concentration-dependent phase-shift (or luminescence lifetime) at multiple modulation frequencies. It was entirely conducted in software (digital signal processing) by using a computer program developed in our laboratories. The digital implementation of the phase estimation algorithm conferred to the measurement system an added value in terms of flexibility and potentiality compared to analog processing systems or those based on a standard lock-in amplifier. The digital nature of the measurement system gives the user full control over the signals, as well as the possibility of implementing advanced signal processing algorithms to improve the performance and functionality of this type of systems. In addition, due to the fact that only a personal computer and an AD/DA board are strictly needed to carry out the generation and post-processing of the digital signals (although in the proposed system a digital oscilloscope was additionally used to record and continuously display the acquired signals), the miniaturization and portability of the measuring system may be possible.

The proposed measurement method was assessed by characterization of a reference oxygen-sensitive film (i.e., a luminescent dye immobilized into a transparent and oxygen-permeable polystyrene matrix). These results were very similar to those obtained on the same sample using a conventional experimental setup based on a commercial lock-in amplifier. In addition, the performance of the entire measurement system as an oxygen sensor was also evaluated. An accuracy better than ± 1 kPa (or $\pm 1\%$ O_2) over the measuring range of 0-50 kPa (or 0-50% O_2) was achieved. A higher accuracy of < 0.2 kPa (or $< 0.2\%$ O_2) was obtained at lower oxygen concentrations over the measuring range of 0-20 kPa (or 0-20% O_2) for short periods of continuous measurement (< 2 min), and at a room temperature of 21 °C. These results showed the viability of the proposed system for measuring O_2 concentration and for characterization of sensing films.

Finally, we think that the proposed measurement system provides the necessary platform for the development of multiples potential applications (oxygen measurements in liquids, in chambers, in packages, etc., or even the measure of other analytes such as CO_2 or pH). Some of the most remarkable features are: the wide adjustable-frequency range, the easy replacement of optical components of the system, the ease of use, the flexibility of the system for the generation and post-processing of the digital signals, as well as the versatile connection via optical fiber of the sensing film to the measurement system.

Acknowledgments

The authors gratefully acknowledge the financial support of the Spanish Ministry of Economy and Competitiveness (Projects CTQ2008-01394 and CTQ2011-25316 and Medina-Rodríguez's grant reference BES-2009-026919) and the Regional Government of Andalusia (Excellence projects P07-FQM-2625 and P07-FQM-2738). The authors also thank M. Marín-Suárez del Toro and F.J. Sainz-Gonzalo for their help in the preparation of the sensing films.

Appendix A. Supplementary data

Supplementary data associated with this article can be found in the Electronic Supporting Information (ESI).

References

- [1] J. Janata, M. Josowicz, P. Vanýsek, D.M. DeVaney, *Chemical Sensors*, *Analytical Chemistry* 70 (1998) 179-208.
- [2] D.B. Papkovsky, T.C. O'Riordan, Emerging applications of phosphorescent metalloporphyrins, *Journal of Fluorescence* 15 (2005) 569-584.
- [3] P. Jamnik, P. Raspor, Methods for monitoring oxidative stress response in yeasts, *Journal of Biochemical and Molecular Toxicology* 19 (2005) 195-203.
- [4] M. Staal, E.I. Prest, J.S. Vrouwenvelder, L.F. Rickelt, M. Köhl, A simple optode based method for imaging O₂ distribution and dynamics in tap water biofilms, *Water Research* 45 (2011) 5027-5037.
- [5] C.A.K. Lange, P. Stavarakas, U.F.O. Luhmann, D.J. De Silva, R.R. Ali, Z.J. Gregor, et al., Intraocular oxygen distribution in advanced proliferative diabetic retinopathy, *American Journal of Ophthalmology* 152 (2012) 406-412.
- [6] K. Xie, X.W. Zhang, L. Huang, Y.T. Wang, Y. Lei, J. Rong, C.W. Qian, Q.L. Xie, Y.F. Wang, A. Hong, S. Xiong, On-line monitoring of oxygen in Tubespin, a novel, small-scale disposable bioreactor, *Cytotechnology* 63 (2011) 345-350.
- [7] X. Ge, M. Hanson, H. Shen, Y. Kostov, K.A. Brorson, D.D. Frey, et al., Validation of an optical sensor-based high-throughput bioreactor system for mammalian cell culture, *Journal of Biotechnology* 122 (2006) 293-306.
- [8] I. Klimant, V. Meyer, M. Köhl, Fiber-optic oxygen microsensors, a new tool in aquatic biology, *Limnology and Oceanography* 40 (1995) 1159-1165.
- [9] B. König, O. Kohls, G. Holst, R.N. Glud, M. Köhl, Fabrication and test of sol - Gel based planar oxygen optodes for use in aquatic sediments, *Marine Chemistry* 97 (2005) 262-276.
- [10] E. Schmäzlin, J.T. Van Dongen, I. Klimant, B. Marmodée, M. Steup, J. Fisahn, et al., An optical multifrequency phase-modulation method using microbeads for measuring intracellular oxygen concentrations in plants, *Biophysical Journal* 89 (2005) 1339-1345.
- [11] Y. Cao, Y.E.L. Koo, R. Kopelman, Poly(decyl methacrylate)-based fluorescent PEBBLE swarm nanosensors for measuring dissolved oxygen in biosamples, *Analyst* 129 (2004) 745-50.

- [12] J.F. Fernández-Sánchez, T. Roth, R. Cannas, M.K. Nazeeruddin, S. Spichiger, M. Graetzel, et al., Novel oxygen sensitive complexes for optical oxygen sensing, *Talanta* 71 (2007) 242-250.
- [13] J.F. Fernández-Sánchez, R. Cannas, S. Spichiger, R. Steiger, U.E. Spichiger-Keller, Novel nanostructured materials to develop oxygen-sensitive films for optical sensors, *Analytica Chimica Acta* 566 (2006) 271-282.
- [14] S.C. Fonseca, F.A.R. Oliveira, J.K. Brecht, K.V. Chau, Influence of low oxygen and high carbon dioxide on shredded Galega kale quality for development of modified atmosphere packages, *Postharvest Biology and Technology* 35 (2005) 279-292.
- [15] T.C. O’Riordan, H. Voraberger, J.P. Kerry, D.B. Papkovsky, Study of migration of active components of phosphorescent oxygen sensors for food packaging applications, *Analytica Chimica Acta* 530 (2005) 135-141.
- [16] F.C. O’Mahony, T.C. O’Riordan, N. Papkovskaia, V.I. Ogurtsov, J.P. Kerry, D.B. Popkovsky, Assessment of oxygen levels in convenience-style muscle-based sous vide products through optical means and impact on shelf-life stability, *Packaging Technology and Science* 17 (2004) 225-234.
- [17] G.A. Holst, T. Köster, E. Voges, D.W. Lübbers, FLOX – an oxygen-flux-measuring system using a phase-modulation method to evaluate the oxygen-dependent fluorescence lifetime, *Sensors and Actuators B* 29 (1995) 231-239.
- [18] K. Tsukada, S. Sakai, K. Hase, H. Minamitani, Development of catheter-type optical oxygen sensor and applications to bioinstrumentation, *Biosensors and Bioelectronics* 18 (2003) 1439-1445.
- [19] O. Ergeneman, G. Dogangil, M.P. Kummer, J.J. Abbott, M.K. Nazeeruddin, B.J. Nelson, A magnetically controlled wireless optical oxygen sensor for intraocular measurements, *IEEE Sensors Journal* 8 (2008) 29-37.
- [20] J.R. Lakowicz, *Principles of Fluorescence Spectroscopy*, 2nd ed., Kluwer Academic, New York, 1999.
- [21] S.M. Borisov, A.S. Vasylevska, C. Krause, O.S. Wolfbeis, Composite luminescent material for dual sensing of oxygen and temperature, *Advanced Functional Materials* 16 (2006) 1536-1542.
- [22] S.M. Borisov, R. Seifner, I. Klimant, A novel planar optical sensor for simultaneous monitoring of oxygen, carbon dioxide, pH and temperature, *Analytical and Bioanalytical Chemistry* 400 (2011) 2463-2474.
- [23] K. Koren, S.M. Borisov, R. Saf, I. Klimant, Strongly phosphorescent iridium(III)-porphyrins – new oxygen indicators with tuneable photophysical properties and functionalities, *European Journal of Inorganic Chemistry* 10 (2011) 1531-1534.
- [24] O.S. Wolfbeis, B.M. Weidgans, F. Baldini, A.N. Chester, J. Homola, S. Martellucci, *Fiber Optic Chemical Sensors and Biosensors: A View Back Optical Chemical Sensors*, Springer Netherlands, 2006, pp. 17-44.

- [25] H. Szmecinski, J. Lakowicz, in: C.D. Geddes, J.R. Lakowicz (Eds.), *Lifetime-Based Sensing Topics in Fluorescence Spectroscopy*, Springer, US, 2002, pp. 295-334.
- [26] G. Orellana, *Luminescent optical sensors*, *Analytical and Bioanalytical Chemistry* 379 (2004) 344-346.
- [27] J. Dakin, B. Culshaw, *Optical Fiber Sensors: Applications, Analysis and Future Trends*, Artech House ed., Norwood, MA, 1997.
- [28] W. Trettnak, C. Kolle, F. Reiningner, C. Dolezal, P. O'Leary, Miniaturized luminescence lifetime-based oxygen sensor instrumentation utilizing a phase modulation technique, *Sensors and Actuators B* 36 (1996) 506-512.
- [29] G. O'Keeffe, B.D. MacCraith, A.K. McEvoy, C.M. McDonagh, J.F. McGilp, Development of a LED-based phase fluorimetric oxygen sensor using evanescent wave excitation of a sol-gel immobilized dye, *Sensors and Actuators B* 29 (1995) 226-230.
- [30] T.S. Yeh, C.S. Chu, Y.L. Lo, Highly sensitive optical fiber oxygen sensor using Pt(II) complex embedded in sol-gel matrices, *Sensors and Actuators B* 119 (2006) 701-707.
- [31] M. Marín-Suárez del Toro, J.F. Fernández-Sánchez, E. Baranoff, M.K. Nazeeruddin, M. Graetzel, A. Fernández-Gutiérrez, Novel luminescent Ir(III) dyes for developing highly sensitive oxygen sensing films, *Talanta* 82 (2010) 620-626.
- [32] M.A. Chan, J.L. Lawless, S.K. Lam, D. Lo, Fiber optic oxygen sensor based on phosphorescence quenching of erythrosin B trapped in silica-gel glasses, *Analytica Chimica Acta* 408 (2000) 33-37.
- [33] C. McDonagh, B.D. MacCraith, A.K. McEvoy, Tailoring of sol-gel films for optical sensing of oxygen in gas and aqueous phase, *Analytical Chemistry* 70 (1) (1998) 45-50.
- [34] B.D. MacCraith, G. O'Keeffe, C. McDonagh, A.K. McEvoy, LED-based fibre optic oxygen sensor using sol-gel coating, *Electronics Letters* 30 (1994) 888-889.
- [35] C. McDonagh, C. Kolle, A.K. McEvoy, D.L. Dowling, A.A. Cafolla, S.J. Cullen, et al., Phase fluorometric dissolved oxygen sensor, *Sensors and Actuators B* 74 (2001) 124-130.
- [36] P. Hartmann, M.J.P. Leiner, M.E. Lippitsch, Response characteristics of luminescent oxygen sensors, *Sensors and Actuators B* 29 (1995) 251-257.
- [37] D.M. Jenkins, C. Zhu, W.W. Su, A simple hybrid circuit for direct determination of fluorescence lifetimes, *Applied Engineering in Agriculture* 24 (2008) 259-263.
- [38] D. Andrzejewski, I. Klimant, H. Podbielska, Method for lifetime-based chemical sensing using the demodulation of the luminescence signal, *Sensors and Actuators B* 84 (2002) 160-166.
- [39] H. Szmecinski, J.R. Lakowicz, Measurement of the intensity of long-lifetime luminophores in the presence of background signals using phase-modulation fluorometry, *Applied Spectroscopy* 53 (1999) 1490-1495.
- [40] E. Crowell, L. Geng, Reduction of multiexponential background in fluorescence with phase-sensitive detection, *Applied Spectroscopy* 55 (2001) 1709-1716.

-
- [41] P. Langer, R. Müller, S. Drost, T. Werner, A new method for filter-free fluorescence measurements, *Sensors and Actuators B* 82 (2002) 1-6.
- [42] R.D. Hippenstiel, *Detection Theory: Applications and Digital Signal Processing*, CRC Press, 2002.
- [43] M. Valledor, J.C. Campo, I. Sánchez-Barragán, J.M. Costa-Fernández, J.C. Álvarez, A. Sanz-Medel, Determination of phosphorescence lifetimes in the presence of high background signals using phase-shift measurements, *Sensors and Actuators B* 113 (2006) 249-258.
- [44] V.I. Ogurtsov, D.B. Papkovsky, Application of frequency spectroscopy to fluorescence-based oxygen sensors, *Sensors and Actuators B* 113 (2) (2006) 608-616.
- [45] D. Giancoli, *Physics for Scientists and Engineers with Modern Physics*, 2nd ed., Prentice Hall, Mishawaka, IN, USA, 1989.
- [46] G.D. Reinhart, P. Marzola, D.M. Jameson, E. Gratton, A method for on-line background subtraction in frequency domain fluorometry, *Journal of Fluorescence* 1 (1991) 153-162.
- [47] V.I. Ogurtsov, D.B. Papkovsky, Selection of modulation frequency of excitation for luminescence lifetime-based oxygen sensors, *Sensors and Actuators B* 51 (1998) 377-381.
- [48] Y. Amao, T. Miyashita, I. Okura, Platinum tetrakis(pentafluorophenyl) porphyrin immobilized in polytrifluoroethylmethacrylate film as a photostable optical oxygen detection material, *Journal of Fluorine Chemistry* 107 (2001) 101-106.
- [49] S.M. Borisov, I. Klimant, Ultrabright oxygen optodes based on cyclometalated iridium(III) coumarin complexes, *Analytical Chemistry* 79 (2007) 7501-7509.
- [50] O.S. Wolfbeis, Materials for fluorescence-based optical chemical sensors, *Journal of Materials Chemistry* 15 (2005) 2657-2669.
- [51] J.N. Demas, B.A. DeGraff, Luminescence-based sensors: microheterogeneous and temperature effects, *Sensors and Actuators B* 11 (1993) 35-41.
- [52] S.S. Lehrer, Solute perturbation of protein fluorescence. The quenching of the tryptophyl fluorescence of model compounds and of lysozyme by iodide ion, *Biochemistry* 10 (1971) 3254-3263.

Appendix A. Supplementary data Electronic Supporting Information (ESI)

An open and low-cost optical-fiber measurement system for the optical detection of oxygen using a multifrequency phase-resolved method

Santiago Medina Rodríguez^{a,b,*}, Ángel de la Torre Vega^{a,*}, Jorge Fernando Fernández Sánchez^b and Alberto Fernández Gutiérrez^b

^a*Department of Signal Theory, Networking and Communications, CITIC-UGR, University of Granada, C/ Periodista Rafael Gómez 2, E-18071 Granada, Spain.*

^b*Department of Analytical Chemistry, Faculty of Sciences, University of Granada, Avda. Fuentenueva s/n, E-18071 Granada, Spain.*

List of Figures

- Fig. ESI-1. Chemical structure of the PtTFPP complex.
- Fig. ESI-2. Schematic diagram of the designed experimental setup for phase-shift measurements taken as a reference system.
- Fig. ESI-3. Luminescence excitation and emission spectra of the oxygen-sensitive film (PtTFPP-PS).
- Fig. ESI-4. Experimental phase difference for 0-15% and 0-100% O₂ plotted against modulation frequency.
- Fig. ESI-5. Typical response-time curve for the oxygen-sensitive film (PtTFPP-PS).
- Fig. ESI-6. Phase-shift measurement of the sensing film vs. oxygen concentration at different modulation frequencies.
- Fig. ESI-7. Lifetime measurement of the sensing film vs. oxygen concentration at different modulation frequencies.
- Fig. ESI-8. Adjustment of the lifetime experimental data ($\tau_{0,\omega}/\tau_{\omega}$) to a two-site Demas model (lifetime calibration curves).
- Figs. ESI-9/ESI-10. Comparison between oxygen concentration values provided by the MFCs (taken as a reference) and oxygen concentration values estimated with the proposed measurement system (based on the multifrequency I/Q method).

List of Tables

- Tables ESI-1/ESI-2. Phase-shift measurements vs. oxygen concentration at 4 different modulation frequencies taken with two different instrumental setups: (1) The proposed measurement system based on I/Q method at a single modulation frequency; (2) The reference measurement system based on a commercial lock-in amplifier.
- Table ESI-3. Parameters of the sensing film-calibration curves obtained by adjusting the experimental multifrequency lifetime data to the Demas model.

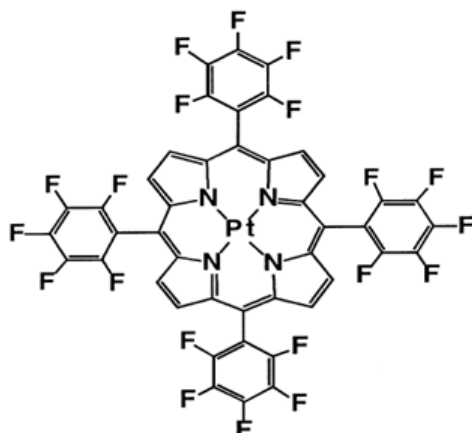


Fig. ESI-1. Chemical structure of the PtTFPP complex (Pt(II) meso-Tetra(pentafluorophenyl)porphine).

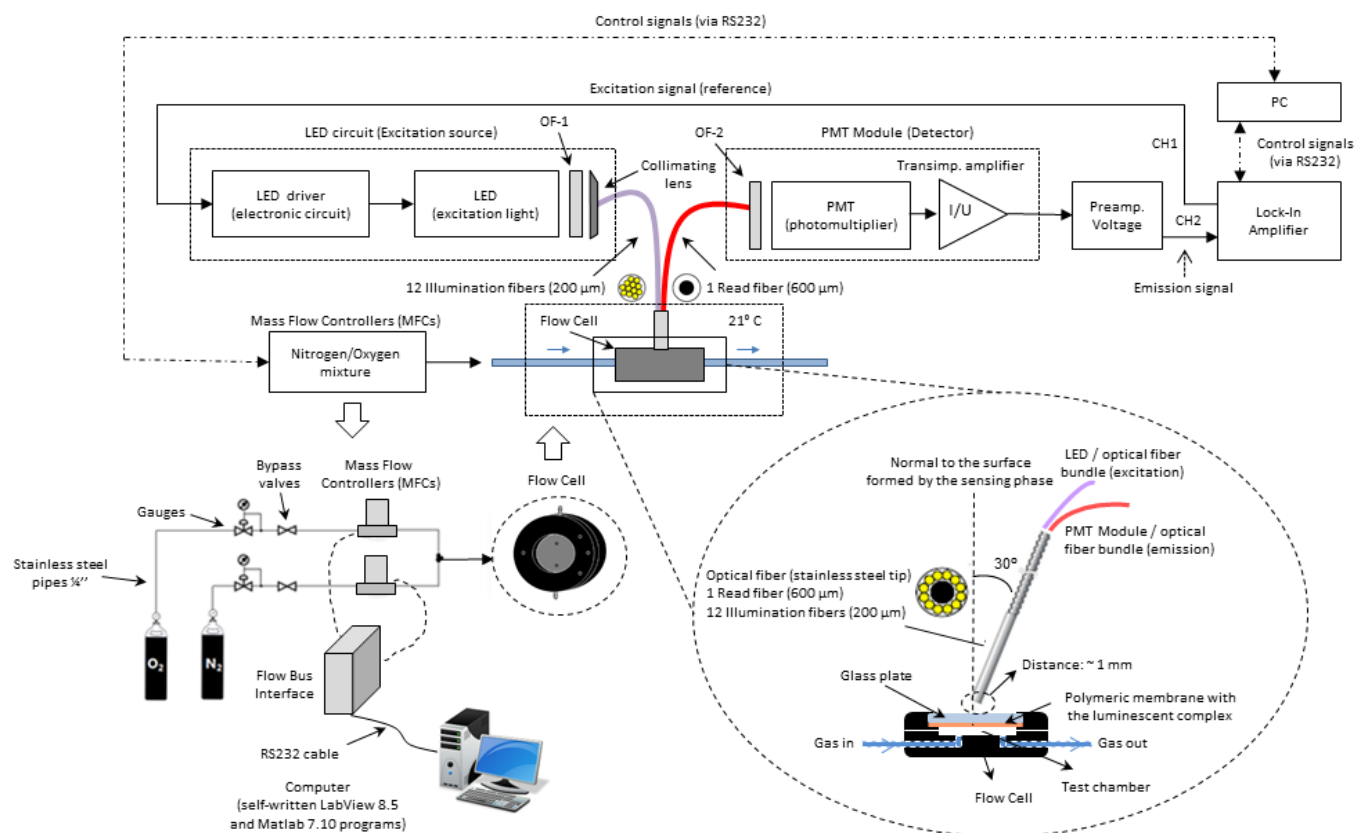


Fig. ESI-2. Schematic diagrams of the designed experimental setup for phase-shift measurements (based on a commercial dual-phase lock-in amplifier, Stanford Research System, model SR830, www.thinksrs.com) and of the flow cell used. Note that in this case the digital oscilloscope of the system based on I/Q method (see Fig. 4.1 of the manuscript) was replaced by a commercial lock-in amplifier (taken as a reference system for measuring the phase-shift).

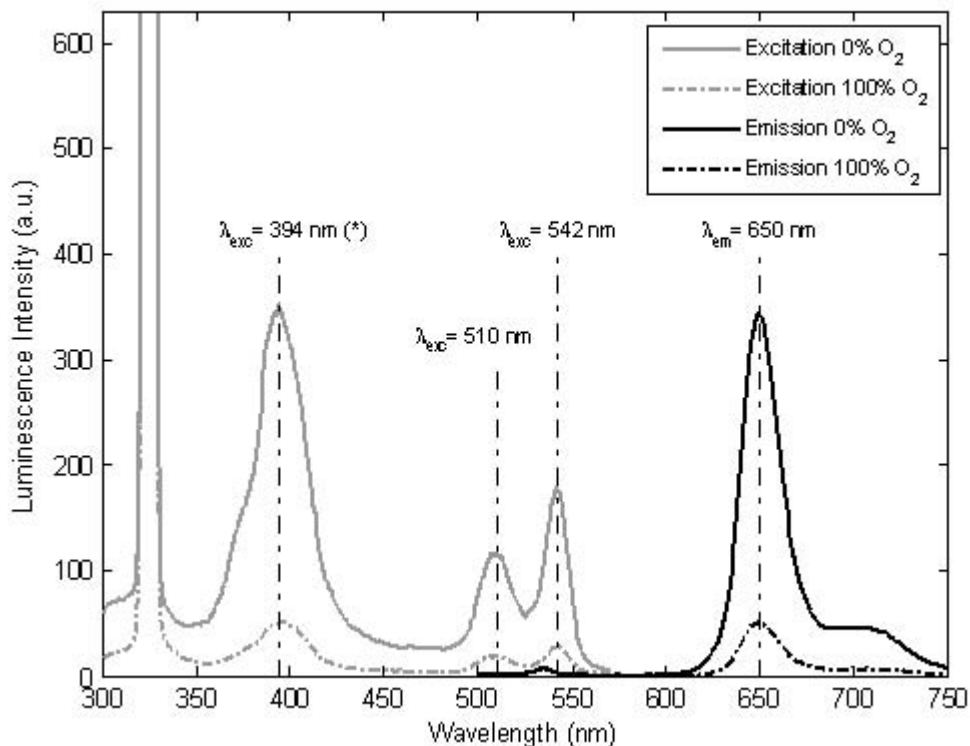


Fig. ESI-3. Luminescence excitation and emission spectra of the oxygen-sensitive dye (PtTFPP) immobilized in a polystyrene (PS) matrix (dye concentration of 1.5 mg mL^{-1} in PS, 198 mg of PS and 3 mg of PtTFPP; film thickness of approximately $4 \mu\text{m}$): (solid, gray line) excitation spectrum in the absence of oxygen (100% N_2); (dotted, gray line) excitation spectrum in the presence of oxygen (100% O_2); (solid, black line) emission spectrum in the absence of oxygen (100% N_2); (dotted, black line) emission spectrum in the presence of oxygen (100% O_2). $\lambda_{max(exc)} = \{394^*, 510, 542\}$ nm (maximum excitation wavelengths), where the asterisk denotes the wavelength selected to excite the sensing film (see dotted vertical lines shown in figure), $\lambda_{max(em)} = 650$ nm (maximum emission wavelength), slits width_(exc/em) = 10/10 nm, detector voltage 550 V, $t_d = 0.001$ ms (delay time), $t_g = 2$ ms (gate time), and a total flow-rate of 200 mL min^{-1} . All measurements were obtained using a Cary Eclipse luminescence spectrophotometer (Varian Inc. - Agilent Technologies., model Cary Eclipse, www.home.agilent.com, CA, USA), at room temperature of 21°C and assuming a constant environmental pressure of approximately 1000 mbar.

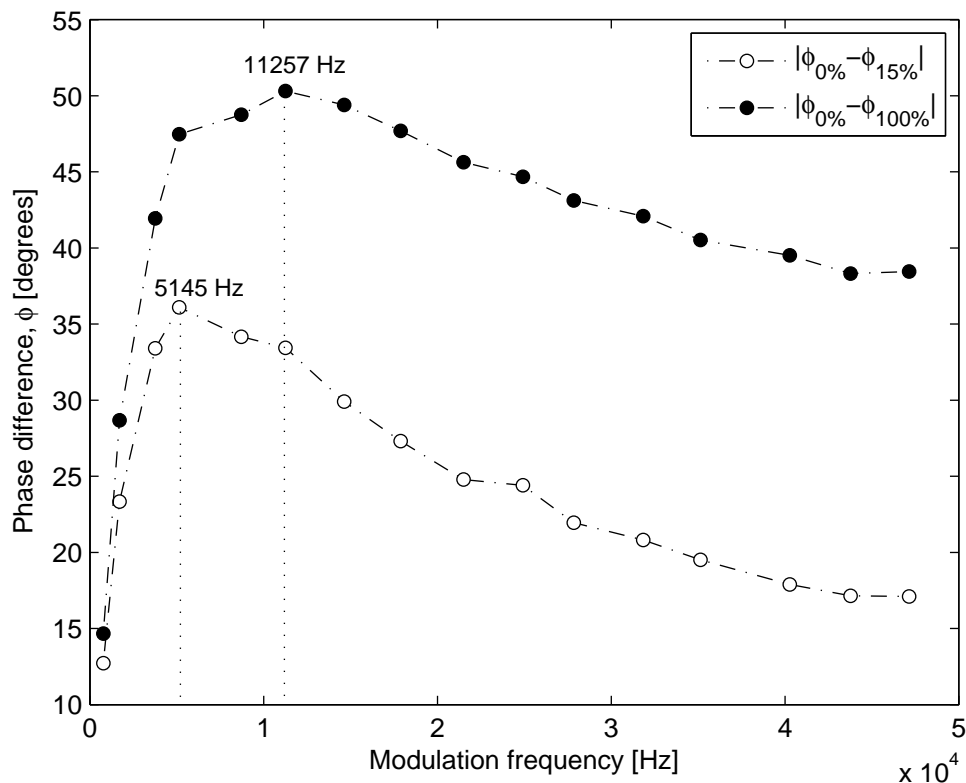


Fig. ESI-4. Experimental phase difference, ϕ (in degrees), between the phase-shift measured at 0% and 15% oxygen ($|\phi_{0\% O_2} - \phi_{15\% O_2}|$) and between 0% and 100% oxygen ($|\phi_{0\% O_2} - \phi_{100\% O_2}|$) plotted against the modulation frequency (in Hz). From this plot, a maximum phase difference of 36° at 5145 Hz (between 0-15% O_2) and another of 50° at 11257 Hz (between 0-100% O_2) were found, and these frequencies were selected as optimal modulation frequencies for these oxygen concentration ranges. All phase-shift measurements were obtained with the proposed measuring system using the multifrequency I/Q method. For this purpose, a multifrequency signal composed of 16 sinusoids with different frequencies (in the range of 769 to 47153 Hz) and equal amplitude (i.e., $M = 16$, $A_i = 0.5$ V in Eq. 6.9 of the manuscript) was used as the excitation signal for modulating the LED light source.

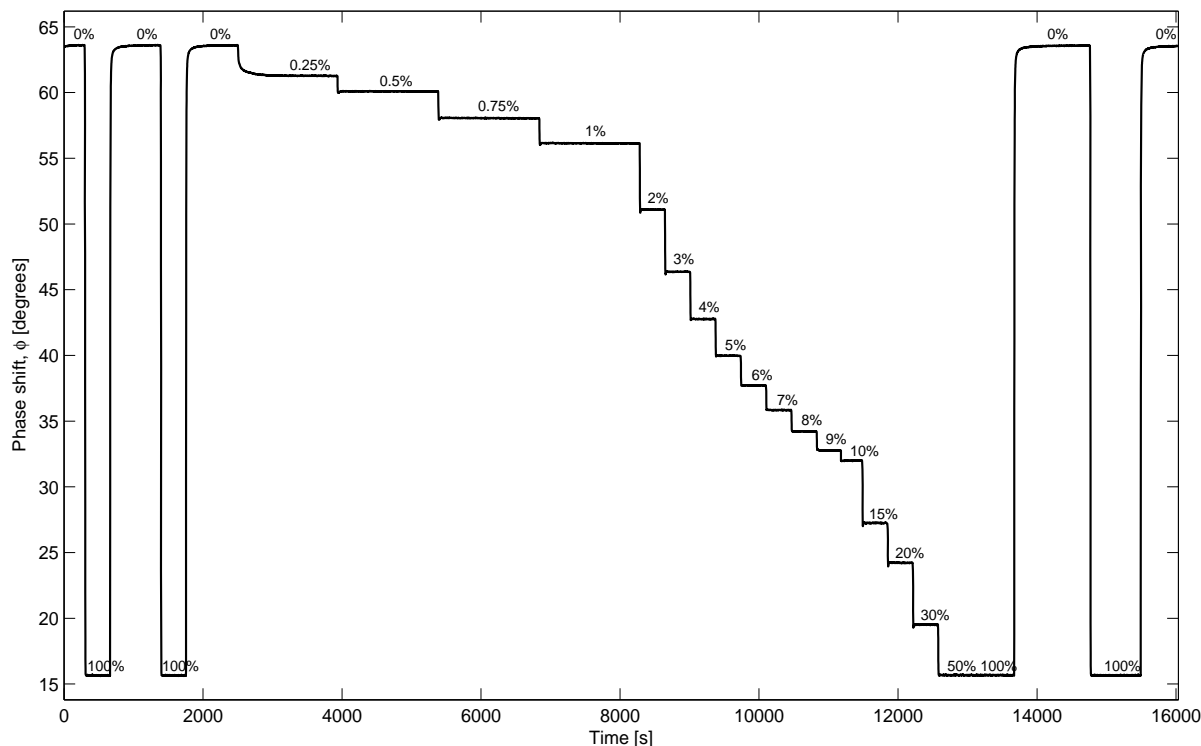


Fig. ESI-5. Typical response-time curve for the PtTFPP-PS sensing film (phase-shift measurement, ϕ (in degrees), at different oxygen concentrations [O_2 (%)] between 0-100% oxygen traced as a function of time). All phase-shift measurements were done with the proposed measurement system using the I/Q method at a fixed modulation frequency of 5145 Hz, in the absence of ambient light, and at room temperature of 21 °C. The oxygen concentrations of the gas passing through the flow cell were calculated in real-time from the measured oxygen/nitrogen flows provided by the the MFCs'control software at a total flow-rate of 200 mL min⁻¹, and assuming a constant environmental pressure of approximately 1000 mbar. From this curve, the response times ($t_{95\%}$) of the sensing film could also be determined, obtaining a fall time < 10 s (when changing from 100% N_2 to 100% O_2) and a rise time < 18 s (when changing from 100% O_2 to 100% N_2). As shown in figure, the phase-shift measurement decreased at higher oxygen concentrations because of the luminescence quenching phenomenon, and the complete reversibility of the phase-shift measurements allowed to monitor increases and decreases of O_2 continuously. The studied sensing film exhibited a high sensitivity over a measurement range of 0-20% O_2 .

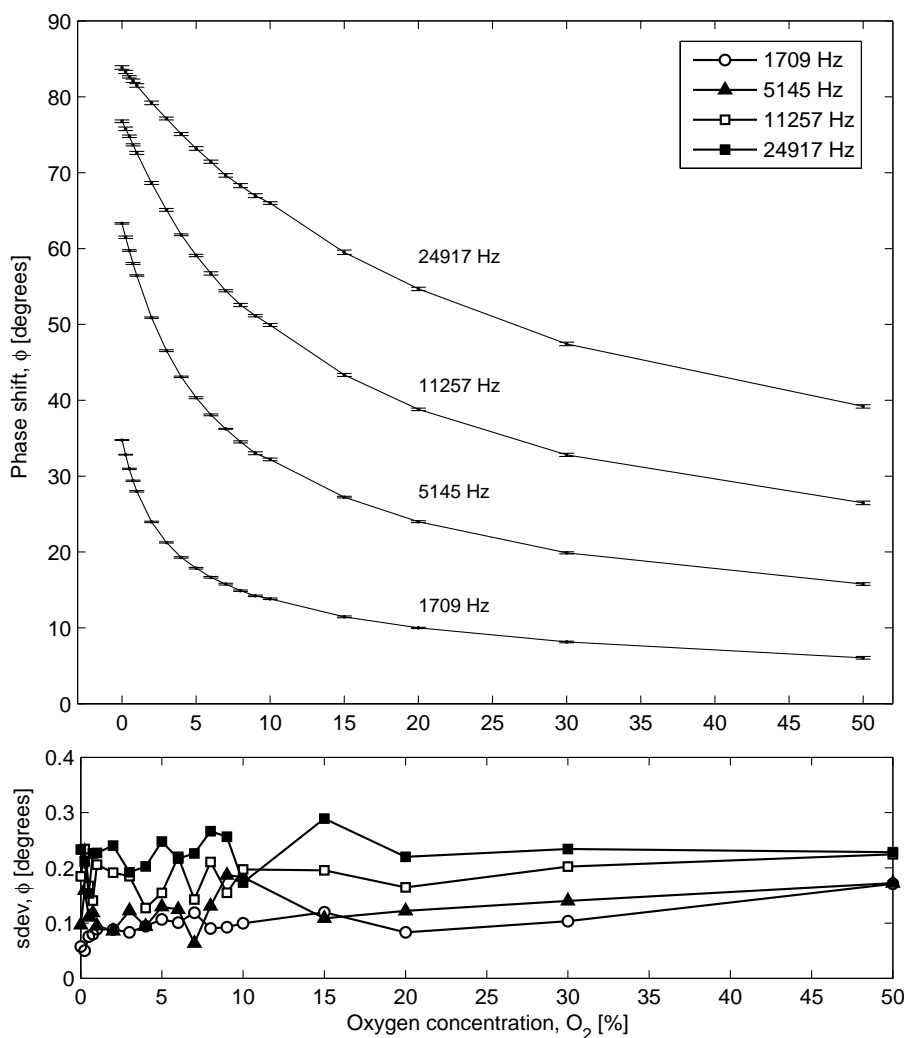


Fig. ESI-6. (Top) Phase-shift measurement of the sensing film versus oxygen concentration at different modulation frequencies. Each point in figure represents the average value of 20 phase-shift measurements, and the error bars show the standard deviation of these measurements. (Bottom) Standard deviation, *sdev* (in degrees), of the phase-shift measurements at different oxygen concentrations. All phase-shift measurements were obtained with the proposed measurement system using the multifrequency I/Q method, in the absence of ambient light, and at room temperature of 21 °C. For this end, a multifrequency signal formed by the summation of 4 sinusoidal functions with different frequencies was chosen as the excitation signal. The frequencies selected for the multifrequency signal were: 1709, 5145, 11257 and 24917 Hz (two of them being the optimal modulation frequencies for the oxygen measurement ranges of 0-15% and 0-100% O₂, respectively, and the other two, additional frequencies above and below these). The amplitude of all sinusoidal components was set at 0.5 V. The oxygen concentrations of the gas passing through the flow cell were calculated in real-time from the measured oxygen/nitrogen flows provided by the the MFCs' control software at a total flow-rate of 200 mL min⁻¹, and assuming a constant environmental pressure of approximately 1000 mbar.

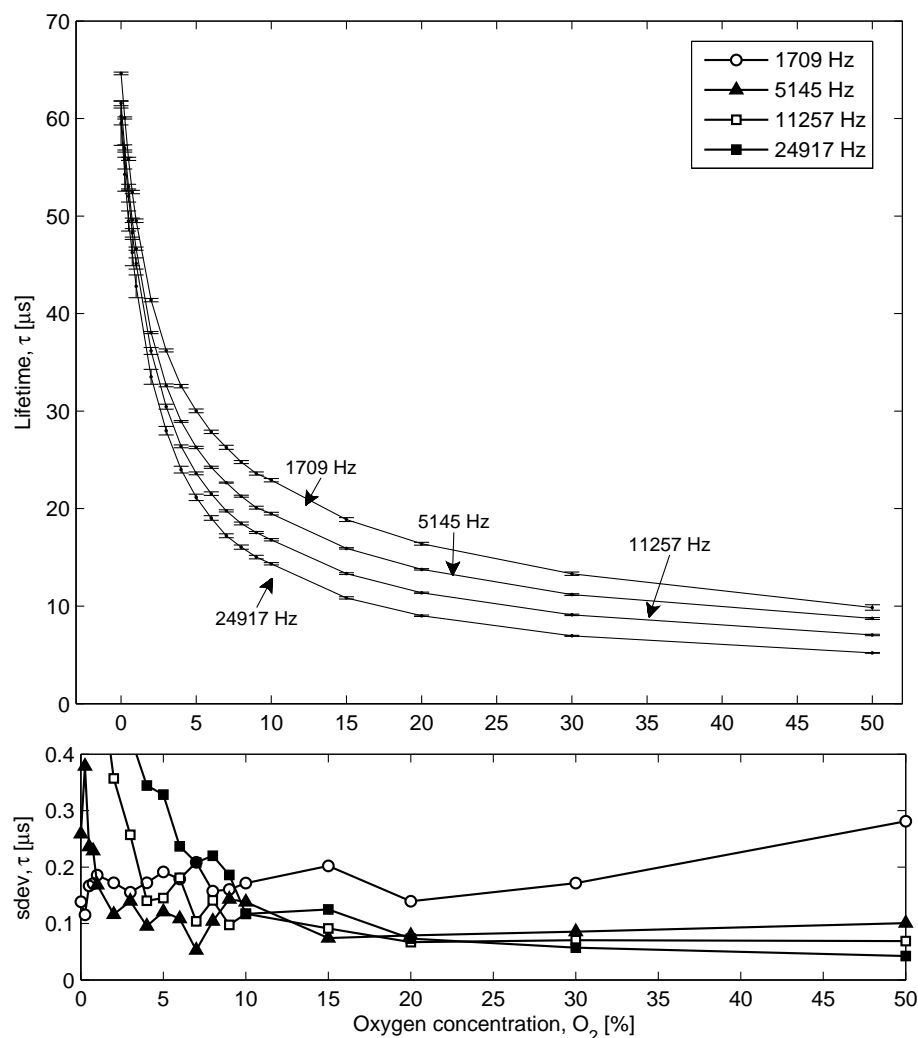


Fig. ESI-7. Idem to Fig. ESI-6, but converting the phase-shift measurements to luminescence lifetimes measurements. (Top) Lifetime measurement of the sensing film versus oxygen concentration at different modulation frequencies. Each point in figure represents the average value of 20 lifetime measurements, and the error bars show the standard deviation of these measurements. (Bottom) Standard deviation, $sdev$ (in μs), of the lifetime measurements at different oxygen concentrations. Luminescence lifetimes were calculated from phase-shift measurements according Eq. 6.1 of the manuscript, assuming an exponential luminescence decay. All phase-shift measurements were obtained with the proposed measurement system using the multifrequency I/Q method, in the absence of ambient light, and at room temperature of 21 °C. For this end, a multifrequency signal formed by the summation of 4 sinusoidal functions with different frequencies was chosen as the excitation signal. The frequencies selected for the multifrequency signal were: 1709, 5145, 11257 and 24917 Hz (two of them being the optimal modulation frequencies for the oxygen measurement ranges of 0-15% and 0-100% O_2 , respectively, and the other two, additional frequencies above and below these). The amplitude of all sinusoidal components was set at 0.5 V. The oxygen concentrations of the gas passing through the flow cell were calculated in real-time from the measured oxygen/nitrogen flows provided by the the MFCs' control software at a total flow-rate of 200 mL min^{-1} , and assuming a constant environmental pressure of approximately 1000 mbar. In this case, the obtained results showed that the sensing film displayed more than one decay time, since different lifetimes were obtained at different modulation frequencies (note that for the ideal case of a single-exponential decay one could use the phase-shift at any frequency to calculate the lifetime). Furthermore, it was also noted that higher modulation frequencies resulted in shorter lifetimes. Hence, in this case, it can be concluded that the lifetimes calculated from the phase-shift values (ϕ_ω), measured at a particular frequency, are only apparent values. These apparent lifetimes are the result of a complex weighting of the individual decay times and amplitudes, which depend on the experimental conditions (such as the measurement method used (phase or modulation) and the modulation frequency). Thus, strictly speaking, one does not actually measure apparent lifetimes. These values are simply interpretations of the measurable quantities (such as the phase and modulation values), which are often difficult to interpret in terms of molecular parameters.

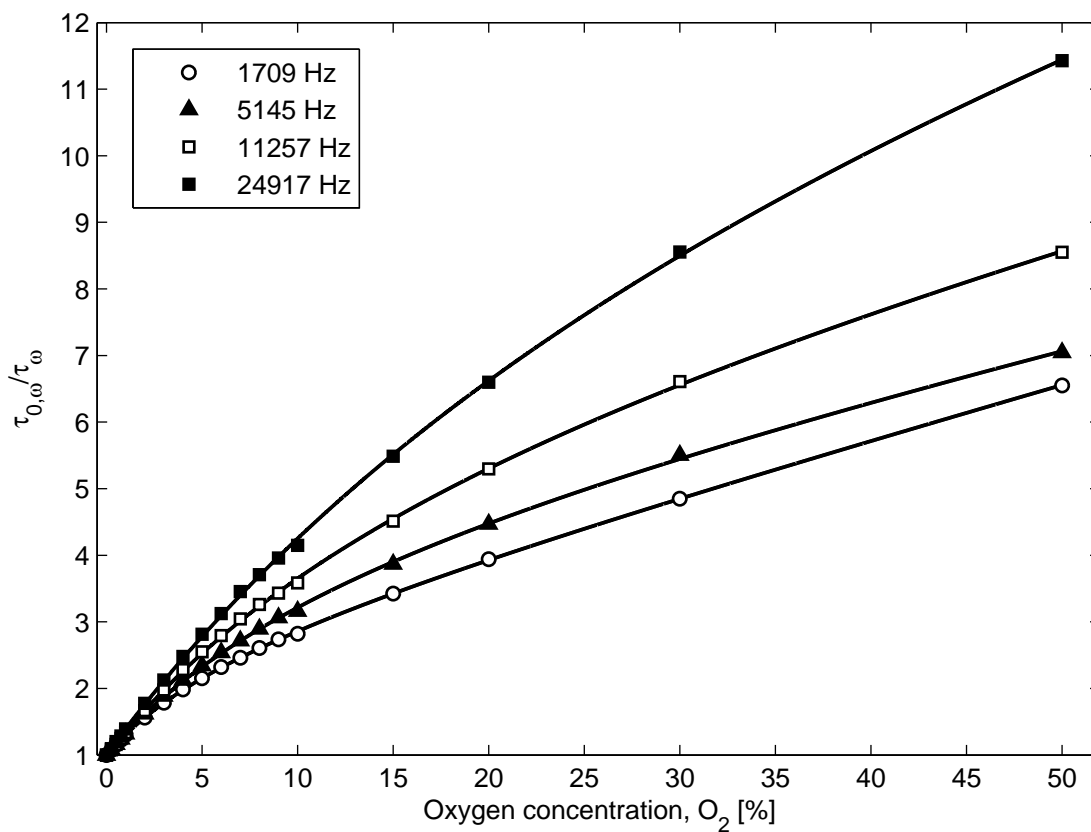
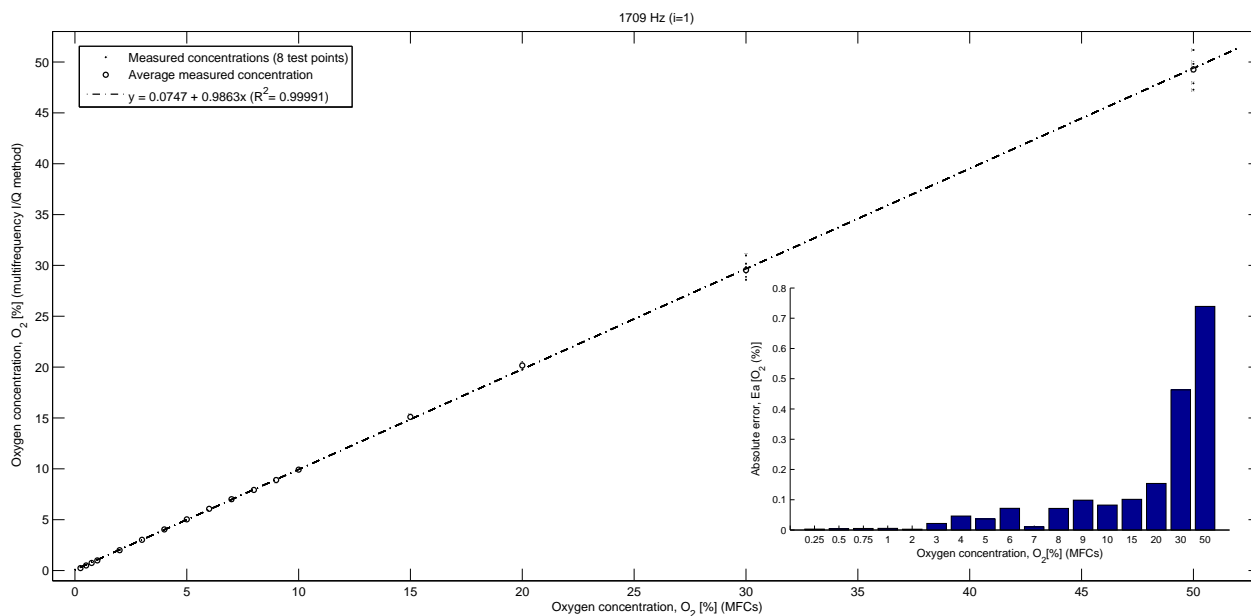
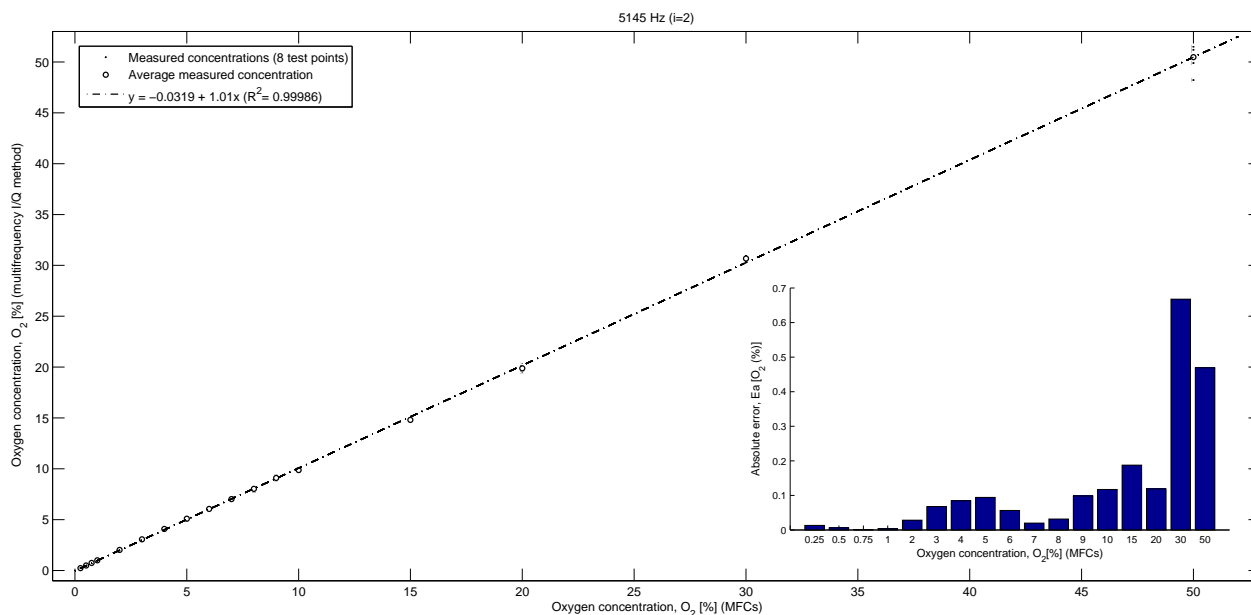


Fig. ESI-8. Calibration curves of normalized lifetime versus oxygen concentration (i.e., $\tau_{0,\omega}/\tau_\omega$ versus $O_2(\%)$) obtained from experimental data, where the subscript ‘0’ refers to the lifetime value in the absence of oxygen and the subscript ‘ ω ’ to the particular frequency component of the multifrequency signal (where $\omega = \{1709, 5145, 11257, 24917\}$ Hz). These lifetime-based calibration curves (solid lines in figure) were obtained individually for each frequency component of the multifrequency signal by adjusting the experimental data ($\tau_{0,\omega}/\tau_\omega$) to a two-site Demas model. In this case, the experimental data were the average lifetime values shown in Fig. ESI-7. The fitting of the experimental data using this model provided very good results (SSE < 0.024 and $R^2 > 0.9998$ in all cases). Table ESI-3 summarizes the parameters obtained for these calibration curves fitted to the Demas model.

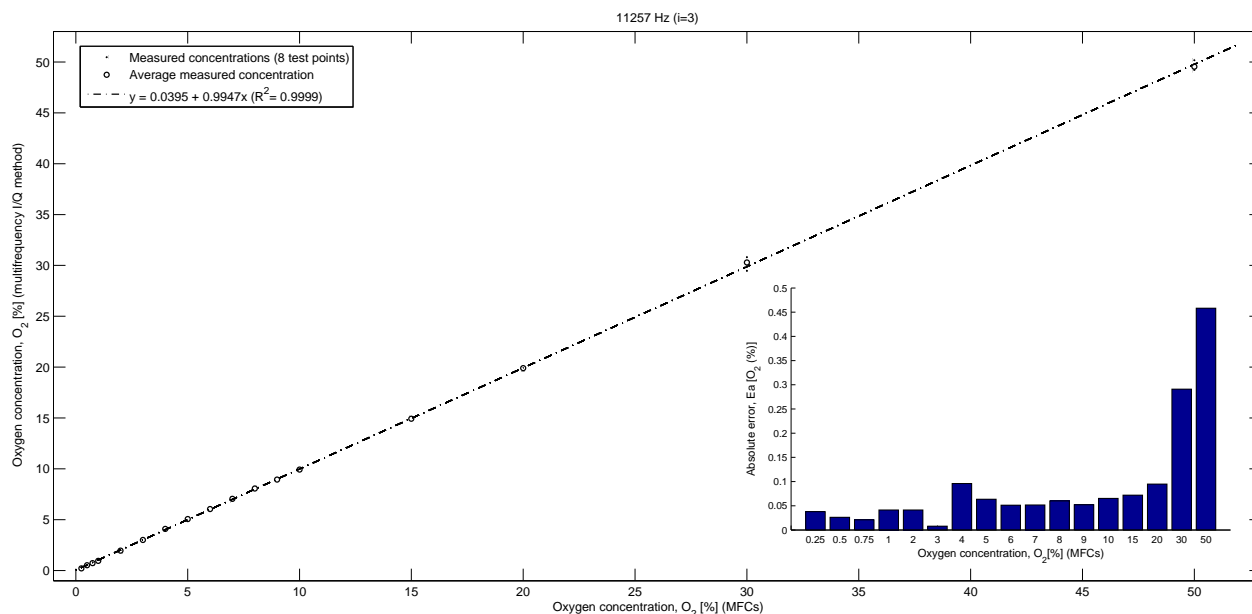


(a)

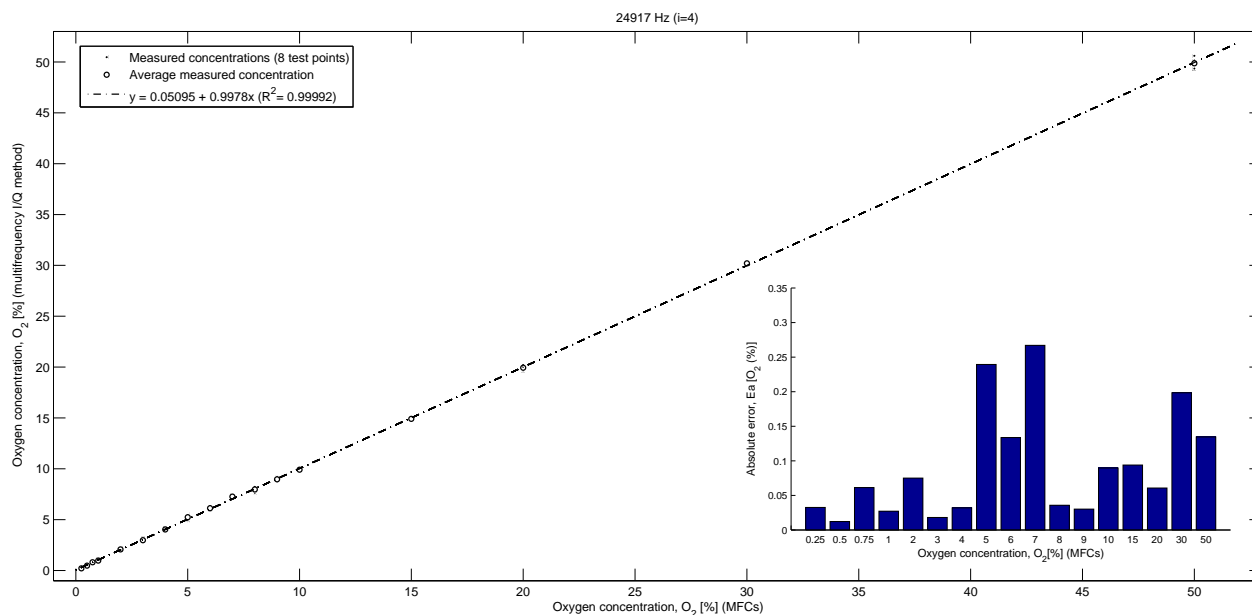


(b)

Fig. ESI-9. Comparison between oxygen concentration values provided by the MFCs (taken as reference) and oxygen concentration values calculated with the proposed measurement system using the multifrequency I/Q method, $[\hat{O}_{2,\omega}]$. For this end, a multifrequency signal formed by the summation of 4 sinusoidal functions with different frequencies (1709, 5145, 11257 and 24917 Hz) and equal amplitude (0.5 V) was used as excitation signal. The oxygen concentration of the gas passing through the flow cell was calculated in real-time from the measured oxygen/nitrogen flows provided by the the MFCs' control software, at a total flow-rate of 200 mL min^{-1} , and assuming a constant environmental pressure of approximately 1000 mbar. All measurements were obtained in the absence of ambient light, and at room temperature of 21°C . The thick points shown in figures correspond to the average value of the estimated oxygen concentration, $[\hat{O}_{2,\omega}]$, calculated from 8 consecutive measurements (fine points). Bar graphs (bottom right of the figures) show the absolute error (expressed in % O_2 or kPa) for each estimated oxygen concentration (i.e., $E_{a,[O_{2,\omega}]} = |[O_{2,MFCs}] - [\hat{O}_{2,\omega}]|$). (a) Values of $[\hat{O}_{2,\omega}]$ obtained for the frequency component of 1709 Hz. (b) Values of $[\hat{O}_{2,\omega}]$ obtained for the frequency component of 5145 Hz.



(a)



(b)

Fig. ESI-10. Idem to Fig. ESI-9. Comparison between oxygen concentration values provided by the MFCs (taken as reference) and oxygen concentration values calculated with the proposed measurement system using the multifrequency I/Q method, $[\hat{O}_{2,\omega}]$. For this end, a multifrequency signal formed by the summation of 4 sinusoidal functions with different frequencies (1709, 5145, 11257 and 24917 Hz) and equal amplitude (0.5 V) was used as excitation signal. The oxygen concentration of the gas passing through the flow cell was calculated in real-time from the measured oxygen/nitrogen flows provided by the the MFCs' control software, at a total flow-rate of 200 mL min^{-1} , and assuming a constant environmental pressure of approximately 1000 mbar. All measurements were obtained in the absence of ambient light, and at room temperature of 21°C . The thick points shown in figures correspond to the average value of the estimated oxygen concentration, $[\hat{O}_{2,\omega}]$, calculated from 8 consecutive measurements (fine points). Bar graphs (bottom right of the figures) show the absolute error (expressed in % O_2 or kPa) for each estimated oxygen concentration (i.e., $E_{a,[O_{2,\omega}]} = |[O_{2,MFCs}] - [\hat{O}_{2,\omega}]|$). (a) Values of $[\hat{O}_{2,\omega}]$ obtained for the frequency component of 11257 Hz. (b) Values of $[\hat{O}_{2,\omega}]$ obtained for the frequency component of 24917 Hz.

Table ESI-1. Phase-shift measurements versus oxygen concentration at 4 different modulation frequencies {1709, 5145, 11257, 24917} Hz. The measurements were taken using two different instrumental setups: (1) The measurement system based on the I/Q method at a single modulation frequency (see Fig. 4.1 of the manuscript); (2) The reference measurement system based on a commercial dual-phase lock-in amplifier (see Fig. ESI-2). Each point in the table represents the average value of 100 phase-shift measurements.

1709 Hz O_2 (%)	Phase-shift (I/Q method)			Phase-shift (lock-in amplifier)			Mean phase-shift (lock-in amplifier) - Phase-shifts. (I/Q method at a simple frequency of 1709 Hz)									
	mean($^\circ$) ^a	sdev($^\circ$) ^b	RSD(%) ^c	mean($^\circ$) ^a	sdev($^\circ$) ^b	RSD(%) ^c	Emean($^\circ$) ^d	E _{max} ($^\circ$) ^e	E _{min} ($^\circ$) ^f	RMSE($^\circ$) ^g	Q(50%) ^h	Q(80%) ^h	Q(85%) ^h	Q(90%) ^h	Q(95%) ^h	Q(99%) ^h
0	34.7346	0.0063	0.0181	34.7359	0.0054	0.0155	0.0046	0.0088	0.0004	0.0056	0.0046	0.008	0.0086	0.0088	0.0088	0.0088
0.25	32.7408	0.0177	0.054	32.7487	0.0134	0.0409	0.0145	0.0289	0.0037	0.0172	0.0127	0.025	0.0276	0.0289	0.0289	0.0289
0.5	30.8635	0.0186	0.0602	30.8988	0.0097	0.0313	0.0353	0.0628	0.0238	0.0388	0.0273	0.0532	0.0596	0.0628	0.0628	0.0628
0.75	29.3185	0.0075	0.0255	29.3319	0.0071	0.0242	0.0133	0.0234	0.007	0.0148	0.0115	0.0208	0.0226	0.0234	0.0234	0.0234
1	27.9487	0.0112	0.04	27.9652	0.0075	0.0268	0.0165	0.0328	0.008	0.0192	0.0127	0.0275	0.031	0.0328	0.0328	0.0328
2	23.8758	0.0055	0.023	23.9011	0.0057	0.0238	0.0253	0.0317	0.0183	0.0257	0.0256	0.03	0.0311	0.0317	0.0317	0.0317
3	21.156	0.0139	0.0657	21.2017	0.0041	0.0193	0.0457	0.0586	0.0265	0.0473	0.0489	0.0568	0.058	0.0586	0.0586	0.0586
4	19.2072	0.0111	0.0577	19.2808	0.0058	0.03	0.0736	0.0889	0.0624	0.0742	0.0716	0.0838	0.0872	0.0889	0.0889	0.0889
5	17.7297	0.0073	0.0411	17.8279	0.0055	0.0308	0.0982	0.1076	0.0901	0.0984	0.0975	0.105	0.1067	0.1076	0.1076	0.1076
6	16.5905	0.0211	0.1271	16.6794	0.0074	0.0443	0.0888	0.1071	0.0586	0.0907	0.0948	0.1044	0.1062	0.1071	0.1071	0.1071
10	13.7449	0.0145	0.1054	13.8814	0.0079	0.0569	0.1365	0.1551	0.1233	0.1371	0.1339	0.1508	0.1536	0.1551	0.1551	0.1551
15	11.3743	0.0132	0.116	11.5071	0.0106	0.0921	0.1328	0.1485	0.1173	0.1333	0.1326	0.145	0.1473	0.1485	0.1485	0.1485
20	9.9121	0.0083	0.0837	10.0715	0.0064	0.0635	0.1594	0.1703	0.1529	0.1595	0.1572	0.1676	0.1694	0.1703	0.1703	0.1703
30	8.0708	0.0177	0.2193	8.2569	0.01	0.1211	0.1861	0.2087	0.1719	0.1868	0.1819	0.2036	0.207	0.2087	0.2087	0.2087
50	5.9837	0.0241	0.4027	6.1672	0.0113	0.1832	0.1835	0.2066	0.1566	0.1847	0.1854	0.2049	0.206	0.2066	0.2066	0.2066

5145 Hz O_2 (%)	Phase-shift (I/Q method)			Phase-shift (lock-in amplifier)			Mean phase-shift (lock-in amplifier) - Phase-shifts. (I/Q method at a simple frequency of 5145 Hz)									
	mean($^\circ$) ^a	sdev($^\circ$) ^b	RSD(%) ^c	mean($^\circ$) ^a	sdev($^\circ$) ^b	RSD(%) ^c	Emean($^\circ$) ^d	E _{max} ($^\circ$) ^e	E _{min} ($^\circ$) ^f	RMSE($^\circ$) ^g	Q(50%) ^h	Q(80%) ^h	Q(85%) ^h	Q(90%) ^h	Q(95%) ^h	Q(99%) ^h
0	63.3901	0.0111	0.0175	63.3736	0.0093	0.0146	0.0165	0.0319	0.0055	0.0191	0.0143	0.0268	0.0302	0.0319	0.0319	0.0319
0.25	61.568	0.0236	0.0383	61.5698	0.0109	0.0177	0.0161	0.036	0.0031	0.0205	0.0127	0.0306	0.0342	0.036	0.036	0.036
0.5	59.7852	0.0105	0.0175	59.7986	0.0128	0.0214	0.0135	0.0277	0.0025	0.0163	0.0119	0.0233	0.0262	0.0277	0.0277	0.0277
0.75	58.0917	0.0244	0.042	58.1036	0.01	0.0172	0.0202	0.0373	0.0015	0.0243	0.0211	0.0342	0.0363	0.0373	0.0373	0.0373
1	56.5181	0.0241	0.0426	56.4961	0.0076	0.0134	0.0232	0.0486	0.0025	0.0303	0.021	0.0447	0.0473	0.0486	0.0486	0.0486
2	50.9505	0.0121	0.0237	50.966	0.0064	0.0125	0.0163	0.0248	0.0014	0.0188	0.0195	0.0245	0.0247	0.0248	0.0248	0.0248
3	46.6097	0.0146	0.0313	46.6422	0.01	0.0214	0.0324	0.0502	0.0153	0.0348	0.0321	0.046	0.0488	0.0502	0.0502	0.0502
4	43.1825	0.0157	0.0363	43.237	0.0089	0.0205	0.0545	0.0744	0.0369	0.0561	0.0533	0.0693	0.0727	0.0744	0.0744	0.0744
5	40.44	0.0142	0.0351	40.5092	0.0079	0.0195	0.0692	0.0892	0.0557	0.0703	0.066	0.0828	0.087	0.0892	0.0892	0.0892
6	38.199	0.0194	0.0507	38.2674	0.0079	0.0206	0.0684	0.0851	0.0473	0.0704	0.0706	0.085	0.0851	0.0851	0.0851	0.0851
10	32.311	0.0202	0.0625	32.4697	0.012	0.0369	0.1587	0.172	0.1292	0.1596	0.1668	0.1719	0.1719	0.172	0.172	0.172
15	27.2928	0.0099	0.0362	27.4709	0.0096	0.0349	0.1782	0.1913	0.1684	0.1784	0.1765	0.1878	0.1901	0.1913	0.1913	0.1913
20	24.0727	0.0311	0.1291	24.2498	0.012	0.0494	0.1772	0.2166	0.143	0.1792	0.1746	0.2068	0.2133	0.2166	0.2166	0.2166
30	19.9447	0.022	0.1103	20.0997	0.0151	0.0751	0.155	0.1839	0.1305	0.1561	0.1528	0.1748	0.1809	0.1839	0.1839	0.1839
50	15.8591	0.0296	0.1866	16.0435	0.0136	0.0847	0.1844	0.2262	0.1624	0.1862	0.1745	0.2136	0.222	0.2262	0.2262	0.2262

^aAverage (mean) of $N = 100$ phase-shift measurements.

^bStandard deviation (sdev) of $N = 100$ phase-shift measurements.

^cRelative standard deviation (RSD(%)) given by: $RSD(\%) = 100 \cdot sdev/mean$.

^dMean absolute error (E_{mean}) given by: $1/N \cdot \sum_{i=1}^N |\bar{\phi}_{(lock-in)} - \phi_i (I/Q \text{ method})|$, where $\bar{\phi}_{(lock-in)}$ is the average phase-shift value obtained with the lock-in amplifier (taken as a reference value: see 5th column of the table).

^eMaximum absolute error (E_{max}) given by: $E_{max} = \max_i \{|\bar{\phi}_{(lock-in)} - \phi_i (I/Q \text{ method})|\}$.

^fMinimum absolute error (E_{min}) given by: $E_{min} = \min_i \{|\bar{\phi}_{(lock-in)} - \phi_i (I/Q \text{ method})|\}$.

^gRoot mean square error (RMSE) given by: $\sqrt{1/N \cdot \sum_{i=1}^N |\bar{\phi}_{(lock-in)} - \phi_i (I/Q \text{ method})|^2}$.

^hQuantiles (50%, 80%, 85%, 90%, 95% and 99%).

Table ESI-2. Phase-shift measurements versus oxygen concentration at 4 different modulation frequencies {1709, 5145, 11257, 24917} Hz. The measurements were taken using two different instrumental setups: (1) The measurement system based on the I/Q method at a single modulation frequency (see Fig. 4.1 of the manuscript); (2) The reference measurement system based on a commercial dual-phase lock-in amplifier (see Fig. ESI-2). Each point in the table represents the average value of 100 phase-shift measurements.

11257 Hz O ₂ (%)	Phase-shift (I/Q method)			Phase-shift (lock-in amplifier)			Mean phase-shift (lock-in amplifier) - Phase-shifts. (I/Q method at a simple frequency of 1709 Hz)									
	mean(°) ^a	sdev(°) ^b	RSD(%) ^c	mean(°) ^a	sdev(°) ^b	RSD(%) ^c	Emean(°) ^d	E _{max} (°) ^e	E _{min} (°) ^f	RMSE(°) ^g	Q(50%) ^h	Q(80%) ^h	Q(85%) ^h	Q(90%) ^h	Q(95%) ^h	Q(99%) ^h
0	76.8602	0.0165	0.0214	76.9004	0.013	0.0169	0.0403	0.06	0.0205	0.0428	0.0403	0.0555	0.0585	0.06	0.06	0.06
0.25	75.8431	0.0331	0.0436	75.8216	0.0162	0.0213	0.0273	0.0609	0.0052	0.0358	0.0216	0.0536	0.0585	0.0609	0.0609	0.0609
0.5	74.7791	0.0313	0.0418	74.7511	0.0211	0.0282	0.0373	0.0471	0.0187	0.039	0.0418	0.0463	0.0468	0.0471	0.0471	0.0471
0.75	73.7046	0.0244	0.0331	73.6935	0.0177	0.024	0.023	0.0299	0.0123	0.0239	0.0249	0.0288	0.0296	0.0299	0.0299	0.0299
1	72.6835	0.0297	0.0408	72.6465	0.0143	0.0196	0.037	0.0726	0.0007	0.0451	0.0374	0.0637	0.0696	0.0726	0.0726	0.0726
2	68.7152	0.0191	0.0277	68.641	0.0173	0.0252	0.0742	0.1021	0.0591	0.076	0.0677	0.0923	0.0989	0.1021	0.1021	0.1021
3	65.163	0.0156	0.0239	65.0665	0.0175	0.0268	0.0965	0.1153	0.0796	0.0974	0.0955	0.1113	0.114	0.1153	0.1153	0.1153
4	61.9204	0.0205	0.0331	61.9285	0.0153	0.0247	0.0173	0.0276	0.0025	0.0196	0.0195	0.0255	0.0269	0.0276	0.0276	0.0276
5	59.1911	0.0243	0.041	59.1862	0.0091	0.0153	0.0202	0.0311	0.0096	0.0216	0.02	0.0281	0.0301	0.0311	0.0311	0.0311
6	56.8032	0.0226	0.0397	56.7748	0.0148	0.026	0.0284	0.0593	0.0078	0.0344	0.0232	0.0505	0.0564	0.0593	0.0593	0.0593
10	49.9792	0.0183	0.0366	49.9195	0.0142	0.0284	0.0597	0.0717	0.0325	0.0618	0.0673	0.0711	0.0715	0.0717	0.0717	0.0717
15	43.4081	0.0245	0.0564	43.3333	0.011	0.0253	0.0748	0.0971	0.0404	0.0777	0.0808	0.0935	0.0959	0.0971	0.0971	0.0971
20	38.8867	0.0229	0.0588	38.7763	0.0107	0.0275	0.1104	0.1323	0.0785	0.1121	0.1153	0.1283	0.131	0.1323	0.1323	0.1323
30	32.8782	0.0327	0.0994	32.7353	0.0123	0.0375	0.1428	0.1752	0.0983	0.1456	0.1489	0.1695	0.1733	0.1752	0.1752	0.1752
50	26.5444	0.0131	0.0493	26.3827	0.0187	0.0708	0.1617	0.1813	0.1535	0.1621	0.156	0.1738	0.1788	0.1813	0.1813	0.1813

24917 Hz O ₂ (%)	Phase-shift (I/Q method)			Phase-shift (lock-in amplifier)			Mean phase-shift (lock-in amplifier) - Phase-shifts. (I/Q method at a simple frequency of 5145 Hz)									
	mean(°) ^a	sdev(°) ^b	RSD(%) ^c	mean(°) ^a	sdev(°) ^b	RSD(%) ^c	Emean(°) ^d	E _{max} (°) ^e	E _{min} (°) ^f	RMSE(°) ^g	Q(50%) ^h	Q(80%) ^h	Q(85%) ^h	Q(90%) ^h	Q(95%) ^h	Q(99%) ^h
0	83.9448	0.0426	0.0507	83.9519	0.0441	0.0525	0.0362	0.0448	0.0189	0.0376	0.0406	0.0439	0.0445	0.0448	0.0448	0.0448
0.25	83.3519	0.0349	0.0418	83.3488	0.032	0.0383	0.0274	0.0415	0.0098	0.0304	0.0291	0.0406	0.0412	0.0415	0.0415	0.0415
0.5	82.7242	0.0319	0.0385	82.6326	0.0315	0.0381	0.0916	0.1244	0.0581	0.0957	0.0919	0.1209	0.1233	0.1244	0.1244	0.1244
0.75	82.2093	0.035	0.0425	82.1633	0.0354	0.043	0.046	0.081	0.0018	0.0551	0.0507	0.0764	0.0795	0.081	0.081	0.081
1	81.579	0.0259	0.0317	81.5176	0.0217	0.0266	0.0614	0.086	0.0267	0.0653	0.0665	0.0827	0.0849	0.086	0.086	0.086
2	79.2935	0.0331	0.0417	79.2129	0.0247	0.0311	0.0807	0.1072	0.0328	0.0856	0.0913	0.1041	0.1062	0.1072	0.1072	0.1072
3	77.2199	0.0286	0.037	77.06	0.026	0.0337	0.16	0.1822	0.1222	0.1619	0.1678	0.1822	0.1822	0.1822	0.1822	0.1822
4	75.1568	0.0309	0.0411	75.0135	0.0393	0.0523	0.1433	0.1712	0.1046	0.1458	0.1488	0.1694	0.1706	0.1712	0.1712	0.1712
5	73.2349	0.0365	0.0498	73.1337	0.023	0.0314	0.1012	0.1306	0.0479	0.1061	0.1132	0.1257	0.129	0.1306	0.1306	0.1306
6	71.5294	0.0316	0.0441	71.3825	0.0219	0.0306	0.1469	0.1826	0.1129	0.1495	0.146	0.1767	0.1807	0.1826	0.1826	0.1826
10	65.969	0.026	0.0394	65.8289	0.0188	0.0285	0.14	0.1627	0.1086	0.1418	0.1444	0.1618	0.1624	0.1627	0.1627	0.1627
15	59.5915	0.0304	0.051	59.4358	0.0178	0.0299	0.1557	0.1785	0.1113	0.1579	0.1665	0.1764	0.1778	0.1785	0.1785	0.1785
20	54.7534	0.0399	0.0728	54.5362	0.0178	0.0326	0.2172	0.2578	0.1757	0.22	0.2177	0.2537	0.2564	0.2578	0.2578	0.2578
30	47.5239	0.035	0.0736	47.3369	0.0225	0.0475	0.187	0.2373	0.1561	0.1894	0.1773	0.2195	0.2314	0.2373	0.2373	0.2373
50	39.2629	0.0381	0.097	39.0667	0.022	0.0563	0.1962	0.2388	0.1531	0.199	0.1965	0.2317	0.2364	0.2388	0.2388	0.2388

^aAverage (mean) of $N = 100$ phase-shift measurements.

^bStandard deviation (sdev) of $N = 100$ phase-shift measurements.

^cRelative standard deviation (RSD(%)) given by: $RSD(\%) = 100 \cdot sdev/mean$.

^dMean absolute error (E_{mean}) given by: $1/N \cdot \sum_{i=1}^N |\bar{\phi}_{(lock-in)} - \phi_i (I/Q \text{ method})|$, where $\bar{\phi}_{(lock-in)}$ is the average phase-shift value obtained with the lock-in amplifier (taken as a reference value: see 5th column of the table).

^eMaximum absolute error (E_{max}) given by: $E_{max} = \max_i \{|\bar{\phi}_{(lock-in)} - \phi_i (I/Q \text{ method})|\}$.

^fMinimum absolute error (E_{min}) given by: $E_{min} = \min_i \{|\bar{\phi}_{(lock-in)} - \phi_i (I/Q \text{ method})|\}$.

^gRoot mean square error (RMSE) given by: $\sqrt{1/N \cdot \sum_{i=1}^N |\bar{\phi}_{(lock-in)} - \phi_i (I/Q \text{ method})|^2}$.

^hQuantiles (50%, 80%, 85%, 90%, 95% and 99%).

Table ESI-3. Parameters of the sensing film-calibration curves obtained by adjusting the experimental multifrequency lifetime data to the Demas model^a.

Freq. (Hz)	f_1	f_2	$K_{SV1} (bar^{-1})$	$K_{SV2} (bar^{-1})$
1709	0.72 ± 0.01	0.27 ± 0.01	46.16 ± 3.40	2.50 ± 0.16
5145	0.83 ± 0.02	0.16 ± 0.01	40.31 ± 3.90	1.17 ± 0.23
11257	0.90 ± 0.02	0.10 ± 0.01	41.66 ± 3.65	0.85 ± 0.24
24917	0.93 ± 0.03	0.05 ± 0.00	40.51 ± 3.58	0.42 ± 0.30

^aA Demas model was used to properly fit experimental data. The fitting of the experimental data using this model provided very good results (SSE < 0.024 and R² > 0.9998 in all cases).

Evaluation of a simple PC-based quadrature detection method at very low SNR for luminescence spectroscopy

Santiago Medina Rodríguez^{a,b,*}, Ángel de la Torre Vega^{a,*}, Jorge Fernando Fernández Sánchez^b and Alberto Fernández Gutiérrez^b

^a*Department of Signal Theory, Networking and Communications, CITIC-UGR, University of Granada, C/ Periodista Rafael Gómez 2, E-18071 Granada, Spain.*

^b*Department of Analytical Chemistry, Faculty of Sciences, University of Granada, Avda. Fuentenueva s/n, E-18071 Granada, Spain.*

Published in *Sensors and Actuators B: Chemical* 192 (2014) 334-340

Evaluation of a simple PC-based quadrature detection method at very low SNR for luminescence spectroscopy

Abstract—We developed a PC-based phase measuring system based on the principles of quadrature detection with ideal features for accurately determining the amplitude and phase of a sinusoidal signal, even in the presence of very high noise levels. This detection technique was implemented via software on a personal computer (PC), and its response was analyzed using experimental tests under different noise conditions using 1 second test signals. Additionally, this technique was implemented and was subsequently evaluated using a real measurement system (a versatile and low-cost optical-fiber measurement system for optically detecting oxygen in the gas phase) under different lighting conditions. The results demonstrate the robustness of the proposed technique to noise and its computational efficiency; these results were similar to those obtained using a measuring instrument commonly used in research laboratories (a commercially available digital lock-in amplifier (LIA)).

keywords: Optical sensor; Photoluminescence; Digital lock-in detection; Quadrature detection; Phase-resolved; Spectroscopy.

5.1 Introduction

DURING the last two decades, there has been considerable interest and tremendous research activity in the field of optical sensing, specifically in real-time monitoring. This attention is justified because optical sensors are important in various areas, including analytical chemistry, environmental sensing, biochemistry, clinical chemistry, and industrial applications [1–7].

Most optical sensors are based on measurements of the luminescence emission intensity [2, 4, 8–10]. Unfortunately, although they are relatively simple and accurate to conduct in the laboratory, they are often inadequate for real applications because the emission intensity is highly influenced by external perturbations [11–13], such as the intensity fluctuations of the exciting light, detector drift, degradation or leaching of the dye, light losses in the optical path, orientation and location of the sensor, concentration of the luminophore, and optical surface quality [12, 14]. Furthermore, another disadvantage of intensity-based measurements is that they are often performed with expensive and bulky instrumentation (typical for luminescence spectrometers used in laboratory measurements [8]) or with portable but equally expensive and specific measuring instruments, such as fiber optic photometers [10] and charge-coupled device (CCD) cameras [3]. These difficulties may be minimized by measuring the luminescence lifetime [15] because it is an intrinsic property of the luminophore. Therefore, lifetime measurements are often preferable when designing reliable and robust optical luminescence sensors [11, 14, 16].

The phase-modulation methods using the phase as analytical signal are the preferred techniques for measuring the luminescence lifetime in the frequency domain [4, 13, 16] because they allow detecting the low-level, slowly varying optical signals that are common in many optical measurement situations (e.g., optical sensors), even when high-level, low frequency optical interference and low frequency ($1/f$) noise are present [17]. Therefore, intensity-modulated optical sources and lock-in detection systems (known as quadrature detection systems) are commonly used to measure lifetime.

To date, various measurement systems based on digital lock-in detection techniques have been reported with ideal features for working with modulated signals at simple or multiple modulation frequencies [12, 18]. Some systems allow better phase resolution and stability [12, 19, 20], fast amplitude and phase computations [18], reduced device size [17], greater versatility [12, 21, 22], and a notable cost reduction [12, 17, 23]. However, very few of these measurement systems have been exhaustively analyzed using real scenarios with different noise conditions, and even fewer have been implemented or evaluated in real-world applications under weak lighting conditions.

In this work, we use a single-frequency digital phase measuring technique (known as the I/Q method) based on the principles of quadrature detection, with ideal features for accurately determining the amplitude and phase of a sinusoidal signal when high noise levels are present. This quadrature detection method is implemented entirely using software on a personal computer, and because all of the signal processing occurs on a computer, full control over the acquired signals and error statistics during every processing stage is possible. This method has been evaluated under different noise conditions using numerically generated analog signals. In addition, we also describe the implementation and evaluation of the I/Q detection method in a versatile and low-cost optical-fiber measurement system to detect oxygen in the gas phase under different lighting conditions as a typical real application. The results from the I/Q method have been compared with those obtained using a commercially available lock-in amplifier (LIA) as a reference under the same experimental conditions.

5.2 Theory

5.2.1 Standard digital lock-in detection (LIA)

In general, for lock-in detection [18–28], there is a source signal ($R(t)$) used as a reference input signal in the lock-in detector. This signal contains a periodic signal of amplitude (A_s), a modulation frequency (f_m), a phase angle (φ_s), and a dc component (dc_s).

$$R(t) = dc_s + A_s \cos(2\pi f_m t + \varphi_s) \quad (5.1)$$

This source signal is used as the excitation signal for a system that yields a measurable response ($M(t)$) that is attenuated in the amplitude and phase shifted according to the following:

$$M(t) = dc_m + A_m \cos(2\pi f_m t + \varphi_m) + \Delta_{noise} \quad (5.2)$$

where dc_m is the dc term, A_m is the amplitude, f_m is the modulation frequency (which is known), φ_m is the phase angle, and Δ_{noise} is an additive noise term.

Essentially, a lock-in detector takes a periodic reference signal $R(t)$ and a noisy input signal $M(t)$ and uses a phase-sensitive detector (PSD) to extract only the portion of the output signal whose frequency matches the reference [28]. Typically, to gain some information about a measured system, the instrument provides the amplitude and the phase angle. In contrast, the dc_m term is usually not useful because it is contaminated with unwanted environmental and/or systematics distortions [18]. When the signal's phase is unknown for the quantity of interest, quadrature detection is used, requiring two reference signals in quadrature (*i.e.*, cosine and sine signals) [18]. During digital lock-in detection [19–23, 25–28], an analog-to-digital converter (ADC) is used to digitize the analog signals. The ADC takes N_s samples of $M(t)$ at a sampling frequency (f_s), yielding the digital signal:

$$M[n] = dc_m + A_m \cos \left[\left(\frac{2\pi f_m n}{f_s} \right) + \varphi_m \right] + \Delta_{noise}[n] \quad (5.3)$$

where n is the index of the n th sample (with $0 \leq n \leq N_s - 1$). The time required to take N_s samples is the measurement time (T_m) and is given by $T_m = N_s/f_s$; it may also be viewed as the settling time for the lock-in filter [18, 28]. The data sampled by the ADC are transferred to a digital processing unit where the computations for the digital lock-in detection are performed [18, 28]. Digital lock-in techniques require digital signals for the cosine and sine waves at the modulation frequency (f_m) [18] that are generally obtained from a numerically generated reference signal stored in the memory of the processing unit. The numerical generation of these reference signals is advantageous because they have no noise (with the exception of the numerical precision errors); however, if the source modulation hardware and the sampling of the ADC are not synchronized, a slight frequency mismatch may occur [18, 20]. The discrete reference signals (cosine and sine) are multiplied by the discrete measured signal ($M[n]$) to yield the ‘in phase’ and ‘quadrature’ components, which are also commonly called the $I[n]$ and $Q[n]$ signals [18, 28]. The measured amplitude (A_m) and the phase (φ_m) of the signal ($M[n]$) can be calculated from the dc terms, I and Q , by filtering $I[n]$ and $Q[n]$ with a low-pass filter ($h_L[n]$). The low-pass filtered versions of $I[n]$ and $Q[n]$ are often called the real (X) and imaginary (Y) parts of the measured sinusoid [18, 28]. The amplitude and phase of the measured sinusoid can be calculated using the real and imaginary parts as follows [18, 28]:

$$A_m = \sqrt{X^2 + Y^2} \quad (5.4)$$

$$\varphi_m = \tan^{-1} \left(\frac{Y}{X} \right) \quad (5.5)$$

5.2.2 Proposed phase measuring technique (I/Q method)

The proposed phase measuring technique (I/Q method) is based on quadrature detection [12, 29], which is well known in the field of digital communications [30]. This technique is relatively

simple to implement using a computer [12, 18] and is less expensive than the commercial measurement equipment used in measuring laboratories to determine the amplitude and phase of a sinusoidal signal measured relative to a reference signal. The I/Q method is a simplified version of the standard digital lock-in detection implemented in most commercial digital lock-in amplifiers; the projections of the input sinusoidal signal on the reference in-phase and quadrature components are calculated using simple arithmetic operations without applying any digital filters. The details and theoretical background of the I/Q detection technique used for simultaneously measuring the amplitude and phase of single and multi-frequency signals have been previously developed by Medina-Rodríguez et al. [12]. In the present work, we are only interested in single-frequency detection, and the X and Y terms for the digital measured signal ($M[n]$) can be calculated using the following expressions [12]:

$$X = \frac{\sum_{n=0}^{N_s-1} M[n] C[n]}{\sqrt{\sum_{n=0}^{N_s-1} C[n]^2}} = \frac{\sum_{n=0}^{N_s-1} M[n] \cos(2\pi f_m n/f_s)}{\sqrt{\sum_{n=0}^{N_s-1} \cos^2(2\pi f_m n/f_s)}} \quad (5.6)$$

$$Y = \frac{\sum_{n=0}^{N_s-1} M[n] S[n]}{\sqrt{\sum_{n=0}^{N_s-1} S[n]^2}} = \frac{\sum_{n=0}^{N_s-1} M[n] \sin(2\pi f_m n/f_s)}{\sqrt{\sum_{n=0}^{N_s-1} \sin^2(2\pi f_m n/f_s)}} \quad (5.7)$$

From the X and Y terms, the amplitude (A_m) and phase (φ_m) of the measured signal ($M[n]$) can be calculated as depicted in (6.4) and (6.5). The discrete signals for the cosine and sine (i.e., $C[n]$ and $S[n]$, respectively) are obtained from a numerically generated reference signal stored on a computer. All discrete signals are sampled at an identical rate (f_s) while having the same length (i.e., a total number of samples equal to N_s) and frequency (f_m) (which is known a priori).

The I/Q method should behave correctly in most cases; however, if the source modulation hardware and the ADC sampling are not synchronized (or if there is frequency drift in the reference source), there may be a slight frequency mismatch, leading to large errors in the signal's phase measurements ($M[n]$), which is a disadvantage relative to commercial LIAs (i.e., lock-in detection technique) in which a PLL (Phase-Locked Loop) is used to engage the frequency of the input signal in real time. Nevertheless, a simple solution to this problem might also be digitally implemented during the I/Q method, although those details are beyond the scope of this work.

The main advantage of the I/Q method versus LIA is its simplicity and flexibility because a very narrow bandwidth for the measured signal $M[n]$ can be achieved (on the order of $1/T_m$, where T_m is the time duration of the signal) without applying any low-pass filtering with optimum parameters dependent on T_m . The phase measurement is obtained using a single frequency (i.e., from in-phase and quadrature signal's projections on the reference frequency of interest f_m) while ignoring the noise from other frequencies. Therefore, only the noise added to the relevant bandwidth of the signal $M[n]$ affects the phase measurement, achieving a very high SNR.

5.3 Experimental

5.3.1 Materials and chemicals

The oxygen-sensitive luminescent dye, Platinum (II) 5,10,15,20-meso-tetrakis-(2,3,4,5,6-pentafluorophenyl)-porphyrin (PtTFPP), was obtained from Frontier Scientific Inc.(www.fronti-ersci.com, UT, USA) and immobilized in a transparent, oxygen-permeable polystyrene matrix (PS; Scientific Polymer Products Inc., www.scientificpolymer.com, Ontario, NY, USA). All components were dissolved in chloroform, which was used for its ability to dissolve both the luminescent dye and polymer [8, 12]. The chloroform was obtained from Sigma-Aldrich (www.sigmaaldrich.com, Química S.A., Madrid, Spain). For the gas mixture, nitrogen and oxygen (99.999% purity) were obtained from Air Liquide (www.airliquide.com, AL Air Liquide España S.A., Madrid, Spain).

5.3.2 Preparation of the oxygen-sensitive film

The cocktail necessary to obtain the sensing film was prepared by dissolving 3 mg of PtTFPP and 198 mg of PS in 2 mL of chloroform (dye concentration of 1.5 mg/mL) [8, 12]. The mixture was shaken with an IKA-Vibramax-VXR (IKA-Labortechnik, Staufen, Germany) until all components had completely dissolved. The oxygen-sensitive membrane was obtained with a Laurell spin-coater (WS-400B-6NPP/LITE, Laurell Technologies, www.laurell.com, North Wales, PA, USA): 200 μ L of the cocktail was injected onto a rotating glass support spinning at 700 rpm. The PtTFPP/PS membrane obtained after the deposition process was a soft reddish color and allowed visible light to pass through it. The resulting layer was approximately 4 μ m thick and was modulated by the viscosity of the cocktail and the spin-coater's rotation speed [8, 12].

5.3.3 Evaluation of the I/Q method using numerically generated analog signals

A personal computer (Intel(R) Core(TM)2 Quad CPU Q9400 at 2.66 GHz, equipped with the numerical computing environment, Matlab 7.10 (MathWorks, www.mathworks.com, Natick, MA, USA)) was used to implement the I/Q method and generate the required digital signals. Two discrete reference signals (cosine and sine) were numerically generated and stored on the computer with the following parameters: $dc = 0$, $A = 1$, $f_m = 5145$ Hz, $f_s = 100$ kHz, $\varphi=0^\circ$, $\Delta_{noise} = 0$, signal duration = 1 s, and $N_s = 100$ kS. In addition, digital test signals with identical lengths (N_s), sampling frequencies (f_s) and modulation frequencies (f_m) but with amplitude of 0.15, randomly phase between 0 and -180° and different levels of additive white Gaussian noise (AWGN) were also generated and stored on the computer. All signals were 1 s in duration. This value was arbitrarily assigned to reduce the processing time and the size of the signal data while remaining long enough to ensure that there was a sufficient number of signal cycles for processing. Additionally, bursts of zeros at the beginning and end of the signals (of 3 s and 1 s duration, respectively) were added to prevent sample loss during the subsequent data acquisition process using an oscilloscope.

These stored digital signals were converted to analog signals using a digital-to-analog converter (DAC) and they were used to validate the I/Q method under different noise levels. In addition, these results were compared with those obtained using a commercial dual-phase digital lock-in amplifier (SR830, Stanford Research Systems, www.thinksrs.com). Electronic Supporting Information (ESI) shows further information about the protocol used for validating the I/Q method by using analog signals.

5.3.4 Measurement system

The control over oxygen concentration and phase-shift measurements was carried out using an ad hoc measurement system designed and built in our laboratory. Fig. 5.1 displays a schematic diagram of the optical-fiber measurement system for sensing oxygen using phase-shift measurements. In this scheme, the PtTFPP-containing sensing film was excited with an ultraviolet LED ($\lambda_{peak} = 395$ nm, angle of illumination 15° , LED diameter 5 mm, luminous power $25 \mu\text{W}$ into a $600 \mu\text{m}$ optical-fiber, model LS-450 LED-395, Ocean Optics, www.oceanoptics.com) filtered through an optical bandpass filter (OF-1) ($\lambda_{central} = 390$ nm, FWHM 18 nm, model MF390-18, Thorlabs GmbH, www.thorlabs.com). The UV-LED light source was sinusoidally modulated at an optimal frequency of 5145 Hz [12]. The numerically generated digital signals were extracted using two analog output channels on an AD/DA board (model NI PCIe-6363/BNC-2120, National Instruments, www.ni.com) at 100 kS/s. One of the channels was used to modulate the current of the LED light source in the LED driving circuit, and the other one was used as an external reference signal for the data acquisition device.

A bifurcated fiber bundle (wavelength range 200-800 nm UV-VIS, 12 illumination fibers $200 \mu\text{m}$ core diameter, 1 read fiber $600 \mu\text{m}$ core diameter, N.A. 0.22, model FCR-7xx200-2, Avantes Inc., www.avantes.com) was used to guide the excitation light toward the sensing film and to guide the luminescence emission back to the detector after passing through an optical bandpass filter (OF-2) ($\lambda_{central} = 630$ nm, FWHM 60 nm, model A10033-03, Hamamatsu Photonics, www.hamamatsu.com). The luminescence was detected with a photomultiplier tube (PMT) (BW DC-1 MHz, model H10723-20, Hamamatsu Photonics). The voltage signal provided by the PMT (only a few tens of millivolts) was amplified with a commercially available low-noise programmable voltage preamplifier (model SIM911 BJT, Stanford Research Systems) and subsequently filtered with a three-stage passive-RC low-pass filter (with filter cut-off frequencies of 20, 27 and 33 kHz for each of the stages, respectively) before being subjected to the data acquisition device: (1) a commercial dual-phase digital lock-in amplifier (model SR830, Stanford Research Systems) and (2) a digital oscilloscope (model WaveRunner 604Zi, LeCroy, www.lecroy.com). For the oscilloscope-based acquisition system, both the excitation signal (the reference) and the emission signal from the sensing film were simultaneously digitized using the digital oscilloscope at 100 kS/s. Signals 1 s in duration (i.e., a 100 kS data buffer) were recorded and transferred via Ethernet from the oscilloscope to the PC. An ad hoc Matlab program was used to digitally process the signals (i.e., calculate the phase-shift between the excitation signal and the emission signal). The average processing time for each phase-shift measurement using the I/Q method was less than 200 ms. Therefore, because the average acquisition time for the signals using the oscilloscope was less than 1.5 s (including the data transfer time from the oscilloscope to the PC), an average total

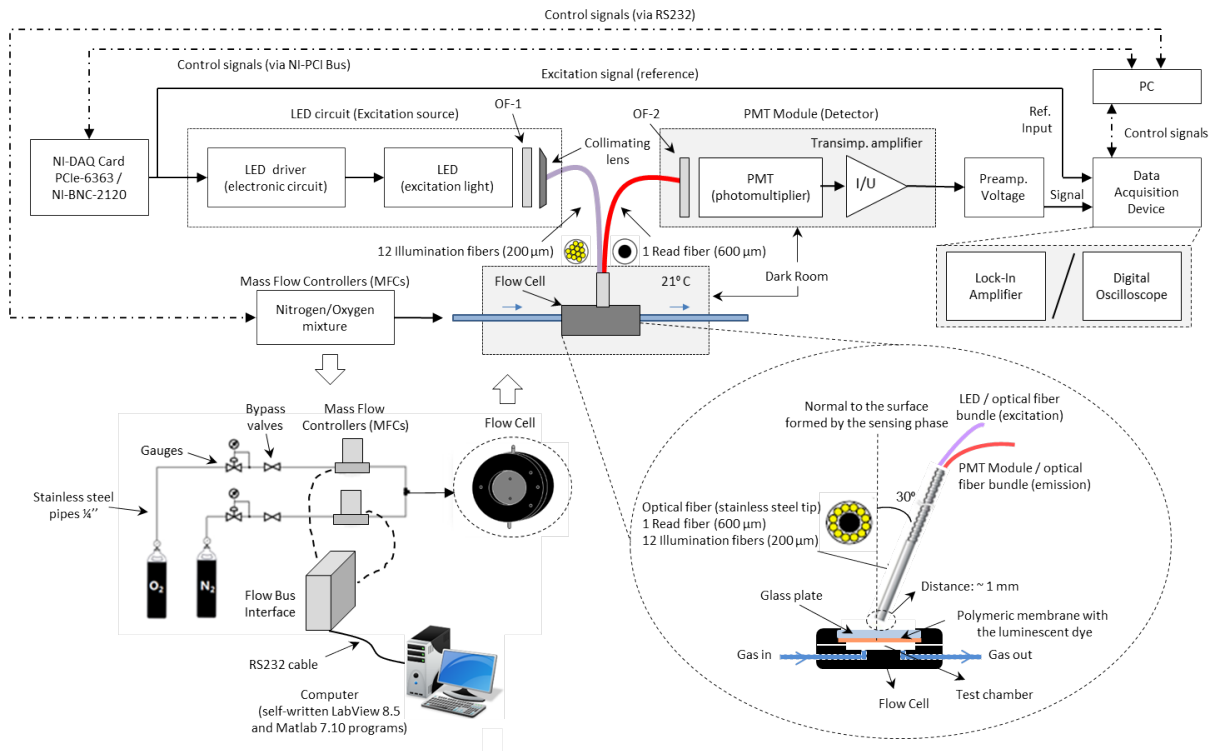


Figure 5.1: Schematic diagram of the experiment designed for measuring the phase-shifts using two different data acquisition devices: (1) a commercial dual-phase lock-in amplifier and (2) a digital oscilloscope connected to a personal computer for further data processing using the I/Q method.

measuring time of less than 1.7 s was necessary to provide each phase-shift measurement; therefore, this system can be used to measure oxygen concentrations in real time.

The additional phase-shift value (i.e., instrumental bias) introduced by the hardware components of the measurement system (AD/DA board, LED driver, PMT, voltage preamplifier, passive-RC low-pass filter, data acquisition device, etc.) was previously estimated for each experimental setup using a red reference LED ($\lambda_{peak} = 660 \text{ nm}$, angle of illumination 50° , LED diameter 5 mm, luminous intensity 2000 mcd typ./20 mA, model L2-0-R5TH50, LED Supply, www.ledsupply.com) in the same spectral range as the sensing film. Subtracting this phase-shift value from the experimental data allowed us to calculate the specific phase-shift value introduced only by the sensing film.

To characterize, calibrate, and evaluate the oxygen-sensitive film in the gas phase, a flow-through cell was specifically designed to hold the sensing film. It was made of black polytetrafluoroethylene (PTFE) to prevent stray reflections and to ensure that the system was chemically inert. Different mixtures of nitrogen and oxygen at a constant flow of 200 mL/min were passed through the flow cell to calibrate (and evaluate) the sensing film. To mix the gases, two mass-flow controllers (MFCs) (EL-FLOW Select F-201CV, Bronkhorst High-Tech, www.bronkhorst.com, Ruurlo, Netherlands) were connected, using copper and stainless steel tubing, to the flow-through cell. The N_2/O_2 -gas station was controlled from a PC using an ad hoc computer program developed in LabVIEW 8.5 and Matlab 7. The PC was connected to a Flow-Bus Interface (Bronkhorst High-Tech) to control the MFCs via a

RS-232 serial port. Finally, both the flow-through cell and the PMT were housed in a dark room (XE25C1, Thorlabs GmbH) to prevent interference from stray light.

All the measurements were performed at room temperature (21 °C). The temperature was continuously monitored using a commercial temperature sensor (MicroLite, Fourtec-Fourier Technologies, www.fouriersystems.com) placed at a point close to the flow cell.

5.3.5 Characterization and test of the oxygen-sensitive film

The spectroscopic behavior of the oxygen-sensitive film (i.e., luminescence excitation and emission spectra in the absence and presence of oxygen) was determined with a Varian Cary-Eclipse luminescence spectrometer (Agilent Technologies, www.home.agilent.com, CA, USA). The parameter settings for the spectroscopic characterization were as follows: $\lambda_{exc} = 394$ nm, $\lambda_{em} = 650$ nm, slit-width_{exc/em} = 10/10 nm, delay time 0.1 ms, gate time 5 ms, flow rate 200 mL/min, and detector voltage 550V. All measurements were performed at room temperature (21 °C).

Phase-shift measurements at different oxygen partial pressures between 0 and 50 kPa O_2 (or 0-50 % O_2 (v/v)) were taken with the two experimental setups illustrated in Fig. 5.1. The phase-shift measurements versus oxygen concentration were used to obtain a typical calibration curve for the sensing film (i.e., Stern-Volmer Plot (SVP)). The fits were performed using Matlab. In addition, the overall responses of the measurement systems were also evaluated under different lighting conditions. For it, the amplitude of the sinusoidal signal used to modulate the current for the LED light source was varied, and then phase-shift measurements at different oxygen concentrations were recorded for each lighting condition (see ESI for further information).

5.4 Results and discussion

5.4.1 Validation of the I/Q method using analog signals

To validate the I/Q method, experimental tests were performed using analog signals with different noise levels and these results were compared to those obtained with LIA (used as reference method).

All the configuration parameters of the LIA were previously optimized to obtain the best response for the phase-shift measurement using signals only 1 s in duration: time constant (TC) of 100 ms, low-pass filter with a slope of 12 dB/octave, AC couple, 1 V sensitivity, low noise reserve, 50/60 Hz Notch filter, sine reference input, and float ground. ESI shows the selection of the TC value.

Table 5.1 and ESI (see Fig. ESI-5) show the statistical results of the absolute phase errors for the experimental tests using the I/Q method and the LIA for a total of 500 statistically independent phase-shift measurements at different signal-to-noise ratio (SNR) conditions. The absolute phase errors are defined as $e_i = |\varphi_i - \hat{\varphi}_i|$ with $i = 1, 2, 3, \dots, 500$, where φ_i is

Table 5.1: Statistical results of the validation of the IQ method using analog signals with different SNR levels.

SNR(dB)	I/Q method					LIA				
	Mean(°)	Sdev(°)	Max(°)	RMSE(°)	Outliers ^a (%)	Mean(°)	Sdev(°)	Max(°)	RMSE(°)	Outliers ^a (%)
-18	1.1122	1.4101	4.2590	1.4115	0.2	1.9036	2.3234	7.5514	2.4047	0.8
-12	0.5688	0.7113	2.1029	0.7210	0.2	1.0047	1.1580	3.7744	1.2641	0.6
-6	0.3019	0.3636	1.0895	0.3798	0	0.4825	0.5862	1.9108	0.6109	0.6
0	0.1453	0.1836	0.5520	0.1837	0	0.2339	0.2912	0.8611	0.2933	0.4
6	0.0750	0.0926	0.2830	0.0941	0	0.1183	0.1492	0.4264	0.1492	0
12	0.0413	0.0487	0.1482	0.0518	0	0.0623	0.0780	0.2304	0.0780	0
18	0.0222	0.0276	0.0840	0.0277	0	0.0349	0.0437	0.1289	0.0438	0
24	0.0158	0.0192	0.0615	0.0196	0	0.0255	0.0313	0.0898	0.0313	0
30	0.0142	0.0177	0.0547	0.0178	0	0.0210	0.0260	0.0763	0.0260	0
36	0.0139	0.0173	0.0510	0.0172	0	0.0186	0.0224	0.0664	0.0229	0

^a Percentage of outliers deleted from the dataset including 500 error measurements (criterion: $e_i > 3 \cdot Sdev$ (dataset)).

the theoretical phase value (known a priori) and $\hat{\varphi}_i$ is the estimated phase value.

It is possible to conclude that both methods provided similar results, although these results appeared to be slightly better for the I/Q method in all cases (i.e., a lower RMS phase error for the different noise conditions tested). For example, for SNRs <18 dB, the I/Q method provided an RMS phase error equivalent to that of the LIA for SNR values that were approximately 4.5 dB lower. For SNRs >18 dB, the RMS phase error stagnated due to the electrical noise introduced by the measurement system's hardware components. The results demonstrate the robustness of the quadrature detection technique toward noise in very low SNR situations, confirming that this detection technique is suitable for measuring the phase of a sinusoidal signal in the presence of high noise levels.

5.4.2 Response of the phase measuring system during a real-world application (oxygen sensor)

A further analysis of the I/Q method was carried out by implementing and evaluating this method using a real measurement system (i.e., a versatile and low-cost optical-fiber measurement system for optically detecting oxygen in the gas phase). The response of the proposed measurement system was assessed by characterizing, calibrating and evaluating a known oxygen-sensitive membrane (PtTFPP/PS) under different lighting conditions. Additionally, these results were also compared to those obtained on the same membrane using a standard measurement system based on a commercial LIA.

Fig. 5.2 displays the Stern-Volmer plots (i.e., φ_0/φ versus oxygen concentration) obtained for the same oxygen-sensitive film by using I/Q and LIA methods. This figure also reveals the fitting of experimental data according to the widely used Demas model [12, 31]. This model assumes that the indicator is localized in two regions of different microenvironments, explaining the deviation from the linearity in the Stern-Volmer plot. Its mathematical expression is given as follows [8, 12]:

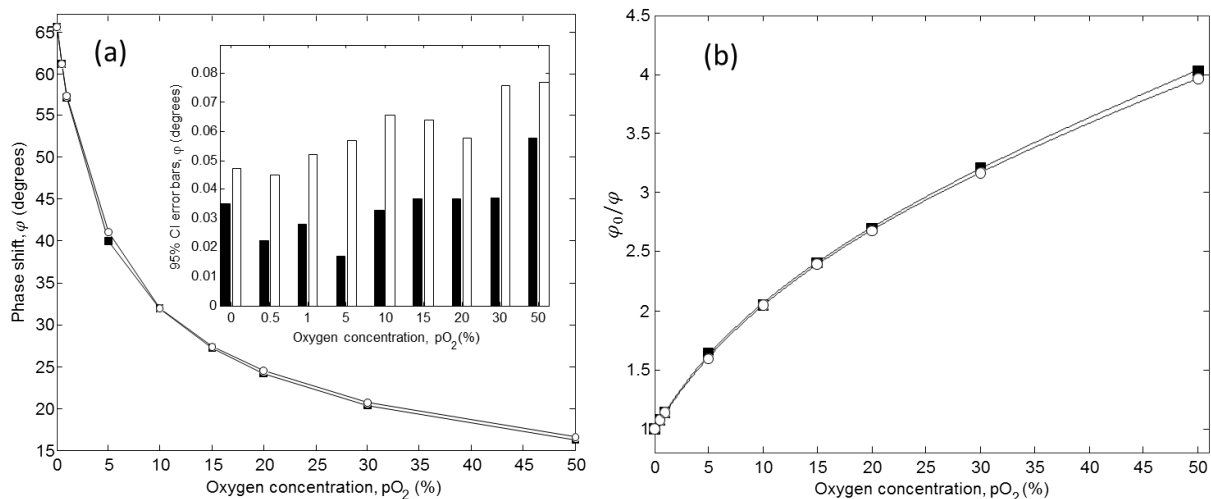


Figure 5.2: Calibration of the oxygen-sensitive film (PtTFPP/PS) using the proposed I/Q method (■, black bars) and LIA (○, white bars). (a) Phase-shift variation versus oxygen concentration. Each point in the figure represents the average of $N=10$ phase-shift measurements with its error ($\varphi \pm \text{error}$; where $\varphi = (1/N) \cdot \sum_{n=1}^N \varphi_n$, and the error bars indicate the 95 % confidence intervals based on Student's t-distribution). (b) Stern-Volmer plots fitted according to the Demas model (solid line).

$$\frac{\varphi_0}{\varphi} = \left[\frac{x_1}{1 + K_{SV1}[O_2]} + \frac{x_2}{1 + K_{SV2}[O_2]} \right]^{-1} \quad (5.8)$$

where φ_0 and φ are the unquenched and quenched phase-shift values (*i.e.*, in the absence and in the presence of oxygen, respectively), $[O_2]$ is the oxygen concentration, x_1 and x_2 are the fractions of the total emission for each site (with $x_1 + x_2 = 1$), and K_{SV1} and K_{SV2} are the Stern-Volmer quenching constants for each microenvironment. ESI (see Table ESI-2) summarizes the fitting parameters for the two setups under study. It is possible to conclude that both measurement setups provided similar calibration curves for the sensing film (after an earlier calibration process to compensate for the instrumental bias). Furthermore, the t_{95} response times for the sensing film were also determined [8, 12], revealing a response time under 10 s when changing from 0 to 50 % O_2 (v/v) and under 18 s when changing from 50 to 0 % O_2 (v/v).

To study the effect of the noise level on the accuracy of the oxygen determination using both systems, several experiments were carried out under different lighting conditions (22, 31, 44, 62, 88, 124, 176, 249, 353, 499, 707 and 1000 mV of amplitude for the LED excitation signal) while assuming a constant 1000 mbar environmental pressure and a 200 mL/min total gas flow at 21 °C. Each oxygen concentration was maintained for 15 min before the measurements, and subsequently, 10 phase-shift measurements were registered for each oxygen concentration and lighting condition with both setups. Using the calibration curves for the sensing film (see Fig. 5.2(b)), the estimated values for the oxygen concentration ($[\hat{O}_2]$) could be calculated from the phase-shift measurements taken with both measurement setups. From these estimated % O_2 (v/v) values (10 values for each of the 9 oxygen concentrations

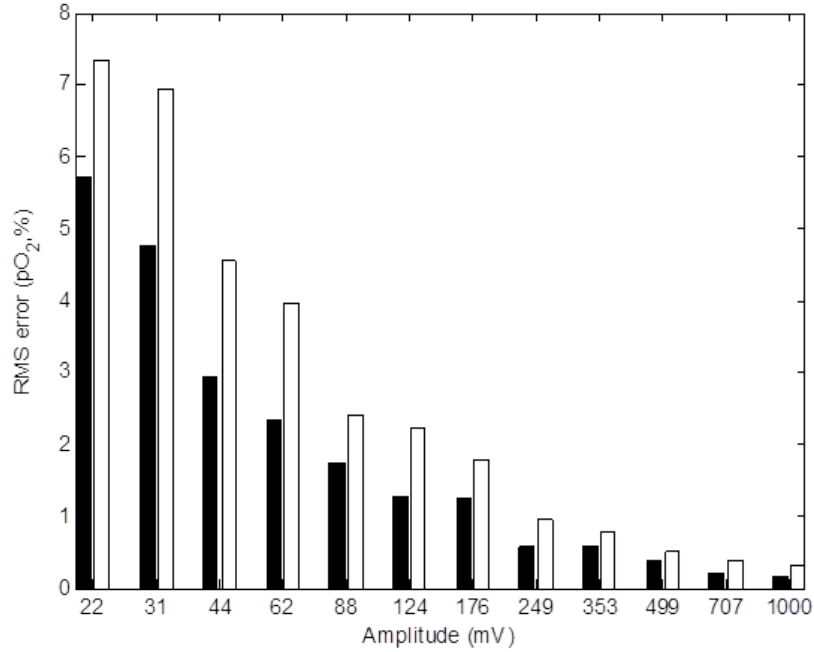


Figure 5.3: Average RMSE values (expressed in units of % O_2 (v/v)) obtained under different lighting conditions using I/Q method (black bars) and LIA system (white bars).

tested), the average RMS error while estimating the oxygen concentration under the different lighting conditions ($RMSE_{A_i}$) was determined:

$$RMSE_{A_i} = \sqrt{\frac{1}{N} \sum_{n=1}^N \left([\widehat{O}_2]_{n, A_i} - [O_2]_{n, MFCs} \right)^2} \quad (5.9)$$

where the subscript A_i denotes a particular lighting condition (or amplitude of the LED excitation signal), N is the total number of measurements (90 in this case), $[\widehat{O}_2]_{n, A_i}$ is the estimated value for a given oxygen concentration, and $[O_2]_{n, MFCs}$ is the true value for the estimated oxygen concentration (provided by the MFCs' control software). The $RMSE_{A_i}$ value (expressed in units of % O_2 (v/v)) was used as a statistic parameter for comparing the response of both measurement setups (see Fig. 5.3). A trend similar to that already observed in the experimental tests using analog signals was obtained for both setups. Slightly higher RMSE values were obtained for the LIA-based oxygen measurement system under all lighting conditions (the average RMSE value was approximately 1.5 times higher than for the I/Q-based measurement system). In all cases, a decrease in the RMSE value for the estimated oxygen concentration at higher amplitudes of the LED excitation signal (i.e., for better lighting conditions) was observed, due to the higher SNR level (or optical power) of the emission signal received by the detector. Therefore, for 0.25-45 % O_2 (v/v), the average RMSE values of 0.16 and 0.31 (in % O_2 (v/v)) were obtained for the I/Q-based and LIA-based systems, respectively, under the most favorable lighting condition studied in this work (1000 mV amplitude); the average RMSE values of 5.72 and 7.34 were obtained for these systems under the worst lighting condition studied (22 mV amplitude). ESI (see Fig. ESI-6) compares the oxygen concentration values measured with the MFCs $[O_2]_{n, MFCs}$ (taken

as reference values) and their corresponding estimated oxygen concentration values $[\hat{O}_2]_{n, A_i}$ under all lighting conditions using the two proposed measurement systems; the mean and standard deviation of 120 points for each oxygen concentration (10 values for each lighting condition) as well as the best-fitting line (i.e., the least squares regression line) through the data for both systems are displayed.

The typical oxygen measurement range for the I/Q-based measurement system was from 0 to 50 % O_2 (v/v) (or from 0 to 50 kPa), with a measurement accuracy of <1 % O_2 (v/v) (or <1 kPa) across the entire measurement range for the 1000 mV amplitude and <13.96 % O_2 (v/v) for the 22 mV amplitude. However, a higher accuracy was obtained at lower oxygen concentrations; the measurement accuracy for <0.2 % O_2 (v/v) (or <0.2 kPa) was reached over the measurement range of 0-20 % O_2 (v/v) (or 0-20 kPa) for the 1000 mV amplitude and <3 % O_2 (v/v) for the 22 mV amplitude. The limit of detection (LOD) for the I/Q-based oxygen sensor was 0.01 % O_2 (v/v) (or 0.01 kPa) under the best lighting condition; LOD was estimated as the oxygen concentration that produced an analytical signal three times the standard deviation of ten blank injections (0 % oxygen (v/v) in this case) [12].

5.5 Conclusions

We presented a single-frequency measurement technique (known as the I/Q method) based on the principles of quadrature detection with ideal features for accurately determining the phase of a sinusoidal signal, even when very high noise levels were present (i.e., under conditions of very low SNR). This detection technique was implemented using only software on a personal computer. To verify the proposed phase estimation method, tests using analog signals 1 s in duration with different SNR levels were carried out and successfully compared to those obtained with a standard measuring instrument used in research laboratories (a commercial digital lock-in amplifier). It can be concluded that I/Q method is robust toward noise, confirming that the quadrature detection technique is suitable for measuring the phase of a sinusoidally modulated signal, even with very low SNR levels.

In addition, the I/Q method was expanded by implementing and evaluating the technique in a real world measurement system (i.e., a versatile and low-cost optical-fiber measurement system for gas phase oxygen sensing), obtaining satisfactory results even when detecting low-level optical signals. Due to the I/Q method can be efficiently implemented using software, miniaturization and portability of the measuring system may be attainable (for example, using an AD/DA board). However, the main advantages over commercial equipment (LIA) are: (1) the ease of use because no parameter settings are necessary (unlike most commercial equipment, where a parameter optimization process is essential for obtaining the best response under each experimental condition) and (2) the low-cost, computational efficiency and flexibility of digital implementation, as well as the full availability of the signals involved in the measuring process. This last feature allows offline signal processing for continuous measurement of the phase over time. This capability might be useful in real-time systems or in applications where very rapid phase changes must be accurately measured. Finally, the I/Q method could be also easily extended to detect amplitude and/or phase at multiple frequencies simultaneously. Thus, this method is ideal for applications using multiple modulation frequencies, including optical chemical sensors, as well as optical and electrical impedance spectroscopy and tomography applications.

References

- [1] J. Janata, M. Josowicz, P. Vanýsek, D.M. DeVaney, *Chemical Sensors*, *Analytical Chemistry* 70 (1998) 179-208.
- [2] D.B. Papkovsky, T.C. O'Riordan, Emerging applications of phosphorescent metalloporphyrins, *Journal of Fluorescence* 15 (2005) 569-584.
- [3] M. Schäferling, The art of fluorescence imaging with chemical sensors, *Angewandte Chemie International Edition* 51 (2012) 3532-3554.
- [4] J.R. Lakowicz, *Principles of Fluorescence Spectroscopy*, 2nd ed., Kluwer Academic, New York, 1999.
- [5] J. Dakin, B. Culshaw, *Optical Fiber Sensors: Applications, Analysis and Future Trends*, Artech House, 1997.
- [6] J.F. Fernández-Sánchez, T. Nezel, R. Steiger, U.E. Spichiger-Keller, Novel optical NO₂-selective sensor based on phthalocyaninato-iron (II) incorporated into a nanostructured matrix, *Sensors and Actuators B: Chemical* 113 (2006) 630-638.
- [7] O.S. Wolfbeis, B.M. Weidgans, F. Baldini, A.N. Chester, J. Homola, S. Martellucci, *Fiber Optic Chemical Sensors and Biosensors: A View Back Optical Chemical Sensors*, Springer, The Netherlands, 2006, pp. 17-44.
- [8] M. Marín-Suárez del Toro, J.F. Fernández-Sánchez, E. Baranoff, M.K. Nazeeruddin, M. Grätzel, A. Fernández-Gutiérrez, Novel luminescent Ir (III) dyes for developing highly sensitive oxygen sensing films, *Talanta*, 82 (2010) 620-626.
- [9] C. McDonagh, C.S. Burke, B.D. MacCraith, *Optical Chemical Sensors*, *Chemical Reviews*, 108 (2008) 400-422.
- [10] F.J. Sainz-Gonzalo, C. Elosua, J.F. Fernández-Sánchez, C. Popovici, I. Fernández, F.L. Ortiz, et al., A novel luminescent optical fibre probe based on immobilized tridentate bis (phosphinic amide)-phosphine oxide for europium (III) ion aqueous detection in situ, *Sensors and Actuators B: Chemical*, 173 (2012) 254-261.
- [11] M. Valledor, J.C. Campo, I. Sánchez-Barragán, J.M. Costa-Fernández, J.C. Álvarez, A. Sanz-Medel, Determination of phosphorescence lifetimes in the presence of high background signals using phase-shift measurements, *Sensors and Actuators, B: Chemical*, 113 (2006) 249-258.
- [12] S. Medina-Rodríguez, A. de la Torre-Vega, J.F. Fernández-Sánchez, A. Fernández-Gutiérrez, An open and low-cost optical-fiber measurement system for the optical detection of oxygen using a multifrequency phase-resolved method, *Sensors and Actuators B: Chemical*, 176 (2013) 1110-1120.
- [13] H. Szmecinski, J.R. Lakowicz, Measurement of the intensity of long-lifetime luminophores in the presence of background signals using phase-modulation fluorometry, *Applied Spectroscopy*, 53 (1999) 1490-1495.

-
- [14] C. McDonagh, C. Kolle, A.K. McEvoy, D.L. Dowling, A.A. Cafolla, S.J. Cullen, et al., Phase fluorometric dissolved oxygen sensor, *Sensors and Actuators, B: Chemical*, 74 (2001) 124-130.
- [15] H. Szmecinski, J. Lakowicz, Lifetime-Based Sensing, in: C.D. Geddes, J.R. Lakowicz (Eds.), *Topics in Fluorescence Spectroscopy*, Springer, USA, 2002, pp. 295-334.
- [16] D. Andrzejewski, I. Klimant, H. Podbielska, Method for lifetime-based chemical sensing using the demodulation of the luminescence signal, *Sensors and Actuators, B: Chemical*, 84 (2002) 160-166.
- [17] A.A. Dorrington, R. Künnemeyer, A Simple microcontroller based Digital lock-in amplifier for the detection of low level optical signals, in: *Proceedings of the The First IEEE International Workshop on Electronic Design, Test and Applications (DELTA '02)*, IEEE Computer Society, 2002, p. 486.
- [18] J.M. Masciotti, J.M. Lasker, A.H. Hielscher, Digital lock-in detection for discriminating multiple modulation frequencies with high accuracy and computational efficiency, *IEEE Transactions on Instrumentation and Measurement*, 57 (2008) 182-189.
- [19] P.A. Probst, A. Jaquier, Multiple-channel digital lock-in amplifier with PPM resolution, *Review of Scientific Instruments*, 65 (1994) 747-750.
- [20] F. Barone, E. Calloni, L. DiFiore, A. Grado, L. Milano, G. Russo, High-performance modular digital lock-in amplifier, *Review of Scientific Instruments*, 66 (1995) 3697-3702.
- [21] S. Carrato, G. Paolucci, R. Tommasini, R. Rosei, Versatile low-cost digital lock-in amplifier suitable for multichannel phase-sensitive detection, *Review of Scientific Instruments*, 60 (1989) 2257-2259.
- [22] G.D. Renkes, L.R. Thorne, W.D. Gwinn, Digital modulator and synchronous demodulator system: An alternative to the analog phase detector, *Review of Scientific Instruments*, 49 (1978) 994-1000.
- [23] X. Wang, Sensitive digital lock-in amplifier using a personal computer, *Review of Scientific Instruments*, 61 (1990) 1999-2001.
- [24] D.P. Blair, P.H. Sydenham, Phase sensitive detection as a means to recover signals buried in noise, *Journal of Physics E: Scientific Instruments*, 8 (1975) 621-627.
- [25] E.D. Morris, H.S. Johnston, Digital phase sensitive detector, *Review of Scientific Instruments*, 39 (1968) 620-621.
- [26] L.A. Barragan, J.I. Artigas, R. Alonso, F. Villuendas, A modular, low-cost, digital signal processor-based lock-in card for measuring optical attenuation, *Review of Scientific Instruments*, 72 (2001) 247-251.
- [27] P.K. Dixon, L. Wu, Broadband digital lock-in amplifier techniques, *Review of Scientific Instruments*, 60 (1989) 3329-3336.
- [28] *Operating Manual and Programming References, SR830 DPS Lock-In Amplifier*, 2.4 ed., Stanford Research Systems, Sunnyvale, California, June 2009, pp. 3-11.

-
- [29] P. Langer, R. Müller, S. Drost, T. Werner, A new method for filter-free fluorescence measurements, *Sensors and Actuators, B: Chemical*, 82 (2002) 1-6.
 - [30] R.D. Hippenstiel, *Detection Theory: Applications and Digital Signal Processing*, CRC Press, University of Texas at Tyler, USA, 2001.
 - [31] J.N. Demas, B.A. DeGraff, Luminescence-based sensors: microheterogeneous and temperature effects, *Sensors and Actuators: B Chemical*, 11 (1993) 35-41.

Appendix A. Supplementary data

Electronic Supporting Information (ESI)

Evaluation of a simple PC-based quadrature detection method at very low SNR for luminescence spectroscopy

Santiago Medina Rodríguez^{a,b}, Ángel de la Torre Vega^a, Jorge F. Fernández Sánchez^b and Alberto Fernández Gutiérrez^b

^a*Department of Signal Theory, Networking and Communications, CITIC-UGR, University of Granada, C/ Periodista Rafael Gómez 2, E-18071 Granada, Spain.*

^b*Department of Analytical Chemistry, Faculty of Sciences, University of Granada, Avda. Fuentenueva s/n, E-18071 Granada, Spain.*

Table of Contents

- A. Validation of the I/Q method by using analog signals.
- B. Analogic signals used for validating the I/Q method implemented into an oxygen sensor.
- C. Selection of the time constant for the LIA system.

List of Figures

- Fig. ESI-1. Experimental systems.
- Fig. ESI-2. Graphical representation of a pair of digital signals (reference and test).
- Fig. ESI-3. Example of the analog sinusoidal signals applied to the LIA method.
- Fig. ESI-4. Analog sinusoidal signals applied to the LIA-based experimental setup.
- Fig. ESI-5. Results obtained for the proposed I/Q algorithm and the LIA.
- Fig. ESI-6. Comparison between the oxygen concentration.

List of Tables

- Table ESI-1. Results (absolute phase errors) of the experimental tests.
- Table ESI-2. Oxygen sensitivity of the sensing film.

A. Validation of the I/Q method by using analog signals

Two discrete reference signals (cosine and sine) were numerically generated and stored on the computer with the following parameters: $dc = 0$, $A = 1$, $f_m = 5145$ Hz, $f_s = 100$ kHz, $\varphi = 0^\circ$, $\Delta_{noise} = 0$, signal duration = 1 s, and $N_s = 100$ kS. Likewise, digital test signals that had identical lengths (N_s), sampling frequencies (f_s), and modulation frequencies (f_m) to the reference signals were also generated and stored on the computer. The amplitude of these test signals was 0.15, while their phase was randomly assigned between 0 and -180° .

In addition, different levels of additive white Gaussian noise (AWGN) were added to the test signals, generating digital signals with different SNR levels. All signals were 1 s in duration; this value was arbitrarily assigned to reduce the processing time and the size of the signal data while remaining long enough to ensure there was a sufficient number of signal cycles for processing. Therefore, longer or shorter duration values would be equally valid. Additionally, bursts of zeros at the beginning and end of the signals (of 3 s and 1 s duration, respectively) were added to prevent sample loss during the subsequent data acquisition process using an oscilloscope. These noisy test signals (of known phase) were subsequently used to validate the I/Q method under different noise levels.

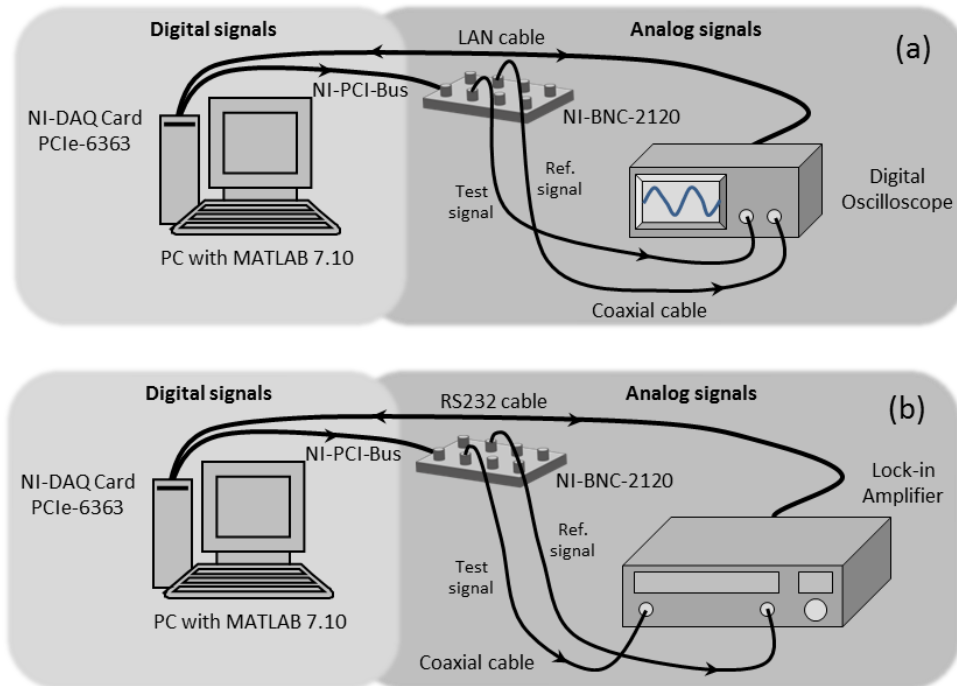


Fig. ESI-1. Experimental systems using (a) the proposed I/Q algorithm and (b) the commercial dual-phase digital lock-in amplifier.

The experimental tests were performed using the experimental setup shown in Fig. ESI-1a. Toward this purpose, the stored digital test signals were converted to analog signals using the digital-to-analog converter (DAC) from a data acquisition board (NI-DAQ PCIe-6363, National Instruments, www.ni.com). As observed in Fig. ESI-1a, two analog signals were generated by the data acquisition board: a cosine reference signal (theoretically noiseless)

called the “Ref. signal” and a noisy test signal (with the same frequency but phase-shifted relative to the reference signal) called the “Test signal”. Both signals were simultaneously extracted using the board’s two analog output channels at 100 kS/s and subsequently transferred via the NI-PCI-Bus to a shielded connector block with signal-labeled BNC connectors (NI-BNC 2120, National Instruments). These two signals were recorded with a digital oscilloscope (WaveRunner 604Zi, LeCroy, www.lecroy.com). Both analog signals (reference and test) were simultaneously digitized by the oscilloscope at 100 kS/s and were transferred using an ethernet cable to a personal computer for further processing. An ad hoc Matlab program was used to perform the digital signal processing (i.e., the I/Q algorithm for calculating the phase-shift between the reference signal and the test signal). A pair of digital signals (reference and test) registered by the digital oscilloscope using this setup can be observed in Fig. ESI-2.

In this figure, both the reference signal (a) and the test signal (b) are sinusoidal signals with identical modulation frequencies ($f_m = 5145$ Hz). The test signal was generated with some amplitude attenuation relative to the reference signal (i.e., $A_{ref} = 1$ V, $A_{test} = 0.15$ V) and with a random phase-shift (i.e., $\varphi_{ref} = 0^\circ$, $\varphi_{test} = -54.22^\circ$ in this example). In addition, some additive white Gaussian noise was added to samples of the clean test signal (b) to generate a noisy test signal with a specific level of SNR (-12 dB in this example) (c).

Additionally, an experimental setup using standard measurement equipment as the phase-sensitive detector (i.e., a commercial dual-phase digital lock-in amplifier, SR830, Stanford Research Systems, www.thinksrs.com) was used to repeat the experimental tests (see Fig. ESI-1b). These experiments allowed us to compare the I/Q method’s results with those of a standard measurement method under identical experimental conditions (i.e., using the same analog signals). Previously, optimizing the LIA parameters was necessary to obtain the best response for analog signals 1 s in duration.

Furthermore, to ensure that the LIA operated with signals only 1 s in duration, analog signals similar to those presented in Fig. ESI-3 were applied to the reference (a) and test (b) signals. Both the reference signal and the test signal contained a burst of zeros at the beginning (2 s duration) and end (1 s duration), as well as a sinusoidal signal of 5145 Hz frequency and a 2 s duration (with a fixed phase value $\varphi_{ref} = 0^\circ$ for the reference signal, and a variable phase value $\varphi_{test}(t)$ for the test signal given by the function displayed in Fig. ESI-3c).

These phase values (φ_1 and φ_2) were known and were randomly assigned between 0 and -180° for each test signal. The transition between φ_1 and φ_2 was performed gradually over 20 ms to avoid phase jumps in the phase-sensitive detector. The reasons for applying these signals to LIA were two-fold. On the one hand, using signals 2 s in duration allowed the reference and test signals to be “locked” to one another using the PLL of the LIA during the first second of signal ($t = 2$ s to $t = 3$ s in Fig. ESI-3b); therefore, when the second half of the test signal was reached ($t = 3$ s), the LIA was ready to measure the phase value (φ_2) of the test signal correctly with respect to the reference signal. On the other hand, because of the test signal’s phase change (from φ_1 to φ_2 in $t = 3$ s), the phase-sensitive detector for the LIA was forced to find a new phase value (φ_2) using only one second of signal (i.e., between $t = 3$ s and $t = 4$ s). This last aspect was crucial for comparing both methods (I/Q method and LIA) under equal conditions because additional experiments (not listed here) revealed that the commercial LIA behaved like an instrument with memory. The phase value (φ_2)

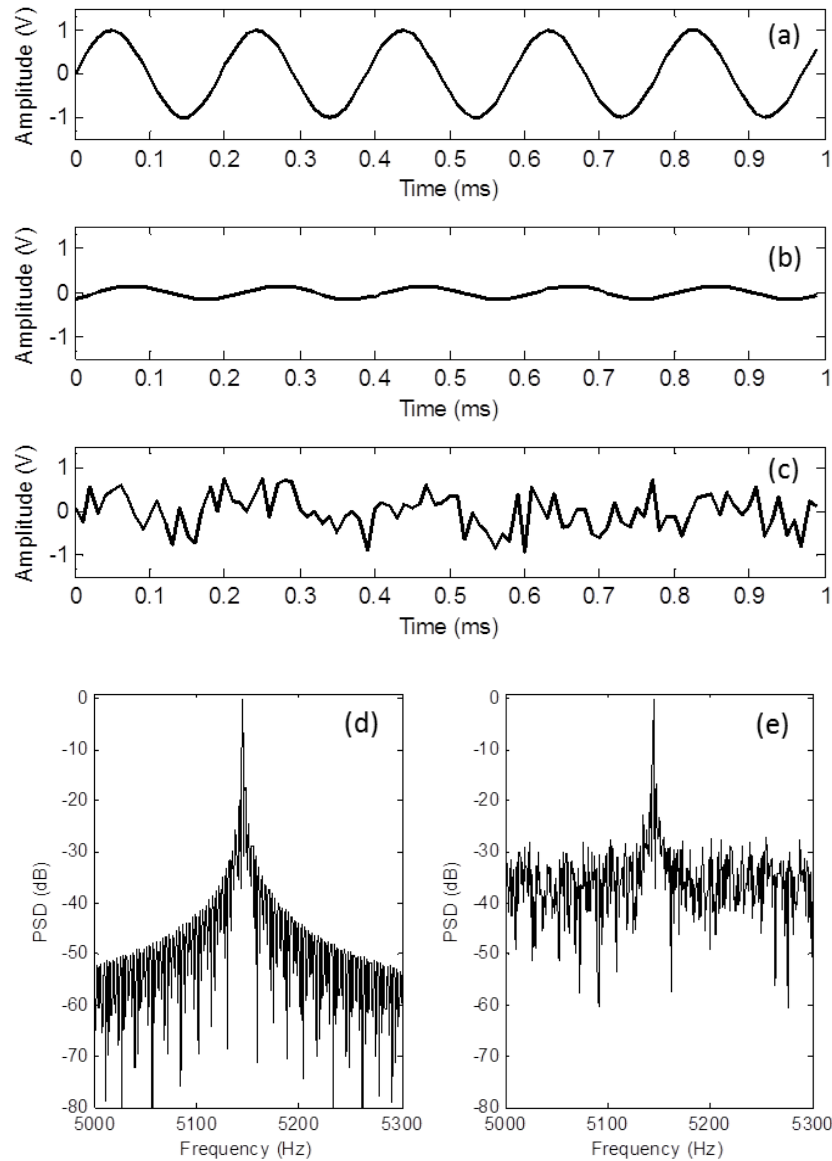


Fig. ESI-2. Graphical representation of a pair of digital signals (reference and test) observed using the digital oscilloscope depicted in Fig. ESI-1a. The parameters of the sinusoidal signals in this example were as follows: $dc_{(ref/test)} = 0$ V, $A_{ref} = 1$ V, $A_{test} = 0.15$ V, $f_m = 5145$ Hz, $\varphi_{ref} = 0^\circ$, $\varphi_{test} = -54.22^\circ$, signal duration = 1 s, $f_s = 100$ kS/s, $N_s = 100$ kS, and $SNR_{test} = -12$ dB. (a)-(c) Time-domain representation between 0 and 1 ms of the digital signals: (a) reference, (b) clean test signal, and (c) test signal with AWGN. (d)-(e) Frequency-domain representation of the digital signals (normalized power spectral density of the reference signal (d) and the noisy test signal (e)).

measured at $t = 4$ s was used as the representative phase value from the LIA for the signal 1 s in duration. To obtain this phase value (φ_2) (near $t = 4$ s), phase-shift measurements were continuously collected and stored in the memory of the LIA (from $t = 0$ s to $t = 5$ s) at 32 measurements/s. Later, this data buffer was transferred to a computer using an RS-232 serial port for further processing (see Fig. ESI-1b). Toward this purpose, an ad hoc Matlab program was used to synchronize both the process of generating the analog signals with a

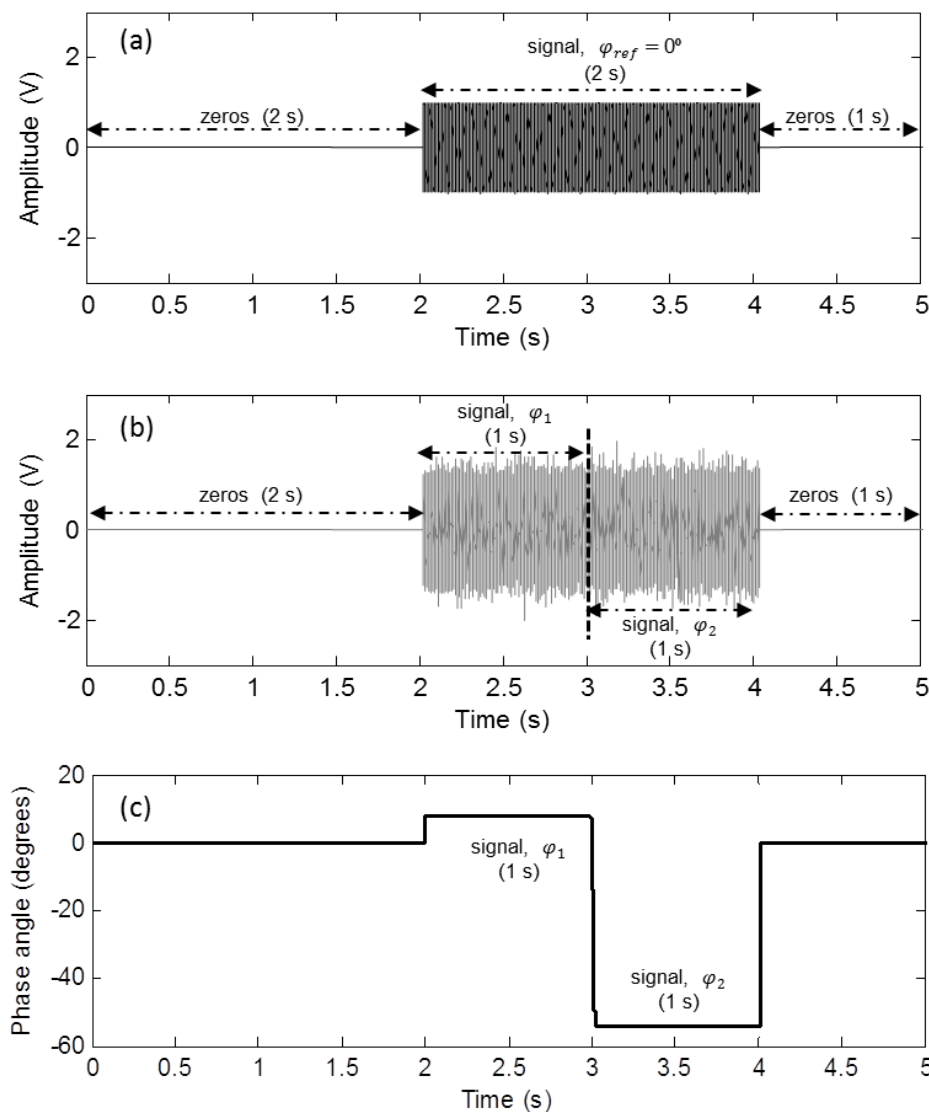


Fig. ESI-3. Example of the analog sinusoidal signals applied to the LIA during the experimental setup depicted in Fig. ESI-1b. (a) Reference signal; with $A_{ref} = 1$ V, $f_m = 5145$ Hz, $\varphi_{ref} = 0^\circ$, and a 2 s duration (excluding zeros). (b) Test signal; with $A_{test} = 0.15$ V, $f_m = 5145$ Hz, $\varphi_{test}(t)$, $SNR = -12$ dB, and a 2 s duration (excluding zeros). (c) Representation of the $\varphi_{test}(t)$ function for the phase of the test signal; where the phase values (φ_1) and (φ_2) (of 8° and -54.22° respectively in this case) were randomly assigned between 0 and -180° for each test signal. The phase value (φ_1) was used only to lock the reference and test signals to one another by the PLL, while the phase value (φ_2) that was used as the true test value was finally measured. Both analog signals (reference and test) were generated with the DAQ-card at 100 kS/s.

DAQ-card and the LIA's reading process. The bursts of zeros flanking the signals prevented any possible data loss during the reading process and facilitated further processing with the computer (the zeros allowed us to clearly identify the signals' beginning and end).

B. Analogic signals used for validating the I/Q method implemented into an oxygen sensor

Lower amplitudes in the excitation signal caused lower currents in the LED driver, leading to lower optical power signals (i.e., signals with lower SNR level). Similar to the experimental tests described in the previous section, a 5145 Hz analog sinusoidal signal 1 s in duration with bursts of zeros at the beginning (3 s duration) and end (1 s duration) was used as the reference and excitation signal in the I/Q-based experimental setup (see Fig. 5.1 of the manuscript). Specific analog signals similar to those displayed in Fig. ESI-3, except without the artificially added noise, were used as the excitation signal for the LED light source (Fig. ESI-4a) and the reference signal (Ref. Input) of the LIA (Fig. ESI-4b) in the LIA-based experimental setup (see Fig. 5.1 of the manuscript). These signals ensured that the LIA operated using signals only 1 s in duration (i.e., from the instant $t = 3$ s to $t = 4$ s in Fig. ESI-4), allowing these results to be compared with those obtained using the I/Q-based measurement system.

C. Selection of the time constant for the LIA system

One of the most important configuration parameters of the LIA is the time constant (TC) of the low-pass filter, which sets the filter bandwidth. The time constant is $1/(2\pi f)$, where f is the -3 dB frequency of the filter. By increasing the time constant, the output becomes steadier and facilitates more reliable measurements because the output noise decreases. A trade-off occurs when real changes in the input signal require many time constants to reflect the output. The time constant reflects the output's response rate and, therefore, the degree of output smoothing. The time constant also determines the equivalent noise bandwidth (ENBW) for the noise measurements (i.e., the effective bandwidth for the Gaussian noise).

In practice, for short time constants, the LIA did not capitalize on the signal over the entire second, and therefore, the uncertainty in the phase measurement was higher than when a full second was used. However, for long time constants, the LIA did not stabilize after one second, mainly due to its slow response. Therefore, the best TC value for the LIA depends on the signal time used while measuring the phase-shift, and therefore, such value must be selected experimentally for each particular measurement condition. However, in practice, the analyzed signals generally are of long duration, and large time constants are often used to obtain more reliable phase-shift measurements in laboratory settings. Obviously, this is only applicable when long duration signals with very slow phase changes are analyzed. Otherwise, the TC value for the LIA must be chosen more carefully.

Table ESI-1 summarizes the results (absolute phase errors) of the experimental tests used to find the best time constant for the LIA's low-pass filter for signals 1 s in duration. The time constant values shown in the table were selected from the front panel of the measurement instrument (LIA), as other intermediate values could not be chosen. As observed in the table (bold values), a minimum RMS phase error was obtained for a time constant of 100 ms in all cases (i.e., for different noise conditions), and therefore, it was chosen as the best TC value to carry out the experimental tests with the LIA. However, it is necessary to clarify that this $TC = 100$ ms may not be the best TC for the LIA for signals of a 1 s duration, and therefore, it is possible that better results could be expected for the LIA if a TC slightly higher or lower

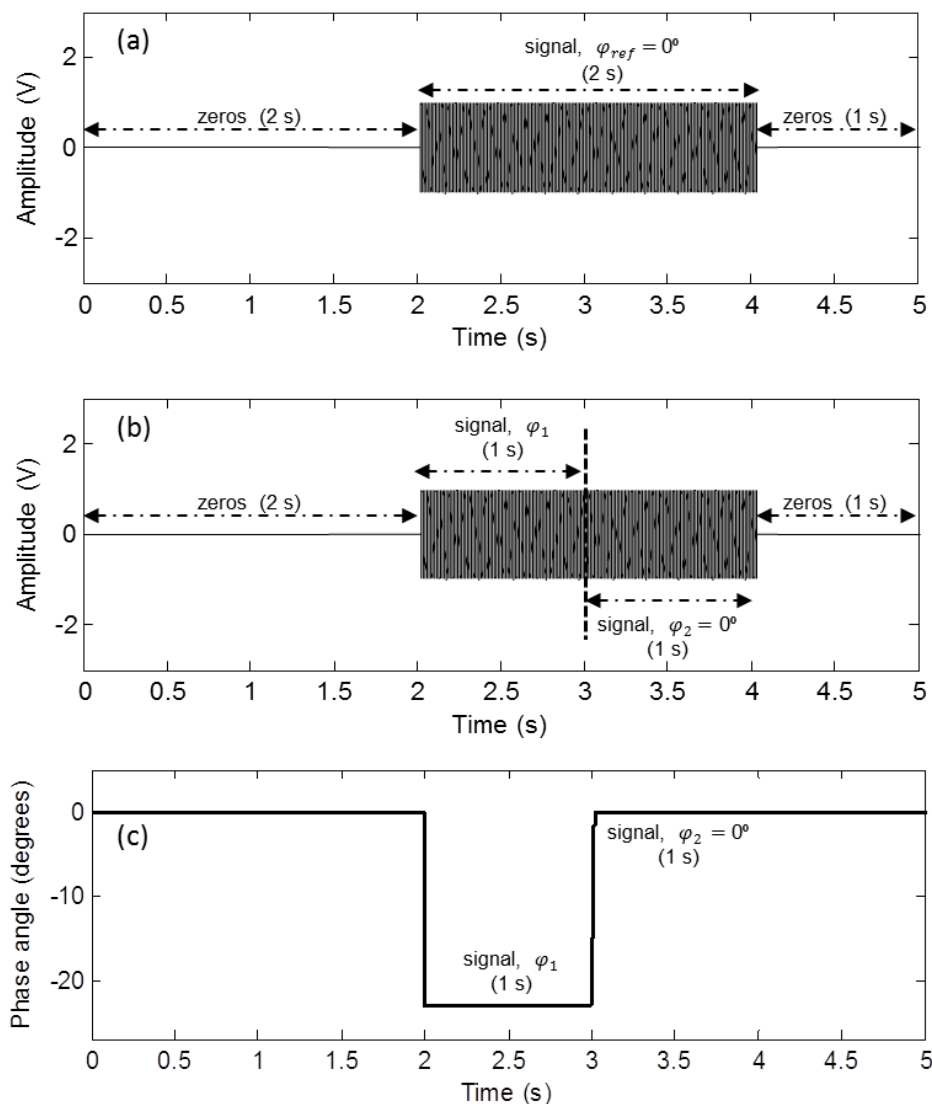


Fig. ESI-4. Analog sinusoidal signals applied to the LIA-based experimental setup. (a) Reference signal (Ref. Input) for the LIA, with $A_{ref} = 1$ V, $f_m = 5145$ Hz, $\varphi_{ref} = 0^\circ$, and a 2 s duration (excluding zeros). (b) Excitation signal for the LED light source, with variable amplitude (A_{exc}) between 22 and 1000 mV for the different lighting conditions, $f_m = 5145$ Hz, $\varphi_{exc}(t)$, and a 2 s duration (excluding zeros). (c) Representation of the $\varphi_{exc}(t)$ function for the phase of the excitation signal. The phase value (φ_1) was randomly assigned between 0 and -180° for each new measurement, while the phase value (φ_2) was set to zero to measure the specific phase-shift value introduced only by the sensing film. Both analog signals (reference and excitation) were generated with the DAQ-card at 100 kS/s.

than 100 ms were selected. Other parameters selected for the LIA were as follows: low-pass filter with a slope of 12 dB/octave, AC couple, 1 V sensitivity, low noise reserve, 50/60 Hz Notch filter, sine reference input, and float ground.

Table ESI-1. Results (absolute phase errors) of the experimental tests carried out to find the best time constant (TC) for the LIA using signals 1 s in duration.

SNR ^a (dB)	TC ^d = 1 ms		TC ^d = 3 ms		TC ^d = 10 ms		TC ^d = 30 ms		TC^d = 100 ms		TC ^d = 300 ms		TC ^d = 1000 ms	
	Mean ^b (°)	RMSE ^c (°)	Mean ^b (°)	RMSE ^c (°)	Mean ^b (°)	RMSE ^c (°)	Mean ^b (°)	RMSE ^c (°)	Mean ^b (°)	RMSE ^c (°)	Mean ^b (°)	RMSE ^c (°)	Mean ^b (°)	RMSE ^c (°)
-18	18.6410	23.5098	12.7646	15.9788	5.4676	6.8749	3.3287	4.0916	1.9036	2.4047	6.6341	7.2147	97.1355	136.1860
-12	8.7651	10.7724	6.4948	7.4987	2.9768	3.7823	1.6457	2.0534	1.0047	1.2641	6.5303	7.0885	97.4191	136.5756
-6	4.2754	5.4711	2.7980	3.3177	1.4730	1.9475	0.7905	0.9959	0.4825	0.6109	6.5175	7.0123	97.5246	136.7455
0	2.2297	2.7483	1.4176	1.7748	0.7001	0.8587	0.4165	0.5103	0.2339	0.2933	6.5319	7.0110	97.6392	136.8179
6	1.1885	1.4866	0.6503	0.7694	0.3445	0.4407	0.2134	0.2566	0.1183	0.1492	6.5252	6.9946	97.4699	136.6102
12	0.5072	0.6584	0.3953	0.4860	0.1647	0.2136	0.1109	0.1365	0.0623	0.0780	6.5364	7.0074	97.5861	136.7536
18	0.4542	0.5559	0.1703	0.2087	0.0951	0.1202	0.0579	0.0720	0.0349	0.0438	6.5213	6.9966	97.7864	136.8915
24	0.3084	0.3655	0.1098	0.1355	0.0446	0.0540	0.0391	0.0501	0.0255	0.0313	6.5222	6.9906	97.6897	136.8878
30	0.2782	0.3490	0.0958	0.1180	0.0247	0.0325	0.0286	0.0375	0.0210	0.0260	6.5222	6.9927	97.6249	136.8274
36	0.2883	0.3551	0.0787	0.0943	0.0172	0.0222	0.0335	0.0422	0.0186	0.0229	6.5328	7.0013	97.6844	136.8174

A total of 500 statistically independent phase-shift measurements were used to obtain each of the values in the table.

^a Signal-to-noise ratio (SNR) of the numerically generated test signals.

^b Mean and ^cRoot-Mean-Square Error (RMSE) of the absolute phase errors obtained from the 500 estimated phase-shift measurements (*i.e.*, $e_i = |\varphi_i - \hat{\varphi}_i|$ with $i = 1, 2, 3, \dots, 500$, where φ_i is the theoretical phase value (known a priori) and $\hat{\varphi}_i$ is the estimated phase value).

^d Time constant (TC) value for the LIA.

All experimental tests were performed with analog signals 1 s in duration.

Table ESI-2. Oxygen sensitivity of the sensing film (PtTFPP/PS) between 0 and 50 % O_2 (v/v) for the two measurement setups displayed in Fig. 5.1 of the manuscript. The Demas model was used to properly fit the experimental data.

Range	Parameter	I/Q method	LIA
0-50%(v/v) O_2	$K_{SV1}(bar^{-1})$	21.42 ± 0.02^a	19.59 ± 0.01
	x_1	0.72 ± 0.03	0.74 ± 0.02
	$K_{SV2}(bar^{-1})$	1.02 ± 0.01	0.81 ± 0.01
	x_2	0.28 ± 0.03	0.26 ± 0.02
	R^2	0.9999	0.9999

^a Parameter \pm error (95 % CI). The same oxygen-sensitive film was used in both measurement setups.

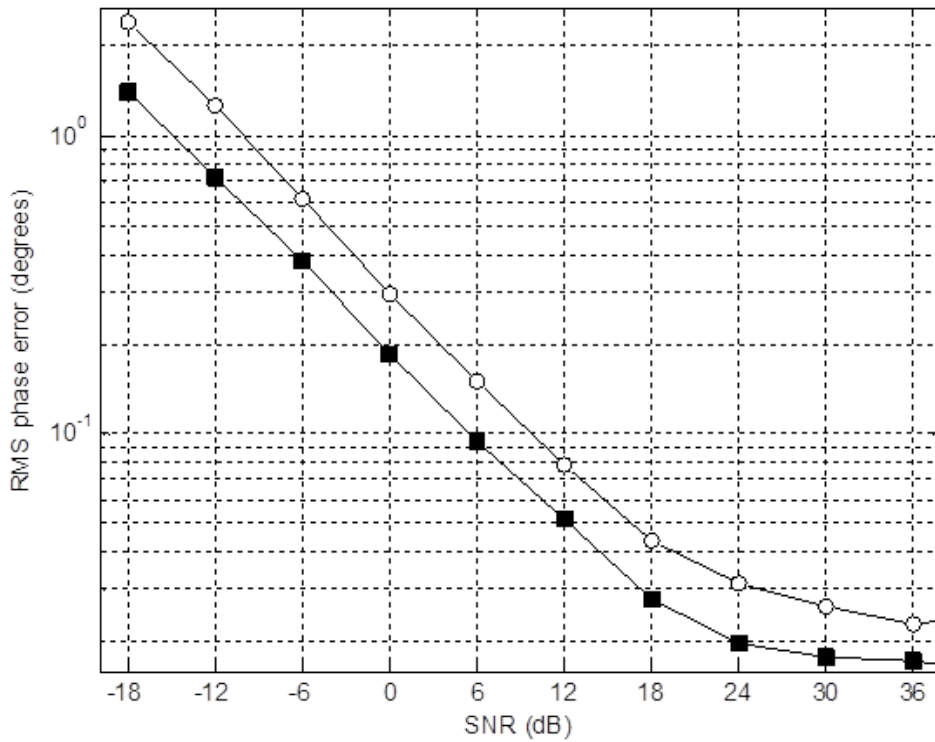


Fig. ESI-5. Results of the experimental tests obtained for the proposed I/Q algorithm and the LIA. RMS phase error versus SNR for the I/Q algorithm (■) and the LIA (○).

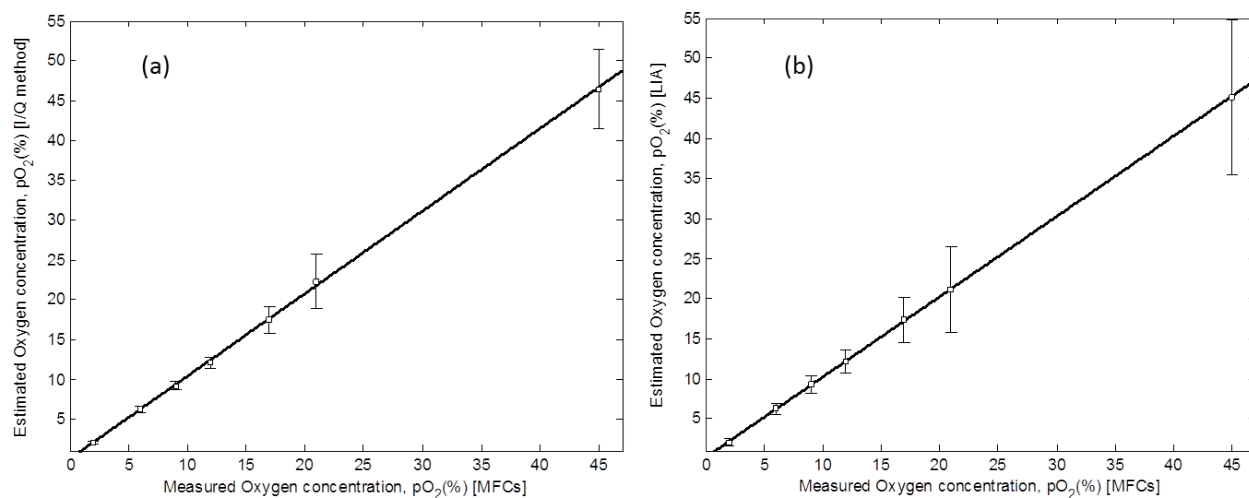


Fig. ESI-6. Comparison between the oxygen concentration values measured with the MFCs, $[O_2]_{n, MFCs}$ (taken as reference values), and their corresponding estimated oxygen concentration values $[\hat{O}_2]_{n, A_i}$ for all lighting conditions using the two oxygen measurement systems proposed in this work: (a) I/Q method and (b) LIA; 120 points for each oxygen concentration were used (10 values for each of the 12 lighting conditions). These figures also display the mean and standard deviation of $[\hat{O}_2]_{n, A_i}$, as well as the best-fitting line (i.e., the least squares regression line) through the data. The parameters for the linear regression analysis ($y = a + bx$) for a 95 % CI were as follows: (a) I/Q method: $a = -0.040 \pm 0.18$, $b = 1.005 \pm 0.010$, $R^2 = 0.9768$; (b) LIA: $a = 0.111 \pm 0.070$, $b = 1.002 \pm 0.010$, and $R^2 = 0.9335$.

A novel multifrequency phase-modulation method using rectangular-wave signals for improving the analytical sensitivity in luminescence spectroscopy

Santiago Medina Rodríguez^{a,b,*}, Ángel de la Torre Vega^a, Francisco J. Sainz Gonzalo^b, Marta Marín Suárez^b, César Elosúa Aguado^c, Francisco J. Arregui^c, Ignacio R. Matías^c, Jorge F. Fernández Sánchez^{b,*} and Alberto Fernández Gutiérrez^b

^a*Department of Signal Theory, Networking and Communications, CITIC-UGR, University of Granada, C/ Periodista Rafael Gómez 2, E-18071 Granada, Spain.*

^b*Department of Analytical Chemistry, Faculty of Sciences, University of Granada, Avda. Fuentenueva s/n, E-18071 Granada, Spain.*

^c*Department of Electrical and Electronic Engineering, Arrosadia Campus, Public University of Navarre, Edificio “Los Tejos”, E-31006 Pamplona, Spain.*

Submitted to *Analytical Chemistry*

A novel multifrequency phase-modulation method using rectangular-wave signals for improving the analytical sensitivity in luminescence spectroscopy

Abstract—We propose a novel multifrequency phase-modulation method for luminescence spectroscopy using a rectangular-wave modulated excitation source with a short duty cycle for (1) improving the analytical sensitivity in the determination of the concentration, and for (2) obtaining more detailed information about the luminescence system. It is based on a simple algorithm which combines multifrequency information provided by the different harmonics of the rectangular-wave signal, which can be easily implemented in existing photoluminescence instruments by replacing the excitation light source (short duty cycle rectangular signal instead of sinusoidal signal) and implementing appropriate digital signal processing after the transducer (implemented in software).

These claims have been demonstrated by using a well-known oxygen-sensing film coated at the end of an optical fibre (a Pt(II) porphyrin immobilized in polystyrene). The experimental results show that the use of the proposed multifrequency phase-modulation method decreases the root mean square error in the analytical determination (from 0.1035 to 0.0053 kPa at 0.5 kPa O₂ and from 1.1087 to 0.1209 kPa at 20 kPa O₂) when it is compared with a conventional phase-modulation method based on a sinusoidally modulated excitation source (under equal luminous power conditions).

keywords: Optical sensing; Phase-resolved; LED; Optical fibre; Square wave; Multifrequency; Spectroscopy.

6.1 Introduction

LIFETIME measurements are preferred in luminescence spectroscopy since they are less susceptible to errors than intensity measurements [1–3]. The luminescent lifetime can be determined using methods that proceed either in the time domain (pulsed methods) or in the frequency domain (phase-modulation methods) [1, 4]. Pulsed measurements are ideally suited for the elimination of the background luminescence and scattering, but they require expensive and complex instrumentation (such as high-speed photodetectors) and high computational cost [1, 2, 5]. On the other hand, lifetime phase-modulation measurements do not require sophisticated instrumentation [6, 7], and allow the use of simple and cheap light sources and electronic devices [2, 8]. Thus, phase-modulation techniques are preferred for designing robust and reliable optical methods [1, 2, 4, 8, 9].

To date, most measurement schemes based on phase-modulation techniques make use of sinusoidally modulated excitation sources, and the phase detection is performed at a single

frequency using commercial lock-in amplifiers [9–12], or either simple analog [13, 14] or digital [2, 15, 16] implementations. However, the generation of a sinusoidal signal is not trivial, and therefore small-size, simple, low-cost and low-power instruments cannot be easily developed for this purpose [17]. In addition, to avoid the alteration of the signal waveform, a continuous operation of the illumination source is required; it implies adding a DC offset to the AC signal and therefore it reduces the useful life of the sensor due to photodegradation processes [9, 18, 19]. Furthermore, the nonlinearities of several devices, such as LEDs, analog filters, amplifiers, photodetectors, etc., may produce a significant distortion in the sinusoidal waveform resulting in undesirable measurement errors [17].

To solve these problems, several authors have proposed the use of train of delta functions or square-wave excitations [4, 5, 20, 21]. They offer a series of advantages with respect to the sinusoidal excitation, such as: (1) an “*on-off*” operation of the light source that reduces the problems of the nonlinear distortion of the signal waveform caused by the nonlinear behaviour of the electronic components; (2) a simpler and lower-cost circuitry (i.e., quartz crystal oscillators, simple logic gates, transistors or microcontrollers); (3) a higher power of signalling (i.e., better signal-to-noise ratio (SNR) for the modulated signal); and (4) a lower power consumption of the excitation light source [22], ideal for its implementation in battery-powered portable devices. In most of these schemes, the sensing phases are excited using LED sources which are modulated with square-wave signals with a 50% duty cycle at a single frequency. Usually, only the information of lifetime estimated from phase-shift or modulation factor of the fundamental harmonic is used [6, 23]. However, another interesting feature of the square signals (in the frequency-domain) is their multifrequency nature [24]. It supplies several advantages with respect to measurements at a single frequency [2, 5], although it has not been sufficiently exploited so far.

As the duty cycle in a rectangular signal decreases, the relative power of the high order harmonics increases [24]. Therefore, a higher number of harmonics are available for multifrequency detection, avoiding the need of preparing complicated multifrequency excitation signals [2] or hard-implementation gated detection schemes [5]. In this paper we study the use of short duty cycle rectangular signals in phase-modulation based luminescence spectroscopy. It provides simultaneous measurements at different frequencies using apparent luminescence lifetimes estimated from modulation or phase-shift for several harmonics, leading to a more complete and reliable analytical characterization of the system and providing a new strategy to obtain more accurate analytical results. In addition, we propose the use of a method, formulated in a statistical framework, for combining information provided by apparent luminescence lifetimes estimated from both modulation and phase-shift at different harmonics. To the best of our knowledge, this is the first time that a multifrequency phase-modulation method with combination of lifetimes for more than one harmonic has been used in luminescence spectroscopy.

To develop the experimental work, an oxygen sensor has been selected as a well-known example of the real applicability of the proposed method. In addition, a fibre optical sensor has been selected in order to have a relatively weak luminescence and low signal-to-noise ratio because it helps to observe the change on the accuracy in the analyte determination.

6.2 Theory: Multifrequency luminescence response using rectangular-wave signals

Conventionally, phase-modulation measurements estimate the luminescence response using a sinusoidally modulated excitation source. The phase-shift and modulation factor are estimated by processing both the excitation and the emission signals at the modulation frequency. The use of short duty-cycle rectangular signals for excitation provides several harmonics with enough amplitude for allowing the simultaneous measurement of the phase-shift and the modulation factor at several frequencies. Since a conventional Lock-In Amplifier (LIA) allows the estimation of these parameters only at one frequency, a multifrequency scheme based on LIA would require a bank of LIAs (one for each harmonic to be used) including an appropriate band-pass filter at the input of each LIA. For the multifrequency analysis of the response we propose an analog-to-digital conversion and the subsequent processing of the recorded digital signal, which can easily be implemented via software in a conventional computer or a micro-controller.

The analysis of the digitized signals (i.e. the excitation $s_{exc}(t)$ and the emission $s_{em}(t)$ signals) is performed in the frequency domain by applying the multifrequency In-phase/Quadrature (I/Q) method [2]. At each harmonic f_i , the in-phase $I_e(f_i)$ and quadrature $Q_e(f_i)$ amplitudes are calculated from the digitized signal $s_e(t)$ as:

$$I_e(f_i) = \frac{1}{K} \sum_{t=0}^{T-1} s_e(t) \cos(2\pi f_i t/f_s) \quad (6.1)$$

$$Q_e(f_i) = \frac{1}{K} \sum_{t=0}^{T-1} s_e(t) \sin(2\pi f_i t/f_s) \quad (6.2)$$

where the subindex e stands for excitation (exc) or emission (em) signals, i is the index of the harmonic, K is a normalization constant, t is the index of the samples, T is the number of samples and f_s is the sampling frequency.

From the in-phase and quadrature amplitudes, the amplitude and phase of the excitation and emission signals can be easily evaluated at each harmonic f_i as:

$$A_e(f_i) = \sqrt{(I_e(f_i))^2 + (Q_e(f_i))^2} \quad (6.3)$$

$$\phi_e(f_i) = -\arctan\left(\frac{Q_e(f_i)}{I_e(f_i)}\right) \quad (6.4)$$

and finally, taking into account the amplitude and phase of both signals, the modulation factor and the phase-shift are estimated at each harmonic as:

$$m(f_i) = \frac{A_{em}(f_i)}{A_{exc}(f_i)} \quad (6.5)$$

$$\varphi(f_i) = \phi_{em}(f_i) - \phi_{exc}(f_i) \quad (6.6)$$

Although modulation factor has been defined in some works as [1]: $(A_{em}(f_i)/A_{exc}(f_i)) / (A_{em}(dc)/A_{exc}(dc))$ (which requires the estimation of the excitation and emission amplitudes at null frequency, i.e. the dc component), we have used the definition in equation (6.5) because it only involves the amplitude at frequency f_i . This is an important practical advantage since the dc components are usually affected by offsets.

One can note that, even though $A_e(f_i)$ and $\phi_e(f_i)$ are biased depending on the normalization constant K and the time reference, $m(f_i)$ and $\varphi(f_i)$ remain invariant to them. The phase-shift based lifetime $\tau_\varphi(f_i)$ can be derived from the phase-shift estimated at each harmonic as [1]:

$$\tau_\varphi(f_i) = \frac{\tan(-\varphi(f_i))}{(2\pi f_i)} \quad (6.7)$$

On the other hand, bearing in mind the relationship between lifetime (τ_q) and intensity (I) at frequency f_i for a single exponential system [25]:

$$I(\tau_q, f) = I_0 \frac{\tau_q}{\tau_0} \frac{1}{\sqrt{1 + (2\pi f_i \tau_q)^2}} \quad (6.8)$$

(where τ_0 is the lifetime at null concentration of the quencher and I_0 is the intensity at low frequency and null concentration), a modulation factor based lifetime (τ_m) can be estimated at each harmonic as (see Supporting Information, SI, section A for further details):

$$\tau_m(f_i) = \tau_0 \frac{m(f_i)/m_0(f_i)}{\sqrt{1 + (2\pi f_i \tau_0)^2 (1 - (m(f_i)/m_0(f_i))^2)}} \quad (6.9)$$

where $m_0(f_i)$ is the modulation factor at null concentration and frequency f_i .

If the system is accurately described by a mono-exponential model, the estimations of $\tau_\varphi(f_i)$ and $\tau_m(f_i)$ obtained at different frequencies would be the same. However, one-site mono exponential model is usually insufficient for describing most real luminescent systems and the lifetimes estimated at different frequencies are not expected to provide the same value. In such situation, these estimations are preferred to be called apparent lifetimes [1].

The proposed method provides, therefore, a procedure for describing accurately the luminescence system at a given quencher concentration, since the apparent lifetimes estimated from modulation factor ($\tau_m(f_i)$) and phase-shift ($\tau_\varphi(f_i)$) can be simultaneously determined at several modulation frequencies with just one measurement.

The determination of the quencher concentration can be performed using calibration curves appropriately fitted from calibration data. Since the proposed method simultaneously provides $\tau_m(f_i)$ and $\tau_\varphi(f_i)$ at several harmonics, different calibration curves can be fitted independently for each parameter. Similarly, from a single signal recording ($s_{em}(t)$ and $s_{exc}(t)$) different independent determinations of the quencher concentration can be estimated.

Using N unbiased and statistically independent determinations of the quencher concentration $\tilde{C}(x_n)$ (each one based on an estimated parameter x_n with $n = 1, 2, \dots, N$), a more accurate estimation \hat{C} can be obtained as the expected value of C using the join probability distribution (see SI section B for details of the mathematical derivation):

$$\hat{C} = \frac{\sum_{n=1}^N \tilde{C}(x_n) \prod_{k \neq n} \sigma_k^2}{\sum_{n=1}^N \prod_{k \neq n} \sigma_k^2} \quad (6.10)$$

where σ_n is the standard error associated to the n^{th} measurement $\tilde{C}(x_n)$, that could also be noted as $SE(\tilde{C}(x_n))$. Since the quencher concentration $\tilde{C}(x_n)$ is estimated from the parameter x_n (being x_n a phase-based apparent lifetime or a modulation-based apparent lifetime) by using the corresponding calibration curve, the standard error $SE(\tilde{C}(x_n))$ can be estimated according to the error propagation theory as:

$$\sigma_n = SE(\tilde{C}(x_n)) = \left| \frac{\partial \tilde{C}(x_n)}{\partial x_n} \right| SE(x_n) \quad (6.11)$$

where $\tilde{C}(x_n)$ is the calibration function describing the quencher concentration as a function of the parameter x_n , and the standard error $SE(x_n)$ should be obtained from several measurements acquired in the operation conditions. However, the estimation of the combined concentration \hat{C} does not require the standard errors, but the standard errors relative to one of them (i.e., if all the standard errors are multiplied by a constant, \hat{C} remains invariant). Therefore, if we accept that under the measurement conditions (due to the unknown noise conditions) the standard errors $SE(x_n)$ (and σ_n) are scaled with a constant that only depends on the SNR, in equation (6.10) \hat{C} remains invariant if we apply the standard errors estimated at a reference SNR condition to the measurements acquired at a different SNR condition. Therefore, the standard errors for equation (6.10) could be estimated from the calibration data.

This way, the proposed method can be applied to combine the information obtained from $\tau_m(f_i)$ and $\tau_\varphi(f_i)$ at different harmonics when the system is excited with a short duty-cycle rectangular-wave signal.

6.3 Experimental

6.3.1 Chemicals and reagents

Platinum (II) meso-tetra(pentafluorophenyl)porphine (PtTFPP) was purchased from Frontier Scientific Inc. (UT, USA) and was used as oxygen sensitive dye. Polystyrene (PS)(280000 g mol⁻¹) which was used as solid support and chloroform (used as solvent) were purchased from Sigma-Aldrich. All chemicals and reagents were of analytical grade and were used as received without further purification.

6.3.2 Preparation of the sensing fibre

A fibre optical sensor has been selected in order to have a relatively weak luminescence and low signal-to-noise ratio. It helps to observe the change on the accuracy in the analyte determination. A multimode plastic-clad silica optical fibre (OFS, Norcross, USA, core/cladding diameters of 200/230 μm , attenuation of 4.28 dB/Km at 650 nm, 1.5 m long, and SMA-905 connector at one end) was cut perpendicularly using a Fujikura CT-20-12 precision fibre cleaver and a Leica DM2500 microscope (Leica Microsystems, Wetzlar, Germany) for visualizing the images of the optical fibre (see SI, Fig. SI-2). A portion (2 cm) of the optical fibre plastic cladding was removed by means of a flame burner. Finally, the optical fibre was cleaned with absolute ethanol for eliminating dirtiness and impurities.

The membrane cocktail was prepared mixing thoroughly 396 mg of PS, 6 mg of PtTFPP and 4.0 mL of chloroform in a glass vial (dye concentration of 1.5 mg mL⁻¹). The mixture was continuously stirred until complete dissolution and coated on the clean, free-cladding optical fibre by dip coating, using a Nadetech ND-R rotatory dip coater (Nadetech Innovations, Pamplona, Spain) [26–28] with a dipping speed of 11 mm/s, dipping time of 1 s and raising speed of 11 mm/s. Finally, the sensing film was dried in an oven at 40 °C during 10 min [26]. SI (see Fig. SI-3) shows some SEM images of the coated optical fibre obtained with a Carl Zeiss FE-SEM Ultra Plus microscope (Carl Zeiss Microscopy, USA). The estimated thickness of the coated layer was 1028 \pm 123 nm (95% confidence interval).

6.3.3 Measurement system

SI (see Fig. SI-1) displays the schematic diagram of the experimental setup used in this work. It is based on simple modifications of the experimental setup described by our research group for implementing the I/Q method [2].

To mix nitrogen and oxygen (both all of 99.999% purity, obtained from Air Liquide España, Spain) two mass-flow controllers (MFCs) (EL-FLOW Select F-201CV, Bronkhorst High-Tech, Ruurlo, Netherlands) connected to a Flow-Bus Interface (Bronkhorst High-Tech, Netherlands) via a RS-232 serial port were used. The MFCs were connected, using copper and stainless steel tubing, to the flow-through cell, which was designed in our laboratory using a standard glass tube (230 mm in length) to hold the optical fibre probe.

The optical fibre probe was excited with an ultraviolet LED (Ocean Optics, LS-450 LED-395, $\lambda_{max} = 391$ nm, angle of illumination 15°, LED diameter 5 mm, luminous power 25 μW) filtered through an optical bandpass filter (OF-1; Thorlabs GmbH, MF390-18, $\lambda_{central} = 390$ nm). This LED was modulated using two different analog current signals: (1) a sine-wave signal of 5145 Hz, and (2) a rectangular-wave signal (with 10% duty cycle) of 1715 Hz. Two identical numerically-generated digital signals were extracted using two analog output channels on an AD/DA board (NI PCIe-6363/BNC-2120, National Instruments, USA) at a sampling rate of 500 kS/s: one for modulating the current of the LED in the LED driving circuit and the other one was used as an external reference signal (see SI, Fig. SI-4 and Fig. SI-5 for further details). The emission signal was transduced with a photomultiplier tube (PMT) with a bandwidth DC-1 MHz (H10723-20, Hamamatsu Photonics, Japan) equipped with an appropriate optical bandpass filter and the PMT output was amplified

and filtered with appropriate analog electronics. Both the excitation signal (the reference) and the emission signal from the sensing film were simultaneously digitized using a digital oscilloscope WaveRunner 604Zi (LeCroy, USA) at 500 kS/s using signals of 5 s in duration (i.e., a 2.5 MS data buffer). The bandwidth of the electronic devices and the sampling rates are large enough for the frequency of the harmonics involved in these experiments and they are also appropriate for the typical lifetimes of the used indicator (that is, for lifetimes in the range of tens of microseconds). The proposed method could also be applied to indicators with shorter lifetimes by using a higher fundamental frequency in the rectangular-wave signals, and hardware components with appropriate bandwidth. In the experimental set-up, the element conditioning the frequency range is the PMT, which has a bandwidth of 1 MHz. This limits the minimum lifetime that can be measured to around 0.1 μ s (for measuring luminophores with a shorter lifetime, a faster PMT should be used, and the preamplifier and analog filters should be redesigned).

All measurements were performed at room temperature (21 °C). The temperature was continuously monitored using a commercial temperature sensor (MicroLite, Fourtec-Fourier Technologies, USA).

6.3.4 Implementation of rectangular-wave modulated excitation in phase-modulation methods

In order to demonstrate the ability of the proposed multifrequency phase-modulation method based on a rectangular-wave modulated excitation source with a short (10%) duty cycle, it was compared with a conventional phase-modulation method based on a sinusoidal modulated excitation signal using the same luminescence system (see Fig. 6.1). To ensure a fair comparison, the waveforms must have equal total excitation energy over the time course of the experiment. Thus, assuming that these waveforms were used to modulate the electrical current of a LED excitation source, all of them must have the same average current level (see horizontal dot-dashed line in Fig. 6.1(a) or amplitude of the DC component (i.e., 0 Hz) in Figs. 6.1(b,1-3)) to ensure the same average electrical power dissipated by the LED (directly related to its average optical output power) [29].

As can be seen in Fig. 6.1(b-2), a 50% duty cycle square-wave excitation has a very rapid falloff in the amplitude of the higher harmonics and only the odd harmonics have non-null amplitude. Therefore, the standard method with square-wave excitation is limited to at most a few harmonics [5]. This drawback can be solved using a short (10%) duty cycle rectangular-wave excitation, which has a slow falloff in the amplitude of both the even and odd harmonics (see Fig. 6.1(b-3)). Thus, rectangular-wave signals are ideal for the multifrequency analysis, since simultaneous measurements of the luminescence are possible at a number of frequencies using the calculated phases and/or amplitudes for several harmonics of the excitation and emission waveforms.

Two types of excitation signals have been used in this study: (1) a conventional sinusoidal signal (frequency: 5145 Hz), used as reference, and (2) the proposed 10% duty cycle rectangular-wave signal (fundamental frequency: 1715 Hz). In the case of the sinusoidal signal, the phase-based apparent lifetime (τ_φ) and the modulation-based apparent lifetime (τ_m) at 5145 Hz have been estimated using the I/Q method [2]. In the case of the rectangular

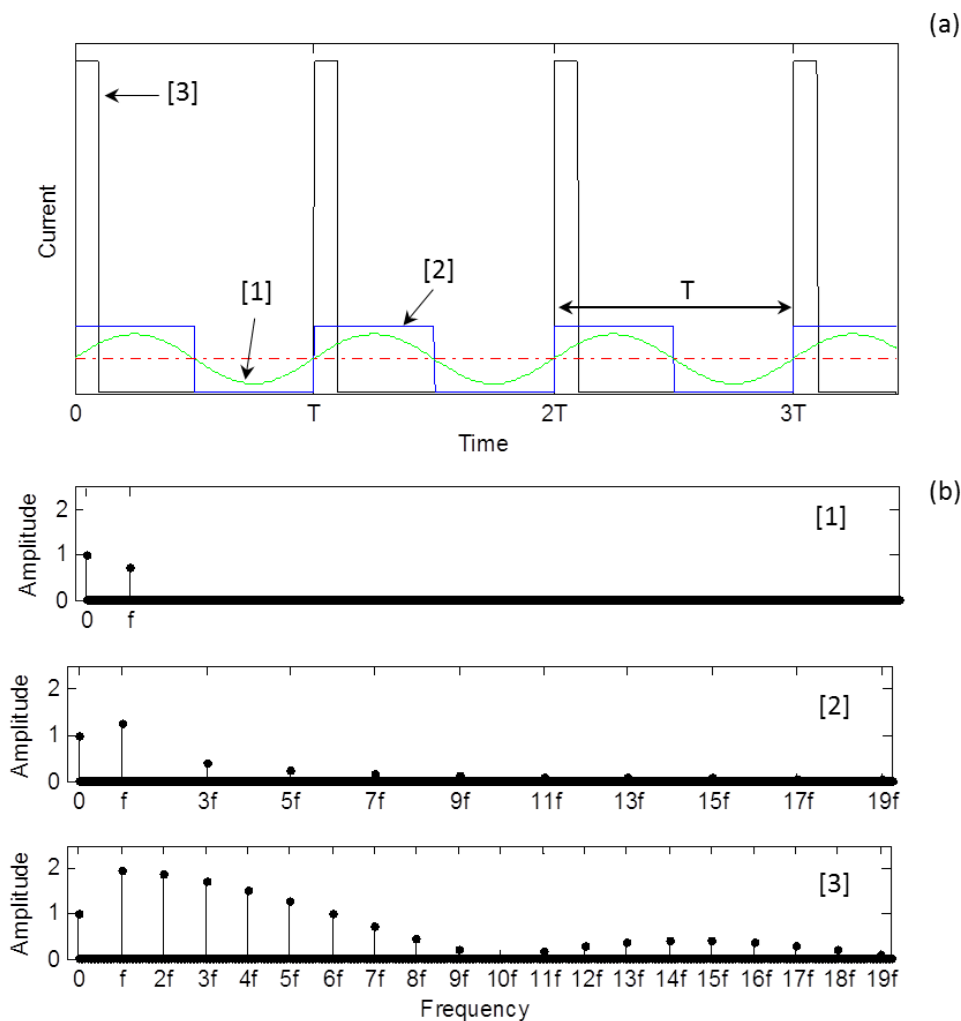


Figure 6.1: Waveform (a) and amplitude spectrum (b) of [1] a sinusoidal wave, [2] a square wave with a 50% duty cycle, and [3] a rectangular wave with a 10% duty cycle with the same average current level (dot-dashed line).

wave, these parameters have been estimated for the 5 first harmonics (i.e. 1715 Hz, 3430 Hz, 5145 Hz, 6860 Hz and 8575 Hz) with the multifrequency I/Q method [2]. SI (see Fig. SI-5) shows some examples of signals and the corresponding spectra.

The implementation of the proposed method requires, on one hand, a rectangular signal (instead of a sinusoidal one) to be used as excitation signal; and, on the second hand, the multifrequency I/Q algorithm to process the recorded digital signal in order to obtain the phase-shift and the modulation factor at each harmonic. In our set-up, the change from a sine-wave signal to a rectangular-wave signal is trivial, since an AD/DA board was used in both cases. However, in general, the use of an on-off rectangular signal simplifies the electronics with respect to the use of sinusoidal signals. On the other hand, the multi frequency I/Q method increases the sophistication of the algorithm, but it just involves digital signal processing (that is easily implemented in software). The acquisition of the digital signals was performed with a digital oscilloscope (which limits the portability) but AD conversion can be easily implemented with an AD/DA board connected to a laptop in order to increase portability.

6.4 Results and discussion

6.4.1 Estimation of the apparent lifetimes and calibration

18 concentrations ranging between 0 and 20 kPa O_2 were evaluated by recording 25 measurements for each concentration level and using both sinusoidal and rectangular-wave signals for exciting the sensing film. The phase-shifts and modulation factors were calculated using equations (6.6) and (6.5), respectively, at the modulation frequency in the case of the sine wave and at the 5 first harmonics for the rectangular wave. The phase based-apparent lifetime (τ_φ) and the modulation-based apparent lifetime (τ_m) were estimated using equations (6.7) and (6.9) from the corresponding phase-shifts and modulation factors. The mean and standard deviation values for phase-shift, modulation factors and the corresponding apparent lifetimes for different concentrations and modulation frequencies (using both sine-wave and rectangular-wave signals) can be seen in SI (see Tables SI-1 to SI-4 and Fig. SI-6).

Fig. 6.2 shows the phase-based apparent lifetime (τ_φ) and the modulation-based apparent lifetime (τ_m) as a function of the modulation frequency, estimated for different oxygen concentrations when the rectangular-wave signal is used. The apparent lifetime decreases from 70 μs to 7 μs when the oxygen concentration increases from 0 to 20 kPa pO_2 . Assuming a mono-exponential luminescence model, for a given oxygen concentration, the phase-based apparent lifetime should be the same as that obtained using modulation factor, and also when they are estimated for different harmonics. However, significant differences are observed. In general, an increase of the apparent lifetime is observed for lower frequencies; this increase is more important when the lifetime is estimated from the phase-shift. At lower concentrations, an increase of the lifetime is also observed for the highest harmonic included in the study. Finally, similar values of τ_φ and τ_m can be observed for lower concentrations (as expected from equation (6.9)), but τ_φ is significantly higher than τ_m for high concentrations. Therefore, this multifrequency analysis of the apparent lifetimes confirms that the mono-exponential luminescence model is insufficient for describing this sensing phase. In this sense, the use of the rectangular-wave signals provides more detailed information and description of the sensing phase than using sine-wave signals since it simultaneously provides information at different frequencies from just one measurement. This is very useful for a complete and fast characterization of the luminescence system.

Due to the variation of the apparent lifetimes among frequencies and between phase-based and modulation-based estimations, calibration oriented to the determination of the oxygen concentration was performed independently for each estimation of the apparent lifetime. The estimated τ_φ and τ_m obtained at different frequencies (see SI, Tables SI-2 for sine-wave signals and SI-4 for rectangular wave signals) were used for calibrating. Calibration curves were obtained by fitting experimental data using the Demas two-site model [30]. The resulting calibration curves and the model parameters are shown in SI for sine-wave and rectangular-wave signals (see SI, Fig. SI-7 and Tables SI-5 and SI-6, respectively). These calibration curves were used for the determination of the oxygen concentration.

When the apparent lifetimes are estimated using rectangular-wave signals, smaller standard deviations are observed even for higher order harmonics (see SI, Tables SI-2 and SI-4). This is due to the higher amplitude of the harmonics (compared to the amplitude of the

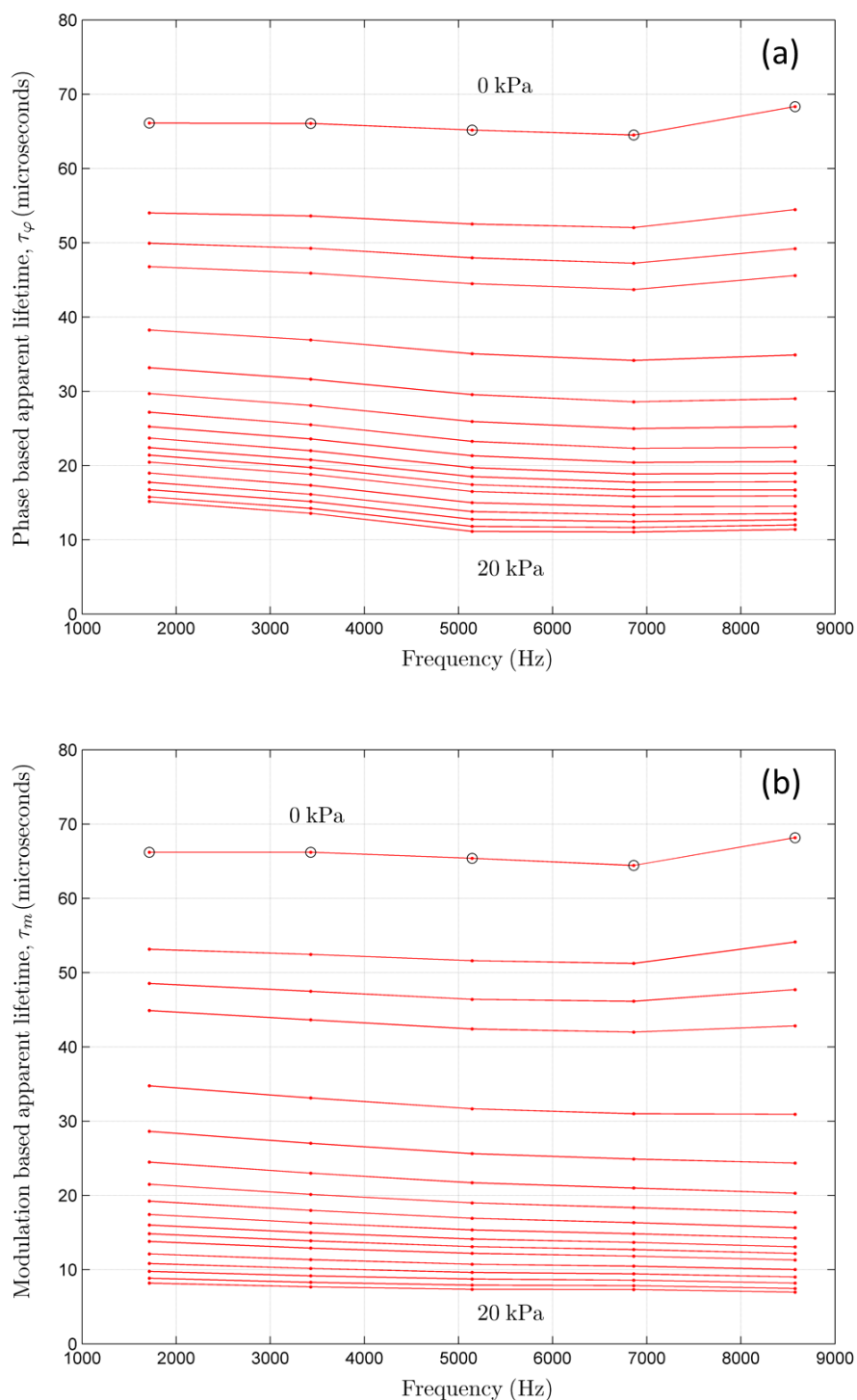


Figure 6.2: Effect of the modulation frequency on the apparent luminescent lifetimes estimated from (a) phase shift and (b) the modulation factor at 0, 0.5, 0.75, 1, 2, 3, 4, 5, 6, 7, 8, 9, 10, 12, 14, 16, 18 and 20 kPa O_2 .

frequency component for the sine-wave signal) at equal illumination conditions, and suggests that the use of the proposed rectangular-wave signals would provide a more accurate

determination of the oxygen concentration.

After the calibration of the system, the analyte concentration can be determined from the recorded signal when the system is excited with a sinusoidal signal or when it is excited with a rectangular-wave signal. In the case of the sinusoidal signal, τ_φ and τ_m are obtained, and two estimations of the analyte concentration ($\widetilde{pO_2}(\tau_\varphi)$ and $\widetilde{pO_2}(\tau_m)$) are available (one from τ_φ and one from τ_m), by applying the corresponding calibration curve. In the case of the rectangular-wave signal, 5 harmonics were analysed, and 10 parameters are available ($\tau_\varphi(f_i)$ and $\tau_m(f_i)$ for $i = 1, \dots, 5$) for each measurement. Therefore, by applying the corresponding calibration curve, 10 independent estimations of the analyte concentration are available ($\widetilde{pO_2}(\tau_\varphi(f_i))$ and $\widetilde{pO_2}(\tau_m(f_i))$ for $i = 1, \dots, 5$).

Therefore, the analyte concentration could be determined by using one of these parameters alone (for each parameter one concentration may be determined) or the estimations from different parameters could be combined in order to increase the accuracy in the determination of the concentration. In the case of sinusoidal signal, only two $\widetilde{pO_2}$ measurements are available while the rectangular-wave signal allows the combination of the information from several harmonics (in our case the combination of up to 10 parameters).

6.4.2 Evaluation of the accuracy of the proposed method

The simple algorithm described in equation (6.10) can be applied to combine the information obtained from $\tau_\varphi(f_i)$ and $\tau_m(f_i)$ when the system is excited with a sinusoidal signal or when it is excited with a rectangular-wave signal. Moreover, the algorithm can be applied to combine multifrequency information provided by the different harmonics in the case of the rectangular-wave signal.

The proposed method has been evaluated using both sinusoidal and rectangular-wave excitation signals. For 17 values of oxygen concentration (ranging between 0.5 kPa and 20 kPa), 25 measurements (different than those used for calibrating) were recorded with each excitation signal (sine-wave and rectangular-wave), using the same sensing film and exciting it with the same average luminous power. For each measurement, estimations of the analyte concentration $\widetilde{pO_2}$ have been obtained from τ_φ and τ_m . Two estimations of concentration based on one parameter have been obtained in the case of sinusoidal excitation signals (one from τ_φ and the other from τ_m). In the case of rectangular-wave excitation signals, 10 estimations of concentration were obtained (from τ_φ and τ_m for the 5 first harmonics). In addition to the concentration estimations based on one parameter, several combinations have been evaluated, including information from τ_φ and τ_m , or combining information from different harmonics in the case of rectangular-wave signals.

The evaluation of the accuracy was based on the Root Mean Square Error (RMSE), using the measurements from the mass-flow controllers as reference. Tables SI-7 to SI-9 show detailed experimental results for both excitation signals, including concentrations estimated from τ_φ , τ_m and the combination of both, and also combining estimations from different harmonics (in the case of rectangular-wave signals). Table 6.1 and Fig. 6.3 summarize these results.

Table 6.1: Accuracy for several combinations with the conventional phase-modulation method (sine-wave modulated excitation at $f_{sin} = 5145$ Hz) and the proposed multifrequency phase-modulation method ($f_1 = 1715$ Hz, $f_2 = 3430$, $f_3 = 5145$, $f_4 = 6860$, and $f_5 = 8575$ Hz) in the determination of pO_2 at four oxygen concentration levels.

Excitation	Parameter	Frequency	RMSE (kPa)			
			0.5 kPa O_2	2.0 kPa O_2	6.0 kPa O_2	20.0 kPa O_2
Sine-wave	τ_φ	f_{sin}	0.1222	0.1825	0.5023	3.0433
	τ_m	f_{sin}	0.1620	0.1630	0.3032	1.2552
	τ_φ, τ_m	f_{sin}	0.1035	0.1358	0.2830	1.1087
Rectangular-wave	τ_φ	f_1	0.0111	0.0243	0.1295	0.7746
		f_2	0.0117	0.0305	0.1093	0.7846
		f_3	0.0247	0.0462	0.1326	0.7564
		f_4	0.0396	0.0686	0.1857	0.8362
		f_5	0.0937	0.1049	0.2980	1.2573
		f_1, f_2	0.0075	0.0210	0.0838	0.4975
		f_1, f_2, f_3	0.0071	0.0206	0.0592	0.4621
		f_1, f_2, f_3, f_4	0.0071	0.0207	0.0527	0.4140
		f_1, f_2, f_3, f_4, f_5	0.0073	0.0204	0.0529	0.3905
Rectangular-wave	τ_m	f_1	0.0086	0.0244	0.0364	0.1914
		f_2	0.0173	0.0313	0.0354	0.1929
		f_3	0.0383	0.0422	0.0535	0.2512
		f_4	0.0783	0.0647	0.0897	0.3153
		f_5	0.2198	0.1324	0.1520	0.3993
		f_1, f_2	0.0083	0.0258	0.0255	0.1619
		f_1, f_2, f_3	0.0087	0.0266	0.0235	0.1449
		f_1, f_2, f_3, f_4	0.0089	0.0268	0.0232	0.1300
		f_1, f_2, f_3, f_4, f_5	0.0092	0.0270	0.0227	0.1269
Rectangular-wave	τ_φ, τ_m	f_1	0.0073	0.0199	0.0345	0.1857
		f_2	0.0082	0.0248	0.0316	0.1864
		f_3	0.0197	0.0369	0.0479	0.2116
		f_4	0.0339	0.0399	0.0857	0.2821
		f_5	0.0888	0.0790	0.1506	0.3817
		f_1, f_2	0.0056	0.0202	0.0253	0.1589
		f_1, f_2, f_3	0.0052	0.0208	0.0223	0.1439
		f_1, f_2, f_3, f_4	0.0052	0.0210	0.0214	0.1250
		f_1, f_2, f_3, f_4, f_5	0.0053	0.0210	0.0207	0.1209

They show that, using the same luminous power, the first harmonics from the rectangular-wave signal provides better accuracy than the sinusoidal signal at low and high concentration levels. This is because the power of these harmonics is higher than that for the fundamental frequency in the sinusoidal signal (and the SNR is consequently higher), as can be seen in Fig. 6.1. Analogously, concentrations estimated from harmonics in the rectangular-wave signals are more accurate for the lower order harmonics due to their higher power (and higher SNR).

Experimental results also show that the procedure proposed for combining information from several parameters for determining analyte concentration is very efficient. The combination of τ_φ and τ_m provides better accuracy than each of them separately, in all the cases. In addition, the proposed method provides an appropriate combination of the information obtained from different harmonics. As can be seen in Table 6.1, the inclusion of a new harmonic generally improves the accuracy in the determination of the analyte concentration, and this is observed for estimations based on τ_φ (RMSE reduced from 0.1295 to 0.0529 kPa at 6 kPa O_2), those based on τ_m (RMSE reduced from 0.0364 to 0.0227 kPa at 6 kPa O_2),

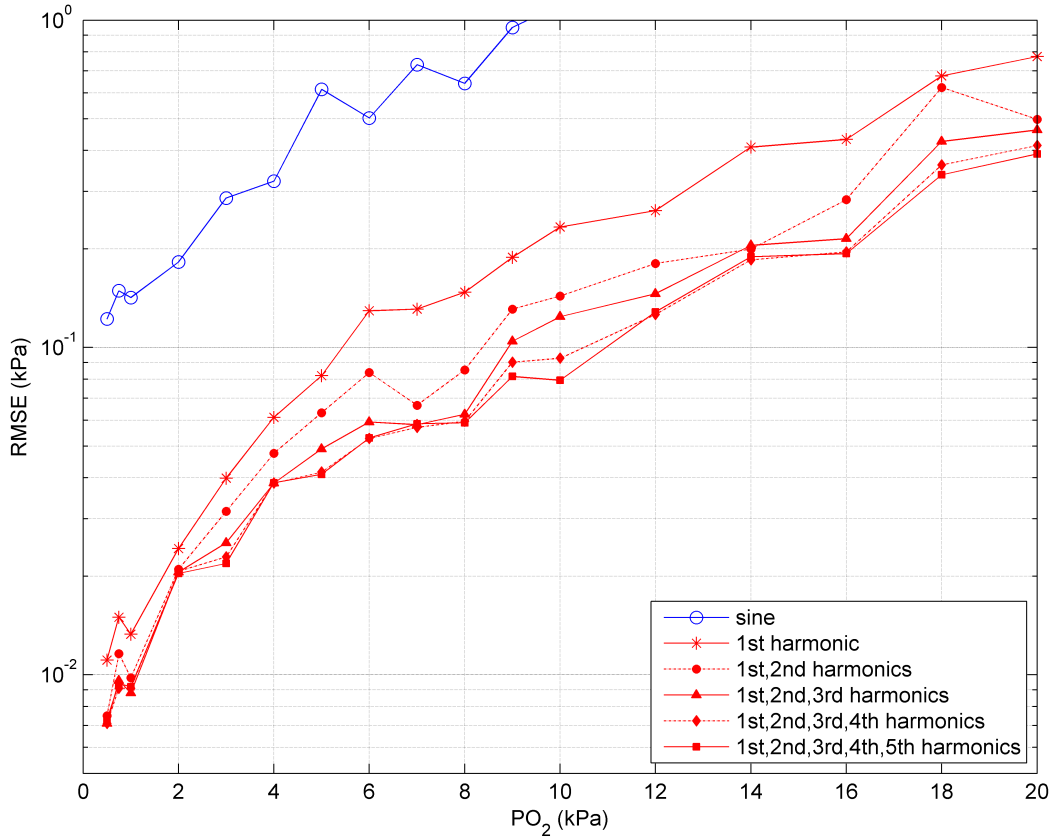


Figure 6.3: RMSE in the determination of pO_2 between 0.5 and 20 kPa using the phase-based apparent lifetime with the conventional phase-modulation method (blue line) and the proposed multifrequency phase-modulation method (red lines) combining the n ($n = 1, 2, \dots, 5$) first harmonics.

or those based on a combination of both τ_φ and τ_m (RMSE reduced from 0.0345 to 0.0207 kPa at 6 kPa O_2). In addition, the experimental results show that the use of the proposed multifrequency phase-modulation method provides a more accurate determination, reducing RMSE from 0.1035 to 0.0053 kPa at 0.5 kPa O_2 and from 1.1087 to 0.1209 kPa at 20 kPa O_2 when it is compared with a conventional phase-modulation method based on a sinusoidally modulated excitation source (under equal luminous power conditions).

The concentration measurements based on τ_m are generally more accurate than those based on τ_φ in all the measurements. This is related to the typical standard error in the estimates of τ_m or τ_φ (see SI, Tables SI-2 and SI-4), and the associated standard error in the concentration estimations due to the error propagation. It was previously described in other works [2, 9]. However, the measurements based on τ_φ are usually preferred since modulation factors are usually more biased by slight modifications in the experimental set-up or luminophore degradation and the measurement procedure based on modulation factor requires more calibration. Fig. 6.3 represents the RMSE in the determination of the oxygen concentration using the phase-based apparent lifetimes. This figure includes the RMSE for the conventional phase-modulation method (using sine-wave signals) and the proposed multifrequency phase-modulation method (using rectangular signals), combining different harmonics. These plots show the improvement derived from the use of the rectangular-wave signals as

well as that derived from the combination of harmonics. Compared with the sine-wave signal, the RMSE in the oxygen determination using τ_φ is in average 6.36 times smaller when the first harmonic is used and 12.08 times smaller when the 5 first harmonics are combined.

6.5 Conclusions

From the results presented in this study, we can conclude that the use of short duty cycle rectangular signals for luminescence measuring systems based on phase-modulation luminescence spectroscopy provides: (1) an improvement in the accuracy for determining the analyte concentration, and (2) a more complete characterization of the luminescence system.

It was demonstrated that the use of rectangular signals, using τ_φ and/or τ_m provides better accuracy than sinusoidal signals. This improvement is mainly associated to the use of more power for signalling (when the same luminous power is used for exciting the sensing fibre). The use of a short duty cycle improves the harmonic/DC power ratio for a number of harmonics, increasing the signal to noise ratio at different frequencies (for a given average luminous power), which reduces the error in the quantification of the analyte concentration. It also allows the combination of several harmonics for determining and quantifying the analyte concentration.

The combination of both analytical signals (τ_φ and τ_m) improves the accuracy provided by either τ_φ or τ_m alone. The procedure proposed for combining information from different estimators has also been successfully applied to combine τ_φ and τ_m information from a number of harmonics. Results show that as more information is included, the relative error decreases, obtaining a RMSE as low as 0.0053 kPa at 0.5 kPa O_2 and 0.12 kPa at 20 kPa O_2 when τ_φ and τ_m from the 5 first harmonics are combined.

The proposed method can be easily implemented in existing photoluminescence instruments since modifications just involve the part of excitation of the light source (short duty cycle rectangular signal instead of sinusoidal signal, which usually implies a simplification of the electronics) and the digital signal processing of the samples after the transducer (that can be implemented in software).

Associated content: Electronic Supporting Information (ESI)

Expressions for the estimation of the apparent lifetimes; procedure for combining several statistically independent measurements; pictures of optical fiber, deposited sensing film and designed set-up; examples of real signals recorded; tables with calibration data; parameters of the fitting models; and detailed experimental results. This material is available free of charge via the Internet at <http://pubs.acs.org>.

References

- [1] Lakowicz, J.R. *Principles of Fluorescence Spectroscopy*, 2nd ed.; Kluwer Academic: New York, 1999.

- [2] Medina-Rodríguez, S.; de la Torre-Vega, A.; Fernández-Sánchez, J. F.; Fernández-Gutiérrez, A. *Sensors and Actuators B: Chemical* **2013**, *176*, 1110-1120.
- [3] Wang, X.D.; Wolfbeis, O.S. *Analytical Chemistry* **2013**, *85*, 487-508.
- [4] McGraw, C.M.; Khalil, G.; Callis, J.B. *The Journal of Physical Chemistry C* **2008**, *112*, 8079-8084.
- [5] Rowe, H.M.; Chan, S.P.; Demas, J.N.; DeGraff, B.A. *Analytical Chemistry* **2002**, *74*, 4821-4827.
- [6] Trettnak, W.; Kolle, C.; Reininger, F.; Dolezal, C.; O'Leary, P. *Sensors and Actuators, B: Chemical* **1996**, *36*, 506-512.
- [7] McDonagh, C.; Kolle, C.; McEvoy, A.K.; Dowling, D.L.; Cafolla, A.A.; Cullen, S.J.; MacCraith, B.D. *Sensors and Actuators, B: Chemical* **2001**, *74*, 124-130.
- [8] Andrzejewski, D.; Klimant, I.; Podbielska, H. *Sensors and Actuators, B: Chemical* **2002**, *84*, 160-166.
- [9] Medina-Rodríguez, S.; Marín-Suárez, M.; Fernández-Sánchez, J.F.; de la Torre-Vega, A.; Baranoff, E.; Fernández-Gutiérrez, A. *Analyst* **2013**, *138*, 4607-4617.
- [10] *Operating Manual and Programming References, SR830 DPS Lock-In Amplifier*, 2.4 ed.; Stanford Research Systems: Sunnyvale, California, June 2009.
- [11] Ergeneman, O.; Chatzipirpiridis, G.; Pokki, J.; Marín-Suárez, M.; Sotiriou, G.A.; Medina-Rodríguez, S.; Fernández-Sánchez, J.F.; Fernández-Gutiérrez, A.; Pané, S.; Nelson, B.J. *IEEE Transactions on Biomedical Engineering* **2012**, *59*, 3104-3109.
- [12] Valledor, M.; Campo, J.C.; Sánchez-Barragán, I.; Costa-Fernández, J.M.; Álvarez, J.C.; Sanz-Medel, A. *Sensors and Actuators B: Chemical* **2006**, *113*, 249-258.
- [13] Holst, G.A.; Köster, T.; Voges, E.; Lübbers, D.W. *Sensors and Actuators: B. Chemical* **1995**, *29*, 231-239.
- [14] O'Keefe, G.; MacCraith, B.D.; McEvoy, A.K.; McDonagh, C.M.; McGilp, J.F. *Sensors and Actuators: B. Chemical* **1995**, *29*, 226-230.
- [15] Masciotti, J.M.; Lasker, J.M.; Hielscher, A.H. *IEEE Transactions on Instrumentation and Measurement* **2008**, *57*, 182-189.
- [16] Langer, P.; Müller, R.; Drost, S.; Werner, T. *Sensors and Actuators, B: Chemical* **2002**, *82*, 1-6.
- [17] Sedra, A.; Smith, K.C. *Microelectronic Circuits*, 6 ed.; Oxford University Press: London, U.K., 2009.
- [18] Marín-Suárez del Toro, M.; Fernández-Sánchez, J.F.; Baranoff, E.; Nazeeruddin, M.K.; Graetzel, M.; Fernández-Gutiérrez, A. *Talanta* **2010**, *82*, 620-626.
- [19] Gao, F.G.; Fay, J.M.; Mathew, G.; Jeevarajan, A.S.; Anderson, M.M. *Journal of Biomedical Optics* **2005**, *10*, 0540051-0540056.

- [20] Philip, J.; Carlsson, K. *Journal of the Optical Society of America A* **2003**, *20*, 368-379.
- [21] Lakowicz, J.R.; Gryczynski, I.; Gryczynski, Z.; Johnson, M.L. *Analytical Biochemistry* **2000**, *277*, 74-85.
- [22] Jinayim, T.; Arunrungrasmi, S.; Tanitteerapan, T.; Mungkung, N. *International Journal of Electrical and Electronics Engineering* **2007**, *22*, 132-137.
- [23] Jenkins, D.M.; Zhu, C.; Su, W.W. *Applied Engineering in Agriculture* **2008**, *24*, 259-263.
- [24] Li Tan, J.J. *Fundamentals of Analog and Digital Signal Processing*, 2 ed.; AuthorHouse, 2008.
- [25] Ogurtsov, V. I.; Papkovsky, D. B. *Sensors and Actuators B: Chemical* **1998**, *51*, 377-381.
- [26] Sainz-Gonzalo, F.J.; Elosua, C.; Fernández-Sánchez, J.F.; Popovici, C.; Fernández, I.; Ortiz, F.L.; Arregui, F.J.; Matías, I.R.; Fernández-Gutiérrez, A. *Sensors and Actuators B: Chemical* **2012**, *173*, 254-261.
- [27] Elosua, C.; Barriain, C.; Matías, I.; Rodríguez, A.; Colacio, E.; Salinas-Castillo, A.; Segura-Carretero, A.; Fernández-Gutiérrez, A. *Sensors* **2008**, *8*, 847-859.
- [28] Elosua, C.; Arregui, F.J.; Zamarreño, C.R.; Barriain, C.; Luquin, A.; Laguna, M.; Matías, I.R. *Sensors and Actuators B: Chemical* **2012**, *173*, 523-529.
- [29] Schubert, E.F. *Light Emitting Diodes* 2ed.; Cambridge University Press, 2006.
- [30] Demas, J.N.; DeGraff, B.A. *Sensors and Actuators B: Chemical* **1993**, *11*, 35-41.

Appendix A. Supplementary data Electronic Supporting Information (ESI)

A novel multifrequency phase-modulation method using rectangular-wave signals for improving the analytical sensitivity in luminescence spectroscopy

Santiago Medina Rodríguez^{a,b,*}, Ángel de la Torre Vega^a, Francisco J. Sainz Gonzalo^b, Marta Marín Suárez^b, César Elosúa Aguado^c, Francisco J. Arregui^c, Ignacio R. Matías^c, Jorge F. Fernández Sánchez^{b,*} and Alberto Fernández Gutiérrez^b

^a*Department of Signal Theory, Networking and Communications, CITIC-UGR, University of Granada, C/ Periodista Rafael Gómez 2, E-18071 Granada, Spain.*

^b*Department of Analytical Chemistry, Faculty of Sciences, University of Granada, Avda. Fuentenueva s/n, E-18071 Granada, Spain.*

^c*Department of Electrical and Electronic Engineering, Arrosadia Campus, Public University of Navarre, Edificio "Los Tejos", E-31006 Pamplona, Spain.*

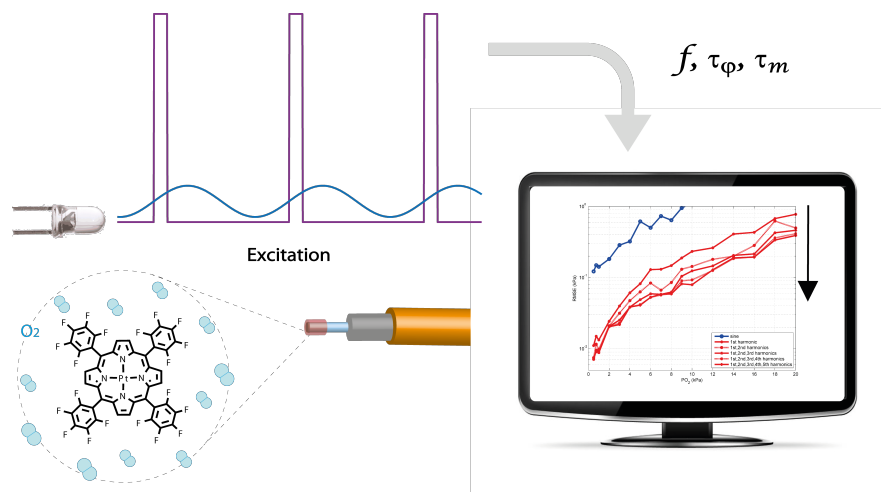
Table of Contents

- A. Estimation of the phase-shift based lifetime and the modulation based lifetime.
- B. Procedure for combining several statistically independent measurements.
 - B.1. Definition of the problem.
 - B.2. Joint probability distribution of x .
 - B.3. Combining two measurements.
 - B.4. Combining three measurements.
 - B.5. Combining N measurements.
 - B.6. Combining N measurements for the estimation of the quencher concentration.
- C. Oxygen measurement system.
- D. Complementary figures.
 - Fig. ESI-2. Optical fibre used.
 - Fig. ESI-3. Deposition of the sensing film on the optical fibre.
 - Fig. ESI-4. Examples of the excitation signals used in this work.

- Fig. ESI-5. Examples of real signals recorded with the oscilloscope.
- Fig. ESI-6. Phase-shift and modulation factor vs frequency.
- Fig. ESI-7. Calibration curves.
- Fig. ESI-8. LED driver circuit designed.
- Fig. ESI-9. Photographs of the optical fibre oxygen sensor.
- Fig. ESI-10. Photograph of the three-stage passive-RC low-pass filter.

E. Complementary tables.

- Table SI-1 to Table SI-4. Calibration data.
- Table SI-5 to Table SI-6. Parameters of the fitting models.
- Table SI-7 to Table SI-9. RMSE in the determination of the oxygen concentration.



Graphical abstract of the manuscript.

A. Estimation of the phase-shift based lifetime and the modulation based lifetime

Luminescence from a mono-exponential luminophore using an intensity modulated excitation at a frequency f presents a luminescence phase-shift $\varphi(f)$ and intensity $I(f)$ described by¹:

$$\varphi(f) = -\arctan(2\pi f\tau_q) \quad (\text{Equation SI-1})$$

$$I(f) = I_0 \frac{\tau_q}{\tau_0} \frac{1}{\sqrt{1 + (2\pi f\tau_q)^2}} \quad (\text{Equation SI-2})$$

where τ_0 is the luminescence lifetime of the luminophore at null quencher concentration, I_0 is the luminescence intensity at null concentration and low frequency (assuming constant excitation intensity at all frequencies), and τ_q is the luminescence lifetime of the luminophore in the presence of the quencher, described by:

$$\tau_q = \frac{\tau_0}{1 + k[Q]} \quad (\text{Equation SI-3})$$

where $[Q]$ is the quencher concentration and k is the Stern-Volmer constant.

From equation (SI-1), the phase-shift based lifetime can be estimated at frequency f as:

$$\tau_\varphi = \frac{\tan(-\varphi(f))}{2\pi f} \quad (\text{Equation SI-4})$$

Similarly, from equation (SI-2), the modulation based lifetime can be derived. In the general case in which the excitation intensity varies across frequencies, equation (SI-2) can be rewritten as:

$$I(f) = I_{exc}(f)M_0 \frac{\tau_q}{\tau_0} \frac{1}{\sqrt{1 + (2\pi f\tau_q)^2}} \quad (\text{Equation SI-5})$$

where $I_{exc}(f)$ is the excitation intensity at frequency f and M_0 is the modulation factor (i.e. ratio between luminescence intensity and excitation intensity) at low frequency and null concentration. Therefore, the modulation factor at frequency f is:

$$m(f) = \frac{I(f)}{I_{exc}(f)} = M_0 \frac{\tau_q}{\tau_0} \frac{1}{\sqrt{1 + (2\pi f\tau_q)^2}} \quad (\text{Equation SI-6})$$

The modulation factor estimated at frequency f for null concentration is therefore:

$$m_0(f) = M_0 \frac{1}{\sqrt{1 + (2\pi f\tau_0)^2}} \quad (\text{Equation SI-7})$$

¹V.I. Ogurtsov and D.B. Papkovsky. Sensors and Actuators B: Chemical 51 (1998) 377-381.

and then, the ratio $m(f)/m_0(f)$ can be written as:

$$\frac{m(f)}{m_0(f)} = \frac{\tau_q \sqrt{1 + (2\pi f \tau_0)^2}}{\tau_0 \sqrt{1 + (2\pi f \tau_q)^2}} \quad (\text{Equation SI-8})$$

Using the following definitions,

$$x \equiv \frac{\tau_q}{\tau_0} \quad A \equiv \frac{m(f)}{m_0(f)} \quad B \equiv \sqrt{1 + (2\pi f \tau_0)^2} \quad C \equiv (2\pi f \tau_0)^2 \quad (\text{Equation SI-9})$$

the equation (SI-8) can be rewritten as:

$$A = x \frac{B}{\sqrt{1 + Cx^2}} \quad (\text{Equation SI-10})$$

or, equivalently:

$$A^2 (1 + Cx^2) = B^2 x^2 \quad (\text{Equation SI-11})$$

which is a 1st degree equation in x^2 that can be easily resolved:

$$x = \frac{A}{\sqrt{B^2 - A^2 C}} \quad (\text{Equation SI-12})$$

and taking into account the previous definitions, the lifetime τ_q (which will be referred to as modulation based lifetime estimated at frequency f , denoted with $\tau_m(f)$) can be estimated as:

$$\tau_m(f) = \tau_0 \frac{m(f)/m_0(f)}{\sqrt{1 + (2\pi f \tau_0)^2 - (2\pi f \tau_0 m(f)/m_0(f))^2}} \quad (\text{Equation SI-13})$$

or equivalently as:

$$\tau_m(f) = \tau_0 \frac{m(f)/m_0(f)}{\sqrt{1 + (2\pi f \tau_0)^2 (1 - (m(f)/m_0(f))^2)}} \quad (\text{Equation SI-14})$$

that is, the lifetime can be estimated with this formula using the modulation factor $m(f)$ at frequency f , the modulation factor for null concentration at this frequency $m_0(f)$ and the lifetime at null concentration τ_0 . The reference parameters τ_0 and $m_0(f)$ should be estimated during the calibration procedure.

Under the assumption of a mono-exponential behavior of the luminescence system, given a concentration $[Q]$ and the corresponding lifetime τ_q , the lifetimes estimated from the phase-shift ($\tau_\varphi(f)$) and from the modulation factor ($\tau_m(f)$) at different modulation frequencies should be equal. However, since this assumption is just a first approach to the behavior of the luminophore, these estimations of the lifetime are not guaranteed to be the same, and they should be referred to as “apparent lifetimes”.

B. Procedure for combining several statistically independent measurements

In this section we present a mathematical derivation describing a procedure for combining several statistically independent measurements into one more robust final measurement.

B.1. Definition of the problem

Let us suppose that we want to estimate an unknown value x from a set of N unbiased statistically independent measurements $\{x_1, x_2, \dots, x_N\}$, each one affected by a standard error $SE(x_n)$ (assuming a general case where the standard errors are not equal). In the case that only the n^{th} measurement is available, if x_n is assumed to be a random process following a normal distribution with mean x (unknown) and standard deviation $SE(x_n)$, the unknown value can be estimated from the measurement x_n as:

$$\hat{x} = x_n \quad (\text{Equation SI-15})$$

and the standard error associated to this estimate would be:

$$SE(\hat{x}) = SE(x_n) \quad (\text{Equation SI-16})$$

Therefore, in the case of just one available measurement, the computation of the expected value and the standard error are evident. The problem of optimally combining the information provided by N statistically independent measurements can be formulated in the following terms:

Given N independent measurements $\{x_1, x_2, \dots, x_N\}$ and their corresponding standard errors $\{SE(x_1), SE(x_2), \dots, SE(x_N)\}$, what is the optimal estimation \hat{x} and the corresponding standard error $SE(\hat{x})$?

Or equivalently:

What are the expressions providing \hat{x} and $SE(\hat{x})$ as a function of $\{x_1, x_2, \dots, x_N\}$ and $\{SE(x_1), SE(x_2), \dots, SE(x_N)\}$?

B.2. Joint probability distribution of x

In the case that only the n^{th} measurement is available, and assumed that x_n follows a normal distribution with mean x and standard deviation $SE(x_n)$, we can describe the probability distribution of x given the observed measurement x_n as:

$$p(x|x_n, SE(x_n)) = \frac{1}{2\pi\sigma_n} \exp\left(-\frac{(x - x_n)^2}{2\sigma_n^2}\right) \quad (\text{Equation SI-17})$$

where σ_n^2 is the variance of the distribution and can be assumed to be $\sigma_n^2 = (SE(x_n))^2$. From this probability distribution, the expected value of x and the corresponding standard error can be easily obtained:

$$\hat{x} = E[x] = \int_{-\infty}^{+\infty} x p(x|x_n, SE(x_n)) dx = x_n \quad (\text{Equation SI-18})$$

$$SE(\hat{x}) = \sqrt{E[(x - \hat{x})^2]} = \sqrt{\int_{-\infty}^{+\infty} (x - \hat{x})^2 p(x|x_n, SE(x_n)) dx} = \sqrt{\sigma_n^2} = SE(x_n) \quad (\text{Equation SI-19})$$

where $E[\cdot]$ denotes expected value. Therefore, the expected value of x and the standard error can be estimated as the mean and the standard deviation of the probability distribution $p(x|x_n, SE(x_n))$.

In the case that 2 statistically independent measurements are available, x_m and x_n , the joint probability distribution would be $p(x|x_m, SE(x_m), x_n, SE(x_n))$. This probability could be obtained by applying the Bayes rule to derive $p(x|A, B)$ in the case of statistical independence of A and B :

$$\begin{aligned} p(x|A, B) &= \frac{p(A, B|x) p(x)}{p(A, B)} = \frac{p(A|x) P(B|x) p(x)}{p(A) p(B)} = \\ &= \frac{p(A|x) p(x)}{p(A)} \frac{p(B|x) p(x)}{p(B)} \frac{1}{p(x)} = p(x|A) p(x|B) \frac{1}{p(x)} \end{aligned} \quad (\text{Equation SI-20})$$

Therefore, taking into account the previous equation, the joint probability distribution of x given two independent measurements, x_m and x_n , would be:

$$p(x|x_m, SE(x_m), x_n, SE(x_n)) = p(x|x_m, SE(x_m)) p(x|x_n, SE(x_n)) \frac{1}{p(x)} \quad (\text{Equation SI-21})$$

Finally, in the case that N statistically independent measurements $\{x_1, x_2, \dots, x_N\}$ are available, the joint probability distribution of x is:

$$p(x|x_1, SE(x_1), x_2, SE(x_2), \dots, x_N, SE(x_N)) = K \prod_{n=1}^N p(x|x_n, SE(x_n)) \quad (\text{Equation SI-22})$$

where K is a constant:

$$K = \frac{1}{(p(x))^{N-1}} \quad (\text{Equation SI-23})$$

Taking into account Equation SI-17, the joint probability distribution of x can be written as:

$$p(x|x_1, SE(x_1), x_2, SE(x_2), \dots, x_N, SE(x_N)) = K \prod_{n=1}^N \frac{1}{2\pi\sigma_n} \exp\left(-\frac{(x - x_n)^2}{2\sigma_n^2}\right) \quad (\text{Equation SI-24})$$

or, equivalently as:

$$p(x|x_1, SE(x_1), x_2, SE(x_2), \dots, x_N, SE(x_N)) = K' \exp\left(\sum_{n=1}^N -\frac{(x-x_n)^2}{2\sigma_n^2}\right) \quad (\text{Equation SI-25})$$

where we have denoted the joint probability distribution with $p(x)$ for simplicity, and the normalization constant K' is:

$$K' = \frac{1}{(p(x))^{N-1}} \prod_{n=1}^N \frac{1}{2\pi\sigma_n} \quad (\text{Equation SI-26})$$

From Equation SI-25, the expected value \hat{x} and the standard error $SE(\hat{x})$ can be estimated in order to combine the information provided by the N available measurements.

Note that the product of several Gaussian functions is also a Gaussian function (because the sum of N 2^{nd} order polynomials within the exponent is also a 2^{nd} order polynomial) and the problem of combining the N measurements is reduced to the problem of estimating the mean \hat{x} and the standard deviation $\sigma_{\hat{x}}$ of the Gaussian function in Equation SI-25. In a Gaussian function with mean μ and standard deviation σ , the exponent can be expanded:

$$-\frac{(x-\mu)^2}{2\sigma^2} = -\frac{1}{2}\left(\frac{x^2}{\sigma^2} - \frac{2\mu x}{\sigma^2} + \frac{\mu^2}{\sigma^2}\right) \quad (\text{Equation SI-27})$$

and therefore, the standard deviation σ can be obtained by identifying the coefficient of x^2 in the second order polynomial in the exponent, and the mean μ by identifying the coefficient of x .

B.3. Combining two measurements

Let us consider the case of two measurements $\{x_1, x_2\}$ with their respective standard errors $\{\sigma_1, \sigma_2\}$. The combined expected value and standard error (that will be noted $x_{1,2}$ and $\sigma_{1,2}$) can be estimated by identifying terms in the 2^{nd} order polynomial in the exponent of the Gaussian probability distribution in Equation SI-25:

$$-\frac{(x-x_1)^2}{2\sigma_1^2} - \frac{(x-x_2)^2}{2\sigma_2^2} = -\frac{(x-x_{1,2})^2}{2\sigma_{1,2}^2} + C \quad (\text{Equation SI-28})$$

where C is a constant. This equation can also be written as:

$$\frac{(x-x_1)^2}{\sigma_1^2} + \frac{(x-x_2)^2}{\sigma_2^2} = \frac{(x-x_{1,2})^2}{\sigma_{1,2}^2} + C' \quad (\text{Equation SI-29})$$

and expanding the terms:

$$\frac{x^2}{\sigma_1^2} + \frac{x^2}{\sigma_2^2} - 2x\frac{x_1}{\sigma_1^2} - 2x\frac{x_2}{\sigma_2^2} + \frac{x_1^2}{\sigma_1^2} + \frac{x_2^2}{\sigma_2^2} = \frac{x^2}{\sigma_{1,2}^2} - 2x\frac{x_{1,2}}{\sigma_{1,2}^2} + \frac{x_{1,2}^2}{\sigma_{1,2}^2} + C' \quad (\text{Equation SI-30})$$

From this equation, $x_{1,2}$ and $\sigma_{1,2}$ can easily be identified:

$$\frac{1}{\sigma_1^2} + \frac{1}{\sigma_2^2} = \frac{1}{\sigma_{1,2}^2} \quad \text{and} \quad \frac{x_1}{\sigma_1^2} + \frac{x_2}{\sigma_2^2} = \frac{x_{1,2}}{\sigma_{1,2}^2} \quad (\text{Equation SI-31})$$

and finally, $x_{1,2}$ and $\sigma_{1,2}$ are:

$$\sigma_{1,2}^2 = \frac{\sigma_1^2 \sigma_2^2}{\sigma_1^2 + \sigma_2^2} = \left(\frac{1}{\sigma_1^2} + \frac{1}{\sigma_2^2} \right)^{-1} \quad \text{and} \quad x_{1,2} = \frac{\sigma_2^2 x_1 + \sigma_1^2 x_2}{\sigma_2^2 + \sigma_1^2} \quad (\text{Equation SI-32})$$

i.e., the resulting expected value $x_{1,2}$ is a weighted average of the measurements (weighted according to the standard errors of the measurements) and the resulting standard error $\sigma_{1,2}$ is a combination of the standard errors of the measurements.

B.4. Combining three measurements

In the case of three measurements $\{x_1, x_2, x_3\}$ with their respective standard errors, $\{\sigma_1, \sigma_2, \sigma_3\}$, a similar derivation would be performed to obtain $x_{1,2,3}$ and $\sigma_{1,2,3}$. However, since adding a new measurement implies adding a new term in the exponent of the resulting Gaussian distribution, and since addition is an associative operation, we can write:

$$\sigma_{1,2,3}^2 = \left(\frac{1}{\sigma_{1,2}^2} + \frac{1}{\sigma_3^2} \right)^{-1} = \left(\frac{1}{\sigma_1^2} + \frac{1}{\sigma_2^2} + \frac{1}{\sigma_3^2} \right)^{-1} \quad (\text{Equation SI-33})$$

and:

$$x_{1,2,3} = \frac{\sigma_3^2 x_{1,2} + \sigma_{1,2}^2 x_3}{\sigma_3^2 + \sigma_{1,2}^2} = \frac{\sigma_2^2 \sigma_3^2 x_1 + \sigma_1^2 \sigma_3^2 x_2 + \sigma_1^2 \sigma_2^2 x_3}{\sigma_2^2 \sigma_3^2 + \sigma_1^2 \sigma_3^2 + \sigma_1^2 \sigma_2^2} \quad (\text{Equation SI-34})$$

which provides again the expected value as a weighted average of the measurements and the standard error as a combination of the standard errors of the measurements.

B.5. Combining N measurements

In the most general case with N statistically independent measurements $\{x_1, x_2, \dots, x_N\}$ and their corresponding standard errors $\{\sigma_1, \sigma_2, \dots, \sigma_N\}$, the expected value \hat{x} and the corresponding standard error $\sigma_{\hat{x}}$ are:

$$\sigma_{\hat{x}}^2 = \left(\sum_{n=1}^N \frac{1}{\sigma_n^2} \right)^{-1} \quad SE(\hat{x}) = \sqrt{\sigma_{\hat{x}}^2} \quad \hat{x} = \frac{\sum_{n=1}^N x_n \prod_{k \neq n} \sigma_k^2}{\sum_{n=1}^N \prod_{k \neq n} \sigma_k^2} \quad (\text{Equation SI-35})$$

which can be proven by mathematical induction.

This way, if a value is estimated with N independent unbiased measurements (each one with its corresponding standard error), the previous results provide the expected value and

the standard error resulting from the combination of the measurements. It should be noted that the expected value is a weighted average of all the measurements. It should also be noted that the standard error is always smaller than each of the standard errors involved in the measurements.

As could be expected, in the case when there is a dominant measurement (its standard error is significantly smaller than those of the other measurements, *i.e.* $\sigma_m \ll \sigma_n \forall n \neq m$), the resulting expected value and standard error would be:

$$\hat{x} \approx x_m \quad \sigma_{\hat{x}} \approx \sigma_m \quad (\text{Equation SI-36})$$

Analogously, if the standard error is the same for all the measurements (*i.e.* $\sigma_n = \sigma \forall n$), the resulting expected value and standard deviations would be:

$$\hat{x} = \frac{1}{N} \sum_{n=1}^N x_n \quad \sigma_{\hat{x}}^2 = \frac{\sigma^2}{N} \Rightarrow \sigma_{\hat{x}} = \frac{\sigma}{\sqrt{N}} \quad (\text{Equation SI-37})$$

From Equation SI-35 one can observe that if standard errors are scaled (with the same constant for all the measurements) the resulting expected value is not affected, and the resulting standard error is affected by the same constant. Therefore, in order to appropriately combine N measurements, we do not need the standard error for each measurement, but the relative standard errors (*i.e.* the standard errors relative to one of them). This could ease the problem of estimating the standard errors in practical situations.

B.6. Combining N measurements for the estimation of the quencher concentration

In this work, the apparent luminescence lifetimes based on phase-shift and modulation factor have been determined (for the only available harmonic in the case of sinusoidal excitation signals and for several harmonics in the case of rectangular-wave excitation signals). From each of these parameters (x_i), the quencher concentration $\tilde{C}(x_i)$ has been measured using the corresponding calibration curve, and the standard error σ_i can also be estimated for each concentration measurement. Assuming that the measurements are unbiased and statistically independent, N of these measurements can be combined, according to the results presented in this section, as:

$$\hat{C} = \frac{\sum_{n=1}^N \tilde{C}(x_n) \prod_{k \neq n} \sigma_k^2}{\sum_{n=1}^N \prod_{k \neq n} \sigma_k^2} \quad (\text{Equation SI-38})$$

providing a more robust determination of the quencher concentration as the expected value of the concentration given the join probability distribution.

C. Oxygen measurement system

Figure SI-1 displays the schematic diagram of the experimental setup used in this work. All the setup was controlled from a PC using an ad hoc computer program developed in LabView 8.5 and MATLAB 7.10.

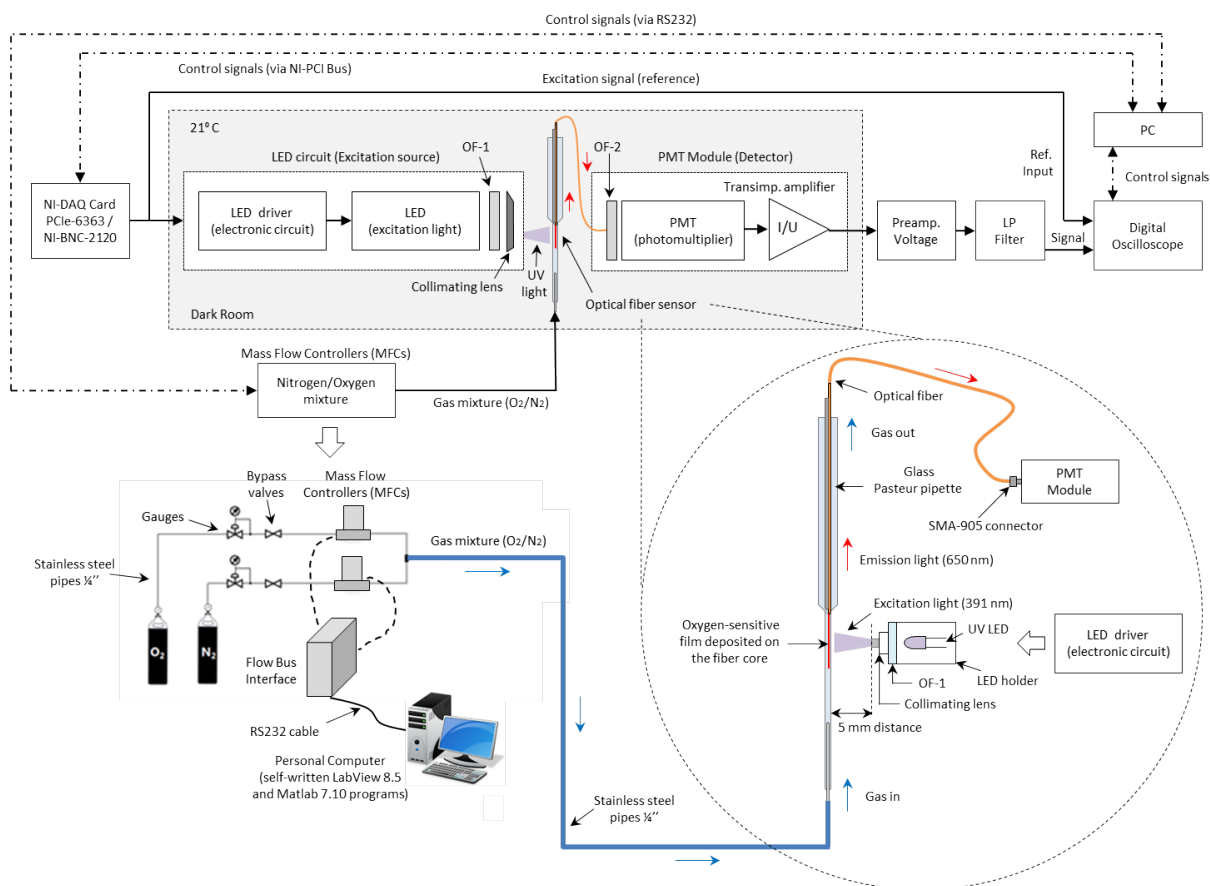


Figure SI-1. Schematic diagram of the designed experimental setup for phase-shift/modulation measurements with the optical fibre sensor.

To mix nitrogen and oxygen (both all of 99.999% purity, obtained from Air Liquide España, Spain) two mass-flow controllers (MFCs) (EL-FLOW Select F-201CV, Bronkhorst High-Tech, Ruurlo, Netherlands) connected to a Flow-Bus Interface (Bronkhorst High-Tech, Netherlands) via a RS-232 serial port were used. The MFCs were connected, using copper and stainless steel tubing, to the flow-through cell, which was designed in our laboratory using a standard glass tube (230 mm in length) to hold the optical fibre probe. A Photomultiplier Tube (PMT) module (Bandwidth DC-1 MHz, H10723-20, Hamamatsu Photonics, Japan) equipped with an optical bandpass filter (OF-2) (Hamamatsu Photonics, A10033-03, $\lambda_{central} = 630$ nm, FWHM = 60 nm) and an analog amplification and filtering system were used as detector system. Both the flow cell and the PMT were housed in a dark room (XE25C1, Thorlabs GmbH) to prevent interference from stray light.

The PtTFPP-coating optical fibre probe was excited with an ultraviolet LED (Ocean Optics, LS-450 LED-395, $\lambda_{max} = 391$ nm, angle of illumination 15° , LED diameter 5 mm, luminous power $25 \mu\text{W}$) filtered through an optical bandpass filter (OF-1; Thorlabs GmbH, MF390-18, $\lambda_{central} = 390$ nm). This LED was modulated using two different analog current signals: (1) a sine-wave signal of 5145 Hz, and (2) a rectangular-wave signal (with 10% duty cycle) of 1715 Hz. Two identical numerically-generated digital signals were extracted using two analog output channels on an AD/DA board (NI PCIe-6363/BNC-2120, National

Instruments, USA) at a sampling rate of 500 kS/s: one for modulating the current of the LED in the LED driving circuit and the other one was used as an external reference signal (see SI, Fig. SI-4 and Fig. SI-5 for further details). Both the excitation signal (the reference) and the emission signal from the sensing film were simultaneously digitized using a digital oscilloscope WaveRunner 604Zi (LeCroy, USA) at 500 kS/s using signals of 5 s in duration (i.e., a 2.5 MS data buffer).

The hardware components of the measurement system (AD/DA board, LED driver, PMT, voltage preamplifier, passive-RC low-pass filter, data acquisition device, etc.) introduce an additional phase-shift (i.e., instrumental bias) to the phase measurement at each working frequency. The bias was previously estimated using a red reference LED ($\lambda_{peak} = 660$ nm, angle of illumination 50° , LED diameter 5 mm, luminous intensity 2000 mcd typ./20 mA, L2-0-R5TH50, LED Supply, USA) in the same spectral range as the sensing film and at the same conditions. The estimated bias was subtracted to the experimental data to calculate the specific phase-shift introduced only by the sensing fibre.

D. Complementary figures

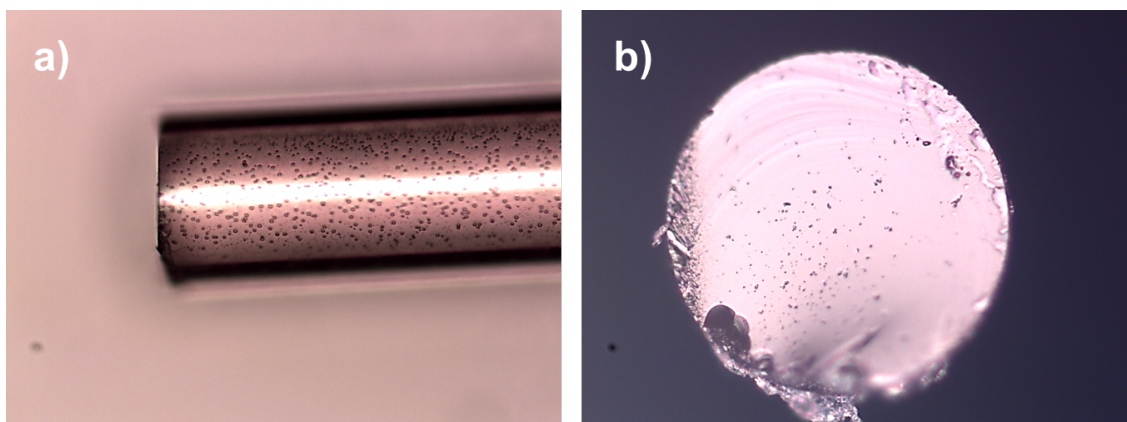


Figure SI-2. Side (a) and front (b) photographs of the optical fibre probe used in this study.

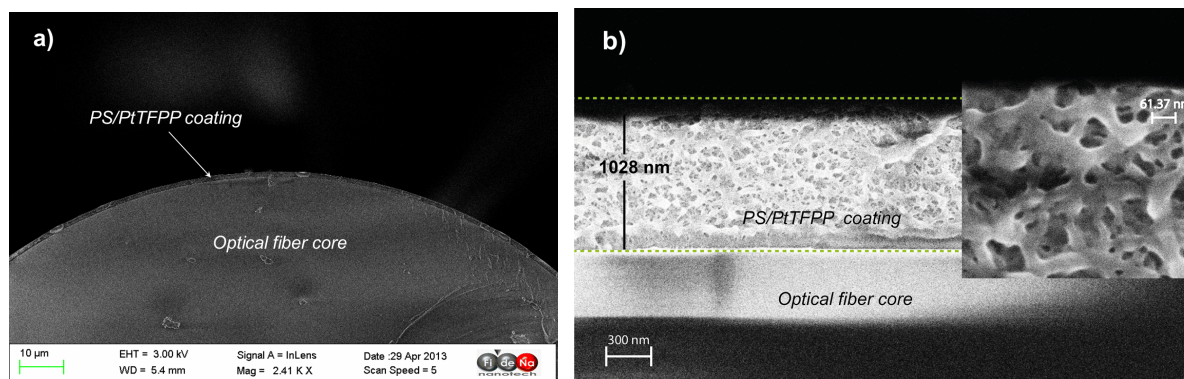


Figure SI-3. Scanning electron microscope (SEM) images of the optical fibre probe with the PS/PtTFPP layer. (a) A cross-sectional image; (b) Zoomed image of the coating. The estimated thickness of the layer was 1028 ± 123 nm (95% confidence interval).

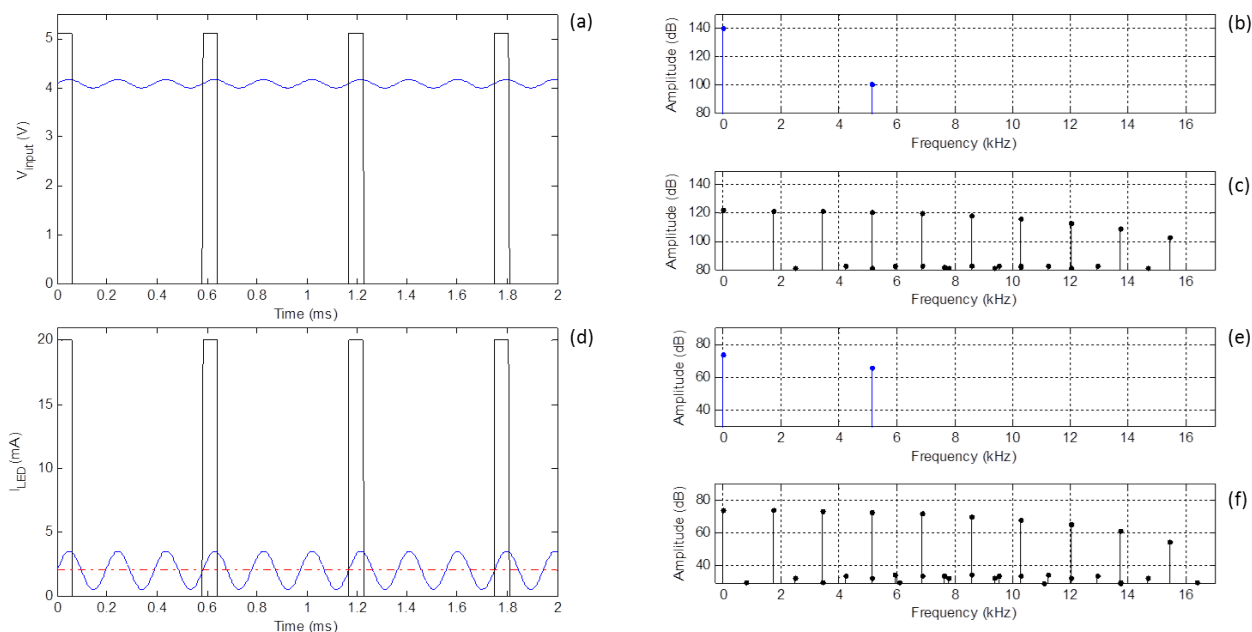


Figure SI-4. Graphical representation of the excitation signals used in this work to experimentally compare the conventional phase-modulation method based on a sinusoidally modulated excitation signal (blue line) and the proposed multifrequency phase-modulation method based on a rectangular-wave modulated excitation signal with a 10% duty cycle (black line). (a) Input voltage signals applied to the base of transistor in the LED driver circuit; (blue line) sine signal with $Amp = 0.085$ V, $dc = 4.09$ V, $freq = 5145$ Hz; (black line) rectangular signal with $Amp = 5$ V, $freq = 1715$ Hz, 10% duty cycle. (d) Current signals applied to the LED in the LED driver circuit; (blue line) sine signal with $Amp = 1.5$ mA, $dc = 2$ mA, $freq = 5145$ Hz; (black line) rectangular signal with $Amp = 20$ mA, $freq = 1715$ Hz, 10% duty cycle; (horizontal dot-dashed red line) average current level (I_{avg}) for both signals (2 mA); I_{avg} is proportional to the average LED optical output power. (b)-(c) Amplitude spectra of the input voltage signals: (b) sine, (c) rectangular. (e)-(f) Amplitude spectra of the current signals applied to the LED: (e) sine, (f) rectangular.

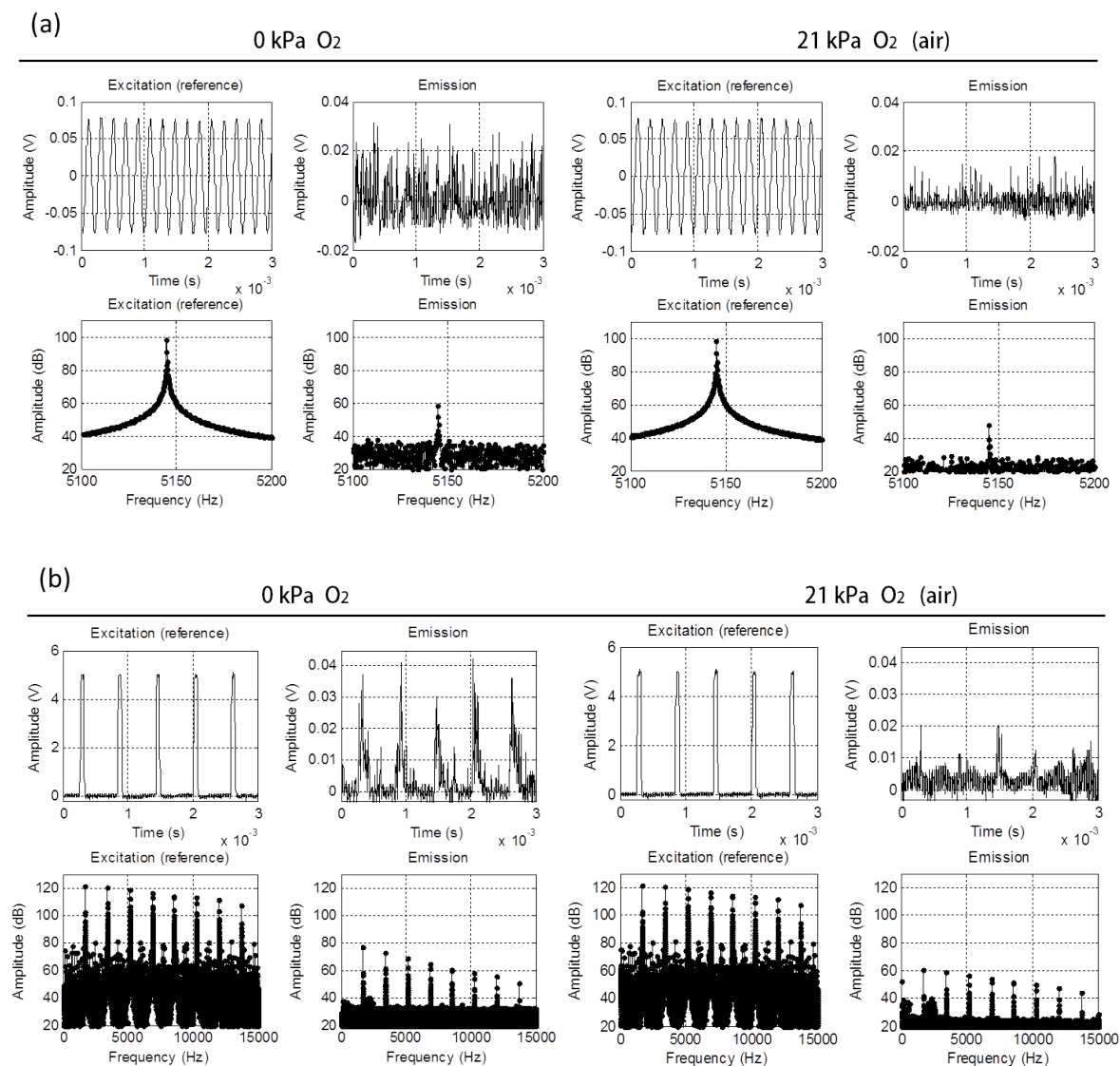


Figure SI-5. Waveforms and amplitude spectra of a pair of analog signals (excitation and emission) when the sensing film was exposed to O₂ atmospheres of 0 and 21 kPa (balance N₂): (a) a sine-wave excitation signal; (b) a rectangular-wave excitation signal with a 10% duty cycle. All signals were of 5 s in duration and were recorded with the digital oscilloscope at a rate of 500 kS/s.

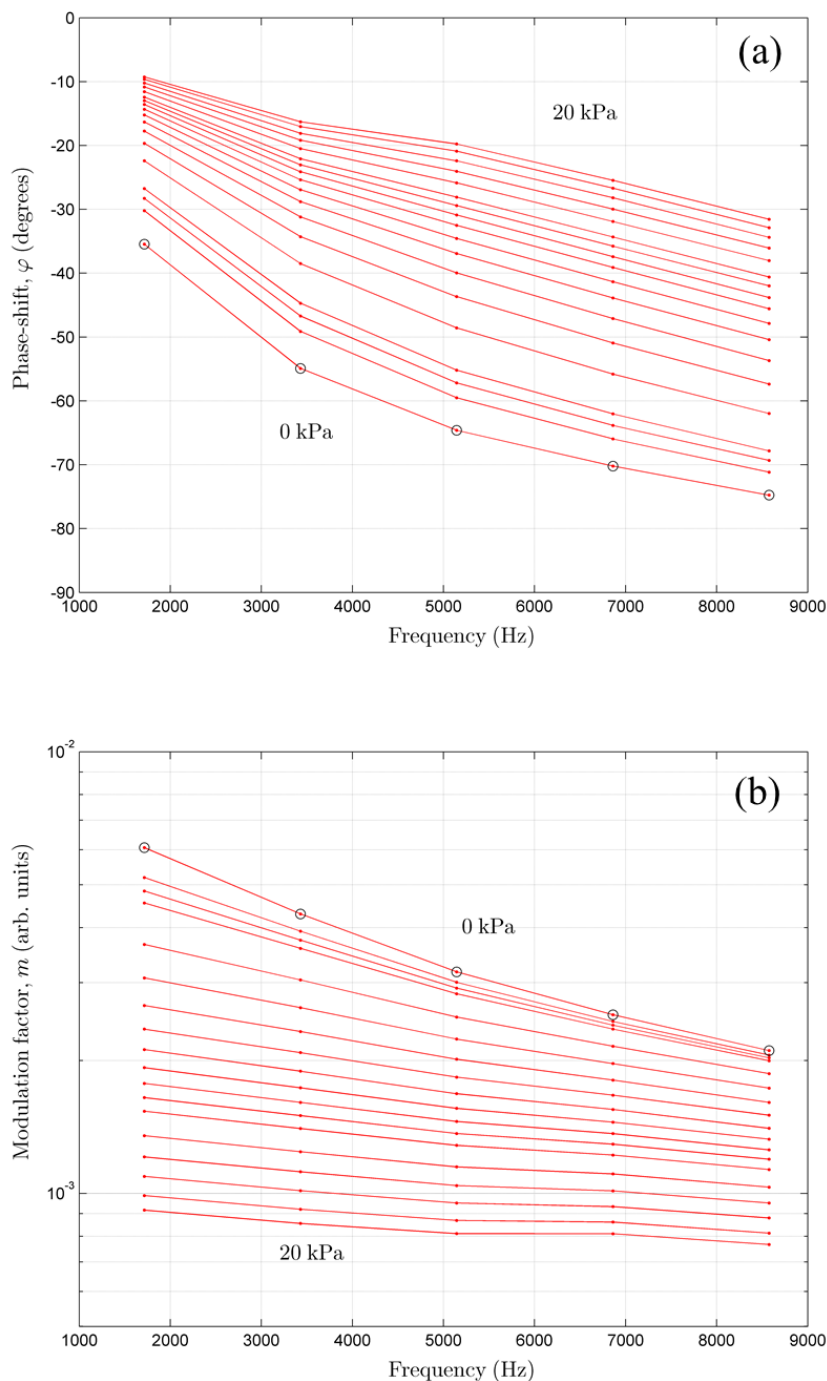


Figure SI-6. Variation of the (a) phase-shift and (b) modulation factor^(*) with the modulation frequency at different oxygen concentrations (0, 0.5, 0.75, 1, 2, 3, 4, 5, 6, 7, 8, 9, 10, 12, 14, 16, 18 and 20 kPa O_2).

^(*) Modulation factors are estimated from the measurements at both channels of the digital oscilloscope. The amplitude of the excitation signal is expressed in volts and the emission signal is also expressed in volts after transduction in the Photomultiplier Tube (PMT) and preamplification. So, modulation factor is expressed in V/V, even though the values would be scaled depending in the configuration of the PMT and the preamplifier. For this reason, the modulation factor is expressed in arbitrary units.

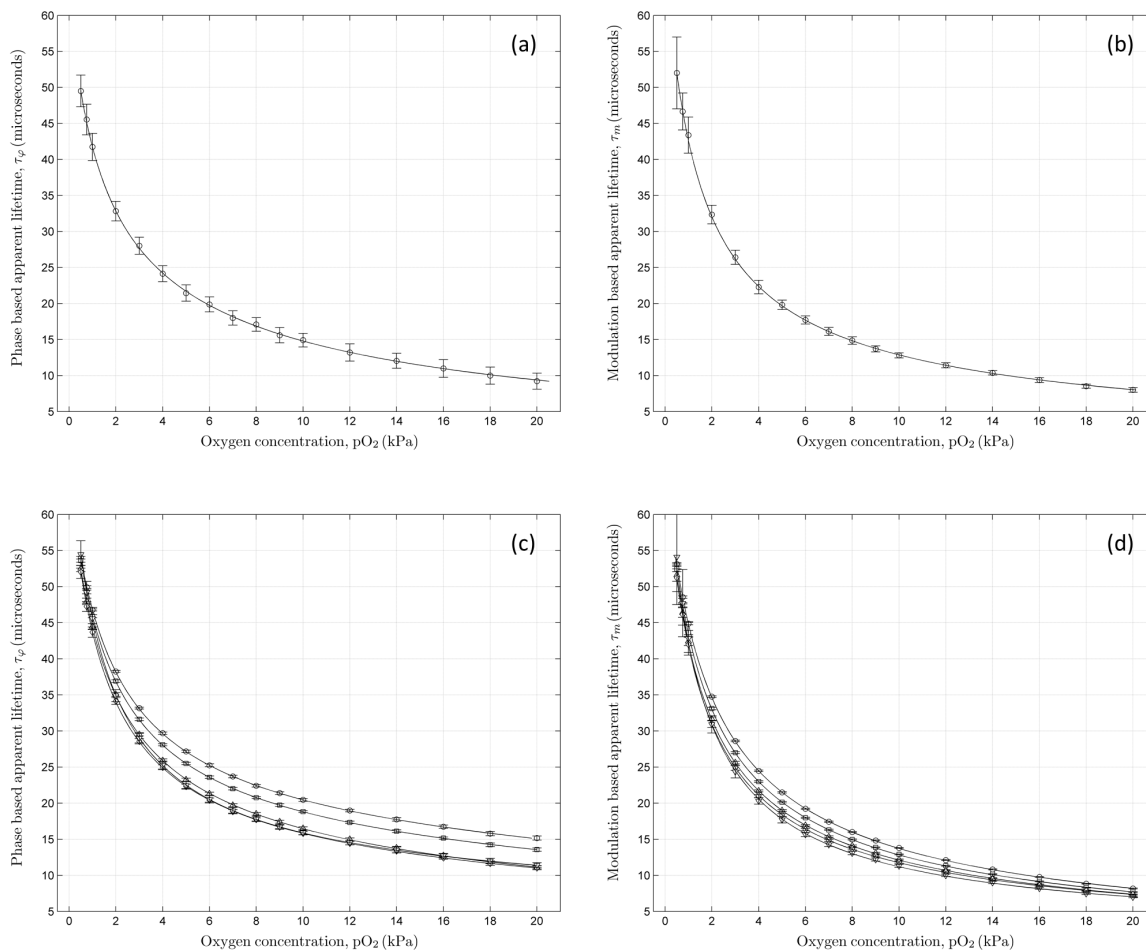


Figure SI-7. Calibration curves for the apparent lifetimes based on phase-shift and modulation factor of the sensing fibre using the conventional phase-modulation method based on a sine-wave modulated excitation at 5145 Hz (a and b), and the proposed multifrequency phase-modulation method based on a rectangular-wave modulated excitation with a 10% duty cycle (c and d) for the first 5 harmonics: 1st harmonic: 1715 Hz (○); 2nd: 3430 Hz (□); 3rd: 5145 Hz (△); 4th: 6860 Hz (◇); 5th: 8575 Hz (▽). Each point represents the average value of 25 measurements with its standard error.

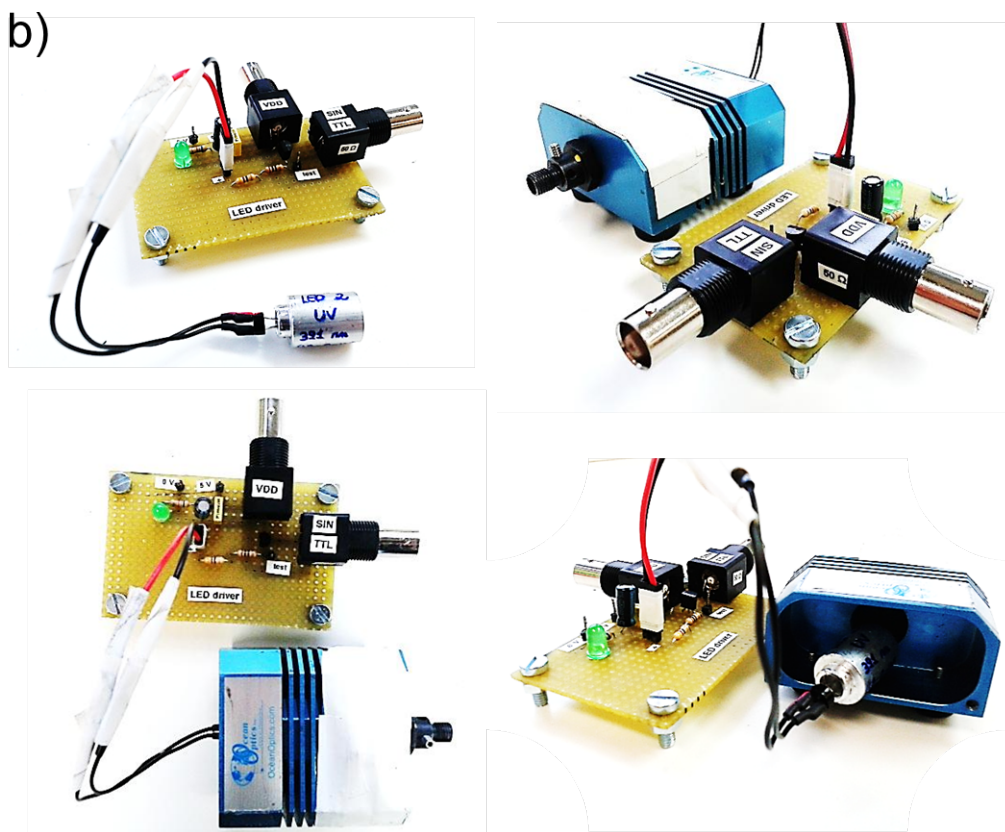
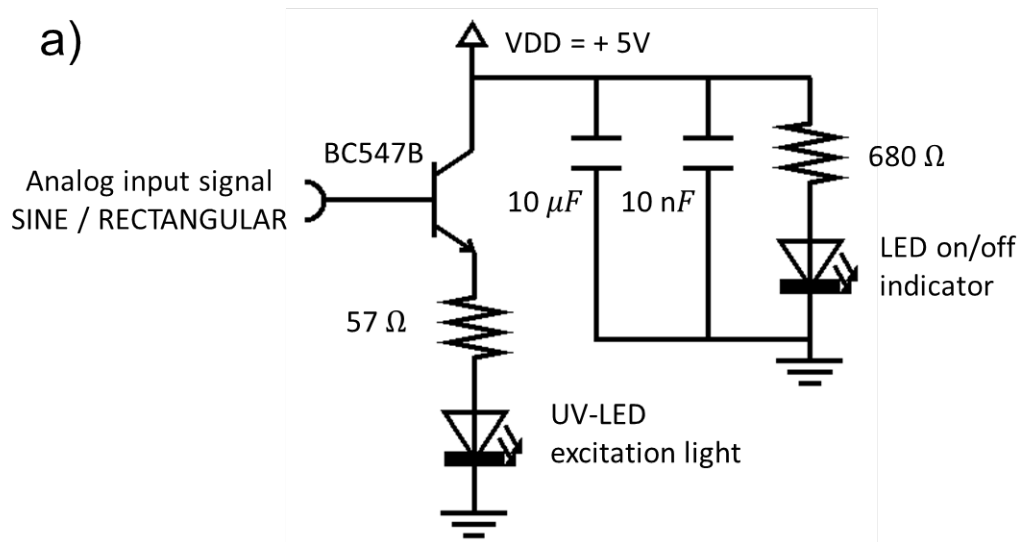


Figure SI-8. LED driver circuit designed to modulate the current of the LED light source in the proposed optical fibre oxygen sensor. (a) Schematic diagram; (b) Photographs from different angles.

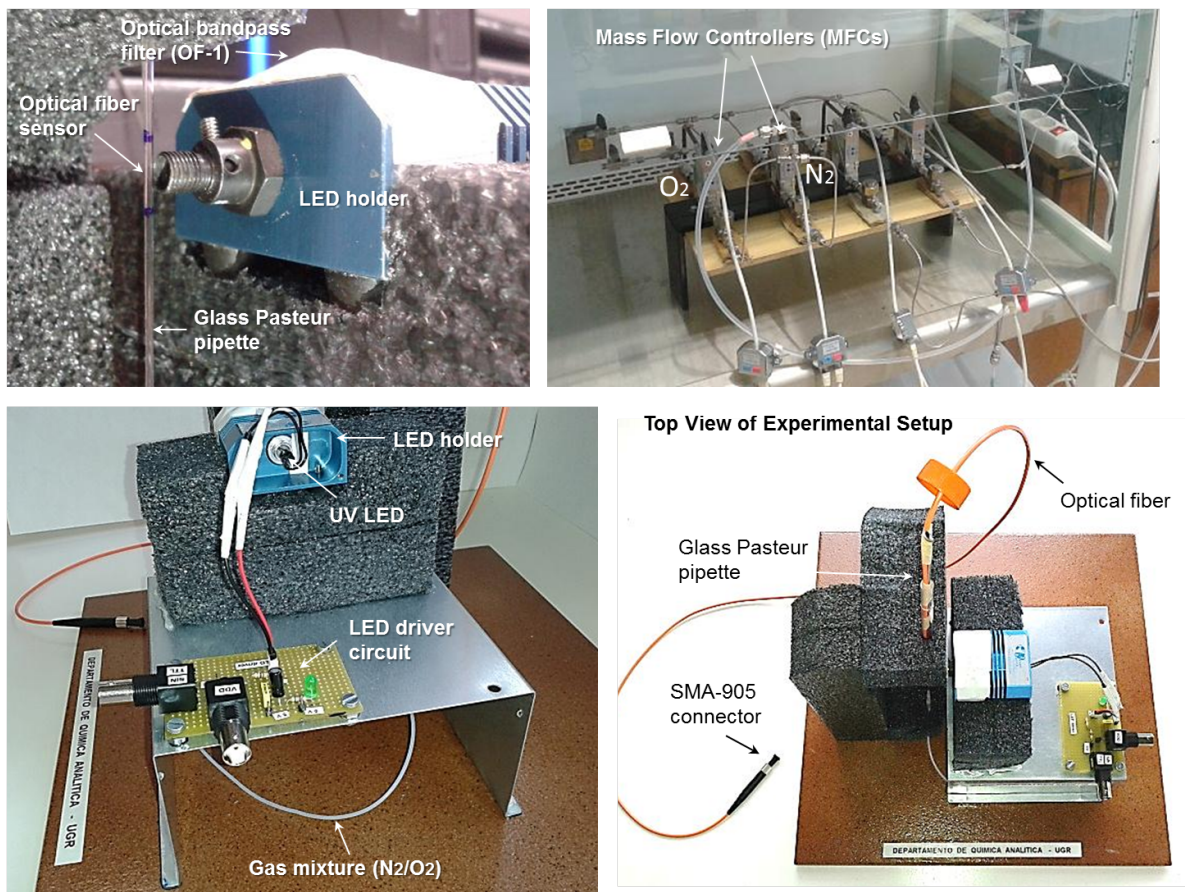


Figure SI-9. Photographs of the different elements that assemble the experimental setup for the optical fibre oxygen sensor described in Figure SI-1.

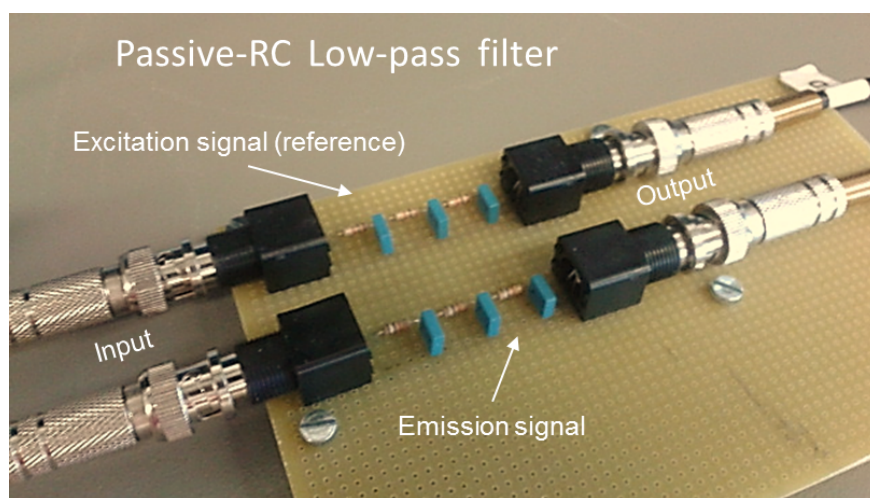


Figure SI-10. Photograph of the three-stage passive-RC low-pass filter (with cut-off frequency of 159 kHz in all stages) designed to filter the excitation and emission signals before the acquisition process. The values of the passive components of the filter were $R=1\text{ k}\Omega$ and $C=1\text{ nF}$.

E. Complementary tables

Table SI-1. Phase-shift and modulation factor for several oxygen concentrations using the conventional phase-modulation method based on a sinusoidally modulated excitation signal at a modulation frequency of 5145 Hz. All the values correspond to the average of 25 measurements.

pO_2 (kPa)	Phase-shift (φ)		Modulation factor (m)	
	Mean (degrees)	Sdev (degrees)	Mean (a.u.) $\times 10^{-3}$	Sdev (a.u.) $\times 10^{-3}$
0.00	63.31	1.26	10.797	0.241
0.50	57.96	1.15	10.362	0.249
0.75	55.78	1.24	10.065	0.172
1.00	53.42	1.24	9.829	0.192
2.00	46.67	1.18	8.729	0.167
3.00	42.14	1.20	7.843	0.168
4.00	37.93	1.27	7.060	0.196
5.00	34.71	1.41	6.516	0.153
6.00	32.70	1.36	6.005	0.143
7.00	30.16	1.37	5.582	0.152
8.00	28.90	1.33	5.233	0.148
9.00	26.74	1.56	4.892	0.128
10.00	25.73	1.43	4.619	0.108
12.00	23.09	1.88	4.184	0.114
14.00	21.25	1.66	3.841	0.102
16.00	19.51	2.01	3.503	0.111
18.00	17.86	1.98	3.206	0.100
20.00	16.58	1.91	3.025	0.118

Table SI-2. Apparent lifetimes based on phase-shift and modulation factor (calibration data) for several oxygen concentrations using the conventional phase-modulation method based on a sinusoidally modulated excitation signal at a modulation frequency of 5145 Hz. All the values correspond to the average of 25 measurements.

pO_2 (kPa)	Phase based apparent lifetime (τ_φ)		Modulation based apparent lifetime (τ_m)	
	Mean (μs)	Sdev (μs)	Mean (μs)	Sdev (μs)
0.00	61.68	3.35	61.80	1.38
0.50	49.51	2.20	52.01	4.99
0.75	45.54	2.13	46.66	2.57
1.00	41.74	1.88	43.37	2.51
2.00	32.82	1.36	32.34	1.30
3.00	28.01	1.18	26.40	0.98
4.00	24.13	1.11	22.28	0.93
5.00	21.45	1.13	19.81	0.65
6.00	19.87	1.04	17.71	0.56
7.00	17.99	0.99	16.11	0.56
8.00	17.09	0.94	14.86	0.52
9.00	15.60	1.06	13.69	0.43
10.00	14.92	0.95	12.79	0.35
12.00	13.20	1.20	11.41	0.35
14.00	12.04	1.04	10.37	0.30
16.00	10.98	1.23	9.37	0.32
18.00	9.98	1.19	8.51	0.29
20.00	9.22	1.12	8.00	0.33

Table SI-3. Phase-shift and modulation factor for several oxygen concentrations at the 5 first harmonics using the proposed multifrequency phase-modulation method. All the values correspond to the average of 25 measurements.

Phase-shift (φ) (mean and standard deviation expressed in degrees)										
# harmonic	(1 st) 1715 Hz		(2 nd) 3430 Hz		(3 rd) 5145 Hz		(4 st) 6860 Hz		(5 st) 8575 Hz	
pO_2 (kPa)	Mean	Sdev	Mean	Sdev	Mean	Sdev	Mean	Sdev	Mean	Sdev
0.00	35.465	0.080	54.913	0.133	64.606	0.225	70.209	0.395	74.760	0.823
0.50	30.200	0.083	49.118	0.122	59.500	0.204	65.963	0.356	71.161	0.613
0.75	28.280	0.087	46.710	0.150	57.176	0.238	63.844	0.328	69.316	0.582
1.00	26.750	0.071	44.696	0.128	55.184	0.232	62.029	0.382	67.824	0.672
2.00	22.400	0.067	38.500	0.132	48.570	0.217	55.803	0.356	61.975	0.564
3.00	19.667	0.070	34.271	0.153	43.678	0.224	50.928	0.359	57.374	0.585
4.00	17.741	0.085	31.183	0.138	39.958	0.232	47.104	0.371	53.691	0.593
5.00	16.321	0.097	28.786	0.157	36.923	0.255	43.881	0.385	50.406	0.636
6.00	15.217	0.114	26.941	0.174	34.564	0.256	41.348	0.397	47.859	0.694
7.00	14.325	0.101	25.367	0.179	32.505	0.283	39.103	0.371	45.580	0.648
8.00	13.576	0.105	24.114	0.129	30.890	0.232	37.407	0.332	43.812	0.566
9.00	12.984	0.105	23.036	0.190	29.399	0.294	35.765	0.399	41.980	0.577
10.00	12.432	0.113	22.082	0.157	28.091	0.288	34.325	0.355	40.597	0.573
12.00	11.559	0.106	20.484	0.191	25.855	0.275	31.908	0.395	38.035	0.555
14.00	10.828	0.141	19.161	0.202	24.037	0.343	29.960	0.484	36.063	0.836
16.00	10.223	0.137	18.091	0.179	22.407	0.300	28.186	0.413	34.384	0.712
18.00	9.646	0.172	17.042	0.282	20.878	0.308	26.676	0.539	32.865	0.770
20.00	9.277	0.172	16.292	0.274	19.769	0.374	25.447	0.517	31.556	0.772
Modulation factor (m) (mean and standard deviation expressed in a.u. $\times 10^{-3}$)										
# harmonic	(1 st) 1715 Hz		(2 nd) 3430 Hz		(3 rd) 5145 Hz		(4 st) 6860 Hz		(5 st) 8575 Hz	
pO_2 (kPa)	Mean	Sdev	Mean	Sdev	Mean	Sdev	Mean	Sdev	Mean	Sdev
0.00	6.0673	0.0156	4.2943	0.0161	3.1752	0.0202	2.5391	0.0243	2.1060	0.0307
0.50	5.1899	0.0128	3.9234	0.0119	3.0074	0.0133	2.4518	0.0157	2.0577	0.0242
0.75	4.8406	0.0133	3.7467	0.0116	2.9175	0.0130	2.4048	0.0159	2.0280	0.0251
1.00	4.5468	0.0124	3.5890	0.0130	2.8330	0.0132	2.3560	0.0147	1.9986	0.0173
2.00	3.6627	0.0103	3.0432	0.0100	2.5082	0.0102	2.1550	0.0121	1.8677	0.0190
3.00	3.0772	0.0109	2.6351	0.0099	2.2366	0.0100	1.9689	0.0127	1.7326	0.0222
4.00	2.6639	0.0106	2.3258	0.0090	2.0138	0.0083	1.8059	0.0103	1.6081	0.0153
5.00	2.3562	0.0100	2.0849	0.0084	1.8341	0.0094	1.6698	0.0118	1.5037	0.0189
6.00	2.1181	0.0078	1.8920	0.0068	1.6825	0.0076	1.5498	0.0100	1.4048	0.0145
7.00	1.9275	0.0092	1.7352	0.0088	1.5587	0.0090	1.4502	0.0104	1.3270	0.0144
8.00	1.7747	0.0071	1.6076	0.0073	1.4557	0.0082	1.3665	0.0108	1.2551	0.0144
9.00	1.6484	0.0068	1.5006	0.0061	1.3673	0.0075	1.2929	0.0100	1.1955	0.0140
10.00	1.5355	0.0069	1.4031	0.0062	1.2852	0.0072	1.2219	0.0113	1.1330	0.0155
12.00	1.3521	0.0069	1.2434	0.0068	1.1489	0.0065	1.1075	0.0087	1.0337	0.0123
14.00	1.2101	0.0064	1.1198	0.0060	1.0420	0.0066	1.0137	0.0081	0.9515	0.0135
16.00	1.0931	0.0059	1.0150	0.0063	0.9517	0.0069	0.9336	0.0098	0.8800	0.0114
18.00	0.9894	0.0057	0.9211	0.0058	0.8692	0.0058	0.8615	0.0075	0.8132	0.0114
20.00	0.9168	0.0057	0.8555	0.0057	0.8113	0.0063	0.8109	0.0076	0.7665	0.0087

Table SI-4. Apparent lifetimes based on phase-shift and modulation factor (calibration data) for several oxygen concentrations at the 5 first harmonics using the proposed multifrequency phase-modulation method. All the values correspond to the average of 25 measurements.

Phase based apparent lifetime (τ_φ) (mean and standard deviation in μs)										
# harmonic	(1 st) 1715 Hz		(2 nd) 3430 Hz		(3 rd) 5145 Hz		(4 st) 6860 Hz		(5 st) 8575 Hz	
$p\text{O}_2$ (kPa)	Mean	Sdev	Mean	Sdev	Mean	Sdev	Mean	Sdev	Mean	Sdev
0.00	66.108	0.195	66.054	0.327	65.170	0.662	64.499	1.394	68.325	3.845
0.50	54.013	0.180	53.601	0.230	52.517	0.428	52.030	0.874	54.458	1.907
0.75	49.928	0.182	49.257	0.259	47.958	0.439	47.248	0.685	49.201	1.511
1.00	46.777	0.143	45.912	0.206	44.484	0.385	43.696	0.707	45.579	1.528
2.00	38.249	0.127	36.909	0.175	35.052	0.268	34.147	0.457	34.886	0.827
3.00	33.167	0.129	31.619	0.181	29.540	0.231	28.579	0.367	29.003	0.656
4.00	29.690	0.152	28.083	0.152	25.919	0.213	24.972	0.325	25.266	0.551
5.00	27.175	0.171	25.495	0.165	23.246	0.215	22.313	0.299	22.447	0.504
6.00	25.243	0.198	23.583	0.178	21.312	0.203	20.418	0.286	20.518	0.500
7.00	23.698	0.174	22.000	0.178	19.712	0.215	18.857	0.249	18.945	0.429
8.00	22.410	0.179	20.769	0.126	18.507	0.170	17.744	0.213	17.809	0.354
9.00	21.398	0.180	19.731	0.182	17.430	0.209	16.712	0.246	16.703	0.339
10.00	20.458	0.192	18.825	0.148	16.512	0.200	15.842	0.211	15.909	0.322
12.00	18.980	0.179	17.334	0.176	14.991	0.184	14.446	0.222	14.521	0.289
14.00	17.749	0.236	16.123	0.184	13.797	0.222	13.374	0.261	13.521	0.415
16.00	16.735	0.229	15.158	0.160	12.755	0.190	12.433	0.216	12.704	0.340
18.00	15.772	0.287	14.224	0.249	11.799	0.191	11.658	0.274	11.994	0.353
20.00	15.160	0.286	13.562	0.241	11.119	0.228	11.041	0.256	11.402	0.346
Modulation based apparent lifetime (τ_m) (mean and standard deviation in μs)										
# harmonic	(1 st) 1715 Hz		(2 nd) 3430 Hz		(3 rd) 5145 Hz		(4 st) 6860 Hz		(5 st) 8575 Hz	
$p\text{O}_2$ (kPa)	Mean	Sdev	Mean	Sdev	Mean	Sdev	Mean	Sdev	Mean	Sdev
0.00	66.200	0.170	66.212	0.249	65.385	0.415	64.428	0.617	68.162	0.994
0.50	53.143	0.173	52.439	0.362	51.599	0.859	51.230	1.917	54.116	6.606
0.75	48.542	0.169	47.477	0.301	46.396	0.664	46.144	1.468	47.707	4.658
1.00	44.879	0.151	43.636	0.297	42.410	0.573	41.981	1.114	42.832	2.325
2.00	34.753	0.112	33.112	0.164	31.660	0.262	30.987	0.483	30.914	1.187
3.00	28.614	0.111	27.003	0.136	25.617	0.194	24.880	0.345	24.350	0.848
4.00	24.481	0.104	22.989	0.110	21.700	0.133	20.983	0.218	20.297	0.424
5.00	21.491	0.096	20.128	0.096	18.983	0.135	18.345	0.212	17.698	0.430
6.00	19.220	0.074	17.970	0.074	16.916	0.099	16.333	0.159	15.652	0.276
7.00	17.426	0.086	16.288	0.092	15.349	0.111	14.833	0.150	14.248	0.246
8.00	16.002	0.066	14.960	0.075	14.115	0.096	13.668	0.145	13.077	0.226
9.00	14.833	0.063	13.872	0.061	13.098	0.084	12.702	0.128	12.178	0.203
10.00	13.794	0.063	12.898	0.062	12.185	0.079	11.817	0.138	11.297	0.211
12.00	12.116	0.063	11.337	0.066	10.727	0.068	10.471	0.099	10.001	0.154
14.00	10.826	0.058	10.153	0.057	9.626	0.067	9.430	0.088	9.008	0.158
16.00	9.766	0.053	9.163	0.059	8.723	0.068	8.578	0.103	8.193	0.127
18.00	8.832	0.051	8.287	0.054	7.914	0.056	7.836	0.076	7.464	0.122
20.00	8.178	0.051	7.680	0.052	7.356	0.060	7.328	0.075	6.973	0.091

Table SI-5. Demas parameters of the calibration of PS/PtTFPP sensing fibre between 0.5-20 kPa O₂ using the conventional phase-modulation method.

Range, pO_2	Apparent phase lifetime (τ_φ)		Apparent modulation lifetime (τ_m)	
0-20 kPa	k_{SV1} (kPa ⁻¹)	0.7677	k_{SV1} (kPa ⁻¹)	0.7429
	k_{SV2} (kPa ⁻¹)	0.0805	k_{SV2} (kPa ⁻¹)	0.0566
	x	0.7259	x	0.8655
	τ_0 (μ s)	62.85	τ_0 (μ s)	68.30
	R^2	0.9994	R^2	0.9998

Table SI-6. Demas parameters of the calibration of PS/PtTFPP sensing fibre between 0.5-20 kPa O₂ using the proposed multifrequency phase-modulation method.

		Apparent phase lifetime (τ_φ)				
		# harmonic				
Range, pO_2	Parameter	(1 st) 1715 Hz	(2 nd) 3430 Hz	(3 rd) 5145 Hz	(4 st) 6860 Hz	(5 st) 8575 Hz
0-20 kPa	k_{SV1} (kPa ⁻¹)	0.5881	0.6154	0.6821	0.6590	0.6585
	k_{SV2} (kPa ⁻¹)	0.0232	0.0248	0.0416	0.0251	0.0117
	x	0.7476	0.7793	0.7905	0.8376	0.8754
	τ_0 (μ s)	65.29	65.84	66.15	65.91	70.02
	R^2	0.99996	0.99996	0.99994	0.99993	0.99992
		Apparent modulation lifetime (τ_m)				
		# harmonic				
Range, pO_2	Parameter	(1 st) 1715 Hz	(2 nd) 3430 Hz	(3 rd) 5145 Hz	(4 st) 6860 Hz	(5 st) 8575 Hz
0-20 kPa	k_{SV1} (kPa ⁻¹)	0.5829	0.6559	0.6830	0.6747	0.7194
	k_{SV2} (kPa ⁻¹)	0.0902	0.0784	0.0553	0.0286	0.0159
	x	0.8380	0.8615	0.8961	0.9278	0.9498
	τ_0 (μ s)	66.09	67.02	66.85	66.84	70.33
	R^2	0.99998	0.99997	0.99995	0.99986	0.99922

Equation for the Demas model:

$$\frac{\tau_0}{\tau} = \left[\frac{x}{1 + k_{SV1} pO_2} + \frac{(1-x)}{1 + k_{SV2} pO_2} \right]^{-1} \quad (\text{Equation SI-39})$$

where τ_0 and τ are the values of the analytical signal (apparent luminescence lifetime) in the absence and the presence of oxygen, respectively; pO_2 is the oxygen concentration, x and $(1-x)$ are the fractions of the total emission for each site, and k_{SV1} and k_{SV2} are the Stern-Volmer quenching constants for each microenvironment.

Table SI-7. Root-Mean-Square Error, RMSE (kPa) obtained in the determination of oxygen concentration (\widehat{pO}_2) using the conventional phase-modulation method. All the values correspond to the average of 25 measurements.

Measured	RMSE (kPa)		
pO_2 , kPa	τ_φ	τ_m	τ_φ, τ_m
0.50	0.1222	0.1620	0.1035
0.75	0.1490	0.1459	0.1133
1.00	0.1421	0.1709	0.1036
2.00	0.1825	0.1630	0.1358
3.00	0.2863	0.2334	0.1775
4.00	0.3222	0.3265	0.2468
5.00	0.6148	0.2293	0.2562
6.00	0.5023	0.3032	0.2830
7.00	0.7318	0.3327	0.3863
8.00	0.6412	0.5014	0.4494
9.00	0.9506	0.4887	0.4321
10.00	1.1159	0.4796	0.4323
12.00	1.7825	0.6053	0.5627
14.00	1.7792	0.6662	0.6796
16.00	2.6974	0.9265	0.9110
18.00	2.8319	1.0103	0.9936
20.00	3.0433	1.2552	1.1087

Table SI-8. Root-Mean-Square Error, RMSE (kPa) obtained in the determination of oxygen concentration ($\widehat{pO_2}$) using the proposed multifrequency phase-modulation method at the 5 first harmonics. All the values correspond to the average of 25 measurements.

RMSE (kPa)									
Measured pO_2 , kPa	1 st harmonic			2 nd harmonic			3 rd harmonic		
	τ_φ	τ_m	τ_φ, τ_m	τ_φ	τ_m	τ_φ, τ_m	τ_φ	τ_m	τ_φ, τ_m
0.50	0.0111	0.0086	0.0073	0.0117	0.0173	0.0082	0.0247	0.0383	0.0197
0.75	0.0150	0.0075	0.0054	0.0172	0.0149	0.0115	0.0270	0.0388	0.0197
1.00	0.0133	0.0117	0.0075	0.0163	0.0213	0.0125	0.0303	0.0390	0.0241
2.00	0.0243	0.0244	0.0199	0.0305	0.0313	0.0248	0.0462	0.0422	0.0369
3.00	0.0399	0.0235	0.0247	0.0468	0.0276	0.0278	0.0571	0.0374	0.0332
4.00	0.0612	0.0263	0.0238	0.0554	0.0280	0.0290	0.0787	0.0357	0.0405
5.00	0.0820	0.0263	0.0250	0.0883	0.0265	0.0314	0.1003	0.0492	0.0456
6.00	0.1295	0.0364	0.0345	0.1093	0.0354	0.0316	0.1326	0.0535	0.0479
7.00	0.1310	0.0520	0.0509	0.1195	0.0609	0.0453	0.1427	0.0692	0.0642
8.00	0.1476	0.0494	0.0446	0.0979	0.0512	0.0472	0.1266	0.0886	0.0720
9.00	0.1886	0.0825	0.0820	0.1883	0.0901	0.0881	0.2037	0.1205	0.1107
10.00	0.2335	0.0989	0.0927	0.1808	0.0979	0.0876	0.2356	0.1216	0.1147
12.00	0.2619	0.1126	0.1067	0.2578	0.1208	0.1158	0.2790	0.1158	0.1089
14.00	0.4096	0.1473	0.1464	0.2824	0.1643	0.1591	0.4299	0.1779	0.1788
16.00	0.4323	0.1254	0.1266	0.2883	0.1503	0.1360	0.4074	0.1999	0.1666
18.00	0.6757	0.2380	0.2335	0.8067	0.2859	0.2810	0.5295	0.3076	0.2967
20.00	0.7746	0.1914	0.1857	0.7846	0.1929	0.1864	0.7564	0.2512	0.2116
Measured pO_2 , kPa	4 th harmonics			5 th harmonics					
	τ_φ	τ_m	τ_φ, τ_m	τ_φ	τ_m	τ_φ, τ_m			
0.50	0.0396	0.0783	0.0339	0.0937	0.2198	0.0888			
0.75	0.0440	0.0830	0.0371	0.0943	0.1948	0.0768			
1.00	0.0573	0.0761	0.0534	0.1236	0.1290	0.1026			
2.00	0.0686	0.0647	0.0399	0.1049	0.1324	0.0790			
3.00	0.0789	0.0714	0.0480	0.1177	0.1785	0.1165			
4.00	0.1267	0.0705	0.0699	0.1899	0.1476	0.1140			
5.00	0.1461	0.0977	0.0891	0.2127	0.2079	0.1505			
6.00	0.1857	0.0897	0.0857	0.2980	0.1520	0.1506			
7.00	0.1942	0.0991	0.0989	0.2795	0.1597	0.1027			
8.00	0.1342	0.1343	0.1166	0.2546	0.1949	0.1599			
9.00	0.2186	0.1775	0.1589	0.3180	0.2606	0.2018			
10.00	0.2823	0.1612	0.1535	0.4087	0.2491	0.2260			
12.00	0.3558	0.1874	0.1697	0.5370	0.2744	0.2307			
14.00	0.4448	0.2234	0.2111	0.8942	0.3934	0.3391			
16.00	0.4555	0.2674	0.2359	0.7374	0.3448	0.3345			
18.00	0.7844	0.3988	0.3908	1.0332	0.5637	0.4766			
20.00	0.8362	0.3153	0.2821	1.2573	0.3993	0.3817			

Table SI-9. Root-Mean-Square Error, RMSE (kPa) obtained in the determination of oxygen concentration (\widehat{pO}_2) using the proposed multifrequency phase-modulation method combining some information from the 5 first harmonics.

RMSE (kPa)									
Measured pO_2 , kPa	1 st harmonic			1 st and 2 nd harmonics			1 st to 3 rd harmonics		
	τ_φ	τ_m	τ_φ, τ_m	τ_φ	τ_m	τ_φ, τ_m	τ_φ	τ_m	τ_φ, τ_m
0.50	0.0111	0.0086	0.0073	0.0075	0.0083	0.0056	0.0071	0.0087	0.0052
0.75	0.0150	0.0075	0.0054	0.0116	0.0068	0.0046	0.0096	0.0076	0.0046
1.00	0.0133	0.0117	0.0075	0.0098	0.0128	0.0062	0.0088	0.0137	0.0064
2.00	0.0243	0.0244	0.0199	0.0210	0.0258	0.0202	0.0206	0.0266	0.0208
3.00	0.0399	0.0235	0.0247	0.0316	0.0194	0.0217	0.0253	0.0181	0.0187
4.00	0.0612	0.0263	0.0238	0.0475	0.0174	0.0211	0.0385	0.0170	0.0199
5.00	0.0820	0.0263	0.0250	0.0632	0.0135	0.0183	0.0490	0.0153	0.0161
6.00	0.1295	0.0364	0.0345	0.0838	0.0255	0.0253	0.0592	0.0235	0.0223
7.00	0.1310	0.0520	0.0509	0.0666	0.0378	0.0344	0.0581	0.0332	0.0305
8.00	0.1476	0.0494	0.0446	0.0854	0.0370	0.0370	0.0625	0.0370	0.0351
9.00	0.1886	0.0825	0.0820	0.1310	0.0724	0.0715	0.1045	0.0732	0.0711
10.00	0.2335	0.0989	0.0927	0.1435	0.0918	0.0819	0.1242	0.0924	0.0839
12.00	0.2619	0.1126	0.1067	0.1806	0.0965	0.0915	0.1460	0.0817	0.0791
14.00	0.4096	0.1473	0.1464	0.1998	0.1280	0.1279	0.2052	0.1208	0.1201
16.00	0.4323	0.1254	0.1266	0.2829	0.0908	0.0903	0.2150	0.0948	0.0888
18.00	0.6757	0.2380	0.2335	0.6232	0.2386	0.2366	0.4260	0.2433	0.2418
20.00	0.7746	0.1914	0.1857	0.4975	0.1619	0.1589	0.4621	0.1449	0.1439

Measured pO_2 , kPa	1 st to 4 st harmonics			1 st to 5 st harmonics		
	τ_φ	τ_m	τ_φ, τ_m	τ_φ	τ_m	τ_φ, τ_m
0.50	0.0071	0.0089	0.0052	0.0073	0.0092	0.0053
0.75	0.0091	0.0075	0.0043	0.0094	0.0075	0.0044
1.00	0.0091	0.0139	0.0069	0.0092	0.0142	0.0070
2.00	0.0207	0.0268	0.0210	0.0204	0.0270	0.0210
3.00	0.0229	0.0174	0.0176	0.0219	0.0168	0.0170
4.00	0.0385	0.0159	0.0187	0.0386	0.0155	0.0178
5.00	0.0416	0.0141	0.0141	0.0410	0.0154	0.0147
6.00	0.0527	0.0232	0.0214	0.0529	0.0227	0.0207
7.00	0.0570	0.0310	0.0292	0.0585	0.0308	0.0277
8.00	0.0595	0.0389	0.0366	0.0589	0.0393	0.0372
9.00	0.0902	0.0759	0.0726	0.0816	0.0781	0.0740
10.00	0.0927	0.0922	0.0808	0.0794	0.0933	0.0819
12.00	0.1261	0.0791	0.0781	0.1284	0.0801	0.0792
14.00	0.1852	0.1143	0.1145	0.1894	0.1158	0.1162
16.00	0.1960	0.0907	0.0850	0.1936	0.0931	0.0873
18.00	0.3613	0.2481	0.2429	0.3371	0.2509	0.2440
20.00	0.4140	0.1300	0.1250	0.3905	0.1269	0.1209

On the calibration of chemical sensors based on photoluminescence: Selecting the appropriate model and criterion

Santiago Medina Rodríguez^{a,b}, Ángel de la Torre Vega^{a,*}, Jorge Fernando Fernández Sánchez^{b,*} and Alberto Fernández Gutiérrez^b

^a*Department of Signal Theory, Networking and Communications, CITIC-UGR, University of Granada, C/ Periodista Rafael Gómez 2, E-18071 Granada, Spain.*

^b*Department of Analytical Chemistry, Faculty of Sciences, University of Granada, Avda. Fuentenueva s/n, E-18071 Granada, Spain.*

Submitted to *Analyst*

On the calibration of chemical sensors based on photoluminescence: Selecting the appropriate model and criterion

Abstract—*In this work we propose a new model for describing the relationship between the photoluminescence response and the analyte concentration and its comparison with classical models (Stern-Volmer, Lehrer and Demas models). This new model can be considered as a variant of the Stern-Volmer model and it provides a good trade-off between the number of parameters and the accuracy with respect to classical models with similar complexity (i.e. with the same number of parameters). In addition, we demonstrate the importance of the optimization criterion used for calibration.*

To demonstrate these claims, we present results from 25 real experiments, involving 7 different oxygen-sensitive sensing phases, using either luminescence intensity or luminescence lifetime as analytical signal, and 3 different instruments (a luminescence spectrometer, a dual-phase lock-in amplifier and a measuring system based on the I/Q method). We provide details for the implementation of the calibration procedures as well as code (compatible with MATLAB and Octave) that performs the calibration for each model and criterion.

keywords: Chemical sensors; Fitting models; Calibration criteria; Polynomial-exponent.

7.1 Introduction

PHOTOLUMINESCENCE sensors require an appropriate calibration for accurately measuring the analyte concentration. Calibration is based on a model describing the relationship between the analytical signal and the concentration, and consists in the estimation of the model parameters that optimally fit some calibration data according to some criterion. Therefore, the calibration procedure, given a model (with M parameters) and some calibration data, consists in the search of the parameter values minimizing the error between the calibration data and the model [1].

The majority of solid-state oxygen sensors display considerable heterogeneity in their physical and luminescent properties which results in complex analytical relationships between the analytical signal (luminescence intensity, or lifetime) and oxygen concentrations [1–5]. In principle, the more complex is the model the most accurate is the fitting of the calibration data. However, calibration measurements are always affected by noise and therefore, more complex models require larger calibration datasets to achieve statistical robustness. Consequently, model complexity increases the risk of over-fitting [6, 7]. On the other hand, the calibration of a model with M parameters is mathematically formulated as an M -dimensional search of the values which minimize the error between the model and the calibration data. Therefore, fitting a complex model implies a multidimensional search for simultaneously optimizing the M parameters, and problems related with searching and convergence usually

increases with the number of parameters [8]. Thus, a good model can be defined as the one providing the best accuracy with the minimum number of parameters. For this reason, the most popular models used in photoluminescence sensors are the 1-site Stern-Volmer (SV) model [9, 10] which provides a basic description, and 2-sites Lehrer (L) [11] and Demas (D) [3, 4, 12, 13] models which are extension of the SV. Other models based on the interaction of the luminophore with the nonuniform environment [14], Gaussian distribution of the luminophore lifetime [15, 16], those based on the physics of diffusion of the analyte into the sensor [5, 17, 18], or dynamic models on the basis of the light emission profiles [19], among others, have been proposed. Such models involve rather complicate mathematical expressions including, in some cases, integrals for the volume of the sensor. These complex models are useful for describing and understanding some aspects of photoluminescence (like dynamic evolution of the response with transitory changes in the analyte concentration). However, since complex models require the calibration of a large number of parameters, their practical applicability in instrumentation is limited [20]. Another property to be considered is the scalability of the model, i.e. the possibility of increasing its complexity when enough calibration data are available. For example, Demas model can be extended to more than 2 sites [13, 15].

The criterion used for fitting the model is a very important aspect to be considered, since the parameters resulting from the calibration process will depend not only on the calibration data but also on the selected criterion [21, 22]. The fitting procedure minimizes the residual error but it is not able to make it null. Therefore the resulting model depends on how the error is defined, i.e. what criterion is used for fitting the parameters. If the aim of the model is to describe the photoluminescence phenomenon, the most reasonable criterion is to minimize the distance between the observed analytical signals and the expected ones [18]. But if the aim of the model is to calibrate an instrument for measuring concentration, the error should be defined as a distance between the observed concentration and the expected one [5]. Some authors [5, 21, 22] have proposed the use of the relative error as criterion for calibration. This criterion is particularly useful when the measuring instrument is designed to operate in a wide range of concentrations.

In this work we propose a new model to describe the relationship between the analytical response and the analyte concentration in chemical sensors based on photoluminescence. It can be considered an extension of the Stern-Volmer model including an additional parameter (3 parameters model). It has been compared with the most commonly used models to describe photoluminescence response: the classical models 1-site Stern-Volmer (2 parameters), and the 2-sites Lehrer (3 parameters) and Demas (4 parameters) models. The proposed model aims to provide a good trade-off between accuracy and number of parameters. In addition, it can be scaled and admits a simple extension to M parameters (with M arbitrarily large), which allows the use of a more complex model depending on the availability of calibration data. As the classical models, the proposed model can be applied to luminescence intensity or luminescence lifetime and it is thought to be of potential use also for enzymatic biosensors coupled with the optical oxygen transducer, and related chemical sensors employing quenching/enhancement of luminescence.

On the other hand, we demonstrate the importance of the calibration criterion by comparing the accuracy provided by different models (the classical ones and the one that we propose) calibrated with three different criteria. Finally, we provide a generic procedure for calibrating the different models (under different criteria), and simplifications particularized to each

case (taking into account the functions involved in the minimization). Electronic Supporting Information (ESI) contains details for the implementation of the calibration procedures and code (compatible with MATLAB and Octave) that provide the calibration for each model and criterion.

7.2 Theory

7.2.1 Reference models included in the study

The three models usually applied to describe the relationship between the analyte concentration and the analytical signal in photoluminescence have been included in this work as reference: the 1-site Stern-Volmer model [9, 10], the Lehrer model [11] and the Demas model [3, 4, 12, 13]. These models will be referred to as SV, L and D, respectively, and are given by the following expressions:

$$\text{Stern-Volmer model (SV): } \quad \frac{\phi_0}{\phi} = 1 + kC \quad (7.1)$$

$$\text{Lehrer model (L): } \quad \frac{\phi_0}{\phi} = \left(\frac{x}{1 + kC} + (1 - x) \right)^{-1} \quad (7.2)$$

$$\text{Demas model (D): } \quad \frac{\phi_0}{\phi} = \left(\frac{x}{1 + k_1C} + \frac{(1 - x)}{1 + k_2C} \right)^{-1} \quad (7.3)$$

where ϕ is the analytical signal (luminescence intensity or luminescence lifetime), C is the analyte concentration and ϕ_0 is the analytical signal at null analyte concentration. The parameters k , k_1 and k_2 are the Stern-Volmer constants. In the Lehrer and Demas models, two sites are considered in the sensor with different constants, and x and $(1 - x)$ represent the relative contribution of each site to the photoluminescence. In the Lehrer model, the constant of the second site is assumed to be null, while in the Demas model, different constants k_1 and k_2 are assumed for each site. Therefore, Stern-Volmer, Lehrer and Demas models require the estimation of 2, 3 and 4 parameters, respectively. Demas model could be generalized to more than two sites (even though every new site would require two additional parameters).

7.2.2 Proposed polynomial-exponent (PE) model

We propose a new model consisting in a polynomial fitting of C with ϕ^α , where parameter α is an exponent affecting the analytical response:

$$C = \sum_{n=0}^p a_n \phi^{n\alpha} = a_0 + a_1 \phi^\alpha + a_2 \phi^{2\alpha} + \dots + a_p \phi^{p\alpha} \quad (7.4)$$

This polynomial-exponent fitting of $C(\phi)$ (which will be referred to as PE model) requires the estimation of $p + 2$ parameters, where p is the polynomial order. If $p = 1$, Eq. (7.4) can

be rewritten as (see ESI, section A.1 for details):

$$\left(\frac{\phi_0}{\phi}\right)^{-\alpha} = 1 + kC \quad (7.5)$$

that is, the model can be considered an extension of SV where a new parameter α is included (or SV can be considered a particular case of PE model, for $\alpha = -1$ and $p = 1$). In order to see the role of the exponent α , a logarithm can be applied to Eq. (7.5). The equation can be rewritten as:

$$\log(1 + kC) = \alpha \log(\phi) + b \quad (7.6)$$

and therefore α would be the slope of a linear regression of $\log(1 + kC)$ and $\log(\phi)$, which provides the exponent describing the dependence of ϕ with $(1 + kC)$. In the case of a uniform distribution of the sensing phase and the quencher, and a monoexponential photoluminescence process, the Stern-Volmer model appropriately describes the analytical response and a value $\alpha = -1$ is expected (i.e. $1/\phi$ linearly increases with $(1 + kC)$). The exponent α provides a simple way for modeling deviations from this dependence associated, for example, to a non uniform distribution of the sensing phase or the quencher [18]. The use of a polynomial order higher than 1 allows to reduce the residual modeling error when enough calibration data are available.

In this work we will evaluate PE models of 1st and 2nd order (i.e. PE1 and PE2 models). Additionally, in order to analyze the role of the exponent included in the model, we will also evaluate the PE2 model in the particular case with $\alpha = -1$, which will be referred to as P2 model (P1 model corresponds to SV model). Therefore, the models to be evaluated in this study are SV, L, D, P2, PE1 and PE2. The mathematical expressions for $\phi(C)$ and $C(\phi)$ for these models can easily be derived from the previous equations and are presented in ESI (section A.2). Table 7.1 summarized the parameters to be fitted in each model.

7.2.3 Sensitivity and response at null concentration

The parameters of SV, L and D models (ϕ_0 , k , x , k_1 and k_2) provide an interpretation related to the photoluminescence phenomenon. The parameters of the proposed model (coefficients a_n and exponent α) cannot directly be interpreted. However, from the functions describing the relationship between C and ϕ , the response at null concentration Φ_0 and the sensitivity K , defined as:

$$\Phi_0 \equiv \lim_{C \rightarrow 0} \phi \quad K \equiv \lim_{C \rightarrow 0} \frac{1}{\phi} \left| \frac{\partial \phi}{\partial C} \right| \quad (7.7)$$

can be easily derived. Mathematical derivations providing these parameters for different models can be found in ESI (section A.3), and resulting Φ_0 and K for each model are summarized in Table 7.1.

7.2.4 Optimization criteria for model calibration

The calibration procedure consists in the estimation of the model parameters $\Lambda = \{\lambda_1, \lambda_2, \dots, \lambda_M\}$ that optimally fit some calibration data. The model with some parameters provides either the function $C = C(\Lambda, \phi)$ or $\phi = \phi(\Lambda, C)$. Given a set of calibration data

Table 7.1: Summary of models included in this study. The parameters to be fitted and expressions for the response at null concentration Φ_0 and the sensitivity K are shown for each model.

Model		Parameters		Φ_0	K
Stern-Volmer	SV	ϕ_0, k	(2)	ϕ_0	k
Lehrer	L	ϕ_0, k, x	(3)	ϕ_0	$k x$
Demas	D	ϕ_0, k_1, k_2, x	(4)	ϕ_0	$k_1 x + k_2 (1 - x)$
Polynomial-2	P2	a_0, a_1, a_2	(3)	$\left(\frac{-a_1 + \sqrt{a_1^2 - 4a_0a_2}}{2a_2}\right)^{-1}$	$\left \frac{1}{a_1\Phi_0^{-1} + 2a_2\Phi_0^{-2}}\right $
Polyn.Exp.1	PE1	a_0, a_1, α	(3)	$\left(\frac{-a_0}{a_1}\right)^{1/\alpha}$	$\left \frac{1}{a_0\alpha}\right $
Polyn.Exp.2	PE2	a_0, a_1, a_2, α	(4)	$\left(\frac{-a_1 + \sqrt{a_1^2 - 4a_0a_2}}{2a_2}\right)^{1/\alpha}$	$\left \frac{1}{\alpha a_1\Phi_0^\alpha + 2\alpha a_2\Phi_0^{2\alpha}}\right $

$\{(\phi_1, C_1), (\phi_2, C_2), \dots, (\phi_N, C_N)\}$, the calibration consists in the minimization of the error between the model and the calibration data:

$$\hat{\Lambda} = \min_{\forall \Lambda}^{-1} E(\Lambda, \{(\phi_1, C_1), (\phi_2, C_2), \dots, (\phi_N, C_N)\}) \quad (7.8)$$

that is, the calibration is an M -dimensional search of the minimum of the error E . This search of the model parameters requires defining the error according to some minimization criterion. The definition of the error to be minimized (and therefore the selected calibration criterion) is relevant, since different criteria will provide different values of the model parameters. If a research study is oriented to understand the photoluminescence phenomenon, the reasonable fitting criterion would define the error to be minimized as the distance between the expected analytical signal $\phi(\Lambda, C_n)$ and the observed analytical signal ϕ_n , averaged for all the calibration data ($n = 1, \dots, N$). Some authors [18, 21, 22] proposed the use of the squared error as minimization criterion:

$$E_a = \sum_{n=1}^N (\phi(\Lambda, C_n) - \phi_n)^2 \quad (7.9)$$

On the other hand, if the aim of the calibration is to optimize the accuracy of an instrument for measuring some analyte concentration, the error to be minimized should be the distance between the concentration expected from the analytical signal $C(\Lambda, \phi_n)$ and the measured concentration C_n [5]:

$$E_b = \sum_{n=1}^N (C(\Lambda, \phi_n) - C_n)^2 \quad (7.10)$$

Some works [5, 21, 22] propose the use of the relative error in concentration as calibration criterion. This criterion is particularly useful when the instrument is intended to measure a wide range of concentrations (since it equalizes the importance of errors at low or high concentrations):

$$E_c = \sum_{n=1}^N \left(\frac{C(\Lambda, \phi_n) - C_n}{C_n} \right)^2 \quad (7.11)$$

The errors defined in the last two criteria can be described with a unique general expression:

$$E_{bw} = \sum_{n=1}^N w_n (C(\Lambda, \phi_n) - C_n)^2 \quad (7.12)$$

where w_n are weights with a value $w_n = 1$ for criterion in Eq. (7.10) and $w_n = 1/C_n^2$ for that in Eq. (7.11). The calibration criteria defined in Eqs. (7.9), (7.10), (7.11) and (7.12) will be referred to as criteria (a), (b), (c) and (bw), respectively.

7.2.5 Calibration formulas for different models and criteria

7.2.5.1 Generic calibration procedure

Calibration consists in the minimization of the error $E(\Lambda, \{(\phi_1, C_1), (\phi_2, C_2), \dots, (\phi_N, C_N)\})$ with respect to the parameters $\Lambda = \{\lambda_1, \lambda_2, \dots, \lambda_M\}$, where E can be defined according to the previous criteria. The minimum of E can be found by finding the zeros of the partials:

$$\frac{\partial E}{\partial \lambda_m} = 0 \quad \forall m = 1, \dots, M \quad (7.13)$$

If we define $f_m(\lambda_m) \equiv \partial E / \partial \lambda_m$, the Newton's method can be applied to the iterative estimation of the roots of $f_m(\lambda_m)$ and therefore to the estimation of the model parameters minimizing E :

$$\lambda_m^{t+1} = \lambda_m^t - \frac{f_m(\lambda_m^t)}{f'_m(\lambda_m^t)} \approx \lambda_m^t - \frac{\epsilon}{2} \frac{E(\lambda_m^t + \epsilon) - E(\lambda_m^t - \epsilon)}{E(\lambda_m^t + \epsilon) + E(\lambda_m^t - \epsilon) - 2E(\lambda_m^t)} \quad (7.14)$$

where t is the iteration, $f'_m(\lambda_m)$ is the derivative of $f_m(\lambda_m)$ with respect to λ_m , and ϵ is an infinitesimal increment in λ_m . The calibration would start with an initialization of the model parameters λ_m^0 . Since the model calibration is an M -dimensional search, at each iteration all the parameters should be independently estimated (more details can be found in ESI, section A.4). However, taking into account the models and criteria, the conditions $f_m(\lambda_m) = 0$ allow to write some of the parameters as a function of the others in some cases, which reduces the dimensionality of the search. In the next sections, the calibration procedure is particularized for each model and criterion. The next sections include only the resulting calibration formulas; the derivations providing these formulas can be found in ESI, section A.5. The calibration algorithms (implemented for MATLAB/Octave) are described and included in ESI, section C.

7.2.5.2 Stern-Volmer model using criterion (a)

The calibration of the Stern-Volmer model requires the estimation of 2 parameters (ϕ_0 and k), and therefore it would be a 2-dimensional search. However, the condition $\partial E_a / \partial \phi_0 = 0$ provides a direct estimation of ϕ_0 as a function of k :

$$\phi_0 = \frac{\sum_n \left(\frac{\phi_n}{1+kC_n} \right)}{\sum_n \left(\frac{1}{1+kC_n} \right)^2} \quad (7.15)$$

which reduces to 1 the dimensionality of the search for this model and criterion (k should be iteratively searched with Eq. (7.14), but not ϕ_0 , which can be directly estimated using Eq. (7.15)).

7.2.5.3 Stern-Volmer model using criteria (b) and (c)

The conditions $\partial E_{bw}/\partial\phi_0 = 0$ and $\partial E_{bw}/\partial k = 0$ directly provide the parameters k and ϕ_0 for the (bw) criterion:

$$k = \frac{S_{\phi\phi}S - S_{\phi}^2}{S_{\phi}S_{C\phi} - S_C S_{\phi\phi}} \quad \phi_0 = \frac{S_{\phi} + kS_C\phi}{S_{\phi\phi}} \quad (7.16)$$

where the following definitions are used: $S \equiv \sum_n w_n$; $S_{\phi} \equiv \sum_n w_n/\phi_n$; $S_C \equiv \sum_n w_n C_n$; $S_{C\phi} \equiv \sum_n w_n C_n/\phi_n$ and $S_{\phi\phi} \equiv \sum_n w_n/\phi_n^2$. These formulas can be particularized to criterion (b) (by using the weights $w_n = 1$) or to criterion (c) (by using the weights $w_n = 1/C_n^2$). For both criteria, the parameters of the Stern-Volmer model can be directly estimated and no iterative procedure is necessary for this calibration.

7.2.5.4 Lehrer model using criterion (a)

The calibration of the Lehrer model requires the estimation of 3 parameters (ϕ_0 , k and x). The conditions $\partial E_a/\partial\phi_0 = 0$ and $\partial E_a/\partial x = 0$ provide a direct estimation of ϕ_0 and x as a function of k :

$$x = \frac{NS_{z\phi} - S_z S_{\phi}}{S_z S_{z\phi} - S_{zz} S_{\phi}} \quad \phi_0 = \frac{S_{z\phi}}{S_z - xS_{zz}} \quad (7.17)$$

where the following definitions have been used: $z_n \equiv kC_n/(1 + kC_n)$; $S_{\phi} \equiv \sum_n \phi_n$; $S_z \equiv \sum_n z_n$; $S_{z\phi} \equiv \sum_n z_n \phi_n$; $S_{zz} \equiv \sum_n z_n^2$. This way, the calibration of the Lehrer model using the (a) criterion becomes a 1-dimensional search of parameter k .

7.2.5.5 Lehrer model using criteria (b) and (c)

The form of the partials of $C(\phi)$ with respect to the different parameters makes the parameter estimation difficult under criteria (b) and (c). An appropriate change of variables allows the reduction of the dimensionality of the search:

$$b_0 \equiv \frac{1}{k} \quad b_1 \equiv \frac{x}{k(1-x)} \quad k' \equiv \frac{1}{\phi_0(1-x)} \quad (7.18)$$

Using the new parameters, the Lehrer model can be written as:

$$C(\phi) = \frac{b_1}{k'\phi - 1} - b_0 \quad (7.19)$$

and the conditions $\partial E_{bw}/\partial b_0 = 0$ and $\partial E_{bw}/\partial b_1 = 0$ provide a direct estimation of the new parameters b_0 and b_1 as a function of the parameter k' :

$$b_0 = \frac{S_{Cz}S_z - S_C S_{zz}}{S_{zz}S - S_z^2} \quad b_1 = \frac{b_0 S_z + S_{Cz}}{S_{zz}} \quad (7.20)$$

where the following definitions were considered: $z_n \equiv 1/(k'\phi_n - 1)$; $S \equiv \sum_n w_n$; $S_z \equiv \sum_n w_n z_n$; $S_C \equiv \sum_n w_n C_n$; $S_{Cz} \equiv \sum_n w_n C_n z_n$; $S_{zz} \equiv \sum_n w_n z_n^2$. This way, for the (b) and (c) criteria (using appropriate weights) the calibration of the Lehrer model with the new parameters becomes a 1-dimensional search of k' . When the iterative search reaches convergence, the parameters k , ϕ_0 and x can be obtained as:

$$k = \frac{1}{b_0} \quad \phi_0 = \frac{b_1 + b_0}{k'b_0} \quad x = \frac{b_1}{b_1 + b_0} \quad (7.21)$$

7.2.5.6 Demas model using criterion (a)

The calibration of the Demas model requires the estimation of 4 parameters (ϕ_0 , x , k_1 and k_2), which would require a 4-dimensional search. By finding the zeros of the partials, ϕ_0 and x can be expressed as a function of k_1 and k_2 , and the calibration can be simplified to a 2-dimensional search. In order to generalize (for the case of criteria (b) and (c)) the formulation for the criterion (a) is derived including weights. The conditions $\partial E_{aw}/\partial\phi_0 = 0$ and $\partial E_{aw}/\partial x = 0$ provide ϕ_0 and x as:

$$x = \frac{S_{y\phi}S_{zy} - S_{yy}S_{z\phi}}{S_{zy}S_{z\phi} - S_{zz}S_{y\phi}} \quad \phi_0 = \frac{S_{z\phi}}{xS_{zz} + S_{zy}} \quad (7.22)$$

using the following definitions: $S_{z\phi} \equiv \sum_n w_n z_n \phi_n$; $S_{y\phi} \equiv \sum_n w_n y_n \phi_n$; $S_{zy} \equiv \sum_n w_n z_n y_n$; $S_{yy} \equiv \sum_n w_n y_n^2$; $S_{zz} \equiv \sum_n w_n z_n^2$, where w_n are the weights (that should be 1 for all the calibration data under the (a) criterion), and y_n and z_n are defined as:

$$y_n \equiv \frac{1}{1 + k_2 C_n} \quad z_n \equiv \frac{1}{1 + k_1 C_n} - \frac{1}{1 + k_2 C_n} \quad (7.23)$$

This way, the calibration of the Demas model using the (a) criterion consists in a 2-dimensional search of k_1 and k_2 .

7.2.5.7 Demas model using criteria (b) and (c)

The form of the partials of $C(\phi)$ with respect to the different parameters makes the parameter estimation difficult under criteria (b) and (c) for the Demas model, and a 4-dimensional search would be necessary. Since the calibration becomes a 2-dimensional search under the (a) criterion (independently of the applied weights), the (b) or (c) criteria could be approached by a calibration using the (a) criterion with appropriate weights. If the (b) criterion is approached with the weighted (a) criterion, the weights are given by:

$$E_{aw} = \sum w_n (\phi(C_n) - \phi_n)^2 \approx \sum_n (C(\phi_n) - C_n)^2 = E_b \quad (7.24)$$

and therefore the weights should be:

$$w_n = \left(\frac{SE(C)}{SE(\phi)} \right)^2 = \left| \frac{\partial C(\phi)}{\partial \phi} \Big|_{\phi_n} \right|^2 = \left| \frac{\partial \phi(C)}{\partial C} \Big|_{C_n} \right|^{-2} \quad (7.25)$$

where $SE(\cdot)$ represents standard error. Taking into account the function $\phi(C)$ for the Demas model, the weights approaching the (b) criterion are:

$$w_n = \left(\frac{\phi_0 x k_1}{(1 + k_1 C_n)^2} + \frac{\phi_0 (1-x) k_2}{(1 + k_2 C_n)^2} \right)^{-2} \quad (7.26)$$

Similarly, the weights to be applied with the (a) criterion for approaching the (c) criterion are:

$$w_n = \frac{1}{C_n^2} \left(\frac{\phi_0 x k_1}{(1 + k_1 C_n)^2} + \frac{\phi_0 (1-x) k_2}{(1 + k_2 C_n)^2} \right)^{-2} \quad (7.27)$$

This way, the procedure for calibrating the Demas model using criterion (b) or (c) under this approach would be a calibration using the weighted (a) criterion, and therefore, it would be a 2-dimensional search of k_1 and k_2 . Since the weights depend on the resulting parameters, in the iterative procedure the weights should be updated to the re-estimated parameters during the search under this approach. However, since the partial $\partial \phi(C)/\partial C$ is strongly constrained by the calibration data, the change of the weights during the iterations is very slight, and therefore this update is not critical for the convergence of the calibration.

7.2.5.8 Polynomial-exponent model using criteria (b) and (c)

The polynomial-exponent model requires the estimation of $(p+2)$ parameters for a p -th order polynomial (i.e. the polynomial coefficients a_0, \dots, a_p and the exponent α). The conditions $\partial E_{bw}/\partial a_i$ (with $i = 0, \dots, p$) constitute a linear equation system that can be written in the matrix form as $A \cdot \vec{a} = \vec{B}$, where the vector \vec{a} contains the coefficients and the elements of A and \vec{B} are:

$$A_{i,j} = \sum_n w_n \phi_n^{(i+j)\alpha} \quad B_i = \sum_n w_n C_n \phi_n^{i\alpha} \quad i, j = 0, \dots, p \quad (7.28)$$

Therefore, for a given value of α , the estimation of the polynomial coefficients is direct and just requires inverting the matrix A . The polynomial coefficients are obtained as $\vec{a} = A^{-1} \cdot \vec{B}$. This way, the calibration of the PE model using the (b) or (c) criteria becomes a 1-dimensional search of the parameter α , independently of the polynomial order p . Appropriate weights must be applied to implement criteria (b) or (c). The polynomial model is a particular case of PE, with constant exponent ($\alpha = -1$), and therefore the calibration of the polynomial model is a direct estimation of the polynomial coefficients.

7.2.5.9 Polynomial-exponent model using criterion (a)

Due to the non-linear behavior of $\phi(C)$ and its derivatives, the calibration of the PE model cannot be simplified under the (a) criterion. In this case, the calibration can be approached

using criterion (b) with appropriate weights. The weights to be applied to approach the (a) criterion are:

$$w_n = \left(\frac{SE(\phi)}{SE(C)} \right)^2 = (a_1 \alpha \phi_n^{\alpha-1} + 2 a_2 \alpha \phi_n^{2\alpha-1} + \dots + p a_p \alpha \phi_n^{p\alpha-1})^{-2} \quad (7.29)$$

and again, the calibration becomes a 1-dimensional search of α . Since the polynomial model can be considered a particular case of the PE model with a constant exponent ($\alpha = -1$), a direct estimation of the polynomial coefficients would be possible. However, in this case, the weights depend on the parameters, and an iterative procedure is recommended.

Therefore, according to the previous derivations, all the calibration procedures can be simplified to a direct estimation or a 1-dimensional search, with the exception of the Demas model, which can be simplified to a 2-dimensional search. In order to achieve these simplifications, the estimation procedures for some models and criteria are based on estimations with other criteria using appropriate weights.

7.3 Experimental

The versatility and accuracy of the proposed model as well as the importance of the calibration criteria have been demonstrated with 25 real experiments previously published by our research group [23–25]. Supporting Information (ESI) shows a detailed description of the 25 experiments (see section B.1). They are based on 7 different oxygen-sensitive sensing phases: PtTFPP - PS (Platinum(II) 5, 10, 15, 20 - meso - tetrakis - (2, 3, 4, 5, 6 - pentafluorophenyl) - porphyrin immobilized in polystyrene) [23], N969-AP200/19 ([Ir(2 - (2, 4 - difluorophenyl) pyridine)₂(4, 4' - dimethylamino - 2, 2' - bipyridine)] (PF6) immobilized into AP200/19 nanostructured aluminium oxide-hydroxide solid support) [24, 25], EB146 - AP200/19 (Ir(2 - (2, 4 - difluoro - 3 - methylesterphenyl) pyridine)₂(4 - (N, N - dimethylamino) picolinate) immobilized into AP200/19) [24, 25], EB146-PSOX (Ir(2 - (2, 4 - difluoro - 3 - methylesterphenyl) pyridine)₂(4 - (N, N - dimethylamino) picolinate) immobilized in polystyrene) [24], N1008-PSOX ([Ir(2 - (2, 4 - difluorophenyl) pyridine)₂(4, 7 - diphenyl - 1, 10 - phenanthroline)](PF6) immobilized into a polystyrene membrane) [24], PtTFPP-AP200/19 (Platinum(II) 5, 10, 15, 20 - meso - tetrakis - (2, 3, 4, 5, 6 - pentafluorophenyl) - porphyrin) immobilized into AP200/19) [25] and N1008 - AP200/19 ([Ir(2 - (2, 4 - difluorophenyl) pyridine)₂(4, 7 - diphenyl - 1, 10 - phenanthroline)](PF6) immobilized into AP200/19) [25]. The sensing phases have been calibrated and tested between several oxygen concentrations: 0.5-20 kPa O₂ (11 experiments), 1.0-10 kPa O₂ (4 experiments), 0.25-10 kPa O₂ (8 experiments) or 0.25-20 kPa O₂ (2 experiments). Experiments involve either luminescence emission intensity or luminescence lifetime as analytical signals: luminescence emission intensity was measured with a Varian Cary-Eclipse luminescence spectrometer (in 4 experiments) [24], luminescence lifetime was estimated from phase-shift (in 16 experiments) and modulation factor (in 5 experiments). Phase shift and modulation factor were measured by phase-resolved luminescence spectroscopy in the frequency domain using a measuring system based on the I/Q method [23] (in 13 experiments) or using a commercial dual-phase lock-in amplifier (LIA) (SR830, Stanford Research Systems) [25] (in 8 experiments).

For each experiment, the analytical signal was obtained at different oxygen concentrations

Table 7.2: Calibration results of experiment 1 for each model and criteria.

Stern-Volmer (SV)				Lehrer (L)				2 nd order Polynomial (P2)			
Parameter	(a)	(b)	(c)	Parameter	(a)	(b)	(c)	Parameter	(a)	(b)	(c)
τ_0 (μs)	55.03	46.27	55.84	τ_0 (μs)	58.61	52.06	58.24	a_0	-1.884	-3.098	-2.054
k (kPa^{-1})	0.2924	0.2050	0.2948	k (kPa^{-1})	0.4323	0.2941	0.4062	a_1	93.35	153.8	104.9
–	–	–	–	x	0.9281	0.9606	0.9393	a_2	1165	574.2	1008
R^2	0.9932	0.9933	0.9876	R^2	0.9993	0.9976	0.9980	R^2	0.9997	0.9979	0.9989
RMSE	1.0884	0.5203	11.121	RMSE	0.3504	0.3112	4.4750	RMSE	0.2415	0.2910	3.3063
iterations	100	1	1	iterations	100	100	100	iterations	100	1	1
Φ_0 (μs)	55.03	46.27	55.84	Φ_0 (μs)	58.61	52.06	58.24	Φ_0 (μs)	59.88	53.14	59.34
K (kPa^{-1})	0.2924	0.2050	0.2948	K (kPa^{-1})	0.4013	0.2825	0.3816	K (kPa^{-1})	0.4527	0.3029	0.4274
1 st order Polynomial-Exp. (PE1)				2 nd order Polynomial-Exp. (PE2)				Demas (D)			
Parameter	(a)	(b)	(c)	Parameter	(a)	(b)	(c)	Parameter	(a)	(b)	(c)
a_0	-1.3193	-2.1988	-1.4135	a_0	-1.0293	-0.7319	-0.9783	τ_0 (μs)	61.35	78.71	61.71
a_1	643.9	410.5	581.7	a_1	1221	1994	1362	k_1 (kPa^{-1})	0.6433	2.1112	0.6838
α	-1.5066	-1.3069	-1.4677	a_2	-11959	-41258	-16300	k_2 (kPa^{-1})	0.0613	0.1194	0.0699
–	–	–	–	α	-1.7113	-1.8863	-1.7478	x	0.7834	0.6510	0.7594
R^2	0.9998	0.9984	0.9993	R^2	0.9999	0.9997	0.9998	R^2	0.9999	0.9993	0.9997
RMSE	0.1921	0.2578	2.5604	RMSE	0.1444	0.1148	1.5248	RMSE	0.1498	0.1693	1.7521
iterations	100	100	100	iterations	100	100	100	iterations	500	500	500
Φ_0 (μs)	60.88	54.67	60.44	Φ_0 (μs)	62.28	65.98	62.59	Φ_0 (μs)	61.35	78.71	61.71
K (kPa^{-1})	0.5031	0.3480	0.4820	K (kPa^{-1})	0.5725	0.7299	0.5900	K (kPa^{-1})	0.5173	1.4161	0.5361

(at least 25 measurements were registered at each concentration level, and the average was estimated after removal of outliers). These measurements were divided into two datasets: one was used for calibration and the other for test; the oxygen concentrations used for calibration and test were always disjunct.

7.4 Results and discussion

7.4.1 Calibration results

The calibration of the different models for criteria (a), (b) and (c) was performed using calibration data, according to the previously described procedures. The models requiring a 1-dimensional search (including the P2 model with the (a) criterion) were calibrated with 100 iterations (even though convergence is reached in the first iterations). The Demas models were calibrated with 500 iterations since these calibrations require a 2-dimensional search. ESI (section B.1) shows the calibration results of the 25 experiments for each model and criteria as well as the response at null concentration (Φ_0) and the sensitivity (K). These results have been exemplified in the manuscript with the results of experiment 1 (see Table 7.2). This table shows the calibrated parameters, the determination coefficient R^2 , and the root mean square error (RMSE). Note that RMSE is expressed in degrees for criterion (a), in kPa for criterion (b) and in relative error (%) for criterion (c).

It is possible to say that all the calibration procedures provide appropriate results. As the

Table 7.3: Root mean square error (RMSE) when the models are calibrated and evaluated with criterion (c): RMS relative error in pO_2 (expressed in %). Analytical signals: τ_ϕ (apparent lifetime estimated from phase-shift), τ_m (apparent lifetime estimated from modulation factor), I (luminescence intensity).

Exper. / sensing phase / signal			RMS relative error in pO_2 (%). Calibration criterion: (c)											
			Calibration data						Test data					
			SV	L	P2	PE1	PE2	D	SV	L	P2	PE1	PE2	D
1	PtTFPP/PS	τ_ϕ	11.12	4.47	3.31	2.56	1.52	1.75	11.09	5.51	4.49	3.76	2.41	2.67
2	PtTFPP/PS	τ_m	8.67	1.46	0.67	0.56	0.34	0.35	9.45	3.36	2.61	2.02	2.23	2.19
3	PtTFPP/PS	τ_ϕ	19.28	3.66	1.13	0.75	0.43	0.42	18.29	3.66	1.07	0.89	0.83	0.87
4	PtTFPP/PS	τ_m	8.77	3.06	2.29	1.12	0.64	0.34	8.48	3.11	2.36	1.29	0.75	0.63
5	PtTFPP/PS	τ_ϕ	18.04	3.62	0.87	0.86	0.64	0.32	17.19	3.51	0.67	0.67	0.60	0.58
6	PtTFPP/PS	τ_m	6.85	1.60	1.13	0.74	0.74	0.58	6.60	1.72	1.27	0.82	0.81	0.71
7	PtTFPP/PS	τ_ϕ	14.71	3.79	1.41	1.04	1.01	0.53	14.11	3.81	1.51	1.08	0.98	0.73
8	PtTFPP/PS	τ_m	8.65	1.53	0.93	1.25	0.86	0.78	8.27	1.69	1.16	1.36	1.10	1.03
9	PtTFPP/PS	τ_ϕ	15.92	2.69	0.75	1.22	0.51	0.32	15.14	2.78	0.78	1.09	0.75	0.71
10	PtTFPP/PS	τ_m	7.85	1.50	1.32	1.85	1.30	1.28	7.57	1.53	1.35	1.79	1.34	1.32
11	PtTFPP/PS	τ_ϕ	15.69	1.51	1.93	2.44	1.26	0.43	15.27	1.98	1.30	1.70	0.77	0.86
12	N969-AP200/19	I	7.93	1.73	1.54	1.52	1.51	1.61	7.08	1.43	1.18	1.12	1.14	1.22
13	EB146-AP200/19	I	9.67	1.52	0.57	0.59	0.54	0.59	8.49	2.19	1.56	1.42	1.50	1.47
14	EB146-PS0X	I	4.86	1.19	1.40	0.94	0.92	0.92	4.69	0.78	1.06	0.35	0.27	0.30
15	N1008-PS0X	I	6.37	0.37	0.92	0.44	0.12	0.15	6.22	0.65	1.17	0.24	0.38	0.39
16	PtTFPP-AP200/19	τ_ϕ	24.05	6.74	2.36	2.40	2.36	1.93	21.47	3.95	4.14	4.49	4.14	3.97
17	N969-AP200/19	τ_ϕ	30.70	5.96	4.84	2.16	1.58	1.24	32.44	7.14	4.60	2.22	2.03	2.18
18	N1008-AP200/19 (repl. 1)	τ_ϕ	30.86	5.59	3.85	1.25	1.25	2.06	31.97	6.82	4.45	1.82	1.83	2.04
19	N1008-AP200/19 (repl. 2)	τ_ϕ	30.94	5.65	3.96	1.77	1.77	2.52	31.38	6.65	5.15	2.65	2.65	2.57
20	N1008-AP200/19 (repl. 3)	τ_ϕ	29.12	5.21	3.24	1.62	1.60	2.32	29.86	5.81	4.10	1.87	1.91	2.07
21	EB146-AP200/19 (repl. 1)	τ_ϕ	28.67	2.77	6.49	4.25	2.89	1.55	29.73	6.60	4.74	3.69	3.50	4.94
22	EB146-AP200/19 (repl. 2)	τ_ϕ	30.17	4.99	8.95	6.09	4.86	3.75	30.46	8.08	5.51	5.87	5.83	6.82
23	EB146-AP200/19 (repl. 3)	τ_ϕ	29.20	5.49	7.55	5.24	4.33	3.74	30.55	8.21	4.01	4.88	5.29	6.28
24	PtTFPP/PS	τ_ϕ	19.66	5.19	1.65	1.65	1.65	1.08	17.98	3.97	1.04	1.02	1.10	1.04
25	PtTFPP/PS	τ_ϕ	9.79	1.89	1.34	1.73	1.32	1.27	8.27	1.41	2.00	3.00	2.14	2.19
Average			17.10	3.33	2.58	1.84	1.44	1.27	16.88	3.85	2.53	2.05	1.85	1.99

complexity of the model increases, the calibration becomes more accurate (providing a higher R^2 and a lower RMSE). In general, the 3 parameter models (L, P2, PE1) are more accurate than the SV model, and the 4 parameter models (PE2 and D) are more accurate than the 3 parameter ones. In this particular experiment, the best models for 3 and 4 parameters are, respectively, PE1 and PE2. It is also remarkable that different calibration criteria provide different model parameters. In the case of simpler models, the differences among criteria can be seen in the calibration curves (in ESI, section B.1). The parameters Φ_0 and K are in the same range for different models and criteria, with the exception of SV and D models when calibrated with the (b) criterion. However, it should be noted that Φ_0 and K are estimated as a limit at $C \rightarrow 0$ with a parametric fitting using calibration data in a range which does not include the null concentration, and therefore, the criterion (b) is the least appropriate for estimating these parameters.

7.4.2 Evaluation of models

In order to compare different models, each one has been evaluated in terms of the RMSE. Depending on the purpose of the calibration, the error to be minimized is selected according to some criterion, and the evaluation should compare the RMSE defined consistently with this criterion. For example, if the model is calibrated in the context of an instrument for measuring concentration aimed to operate in a wide range of concentrations, the (c) criterion is the most recommendable, and the evaluation should compare the RMSE defined in terms of relative error in concentration.

Table 7.3 represents the RMS relative error of pO_2 (in %) for the 25 experiments using the different models calibrated with the (c) criterion. Similar tables (with RMSE for calibration and test data) for criteria (a) and (b) can be found in ESI (section B.2). The RMS relative error is evaluated using both the calibration and test data. The typical behavior is that RMSE decreases for more complex models. The last line shows the RMSE averaged for all the experiments. Taking into account the averaged RMSE for calibration data, the best 3 parameter model is PE1 (even though for some particular experiments P2 or L models perform better), and the best 4 parameter model is D (even though sometimes PE2 performs better). The RMSE estimated with the test data shows similar results than for calibration data for the 2 and 3 parameter models. However, results with the 4 parameter models are significantly worse compared with those using calibration data. This reveals some degree of over-fitting of the Demas model and PE2 to the calibration data. Over-fitting is more important in the Demas model, and PE2 results with test data are slightly better than those for the Demas model. It is also remarkable that PE1 model shows a RMSE that is closer to the PE2 or Demas models than to the other 3 parameter models.

Table 7.4 contains the RMSE averaged for the 25 experiments for all models and criteria using calibration and test data. In the case of the (a) criterion, only the experiments involving the luminescence lifetime as analytical signal were included (in order to obtain a coherent average). The behavior of the RMSE for criteria (a) and (b) is similar to that described for criterion (c): On one hand, PE1 performs significantly better than SV, L or P2 for both calibration and test data, and its accuracy is closer to that of PE2 or D models. On the other hand, D performs significantly better than PE2 with calibration data, but similarly with test data.

Table 7.4: RMSE averaged for the 25 experiments, using different models and calibration criteria. RMSE evaluated from calibration (calib.) and test data.

Evaluation criterion			SV	L	P2	PE1	PE2	D
RMS error in τ (μs)*	(a)	calib.	0.859	0.153	0.088	0.087	0.059	0.048
RMS error in τ (μs)*	(a)	test	0.822	0.167	0.106	0.101	0.080	0.080
RMS error in pO_2 (kPa)	(b)	calib.	0.726	0.145	0.121	0.091	0.068	0.064
RMS error in pO_2 (kPa)	(b)	test	0.586	0.174	0.147	0.139	0.139	0.136
RMS relat. error in pO_2 (%)	(c)	calib.	17.10	3.328	2.576	1.843	1.439	1.273
RMS relat. error in pO_2 (%)	(c)	test	16.88	3.854	2.532	2.045	1.851	1.993

*For the (a) criterion, only the 21 experiments using luminescence lifetime as analytical signal were considered.

Table 7.5: Relative degradation associated to over-fitting (D_{OF}) for different models and criteria when $RMSE_{test}$ is compared with $RMSE_{cal}$.

critereon	SV	L	P2	PE1	PE2	D
(a)	-0.043	0.094	0.198	0.163	0.347	0.681
(b)	-0.192	0.202	0.219	0.520	1.052	1.124
(c)	-0.013	0.158	-0.017	0.110	0.287	0.566

7.4.3 Complexity of the model and over-fitting

The model complexity is one important aspect to be considered when a model is used to represent the relationship between the analytical signal and the concentration. Most of the models can usually increase the complexity by including new parameters. That is the case of the Demas model, which can be extended to more than 2 sites, or the PE model, which can be extended to an arbitrary polynomial order. Increasing the number of parameters reduces the RMSE for the calibration data (in fact, if the number of parameters to be calibrated is equal to the number of points in the calibration dataset, the calibration RMSE is expected to be null). However, reducing the error in the calibration data does not always imply an improvement in the model, and sometimes the RMSE estimated from a test dataset (i.e. with data different to those used for calibration) increases because of an over-fitting of the model parameters to the calibration data.

In order to evaluate the degree of over-fitting, we have defined the relative degradation D_{OF} when RMSE from test data is compared with RMSE from calibration data:

$$D_{OF} = \frac{RMSE_{test} - RMSE_{cal}}{RMSE_{cal}} \quad (7.30)$$

This relative degradation can be estimated for different criteria (i.e., using the appropriate RMSE according to criteria (a), (b) or (c)). Table 7.5 shows the relative degradation resulting from the averaged RMSE values in table 7.4. This table shows that more complex models (i.e. including more parameters) degrades more than simpler models, in the sense that test RMSE significantly increases with respect to calibration RMSE. Demas model is strongly affected by over-fitting, as well as PE2 when it is calibrated with criterion (b). The SV (and the P2 for the (c) criterion) shows a negative degradation index (i.e. better RMSE for test data than for calibration data). This is because the range of test data is always included in the range of calibration data, and when the model does not properly represent the function $C(\phi)$ or $\phi(C)$, the errors tends to be greater in the limits of the interval. According to tables 7.4 and 7.5, the most recommendable model (in average for the 25 experiments and with the considered size in the calibration datasets) would be PE2 when using criteria (a) and (c) and PE1 for criterion (b). However, if more data were considered in the calibration dataset, more complex models could be considered to achieve the best accuracy. In that sense, the scalability of the PE- p model (that always requires a 1-dimensional search) is a promising solution for adapting the model complexity to the available calibration dataset.

Table 7.6: RMSE averaged for the 25 experiments, for each model and criterion. For each model, the criteria used for calibration are in different columns; the criteria used for evaluation are in different rows. RMSE evaluated with calibration and test data.

Calibration data	SV			L			P2			PE1			PE2			D		
	(a)	(b)	(c)	(a)	(b)	(c)	(a)	(b)	(c)	(a)	(b)	(c)	(a)	(b)	(c)	(a)	(b)	(c)
RMSE τ (μs)*	0.86	2.26	0.94	0.15	0.61	0.18	0.09	0.33	0.10	0.09	0.27	0.09	0.06	0.23	0.06	0.05	0.15	0.05
RMSE pO_2 (kPa)	1.54	0.73	1.60	0.56	0.15	0.26	0.27	0.12	0.20	0.19	0.09	0.13	0.14	0.07	0.10	0.11	0.06	0.09
RMSE relat. pO_2 (%)	33.0	94.6	17.1	4.80	13.8	3.33	3.00	10.1	2.58	2.15	4.99	1.84	1.64	3.68	1.44	1.40	3.42	1.27
Test data	SV			L			P2			PE1			PE2			D		
	(a)	(b)	(c)	(a)	(b)	(c)	(a)	(b)	(c)	(a)	(b)	(c)	(a)	(b)	(c)	(a)	(b)	(c)
RMSE τ (μs)*	0.82	1.54	0.96	0.17	0.38	0.21	0.11	0.24	0.12	0.10	0.19	0.11	0.08	0.14	0.08	0.08	0.12	0.08
RMSE pO_2 (kPa)	1.19	0.59	1.28	0.45	0.17	0.26	0.17	0.15	0.13	0.14	0.14	0.12	0.14	0.14	0.13	0.16	0.14	0.14
RMSE relat. pO_2 (%)	16.5	34.6	16.9	4.91	5.06	3.85	2.56	4.96	2.53	2.02	3.03	2.05	1.94	2.61	1.85	2.24	2.56	1.99

*For the (a) criterion, only the 21 experiments using luminescence lifetime as analytical signal were considered.

7.4.4 Comparison of different calibration criteria

The comparison of the model parameters resulting from calibration with different criteria shows the relevance of the criterion selected for calibration. In order to understand the role of the calibration criterion, the models calibrated with each criterion were evaluated taking into account the RMSE corresponding to analytical signal error (either intensity or luminescence lifetime), the concentration error (in kPa) and the relative concentration error (in %), i.e. using the RMSE consistent to different criteria.

For each one of the 25 experiments, the models SV, L, P2, PE1, PE2 and D have been calibrated according to criteria (a), (b) and (c), and each model calibrated with each criterion has been evaluated in terms of the three definitions of RMSE (i.e., RMSE consistent with criteria (a), (b) and (c)). So, for each model, there is a 3×3 table of RMSE results, a column for each calibration criterion and a row for RMSE defined according to each evaluation criterion. These 3×3 tables for each model and experiment are available in ESI (section B.1) for both calibration and test data. Table 7.6 presents the average for all the experiments (since the analytical signal is luminescence lifetime only for 21 experiments, the averages for the RMSE errors based on criterion (a) were estimated only from these experiments).

When the 3×3 table of RMSE results for each model is analyzed, the results in a row can be compared among them (a row compares a RMSE estimated with the same criterion and expressed in the same units), and the element showing the minimum error indicates which is the most appropriate calibration criterion for minimizing such RMSE. As can be seen in Table 7.6 (and in ESI for each particular experiment), for calibration data the minimum RMSE is always reached for the elements in the diagonal of each 3×3 table, i.e. when the calibration criterion match the evaluation criterion. This tendency is also observed for test data (even though it is not verified in some particular experiments for some models due to the statistical error affecting the calibration and test data). This result indicates that calibration criterion should be selected consistently with the purpose of the calibration (i.e. if we are concerned about the error in phase-shift, the error in concentration or the relative error in concentration, the calibration should use criteria (a), (b) or (c), respectively). On

the other hand, the differences in the resulting RMSE errors show the importance of selecting the appropriate criterion and the impact of using a non appropriate criterion.

7.5 Conclusions

In this paper we propose a new model for describing the relationship between the analytical signal and the analyte concentration in chemical sensors based on photoluminescence. This model represent the concentration C as a p -th order polynomial of ϕ^α , where ϕ is the analytical signal and α is an exponent to be fitted. The proposed model can be considered an extension of the Stern-Volmer model (it is identical to the Stern-Volmer model for $p = 1$ and $\alpha = -1$). We provide an easy calibration procedure of the model for different calibration criteria: the calibration procedure becomes a 1-dimensional search independently of the polynomial order. The proposed model (for order 1 and 2) has been compared with other models in 25 experiments of photoluminescence with disjoint datasets for calibration and test and using different calibration criteria. The proposed model provides the best trade-off between accuracy and complexity: the PE1 model (with only 3 parameters) provide an accuracy that is closer to the 4 parameter models than to the 3 parameter models. The PE2 model (with 4 parameters) provides similar results (for the test data) than the Demas model (also with 4 parameters) but with significantly lower over-fitting. Additionally, the proposed model can easily be scaled to a higher polynomial order in the case when more calibration data are available, because calibration procedure is a 1-dimensional search independently of the polynomial order.

Even though the parameters of the proposed model do not have a direct physical interpretation, the response of the model at null concentration Φ_0 and the sensitivity K can be derived from the model parameters. Appropriate formulas are provided for Φ_0 and K , and consistent results are observed when these parameters estimated for the proposed model are compared to those from other existing models.

If we consider particular experiments, the model that best fit concentration and analytical signal data changes from one experiment to other (sometimes Demas performs better than PE2, sometimes PE2 is better than Demas). In this sense, the proposed model can be considered as an alternative to Demas model. The model to be applied to fit the data should be the simplest one providing the best accuracy with the lowest degradation between calibration and test, and the optimal model (regarding model family and number of parameter) could change among different photoluminescence experiments.

The experimental results presented in this paper also show the importance of the calibration criterion. For each model, different criteria provides different model parameters, since calibration criteria determines the definition of the error to be minimized. The optimal fitting for a given criterion is reached when the calibration is performed consistently with the criterion. We have considered three different calibration criteria in this work: minimization of the square error in the analytical signal (a), minimization of the square error in concentration (b) and minimization of the square relative error in the concentration (c). Criterion (a) is appropriate for the study of photoluminescence; criteria (b) and (c) are more appropriate for instrumentation oriented to concentration measurements. In the last case, criterion (c) is

preferable when the instrument is intended to measure concentrations in a wide range.

In the paper, we provide a generic procedure for calibration of the different models and criteria, and simplifications particularized to each case (taking into account the functions involved in the minimization). ESI contains details for the implementation of the calibration procedures and code (compatible with MATLAB and Octave) that provide the calibration for each model and criterion.

Acknowledgments

The authors gratefully acknowledge the financial support of the Spanish Ministry of Economy and Competitiveness (Projects CTQ2008-01394 and CTQ2011-25316, and Medina-Rodríguez's grant, reference BES-2009-026919) and the Regional Government of Andalusia (Excellence projects P07-FQM-2625 and P07-FQM-2738).

Appendix. Electronic Supporting Information (ESI)

Electronic Supporting Information (ESI) available: [(A) complementary mathematical formulation related to the models, criteria and calibration procedures; (B) detailed experimental results for the 25 experiments included in the study; and (C) MATLAB/Octave code implementing calibration and evaluation for all the models and criteria considered in this study (also available in file Photoluminescence_models.zip)]. See DOI: 10.1039/b000000x/.

References

- [1] Papkovsky, D. B. In *Methods Enzymology*; Sen, C. K., Semenza, G. L., Eds., 2004; Vol. 383, pp 715-734.
- [2] Ogurtsov, V. I.; Papkovsky, D. B. *Sensors and Actuators B-Chemical* **2006**, *113*, 917-929.
- [3] Demas, J. N.; DeGraff, B. A.; Xu, W. *Analytical Chemistry* **1995**, *67*, 1377-1380.
- [4] Demas, J. N.; DeGraff, B. A. *Sensors and Actuators B: Chemical* **1993**, *11*, 35-41.
- [5] Ogurtsov, V. I.; Papkovsky, D. B.; Papkovskaia, N. Y. *Sensors and Actuators B-Chemical* **2001**, *81*, 17-24.
- [6] Hawkins, D. M. *Journal of Chemical Information and Computer Sciences* **2004**, *44*, 1-12.
- [7] Faber, N. M.; Rajkó, R. *Analytica Chimica Acta* **2007**, *595*, 98-106.
- [8] Fletcher, R. *Practical Methods of Optimization*, Second Edition ed.; JOHN WILEY & SONS, 2008.

- [9] Lakowicz, J. R. *Principles of Fluorescence Spectroscopy*, 2nd ed.; Kluwer Academic: New York, 1999.
- [10] Wolfbeis, O. S. *Fiber Optic Chemical Sensors and Biosensors* CRC Press: Boca Raton, MA, 1991.
- [11] Lehrer, S. *Biochemistry* **1971**, *10*, 3254-3263.
- [12] Eftink, M. R.; Ghiron, C. A. *Biochemistry* **1976**, *15*, 672-680.
- [13] Carraway, E. R.; Demas, J. N.; DeGraff, B. A.; Bacon, J. R. *Analytical Chemistry* **1991**, *63*, 337-342.
- [14] Draxler, S.; Lippitsch, M. E.; Klimant, I.; Kraus, H.; Wolfbeis, O. S. *The Journal of Physical Chemistry* **1995**, *99*, 3162-3167.
- [15] Mills, A. *Sensors and Actuators B: Chemical* **1998**, *51*, 69-76.
- [16] Mills, A. *Analyst* **1999**, *124*, 1301-1307.
- [17] Bossi, M. L.; Daraio, M. E.; F. Aramendía, P. *Journal of Photochemistry and Photobiology A: Chemistry* **1999**, *120*, 15-21.
- [18] Ogurtsov, V. I.; Papkovsky, D. B. *Sensors and Actuators B-Chemical* **2003**, *88*, 89-100.
- [19] Badocco, D.; Mondin, A.; Fusar, A.; Pastore, P. *Journal of Physical Chemistry C* **2009**, *113*, 20467-20475.
- [20] Trettnak, W.; Gruber, W.; Reiningger, F.; Klimant, I. *Sensors and Actuators B: Chemical* **1995**, *29*, 219-225.
- [21] Korn, G. A.; T.M.Korn *Mathematical Handbook for Scientists and Engineers*, 1968.
- [22] Himmelblau, D. M. *Process Analysis by Statistical Methods*; Wiley: New York, 1970.
- [23] Medina-Rodríguez, S.; de la Torre-Vega, A.; Fernández-Sánchez, J. F.; Fernández-Gutiérrez, A. *Sensors and Actuators B: Chemical* **2013**, *176*, 1110-1120.
- [24] Marín-Suárez del Toro, M.; Fernández-Sánchez, J. F.; Baranoff, E.; Nazeeruddin, M. K.; Graetzel, M.; Fernández-Gutiérrez, A. *Talanta* **2010**, *82*, 620-626.
- [25] Medina-Rodríguez, S.; Marín-Suárez, M.; Fernández-Sánchez, J. F.; de la Torre-Vega, A.; Baranoff, E.; Fernández-Gutiérrez, A. *Analyst* **2013**, *138*, 4607-4617.

Appendix. Electronic Supporting Information (ESI)

On the calibration of chemical sensors based on photoluminescence: Selecting the appropriate model and criterion

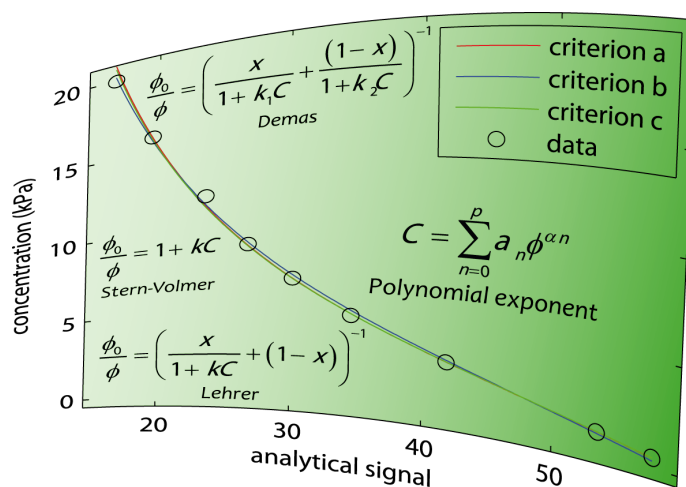
Santiago Medina Rodríguez^{a,b}, Ángel de la Torre Vega^{a,*}, Jorge Fernando Fernández Sánchez^{b,*} and Alberto Fernández Gutiérrez^b

^aDepartment of Signal Theory, Networking and Communications, CITIC-UGR, University of Granada, C/ Periodista Rafael Gómez 2, E-18071 Granada, Spain.

^bDepartment of Analytical Chemistry, Faculty of Sciences, University of Granada, Avda. Fuentenueva s/n, E-18071 Granada, Spain.

Table of Contents

- Graphical abstract of the manuscript.
- Supporting Information.



Graphical abstract of the manuscript

Electronic Supporting Information

On the calibration of chemical sensors based on photoluminescence: Selecting the appropriate model and criterion

Santiago Medina-Rodríguez^{a,b}, Ángel de la Torre-Vega^{a,*},
Jorge Fernando Fernández-Sánchez^{b,*} and Alberto Fernández-Gutiérrez^b

^aDepartment of Signal Theory, Networking and Communications, CITIC-UGR, University of Granada, C/ Periodista Rafael Gómez 2, E-18071 Granada, Spain.

^bDepartment of Analytical Chemistry, Faculty of Sciences, University of Granada, Avda. Fuentenueva s/n, E-18071 Granada, Spain.

*Corresponding authors. Tel.: +34 958 240451; fax: +34 958243328. E-mail: atv@ugr.es (A. de la Torre-Vega); jffernan@ugr.es (J.F. Fernández-Sánchez).

Contents

A	Complementary mathematical formulation	2
A.1	Relationship between the 1st order Polynomial-Exponential (PE1) model and the Stern-Volmer (SV) model	2
A.2	$C(\phi)$ and $\phi(C)$ for different models	2
A.3	Sensitivity and response at null concentration	3
A.4	Generic calibration procedure	4
A.5	Calibration formulas for different models and criteria	5
A.5.1	Stern-Volmer model using criterion (a)	5
A.5.2	Stern-Volmer model using criteria (b) and (c)	5
A.5.3	Lehrer model using criterion (a)	6
A.5.4	Lehrer model using criteria (b) and (c)	6
A.5.5	Demas model using criterion (a)	7
A.5.6	Polynomial-Exponent model using criteria (b) and (c)	8
B	Detailed experimental results	9
B.1	Calibration and evaluation results for each experiment	9
B.2	Summary of evaluation results with criteria (a) and (b)	60
C	Software implementation for model calibration and evaluation	61
C.1	Contents of the directory	61
C.2	Help and examples	62
C.3	How to use functions and scripts	62
C.4	Compatibility MATLAB/Octave	62
C.5	Authors of the software	63
C.6	Files included in the directory PHOTOLUMINESCENCE_MODELS	63
C.6.1	Functions for model calibration	64
C.6.2	Functions for model evaluation	77
C.6.3	Function for performing a complete study	79
C.6.4	Scripts for model calibration and evaluation	86
C.6.5	Some data files with input data for calibration/test, and output data from scripts	90

Appendix A

Complementary mathematical formulation

A.1 Relationship between the 1st order Polynomial-Exponential (PE1) model and the Stern-Volmer (SV) model

The 1st order polynomial-exponent (PE1) model describes the concentration as a function of the analytical signal as:

$$C = a_0 + a_1\phi^\alpha \quad (\text{A.1})$$

This equation can be written as:

$$\frac{-a_1/a_0}{\phi^{-\alpha}} = 1 - \frac{1}{a_0}C \quad (\text{A.2})$$

and with appropriate definitions, the PE1 model can be rewritten as:

$$\left(\frac{\phi_0}{\phi}\right)^{-\alpha} = 1 + kC \quad \left(\begin{array}{l} \phi_0^{-\alpha} \equiv -a_1/a_0 \\ k \equiv -1/a_0 \end{array}\right) \quad (\text{A.3})$$

i.e., the PE1 model can be considered an extension of the Stern-Volmer model where an exponent $-\alpha$ is included in the left-hand side. The Stern-Volmer model can therefore be considered a particular case of PE1 model (for $\alpha = -1$) and one could expect that the calibration of PE1 model provides a value of α around -1 .

A.2 $C(\phi)$ and $\phi(C)$ for different models

The mathematical formulas describing the models are rather simple in some ones and more complicated in some others. This section provides mathematical expressions for $C(\phi)$ and $\phi(C)$ for each model included in this study, since these expressions are required in some derivations.

Stern-Volmer model (SV)

$$\frac{\phi_0}{\phi} = 1 + kC \quad \Rightarrow \quad \phi(C) = \frac{\phi_0}{1 + kC} \quad C(\phi) = \frac{1}{k} \left(\frac{\phi_0}{\phi} - 1 \right) \quad (\text{A.4})$$

Lehrer model (L)

$$\frac{\phi_0}{\phi} = \left(\frac{x}{1 + kC} + (1 - x) \right)^{-1} \quad \Rightarrow \quad \phi(C) = \phi_0 \left(\frac{x}{1 + kC} + (1 - x) \right) \quad C(\phi) = \frac{\phi_0 - \phi}{k\phi - k\phi_0 + xk\phi_0} \quad (\text{A.5})$$

Demas model (D)

$$\frac{\phi_0}{\phi} = \left(\frac{x}{1 + k_1C} + \frac{(1-x)}{1 + k_2C} \right)^{-1} \quad \Rightarrow \quad \phi(C) = \phi_0 \left(\frac{x}{1 + k_1C} + \frac{(1-x)}{1 + k_2C} \right)$$

$$C(\phi) = \frac{-b + \sqrt{b^2 - 4ac}}{2a} \quad \text{where: } \begin{cases} a = k_1k_2\phi \\ b = (k_1 + k_2)\phi - (1-x)k_1\phi_0 - xk_2\phi_0 \\ c = \phi - \phi_0 \end{cases} \quad (\text{A.6})$$

1st order polynomial-exponent model (PE1)

$$C(\phi) = a_0 + a_1\phi^\alpha \quad \phi(C) = \left(\frac{C - a_0}{a_1}\right)^{1/\alpha} \quad (\text{A.7})$$

2nd order polynomial-exponent model (PE2)

$$C(\phi) = a_0 + a_1\phi^\alpha + a_2\phi^{2\alpha} \quad \phi(C) = \left(\frac{-a_1 + \sqrt{a_1^2 - 4a_2(a_0 - C)}}{2a_2}\right)^{1/\alpha} \quad (\text{A.8})$$

2nd order polynomial model (P2)

$$C(\phi) = a_0 + a_1\phi^{-1} + a_2\phi^{-2} \quad \phi(C) = \left(\frac{-a_1 + \sqrt{a_1^2 - 4a_2(a_0 - C)}}{2a_2}\right)^{-1} \quad (\text{A.9})$$

A.3 Sensitivity and response at null concentration

The response at null concentration Φ_0 and the sensitivity K are defined, respectively as:

$$\Phi_0 \equiv \lim_{C \rightarrow 0} \phi(C) \quad K \equiv \lim_{C \rightarrow 0} \frac{1}{\phi(C)} \left| \frac{\partial \phi(C)}{\partial C} \right| = \lim_{C \rightarrow 0} \frac{1}{\Phi_0} \left| \frac{\partial \phi(C)}{\partial C} \right| = \lim_{C \rightarrow 0} \frac{1}{\Phi_0} \left| \frac{\partial C(\phi)}{\partial \phi} \right|^{-1} \quad (\text{A.10})$$

From these definitions, Φ_0 and K can be derived.

Stern-Volmer model (SV)

$$\phi(C) = \frac{\phi_0}{1 + kC} \quad \frac{\partial \phi(C)}{\partial C} = \frac{-\phi_0 k}{(1 + kC)^2} \quad (\text{A.11})$$

$$\Phi_0 = \lim_{C \rightarrow 0} \frac{\phi_0}{1 + kC} = \phi_0 \quad K = \lim_{C \rightarrow 0} \frac{1}{\phi_0} \left| \frac{-\phi_0 k}{(1 + kC)^2} \right| = k \quad (\text{A.12})$$

Lehrer model (L)

$$\phi(C) = \phi_0 \left(\frac{x}{1 + kC} + (1 - x) \right) \quad \frac{\partial \phi(C)}{\partial C} = \frac{-\phi_0 k x}{(1 + kC)^2} \quad (\text{A.13})$$

$$\Phi_0 = \lim_{C \rightarrow 0} \phi_0 \left(\frac{x}{1 + kC} + (1 - x) \right) = \phi_0 \quad K = \lim_{C \rightarrow 0} \frac{1}{\phi_0} \left| \frac{-\phi_0 k x}{(1 + kC)^2} \right| = k x \quad (\text{A.14})$$

Demas model (D)

$$\phi(C) = \phi_0 \left(\frac{x}{1 + k_1 C} + \frac{(1 - x)}{1 + k_2 C} \right) \quad \frac{\partial \phi(C)}{\partial C} = \left(\frac{-\phi_0 k_1 x}{(1 + k_1 C)^2} - \frac{\phi_0 k_2 (1 - x)}{(1 + k_2 C)^2} \right) \quad (\text{A.15})$$

$$\Phi_0 = \lim_{C \rightarrow 0} \phi_0 \left(\frac{x}{1 + k_1 C} + \frac{(1 - x)}{1 + k_2 C} \right) = \phi_0 \quad (\text{A.16})$$

$$K = \lim_{C \rightarrow 0} \frac{1}{\phi_0} \left| \left(\frac{-\phi_0 k_1 x}{(1 + k_1 C)^2} - \frac{\phi_0 k_2 (1 - x)}{(1 + k_2 C)^2} \right) \right| = k_1 x + k_2 (1 - x) \quad (\text{A.17})$$

1st order polynomial-exponent model (PE1)

$$C(\phi) = a_0 + a_1\phi^\alpha \quad \phi(C) = \left(\frac{C - a_0}{a_1}\right)^{1/\alpha} \quad \frac{\partial \phi(C)}{\partial C} = \left(\frac{\partial C(\phi)}{\partial \phi}\right)^{-1} = \frac{1}{a_1 \alpha \phi^{\alpha-1}} \quad (\text{A.18})$$

$$\Phi_0 = \lim_{C \rightarrow 0} \left(\frac{C - a_0}{a_1}\right)^{1/\alpha} = \left(\frac{-a_0}{a_1}\right)^{1/\alpha} \quad K = \lim_{C \rightarrow 0} \frac{1}{\phi} \left| \frac{1}{a_1 \alpha \phi^{\alpha-1}} \right| = \left| \frac{1}{a_1 \alpha \Phi_0^\alpha} \right| = \left| \frac{1}{a_1 \alpha (-a_0/a_1)} \right| = \left| \frac{1}{a_0 \alpha} \right| \quad (\text{A.19})$$

2nd order polynomial-exponent model (PE2)

$$C(\phi) = a_0 + a_1\phi^\alpha + a_2\phi^{2\alpha} \quad \phi(C) = \left(\frac{-a_1 + \sqrt{a_1^2 - 4a_2(a_0 - C)}}{2a_2} \right)^{1/\alpha} \quad (\text{A.20})$$

$$\frac{\partial\phi(C)}{\partial C} = \left(\frac{\partial C(\phi)}{\partial\phi} \right)^{-1} = \frac{1}{\alpha a_1\phi^{\alpha-1} + 2\alpha a_2\phi^{2\alpha-1}} \quad (\text{A.21})$$

$$\Phi_0 = \lim_{C \rightarrow 0} \left(\frac{-a_1 + \sqrt{a_1^2 - 4a_2(a_0 - C)}}{2a_2} \right)^{1/\alpha} = \left(\frac{-a_1 + \sqrt{a_1^2 - 4a_0a_2}}{2a_2} \right)^{1/\alpha} \quad (\text{A.22})$$

$$K = \lim_{C \rightarrow 0} \frac{1}{\phi} \left| \frac{1}{\alpha a_1\phi^{\alpha-1} + 2\alpha a_2\phi^{2\alpha-1}} \right| = \left| \frac{1}{\alpha a_1\Phi_0^\alpha + 2\alpha a_2\Phi_0^{2\alpha}} \right| \quad (\text{A.23})$$

2nd order polynomial model (P2)

$$C(\phi) = a_0 + a_1\phi^{-1} + a_2\phi^{-2} \quad \phi(C) = \left(\frac{-a_1 + \sqrt{a_1^2 - 4a_2(a_0 - C)}}{2a_2} \right)^{-1} \quad (\text{A.24})$$

$$\frac{\partial\phi(C)}{\partial C} = \left(\frac{\partial C(\phi)}{\partial\phi} \right)^{-1} = \frac{-1}{a_1\phi^{-2} + 2a_2\phi^{-3}} \quad (\text{A.25})$$

$$\Phi_0 = \lim_{C \rightarrow 0} \left(\frac{-a_1 + \sqrt{a_1^2 - 4a_2(a_0 - C)}}{2a_2} \right)^{-1} = \left(\frac{-a_1 + \sqrt{a_1^2 - 4a_0a_2}}{2a_2} \right)^{-1} \quad (\text{A.26})$$

$$K = \lim_{C \rightarrow 0} \frac{1}{\phi} \left| \frac{-1}{a_1\phi^{-2} + 2a_2\phi^{-3}} \right| = \left| \frac{1}{a_1\Phi_0^{-1} + 2a_2\Phi_0^{-2}} \right| \quad (\text{A.27})$$

A.4 Generic calibration procedure

Calibration consists in the minimization of the error function $E(\Lambda, \{(\phi_1, C_1), (\phi_2, C_2), \dots, (\phi_N, C_N)\})$ with respect to the parameters $\Lambda = \{\lambda_1, \lambda_2, \dots, \lambda_M\}$. The error E is minimized by finding the zeros of the partials:

$$\frac{\partial E}{\partial \lambda_m} = 0 \quad \forall m = 1, \dots, M \quad (\text{A.28})$$

If we define:

$$f_m(\lambda_m) \equiv \frac{\partial E}{\partial \lambda_m} \quad (\text{A.29})$$

the minimization of the error E is equivalent to finding the values λ_m that simultaneously cancel $f_m(\lambda_m)$ for each m . The Newton's method can be applied for the iterative estimation of the roots of $f_m(\lambda_m)$ (and therefore to the estimation of the model parameters minimizing E):

$$\lambda_m^{t+1} = \lambda_m^t - \frac{f_m(\lambda_m^t)}{f'_m(\lambda_m^t)} \quad (\text{A.30})$$

where t is the iteration and $f'_m(\lambda_m)$ is the derivative of $f_m(\lambda_m)$ with respect to λ_m . This method provides a generic procedure for calibration where the parameter λ_m can be calculated at iteration $t + 1$ from its value at iteration t . The calibration would start with an initialization of the model parameters λ_m^0 . If we evaluate $E(\lambda_m^t)$, $E(\lambda_m^t + \epsilon)$ and $E(\lambda_m^t - \epsilon)$ (being ϵ an infinitesimal increment in λ_m), the following approaches are possible:

$$f_m(\lambda_m^t) \approx \frac{E(\lambda_m^t + \epsilon) - E(\lambda_m^t - \epsilon)}{2\epsilon} \quad \left. \frac{\partial f_m(\lambda_m)}{\partial \lambda_m} \right|_{\lambda_m^t} \approx \frac{E(\lambda_m^t + \epsilon) + E(\lambda_m^t - \epsilon) - 2E(\lambda_m^t)}{\epsilon^2} \quad (\text{A.31})$$

and the iterative procedure can be expressed as:

$$\lambda_m^{t+1} \approx \lambda_m^t - \frac{\epsilon}{2} \frac{E(\lambda_m^t + \epsilon) - E(\lambda_m^t - \epsilon)}{E(\lambda_m^t + \epsilon) + E(\lambda_m^t - \epsilon) - 2E(\lambda_m^t)} \quad (\text{A.32})$$

Therefore, given the calibration data, the iterative procedure would be carried out as follows:

1. The model parameters are initialized: $\lambda_m^0 \quad \forall m = 1, \dots, M$.
2. For each iteration t , until convergence:
 - (a) For each parameter to optimize λ_m , errors are calculated:
 - $E(\lambda_1^t, \dots, \lambda_m^t, \dots, \lambda_M^t)$
 - $E(\lambda_1^t, \dots, \lambda_m^t + \epsilon, \dots, \lambda_M^t)$
 - $E(\lambda_1^t, \dots, \lambda_m^t - \epsilon, \dots, \lambda_M^t)$
 - (b) λ_m^{t+1} is estimated using equation (A.32).
3. When convergence is reached, the calibrated model parameters are $\hat{\Lambda} = \{\hat{\lambda}_1, \hat{\lambda}_2, \dots, \hat{\lambda}_M\}$ and the minimized calibration error would be $E(\hat{\Lambda}, \{(x_1, C_1), (x_2, C_2), \dots, (x_N, C_N)\})$.

This generic calibration procedure has the disadvantage of being a M -dimensional search, and at each iteration all the parameters should be independently estimated. However, taking into account the models and criteria, the conditions $f_m(\lambda_m) = 0$ allow to write some of the parameters as a function of the others in some cases, which reduces the dimensionality of the search. In the next section, the calibration procedure is particularized for each model and criterion.

A.5 Calibration formulas for different models and criteria

A.5.1 Stern-Volmer model using criterion (a)

$$\phi(C) = \frac{\phi_0}{1+kC} \quad E_a = \sum_n \left(\frac{\phi_0}{1+kC_n} - \phi_n \right)^2 \quad (\text{A.33})$$

$$\frac{\partial E_a}{\partial \phi_0} = 2 \sum_n \left(\frac{\phi_0}{1+kC_n} - \phi_n \right) \frac{1}{1+kC_n} \quad (\text{A.34})$$

$$\frac{\partial E_a}{\partial \phi_0} = 0 \Leftrightarrow \phi_0 \sum_n \left(\frac{1}{1+kC_n} \right)^2 = \sum_n \frac{\phi_n}{1+kC_n} \Leftrightarrow \boxed{\phi_0 = \frac{\sum_n \left(\frac{\phi_n}{1+kC_n} \right)}{\sum_n \left(\frac{1}{1+kC_n} \right)^2}} \quad (\text{A.35})$$

A.5.2 Stern-Volmer model using criteria (b) and (c)

$$C(\phi) = \frac{1}{k} \left(\frac{\phi_0}{\phi} - 1 \right) \quad E_{bw} = \sum_n w_n \left(\frac{1}{k} \left(\frac{\phi_0}{\phi_n} - 1 \right) - C_n \right)^2 \quad (\text{A.36})$$

$$\frac{\partial E_{bw}}{\partial \phi_0} = 2 \sum_n w_n \left(\frac{1}{k} \left(\frac{\phi_0}{\phi_n} - 1 \right) - C_n \right) \frac{1}{k\phi_n} \quad \frac{\partial E_{bw}}{\partial k} = 2 \sum_n w_n \left(\frac{1}{k} \left(\frac{\phi_0}{\phi_n} - 1 \right) - C_n \right) \left(\frac{-1}{k^2} \right) \left(\frac{\phi_0}{\phi_n} - 1 \right) \quad (\text{A.37})$$

$$\frac{\partial E_{bw}}{\partial \phi_0} = 0 \Leftrightarrow \phi_0 \sum_n \frac{w_n}{\phi_n^2} - \sum_n \frac{w_n}{\phi_n} = k \sum_n \frac{w_n C_n}{\phi_n} \quad (\text{A.38})$$

$$\frac{\partial E_{bw}}{\partial k} = 0 \Leftrightarrow k\phi_0 \sum_n \frac{w_n C_n}{\phi_n} - k \sum_n w_n C_n = \phi_0^2 \sum_n \frac{w_n}{\phi_n^2} - 2\phi_0 \sum_n \frac{w_n}{\phi_n} + \sum_n w_n \quad (\text{A.39})$$

Using the following definitions:

$$S \equiv \sum_n w_n \quad S_\phi \equiv \sum_n \frac{w_n}{\phi_n} \quad S_C \equiv \sum_n w_n C_n \quad S_{C\phi} \equiv \sum_n \frac{w_n C_n}{\phi_n} \quad S_{\phi\phi} \equiv \sum_n \frac{w_n}{\phi_n^2} \quad (\text{A.40})$$

the conditions $\partial E_{bw}/\partial \phi_0 = 0$ and $\partial E_{bw}/\partial k = 0$ can be rewritten as:

$$\phi_0 S_{\phi\phi} - S_\phi = k S_{C\phi} \quad k\phi_0 S_{C\phi} - k S_C = \phi_0^2 S_{\phi\phi} - 2\phi_0 S_\phi + S \quad (\text{A.41})$$

and from these equations, k and ϕ_0 are obtained as:

$$\boxed{k = \frac{S_{\phi\phi} S - S_\phi^2}{S_\phi S_{C\phi} - S_C S_{\phi\phi}} \quad \phi_0 = \frac{S_\phi + k S_{C\phi}}{S_{\phi\phi}}} \quad (\text{A.42})$$

A.5.3 Lehrer model using criterion (a)

$$\phi(C) = \phi_0 \left(\frac{x}{1+kC} + (1-x) \right) \quad E_a = \sum_n \left(\phi_0 \left(\frac{x}{1+kC_n} + (1-x) \right) - \phi_n \right)^2 \quad (\text{A.43})$$

If we define $z_n \equiv kC_n/(1+kC_n)$ the previous expressions can be rewritten as:

$$\phi(C) = \phi_0(1-xz_n) \quad E_a = \sum_n (\phi_0(1-xz_n) - \phi_n)^2 \quad (\text{A.44})$$

$$\frac{\partial E_a}{\partial \phi_0} = 2 \sum_n (\phi_0(1-xz_n) - \phi_n)(1-xz_n) \quad \frac{\partial E_a}{\partial x} = -2 \sum_n (\phi_0(1-xz_n) - \phi_n)(\phi_0 z_n) \quad (\text{A.45})$$

$$\frac{\partial E_a}{\partial \phi_0} = 0 \Leftrightarrow \phi_0 \sum_n (1-xz_n)^2 = \sum_n \phi_n(1-xz_n) \quad (\text{A.46})$$

$$\frac{\partial E_a}{\partial x} = 0 \Leftrightarrow \phi_0 \sum_n (1-xz_n)z_n = \sum_n \phi_n z_n \quad (\text{A.47})$$

Using the following definitions:

$$S_\phi \equiv \sum_n \phi_n \quad S_z \equiv \sum_n z_n \quad S_{z\phi} \equiv \sum_n z_n \phi_n \quad S_{zz} \equiv \sum_n z_n^2 \quad (\text{A.48})$$

the conditions $\partial E_a/\partial \phi_0 = 0$ and $\partial E_a/\partial x = 0$ can be rewritten as:

$$\phi_0 x^2 S_{zz} + \phi_0 N - 2\phi_0 x S_z = S_\phi - x S_{z\phi} \quad \phi_0 S_z - \phi_0 x S_{zz} = S_{z\phi} \quad (\text{A.49})$$

and from these equations, x and ϕ_0 are obtained as:

$$\boxed{x = \frac{N S_{z\phi} - S_z S_\phi}{S_z S_{z\phi} - S_{zz} S_\phi} \quad \phi_0 = \frac{S_{z\phi}}{S_z - x S_{zz}}} \quad (\text{A.50})$$

A.5.4 Lehrer model using criteria (b) and (c)

Due to the no-linear dependencies of $C(\phi)$ with the model parameters:

$$C(\phi) = \frac{\phi_0 - \phi}{k\phi - k\phi_0 + xk\phi_0} \quad (\text{A.51})$$

the parameter estimation is difficult for criteria (b) and (c). With an appropriate change of variables:

$$b_0 \equiv \frac{1}{k} \quad b_1 \equiv \frac{x}{k(1-x)} \quad k' \equiv \frac{1}{\phi_0(1-x)} \quad (\text{A.52})$$

the function $C(\phi)$ and the error E_{bw} can be written as:

$$C(\phi) = \frac{b_1}{k'\phi - 1} - b_0 \quad E_{bw} = \sum_n w_n \left(\frac{b_1}{k'\phi_n - 1} - b_0 - C_n \right)^2 \quad (\text{A.53})$$

and defining $z_n = 1/(k'\phi_n - 1)$, the error and the derivatives can be written as:

$$C(\phi) = b_1 z_n - b_0 \quad E_{bw} = \sum_n w_n (b_1 z_n - b_0 - C_n)^2 \quad (\text{A.54})$$

$$\frac{\partial E_{bw}}{\partial b_0} = -2 \sum_n w_n (b_1 z_n - b_0 - C_n) \quad \frac{\partial E_{bw}}{\partial b_1} = 2 \sum_n w_n (b_1 z_n - b_0 - C_n) z_n \quad (\text{A.55})$$

$$\frac{\partial E_{bw}}{\partial b_0} = 0 \Leftrightarrow b_1 \sum_n w_n z_n - b_0 \sum_n w_n - \sum_n w_n C_n = 0 \quad (\text{A.56})$$

$$\frac{\partial E_{bw}}{\partial b_1} = 0 \Leftrightarrow b_1 \sum_n w_n z_n^2 - b_0 \sum_n w_n^2 - \sum_n w_n C_n z_n = 0 \quad (\text{A.57})$$

Using the following definitions:

$$S \equiv \sum_n w_n \quad S_z \equiv \sum_n w_n z_n \quad S_C \equiv \sum_n w_n C_n \quad S_{Cz} \equiv \sum_n w_n C_n z_n \quad S_{zz} \equiv \sum_n w_n z_n^2 \quad (\text{A.58})$$

the conditions $\partial E_{bw}/\partial b_0 = 0$ and $\partial E_{bw}/\partial b_1 = 0$ can be rewritten as:

$$b_1 S_z - b_0 S - S_C = 0 \quad b_1 S_{zz} - b_0 S_z - S_{Cz} = 0 \quad (\text{A.59})$$

and from these equations, b_0 and b_1 are obtained as:

$$\boxed{b_0 = \frac{S_{Cz} S_z - S_C S_{zz}}{S_{zz} S - S_z^2} \quad b_1 = \frac{b_0 S_z + S_{Cz}}{S_{zz}}} \quad (\text{A.60})$$

Finally, from b_0 , b_1 and k' are found, k , ϕ_0 and x can be obtained as:

$$k = \frac{1}{b_0} \quad x = \frac{b_1}{b_1 + b_0} \quad \phi_0 = \frac{b_1 + b_0}{k' b_0} \quad (\text{A.61})$$

A.5.5 Demas model using criterion (a)

$$\phi(C) = \phi_0 \left(\frac{x}{1 + k_1 C} + \frac{(1-x)}{1 + k_2 C} \right) \quad E_{aw} = \sum_n w_n \left(\phi_0 \left(\frac{x}{1 + k_1 C_n} + \frac{(1-x)}{1 + k_2 C_n} \right) - \phi_n \right)^2 \quad (\text{A.62})$$

Using the following definitions:

$$y_n \equiv \frac{1}{1 + k_2 C_n} \quad z_n \equiv \frac{1}{1 + k_1 C_n} - \frac{1}{1 + k_2 C_n} \quad (\text{A.63})$$

the previous expressions can be written as:

$$\phi(C) = \phi_0 (x z_n + y_n) \quad E_{aw} = \sum_n w_n (\phi_0 (x z_n + y_n) - \phi_n)^2 \quad (\text{A.64})$$

$$\frac{\partial E_{aw}}{\partial \phi_0} = 2 \sum_n w_n (\phi_0 (x z_n + y_n) - \phi_n) (x z_n + y_n) \quad \frac{\partial E_{aw}}{\partial x} = 2 \sum_n w_n (\phi_0 (x z_n + y_n) - \phi_n) \phi_0 z_n \quad (\text{A.65})$$

$$\frac{\partial E_{aw}}{\partial \phi_0} = 0 \Leftrightarrow \phi_0 \sum_n w_n (x z_n + y_n)^2 = \sum_n w_n (x z_n + y_n) \phi_n \quad (\text{A.66})$$

$$\frac{\partial E_{aw}}{\partial x} = 0 \Leftrightarrow \phi_0 \sum_n w_n z_n (x z_n + y_n) = \sum_n w_n z_n \phi_n \quad (\text{A.67})$$

Using the following definitions:

$$S_{z\phi} \equiv \sum_n w_n z_n \phi_n \quad S_{y\phi} \equiv \sum_n w_n y_n \phi_n \quad S_{zy} \equiv \sum_n w_n z_n y_n \quad S_{yy} \equiv \sum_n w_n y_n^2 \quad S_{zz} \equiv \sum_n w_n z_n^2 \quad (\text{A.68})$$

the conditions $\partial E_{aw}/\partial \phi_0 = 0$ and $\partial E_{aw}/\partial x = 0$ can be rewritten as:

$$\phi_0 x^2 S_{zz} + 2\phi_0 x S_{zy} + \phi_0 S_{yy} = x S_{z\phi} + S_{y\phi} \quad \phi_0 x S_{zz} + 2\phi_0 S_{zy} = S_{z\phi} \quad (\text{A.69})$$

and from these equations x and ϕ_0 are obtained as:

$$\boxed{x = \frac{S_{y\phi} S_{zy} - S_{yy} S_{z\phi}}{S_{zy} S_{z\phi} - S_{zz} S_{y\phi}} \quad \phi_0 = \frac{S_{z\phi}}{x S_{zz} + S_{zy}}} \quad (\text{A.70})$$

A.5.6 Polynomial-Exponent model using criteria (b) and (c)

$$C(\phi) = a_0 + a_1\phi^\alpha + a_2\phi^{2\alpha} + \dots + a_p\phi^{p\alpha} \quad E_{bw} = \sum_n w_n (C(\phi_n) - C_n)^2 \quad (\text{A.71})$$

$$\frac{\partial E_{bw}}{\partial a_0} = 2 \sum_n w_n (a_0 + a_1\phi_n^\alpha + a_2\phi_n^{2\alpha} + \dots + a_p\phi_n^{p\alpha} - C_n) \quad (\text{A.72})$$

$$\frac{\partial E_{bw}}{\partial a_1} = 2 \sum_n w_n (a_0 + a_1\phi_n^\alpha + a_2\phi_n^{2\alpha} + \dots + a_p\phi_n^{p\alpha} - C_n)\phi_n^\alpha \quad (\text{A.73})$$

$$\frac{\partial E_{bw}}{\partial a_2} = 2 \sum_n w_n (a_0 + a_1\phi_n^\alpha + a_2\phi_n^{2\alpha} + \dots + a_p\phi_n^{p\alpha} - C_n)\phi_n^{2\alpha} \quad (\text{A.74})$$

⋮

$$\frac{\partial E_{bw}}{\partial a_p} = 2 \sum_n w_n (a_0 + a_1\phi_n^\alpha + a_2\phi_n^{2\alpha} + \dots + a_p\phi_n^{p\alpha} - C_n)\phi_n^{p\alpha} \quad (\text{A.75})$$

The conditions $\partial E_{bw}/\partial a_i = 0$ (with $i = 0, \dots, p$) constitute a linear equation system:

$$\frac{\partial E_{bw}}{\partial a_0} = 0 \quad \Leftrightarrow \quad a_0 \sum_n w_n + a_1 \sum_n w_n \phi_n^\alpha + a_2 \sum_n w_n \phi_n^{2\alpha} + \dots + a_p \sum_n w_n \phi_n^{p\alpha} = \sum_n w_n C_n \quad (\text{A.76})$$

$$\frac{\partial E_{bw}}{\partial a_1} = 0 \quad \Leftrightarrow \quad a_0 \sum_n w_n \phi_n^\alpha + a_1 \sum_n w_n \phi_n^{2\alpha} + a_2 \sum_n w_n \phi_n^{3\alpha} + \dots + a_p \sum_n w_n \phi_n^{(p+1)\alpha} = \sum_n w_n C_n \phi_n^\alpha \quad (\text{A.77})$$

$$\frac{\partial E_{bw}}{\partial a_2} = 0 \quad \Leftrightarrow \quad a_0 \sum_n w_n \phi_n^{2\alpha} + a_1 \sum_n w_n \phi_n^{3\alpha} + a_2 \sum_n w_n \phi_n^{4\alpha} + \dots + a_p \sum_n w_n \phi_n^{(p+2)\alpha} = \sum_n w_n C_n \phi_n^{2\alpha} \quad (\text{A.78})$$

⋮

$$\frac{\partial E_{bw}}{\partial a_p} = 0 \quad \Leftrightarrow \quad a_0 \sum_n w_n \phi_n^{p\alpha} + a_1 \sum_n w_n \phi_n^{(p+1)\alpha} + a_2 \sum_n w_n \phi_n^{(p+2)\alpha} + \dots + a_p \sum_n w_n \phi_n^{(2p)\alpha} = \sum_n w_n C_n \phi_n^{p\alpha} \quad (\text{A.79})$$

This equation system can be written in matrix form as:

$$A \cdot \vec{a} = \vec{B} \quad (\text{A.80})$$

where the vector \vec{a} contains the polynomial coefficients a_0, \dots, a_p , and A and \vec{B} are, respectively, a square matrix and a column vector whose components are:

$$A_{i,j} = \sum_n w_n \phi_n^{(i+j)\alpha} \quad B_i = \sum_n w_n C_n \phi_n^{i\alpha} \quad i, j = 0, \dots, p \quad (\text{A.81})$$

and therefore, given α , the polynomial coefficients are directly obtained by inverting the matrix A as:

$$\boxed{\vec{a} = A^{-1} \cdot \vec{B}} \quad (\text{A.82})$$

Appendix B

Detailed experimental results

B.1 Calibration and evaluation results for each experiment

The evaluation of the described models using different criteria has been performed with 25 experiments, each one using a different set of calibration and evaluation data. The calibration data, evaluation data and the results of the calibration and evaluation with each model and criterion are presented in this section for each experiment.

The 25 experiments included in this study involve 7 different oxygen-sensitive sensing phases, which have been calibrated and tested between several oxygen concentrations. Two different analytical signals (luminescence lifetime or luminescence intensity), measured with different instruments and procedures, are used in each experiment.

For each experiment, a report is provided, containing the following information:

- Table 1.- Description of the experiment: description of the sensing phase, analyte, concentration range, analytical signal, measurement method, instrument, measurement procedure and references.
- Table 2.- Calibration and test data for the experiment, including number of measurements involved in each data, mean/standard deviation of the analytical signal (after removing outliers), for both calibration and test datasets.
- Figure 1.- Calibration curves for different models (at each plot) and criteria (in red, blue and green for criteria (a), (b) and (c), respectively). The calibration data are also represented with circles.
- Table 3.- Calibration results for each model and criterion. The table shows, for each case, the calibrated parameters, the determination coefficient R^2 , and the root mean square error (RMSE) expressed in degrees for criterion (a), in kPa for criterion (b) and in relative error (%) for criterion (c). The response at null concentration Φ_0 and the sensitivity K are also included for each model and criterion.
- Tables 4 and 5.- Evaluation of each model/criterion in terms of RMSE in analytical signal, RMSE in cocentration and RMS relative error in concentration. Table 4 includes evaluation for calibration data and Table 5 for test data.

Experiment 1

page 1/2

Table 1: Sensing phase information

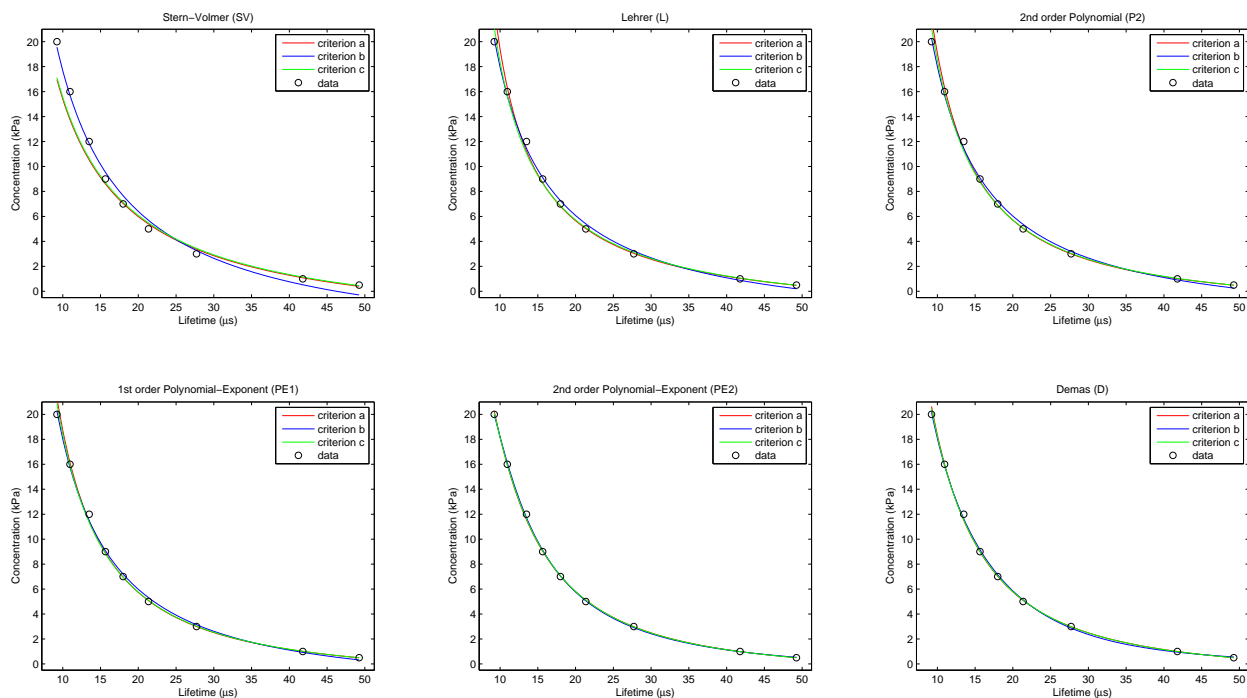
Name:	PtTFPP/PS
Description:	An oxygen-sensing film coated at the end of an optical fibre (a Platinum(II) 5,10,15,20-meso-tetrakis-(2,3,4,5,6-pentafluorophenyl)-porphyrin immobilized in polystyrene).
Analyte:	Partial pressure of oxygen in the gas phase (pO_2 , kPa); Range: 0.5-20 kPa.
Analytical signal:	(Measurement method): Luminescence lifetime in the frequency domain (<i>i.e.</i> , apparent lifetime estimated from phase-shift) using a phase-modulation method. (Instrumentation): Measurement system based on the I/Q method; Excitation signal: Sinusoidal-wave at 5145 Hz (see reference).
Reference(s):	Medina-Rodríguez, S.; de la Torre-Vega, A.; Fernández-Sánchez, J. F.; Fernández-Gutiérrez, A. <i>Sensors and Actuators B: Chemical</i> 2013 , 176, 1110-1120.

1.- Experimental data (calibration and test)

Table 2: Experimental data (*i.e.*, calibration and test data); apparent phase-shift lifetime measurements (τ_ϕ , in microseconds) for several oxygen concentrations (pO_2 , in kPa) at room temperature (21 °C). All the values correspond to the average of 25 measurements.

Calibration data (τ_ϕ , in microseconds)			Test data (τ_ϕ , in microseconds)		
pO_2 (kPa)	Mean (μs)	Sdev (μs)	pO_2 (kPa)	Mean (μs)	Sdev (μs)
0.50	49.2411	0.5688	0.75	45.4119	0.5965
1.00	41.7845	0.7215	2.00	32.4933	0.6855
3.00	27.7127	0.6510	4.00	24.2433	0.8132
5.00	21.3608	0.6588	6.00	19.9944	0.8494
7.00	17.9941	0.7267	8.00	17.0082	0.8271
9.00	15.6490	0.9316	10.00	15.0475	0.7362
12.00	13.4975	1.0385	14.00	12.0687	0.9148
16.00	10.9609	1.0703	18.00	9.8983	1.2176
20.00	9.2335	1.1885			

2.- Calibration curves: models and criteria


Figure 1: Calibration curves for the apparent phase-shift lifetime measurements (calibration data) of the sensing phase using different models and criteria. Models: Stern-Volmer (SV) (2 parameters), Lehrer (L) (3 parameters), 2nd order Polynomial (P2) (3 parameters), 1st order Polynomial-Exponent (PE1) (3 parameters), 2nd order Polynomial-Exponent (PE2) (4 parameters), Demas (D) (4 parameters). Criteria: (a) minimum mean square error (MSE) in τ_ϕ , (b) minimum mean square error (MSE) in pO_2 , (c) minimum mean square relative error in pO_2 .

Experiment 1

3.- Parameters of the fitting models for different criteria

Table 3: Parameters of the fitting models for different criteria: (a) minimum mean square error (MSE) in τ_ϕ , (b) minimum mean square error (MSE) in pO_2 , (c) minimum mean square relative error in pO_2 . RMSE is expressed in microseconds for criterion (a), in kPa for criterion (b) and in relative error (%) for criterion (c). Calibration data used are shown in Table 2.

Range	Stern-Volmer (SV)			Lehrer (L)			2 nd order Polynomial (P2)					
pO_2	Parameter	(a)	(b)	(c)	Parameter	(a)	(b)	(c)	Parameter	(a)	(b)	(c)
0.5-20 (kPa)	τ_0 (μs)	55.0305	46.2695	55.8358	τ_0 (μs)	58.6094	52.0615	58.2358	a_0	-1.8839	-3.0979	-2.0536
	k (kPa^{-1})	0.2924	0.2050	0.2948	k (kPa^{-1})	0.4323	0.2941	0.4062	a_1	93.3546	153.823	104.859
	—	—	—	—	x	0.9281	0.9606	0.9393	a_2	1165.39	574.207	1008.25
	R^2	0.99321	0.99332	0.98763	R^2	0.99930	0.99761	0.99800	R^2	0.99967	0.99791	0.99891
	RMSE	1.0884	0.5203	11.1207	RMSE	0.3504	0.3112	4.4750	RMSE	0.2415	0.2910	3.3063
	iterations	100	1	1	iterations	100	100	100	iterations	100	1	1
0.5-20 (kPa)	Φ_0 (μs)	55.0305	46.2695	55.8358	Φ_0 (μs)	58.6094	52.0615	58.2358	Φ_0 (μs)	59.8828	53.1422	59.3367
	K (kPa^{-1})	0.2924	0.2050	0.2948	K (kPa^{-1})	0.4013	0.2825	0.3816	K (kPa^{-1})	0.4527	0.3029	0.4274
Range	1 st order Polynomial-Exponent (PE1)			2 nd order Polynomial-Exponent (PE2)			Demas (D)					
pO_2	Parameter	(a)	(b)	(c)	Parameter	(a)	(b)	(c)	Parameter	(a)	(b)	(c)
0.5-20 (kPa)	a_0	-1.3193	-2.1988	-1.4135	a_0	-1.0293	-0.7319	-0.9783	τ_0 (μs)	61.3469	78.7094	61.7059
	a_1	643.926	410.529	581.72	a_1	1221.5	1994	1362.34	k_1 (kPa^{-1})	0.6433	2.1112	0.6838
	α	-1.5066	-1.3069	-1.4677	a_2	-11959.2	-41258.1	-16300.6	k_2 (kPa^{-1})	0.0613	0.1194	0.0699
	—	—	—	—	α	-1.7113	-1.8863	-1.7478	x	0.7834	0.6510	0.7594
	R^2	0.99979	0.99836	0.99934	R^2	0.99988	0.99968	0.99977	R^2	0.99987	0.99929	0.99969
	RMSE	0.1921	0.2578	2.5604	RMSE	0.1444	0.1148	1.5248	RMSE	0.1498	0.1693	1.7521
iterations	100	100	100	iterations	100	100	100	iterations	500	500	500	
0.5-20 (kPa)	Φ_0 (μs)	60.8825	54.6723	60.4350	Φ_0 (μs)	62.2808	65.9795	62.5949	Φ_0 (μs)	61.3469	78.7094	61.7059
	K (kPa^{-1})	0.5031	0.3480	0.4820	K (kPa^{-1})	0.5725	0.7299	0.5900	K (kPa^{-1})	0.5173	1.4161	0.5361

4.- Accuracy of the fitting models for different criteria using calibration data

Table 4: Accuracy (root mean square error, RMSE) of the fitting models for different criteria: (a) minimum mean square error (MSE) in τ_ϕ , (b) minimum mean square error (MSE) in pO_2 , (c) minimum mean square relative error in pO_2 . Calibration data were used for evaluating the models (see Table 2).

Range	Stern-Volmer (SV)			Lehrer (L)			2 nd order Polynomial (P2)					
pO_2	Evaluation (criterion)	(a)	(b)	(c)	Evaluation (criterion)	(a)	(b)	(c)	Evaluation (criterion)	(a)	(b)	(c)
0.5-20 (kPa)	RMSE τ_ϕ (μs)	1.0884	2.7674	1.1346	RMSE τ_ϕ (μs)	0.3504	1.3392	0.4040	RMSE τ_ϕ (μs)	0.2415	1.1327	0.2730
	RMSE pO_2 (kPa)	1.3714	0.5203	1.2979	RMSE pO_2 (kPa)	0.9636	0.3112	0.5310	RMSE pO_2 (kPa)	0.6722	0.2910	0.4621
	RMSE relat. pO_2 (%)	11.8671	55.6884	11.1207	RMSE relat. pO_2 (%)	5.5855	20.6362	4.4750	RMSE relat. pO_2 (%)	3.7690	16.5374	3.3063
Range	1 st order Polynomial-Exponent (PE1)			2 nd order Polynomial-Exponent (PE2)			Demas (D)					
pO_2	Evaluation (criterion)	(a)	(b)	(c)	Evaluation (criterion)	(a)	(b)	(c)	Evaluation (criterion)	(a)	(b)	(c)
0.5-20 (kPa)	RMSE τ_ϕ (μs)	0.1921	0.9376	0.2086	RMSE τ_ϕ (μs)	0.1444	0.2865	0.1484	RMSE τ_ϕ (μs)	0.1498	0.6374	0.1540
	RMSE pO_2 (kPa)	0.4749	0.2578	0.3670	RMSE pO_2 (kPa)	0.1735	0.1148	0.1463	RMSE pO_2 (kPa)	0.2657	0.1693	0.2263
	RMSE relat. pO_2 (%)	2.7674	12.5307	2.5604	RMSE relat. pO_2 (%)	1.5633	2.6442	1.5248	RMSE relat. pO_2 (%)	1.8224	4.8828	1.7521

5.- Accuracy of the fitting models for different criteria using test data

Table 5: Accuracy (root mean square error, RMSE) of the fitting models for different criteria: (a) minimum mean square error (MSE) in τ_ϕ , (b) minimum mean square error (MSE) in pO_2 , (c) minimum mean square relative error in pO_2 . Test data were used for evaluating the models (see Table 2).

Range	Stern-Volmer (SV)			Lehrer (L)			2 nd order Polynomial (P2)					
pO_2	Evaluation (criterion)	(a)	(b)	(c)	Evaluation (criterion)	(a)	(b)	(c)	Evaluation (criterion)	(a)	(b)	(c)
0.75-18 (kPa)	RMSE τ_ϕ (μs)	1.1442	1.9538	1.2450	RMSE τ_ϕ (μs)	0.5306	0.9749	0.5962	RMSE τ_ϕ (μs)	0.4124	0.8452	0.4617
	RMSE pO_2 (kPa)	1.1367	0.3527	1.0653	RMSE pO_2 (kPa)	0.7280	0.2539	0.4843	RMSE pO_2 (kPa)	0.5724	0.2492	0.4398
	RMSE relat. pO_2 (%)	10.5064	31.4162	11.0864	RMSE relat. pO_2 (%)	5.8298	11.6237	5.5139	RMSE relat. pO_2 (%)	4.5536	9.5275	4.4927
Range	1 st order Polynomial-Exponent (PE1)			2 nd order Polynomial-Exponent (PE2)			Demas (D)					
pO_2	Evaluation (criterion)	(a)	(b)	(c)	Evaluation (criterion)	(a)	(b)	(c)	Evaluation (criterion)	(a)	(b)	(c)
0.75-18 (kPa)	RMSE τ_ϕ (μs)	0.3568	0.7177	0.3817	RMSE τ_ϕ (μs)	0.2623	0.2258	0.2481	RMSE τ_ϕ (μs)	0.2845	0.2710	0.2671
	RMSE pO_2 (kPa)	0.4396	0.2288	0.3706	RMSE pO_2 (kPa)	0.2355	0.2061	0.2101	RMSE pO_2 (kPa)	0.2986	0.1767	0.2620
	RMSE relat. pO_2 (%)	3.7827	7.6678	3.7623	RMSE relat. pO_2 (%)	2.5739	2.2339	2.4076	RMSE relat. pO_2 (%)	2.8915	2.3614	2.6749

Experiment 2

page 1/2

Table 1: Sensing phase information

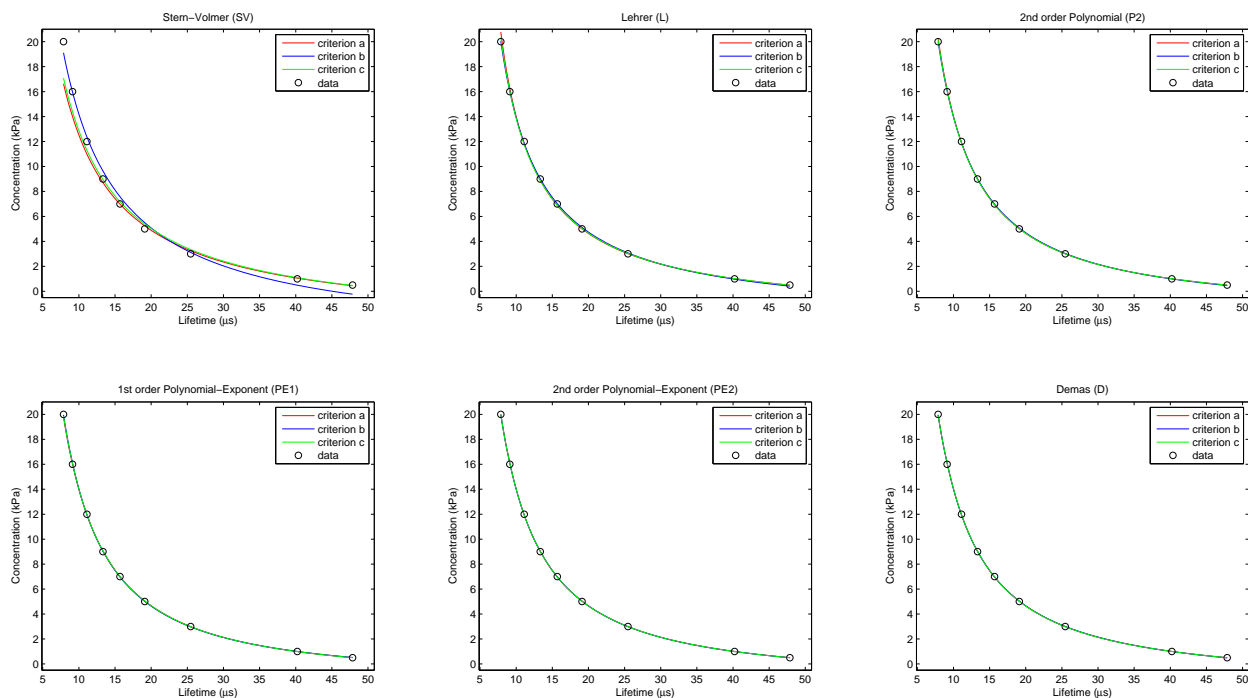
Name:	PtTFPP/PS
Description:	An oxygen-sensing film coated at the end of an optical fibre (a Platinum(II) 5,10,15,20-meso-tetrakis-(2,3,4,5,6-pentafluorophenyl)-porphyrin immobilized in polystyrene).
Analyte:	Partial pressure of oxygen in the gas phase (pO_2 , kPa); Range: 0.5-20 kPa.
Analytical signal:	(Measurement method): Luminescence lifetime in the frequency domain (<i>i.e.</i> , apparent lifetime estimated from modulation factor) using a phase-modulation method. (Instrumentation): Measurement system based on the I/Q method; Excitation signal: Sinusoidal-wave at 5145 Hz (see reference).
Reference(s):	Medina-Rodríguez, S.; de la Torre-Vega, A.; Fernández-Sánchez, J. F.; Fernández-Gutiérrez, A. <i>Sensors and Actuators B: Chemical</i> 2013 , 176, 1110-1120.

1.- Experimental data (calibration and test)

Table 2: Experimental data (*i.e.*, calibration and test data); apparent modulation lifetime measurements (τ_m , in microseconds) for several oxygen concentrations (pO_2 , in kPa) at room temperature (21 °C). All the values correspond to the average of 25 measurements.

Calibration data (τ_m , in microseconds)			Test data (τ_m , in microseconds)		
pO_2 (kPa)	Mean (μs)	Sdev (μs)	pO_2 (kPa)	Mean (μs)	Sdev (μs)
0.50	47.8615	0.7356	0.75	43.3201	0.4174
1.00	40.2136	0.4810	2.00	30.7622	0.4457
3.00	25.4641	0.3636	4.00	21.3545	0.4377
5.00	19.1103	0.4520	6.00	17.2656	0.3634
7.00	15.6865	0.4387	8.00	14.4929	0.3115
9.00	13.3328	0.2955	10.00	12.5431	0.2597
12.00	11.1114	0.2650	14.00	10.2103	0.2057
16.00	9.1234	0.2240	18.00	8.3423	0.2610
20.00	7.8771	0.2733			

2.- Calibration curves: models and criteria


Figure 1: Calibration curves for the apparent modulation lifetime measurements (calibration data) of the sensing phase using different models and criteria. Models: Stern-Volmer (SV) (2 parameters), Lehrer (L) (3 parameters), 2nd order Polynomial (P2) (3 parameters), 1st order Polynomial-Exponent (PE1) (3 parameters), 2nd order Polynomial-Exponent (PE2) (4 parameters), Demas (D) (4 parameters). Criteria: (a) minimum mean square error (MSE) in τ_m , (b) minimum mean square error (MSE) in pO_2 , (c) minimum mean square relative error in pO_2 .

Experiment 2

3.- Parameters of the fitting models for different criteria

Table 3: Parameters of the fitting models for different criteria: (a) minimum mean square error (MSE) in τ_m , (b) minimum mean square error (MSE) in pO_2 , (c) minimum mean square relative error in pO_2 . RMSE is expressed in microseconds for criterion (a), in kPa for criterion (b) and in relative error (%) for criterion (c). Calibration data used are shown in Table 2.

Range	Stern-Volmer (SV)			Lehrer (L)			2 nd order Polynomial (P2)					
pO_2	Parameter	(a)	(b)	(c)	Parameter	(a)	(b)	(c)	Parameter	(a)	(b)	(c)
0.5-20 (kPa)	τ_0 (μs)	55.6790	45.1056	55.8429	τ_0 (μs)	58.6696	55.9526	58.5088	a_0	-1.8733	-2.0373	-1.8994
	k (kPa^{-1})	0.3650	0.2474	0.3565	k (kPa^{-1})	0.4871	0.4273	0.4765	a_1	101.451	109.167	103.126
	–	–	–	–	x	0.9513	0.9595	0.9546	a_2	575.82	508.138	555.686
	R^2	0.99655	0.99250	0.99248	R^2	0.99991	0.99986	0.99979	R^2	0.99998	0.99995	0.99996
	RMSE	0.7861	0.5513	0.6733	RMSE	0.1246	0.0745	1.4637	RMSE	0.0553	0.0443	0.6662
	iterations	100	1	1	iterations	100	100	100	iterations	100	1	1
	Φ_0 (μs)	55.6790	45.1056	55.8429	Φ_0 (μs)	58.6696	55.9526	58.5088	Φ_0 (μs)	59.3361	57.8916	59.2347
	K (kPa^{-1})	0.3650	0.2474	0.3565	K (kPa^{-1})	0.4633	0.4100	0.4549	K (kPa^{-1})	0.4910	0.4568	0.4860
Range	1 st order Polynomial-Exponent (PE1)			2 nd order Polynomial-Exponent (PE2)			Demas (D)					
pO_2	Parameter	(a)	(b)	(c)	Parameter	(a)	(b)	(c)	Parameter	(a)	(b)	(c)
0.5-20 (kPa)	a_0	-1.3583	-1.2513	-1.3382	a_0	-1.7960	-1.4262	-1.7685	τ_0 (μs)	59.6257	59.0225	59.6268
	a_1	340.465	362.976	347.306	a_1	24.8776	293.389	22.1383	k_1 (kPa^{-1})	0.5508	0.5245	0.5503
	α	-1.3467	-1.3759	-1.3547	a_2	403.576	297.336	396.291	k_2 (kPa^{-1})	0.0320	0.0252	0.0316
	–	–	–	–	α	-0.7710	-1.3007	-0.7607	x	0.9077	0.9199	0.9083
	R^2	0.99998	0.99997	0.99997	R^2	0.99999	0.99997	0.99999	R^2	0.99999	0.99997	0.99999
	RMSE	0.0548	0.0375	0.5585	RMSE	0.0319	0.0332	0.3435	RMSE	0.0314	0.0368	0.3456
	iterations	100	100	100	iterations	100	100	100	iterations	500	500	500
	Φ_0 (μs)	60.4605	61.6187	60.5479	Φ_0 (μs)	59.8047	60.2637	59.8518	Φ_0 (μs)	59.6257	59.0225	59.6268
	K (kPa^{-1})	0.5467	0.5808	0.5516	K (kPa^{-1})	0.5125	0.5364	0.5150	K (kPa^{-1})	0.5029	0.4845	0.5027

4.- Accuracy of the fitting models for different criteria using calibration data

Table 4: Accuracy (root mean square error, RMSE) of the fitting models for different criteria: (a) minimum mean square error (MSE) in τ_m , (b) minimum mean square error (MSE) in pO_2 , (c) minimum mean square relative error in pO_2 . Calibration data were used for evaluating the models (see Table 2).

Range	Stern-Volmer (SV)			Lehrer (L)			2 nd order Polynomial (P2)					
pO_2	Evaluation (criterion)	(a)	(b)	(c)	Evaluation (criterion)	(a)	(b)	(c)	Evaluation (criterion)	(a)	(b)	(c)
0.5-20 (kPa)	RMSE τ_m (μs)	0.7861	2.9550	0.8416	RMSE τ_m (μs)	0.1246	0.4890	0.1419	RMSE τ_m (μs)	0.0553	0.2156	0.0611
	RMSE pO_2 (kPa)	1.3617	0.5513	1.1552	RMSE pO_2 (kPa)	0.2822	0.0745	0.1501	RMSE pO_2 (kPa)	0.1156	0.0443	0.0736
	RMSE relat. pO_2 (%)	9.1780	51.9854	8.6733	RMSE relat. pO_2 (%)	1.7673	5.8627	1.4637	RMSE relat. pO_2 (%)	0.7510	2.4128	0.6662
Range	1 st order Polynomial-Exponent (PE1)			2 nd order Polynomial-Exponent (PE2)			Demas (D)					
pO_2	Evaluation (criterion)	(a)	(b)	(c)	Evaluation (criterion)	(a)	(b)	(c)	Evaluation (criterion)	(a)	(b)	(c)
0.5-20 (kPa)	RMSE τ_m (μs)	0.0548	0.1424	0.0582	RMSE τ_m (μs)	0.0319	0.0402	0.0321	RMSE τ_m (μs)	0.0314	0.0692	0.0315
	RMSE pO_2 (kPa)	0.0813	0.0375	0.0538	RMSE pO_2 (kPa)	0.0355	0.0332	0.0340	RMSE pO_2 (kPa)	0.0403	0.0368	0.0395
	RMSE relat. pO_2 (%)	0.6091	1.4166	0.5585	RMSE relat. pO_2 (%)	0.3471	0.3967	0.3435	RMSE relat. pO_2 (%)	0.3466	0.7560	0.3456

5.- Accuracy of the fitting models for different criteria using test data

Table 5: Accuracy (root mean square error, RMSE) of the fitting models for different criteria: (a) minimum mean square error (MSE) in τ_m , (b) minimum mean square error (MSE) in pO_2 , (c) minimum mean square relative error in pO_2 . Test data were used for evaluating the models (see Table 2).

Range	Stern-Volmer (SV)			Lehrer (L)			2 nd order Polynomial (P2)					
pO_2	Evaluation (criterion)	(a)	(b)	(c)	Evaluation (criterion)	(a)	(b)	(c)	Evaluation (criterion)	(a)	(b)	(c)
0.75-18 (kPa)	RMSE τ_m (μs)	0.8971	1.9784	1.0321	RMSE τ_m (μs)	0.2991	0.3507	0.3449	RMSE τ_m (μs)	0.2458	0.2528	0.2640
	RMSE pO_2 (kPa)	1.1098	0.4286	0.9214	RMSE pO_2 (kPa)	0.3623	0.2429	0.3045	RMSE pO_2 (kPa)	0.2611	0.2239	0.2471
	RMSE relat. pO_2 (%)	8.9014	28.2498	9.4462	RMSE relat. pO_2 (%)	3.1964	3.2421	3.3593	RMSE relat. pO_2 (%)	2.5114	2.3923	2.6140
Range	1 st order Polynomial-Exponent (PE1)			2 nd order Polynomial-Exponent (PE2)			Demas (D)					
pO_2	Evaluation (criterion)	(a)	(b)	(c)	Evaluation (criterion)	(a)	(b)	(c)	Evaluation (criterion)	(a)	(b)	(c)
0.75-18 (kPa)	RMSE τ_m (μs)	0.2189	0.2347	0.2064	RMSE τ_m (μs)	0.2278	0.2178	0.2265	RMSE τ_m (μs)	0.2237	0.2324	0.2241
	RMSE pO_2 (kPa)	0.1884	0.1998	0.1878	RMSE pO_2 (kPa)	0.2131	0.2083	0.2101	RMSE pO_2 (kPa)	0.1985	0.2097	0.2001
	RMSE relat. pO_2 (%)	2.1259	2.2677	2.0246	RMSE relat. pO_2 (%)	2.2523	2.1667	2.2347	RMSE relat. pO_2 (%)	2.1838	2.2557	2.1915

Experiment 3

page 1/2

Table 1: Sensing phase information

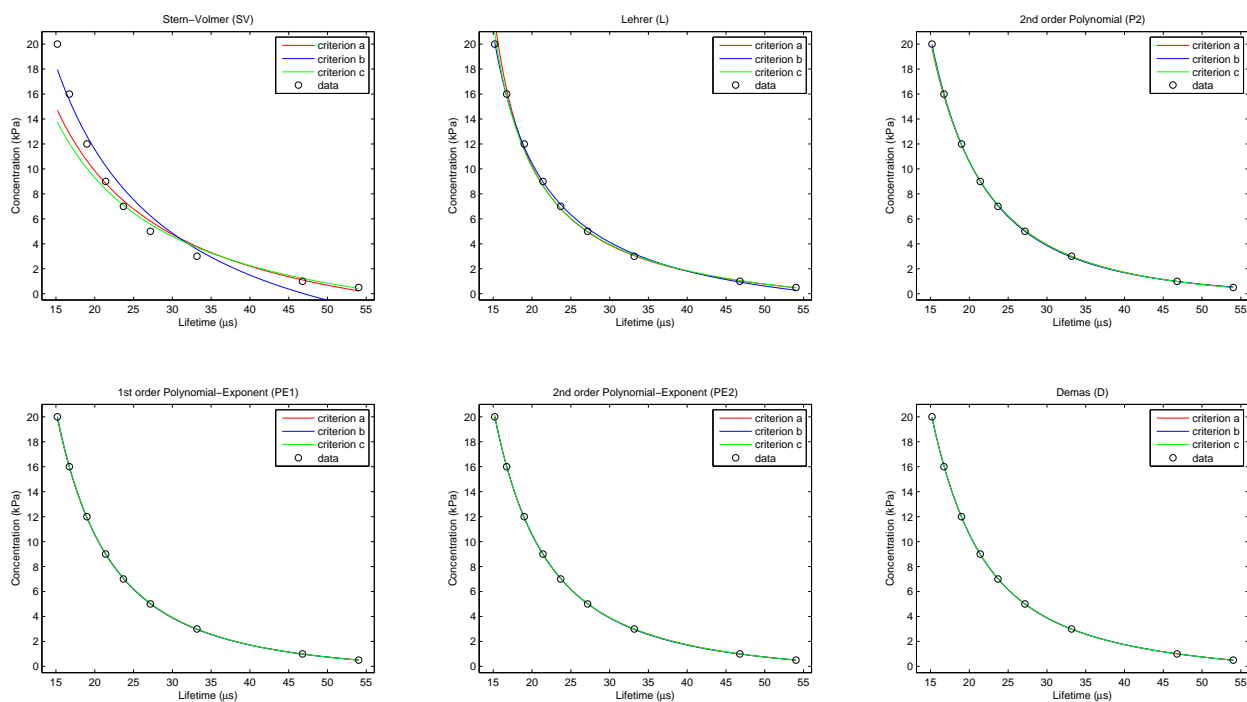
Name:	PtTFPP/PS
Description:	An oxygen-sensing film coated at the end of an optical fibre (a Platinum(II) 5,10,15,20-meso-tetrakis-(2,3,4,5,6-pentafluorophenyl)-porphyrin immobilized in polystyrene).
Analyte:	Partial pressure of oxygen in the gas phase (pO_2 , kPa); Range: 0.5-20 kPa.
Analytical signal:	(Measurement method): Luminescence lifetime in the frequency domain (<i>i.e.</i> , apparent lifetime estimated from phase-shift) using a phase-modulation method. (Instrumentation): Measurement system based on the multifrequency I/Q method (see reference); Excitation signal: 10% duty cycle rectangular-wave (fundamental frequency: 1715 Hz); Measurement frequency: 1 st harmonic (1715 Hz).
Reference(s):	Medina-Rodríguez, S.; de la Torre-Vega, A.; Fernández-Sánchez, J. F.; Fernández-Gutiérrez, A. <i>Sensors and Actuators B: Chemical</i> 2013 , 176, 1110-1120.

1.- Experimental data (calibration and test)

Table 2: Experimental data (*i.e.*, calibration and test data); apparent phase-shift lifetime measurements (τ_ϕ , in microseconds) for several oxygen concentrations (pO_2 , in kPa) at room temperature (21 °C). All the values correspond to the average of 25 measurements.

Calibration data (τ_ϕ , in microseconds)			Test data (τ_ϕ , in microseconds)		
pO_2 (kPa)	Mean (μs)	Sdev (μs)	pO_2 (kPa)	Mean (μs)	Sdev (μs)
0.50	54.0257	0.0918	0.75	49.9349	0.0956
1.00	46.7773	0.0887	2.00	38.2474	0.0707
3.00	33.1722	0.0776	4.00	29.6878	0.1001
5.00	27.1615	0.1085	6.00	25.2382	0.1214
7.00	23.6878	0.1146	8.00	22.4154	0.1141
9.00	21.3972	0.1145	10.00	20.4579	0.1344
12.00	18.9901	0.1134	14.00	17.7608	0.1505
16.00	16.7298	0.1550	18.00	15.7708	0.1821
20.00	15.1776	0.1974			

2.- Calibration curves: models and criteria


Figure 1: Calibration curves for the apparent phase-shift lifetime measurements (calibration data) of the sensing phase using different models and criteria. Models: Stern-Volmer (SV) (2 parameters), Lehrer (L) (3 parameters), 2nd order Polynomial (P2) (3 parameters), 1st order Polynomial-Exponent (PE1) (3 parameters), 2nd order Polynomial-Exponent (PE2) (4 parameters), Demas (D) (4 parameters). Criteria: (a) minimum mean square error (MSE) in τ_ϕ , (b) minimum mean square error (MSE) in pO_2 , (c) minimum mean square relative error in pO_2 .

Experiment 3

3.- Parameters of the fitting models for different criteria

Table 3: Parameters of the fitting models for different criteria: (a) minimum mean square error (MSE) in τ_ϕ , (b) minimum mean square error (MSE) in pO_2 , (c) minimum mean square relative error in pO_2 . RMSE is expressed in microseconds for criterion (a), in kPa for criterion (b) and in relative error (%) for criterion (c). Calibration data used are shown in Table 2.

Range	Stern-Volmer (SV)			Lehrer (L)			2 nd order Polynomial (P2)					
pO_2	Parameter	(a)	(b)	(c)	Parameter	(a)	(b)	(c)	Parameter	(a)	(b)	(c)
0.5-20 (kPa)	τ_0 (μs)	56.2872	46.9722	58.8652	τ_0 (μs)	62.8756	58.0762	62.7356	a_0	-0.5042	-0.0633	-0.4421
	k (kPa^{-1})	0.1843	0.1166	0.2091	k (kPa^{-1})	0.4204	0.3150	0.4040	a_1	-43.6061	-73.5763	-48.658
	—	—	—	—	x	0.8407	0.8549	0.8478	a_2	5300.1	5734.32	5390.15
	R^2	0.97322	0.96205	0.96281	R^2	0.99944	0.99917	0.99866	R^2	0.99993	0.99997	0.99987
	RMSE	2.1052	1.2406	19.2846	RMSE	0.3042	0.1830	3.6554	RMSE	0.1111	0.0367	1.1270
	iterations	100	1	1	iterations	100	100	100	iterations	100	1	1
0.5-20 (kPa)	Φ_0 (μs)	56.2872	46.9722	58.8652	Φ_0 (μs)	62.8756	58.0762	62.7356	Φ_0 (μs)	68.0290	73.3152	68.3388
	K (kPa^{-1})	0.1843	0.1166	0.2091	K (kPa^{-1})	0.3534	0.2693	0.3426	K (kPa^{-1})	0.6062	0.8849	0.6264
	—	—	—	—	—	—	—	—	—	—	—	—
	—	—	—	—	—	—	—	—	—	—	—	—
	—	—	—	—	—	—	—	—	—	—	—	—
	—	—	—	—	—	—	—	—	—	—	—	—
Range	1 st order Polynomial-Exponent (PE1)			2 nd order Polynomial-Exponent (PE2)			Demas (D)					
pO_2	Parameter	(a)	(b)	(c)	Parameter	(a)	(b)	(c)	Parameter	(a)	(b)	(c)
0.5-20 (kPa)	a_0	-0.8295	-0.7663	-0.8176	a_0	-1.2257	-0.6602	-1.1935	τ_0 (μs)	65.1484	64.6276	65.1771
	a_1	7331.81	8153.93	7558.05	a_1	161.173	-15.3234	130.515	k_1 (kPa^{-1})	0.5785	0.5497	0.5783
	α	-2.1588	-2.1959	-2.1688	a_2	15046.5	7638.11	13495.7	k_2 (kPa^{-1})	0.0219	0.0198	0.0217
	—	—	—	—	α	-1.2578	-1.0798	-1.2309	x	0.7515	0.7609	0.7526
	R^2	0.99996	0.99998	0.99994	R^2	0.99999	0.99998	0.99998	R^2	0.99999	0.99998	0.99998
	RMSE	0.0768	0.0317	0.7476	RMSE	0.0380	0.0314	0.4256	RMSE	0.0457	0.0271	0.4217
iterations	100	100	100	iterations	100	100	100	iterations	500	500	500	
0.5-20 (kPa)	Φ_0 (μs)	67.3036	68.2124	67.3898	Φ_0 (μs)	66.0609	68.8899	66.1740	Φ_0 (μs)	65.1484	64.6276	65.1771
	K (kPa^{-1})	0.5584	0.5943	0.5640	K (kPa^{-1})	0.4898	0.6261	0.4960	K (kPa^{-1})	0.4402	0.4230	0.4406
	—	—	—	—	—	—	—	—	—	—	—	—
	—	—	—	—	—	—	—	—	—	—	—	—
	—	—	—	—	—	—	—	—	—	—	—	—
	—	—	—	—	—	—	—	—	—	—	—	—

4.- Accuracy of the fitting models for different criteria using calibration data

Table 4: Accuracy (root mean square error, RMSE) of the fitting models for different criteria: (a) minimum mean square error (MSE) in τ_ϕ , (b) minimum mean square error (MSE) in pO_2 , (c) minimum mean square relative error in pO_2 . Calibration data were used for evaluating the models (see Table 2).

Range	Stern-Volmer (SV)			Lehrer (L)			2 nd order Polynomial (P2)					
pO_2	Evaluation (criterion)	(a)	(b)	(c)	Evaluation (criterion)	(a)	(b)	(c)	Evaluation (criterion)	(a)	(b)	(c)
0.5-20 (kPa)	RMSE τ_ϕ (μs)	2.1052	3.8405	2.2709	RMSE τ_ϕ (μs)	0.3042	0.9818	0.3391	RMSE τ_ϕ (μs)	0.1111	0.3078	0.1158
	RMSE pO_2 (kPa)	2.1483	1.2406	2.5753	RMSE pO_2 (kPa)	0.6955	0.1830	0.3792	RMSE pO_2 (kPa)	0.1470	0.0367	0.1027
	RMSE relat. pO_2 (%)	24.2636	113.4885	19.2846	RMSE relat. pO_2 (%)	4.3830	14.9805	3.6554	RMSE relat. pO_2 (%)	1.1831	2.8079	1.1270
Range	1 st order Polynomial-Exponent (PE1)			2 nd order Polynomial-Exponent (PE2)			Demas (D)					
pO_2	Evaluation (criterion)	(a)	(b)	(c)	Evaluation (criterion)	(a)	(b)	(c)	Evaluation (criterion)	(a)	(b)	(c)
0.5-20 (kPa)	RMSE τ_ϕ (μs)	0.0768	0.1088	0.0791	RMSE τ_ϕ (μs)	0.0380	0.1403	0.0389	RMSE τ_ϕ (μs)	0.0457	0.0649	0.0464
	RMSE pO_2 (kPa)	0.0755	0.0317	0.0503	RMSE pO_2 (kPa)	0.0545	0.0314	0.0462	RMSE pO_2 (kPa)	0.0374	0.0271	0.0330
	RMSE relat. pO_2 (%)	0.7787	1.0476	0.7476	RMSE relat. pO_2 (%)	0.4361	1.3594	0.4256	RMSE relat. pO_2 (%)	0.4317	0.7066	0.4217

5.- Accuracy of the fitting models for different criteria using test data

Table 5: Accuracy (root mean square error, RMSE) of the fitting models for different criteria: (a) minimum mean square error (MSE) in τ_ϕ , (b) minimum mean square error (MSE) in pO_2 , (c) minimum mean square relative error in pO_2 . Test data were used for evaluating the models (see Table 2).

Range	Stern-Volmer (SV)			Lehrer (L)			2 nd order Polynomial (P2)					
pO_2	Evaluation (criterion)	(a)	(b)	(c)	Evaluation (criterion)	(a)	(b)	(c)	Evaluation (criterion)	(a)	(b)	(c)
0.75-18 (kPa)	RMSE τ_ϕ (μs)	1.9463	2.7865	2.2187	RMSE τ_ϕ (μs)	0.2944	0.6030	0.3661	RMSE τ_ϕ (μs)	0.0980	0.1801	0.1119
	RMSE pO_2 (kPa)	1.7040	1.0454	2.0923	RMSE pO_2 (kPa)	0.5458	0.1952	0.3370	RMSE pO_2 (kPa)	0.0766	0.1227	0.0844
	RMSE relat. pO_2 (%)	16.6982	61.0064	18.2945	RMSE relat. pO_2 (%)	3.7791	6.8423	3.6609	RMSE relat. pO_2 (%)	0.9574	1.5571	1.0742
Range	1 st order Polynomial-Exponent (PE1)			2 nd order Polynomial-Exponent (PE2)			Demas (D)					
pO_2	Evaluation (criterion)	(a)	(b)	(c)	Evaluation (criterion)	(a)	(b)	(c)	Evaluation (criterion)	(a)	(b)	(c)
0.75-18 (kPa)	RMSE τ_ϕ (μs)	0.0791	0.1011	0.0870	RMSE τ_ϕ (μs)	0.0663	0.1133	0.0652	RMSE τ_ϕ (μs)	0.0721	0.0652	0.0756
	RMSE pO_2 (kPa)	0.0872	0.1223	0.1030	RMSE pO_2 (kPa)	0.1406	0.1222	0.1325	RMSE pO_2 (kPa)	0.1143	0.1245	0.1196
	RMSE relat. pO_2 (%)	0.8083	1.0033	0.8935	RMSE relat. pO_2 (%)	0.8687	1.0846	0.8336	RMSE relat. pO_2 (%)	0.8291	0.8068	0.8666

Experiment 4

page 1/2

Table 1: Sensing phase information

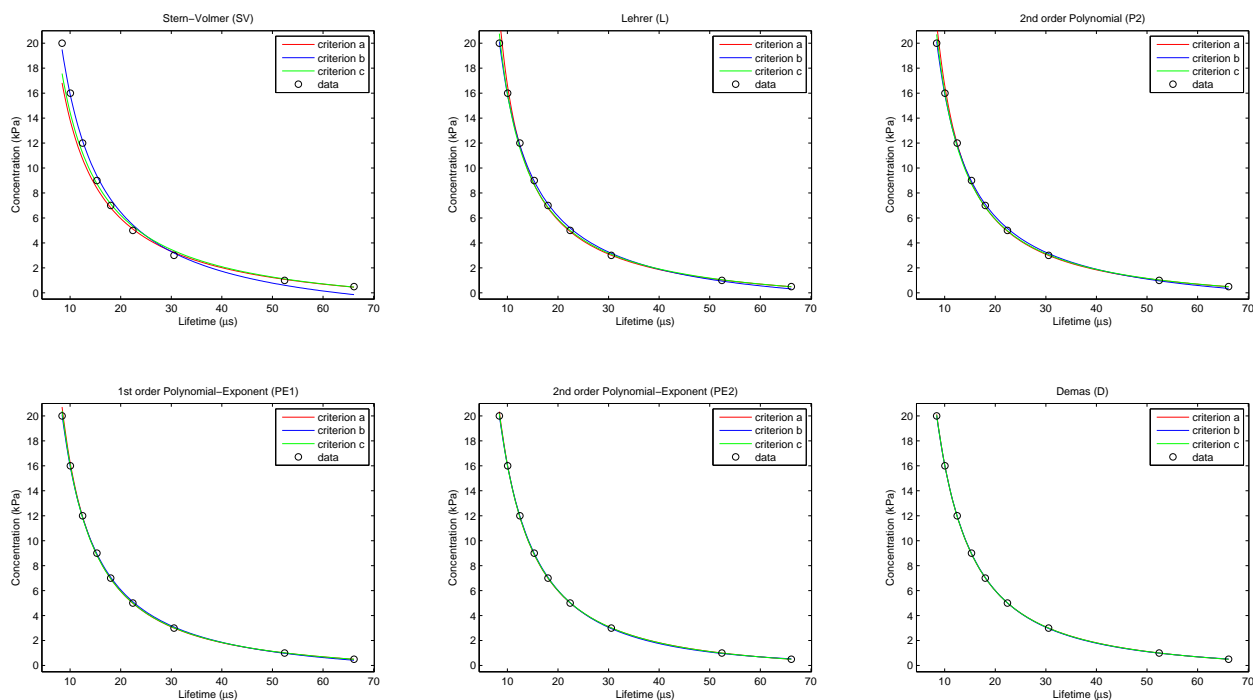
Name:	PtTFPP/PS
Description:	An oxygen-sensing film coated at the end of an optical fibre (a Platinum(II) 5,10,15,20-meso-tetrakis-(2,3,4,5,6-pentafluorophenyl)-porphyrin immobilized in polystyrene).
Analyte:	Partial pressure of oxygen in the gas phase (pO_2 , kPa); Range: 0.5-20 kPa.
Analytical signal:	(Measurement method): Luminescence lifetime in the frequency domain (<i>i.e.</i> , apparent lifetime estimated from modulation factor) using a phase-modulation method. (Instrumentation): Measurement system based on the multifrequency I/Q method (see reference); Excitation signal: 10% duty cycle rectangular-wave (fundamental frequency: 1715 Hz); Measurement frequency: 2 nd harmonic (3430 Hz).
Reference(s):	Medina-Rodríguez, S.; de la Torre-Vega, A.; Fernández-Sánchez, J. F.; Fernández-Gutiérrez, A. <i>Sensors and Actuators B: Chemical</i> 2013 , 176, 1110-1120.

1.- Experimental data (calibration and test)

Table 2: Experimental data (*i.e.*, calibration and test data); apparent modulation lifetime measurements (τ_m , in microseconds) for several oxygen concentrations (pO_2 , in kPa) at room temperature (21 °C). All the values correspond to the average of 25 measurements.

Calibration data (τ_m , in microseconds)			Test data (τ_m , in microseconds)		
pO_2 (kPa)	Mean (μs)	Sdev (μs)	pO_2 (kPa)	Mean (μs)	Sdev (μs)
0.50	66.1203	0.0723	0.75	58.1632	0.0746
1.00	52.4002	0.0719	2.00	38.1310	0.0672
3.00	30.5343	0.0587	4.00	25.7403	0.0526
5.00	22.4103	0.0542	6.00	19.9292	0.0486
7.00	18.0187	0.0595	8.00	16.5151	0.0439
9.00	15.2963	0.0424	10.00	14.2063	0.0401
12.00	12.4657	0.0449	14.00	11.1471	0.0387
16.00	10.0526	0.0460	18.00	9.0844	0.0404
20.00	8.4178	0.0348			

2.- Calibration curves: models and criteria


Figure 1: Calibration curves for the apparent modulation lifetime measurements (calibration data) of the sensing phase using different models and criteria. Models: Stern-Volmer (SV) (2 parameters), Lehrer (L) (3 parameters), 2nd order Polynomial (P2) (3 parameters), 1st order Polynomial-Exponent (PE1) (3 parameters), 2nd order Polynomial-Exponent (PE2) (4 parameters), Demas (D) (4 parameters). Criteria: (a) minimum mean square error (MSE) in τ_m , (b) minimum mean square error (MSE) in pO_2 , (c) minimum mean square relative error in pO_2 .

Experiment 4

3.- Parameters of the fitting models for different criteria

Table 3: Parameters of the fitting models for different criteria: (a) minimum mean square error (MSE) in τ_m , (b) minimum mean square error (MSE) in pO_2 , (c) minimum mean square relative error in pO_2 . RMSE is expressed in microseconds for criterion (a), in kPa for criterion (b) and in relative error (%) for criterion (c). Calibration data used are shown in Table 2.

Range	Stern-Volmer (SV)				Lehrer (L)				2 nd order Polynomial (P2)			
pO_2	Parameter	(a)	(b)	(c)	Parameter	(a)	(b)	(c)	Parameter	(a)	(b)	(c)
0.5-20 (kPa)	τ_0 (μs)	81.6688	62.9791	81.1457	τ_0 (μs)	87.3905	76.3667	86.0315	a_0	-1.2967	-1.8556	-1.4153
	k (kPa^{-1})	0.5174	0.3325	0.4917	k (kPa^{-1})	0.6920	0.5013	0.6434	a_1	107.572	140.484	117.312
	-	-	-	-	x	0.9623	0.9779	0.9697	a_2	718.376	376.584	580.099
	R^2	0.99662	0.99584	0.99231	R^2	0.99965	0.99944	0.99906	R^2	0.99984	0.99957	0.99948
	RMSE	1.1070	0.4106	8.7671	RMSE	0.3585	0.1512	3.0631	RMSE	0.2432	0.1322	2.2866
	iterations	100	1	1	iterations	100	100	100	iterations	100	1	1
	Φ_0 (μs)	81.6688	62.9791	81.1457	Φ_0 (μs)	87.3905	76.3667	86.0315	Φ_0 (μs)	89.1711	78.2994	87.5719
	K (kPa^{-1})	0.5174	0.3325	0.4917	K (kPa^{-1})	0.6659	0.4902	0.6239	K (kPa^{-1})	0.7210	0.5216	0.6707
Range	1 st order Polynomial-Exponent (PE1)				2 nd order Polynomial-Exponent (PE2)				Demas (D)			
pO_2	Parameter	(a)	(b)	(c)	Parameter	(a)	(b)	(c)	Parameter	(a)	(b)	(c)
0.5-20 (kPa)	a_0	-0.8992	-1.2397	-0.9558	a_0	-0.2993	3.9680	0.1589	τ_0 (μs)	92.4153	97.5239	92.6869
	a_1	366.518	299.125	343.803	a_1	-17.2121	-64.2367	-25.5074	k_1 (kPa^{-1})	0.9448	1.1803	0.9618
	α	-1.3287	-1.2391	-1.3042	a_2	313.455	269.113	293.289	k_2 (kPa^{-1})	0.0857	0.1144	0.0901
	-	-	-	-	α	-0.5883	-0.4405	-0.5523	x	0.8702	0.8263	0.8643
	R^2	0.99997	0.99981	0.99987	R^2	0.99999	0.99997	0.99996	R^2	1.00000	0.99998	0.99999
	RMSE	0.1021	0.0883	1.1233	RMSE	0.0655	0.0369	0.6399	RMSE	0.0339	0.0267	0.3355
iterations	100	100	100	iterations	100	100	100	iterations	500	500	500	
	Φ_0 (μs)	92.1573	83.7048	91.1525	Φ_0 (μs)	94.6382	109.4278	96.3891	Φ_0 (μs)	92.4153	97.5239	92.6869
	K (kPa^{-1})	0.8370	0.6510	0.8022	K (kPa^{-1})	0.9536	1.5524	1.0477	K (kPa^{-1})	0.8333	0.9952	0.8435

4.- Accuracy of the fitting models for different criteria using calibration data

Table 4: Accuracy (root mean square error, RMSE) of the fitting models for different criteria: (a) minimum mean square error (MSE) in τ_m , (b) minimum mean square error (MSE) in pO_2 , (c) minimum mean square relative error in pO_2 . Calibration data were used for evaluating the models (see Table 2).

Range	Stern-Volmer (SV)				Lehrer (L)				2 nd order Polynomial (P2)			
pO_2	Evaluation (criterion)	(a)	(b)	(c)	Evaluation (criterion)	(a)	(b)	(c)	Evaluation (criterion)	(a)	(b)	(c)
0.5-20 (kPa)	RMSE τ_m (μs)	1.1070	4.4335	1.2237	RMSE τ_m (μs)	0.3585	1.6532	0.4410	RMSE τ_m (μs)	0.2432	1.3656	0.3111
	RMSE pO_2 (kPa)	1.3824	0.4106	1.0272	RMSE pO_2 (kPa)	0.7896	0.1512	0.3174	RMSE pO_2 (kPa)	0.5722	0.1322	0.2716
	RMSE relat. pO_2 (%)	9.5769	45.0626	8.7671	RMSE relat. pO_2 (%)	4.4637	12.5768	3.0631	RMSE relat. pO_2 (%)	3.1535	9.9666	2.2866
Range	1 st order Polynomial-Exponent (PE1)				2 nd order Polynomial-Exponent (PE2)				Demas (D)			
pO_2	Evaluation (criterion)	(a)	(b)	(c)	Evaluation (criterion)	(a)	(b)	(c)	Evaluation (criterion)	(a)	(b)	(c)
0.5-20 (kPa)	RMSE τ_m (μs)	0.1021	0.8535	0.1313	RMSE τ_m (μs)	0.0655	0.5973	0.0793	RMSE τ_m (μs)	0.0339	0.2198	0.0364
	RMSE pO_2 (kPa)	0.2512	0.0883	0.1546	RMSE pO_2 (kPa)	0.1253	0.0369	0.0767	RMSE pO_2 (kPa)	0.0511	0.0267	0.0401
	RMSE relat. pO_2 (%)	1.3726	5.5099	1.1233	RMSE relat. pO_2 (%)	0.7566	2.5807	0.6399	RMSE relat. pO_2 (%)	0.3546	1.1486	0.3355

5.- Accuracy of the fitting models for different criteria using test data

Table 5: Accuracy (root mean square error, RMSE) of the fitting models for different criteria: (a) minimum mean square error (MSE) in τ_m , (b) minimum mean square error (MSE) in pO_2 , (c) minimum mean square relative error in pO_2 . Test data were used for evaluating the models (see Table 2).

Range	Stern-Volmer (SV)				Lehrer (L)				2 nd order Polynomial (P2)			
pO_2	Evaluation (criterion)	(a)	(b)	(c)	Evaluation (criterion)	(a)	(b)	(c)	Evaluation (criterion)	(a)	(b)	(c)
0.75-18 (kPa)	RMSE τ_m (μs)	1.0878	2.8220	1.3057	RMSE τ_m (μs)	0.3490	0.8944	0.4766	RMSE τ_m (μs)	0.2462	0.7174	0.3396
	RMSE pO_2 (kPa)	1.1502	0.3476	0.8272	RMSE pO_2 (kPa)	0.5645	0.1512	0.2659	RMSE pO_2 (kPa)	0.4526	0.1383	0.2375
	RMSE relat. pO_2 (%)	8.6655	24.1247	8.4827	RMSE relat. pO_2 (%)	3.7144	5.7364	3.1138	RMSE relat. pO_2 (%)	2.8108	4.4493	2.3613
Range	1 st order Polynomial-Exponent (PE1)				2 nd order Polynomial-Exponent (PE2)				Demas (D)			
pO_2	Evaluation (criterion)	(a)	(b)	(c)	Evaluation (criterion)	(a)	(b)	(c)	Evaluation (criterion)	(a)	(b)	(c)
0.75-18 (kPa)	RMSE τ_m (μs)	0.1262	0.4288	0.1632	RMSE τ_m (μs)	0.0819	0.2348	0.0744	RMSE τ_m (μs)	0.0804	0.1526	0.0769
	RMSE pO_2 (kPa)	0.2300	0.1077	0.1596	RMSE pO_2 (kPa)	0.1413	0.0782	0.1060	RMSE pO_2 (kPa)	0.0960	0.0744	0.0863
	RMSE relat. pO_2 (%)	1.4132	2.5268	1.2863	RMSE relat. pO_2 (%)	0.9038	1.3057	0.7549	RMSE relat. pO_2 (%)	0.6667	0.8831	0.6250

Experiment 5

page 1/2

Table 1: Sensing phase information

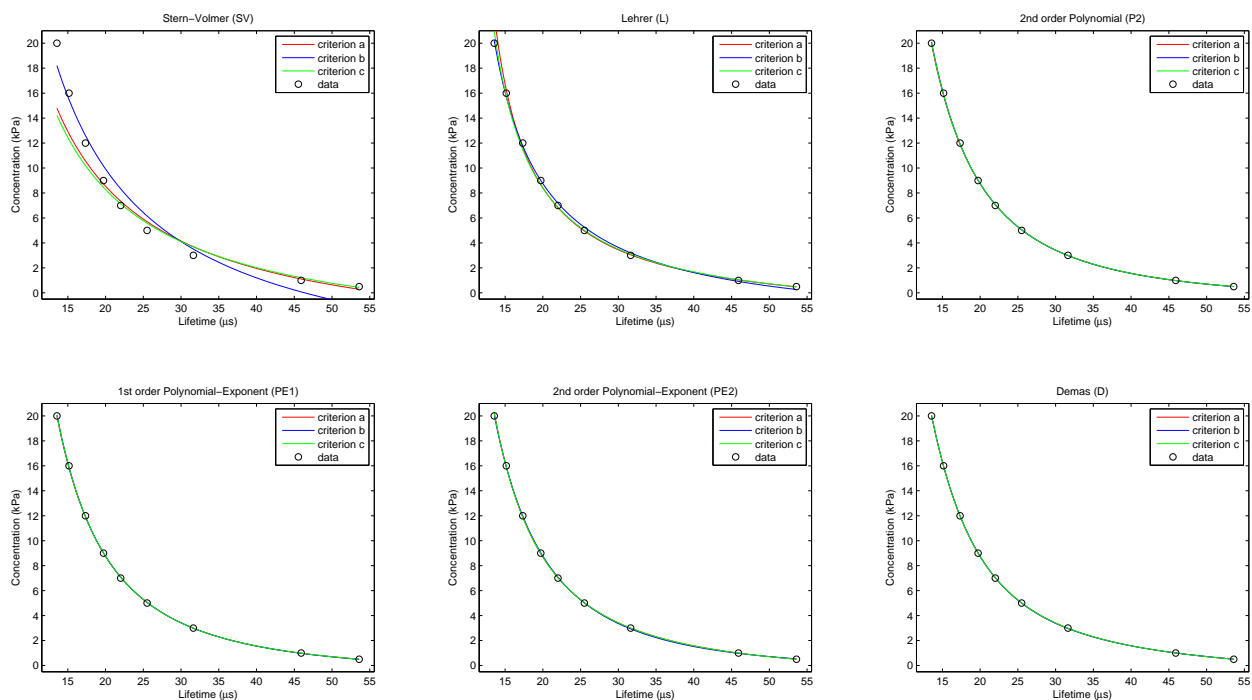
Name:	PtTFPP/PS
Description:	An oxygen-sensing film coated at the end of an optical fibre (a Platinum(II) 5,10,15,20-meso-tetrakis-(2,3,4,5,6-pentafluorophenyl)-porphyrin immobilized in polystyrene).
Analyte:	Partial pressure of oxygen in the gas phase (pO_2 , kPa); Range: 0.5-20 kPa.
Analytical signal:	(Measurement method): Luminescence lifetime in the frequency domain (<i>i.e.</i> , apparent lifetime estimated from phase-shift) using a phase-modulation method. (Instrumentation): Measurement system based on the multifrequency I/Q method (see reference); Excitation signal: 10% duty cycle rectangular-wave (fundamental frequency: 1715 Hz); Measurement frequency: 2 nd harmonic (3430 Hz).
Reference(s):	Medina-Rodríguez, S.; de la Torre-Vega, A.; Fernández-Sánchez, J. F.; Fernández-Gutiérrez, A. <i>Sensors and Actuators B: Chemical</i> 2013 , 176, 1110-1120.

1.- Experimental data (calibration and test)

Table 2: Experimental data (*i.e.*, calibration and test data); apparent phase-shift lifetime measurements (τ_ϕ , in microseconds) for several oxygen concentrations (pO_2 , in kPa) at room temperature (21 °C). All the values correspond to the average of 25 measurements.

Calibration data (τ_ϕ , in microseconds)			Test data (τ_ϕ , in microseconds)		
pO_2 (kPa)	Mean (μs)	Sdev (μs)	pO_2 (kPa)	Mean (μs)	Sdev (μs)
0.50	53.5916	0.0669	0.75	49.2501	0.0874
1.00	45.9113	0.0775	2.00	36.9030	0.0729
3.00	31.6271	0.0946	4.00	28.0799	0.0733
5.00	25.4994	0.0835	6.00	23.5797	0.1107
7.00	22.0011	0.1007	8.00	20.7684	0.0775
9.00	19.7315	0.0940	10.00	18.8299	0.0845
12.00	17.3437	0.1072	14.00	16.1179	0.1071
16.00	15.1621	0.0973	18.00	14.2264	0.1464
20.00	13.5607	0.1340			

2.- Calibration curves: models and criteria


Figure 1: Calibration curves for the apparent phase-shift lifetime measurements (calibration data) of the sensing phase using different models and criteria. Models: Stern-Volmer (SV) (2 parameters), Lehrer (L) (3 parameters), 2nd order Polynomial (P2) (3 parameters), 1st order Polynomial-Exponent (PE1) (3 parameters), 2nd order Polynomial-Exponent (PE2) (4 parameters), Demas (D) (4 parameters). Criteria: (a) minimum mean square error (MSE) in τ_ϕ , (b) minimum mean square error (MSE) in pO_2 , (c) minimum mean square relative error in pO_2 .

Experiment 5

3.- Parameters of the fitting models for different criteria

Table 3: Parameters of the fitting models for different criteria: (a) minimum mean square error (MSE) in τ_ϕ , (b) minimum mean square error (MSE) in pO_2 , (c) minimum mean square relative error in pO_2 . RMSE is expressed in microseconds for criterion (a), in kPa for criterion (b) and in relative error (%) for criterion (c). Calibration data used are shown in Table 2.

Range	Stern-Volmer (SV)			Lehrer (L)			2 nd order Polynomial (P2)						
pO_2	Parameter	(a)	(b)	(c)	Parameter	(a)	(b)	(c)	Parameter	(a)	(b)	(c)	
0.5-20 (kPa)	τ_0 (μs)	56.9092	46.3770	59.0720	τ_0 (μs)	63.4096	57.6964	63.1159	a_0	-0.8573	-0.7800	-0.8228	
	k (kPa^{-1})	0.2160	0.1329	0.2360	k (kPa^{-1})	0.4528	0.3300	0.4309	a_1	2.14343	-4.15649	-0.625853	
	-	-	-	-	x	0.8643	0.8796	0.8720	a_2	3793.21	3894.54	3840.89	
	R^2	0.97822	0.96793	0.96747	R^2	0.99950	0.99889	0.99869	R^2	0.99996	0.99990	0.99992	
	RMSE	1.9556	1.1405	18.0361	RMSE	0.2968	0.2123	3.6240	RMSE	0.0884	0.0629	0.8668	
	iterations	100	1	1	iterations	100	100	100	iterations	100	1	1	
0.5-20 (kPa)	Φ_0 (μs)	56.9092	46.3770	59.0720	Φ_0 (μs)	63.4096	57.6964	63.1159	Φ_0 (μs)	67.7810	68.0481	67.9449	
	K (kPa^{-1})	0.2160	0.1329	0.2360	K (kPa^{-1})	0.3914	0.2903	0.3757	K (kPa^{-1})	0.5942	0.6169	0.6043	
	1 st order Polynomial-Exponent (PE1)			2 nd order Polynomial-Exponent (PE2)			Demas (D)						
	pO_2	Parameter	(a)	(b)	(c)	Parameter	(a)	(b)	(c)	Parameter	(a)	(b)	(c)
	0.5-20 (kPa)	a_0	-0.8324	-0.8320	-0.8205	a_0	-1.2360	0.3275	-1.1716	τ_0 (μs)	65.7472	66.7099	65.8042
		a_1	3797.05	3937.61	3905.26	a_1	118.793	-73.268	77.9569	k_1 (kPa^{-1})	0.6100	0.6543	0.6132
α		-1.9973	-2.0089	-2.0068	a_2	7308.61	2653.57	6032.53	k_2 (kPa^{-1})	0.0243	0.0269	0.0245	
-		-	-	-	α	-1.1749	-0.8789	-1.1238	x	0.7810	0.7716	0.7801	
R^2		0.99995	0.99990	0.99993	R^2	0.99998	0.99993	0.99996	R^2	0.99999	0.99999	0.99999	
RMSE		0.0895	0.0636	0.8588	RMSE	0.0520	0.0536	0.6448	RMSE	0.0331	0.0227	0.3163	
iterations	100	100	100	iterations	100	100	100	iterations	500	500	500		
0.5-20 (kPa)	Φ_0 (μs)	67.9272	67.5116	68.0148	Φ_0 (μs)	66.5652	76.9057	66.7945	Φ_0 (μs)	65.7472	66.7099	65.8042	
	K (kPa^{-1})	0.6015	0.5983	0.6074	K (kPa^{-1})	0.5268	1.1889	0.5395	K (kPa^{-1})	0.4817	0.5110	0.4837	

4.- Accuracy of the fitting models for different criteria using calibration data

Table 4: Accuracy (root mean square error, RMSE) of the fitting models for different criteria: (a) minimum mean square error (MSE) in τ_ϕ , (b) minimum mean square error (MSE) in pO_2 , (c) minimum mean square relative error in pO_2 . Calibration data were used for evaluating the models (see Table 2).

Range	Stern-Volmer (SV)			Lehrer (L)			2 nd order Polynomial (P2)					
pO_2	Evaluation (criterion)	(a)	(b)	(c)	Evaluation (criterion)	(a)	(b)	(c)	Evaluation (criterion)	(a)	(b)	(c)
0.5-20 (kPa)	RMSE τ_ϕ (μs)	1.9556	3.9713	2.0587	RMSE τ_ϕ (μs)	0.2968	1.1213	0.3394	RMSE τ_ϕ (μs)	0.0884	0.1142	0.0913
	RMSE pO_2 (kPa)	2.1340	1.1405	2.3987	RMSE pO_2 (kPa)	0.7600	0.2123	0.4066	RMSE pO_2 (kPa)	0.0923	0.0629	0.0698
	RMSE relat. pO_2 (%)	20.9530	106.2052	18.0361	RMSE relat. pO_2 (%)	4.4972	16.1074	3.6240	RMSE relat. pO_2 (%)	0.9050	0.9917	0.8668
1 st order Polynomial-Exponent (PE1)			2 nd order Polynomial-Exponent (PE2)			Demas (D)						
pO_2	Evaluation (criterion)	(a)	(b)	(c)	Evaluation (criterion)	(a)	(b)	(c)	Evaluation (criterion)	(a)	(b)	(c)
0.5-20 (kPa)	RMSE τ_ϕ (μs)	0.0895	0.1410	0.0918	RMSE τ_ϕ (μs)	0.0520	0.3348	0.0553	RMSE τ_ϕ (μs)	0.0331	0.0947	0.0334
	RMSE pO_2 (kPa)	0.0822	0.0636	0.0663	RMSE pO_2 (kPa)	0.1081	0.0536	0.0878	RMSE pO_2 (kPa)	0.0305	0.0227	0.0292
	RMSE relat. pO_2 (%)	0.8894	1.2494	0.8588	RMSE relat. pO_2 (%)	0.6787	2.7766	0.6448	RMSE relat. pO_2 (%)	0.3197	0.9129	0.3163

5.- Accuracy of the fitting models for different criteria using test data

Table 5: Accuracy (root mean square error, RMSE) of the fitting models for different criteria: (a) minimum mean square error (MSE) in τ_ϕ , (b) minimum mean square error (MSE) in pO_2 , (c) minimum mean square relative error in pO_2 . Test data were used for evaluating the models (see Table 2).

Range	Stern-Volmer (SV)			Lehrer (L)			2 nd order Polynomial (P2)					
pO_2	Evaluation (criterion)	(a)	(b)	(c)	Evaluation (criterion)	(a)	(b)	(c)	Evaluation (criterion)	(a)	(b)	(c)
0.75-18 (kPa)	RMSE τ_ϕ (μs)	1.8317	2.8353	2.0486	RMSE τ_ϕ (μs)	0.2885	0.6857	0.3707	RMSE τ_ϕ (μs)	0.0647	0.1005	0.0712
	RMSE pO_2 (kPa)	1.7200	0.9681	1.9608	RMSE pO_2 (kPa)	0.4959	0.1709	0.2911	RMSE pO_2 (kPa)	0.0551	0.0685	0.0569
	RMSE relat. pO_2 (%)	15.5331	57.5322	17.1870	RMSE relat. pO_2 (%)	3.5565	7.5611	3.5062	RMSE relat. pO_2 (%)	0.6295	0.8801	0.6660
1 st order Polynomial-Exponent (PE1)			2 nd order Polynomial-Exponent (PE2)			Demas (D)						
pO_2	Evaluation (criterion)	(a)	(b)	(c)	Evaluation (criterion)	(a)	(b)	(c)	Evaluation (criterion)	(a)	(b)	(c)
0.75-18 (kPa)	RMSE τ_ϕ (μs)	0.0661	0.1180	0.0727	RMSE τ_ϕ (μs)	0.0545	0.1858	0.0505	RMSE τ_ϕ (μs)	0.0549	0.1017	0.0563
	RMSE pO_2 (kPa)	0.0533	0.0685	0.0603	RMSE pO_2 (kPa)	0.1045	0.0705	0.0863	RMSE pO_2 (kPa)	0.0720	0.0712	0.0719
	RMSE relat. pO_2 (%)	0.6282	1.0335	0.6750	RMSE relat. pO_2 (%)	0.6890	1.4695	0.6019	RMSE relat. pO_2 (%)	0.5772	0.9052	0.5845

Experiment 6

page 1/2

Table 1: Sensing phase information

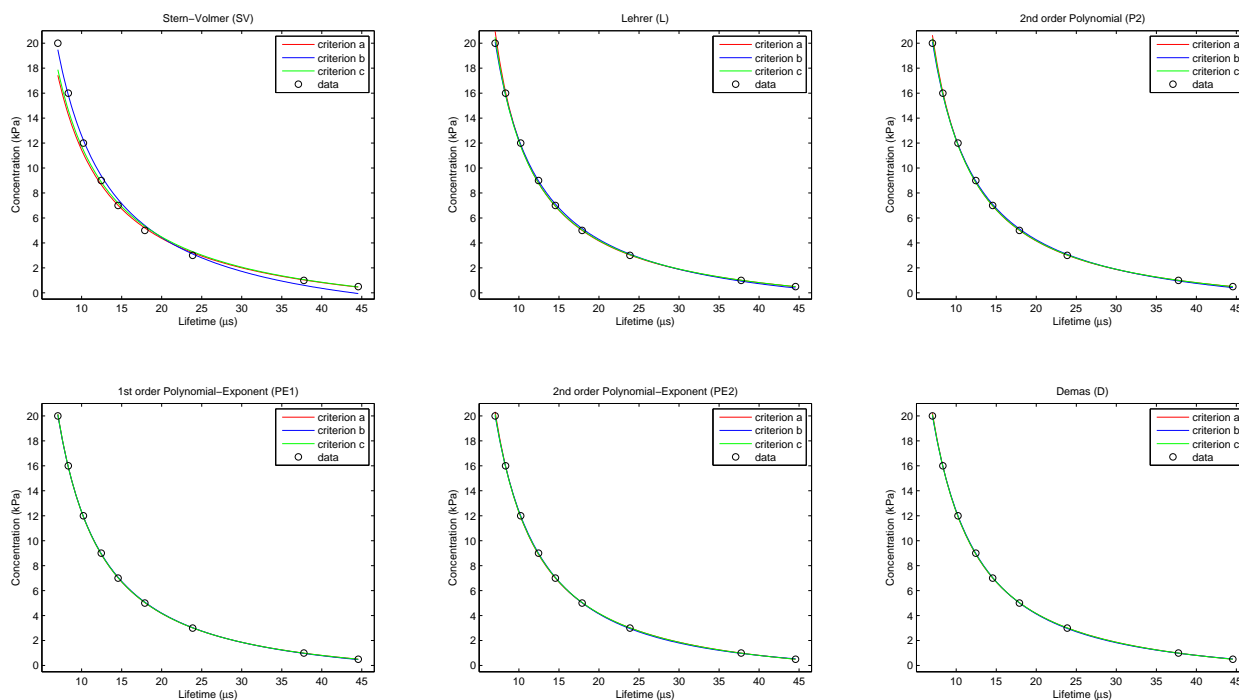
Name:	PtTFPP/PS
Description:	An oxygen-sensing film coated at the end of an optical fibre (a Platinum(II) 5,10,15,20-meso-tetrakis-(2,3,4,5,6-pentafluorophenyl)-porphyrin immobilized in polystyrene).
Analyte:	Partial pressure of oxygen in the gas phase (pO_2 , kPa); Range: 0.5-20 kPa.
Analytical signal:	(Measurement method): Luminescence lifetime in the frequency domain (<i>i.e.</i> , apparent lifetime estimated from modulation factor) using a phase-modulation method. (Instrumentation): Measurement system based on the multifrequency I/Q method (see reference); Excitation signal: 10% duty cycle rectangular-wave (fundamental frequency: 1715 Hz); Measurement frequency: 3 rd harmonic (5145 Hz).
Reference(s):	Medina-Rodríguez, S.; de la Torre-Vega, A.; Fernández-Sánchez, J. F.; Fernández-Gutiérrez, A. <i>Sensors and Actuators B: Chemical</i> 2013 , 176, 1110-1120.

1.- Experimental data (calibration and test)

Table 2: Experimental data (*i.e.*, calibration and test data); apparent modulation lifetime measurements (τ_m , in microseconds) for several oxygen concentrations (pO_2 , in kPa) at room temperature (21 °C). All the values correspond to the average of 25 measurements.

Calibration data (τ_m , in microseconds)			Test data (τ_m , in microseconds)		
pO_2 (kPa)	Mean (μs)	Sdev (μs)	pO_2 (kPa)	Mean (μs)	Sdev (μs)
0.50	44.5529	0.0780	0.75	40.8198	0.0657
1.00	37.7638	0.0717	2.00	29.0900	0.0602
3.00	23.8634	0.0532	4.00	20.3738	0.0479
5.00	17.8995	0.0522	6.00	15.9990	0.0437
7.00	14.5527	0.0484	8.00	13.4031	0.0464
9.00	12.4541	0.0467	10.00	11.5974	0.0437
12.00	10.2204	0.0388	14.00	9.1842	0.0301
16.00	8.3287	0.0415	18.00	7.5558	0.0354
20.00	7.0297	0.0382			

2.- Calibration curves: models and criteria


Figure 1: Calibration curves for the apparent modulation lifetime measurements (calibration data) of the sensing phase using different models and criteria. Models: Stern-Volmer (SV) (2 parameters), Lehrer (L) (3 parameters), 2nd order Polynomial (P2) (3 parameters), 1st order Polynomial-Exponent (PE1) (3 parameters), 2nd order Polynomial-Exponent (PE2) (4 parameters), Demas (D) (4 parameters). Criteria: (a) minimum mean square error (MSE) in τ_m , (b) minimum mean square error (MSE) in pO_2 , (c) minimum mean square relative error in pO_2 .

Experiment 6

3.- Parameters of the fitting models for different criteria

Table 3: Parameters of the fitting models for different criteria: (a) minimum mean square error (MSE) in τ_m , (b) minimum mean square error (MSE) in pO_2 , (c) minimum mean square relative error in pO_2 . RMSE is expressed in microseconds for criterion (a), in kPa for criterion (b) and in relative error (%) for criterion (c). Calibration data used are shown in Table 2.

Range	Stern-Volmer (SV)			Lehrer (L)			2 nd order Polynomial (P2)					
pO_2	Parameter	(a)	(b)	(c)	Parameter	(a)	(b)	(c)	Parameter	(a)	(b)	(c)
0.5-20 (kPa)	τ_0 (μs)	52.1230	43.8904	52.1653	τ_0 (μs)	54.2764	51.0813	54.0530	a_0	-2.0469	-2.3974	-2.1001
	k (kPa^{-1})	0.3680	0.2692	0.3591	k (kPa^{-1})	0.4617	0.3912	0.4491	a_1	104.84	119.318	107.855
	-	-	-	-	x	0.9604	0.9720	0.9646	a_2	384.153	273.59	352.945
	R^2	0.99780	0.99626	0.99530	R^2	0.99991	0.99968	0.99974	R^2	0.99996	0.99978	0.99987
	RMSE	0.5898	0.3893	6.8532	RMSE	0.1187	0.1133	1.6049	RMSE	0.0798	0.0953	1.1291
	iterations	100	1	1	iterations	100	100	100	iterations	100	1	1
0.5-20 (kPa)	Φ_0 (μs)	52.1230	43.8904	52.1653	Φ_0 (μs)	54.2764	51.0813	54.0530	Φ_0 (μs)	54.6528	51.9654	54.4434
	K (kPa^{-1})	0.3680	0.2692	0.3591	K (kPa^{-1})	0.4434	0.3802	0.4332	K (kPa^{-1})	0.4597	0.4002	0.4506
	1 st order Polynomial-Exponent (PE1)			2 nd order Polynomial-Exponent (PE2)			Demas (D)					
	a_0	-1.5626	-1.6928	-1.5750	a_0	-1.9826	1.6587	-1.5654	τ_0 (μs)	55.0351	56.8869	55.0893
	a_1	259.999	249.334	258.904	a_1	18.1487	-44.6171	262.616	k_1 (kPa^{-1})	0.5168	0.6423	0.5257
	α	-1.2734	-1.2503	-1.2710	a_2	287.884	240.02	-17.9787	k_2 (kPa^{-1})	0.0372	0.0776	0.0444
0.5-20 (kPa)	-	-	-	α	-0.7136	-0.4898	-1.2758	x	0.9165	0.8391	0.9067	
	R^2	0.99997	0.99991	0.99994	R^2	0.99998	0.99997	0.99994	R^2	0.99998	0.99998	0.99997
	RMSE	0.0712	0.0590	0.7430	RMSE	0.0620	0.0350	0.7425	RMSE	0.0525	0.0267	0.5825
	iterations	100	100	100	iterations	100	100	100	iterations	500	500	500
	Φ_0 (μs)	55.4940	54.2104	55.3934	Φ_0 (μs)	55.0571	60.1034	55.4201	Φ_0 (μs)	55.0351	56.8869	55.0893
	K (kPa^{-1})	0.5025	0.4725	0.4996	K (kPa^{-1})	0.4789	0.7606	0.5009	K (kPa^{-1})	0.4768	0.5514	0.4808

4.- Accuracy of the fitting models for different criteria using calibration data

Table 4: Accuracy (root mean square error, RMSE) of the fitting models for different criteria: (a) minimum mean square error (MSE) in τ_m , (b) minimum mean square error (MSE) in pO_2 , (c) minimum mean square relative error in pO_2 . Calibration data were used for evaluating the models (see Table 2).

Range	Stern-Volmer (SV)			Lehrer (L)			2 nd order Polynomial (P2)					
pO_2	Evaluation (criterion)	(a)	(b)	(c)	Evaluation (criterion)	(a)	(b)	(c)	Evaluation (criterion)	(a)	(b)	(c)
0.5-20 (kPa)	RMSE τ_m (μs)	0.5898	2.2617	0.6384	RMSE τ_m (μs)	0.1187	0.6027	0.1388	RMSE τ_m (μs)	0.0798	0.4559	0.0916
	RMSE pO_2 (kPa)	1.0780	0.3893	0.8747	RMSE pO_2 (kPa)	0.3356	0.1133	0.1977	RMSE pO_2 (kPa)	0.2244	0.0953	0.1528
	RMSE relat. pO_2 (%)	7.3236	39.5328	6.8532	RMSE relat. pO_2 (%)	1.9402	8.0014	1.6049	RMSE relat. pO_2 (%)	1.2880	5.8131	1.1291
1 st order Polynomial-Exponent (PE1)			2 nd order Polynomial-Exponent (PE2)			Demas (D)						
pO_2	Evaluation (criterion)	(a)	(b)	(c)	Evaluation (criterion)	(a)	(b)	(c)	Evaluation (criterion)	(a)	(b)	(c)
0.5-20 (kPa)	RMSE τ_m (μs)	0.0712	0.2147	0.0725	RMSE τ_m (μs)	0.0620	0.2547	0.0731	RMSE τ_m (μs)	0.0525	0.1548	0.0560
	RMSE pO_2 (kPa)	0.0690	0.0590	0.0671	RMSE pO_2 (kPa)	0.1214	0.0350	0.0645	RMSE pO_2 (kPa)	0.0826	0.0267	0.0539
	RMSE relat. pO_2 (%)	0.7582	2.3621	0.7430	RMSE relat. pO_2 (%)	0.8197	2.4460	0.7425	RMSE relat. pO_2 (%)	0.6375	1.6086	0.5825

5.- Accuracy of the fitting models for different criteria using test data

Table 5: Accuracy (root mean square error, RMSE) of the fitting models for different criteria: (a) minimum mean square error (MSE) in τ_m , (b) minimum mean square error (MSE) in pO_2 , (c) minimum mean square relative error in pO_2 . Test data were used for evaluating the models (see Table 2).

Range	Stern-Volmer (SV)			Lehrer (L)			2 nd order Polynomial (P2)					
pO_2	Evaluation (criterion)	(a)	(b)	(c)	Evaluation (criterion)	(a)	(b)	(c)	Evaluation (criterion)	(a)	(b)	(c)
0.75-18 (kPa)	RMSE τ_m (μs)	0.5825	1.5956	0.6814	RMSE τ_m (μs)	0.1255	0.4033	0.1604	RMSE τ_m (μs)	0.0866	0.3074	0.1067
	RMSE pO_2 (kPa)	0.8610	0.3322	0.6790	RMSE pO_2 (kPa)	0.2707	0.1240	0.1831	RMSE pO_2 (kPa)	0.2084	0.1132	0.1575
	RMSE relat. pO_2 (%)	6.4371	22.7087	6.5954	RMSE relat. pO_2 (%)	1.8117	4.3502	1.7226	RMSE relat. pO_2 (%)	1.3274	3.2160	1.2681
1 st order Polynomial-Exponent (PE1)			2 nd order Polynomial-Exponent (PE2)			Demas (D)						
pO_2	Evaluation (criterion)	(a)	(b)	(c)	Evaluation (criterion)	(a)	(b)	(c)	Evaluation (criterion)	(a)	(b)	(c)
0.75-18 (kPa)	RMSE τ_m (μs)	0.0653	0.1650	0.0694	RMSE τ_m (μs)	0.0648	0.1505	0.0695	RMSE τ_m (μs)	0.0558	0.1050	0.0571
	RMSE pO_2 (kPa)	0.1014	0.0917	0.1007	RMSE pO_2 (kPa)	0.1409	0.0796	0.0989	RMSE pO_2 (kPa)	0.1188	0.0772	0.0967
	RMSE relat. pO_2 (%)	0.7953	1.6655	0.8187	RMSE relat. pO_2 (%)	0.9338	1.2580	0.8131	RMSE relat. pO_2 (%)	0.7889	0.9184	0.7148

Experiment 7

page 1/2

Table 1: Sensing phase information

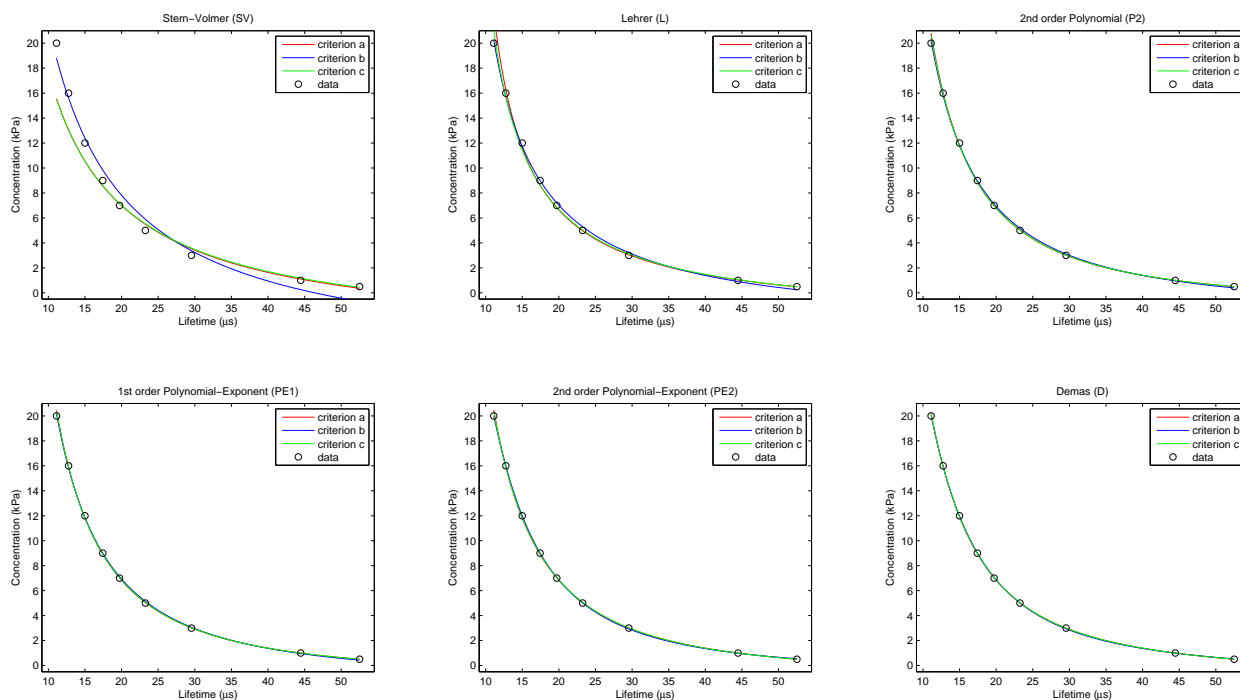
Name:	PtTFPP/PS
Description:	An oxygen-sensing film coated at the end of an optical fibre (a Platinum(II) 5,10,15,20-meso-tetrakis-(2,3,4,5,6-pentafluorophenyl)-porphyrin immobilized in polystyrene).
Analyte:	Partial pressure of oxygen in the gas phase (pO_2 , kPa); Range: 0.5-20 kPa.
Analytical signal:	(Measurement method): Luminescence lifetime in the frequency domain (<i>i.e.</i> , apparent lifetime estimated from phase-shift) using a phase-modulation method. (Instrumentation): Measurement system based on the multifrequency I/Q method (see reference); Excitation signal: 10% duty cycle rectangular-wave (fundamental frequency: 1715 Hz); Measurement frequency: 3 rd harmonic (5145 Hz).
Reference(s):	Medina-Rodríguez, S.; de la Torre-Vega, A.; Fernández-Sánchez, J. F.; Fernández-Gutiérrez, A. <i>Sensors and Actuators B: Chemical</i> 2013 , 176, 1110-1120.

1.- Experimental data (calibration and test)

Table 2: Experimental data (*i.e.*, calibration and test data); apparent phase-shift lifetime measurements (τ_ϕ , in microseconds) for several oxygen concentrations (pO_2 , in kPa) at room temperature (21 °C). All the values correspond to the average of 25 measurements.

Calibration data (τ_ϕ , in microseconds)			Test data (τ_ϕ , in microseconds)		
pO_2 (kPa)	Mean (μs)	Sdev (μs)	pO_2 (kPa)	Mean (μs)	Sdev (μs)
0.50	52.5073	0.0742	0.75	47.9429	0.0942
1.00	44.4632	0.0777	2.00	35.0347	0.0728
3.00	29.5475	0.0906	4.00	25.9280	0.0761
5.00	23.2507	0.1043	6.00	21.3109	0.1006
7.00	19.7186	0.0960	8.00	18.5124	0.0894
9.00	17.4309	0.1178	10.00	16.5097	0.1142
12.00	14.9955	0.0939	14.00	13.7952	0.1233
16.00	12.7613	0.1173	18.00	11.7856	0.1108
20.00	11.1091	0.1334			

2.- Calibration curves: models and criteria


Figure 1: Calibration curves for the apparent phase-shift lifetime measurements (calibration data) of the sensing phase using different models and criteria. Models: Stern-Volmer (SV) (2 parameters), Lehrer (L) (3 parameters), 2nd order Polynomial (P2) (3 parameters), 1st order Polynomial-Exponent (PE1) (3 parameters), 2nd order Polynomial-Exponent (PE2) (4 parameters), Demas (D) (4 parameters). Criteria: (a) minimum mean square error (MSE) in τ_ϕ , (b) minimum mean square error (MSE) in pO_2 , (c) minimum mean square relative error in pO_2 .

Experiment 7

3.- Parameters of the fitting models for different criteria

Table 3: Parameters of the fitting models for different criteria: (a) minimum mean square error (MSE) in τ_ϕ , (b) minimum mean square error (MSE) in pO_2 , (c) minimum mean square relative error in pO_2 . RMSE is expressed in microseconds for criterion (a), in kPa for criterion (b) and in relative error (%) for criterion (c). Calibration data used are shown in Table 2.

Range	Stern-Volmer (SV)			Lehrer (L)			2 nd order Polynomial (P2)					
pO_2	Parameter	(a)	(b)	(c)	Parameter	(a)	(b)	(c)	Parameter	(a)	(b)	(c)
0.5-20 (kPa)	τ_0 (μs)	57.6398	46.3746	58.9845	τ_0 (μs)	63.0163	56.5213	62.6016	a_0	-1.3949	-2.0079	-1.4650
	k (kPa^{-1})	0.2693	0.1688	0.2781	k (kPa^{-1})	0.4692	0.3329	0.4428	a_1	59.9759	93.669	65.0005
	–	–	–	–	x	0.9020	0.9227	0.9109	a_2	2072.25	1701.03	1998.59
	R^2	0.98740	0.98255	0.97838	R^2	0.99947	0.99867	0.99856	R^2	0.99995	0.99945	0.99980
	RMSE	1.5371	0.8412	14.7051	RMSE	0.3139	0.2321	3.7928	RMSE	0.1013	0.1489	1.4098
iterations	100	1	1	iterations	100	100	100	iterations	100	1	1	
	Φ_0 (μs)	57.6398	46.3746	58.9845	Φ_0 (μs)	63.0163	56.5213	62.6016	Φ_0 (μs)	65.6312	60.6251	65.2713
	K (kPa^{-1})	0.2693	0.1688	0.2781	K (kPa^{-1})	0.4232	0.3072	0.4033	K (kPa^{-1})	0.5330	0.4047	0.5170
Range	1 st order Polynomial-Exponent (PE1)			2 nd order Polynomial-Exponent (PE2)			Demas (D)					
pO_2	Parameter	(a)	(b)	(c)	Parameter	(a)	(b)	(c)	Parameter	(a)	(b)	(c)
0.5-20 (kPa)	a_0	-0.9892	-1.2544	-1.0090	a_0	-1.0466	-0.5895	-0.7461	τ_0 (μs)	65.6701	68.8689	65.8121
	a_1	1335.95	1105.3	1301.77	a_1	4.57456	3267.3	-15.4715	k_1 (kPa^{-1})	0.6481	0.8240	0.6602
	α	-1.7163	-1.6379	-1.7066	a_2	1387.51	-84048.6	1156.02	k_2 (kPa^{-1})	0.0370	0.0502	0.0390
	–	–	–	–	α	-0.8706	-2.0096	-0.8113	x	0.8039	0.7639	0.7983
	R^2	0.99996	0.99965	0.99989	R^2	0.99996	0.99997	0.99990	R^2	0.99999	0.99995	0.99997
RMSE	0.0847	0.1186	1.0393	RMSE	0.0843	0.0345	1.0052	RMSE	0.0463	0.0434	0.5350	
iterations	100	100	100	iterations	100	100	100	iterations	500	500	500	
	Φ_0 (μs)	66.6843	62.8150	66.4849	Φ_0 (μs)	66.5515	72.7643	67.0995	Φ_0 (μs)	65.6701	68.8689	65.8121
	K (kPa^{-1})	0.5890	0.4867	0.5807	K (kPa^{-1})	0.5816	0.8481	0.6156	K (kPa^{-1})	0.5283	0.6413	0.5349

4.- Accuracy of the fitting models for different criteria using calibration data

Table 4: Accuracy (root mean square error, RMSE) of the fitting models for different criteria: (a) minimum mean square error (MSE) in τ_ϕ , (b) minimum mean square error (MSE) in pO_2 , (c) minimum mean square relative error in pO_2 . Calibration data were used for evaluating the models (see Table 2).

Range	Stern-Volmer (SV)			Lehrer (L)			2 nd order Polynomial (P2)					
pO_2	Evaluation (criterion)	(a)	(b)	(c)	Evaluation (criterion)	(a)	(b)	(c)	Evaluation (criterion)	(a)	(b)	(c)
0.5-20 (kPa)	RMSE τ_ϕ (μs)	1.5371	3.7520	1.5933	RMSE τ_ϕ (μs)	0.3139	1.2543	0.3646	RMSE τ_ϕ (μs)	0.1013	0.6532	0.1117
	RMSE pO_2 (kPa)	1.8634	0.8412	1.8876	RMSE pO_2 (kPa)	0.8343	0.2321	0.4350	RMSE pO_2 (kPa)	0.2758	0.1489	0.2193
	RMSE relat. pO_2 (%)	15.8640	83.8133	14.7051	RMSE relat. pO_2 (%)	4.8217	17.2886	3.7928	RMSE relat. pO_2 (%)	1.5171	7.5110	1.4098
Range	1 st order Polynomial-Exponent (PE1)			2 nd order Polynomial-Exponent (PE2)			Demas (D)					
pO_2	Evaluation (criterion)	(a)	(b)	(c)	Evaluation (criterion)	(a)	(b)	(c)	Evaluation (criterion)	(a)	(b)	(c)
0.5-20 (kPa)	RMSE τ_ϕ (μs)	0.0847	0.5013	0.0871	RMSE τ_ϕ (μs)	0.0843	0.3528	0.0918	RMSE τ_ϕ (μs)	0.0463	0.2295	0.0485
	RMSE pO_2 (kPa)	0.1673	0.1186	0.1515	RMSE pO_2 (kPa)	0.1764	0.0345	0.1322	RMSE pO_2 (kPa)	0.0840	0.0434	0.0696
	RMSE relat. pO_2 (%)	1.0611	5.2192	1.0393	RMSE relat. pO_2 (%)	1.0875	2.9162	1.0052	RMSE relat. pO_2 (%)	0.5588	2.0259	0.5350

5.- Accuracy of the fitting models for different criteria using test data

Table 5: Accuracy (root mean square error, RMSE) of the fitting models for different criteria: (a) minimum mean square error (MSE) in τ_ϕ , (b) minimum mean square error (MSE) in pO_2 , (c) minimum mean square relative error in pO_2 . Test data were used for evaluating the models (see Table 2).

Range	Stern-Volmer (SV)			Lehrer (L)			2 nd order Polynomial (P2)					
pO_2	Evaluation (criterion)	(a)	(b)	(c)	Evaluation (criterion)	(a)	(b)	(c)	Evaluation (criterion)	(a)	(b)	(c)
0.75-18 (kPa)	RMSE τ_ϕ (μs)	1.4686	2.6054	1.6338	RMSE τ_ϕ (μs)	0.3148	0.7689	0.4061	RMSE τ_ϕ (μs)	0.1143	0.3778	0.1310
	RMSE pO_2 (kPa)	1.5245	0.7090	1.5465	RMSE pO_2 (kPa)	0.5561	0.2065	0.3399	RMSE pO_2 (kPa)	0.2341	0.1434	0.1968
	RMSE relat. pO_2 (%)	12.7540	45.5424	14.1130	RMSE relat. pO_2 (%)	3.9155	8.2470	3.8091	RMSE relat. pO_2 (%)	1.5185	3.5686	1.5114
Range	1 st order Polynomial-Exponent (PE1)			2 nd order Polynomial-Exponent (PE2)			Demas (D)					
pO_2	Evaluation (criterion)	(a)	(b)	(c)	Evaluation (criterion)	(a)	(b)	(c)	Evaluation (criterion)	(a)	(b)	(c)
0.75-18 (kPa)	RMSE τ_ϕ (μs)	0.0847	0.3000	0.0875	RMSE τ_ϕ (μs)	0.0867	0.2057	0.0806	RMSE τ_ϕ (μs)	0.0694	0.1740	0.0653
	RMSE pO_2 (kPa)	0.1612	0.1209	0.1503	RMSE pO_2 (kPa)	0.1674	0.0890	0.1364	RMSE pO_2 (kPa)	0.1154	0.0834	0.1034
	RMSE relat. pO_2 (%)	1.0880	2.7560	1.0768	RMSE relat. pO_2 (%)	1.1217	1.5687	0.9810	RMSE relat. pO_2 (%)	0.8052	1.3547	0.7343

Experiment 8

page 1/2

Table 1: Sensing phase information

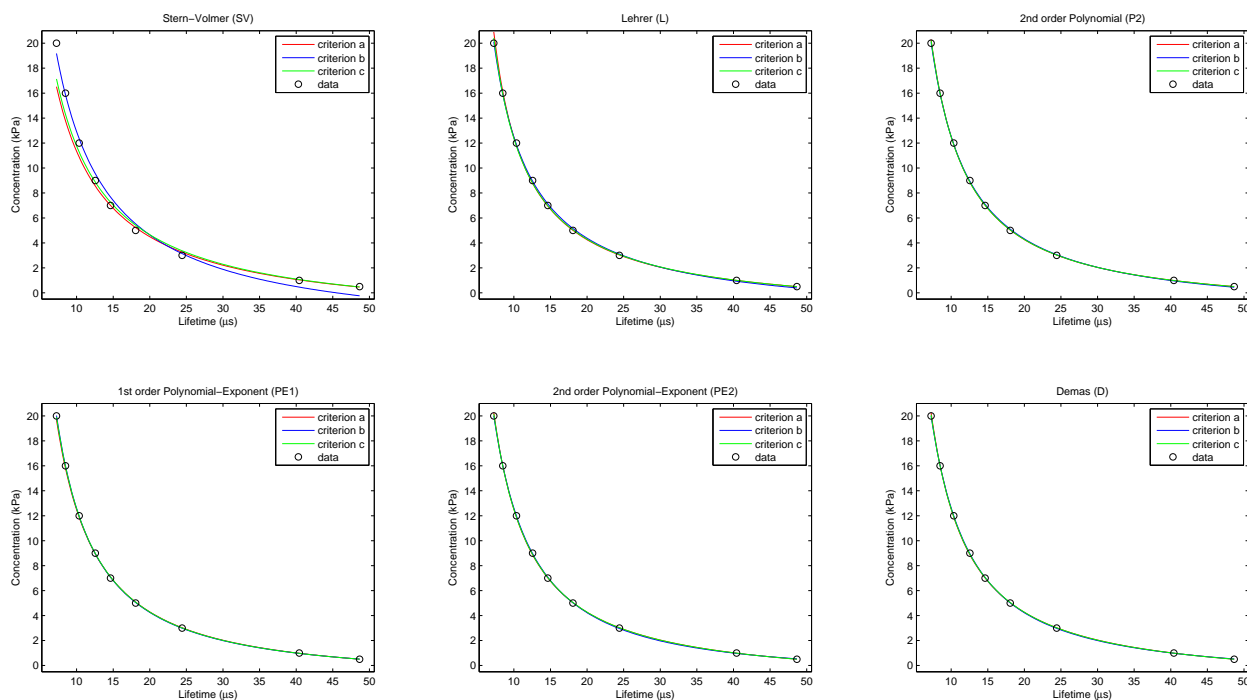
Name:	PtTFPP/PS
Description:	An oxygen-sensing film coated at the end of an optical fibre (a Platinum(II) 5,10,15,20-meso-tetrakis-(2,3,4,5,6-pentafluorophenyl)-porphyrin immobilized in polystyrene).
Analyte:	Partial pressure of oxygen in the gas phase (pO_2 , kPa); Range: 0.5-20 kPa.
Analytical signal:	(Measurement method): Luminescence lifetime in the frequency domain (<i>i.e.</i> , apparent lifetime estimated from modulation factor) using a phase-modulation method. (Instrumentation): Measurement system based on the multifrequency I/Q method (see reference); Excitation signal: 10% duty cycle rectangular-wave (fundamental frequency: 1715 Hz); Measurement frequency: 4 th harmonic (6860 Hz).
Reference(s):	Medina-Rodríguez, S.; de la Torre-Vega, A.; Fernández-Sánchez, J. F.; Fernández-Gutiérrez, A. <i>Sensors and Actuators B: Chemical</i> 2013 , 176, 1110-1120.

1.- Experimental data (calibration and test)

Table 2: Experimental data (*i.e.*, calibration and test data); apparent modulation lifetime measurements (τ_m , in microseconds) for several oxygen concentrations (pO_2 , in kPa) at room temperature (21 °C). All the values correspond to the average of 25 measurements.

Calibration data (τ_m , in microseconds)			Test data (τ_m , in microseconds)		
pO_2 (kPa)	Mean (μs)	Sdev (μs)	pO_2 (kPa)	Mean (μs)	Sdev (μs)
0.50	48.6613	0.0995	0.75	44.2521	0.0809
1.00	40.4194	0.0856	2.00	30.2247	0.0785
3.00	24.4148	0.0772	4.00	20.6403	0.0550
5.00	18.0660	0.0685	6.00	16.1033	0.0587
7.00	14.6429	0.0585	8.00	13.5028	0.0605
9.00	12.5536	0.0558	10.00	11.6843	0.0740
12.00	10.3582	0.0510	14.00	9.3293	0.0401
16.00	8.4911	0.0590	18.00	7.7560	0.0404
20.00	7.2572	0.0434			

2.- Calibration curves: models and criteria


Figure 1: Calibration curves for the apparent modulation lifetime measurements (calibration data) of the sensing phase using different models and criteria. Models: Stern-Volmer (SV) (2 parameters), Lehrer (L) (3 parameters), 2nd order Polynomial (P2) (3 parameters), 1st order Polynomial-Exponent (PE1) (3 parameters), 2nd order Polynomial-Exponent (PE2) (4 parameters), Demas (D) (4 parameters). Criteria: (a) minimum mean square error (MSE) in τ_m , (b) minimum mean square error (MSE) in pO_2 , (c) minimum mean square relative error in pO_2 .

Experiment 8

3.- Parameters of the fitting models for different criteria

Table 3: Parameters of the fitting models for different criteria: (a) minimum mean square error (MSE) in τ_m , (b) minimum mean square error (MSE) in pO_2 , (c) minimum mean square relative error in pO_2 . RMSE is expressed in microseconds for criterion (a), in kPa for criterion (b) and in relative error (%) for criterion (c). Calibration data used are shown in Table 2.

Range	Stern-Volmer (SV)			Lehrer (L)			2 nd order Polynomial (P2)					
pO_2	Parameter	(a)	(b)	(c)	Parameter	(a)	(b)	(c)	Parameter	(a)	(b)	(c)
0.5-20 (kPa)	τ_0 (μs)	58.2412	45.5114	58.0471	τ_0 (μs)	61.6287	57.3905	61.2433	a_0	-1.6399	-1.8333	-1.6611
	k (kPa^{-1})	0.4253	0.2749	0.4084	k (kPa^{-1})	0.5633	0.4749	0.5464	a_1	94.683	102.659	95.8379
	–	–	–	–	x	0.9572	0.9650	0.9605	a_2	468.184	409.195	457.466
	R^2	0.99680	0.99260	0.99252	R^2	0.99993	0.99969	0.99976	R^2	0.99996	0.99986	0.99991
	RMSE	0.7844	0.5478	0.6472	RMSE	0.1164	0.1124	1.5335	RMSE	0.0884	0.0763	0.9329
	iterations	100	1	1	iterations	100	100	100	iterations	100	1	1
	Φ_0 (μs)	58.2412	45.5114	58.0471	Φ_0 (μs)	61.6287	57.3905	61.2433	Φ_0 (μs)	62.3184	59.7345	62.1284
	K (kPa^{-1})	0.4253	0.2749	0.4084	K (kPa^{-1})	0.5391	0.4583	0.5248	K (kPa^{-1})	0.5680	0.5134	0.5619
Range	1 st order Polynomial-Exponent (PE1)			2 nd order Polynomial-Exponent (PE2)			Demas (D)					
pO_2	Parameter	(a)	(b)	(c)	Parameter	(a)	(b)	(c)	Parameter	(a)	(b)	(c)
0.5-20 (kPa)	a_0	-1.1908	-1.0960	-1.1469	a_0	-1.6958	-0.4224	-1.7148	τ_0 (μs)	62.2422	64.4681	62.4030
	a_1	284.712	309.55	298.467	a_1	71.3608	-15.3785	43.6464	k_1 (kPa^{-1})	0.6005	0.7124	0.6153
	α	-1.3184	-1.3545	-1.3375	a_2	436.639	295.455	382.36	k_2 (kPa^{-1})	0.0185	0.0469	0.0265
	–	–	–	–	α	-0.9344	-0.6241	-0.8412	x	0.9376	0.8957	0.9282
	R^2	0.99989	0.99996	0.99984	R^2	0.99996	0.99997	0.99993	R^2	0.99996	0.99998	0.99994
	RMSE	0.1487	0.0381	1.2528	RMSE	0.0870	0.0337	0.8619	RMSE	0.0822	0.0264	0.7753
	iterations	100	100	100	iterations	100	100	100	iterations	500	500	500
	Φ_0 (μs)	63.6946	64.4835	63.9483	Φ_0 (μs)	62.2979	67.8799	62.3639	Φ_0 (μs)	62.2422	64.4681	62.4030
	K (kPa^{-1})	0.6369	0.6736	0.6519	K (kPa^{-1})	0.5665	0.8214	0.5715	K (kPa^{-1})	0.5641	0.6430	0.5730

4.- Accuracy of the fitting models for different criteria using calibration data

Table 4: Accuracy (root mean square error, RMSE) of the fitting models for different criteria: (a) minimum mean square error (MSE) in τ_m , (b) minimum mean square error (MSE) in pO_2 , (c) minimum mean square relative error in pO_2 . Calibration data were used for evaluating the models (see Table 2).

Range	Stern-Volmer (SV)			Lehrer (L)			2 nd order Polynomial (P2)					
pO_2	Evaluation (criterion)	(a)	(b)	(c)	Evaluation (criterion)	(a)	(b)	(c)	Evaluation (criterion)	(a)	(b)	(c)
0.5-20 (kPa)	RMSE τ_m (μs)	0.7844	3.3308	0.8560	RMSE τ_m (μs)	0.1164	0.7224	0.1394	RMSE τ_m (μs)	0.0884	0.3982	0.0910
	RMSE pO_2 (kPa)	1.4398	0.5478	1.1573	RMSE pO_2 (kPa)	0.3209	0.1124	0.1868	RMSE pO_2 (kPa)	0.1175	0.0763	0.1022
	RMSE relat. pO_2 (%)	9.2637	52.5581	8.6472	RMSE relat. pO_2 (%)	1.8735	7.6309	1.5335	RMSE relat. pO_2 (%)	0.9593	3.8402	0.9329
Range	1 st order Polynomial-Exponent (PE1)			2 nd order Polynomial-Exponent (PE2)			Demas (D)					
pO_2	Evaluation (criterion)	(a)	(b)	(c)	Evaluation (criterion)	(a)	(b)	(c)	Evaluation (criterion)	(a)	(b)	(c)
0.5-20 (kPa)	RMSE τ_m (μs)	0.1487	0.1759	0.1576	RMSE τ_m (μs)	0.0870	0.3096	0.0930	RMSE τ_m (μs)	0.0822	0.1922	0.0886
	RMSE pO_2 (kPa)	0.1440	0.0381	0.0579	RMSE pO_2 (kPa)	0.1060	0.0337	0.0757	RMSE pO_2 (kPa)	0.1052	0.0264	0.0554
	RMSE relat. pO_2 (%)	1.4036	1.3347	1.2528	RMSE relat. pO_2 (%)	0.9183	2.4427	0.8619	RMSE relat. pO_2 (%)	0.8799	1.6334	0.7753

5.- Accuracy of the fitting models for different criteria using test data

Table 5: Accuracy (root mean square error, RMSE) of the fitting models for different criteria: (a) minimum mean square error (MSE) in τ_m , (b) minimum mean square error (MSE) in pO_2 , (c) minimum mean square relative error in pO_2 . Test data were used for evaluating the models (see Table 2).

Range	Stern-Volmer (SV)			Lehrer (L)			2 nd order Polynomial (P2)					
pO_2	Evaluation (criterion)	(a)	(b)	(c)	Evaluation (criterion)	(a)	(b)	(c)	Evaluation (criterion)	(a)	(b)	(c)
0.75-18 (kPa)	RMSE τ_m (μs)	0.7823	2.4036	0.9147	RMSE τ_m (μs)	0.1332	0.5397	0.1704	RMSE τ_m (μs)	0.1041	0.3343	0.1141
	RMSE pO_2 (kPa)	1.1531	0.4710	0.8990	RMSE pO_2 (kPa)	0.2635	0.1275	0.1763	RMSE pO_2 (kPa)	0.1392	0.1053	0.1268
	RMSE relat. pO_2 (%)	8.3036	31.2119	8.2685	RMSE relat. pO_2 (%)	1.7989	4.8504	1.6851	RMSE relat. pO_2 (%)	1.1375	2.8672	1.1631
Range	1 st order Polynomial-Exponent (PE1)			2 nd order Polynomial-Exponent (PE2)			Demas (D)					
pO_2	Evaluation (criterion)	(a)	(b)	(c)	Evaluation (criterion)	(a)	(b)	(c)	Evaluation (criterion)	(a)	(b)	(c)
0.75-18 (kPa)	RMSE τ_m (μs)	0.1459	0.1738	0.1646	RMSE τ_m (μs)	0.1028	0.1719	0.1129	RMSE τ_m (μs)	0.0993	0.1108	0.1080
	RMSE pO_2 (kPa)	0.0906	0.0852	0.0722	RMSE pO_2 (kPa)	0.1313	0.0826	0.1096	RMSE pO_2 (kPa)	0.1350	0.0812	0.1000
	RMSE relat. pO_2 (%)	1.3030	1.3821	1.3640	RMSE relat. pO_2 (%)	1.1034	1.2913	1.0973	RMSE relat. pO_2 (%)	1.0869	0.8981	1.0268

Experiment 9

page 1/2

Table 1: Sensing phase information

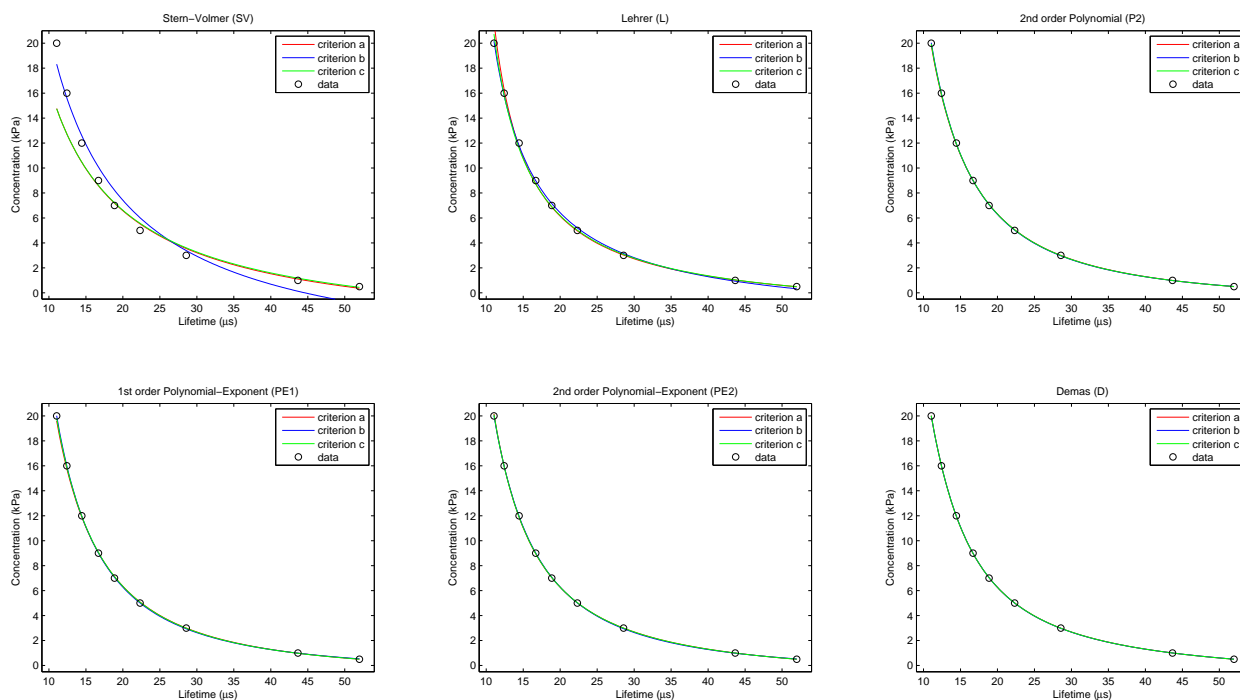
Name:	PtTFPP/PS
Description:	An oxygen-sensing film coated at the end of an optical fibre (a Platinum(II) 5,10,15,20-meso-tetrakis-(2,3,4,5,6-pentafluorophenyl)-porphyrin immobilized in polystyrene).
Analyte:	Partial pressure of oxygen in the gas phase (pO_2 , kPa); Range: 0.5-20 kPa.
Analytical signal:	(Measurement method): Luminescence lifetime in the frequency domain (<i>i.e.</i> , apparent lifetime estimated from phase-shift) using a phase-modulation method. (Instrumentation): Measurement system based on the multifrequency I/Q method (see reference); Excitation signal: 10% duty cycle rectangular-wave (fundamental frequency: 1715 Hz); Measurement frequency: 4 th harmonic (6860 Hz).
Reference(s):	Medina-Rodríguez, S.; de la Torre-Vega, A.; Fernández-Sánchez, J. F.; Fernández-Gutiérrez, A. <i>Sensors and Actuators B: Chemical</i> 2013 , 176, 1110-1120.

1.- Experimental data (calibration and test)

Table 2: Experimental data (*i.e.*, calibration and test data); apparent phase-shift lifetime measurements (τ_{ϕ} , in microseconds) for several oxygen concentrations (pO_2 , in kPa) at room temperature (21 °C). All the values correspond to the average of 25 measurements.

pO_2 (kPa)	Calibration data (τ_{ϕ} , in microseconds)		Test data (τ_{ϕ} , in microseconds)		
	Mean (μs)	Sdev (μs)	pO_2 (kPa)	Mean (μs)	Sdev (μs)
0.50	51.9833	0.1071	0.75	47.2283	0.0965
1.00	43.6677	0.1023	2.00	34.1379	0.1009
3.00	28.5701	0.1062	4.00	24.9613	0.1053
5.00	22.3270	0.1179	6.00	20.4099	0.1159
7.00	18.8574	0.1068	8.00	17.7399	0.0864
9.00	16.6995	0.1048	10.00	15.8421	0.1008
12.00	14.4392	0.1108	14.00	13.3723	0.1407
16.00	12.4268	0.1069	18.00	11.6526	0.1415
20.00	11.0441	0.1263			

2.- Calibration curves: models and criteria


Figure 1: Calibration curves for the apparent phase-shift lifetime measurements (calibration data) of the sensing phase using different models and criteria. Models: Stern-Volmer (SV) (2 parameters), Lehrer (L) (3 parameters), 2nd order Polynomial (P2) (3 parameters), 1st order Polynomial-Exponent (PE1) (3 parameters), 2nd order Polynomial-Exponent (PE2) (4 parameters), Demas (D) (4 parameters). Criteria: (a) minimum mean square error (MSE) in τ_{ϕ} , (b) minimum mean square error (MSE) in pO_2 , (c) minimum mean square relative error in pO_2 .

Experiment 9

3.- Parameters of the fitting models for different criteria

Table 3: Parameters of the fitting models for different criteria: (a) minimum mean square error (MSE) in τ_ϕ , (b) minimum mean square error (MSE) in pO_2 , (c) minimum mean square relative error in pO_2 . RMSE is expressed in microseconds for criterion (a), in kPa for criterion (b) and in relative error (%) for criterion (c). Calibration data used are shown in Table 2.

Range	Stern-Volmer (SV)			Lehrer (L)			2 nd order Polynomial (P2)					
pO_2	Parameter	(a)	(b)	(c)	Parameter	(a)	(b)	(c)	Parameter	(a)	(b)	(c)
0.5-20 (kPa)	τ_0 (μs)	57.3708	44.6047	58.7108	τ_0 (μs)	63.6292	58.1055	63.2260	a_0	-1.1740	-1.0610	-1.1370
	k (kPa^{-1})	0.2842	0.1659	0.2926	k (kPa^{-1})	0.5228	0.4027	0.4994	a_1	48.1026	40.79	45.4099
	—	—	—	—	x	0.8993	0.9097	0.9050	a_2	2029.98	2122.7	2069.75
	R^2	0.98523	0.97323	0.97464	R^2	0.99974	0.99937	0.99928	R^2	0.99997	0.99997	0.99994
	RMSE	1.6531	1.0420	15.9247	RMSE	0.2179	0.1600	2.6889	RMSE	0.0765	0.0371	0.7491
	iterations	100	1	1	iterations	100	100	100	iterations	100	1	1
0.5-20 (kPa)	Φ_0 (μs)	57.3708	44.6047	58.7108	Φ_0 (μs)	63.6292	58.1055	63.2260	Φ_0 (μs)	66.8432	67.9075	67.0777
	K (kPa^{-1})	0.2842	0.1659	0.2926	K (kPa^{-1})	0.4701	0.3663	0.4520	K (kPa^{-1})	0.6141	0.6573	0.6262
Range	1 st order Polynomial-Exponent (PE1)			2 nd order Polynomial-Exponent (PE2)			Demas (D)					
pO_2	Parameter	(a)	(b)	(c)	Parameter	(a)	(b)	(c)	Parameter	(a)	(b)	(c)
0.5-20 (kPa)	a_0	-0.8263	-0.6674	-0.7865	a_0	-1.2767	-0.8248	-1.2847	τ_0 (μs)	65.4329	66.0420	65.4921
	a_1	1407.86	1708.82	1509.09	a_1	196.745	12.7944	135.824	k_1 (kPa^{-1})	0.6371	0.6634	0.6404
	α	-1.7625	-1.8379	-1.7878	a_2	4102.89	1833.51	3289.12	k_2 (kPa^{-1})	0.0223	0.0244	0.0227
	—	—	—	—	α	-1.2294	-0.9456	-1.1536	x	0.8446	0.8386	0.8436
	R^2	0.99991	0.99997	0.99985	R^2	0.99999	0.99997	0.99997	R^2	0.99999	0.99999	0.99999
	RMSE	0.1286	0.0356	1.2189	RMSE	0.0434	0.0349	0.5149	RMSE	0.0338	0.0206	0.3244
iterations	100	100	100	iterations	100	100	100	iterations	500	500	500	
0.5-20 (kPa)	Φ_0 (μs)	68.1421	71.5320	68.6057	Φ_0 (μs)	66.0559	69.9900	66.1829	Φ_0 (μs)	65.4329	66.0420	65.4921
	K (kPa^{-1})	0.6866	0.8153	0.7112	K (kPa^{-1})	0.5752	0.7452	0.5811	K (kPa^{-1})	0.5416	0.5602	0.5438

4.- Accuracy of the fitting models for different criteria using calibration data

Table 4: Accuracy (root mean square error, RMSE) of the fitting models for different criteria: (a) minimum mean square error (MSE) in τ_ϕ , (b) minimum mean square error (MSE) in pO_2 , (c) minimum mean square relative error in pO_2 . Calibration data were used for evaluating the models (see Table 2).

Range	Stern-Volmer (SV)			Lehrer (L)			2 nd order Polynomial (P2)					
pO_2	Evaluation (criterion)	(a)	(b)	(c)	Evaluation (criterion)	(a)	(b)	(c)	Evaluation (criterion)	(a)	(b)	(c)
0.5-20 (kPa)	RMSE τ_ϕ (μs)	1.6531	4.1748	1.7064	RMSE τ_ϕ (μs)	0.2179	0.9834	0.2565	RMSE τ_ϕ (μs)	0.0765	0.1107	0.0817
	RMSE pO_2 (kPa)	2.1427	1.0420	2.1470	RMSE pO_2 (kPa)	0.5916	0.1600	0.3043	RMSE pO_2 (kPa)	0.0926	0.0371	0.0525
	RMSE relat. pO_2 (%)	16.9364	95.5817	15.9247	RMSE relat. pO_2 (%)	3.4301	12.0905	2.6889	RMSE relat. pO_2 (%)	0.8194	0.9442	0.7491
Range	1 st order Polynomial-Exponent (PE1)			2 nd order Polynomial-Exponent (PE2)			Demas (D)					
pO_2	Evaluation (criterion)	(a)	(b)	(c)	Evaluation (criterion)	(a)	(b)	(c)	Evaluation (criterion)	(a)	(b)	(c)
0.5-20 (kPa)	RMSE τ_ϕ (μs)	0.1286	0.2860	0.1393	RMSE τ_ϕ (μs)	0.0434	0.2115	0.0460	RMSE τ_ϕ (μs)	0.0338	0.0642	0.0341
	RMSE pO_2 (kPa)	0.1685	0.0356	0.0892	RMSE pO_2 (kPa)	0.0722	0.0349	0.0569	RMSE pO_2 (kPa)	0.0248	0.0206	0.0235
	RMSE relat. pO_2 (%)	1.3532	2.3543	1.2189	RMSE relat. pO_2 (%)	0.5414	1.7797	0.5149	RMSE relat. pO_2 (%)	0.3272	0.5795	0.3244

5.- Accuracy of the fitting models for different criteria using test data

Table 5: Accuracy (root mean square error, RMSE) of the fitting models for different criteria: (a) minimum mean square error (MSE) in τ_ϕ , (b) minimum mean square error (MSE) in pO_2 , (c) minimum mean square relative error in pO_2 . Test data were used for evaluating the models (see Table 2).

Range	Stern-Volmer (SV)			Lehrer (L)			2 nd order Polynomial (P2)					
pO_2	Evaluation (criterion)	(a)	(b)	(c)	Evaluation (criterion)	(a)	(b)	(c)	Evaluation (criterion)	(a)	(b)	(c)
0.75-18 (kPa)	RMSE τ_ϕ (μs)	1.5662	2.9132	1.7278	RMSE τ_ϕ (μs)	0.2195	0.5566	0.2843	RMSE τ_ϕ (μs)	0.0845	0.1201	0.0893
	RMSE pO_2 (kPa)	1.7562	0.8767	1.7601	RMSE pO_2 (kPa)	0.3765	0.1553	0.2446	RMSE pO_2 (kPa)	0.0908	0.0607	0.0637
	RMSE relat. pO_2 (%)	13.8586	52.4513	15.1393	RMSE relat. pO_2 (%)	2.7790	5.5341	2.7764	RMSE relat. pO_2 (%)	0.8497	0.9467	0.7781
Range	1 st order Polynomial-Exponent (PE1)			2 nd order Polynomial-Exponent (PE2)			Demas (D)					
pO_2	Evaluation (criterion)	(a)	(b)	(c)	Evaluation (criterion)	(a)	(b)	(c)	Evaluation (criterion)	(a)	(b)	(c)
0.75-18 (kPa)	RMSE τ_ϕ (μs)	0.1142	0.1990	0.1318	RMSE τ_ϕ (μs)	0.0765	0.1680	0.0747	RMSE τ_ϕ (μs)	0.0787	0.1075	0.0802
	RMSE pO_2 (kPa)	0.1304	0.0577	0.0713	RMSE pO_2 (kPa)	0.0863	0.0580	0.0775	RMSE pO_2 (kPa)	0.0571	0.0506	0.0554
	RMSE relat. pO_2 (%)	1.1523	1.4794	1.0893	RMSE relat. pO_2 (%)	0.7981	1.2665	0.7487	RMSE relat. pO_2 (%)	0.7099	0.8832	0.7116

Experiment 10

page 1/2

Table 1: Sensing phase information

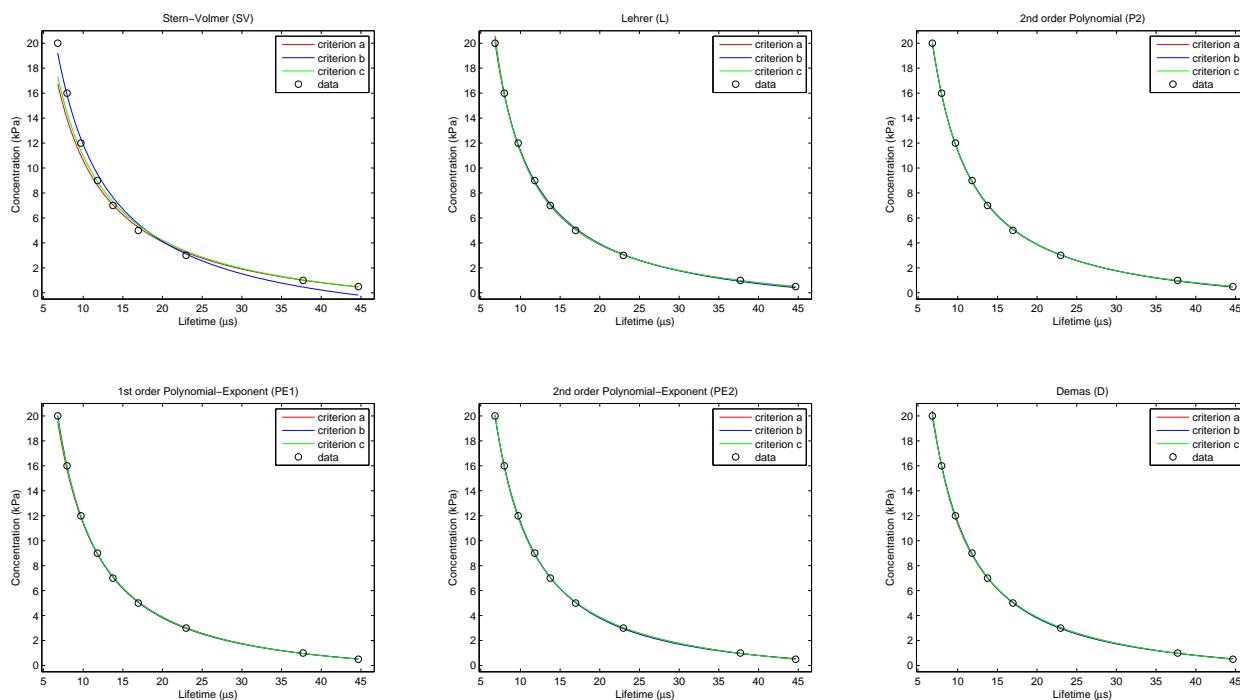
Name:	PtTFPP/PS
Description:	An oxygen-sensing film coated at the end of an optical fibre (a Platinum(II) 5,10,15,20-meso-tetrakis-(2,3,4,5,6-pentafluorophenyl)-porphyrin immobilized in polystyrene).
Analyte:	Partial pressure of oxygen in the gas phase (pO_2 , kPa); Range: 0.5-20 kPa.
Analytical signal:	(Measurement method): Luminescence lifetime in the frequency domain (<i>i.e.</i> , apparent lifetime estimated from modulation factor) using a phase-modulation method. (Instrumentation): Measurement system based on the multifrequency I/Q method (see reference); Excitation signal: 10% duty cycle rectangular-wave (fundamental frequency: 1715 Hz); Measurement frequency: 5 th harmonic (8575 Hz).
Reference(s):	Medina-Rodríguez, S.; de la Torre-Vega, A.; Fernández-Sánchez, J. F.; Fernández-Gutiérrez, A. <i>Sensors and Actuators B: Chemical</i> 2013 , 176, 1110-1120.

1.- Experimental data (calibration and test)

Table 2: Experimental data (*i.e.*, calibration and test data); apparent modulation lifetime measurements (τ_m , in microseconds) for several oxygen concentrations (pO_2 , in kPa) at room temperature (21 °C). All the values correspond to the average of 25 measurements.

Calibration data (τ_m , in microseconds)			Test data (τ_m , in microseconds)		
pO_2 (kPa)	Mean (μs)	Sdev (μs)	pO_2 (kPa)	Mean (μs)	Sdev (μs)
0.50	44.6739	0.1137	0.75	40.7691	0.1459
1.00	37.7027	0.1012	2.00	28.5414	0.1125
3.00	22.9737	0.1441	4.00	19.3576	0.0935
5.00	16.9540	0.1119	6.00	15.0719	0.0814
7.00	13.7601	0.0783	8.00	12.6524	0.0752
9.00	11.8088	0.0666	10.00	10.9651	0.0867
12.00	9.7173	0.0643	14.00	8.7656	0.0730
16.00	7.9769	0.0723	18.00	7.2715	0.0697
20.00	6.8008	0.0554			

2.- Calibration curves: models and criteria


Figure 1: Calibration curves for the apparent modulation lifetime measurements (calibration data) of the sensing phase using different models and criteria. Models: Stern-Volmer (SV) (2 parameters), Lehrer (L) (3 parameters), 2nd order Polynomial (P2) (3 parameters), 1st order Polynomial-Exponent (PE1) (3 parameters), 2nd order Polynomial-Exponent (PE2) (4 parameters), Demas (D) (4 parameters). Criteria: (a) minimum mean square error (MSE) in τ_m , (b) minimum mean square error (MSE) in pO_2 , (c) minimum mean square relative error in pO_2 .

Experiment 10

3.- Parameters of the fitting models for different criteria

Table 3: Parameters of the fitting models for different criteria: (a) minimum mean square error (MSE) in τ_m , (b) minimum mean square error (MSE) in pO_2 , (c) minimum mean square relative error in pO_2 . RMSE is expressed in microseconds for criterion (a), in kPa for criterion (b) and in relative error (%) for criterion (c). Calibration data used are shown in Table 2.

Range	Stern-Volmer (SV)			Lehrer (L)			2 nd order Polynomial (P2)					
pO_2	Parameter	(a)	(b)	(c)	Parameter	(a)	(b)	(c)	Parameter	(a)	(b)	(c)
0.5-20 (kPa)	τ_0 (μs)	53.2961	42.4670	53.0768	τ_0 (μs)	55.9263	52.8405	55.6356	a_0	-1.8014	-1.9229	-1.8083
	k (kPa^{-1})	0.4079	0.2728	0.3923	k (kPa^{-1})	0.5236	0.4589	0.5126	a_1	95.0124	98.965	95.0951
	—	—	—	—	x	0.9599	0.9657	0.9619	a_2	366.391	345.073	368.954
	R^2	0.99734	0.99324	0.99384	R^2	0.99989	0.99970	0.99978	R^2	0.99988	0.99985	0.99982
	RMSE	0.6581	0.5236	7.8505	RMSE	0.1319	0.1111	1.4970	RMSE	0.1395	0.0788	1.3241
iterations	100	1	1	iterations	100	100	100	iterations	100	1	1	
	Φ_0 (μs)	53.2961	42.4670	53.0768	Φ_0 (μs)	55.9263	52.8405	55.6356	Φ_0 (μs)	56.3543	54.7449	56.2174
	K (kPa^{-1})	0.4079	0.2728	0.3923	K (kPa^{-1})	0.5026	0.4432	0.4930	K (kPa^{-1})	0.5217	0.4907	0.5195
Range	1 st order Polynomial-Exponent (PE1)			2 nd order Polynomial-Exponent (PE2)			Demas (D)					
pO_2	Parameter	(a)	(b)	(c)	Parameter	(a)	(b)	(c)	Parameter	(a)	(b)	(c)
0.5-20 (kPa)	a_0	-1.3570	-1.1813	-1.2957	a_0	-1.8726	-0.5313	-1.8903	τ_0 (μs)	56.0683	58.7995	56.1335
	a_1	244.007	276.9	259.226	a_1	74.2069	-14.0569	68.4545	k_1 (kPa^{-1})	0.5328	0.6748	0.5443
	α	-1.2822	-1.3399	-1.3074	a_2	352.705	267.396	351.02	k_2 (kPa^{-1})	0.0056	0.0470	0.0151
	—	—	—	—	α	-0.9384	-0.6198	-0.9204	x	0.9545	0.8954	0.9449
	R^2	0.99976	0.99995	0.99966	R^2	0.99988	0.99996	0.99983	R^2	0.99990	0.99997	0.99984
RMSE	0.1990	0.0455	1.8487	RMSE	0.1377	0.0423	1.3042	RMSE	0.1297	0.0341	1.2790	
iterations	100	100	100	iterations	100	100	100	iterations	500	500	500	
	Φ_0 (μs)	57.3554	58.7107	57.5612	Φ_0 (μs)	56.2956	61.2646	56.1811	Φ_0 (μs)	56.0683	58.7995	56.1335
	K (kPa^{-1})	0.5747	0.6317	0.5903	K (kPa^{-1})	0.5185	0.7471	0.5170	K (kPa^{-1})	0.5088	0.6091	0.5152

4.- Accuracy of the fitting models for different criteria using calibration data

Table 4: Accuracy (root mean square error, RMSE) of the fitting models for different criteria: (a) minimum mean square error (MSE) in τ_m , (b) minimum mean square error (MSE) in pO_2 , (c) minimum mean square relative error in pO_2 . Calibration data were used for evaluating the models (see Table 2).

Range	Stern-Volmer (SV)			Lehrer (L)			2 nd order Polynomial (P2)					
pO_2	Evaluation (criterion)	(a)	(b)	(c)	Evaluation (criterion)	(a)	(b)	(c)	Evaluation (criterion)	(a)	(b)	(c)
0.5-20 (kPa)	RMSE τ_m (μs)	0.6581	2.8745	0.7185	RMSE τ_m (μs)	0.1319	0.5706	0.1403	RMSE τ_m (μs)	0.1395	0.3148	0.1419
	RMSE pO_2 (kPa)	1.3360	0.5236	1.0723	RMSE pO_2 (kPa)	0.2178	0.1111	0.1572	RMSE pO_2 (kPa)	0.0893	0.0788	0.0866
	RMSE relat. pO_2 (%)	8.4161	49.1028	7.8505	RMSE relat. pO_2 (%)	1.6237	6.4659	1.4970	RMSE relat. pO_2 (%)	1.3650	3.1442	1.3241
Range	1 st order Polynomial-Exponent (PE1)			2 nd order Polynomial-Exponent (PE2)			Demas (D)					
pO_2	Evaluation (criterion)	(a)	(b)	(c)	Evaluation (criterion)	(a)	(b)	(c)	Evaluation (criterion)	(a)	(b)	(c)
0.5-20 (kPa)	RMSE τ_m (μs)	0.1990	0.2451	0.2105	RMSE τ_m (μs)	0.1377	0.3654	0.1405	RMSE τ_m (μs)	0.1297	0.2764	0.1372
	RMSE pO_2 (kPa)	0.2055	0.0455	0.0881	RMSE pO_2 (kPa)	0.0883	0.0423	0.0816	RMSE pO_2 (kPa)	0.1546	0.0341	0.0836
	RMSE relat. pO_2 (%)	2.0447	2.1619	1.8487	RMSE relat. pO_2 (%)	1.3502	3.2684	1.3042	RMSE relat. pO_2 (%)	1.4214	2.6385	1.2790

5.- Accuracy of the fitting models for different criteria using test data

Table 5: Accuracy (root mean square error, RMSE) of the fitting models for different criteria: (a) minimum mean square error (MSE) in τ_m , (b) minimum mean square error (MSE) in pO_2 , (c) minimum mean square relative error in pO_2 . Test data were used for evaluating the models (see Table 2).

Range	Stern-Volmer (SV)			Lehrer (L)			2 nd order Polynomial (P2)					
pO_2	Evaluation (criterion)	(a)	(b)	(c)	Evaluation (criterion)	(a)	(b)	(c)	Evaluation (criterion)	(a)	(b)	(c)
0.75-18 (kPa)	RMSE τ_m (μs)	0.6435	2.0674	0.7623	RMSE τ_m (μs)	0.1205	0.4087	0.1395	RMSE τ_m (μs)	0.1275	0.2515	0.1343
	RMSE pO_2 (kPa)	1.0609	0.4672	0.8284	RMSE pO_2 (kPa)	0.1968	0.1377	0.1588	RMSE pO_2 (kPa)	0.1142	0.1174	0.1199
	RMSE relat. pO_2 (%)	7.5168	29.0686	7.5651	RMSE relat. pO_2 (%)	1.5114	4.0606	1.5303	RMSE relat. pO_2 (%)	1.2918	2.3951	1.3497
Range	1 st order Polynomial-Exponent (PE1)			2 nd order Polynomial-Exponent (PE2)			Demas (D)					
pO_2	Evaluation (criterion)	(a)	(b)	(c)	Evaluation (criterion)	(a)	(b)	(c)	Evaluation (criterion)	(a)	(b)	(c)
0.75-18 (kPa)	RMSE τ_m (μs)	0.1773	0.2029	0.1975	RMSE τ_m (μs)	0.1268	0.2407	0.1338	RMSE τ_m (μs)	0.1187	0.1973	0.1307
	RMSE pO_2 (kPa)	0.1396	0.1002	0.0952	RMSE pO_2 (kPa)	0.1114	0.0985	0.1167	RMSE pO_2 (kPa)	0.1619	0.0946	0.1205
	RMSE relat. pO_2 (%)	1.7553	1.6868	1.7918	RMSE relat. pO_2 (%)	1.2820	1.9106	1.3378	RMSE relat. pO_2 (%)	1.3652	1.5901	1.3223

Experiment 11

page 1/2

Table 1: Sensing phase information

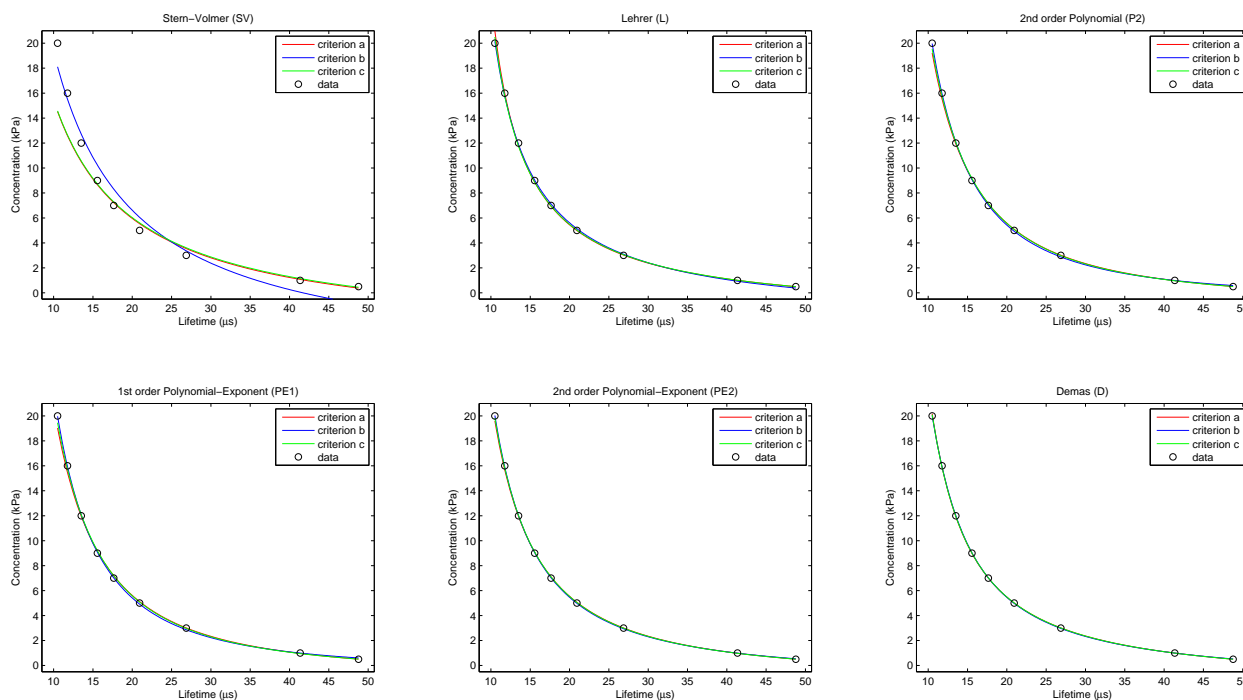
Name:	PtTFPP/PS
Description:	An oxygen-sensing film coated at the end of an optical fibre (a Platinum(II) 5,10,15,20-meso-tetrakis-(2,3,4,5,6-pentafluorophenyl)-porphyrin immobilized in polystyrene).
Analyte:	Partial pressure of oxygen in the gas phase (pO_2 , kPa); Range: 0.5-20 kPa.
Analytical signal:	(Measurement method): Luminescence lifetime in the frequency domain (<i>i.e.</i> , apparent lifetime estimated from phase-shift) using a phase-modulation method. (Instrumentation): Measurement system based on the multifrequency I/Q method (see reference); Excitation signal: 10% duty cycle rectangular-wave (fundamental frequency: 1715 Hz); Measurement frequency: 5 th harmonic (8575 Hz).
Reference(s):	Medina-Rodríguez, S.; de la Torre-Vega, A.; Fernández-Sánchez, J. F.; Fernández-Gutiérrez, A. <i>Sensors and Actuators B: Chemical</i> 2013 , 176, 1110-1120.

1.- Experimental data (calibration and test)

Table 2: Experimental data (*i.e.*, calibration and test data); apparent phase-shift lifetime measurements (τ_ϕ , in microseconds) for several oxygen concentrations (pO_2 , in kPa) at room temperature (21 °C). All the values correspond to the average of 25 measurements.

pO_2 (kPa)	Calibration data (τ_ϕ , in microseconds)		Test data (τ_ϕ , in microseconds)		
	Mean (μs)	Sdev (μs)	pO_2 (kPa)	Mean (μs)	Sdev (μs)
0.50	48.7726	0.1461	0.75	44.4270	0.1345
1.00	41.3500	0.1415	2.00	32.1099	0.1158
3.00	26.8674	0.1153	4.00	23.4718	0.1442
5.00	20.9332	0.1419	6.00	19.1177	0.1625
7.00	17.6530	0.1496	8.00	16.5792	0.1341
9.00	15.5607	0.1183	10.00	14.8080	0.1233
12.00	13.5103	0.1208	14.00	12.5463	0.2058
16.00	11.7566	0.1627	18.00	11.0906	0.1721
20.00	10.5028	0.1445			

2.- Calibration curves: models and criteria


Figure 1: Calibration curves for the apparent phase-shift lifetime measurements (calibration data) of the sensing phase using different models and criteria. Models: Stern-Volmer (SV) (2 parameters), Lehrer (L) (3 parameters), 2nd order Polynomial (P2) (3 parameters), 1st order Polynomial-Exponent (PE1) (3 parameters), 2nd order Polynomial-Exponent (PE2) (4 parameters), Demas (D) (4 parameters). Criteria: (a) minimum mean square error (MSE) in τ_ϕ , (b) minimum mean square error (MSE) in pO_2 , (c) minimum mean square relative error in pO_2 .

Experiment 11

3.- Parameters of the fitting models for different criteria

Table 3: Parameters of the fitting models for different criteria: (a) minimum mean square error (MSE) in τ_ϕ , (b) minimum mean square error (MSE) in pO_2 , (c) minimum mean square relative error in pO_2 . RMSE is expressed in microseconds for criterion (a), in kPa for criterion (b) and in relative error (%) for criterion (c). Calibration data used are shown in Table 2.

Range	Stern-Volmer (SV)			Lehrer (L)			2 nd order Polynomial (P2)						
pO_2	Parameter	(a)	(b)	(c)	Parameter	(a)	(b)	(c)	Parameter	(a)	(b)	(c)	
0.5-20 (kPa)	τ_0 (μs)	54.0611	41.7127	55.1648	τ_0 (μs)	59.8990	56.1157	59.6190	a_0	-1.2374	-0.6177	-1.1271	
	k (kPa^{-1})	0.2856	0.1641	0.2917	k (kPa^{-1})	0.5228	0.4396	0.5083	a_1	49.5531	15.3949	42.0337	
	–	–	–	–	x	0.8998	0.9046	0.9029	a_2	1735.6	2109.66	1838.47	
	R^2	0.98533	0.96820	0.97539	R^2	0.99994	0.99958	0.99977	R^2	0.99981	0.99988	0.99963	
	RMSE	1.5517	1.1357	1.56862	RMSE	0.0995	0.1308	1.5077	RMSE	0.1769	0.0697	1.9315	
	iterations	100	1	1	iterations	100	100	100	iterations	100	1	1	
0.5-20 (kPa)	Φ_0 (μs)	54.0611	41.7127	55.1648	Φ_0 (μs)	59.8990	56.1157	59.6190	Φ_0 (μs)	62.4928	72.2184	63.1325	
	K (kPa^{-1})	0.2856	0.1641	0.2917	K (kPa^{-1})	0.4705	0.3976	0.4589	K (kPa^{-1})	0.5946	0.9783	0.6296	
	1 st order Polynomial-Exponent (PE1)			2 nd order Polynomial-Exponent (PE2)			Demas (D)						
	pO_2	Parameter	(a)	(b)	(c)	Parameter	(a)	(b)	(c)	Parameter	(a)	(b)	(c)
	0.5-20 (kPa)	a_0	-0.8539	-0.4315	-0.7702	a_0	-1.2630	-1.0968	-1.2098	τ_0 (μs)	60.5573	62.0734	60.6308
		a_1	1203.47	1959.3	1383.9	a_1	254.137	229.833	277.943	k_1 (kPa^{-1})	0.5654	0.6308	0.5721
α		-1.7446	-1.9410	-1.7970	a_2	4119.39	4816.04	4702.46	k_2 (kPa^{-1})	0.0093	0.0159	0.0108	
–		–	–	–	α	-1.3028	-1.3043	-1.3322	x	0.8780	0.8602	0.8743	
R^2		0.99967	0.99986	0.99941	R^2	0.99991	0.99995	0.99984	R^2	0.99999	0.99998	0.99998	
RMSE		0.2341	0.0763	2.4384	RMSE	0.1245	0.0442	1.2558	RMSE	0.0362	0.0293	0.4283	
iterations	100	100	100	iterations	100	100	100	iterations	500	500	500		
0.5-20 (kPa)	Φ_0 (μs)	63.8234	76.5792	64.7286	Φ_0 (μs)	61.9827	64.3988	62.2429	Φ_0 (μs)	60.5573	62.0734	60.6308	
	K (kPa^{-1})	0.6712	1.1939	0.7225	K (kPa^{-1})	0.5681	0.6449	0.5829	K (kPa^{-1})	0.4975	0.5448	0.5015	

4.- Accuracy of the fitting models for different criteria using calibration data

Table 4: Accuracy (root mean square error, RMSE) of the fitting models for different criteria: (a) minimum mean square error (MSE) in τ_ϕ , (b) minimum mean square error (MSE) in pO_2 , (c) minimum mean square relative error in pO_2 . Calibration data were used for evaluating the models (see Table 2).

Range	Stern-Volmer (SV)			Lehrer (L)			2 nd order Polynomial (P2)					
pO_2	Evaluation (criterion)	(a)	(b)	(c)	Evaluation (criterion)	(a)	(b)	(c)	Evaluation (criterion)	(a)	(b)	(c)
0.5-20 (kPa)	RMSE τ_ϕ (μs)	1.5517	4.0237	1.5962	RMSE τ_ϕ (μs)	0.0995	0.6715	0.1220	RMSE τ_ϕ (μs)	0.1769	0.7245	0.1956
	RMSE pO_2 (kPa)	2.2257	1.1357	2.2002	RMSE pO_2 (kPa)	0.3376	0.1308	0.2069	RMSE pO_2 (kPa)	0.3124	0.0697	0.1929
	RMSE relat. pO_2 (%)	16.5464	98.1175	15.6862	RMSE relat. pO_2 (%)	1.8506	8.1634	1.5077	RMSE relat. pO_2 (%)	2.1497	5.8617	1.9315
1 st order Polynomial-Exponent (PE1)			2 nd order Polynomial-Exponent (PE2)			Demas (D)						
pO_2	Evaluation (criterion)	(a)	(b)	(c)	Evaluation (criterion)	(a)	(b)	(c)	Evaluation (criterion)	(a)	(b)	(c)
0.5-20 (kPa)	RMSE τ_ϕ (μs)	0.2341	0.9351	0.2578	RMSE τ_ϕ (μs)	0.1245	0.2767	0.1352	RMSE τ_ϕ (μs)	0.0362	0.1518	0.0395
	RMSE pO_2 (kPa)	0.3760	0.0763	0.2266	RMSE pO_2 (kPa)	0.1778	0.0442	0.0925	RMSE pO_2 (kPa)	0.0728	0.0293	0.0514
	RMSE relat. pO_2 (%)	2.7005	7.1541	2.4384	RMSE relat. pO_2 (%)	1.4094	2.6032	1.2558	RMSE relat. pO_2 (%)	0.4778	1.5404	0.4283

5.- Accuracy of the fitting models for different criteria using test data

Table 5: Accuracy (root mean square error, RMSE) of the fitting models for different criteria: (a) minimum mean square error (MSE) in τ_ϕ , (b) minimum mean square error (MSE) in pO_2 , (c) minimum mean square relative error in pO_2 . Test data were used for evaluating the models (see Table 2).

Range	Stern-Volmer (SV)			Lehrer (L)			2 nd order Polynomial (P2)					
pO_2	Evaluation (criterion)	(a)	(b)	(c)	Evaluation (criterion)	(a)	(b)	(c)	Evaluation (criterion)	(a)	(b)	(c)
0.75-18 (kPa)	RMSE τ_ϕ (μs)	1.4958	2.8177	1.6395	RMSE τ_ϕ (μs)	0.1650	0.3540	0.2024	RMSE τ_ϕ (μs)	0.1214	0.4037	0.1180
	RMSE pO_2 (kPa)	1.8252	0.9599	1.8021	RMSE pO_2 (kPa)	0.1654	0.1130	0.1436	RMSE pO_2 (kPa)	0.2547	0.0691	0.1549
	RMSE relat. pO_2 (%)	14.0904	54.3288	15.2712	RMSE relat. pO_2 (%)	1.7652	3.5926	1.9763	RMSE relat. pO_2 (%)	1.6663	3.0308	1.2985
1 st order Polynomial-Exponent (PE1)			2 nd order Polynomial-Exponent (PE2)			Demas (D)						
pO_2	Evaluation (criterion)	(a)	(b)	(c)	Evaluation (criterion)	(a)	(b)	(c)	Evaluation (criterion)	(a)	(b)	(c)
0.75-18 (kPa)	RMSE τ_ϕ (μs)	0.1533	0.4957	0.1686	RMSE τ_ϕ (μs)	0.0867	0.1930	0.0736	RMSE τ_ϕ (μs)	0.1027	0.1555	0.0909
	RMSE pO_2 (kPa)	0.2956	0.0758	0.1762	RMSE pO_2 (kPa)	0.1608	0.0455	0.0862	RMSE pO_2 (kPa)	0.0554	0.0376	0.0486
	RMSE relat. pO_2 (%)	2.0060	3.6030	1.7037	RMSE relat. pO_2 (%)	1.1205	1.5741	0.7650	RMSE relat. pO_2 (%)	0.9840	1.3500	0.8632

Experiment 12

page 1/2

Table 1: Sensing phase information

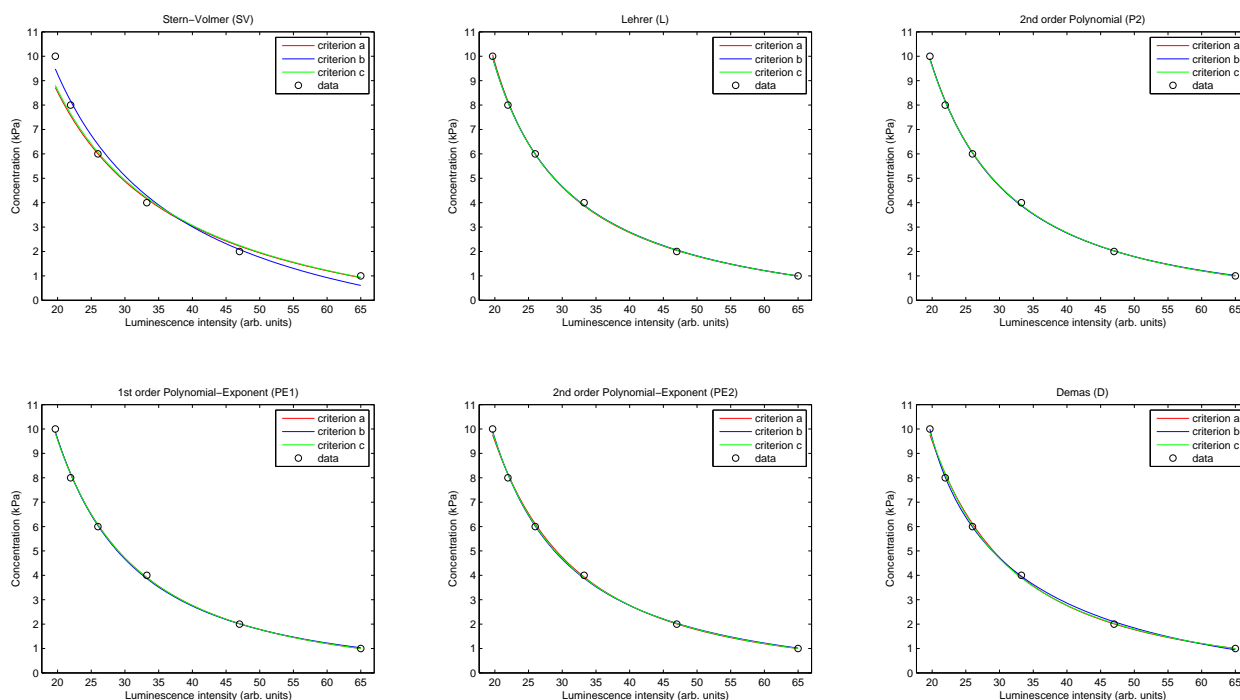
Name:	N969-AP200/19
Description:	An oxygen-sensing dye ($[\text{Ir}(2\text{-}(2,4\text{-difluorophenyl)pyridine})_2(4,4'\text{-dimethylamino-2,2'}\text{-bipyridine})](\text{PF}_6)$) immobilized into AP200/19 (a nanostructured aluminium oxide-hydroxide solid support).
Analyte:	Partial pressure of oxygen in the gas phase ($p\text{O}_2$, kPa); Range: 1-10 kPa.
Analytical signal:	(Measurement method): Luminescence intensity measurements (in arbitrary units). (Instrumentation): A Varian Cary-Eclipse luminescence spectrometer (see reference).
Reference(s):	Marín-Suárez del Toro, M.; Fernández-Sánchez, J.F.; Baranoff, E.; Nazeeruddin, M.K.; Grätzel, M.; Fernández-Gutiérrez, A. <i>Talanta</i> 2010 , 82, 620-626.

1.- Experimental data (calibration and test)

Table 2: Experimental data (*i.e.*, calibration and test data); luminescence intensity measurements (I , in arbitrary units) for several oxygen concentrations ($p\text{O}_2$, in kPa, at room temperature (21 °C)). All the values correspond to the average of 50 measurements.

Calibration data (luminescence intensity, in a.u.)			Test data (luminescence intensity, in a.u.)		
$p\text{O}_2$ (kPa)	Mean (a.u.)	Sdev (a.u.)	$p\text{O}_2$ (kPa)	Mean (a.u.)	Sdev (a.u.)
1.00	65.0003	0.8707	3.00	38.2012	0.3712
2.00	46.9953	0.8629	5.00	29.2062	0.2546
4.00	33.2425	0.1840	7.00	23.7255	0.5223
6.00	25.9853	0.2102	9.00	20.6583	0.1608
8.00	21.9394	0.1902			
10.00	19.6626	0.1961			

2.- Calibration curves: models and criteria


Figure 1: Calibration curves for the luminescence intensity measurements (calibration data) of the sensing phase using different models and criteria. Models: Stern-Volmer (SV) (2 parameters), Lehrer (L) (3 parameters), 2nd order Polynomial (P2) (3 parameters), 1st order Polynomial-Exponent (PE1) (3 parameters), 2nd order Polynomial-Exponent (PE2) (4 parameters), Demas (D) (4 parameters). Criteria: (a) minimum mean square error (MSE) in I , (b) minimum mean square error (MSE) in $p\text{O}_2$, (c) minimum mean square relative error in $p\text{O}_2$.

Experiment 12

3.- Parameters of the fitting models for different criteria

Table 3: Parameters of the fitting models for different criteria: (a) minimum mean square error (MSE) in I , (b) minimum mean square error (MSE) in pO_2 , (c) minimum mean square relative error in pO_2 . RMSE is expressed in arbitrary units for criterion (a), in kPa for criterion (b) and in relative error (%) for criterion (c). Calibration data used are shown in Table 2.

Range	Stern-Volmer (SV)				Lehrer (L)				2 nd order Polynomial (P2)			
pO_2	Parameter	(a)	(b)	(c)	Parameter	(a)	(b)	(c)	Parameter	(a)	(b)	(c)
1-10 (kPa)	I_0 (a.u.)	89.5458	77.1782	89.7495	I_0 (a.u.)	110.0106	108.3270	108.5145	a_0	-0.8237	-0.7332	-0.8612
	k (kPa ⁻¹)	0.4075	0.3085	0.4046	k (kPa ⁻¹)	0.8003	0.7624	0.7698	a_1	78.2044	72.4835	81.6659
	–	–	–	–	x	0.9232	0.9265	0.9256	a_2	2613.27	2685.16	2543.31
	R^2	0.99155	0.98873	0.99371	R^2	0.99953	0.99951	0.99970	R^2	0.99973	0.99918	0.99976
	RMSE	1.4692	0.3380	7.9335	RMSE	0.3457	0.0704	1.7316	RMSE	0.2635	0.0910	1.5435
	iterations	100	1	1	iterations	100	100	100	iterations	100	1	1
1-10 (kPa)	Φ_0 (a.u.)	89.5458	77.1782	89.7495	Φ_0 (a.u.)	110.0106	108.3270	108.5145	Φ_0 (a.u.)	121.1292	127.5702	119.5298
	K (kPa ⁻¹)	0.4075	0.3085	0.4046	K (kPa ⁻¹)	0.7389	0.7063	0.7125	K (kPa ⁻¹)	0.9982	1.1134	0.9622
Range	1 st order Polynomial-Exponent (PE1)				2 nd order Polynomial-Exponent (PE2)				Demas (D)			
pO_2	Parameter	(a)	(b)	(c)	Parameter	(a)	(b)	(c)	Parameter	(a)	(b)	(c)
1-10 (kPa)	a_0	-0.4570	-0.2977	-0.4653	a_0	1.6313	-0.7064	-0.5539	I_0 (a.u.)	130.1773	96.8086	115.9785
	a_1	1354.3	1629.14	1330.61	a_1	-61.4495	356.141	961.496	k_1 (kPa ⁻¹)	1.4323	0.5464	0.9779
	α	-1.6375	-1.7036	-1.6320	a_2	658.736	7173.29	6931.96	k_2 (kPa ⁻¹)	0.0807	-0.0414	0.0363
	–	–	–	–	α	-0.6005	-1.2976	-1.5429	x	0.8288	0.9688	0.8822
	R^2	0.99977	0.99907	0.99977	R^2	0.99979	0.99926	0.99977	R^2	0.99976	0.99975	0.99974
	RMSE	0.2435	0.0970	1.5243	RMSE	0.2292	0.0864	1.5119	RMSE	0.2491	0.0501	1.6082
iterations	100	100	100	iterations	100	100	100	iterations	500	500	500	
1-10 (kPa)	Φ_0 (a.u.)	131.8682	156.4290	131.1809	Φ_0 (a.u.)	122.6312	124.5790	126.1203	Φ_0 (a.u.)	130.1773	96.8086	115.9785
	K (kPa ⁻¹)	1.3363	1.9716	1.3168	K (kPa ⁻¹)	1.4642	1.0520	1.1653	K (kPa ⁻¹)	1.2009	0.5281	0.8670

4.- Accuracy of the fitting models for different criteria using calibration data

Table 4: Accuracy (root mean square error, RMSE) of the fitting models for different criteria: (a) minimum mean square error (MSE) in I , (b) minimum mean square error (MSE) in pO_2 , (c) minimum mean square relative error in pO_2 . Calibration data were used for evaluating the models (see Table 2).

Range	Stern-Volmer (SV)				Lehrer (L)				2 nd order Polynomial (P2)			
pO_2	Evaluation (criterion)	(a)	(b)	(c)	Evaluation (criterion)	(a)	(b)	(c)	Evaluation (criterion)	(a)	(b)	(c)
1-10 (kPa)	RMSE I (a.u.)	1.4692	2.5927	1.4855	RMSE I (a.u.)	0.3457	0.3655	0.3544	RMSE I (a.u.)	0.2635	0.3446	0.2668
	RMSE pO_2 (kPa)	0.5639	0.3380	0.5255	RMSE pO_2 (kPa)	0.0892	0.0704	0.0710	RMSE pO_2 (kPa)	0.0927	0.0910	0.0927
	RMSE relat. pO_2 (%)	8.0171	16.7423	7.9335	RMSE relat. pO_2 (%)	1.8218	1.7512	1.7316	RMSE relat. pO_2 (%)	1.5627	1.7727	1.5435
Range	1 st order Polynomial-Exponent (PE1)				2 nd order Polynomial-Exponent (PE2)				Demas (D)			
pO_2	Evaluation (criterion)	(a)	(b)	(c)	Evaluation (criterion)	(a)	(b)	(c)	Evaluation (criterion)	(a)	(b)	(c)
1-10 (kPa)	RMSE I (a.u.)	0.2435	0.4674	0.2441	RMSE I (a.u.)	0.2292	0.3540	0.2529	RMSE I (a.u.)	0.2491	0.6726	0.2785
	RMSE pO_2 (kPa)	0.1014	0.0970	0.1026	RMSE pO_2 (kPa)	0.1254	0.0864	0.0956	RMSE pO_2 (kPa)	0.1290	0.0501	0.0965
	RMSE relat. pO_2 (%)	1.5282	2.1044	1.5243	RMSE relat. pO_2 (%)	1.5996	1.7824	1.5119	RMSE relat. pO_2 (%)	1.6986	3.0548	1.6082

5.- Accuracy of the fitting models for different criteria using test data

Table 5: Accuracy (root mean square error, RMSE) of the fitting models for different criteria: (a) minimum mean square error (MSE) in I , (b) minimum mean square error (MSE) in pO_2 , (c) minimum mean square relative error in pO_2 . Test data were used for evaluating the models (see Table 2).

Range	Stern-Volmer (SV)				Lehrer (L)				2 nd order Polynomial (P2)			
pO_2	Evaluation (criterion)	(a)	(b)	(c)	Evaluation (criterion)	(a)	(b)	(c)	Evaluation (criterion)	(a)	(b)	(c)
3-9 (kPa)	RMSE I (a.u.)	1.3076	1.1608	1.3735	RMSE I (a.u.)	0.2535	0.2482	0.2434	RMSE I (a.u.)	0.1889	0.1962	0.1828
	RMSE pO_2 (kPa)	0.4471	0.2775	0.4127	RMSE pO_2 (kPa)	0.1028	0.0709	0.0754	RMSE pO_2 (kPa)	0.0829	0.0771	0.0704
	RMSE relat. pO_2 (%)	6.9049	6.4716	7.0781	RMSE relat. pO_2 (%)	1.6486	1.4116	1.4337	RMSE relat. pO_2 (%)	1.2787	1.2844	1.1761
Range	1 st order Polynomial-Exponent (PE1)				2 nd order Polynomial-Exponent (PE2)				Demas (D)			
pO_2	Evaluation (criterion)	(a)	(b)	(c)	Evaluation (criterion)	(a)	(b)	(c)	Evaluation (criterion)	(a)	(b)	(c)
3-9 (kPa)	RMSE I (a.u.)	0.1737	0.2038	0.1698	RMSE I (a.u.)	0.1735	0.2034	0.1761	RMSE I (a.u.)	0.1703	0.4135	0.1871
	RMSE pO_2 (kPa)	0.0752	0.0810	0.0697	RMSE pO_2 (kPa)	0.0742	0.0761	0.0690	RMSE pO_2 (kPa)	0.0793	0.0682	0.0752
	RMSE relat. pO_2 (%)	1.1685	1.3422	1.1189	RMSE relat. pO_2 (%)	1.1492	1.3044	1.1393	RMSE relat. pO_2 (%)	1.1806	2.0089	1.2243

Experiment 13

page 1/2

Table 1: Sensing phase information

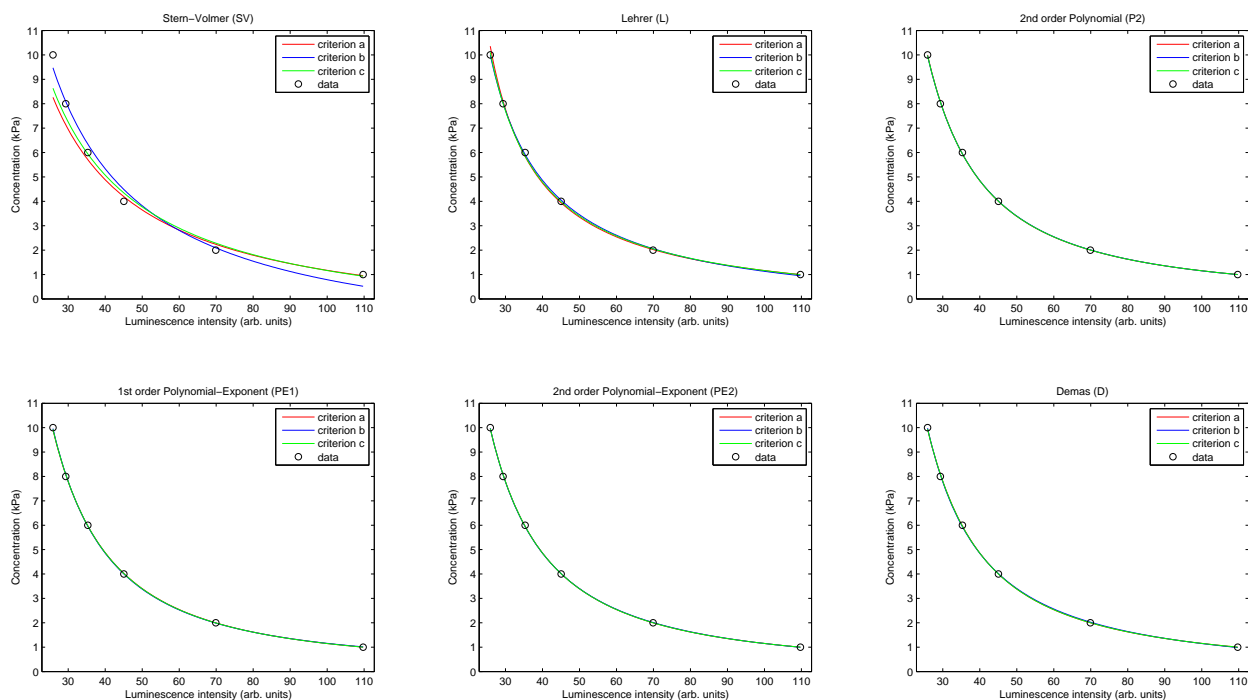
Name:	EB146-AP200/19
Description:	An oxygen-sensing dye (Ir(2-(2,4-difluoro-3-methylesterphenyl)pyridine) ₂ (4-(N,N-dimethylamino)picolinate)) immobilized into AP200/19 (a nanostructured aluminium oxide-hydroxide solid support).
Analyte:	Partial pressure of oxygen in the gas phase (pO_2 , kPa); Range: 1-10 kPa.
Analytical signal:	(Measurement method): Luminescence intensity measurements (in arbitrary units). (Instrumentation): A Varian Cary-Eclipse luminescence spectrometer (see reference).
Reference(s):	Marín-Suárez del Toro, M.; Fernández-Sánchez, J.F.; Baranoff, E.; Nazeeruddin, M.K.; Grätzel, M.; Fernández-Gutiérrez, A. <i>Talanta</i> 2010 , <i>82</i> , 620-626.

1.- Experimental data (calibration and test)

Table 2: Experimental data (*i.e.*, calibration and test data); luminescence intensity measurements (I , in arbitrary units) for several oxygen concentrations (pO_2 , in kPa) at room temperature (21 °C). All the values correspond to the average of 50 measurements.

Calibration data (luminescence intensity, in a.u.)			Test data (luminescence intensity, in a.u.)		
pO_2 (kPa)	Mean (a.u.)	Sdev (a.u.)	pO_2 (kPa)	Mean (a.u.)	Sdev (a.u.)
1.00	109.7275	0.3470	3.00	54.1529	0.2511
2.00	69.9040	0.3555	5.00	39.1459	0.2787
4.00	45.0438	0.2356	7.00	32.3710	0.2337
6.00	35.3143	0.2885	9.00	27.1419	0.1622
8.00	29.3446	0.2592			
10.00	25.8762	0.1709			

2.- Calibration curves: models and criteria


Figure 1: Calibration curves for the luminescence intensity measurements (calibration data) of the sensing phase using different models and criteria. Models: Stern-Volmer (SV) (2 parameters), Lehrer (L) (3 parameters), 2nd order Polynomial (P2) (3 parameters), 1st order Polynomial-Exponent (PE1) (3 parameters), 2nd order Polynomial-Exponent (PE2) (4 parameters), Demas (D) (4 parameters). Criteria: (a) minimum mean square error (MSE) in I , (b) minimum mean square error (MSE) in pO_2 , (c) minimum mean square relative error in pO_2 .

Experiment 13

3.- Parameters of the fitting models for different criteria

Table 3: Parameters of the fitting models for different criteria: (a) minimum mean square error (MSE) in I , (b) minimum mean square error (MSE) in pO_2 , (c) minimum mean square relative error in pO_2 . RMSE is expressed in arbitrary units for criterion (a), in kPa for criterion (b) and in relative error (%) for criterion (c). Calibration data used are shown in Table 2.

Range	Stern-Volmer (SV)				Lehrer (L)				2 nd order Polynomial (P2)			
pO_2	Parameter	(a)	(b)	(c)	Parameter	(a)	(b)	(c)	Parameter	(a)	(b)	(c)
1-10 (kPa)	I_0 (a.u.)	189.8502	135.1251	180.3810	I_0 (a.u.)	315.5584	244.8967	285.9766	a_0	-0.1590	-0.1946	-0.1748
	k (kPa ⁻¹)	0.7669	0.4457	0.6915	k (kPa ⁻¹)	2.1253	1.4341	1.8118	a_1	85.2649	89.8964	87.4975
	–	–	–	–	x	0.9597	0.9567	0.9592	a_2	4597.74	4480.21	4535.6
	R^2	0.98871	0.98555	0.99064	R^2	0.99980	0.99974	0.99977	R^2	0.99998	0.99985	0.99997
	RMSE	3.1200	0.3828	9.6724	RMSE	0.4142	0.0510	1.5167	RMSE	0.1150	0.0395	0.5742
	iterations	100	1	1	iterations	100	100	100	iterations	100	1	1
	Φ_0 (a.u.)	189.8502	135.1251	180.3810	Φ_0 (a.u.)	315.5584	244.8967	285.9766	Φ_0 (a.u.)	585.5601	507.2642	547.7759
	K (kPa ⁻¹)	0.7669	0.4457	0.6915	K (kPa ⁻¹)	2.0396	1.3720	1.7379	K (kPa ⁻¹)	5.7994	4.7161	5.2642
Range	1 st order Polynomial-Exponent (PE1)				2 nd order Polynomial-Exponent (PE2)				Demas (D)			
pO_2	Parameter	(a)	(b)	(c)	Parameter	(a)	(b)	(c)	Parameter	(a)	(b)	(c)
1-10 (kPa)	a_0	0.1006	0.1565	0.1129	a_0	0.0538	-0.0557	0.0523	I_0 (a.u.)	447.3870	319.0493	431.1766
	a_1	2130.8	2379.53	2200.12	a_1	1584.22	934.397	1571.05	k_1 (kPa ⁻¹)	3.8477	2.2792	3.6369
	α	-1.6539	-1.6881	-1.6635	a_2	20095.7	21335.4	20265.1	k_2 (kPa ⁻¹)	0.0566	0.0303	0.0533
	–	–	–	–	α	-1.5817	-1.4507	-1.5796	x	0.9473	0.9463	0.9472
	R^2	0.99998	0.99982	0.99997	R^2	0.99999	0.99985	0.99997	R^2	0.99999	0.99983	0.99997
	RMSE	0.1218	0.0427	0.5870	RMSE	0.1065	0.0384	0.5400	RMSE	0.1080	0.0418	0.5891
	Φ_0 (a.u.)	133.1895	85.8683	118.4704	Φ_0 (a.u.)	269.9032	817.3094	277.5963	Φ_0 (a.u.)	447.3870	319.0493	431.1766
	K (kPa ⁻¹)	6.0095	3.7846	5.3250	K (kPa ⁻¹)	11.7497	12.3513	12.1215	K (kPa ⁻¹)	3.6481	2.1583	3.4475

4.- Accuracy of the fitting models for different criteria using calibration data

Table 4: Accuracy (root mean square error, RMSE) of the fitting models for different criteria: (a) minimum mean square error (MSE) in I , (b) minimum mean square error (MSE) in pO_2 , (c) minimum mean square relative error in pO_2 . Calibration data were used for evaluating the models (see Table 2).

Range	Stern-Volmer (SV)				Lehrer (L)				2 nd order Polynomial (P2)			
pO_2	Evaluation (criterion)	(a)	(b)	(c)	Evaluation (criterion)	(a)	(b)	(c)	Evaluation (criterion)	(a)	(b)	(c)
1-10 (kPa)	RMSE I (a.u.)	3.1200	6.8628	3.2609	RMSE I (a.u.)	0.4142	1.2943	0.5429	RMSE I (a.u.)	0.1150	0.1625	0.1224
	RMSE pO_2 (kPa)	0.8114	0.3828	0.6303	RMSE pO_2 (kPa)	0.1683	0.0510	0.0770	RMSE pO_2 (kPa)	0.0423	0.0395	0.0399
	RMSE relat. pO_2 (%)	10.2477	20.5831	9.6724	RMSE relat. pO_2 (%)	2.0624	2.4466	1.5167	RMSE relat. pO_2 (%)	0.5903	0.5924	0.5742
Range	1 st order Polynomial-Exponent (PE1)				2 nd order Polynomial-Exponent (PE2)				Demas (D)			
pO_2	Evaluation (criterion)	(a)	(b)	(c)	Evaluation (criterion)	(a)	(b)	(c)	Evaluation (criterion)	(a)	(b)	(c)
1-10 (kPa)	RMSE I (a.u.)	0.1218	0.4047	0.1306	RMSE I (a.u.)	0.1065	0.2105	0.1065	RMSE I (a.u.)	0.1080	0.4933	0.1106
	RMSE pO_2 (kPa)	0.0486	0.0427	0.0451	RMSE pO_2 (kPa)	0.0396	0.0384	0.0396	RMSE pO_2 (kPa)	0.0478	0.0418	0.0461
	RMSE relat. pO_2 (%)	0.6038	0.7764	0.5870	RMSE relat. pO_2 (%)	0.5400	0.6294	0.5400	RMSE relat. pO_2 (%)	0.5915	1.0128	0.5891

5.- Accuracy of the fitting models for different criteria using test data

Table 5: Accuracy (root mean square error, RMSE) of the fitting models for different criteria: (a) minimum mean square error (MSE) in I , (b) minimum mean square error (MSE) in pO_2 , (c) minimum mean square relative error in pO_2 . Test data were used for evaluating the models (see Table 2).

Range	Stern-Volmer (SV)				Lehrer (L)				2 nd order Polynomial (P2)			
pO_2	Evaluation (criterion)	(a)	(b)	(c)	Evaluation (criterion)	(a)	(b)	(c)	Evaluation (criterion)	(a)	(b)	(c)
3-9 (kPa)	RMSE I (a.u.)	2.6270	2.2887	2.6953	RMSE I (a.u.)	0.5023	0.4530	0.3985	RMSE I (a.u.)	0.2954	0.2770	0.2852
	RMSE pO_2 (kPa)	0.6895	0.3150	0.5084	RMSE pO_2 (kPa)	0.2358	0.1360	0.1678	RMSE pO_2 (kPa)	0.1318	0.1230	0.1259
	RMSE relat. pO_2 (%)	9.2242	7.8065	8.4936	RMSE relat. pO_2 (%)	2.9180	1.9495	2.1895	RMSE relat. pO_2 (%)	1.6187	1.5265	1.5619
Range	1 st order Polynomial-Exponent (PE1)				2 nd order Polynomial-Exponent (PE2)				Demas (D)			
pO_2	Evaluation (criterion)	(a)	(b)	(c)	Evaluation (criterion)	(a)	(b)	(c)	Evaluation (criterion)	(a)	(b)	(c)
3-9 (kPa)	RMSE I (a.u.)	0.2645	0.3009	0.2722	RMSE I (a.u.)	0.2775	0.2790	0.2774	RMSE I (a.u.)	0.2787	0.2843	0.2808
	RMSE pO_2 (kPa)	0.1069	0.1199	0.1123	RMSE pO_2 (kPa)	0.1203	0.1240	0.1201	RMSE pO_2 (kPa)	0.1153	0.1266	0.1183
	RMSE relat. pO_2 (%)	1.3774	1.5243	1.4246	RMSE relat. pO_2 (%)	1.5017	1.5437	1.5008	RMSE relat. pO_2 (%)	1.4435	1.5743	1.4724

Experiment 14

page 1/2

Table 1: Sensing phase information

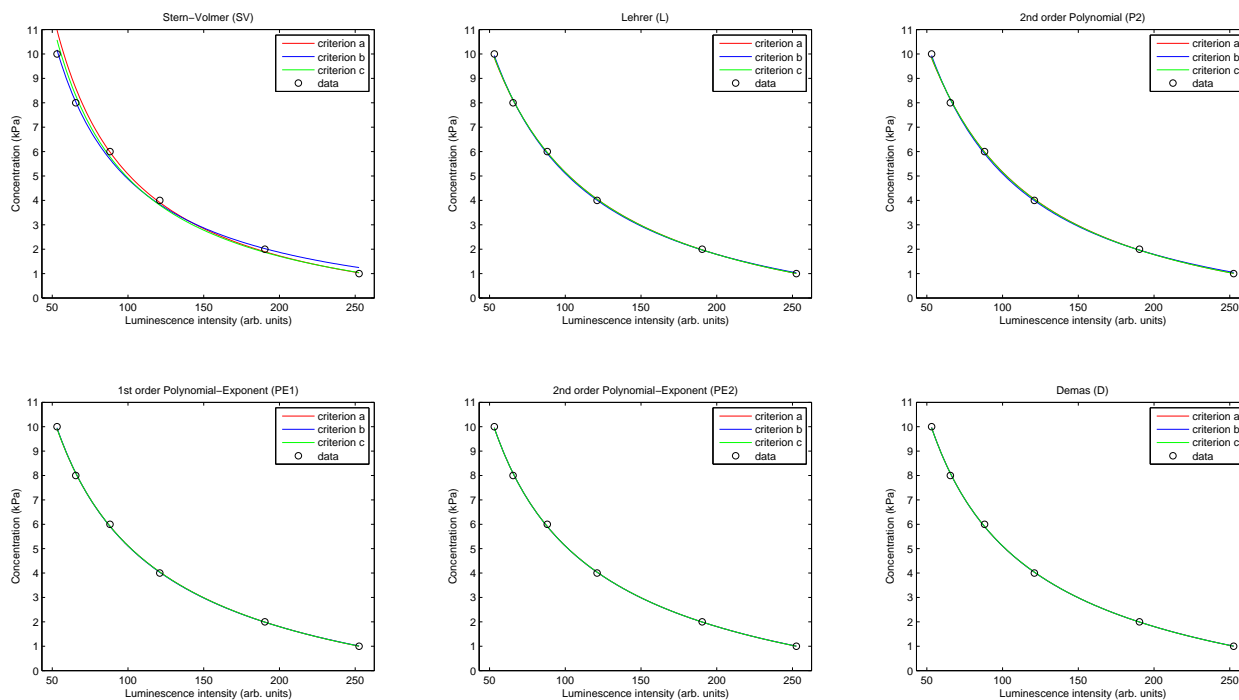
Name:	EB146-PSOX
Description:	An oxygen-sensing dye (Ir(2-(2,4-difluoro-3-methylesterphenyl)pyridine) ₂ (4-(N,N-dimethylamino)picolinate)) immobilized into a polystyrene membrane.
Analyte:	Partial pressure of oxygen in the gas phase (pO_2 , kPa); Range: 1-10 kPa.
Analytical signal:	(Measurement method): Luminescence intensity measurements (in arbitrary units). (Instrumentation): A Varian Cary-Eclipse luminescence spectrometer (see reference).
Reference(s):	Marín-Suárez del Toro, M.; Fernández-Sánchez, J.F.; Baranoff, E.; Nazeeruddin, M.K.; Grätzel, M.; Fernández-Gutiérrez, A. <i>Talanta</i> 2010 , 82, 620-626.

1.- Experimental data (calibration and test)

Table 2: Experimental data (*i.e.*, calibration and test data); luminescence intensity measurements (I , in arbitrary units) for several oxygen concentrations (pO_2 , in kPa) at room temperature (21 °C). All the values correspond to the average of 50 measurements.

Calibration data (luminescence intensity, in a.u.)			Test data (luminescence intensity, in a.u.)		
pO_2 (kPa)	Mean (a.u.)	Sdev (a.u.)	pO_2 (kPa)	Mean (a.u.)	Sdev (a.u.)
1.00	252.5822	11.6378	3.00	149.6979	13.3901
2.00	190.3578	17.6393	5.00	101.6995	5.1459
4.00	120.9905	8.3626	7.00	75.1897	2.9237
6.00	88.1332	1.9210	9.00	58.7116	4.6095
8.00	65.5084	2.7984			
10.00	53.1518	2.0899			

2.- Calibration curves: models and criteria


Figure 1: Calibration curves for the luminescence intensity measurements (calibration data) of the sensing phase using different models and criteria. Models: Stern-Volmer (SV) (2 parameters), Lehrer (L) (3 parameters), 2nd order Polynomial (P2) (3 parameters), 1st order Polynomial-Exponent (PE1) (3 parameters), 2nd order Polynomial-Exponent (PE2) (4 parameters), Demas (D) (4 parameters). Criteria: (a) minimum mean square error (MSE) in I , (b) minimum mean square error (MSE) in pO_2 , (c) minimum mean square relative error in pO_2 .

Experiment 14

3.- Parameters of the fitting models for different criteria

Table 3: Parameters of the fitting models for different criteria: (a) minimum mean square error (MSE) in I , (b) minimum mean square error (MSE) in pO_2 , (c) minimum mean square relative error in pO_2 . RMSE is expressed in arbitrary units for criterion (a), in kPa for criterion (b) and in relative error (%) for criterion (c). Calibration data used are shown in Table 2.

Range	Stern-Volmer (SV)			Lehrer (L)			2 nd order Polynomial (P2)					
pO_2	Parameter	(a)	(b)	(c)	Parameter	(a)	(b)	(c)	Parameter	(a)	(b)	(c)
1-10 (kPa)	I_0 (a.u.)	412.5143	530.1994	427.4725	I_0 (a.u.)	372.8672	386.5797	373.7612	a_0	-2.1441	-1.9251	-2.1186
	k (kPa ⁻¹)	0.6155	0.8823	0.6658	k (kPa ⁻¹)	0.4371	0.4823	0.4420	a_1	838.809	782.766	830.292
	–	–	–	–	x	1.0566	1.0424	1.0543	a_2	-10762.1	-8083.74	-10292.2
	R^2	0.99744	0.99640	0.99763	R^2	0.99982	0.99953	0.99986	R^2	0.99974	0.99944	0.99980
	RMSE	3.6088	0.1912	4.8634	RMSE	0.9483	0.0689	1.1879	RMSE	1.1398	0.0752	1.3995
iterations	100	1	1	iterations	100	100	100	iterations	100	1	1	
	Φ_0 (a.u.)	412.5143	530.1994	427.4725	Φ_0 (a.u.)	372.8672	386.5797	373.7612	Φ_0 (a.u.)	377.9399	396.0056	379.0855
	K (kPa ⁻¹)	0.6155	0.8823	0.6658	K (kPa ⁻¹)	0.4619	0.5028	0.4660	K (kPa ⁻¹)	0.4834	0.5337	0.4885
Range	1 st order Polynomial-Exponent (PE1)			2 nd order Polynomial-Exponent (PE2)			Demas (D)					
pO_2	Parameter	(a)	(b)	(c)	Parameter	(a)	(b)	(c)	Parameter	(a)	(b)	(c)
1-10 (kPa)	a_0	-3.5007	-3.3319	-3.4852	a_0	-4.3174	-4.1489	-4.2782	I_0 (a.u.)	358.5628	359.5827	359.8430
	a_1	217.781	230.113	219.239	a_1	73.1353	95.0032	82.7668	k_1 (kPa ⁻¹)	0.2365	0.2631	0.2945
	α	-0.7012	-0.7177	-0.7030	a_2	262.184	270.221	262.392	k_2 (kPa ⁻¹)	0.2095	0.1849	0.1493
	–	–	–	–	α	-0.5090	-0.5499	-0.5263	x	6.7555	2.6946	1.7205
	R^2	0.99990	0.99964	0.99991	R^2	0.99990	0.99965	0.99992	R^2	0.99990	0.99966	0.99992
	RMSE	0.7296	0.0606	0.9357	RMSE	0.7120	0.0593	0.9156	RMSE	0.7103	0.0590	0.9177
	iterations	100	100	100	iterations	100	100	100	iterations	500	500	500
	Φ_0 (a.u.)	361.6598	365.2105	361.7726	Φ_0 (a.u.)	359.1432	360.3159	358.9987	Φ_0 (a.u.)	358.5628	359.5827	359.8430
	K (kPa ⁻¹)	0.4074	0.4182	0.4081	K (kPa ⁻¹)	0.3950	0.3983	0.3946	K (kPa ⁻¹)	0.3921	0.3956	0.3992

4.- Accuracy of the fitting models for different criteria using calibration data

Table 4: Accuracy (root mean square error, RMSE) of the fitting models for different criteria: (a) minimum mean square error (MSE) in I , (b) minimum mean square error (MSE) in pO_2 , (c) minimum mean square relative error in pO_2 . Calibration data were used for evaluating the models (see Table 2).

Range	Stern-Volmer (SV)			Lehrer (L)			2 nd order Polynomial (P2)					
pO_2	Evaluation (criterion)	(a)	(b)	(c)	Evaluation (criterion)	(a)	(b)	(c)	Evaluation (criterion)	(a)	(b)	(c)
1-10 (kPa)	RMSE I (a.u.)	3.6088	12.1096	4.1194	RMSE I (a.u.)	0.9483	1.4876	0.9585	RMSE I (a.u.)	1.1398	2.0091	1.1537
	RMSE pO_2 (kPa)	0.4751	0.1912	0.2964	RMSE pO_2 (kPa)	0.0834	0.0689	0.0779	RMSE pO_2 (kPa)	0.0977	0.0752	0.0899
	RMSE relat. pO_2 (%)	5.6873	10.4356	4.8634	RMSE relat. pO_2 (%)	1.2006	1.7400	1.1879	RMSE relat. pO_2 (%)	1.4200	2.2734	1.3995
Range	1 st order Polynomial-Exponent (PE1)			2 nd order Polynomial-Exponent (PE2)			Demas (D)					
pO_2	Evaluation (criterion)	(a)	(b)	(c)	Evaluation (criterion)	(a)	(b)	(c)	Evaluation (criterion)	(a)	(b)	(c)
1-10 (kPa)	RMSE I (a.u.)	0.7296	0.7834	0.7299	RMSE I (a.u.)	0.7120	0.7194	0.7124	RMSE I (a.u.)	0.7103	0.7150	0.7150
	RMSE pO_2 (kPa)	0.0619	0.0606	0.0615	RMSE pO_2 (kPa)	0.0594	0.0593	0.0595	RMSE pO_2 (kPa)	0.0590	0.0590	0.0593
	RMSE relat. pO_2 (%)	0.9368	1.0042	0.9357	RMSE relat. pO_2 (%)	0.9160	0.9287	0.9156	RMSE relat. pO_2 (%)	0.9152	0.9225	0.9177

5.- Accuracy of the fitting models for different criteria using test data

Table 5: Accuracy (root mean square error, RMSE) of the fitting models for different criteria: (a) minimum mean square error (MSE) in I , (b) minimum mean square error (MSE) in pO_2 , (c) minimum mean square relative error in pO_2 . Test data were used for evaluating the models (see Table 2).

Range	Stern-Volmer (SV)			Lehrer (L)			2 nd order Polynomial (P2)					
pO_2	Evaluation (criterion)	(a)	(b)	(c)	Evaluation (criterion)	(a)	(b)	(c)	Evaluation (criterion)	(a)	(b)	(c)
3-9 (kPa)	RMSE I (a.u.)	3.4841	2.9378	4.0250	RMSE I (a.u.)	0.5955	0.7660	0.6234	RMSE I (a.u.)	0.8424	1.0002	0.8550
	RMSE pO_2 (kPa)	0.4272	0.1540	0.2601	RMSE pO_2 (kPa)	0.0443	0.0421	0.0465	RMSE pO_2 (kPa)	0.0644	0.0507	0.0625
	RMSE relat. pO_2 (%)	5.4490	3.2125	4.6937	RMSE relat. pO_2 (%)	0.7453	0.8497	0.7782	RMSE relat. pO_2 (%)	1.0647	1.0885	1.0578
Range	1 st order Polynomial-Exponent (PE1)			2 nd order Polynomial-Exponent (PE2)			Demas (D)					
pO_2	Evaluation (criterion)	(a)	(b)	(c)	Evaluation (criterion)	(a)	(b)	(c)	Evaluation (criterion)	(a)	(b)	(c)
3-9 (kPa)	RMSE I (a.u.)	0.2525	0.2895	0.2647	RMSE I (a.u.)	0.1989	0.1932	0.1910	RMSE I (a.u.)	0.1878	0.1840	0.2109
	RMSE pO_2 (kPa)	0.0222	0.0256	0.0241	RMSE pO_2 (kPa)	0.0219	0.0221	0.0208	RMSE pO_2 (kPa)	0.0230	0.0223	0.0231
	RMSE relat. pO_2 (%)	0.3323	0.3725	0.3519	RMSE relat. pO_2 (%)	0.2856	0.2809	0.2728	RMSE relat. pO_2 (%)	0.2830	0.2755	0.3017

Experiment 15

page 1/2

Table 1: Sensing phase information

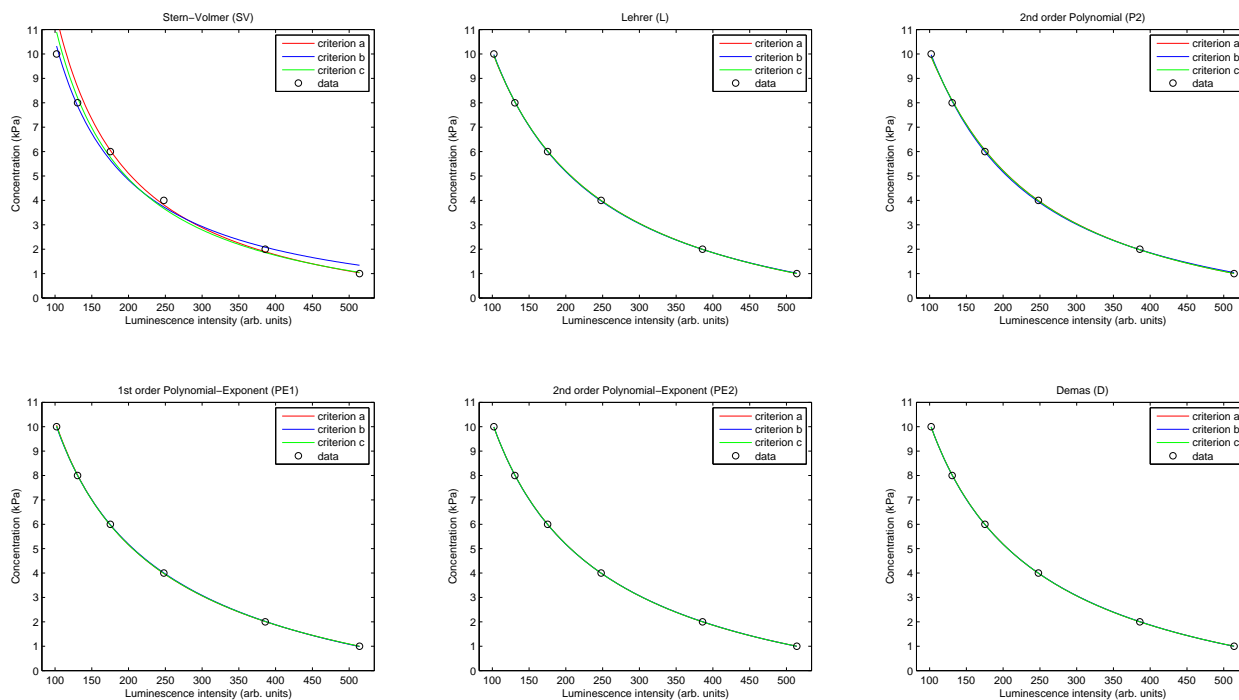
Name:	N1008-PSOX
Description:	An oxygen-sensing dye ($[\text{Ir}(2\text{-}(2,4\text{-difluorophenyl})\text{pyridine})_2(4,7\text{-diphenyl-1,10-phenanthroline})](\text{PF}_6)$) immobilized into a polystyrene membrane.
Analyte:	Partial pressure of oxygen in the gas phase ($p\text{O}_2$, kPa); Range: 1-10 kPa.
Analytical signal:	(Measurement method): Luminescence intensity measurements (in arbitrary units). (Instrumentation): A Varian Cary-Eclipse luminescence spectrometer (see reference).
Reference(s):	Marín-Suárez del Toro, M.; Fernández-Sánchez, J.F.; Baranoff, E.; Nazeeruddin, M.K.; Grätzel, M.; Fernández-Gutiérrez, A. <i>Talanta</i> 2010 , 82, 620-626.

1.- Experimental data (calibration and test)

Table 2: Experimental data (*i.e.*, calibration and test data); luminescence intensity measurements (I , in arbitrary units) for several oxygen concentrations ($p\text{O}_2$, in kPa) at room temperature (21 °C). All the values correspond to the average of 50 measurements.

Calibration data (luminescence intensity, in a.u.)			Test data (luminescence intensity, in a.u.)		
$p\text{O}_2$ (kPa)	Mean (a.u.)	Sdev (a.u.)	$p\text{O}_2$ (kPa)	Mean (a.u.)	Sdev (a.u.)
1.00	514.1325	1.6743	3.00	304.8134	1.0691
2.00	385.8328	1.8055	5.00	206.2071	1.2703
4.00	247.9520	1.1513	7.00	149.5237	1.0363
6.00	175.1547	0.7471	9.00	115.0019	0.6323
8.00	130.6879	1.0485			
10.00	102.0667	0.4338			

2.- Calibration curves: models and criteria


Figure 1: Calibration curves for the luminescence intensity measurements (calibration data) of the sensing phase using different models and criteria. Models: Stern-Volmer (SV) (2 parameters), Lehrer (L) (3 parameters), 2nd order Polynomial (P2) (3 parameters), 1st order Polynomial-Exponent (PE1) (3 parameters), 2nd order Polynomial-Exponent (PE2) (4 parameters), Demas (D) (4 parameters). Criteria: (a) minimum mean square error (MSE) in I , (b) minimum mean square error (MSE) in $p\text{O}_2$, (c) minimum mean square relative error in $p\text{O}_2$.

Experiment 15

page 2/2

3.- Parameters of the fitting models for different criteria

Table 3: Parameters of the fitting models for different criteria: (a) minimum mean square error (MSE) in I , (b) minimum mean square error (MSE) in pO_2 , (c) minimum mean square relative error in pO_2 . RMSE is expressed in arbitrary units for criterion (a), in kPa for criterion (b) and in relative error (%) for criterion (c). Calibration data used are shown in Table 2.

Range	Stern-Volmer (SV)			Lehrer (L)			2 nd order Polynomial (P2)					
pO_2	Parameter	(a)	(b)	(c)	Parameter	(a)	(b)	(c)	Parameter	(a)	(b)	(c)
1-10 (kPa)	I_0 (a.u.)	852.8149	1293.8034	902.0805	I_0 (a.u.)	750.2269	763.7221	751.2685	a_0	-2.1886	-2.0051	-2.1694
	k (kPa ⁻¹)	0.6390	1.1307	0.7190	k (kPa ⁻¹)	0.4138	0.4350	0.4163	a_1	1743.85	1651.86	1731.31
	—	—	—	—	x	1.0742	1.0659	1.0728	a_2	-52250.5	-43852	-50975.8
	R^2	0.99619	0.99273	0.99594	R^2	0.99999	0.99995	0.99999	R^2	0.99989	0.99982	0.99991
	RMSE	9.0686	0.2716	6.3740	RMSE	0.5523	0.0219	0.3717	RMSE	1.5250	0.0422	0.9232
	iterations	100	1	1	iterations	100	100	100	iterations	100	1	1
	Φ_0 (a.u.)	852.8149	1293.8034	902.0805	Φ_0 (a.u.)	750.2269	763.7221	751.2685	Φ_0 (a.u.)	765.5955	796.3569	767.4489
	K (kPa ⁻¹)	0.6390	1.1307	0.7190	K (kPa ⁻¹)	0.4445	0.4637	0.4466	K (kPa ⁻¹)	0.4763	0.5165	0.4801
Range	1 st order Polynomial-Exponent (PE1)			2 nd order Polynomial-Exponent (PE2)			Demas (D)					
pO_2	Parameter	(a)	(b)	(c)	Parameter	(a)	(b)	(c)	Parameter	(a)	(b)	(c)
1-10 (kPa)	a_0	-4.1141	-4.5141	-4.1843	a_0	48.2706	10.8223	38.1884	I_0 (a.u.)	741.2788	731.3712	740.2958
	a_1	262.528	233.344	255.363	a_1	-256.249	-113.541	-221.974	k_1 (kPa ⁻¹)	0.3801	0.3438	0.3755
	α	-0.6310	-0.6004	-0.6243	a_2	331.431	253.274	311.647	k_2 (kPa ⁻¹)	0.0297	0.0575	0.0343
	—	—	—	—	α	-0.1212	-0.1770	-0.1305	x	1.1260	1.2095	1.1360
	R^2	0.99997	0.99998	0.99998	R^2	1.00000	0.99999	1.00000	R^2	1.00000	0.99999	1.00000
	RMSE	0.7771	0.0125	0.4450	RMSE	0.1765	0.0076	0.1226	RMSE	0.2331	0.0079	0.1511
iterations	100	100	100	iterations	100	100	100	iterations	500	500	500	
	Φ_0 (a.u.)	725.1850	714.3232	724.1468	Φ_0 (a.u.)	748.9788	735.1467	747.2922	Φ_0 (a.u.)	741.2788	731.3712	740.2958
	K (kPa ⁻¹)	0.3852	0.3690	0.3828	K (kPa ⁻¹)	0.4503	0.4139	0.4450	K (kPa ⁻¹)	0.4243	0.4038	0.4218

4.- Accuracy of the fitting models for different criteria using calibration data

Table 4: Accuracy (root mean square error, RMSE) of the fitting models for different criteria: (a) minimum mean square error (MSE) in I , (b) minimum mean square error (MSE) in pO_2 , (c) minimum mean square relative error in pO_2 . Calibration data were used for evaluating the models (see Table 2).

Range	Stern-Volmer (SV)			Lehrer (L)			2 nd order Polynomial (P2)					
pO_2	Evaluation (criterion)	(a)	(b)	(c)	Evaluation (criterion)	(a)	(b)	(c)	Evaluation (criterion)	(a)	(b)	(c)
1-10 (kPa)	RMSE I (a.u.)	9.0686	38.8715	10.7856	RMSE I (a.u.)	0.5523	1.3275	0.5700	RMSE I (a.u.)	1.5250	3.4070	1.5532
	RMSE pO_2 (kPa)	0.6775	0.2716	0.4163	RMSE pO_2 (kPa)	0.0325	0.0219	0.0287	RMSE pO_2 (kPa)	0.0682	0.0422	0.0613
	RMSE relat. pO_2 (%)	7.6734	14.5711	6.3740	RMSE relat. pO_2 (%)	0.3820	0.7682	0.3717	RMSE relat. pO_2 (%)	0.9406	1.8786	0.9232
Range	1 st order Polynomial-Exponent (PE1)			2 nd order Polynomial-Exponent (PE2)			Demas (D)					
pO_2	Evaluation (criterion)	(a)	(b)	(c)	Evaluation (criterion)	(a)	(b)	(c)	Evaluation (criterion)	(a)	(b)	(c)
1-10 (kPa)	RMSE I (a.u.)	0.7771	1.2452	0.8047	RMSE I (a.u.)	0.1765	0.4178	0.1832	RMSE I (a.u.)	0.2331	0.5046	0.2422
	RMSE pO_2 (kPa)	0.0306	0.0125	0.0220	RMSE pO_2 (kPa)	0.0108	0.0076	0.0095	RMSE pO_2 (kPa)	0.0124	0.0079	0.0105
	RMSE relat. pO_2 (%)	0.4691	0.7340	0.4450	RMSE relat. pO_2 (%)	0.1267	0.2345	0.1226	RMSE relat. pO_2 (%)	0.1567	0.2841	0.1511

5.- Accuracy of the fitting models for different criteria using test data

Table 5: Accuracy (root mean square error, RMSE) of the fitting models for different criteria: (a) minimum mean square error (MSE) in I , (b) minimum mean square error (MSE) in pO_2 , (c) minimum mean square relative error in pO_2 . Test data were used for evaluating the models (see Table 2).

Range	Stern-Volmer (SV)			Lehrer (L)			2 nd order Polynomial (P2)					
pO_2	Evaluation (criterion)	(a)	(b)	(c)	Evaluation (criterion)	(a)	(b)	(c)	Evaluation (criterion)	(a)	(b)	(c)
3-9 (kPa)	RMSE I (a.u.)	9.1010	8.1006	11.1186	RMSE I (a.u.)	1.0139	1.2231	1.0677	RMSE I (a.u.)	1.9183	2.1972	1.9547
	RMSE pO_2 (kPa)	0.5607	0.2164	0.3312	RMSE pO_2 (kPa)	0.0400	0.0366	0.0411	RMSE pO_2 (kPa)	0.0738	0.0557	0.0706
	RMSE relat. pO_2 (%)	7.1132	4.3387	6.2184	RMSE relat. pO_2 (%)	0.6245	0.6848	0.6515	RMSE relat. pO_2 (%)	1.1747	1.1777	1.1681
Range	1 st order Polynomial-Exponent (PE1)			2 nd order Polynomial-Exponent (PE2)			Demas (D)					
pO_2	Evaluation (criterion)	(a)	(b)	(c)	Evaluation (criterion)	(a)	(b)	(c)	Evaluation (criterion)	(a)	(b)	(c)
3-9 (kPa)	RMSE I (a.u.)	0.5294	0.5477	0.3998	RMSE I (a.u.)	0.6237	0.4589	0.6061	RMSE I (a.u.)	0.6613	0.4436	0.6247
	RMSE pO_2 (kPa)	0.0242	0.0162	0.0153	RMSE pO_2 (kPa)	0.0260	0.0210	0.0252	RMSE pO_2 (kPa)	0.0273	0.0205	0.0258
	RMSE relat. pO_2 (%)	0.3414	0.3046	0.2425	RMSE relat. pO_2 (%)	0.3926	0.3012	0.3813	RMSE relat. pO_2 (%)	0.4148	0.2926	0.3918

Experiment 16

page 1/2

Table 1: Sensing phase information

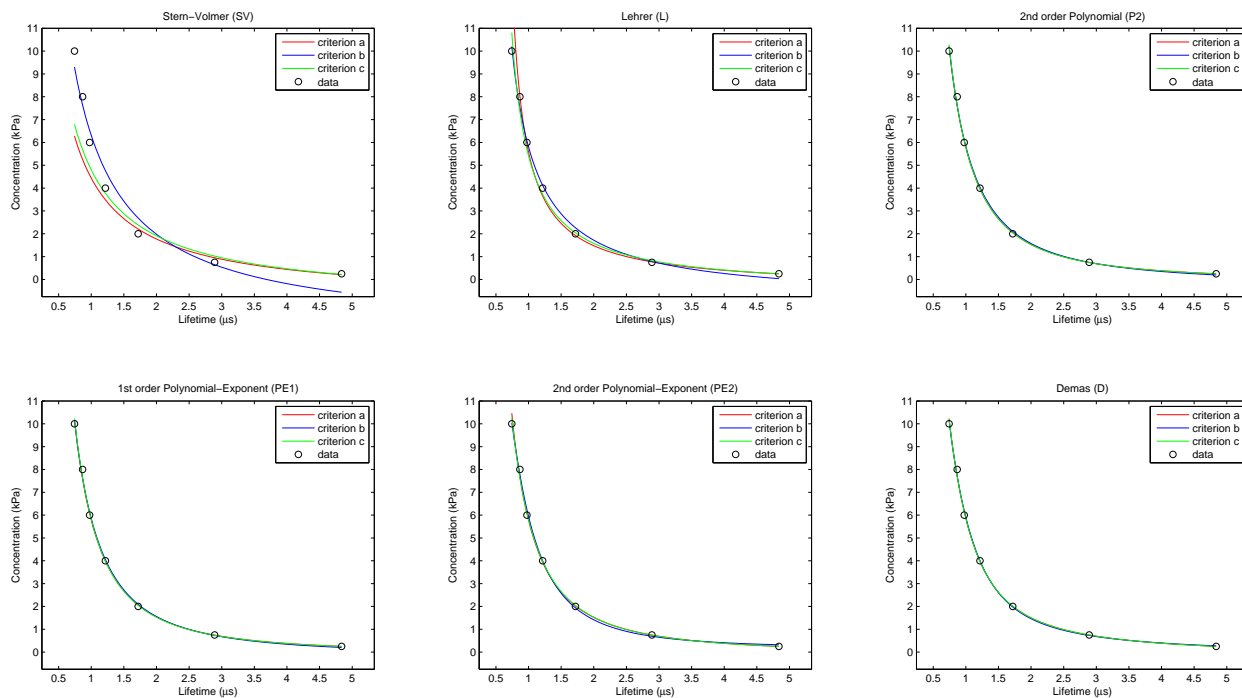
Name:	PtTFPP-AP200/19
Description:	An oxygen-sensing dye (Platinum(II) 5,10,15,20-meso-tetrakis-(2,3,4,5,6-pentafluorophenyl)-porphyrin) immobilized into AP200/19 (a nanostructured aluminium oxide-hydroxide solid support).
Analyte:	Partial pressure of oxygen in the gas phase (pO_2 , kPa); Range: 0.25-10 kPa.
Analytical signal:	(Measurement method): Luminescence lifetime in the frequency domain (<i>i.e.</i> , apparent lifetime estimated from phase-shift) using a phase-modulation method. (Instrumentation): A dual-phase lock-in amplifier (LIA) (SR830, Stanford Research Systems); Excitation signal: Sinusoidal-wave at 40100 Hz (see reference).
Reference(s):	Medina-Rodríguez, S.; Marín-Suárez, M.; Fernández-Sánchez, J.F.; de la Torre-Vega, A.; Baranoff, E.; Fernández-Gutiérrez, A. <i>Analyst</i> 2013 , 138, 4607-4617.

1.- Experimental data (calibration and test)

Table 2: Experimental data (*i.e.*, calibration and test data); apparent phase-shift lifetime measurements (τ_ϕ , in microseconds) for several oxygen concentrations (pO_2 , in kPa) at room temperature (21 °C). All the values correspond to the average of 25 measurements.

Calibration data (τ_ϕ , in microseconds)			Test data (τ_ϕ , in microseconds)		
pO_2 (kPa)	Mean (μs)	Sdev (μs)	pO_2 (kPa)	Mean (μs)	Sdev (μs)
0.25	4.8379	0.0116	0.50	3.6174	0.0371
0.75	2.8917	0.0051	1.00	2.5886	0.0024
2.00	1.7192	0.0024	3.00	1.4000	0.0024
4.00	1.2168	0.0031	5.00	1.0720	0.0033
6.00	0.9757	0.0030	7.00	0.8995	0.0028
8.00	0.8678	0.0029	9.00	0.7839	0.0026
10.00	0.7429	0.0026			

2.- Calibration curves: models and criteria


Figure 1: Calibration curves for the apparent phase-shift lifetime measurements (calibration data) of the sensing phase using different models and criteria. Models: Stern-Volmer (SV) (2 parameters), Lehrer (L) (3 parameters), 2nd order Polynomial (P2) (3 parameters), 1st order Polynomial-Exponent (PE1) (3 parameters), 2nd order Polynomial-Exponent (PE2) (4 parameters), Demas (D) (4 parameters). Criteria: (a) minimum mean square error (MSE) in τ_ϕ , (b) minimum mean square error (MSE) in pO_2 , (c) minimum mean square relative error in pO_2 .

Experiment 16

3.- Parameters of the fitting models for different criteria

Table 3: Parameters of the fitting models for different criteria: (a) minimum mean square error (MSE) in τ_ϕ , (b) minimum mean square error (MSE) in pO_2 , (c) minimum mean square relative error in pO_2 . RMSE is expressed in microseconds for criterion (a), in kPa for criterion (b) and in relative error (%) for criterion (c). Calibration data used are shown in Table 2.

Range	Stern-Volmer (SV)			Lehrer (L)			2 nd order Polynomial (P2)						
pO_2	Parameter	(a)	(b)	(c)	Parameter	(a)	(b)	(c)	Parameter	(a)	(b)	(c)	
0.25-10 (kPa)	τ_0 (μs)	5.9749	3.6879	5.9357	τ_0 (μs)	7.6321	5.0129	7.0433	a_0	-0.1152	-0.2751	-0.1048	
	k (kPa^{-1})	1.1210	0.4260	1.0286	k (kPa^{-1})	2.6196	1.0611	2.0746	a_1	0.69275	1.29313	0.630369	
	—	—	—	—	x	0.9285	0.9305	0.9344	a_2	5.19773	4.81538	5.2634	
	R^2	0.97282	0.96853	0.94214	R^2	0.99922	0.99513	0.99545	R^2	0.99991	0.99740	0.99944	
	RMSE	0.2279	0.6121	24.0549	RMSE	0.0386	0.2407	6.7432	RMSE	0.0130	0.1760	2.3650	
	iterations	100	1	1	iterations	100	100	100	iterations	100	1	1	
0.25-10 (kPa)	Φ_0 (μs)	5.9749	3.6879	5.9357	Φ_0 (μs)	7.6321	5.0129	7.0433	Φ_0 (μs)	10.3691	7.1485	10.7046	
	K (kPa^{-1})	1.1210	0.4260	1.0286	K (kPa^{-1})	2.4323	0.9873	1.9385	K (kPa^{-1})	6.1164	2.7074	6.6333	
	1 st order Polynomial-Exponent (PE1)			2 nd order Polynomial-Exponent (PE2)			Demas (D)						
	pO_2	Parameter	(a)	(b)	(c)	Parameter	(a)	(b)	(c)	Parameter	(a)	(b)	(c)
	0.25-10 (kPa)	a_0	-0.0533	-0.1330	-0.0437	a_0	-0.1719	0.1648	-0.1053	τ_0 (μs)	8.4522	11.2232	8.5133
		a_1	5.8378	5.98796	5.84794	a_1	1.81392	6.6606	0.636156	k_1 (kPa^{-1})	3.6717	6.1927	3.7476
α		-1.8755	-1.8249	-1.8958	a_2	4.1356	-0.880038	5.25796	k_2 (kPa^{-1})	0.0688	0.0921	0.0715	
—		—	—	—	α	-1.1309	-2.3764	-1.0005	x	0.8895	0.8993	0.8882	
R^2		0.99988	0.99759	0.99942	R^2	0.99993	0.99849	0.99944	R^2	0.99996	0.99830	0.99963	
RMSE		0.0150	0.1695	2.4049	RMSE	0.0114	0.1339	2.3650	RMSE	0.0092	0.1425	1.9350	
iterations	100	100	100	iterations	100	100	100	iterations	500	500	500		
0.25-10 (kPa)	Φ_0 (μs)	12.2271	8.0528	13.2338	Φ_0 (μs)	9.3176	1.1694	10.6918	Φ_0 (μs)	8.4522	11.2232	8.5133	
	K (kPa^{-1})	9.9969	4.1187	12.0699	K (kPa^{-1})	4.4558	2.5446	6.6108	K (kPa^{-1})	3.2737	5.5786	3.3366	

4.- Accuracy of the fitting models for different criteria using calibration data

Table 4: Accuracy (root mean square error, RMSE) of the fitting models for different criteria: (a) minimum mean square error (MSE) in τ_ϕ , (b) minimum mean square error (MSE) in pO_2 , (c) minimum mean square relative error in pO_2 . Calibration data were used for evaluating the models (see Table 2).

Range	Stern-Volmer (SV)			Lehrer (L)			2 nd order Polynomial (P2)					
pO_2	Evaluation (criterion)	(a)	(b)	(c)	Evaluation (criterion)	(a)	(b)	(c)	Evaluation (criterion)	(a)	(b)	(c)
0.25-10 (kPa)	RMSE τ_ϕ (μs)	0.2279	0.5827	0.2380	RMSE τ_ϕ (μs)	0.0386	0.3080	0.0628	RMSE τ_ϕ (μs)	0.0130	0.1293	0.0133
	RMSE pO_2 (kPa)	1.8430	0.6121	1.5610	RMSE pO_2 (kPa)	1.2654	0.2407	0.4277	RMSE pO_2 (kPa)	0.1829	0.1760	0.1845
	RMSE relat. pO_2 (%)	25.0243	123.2473	24.0549	RMSE relat. pO_2 (%)	13.1458	32.7881	6.7432	RMSE relat. pO_2 (%)	2.3839	8.4045	2.3650
1 st order Polynomial-Exponent (PE1)			2 nd order Polynomial-Exponent (PE2)			Demas (D)						
pO_2	Evaluation (criterion)	(a)	(b)	(c)	Evaluation (criterion)	(a)	(b)	(c)	Evaluation (criterion)	(a)	(b)	(c)
0.25-10 (kPa)	RMSE τ_ϕ (μs)	0.0150	0.1257	0.0158	RMSE τ_ϕ (μs)	0.0114	0.5387	0.0133	RMSE τ_ϕ (μs)	0.0092	0.0884	0.0093
	RMSE pO_2 (kPa)	0.1767	0.1695	0.1759	RMSE pO_2 (kPa)	0.2219	0.1339	0.1846	RMSE pO_2 (kPa)	0.1566	0.1425	0.1524
	RMSE relat. pO_2 (%)	2.4694	7.5434	2.4049	RMSE relat. pO_2 (%)	2.5552	11.4101	2.3650	RMSE relat. pO_2 (%)	1.9574	4.3814	1.9350

5.- Accuracy of the fitting models for different criteria using test data

Table 5: Accuracy (root mean square error, RMSE) of the fitting models for different criteria: (a) minimum mean square error (MSE) in τ_ϕ , (b) minimum mean square error (MSE) in pO_2 , (c) minimum mean square relative error in pO_2 . Test data were used for evaluating the models (see Table 2).

Range	Stern-Volmer (SV)			Lehrer (L)			2 nd order Polynomial (P2)					
pO_2	Evaluation (criterion)	(a)	(b)	(c)	Evaluation (criterion)	(a)	(b)	(c)	Evaluation (criterion)	(a)	(b)	(c)
0.5-9 (kPa)	RMSE τ_ϕ (μs)	0.1984	0.2561	0.2207	RMSE τ_ϕ (μs)	0.0474	0.0948	0.0362	RMSE τ_ϕ (μs)	0.0553	0.0712	0.0589
	RMSE pO_2 (kPa)	1.5449	0.5168	1.2706	RMSE pO_2 (kPa)	0.8230	0.1352	0.2176	RMSE pO_2 (kPa)	0.1064	0.1219	0.1239
	RMSE relat. pO_2 (%)	21.8339	39.3040	21.4717	RMSE relat. pO_2 (%)	10.0194	8.7460	3.9538	RMSE relat. pO_2 (%)	3.8632	5.1231	4.1442
1 st order Polynomial-Exponent (PE1)			2 nd order Polynomial-Exponent (PE2)			Demas (D)						
pO_2	Evaluation (criterion)	(a)	(b)	(c)	Evaluation (criterion)	(a)	(b)	(c)	Evaluation (criterion)	(a)	(b)	(c)
0.5-9 (kPa)	RMSE τ_ϕ (μs)	0.0587	0.0891	0.0650	RMSE τ_ϕ (μs)	0.0524	0.0973	0.0589	RMSE τ_ϕ (μs)	0.0511	0.0693	0.0526
	RMSE pO_2 (kPa)	0.0868	0.1295	0.1173	RMSE pO_2 (kPa)	0.1715	0.1786	0.1240	RMSE pO_2 (kPa)	0.1497	0.1538	0.1457
	RMSE relat. pO_2 (%)	4.0277	6.2356	4.4934	RMSE relat. pO_2 (%)	3.9795	6.8621	4.1416	RMSE relat. pO_2 (%)	3.8961	5.0706	3.9743

Experiment 17

page 1/2

Table 1: Sensing phase information

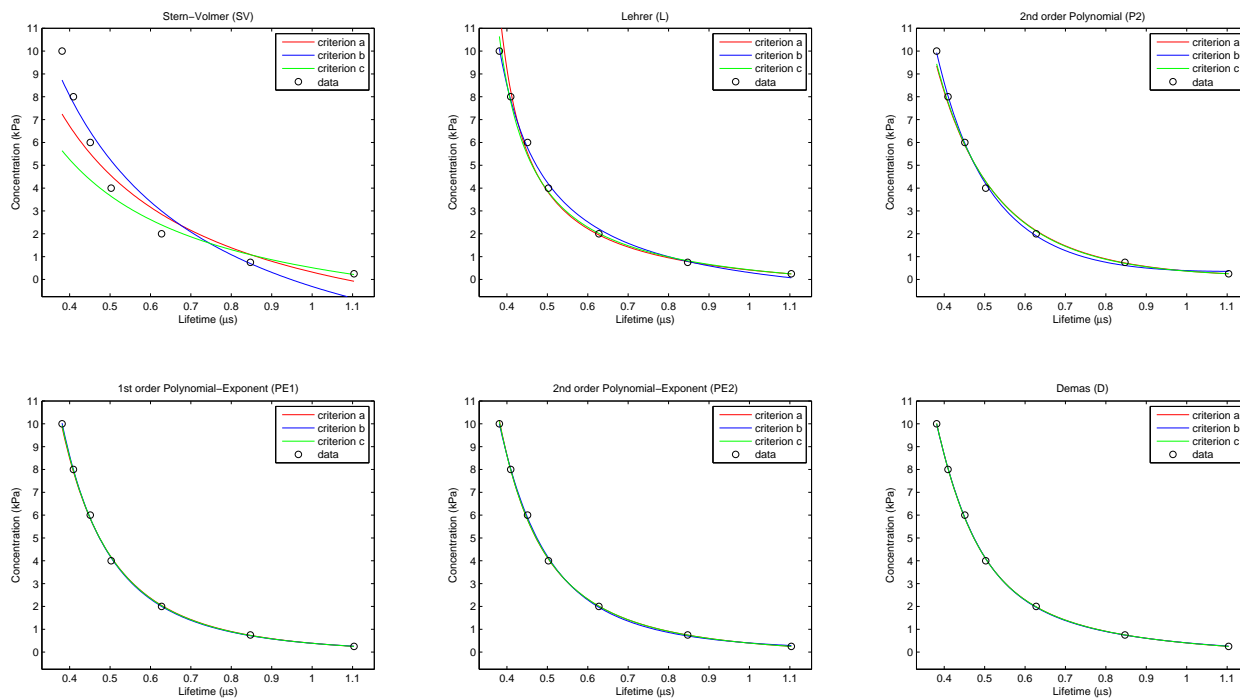
Name:	N969-AP200/19
Description:	An oxygen-sensing dye ($[\text{Ir}(2\text{-}(2,4\text{-difluorophenyl)pyridine})_2(4,4'\text{-dimethylamino-2,2'}\text{-bipyridine})](\text{PF}_6))$ immobilized into AP200/19 (a nanostructured aluminium oxide-hydroxide solid support).
Analyte:	Partial pressure of oxygen in the gas phase (pO_2 , kPa); Range: 0.25-10 kPa.
Analytical signal:	(Measurement method): Luminescence lifetime in the frequency domain (<i>i.e.</i> , apparent lifetime estimated from phase-shift) using a phase-modulation method. (Instrumentation): A dual-phase lock-in amplifier (LIA) (SR830, Stanford Research Systems); Excitation signal: Sinusoidal-wave at 94100 Hz (see reference).
Reference(s):	Medina-Rodríguez, S.; Marín-Suárez, M.; Fernández-Sánchez, J.F.; de la Torre-Vega, A.; Baranoff, E.; Fernández-Gutiérrez, A. <i>Analyst</i> 2013 , 138, 4607-4617.

1.- Experimental data (calibration and test)

Table 2: Experimental data (*i.e.*, calibration and test data); apparent phase-shift lifetime measurements (τ_ϕ , in microseconds) for several oxygen concentrations (pO_2 , in kPa) at room temperature (21 °C). All the values correspond to the average of 25 measurements.

Calibration data (τ_ϕ , in microseconds)			Test data (τ_ϕ , in microseconds)		
pO_2 (kPa)	Mean (μs)	Sdev (μs)	pO_2 (kPa)	Mean (μs)	Sdev (μs)
0.25	1.1037	0.0009	0.50	0.9418	0.0002
0.75	0.8473	0.0001	1.00	0.7815	0.0002
2.00	0.6275	0.0002	3.00	0.5550	0.0001
4.00	0.5028	0.0002	5.00	0.4711	0.0001
6.00	0.4510	0.0001	7.00	0.4299	0.0002
8.00	0.4092	0.0002	9.00	0.3908	0.0002
10.00	0.3813	0.0002			

2.- Calibration curves: models and criteria


Figure 1: Calibration curves for the apparent phase-shift lifetime measurements (calibration data) of the sensing phase using different models and criteria. Models: Stern-Volmer (SV) (2 parameters), Lehrer (L) (3 parameters), 2nd order Polynomial (P2) (3 parameters), 1st order Polynomial-Exponent (PE1) (3 parameters), 2nd order Polynomial-Exponent (PE2) (4 parameters), Demas (D) (4 parameters). Criteria: (a) minimum mean square error (MSE) in τ_ϕ , (b) minimum mean square error (MSE) in pO_2 , (c) minimum mean square relative error in pO_2 .

Experiment 17

3.- Parameters of the fitting models for different criteria

Table 3: Parameters of the fitting models for different criteria: (a) minimum mean square error (MSE) in τ_ϕ , (b) minimum mean square error (MSE) in pO_2 , (c) minimum mean square relative error in pO_2 . RMSE is expressed in microseconds for criterion (a), in kPa for criterion (b) and in relative error (%) for criterion (c). Calibration data used are shown in Table 2.

Range	Stern-Volmer (SV)			Lehrer (L)			2 nd order Polynomial (P2)					
pO_2	Parameter	(a)	(b)	(c)	Parameter	(a)	(b)	(c)	Parameter	(a)	(b)	(c)
0.25-10 (kPa)	τ_0 (μs)	1.0818	0.9477	1.1941	τ_0 (μs)	1.3204	1.1432	1.3016	a_0	1.3507	2.9545	1.4968
	k (kPa^{-1})	0.2537	0.1702	0.3779	k (kPa^{-1})	1.1219	0.6416	1.0053	a_1	-3.46422	-5.78587	-3.69654
	–	–	–	–	x	0.7645	0.7692	0.7732	a_2	2.48373	3.22029	2.56421
	R^2	0.93140	0.93385	0.90578	R^2	0.99883	0.99765	0.99645	R^2	0.99885	0.99903	0.99766
	RMSE	0.0649	0.8874	30.6952	RMSE	0.0085	0.1672	5.9569	RMSE	0.0084	0.1076	4.8418
	iterations	100	1	1	iterations	100	100	100	iterations	100	1	1
	Φ_0 (μs)	1.0818	0.9477	1.1941	Φ_0 (μs)	1.3204	1.1432	1.3016	Φ_0 (μs)	1.2823	0.9792	1.2348
	K (kPa^{-1})	0.2537	0.1702	0.3779	K (kPa^{-1})	0.8577	0.4935	0.7772	K (kPa^{-1})	1.1385	0.4878	1.0073
Range	1 st order Polynomial-Exponent (PE1)			2 nd order Polynomial-Exponent (PE2)			Demas (D)					
pO_2	Parameter	(a)	(b)	(c)	Parameter	(a)	(b)	(c)	Parameter	(a)	(b)	(c)
0.25-10 (kPa)	a_0	-0.1400	-0.0959	-0.1258	a_0	-0.2990	0.0059	-0.3007	τ_0 (μs)	1.3818	1.4260	1.3818
	a_1	0.528311	0.482328	0.511824	a_1	0.594628	0.397549	0.545131	k_1 (kPa^{-1})	1.6060	1.8144	1.6044
	α	-3.0484	-3.1568	-3.0884	a_2	0.100596	-0.00151551	0.150784	k_2 (kPa^{-1})	0.0296	0.0326	0.0294
	–	–	–	–	α	-2.1110	-3.4615	-1.9718	x	0.6952	0.6936	0.6956
	R^2	0.99977	0.99953	0.99953	R^2	0.99992	0.99959	0.99975	R^2	0.99994	0.99969	0.99985
	RMSE	0.0038	0.0746	2.1624	RMSE	0.0023	0.0698	1.5755	RMSE	0.0018	0.0606	1.2376
iterations	100	100	100	iterations	100	100	100	iterations	500	500	500	
	Φ_0 (μs)	1.5459	1.6680	1.5753	Φ_0 (μs)	1.4357	2.0741	1.4416	Φ_0 (μs)	1.3818	1.4260	1.3818
	K (kPa^{-1})	2.3429	3.3024	2.5742	K (kPa^{-1})	1.4766	48.6612	1.5080	K (kPa^{-1})	1.1254	1.2685	1.1249

4.- Accuracy of the fitting models for different criteria using calibration data

Table 4: Accuracy (root mean square error, RMSE) of the fitting models for different criteria: (a) minimum mean square error (MSE) in τ_ϕ , (b) minimum mean square error (MSE) in pO_2 , (c) minimum mean square relative error in pO_2 . Calibration data were used for evaluating the models (see Table 2).

Range	Stern-Volmer (SV)			Lehrer (L)			2 nd order Polynomial (P2)					
pO_2	Evaluation (criterion)	(a)	(b)	(c)	Evaluation (criterion)	(a)	(b)	(c)	Evaluation (criterion)	(a)	(b)	(c)
0.25-10 (kPa)	RMSE τ_ϕ (μs)	0.0649	0.0839	0.0827	RMSE τ_ϕ (μs)	0.0085	0.0325	0.0103	RMSE τ_ϕ (μs)	0.0084	0.0132	0.0086
	RMSE pO_2 (kPa)	1.2760	0.8874	2.0922	RMSE pO_2 (kPa)	0.7543	0.1672	0.3421	RMSE pO_2 (kPa)	0.2970	0.1076	0.2591
	RMSE relat. pO_2 (%)	56.6930	164.9727	30.6952	RMSE relat. pO_2 (%)	8.4317	27.1822	5.9569	RMSE relat. pO_2 (%)	4.9515	17.6210	4.8418
Range	1 st order Polynomial-Exponent (PE1)			2 nd order Polynomial-Exponent (PE2)			Demas (D)					
pO_2	Evaluation (criterion)	(a)	(b)	(c)	Evaluation (criterion)	(a)	(b)	(c)	Evaluation (criterion)	(a)	(b)	(c)
0.25-10 (kPa)	RMSE τ_ϕ (μs)	0.0038	0.0053	0.0039	RMSE τ_ϕ (μs)	0.0023	0.0187	0.0023	RMSE τ_ϕ (μs)	0.0018	0.0045	0.0018
	RMSE pO_2 (kPa)	0.1088	0.0746	0.0860	RMSE pO_2 (kPa)	0.1007	0.0698	0.0912	RMSE pO_2 (kPa)	0.0625	0.0606	0.0629
	RMSE relat. pO_2 (%)	2.2465	2.4862	2.1624	RMSE relat. pO_2 (%)	1.6000	6.3014	1.5755	RMSE relat. pO_2 (%)	1.2381	2.2724	1.2376

5.- Accuracy of the fitting models for different criteria using test data

Table 5: Accuracy (root mean square error, RMSE) of the fitting models for different criteria: (a) minimum mean square error (MSE) in τ_ϕ , (b) minimum mean square error (MSE) in pO_2 , (c) minimum mean square relative error in pO_2 . Test data were used for evaluating the models (see Table 2).

Range	Stern-Volmer (SV)			Lehrer (L)			2 nd order Polynomial (P2)					
pO_2	Evaluation (criterion)	(a)	(b)	(c)	Evaluation (criterion)	(a)	(b)	(c)	Evaluation (criterion)	(a)	(b)	(c)
0.5-9 (kPa)	RMSE τ_ϕ (μs)	0.0514	0.0460	0.0809	RMSE τ_ϕ (μs)	0.0104	0.0101	0.0132	RMSE τ_ϕ (μs)	0.0078	0.0231	0.0094
	RMSE pO_2 (kPa)	1.0000	0.6963	1.7813	RMSE pO_2 (kPa)	0.5942	0.1740	0.3317	RMSE pO_2 (kPa)	0.1828	0.1464	0.1586
	RMSE relat. pO_2 (%)	26.7017	43.0259	32.4382	RMSE relat. pO_2 (%)	8.0059	5.5542	7.1408	RMSE relat. pO_2 (%)	4.1206	8.8455	4.6024
Range	1 st order Polynomial-Exponent (PE1)			2 nd order Polynomial-Exponent (PE2)			Demas (D)					
pO_2	Evaluation (criterion)	(a)	(b)	(c)	Evaluation (criterion)	(a)	(b)	(c)	Evaluation (criterion)	(a)	(b)	(c)
0.5-9 (kPa)	RMSE τ_ϕ (μs)	0.0032	0.0055	0.0041	RMSE τ_ϕ (μs)	0.0030	0.0072	0.0029	RMSE τ_ϕ (μs)	0.0038	0.0047	0.0038
	RMSE pO_2 (kPa)	0.1092	0.1350	0.1175	RMSE pO_2 (kPa)	0.1624	0.1331	0.1520	RMSE pO_2 (kPa)	0.1345	0.1315	0.1360
	RMSE relat. pO_2 (%)	1.9162	2.7581	2.2194	RMSE relat. pO_2 (%)	2.1300	3.3714	2.0257	RMSE relat. pO_2 (%)	2.1577	2.4333	2.1768

Experiment 18

page 1/2

Table 1: Sensing phase information

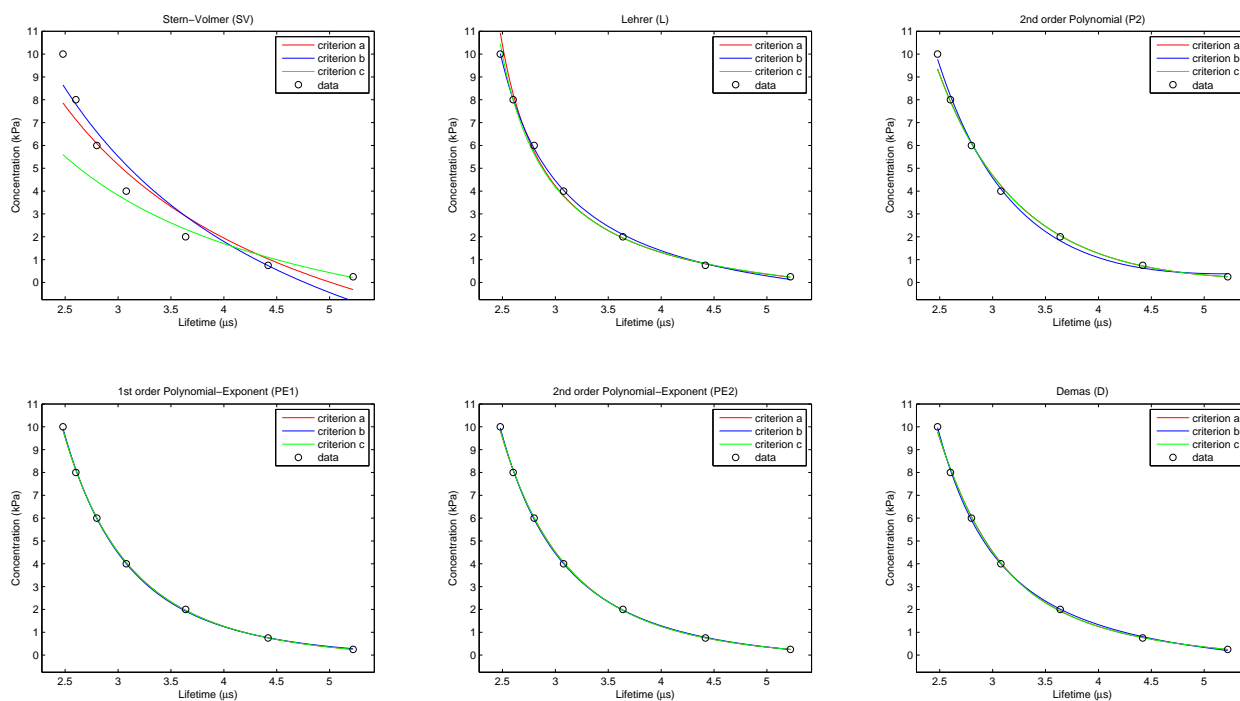
Name:	N1008-AP200/19 (replica 1)
Description:	An oxygen-sensing dye ($[\text{Ir}(2\text{-}(2,4\text{-difluorophenyl})\text{pyridine})_2(4,7\text{-diphenyl-}1,10\text{-phenanthroline})](\text{PF}_6))$ immobilized into AP200/19 (a nanostructured aluminium oxide-hydroxide solid support).
Analyte:	Partial pressure of oxygen in the gas phase (pO_2 , kPa); Range: 0.25-10 kPa.
Analytical signal:	(Measurement method): Luminescence lifetime in the frequency domain (<i>i.e.</i> , apparent lifetime estimated from phase-shift) using a phase-modulation method. (Instrumentation): A dual-phase lock-in amplifier (LIA) (SR830, Stanford Research Systems); Excitation signal: Sinusoidal-wave at 30100 Hz (see reference).
Reference(s):	Medina-Rodríguez, S.; Marín-Suárez, M.; Fernández-Sánchez, J.F.; de la Torre-Vega, A.; Baranoff, E.; Fernández-Gutiérrez, A. <i>Analyst</i> 2013 , 138, 4607-4617.

1.- Experimental data (calibration and test)

Table 2: Experimental data (*i.e.*, calibration and test data); apparent phase-shift lifetime measurements (τ_ϕ , in microseconds) for several oxygen concentrations (pO_2 , in kPa) at room temperature (21 °C). All the values correspond to the average of 25 measurements.

Calibration data (τ_ϕ , in microseconds)			Test data (τ_ϕ , in microseconds)		
pO_2 (kPa)	Mean (μs)	Sdev (μs)	pO_2 (kPa)	Mean (μs)	Sdev (μs)
0.25	5.2215	0.0043	0.50	4.7634	0.0015
0.75	4.4184	0.0010	1.00	4.1797	0.0009
2.00	3.6386	0.0006	3.00	3.3196	0.0004
4.00	3.0773	0.0005	5.00	2.9273	0.0005
6.00	2.7994	0.0005	7.00	2.6932	0.0006
8.00	2.6013	0.0005	9.00	2.5191	0.0004
10.00	2.4796	0.0004			

2.- Calibration curves: models and criteria


Figure 1: Calibration curves for the apparent phase-shift lifetime measurements (calibration data) of the sensing phase using different models and criteria. Models: Stern-Volmer (SV) (2 parameters), Lehrer (L) (3 parameters), 2nd order Polynomial (P2) (3 parameters), 1st order Polynomial-Exponent (PE1) (3 parameters), 2nd order Polynomial-Exponent (PE2) (4 parameters), Demas (D) (4 parameters). Criteria: (a) minimum mean square error (MSE) in τ_ϕ , (b) minimum mean square error (MSE) in pO_2 , (c) minimum mean square relative error in pO_2 .

Experiment 18

3.- Parameters of the fitting models for different criteria

Table 3: Parameters of the fitting models for different criteria: (a) minimum mean square error (MSE) in τ_ϕ , (b) minimum mean square error (MSE) in pO_2 , (c) minimum mean square relative error in pO_2 . RMSE is expressed in microseconds for criterion (a), in kPa for criterion (b) and in relative error (%) for criterion (c). Calibration data used are shown in Table 2.

Range	Stern-Volmer (SV)			Lehrer (L)			2 nd order Polynomial (P2)					
pO_2	Parameter	(a)	(b)	(c)	Parameter	(a)	(b)	(c)	Parameter	(a)	(b)	(c)
0.25-10 (kPa)	τ_0 (μs)	5.0111	4.7650	5.4639	τ_0 (μs)	5.7126	5.4317	5.7372	a_0	4.8602	8.1159	4.8362
	k (kPa^{-1})	0.1299	0.1066	0.2151	k (kPa^{-1})	0.6644	0.4824	0.6595	a_1	-55.8912	-80.6503	-55.6472
	–	–	–	–	x	0.6439	0.6559	0.6502	a_2	166.178	210.165	165.57
	R^2	0.93185	0.93414	0.90475	R^2	0.99836	0.99940	0.99687	R^2	0.99907	0.99798	0.99852
	RMSE	0.2483	0.8855	30.8620	RMSE	0.0385	0.0848	5.5924	RMSE	0.0290	0.1551	3.8465
	iterations	100	1	1	iterations	100	100	100	iterations	100	1	1
	Φ_0 (μs)	5.0111	4.7650	5.4639	Φ_0 (μs)	5.7126	5.4317	5.7372	Φ_0 (μs)	5.7499	4.9687	5.7532
	K (kPa^{-1})	0.1299	0.1066	0.2151	K (kPa^{-1})	0.4278	0.3164	0.4288	K (kPa^{-1})	0.5658	0.2853	0.5675
Range	1 st order Polynomial-Exponent (PE1)			2 nd order Polynomial-Exponent (PE2)			Demas (D)					
pO_2	Parameter	(a)	(b)	(c)	Parameter	(a)	(b)	(c)	Parameter	(a)	(b)	(c)
0.25-10 (kPa)	a_0	-0.3022	-0.2138	-0.2987	a_0	-0.2592	-0.4828	-0.3147	τ_0 (μs)	5.9098	5.6294	5.9059
	a_1	353.241	402.142	355.769	a_1	-2.36265	123.199	0.994957	k_1 (kPa^{-1})	1.0871	0.6763	1.0624
	α	-3.9099	-4.0539	-3.9177	a_2	337.986	961.68	362.28	k_2 (kPa^{-1})	0.0248	0.0105	0.0236
	–	–	–	–	α	-1.9116	-3.1314	-1.9766	x	0.5359	0.5990	0.5416
	R^2	0.99991	0.99964	0.99984	R^2	0.99991	0.99978	0.99984	R^2	0.99972	0.99972	0.99958
	RMSE	0.0092	0.0656	1.2541	RMSE	0.0091	0.0507	1.2532	RMSE	0.0159	0.0578	2.0592
iterations	100	100	100	iterations	100	100	100	iterations	500	500	500	
	Φ_0 (μs)	6.0901	6.4229	6.0975	Φ_0 (μs)	6.1128	5.9248	6.0890	Φ_0 (μs)	5.9098	5.6294	5.9059
	K (kPa^{-1})	0.8464	1.1540	0.8546	K (kPa^{-1})	0.8828	0.6429	0.8411	K (kPa^{-1})	0.5942	0.4093	0.5863

4.- Accuracy of the fitting models for different criteria using calibration data

Table 4: Accuracy (root mean square error, RMSE) of the fitting models for different criteria: (a) minimum mean square error (MSE) in τ_ϕ , (b) minimum mean square error (MSE) in pO_2 , (c) minimum mean square relative error in pO_2 . Calibration data were used for evaluating the models (see Table 2).

Range	Stern-Volmer (SV)			Lehrer (L)			2 nd order Polynomial (P2)					
pO_2	Evaluation (criterion)	(a)	(b)	(c)	Evaluation (criterion)	(a)	(b)	(c)	Evaluation (criterion)	(a)	(b)	(c)
0.25-10 (kPa)	RMSE τ_ϕ (μs)	0.2483	0.2756	0.4167	RMSE τ_ϕ (μs)	0.0385	0.0724	0.0410	RMSE τ_ϕ (μs)	0.0290	0.0369	0.0290
	RMSE pO_2 (kPa)	1.0185	0.8855	2.0907	RMSE pO_2 (kPa)	0.3870	0.0848	0.2420	RMSE pO_2 (kPa)	0.2682	0.1551	0.2757
	RMSE relat. pO_2 (%)	88.3708	163.1592	30.8620	RMSE relat. pO_2 (%)	6.3316	18.6450	5.5924	RMSE relat. pO_2 (%)	3.8518	20.7261	3.8465
Range	1 st order Polynomial-Exponent (PE1)			2 nd order Polynomial-Exponent (PE2)			Demas (D)					
pO_2	Evaluation (criterion)	(a)	(b)	(c)	Evaluation (criterion)	(a)	(b)	(c)	Evaluation (criterion)	(a)	(b)	(c)
0.25-10 (kPa)	RMSE τ_ϕ (μs)	0.0092	0.0344	0.0092	RMSE τ_ϕ (μs)	0.0091	0.0141	0.0092	RMSE τ_ϕ (μs)	0.0159	0.0396	0.0160
	RMSE pO_2 (kPa)	0.0774	0.0656	0.0761	RMSE pO_2 (kPa)	0.0820	0.0507	0.0744	RMSE pO_2 (kPa)	0.1149	0.0578	0.1042
	RMSE relat. pO_2 (%)	1.2585	4.9861	1.2541	RMSE relat. pO_2 (%)	1.2681	1.9103	1.2532	RMSE relat. pO_2 (%)	2.0858	8.0371	2.0592

5.- Accuracy of the fitting models for different criteria using test data

Table 5: Accuracy (root mean square error, RMSE) of the fitting models for different criteria: (a) minimum mean square error (MSE) in τ_ϕ , (b) minimum mean square error (MSE) in pO_2 , (c) minimum mean square relative error in pO_2 . Test data were used for evaluating the models (see Table 2).

Range	Stern-Volmer (SV)			Lehrer (L)			2 nd order Polynomial (P2)					
pO_2	Evaluation (criterion)	(a)	(b)	(c)	Evaluation (criterion)	(a)	(b)	(c)	Evaluation (criterion)	(a)	(b)	(c)
0.5-9 (kPa)	RMSE τ_ϕ (μs)	0.1875	0.1824	0.3899	RMSE τ_ϕ (μs)	0.0447	0.0404	0.0509	RMSE τ_ϕ (μs)	0.0348	0.0739	0.0343
	RMSE pO_2 (kPa)	0.7565	0.6787	1.7699	RMSE pO_2 (kPa)	0.4055	0.1422	0.3010	RMSE pO_2 (kPa)	0.0988	0.1378	0.1003
	RMSE relat. pO_2 (%)	27.4424	45.7149	31.9702	RMSE relat. pO_2 (%)	6.6482	5.5812	6.8166	RMSE relat. pO_2 (%)	4.5171	7.7727	4.4501
Range	1 st order Polynomial-Exponent (PE1)			2 nd order Polynomial-Exponent (PE2)			Demas (D)					
pO_2	Evaluation (criterion)	(a)	(b)	(c)	Evaluation (criterion)	(a)	(b)	(c)	Evaluation (criterion)	(a)	(b)	(c)
0.5-9 (kPa)	RMSE τ_ϕ (μs)	0.0130	0.0147	0.0132	RMSE τ_ϕ (μs)	0.0130	0.0181	0.0132	RMSE τ_ϕ (μs)	0.0139	0.0295	0.0152
	RMSE pO_2 (kPa)	0.0992	0.1277	0.1009	RMSE pO_2 (kPa)	0.0941	0.1287	0.1026	RMSE pO_2 (kPa)	0.1074	0.1371	0.1123
	RMSE relat. pO_2 (%)	1.7955	2.0681	1.8246	RMSE relat. pO_2 (%)	1.7790	2.4220	1.8312	RMSE relat. pO_2 (%)	1.8928	3.7842	2.0439

Experiment 19

page 1/2

Table 1: Sensing phase information

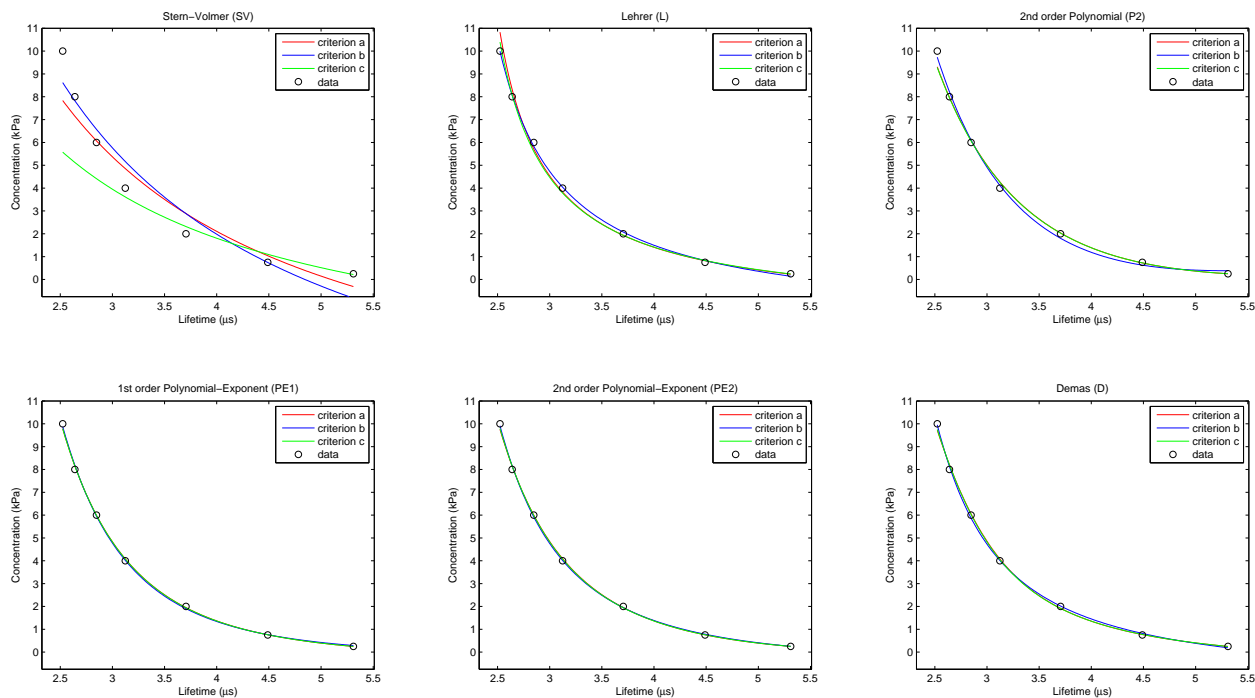
Name:	N1008-AP200/19 (replica 2)
Description:	An oxygen-sensing dye ($[\text{Ir}(2\text{-}(2,4\text{-difluorophenyl})\text{pyridine})_2(4,7\text{-diphenyl-}1,10\text{-phenanthroline})](\text{PF}_6))$ immobilized into AP200/19 (a nanostructured aluminium oxide-hydroxide solid support).
Analyte:	Partial pressure of oxygen in the gas phase (pO_2 , kPa); Range: 0.25-10 kPa.
Analytical signal:	(Measurement method): Luminescence lifetime in the frequency domain (<i>i.e.</i> , apparent lifetime estimated from phase-shift) using a phase-modulation method. (Instrumentation): A dual-phase lock-in amplifier (LIA) (SR830, Stanford Research Systems); Excitation signal: Sinusoidal-wave at 30100 Hz (see reference).
Reference(s):	Medina-Rodríguez, S.; Marín-Suárez, M.; Fernández-Sánchez, J.F.; de la Torre-Vega, A.; Baranoff, E.; Fernández-Gutiérrez, A. <i>Analyst</i> 2013 , 138, 4607-4617.

1.- Experimental data (calibration and test)

Table 2: Experimental data (*i.e.*, calibration and test data); apparent phase-shift lifetime measurements (τ_ϕ , in microseconds) for several oxygen concentrations (pO_2 , in kPa) at room temperature (21 °C). All the values correspond to the average of 25 measurements.

Calibration data (τ_ϕ , in microseconds)			Test data (τ_ϕ , in microseconds)		
pO_2 (kPa)	Mean (μs)	Sdev (μs)	pO_2 (kPa)	Mean (μs)	Sdev (μs)
0.25	5.3101	0.0028	0.50	4.8618	0.0040
0.75	4.4891	0.0026	1.00	4.2470	0.0015
2.00	3.7055	0.0012	3.00	3.3836	0.0010
4.00	3.1233	0.0011	5.00	2.9806	0.0009
6.00	2.8475	0.0008	7.00	2.7362	0.0007
8.00	2.6398	0.0007	9.00	2.5646	0.0008
10.00	2.5237	0.0007			

2.- Calibration curves: models and criteria


Figure 1: Calibration curves for the apparent phase-shift lifetime measurements (calibration data) of the sensing phase using different models and criteria. Models: Stern-Volmer (SV) (2 parameters), Lehrer (L) (3 parameters), 2nd order Polynomial (P2) (3 parameters), 1st order Polynomial-Exponent (PE1) (3 parameters), 2nd order Polynomial-Exponent (PE2) (4 parameters), Demas (D) (4 parameters). Criteria: (a) minimum mean square error (MSE) in τ_ϕ , (b) minimum mean square error (MSE) in pO_2 , (c) minimum mean square relative error in pO_2 .

Experiment 19

page 2/2

3.- Parameters of the fitting models for different criteria

Table 3: Parameters of the fitting models for different criteria: (a) minimum mean square error (MSE) in τ_ϕ , (b) minimum mean square error (MSE) in pO_2 , (c) minimum mean square relative error in pO_2 . RMSE is expressed in microseconds for criterion (a), in kPa for criterion (b) and in relative error (%) for criterion (c). Calibration data used are shown in Table 2.

Range	Stern-Volmer (SV)			Lehrer (L)			2 nd order Polynomial (P2)						
pO_2	Parameter	(a)	(b)	(c)	Parameter	(a)	(b)	(c)	Parameter	(a)	(b)	(c)	
0.25-10 (kPa)	τ_0 (μs)	5.0957	4.8458	5.5569	τ_0 (μs)	5.8080	5.5475	5.8371	a_0	4.8616	8.1941	4.8279	
	k (kPa^{-1})	0.1301	0.1067	0.2156	k (kPa^{-1})	0.6636	0.4947	0.6632	a_1	-56.8228	-82.5495	-56.487	
	–	–	–	–	x	0.6442	0.6553	0.6500	a_2	171.733	218.124	170.911	
	R^2	0.93185	0.93343	0.90425	R^2	0.99827	0.99929	0.99681	R^2	0.99902	0.99736	0.99843	
	RMSE	0.2526	0.8902	30.9441	RMSE	0.0402	0.0921	5.6480	RMSE	0.0304	0.1774	3.9598	
	iterations	100	1	1	iterations	100	100	100	iterations	100	1	1	
0.25-10 (kPa)	Φ_0 (μs)	5.0957	4.8458	5.5569	Φ_0 (μs)	5.8080	5.5475	5.8371	Φ_0 (μs)	5.8440	5.0371	5.8500	
	K (kPa^{-1})	0.1301	0.1067	0.2156	K (kPa^{-1})	0.4275	0.3242	0.4311	K (kPa^{-1})	0.5647	0.2819	0.5678	
	1 st order Polynomial-Exponent (PE1)			2 nd order Polynomial-Exponent (PE2)			Demas (D)						
	pO_2	Parameter	(a)	(b)	(c)	Parameter	(a)	(b)	(c)	Parameter	(a)	(b)	(c)
	0.25-10 (kPa)	a_0	-0.3027	-0.1906	-0.2979	a_0	-0.2234	-0.4625	-0.3037	τ_0 (μs)	6.0072	5.6815	6.0027
		a_1	375.264	444.05	378.775	a_1	-4.22052	125.233	0.365213	k_1 (kPa^{-1})	1.0822	0.6212	1.0532
α		-3.9065	-4.0901	-3.9167	a_2	346.698	1104.27	381.32	k_2 (kPa^{-1})	0.0247	0.0073	0.0232	
–		–	–	–	α	-1.8775	-3.1215	-1.9647	x	0.5368	0.6154	0.5437	
R^2		0.99981	0.99924	0.99969	R^2	0.99982	0.99945	0.99969	R^2	0.99959	0.99944	0.99937	
RMSE		0.0132	0.0951	1.7746	RMSE	0.0131	0.0807	1.7746	RMSE	0.0197	0.0818	2.5161	
iterations	100	100	100	iterations	100	100	100	iterations	500	500	500		
0.25-10 (kPa)	Φ_0 (μs)	6.1922	6.6570	6.2028	Φ_0 (μs)	6.2347	6.0761	6.1997	Φ_0 (μs)	6.0072	5.6815	6.0027	
	K (kPa^{-1})	0.8457	1.2827	0.8572	K (kPa^{-1})	0.9142	0.6721	0.8522	K (kPa^{-1})	0.5924	0.3851	0.5831	

4.- Accuracy of the fitting models for different criteria using calibration data

Table 4: Accuracy (root mean square error, RMSE) of the fitting models for different criteria: (a) minimum mean square error (MSE) in τ_ϕ , (b) minimum mean square error (MSE) in pO_2 , (c) minimum mean square relative error in pO_2 . Calibration data were used for evaluating the models (see Table 2).

Range	Stern-Volmer (SV)			Lehrer (L)			2 nd order Polynomial (P2)					
pO_2	Evaluation (criterion)	(a)	(b)	(c)	Evaluation (criterion)	(a)	(b)	(c)	Evaluation (criterion)	(a)	(b)	(c)
0.25-10 (kPa)	RMSE τ_ϕ (μs)	0.2526	0.2803	0.4246	RMSE τ_ϕ (μs)	0.0402	0.0694	0.0426	RMSE τ_ϕ (μs)	0.0304	0.0446	0.0304
	RMSE pO_2 (kPa)	1.0225	0.8902	2.0954	RMSE pO_2 (kPa)	0.3616	0.0921	0.2313	RMSE pO_2 (kPa)	0.2832	0.1774	0.2919
	RMSE relat. pO_2 (%)	88.4261	163.0224	30.9441	RMSE relat. pO_2 (%)	6.3459	17.0354	5.6480	RMSE relat. pO_2 (%)	3.9666	21.5776	3.9598
1 st order Polynomial-Exponent (PE1)			2 nd order Polynomial-Exponent (PE2)			Demas (D)						
pO_2	Evaluation (criterion)	(a)	(b)	(c)	Evaluation (criterion)	(a)	(b)	(c)	Evaluation (criterion)	(a)	(b)	(c)
0.25-10 (kPa)	RMSE τ_ϕ (μs)	0.0132	0.0466	0.0132	RMSE τ_ϕ (μs)	0.0131	0.0181	0.0132	RMSE τ_ϕ (μs)	0.0197	0.0474	0.0199
	RMSE pO_2 (kPa)	0.1081	0.0951	0.1069	RMSE pO_2 (kPa)	0.1155	0.0807	0.1063	RMSE pO_2 (kPa)	0.1402	0.0818	0.1285
	RMSE relat. pO_2 (%)	1.7813	6.4349	1.7746	RMSE relat. pO_2 (%)	1.7940	2.2959	1.7746	RMSE relat. pO_2 (%)	2.5466	9.8465	2.5161

5.- Accuracy of the fitting models for different criteria using test data

Table 5: Accuracy (root mean square error, RMSE) of the fitting models for different criteria: (a) minimum mean square error (MSE) in τ_ϕ , (b) minimum mean square error (MSE) in pO_2 , (c) minimum mean square relative error in pO_2 . Test data were used for evaluating the models (see Table 2).

Range	Stern-Volmer (SV)			Lehrer (L)			2 nd order Polynomial (P2)					
pO_2	Evaluation (criterion)	(a)	(b)	(c)	Evaluation (criterion)	(a)	(b)	(c)	Evaluation (criterion)	(a)	(b)	(c)
0.5-9 (kPa)	RMSE τ_ϕ (μs)	0.1904	0.1871	0.3980	RMSE τ_ϕ (μs)	0.0466	0.0438	0.0522	RMSE τ_ϕ (μs)	0.0414	0.0811	0.0409
	RMSE pO_2 (kPa)	0.7568	0.6738	1.7790	RMSE pO_2 (kPa)	0.3747	0.1336	0.2908	RMSE pO_2 (kPa)	0.1000	0.1323	0.1048
	RMSE relat. pO_2 (%)	28.2626	48.1130	31.3753	RMSE relat. pO_2 (%)	6.4818	5.9587	6.6523	RMSE relat. pO_2 (%)	5.2153	8.0618	5.1511
1 st order Polynomial-Exponent (PE1)			2 nd order Polynomial-Exponent (PE2)			Demas (D)						
pO_2	Evaluation (criterion)	(a)	(b)	(c)	Evaluation (criterion)	(a)	(b)	(c)	Evaluation (criterion)	(a)	(b)	(c)
0.5-9 (kPa)	RMSE τ_ϕ (μs)	0.0202	0.0190	0.0206	RMSE τ_ϕ (μs)	0.0205	0.0225	0.0206	RMSE τ_ϕ (μs)	0.0189	0.0361	0.0200
	RMSE pO_2 (kPa)	0.0844	0.1234	0.0861	RMSE pO_2 (kPa)	0.0757	0.1232	0.0867	RMSE pO_2 (kPa)	0.0995	0.1325	0.1064
	RMSE relat. pO_2 (%)	2.6045	2.5226	2.6528	RMSE relat. pO_2 (%)	2.6259	2.8648	2.6514	RMSE relat. pO_2 (%)	2.4573	4.5820	2.5738

Experiment 20

page 1/2

Table 1: Sensing phase information

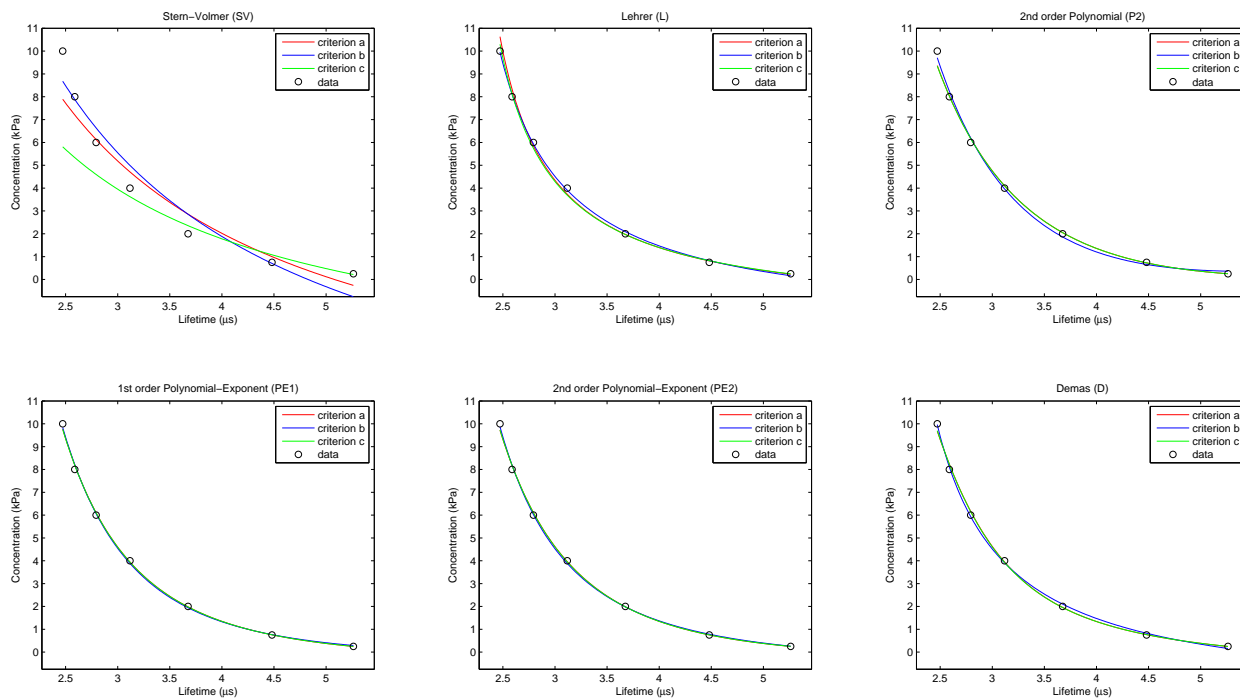
Name:	N1008-AP200/19 (replica 3)
Description:	An oxygen-sensing dye ($[\text{Ir}(2\text{-}(2,4\text{-difluorophenyl})\text{pyridine})_2(4,7\text{-diphenyl-}1,10\text{-phenanthroline})](\text{PF}_6))$ immobilized into AP200/19 (a nanostructured aluminium oxide-hydroxide solid support).
Analyte:	Partial pressure of oxygen in the gas phase ($p\text{O}_2$, kPa); Range: 0.25-10 kPa.
Analytical signal:	(Measurement method): Luminescence lifetime in the frequency domain (<i>i.e.</i> , apparent lifetime estimated from phase-shift) using a phase-modulation method. (Instrumentation): A dual-phase lock-in amplifier (LIA) (SR830, Stanford Research Systems); Excitation signal: Sinusoidal-wave at 30100 Hz (see reference).
Reference(s):	Medina-Rodríguez, S.; Marín-Suárez, M.; Fernández-Sánchez, J.F.; de la Torre-Vega, A.; Baranoff, E.; Fernández-Gutiérrez, A. <i>Analyst</i> 2013 , 138, 4607-4617.

1.- Experimental data (calibration and test)

Table 2: Experimental data (*i.e.*, calibration and test data); apparent phase-shift lifetime measurements (τ_ϕ , in microseconds) for several oxygen concentrations ($p\text{O}_2$, in kPa) at room temperature (21 °C). All the values correspond to the average of 25 measurements.

Calibration data (τ_ϕ , in microseconds)			Test data (τ_ϕ , in microseconds)		
$p\text{O}_2$ (kPa)	Mean (μs)	Sdev (μs)	$p\text{O}_2$ (kPa)	Mean (μs)	Sdev (μs)
0.25	5.2619	0.0032	0.50	4.8199	0.0006
0.75	4.4810	0.0007	1.00	4.2401	0.0007
2.00	3.6755	0.0006	3.00	3.3377	0.0003
4.00	3.1177	0.0005	5.00	2.9312	0.0004
6.00	2.7929	0.0005	7.00	2.6773	0.0005
8.00	2.5882	0.0004	9.00	2.5086	0.0005
10.00	2.4724	0.0005			

2.- Calibration curves: models and criteria


Figure 1: Calibration curves for the apparent phase-shift lifetime measurements (calibration data) of the sensing phase using different models and criteria. Models: Stern-Volmer (SV) (2 parameters), Lehrer (L) (3 parameters), 2nd order Polynomial (P2) (3 parameters), 1st order Polynomial-Exponent (PE1) (3 parameters), 2nd order Polynomial-Exponent (PE2) (4 parameters), Demas (D) (4 parameters). Criteria: (a) minimum mean square error (MSE) in τ_ϕ , (b) minimum mean square error (MSE) in $p\text{O}_2$, (c) minimum mean square relative error in $p\text{O}_2$.

Experiment 20

3.- Parameters of the fitting models for different criteria

Table 3: Parameters of the fitting models for different criteria: (a) minimum mean square error (MSE) in τ_ϕ , (b) minimum mean square error (MSE) in pO_2 , (c) minimum mean square relative error in pO_2 . RMSE is expressed in microseconds for criterion (a), in kPa for criterion (b) and in relative error (%) for criterion (c). Calibration data used are shown in Table 2.

Range	Stern-Volmer (SV)			Lehrer (L)			2 nd order Polynomial (P2)					
pO_2	Parameter	(a)	(b)	(c)	Parameter	(a)	(b)	(c)	Parameter	(a)	(b)	(c)
0.25-10 (kPa)	τ_0 (μs)	5.0799	4.8263	5.5027	τ_0 (μs)	5.7248	5.5326	5.7577	a_0	4.1163	6.7698	4.0853
	k (kPa^{-1})	0.1336	0.1097	0.2110	k (kPa^{-1})	0.6086	0.4811	0.6145	a_1	-49.8585	-70.0443	-49.582
	–	–	–	–	x	0.6559	0.6686	0.6607	a_2	155.346	191.15	154.745
	R^2	0.94061	0.94124	0.91523	R^2	0.99847	0.99942	0.99728	R^2	0.99933	0.99734	0.99895
	RMSE	0.2372	0.8364	29.1158	RMSE	0.0381	0.0834	5.2131	RMSE	0.0252	0.1781	3.2391
	iterations	100	1	1	iterations	100	100	100	iterations	100	1	1
	Φ_0 (μs)	5.0799	4.8263	5.5027	Φ_0 (μs)	5.7248	5.5326	5.7577	Φ_0 (μs)	6.0562	5.1733	6.0683
	K (kPa^{-1})	0.1336	0.1097	0.2110	K (kPa^{-1})	0.3992	0.3217	0.4060	K (kPa^{-1})	0.7243	0.3234	0.7337
Range	1 st order Polynomial-Exponent (PE1)			2 nd order Polynomial-Exponent (PE2)			Demas (D)					
pO_2	Parameter	(a)	(b)	(c)	Parameter	(a)	(b)	(c)	Parameter	(a)	(b)	(c)
0.25-10 (kPa)	a_0	-0.3839	-0.2679	-0.3812	a_0	-0.2144	-0.5474	-0.2795	τ_0 (μs)	5.9071	5.5210	5.9065
	a_1	282.357	324.553	282.879	a_1	-6.75101	101.179	-4.42934	k_1 (kPa^{-1})	0.9955	0.4720	0.9796
	α	-3.6740	-3.8329	-3.6771	a_2	251.465	685.784	262.25	k_2 (kPa^{-1})	0.0266	-0.0006	0.0256
	–	–	–	–	α	-1.7103	-2.9398	-1.7560	x	0.5371	0.6722	0.5420
	R^2	0.99986	0.99888	0.99974	R^2	0.99987	0.99917	0.99974	R^2	0.99969	0.99941	0.99946
	RMSE	0.0113	0.1156	1.6161	RMSE	0.0111	0.0992	1.6007	RMSE	0.0172	0.0835	2.3159
iterations	100	100	100	iterations	100	100	100	iterations	500	500	500	
	Φ_0 (μs)	6.0289	6.3744	6.0342	Φ_0 (μs)	6.0858	5.9733	6.0679	Φ_0 (μs)	5.9071	5.5210	5.9065
	K (kPa^{-1})	0.7090	0.9738	0.7134	K (kPa^{-1})	0.7940	0.6009	0.7636	K (kPa^{-1})	0.5470	0.3170	0.5427

4.- Accuracy of the fitting models for different criteria using calibration data

Table 4: Accuracy (root mean square error, RMSE) of the fitting models for different criteria: (a) minimum mean square error (MSE) in τ_ϕ , (b) minimum mean square error (MSE) in pO_2 , (c) minimum mean square relative error in pO_2 . Calibration data were used for evaluating the models (see Table 2).

Range	Stern-Volmer (SV)			Lehrer (L)			2 nd order Polynomial (P2)					
pO_2	Evaluation (criterion)	(a)	(b)	(c)	Evaluation (criterion)	(a)	(b)	(c)	Evaluation (criterion)	(a)	(b)	(c)
0.25-10 (kPa)	RMSE τ_ϕ (μs)	0.2372	0.2668	0.3872	RMSE τ_ϕ (μs)	0.0381	0.0578	0.0403	RMSE τ_ϕ (μs)	0.0252	0.0422	0.0252
	RMSE pO_2 (kPa)	0.9750	0.8364	1.9642	RMSE pO_2 (kPa)	0.2953	0.0834	0.1973	RMSE pO_2 (kPa)	0.2544	0.1781	0.2592
	RMSE relat. pO_2 (%)	80.4098	153.2015	29.1158	RMSE relat. pO_2 (%)	5.8598	13.7017	5.2131	RMSE relat. pO_2 (%)	3.2415	17.8660	3.2391
Range	1 st order Polynomial-Exponent (PE1)			2 nd order Polynomial-Exponent (PE2)			Demas (D)					
pO_2	Evaluation (criterion)	(a)	(b)	(c)	Evaluation (criterion)	(a)	(b)	(c)	Evaluation (criterion)	(a)	(b)	(c)
0.25-10 (kPa)	RMSE τ_ϕ (μs)	0.0113	0.0430	0.0114	RMSE τ_ϕ (μs)	0.0111	0.0197	0.0111	RMSE τ_ϕ (μs)	0.0172	0.0598	0.0173
	RMSE pO_2 (kPa)	0.1233	0.1156	0.1234	RMSE pO_2 (kPa)	0.1337	0.0992	0.1298	RMSE pO_2 (kPa)	0.1637	0.0835	0.1573
	RMSE relat. pO_2 (%)	1.6210	6.5355	1.6161	RMSE relat. pO_2 (%)	1.6076	2.7508	1.6007	RMSE relat. pO_2 (%)	2.3235	14.4288	2.3159

5.- Accuracy of the fitting models for different criteria using test data

Table 5: Accuracy (root mean square error, RMSE) of the fitting models for different criteria: (a) minimum mean square error (MSE) in τ_ϕ , (b) minimum mean square error (MSE) in pO_2 , (c) minimum mean square relative error in pO_2 . Test data were used for evaluating the models (see Table 2).

Range	Stern-Volmer (SV)			Lehrer (L)			2 nd order Polynomial (P2)					
pO_2	Evaluation (criterion)	(a)	(b)	(c)	Evaluation (criterion)	(a)	(b)	(c)	Evaluation (criterion)	(a)	(b)	(c)
0.5-9 (kPa)	RMSE τ_ϕ (μs)	0.1832	0.1833	0.3566	RMSE τ_ϕ (μs)	0.0392	0.0385	0.0440	RMSE τ_ϕ (μs)	0.0322	0.0537	0.0316
	RMSE pO_2 (kPa)	0.7242	0.6678	1.6375	RMSE pO_2 (kPa)	0.3496	0.1409	0.2577	RMSE pO_2 (kPa)	0.1188	0.1625	0.1160
	RMSE relat. pO_2 (%)	25.6190	44.4273	29.8635	RMSE relat. pO_2 (%)	5.7171	5.0297	5.8146	RMSE relat. pO_2 (%)	4.1773	6.0072	4.1030
Range	1 st order Polynomial-Exponent (PE1)			2 nd order Polynomial-Exponent (PE2)			Demas (D)					
pO_2	Evaluation (criterion)	(a)	(b)	(c)	Evaluation (criterion)	(a)	(b)	(c)	Evaluation (criterion)	(a)	(b)	(c)
0.5-9 (kPa)	RMSE τ_ϕ (μs)	0.0136	0.0167	0.0132	RMSE τ_ϕ (μs)	0.0141	0.0196	0.0136	RMSE τ_ϕ (μs)	0.0151	0.0391	0.0151
	RMSE pO_2 (kPa)	0.1269	0.1421	0.1228	RMSE pO_2 (kPa)	0.1180	0.1391	0.1182	RMSE pO_2 (kPa)	0.1405	0.1416	0.1388
	RMSE relat. pO_2 (%)	1.9235	2.2900	1.8664	RMSE relat. pO_2 (%)	1.9714	2.6099	1.9059	RMSE relat. pO_2 (%)	2.0881	5.1328	2.0738

Experiment 21

page 1/2

Table 1: Sensing phase information

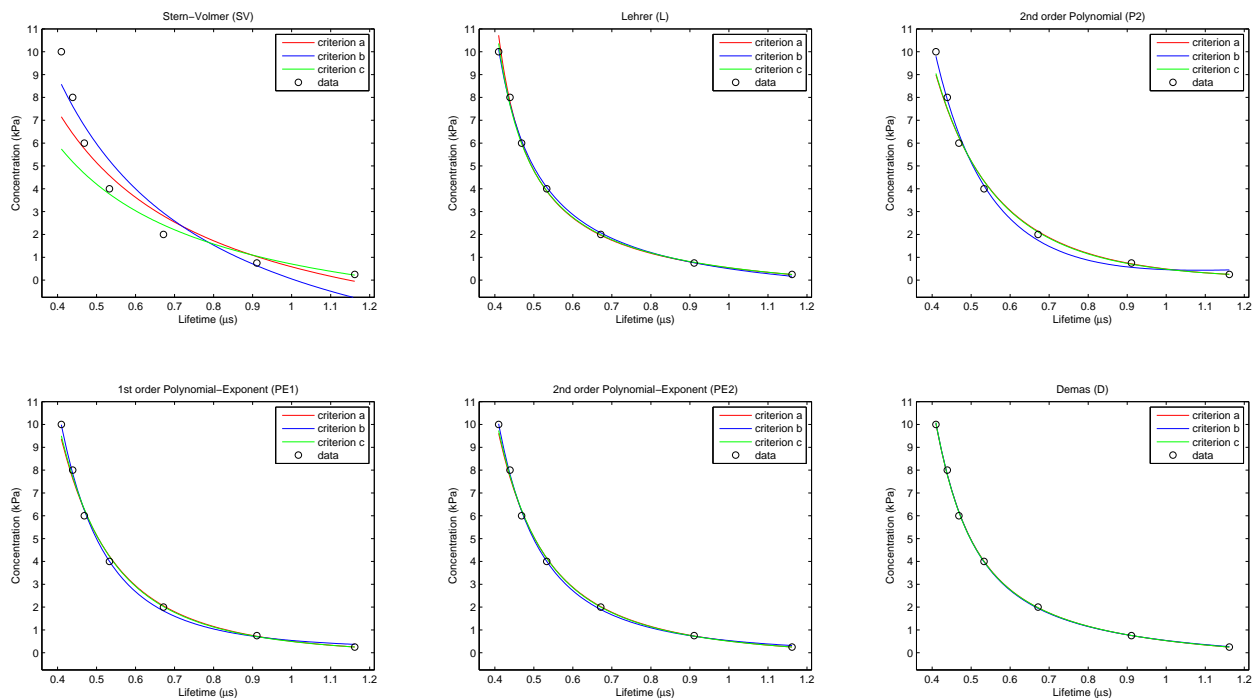
Name:	EB146-AP200/19 (replica 1)
Description:	An oxygen-sensing dye (Ir(2-(2,4-difluoro-3-methylesterphenyl)pyridine) ₂ (4-(N,N-dimethylamino)picolinate)) immobilized into AP200/19 (a nanostructured aluminium oxide-hydroxide solid support).
Analyte:	Partial pressure of oxygen in the gas phase (pO_2 , kPa); Range: 0.25-10 kPa.
Analytical signal:	(Measurement method): Luminescence lifetime in the frequency domain (<i>i.e.</i> , apparent lifetime estimated from phase-shift) using a phase-modulation method. (Instrumentation): A dual-phase lock-in amplifier (LIA) (SR830, Stanford Research Systems); Excitation signal: Sinusoidal-wave at 94100 Hz (see reference).
Reference(s):	Medina-Rodríguez, S.; Marín-Suárez, M.; Fernández-Sánchez, J.F.; de la Torre-Vega, A.; Baranoff, E.; Fernández-Gutiérrez, A. <i>Analyst</i> 2013 , 138, 4607-4617.

1.- Experimental data (calibration and test)

Table 2: Experimental data (*i.e.*, calibration and test data); apparent phase-shift lifetime measurements (τ_ϕ , in microseconds) for several oxygen concentrations (pO_2 , in kPa) at room temperature (21 °C). All the values correspond to the average of 25 measurements.

Calibration data (τ_ϕ , in microseconds)			Test data (τ_ϕ , in microseconds)		
pO_2 (kPa)	Mean (μs)	Sdev (μs)	pO_2 (kPa)	Mean (μs)	Sdev (μs)
0.25	1.1617	0.0010	0.50	1.0019	0.0006
0.75	0.9108	0.0004	1.00	0.8477	0.0003
2.00	0.6714	0.0002	3.00	0.5932	0.0001
4.00	0.5330	0.0002	5.00	0.5027	0.0002
6.00	0.4687	0.0002	7.00	0.4566	0.0001
8.00	0.4390	0.0002	9.00	0.4141	0.0003
10.00	0.4098	0.0002			

2.- Calibration curves: models and criteria


Figure 1: Calibration curves for the apparent phase-shift lifetime measurements (calibration data) of the sensing phase using different models and criteria. Models: Stern-Volmer (SV) (2 parameters), Lehrer (L) (3 parameters), 2nd order Polynomial (P2) (3 parameters), 1st order Polynomial-Exponent (PE1) (3 parameters), 2nd order Polynomial-Exponent (PE2) (4 parameters), Demas (D) (4 parameters). Criteria: (a) minimum mean square error (MSE) in τ_ϕ , (b) minimum mean square error (MSE) in pO_2 , (c) minimum mean square relative error in pO_2 .

Experiment 21

3.- Parameters of the fitting models for different criteria

Table 3: Parameters of the fitting models for different criteria: (a) minimum mean square error (MSE) in τ_ϕ , (b) minimum mean square error (MSE) in pO_2 , (c) minimum mean square relative error in pO_2 . RMSE is expressed in microseconds for criterion (a), in kPa for criterion (b) and in relative error (%) for criterion (c). Calibration data used are shown in Table 2.

Range	Stern-Volmer (SV)				Lehrer (L)				2 nd order Polynomial (P2)			
pO_2	Parameter	(a)	(b)	(c)	Parameter	(a)	(b)	(c)	Parameter	(a)	(b)	(c)
0.25-10 (kPa)	τ_0 (μs)	1.1466	1.0089	1.2528	τ_0 (μs)	1.3727	1.2766	1.3669	a_0	1.0891	3.8773	1.2397
	k (kPa^{-1})	0.2514	0.1705	0.3582	k (kPa^{-1})	1.0193	0.7891	0.9815	a_1	-3.26781	-7.47827	-3.51462
	–	–	–	–	x	0.7656	0.7640	0.7691	a_2	2.66644	4.05957	2.75183
	R^2	0.93703	0.92512	0.91779	R^2	0.99975	0.99847	0.99923	R^2	0.99798	0.99561	0.99578
	RMSE	0.0656	0.9442	28.6719	RMSE	0.0042	0.1351	2.7717	RMSE	0.0118	0.2287	6.4936
	iterations	100	1	1	iterations	100	100	100	iterations	100	1	1
	Φ_0 (μs)	1.1466	1.0089	1.2528	Φ_0 (μs)	1.3727	1.2766	1.3669	Φ_0 (μs)	1.5003	0.9644	1.4175
	K (kPa^{-1})	0.2514	0.1705	0.3582	K (kPa^{-1})	0.7804	0.6029	0.7548	K (kPa^{-1})	1.6163	0.3857	1.3102
Range	1 st order Polynomial-Exponent (PE1)				2 nd order Polynomial-Exponent (PE2)				Demas (D)			
pO_2	Parameter	(a)	(b)	(c)	Parameter	(a)	(b)	(c)	Parameter	(a)	(b)	(c)
0.25-10 (kPa)	a_0	-0.2021	0.1231	-0.1694	a_0	-0.3510	-0.1152	-0.3210	τ_0 (μs)	1.3928	1.4351	1.3911
	a_1	0.704882	0.41664	0.663309	a_1	0.781315	0.603316	0.754029	k_1 (kPa^{-1})	1.1641	1.2911	1.1466
	α	-2.9242	-3.5473	-3.0038	a_2	0.0825912	0.0458064	0.0738015	k_2 (kPa^{-1})	0.0124	0.0140	0.0109
	–	–	–	–	α	-2.2176	-2.5456	-2.2785	x	0.7343	0.7341	0.7382
	R^2	0.99920	0.99848	0.99819	R^2	0.99968	0.99891	0.99917	R^2	0.99992	0.99915	0.99976
	RMSE	0.0074	0.1343	4.2530	RMSE	0.0047	0.1141	2.8857	RMSE	0.0023	0.1005	1.5502
iterations	100	100	100	iterations	100	100	100	iterations	500	500	500	
	Φ_0 (μs)	1.5330	0.8924	1.5751	Φ_0 (μs)	1.4636	1.9274	1.4800	Φ_0 (μs)	1.3928	1.4351	1.3911
	K (kPa^{-1})	1.6921	2.2903	1.9648	K (kPa^{-1})	1.2313	3.3639	1.3166	K (kPa^{-1})	0.8581	0.9515	0.8493

4.- Accuracy of the fitting models for different criteria using calibration data

Table 4: Accuracy (root mean square error, RMSE) of the fitting models for different criteria: (a) minimum mean square error (MSE) in τ_ϕ , (b) minimum mean square error (MSE) in pO_2 , (c) minimum mean square relative error in pO_2 . Calibration data were used for evaluating the models (see Table 2).

Range	Stern-Volmer (SV)				Lehrer (L)				2 nd order Polynomial (P2)			
pO_2	Evaluation (criterion)	(a)	(b)	(c)	Evaluation (criterion)	(a)	(b)	(c)	Evaluation (criterion)	(a)	(b)	(c)
0.25-10 (kPa)	RMSE τ_ϕ (μs)	0.0656	0.0856	0.0816	RMSE τ_ϕ (μs)	0.0042	0.0178	0.0048	RMSE τ_ϕ (μs)	0.0118	0.0518	0.0119
	RMSE pO_2 (kPa)	1.3012	0.9442	2.0064	RMSE pO_2 (kPa)	0.2858	0.1351	0.1887	RMSE pO_2 (kPa)	0.4604	0.2287	0.4366
	RMSE relat. pO_2 (%)	52.1663	156.1743	28.6719	RMSE relat. pO_2 (%)	3.2926	12.4225	2.7717	RMSE relat. pO_2 (%)	6.5836	31.9399	6.4936
Range	1 st order Polynomial-Exponent (PE1)				2 nd order Polynomial-Exponent (PE2)				Demas (D)			
pO_2	Evaluation (criterion)	(a)	(b)	(c)	Evaluation (criterion)	(a)	(b)	(c)	Evaluation (criterion)	(a)	(b)	(c)
0.25-10 (kPa)	RMSE τ_ϕ (μs)	0.0074	0.0899	0.0078	RMSE τ_ϕ (μs)	0.0047	0.0298	0.0050	RMSE τ_ϕ (μs)	0.0023	0.0064	0.0023
	RMSE pO_2 (kPa)	0.3076	0.1343	0.2605	RMSE pO_2 (kPa)	0.2138	0.1141	0.1757	RMSE pO_2 (kPa)	0.1017	0.1005	0.1026
	RMSE relat. pO_2 (%)	4.4066	18.3289	4.2530	RMSE relat. pO_2 (%)	3.0114	10.6848	2.8857	RMSE relat. pO_2 (%)	1.5659	3.4421	1.5502

5.- Accuracy of the fitting models for different criteria using test data

Table 5: Accuracy (root mean square error, RMSE) of the fitting models for different criteria: (a) minimum mean square error (MSE) in τ_ϕ , (b) minimum mean square error (MSE) in pO_2 , (c) minimum mean square relative error in pO_2 . Test data were used for evaluating the models (see Table 2).

Range	Stern-Volmer (SV)				Lehrer (L)				2 nd order Polynomial (P2)			
pO_2	Evaluation (criterion)	(a)	(b)	(c)	Evaluation (criterion)	(a)	(b)	(c)	Evaluation (criterion)	(a)	(b)	(c)
0.5-9 (kPa)	RMSE τ_ϕ (μs)	0.0488	0.0465	0.0774	RMSE τ_ϕ (μs)	0.0105	0.0044	0.0107	RMSE τ_ϕ (μs)	0.0083	0.0370	0.0103
	RMSE pO_2 (kPa)	0.9583	0.6609	1.6630	RMSE pO_2 (kPa)	0.5204	0.3121	0.4158	RMSE pO_2 (kPa)	0.1775	0.2497	0.1585
	RMSE relat. pO_2 (%)	22.6763	41.4242	29.7263	RMSE relat. pO_2 (%)	7.2768	3.8024	6.5991	RMSE relat. pO_2 (%)	4.0934	13.0211	4.7403
Range	1 st order Polynomial-Exponent (PE1)				2 nd order Polynomial-Exponent (PE2)				Demas (D)			
pO_2	Evaluation (criterion)	(a)	(b)	(c)	Evaluation (criterion)	(a)	(b)	(c)	Evaluation (criterion)	(a)	(b)	(c)
0.5-9 (kPa)	RMSE τ_ϕ (μs)	0.0065	0.0197	0.0086	RMSE τ_ϕ (μs)	0.0063	0.0140	0.0075	RMSE τ_ϕ (μs)	0.0084	0.0105	0.0087
	RMSE pO_2 (kPa)	0.1060	0.2879	0.1194	RMSE pO_2 (kPa)	0.1549	0.2956	0.1854	RMSE pO_2 (kPa)	0.2957	0.3095	0.3136
	RMSE relat. pO_2 (%)	2.9014	7.4259	3.6901	RMSE relat. pO_2 (%)	2.9719	6.0843	3.5002	RMSE relat. pO_2 (%)	4.6972	5.4114	4.9424

Experiment 22

page 1/2

Table 1: Sensing phase information

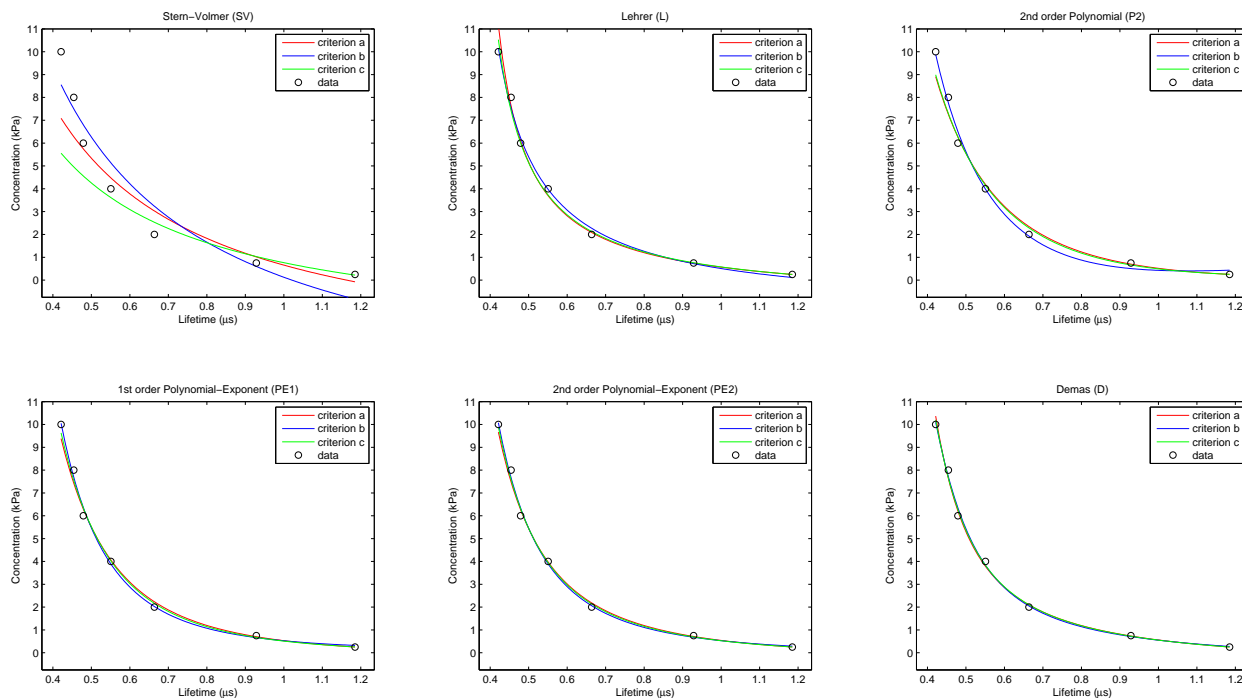
Name:	EB146-AP200/19 (replica 2)
Description:	An oxygen-sensing dye (Ir(2-(2,4-difluoro-3-methylesterphenyl)pyridine) ₂ (4-(N,N-dimethylamino)picolinate)) immobilized into AP200/19 (a nanostructured aluminium oxide-hydroxide solid support).
Analyte:	Partial pressure of oxygen in the gas phase (pO_2 , kPa); Range: 0.25-10 kPa.
Analytical signal:	(Measurement method): Luminescence lifetime in the frequency domain (<i>i.e.</i> , apparent lifetime estimated from phase-shift) using a phase-modulation method. (Instrumentation): A dual-phase lock-in amplifier (LIA) (SR830, Stanford Research Systems); Excitation signal: Sinusoidal-wave at 94100 Hz (see reference).
Reference(s):	Medina-Rodríguez, S.; Marín-Suárez, M.; Fernández-Sánchez, J.F.; de la Torre-Vega, A.; Baranoff, E.; Fernández-Gutiérrez, A. <i>Analyst</i> 2013 , 138, 4607-4617.

1.- Experimental data (calibration and test)

Table 2: Experimental data (*i.e.*, calibration and test data); apparent phase-shift lifetime measurements (τ_ϕ , in microseconds) for several oxygen concentrations (pO_2 , in kPa) at room temperature (21 °C). All the values correspond to the average of 25 measurements.

Calibration data (τ_ϕ , in microseconds)			Test data (τ_ϕ , in microseconds)		
pO_2 (kPa)	Mean (μs)	Sdev (μs)	pO_2 (kPa)	Mean (μs)	Sdev (μs)
0.25	1.1849	0.0012	0.50	1.0177	0.0005
0.75	0.9286	0.0006	1.00	0.8583	0.0004
2.00	0.6636	0.0003	3.00	0.6104	0.0002
4.00	0.5507	0.0002	5.00	0.5103	0.0001
6.00	0.4792	0.0001	7.00	0.4602	0.0002
8.00	0.4544	0.0002	9.00	0.4229	0.0002
10.00	0.4214	0.0001			

2.- Calibration curves: models and criteria


Figure 1: Calibration curves for the apparent phase-shift lifetime measurements (calibration data) of the sensing phase using different models and criteria. Models: Stern-Volmer (SV) (2 parameters), Lehrer (L) (3 parameters), 2nd order Polynomial (P2) (3 parameters), 1st order Polynomial-Exponent (PE1) (3 parameters), 2nd order Polynomial-Exponent (PE2) (4 parameters), Demas (D) (4 parameters). Criteria: (a) minimum mean square error (MSE) in τ_ϕ , (b) minimum mean square error (MSE) in pO_2 , (c) minimum mean square relative error in pO_2 .

Experiment 22

3.- Parameters of the fitting models for different criteria

Table 3: Parameters of the fitting models for different criteria: (a) minimum mean square error (MSE) in τ_ϕ , (b) minimum mean square error (MSE) in pO_2 , (c) minimum mean square relative error in pO_2 . RMSE is expressed in microseconds for criterion (a), in kPa for criterion (b) and in relative error (%) for criterion (c). Calibration data used are shown in Table 2.

Range	Stern-Volmer (SV)			Lehrer (L)			2 nd order Polynomial (P2)					
pO_2	Parameter	(a)	(b)	(c)	Parameter	(a)	(b)	(c)	Parameter	(a)	(b)	(c)
0.25-10 (kPa)	τ_0 (μs)	1.1633	1.0211	1.2805	τ_0 (μs)	1.4243	1.2600	1.4082	a_0	1.2552	4.3004	1.5567
	k (kPa^{-1})	0.2485	0.1663	0.3668	k (kPa^{-1})	1.1358	0.7431	1.0569	a_1	-3.62392	-8.40561	-4.12253
	–	–	–	–	x	0.7596	0.7537	0.7637	a_2	2.8861	4.53366	3.05781
	R^2	0.92518	0.91609	0.90896	R^2	0.99926	0.99525	0.99751	R^2	0.99580	0.99490	0.99199
	RMSE	0.0724	0.9995	30.1732	RMSE	0.0072	0.2378	4.9907	RMSE	0.0172	0.2465	8.9505
iterations	100	1	1	iterations	100	100	100	iterations	100	1	1	
	Φ_0 (μs)	1.1633	1.0211	1.2805	Φ_0 (μs)	1.4243	1.2600	1.4082	Φ_0 (μs)	1.4436	0.9773	1.3242
	K (kPa^{-1})	0.2485	0.1663	0.3668	K (kPa^{-1})	0.8627	0.5600	0.8072	K (kPa^{-1})	1.3013	0.3792	0.9802
Range	1 st order Polynomial-Exponent (PE1)			2 nd order Polynomial-Exponent (PE2)			Demas (D)					
pO_2	Parameter	(a)	(b)	(c)	Parameter	(a)	(b)	(c)	Parameter	(a)	(b)	(c)
0.25-10 (kPa)	a_0	-0.1545	0.0803	-0.0962	a_0	-0.2929	-0.1281	-0.2448	τ_0 (μs)	1.4425	1.5494	1.4507
	a_1	0.685296	0.445461	0.606971	a_1	0.744162	0.453999	0.692706	k_1 (kPa^{-1})	1.2655	1.7467	1.3350
	α	-3.0468	-3.5972	-3.2103	a_2	0.0898494	0.203319	0.079418	k_2 (kPa^{-1})	0.0096	0.0214	0.0138
	–	–	–	–	α	-2.2800	-2.0840	-2.3690	x	0.7361	0.7161	0.7252
	R^2	0.99787	0.99687	0.99629	R^2	0.99866	0.99693	0.99763	R^2	0.99940	0.99703	0.99859
	RMSE	0.0122	0.1931	6.0907	RMSE	0.0097	0.1913	4.8636	RMSE	0.0065	0.1880	3.7531
	iterations	100	100	100	iterations	100	100	100	iterations	500	500	500
	Φ_0 (μs)	1.6307	1.0340	1.7747	Φ_0 (μs)	1.5348	1.9322	1.5766	Φ_0 (μs)	1.4425	1.5494	1.4507
	K (kPa^{-1})	2.1250	3.4604	3.2365	K (kPa^{-1})	1.4348	3.3989	1.6623	K (kPa^{-1})	0.9341	1.2568	0.9719

4.- Accuracy of the fitting models for different criteria using calibration data

Table 4: Accuracy (root mean square error, RMSE) of the fitting models for different criteria: (a) minimum mean square error (MSE) in τ_ϕ , (b) minimum mean square error (MSE) in pO_2 , (c) minimum mean square relative error in pO_2 . Calibration data were used for evaluating the models (see Table 2).

Range	Stern-Volmer (SV)			Lehrer (L)			2 nd order Polynomial (P2)					
pO_2	Evaluation (criterion)	(a)	(b)	(c)	Evaluation (criterion)	(a)	(b)	(c)	Evaluation (criterion)	(a)	(b)	(c)
0.25-10 (kPa)	RMSE τ_ϕ (μs)	0.0724	0.0921	0.0902	RMSE τ_ϕ (μs)	0.0072	0.0302	0.0081	RMSE τ_ϕ (μs)	0.0172	0.0601	0.0175
	RMSE pO_2 (kPa)	1.3620	0.9995	2.1244	RMSE pO_2 (kPa)	0.4839	0.2378	0.3194	RMSE pO_2 (kPa)	0.5313	0.2465	0.4933
	RMSE relat. pO_2 (%)	56.1888	165.8311	30.1732	RMSE relat. pO_2 (%)	5.8651	21.1719	4.9907	RMSE relat. pO_2 (%)	9.2313	30.8437	8.9505
Range	1 st order Polynomial-Exponent (PE1)			2 nd order Polynomial-Exponent (PE2)			Demas (D)					
pO_2	Evaluation (criterion)	(a)	(b)	(c)	Evaluation (criterion)	(a)	(b)	(c)	Evaluation (criterion)	(a)	(b)	(c)
0.25-10 (kPa)	RMSE τ_ϕ (μs)	0.0122	0.0486	0.0130	RMSE τ_ϕ (μs)	0.0097	0.0215	0.0102	RMSE τ_ϕ (μs)	0.0065	0.0120	0.0066
	RMSE pO_2 (kPa)	0.3514	0.1931	0.2677	RMSE pO_2 (kPa)	0.2643	0.1913	0.2113	RMSE pO_2 (kPa)	0.2317	0.1880	0.1991
	RMSE relat. pO_2 (%)	6.5034	12.1760	6.0907	RMSE relat. pO_2 (%)	5.1384	7.8084	4.8636	RMSE relat. pO_2 (%)	3.8932	5.5799	3.7531

5.- Accuracy of the fitting models for different criteria using test data

Table 5: Accuracy (root mean square error, RMSE) of the fitting models for different criteria: (a) minimum mean square error (MSE) in τ_ϕ , (b) minimum mean square error (MSE) in pO_2 , (c) minimum mean square relative error in pO_2 . Test data were used for evaluating the models (see Table 2).

Range	Stern-Volmer (SV)			Lehrer (L)			2 nd order Polynomial (P2)					
pO_2	Evaluation (criterion)	(a)	(b)	(c)	Evaluation (criterion)	(a)	(b)	(c)	Evaluation (criterion)	(a)	(b)	(c)
0.5-9 (kPa)	RMSE τ_ϕ (μs)	0.0487	0.0474	0.0813	RMSE τ_ϕ (μs)	0.0136	0.0082	0.0125	RMSE τ_ϕ (μs)	0.0072	0.0493	0.0130
	RMSE pO_2 (kPa)	0.9282	0.6755	1.7112	RMSE pO_2 (kPa)	0.8191	0.4233	0.5661	RMSE pO_2 (kPa)	0.1256	0.4216	0.1082
	RMSE relat. pO_2 (%)	23.0158	42.9911	30.4558	RMSE relat. pO_2 (%)	10.5242	5.8469	8.0788	RMSE relat. pO_2 (%)	3.4082	16.5942	5.5078
Range	1 st order Polynomial-Exponent (PE1)			2 nd order Polynomial-Exponent (PE2)			Demas (D)					
pO_2	Evaluation (criterion)	(a)	(b)	(c)	Evaluation (criterion)	(a)	(b)	(c)	Evaluation (criterion)	(a)	(b)	(c)
0.5-9 (kPa)	RMSE τ_ϕ (μs)	0.0074	0.0189	0.0130	RMSE τ_ϕ (μs)	0.0081	0.0158	0.0114	RMSE τ_ϕ (μs)	0.0119	0.0143	0.0114
	RMSE pO_2 (kPa)	0.1497	0.4274	0.2537	RMSE pO_2 (kPa)	0.2465	0.4271	0.3406	RMSE pO_2 (kPa)	0.5230	0.4442	0.4660
	RMSE relat. pO_2 (%)	3.4306	8.6154	5.8653	RMSE relat. pO_2 (%)	4.1819	7.7034	5.8314	RMSE relat. pO_2 (%)	7.4328	7.4390	6.8174

Experiment 23

page 1/2

Table 1: Sensing phase information

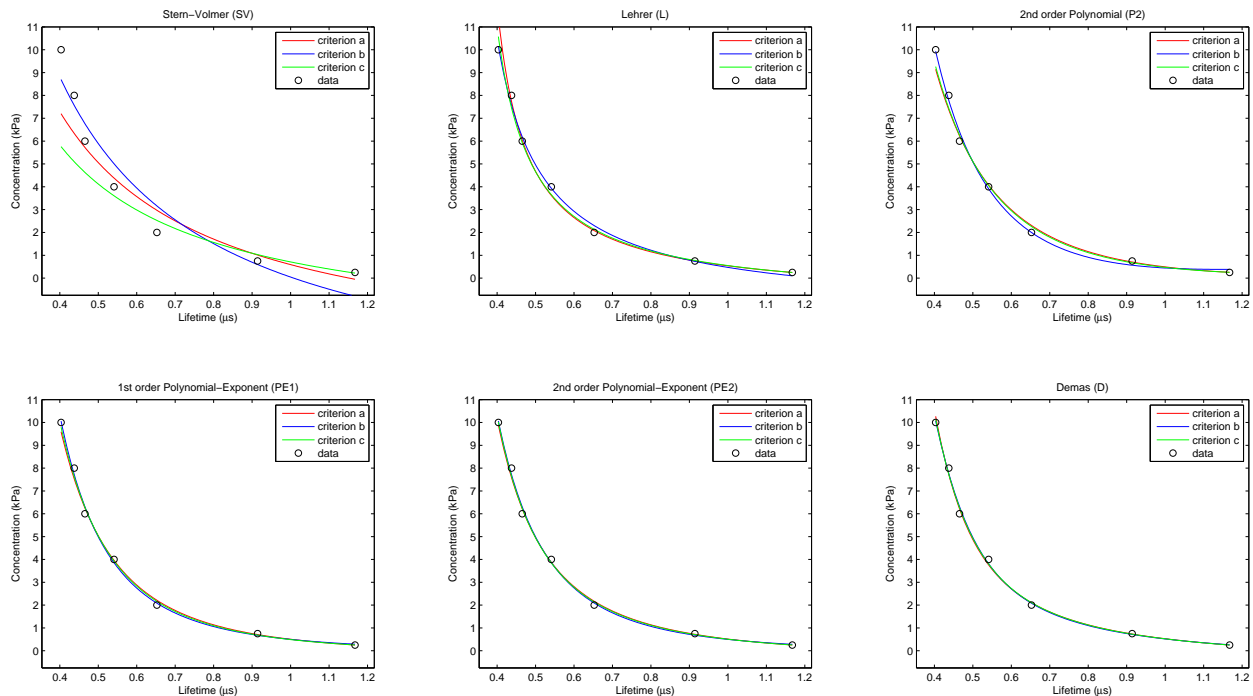
Name:	EB146-AP200/19 (replica 3)
Description:	An oxygen-sensing dye (Ir(2-(2,4-difluoro-3-methylesterphenyl)pyridine) ₂ (4-(N,N-dimethylamino)picolinate)) immobilized into AP200/19 (a nanostructured aluminium oxide-hydroxide solid support).
Analyte:	Partial pressure of oxygen in the gas phase (pO_2 , kPa); Range: 0.25-10 kPa.
Analytical signal:	(Measurement method): Luminescence lifetime in the frequency domain (<i>i.e.</i> , apparent lifetime estimated from phase-shift) using a phase-modulation method. (Instrumentation): A dual-phase lock-in amplifier (LIA) (SR830, Stanford Research Systems); Excitation signal: Sinusoidal-wave at 94100 Hz (see reference).
Reference(s):	Medina-Rodríguez, S.; Marín-Suárez, M.; Fernández-Sánchez, J.F.; de la Torre-Vega, A.; Baranoff, E.; Fernández-Gutiérrez, A. <i>Analyst</i> 2013 , 138, 4607-4617.

1.- Experimental data (calibration and test)

Table 2: Experimental data (*i.e.*, calibration and test data); apparent phase-shift lifetime measurements (τ_ϕ , in microseconds) for several oxygen concentrations (pO_2 , in kPa) at room temperature (21 °C). All the values correspond to the average of 25 measurements.

Calibration data (τ_ϕ , in microseconds)			Test data (τ_ϕ , in microseconds)		
pO_2 (kPa)	Mean (μs)	Sdev (μs)	pO_2 (kPa)	Mean (μs)	Sdev (μs)
0.25	1.1675	0.0006	0.50	0.9981	0.0001
0.75	0.9141	0.0002	1.00	0.8405	0.0001
2.00	0.6524	0.0001	3.00	0.5994	0.0002
4.00	0.5410	0.0001	5.00	0.4969	0.0002
6.00	0.4654	0.0002	7.00	0.4432	0.0002
8.00	0.4374	0.0002	9.00	0.4070	0.0002
10.00	0.4033	0.0002			

2.- Calibration curves: models and criteria


Figure 1: Calibration curves for the apparent phase-shift lifetime measurements (calibration data) of the sensing phase using different models and criteria. Models: Stern-Volmer (SV) (2 parameters), Lehrer (L) (3 parameters), 2nd order Polynomial (P2) (3 parameters), 1st order Polynomial-Exponent (PE1) (3 parameters), 2nd order Polynomial-Exponent (PE2) (4 parameters), Demas (D) (4 parameters). Criteria: (a) minimum mean square error (MSE) in τ_ϕ , (b) minimum mean square error (MSE) in pO_2 , (c) minimum mean square relative error in pO_2 .

Experiment 23

3.- Parameters of the fitting models for different criteria

Table 3: Parameters of the fitting models for different criteria: (a) minimum mean square error (MSE) in τ_ϕ , (b) minimum mean square error (MSE) in pO_2 , (c) minimum mean square relative error in pO_2 . RMSE is expressed in microseconds for criterion (a), in kPa for criterion (b) and in relative error (%) for criterion (c). Calibration data used are shown in Table 2.

Range	Stern-Volmer (SV)			Lehrer (L)			2 nd order Polynomial (P2)					
pO_2	Parameter	(a)	(b)	(c)	Parameter	(a)	(b)	(c)	Parameter	(a)	(b)	(c)
0.25-10 (kPa)	τ_0 (μs)	1.1527	1.0081	1.2625	τ_0 (μs)	1.3951	1.2289	1.3779	a_0	1.0382	3.1966	1.3006
	k (kPa^{-1})	0.2581	0.1724	0.3700	k (kPa^{-1})	1.0837	0.6794	0.9943	a_1	-3.12714	-6.45263	-3.56071
	—	—	—	—	x	0.7683	0.7691	0.7745	a_2	2.57995	3.7	2.7315
	R^2	0.93317	0.92869	0.91471	R^2	0.99900	0.99576	0.99699	R^2	0.99694	0.99660	0.99430
	RMSE	0.0684	0.9214	29.2045	RMSE	0.0084	0.2247	5.4906	RMSE	0.0146	0.2012	7.5496
	iterations	100	1	1	iterations	100	100	100	iterations	100	1	1
	Φ_0 (μs)	1.1527	1.0081	1.2625	Φ_0 (μs)	1.3951	1.2289	1.3779	Φ_0 (μs)	1.5061	1.0093	1.3689
	K (kPa^{-1})	0.2581	0.1724	0.3700	K (kPa^{-1})	0.8326	0.5225	0.7701	K (kPa^{-1})	1.6303	0.4517	1.1710
Range	1 st order Polynomial-Exponent (PE1)			2 nd order Polynomial-Exponent (PE2)			Demas (D)					
pO_2	Parameter	(a)	(b)	(c)	Parameter	(a)	(b)	(c)	Parameter	(a)	(b)	(c)
0.25-10 (kPa)	a_0	-0.1832	-0.0301	-0.1380	a_0	-0.3326	-0.0962	-0.3030	τ_0 (μs)	1.4243	1.4782	1.4314
	a_1	0.68727	0.528298	0.628545	a_1	0.753072	0.139337	0.719731	k_1 (kPa^{-1})	1.2952	1.5864	1.3602
	α	-2.9243	-3.2486	-3.0398	a_2	0.0935784	0.455671	0.0892985	k_2 (kPa^{-1})	0.0165	0.0261	0.0206
	—	—	—	—	α	-2.1707	-1.6739	-2.2124	x	0.7284	0.7082	0.7180
	R^2	0.99839	0.99747	0.99725	R^2	0.99895	0.99747	0.99813	R^2	0.99936	0.99752	0.99860
	RMSE	0.0106	0.1737	5.2416	RMSE	0.0086	0.1736	4.3270	RMSE	0.0067	0.1719	3.7378
	Φ_0 (μs)	1.5716	2.4148	1.6468	Φ_0 (μs)	1.4916	1.9343	1.5114	Φ_0 (μs)	1.4243	1.4782	1.4314
	K (kPa^{-1})	1.8666	10.2150	2.3843	K (kPa^{-1})	1.3196	4.0836	1.4243	K (kPa^{-1})	0.9480	1.1310	0.9825

4.- Accuracy of the fitting models for different criteria using calibration data

Table 4: Accuracy (root mean square error, RMSE) of the fitting models for different criteria: (a) minimum mean square error (MSE) in τ_ϕ , (b) minimum mean square error (MSE) in pO_2 , (c) minimum mean square relative error in pO_2 . Calibration data were used for evaluating the models (see Table 2).

Range	Stern-Volmer (SV)			Lehrer (L)			2 nd order Polynomial (P2)					
pO_2	Evaluation (criterion)	(a)	(b)	(c)	Evaluation (criterion)	(a)	(b)	(c)	Evaluation (criterion)	(a)	(b)	(c)
0.25-10 (kPa)	RMSE τ_ϕ (μs)	0.0684	0.0891	0.0842	RMSE τ_ϕ (μs)	0.0084	0.0313	0.0096	RMSE τ_ϕ (μs)	0.0146	0.0286	0.0150
	RMSE pO_2 (kPa)	1.3057	0.9214	2.0289	RMSE pO_2 (kPa)	0.5692	0.2247	0.3306	RMSE pO_2 (kPa)	0.4276	0.2012	0.3789
	RMSE relat. pO_2 (%)	52.3783	159.6840	29.2045	RMSE relat. pO_2 (%)	6.7969	23.1802	5.4906	RMSE relat. pO_2 (%)	7.7850	22.5065	7.5496
Range	1 st order Polynomial-Exponent (PE1)			2 nd order Polynomial-Exponent (PE2)			Demas (D)					
pO_2	Evaluation (criterion)	(a)	(b)	(c)	Evaluation (criterion)	(a)	(b)	(c)	Evaluation (criterion)	(a)	(b)	(c)
0.25-10 (kPa)	RMSE τ_ϕ (μs)	0.0106	0.0215	0.0111	RMSE τ_ϕ (μs)	0.0086	0.0178	0.0087	RMSE τ_ϕ (μs)	0.0067	0.0083	0.0068
	RMSE pO_2 (kPa)	0.2662	0.1737	0.2088	RMSE pO_2 (kPa)	0.1975	0.1736	0.1800	RMSE pO_2 (kPa)	0.1953	0.1719	0.1764
	RMSE relat. pO_2 (%)	5.5128	7.6706	5.2416	RMSE relat. pO_2 (%)	4.4484	6.8356	4.3270	RMSE relat. pO_2 (%)	3.8008	4.2155	3.7378

5.- Accuracy of the fitting models for different criteria using test data

Table 5: Accuracy (root mean square error, RMSE) of the fitting models for different criteria: (a) minimum mean square error (MSE) in τ_ϕ , (b) minimum mean square error (MSE) in pO_2 , (c) minimum mean square relative error in pO_2 . Test data were used for evaluating the models (see Table 2).

Range	Stern-Volmer (SV)			Lehrer (L)			2 nd order Polynomial (P2)					
pO_2	Evaluation (criterion)	(a)	(b)	(c)	Evaluation (criterion)	(a)	(b)	(c)	Evaluation (criterion)	(a)	(b)	(c)
0.5-9 (kPa)	RMSE τ_ϕ (μs)	0.0474	0.0444	0.0771	RMSE τ_ϕ (μs)	0.0148	0.0065	0.0146	RMSE τ_ϕ (μs)	0.0043	0.0318	0.0090
	RMSE pO_2 (kPa)	0.8941	0.6335	1.6281	RMSE pO_2 (kPa)	0.8014	0.3496	0.4915	RMSE pO_2 (kPa)	0.0973	0.3781	0.1131
	RMSE relat. pO_2 (%)	23.3935	39.8003	30.5495	RMSE relat. pO_2 (%)	10.7010	4.6782	8.2144	RMSE relat. pO_2 (%)	2.1857	12.2953	4.0065
Range	1 st order Polynomial-Exponent (PE1)			2 nd order Polynomial-Exponent (PE2)			Demas (D)					
pO_2	Evaluation (criterion)	(a)	(b)	(c)	Evaluation (criterion)	(a)	(b)	(c)	Evaluation (criterion)	(a)	(b)	(c)
0.5-9 (kPa)	RMSE τ_ϕ (μs)	0.0063	0.0135	0.0095	RMSE τ_ϕ (μs)	0.0082	0.0129	0.0094	RMSE τ_ϕ (μs)	0.0117	0.0120	0.0110
	RMSE pO_2 (kPa)	0.1845	0.3711	0.2657	RMSE pO_2 (kPa)	0.2819	0.3705	0.3359	RMSE pO_2 (kPa)	0.4316	0.3867	0.3964
	RMSE relat. pO_2 (%)	3.3153	6.7930	4.8759	RMSE relat. pO_2 (%)	4.5349	6.6024	5.2867	RMSE relat. pO_2 (%)	6.7397	6.4951	6.2756

Experiment 24

page 1/2

Table 1: Sensing phase information

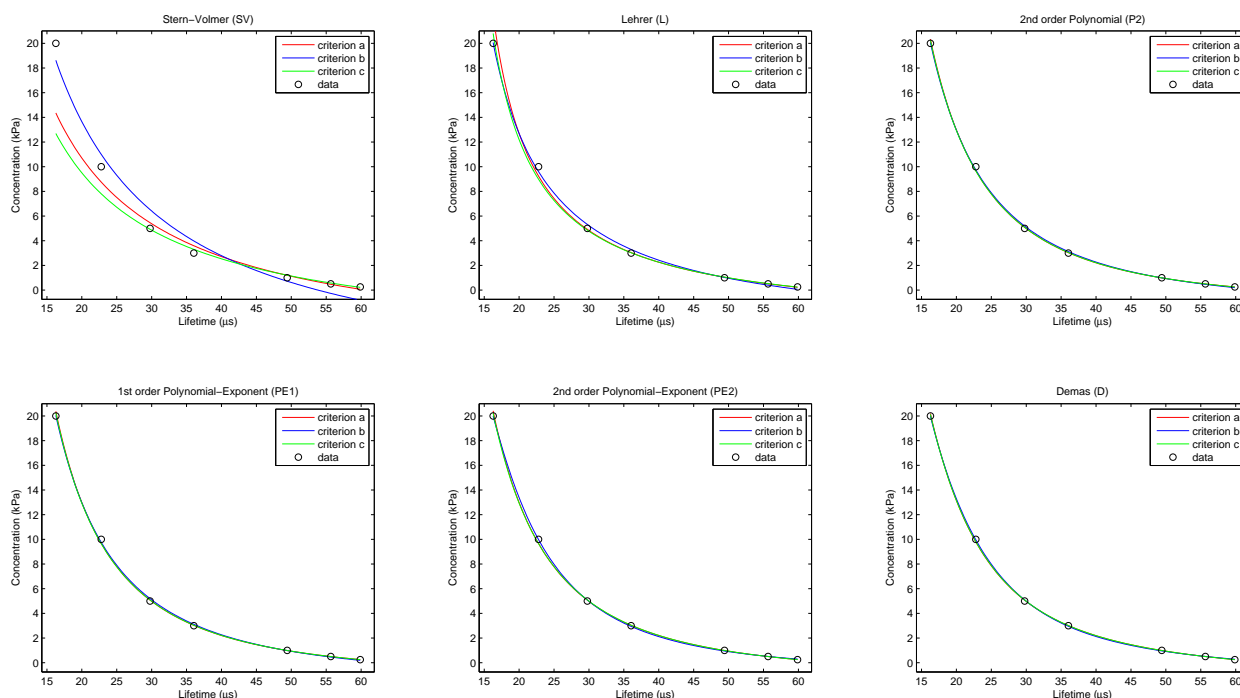
Name:	PtTFPP/PS
Description:	An oxygen-sensing dye (a Platinum(II) 5,10,15,20-meso-tetrakis-(2,3,4,5,6-pentafluorophenyl)-porphyrin) immobilized in polystyrene.
Analyte:	Partial pressure of oxygen in the gas phase (pO_2 , kPa); Range: 0.25-20 kPa.
Analytical signal:	(Measurement method): Luminescence lifetime in the frequency domain (<i>i.e.</i> , apparent lifetime estimated from phase-shift) using a phase-modulation method. (Instrumentation): Measurement system based on the I/Q method; Excitation signal: Sinusoidal-wave at 1709 Hz (see reference).
Reference(s):	Medina-Rodríguez, S.; de la Torre-Vega, A.; Fernández-Sánchez, J. F.; Fernández-Gutiérrez, A. <i>Sensors and Actuators B: Chemical</i> 2013 , 176, 1110-1120.

1.- Experimental data (calibration and test)

Table 2: Experimental data (*i.e.*, calibration and test data); apparent phase-shift lifetime measurements (τ_ϕ , in microseconds) for several oxygen concentrations (pO_2 , in kPa) at room temperature (21 °C). All the values correspond to the average of 25 measurements.

Calibration data (τ_ϕ , in microseconds)			Test data (τ_ϕ , in microseconds)		
pO_2 (kPa)	Mean (μs)	Sdev (μs)	pO_2 (kPa)	Mean (μs)	Sdev (μs)
0.25	59.8805	0.0288	0.75	52.3003	0.0122
0.50	55.6551	0.0302	2.00	41.2214	0.0089
1.00	49.4099	0.0182	4.00	32.4436	0.0180
3.00	36.0395	0.0226	6.00	27.7457	0.0343
5.00	29.7740	0.0119	15.00	18.7343	0.0215
10.00	22.7794	0.0236			
20.00	16.2736	0.0135			

2.- Calibration curves: models and criteria


Figure 1: Calibration curves for the apparent phase-shift lifetime measurements (calibration data) of the sensing phase using different models and criteria. Models: Stern-Volmer (SV) (2 parameters), Lehrer (L) (3 parameters), 2nd order Polynomial (P2) (3 parameters), 1st order Polynomial-Exponent (PE1) (3 parameters), 2nd order Polynomial-Exponent (PE2) (4 parameters), Demas (D) (4 parameters). Criteria: (a) minimum mean square error (MSE) in τ_ϕ , (b) minimum mean square error (MSE) in pO_2 , (c) minimum mean square relative error in pO_2 .

Experiment 24

3.- Parameters of the fitting models for different criteria

Table 3: Parameters of the fitting models for different criteria: (a) minimum mean square error (MSE) in τ_ϕ , (b) minimum mean square error (MSE) in pO_2 , (c) minimum mean square relative error in pO_2 . RMSE is expressed in microseconds for criterion (a), in kPa for criterion (b) and in relative error (%) for criterion (c). Calibration data used are shown in Table 2.

Range	Stern-Volmer (SV)				Lehrer (L)				2 nd order Polynomial (P2)			
pO_2	Parameter	(a)	(b)	(c)	Parameter	(a)	(b)	(c)	Parameter	(a)	(b)	(c)
0.25-20 (kPa)	τ_0 (μs)	60.6027	53.8065	62.8443	τ_0 (μs)	63.9008	60.7216	64.1699	a_0	-1.2330	-1.7562	-1.2944
	k (kPa^{-1})	0.1897	0.1238	0.2255	k (kPa^{-1})	0.3562	0.2671	0.3543	a_1	-8.85694	27.8895	-3.7773
	—	—	—	—	x	0.8391	0.8686	0.8477	a_2	5858.12	5325.23	5765.53
	R^2	0.98134	0.97426	0.96135	R^2	0.99922	0.99871	0.99731	R^2	0.99988	0.99958	0.99973
	RMSE	2.1250	1.0670	19.6591	RMSE	0.4332	0.2385	5.1897	RMSE	0.1687	0.1365	1.6509
	iterations	100	1	1	iterations	100	100	100	iterations	100	1	1
0.25-20 (kPa)	Φ_0 (μs)	60.6027	53.8065	62.8443	Φ_0 (μs)	63.9008	60.7216	64.1699	Φ_0 (μs)	65.4293	63.5759	65.2976
	K (kPa^{-1})	0.1897	0.1238	0.2255	K (kPa^{-1})	0.2989	0.2320	0.3004	K (kPa^{-1})	0.3844	0.3253	0.3778
	—	—	—	—	—	—	—	—	—	—	—	—
	R^2	0.99988	0.99961	0.99973	R^2	0.99988	0.99995	0.99973	R^2	0.99995	0.99995	0.99988
	RMSE	0.1678	0.1309	1.6527	RMSE	0.1673	0.0457	1.6496	RMSE	0.1112	0.0461	1.0805
	iterations	100	100	100	iterations	100	100	100	iterations	500	500	500
0.25-20 (kPa)	α_0	-1.2894	-1.5744	-1.3197	α_0	-1.3557	-0.7896	-1.2497	τ_0 (μs)	65.1289	66.8264	65.1248
	α_1	6218	4618.23	5891.66	α_1	11.5468	28764.3	-10.2307	k_1 (kPa^{-1})	0.4991	0.6556	0.5036
	α	-2.0287	-1.9228	-2.0111	α_2	6660.01	-7.58059e+006	5530.88	k_2 (kPa^{-1})	0.0289	0.0407	0.0301
	—	—	—	—	α	-1.0313	-2.4866	-0.9897	x	0.7049	0.6405	0.6995
	R^2	0.99988	0.99961	0.99973	R^2	0.99988	0.99995	0.99973	R^2	0.99995	0.99995	0.99988
	RMSE	0.1678	0.1309	1.6527	RMSE	0.1673	0.0457	1.6496	RMSE	0.1112	0.0461	1.0805
0.25-20 (kPa)	Φ_0 (μs)	65.4000	63.5727	65.2836	Φ_0 (μs)	65.3564	68.0931	65.3176	Φ_0 (μs)	65.1289	66.8264	65.1248
	K (kPa^{-1})	0.3823	0.3303	0.3768	K (kPa^{-1})	0.3793	0.5130	0.3794	K (kPa^{-1})	0.3603	0.4346	0.3613
	—	—	—	—	—	—	—	—	—	—	—	—
	R^2	0.99988	0.99961	0.99973	R^2	0.99988	0.99995	0.99973	R^2	0.99995	0.99995	0.99988
	RMSE	0.1678	0.1309	1.6527	RMSE	0.1673	0.0457	1.6496	RMSE	0.1112	0.0461	1.0805
	iterations	100	100	100	iterations	100	100	100	iterations	500	500	500

4.- Accuracy of the fitting models for different criteria using calibration data

Table 4: Accuracy (root mean square error, RMSE) of the fitting models for different criteria: (a) minimum mean square error (MSE) in τ_ϕ , (b) minimum mean square error (MSE) in pO_2 , (c) minimum mean square relative error in pO_2 . Calibration data were used for evaluating the models (see Table 2).

Range	Stern-Volmer (SV)				Lehrer (L)				2 nd order Polynomial (P2)			
pO_2	Evaluation (criterion)	(a)	(b)	(c)	Evaluation (criterion)	(a)	(b)	(c)	Evaluation (criterion)	(a)	(b)	(c)
0.25-20 (kPa)	RMSE τ_ϕ (μs)	2.1250	3.9766	2.4556	RMSE τ_ϕ (μs)	0.4332	1.1774	0.4891	RMSE τ_ϕ (μs)	0.1687	0.4858	0.1718
	RMSE pO_2 (kPa)	2.2052	1.0670	2.8878	RMSE pO_2 (kPa)	0.9225	0.2385	0.4924	RMSE pO_2 (kPa)	0.1834	0.1365	0.1648
	RMSE relat. pO_2 (%)	32.5183	172.9540	19.6591	RMSE relat. pO_2 (%)	6.5152	30.0213	5.1897	RMSE relat. pO_2 (%)	1.7081	9.0916	1.6509
0.25-20 (kPa)	1 st order Polynomial-Exponent (PE1)				2 nd order Polynomial-Exponent (PE2)				Demas (D)			
	Evaluation (criterion)	(a)	(b)	(c)	Evaluation (criterion)	(a)	(b)	(c)	Evaluation (criterion)	(a)	(b)	(c)
	RMSE τ_ϕ (μs)	0.1678	0.5146	0.1716	RMSE τ_ϕ (μs)	0.1673	0.4638	0.1727	RMSE τ_ϕ (μs)	0.1112	0.3330	0.1133
	RMSE pO_2 (kPa)	0.1948	0.1309	0.1667	RMSE pO_2 (kPa)	0.2056	0.0457	0.1598	RMSE pO_2 (kPa)	0.1135	0.0461	0.0943
	RMSE relat. pO_2 (%)	1.7149	9.6059	1.6527	RMSE relat. pO_2 (%)	1.7203	7.0784	1.6496	RMSE relat. pO_2 (%)	1.1076	5.1689	1.0805

5.- Accuracy of the fitting models for different criteria using test data

Table 5: Accuracy (root mean square error, RMSE) of the fitting models for different criteria: (a) minimum mean square error (MSE) in τ_ϕ , (b) minimum mean square error (MSE) in pO_2 , (c) minimum mean square relative error in pO_2 . Test data were used for evaluating the models (see Table 2).

Range	Stern-Volmer (SV)				Lehrer (L)				2 nd order Polynomial (P2)			
pO_2	Evaluation (criterion)	(a)	(b)	(c)	Evaluation (criterion)	(a)	(b)	(c)	Evaluation (criterion)	(a)	(b)	(c)
0.75-15 (kPa)	RMSE τ_ϕ (μs)	2.0577	2.6574	2.3331	RMSE τ_ϕ (μs)	0.2712	0.7488	0.4064	RMSE τ_ϕ (μs)	0.1115	0.3300	0.1171
	RMSE pO_2 (kPa)	1.4833	0.9738	2.0528	RMSE pO_2 (kPa)	0.0889	0.2667	0.3350	RMSE pO_2 (kPa)	0.0378	0.1156	0.0505
	RMSE relat. pO_2 (%)	16.6639	37.6370	17.9801	RMSE relat. pO_2 (%)	2.4292	6.5302	3.9653	RMSE relat. pO_2 (%)	1.0177	2.9703	1.0440
0.75-15 (kPa)	1 st order Polynomial-Exponent (PE1)				2 nd order Polynomial-Exponent (PE2)				Demas (D)			
	Evaluation (criterion)	(a)	(b)	(c)	Evaluation (criterion)	(a)	(b)	(c)	Evaluation (criterion)	(a)	(b)	(c)
	RMSE τ_ϕ (μs)	0.1056	0.3439	0.1142	RMSE τ_ϕ (μs)	0.0985	0.3301	0.1229	RMSE τ_ϕ (μs)	0.0961	0.2825	0.1120
	RMSE pO_2 (kPa)	0.0351	0.1168	0.0501	RMSE pO_2 (kPa)	0.0326	0.1706	0.0530	RMSE pO_2 (kPa)	0.0707	0.1210	0.0712
	RMSE relat. pO_2 (%)	0.9633	3.1934	1.0166	RMSE relat. pO_2 (%)	0.8959	2.9456	1.0973	RMSE relat. pO_2 (%)	0.9025	2.4862	1.0396

Experiment 25

page 1/2

Table 1: Sensing phase information

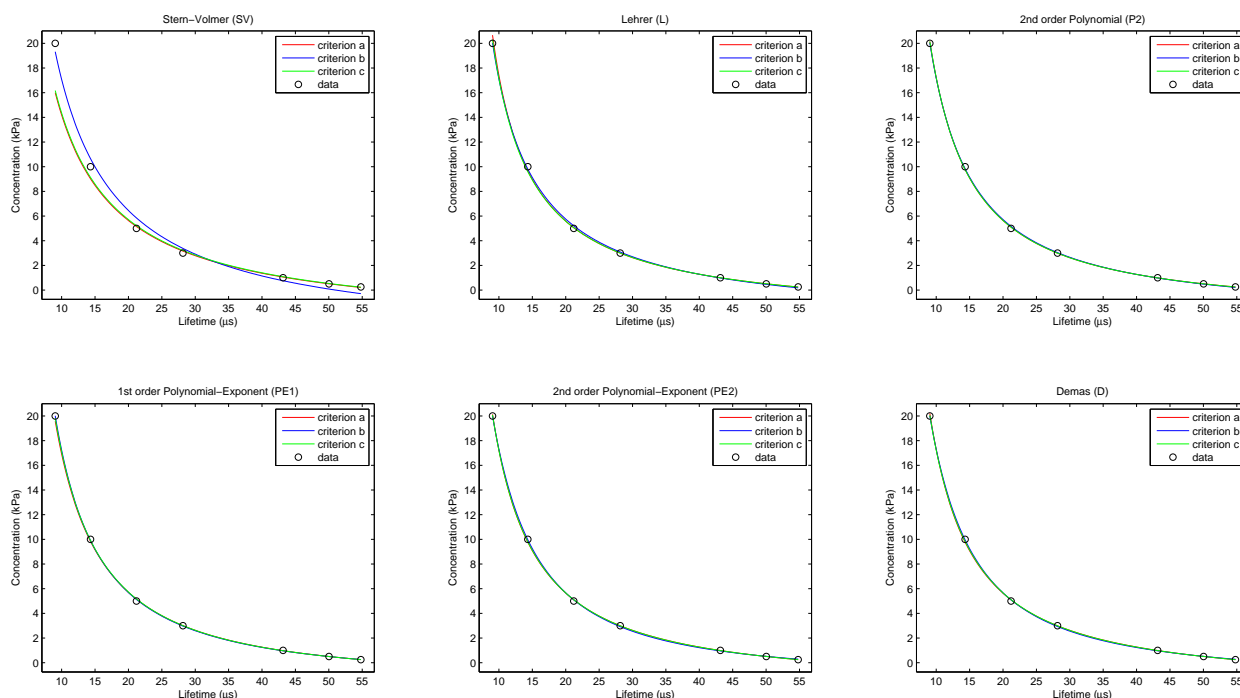
Name:	PtTFPP/PS
Description:	An oxygen-sensing dye (a Platinum(II) 5,10,15,20-meso-tetrakis-(2,3,4,5,6-pentafluorophenyl)-porphyrin) immobilized in polystyrene.
Analyte:	Partial pressure of oxygen in the gas phase (pO_2 , kPa); Range: 0.25-20 kPa.
Analytical signal:	(Measurement method): Luminescence lifetime in the frequency domain (<i>i.e.</i> , apparent lifetime estimated from phase-shift) using a phase-modulation method. (Instrumentation): Measurement system based on the I/Q method; Excitation signal: Sinusoidal-wave at 24917 Hz (see reference).
Reference(s):	Medina-Rodríguez, S.; de la Torre-Vega, A.; Fernández-Sánchez, J. F.; Fernández-Gutiérrez, A. <i>Sensors and Actuators B: Chemical</i> 2013 , 176, 1110-1120.

1.- Experimental data (calibration and test)

Table 2: Experimental data (*i.e.*, calibration and test data); apparent phase-shift lifetime measurements (τ_ϕ , in microseconds) for several oxygen concentrations (pO_2 , in kPa) at room temperature (21 °C). All the values correspond to the average of 25 measurements.

Calibration data (τ_ϕ , in microseconds)			Test data (τ_ϕ , in microseconds)		
pO_2 (kPa)	Mean (μs)	Sdev (μs)	pO_2 (kPa)	Mean (μs)	Sdev (μs)
0.25	54.8017	0.0039	0.75	46.6855	0.0039
0.50	50.0291	0.0036	2.00	33.7834	0.0037
1.00	43.1460	0.0029	4.00	24.1018	0.0034
3.00	28.1595	0.0032	6.00	19.1225	0.0035
5.00	21.2028	0.0041	15.00	10.8834	0.0034
10.00	14.3255	0.0029			
20.00	9.0391	0.0044			

2.- Calibration curves: models and criteria


Figure 1: Calibration curves for the apparent phase-shift lifetime measurements (calibration data) of the sensing phase using different models and criteria. Models: Stern-Volmer (SV) (2 parameters), Lehrer (L) (3 parameters), 2nd order Polynomial (P2) (3 parameters), 1st order Polynomial-Exponent (PE1) (3 parameters), 2nd order Polynomial-Exponent (PE2) (4 parameters), Demas (D) (4 parameters). Criteria: (a) minimum mean square error (MSE) in τ_ϕ , (b) minimum mean square error (MSE) in pO_2 , (c) minimum mean square relative error in pO_2 .

Experiment 25

3.- Parameters of the fitting models for different criteria

Table 3: Parameters of the fitting models for different criteria: (a) minimum mean square error (MSE) in τ_ϕ , (b) minimum mean square error (MSE) in pO_2 , (c) minimum mean square relative error in pO_2 . RMSE is expressed in microseconds for criterion (a), in kPa for criterion (b) and in relative error (%) for criterion (c). Calibration data used are shown in Table 2.

Range	Stern-Volmer (SV)				Lehrer (L)				2 nd order Polynomial (P2)				
pO_2	Parameter	(a)	(b)	(c)	Parameter	(a)	(b)	(c)	Parameter	(a)	(b)	(c)	
0.25-20 (kPa)	τ_0 (μs)	58.7771	51.0053	59.2221	τ_0 (μs)	60.2508	58.4208	60.2667	a_0	-2.1664	-2.3206	-2.1661	
	k (kPa^{-1})	0.3440	0.2403	0.3433	k (kPa^{-1})	0.4306	0.3845	0.4276	a_1	118.709	126.564	118.677	
	–	–	–	–	x	0.9455	0.9550	0.9480	a_2	749.952	682.351	750.205	
	R^2	0.99729	0.99264	0.99041	R^2	0.99991	0.99968	0.99964	R^2	0.99993	0.99981	0.99982	
	RMSE	0.8662	0.5704	0.97936	RMSE	0.1564	0.1181	1.8854	RMSE	0.1386	0.0908	1.3448	
	iterations	100	1	1	iterations	100	100	100	iterations	100	1	1	
0.25-20 (kPa)	Φ_0 (μs)	58.7771	51.0053	59.2221	Φ_0 (μs)	60.2508	58.4208	60.2667	Φ_0 (μs)	60.5168	59.4824	60.5113	
	K (kPa^{-1})	0.3440	0.2403	0.3433	K (kPa^{-1})	0.4071	0.3672	0.4053	K (kPa^{-1})	0.4217	0.3979	0.4218	
	Range	1 st order Polynomial-Exponent (PE1)				2 nd order Polynomial-Exponent (PE2)				Demas (D)			
	pO_2	Parameter	(a)	(b)	(c)	Parameter	(a)	(b)	(c)	Parameter	(a)	(b)	(c)
	0.25-20 (kPa)	a_0	-1.6740	-1.5595	-1.6539	a_0	-2.1939	-1.2551	-2.2264	τ_0 (μs)	60.4636	61.9825	60.5542
a_1		398.887	443.512	414.088	a_1	104.695	668.936	64.099	k_1 (kPa^{-1})	0.4516	0.5628	0.4641	
α		-1.3318	-1.3731	-1.3441	a_2	719.828	-2022.73	614.913	k_2 (kPa^{-1})	0.0151	0.0519	0.0236	
–		–	–	–	α	-0.9714	-1.5148	-0.8759	x	0.9239	0.8430	0.9099	
R^2		0.99986	0.99991	0.99970	R^2	0.99993	0.99993	0.99983	R^2	0.99994	0.99994	0.99984	
RMSE		0.1938	0.0642	1.7320	RMSE	0.1384	0.0540	1.3185	RMSE	0.1331	0.0502	1.2667	
iterations	100	100	100	iterations	100	100	100	iterations	500	500	500		
0.25-20 (kPa)	Φ_0 (μs)	60.9341	61.2460	60.8845	Φ_0 (μs)	60.5137	62.8559	60.5496	Φ_0 (μs)	60.4636	61.9825	60.5542	
	K (kPa^{-1})	0.4485	0.4670	0.4498	K (kPa^{-1})	0.4215	0.5290	0.4243	K (kPa^{-1})	0.4184	0.4825	0.4245	

4.- Accuracy of the fitting models for different criteria using calibration data

Table 4: Accuracy (root mean square error, RMSE) of the fitting models for different criteria: (a) minimum mean square error (MSE) in τ_ϕ , (b) minimum mean square error (MSE) in pO_2 , (c) minimum mean square relative error in pO_2 . Calibration data were used for evaluating the models (see Table 2).

Range	Stern-Volmer (SV)				Lehrer (L)				2 nd order Polynomial (P2)			
pO_2	Evaluation (criterion)	(a)	(b)	(c)	Evaluation (criterion)	(a)	(b)	(c)	Evaluation (criterion)	(a)	(b)	(c)
0.25-20 (kPa)	RMSE τ_ϕ (μs)	0.8662	3.2856	0.9121	RMSE τ_ϕ (μs)	0.1564	0.5948	0.1645	RMSE τ_ϕ (μs)	0.1386	0.3364	0.1386
	RMSE pO_2 (kPa)	1.5599	0.5704	1.4889	RMSE pO_2 (kPa)	0.2830	0.1181	0.1880	RMSE pO_2 (kPa)	0.1084	0.0908	0.1085
	RMSE relat. pO_2 (%)	10.7585	88.2028	9.7936	RMSE relat. pO_2 (%)	2.0607	11.1505	1.8854	RMSE relat. pO_2 (%)	1.3457	5.5615	1.3448
Range	1 st order Polynomial-Exponent (PE1)				2 nd order Polynomial-Exponent (PE2)				Demas (D)			
pO_2	Evaluation (criterion)	(a)	(b)	(c)	Evaluation (criterion)	(a)	(b)	(c)	Evaluation (criterion)	(a)	(b)	(c)
0.25-20 (kPa)	RMSE τ_ϕ (μs)	0.1938	0.2228	0.2010	RMSE τ_ϕ (μs)	0.1384	0.4490	0.1421	RMSE τ_ϕ (μs)	0.1331	0.3343	0.1395
	RMSE pO_2 (kPa)	0.1796	0.0642	0.1005	RMSE pO_2 (kPa)	0.1056	0.0540	0.0926	RMSE pO_2 (kPa)	0.1235	0.0502	0.0807
	RMSE relat. pO_2 (%)	1.8811	2.0875	1.7320	RMSE relat. pO_2 (%)	1.3393	6.1783	1.3185	RMSE relat. pO_2 (%)	1.3476	4.5336	1.2667

5.- Accuracy of the fitting models for different criteria using test data

Table 5: Accuracy (root mean square error, RMSE) of the fitting models for different criteria: (a) minimum mean square error (MSE) in τ_ϕ , (b) minimum mean square error (MSE) in pO_2 , (c) minimum mean square relative error in pO_2 . Test data were used for evaluating the models (see Table 2).

Range	Stern-Volmer (SV)				Lehrer (L)				2 nd order Polynomial (P2)			
pO_2	Evaluation (criterion)	(a)	(b)	(c)	Evaluation (criterion)	(a)	(b)	(c)	Evaluation (criterion)	(a)	(b)	(c)
0.75-15 (kPa)	RMSE τ_ϕ (μs)	0.8110	1.9626	0.9261	RMSE τ_ϕ (μs)	0.1698	0.4723	0.1565	RMSE τ_ϕ (μs)	0.2176	0.3603	0.2188
	RMSE pO_2 (kPa)	0.9924	0.5585	0.9342	RMSE pO_2 (kPa)	0.0453	0.1185	0.0477	RMSE pO_2 (kPa)	0.0586	0.0954	0.0581
	RMSE relat. pO_2 (%)	7.6743	24.1421	8.2658	RMSE relat. pO_2 (%)	1.5606	4.2971	1.4076	RMSE relat. pO_2 (%)	1.9864	3.3021	1.9990
Range	1 st order Polynomial-Exponent (PE1)				2 nd order Polynomial-Exponent (PE2)				Demas (D)			
pO_2	Evaluation (criterion)	(a)	(b)	(c)	Evaluation (criterion)	(a)	(b)	(c)	Evaluation (criterion)	(a)	(b)	(c)
0.75-15 (kPa)	RMSE τ_ϕ (μs)	0.3011	0.3479	0.3344	RMSE τ_ϕ (μs)	0.2177	0.3844	0.2342	RMSE τ_ϕ (μs)	0.2070	0.3321	0.2387
	RMSE pO_2 (kPa)	0.0896	0.1050	0.1026	RMSE pO_2 (kPa)	0.0585	0.1385	0.0674	RMSE pO_2 (kPa)	0.0679	0.1333	0.0845
	RMSE relat. pO_2 (%)	2.7001	3.1104	3.0037	RMSE relat. pO_2 (%)	1.9868	3.2176	2.1359	RMSE relat. pO_2 (%)	1.9099	2.8541	2.1924

B.2 Summary of evaluation results with criteria (a) and (b)

Table B.1: Root mean square error (RMSE) when the models are calibrated and evaluated with criterion (a): RMSE in analytical signal (expressed in appropriate units). Analytical signals: τ_ϕ (apparent lifetime estimated from phase-shift), τ_m (apparent lifetime estimated from modulation factor), I (luminescence intensity).

Calibration criterion: (a)			RMS error in the analytical signal (in appropriate units)											
Experiment	Sensing phase	Analytical signal	Calibration data						Test data					
			SV	L	P2	PE1	PE2	D	SV	L	P2	PE1	PE2	D
1	PtTFPP/PS	τ_ϕ	1.0884	0.3504	0.2415	0.1921	0.1444	0.1498	1.1442	0.5306	0.4124	0.3568	0.2623	0.2845
2	PtTFPP/PS	τ_m	0.7861	0.1246	0.0553	0.0548	0.0319	0.0314	0.8971	0.2991	0.2458	0.2189	0.2278	0.2237
3	PtTFPP/PS	τ_ϕ	2.1052	0.3042	0.1111	0.0768	0.0380	0.0457	1.9463	0.2944	0.0980	0.0791	0.0663	0.0721
4	PtTFPP/PS	τ_m	1.1070	0.3585	0.2432	0.1021	0.0655	0.0339	1.0878	0.3490	0.2462	0.1262	0.0819	0.0804
5	PtTFPP/PS	τ_ϕ	1.9556	0.2968	0.0884	0.0895	0.0520	0.0331	1.8317	0.2885	0.0647	0.0661	0.0545	0.0549
6	PtTFPP/PS	τ_m	0.5898	0.1187	0.0798	0.0712	0.0620	0.0525	0.5825	0.1255	0.0866	0.0653	0.0648	0.0558
7	PtTFPP/PS	τ_ϕ	1.5371	0.3139	0.1013	0.0847	0.0843	0.0463	1.4686	0.3148	0.1143	0.0847	0.0867	0.0694
8	PtTFPP/PS	τ_m	0.7844	0.1164	0.0884	0.1487	0.0870	0.0822	0.7823	0.1332	0.1041	0.1459	0.1028	0.0993
9	PtTFPP/PS	τ_ϕ	1.6531	0.2179	0.0765	0.1286	0.0434	0.0338	1.5662	0.2195	0.0845	0.1142	0.0765	0.0787
10	PtTFPP/PS	τ_m	0.6581	0.1319	0.1395	0.1990	0.1377	0.1297	0.6435	0.1205	0.1275	0.1773	0.1268	0.1187
11	PtTFPP/PS	τ_ϕ	1.5517	0.0995	0.1769	0.2341	0.1245	0.0362	1.4958	0.1650	0.1214	0.1533	0.0867	0.1027
12	N969-AP200/19	I	1.4692	0.3457	0.2635	0.2435	0.2292	0.2491	1.3076	0.2535	0.1889	0.1737	0.1735	0.1703
13	EB146-AP200/19	I	3.1200	0.4142	0.1150	0.1218	0.1065	0.1080	2.6270	0.5023	0.2954	0.2645	0.2775	0.2787
14	EB146-PS0X	I	3.6088	0.9483	1.1398	0.7296	0.7120	0.7103	3.4841	0.5955	0.8424	0.2525	0.1989	0.1878
15	N1008-PS0X	I	9.0686	0.5523	1.5250	0.7771	0.1765	0.2331	9.1010	0.1039	1.9183	0.5294	0.6237	0.6613
16	PtTFPP-AP200/19	τ_ϕ	0.2279	0.0386	0.0130	0.0150	0.0114	0.0092	0.1984	0.0474	0.0553	0.0587	0.0524	0.0511
17	N969-AP200/19	τ_ϕ	0.0649	0.0085	0.0084	0.0038	0.0023	0.0018	0.0514	0.0104	0.0078	0.0032	0.0030	0.0038
18	N1008-AP200/19 (repl. 1)	τ_ϕ	0.2483	0.0385	0.0290	0.0092	0.0091	0.0159	0.1875	0.0447	0.0348	0.0130	0.0130	0.0139
19	N1008-AP200/19 (repl. 2)	τ_ϕ	0.2526	0.0402	0.0304	0.0132	0.0131	0.0197	0.1904	0.0466	0.0414	0.0202	0.0205	0.0189
20	N1008-AP200/19 (repl. 3)	τ_ϕ	0.2372	0.0381	0.0252	0.0113	0.0111	0.0172	0.1832	0.0392	0.0322	0.0136	0.0141	0.0151
21	EB146-AP200/19 (repl. 1)	τ_ϕ	0.0656	0.0042	0.0118	0.0074	0.0047	0.0023	0.0488	0.0105	0.0083	0.0065	0.0063	0.0084
22	EB146-AP200/19 (repl. 2)	τ_ϕ	0.0724	0.0072	0.0172	0.0122	0.0097	0.0065	0.0487	0.0136	0.0072	0.0074	0.0081	0.0119
23	EB146-AP200/19 (repl. 3)	τ_ϕ	0.0684	0.0084	0.0146	0.0106	0.0086	0.0067	0.0474	0.0148	0.0043	0.0063	0.0082	0.0117
24	PtTFPP/PS	τ_ϕ	2.1250	0.4332	0.1687	0.1678	0.1673	0.1112	2.0577	0.2712	0.1115	0.1056	0.0985	0.0961
25	PtTFPP/PS	τ_ϕ	0.8662	0.1564	0.1386	0.1938	0.1384	0.1331	0.8110	0.1698	0.2176	0.3011	0.2177	0.2070
Mean RMS error in τ (μs)			0.8593	0.1527	0.0885	0.0870	0.0594	0.0475	0.8224	0.1671	0.1060	0.1011	0.0799	0.0799
Mean RMS error in I (arb. units)			4.3166	0.5651	0.7608	0.4680	0.3060	0.3251	4.1299	0.5913	0.8113	0.3050	0.3184	0.3245

Table B.2: Root mean square error (RMSE) when the models are calibrated and evaluated with criterion (b): RMSE in pO_2 (kPa). Analytical signals: τ_ϕ (apparent lifetime estimated from phase-shift), τ_m (apparent lifetime estimated from modulation factor), I (luminescence intensity).

Calibration criterion: (b)			RMS error in pO_2 (expressed in kPa)											
Experiment	Sensing phase	Analytical signal	Calibration data						Test data					
			SV	L	P2	PE1	PE2	D	SV	L	P2	PE1	PE2	D
1	PtTFPP/PS	τ_ϕ	0.5203	0.3112	0.2910	0.2578	0.1148	0.1693	0.3527	0.2539	0.2492	0.2288	0.2061	0.1767
2	PtTFPP/PS	τ_m	0.5513	0.0745	0.0443	0.0375	0.0332	0.0368	0.4286	0.2429	0.2239	0.1998	0.2083	0.2097
3	PtTFPP/PS	τ_ϕ	1.2406	0.1830	0.0367	0.0317	0.0314	0.0271	1.0454	0.1952	0.1227	0.1223	0.1222	0.1245
4	PtTFPP/PS	τ_m	0.4106	0.1512	0.1322	0.0883	0.0369	0.0267	0.3476	0.1512	0.1383	0.1077	0.0782	0.0744
5	PtTFPP/PS	τ_ϕ	1.1405	0.2123	0.0629	0.0636	0.0536	0.0227	0.9681	0.1709	0.0685	0.0685	0.0705	0.0712
6	PtTFPP/PS	τ_m	0.3893	0.1133	0.0953	0.0590	0.0350	0.0267	0.3322	0.1240	0.1132	0.0917	0.0796	0.0772
7	PtTFPP/PS	τ_ϕ	0.8412	0.2321	0.1489	0.1186	0.0345	0.0434	0.7090	0.2065	0.1434	0.1209	0.0890	0.0834
8	PtTFPP/PS	τ_m	0.5478	0.1124	0.0763	0.0381	0.0337	0.0264	0.4710	0.1275	0.1053	0.0852	0.0826	0.0812
9	PtTFPP/PS	τ_ϕ	1.0420	0.1600	0.0371	0.0356	0.0349	0.0206	0.8767	0.1553	0.0607	0.0577	0.0580	0.0506
10	PtTFPP/PS	τ_m	0.5236	0.1111	0.0788	0.0455	0.0423	0.0341	0.4672	0.1377	0.1174	0.1002	0.0985	0.0946
11	PtTFPP/PS	τ_ϕ	1.1357	0.1308	0.0697	0.0763	0.0442	0.0293	0.9599	0.1130	0.0691	0.0758	0.0455	0.0376
12	N969-AP200/19	I	0.3380	0.0704	0.0910	0.0970	0.0864	0.0501	0.2775	0.0709	0.0771	0.0810	0.0761	0.0682
13	EB146-AP200/19	I	0.3828	0.0510	0.0395	0.0427	0.0384	0.0418	0.3150	0.1360	0.1230	0.1199	0.1240	0.1266
14	EB146-PS0X	I	0.1912	0.0689	0.0752	0.0606	0.0593	0.0590	0.1540	0.0421	0.0507	0.0256	0.0221	0.0223
15	N1008-PS0X	I	0.2716	0.0219	0.0422	0.0125	0.0076	0.0079	0.2164	0.0366	0.0557	0.0162	0.0210	0.0205
16	PtTFPP-AP200/19	τ_ϕ	0.6121	0.2407	0.1760	0.1695	0.1339	0.1425	0.5168	0.1352	0.1219	0.1295	0.1786	0.1538
17	N969-AP200/19	τ_ϕ	0.8874	0.1672	0.1076	0.0746	0.0698	0.0606	0.6963	0.1740	0.1464	0.1350	0.1331	0.1315
18	N1008-AP200/19 (repl. 1)	τ_ϕ	0.8855	0.0848	0.1551	0.0656	0.0507	0.0578	0.6787	0.1422	0.1378	0.1277	0.1287	0.1371
19	N1008-AP200/19 (repl. 2)	τ_ϕ	0.8902	0.0921	0.1774	0.0951	0.0807	0.0818	0.6738	0.1336	0.1323	0.1234	0.1232	0.1325
20	N1008-AP200/19 (repl. 3)	τ_ϕ	0.8364	0.0834	0.1781	0.1156	0.0992	0.0835	0.6678	0.1409	0.1625	0.1421	0.1391	0.1416
21	EB146-AP200/19 (repl. 1)	τ_ϕ	0.9442	0.1351	0.2287	0.1343	0.1141	0.1005	0.6609	0.3121	0.2497	0.2879	0.2956	0.3095
22	EB146-AP200/19 (repl. 2)	τ_ϕ	0.9995	0.2378	0.2465	0.1931	0.1913	0.1880	0.6755	0.4233	0.4216	0.4274	0.4271	0.4442
23	EB146-AP200/19 (repl. 3)	τ_ϕ	0.9214	0.2247	0.2012	0.1737	0.1736	0.1719	0.6335	0.3496	0.3781	0.3711	0.3705	0.3867
24	PtTFPP/PS	τ_ϕ	1.0670	0.2385	0.1365	0.1309	0.0457	0.0461	0.9738	0.2667	0.1156	0.1168	0.1706	0.1210
25	PtTFPP/PS	τ_ϕ	0.5704	0.1181	0.0908	0.0642	0.0540	0.0502	0.5585	0.1185	0.0954	0.1050	0.1385	0.1333
Mean RMS error in pO_2 (kPa)			0.7256	0.1451	0.1208	0.0913	0.0680	0.0642	0.5863	0.1744	0.1472	0.1387	0.1395	0.1364

Appendix C

Software implementation for model calibration and evaluation

The directory PHOTOLUMINESCENCE_MODELS contains some MATLAB/Octave functions and scripts to perform model fitting (calibration) for several models describing photoluminescence response, with different criteria. Some data files (to perform calibration and evaluation of the models) are also included.

Model fitting consists in finding the model parameters minimizing the error between the model and some calibration data. Calibration / evaluation data consists of pairs of values (C_n, ϕ_n) , where C_n and ϕ_n are the data representing the concentration and analytical signal, respectively.

Models that can be fitted are:

- Stern-Volmer model (SV)
- Lehrer model (L)
- Demas model (D)
- Polynomial model, 2nd order (P2)
- Polynomial-Exponent model, 1st order (PE1)
- Polynomial-Exponent model, 2nd order (PE2)

Criteria used for fitting are:

- Error in ϕ_n : criterion (a)
- Error in C_n : criterion (b)
- Relative error in C_n : criterion (c)

C.1 Contents of the directory

The directory contains the following files:

1. Information:
 - info.pdf
2. MATLAB/Octave functions for model calibration:
 - model_SV.m (SV model fitting with criteria (a), (b) or (c))
 - model_L.m (L model fitting with criteria (a), (b) or (c))
 - model_D.m (D model fitting with criteria (a), (b) or (c))
 - model_P2.m (P2 model fitting with criteria (a), (b) or (c))
 - model_PE1.m (PE1 model fitting with criteria (a), (b) or (c))
 - model_PE2.m (PE2 model fitting with criteria (a), (b) or (c))
3. MATLAB/Octave functions for model evaluation:
 - evaluation_demas.m (evaluation models SV, L, D for all criteria)
 - evaluation_polynom.m (evaluation models P2, PE1, PE2 for all criteria)
4. MATLAB/Octave function performing a complete study with all models and criteria:
 - complete_study.m (it combines functions for model calibration/evaluation)
5. Data files for calibration / test:

- exp_1_cal.txt; exp_1_test.txt; (calibration/test data for experiment 1)
 - exp_2_cal.txt; exp_2_test.txt; (calibration/test data for experiment 2)
 - exp_3_cal.txt; exp_3_test.txt; (calibration/test data for experiment 3)
6. Three MATLAB/Octave scripts performing calibration/evaluation with some data files:
- script_models_simple.m
 - script_models_complex.m
 - script_complete_study.m
7. A text file with the output of the script "script_complete_study.m":
- out_complete_study.txt

C.2 Help and examples

All the functions and scripts provide information by typing:

```
help <function/script>
```

Example:

```
help model.SV
```

```
help script_complete_study
```

The help information includes both descriptions and examples.

For a fast use of this software, just type the following line in a MATLAB/Octave command window:

```
script_complete_study
```

C.3 How to use functions and scripts

- The functions are intended not to be modified.
- The scripts illustrate how to use the functions. Users can modify the scripts or create new scripts to process data according to their requirements.
- The script "script_complete_study.m" allows a user not experienced with MATLAB/Octave to perform a complete analysis of some data with minimal changes in the script. Note that most of the content of this script are comments explaining how to use or modify the script (the script just contains 8 lines of code). Type "help script_complete_study" for details.
- The script "script_models_simple.m" is a very simple script providing calibration and evaluation with model Lehrer, criterion (a). This script illustrates how the functions for calibration and evaluation can be used.
- The script "script_models_complex.m" provides calibration and evaluation for all the models and criteria. This script illustrates how to use the functions for a complex study.
- The easiest way of calibrating a model with new data is:
 - Write the calibration data into a text file (two columns, for C_n and ϕ_n).
 - Write the test data (if evaluation will be done with different data).
 - Modify or create a script to read the new data files and process the data.
 - Execute the script by typing the script name in a command window of MATLAB or Octave.

C.4 Compatibility MATLAB/Octave

These scripts/functions were developed with MATLAB. They have also been tested with Octave (version 3.6.4). Both provide the same results. However, due to differences in syntax, there are some details that should be taken into account when this code is run in Octave:

- The first time the functions and scripts are run, a lot of warnings (reporting issues related to MATLAB/Octave compatibility) are displayed, but not the next times.
- After a modification of a script, the first time it is run, the warnings are displayed again.
- The command "warning off" could reduce the warnings (depending on the Octave version).
- When a script/function produces an output that cannot be displayed in one screen of the console, usually Octave filters the output with the Unix command "more". It can be deactivated or reactivated by typing "more" in the command window.

C.5 Authors of the software

This software has been developed in November 2013 by: S. Medina-Rodríguez, A. de la Torre-Vega, J.F. Fernández-Sánchez and A. Fernández-Gutiérrez (smedina@ugr.es, atv@ugr.es, jffernan@ugr.es, albertof@ugr.es). The authors are with the Department of Signal Theory, Networking and Communications and with the Department of Analytical Chemistry, University of Granada (Spain).

C.6 Files included in the directory PHOTOLUMINESCENCE_MODELS

The next pages contains the code of the different functions and scripts, as well as the data files (for calibration and evaluation) and the output files.

C.6.1 Functions for model calibration

Function for fitting the Stern-Volmer model: model_SV.m

```

%%%%%%%%%%%%%%%%%%%%%%%%%%%%%%%%%%%%%%%%%%%%%%%%%%%%%%%%%%%%%%%%%%%%%%%%
% function [phi_0,k,R2,Erms] = model_SV(phi_n,C_n,NITER,CRITERION,DIAGRAM,REPORT)
%%%%%%%%%%%%%%%%%%%%%%%%%%%%%%%%%%%%%%%%%%%%%%%%%%%%%%%%%%%%%%%%%%%%%%%%
%%% Developed by S. Medina-Rodriguez, A. de la Torre-Vega,
%%% J.F. Fernandez-Sanchez and A. Fernandez-Gutierrez
%%% (smedina@ugr.es, atv@ugr.es, jffernan@ugr.es, albertof@ugr.es)
%%% Dpt. Analytical Chemistry / Dpt. Signal Theory Networking and Communications
%%% University of Granada, Nov 2013
%%%%%%%%%%%%%%%%%%%%%%%%%%%%%%%%%%%%%%%%%%%%%%%%%%%%%%%%%%%%%%%%%%%%%%%%
% This function provides an estimation of the parameters of the
% Stern-Volmer model given observations of photoluminiscece consisting on
% analytical signal and concentration (phi_n, C_n)
% The variable NITER indicates the number of iterations (valid only for
% criterion 'A')
% The variable CRITERION defines the calibration criterion ('A' 'B' 'C')
% The variables DIAGRAM and REPORT provides some information and plots
% while the model parameters are estimated
% The output parameters are:
% phi_0 phi_0 of Stern-Volmer model
% k k of Stern-Volmer model
% R2 Determination coefficient
% Erms RMS error for calibration data
% Stern-Volmer model:
% (phi_0/phi) = 1 + k C
%
% Procedure for optimization:
% for criteria b and c, it is a direct estimation
% for criterion a, it is a 1-D search implemented with Newton's method
%
% Example:
% C_n=[0.01 0.03 0.1 0.3 1];
% phi_n=[35 30 25 20 15];
% [phi_0,k,R2,Erms] = model_SV(phi_n,C_n,100,'c',1,1);
%%%%%%%%%%%%%%%%%%%%%%%%%%%%%%%%%%%%%%%%%%%%%%%%%%%%%%%%%%%%%%%%%%%%%%%%
function [phi_0,k,R2,Erms] = model_SV(phi_n,C_n,NITER,CRITERION,DIAGRAM,REPORT)
N=length(C_n);
if N~=length(phi_n)
    fprintf('Error: phi_n and C_n should have the same length\n');
    phi_0=[]; k=[]; R2=[]; Erms=[]; return;
end

switch lower(CRITERION)
    case 'b'
        w_n = ones(size(C_n));
        [phi_0,k,R2,Erms]=SV_estimation(phi_n,C_n,w_n,'b');
    case 'c'
        cond = C_n>0;
        if sum(cond)~=length(phi_n)
            fprintf('...Warning!: null concentration ignored for (c) criterion.\n');
            phi_n=phi_n(cond); C_n=C_n(cond);
        end
        w_n = 1./(C_n.*C_n);
        [phi_0,k,R2,Erms]=SV_estimation(phi_n,C_n,w_n,'c');
    case 'a'
        Report_iterations = 0;
        [phi_0,k,R2,Erms]=SV_estimation_a(phi_n,C_n,NITER,Report_iterations);
    otherwise
        fprintf('Error: CRITERION should be ''a'' ''A'' ''b'' ''B'' ''c'' or ''C''\n');
        phi_0=[]; k=[]; R2=[]; Erms=[]; return;
end

if DIAGRAM
    figure(DIAGRAM)
    D_phi=(max(phi_n)-min(phi_n))/200;
    x = min(phi_n):D_phi:max(phi_n);
    y = ((phi_0./x) - 1)/k;
    plot(x,y,'-r',phi_n,C_n,'ok')
    xlabel('analytical signal')
    ylabel('concentration (%)')
end
if REPORT, fprintf('St-Vol(%s): E=%4f R2=%4f phi_0=%4f k=%4f\n',...
    CRITERION,Erms,R2,phi_0,k); end;
return;
%%%%%%%%%%%%%%%%%%%%%%%%%%%%%%%%%%%%%%%%%%%%%%%%%%%%%%%%%%%%%%%%%%%%%%%%
function [phi_0,k,R2,Erms]=SV_estimation(phi_n,C_n,w_n,CRITERION)
% direct estimation of phi_0 and k for criteria (b) and (c)
p=1./phi_n;
S=sum(w_n);
Sp=sum(w_n.*p);
Sc=sum(w_n.*C_n);

```

```

Scp=sum(w_n.*C_n.*p);
Spp=sum(w_n.*p.*p);

k = (Spp*S - Sp*Sp)/(Sp*Scp - Sc*Spp);
phi_0 = (Sp + k*Scp)/Spp;

% statistical results
C_estim = (phi_0./phi_n-1)/k;
SS_res = mean(w_n.*(C_estim - C_n).^2);
Erms = sqrt(SS_res);
mu = mean(C_n);
SS_tot = mean(w_n.*(C_n - mu).^2);
R2 = 1 - SS_res/SS_tot;
if CRITERION == 'c'
    R2=1-SS_res;
end
return;
%%%%%%%%%%%%%%%%%%%%%%%%%%%%%%%%%%%%%%%%%%%%%%%%%%%%%%%%%%%%%%%%%%%%%%%%
function [phi_0,k,R2,Erms]=SV_estimation_a(phi_n,C_n,NITER,REPORT)
% iterative estimation of phi_0 and k for criterion (a)
% first step: initialization by exhaustive search
w_n=ones(size(C_n));
[phi_0,k]=SV_estimation(phi_n,C_n,w_n,'b');
k_search = k.*10.^(-1.5:0.1:1.5); % exhaustive search around "k" provided by (b) criterion
k_ref=0.0; E0_ref=1e30;
for iter = 1:length(k_search)
    [E0] = Error_estimation(phi_n,C_n,k_search(iter));
    if E0<E0_ref, E0_ref=E0; k_ref=k_search(iter); end;
    if REPORT, fprintf('Init: k=%f E=%f\n',k_search(iter),sqrt(E0)); end;
end
k=k_ref;
% using k as initialization, 1-Dim search using Newton's method:
for iter=1:NITER
    epsilon = abs(k/1000);
    x0=k; xa=x0-epsilon; xb=x0+epsilon;
    [E0,phi_0] = Error_estimation(phi_n,C_n,x0);
    [Ea] = Error_estimation(phi_n,C_n,xa);
    [Eb] = Error_estimation(phi_n,C_n,xb);
    Dx0=-epsilon/2*(Eb-Ea)/(Eb+Ea-2*E0);
    if REPORT, fprintf('Iter:%d E:%f phi_0:%f k:%f\n',iter,sqrt(E0),phi_0,k); end;
    % usually, k=k+Dx0; however Newton's method finds minima or maxima...
    % so, we analyze several options to guarantee minimization
    Dx=[1 0.5 -0.5 -1].*Dx0;
    E0_verify=E0; k0=k;
    for idx=1:4
        [E_verify] = Error_estimation(phi_n,C_n,k0+Dx(idx));
        if E_verify<E0_verify
            E0_verify=E_verify;
            k=k0+Dx(idx);
        end
    end
    if E0_verify==E0
        k=k0+0.05*Dx0;
    end
end
[E0,phi_0] = Error_estimation(phi_n,C_n,k);

% statistical results
z=1./(1+k*C_n);
phi_estim = phi_0*z;
SS_res = mean((phi_estim - phi_n).^2);
Erms = sqrt(SS_res);
mu = mean(phi_n);
SS_tot = mean((phi_n - mu).^2);
R2 = 1 - SS_res/SS_tot;
return;
%%%%%%%%%%%%%%%%%%%%%%%%%%%%%%%%%%%%%%%%%%%%%%%%%%%%%%%%%%%%%%%%%%%%%%%%
function [E,phi_0] = Error_estimation(phi_n,C_n,k)

z=1./(1+k*C_n);
phi_0 = sum(phi_n.*z)/sum(z.^2);
phi_estim = phi_0*z;
E = mean((phi_estim - phi_n).^2);
return;
%%%%%%%%%%%%%%%%%%%%%%%%%%%%%%%%%%%%%%%%%%%%%%%%%%%%%%%%%%%%%%%%%%%%%%%%

```

Function for fitting the Lehrer model: model_L.m

```

%%%%%%%%%%%%%%%%%%%%%%%%%%%%%%%%%%%%%%%%%%%%%%%%%%%%%%%%%%%%%%%%%%%%%%%%
% function [phi_0,k,x,K,R2,Erms] = model_L(phi_n,C_n,NITER,CRITERION,DIAGRAM,REPORT,LIMIT)
%%%%%%%%%%%%%%%%%%%%%%%%%%%%%%%%%%%%%%%%%%%%%%%%%%%%%%%%%%%%%%%%%%%%%%%%

```

```

%%% Developed by S. Medina-Rodriguez, A. de la Torre-Vega,
%%% J.F. Fernandez-Sanchez and A. Fernandez-Gutierrez
%%% (smedina@ugr.es, atv@ugr.es, jffernan@ugr.es, albertof@ugr.es)
%%% Dpt. Analytical Chemistry / Dpt. Signal Theory Networking and Communications
%%% University of Granada, Nov 2013
%%%%%%%%%%%%%%%%%%%%%%%%%%%%%%%%%%%%%%%%%%%%%%%%%%%%%%%%%%%%%%%%%%%%%%%%
% This function provides an estimation of the parameters of the
% Lehrer model given observations of photoluminisce consisting on
% analytical signal and concentration (phi_n, C_n)
% The variable NITER indicates the number of iterations
% The variable CRITERION defines the calibration criterion ('A' 'B' 'C')
% The variables DIAGRAM and REPORT provides some information and plots
% The variable LIMIT, when 1, forces k>=0, x>0 and x<1
% while the model parameters are estimated
% The output parameters are:
%   phi_0      phi_0 of Lehrer model
%   k          k of Lehrer model
%   x          fraction of radiative deactivation
%   K          corrected sensitivity
%   R2         Determination coefficient
%   Erms       RMS error for calibration data
% Lehrer model:
%   (phi_0/phi) = ( x / (1 + k C) + (1-x) ) .^(-1)
%
% Procedure for optimization:
%   it is a 1-D search implemented with Newton's method
%
% Example:
%   C_n=[0.01 0.03 0.1 0.3 1];
%   phi_n=[35 30 25 20 15];
%   [phi_0,k,x,K,R2,Erms] = model_L(phi_n,C_n,100,'c',1,1,0);
%%%%%%%%%%%%%%%%%%%%%%%%%%%%%%%%%%%%%%%%%%%%%%%%%%%%%%%%%%%%%%%%%%%%%%%%
function [phi_0,k,x,K,R2,Erms] = model_L(phi_n,C_n,NITER,CRITERION,DIAGRAM,REPORT,LIMIT)
N=length(C_n);
if N~=length(phi_n)
    fprintf('Error: phi_n and C_n should have the same length\n');
    phi_0=[]; k=[]; x=[]; K=[]; R2=[]; Erms=[]; return;
end

Report_iterations = 0;
switch lower(CRITERION)
    case 'b'
        w_n = ones(size(C_n));
        [phi_0,k,x,R2,Erms]=L_estimation(phi_n,C_n,w_n,'b',NITER,Report_iterations,LIMIT);
    case 'c'
        cond = C_n>0;
        if sum(cond)~=length(phi_n)
            fprintf('...Warning!: null concentration ignored for (c) criterion.\n');
            phi_n=phi_n(cond); C_n=C_n(cond);
        end
        w_n = 1./(C_n.*C_n);
        [phi_0,k,x,R2,Erms]=L_estimation(phi_n,C_n,w_n,'c',NITER,Report_iterations,LIMIT);
    case 'a'
        [phi_0,k,x,R2,Erms]=L_estimation_a(phi_n,C_n,NITER,Report_iterations,LIMIT);
    otherwise
        fprintf('Error: CRITERION should be ''a'' ''A'' ''b'' ''B'' ''c'' or ''C''\n');
        phi_0=[]; k=[]; x=[]; K=[]; R2=[]; Erms=[]; return;
end

K=k*x;
if DIAGRAM
    figure(DIAGRAM)
    D_phi=(max(phi_n)-min(phi_n))/200;
    x_grafica = min(phi_n):D_phi:max(phi_n);
    A=phi_0-x_grafica;
    B=(x_grafica-phi_0+x*phi_0)*k;
    y=A./B;
    plot(x_grafica,y,'-r',phi_n,C_n,'ok')
    xlabel('analytical signal')
    ylabel('concentration (%)')
end
if REPORT
    fprintf('Lehrer(%s): E=%.4f R2=%.4f phi_0=%.4f k=%.4f x=%.4f K=%.4f\n',...
        CRITERION,Erms,R2,phi_0,k,x,K);
end
return;
%%%%%%%%%%%%%%%%%%%%%%%%%%%%%%%%%%%%%%%%%%%%%%%%%%%%%%%%%%%%%%%%%%%%%%%%
function [phi_0,k,x,R2,Erms]=L_estimation(phi_n,C_n,w_n,CRITERION,NITER,REPORT,LIMIT)
% iterative estimation of phi_0 and k for criteria (b) and (c)
kl=1;
kl_search = kl.*10.^(-4:0.25:4); % exhaustive search around "kl"
kl_ref=0.0; E0_ref=1e30;
for iter = 1:length(kl_search)
    [E0] = Error_estimation_L_bc(phi_n,C_n,w_n,kl_search(iter),LIMIT);
end

```

```

    if E0<E0_ref, E0_ref=E0; k1_ref=k1_search(iter); end;
    if REPORT, fprintf('Init: k1=%f   E=%f\n',k1_search(iter),sqrt(E0)); end;
end
k1=k1_ref;
% using k1 as initialization, 1-Dim search using Newton's method:
for iter=1:NITER
    epsilon = abs(k1/1000);
    x0=k1; xa=x0-epsilon; xb=x0+epsilon;
    [E0,phi_0,k,x] = Error_estimation_L_bc(phi_n,C_n,w_n,x0,LIMIT);
    [Ea] = Error_estimation_L_bc(phi_n,C_n,w_n,xa,LIMIT);
    [Eb] = Error_estimation_L_bc(phi_n,C_n,w_n,xb,LIMIT);
    Dx0=-epsilon/2*(Eb-Ea)/(Eb+Ea-2*E0);
    if REPORT, fprintf('Iter:%d E:%f phi_0:%f k:%f x:%f k1=%f\n',iter,sqrt(E0),phi_0,k,x,k1); end;
    % usually, k1=k1+Dx0; however Newton's method finds minima or maxima...
    % so, we analyze several options to guarantee minimization
    Dx=[1 0.5 -0.5 -1].*Dx0;
    E0_verify=E0; k0=k1;
    for idx=1:4
        [E_verify] = Error_estimation_L_bc(phi_n,C_n,w_n,k0+Dx(idx),LIMIT);
        if E_verify<E0_verify
            E0_verify=E_verify;
            k1=k0+Dx(idx);
        end
    end
    if E0_verify==E0
        k1=k0+0.05*Dx0;
    end
end
[E0,phi_0,k,x] = Error_estimation_L_bc(phi_n,C_n,w_n,k1,LIMIT);

% statistical results
A=phi_0-phi_n;
B=(phi_n-phi_0+x*phi_0)*k;
C_estim = A./B;
SS_res = mean(w_n.*(C_estim - C_n).^2);
Erms = sqrt(SS_res);
mu = mean(C_n);
SS_tot = mean(w_n.*(C_n - mu).^2);
R2 = 1 - SS_res/SS_tot;
if CRITERION == 'c'
    R2=1-SS_res;
end
return;
%%%%%%%%%%%%%%%%%%%%%%%%%%%%%%%%%%%%%%%%%%%%%%%%%%%%%%%%%%%%%%%%%%%%%%%%
function [phi_0,k,x,R2,Erms]=L_estimation_a(phi_n,C_n,NITER,REPORT,LIMIT)
% iterative estimation of phi_0 and k for criterion (a)
k=1;
k_search = k.*10.^(-4:0.25:4); % exhaustive search around "k"
k_ref=0.0; E0_ref=1e30;
for iter = 1:length(k_search)
    [E0] = Error_estimation_L_a(phi_n,C_n,k_search(iter),LIMIT);
    if E0<E0_ref, E0_ref=E0; k_ref=k_search(iter); end;
    if REPORT, fprintf('Init: k1=%f   E=%f\n',k_search(iter),sqrt(E0)); end;
end
k=k_ref;
% using k as initialization, 1-Dim search using Newton's method:
for iter=1:NITER
    epsilon = abs(k/1000);
    x0=k; xa=x0-epsilon; xb=x0+epsilon;
    [E0,phi_0,x] = Error_estimation_L_a(phi_n,C_n,x0,LIMIT);
    [Ea] = Error_estimation_L_a(phi_n,C_n,xa,LIMIT);
    [Eb] = Error_estimation_L_a(phi_n,C_n,xb,LIMIT);
    Dx0=-epsilon/2*(Eb-Ea)/(Eb+Ea-2*E0);
    if REPORT, fprintf('Iter:%d E:%f phi_0:%f k:%f x:%f\n',iter,sqrt(E0),phi_0,k,x); end;
    % usually, k=k+Dx0; however Newton's method finds minima or maxima...
    % so, we analyze several options to guarantee minimization
    Dx=[1 0.5 -0.5 -1].*Dx0;
    E0_verify=E0; k0=k;
    for idx=1:4
        [E_verify] = Error_estimation_L_a(phi_n,C_n,k0+Dx(idx),LIMIT);
        if E_verify<E0_verify
            E0_verify=E_verify;
            k=k0+Dx(idx);
        end
    end
    if E0_verify==E0
        k=k0+0.05*Dx0;
    end
end
[E,phi_0,x] = Error_estimation_L_a(phi_n,C_n,k,LIMIT);

% statistical results
z=x./(1+k*C_n);
phi_estim = phi_0*(z+1-x);

```

```

SS_res = mean((phi_estim - phi_n).^2);
Erms = sqrt(SS_res);
mu = mean(phi_n);
SS_tot = mean((phi_n - mu).^2);
R2 = 1 - SS_res/SS_tot;
return;
%%%%%%%%%%%%%%%%%%%%%%%%%%%%%%%%%%%%%%%%%%%%%%%%%%%%%%%%%%%%%%%%%%%%%%%%
function [E,phi_0,k,x] = Error_estimation_L_bc(phi_n,C_n,w_n,k1,LIMIT)
% definitions
z=1./(k1*phi_n-1);
S=sum(w_n);
Sz=sum(w_n.*z);
Sc=sum(w_n.*C_n);
Scz=sum(w_n.*C_n.*z);
Szz=sum(w_n.*z.*z);
% estimations
b0=(Scz*Sz-Sc*Szz)/(Szz*S-Sz*Sz);
b1=(b0*Sz+Sc)/Szz;
% model for k1 and error
k=1/b0; phi_0=(b1+b0)/(k1*b0); x=b1/(b1+b0);
if LIMIT
    if x<=0, x=0.00001; end;
    if x>=1, x=0.99999; end;
    b1=x/(k*(1-x)); phi_0=(b1+b0)/(k1*b0);
end
C_estim = b1./(k1*phi_n - 1) - b0;
E = mean(w_n.*(C_estim - C_n).^2);
return;
%%%%%%%%%%%%%%%%%%%%%%%%%%%%%%%%%%%%%%%%%%%%%%%%%%%%%%%%%%%%%%%%%%%%%%%%
function [E,phi_0,x] = Error_estimation_L_a(phi_n,C_n,k,LIMIT)
% definitions
z=k*C_n./(1+k*C_n);
N=length(phi_n);
Sf=sum(phi_n);
Sz=sum(z);
Szf=sum(z.*phi_n);
Szz=sum(z.*z);
% estimations
x=(N*Szf-Sz*Sf)/(Sz*Szf-Szz*Sf);
if LIMIT
    if x<=0, x=0.00001; end;
    if x>=1, x=0.99999; end;
end
phi_0=Szf/(Sz-x*Szz);
% model for k1 and error
phi_estim = phi_0*(x./(1+k*C_n) + (1-x));
E = mean((phi_estim - phi_n).^2);
return;
%%%%%%%%%%%%%%%%%%%%%%%%%%%%%%%%%%%%%%%%%%%%%%%%%%%%%%%%%%%%%%%%%%%%%%%%

```

Function for fitting the Demas model: model_D.m

```

%%%%%%%%%%%%%%%%%%%%%%%%%%%%%%%%%%%%%%%%%%%%%%%%%%%%%%%%%%%%%%%%%%%%%%%%
% function [phi_0,k1,k2,x,K,R2,Erms] = model_D(phi_n,C_n,NITER,CRITERION,DIAGRAM,REPORT,LIMIT)
%%%%%%%%%%%%%%%%%%%%%%%%%%%%%%%%%%%%%%%%%%%%%%%%%%%%%%%%%%%%%%%%%%%%%%%%
%% Developed by S. Medina-Rodriguez, A. de la Torre-Vega,
%% J.F. Fernandez-Sanchez and A. Fernandez-Gutierrez
%% (smedina@ugr.es, atv@ugr.es, jffernan@ugr.es, albertof@ugr.es)
%% Dpt. Analytical Chemistry / Dpt. Signal Theory Networking and Communications
%% University of Granada, Nov 2013
%%%%%%%%%%%%%%%%%%%%%%%%%%%%%%%%%%%%%%%%%%%%%%%%%%%%%%%%%%%%%%%%%%%%%%%%
% This function provides an estimation of the parameters of the
% Demas model given observations of photoluminiscece consisting on
% analytical signal and concentration (phi_n, C_n)
% The variable NITER indicates the number of iterations
% The variable CRITERION defines the calibration criterion ('A' 'B' 'C')
% The variables DIAGRAM and REPORT provides some information and plots
% The variable LIMIT, when 1, forces k1>k2, k2>=0, x>0 and x<1
% while the model parameters are estimated
% The output parameters are:
% phi_0 phi_0 of Demas model
% k1 k of Demas model 1st site
% k2 k of Demas model 2nd site
% x fraction of 1st site / 2nd site
% K corrected sensitivity
% R2 Determination coefficient
% Erms RMS error for calibration data
% Demas model:
% (phi_0/phi) = ( x / (1 + k1 C) + (1-x) / (1 + k2 C) ).^(-1)
%
% Procedure for optimization:

```



```

% it is a 2-D search implemented with Newton's method
%
% Example:
% C_n=[0.01 0.03 0.1 0.3 1];
% phi_n=[35 30 25 20 15];
% [phi_0,k1,k2,x,K,R2,Erms] = model_D(phi_n,C_n,500,'c',1,1,0);
%%%%%%%%%%%%%%%%%%%%%%%%%%%%%%%%%%%%%%%%%%%%%%%%%%%%%%%%%%%%%%%%%%%%%%%%
function [phi_0,k1,k2,x,K,R2,Erms] = model_D(phi_n,C_n,NITER,CRITERION,DIAGRAM,REPORT,LIMIT)
N=length(C_n);
if N~=length(phi_n)
    fprintf('Error: phi_n and C_n should have the same length\n');
    phi_0=[]; k1=[]; k2=[]; x=[]; K=[]; R2=[]; Erms=[]; return;
end

Report_iterations = 0;
switch lower(CRITERION)
    case 'b'
        w_n = ones(size(C_n));
        [phi_0,k1,k2,x,R2,Erms]=D_estimation_bc(phi_n,C_n,w_n,'b',NITER,Report_iterations,LIMIT);
    case 'c'
        cond = C_n>0;
        if sum(cond)~=length(phi_n)
            fprintf('...Warning!: null concentration ignored for (c) criterion.\n');
            phi_n=phi_n(cond); C_n=C_n(cond);
        end
        w_n = 1./(C_n.*C_n);
        [phi_0,k1,k2,x,R2,Erms]=D_estimation_bc(phi_n,C_n,w_n,'c',NITER,Report_iterations,LIMIT);
    case 'a'
        w_n = ones(size(C_n));
        [phi_0,k1,k2,x,R2,Erms]=D_estimation_a(phi_n,C_n,w_n,NITER,Report_iterations,LIMIT);
    otherwise
        fprintf('Error: CRITERION should be ''a'' ''A'' ''b'' ''B'' ''c'' or ''C''\n');
        phi_0=[]; k1=[]; k2=[]; x=[]; K=[]; R2=[]; Erms=[]; return;
end

K=k1*x+k2*(1-x);
if DIAGRAM
    figure(DIAGRAM)
    D_phi=(max(phi_n)-min(phi_n))/200;
    x_grafica = min(phi_n):D_phi:max(phi_n);
    y=estimation_C_demas(x_grafica,phi_0,k1,k2,x);
    plot(x_grafica,y,'-r',phi_n,C_n,'ok')
    xlabel('analytical signal')
    ylabel('concentration (%)')
end
if REPORT
    fprintf('Demas(%s): E=%4f R2=%4f phi_0=%4f k1=%4f k2=%4f x=%4f K=%4f\n',...
        CRITERION,Erms,R2,phi_0,k1,k2,x,K);
end
return;
%%%%%%%%%%%%%%%%%%%%%%%%%%%%%%%%%%%%%%%%%%%%%%%%%%%%%%%%%%%%%%%%%%%%%%%%
function [C]=estimation_C_demas(phi_n,phi_0,k1,k2,x)
a = k1*k2*phi_n;
b = (k1+k2)*phi_n - k1*phi_0 - x*k2*phi_0 + x*k1*phi_0;
c = phi_n - phi_0;
R=b.*b-4*a.*c;
C=(-b+sqrt(R))./(2*a);
return;
%%%%%%%%%%%%%%%%%%%%%%%%%%%%%%%%%%%%%%%%%%%%%%%%%%%%%%%%%%%%%%%%%%%%%%%%
function [phi_0,k1,k2,x,R2,Erms]=D_estimation_bc(phi_n,C_n,w_n,CRITERION,NITER,REPORT,LIMIT)
% iterative estimation of k1 and k2 for criteria (b) and (c)
% first step: initialization with Demas(a)
w_a=ones(size(C_n));
[phi_0,k1,k2,x]=D_estimation_a(phi_n,C_n,w_a,ceil(NITER/2),0,LIMIT);
% reestimation of weights:
for iter=1:5
    A1=phi_0*x*k1./(1+k1*C_n).^2;
    A2=phi_0*(1-x)*k2./(1+k2*C_n).^2;
    w_a=w_n.*(A1+A2).^(-2);
    [phi_0,k1,k2,x]=D_estimation_a(phi_n,C_n,w_a,ceil(NITER/5),0,LIMIT);
    C_estim=estimation_C_demas(phi_n,phi_0,k1,k2,x);
    E0=mean(w_n.*(C_estim - C_n).^2);
    if REPORT, fprintf('Iter:%d E:%f phi_0:%f k1:%f k2:%f x:%f\n',iter*ceil(NITER/5),sqrt(E0),phi_0,k1,k2,x); end;
end

% statistical results
C_estim=estimation_C_demas(phi_n,phi_0,k1,k2,x);
SS_res = mean(w_n.*(C_estim - C_n).^2);
Erms = sqrt(SS_res);
mu = mean(C_n);
SS_tot = mean(w_n.*(C_n - mu).^2);
R2 = 1 - SS_res/SS_tot;
if CRITERION == 'c'
    R2=1-SS_res;
end

```

```

end
return;
%%%%%%%%%%%%%%%%%%%%%%%%%%%%%%%%%%%%%%%%%%%%%%%%%%%%%%%%%%%%%%%%%%%%%%%%
function [phi_0,k1,k2,x,R2,Erms]=D_estimation_a(phi_n,C_n,w_n,NITER,REPORT,LIMIT)
% iterative estimation of k1 and k2 for criterion (a)
% initialization with Lehrer model:
[phi_0,k] = model_L(phi_n,C_n,100,'a',0,0,LIMIT);
k1=k;
k2=k/100;

% using k1 and k2 as initialization, 2-Dim search using Newton's method:
for iter=1:NITER
% estimation of k1
epsilon = abs(k1/1000);
x0=k1; xa=x0-epsilon; xb=x0+epsilon;
[E0,phi_0,x] = Error_estimation_D_a(phi_n,C_n,w_n,x0,k2,LIMIT);
[Ea] = Error_estimation_D_a(phi_n,C_n,w_n,xa,k2,LIMIT);
[Eb] = Error_estimation_D_a(phi_n,C_n,w_n,xb,k2,LIMIT);
Dx0=-epsilon/2*(Eb-Ea)/(Eb+Ea-2*E0);
if REPORT, fprintf('Iter:%d E:%f phi_0:%f k1:%f k2:%f x:%f\n',iter,sqrt(E0),phi_0,k1,k2,x); end;
% usually, k=k+Dx0; however Newton's method finds minima or maxima...
% so, we analyze several options to guarantee minimization
Dx=[1 0.5 -0.5 -1].*Dx0;
E0_verify=E0; k0=k1;
for idx=1:4
[E_verify] = Error_estimation_D_a(phi_n,C_n,w_n,k0+Dx(idx),k2,LIMIT);
if E_verify<E0_verify && (k0+Dx(idx))>1.001*k2 % k1>k2 is forced
if LIMIT
if k0+Dx(idx)>0, E0_verify=E_verify; k1=k0+Dx(idx); end;
else
E0_verify=E_verify; k1=k0+Dx(idx);
end
end
end
if E0_verify==E0 && k0+0.005*Dx0>0
k1=k0+0.005*Dx0;
end
% estimation of k2
epsilon = abs(k2/1000);
x0=k2; xa=x0-epsilon; xb=x0+epsilon;
[E0,phi_0,x] = Error_estimation_D_a(phi_n,C_n,w_n,k1,x0,LIMIT);
[Ea] = Error_estimation_D_a(phi_n,C_n,w_n,k1,xa,LIMIT);
[Eb] = Error_estimation_D_a(phi_n,C_n,w_n,k1,xb,LIMIT);
Dx0=-epsilon/2*(Eb-Ea)/(Eb+Ea-2*E0);
if REPORT, fprintf('Iter:%d E:%f phi_0:%f k1:%f k2:%f x:%f\n',iter,sqrt(E0),phi_0,k1,k2,x); end;
% usually, k=k+Dx0; however Newton's method finds minima or maxima...
% so, we analyze several options to guarantee minimization
Dx=[1 0.5 -0.5 -1].*Dx0;
E0_verify=E0; k0=k2;
for idx=1:4
[E_verify] = Error_estimation_D_a(phi_n,C_n,w_n,k1,k0+Dx(idx),LIMIT);
if E_verify<E0_verify && (k0+Dx(idx))<0.999*k1 % k1>k2 is forced
if LIMIT
if k0+Dx(idx)>0, E0_verify=E_verify; k2=k0+Dx(idx); end;
else
E0_verify=E_verify; k2=k0+Dx(idx);
end
end
end
if E0_verify==E0 && k0+0.005*Dx0>0
k2=k0+0.005*Dx0;
end
end
[E,phi_0,x] = Error_estimation_D_a(phi_n,C_n,w_n,k1,k2,LIMIT);

% statistical results
z=x./(1+k1*C_n)+(1-x)./(1+k2*C_n);
phi_estim = phi_0*z;
SS_res = mean((phi_estim - phi_n).^2);
Erms = sqrt(SS_res);
mu = mean(phi_n);
SS_tot = mean((phi_n - mu).^2);
R2 = 1 - SS_res/SS_tot;
return;
%%%%%%%%%%%%%%%%%%%%%%%%%%%%%%%%%%%%%%%%%%%%%%%%%%%%%%%%%%%%%%%%%%%%%%%%
function [E,phi_0,x] = Error_estimation_D_a(phi_n,C_n,w_n,k1,k2,LIMIT)
% definitions
y=1./(1+k2*C_n);
z=1./(1+k1*C_n)-1./(1+k2*C_n);
Szf=sum(w_n.*z.*phi_n);
Syf=sum(w_n.*y.*phi_n);
Szy=sum(w_n.*z.*y);
Syy=sum(w_n.*y.*y);
Szz=sum(w_n.*z.*z);

```

```

% estimations
x=(Syf*Szy-Syy*Szf)/(Szy*Szf-Szz*Syf);
if LIMIT
    if x<=0, x=0.00001; end;
    if x>=1, x=0.99999; end;
end
phi_0=Szf/(x*Szz+Szy);
% model for k1 and error
phi_estim = phi_0*(x./(1+k1*C_n) + (1-x)./(1+k2*C_n));
E = mean(w_n.*(phi_estim - phi_n).^2);
return;
%%%%%%%%%%%%%%%%%%%%%%%%%%%%%%%%%%%%%%%%%%%%%%%%%%%%%%%%%%%%%%%%%%%%%%%%

```

Function for fitting the Polynomial model 2nd order: model_P2.m

```

%%%%%%%%%%%%%%%%%%%%%%%%%%%%%%%%%%%%%%%%%%%%%%%%%%%%%%%%%%%%%%%%%%%%%%%%
% function [a0,a1,a2,PHI_0,K,R2,Erms] = model_P2(phi_n,C_n,NITER,CRITERION,DIAGRAM,REPORT)
%%%%%%%%%%%%%%%%%%%%%%%%%%%%%%%%%%%%%%%%%%%%%%%%%%%%%%%%%%%%%%%%%%%%%%%%
%%% Developed by S. Medina-Rodriguez, A. de la Torre-Vega,
%%% J.F. Fernandez-Sanchez and A. Fernandez-Gutierrez
%%% (smedina@ugr.es, atv@ugr.es, jffernan@ugr.es, albertof@ugr.es)
%%% Dpt. Analytical Chemistry / Dpt. Signal Theory Networking and Communications
%%% University of Granada, Nov 2013
%%%%%%%%%%%%%%%%%%%%%%%%%%%%%%%%%%%%%%%%%%%%%%%%%%%%%%%%%%%%%%%%%%%%%%%%
% This function provides an estimation of the parameters of the
% 2nd order Polynomic model (P2) given observations of
% photoluminiscece consisting on analytical signal and concentration (phi_n, C_n)
% The variable NITER indicates the number of iterations
% The variable CRITERION defines the calibration criterion ('A' 'B' 'C')
% The variables DIAGRAM and REPORT provides some information and plots
% while the model parameters are estimated
% The output parameters are:
%   a0,a1,a2   The polynomial coefficients
%   PHI_0      The response of the model at null concentration
%   K          The sensitivity of the model
%   R2         Determination coefficient
%   Erms       RMS error for calibration data
% PE2 model:
%   C = a0 + a1 / phi + a2 / phi^2
%
% Procedure for optimization:
%   it is a direct estimation for criteria (b) and (c);
%   it is an iterative procedure for criterion (a)
%
% Example:
%   C_n=[0.01 0.03 0.1 0.3 1];
%   phi_n=[35 30 25 20 15];
%   [a0,a1,a2,PHI_0,K,R2,Erms] = model_P2(phi_n,C_n,100,'c',1,1);
%%%%%%%%%%%%%%%%%%%%%%%%%%%%%%%%%%%%%%%%%%%%%%%%%%%%%%%%%%%%%%%%%%%%%%%%
function [a0,a1,a2,PHI_0,K,R2,Erms] = model_P2(phi_n,C_n,NITER,CRITERION,DIAGRAM,REPORT)
N=length(C_n);
if N~=length(phi_n)
    fprintf('Error: phi_n and C_n should have the same length\n');
    a0=[]; a1=[]; a2=[]; K=[]; PHI_0=[]; R2=[]; Erms=[]; return;
end

Report_iterations = 0;
switch lower(CRITERION)
    case 'b'
        w_n = ones(size(C_n));
        [a0,a1,a2,R2,Erms]=P2_estimation_bc(phi_n,C_n,w_n,'b');
    case 'c'
        cond = C_n>0;
        if sum(cond)~=length(phi_n)
            fprintf('...Warning!: null concentration ignored for (c) criterion.\n');
            phi_n=phi_n(cond); C_n=C_n(cond);
        end
        w_n = 1./(C_n.*C_n);
        [a0,a1,a2,R2,Erms]=P2_estimation_bc(phi_n,C_n,w_n,'c');
    case 'a'
        [a0,a1,a2,R2,Erms]=P2_estimation_a(phi_n,C_n,NITER,Report_iterations);
    otherwise
        fprintf('Error: CRITERION should be ''a'' ''A'' ''b'' ''B'' ''c'' or ''C''\n');
        a0=[]; a1=[]; a2=[]; K=[]; PHI_0=[]; R2=[]; Erms=[]; return;
end

PHI_0 = ((-a1 + sqrt(a1*a1-4*a0*a2))/(2*a2))^( -1);
K = abs(1/(a1*PHI_0^( -1)+2*a2*PHI_0^( -2)));
if DIAGRAM
    figure(DIAGRAM)
    D_phi=(max(phi_n)-min(phi_n))/200;

```

```

x_grafica = min(phi_n):D_phi:max(phi_n);
y=a0+a1*x_grafica.^(-1)+a2*x_grafica.^(-2);
plot(x_grafica,y,'-r',phi_n,C_n,'ok')
xlabel('analytical signal')
ylabel('concentration (%)')
end
if REPORT
    fprintf('Pol-2(%s): E=%4f R2=%4f a0=%4f a1=%4f a2=%4f PHI_0=%4f K=%4f\n',...
        CRITERION,Erms,R2,a0,a1,a2,PHI_0,K);
end
return;
%%%%%%%%%%%%%%%%%%%%%%%%%%%%%%%%%%%%%%%%%%%%%%%%%%%%%%%%%%%%%%%%%%%%%%%%
function [a0,a1,a2,R2,Erms]=P2_estimation_a(phi_n,C_n,NITER,REPORT)
% pre-scaling
phi_scale=max(phi_n);
phi_n=phi_n/phi_scale;
% iterative estimation for criterion (a)
% first step: initalization with P2(c)
w_a=zeros(size(C_n));
cond=C_n>0;
w_a(cond)=1./(C_n(cond).^2);
[a0,a1,a2]=P2_estimation_bc(phi_n,C_n,w_a,'c');
% reestimation of weights and new iterations:
for iter=1:NITER
    w_a=(a1./(phi_n.^2)+2*a2./(phi_n.^3)).^(-2);
    [a0,a1,a2,R2,Erms]=P2_estimation_bc(phi_n,C_n,w_a,'c');
    if REPORT, fprintf('Iter:%d E:%f a0:%f a1:%f a2:%f\n',iter,Erms,a0,a1,a2); end;
end
% de-scaling
phi_n=phi_n*phi_scale;
a1=a1*phi_scale;
a2=a2*phi_scale*phi_scale;
% statistical results
phi_estim = ((-a1+sqrt(a1*a1-4*a2*(a0-C_n)))/(2*a2)).^(-1);
SS_res = mean((phi_estim - phi_n).^2);
Erms = sqrt(SS_res);
mu = mean(phi_n);
SS_tot = mean((phi_n - mu).^2);
R2 = 1 - SS_res/SS_tot;
return;
%%%%%%%%%%%%%%%%%%%%%%%%%%%%%%%%%%%%%%%%%%%%%%%%%%%%%%%%%%%%%%%%%%%%%%%%
function [a0,a1,a2,R2,Erms]=P2_estimation_bc(phi_n,C_n,w_n,CRITERION)
% pre-scaling
phi_scale=max(phi_n);
phi_n=phi_n/phi_scale;
alpha=-1;
[E0,a0,a1,a2] = Error_estimation_PE2_bc(phi_n,C_n,w_n,alpha);
% de-scaling
phi_n=phi_n*phi_scale;
a1=a1/phi_scale^alpha;
a2=a2/phi_scale^(2+alpha);
% statistical results
C_estim=a0+a1*phi_n.^alpha+a2*phi_n^(2+alpha);
SS_res = mean(w_n.*(C_estim - C_n).^2);
Erms = sqrt(SS_res);
mu = mean(C_n);
SS_tot = mean(w_n.*(C_n - mu).^2);
R2 = 1 - SS_res/SS_tot;
if CRITERION == 'c'
    R2=1-SS_res;
end
return;
%%%%%%%%%%%%%%%%%%%%%%%%%%%%%%%%%%%%%%%%%%%%%%%%%%%%%%%%%%%%%%%%%%%%%%%%
function [E,a0,a1,a2] = Error_estimation_PE2_bc(phi_n,C_n,w_n,alpha)
% definitions
f=phi_n.^alpha;
X=ones(size(C_n));
Xf=X.*f; Xff=Xf.*f; Xfff=Xff.*f; Xffff=Xfff.*f;
Xc=C_n; Xcf=Xc.*f; Xcff=Xcf.*f;
% elements of matrices
A0=sum(w_n.*X); A1=sum(w_n.*Xf); A2=sum(w_n.*Xff);
A3=sum(w_n.*Xfff); A4=sum(w_n.*Xffff);
B0=sum(w_n.*Xc); B1=sum(w_n.*Xcf); B2=sum(w_n.*Xcff);
% matrices
A=[A0 A1 A2; A1 A2 A3; A2 A3 A4];
B=[B0; B1; B2];
% coeficients a0 a1 a2:
x=A\B; a0=x(1); a1=x(2); a2=x(3);
% error estimation
C_estim = a0 + a1*f + a2*f.*f;
E=mean(w_n.*(C_estim-C_n).^2);
return;
%%%%%%%%%%%%%%%%%%%%%%%%%%%%%%%%%%%%%%%%%%%%%%%%%%%%%%%%%%%%%%%%%%%%%%%%

```

Function for fitting the Polynomial-Exponent model 1st order: model_PE1.m

```

%%%%%%%%%%%%%%%%%%%%%%%%%%%%%%%%%%%%%%%%%%%%%%%%%%%%%%%%%%%%%%%%%%%%%%%%
% function [a0,a1,alpha,PHI_0,K,R2,Erms] = model_PE1(phi_n,C_n,NITER,CRITERION,DIAGRAM,REPORT)
%%%%%%%%%%%%%%%%%%%%%%%%%%%%%%%%%%%%%%%%%%%%%%%%%%%%%%%%%%%%%%%%%%%%%%%%
%%% Developed by S. Medina-Rodriguez, A. de la Torre-Vega,
%%% J.F. Fernandez-Sanchez and A. Fernandez-Gutierrez
%%% (smedina@ugr.es, atv@ugr.es, jffernan@ugr.es, albertof@ugr.es)
%%% Dpt. Analytical Chemistry / Dpt. Signal Theory Networking and Communications
%%% University of Granada, Nov 2013
%%%%%%%%%%%%%%%%%%%%%%%%%%%%%%%%%%%%%%%%%%%%%%%%%%%%%%%%%%%%%%%%%%%%%%%%
% This function provides an estimation of the parameters of the
% 1st order Polynomial-Exponent model (PE1) given observations of
% photoluminescence consisting on analytical signal and concentration (phi_n, C_n)
% The variable NITER indicates the number of iterations
% The variable CRITERION defines the calibration criterion ('A' 'B' 'C')
% The variables DIAGRAM and REPORT provides some information and plots
% while the model parameters are estimated
% The output parameters are:
%   a0,a1      The polynomial coefficients
%   alpha      The exponent
%   PHI_0      The response of the model at null concentration
%   K          The sensitivity of the model
%   R2         Determination coefficient
%   Erms       RMS error for calibration data
% PE2 model:
%   C = a0 + a1 phi^alpha
%
% Procedure for optimization:
%   it is a 1-D search implemented with Newton's method
%
% Example:
%   C_n=[0.01 0.03 0.1 0.3 1];
%   phi_n=[35 30 25 20 15];
%   [a0,a1,alpha,PHI_0,K,R2,Erms] = model_PE1(phi_n,C_n,100,'c',1,1);
%%%%%%%%%%%%%%%%%%%%%%%%%%%%%%%%%%%%%%%%%%%%%%%%%%%%%%%%%%%%%%%%%%%%%%%%
function [a0,a1,alpha,PHI_0,K,R2,Erms] = model_PE1(phi_n,C_n,NITER,CRITERION,DIAGRAM,REPORT)
N=length(C_n);
if N~=length(phi_n)
    fprintf('Error: phi_n and C_n should have the same length\n');
    a0=[]; a1=[]; alpha=[]; K=[]; PHI_0=[]; R2=[]; Erms=[]; return;
end

Report_iterations = 0;
switch lower(CRITERION)
    case 'b'
        w_n = ones(size(C_n));
        [a0,a1,alpha,R2,Erms]=PE1_estimation_bc(phi_n,C_n,w_n,'b',NITER,Report_iterations);
    case 'c'
        cond = C_n>0;
        if sum(cond)~=length(phi_n)
            fprintf('...Warning!: null concentration ignored for (c) criterion.\n');
            phi_n=phi_n(cond); C_n=C_n(cond);
        end
        w_n = 1./(C_n.*C_n);
        [a0,a1,alpha,R2,Erms]=PE1_estimation_bc(phi_n,C_n,w_n,'c',NITER,Report_iterations);
    case 'a'
        [a0,a1,alpha,R2,Erms]=PE1_estimation_a(phi_n,C_n,NITER,Report_iterations);
    otherwise
        fprintf('Error: CRITERION should be ''a'' ''A'' ''b'' ''B'' ''c'' or ''C''\n');
        a0=[]; a1=[]; alpha=[]; K=[]; PHI_0=[]; R2=[]; Erms=[]; return;
end

PHI_0 = (-a0/a1).^(1/alpha);
K = abs(1/(a0*alpha));
if DIAGRAM
    figure(DIAGRAM)
    D_phi=(max(phi_n)-min(phi_n))/200;
    x_grafica = min(phi_n):D_phi:max(phi_n);
    y=a0+a1*x_grafica.^alpha;
    plot(x_grafica,y,'-r',phi_n,C_n,'ok')
    xlabel('analytical signal')
    ylabel('concentration (%)')
end
if REPORT
    fprintf('Pol.E-1(%s): E=%4f R2=%4f a0=%4f a1=%4f alpha=%4f PHI_0=%4f K=%f\n',...
        CRITERION,Erms,R2,a0,a1,alpha,PHI_0,K);
end
return;
%%%%%%%%%%%%%%%%%%%%%%%%%%%%%%%%%%%%%%%%%%%%%%%%%%%%%%%%%%%%%%%%%%%%%%%%
function [a0,a1,alpha,R2,Erms]=PE1_estimation_a(phi_n,C_n,NITER,REPORT)

```

```

% pre-scaling
phi_scale=max(phi_n);
phi_n=phi_n/phi_scale;
% iterative estimation of alpha for criterion (a)
% first step: initialization with PE2(c)
w_a=zeros(size(C_n));
cond=C_n>0;
w_a(cond)=1./(C_n(cond).^2);
[a0,a1,alpha]=PE1_estimation_bc(phi_n,C_n,w_a,'c',ceil(NITER/2),0);
% reestimation of weights and new iterations:
for iter=1:5
    f1=phi_n.^(alpha-1);
    w_a=(abs(a1*alpha*f1)).^(-2);
    [a0,a1,alpha]=PE1_estimation_bc(phi_n,C_n,w_a,'c',ceil(NITER/5),0);
    phi_estim = ((C_n-a0)/a1).^(1/alpha);
    E0=mean((phi_estim - phi_n).^2);
    if REPORT, fprintf('Iter:%d E:%f a0:%f a1:%f alpha:%f\n',iter*ceil(NITER/5),sqrt(E0),a0,a1,alpha); end;
end
% de-scaling
phi_n=phi_n*phi_scale;
a1=a1/phi_scale^alpha;
% statistical results
phi_estim = ((C_n-a0)/a1).^(1/alpha);
SS_res = mean((phi_estim - phi_n).^2);
Erms = sqrt(SS_res);
mu = mean(phi_n);
SS_tot = mean((phi_n - mu).^2);
R2 = 1 - SS_res/SS_tot;
return;
%%%%%%%%%%%%%%%%%%%%%%%%%%%%%%%%%%%%%%%%%%%%%%%%%%%%%%%%%%%%%%%%%%%%%%%%
function [a0,a1,alpha,R2,Erms]=PE1_estimation_bc(phi_n,C_n,w_n,CRITERION,NITER,REPORT)
% pre-scaling
phi_scale=max(phi_n);
phi_n=phi_n/phi_scale;
% initialization of alpha:
alpha_search = -1.*10.^(-2:0.1:2); % exhaustive search around -1
alpha_ref=0.0; E0_ref=1e30;
warning('off');
for iter = 1:length(alpha_search)
    [E0] = Error_estimation_PE1_bc(phi_n,C_n,w_n,alpha_search(iter));
    if E0<E0_ref, E0_ref=E0; alpha_ref=alpha_search(iter); end;
    if REPORT, fprintf('Init: alpha=%f E=%f\n',alpha_search(iter),sqrt(E0)); end;
end
warning('on');
alpha=alpha_ref;
% using alpha as initialization, 1-Dim search using Newton's method:
for iter=1:NITER
    epsilon = abs(alpha/1000);
    x0=alpha; xa=x0-epsilon; xb=x0+epsilon;
    [E0,a0,a1] = Error_estimation_PE1_bc(phi_n,C_n,w_n,x0);
    [Ea] = Error_estimation_PE1_bc(phi_n,C_n,w_n,xa);
    [Eb] = Error_estimation_PE1_bc(phi_n,C_n,w_n,xb);
    Dx0=-epsilon/2*(Eb-Ea)/(Eb+Ea-2*E0);
    if REPORT, fprintf('Iter:%d E:%f a0:%f a1:%f alpha:%f\n',iter,sqrt(E0),a0,a1,alpha); end;
    % usually, k=k+Dx0; however Newton's method finds minima or maxima...
    % so, we analyze several options to guarantee minimization
    Dx=[1 0.5 -0.5 -1].*Dx0;
    E0_verify=E0; alpha0=alpha;
    for idx=1:4
        [E_verify] = Error_estimation_PE1_bc(phi_n,C_n,w_n,alpha0+Dx(idx));
        if E_verify<E0_verify
            E0_verify=E_verify;
            alpha=alpha0+Dx(idx);
        end
    end
    if E0_verify==E0
        alpha=alpha0+0.05*Dx0;
    end
end
[E0,a0,a1] = Error_estimation_PE1_bc(phi_n,C_n,w_n,alpha);
% de-scaling
phi_n=phi_n*phi_scale;
a1=a1/phi_scale^alpha;
% statistical results
C_estim=a0+a1*phi_n.^alpha;
SS_res = mean(w_n.*(C_estim - C_n).^2);
Erms = sqrt(SS_res);
mu = mean(C_n);
SS_tot = mean(w_n.*(C_n - mu).^2);
R2 = 1 - SS_res/SS_tot;
if CRITERION == 'c'
    R2=1-SS_res;
end
return;

```

```

%%%%%%%%%%%%%%%%%%%%%%%%%%%%%%%%%%%%%%%%%%%%%%%%%%%%%%%%%%%%%%%%%%%%%%%%
function [E,a0,a1] = Error_estimation_PE1_bc(phi_n,C_n,w_n,alpha)
% definitions
f=phi_n.^alpha;
X=ones(size(C_n));
Xf=X.*f; Xff=Xf.*f;
Xc=C_n; Xcf=Xc.*f;
% elements of matrices
A0=sum(w_n.*X); A1=sum(w_n.*Xf); A2=sum(w_n.*Xff);
B0=sum(w_n.*Xc); B1=sum(w_n.*Xcf);
% matrices
A=[A0 A1; A1 A2];
B=[B0; B1];
% coefficients a0 a1 a2:
x=A\B; a0=x(1); a1=x(2);
% error estimation
C_estim = a0 + a1*f;
E=mean(w_n.*(C_estim-C_n).^2);
return;
%%%%%%%%%%%%%%%%%%%%%%%%%%%%%%%%%%%%%%%%%%%%%%%%%%%%%%%%%%%%%%%%%%%%%%%%

```

Function for fitting the Polynomial-Exponent model 2nd order: model_PE2.m

```

%%%%%%%%%%%%%%%%%%%%%%%%%%%%%%%%%%%%%%%%%%%%%%%%%%%%%%%%%%%%%%%%%%%%%%%%
% function [a0,a1,a2,alpha,PHI_0,K,R2,Erms] = model_PE2(phi_n,C_n,NITER,CRITERION,DIAGRAM,REPORT)
%%%%%%%%%%%%%%%%%%%%%%%%%%%%%%%%%%%%%%%%%%%%%%%%%%%%%%%%%%%%%%%%%%%%%%%%
%%% Developed by S. Medina-Rodriguez, A. de la Torre-Vega,
%%% J.F. Fernandez-Sanchez and A. Fernandez-Gutierrez
%%% (smedina@ugr.es, atv@ugr.es, jffernan@ugr.es, albertof@ugr.es)
%%% Dpt. Analytical Chemistry / Dpt. Signal Theory Networking and Communications
%%% University of Granada, Nov 2013
%%%%%%%%%%%%%%%%%%%%%%%%%%%%%%%%%%%%%%%%%%%%%%%%%%%%%%%%%%%%%%%%%%%%%%%%
% This function provides an estimation of the parameters of the
% 2nd order Polynomic-Exponent model (PE2) given observations of
% photoluminiscece consisting on analytical signal and concentration (phi_n, C_n)
% The variable NITER indicates the number of iterations
% The variable CRITERION defines the calibration criterion ('A' 'B' 'C')
% The variables DIAGRAM and REPORT provides some information and plots
% while the model parameters are estimated
% The output parameters are:
%   a0,a1,a2   The polynomial coefficients
%   alpha      The exponent
%   PHI_0      The response of the model at null concentration
%   K          The sensitivity of the model
%   R2         Determination coefficient
%   Erms       RMS error for calibration data
% PE2 model:
%   C = a0 + a1 phi^alpha + a2 phi^(2*alpha)
%
% Procedure for optimization:
%   it is a 1-D search implemented with Newton's method
%
% Example:
%   C_n=[0.01 0.03 0.1 0.3 1];
%   phi_n=[35 30 25 20 15];
%   [a0,a1,a2,alpha,PHI_0,K,R2,Erms] = model_PE2(phi_n,C_n,100,'c',1,1);
%%%%%%%%%%%%%%%%%%%%%%%%%%%%%%%%%%%%%%%%%%%%%%%%%%%%%%%%%%%%%%%%%%%%%%%%
function [a0,a1,a2,alpha,PHI_0,K,R2,Erms] = model_PE2(phi_n,C_n,NITER,CRITERION,DIAGRAM,REPORT)
N=length(C_n);
if N~=length(phi_n)
    fprintf('Error: phi_n and C_n should have the same length\n');
    a0=[]; a1=[]; a2=[]; alpha=[]; K=[]; PHI_0=[]; R2=[]; Erms=[]; return;
end

Report_iterations = 0;
switch lower(CRITERION)
    case 'b'
        w_n = ones(size(C_n));
        [a0,a1,a2,alpha,R2,Erms]=PE2_estimation_bc(phi_n,C_n,w_n,'b',NITER,Report_iterations);
    case 'c'
        cond = C_n>0;
        if sum(cond)~=length(phi_n)
            fprintf('...Warning!: null concentration ignored for (c) criterion.\n');
            phi_n=phi_n(cond); C_n=C_n(cond);
        end
        w_n = 1./(C_n.*C_n);
        [a0,a1,a2,alpha,R2,Erms]=PE2_estimation_bc(phi_n,C_n,w_n,'c',NITER,Report_iterations);
    case 'a'
        [a0,a1,a2,alpha,R2,Erms]=PE2_estimation_a(phi_n,C_n,NITER,Report_iterations);
    otherwise
        fprintf('Error: CRITERION should be ''a'' ''A'' ''b'' ''B'' ''c'' or ''C''\n');

```

```

    a0=[]; a1=[]; a2=[]; alpha=[]; K=[]; PHI_0=[]; R2=[]; Erms=[]; return;
end

PHI_0 = ((-a1 + sqrt(a1*a1-4*a0*a2))/(2*a2))^(1/alpha);
K = abs(1/(alpha*a1*PHI_0^alpha+2*alpha*a2*PHI_0^(2*alpha)));
if DIAGRAM
    figure(DIAGRAM)
    D_phi=(max(phi_n)-min(phi_n))/200;
    x_grafica = min(phi_n):D_phi:max(phi_n);
    y=a0+a1*x_grafica.^alpha+a2*x_grafica.^(2*alpha);
    plot(x_grafica,y,'-r',phi_n,C_n,'ok')
    xlabel('analytical signal')
    ylabel('concentration (%)')
end
if REPORT
    fprintf('Pol.E-2(%s): E=%.4f R2=%.4f a0=%.4f a1=%.4f a2=%.4f alpha=%.4f PHI_0=%.4f K=%f\n',...
        CRITERION,Erms,R2,a0,a1,a2,alpha,PHI_0,K);
end
return;
%%%%%%%%%%%%%%%%%%%%%%%%%%%%%%%%%%%%%%%%%%%%%%%%%%%%%%%%%%%%%%%%%%%%%%%%
function [a0,a1,a2,alpha,R2,Erms]=PE2_estimation_a(phi_n,C_n,NITER,REPORT)
% pre-scaling
phi_scale=max(phi_n);
phi_n=phi_n/phi_scale;
% iterative estimation of alpha for criterion (a)
% first step: initialization with PE2(c)
w_a=zeros(size(C_n));
cond=C_n>0;
w_a(cond)=1./(C_n(cond).^2);
[a0,a1,a2,alpha]=PE2_estimation_bc(phi_n,C_n,w_a,'c',ceil(NITER/2),0);
% reestimation of weights and new iterations:
for iter=1:5
    f1=phi_n.^(alpha-1);
    f2=phi_n.^(2*alpha-1);
    w_a=(abs(a1*alpha*f1 + 2*a2*alpha*f2)).^(-2);
    [a0,a1,a2,alpha]=PE2_estimation_bc(phi_n,C_n,w_a,'c',ceil(NITER/5),0);
    phi_estim = ((-a1+sqrt(a1*a1-4*a2*(a0-C_n)))/(2*a2)).^(1/alpha);
    E0=mean((phi_estim - phi_n).^2);
    if REPORT, fprintf('Iter:%d E:%f a0:%f a1:%f a2:%f alpha:%f\n',iter*ceil(NITER/5),sqrt(E0),a0,a1,a2,alpha); end;
end
% de-scaling
phi_n=phi_n*phi_scale;
a1=a1/phi_scale^alpha;
a2=a2/phi_scale^(2*alpha);
% statistical results
phi_estim = ((-a1+sqrt(a1*a1-4*a2*(a0-C_n)))/(2*a2)).^(1/alpha);
SS_res = mean((phi_estim - phi_n).^2);
Erms = sqrt(SS_res);
mu = mean(phi_n);
SS_tot = mean((phi_n - mu).^2);
R2 = 1 - SS_res/SS_tot;
return;
%%%%%%%%%%%%%%%%%%%%%%%%%%%%%%%%%%%%%%%%%%%%%%%%%%%%%%%%%%%%%%%%%%%%%%%%
function [a0,a1,a2,alpha,R2,Erms]=PE2_estimation_bc(phi_n,C_n,w_n,CRITERION,NITER,REPORT)
% pre-scaling
phi_scale=max(phi_n);
phi_n=phi_n/phi_scale;
% initialization of alpha:
alpha_search = -1.*10.^(-2:0.1:2); % exhaustive search around -1
alpha_ref=0.0; E0_ref=1e30;
warning('off');
for iter = 1:length(alpha_search)
    [E0] = Error_estimation_PE2_bc(phi_n,C_n,w_n,alpha_search(iter));
    if E0<E0_ref, E0_ref=E0; alpha_ref=alpha_search(iter); end;
    if REPORT, fprintf('Init: alpha=%f E=%f\n',alpha_search(iter),sqrt(E0)); end;
end
warning('on');
alpha=alpha_ref;
% using alpha as initialization, 1-Dim search using Newton's method:
for iter=1:NITER
    epsilon = abs(alpha/1000);
    x0=alpha; xa=x0-epsilon; xb=x0+epsilon;
    [E0,a0,a1,a2] = Error_estimation_PE2_bc(phi_n,C_n,w_n,x0);
    [Ea] = Error_estimation_PE2_bc(phi_n,C_n,w_n,xa);
    [Eb] = Error_estimation_PE2_bc(phi_n,C_n,w_n,xb);
    Dx0=-epsilon/2*(Eb-Ea)/(Eb+Ea-2*E0);
    if REPORT, fprintf('Iter:%d E:%f a0:%f a1:%f a2:%f alpha:%f\n',iter,sqrt(E0),a0,a1,a2,alpha); end;
    % usually, k=k+Dx0; however Newton's method finds minima or maxima...
    % so, we analyze several options to guarantee minimization
    Dx=[1 0.5 -0.5 -1].*Dx0;
    E0_verify=E0; alpha0=alpha;
    for idx=1:4
        [E_verify] = Error_estimation_PE2_bc(phi_n,C_n,w_n,alpha0+Dx(idx));
        if E_verify<E0_verify

```



```

        E0_verify=E_verify;
        alpha=alpha0+Dx(idx);
    end
end
if E0_verify==E0
    alpha=alpha0+0.05*Dx0;
end
end
[E0,a0,a1,a2] = Error_estimation_PE2_bc(phi_n,C_n,w_n,alpha);
% de-scaling
phi_n=phi_n*phi_scale;
a1=a1/phi_scale^alpha;
a2=a2/phi_scale^(2*alpha);
% statistical results
C_estim=a0+a1*phi_n.^alpha+a2*phi_n.^(2*alpha);
SS_res = mean(w_n.*(C_estim - C_n).^2);
Erms = sqrt(SS_res);
mu = mean(C_n);
SS_tot = mean(w_n.*(C_n - mu).^2);
R2 = 1 - SS_res/SS_tot;
if CRITERION == 'c'
    R2=1-SS_res;
end
return;
%%%%%%%%%%%%%%%%%%%%%%%%%%%%%%%%%%%%%%%%%%%%%%%%%%%%%%%%%%%%%%%%%%%%%%%%
function [E,a0,a1,a2] = Error_estimation_PE2_bc(phi_n,C_n,w_n,alpha)
% definitions
f=phi_n.^alpha;
X=ones(size(C_n));
Xf=X.*f; Xff=Xf.*f; Xfff=Xff.*f; Xffff=Xfff.*f;
Xc=C_n; Xcf=Xc.*f; Xcff=Xcf.*f;
% elements of matrices
A0=sum(w_n.*X); A1=sum(w_n.*Xf); A2=sum(w_n.*Xff);
A3=sum(w_n.*Xfff); A4=sum(w_n.*Xffff);
B0=sum(w_n.*Xc); B1=sum(w_n.*Xcf); B2=sum(w_n.*Xcff);
% matrices
A=[A0 A1 A2; A1 A2 A3; A2 A3 A4];
B=[B0; B1; B2];
% coefficients a0 a1 a2:
x=A\B; a0=x(1); a1=x(2); a2=x(3);
% error estimation
C_estim = a0 + a1*f + a2*f.*f;
E=mean(w_n.*(C_estim-C_n).^2);
return;
%%%%%%%%%%%%%%%%%%%%%%%%%%%%%%%%%%%%%%%%%%%%%%%%%%%%%%%%%%%%%%%%%%%%%%%%

```

C.6.2 Functions for model evaluation

Function for evaluation of the Stern-Volmer, Lehrer and Demas models: `evaluation_demas.m`

```

%%%%%%%%%%%%%%%%%%%%%%%%%%%%%%%%%%%%%%%%%%%%%%%%%%%%%%%%%%%%%%%%%%%%%%%%
% function [Ea,R2a,Eb,R2b,Ec,R2c] = evaluation_demas(phi_n,C_n,phi_0,k1,k2,x,DIAGRAM,REPORT)
%%%%%%%%%%%%%%%%%%%%%%%%%%%%%%%%%%%%%%%%%%%%%%%%%%%%%%%%%%%%%%%%%%%%%%%%
%%% Developed by S. Medina-Rodriguez, A. de la Torre-Vega,
%%% J.F. Fernandez-Sanchez and A. Fernandez-Gutierrez
%%% (smedina@ugr.es, atv@ugr.es, jffernan@ugr.es, albertof@ugr.es)
%%% Dpt. Analytical Chemistry / Dpt. Signal Theory Networking and Communications
%%% University of Granada, Nov 2013
%%%%%%%%%%%%%%%%%%%%%%%%%%%%%%%%%%%%%%%%%%%%%%%%%%%%%%%%%%%%%%%%%%%%%%%%
% Input parameters:
% phi_n, C_n: data to be evaluated
% phi_0, k1, k2, x: parameters of a Demas model
% if k2=0: Lehrer model
% if k2=0, x=1: Stern-Volmer model
% DIAGRAM, REPORT: boolean variables to plot or print result (0 or 1)
% Output parameters:
% Ea, Eb, Ec: RMS Errors according to criteria (a), (b) and (c)
% R2a, R2b, R2c: Determination coefficients R^2 according to criteria (a), (b) or (c)
% Example:
% C_n=[0.01 0.03 0.1 0.3 1];
% phi_n=[35 30 25 20 15];
% [phi_0,k1,k2,x,K,R2,Erms] = model_D(phi_n,C_n,500,'c',1,1,0);
% [Ea,R2a,Eb,R2b,Ec,R2c] = evaluation_demas(phi_n,C_n,phi_0,k1,k2,x,2,1);
%%%%%%%%%%%%%%%%%%%%%%%%%%%%%%%%%%%%%%%%%%%%%%%%%%%%%%%%%%%%%%%%%%%%%%%%
function [Ea,R2a,Eb,R2b,Ec,R2c] = evaluation_demas(phi_n,C_n,phi_0,k1,k2,x,DIAGRAM,REPORT)

% first, we compute the plot (phi,C) for the model and parameters
x_range=max(C_n)-min(C_n);
x_ini=max((min(C_n)-x_range/25),1e-4);
x_max=max(C_n)+x_range/25;

```

```

Dx=x_range/1000;
C=x_ini:Dx:x_max;

A1=x./(1+k1*C);
A2=(1-x)./(1+k2*C);
B=(A1+A2);
phi=B*phi_0;

% diagram
if DIAGRAM
    figure(DIAGRAM)
    plot(phi,C,'r-',phi_n,C_n,'ok');
    xlabel('analytical signal')
    ylabel('concentration (%)')
end

% evaluation, criterion (a)
phi_estim = phi_0 .* (x./(1+k1*C_n) + (1-x)./(1+k2*C_n));
SS_res=mean((phi_estim-phi_n).^2);
E2=SS_res;
Ea=sqrt(E2);
mu=mean(phi_n);
SS_tot=mean((phi_n-mu).^2);
R2a=1-SS_res/SS_tot;

% evaluation, criterion (b)
if k2
    a_demas = k1*k2*phi_n;
    b_demas = (k1+k2)*phi_n - (1-x)*k1*phi_0 - x*k2*phi_0;
    c_demas = phi_n - phi_0;
    C_estim = (-b_demas + sqrt(b_demas.*b_demas - 4*a_demas.*c_demas))./(2*a_demas);
else
    C_estim = (phi_0-phi_n)./(phi_n - phi_0 + x*phi_0)/k1;
end
SS_res=mean((C_estim-C_n).^2);
E2=SS_res;
Eb=sqrt(E2);
mu=mean(C_n);
SS_tot=mean((C_n-mu).^2);
R2b=1-SS_res/SS_tot;

% evaluation, criterion (c)
cond=C_n>0;
SS_res=mean((C_estim(cond)./C_n(cond)-1).^2);
E2=SS_res;
Ec=sqrt(E2);
R2c=1-SS_res;

if REPORT
    fprintf('Ea=%f Eb=%f Ec=%f R2a=%f R2b=%f R2c=%f\n',Ea,Eb,Ec,R2a,R2b,R2c)
end

return;

```

Function for evaluation of the Polynomial and Polynomial-Exponent models: evaluation_polynom.m

```

%%%%%%%%%%%%%%%%%%%%%%%%%%%%%%%%%%%%%%%%%%%%%%%%%%%%%%%%%%%%%%%%%%%%%%%%
% function [Ea,R2a,Eb,R2b,Ec,R2c] = evaluation_polynom(phi_n,C_n,alpha,a0,a1,a2,DIAGRAM,REPORT)
%%%%%%%%%%%%%%%%%%%%%%%%%%%%%%%%%%%%%%%%%%%%%%%%%%%%%%%%%%%%%%%%%%%%%%%%
%%% Developed by S. Medina-Rodriguez, A. de la Torre-Vega,
%%% J.F. Fernandez-Sanchez and A. Fernandez-Gutierrez
%%% (smedina@ugr.es, atv@ugr.es, jffernan@ugr.es, albertof@ugr.es)
%%% Dpt. Analytical Chemistry / Dpt. Signal Theory Networking and Communications
%%% University of Granada, Nov 2013
%%%%%%%%%%%%%%%%%%%%%%%%%%%%%%%%%%%%%%%%%%%%%%%%%%%%%%%%%%%%%%%%%%%%%%%%
% Input parameters:
% phi_n, C_n: data to be evaluated
% alpha, a0, a1, a2 parameters of a PE-2 model
% if a2=0: PE-1 model
% if alpha=-1: P-2 model
% if alpha=-1, a2=0: P-1 model (equivalent to a Stern-Volmer model)
% DIAGRAM, REPORT: boolean variables to plot or print result (0 or 1)
% Output parameters:
% Ea, Eb, Ec: RMS Errors according to criteria (a), (b) and (c)
% R2a, R2b, R2c: Determination coefficients R^2 according to criteria (a), (b) or (c)
% Example:
% C_n=[0.01 0.03 0.1 0.3 1];
% phi_n=[35 30 25 20 15];
% [a0,a1,a2,alpha,PHI_0,K,R2,Erms] = model_PE2(phi_n,C_n,100,'c',1,1);
% [Ea,R2a,Eb,R2b,Ec,R2c] = evaluation_polynom(phi_n,C_n,alpha,a0,a1,a2,2,1);
%%%%%%%%%%%%%%%%%%%%%%%%%%%%%%%%%%%%%%%%%%%%%%%%%%%%%%%%%%%%%%%%%%%%%%%%

```

```

function [Ea,R2a,Eb,R2b,Ec,R2c] = evaluation_polynom(phi_n,C_n,alpha,a0,a1,a2,DIAGRAM,REPORT)

% first, we compute the plot (phi,C) for the model and parameters
x_range=max(phi_n)-min(phi_n);
x_ini=max((min(phi_n)-x_range/25),1e-4);
x_max=max(phi_n)+x_range/25;
Dx=x_range/1000;
phi=x_ini:Dx:x_max;
C=a0+a1*phi.^alpha+a2*phi.^(2*alpha);

% diagram
if DIAGRAM
    figure(DIAGRAM)
    plot(phi,C,'r-',phi_n,C_n,'ok');
    xlabel('analytical signal')
    ylabel('concentration (%)')
end

% evaluation, criterion (a)
if a2
    phi_estim = ((-a1+sqrt(a1*a1-4*a2*(a0-C_n)))./(2*a2)).^(1/alpha);
else
    phi_estim = ((C_n-a0)./a1).^(1/alpha);
end
SS_res=mean((phi_estim-phi_n).^2);
E2=SS_res;
Ea=sqrt(E2);
mu=mean(phi_n);
SS_tot=mean((phi_n-mu).^2);
R2a=1-SS_res/SS_tot;

% evaluation, criterion (b)
C_estim = a0 + a1.*phi_n.^alpha + a2.*phi_n.^(2*alpha);
SS_res=mean((C_estim-C_n).^2);
E2=SS_res;
Eb=sqrt(E2);
mu=mean(C_n);
SS_tot=mean((C_n-mu).^2);
R2b=1-SS_res/SS_tot;

% evaluation, criterion (c)
cond=C_n>0;
SS_res=mean((C_estim(cond)./C_n(cond)-1).^2);
E2=SS_res;
Ec=sqrt(E2);
R2c=1-SS_res;

if REPORT
    fprintf('Ea=%f Eb=%f Ec=%f R2a=%f R2b=%f R2c=%f\n',Ea,Eb,Ec,R2a,R2b,R2c)
end

return;

```

C.6.3 Function for performing a complete study

Function complete_study.m

```

%%%%%%%%%%%%%%%%%%%%%%%%%%%%%%%%%%%%%%%%%%%%%%%%%%%%%%%%%%%%%%%%%%%%%%%%
% function complete_study(phi_n_cal,C_n_cal,phi_n_test,C_n_test,LIMIT,file_out)
%%%%%%%%%%%%%%%%%%%%%%%%%%%%%%%%%%%%%%%%%%%%%%%%%%%%%%%%%%%%%%%%%%%%%%%%
%% Developed by S. Medina-Rodriguez, A. de la Torre-Vega,
%% J.F. Fernandez-Sanchez and A. Fernandez-Gutierrez
%% (smedina@ugr.es, atv@ugr.es, jffernan@ugr.es, albertof@ugr.es)
%% Dpt. Analytical Chemistry / Dpt. Signal Theory Networking and Communications
%% University of Granada, Nov 2013
%%%%%%%%%%%%%%%%%%%%%%%%%%%%%%%%%%%%%%%%%%%%%%%%%%%%%%%%%%%%%%%%%%%%%%%%
% This function performs a complete study of photoluminescence - concetration
% data according to the experiments performed in the article.
% The study includes fitting of input data with different models and
% criteria. Models included in the study are: Stern-Volmer, Lehrer,
% Polynomial-2, Polynomial-Exponent-1, Polynomial-Exponent-2 and Demas.
% Criteria included in the study are (a), (b) and (c).
% The study includes:
% * fitting each model according to each criterion, using calibration data
% * reporting results of fitting procedure (parameters of the model, RMS error, R2)
% * plotting the curves provided by the models, the calibration data
% and the test data
% * evaluation of calibration data with each model
% * evaluation of test data with each model
%
%

```

```

% The results of the calibration and evaluation are presented in the
% command window, and are also written in a text file.
%
% Input parameters:
% * phi_n_cal    vector containing the analytical signal (calibration data)
% * C_n_cal      vector containing the concentration (calibration data)
% * phi_n_test   vector containing the analytical signal (test data)
% * C_n_test     vector containing the concentration (test data)
% * LIMIT        when 1, forces k1>k2, k2>=0, x>0 and x<1 in Demas/Lehrer models
% * file_name    name of the output file where results are written
%
% Example:
%   C_n=[0.01 0.03 0.1 0.3 1];
%   phi_n=[35 30 25 20 15];
%   complete_study(phi_n,C_n,phi_n,C_n,0,'tmp.txt');
%%%%%%%%%%%%%%%%%%%%%%%%%%%%%%%%%%%%%%%%%%%%%%%%%%%%%%%%%%%%%%%%%%%%%%%%
function complete_study(phi_n_cal,C_n_cal,phi_n_test,C_n_test,LIMIT,file_out)

%% checking that C and phi vectors have the same length
if length(phi_n_cal)~=length(C_n_cal)
    fprintf('Error: phi_n_cal and C_n_cal should have the same length\n');
    return;
end
if length(phi_n_test)~=length(C_n_test)
    fprintf('Error: phi_n_test and C_n_test should have the same length\n');
    return;
end

%% independent variables for plots
DC=(max(C_n_cal)-min(C_n_cal))/200;
C=min(C_n_cal):DC:max(C_n_cal);
Dphi=(max(phi_n_cal)-min(phi_n_cal))/200;
phi=min(phi_n_cal):Dphi:max(phi_n_cal);
Range_x = [ min(phi)-10*Dphi max(phi)+10*Dphi ];
Range_y = [ min(C)-10*DC max(C)+10*DC ];

%% opening output file for results
f=fopen(file_out,'wt');

%% printing calibration data / test data
fprintf('=====\n');
fprintf('Calibration data: (C_n_cal,phi_n_cal)\n');
for n=1:length(phi_n_cal)
    fprintf('%20.12f      %20.12f\n',C_n_cal(n),phi_n_cal(n));
end
fprintf('Test data: (C_n_test,phi_n_test)\n');
for n=1:length(phi_n_test)
    fprintf('%20.12f      %20.12f\n',C_n_test(n),phi_n_test(n));
end
fprintf('=====\n');
% printing calibration data / test data in output file
fprintf(f,'=====\n');
fprintf(f,'Calibration data: (C_n_cal,phi_n_cal)\n');
for n=1:length(phi_n_cal)
    fprintf(f,'%20.12f      %20.12f\n',C_n_cal(n),phi_n_cal(n));
end
fprintf(f,'Test data: (C_n_test,phi_n_test)\n');
for n=1:length(phi_n_test)
    fprintf(f,'%20.12f      %20.12f\n',C_n_test(n),phi_n_test(n));
end
fprintf(f,'=====\n');

%% STERN VOLMER calibration
[phi_0_a,k_a,R2_a,Erms_a] = model_SV(phi_n_cal,C_n_cal,100,'a',0,0);
[phi_0_b,k_b,R2_b,Erms_b] = model_SV(phi_n_cal,C_n_cal,1,'b',0,0);
[phi_0_c,k_c,R2_c,Erms_c] = model_SV(phi_n_cal,C_n_cal,1,'c',0,0);
% Reporting calibration
fprintf('STERN-VOLMER calibration\n');
fprintf('Parameter      (a)      (b)      (c)\n');
fprintf('phi_0:      %10.6f %10.6f %10.6f\n',phi_0_a,phi_0_b,phi_0_c);
fprintf('k:          %10.6f %10.6f %10.6f\n',k_a,k_b,k_c);
fprintf('R2:         %10.8f %10.8f %10.8f\n',R2_a,R2_b,R2_c);
fprintf('RMSE:       %10.6f %10.6f %10.6f\n',Erms_a,Erms_b,Erms_c*100);
fprintf('Iter.:      %10d %10d %10d\n',100,1,1);
fprintf('-----\n');
fprintf('Phi_0:      %10.6f %10.6f %10.6f\n',phi_0_a,phi_0_b,phi_0_c);
fprintf('K:          %10.6f %10.6f %10.6f\n',k_a,k_b,k_c);
fprintf('=====\n');
% Reporting calibration in output file
fprintf(f,'STERN-VOLMER calibration\n');
fprintf(f,'Parameter      (a)      (b)      (c)\n');
fprintf(f,'phi_0:      %10.6f %10.6f %10.6f\n',phi_0_a,phi_0_b,phi_0_c);
fprintf(f,'k:          %10.6f %10.6f %10.6f\n',k_a,k_b,k_c);
fprintf(f,'R2:         %10.8f %10.8f %10.8f\n',R2_a,R2_b,R2_c);

```

```

fprintf(f,'RMSE:      %10.6f %10.6f %10.6f\n',Erms_a,Erms_b,Erms_c*100);
fprintf(f,'Iter.:    %10d %10d %10d\n',100,1,1);
fprintf(f,'-----\n');
fprintf(f,'Phi_0:     %10.6f %10.6f %10.6f\n',phi_0_a,phi_0_b,phi_0_c);
fprintf(f,'K:         %10.6f %10.6f %10.6f\n',k_a,k_b,k_c);
fprintf(f,'===== \n');
% plot with calibration curves
phi_a=phi_0_a./(1+k_a*C);
phi_b=phi_0_b./(1+k_b*C);
phi_c=phi_0_c./(1+k_c*C);
figure(1)
p_fig=plot(phi_a,C,'-r',phi_b,C,'-b',phi_c,C,'-g',phi_n_cal,C_n_cal,'ok',phi_n_test,C_n_test,'dk');
set(p_fig(4),'MarkerSize',6,'MarkerFaceColor','k')
set(p_fig(5),'MarkerSize',6)
xlim(Range_x); ylim(Range_y); grid('on');
title(sprintf('Stern-Volmer R2a=%0.8f R2b=%0.8f R2c=%0.8f',R2_a,R2_b,R2_c))
xlabel('analytical signal');
ylabel('concentration');
legend('criterion (a)','criterion (b)','criterion (c)', ' calib. data', ' test data');
% evaluation with calibration data
[Ea_a,R2a_a,Ea_b,R2a_b,Ea_c] = evaluation_demas(phi_n_cal,C_n_cal,phi_0_a,k_a,0,1,0,0);
[Eb_a,R2b_a,Eb_b,R2b_b,Eb_c] = evaluation_demas(phi_n_cal,C_n_cal,phi_0_b,k_b,0,1,0,0);
[Ec_a,R2c_a,Ec_b,R2c_b,Ec_c] = evaluation_demas(phi_n_cal,C_n_cal,phi_0_c,k_c,0,1,0,0);
fprintf('S-V, evaluation with calibration data      S-V(a)      S-V(b)      S-V(c)\n');
fprintf('evaluation with crit. (a) RMSE (signal):    %0.4f      %0.4f      %0.4f\n',Ea_a,Eb_a,Ec_a);
fprintf('evaluation with crit. (b) RMSE (conc):       %0.4f      %0.4f      %0.4f\n',Ea_b,Eb_b,Ec_b);
fprintf('evaluation with crit. (c) RMSE (%%):          %0.4f      %0.4f      %0.4f\n',Ea_c*100,Eb_c*100,Ec_c*100);
fprintf('S-V, evaluation with calibration data      S-V(a)      S-V(b)      S-V(c)\n');
fprintf('evaluation with crit. (a) RMSE (signal):    %0.4f      %0.4f      %0.4f\n',Ea_a,Eb_a,Ec_a);
fprintf('evaluation with crit. (b) RMSE (conc):       %0.4f      %0.4f      %0.4f\n',Ea_b,Eb_b,Ec_b);
fprintf('evaluation with crit. (c) RMSE (%%):          %0.4f      %0.4f      %0.4f\n',Ea_c*100,Eb_c*100,Ec_c*100);
% evaluation with test data
[Ea_a,R2a_a,Ea_b,R2a_b,Ea_c] = evaluation_demas(phi_n_test,C_n_test,phi_0_a,k_a,0,1,0,0);
[Eb_a,R2b_a,Eb_b,R2b_b,Eb_c] = evaluation_demas(phi_n_test,C_n_test,phi_0_b,k_b,0,1,0,0);
[Ec_a,R2c_a,Ec_b,R2c_b,Ec_c] = evaluation_demas(phi_n_test,C_n_test,phi_0_c,k_c,0,1,0,0);
fprintf('-----\n');
fprintf('S-V, evaluation with test data      S-V(a)      S-V(b)      S-V(c)\n');
fprintf('evaluation with crit. (a) RMSE (signal):    %0.4f      %0.4f      %0.4f\n',Ea_a,Eb_a,Ec_a);
fprintf('evaluation with crit. (b) RMSE (conc):       %0.4f      %0.4f      %0.4f\n',Ea_b,Eb_b,Ec_b);
fprintf('evaluation with crit. (c) RMSE (%%):          %0.4f      %0.4f      %0.4f\n',Ea_c*100,Eb_c*100,Ec_c*100);
fprintf('===== \n');
fprintf(f,'-----\n');
fprintf('S-V, evaluation with test data      S-V(a)      S-V(b)      S-V(c)\n');
fprintf('evaluation with crit. (a) RMSE (signal):    %0.4f      %0.4f      %0.4f\n',Ea_a,Eb_a,Ec_a);
fprintf('evaluation with crit. (b) RMSE (conc):       %0.4f      %0.4f      %0.4f\n',Ea_b,Eb_b,Ec_b);
fprintf('evaluation with crit. (c) RMSE (%%):          %0.4f      %0.4f      %0.4f\n',Ea_c*100,Eb_c*100,Ec_c*100);
fprintf(f,'===== \n');

%% LEHRER calibration
[phi_0_a,k_a,x_a,K_a,R2_a,Erms_a] = model_L(phi_n_cal,C_n_cal,100,'a',0,0,LIMIT);
[phi_0_b,k_b,x_b,K_b,R2_b,Erms_b] = model_L(phi_n_cal,C_n_cal,100,'b',0,0,LIMIT);
[phi_0_c,k_c,x_c,K_c,R2_c,Erms_c] = model_L(phi_n_cal,C_n_cal,100,'c',0,0,LIMIT);
% Reporting calibration
fprintf('LEHRER calibration\n');
fprintf('Parameter      (a)          (b)          (c)\n');
fprintf('phi_0:          %10.6f %10.6f %10.6f\n',phi_0_a,phi_0_b,phi_0_c);
fprintf('k:              %10.6f %10.6f %10.6f\n',k_a,k_b,k_c);
fprintf('x:              %10.6f %10.6f %10.6f\n',x_a,x_b,x_c);
fprintf('R2:             %10.8f %10.8f %10.8f\n',R2_a,R2_b,R2_c);
fprintf('RMSE:          %10.6f %10.6f %10.6f\n',Erms_a,Erms_b,Erms_c*100);
fprintf('Iter.:         %10d %10d %10d\n',100,100,100);
fprintf('-----\n');
fprintf('Phi_0:         %10.6f %10.6f %10.6f\n',phi_0_a,phi_0_b,phi_0_c);
fprintf('K:             %10.6f %10.6f %10.6f\n',K_a,K_b,K_c);
fprintf('===== \n');
% Reporting calibration in output file
fprintf(f,'LEHRER calibration\n');
fprintf(f,'Parameter      (a)          (b)          (c)\n');
fprintf(f,'phi_0:          %10.6f %10.6f %10.6f\n',phi_0_a,phi_0_b,phi_0_c);
fprintf(f,'k:              %10.6f %10.6f %10.6f\n',k_a,k_b,k_c);
fprintf(f,'x:              %10.6f %10.6f %10.6f\n',x_a,x_b,x_c);
fprintf(f,'R2:             %10.8f %10.8f %10.8f\n',R2_a,R2_b,R2_c);
fprintf(f,'RMSE:          %10.6f %10.6f %10.6f\n',Erms_a,Erms_b,Erms_c*100);
fprintf(f,'Iter.:         %10d %10d %10d\n',100,100,100);
fprintf(f,'-----\n');
fprintf(f,'Phi_0:         %10.6f %10.6f %10.6f\n',phi_0_a,phi_0_b,phi_0_c);
fprintf(f,'K:             %10.6f %10.6f %10.6f\n',K_a,K_b,K_c);
fprintf(f,'===== \n');
% plot with calibration curves
phi_a=phi_0_a*(x_a./(1+k_a*C)+1-x_a);
phi_b=phi_0_b*(x_b./(1+k_b*C)+1-x_b);
phi_c=phi_0_c*(x_c./(1+k_c*C)+1-x_c);
figure(2)
p_fig=plot(phi_a,C,'-r',phi_b,C,'-b',phi_c,C,'-g',phi_n_cal,C_n_cal,'ok',phi_n_test,C_n_test,'dk');

```

```

set(p_fig(4),'MarkerSize',6,'MarkerFaceColor','k')
set(p_fig(5),'MarkerSize',6)
xlim(Range_x); ylim(Range_y); grid on;
title(sprintf('Lehrer R2a=%0.8f R2b=%0.8f R2c=%0.8f',R2_a,R2_b,R2_c))
xlabel('analytical signal');
ylabel('concentration');
legend('criterion (a)','criterion (b)','criterion (c)', 'calib. data', 'test data');
% evaluation with calibration data
[Ea_a,R2a_a,Ea_b,R2a_b,Ea_c] = evaluation_demas(phi_n_cal,C_n_cal,phi_0_a,k_a,0,x_a,0,0);
[Eb_a,R2b_a,Eb_b,R2b_b,Eb_c] = evaluation_demas(phi_n_cal,C_n_cal,phi_0_b,k_b,0,x_b,0,0);
[Ec_a,R2c_a,Ec_b,R2c_b,Ec_c] = evaluation_demas(phi_n_cal,C_n_cal,phi_0_c,k_c,0,x_c,0,0);
fprintf('L, evaluation with calibration data L(a) L(b) L(c)\n');
fprintf('evaluation with crit. (a) RMSE (signal): %0.4f %0.4f %0.4f\n',Ea_a,Eb_a,Ec_a);
fprintf('evaluation with crit. (b) RMSE (conc): %0.4f %0.4f %0.4f\n',Ea_b,Eb_b,Ec_b);
fprintf('evaluation with crit. (c) RMSE (%): %0.4f %0.4f %0.4f\n',Ea_c*100,Eb_c*100,Ec_c*100);
fprintf(f,'L, evaluation with calibration data L(a) L(b) L(c)\n');
fprintf(f,'evaluation with crit. (a) RMSE (signal): %0.4f %0.4f %0.4f\n',Ea_a,Eb_a,Ec_a);
fprintf(f,'evaluation with crit. (b) RMSE (conc): %0.4f %0.4f %0.4f\n',Ea_b,Eb_b,Ec_b);
fprintf(f,'evaluation with crit. (c) RMSE (%): %0.4f %0.4f %0.4f\n',Ea_c*100,Eb_c*100,Ec_c*100);
% evaluation with test data
[Ea_a,R2a_a,Ea_b,R2a_b,Ea_c] = evaluation_demas(phi_n_test,C_n_test,phi_0_a,k_a,0,x_a,0,0);
[Eb_a,R2b_a,Eb_b,R2b_b,Eb_c] = evaluation_demas(phi_n_test,C_n_test,phi_0_b,k_b,0,x_b,0,0);
[Ec_a,R2c_a,Ec_b,R2c_b,Ec_c] = evaluation_demas(phi_n_test,C_n_test,phi_0_c,k_c,0,x_c,0,0);
fprintf('-----\n');
fprintf('L, evaluation with test data L(a) L(b) L(c)\n');
fprintf('evaluation with crit. (a) RMSE (signal): %0.4f %0.4f %0.4f\n',Ea_a,Eb_a,Ec_a);
fprintf('evaluation with crit. (b) RMSE (conc): %0.4f %0.4f %0.4f\n',Ea_b,Eb_b,Ec_b);
fprintf('evaluation with crit. (c) RMSE (%): %0.4f %0.4f %0.4f\n',Ea_c*100,Eb_c*100,Ec_c*100);
fprintf('-----\n');
fprintf(f,'-----\n');
fprintf(f,'L, evaluation with test data L(a) L(b) L(c)\n');
fprintf(f,'evaluation with crit. (a) RMSE (signal): %0.4f %0.4f %0.4f\n',Ea_a,Eb_a,Ec_a);
fprintf(f,'evaluation with crit. (b) RMSE (conc): %0.4f %0.4f %0.4f\n',Ea_b,Eb_b,Ec_b);
fprintf(f,'evaluation with crit. (c) RMSE (%): %0.4f %0.4f %0.4f\n',Ea_c*100,Eb_c*100,Ec_c*100);
fprintf(f,'-----\n');

%% P2 calibration
[a0_a,a1_a,a2_a,PHI_0_a,K_a,R2_a,Erms_a] = model_P2(phi_n_cal,C_n_cal,100,'a',0,0);
[a0_b,a1_b,a2_b,PHI_0_b,K_b,R2_b,Erms_b] = model_P2(phi_n_cal,C_n_cal,1,'b',0,0);
[a0_c,a1_c,a2_c,PHI_0_c,K_c,R2_c,Erms_c] = model_P2(phi_n_cal,C_n_cal,1,'c',0,0);
% Reporting calibration
fprintf('POLYNOMIAL-2nd DEGREE calibration\n');
fprintf('Parameter (a) (b) (c)\n');
fprintf('a_0: %0.6f %0.6f %0.6f\n',a0_a,a0_b,a0_c);
fprintf('a_1: %0.6f %0.6f %0.6f\n',a1_a,a1_b,a1_c);
fprintf('a_2: %0.6f %0.6f %0.6f\n',a2_a,a2_b,a2_c);
fprintf('R2: %0.8f %0.8f %0.8f\n',R2_a,R2_b,R2_c);
fprintf('RMSE: %0.6f %0.6f %0.6f\n',Erms_a,Erms_b,Erms_c*100);
fprintf('Iter.: %0d %0d %0d\n',100,1,1);
fprintf('-----\n');
fprintf('Phi_0: %0.6f %0.6f %0.6f\n',PHI_0_a,PHI_0_b,PHI_0_c);
fprintf('K: %0.6f %0.6f %0.6f\n',K_a,K_b,K_c);
fprintf('-----\n');
% Reporting calibration in output file
fprintf(f,'POLYNOMIAL-2nd DEGREE calibration\n');
fprintf(f,'Parameter (a) (b) (c)\n');
fprintf(f,'a_0: %0.6f %0.6f %0.6f\n',a0_a,a0_b,a0_c);
fprintf(f,'a_1: %0.6f %0.6f %0.6f\n',a1_a,a1_b,a1_c);
fprintf(f,'a_2: %0.6f %0.6f %0.6f\n',a2_a,a2_b,a2_c);
fprintf(f,'R2: %0.8f %0.8f %0.8f\n',R2_a,R2_b,R2_c);
fprintf(f,'RMSE: %0.6f %0.6f %0.6f\n',Erms_a,Erms_b,Erms_c*100);
fprintf(f,'Iter.: %0d %0d %0d\n',100,1,1);
fprintf(f,'-----\n');
fprintf(f,'Phi_0: %0.6f %0.6f %0.6f\n',PHI_0_a,PHI_0_b,PHI_0_c);
fprintf(f,'K: %0.6f %0.6f %0.6f\n',K_a,K_b,K_c);
fprintf(f,'-----\n');
% plot with calibration curves
C_a=a0_a+a1_a./phi+a2_a./phi./phi;
C_b=a0_b+a1_b./phi+a2_b./phi./phi;
C_c=a0_c+a1_c./phi+a2_c./phi./phi;
figure(3)
p_fig=plot(phi,C_a,'-r',phi,C_b,'-b',phi,C_c,'-g',phi_n_cal,C_n_cal,'ok',phi_n_test,C_n_test,'dk');
set(p_fig(4),'MarkerSize',6,'MarkerFaceColor','k')
set(p_fig(5),'MarkerSize',6)
xlim(Range_x); ylim(Range_y); grid on;
title(sprintf('Polynom.2 R2a=%0.8f R2b=%0.8f R2c=%0.8f',R2_a,R2_b,R2_c))
xlabel('analytical signal');
ylabel('concentration');
legend('criterion (a)','criterion (b)','criterion (c)', 'calib. data', 'test data');
% evaluation with calibration data
[Ea_a,R2a_a,Ea_b,R2a_b,Ea_c] = evaluation_polynom(phi_n_cal,C_n_cal,-1,a0_a,a1_a,a2_a,0,0);
[Eb_a,R2b_a,Eb_b,R2b_b,Eb_c] = evaluation_polynom(phi_n_cal,C_n_cal,-1,a0_b,a1_b,a2_b,0,0);
[Ec_a,R2c_a,Ec_b,R2c_b,Ec_c] = evaluation_polynom(phi_n_cal,C_n_cal,-1,a0_c,a1_c,a2_c,0,0);
fprintf('P2, evaluation with calibration data P2(a) P2(b) P2(c)\n');

```

```

fprintf('evaluation with crit. (a) RMSE (signal):      %.4f      %.4f      %.4f\n', Ea_a, Eb_a, Ec_a);
fprintf('evaluation with crit. (b) RMSE (conc):      %.4f      %.4f      %.4f\n', Ea_b, Eb_b, Ec_b);
fprintf('evaluation with crit. (c) RMSE (%%):      %.4f      %.4f      %.4f\n', Ea_c*100, Eb_c*100, Ec_c*100);
fprintf(f, 'P2, evaluation with calibration data      P2 (a)      P2 (b)      P2 (c)\n');
fprintf(f, 'evaluation with crit. (a) RMSE (signal):  %.4f      %.4f      %.4f\n', Ea_a, Eb_a, Ec_a);
fprintf(f, 'evaluation with crit. (b) RMSE (conc):    %.4f      %.4f      %.4f\n', Ea_b, Eb_b, Ec_b);
fprintf(f, 'evaluation with crit. (c) RMSE (%%):      %.4f      %.4f      %.4f\n', Ea_c*100, Eb_c*100, Ec_c*100);
% evaluation with test data
[Ea_a, R2a_a, Ea_b, R2a_b, Ea_c] = evaluation_polynom(phi_n_test, C_n_test, -1, a0_a, al_a, a2_a, 0, 0);
[Eb_a, R2b_a, Eb_b, R2b_b, Eb_c] = evaluation_polynom(phi_n_test, C_n_test, -1, a0_b, al_b, a2_b, 0, 0);
[Ec_a, R2c_a, Ec_b, R2c_b, Ec_c] = evaluation_polynom(phi_n_test, C_n_test, -1, a0_c, al_c, a2_c, 0, 0);
fprintf('-----\n');
fprintf('P2, evaluation with test data      P2 (a)      P2 (b)      P2 (c)\n');
fprintf('evaluation with crit. (a) RMSE (signal):  %.4f      %.4f      %.4f\n', Ea_a, Eb_a, Ec_a);
fprintf('evaluation with crit. (b) RMSE (conc):    %.4f      %.4f      %.4f\n', Ea_b, Eb_b, Ec_b);
fprintf('evaluation with crit. (c) RMSE (%%):      %.4f      %.4f      %.4f\n', Ea_c*100, Eb_c*100, Ec_c*100);
fprintf('-----\n');
fprintf(f, '-----\n');
fprintf(f, 'P2, evaluation with test data      P2 (a)      P2 (b)      P2 (c)\n');
fprintf(f, 'evaluation with crit. (a) RMSE (signal):  %.4f      %.4f      %.4f\n', Ea_a, Eb_a, Ec_a);
fprintf(f, 'evaluation with crit. (b) RMSE (conc):    %.4f      %.4f      %.4f\n', Ea_b, Eb_b, Ec_b);
fprintf(f, 'evaluation with crit. (c) RMSE (%%):      %.4f      %.4f      %.4f\n', Ea_c*100, Eb_c*100, Ec_c*100);
fprintf(f, '-----\n');

%% PE1 calibration
[a0_a, al_a, alpha_a, PHI_0_a, K_a, R2_a, Erms_a] = model_PE1(phi_n_cal, C_n_cal, 100, 'a', 0, 0);
[a0_b, al_b, alpha_b, PHI_0_b, K_b, R2_b, Erms_b] = model_PE1(phi_n_cal, C_n_cal, 100, 'b', 0, 0);
[a0_c, al_c, alpha_c, PHI_0_c, K_c, R2_c, Erms_c] = model_PE1(phi_n_cal, C_n_cal, 100, 'c', 0, 0);
% Reporting calibration
fprintf('POLINOMIAL-EXPONENT-1st DEGREE calibration\n');
fprintf('Parameter      (a)      (b)      (c)\n');
fprintf('a_0:      %10.6f %10.6f %10.6f\n', a0_a, a0_b, a0_c);
fprintf('a_1:      %10.6f %10.6f %10.6f\n', al_a, al_b, al_c);
fprintf('alpha:    %10.6f %10.6f %10.6f\n', alpha_a, alpha_b, alpha_c);
fprintf('R2:      %10.8f %10.8f %10.8f\n', R2_a, R2_b, R2_c);
fprintf('RMSE:    %10.6f %10.6f %10.6f\n', Erms_a, Erms_b, Erms_c*100);
fprintf('Iter.:   %10d %10d %10d\n', 100, 100, 100);
fprintf('-----\n');
fprintf('Phi_0:   %10.6f %10.6f %10.6f\n', PHI_0_a, PHI_0_b, PHI_0_c);
fprintf('K:      %10.6f %10.6f %10.6f\n', K_a, K_b, K_c);
fprintf('-----\n');
% Reporting calibration in output file
fprintf(f, 'POLINOMIAL-EXPONENT-1st DEGREE calibration\n');
fprintf(f, 'Parameter      (a)      (b)      (c)\n');
fprintf(f, 'a_0:      %10.6f %10.6f %10.6f\n', a0_a, a0_b, a0_c);
fprintf(f, 'a_1:      %10.6f %10.6f %10.6f\n', al_a, al_b, al_c);
fprintf(f, 'alpha:    %10.6f %10.6f %10.6f\n', alpha_a, alpha_b, alpha_c);
fprintf(f, 'R2:      %10.8f %10.8f %10.8f\n', R2_a, R2_b, R2_c);
fprintf(f, 'RMSE:    %10.6f %10.6f %10.6f\n', Erms_a, Erms_b, Erms_c*100);
fprintf(f, 'Iter.:   %10d %10d %10d\n', 100, 100, 100);
fprintf(f, '-----\n');
fprintf(f, 'Phi_0:   %10.6f %10.6f %10.6f\n', PHI_0_a, PHI_0_b, PHI_0_c);
fprintf(f, 'K:      %10.6f %10.6f %10.6f\n', K_a, K_b, K_c);
fprintf(f, '-----\n');
% plot with calibration curves
C_a=a0_a+al_a.*(phi.^(alpha_a));
C_b=a0_b+al_b.*(phi.^(alpha_b));
C_c=a0_c+al_c.*(phi.^(alpha_c));
figure(4)
p_fig=plot(phi, C_a, '-r', phi, C_b, '-b', phi, C_c, '-g', phi_n_cal, C_n_cal, 'ok', phi_n_test, C_n_test, 'dk');
set(p_fig(4), 'MarkerSize', 6, 'MarkerFaceColor', 'k')
set(p_fig(5), 'MarkerSize', 6)
xlim(Range_x); ylim(Range_y); grid on;
title(sprintf('Polynom-Exp.1 R2a=%0.8f R2b=%0.8f R2c=%0.8f', R2_a, R2_b, R2_c))
xlabel('analytical signal')
ylabel('concentration')
legend('criterion (a)', 'criterion (b)', 'criterion (c)', 'calib. data', 'test data');
% evaluation with calibration data
[Ea_a, R2a_a, Ea_b, R2a_b, Ea_c] = evaluation_polynom(phi_n_cal, C_n_cal, alpha_a, a0_a, al_a, 0, 0, 0);
[Eb_a, R2b_a, Eb_b, R2b_b, Eb_c] = evaluation_polynom(phi_n_cal, C_n_cal, alpha_b, a0_b, al_b, 0, 0, 0);
[Ec_a, R2c_a, Ec_b, R2c_b, Ec_c] = evaluation_polynom(phi_n_cal, C_n_cal, alpha_c, a0_c, al_c, 0, 0, 0);
fprintf('PE1, evaluation with calibration data      PE1 (a)      PE1 (b)      PE1 (c)\n');
fprintf('evaluation with crit. (a) RMSE (signal):  %.4f      %.4f      %.4f\n', Ea_a, Eb_a, Ec_a);
fprintf('evaluation with crit. (b) RMSE (conc):    %.4f      %.4f      %.4f\n', Ea_b, Eb_b, Ec_b);
fprintf('evaluation with crit. (c) RMSE (%%):      %.4f      %.4f      %.4f\n', Ea_c*100, Eb_c*100, Ec_c*100);
fprintf(f, 'PE1, evaluation with calibration data      PE1 (a)      PE1 (b)      PE1 (c)\n');
fprintf(f, 'evaluation with crit. (a) RMSE (signal):  %.4f      %.4f      %.4f\n', Ea_a, Eb_a, Ec_a);
fprintf(f, 'evaluation with crit. (b) RMSE (conc):    %.4f      %.4f      %.4f\n', Ea_b, Eb_b, Ec_b);
fprintf(f, 'evaluation with crit. (c) RMSE (%%):      %.4f      %.4f      %.4f\n', Ea_c*100, Eb_c*100, Ec_c*100);
% evaluation with test data
[Ea_a, R2a_a, Ea_b, R2a_b, Ea_c] = evaluation_polynom(phi_n_test, C_n_test, alpha_a, a0_a, al_a, 0, 0, 0);
[Eb_a, R2b_a, Eb_b, R2b_b, Eb_c] = evaluation_polynom(phi_n_test, C_n_test, alpha_b, a0_b, al_b, 0, 0, 0);
[Ec_a, R2c_a, Ec_b, R2c_b, Ec_c] = evaluation_polynom(phi_n_test, C_n_test, alpha_c, a0_c, al_c, 0, 0, 0);
fprintf('-----\n');

```

```

fprintf('PE1, evaluation with test data                PE1 (a)    PE1 (b)    PE1 (c)\n');
fprintf('evaluation with crit. (a) RMSE (signal):      % .4f      % .4f      % .4f\n', Ea_a, Eb_a, Ec_a);
fprintf('evaluation with crit. (b) RMSE (conc):        % .4f      % .4f      % .4f\n', Ea_b, Eb_b, Ec_b);
fprintf('evaluation with crit. (c) RMSE (%):            % .4f      % .4f      % .4f\n', Ea_c*100, Eb_c*100, Ec_c*100);
fprintf('===== \n');
fprintf(f, '-----\n');
fprintf(f, 'PE1, evaluation with test data                PE1 (a)    PE1 (b)    PE1 (c)\n');
fprintf(f, 'evaluation with crit. (a) RMSE (signal):          % .4f      % .4f      % .4f\n', Ea_a, Eb_a, Ec_a);
fprintf(f, 'evaluation with crit. (b) RMSE (conc):            % .4f      % .4f      % .4f\n', Ea_b, Eb_b, Ec_b);
fprintf(f, 'evaluation with crit. (c) RMSE (%):                % .4f      % .4f      % .4f\n', Ea_c*100, Eb_c*100, Ec_c*100);
fprintf(f, '===== \n');

%% PE2 calibration
[a0_a, a1_a, a2_a, alpha_a, PHI_0_a, K_a, R2_a, Erms_a] = model_PE2(phi_n_cal, C_n_cal, 100, 'a', 0, 0);
[a0_b, a1_b, a2_b, alpha_b, PHI_0_b, K_b, R2_b, Erms_b] = model_PE2(phi_n_cal, C_n_cal, 100, 'b', 0, 0);
[a0_c, a1_c, a2_c, alpha_c, PHI_0_c, K_c, R2_c, Erms_c] = model_PE2(phi_n_cal, C_n_cal, 100, 'c', 0, 0);
% Reporting calibration
fprintf('POLYNOMIAL-EXPONENT-2nd DEGREE calibration\n');
fprintf('Parameter      (a)      (b)      (c)\n');
fprintf('a_0:             %10.6f %10.6f %10.6f\n', a0_a, a0_b, a0_c);
fprintf('a_1:             %10.6f %10.6f %10.6f\n', a1_a, a1_b, a1_c);
fprintf('a_2:             %10.6f %10.6f %10.6f\n', a2_a, a2_b, a2_c);
fprintf('alpha:           %10.6f %10.6f %10.6f\n', alpha_a, alpha_b, alpha_c);
fprintf('R2:              %10.8f %10.8f %10.8f\n', R2_a, R2_b, R2_c);
fprintf('RMSE:           %10.6f %10.6f %10.6f\n', Erms_a, Erms_b, Erms_c*100);
fprintf('Iter.:          %10d %10d %10d\n', 100, 100, 100);
fprintf('-----\n');
fprintf('Phi_0:          %10.6f %10.6f %10.6f\n', PHI_0_a, PHI_0_b, PHI_0_c);
fprintf('K:              %10.6f %10.6f %10.6f\n', K_a, K_b, K_c);
fprintf('===== \n');
% Reporting calibration in output file
fprintf(f, 'POLYNOMIAL-EXPONENT-2nd DEGREE calibration\n');
fprintf(f, 'Parameter      (a)      (b)      (c)\n');
fprintf(f, 'a_0:             %10.6f %10.6f %10.6f\n', a0_a, a0_b, a0_c);
fprintf(f, 'a_1:             %10.6f %10.6f %10.6f\n', a1_a, a1_b, a1_c);
fprintf(f, 'a_2:             %10.6f %10.6f %10.6f\n', a2_a, a2_b, a2_c);
fprintf(f, 'alpha:           %10.6f %10.6f %10.6f\n', alpha_a, alpha_b, alpha_c);
fprintf(f, 'R2:              %10.8f %10.8f %10.8f\n', R2_a, R2_b, R2_c);
fprintf(f, 'RMSE:           %10.6f %10.6f %10.6f\n', Erms_a, Erms_b, Erms_c*100);
fprintf(f, 'Iter.:          %10d %10d %10d\n', 100, 100, 100);
fprintf(f, '-----\n');
fprintf(f, 'Phi_0:          %10.6f %10.6f %10.6f\n', PHI_0_a, PHI_0_b, PHI_0_c);
fprintf(f, 'K:              %10.6f %10.6f %10.6f\n', K_a, K_b, K_c);
fprintf(f, '===== \n');
% plot with calibration curves
C_a=a0_a+a1_a.*(phi.^(alpha_a))+a2_a.*(phi.^(2*alpha_a));
C_b=a0_b+a1_b.*phi.^(alpha_b)+a2_b.*(phi.^(2*alpha_b));
C_c=a0_c+a1_c.*phi.^(alpha_c)+a2_c.*(phi.^(2*alpha_c));
figure(5)
p_fig=plot(phi, C_a, '-r', phi, C_b, '-b', phi, C_c, '-g', phi_n_cal, C_n_cal, 'ok', phi_n_test, C_n_test, 'dk');
set(p_fig(4), 'MarkerSize', 6, 'MarkerFaceColor', 'k');
set(p_fig(5), 'MarkerSize', 6)
xlim(Range_x); ylim(Range_y); grid on;
title(sprintf('Polynom-Exp.2 R2a=% .8f R2b=% .8f R2c=% .8f', R2_a, R2_b, R2_c))
xlabel('analytical signal');
ylabel('concentration');
legend('criterion (a)', 'criterion (b)', 'criterion (c)', 'calib. data', 'test data');
% evaluation with calibration data
[Ea_a, R2a_a, Ea_b, R2a_b, Ea_c] = evaluation_polynom(phi_n_cal, C_n_cal, alpha_a, a0_a, a1_a, a2_a, 0, 0);
[Eb_a, R2b_a, Eb_b, R2b_b, Eb_c] = evaluation_polynom(phi_n_cal, C_n_cal, alpha_b, a0_b, a1_b, a2_b, 0, 0);
[Ec_a, R2c_a, Ec_b, R2c_b, Ec_c] = evaluation_polynom(phi_n_cal, C_n_cal, alpha_c, a0_c, a1_c, a2_c, 0, 0);
fprintf('PE2, evaluation with calibration data                PE2 (a)    PE2 (b)    PE2 (c)\n');
fprintf('evaluation with crit. (a) RMSE (signal):            % .4f      % .4f      % .4f\n', Ea_a, Eb_a, Ec_a);
fprintf('evaluation with crit. (b) RMSE (conc):              % .4f      % .4f      % .4f\n', Ea_b, Eb_b, Ec_b);
fprintf('evaluation with crit. (c) RMSE (%):                 % .4f      % .4f      % .4f\n', Ea_c*100, Eb_c*100, Ec_c*100);
fprintf(f, 'PE2, evaluation with calibration data                PE2 (a)    PE2 (b)    PE2 (c)\n');
fprintf(f, 'evaluation with crit. (a) RMSE (signal):            % .4f      % .4f      % .4f\n', Ea_a, Eb_a, Ec_a);
fprintf(f, 'evaluation with crit. (b) RMSE (conc):              % .4f      % .4f      % .4f\n', Ea_b, Eb_b, Ec_b);
fprintf(f, 'evaluation with crit. (c) RMSE (%):                 % .4f      % .4f      % .4f\n', Ea_c*100, Eb_c*100, Ec_c*100);
% evaluation with test data
[Ea_a, R2a_a, Ea_b, R2a_b, Ea_c] = evaluation_polynom(phi_n_test, C_n_test, alpha_a, a0_a, a1_a, a2_a, 0, 0);
[Eb_a, R2b_a, Eb_b, R2b_b, Eb_c] = evaluation_polynom(phi_n_test, C_n_test, alpha_b, a0_b, a1_b, a2_b, 0, 0);
[Ec_a, R2c_a, Ec_b, R2c_b, Ec_c] = evaluation_polynom(phi_n_test, C_n_test, alpha_c, a0_c, a1_c, a2_c, 0, 0);
fprintf('-----\n');
fprintf(f, 'PE2, evaluation with test data                PE2 (a)    PE2 (b)    PE2 (c)\n');
fprintf(f, 'evaluation with crit. (a) RMSE (signal):            % .4f      % .4f      % .4f\n', Ea_a, Eb_a, Ec_a);
fprintf(f, 'evaluation with crit. (b) RMSE (conc):              % .4f      % .4f      % .4f\n', Ea_b, Eb_b, Ec_b);
fprintf(f, 'evaluation with crit. (c) RMSE (%):                 % .4f      % .4f      % .4f\n', Ea_c*100, Eb_c*100, Ec_c*100);
fprintf(f, '===== \n');
fprintf(f, '-----\n');
fprintf(f, 'PE2, evaluation with test data                PE2 (a)    PE2 (b)    PE2 (c)\n');
fprintf(f, 'evaluation with crit. (a) RMSE (signal):            % .4f      % .4f      % .4f\n', Ea_a, Eb_a, Ec_a);
fprintf(f, 'evaluation with crit. (b) RMSE (conc):              % .4f      % .4f      % .4f\n', Ea_b, Eb_b, Ec_b);
fprintf(f, 'evaluation with crit. (c) RMSE (%):                 % .4f      % .4f      % .4f\n', Ea_c*100, Eb_c*100, Ec_c*100);

```



```

fprintf(f,'=====\\n');

%% DEMAS calibration
[phi_0_a,k1_a,k2_a,x_a,K_a,R2_a,Erms_a] = model_D(phi_n_cal,C_n_cal,500,'a',0,0,LIMIT);
[phi_0_b,k1_b,k2_b,x_b,K_b,R2_b,Erms_b] = model_D(phi_n_cal,C_n_cal,500,'b',0,0,LIMIT);
[phi_0_c,k1_c,k2_c,x_c,K_c,R2_c,Erms_c] = model_D(phi_n_cal,C_n_cal,500,'c',0,0,LIMIT);
% Reporting calibration
fprintf('DEMAS calibration\\n');
fprintf('Parameter          (a)          (b)          (c)\\n');
fprintf('phi_0:      %10.6f %10.6f %10.6f\\n',phi_0_a,phi_0_b,phi_0_c);
fprintf('k1:        %10.6f %10.6f %10.6f\\n',k1_a,k1_b,k1_c);
fprintf('k2:        %10.6f %10.6f %10.6f\\n',k2_a,k2_b,k2_c);
fprintf('x:         %10.6f %10.6f %10.6f\\n',x_a,x_b,x_c);
fprintf('R2:        %10.8f %10.8f %10.8f\\n',R2_a,R2_b,R2_c);
fprintf('RMSE:     %10.6f %10.6f %10.6f\\n',Erms_a,Erms_b,Erms_c*100);
fprintf('Iter.:    %10d %10d %10d\\n',500,500,500);
fprintf('-----\\n');
fprintf('Phi_0:     %10.6f %10.6f %10.6f\\n',phi_0_a,phi_0_b,phi_0_c);
fprintf('K:         %10.6f %10.6f %10.6f\\n',K_a,K_b,K_c);
fprintf('=====\\n');
% Reporting calibration in output file
fprintf(f,'DEMAS calibration\\n');
fprintf(f,'Parameter          (a)          (b)          (c)\\n');
fprintf(f,'phi_0:      %10.6f %10.6f %10.6f\\n',phi_0_a,phi_0_b,phi_0_c);
fprintf(f,'k1:        %10.6f %10.6f %10.6f\\n',k1_a,k1_b,k1_c);
fprintf(f,'k2:        %10.6f %10.6f %10.6f\\n',k2_a,k2_b,k2_c);
fprintf(f,'x:         %10.6f %10.6f %10.6f\\n',x_a,x_b,x_c);
fprintf(f,'R2:        %10.8f %10.8f %10.8f\\n',R2_a,R2_b,R2_c);
fprintf(f,'RMSE:     %10.6f %10.6f %10.6f\\n',Erms_a,Erms_b,Erms_c*100);
fprintf(f,'Iter.:    %10d %10d %10d\\n',500,500,500);
fprintf(f,'-----\\n');
fprintf(f,'Phi_0:     %10.6f %10.6f %10.6f\\n',phi_0_a,phi_0_b,phi_0_c);
fprintf(f,'K:         %10.6f %10.6f %10.6f\\n',K_a,K_b,K_c);
fprintf(f,'=====\\n');
% plot with calibration curves
phi_a=phi_0_a*(x_a./(1+k1_a*C)+(1-x_a)/(1+k2_a*C));
phi_b=phi_0_b*(x_b./(1+k1_b*C)+(1-x_b)/(1+k2_b*C));
phi_c=phi_0_c*(x_c./(1+k1_c*C)+(1-x_c)/(1+k2_c*C));
figure(6)
p_fig=plot(phi_a,C,'-r',phi_b,C,'-b',phi_c,C,'-g',phi_n_cal,C_n_cal,'ok',phi_n_test,C_n_test,'dk');
set(p_fig(4),'MarkerSize',6,'MarkerFaceColor','k')
set(p_fig(5),'MarkerSize',6)
xlim(Range_x); ylim(Range_y); grid on;
title(sprintf('Demas R2a=%0.8f R2b=%0.8f R2c=%0.8f',R2_a,R2_b,R2_c))
xlabel('analytical signal');
ylabel('concentration');
legend('criterion (a)', 'criterion (b)', 'criterion (c)', 'calib. data', 'test data');
% evaluation with calibration data
[Ea_a,R2a_a,Ea_b,R2a_b,Ea_c] = evaluation_demas(phi_n_cal,C_n_cal,phi_0_a,k1_a,k2_a,x_a,0,0);
[Eb_a,R2b_a,Eb_b,R2b_b,Eb_c] = evaluation_demas(phi_n_cal,C_n_cal,phi_0_b,k1_b,k2_b,x_b,0,0);
[Ec_a,R2c_a,Ec_b,R2c_b,Ec_c] = evaluation_demas(phi_n_cal,C_n_cal,phi_0_c,k1_c,k2_c,x_c,0,0);
fprintf('D, evaluation with calibration data          D(a)          D(b)          D(c)\\n');
fprintf('evaluation with crit. (a) RMSE (signal):      %0.4f %0.4f %0.4f\\n',Ea_a,Eb_a,Ec_a);
fprintf('evaluation with crit. (b) RMSE (conc):        %0.4f %0.4f %0.4f\\n',Ea_b,Eb_b,Ec_b);
fprintf('evaluation with crit. (c) RMSE (%%):          %0.4f %0.4f %0.4f\\n',Ea_c*100,Eb_c*100,Ec_c*100);
fprintf(f,'D, evaluation with calibration data          D(a)          D(b)          D(c)\\n');
fprintf(f,'evaluation with crit. (a) RMSE (signal):      %0.4f %0.4f %0.4f\\n',Ea_a,Eb_a,Ec_a);
fprintf(f,'evaluation with crit. (b) RMSE (conc):        %0.4f %0.4f %0.4f\\n',Ea_b,Eb_b,Ec_b);
fprintf(f,'evaluation with crit. (c) RMSE (%%):          %0.4f %0.4f %0.4f\\n',Ea_c*100,Eb_c*100,Ec_c*100);
% evaluation with test data
[Ea_a,R2a_a,Ea_b,R2a_b,Ea_c] = evaluation_demas(phi_n_test,C_n_test,phi_0_a,k1_a,k2_a,x_a,0,0);
[Eb_a,R2b_a,Eb_b,R2b_b,Eb_c] = evaluation_demas(phi_n_test,C_n_test,phi_0_b,k1_b,k2_b,x_b,0,0);
[Ec_a,R2c_a,Ec_b,R2c_b,Ec_c] = evaluation_demas(phi_n_test,C_n_test,phi_0_c,k1_c,k2_c,x_c,0,0);
fprintf('-----\\n');
fprintf('D, evaluation with test data          D(a)          D(b)          D(c)\\n');
fprintf('evaluation with crit. (a) RMSE (signal):      %0.4f %0.4f %0.4f\\n',Ea_a,Eb_a,Ec_a);
fprintf('evaluation with crit. (b) RMSE (conc):        %0.4f %0.4f %0.4f\\n',Ea_b,Eb_b,Ec_b);
fprintf('evaluation with crit. (c) RMSE (%%):          %0.4f %0.4f %0.4f\\n',Ea_c*100,Eb_c*100,Ec_c*100);
fprintf(f,'-----\\n');
fprintf(f,'D, evaluation with test data          D(a)          D(b)          D(c)\\n');
fprintf(f,'evaluation with crit. (a) RMSE (signal):      %0.4f %0.4f %0.4f\\n',Ea_a,Eb_a,Ec_a);
fprintf(f,'evaluation with crit. (b) RMSE (conc):        %0.4f %0.4f %0.4f\\n',Ea_b,Eb_b,Ec_b);
fprintf(f,'evaluation with crit. (c) RMSE (%%):          %0.4f %0.4f %0.4f\\n',Ea_c*100,Eb_c*100,Ec_c*100);
fprintf(f,'=====\\n');

%%
% closing output file
fclose(f);

%%%%%%%%%%%%%%%%%%%%%%%%%%%%%%%%%%%%%%%%%%%%%%%%%%%%%%%%%%%%%%%%%%%%%%%%

```

C.6.4 Scripts for model calibration and evaluation

A very simple script: script_models_simple.m

```

%%%%%%%%%%%%%%%%%%%%%%%%%%%%%%%%%%%%%%%%%%%%%%%%%%%%%%%%%%%%%%%%%%%%%%%%
% script_models_simple.m
%%%%%%%%%%%%%%%%%%%%%%%%%%%%%%%%%%%%%%%%%%%%%%%%%%%%%%%%%%%%%%%%%%%%%%%%
%%% Developed by S. Medina-Rodriguez, A. de la Torre-Vega,
%%% J.F. Fernandez-Sanchez and A. Fernandez-Gutierrez
%%% (smedina@ugr.es, atv@ugr.es, jffernan@ugr.es, albertof@ugr.es)
%%% Dpt. Analytical Chemistry / Dpt. Signal Theory Networking and Communications
%%% University of Granada, Nov 2013
%%%%%%%%%%%%%%%%%%%%%%%%%%%%%%%%%%%%%%%%%%%%%%%%%%%%%%%%%%%%%%%%%%%%%%%%
% To perform parameter fitting of the models describing the relation
% between analyte concentration and chemical signal C(phi) or phi(C)
% Simple script: only for L(a): Lehrer model, calibrated with criterion (a)
% To run it, just type:
%   script_models_simple
% in a MATLAB or OCTAVE console.
%%%%%%%%%%%%%%%%%%%%%%%%%%%%%%%%%%%%%%%%%%%%%%%%%%%%%%%%%%%%%%%%%%%%%%%%
clear;

% Files with data for calibration / test
% These are ASCII files with 2 columns
% 1st column for concentration; 2nd column for analytical signal
file_calibration = 'exp_1_cal.txt';
file_test = 'exp_1_test.txt';
% Loading calibration data
A_cal=load(file_calibration);
C_n_cal=A_cal(:,1);
phi_n_cal=A_cal(:,2);
% Loading test data
A_test=load(file_test);
C_n_test=A_test(:,1);
phi_n_test=A_test(:,2);
fprintf('\nCALIBRATION DATAFILE: %s    TEST DATAFILE: %s\n',file_calibration,file_test);

LIMIT = 0; % if LIMIT = 1, this forces the Lehrer model to provide k>0, x>0 and x<1

% Fitting Lehrer model with criterion (a)
% 100 iterations; criterion (a);
% plots represented in figure 1; reporting results
% FITTING L(a) MODEL WITH CALIBRATION DATA
fprintf('FITTING A LEHRER MODEL WITH (a) CRITERION\n')
[phi_0_a,k_a,x_a,K,R2,Erms] = model_L(phi_n_cal,C_n_cal,100,'a',1,1,LIMIT);

% Evaluation of fitted model. Model fitted with (a) criterion is evaluated
% with criteria (a), (b) and (c)
% EVALUATION FOR CALIBRATION DATA (plots in figure 2; reporting results)
fprintf('EVALUATION OF THE LEHRER(a) MODEL WITH (a),(b),(c) CRITERIA USING CALIBRATION DATA\n')
[Ea_a,R2a_a,Ea_b,R2a_b,Ea_c,R2a_c] = evaluation_demas(phi_n_cal,C_n_cal,phi_0_a,k_a,0,x_a,2,1);
% EVALUATION FOR TEST DATA (plots in figure 3; reporting results)
fprintf('EVALUATION OF THE LEHRER(A) MODEL WITH (a),(b),(c) CRITERIA USING TEST DATA\n')
[Ea_a,R2a_a,Ea_b,R2a_b,Ea_c,R2a_c] = evaluation_demas(phi_n_test,C_n_test,phi_0_a,k_a,0,x_a,3,1);

% END OF SCRIPT
%****

```

A more complex script: script_models_complex.m

```

%%%%%%%%%%%%%%%%%%%%%%%%%%%%%%%%%%%%%%%%%%%%%%%%%%%%%%%%%%%%%%%%%%%%%%%%
% script_models_complex.m
%%%%%%%%%%%%%%%%%%%%%%%%%%%%%%%%%%%%%%%%%%%%%%%%%%%%%%%%%%%%%%%%%%%%%%%%
%%% Developed by S. Medina-Rodriguez, A. de la Torre-Vega,
%%% J.F. Fernandez-Sanchez and A. Fernandez-Gutierrez
%%% (smedina@ugr.es, atv@ugr.es, jffernan@ugr.es, albertof@ugr.es)
%%% Dpt. Analytical Chemistry / Dpt. Signal Theory Networking and Communications
%%% University of Granada, Nov 2013
%%%%%%%%%%%%%%%%%%%%%%%%%%%%%%%%%%%%%%%%%%%%%%%%%%%%%%%%%%%%%%%%%%%%%%%%
% To perform parameter fitting of the models describing the relation
% between analyte concentration and chemical signal C(phi) or phi(C)
% Complex script: for all models and criteria
% Example of use (saving output in file 'output_1.txt'):
%   diary('output_1.txt');
%   script_models_complex
%   diary('off');

```

```

% Simplest way to run it: just type:
% script_models_complex
% in a MATLAB or OCTAVE console.
%%%%%%%%%%%%%%%%%%%%%%%%%%%%%%%%%%%%%%%%%%%%%%%%%%%%%%%%%%%%%%%%%%%%%%%%
clear;

% LOADING DATA
% Files with data for calibration / test
% These are ASCII files with 2 columns
% 1st column for concentration; 2nd column for analytical signal
file_calibration = 'exp_1_cal.txt';
file_test = 'exp_1_test.txt';
% Loading calibration data
A_cal=load(file_calibration);
C_n_cal=A_cal(:,1);
phi_n_cal=A_cal(:,2);
% Loading test data
A_test=load(file_test);
C_n_test=A_test(:,1);
phi_n_test=A_test(:,2);
fprintf('\nCalibration datafile: %s    Test datafile: %s\n',file_calibration,file_test);

LIMIT = 0; % when 0, Lehrer and Demas models are computed without restrictions

% STERN-VOLMER MODEL
fprintf('\n===== \n');
fprintf('STERN-VOLMER MODEL: Calibration (a), (b) and (c)\n');
% S-V (a), (b) and (c) calibration
[phi_0_a,k_a,R2,Erms] = model_SV(phi_n_cal,C_n_cal,100,'a',0,1);
[phi_0_b,k_b,R2,Erms] = model_SV(phi_n_cal,C_n_cal,1,'b',0,1);
[phi_0_c,k_c,R2,Erms] = model_SV(phi_n_cal,C_n_cal,1,'c',0,1);
% evaluation with calibration data
[Ea_a,R2a_a,Ea_b,R2a_b,Ea_c,R2a_c] = evaluation_demas(phi_n_cal,C_n_cal,phi_0_a,k_a,0,1,0,0);
[Eb_a,R2b_a,Eb_b,R2b_b,Eb_c,R2b_c] = evaluation_demas(phi_n_cal,C_n_cal,phi_0_b,k_b,0,1,0,0);
[Ec_a,R2c_a,Ec_b,R2c_b,Ec_c,R2c_c] = evaluation_demas(phi_n_cal,C_n_cal,phi_0_c,k_c,0,1,0,0);
fprintf('----- \n');
fprintf('S-V, evaluation with calibration data      S-V(a)    S-V(b)    S-V(c)\n');
fprintf('evaluation with crit. (a) RMSE (signal):    % .4f    % .4f    % .4f\n', Ea_a,Eb_a,Ec_a);
fprintf('evaluation with crit. (b) RMSE (conc):       % .4f    % .4f    % .4f\n', Ea_b,Eb_b,Ec_b);
fprintf('evaluation with crit. (c) RMSE (%):          % .4f    % .4f    % .4f\n', Ea_c*100,Eb_c*100,Ec_c*100);
% evaluation with test data
[Ea_a,R2a_a,Ea_b,R2a_b,Ea_c,R2a_c] = evaluation_demas(phi_n_test,C_n_test,phi_0_a,k_a,0,1,0,0);
[Eb_a,R2b_a,Eb_b,R2b_b,Eb_c,R2b_c] = evaluation_demas(phi_n_test,C_n_test,phi_0_b,k_b,0,1,0,0);
[Ec_a,R2c_a,Ec_b,R2c_b,Ec_c,R2c_c] = evaluation_demas(phi_n_test,C_n_test,phi_0_c,k_c,0,1,0,0);
fprintf('----- \n');
fprintf('S-V, evaluation with test data      S-V(a)    S-V(b)    S-V(c)\n');
fprintf('evaluation with crit. (a) RMSE (signal):    % .4f    % .4f    % .4f\n', Ea_a,Eb_a,Ec_a);
fprintf('evaluation with crit. (b) RMSE (conc):       % .4f    % .4f    % .4f\n', Ea_b,Eb_b,Ec_b);
fprintf('evaluation with crit. (c) RMSE (%):          % .4f    % .4f    % .4f\n', Ea_c*100,Eb_c*100,Ec_c*100);
fprintf('===== \n');

% LEHRER MODEL
fprintf('\n===== \n');
fprintf('LEHRER MODEL: Calibration (a), (b) and (c)\n');
% L (a), (b) and (c) calibration
[phi_0_a,k_a,x_a,K,R2,Erms] = model_L(phi_n_cal,C_n_cal,100,'a',0,1,LIMIT);
[phi_0_b,k_b,x_b,K,R2,Erms] = model_L(phi_n_cal,C_n_cal,100,'b',0,1,LIMIT);
[phi_0_c,k_c,x_c,K,R2,Erms] = model_L(phi_n_cal,C_n_cal,100,'c',0,1,LIMIT);
% evaluation with calibration data
[Ea_a,R2a_a,Ea_b,R2a_b,Ea_c,R2a_c] = evaluation_demas(phi_n_cal,C_n_cal,phi_0_a,k_a,0,x_a,0,0);
[Eb_a,R2b_a,Eb_b,R2b_b,Eb_c,R2b_c] = evaluation_demas(phi_n_cal,C_n_cal,phi_0_b,k_b,0,x_b,0,0);
[Ec_a,R2c_a,Ec_b,R2c_b,Ec_c,R2c_c] = evaluation_demas(phi_n_cal,C_n_cal,phi_0_c,k_c,0,x_c,0,0);
fprintf('----- \n');
fprintf('L, evaluation with calibration data      L(a)      L(b)      L(c)\n');
fprintf('evaluation with crit. (a) RMSE (signal):    % .4f    % .4f    % .4f\n', Ea_a,Eb_a,Ec_a);
fprintf('evaluation with crit. (b) RMSE (conc):       % .4f    % .4f    % .4f\n', Ea_b,Eb_b,Ec_b);
fprintf('evaluation with crit. (c) RMSE (%):          % .4f    % .4f    % .4f\n', Ea_c*100,Eb_c*100,Ec_c*100);
% evaluation with test data
[Ea_a,R2a_a,Ea_b,R2a_b,Ea_c,R2a_c] = evaluation_demas(phi_n_test,C_n_test,phi_0_a,k_a,0,x_a,0,0);
[Eb_a,R2b_a,Eb_b,R2b_b,Eb_c,R2b_c] = evaluation_demas(phi_n_test,C_n_test,phi_0_b,k_b,0,x_b,0,0);
[Ec_a,R2c_a,Ec_b,R2c_b,Ec_c,R2c_c] = evaluation_demas(phi_n_test,C_n_test,phi_0_c,k_c,0,x_c,0,0);
fprintf('----- \n');
fprintf('L, evaluation with test data      L(a)      L(b)      L(c)\n');
fprintf('evaluation with crit. (a) RMSE (signal):    % .4f    % .4f    % .4f\n', Ea_a,Eb_a,Ec_a);
fprintf('evaluation with crit. (b) RMSE (conc):       % .4f    % .4f    % .4f\n', Ea_b,Eb_b,Ec_b);
fprintf('evaluation with crit. (c) RMSE (%):          % .4f    % .4f    % .4f\n', Ea_c*100,Eb_c*100,Ec_c*100);
fprintf('===== \n');

% POLYNOMIAL 2nd DEGREE MODEL
fprintf('\n===== \n');
fprintf('POLYNOMIAL P2 MODEL: Calibration (a), (b) and (c)\n');
% P2 (a), (b) and (c) calibration
[a0_a,a1_a,a2_a,PHI_0,K,R2,Erms] = model_P2(phi_n_cal,C_n_cal,100,'a',0,1);
[a0_b,a1_b,a2_b,PHI_0,K,R2,Erms] = model_P2(phi_n_cal,C_n_cal,1,'b',0,1);

```

```

[a0_c,a1_c,a2_c,PHI_0,K,R2,Erms] = model_P2(phi_n_cal,C_n_cal,1,'c',0,1);
% evaluation with calibration data
[ Ea_a,R2a_a,Ea_b,R2a_b,Ea_c,R2a_c ] = evaluation_polynom(phi_n_cal,C_n_cal,-1,a0_a,a1_a,a2_a,0,0);
[ Eb_a,R2b_a,Eb_b,R2b_b,Eb_c,R2b_c ] = evaluation_polynom(phi_n_cal,C_n_cal,-1,a0_b,a1_b,a2_b,0,0);
[ Ec_a,R2c_a,Ec_b,R2c_b,Ec_c,R2c_c ] = evaluation_polynom(phi_n_cal,C_n_cal,-1,a0_c,a1_c,a2_c,0,0);
fprintf('-----\n');
fprintf('P2, evaluation with calibration data          P2 (a)      P2 (b)      P2 (c)\n');
fprintf('evaluation with crit. (a) RMSE (signal):      % .4f      % .4f      % .4f\n', Ea_a,Eb_a,Ec_a);
fprintf('evaluation with crit. (b) RMSE (conc):         % .4f      % .4f      % .4f\n', Ea_b,Eb_b,Ec_b);
fprintf('evaluation with crit. (c) RMSE (%):             % .4f      % .4f      % .4f\n', Ea_c*100,Eb_c*100,Ec_c*100);
% evaluation with test data
[ Ea_a,R2a_a,Ea_b,R2a_b,Ea_c,R2a_c ] = evaluation_polynom(phi_n_test,C_n_test,-1,a0_a,a1_a,a2_a,0,0);
[ Eb_a,R2b_a,Eb_b,R2b_b,Eb_c,R2b_c ] = evaluation_polynom(phi_n_test,C_n_test,-1,a0_b,a1_b,a2_b,0,0);
[ Ec_a,R2c_a,Ec_b,R2c_b,Ec_c,R2c_c ] = evaluation_polynom(phi_n_test,C_n_test,-1,a0_c,a1_c,a2_c,0,0);
fprintf('-----\n');
fprintf('P2, evaluation with test data          P2 (a)      P2 (b)      P2 (c)\n');
fprintf('evaluation with crit. (a) RMSE (signal):      % .4f      % .4f      % .4f\n', Ea_a,Eb_a,Ec_a);
fprintf('evaluation with crit. (b) RMSE (conc):         % .4f      % .4f      % .4f\n', Ea_b,Eb_b,Ec_b);
fprintf('evaluation with crit. (c) RMSE (%):             % .4f      % .4f      % .4f\n', Ea_c*100,Eb_c*100,Ec_c*100);
fprintf('===== \n');

% POLYNOMIAL-EXPONENT 1st DEGREE MODEL
fprintf('\n===== \n');
fprintf('POLYNOMIAL-EXPONENT PE-1 MODEL: Calibration (a), (b) and (c)\n');
% PE-1 (a), (b) and(c) calibration
[a0_a,a1_a,alpha_a,PHI_0,K,R2,Erms] = model_PE1(phi_n_cal,C_n_cal,100,'a',0,1);
[a0_b,a1_b,alpha_b,PHI_0,K,R2,Erms] = model_PE1(phi_n_cal,C_n_cal,100,'b',0,1);
[a0_c,a1_c,alpha_c,PHI_0,K,R2,Erms] = model_PE1(phi_n_cal,C_n_cal,100,'c',0,1);
% evaluation with calibration data
[ Ea_a,R2a_a,Ea_b,R2a_b,Ea_c,R2a_c ] = evaluation_polynom(phi_n_cal,C_n_cal,alpha_a,a0_a,a1_a,0,0,0);
[ Eb_a,R2b_a,Eb_b,R2b_b,Eb_c,R2b_c ] = evaluation_polynom(phi_n_cal,C_n_cal,alpha_b,a0_b,a1_b,0,0,0);
[ Ec_a,R2c_a,Ec_b,R2c_b,Ec_c,R2c_c ] = evaluation_polynom(phi_n_cal,C_n_cal,alpha_c,a0_c,a1_c,0,0,0);
fprintf('-----\n');
fprintf('PE1, evaluation with calibration data          PE1 (a)      PE1 (b)      PE1 (c)\n');
fprintf('evaluation with crit. (a) RMSE (signal):      % .4f      % .4f      % .4f\n', Ea_a,Eb_a,Ec_a);
fprintf('evaluation with crit. (b) RMSE (conc):         % .4f      % .4f      % .4f\n', Ea_b,Eb_b,Ec_b);
fprintf('evaluation with crit. (c) RMSE (%):             % .4f      % .4f      % .4f\n', Ea_c*100,Eb_c*100,Ec_c*100);
% evaluation with test data
[ Ea_a,R2a_a,Ea_b,R2a_b,Ea_c,R2a_c ] = evaluation_polynom(phi_n_test,C_n_test,alpha_a,a0_a,a1_a,0,0,0);
[ Eb_a,R2b_a,Eb_b,R2b_b,Eb_c,R2b_c ] = evaluation_polynom(phi_n_test,C_n_test,alpha_b,a0_b,a1_b,0,0,0);
[ Ec_a,R2c_a,Ec_b,R2c_b,Ec_c,R2c_c ] = evaluation_polynom(phi_n_test,C_n_test,alpha_c,a0_c,a1_c,0,0,0);
fprintf('-----\n');
fprintf('PE1, evaluation with test data          PE1 (a)      PE1 (b)      PE1 (c)\n');
fprintf('evaluation with crit. (a) RMSE (signal):      % .4f      % .4f      % .4f\n', Ea_a,Eb_a,Ec_a);
fprintf('evaluation with crit. (b) RMSE (conc):         % .4f      % .4f      % .4f\n', Ea_b,Eb_b,Ec_b);
fprintf('evaluation with crit. (c) RMSE (%):             % .4f      % .4f      % .4f\n', Ea_c*100,Eb_c*100,Ec_c*100);
fprintf('===== \n');

% POLYNOMIAL-EXPONENT 2nd DEGREE MODEL
fprintf('\n===== \n');
fprintf('POLYNOMIAL-EXPONENT PE-2 MODEL: Calibration (a), (b) and (c)\n');
% PE-2 (a), (b) and(c) calibration
[a0_a,a1_a,a2_a,alpha_a,PHI_0,K,R2,Erms] = model_PE2(phi_n_cal,C_n_cal,100,'a',0,1);
[a0_b,a1_b,a2_b,alpha_b,PHI_0,K,R2,Erms] = model_PE2(phi_n_cal,C_n_cal,100,'b',0,1);
[a0_c,a1_c,a2_c,alpha_c,PHI_0,K,R2,Erms] = model_PE2(phi_n_cal,C_n_cal,100,'c',0,1);
% evaluation with calibration data
[ Ea_a,R2a_a,Ea_b,R2a_b,Ea_c,R2a_c ] = evaluation_polynom(phi_n_cal,C_n_cal,alpha_a,a0_a,a1_a,a2_a,0,0);
[ Eb_a,R2b_a,Eb_b,R2b_b,Eb_c,R2b_c ] = evaluation_polynom(phi_n_cal,C_n_cal,alpha_b,a0_b,a1_b,a2_b,0,0);
[ Ec_a,R2c_a,Ec_b,R2c_b,Ec_c,R2c_c ] = evaluation_polynom(phi_n_cal,C_n_cal,alpha_c,a0_c,a1_c,a2_c,0,0);
fprintf('-----\n');
fprintf('PE2, evaluation with calibration data          PE2 (a)      PE2 (b)      PE2 (c)\n');
fprintf('evaluation with crit. (a) RMSE (signal):      % .4f      % .4f      % .4f\n', Ea_a,Eb_a,Ec_a);
fprintf('evaluation with crit. (b) RMSE (conc):         % .4f      % .4f      % .4f\n', Ea_b,Eb_b,Ec_b);
fprintf('evaluation with crit. (c) RMSE (%):             % .4f      % .4f      % .4f\n', Ea_c*100,Eb_c*100,Ec_c*100);
% evaluation with test data
[ Ea_a,R2a_a,Ea_b,R2a_b,Ea_c,R2a_c ] = evaluation_polynom(phi_n_test,C_n_test,alpha_a,a0_a,a1_a,a2_a,0,0);
[ Eb_a,R2b_a,Eb_b,R2b_b,Eb_c,R2b_c ] = evaluation_polynom(phi_n_test,C_n_test,alpha_b,a0_b,a1_b,a2_b,0,0);
[ Ec_a,R2c_a,Ec_b,R2c_b,Ec_c,R2c_c ] = evaluation_polynom(phi_n_test,C_n_test,alpha_c,a0_c,a1_c,a2_c,0,0);
fprintf('-----\n');
fprintf('PE2, evaluation with test data          PE2 (a)      PE2 (b)      PE2 (c)\n');
fprintf('evaluation with crit. (a) RMSE (signal):      % .4f      % .4f      % .4f\n', Ea_a,Eb_a,Ec_a);
fprintf('evaluation with crit. (b) RMSE (conc):         % .4f      % .4f      % .4f\n', Ea_b,Eb_b,Ec_b);
fprintf('evaluation with crit. (c) RMSE (%):             % .4f      % .4f      % .4f\n', Ea_c*100,Eb_c*100,Ec_c*100);
fprintf('===== \n');

% DEMAS MODEL
fprintf('\n===== \n');
fprintf('DEMAS MODEL: Calibration (a), (b) and (c)\n');
% D (a), (b) and(c) calibration
[phi_0_a,k1_a,k2_a,x_a,K,R2,Erms] = model_D(phi_n_cal,C_n_cal,500,'a',0,1,LIMIT);
[phi_0_b,k1_b,k2_b,x_b,K,R2,Erms] = model_D(phi_n_cal,C_n_cal,500,'b',0,1,LIMIT);
[phi_0_c,k1_c,k2_c,x_c,K,R2,Erms] = model_D(phi_n_cal,C_n_cal,500,'c',0,1,LIMIT);
% evaluation with calibration data
[ Ea_a,R2a_a,Ea_b,R2a_b,Ea_c,R2a_c ] = evaluation_demas(phi_n_cal,C_n_cal,phi_0_a,k1_a,k2_a,x_a,0,0);

```

```
[Eb_a,R2b_a,Eb_b,R2b_b,Eb_c,R2b_c] = evaluation_demas(phi_n_cal,C_n_cal,phi_0_b,k1_b,k2_b,x_b,0,0);
[Ec_a,R2c_a,Ec_b,R2c_b,Ec_c,R2c_c] = evaluation_demas(phi_n_cal,C_n_cal,phi_0_c,k1_c,k2_c,x_c,0,0);
fprintf('-----\n');
fprintf('D, evaluation with calibration data          D(a)          D(b)          D(c)\n');
fprintf('evaluation with crit. (a) RMSE (signal):      %.4f          %.4f          %.4f\n', Ea_a,Eb_a,Ec_a);
fprintf('evaluation with crit. (b) RMSE (conc):         %.4f          %.4f          %.4f\n', Ea_b,Eb_b,Ec_b);
fprintf('evaluation with crit. (c) RMSE (%):             %.4f          %.4f          %.4f\n', Ea_c*100,Eb_c*100,Ec_c*100);
% evaluation with test data
[Ea_a,R2a_a,Ea_b,R2a_b,Ea_c,R2a_c] = evaluation_demas(phi_n_test,C_n_test,phi_0_a,k1_a,k2_a,x_a,0,0);
[Eb_a,R2b_a,Eb_b,R2b_b,Eb_c,R2b_c] = evaluation_demas(phi_n_test,C_n_test,phi_0_b,k1_b,k2_b,x_b,0,0);
[Ec_a,R2c_a,Ec_b,R2c_b,Ec_c,R2c_c] = evaluation_demas(phi_n_test,C_n_test,phi_0_c,k1_c,k2_c,x_c,0,0);
fprintf('-----\n');
fprintf('D, evaluation with test data          D(a)          D(b)          D(c)\n');
fprintf('evaluation with crit. (a) RMSE (signal):      %.4f          %.4f          %.4f\n', Ea_a,Eb_a,Ec_a);
fprintf('evaluation with crit. (b) RMSE (conc):         %.4f          %.4f          %.4f\n', Ea_b,Eb_b,Ec_b);
fprintf('evaluation with crit. (c) RMSE (%):             %.4f          %.4f          %.4f\n', Ea_c*100,Eb_c*100,Ec_c*100);
fprintf('===== \n');
#####
```

Script performing the complete study: script_complete_study.m

```
#####
% script_complete_study.m
#####
%%% Developed by S. Medina-Rodriguez, A. de la Torre-Vega,
%%% J.F. Fernandez-Sanchez and A. Fernandez-Gutierrez
%%% (smedina@ugr.es, atv@ugr.es, jffernan@ugr.es, albertof@ugr.es)
%%% Dpt. Analytical Chemistry / Dpt. Signal Theory Networking and Communications
%%% University of Granada, Nov 2013
#####
% This script performs a complete study of the data with different
% models and criteria using the function "complete_study.m". The study
% involves the calibration of each model with each criterion using the
% calibration data, and the evaluation of each model using calibration and
% test data. Results are reported in the command window and also in a text
% file. The script allows to prepare the calibration and test data easily.
%
% In order to prepare this script for new data, the following step should
% be done:
% 1.- Prepare your calibration data. See comments below.
% 2.- Prepare your test data. See comments below.
% 3.- Select if k,x (in Lehrer model) and k1,k2,x (in Demas model) should
% be limited to k>0, x>0, x<1 (Lehrer); k1>0, k2>0, x>0, x<1 (Demas), by
% setting the variable LIMIT to 0 or 1; (see line 115)
% 4.- Select the name of the output file (see line 122)
% 5.- The function complete_study() performs all the calibrations and
% tests (see line 127)
%
% Calibration data are values of concentration (C_n) and analytical signal
% (phi_n). Calibration data are prepared by writing concentration and
% analytical signal:
% C_cal=[C1 C2 ... CN];
% phi_cal=[phi1 phi2 ... phiN];
% i.e., the values of concentration and the corresponding analytical signal
% at each concentration separated by a space.
% VERY IMPORTANT: there should be the same number of elements in C_cal and
% phi_cal.
% Preparing test data is similar.
%
% In order to prepare data, modify lines 88 and 89 for calibration data:
% C_cal=[0.5 1.0 3.0 5.0 7.0 9.0 12.0 16.0 20.0];
% phi_cal=[49.2411 41.7845 27.7127 21.3608 17.9941 15.6490 13.4975 10.9609 9.2335];
% and modify lines 99 and 100 for test data:
% C_test=[0.75 2.0 4.0 6.0 8.0 10.0 14.0 18.0];
% phi_test=[45.4119 32.4933 24.2433 19.9944 17.0082 15.0475 12.0687 9.8983];
%
% Alternatively, one could prepare the calibration/test data from text files,
% where data are written in two columns (first column for concentration C,
% second for analytical signal phi). For example:
% Loading calibration data
% A_cal=load('exp_1_cal.tex');
% C_n_cal=A_cal(:,1);
% phi_n_cal=A_cal(:,2);
% Loading test data
% A_test=load('exp_1_test.tex');
% C_n_test=A_test(:,1);
% phi_n_test=A_test(:,2);
% See the data file "exp_1_cal.tex" to see an example of how to prepare
% the data in a file. Data are in two columns separated by a space:
% C1 phi1
% C2 phi2
```

```

% .....
% CN    phiN
%
% In order to read calibration/test data from files do the next steps:
% 1. Prepare the calibration and test data in text files
% 2. Comment lines 88, 89, 99, 100
% 3. Uncomment lines 103, 104, 105, 107, 108, 109
% 4. Modify the line 103 to set the file name where the calibration data
%    are written.
% 5. Modify the line 107 to set the file name where the calibration data
%    are written.
%
%
% To run the script, just type:
%   script_complete_study
% in a MATLAB or OCTAVE console.
%%%%%%%%%%%%%%%%%%%%%%%%%%%%%%%%%%%%%%%%%%%%%%%%%%%%%%%%%%%%%%%%%%%%%%%%
clear; % This clear all the variables before starting with computations

% PREPARING CALIBRATION DATA
% Concentration and analytical signal used for calibration
% Concentration: list of values separated by spaces
% Analytical signal: list of values separated by spaces
% There should be the same number of values in both
% Example:
%   C_cal=[0.01 0.03 0.1 0.3 1];
%   phi_cal=[35 30 25 20 15];
C_cal=[0.5 1.0 3.0 5.0 7.0 9.0 12.0 16.0 20.0];
phi_cal=[49.2411 41.7845 27.7127 21.3608 17.9941 15.6490 13.4975 10.9609 9.2335];

% PREPARING TEST DATA
% Concentration and analytical signal used for test
% Concentration: list of values separated by spaces
% Analytical signal: list of values separated by spaces
% There should be the same number of values in both
% Example:
%   C_test=[0.01 0.03 0.1 0.3 1];
%   phi_test=[35 30 25 20 15];
C_test=[0.75 2.0 4.0 6.0 8.0 10.0 14.0 18.0];
phi_test=[45.4119 32.4933 24.2433 19.9944 17.0082 15.0475 12.0687 9.8983];

% PREPARING CALIBRATION DATA FROM FILE (uncomment these lines in that case)
%   A_cal=load('exp_1_cal.tex');
%   C_n_cal=A_cal(:,1);
%   phi_n_cal=A_cal(:,2);
% PREPARING TEST DATA FROM FILE (uncomment these lines in that case)
%   A_test=load('exp_1_test.tex');
%   C_n_test=A_test(:,1);
%   phi_n_test=A_test(:,2);

% SELECTING LIMIT FOR LEHRER AND DEMAS MODEL
% LIMIT=0; computes Lehrer and Demas models without restrictions
% LIMIT=1; computes Lehrer and Demas models with restrictions:
%   k>0, x>0, x<1 (Lehrer); k1>0, k2>0, x>0, x<1 (Demas)
LIMIT = 0;

% SELECTING THE NAME FOR THE OUTPUT FILE
% The output file is written as plain text. So, recommended extension is ".txt"
% A new file will be created with this name. If the file exists, it will be
% overwritten. All the results are displayed in the command line and also
% written in the output file.
file_out = 'out_complete_study.txt';

% RUNNING THE FUNCTION WITH APPROPRIATE PARAMETERS
% This function performs calibrations and evaluations according to the
% configuration:
complete_study(phi_cal,C_cal,phi_test,C_test,LIMIT,file_out);

% END OF SCRIPT
%%%%

```

C.6.5 Some data files with input data for calibration/test, and output data from scripts

Calibration file for experiment 1: exp_1_cal.txt

```

0.50 49.2411
1.00 41.7845
3.00 27.7127
5.00 21.3608
7.00 17.9941

```

```
9.00 15.6490
12.00 13.4975
16.00 10.9609
20.00 9.2335
```

Test file for experiment 1: exp_1_test.txt

```
0.75 45.4119
2.00 32.4933
4.00 24.2433
6.00 19.9944
8.00 17.0082
10.00 15.0475
14.00 12.0687
18.00 9.8983
```

Calibration file for experiment 2: exp_2_cal.txt

```
0.50 47.8615
1.00 40.2136
3.00 25.4641
5.00 19.1103
7.00 15.6865
9.00 13.3328
12.00 11.1114
16.00 9.1234
20.00 7.8771
```

Test file for experiment 2: exp_2_test.txt

```
0.75 43.3201
2.00 30.7622
4.00 21.3545
6.00 17.2656
8.00 14.4929
10.00 12.5431
14.00 10.2103
18.00 8.3423
```

Calibration file for experiment 3: exp_3_cal.txt

```
0.50 54.0257
1.00 46.7773
3.00 33.1722
5.00 27.1615
7.00 23.6878
9.00 21.3972
12.00 18.9901
16.00 16.7298
20.00 15.1776
```

Test file for experiment 3: exp_3_test.txt

```
0.75 49.9349
2.00 38.2474
4.00 29.6878
6.00 25.2382
8.00 22.4154
10.00 20.4579
14.00 17.7608
18.00 15.7708
```

Output of script_complete_study.m with experiment 1: out_complete_study.txt

```

=====
Calibration data: (C_n_cal,phi_n_cal)
0.500000000000    49.241100000000
1.000000000000    41.784500000000
3.000000000000    27.712700000000
5.000000000000    21.360800000000
7.000000000000    17.994100000000
9.000000000000    15.649000000000
12.000000000000   13.497500000000
16.000000000000   10.960900000000
20.000000000000    9.233500000000
Test data: (C_n_test,phi_n_test)
0.750000000000    45.411900000000
2.000000000000    32.493300000000
4.000000000000    24.243300000000
6.000000000000    19.994400000000
8.000000000000    17.008200000000
10.000000000000   15.047500000000
14.000000000000   12.068700000000
18.000000000000    9.898300000000
=====
STERN-VOLMER calibration
Parameter      (a)      (b)      (c)
phi_0:    55.030567  46.269568  55.835803
k:         0.292397  0.205050  0.294822
R2:        0.99320931 0.99332426 0.98763289
RMSE:      1.088454  0.520325  11.120749
Iter.:      100      1         1
-----
Phi_0:      55.030567  46.269568  55.835803
K:          0.292397  0.205050  0.294822
=====
S-V, evaluation with calibration data      S-V(a)      S-V(b)      S-V(c)
evaluation with crit. (a) RMSE (signal):    1.0885      2.7673      1.1346
evaluation with crit. (b) RMSE (conc):      1.3714      0.5203      1.2979
evaluation with crit. (c) RMSE (%):         11.8672     55.6881     11.1207
-----
S-V, evaluation with test data              S-V(a)      S-V(b)      S-V(c)
evaluation with crit. (a) RMSE (signal):    1.1442     1.9538     1.2450
evaluation with crit. (b) RMSE (conc):      1.1367     0.3527     1.0653
evaluation with crit. (c) RMSE (%):         10.5064     31.4158     11.0865
=====
LEHRER calibration
Parameter      (a)      (b)      (c)
phi_0:    58.609412  52.061466  58.235861
k:         0.432345  0.294048  0.406246
x:         0.928130  0.960641  0.939276
R2:        0.99929635 0.99761230 0.99799732
RMSE:      0.350374  0.311183  4.475131
Iter.:      100      100      100
-----
Phi_0:      58.609412  52.061466  58.235861
K:          0.401272  0.282474  0.381577
=====
L, evaluation with calibration data          L(a)      L(b)      L(c)
evaluation with crit. (a) RMSE (signal):    0.3504     1.3392     0.4041
evaluation with crit. (b) RMSE (conc):      0.9636     0.3112     0.5310
evaluation with crit. (c) RMSE (%):         5.5857     20.6367     4.4751
-----
L, evaluation with test data                  L(a)      L(b)      L(c)
evaluation with crit. (a) RMSE (signal):    0.5306     0.9749     0.5962
evaluation with crit. (b) RMSE (conc):      0.7280     0.2539     0.4842
evaluation with crit. (c) RMSE (%):         5.8297     11.6238     5.5138
=====
POLINOMIAL-2nd DEGREE calibration
Parameter      (a)      (b)      (c)
a_0:    -1.883936  -3.097917  -2.053558
a_1:     93.354204 153.824899 104.859379
a_2:    1165.399219 574.194234 1008.252164
R2:      0.99966580 0.99791243 0.99890671
RMSE:    0.241465  0.290969  3.306490
Iter.:    100      1         1
-----
Phi_0:      59.882866  53.142087  59.336723
K:          0.452709  0.302917  0.427364
=====
P2, evaluation with calibration data          P2(a)      P2(b)      P2(c)
evaluation with crit. (a) RMSE (signal):    0.2415     1.1327     0.2731
evaluation with crit. (b) RMSE (conc):      0.6722     0.2910     0.4621
evaluation with crit. (c) RMSE (%):         3.7691     16.5380     3.3065
-----
P2, evaluation with test data                  P2(a)      P2(b)      P2(c)

```



```

evaluation with crit. (a) RMSE (signal):    0.4124    0.8452    0.4617
evaluation with crit. (b) RMSE (conc):     0.5724    0.2492    0.4398
evaluation with crit. (c) RMSE (%):        4.5535    9.5277    4.4926

```

```

=====
POLINOMIAL-EXPONENT-1st DEGREE calibration
Parameter      (a)      (b)      (c)
a_0:          -1.319260 -2.198806 -1.413456
a_1:           643.930645 410.523471 581.721810
alpha:        -1.506595 -1.306937 -1.467720
R2:           0.99978840 0.99836051 0.99934436
RMSE:         0.192136  0.257857  2.560554
Iter.:         100      100      100

```

```

-----
Phi_0:         60.882546  54.672111  60.435031
K:             0.503122  0.347983  0.482031

```

```

=====
PE1, evaluation with calibration data      PE1(a)    PE1(b)    PE1(c)
evaluation with crit. (a) RMSE (signal):  0.1921    0.9376    0.2086
evaluation with crit. (b) RMSE (conc):    0.4749    0.2579    0.3670
evaluation with crit. (c) RMSE (%):       2.7676    12.5313   2.5606

```

```

-----
PE1, evaluation with test data            PE1(a)    PE1(b)    PE1(c)
evaluation with crit. (a) RMSE (signal):  0.3568    0.7177    0.3817
evaluation with crit. (b) RMSE (conc):    0.4396    0.2288    0.3705
evaluation with crit. (c) RMSE (%):       3.7825    7.6679    3.7622

```

```

=====
POLINOMIAL-EXPONENT-2nd DEGREE calibration
Parameter      (a)      (b)      (c)
a_0:          -1.029316 -0.731937 -0.978258
a_1:          1221.543408 1994.035027 1362.395894
a_2:          -11960.433929 -41259.702102 -16302.284602
alpha:        -1.711329 -1.886285 -1.747843
R2:           0.99988051 0.99967511 0.99976745
RMSE:         0.144386  0.114786  1.524958
Iter.:         100      100      100

```

```

-----
Phi_0:         62.280907  65.979314  62.595036
K:             0.572501  0.729930  0.590008

```

```

=====
PE2, evaluation with calibration data      PE2(a)    PE2(b)    PE2(c)
evaluation with crit. (a) RMSE (signal):  0.1444    0.2865    0.1484
evaluation with crit. (b) RMSE (conc):    0.1735    0.1148    0.1463
evaluation with crit. (c) RMSE (%):       1.5634    2.6440    1.5250

```

```

-----
PE2, evaluation with test data            PE2(a)    PE2(b)    PE2(c)
evaluation with crit. (a) RMSE (signal):  0.2623    0.2258    0.2481
evaluation with crit. (b) RMSE (conc):    0.2354    0.2061    0.2100
evaluation with crit. (c) RMSE (%):       2.5737    2.2338    2.4074

```

```

=====
DEMAs calibration
Parameter      (a)      (b)      (c)
phi_0:         61.347029  78.712409  61.706000
k1:            0.643318  2.111436  0.683808
k2:            0.061307  0.119410  0.069900
x:             0.783420  0.651016  0.759354
R2:           0.99987134 0.99929308 0.99969296
RMSE:         0.149819  0.169321  1.752266
Iter.:         500      500      500

```

```

-----
Phi_0:         61.347029  78.712409  61.706000
K:             0.517266  1.416250  0.536074

```

```

=====
D, evaluation with calibration data      D(a)      D(b)      D(c)
evaluation with crit. (a) RMSE (signal):  0.1498    0.6375    0.1540
evaluation with crit. (b) RMSE (conc):    0.2657    0.1693    0.2264
evaluation with crit. (c) RMSE (%):       1.8226    4.8831    1.7523

```

```

-----
D, evaluation with test data            D(a)      D(b)      D(c)
evaluation with crit. (a) RMSE (signal):  0.2845    0.2710    0.2671
evaluation with crit. (b) RMSE (conc):    0.2986    0.1766    0.2619
evaluation with crit. (c) RMSE (%):       2.8914    2.3613    2.6747

```

Conclusiones

1. Se ha desarrollado un banco de pruebas de laboratorio para la caracterización y evaluación de una amplia variedad de fases sensoras ópticas. La modularidad del sistema de medida desarrollado y su amplia gama instrumental le confieren una gran versatilidad y flexibilidad, permitiendo que pueda ser adaptado fácilmente a casi cualquier tipo de diseño experimental (sustituyendo algunos de sus componentes por otros).

Este sistema permite, al menos, la adquisición de dos tipos de medidas luminiscentes: (1) medidas de intensidad de la luminiscencia, y (2) medidas de tiempo de vida de luminiscencia en el dominio de la frecuencia. Otra característica importante del sistema es que todos sus instrumentos pueden ser controlados remotamente desde un único ordenador central, lo que permite automatizar el proceso de medida.

Una de las características que proporcionan más versatilidad y potencia al sistema de medida desarrollado es la adquisición y digitalización de las señales para su posterior tratamiento mediante técnicas de procesamiento digital de señales. La naturaleza digital del sistema permite un control total sobre las señales adquiridas, así como la implementación de algoritmos avanzados de procesamiento de señal que han permitido mejorar la respuesta (sensibilidad analítica) y la funcionalidad de este tipo de sistemas, y permitirían la miniaturización y portabilidad de instrumentos basados en el sistema desarrollado. Así pues, el sistema de medida propuesto en esta memoria proporciona la plataforma necesaria para el desarrollo de múltiples aplicaciones potenciales en el ámbito de la Química Analítica, que van desde la completa caracterización y evaluación de fases sensoras ópticas, hasta el desarrollo, implementación y evaluación de nuevos algoritmos de medida que permitan mejorar la sensibilidad analítica de los sistemas desarrollados, la reducción del coste de sus componentes, o simplemente su miniaturización. En definitiva, puede decirse que el banco de pruebas desarrollado ha permitido iniciar una nueva y prometedora línea de investigación multidisciplinar en los Grupos de Investigación FQM-297 y TIC-123 de la Universidad de Granada, siendo los resultados de esta Tesis un claro ejemplo de su potencialidad y aplicabilidad.

2. Se ha llevado a cabo el desarrollo y caracterización una fase sensora óptica para la determinación de dióxido de carbono (CO_2) tanto en muestras acuosas como gaseosas, la cual ha sido utilizada para desarrollar un optosensor de CO_2 usando el sistema de medida propuesto en esta Tesis (configuración basada en medidas de intensidad). Esta fase sensora se basa en la inmovilización de un agente de transferencia de fase (hidróxido de tetraoctil amonio (TONOH)) en un co-polímero funcionalizado con un indicador luminiscente sensible al pH. Así, se ha optimizado el efecto de la concentración

de TONOH y la influencia de parámetros externos tales como la velocidad de flujo, la humedad y otros gases interferentes (O_2 , CO, NO_2), determinándose que el NO_2 puede ser considerado como una especie interferente cuando su concentración es superior a 1 ppm. La fase sensora presenta un intervalo dinámico lineal entre 7.7 y 40 % CO_2 (v/v) en fase gaseosa y entre 4.4 y 60 % CO_2 (v/v) en fase acuosa, con límites de detección de 1.3 y 2.3 % CO_2 (v/v) respectivamente, un tiempo de respuesta rápido ($t_{95} = 5$ s de 0 a 20 % CO_2 (v/v) en fase gaseosa) y una buena estabilidad opto-térmica. Para demostrar la aplicabilidad y versatilidad de la fase sensora se ha desarrollado un sensor de fibra óptica con un intervalo dinámico lineal de 1.4-40 % CO_2 (v/v) y un excelente límite de detección (0.4 % CO_2 (v/v)) en fase gaseosa.

3. Se han caracterizado cuatro fases sensoras ópticas sensibles a oxígeno, una basada en un complejo de platino (PtTFPP) y otras tres basadas en complejos de iridio (N969, N1008 y EB146), inmovilizados todos ellos sobre un soporte nanoestructurado de óxido hidróxido de aluminio (AP200/19). Dicha caracterización ha sido realizada con el sistema de medida propuesto en esta memoria usando medidas de desplazamiento de fase (medidas de tiempo de vida en el dominio de la frecuencia). Todas las fases sensoras han demostrado poseer una excelente sensibilidad para detectar muy bajas concentraciones de oxígeno, siendo especialmente significativo el caso de la fase sensora PtTFPP-AP200/19, la cual presenta la mejor sensibilidad, con una constante de Stern-Volmer (k_{SV}) de $3102 \pm 132 \text{ bar}^{-1}$ en el intervalo de 0 a 1 % O_2 y de $2568 \pm 614 \text{ bar}^{-1}$ en el intervalo de 0 a 10 % O_2 . La k_{SV} de la membrana PtTFPP-AP200/19 en el intervalo de 0 a 10 % O_2 ha resultado ser unas 62 veces mayor que la de una membrana PtTFPP-PS (poliestireno), o unas 8 veces mayor que la k_{SV} obtenida en el intervalo de 0 a 1 % O_2 cuando el indicador PtTFPP es inmovilizado en partículas de sílice. Los resultados obtenidos demuestran que la fase sensora PtTFPP-AP200/19, caracterizada con medidas de desplazamiento de fase, es una de las membranas más sensibles a oxígeno propuestas en la literatura.
4. Se ha desarrollado un sensor de fibra óptica versátil y de bajo coste para la determinación de oxígeno usando un método de modulación de fase multifrecuencia (llamado método I/Q multifrecuencia). Este método se basa en los principios de la detección en cuadratura, y es capaz de determinar en una sola medida el desplazamiento de fase (el cual varía con la concentración de oxígeno) en múltiples frecuencias de modulación. El procesamiento digital del algoritmo de estimación de la fase confiere al sistema de medida un valor añadido en términos de flexibilidad y potencialidad, comparado con otros sistemas que realizan un procesamiento analógico o que están basados en detectores de fase-fija (*Lock-In Amplifiers*, LIAs) comerciales. La naturaleza digital del sistema de medida proporciona al usuario un control total sobre las señales, así como la posibilidad de implementar algoritmos avanzados de procesamiento de señal para mejorar la precisión y funcionalidad de este tipo de sistemas. Además, el procesamiento digital también permitiría la miniaturización del sensor y, por tanto, su portabilidad.

Para demostrar su aplicabilidad, el método de medida propuesto ha sido evaluado usando una fase sensora óptica de referencia sensible a oxígeno (un complejo de Pt(II) inmovilizado en una matriz polimérica), obteniéndose unos resultados similares a los obtenidos con un equipo comercial de referencia (LIA). El sensor ha proporcionado una precisión mayor de ± 1 kPa (o 1 % O_2) en el intervalo de medida de 0-50 kPa (o 0-50 %

O₂), y de ± 0.2 kPa (o 0.2% O₂) en el intervalo de medida de 0-20 kPa (o 0-20 % O₂), para periodos cortos de medida continua (< 2 min) y a temperatura ambiente de 21 °C. Las principales características del sistema propuesto son: amplio intervalo de frecuencias de operación, sencilla sustitución de sus componentes ópticos, facilidad de uso, flexibilidad del sistema para la generación y el post-procesamiento de las señales digitales, y la versátil conexión de la muestra con el sistema de medida usando una fibra óptica.

5. Se ha evaluado la precisión del método I/Q para distintas condiciones de ruido. Para ello, se ha realizado un conjunto de pruebas experimentales usando señales sinusoidales analógicas con diferentes niveles de ruido blanco gaussiano aditivo (AWGN), y se han comparado los resultados obtenidos con los proporcionados por un equipo de medida de referencia (un LIA comercial), obteniéndose resultados muy similares en ambos casos. Sin embargo, es importante señalar que el método I/Q permite una implementación más versátil y barata que un instrumento que requiera un LIA, siendo éste el gran aporte de este trabajo. Estos resultados confirman que la técnica de detección en cuadratura es ideal para la medida de la fase de una señal sinusoidal con niveles de SNR muy bajos, llegando a proporcionar medidas razonables con SNRs inferiores a -18 dB. Asimismo, la respuesta del método I/Q también ha sido evaluada en un sistema real de medida (un sensor de oxígeno de fibra óptica basado en un método de modulación de fase) para demostrar su validez en aplicaciones de espectroscopia de luminiscencia bajo diferentes condiciones de iluminación. Los resultados obtenidos han sido aceptables incluso para señales ópticas de muy baja intensidad, obteniendo mejores resultados para bajas concentraciones de oxígeno (intervalo de medida de 0-20 kPa O₂), con valores de precisión en la estimación de la concentración < 0.2 y < 3 kPa O₂ para la mejor y peor condición de iluminación respectivamente. El límite de detección (LOD) del sensor para la mejor condición de iluminación ha sido de 0.01 % (v/v) O₂. Estos resultados también han sido comparados satisfactoriamente con los de un sistema de medida convencional basado en un LIA comercial.
6. Se ha propuesto un nuevo método de modulación de fase multifrecuencia para mejorar la sensibilidad analítica en espectroscopia de luminiscencia basado en la utilización de una señal de excitación rectangular con un ciclo de trabajo corto. Los resultados obtenidos han demostrado que la utilización de esta señal de excitación proporciona las siguientes ventajas: (1) una mayor exactitud en la determinación de la concentración del analito, y (2) una caracterización más completa del sistema luminiscente. Además, este método permite la combinación de varios armónicos de la señal para determinar y cuantificar la concentración de analito, así como combinar la información de varias señales analíticas (τ_φ y τ_m) para mejorar la exactitud proporcionada por cada una de ellas por separado. Los resultados muestran que a medida que se combina una mayor cantidad de información, el RMSE se reduce, obteniéndose un RMSE inferior a 0.0053 kPa a 0.5 kPa de O₂ y de 0.12 kPa a 20 kPa de O₂ cuando son combinadas las medidas de τ_φ y τ_m de los 5 primeros armónicos. El método propuesto puede ser fácilmente implementado en los instrumentos de fotoluminiscencia actuales, ya que solo afecta a la parte que modula la fuente de luz de excitación (uso de una señal rectangular con un ciclo de trabajo corto en lugar de una señal sinusoidal, lo cual implica normalmente una simplificación de la electrónica) y al procesamiento digital de las muestras después

del transductor (que puede ser implementado en software).

7. Se ha propuesto un nuevo modelo de calibración para sensores ópticos luminiscentes. Este modelo representa la concentración de analito C como un polinomio de ϕ^α de orden p , donde ϕ es la señal analítica y α es un exponente que debe ser ajustado. Dicho modelo puede considerarse una extensión del modelo de Stern-Volmer (siendo idéntico a éste cuando $p = 1$ y $\alpha = -1$). El modelo propuesto (para orden 1 y 2) ha sido comparado con los modelos clásicos propuestos en la literatura (Stern-Volmer, Lehrer y Demas) considerando 25 experimentos, y usando diferentes criterios de calibración: (a) minimización del error cuadrático en la señal analítica, (b) minimización del error cuadrático en la concentración, y (c) minimización del error relativo cuadrático en la concentración. El criterio (a) es apropiado para el estudio de la fotoluminiscencia, mientras que los criterios (b) y (c) son más apropiados para instrumentación orientada a la medida de concentraciones. En este último caso, si el intervalo de concentraciones a medir es amplio, el criterio (c) parece ser el más adecuado. Los resultados obtenidos han puesto de manifiesto la importancia del criterio de calibración, demostrándose que el ajuste óptimo para un criterio dado se consigue cuando la calibración es consistente con el criterio. El modelo propuesto ha ofrecido el mejor compromiso entre exactitud y complejidad, presentando la ventaja añadida de poder ser escalado fácilmente a un orden polinómico más alto en el caso de que se disponga de un mayor número de datos de calibración, ya que su procedimiento de calibración es una búsqueda unidimensional independientemente del orden del polinomio.

Conclusions

1. A laboratory test bench was developed for characterisation and evaluation of a wide variety of optical sensing phases. The modularity of the measurement system developed and its wide instrumental range give it great versatility and flexibility, allowing it to be easily adapted to almost any type of experimental design (replacing some of its components with others).

This system allows, as a minimum, the acquisition of at least two types of luminescent measurements: (1) luminescence intensity measurements, and (2) luminescence lifetime measurements in the frequency domain. Another important feature of the system is that all instruments can be controlled remotely from a single central computer, which allows the measurement process to be automated.

One of the characteristics that provides the measurement system developed greater versatility and potentiality is the acquisition and digitisation of signals for further processing using digital signal processing techniques. The digital nature of the system allows full control over the acquired signals and the implementation of advanced signal processing algorithms that have improved the response (analytical sensitivity) and the functionality of these systems, and will allow for miniaturisation and portability of instruments based on the system developed. Thus, the measurement system proposed herein provides the platform required for the development of multiple potential applications in the field of analytical chemistry, ranging from the complete characterisation and evaluation of optical sensing phases to the development, implementation and evaluation of new algorithms to improve the analytical sensitivity of the systems developed, reducing the cost of their components, or just their miniaturisation. To sum up, we can say that the laboratory test bench developed has allowed for the start of a new and promising multidisciplinary research topic in Groups FQM-297 and TIC-123 from the University of Granada, the results of this Thesis being a clear example of its potential and applicability.

2. The development and characterisation of an optical sensing phase was completed for determining carbon dioxide (CO_2) both in aqueous and gaseous media, which has been used to develop a CO_2 optosensor using the measurement system proposed in this Thesis (configuration based on intensity measurements). This sensing phase is based on the immobilisation of a phase transfer agent (tetraoctyl ammonium hydroxide (TONOH)) in a functionalised co-polymer with a pH-sensitive luminescence indicator. Thus, the effect of TONOH concentration and the influence of external parameters such as flow rate, humidity and other interfering gases (O_2 , CO , NO_2) were optimised and evaluated,

determined that NO_2 can be considered as an interfering species when its concentration is higher than 1 ppm. The sensing phase showed a linear dynamic range between 7.7 and 40% CO_2 (v/v) in the gaseous media and between 4.4 and 60% CO_2 (v/v) in aqueous media, with detection limits of 1.3 and 2.3% CO_2 (v/v) respectively, a fast response time ($t_{95} = 5$ s from 0 to 20% CO_2 (v/v) in the gaseous media) and good opto-thermal stability. To demonstrate the applicability and versatility of this sensing phase, a fibre optical sensor were developed. It had a linear dynamic range of 1.4-40% CO_2 (v/v) and an excellent detection limit (0.4% CO_2 (v/v) in gaseous media.

3. Four oxygen-sensitive optical sensing phases were characterised, one based on a platinum complex (PtTFPP) and three based on iridium complexes (N969, N1008 and EB146), all immobilised onto a nanostructured aluminium hydroxide oxide support (AP200/19). This characterisation was performed with the system proposed herein using phase shift measurements (lifetime measurements in the frequency domain). All sensing phases demonstrated excellent sensitivity to detect ultra-low concentrations of oxygen, this being especially significant in the PtTFPP-AP200/19, which had the best sensitivity, with a Stern-Volmer constant (k_{SV}) of $3102 \pm 132 \text{ bar}^{-1}$ in the range 0 to 1% O_2 and $2568 \pm 614 \text{ bar}^{-1}$ in the range 0 to 10% O_2 . The k_{SV} of the PtTFPP-AP200/19 membrane in the range 0 to 10% O_2 had proven to be about 62 times greater than that of a PtTFPP-PS (polystyrene) membrane, or about 8 times greater than the k_{SV} obtained in the range 0 to 1% O_2 when the PtTFPP indicator is immobilised on silica particles. The results obtained showed that the PtTFPP-AP200/19 sensing phase, characterized by phase shift measurements, is one of the most oxygen sensitive membranes proposed in the literature.
4. We have developed a versatile and low-cost fibre optic sensor for oxygen determination using a multi-frequency phase-modulation method (called I/Q multi-frequency method). This method is based on the principles of quadrature detection, and is capable of determining the phase shift (which varies with oxygen concentration) at multiple modulation frequencies using a single measurement. The digital processing algorithm for estimating the phase shift gives the measurement system added value in terms of flexibility and potential, compared to other systems that perform analog processing or that are based on commercial Lock-In Amplifiers (LIAs). The digital nature of the measurement system gives the user full control over the signals as well as the ability to implement advanced signal processing algorithms to improve the accuracy and functionality of such systems. Furthermore, digital processing also allows for miniaturisation of the sensor and therefore portability.

To demonstrate its applicability, the proposed measurement method was evaluated using a reference oxygen-sensitive optical sensing phase (a complex of Pt(II) immobilised on a polymer matrix), obtaining similar results to those obtained with a reference commercial equipment (LIA). The sensor provided greater accuracy of ± 1 kPa (or 1% O_2) in the measurement range 0-50 kPa (or 0-50% O_2) and ± 0.2 kPa (or 0.2% O_2) in the measuring range 0-20 kPa (or 0-20% O_2), for short periods of continuous measurement (< 2 min) and at room temperature of 21 °C. The main characteristics of the system proposed are its wide range of operating frequencies, the simple replacement of optical components, ease of use, flexibility of the system for the generation and post-processing of digital signals, and versatile connection of the sample with the measurement system

using optical fibres.

5. We assessed the accuracy of the I/Q method for different noise conditions. To do this, we carried out a series of experimental tests using analog sinusoidal signals with different levels of Additive White Gaussian Noise (AWGN), and compared the results with those provided by a reference measurement equipment (a commercial LIA). Very similar results were achieved in both cases. However, it is important to note that the I/Q method allows for a more versatile and inexpensive implementation than an instrument that requires a LIA, which is the major contribution of this work. These results confirmed that the quadrature detection technique is ideal for measuring the phase of a sinusoidal signal with the lowest SNR levels, providing reasonable measurements with SNRs lower than -18 dB. Additionally, the response of the I/Q method was also evaluated in a real measurement system (fibre optic oxygen sensor based on a phase-modulation method) to demonstrate its validity in luminescence spectroscopy operating under different lighting conditions. The results were acceptable even for optical signals of very low intensity, obtaining better results for low oxygen concentrations (range 0-20 kPa O₂), with accuracy values in estimating the concentration of < 0.2 and < 3 kPa O₂ for better and worse lighting conditions respectively. The limit of detection (LOD) for the best lighting conditions was 0.01% (v/v) O₂. These results were also successfully compared with a conventional measurement system based on a commercial LIA.
6. A new multi-frequency phase-modulation method was proposed to improve analytical sensitivity in luminescence spectroscopy using a rectangular excitation signal with a short duty cycle. The results obtained showed that the use of this excitation signal provides the following advantages: (1) greater accuracy in determining analyte concentration, and (2) a more complete characterisation of the luminescent system. Furthermore, this method allows the combination of several harmonics of the signal to determine and quantify the analyte concentration, and to combine information from several analytical signals (τ_φ and τ_m) to enhance the accuracy provided by each of them separately. The results showed that as a greater amount of information is combined, the RMSE is reduced, resulting in a lower RMSE at 0.0053 kPa to 0.5 kPa O₂ and from 0.12 kPa to 20 kPa O₂ when combined measurements τ_φ and τ_m of the first 5 harmonics. The proposed method can be easily implemented in existing photoluminescence instruments, since it only affects the part that modulates the excitation light source (using a rectangular signal with a short duty cycle instead of a sinusoidal signal, which usually involves simplification of the electronics) and the digital processing of the samples after the transducer (which may be implemented in software).
7. We have proposed a new calibration model for luminescent optical sensors. This model represents the analyte concentration C as a p -th order polynomial of ϕ^α where ϕ is the analytical signal and α is an exponent to be adjusted. This model can be considered an extension of the Stern-Volmer model (being identical to it when $p = 1$ and $\alpha = -1$). The model proposed (for order 1 and 2) was compared with classical models proposed in the literature (Stern-Volmer, Lehrer and Demas) considering 25 experiments, and using different calibration criteria: (a) minimising the squared error in the analytical signal, (b) minimising the squared error in the concentration, and (c) minimising the relative squared error in the concentration. Criterion (a) is appropriate for the study of photoluminescence, while criteria (b) and (c) are more appropriate for concentration

orientated measurement instrumentation. In the latter case, if the concentration range measured is large, criterion (c) appears to be the most appropriate. The results obtained highlighted the importance of calibration criteria, showing that the optimal fitting for a given criterion is achieved when calibration is consistent with the criterion. The model proposed provided the best compromise between accuracy and complexity, presenting the additional advantage of being easily scaled to a higher polynomial order in the case of the availability of a larger amount of calibration data since its calibration procedure is a one-dimensional search independent of the polynomial order.

APÉNDICES



Apéndice I:

Sensores ópticos en sistemas de análisis en flujo

VALCÁRCEL y Luque de Castro [337] establecieron una clasificación de los sensores ópticos en sistemas de flujo. Propusieron dos grandes grupos: los sensores tipo sonda y los sensores tipo célula de flujo. En su clasificación, el uso de fibras ópticas es exclusivo de los sensores tipo sonda. La principal diferencia entre ambos grupos radica en el hecho de que los sensores de fibra óptica (tipo sonda) pueden emplearse tanto para llevar a cabo medidas en estado estacionario como en continuo, mientras que los de tipo célula de flujo necesitan imperiosamente un sistema de flujo continuo para trabajar correctamente [1].

Hasta la fecha, la mayor parte de los sensores ópticos desarrollados en sistemas de flujo pueden clasificarse en función de donde tiene lugar la reacción y la detección (véase la Figura 6). Valcárcel y Luque de Castro establecieron dos categorías básicas [8]: (1) sensores tipo sonda, donde la fase sensora se encuentra inmovilizada sobre la propia fibra óptica inmersa en la corriente de un flujo, y (2) sensores tipo célula de flujo (optosensores convencionales y no convencionales), donde la fase sensora se halla inmovilizada en una celda de flujo.

La realización simultánea de la etapa de retención del analito y del proceso de detección óptica en un sistema de análisis por inyección en flujo (FIA), abre un nuevo horizonte de posibilidades para superar muchos de los inconvenientes asociados a los sensores ópticos [70, 338, 339].

La metodología proporcionada por las técnicas FIA ofrece numerosas ventajas analíticas, tales como: un fundamento sencillo, equipamiento de bajo coste, bajo consumo de muestra y reactivos, elevada frecuencia de muestreo y fácil automatización. Las técnicas FIA se engloban dentro de los métodos cinéticos, y por consiguiente, éstas presentan generalmente una mayor selectividad que las correspondientes técnicas manuales [98]. Finalmente, cabe destacar la casi universalidad de las técnicas FIA, dado que su carácter modular las hace sencillas de adaptar a cualquier necesidad analítica concreta [70]. El gran desarrollo actual de estas técnicas se debe fundamentalmente a su excelente versatilidad.

Un sistema FIA ordinario está constituido básicamente por cuatro partes esenciales: (1) una unidad de propulsión, que impulsa un gas inerte o un portador a lo largo del sistema (generalmente se trata de una bomba peristáltica), (2) un sistema de inyección, por donde se introduce la muestra (generalmente se trata de una válvula de cuatro o seis vías), (3) una zona de reacción, donde puede o no existir alguna reacción adicional, y (4) un sistema de detección, donde se encuentra la celda de flujo [70].

La técnica FIA consiste básicamente en una inyección o inserción directa de la muestra líquida en un flujo continuo y no segmentado. De este modo, la muestra es arrastrada a través del flujo del sistema, teniendo o no lugar uno o varios procesos de reacción adicionales entre ésta y el fluido portador. La muestra se hace pasar por un sistema de detección adecuado para la realización de mediciones en continuo, el cual proporciona una señal analítica transitoria que está relacionada con la concentración de la especie a determinar (analito).

Habitualmente, las condiciones experimentales llevadas a cabo en los sistemas FIA originan una mezcla incompleta del bolo de muestra inyectado en el flujo portador. Dicha dispersión de la muestra suele estar controlada por diversos factores, tales como la velocidad de flujo, el diseño geométrico del sistema, la longitud y el diámetro de los tubos y el volumen de inyección de muestra. Así pues, una elevada reproducibilidad del tiempo de operación es considerada una característica fundamental de esta metodología, debido a que las medidas se realizan en condiciones de no equilibrio [98]. La bibliografía recoge de forma detallada un amplio tratamiento de esta temática [340].

Los sistemas de análisis en flujo pueden ofrecer soluciones a algunos de los problemas que limitan la utilidad práctica de los sensores químicos [341], como por ejemplo, el inconveniente de tener tiempos de respuesta elevados como consecuencia de los lentos procesos de difusión del analito desde la muestra a la fase activa. Cuando se trabaja con sistemas FIA, dichos tiempos de respuesta pueden ser minimizados mediante la incorporación de un pequeño bolo de muestra en un flujo portador que fuerza el paso de la muestra a través de la fase sensora de forma transitoria. Asimismo, el tiempo de exposición en análisis por inyección en flujo se puede utilizar para realizar una discriminación cinética entre el analito y otras sustancias interferentes, siempre y cuando éstas presenten velocidades de difusión o de reacción diferentes [1]. Otra característica destacable de los sistemas FIA es su facilidad para acoplar un sistema de regeneración de la fase sensora (en caso de irreversibilidad en la reacción de reconocimiento) [340].

Una de las características más relevantes de los sensores tipo célula de flujo es su total compatibilidad con sistemas FIA. Así pues, la conjunción de las características intrínsecas de los sistemas de inyección en flujo (automatización, flexibilidad, acondicionamiento y calibrados de muestra sencillos, desarrollo previo de reacciones químicas, etc.) junto con la utilización de fases sensoras (selectividad, preconcentración del analito, etc.), posibilitan su aplicación a toda clase de muestras reales [70, 98, 340].

Las principales ventajas de tipo práctico que se pueden conseguir al introducir interfaces sólidas en sistemas de análisis en flujo, son las siguientes [340]:

- *Aumento de la sensibilidad* empleando fases sólidas, debido a que la sensibilidad de los sistemas de análisis en flujo puede incrementarse por: (1) *Preconcentración en línea o in situ*: es uno de los métodos más efectivos para incrementar la sensibilidad. Desde el punto de vista físico, la preconcentración puede obtenerse acoplando una unidad apropiada de separación (por ejemplo una microcolumna con un relleno adecuado) en el sistema en flujo. Si la fase sólida se encuentra localizada en la célula de flujo de un detector óptico no destructivo, se obtiene un sistema particular de preconcentración *in situ*, que combina ambos procesos de retención y detección [342]. Este sistema de preconcentración es el que tiene lugar en los optosensores. (2) *Disminución de la dilución*:

históricamente, los primeros reactores sólidos utilizados en el desarrollo de sistemas FIA fueron de naturaleza redox [343], ya que de este modo se evita la correspondiente dilución empleando un reductor adicional. (3) *Aumento de la estabilidad de los reactivos*: los reactivos (por ejemplo, enzimas) inmovilizados sobre soportes apropiados tienen una mayor estabilidad que en disolución, y se han empleado ampliamente en sistemas FIA tanto para determinar substratos [344, 345], como actividades enzimáticas [346].

- *Aumento de la selectividad* utilizando fases sólidas. Los métodos FIA son más selectivos que sus homólogos manuales. Esto es debido a que las medidas se realizan sin alcanzar las condiciones de equilibrio, por lo que se eliminan las interferencias de aquellas especies que reaccionen más lentamente que el analito [347].

Los optosensores deben reunir una serie de características para garantizar un funcionamiento adecuado: (1) el sistema debe ser reversible (o fácilmente regenerable si es irreversible), (2) la cinética de los procesos que tengan lugar debe ser rápida, (3) la fase de reconocimiento químico debe ser robusta, y (4) la fase sensora y el sistema de detección deben ser totalmente compatibles, lo cual no siempre es posible.

Como conclusión, podemos señalar que los optosensores en sistemas de flujo presentan pues una serie de ventajas frente a otro tipo de sensores, como son [98, 340]:

- Una mayor sensibilidad al reducirse la dispersión de la muestra inyectada.
- Una mejora indirecta de la selectividad eliminando especies interferentes y señales parásitas a través de medidas cinéticas.
- Una rápida regeneración de la fase sensora, de forma simple y automática, en el caso de irreversibilidad del mecanismo de reconocimiento.
- Una mejora de las características intrínsecas de los sensores derivada del empleo de la técnica FIA: acondicionamiento y desarrollo de métodos sencillos, automatización, desarrollo previo de reacciones químicas, flexibilidad, etc.

Por el contrario, las principales desventajas de los optosensores son [98, 340]:

- La necesidad de un sistema para impulsar la muestra.
- La dificultad de monitorización en zonas remotas.
- La necesidad de compatibilidad entre la zona sensible y el detector.
- Problemas derivados de la cinética si los procesos de separación y reacción son demasiado lentos.

Por último, cabe destacar el importante auge experimentado por los optosensores en los últimos años, especialmente en aplicaciones relacionadas con los análisis clínicos y farmacéuticos [348–350], la detección de pesticidas [106, 351, 352], o el análisis de contaminantes orgánicos en aguas [353–355].

Apéndice II:

Sensores ópticos tipo sonda (Optodos)

EL uso de fibras ópticas en el ámbito del análisis químico y bioquímico tuvo sus orígenes en los años 60 [1], en particular con el desarrollo de un oxímetro para la medida de oxígeno en la sangre [356, 357]. Durante los años siguientes, importantes avances en el campo de la transmisión de luz a través de fibras ópticas dieron lugar a la aparición de nuevas ideas en el campo de los sensores ópticos. Además, se introdujeron nuevos conceptos en cuanto a microsondas [1, 358], técnicas espectroscópicas de fibra óptica [359] y experimentos con sensores de oxígeno en continuo [200]. Estos primeros desarrollos abrieron el camino a otras muchas propuestas llevadas a cabo en años posteriores, como la espectroscopía Raman con fibra óptica [360], el primer sensor de pH de fibra óptica [361, 362], o la aparición del primer espectrofotómetro de fibra óptica comercial.

Hasta hace pocos años, los sensores electroquímicos (electrodo de pH, electrodo de fluoruros, etc.) eran los más estudiados y los que tenían una mayor aplicación en Química Analítica [1]. Sin embargo, en los últimos años se ha producido un espectacular progreso en el campo de los sensores ópticos gracias a la colaboración de especialistas procedentes de muy diversas áreas. La industria de las telecomunicaciones ha proporcionado fibras ópticas de bajo coste y altas prestaciones que permiten la transmisión de señales a largas distancias, tanto en la región del visible (VIS, 390-700 nm) como en las regiones del ultravioleta (UV, 300-400 nm) o en la zona del infrarrojo (NIR-MIR, 750-2000 nm) [52]. Además, el desarrollo de nuevas fuentes luminosas como los láseres, los diodos LEDs o la tecnología de estado sólido, así como el avance en el campo de la detección óptica con detectores cada vez más sensibles y de bajo coste, han catapultado el desarrollo de los sensores ópticos basados en fibra óptica hasta un lugar privilegiado en este moderno campo de los sensores (bio)químicos [1].

Los sensores químicos de naturaleza óptica basados en fibra óptica suelen ser denominados con el nombre de *optodos* (del griego “*óptico*” y “*camino*”) u *optrodos* (del inglés, “*optical electrode*”). Otro término utilizado a veces para referirse a este tipo de sensores es el de FOCS (del inglés, “*Fiber Optic Chemical Sensors*”).

Un optodo es un dispositivo constituido básicamente por una fase sensora (o membrana ópticamente activa) soportada sobre una guía de onda. Como ya mencionamos anteriormente, las guías de ondas más comúnmente usadas para dispositivos sensores son aquellas que presentan una morfología cilíndrica, es decir, las fibras ópticas [50, 298, 363]. Sin embargo, también se han desarrollado algunos optodos basados en guías de ondas planas (véase la Figura 7), dando lugar a los llamados optodos de geometría plana o de tipo chip [364-369].

Los sensores ópticos (y particularmente los optodos) poseen un gran número de ventajas potenciales que los hace mucho más atractivos que otro tipo de sensores químicos, particularmente los electroquímicos [370–372]. Algunas de estas ventajas se mencionan a continuación:

- 1) A diferencia de los sensores potenciométricos, donde se miden diferencias relativas entre dos potenciales eléctricos, los sensores ópticos no necesitan de un sistema de referencia.
- 2) Los sensores de fibra óptica son elementos completamente pasivos: por un lado no necesitan alimentación eléctrica y por otro no se tienen que polarizar para estar operativos (lo que ocurre con los sensores basados en semiconductores). La mayoría de ellos están constituidos por materiales químicamente inertes, lo que les confiere pasividad eléctrica y química. La ausencia de señales eléctricas es muy atractiva en aplicaciones relacionadas con el transporte y almacenaje de disolventes químicos: generalmente estos productos son altamente inflamables, por lo que una chispa eléctrica podría generar una explosión. También podrían ser utilizados para identificar atmósferas con elevado riesgo de explosión o con una concentración anormal de vapores orgánicos. En el caso de los sensores eléctricos, esto supone un riesgo importante y además, las medidas las debe realizar un operario *in-situ* con el correspondiente dispositivo, mientras que la fibra óptica permitiría realizarlas remotamente [52]. En determinadas aplicaciones, como es el caso de las medidas biomédicas *in vivo*, los sensores ópticos son más seguros que los electroquímicos, ya que evitan el riesgo de sufrir un *shock* eléctrico.
- 3) La comunicación con los sensores de fibra óptica no se ve afectada por interferencias electromagnéticas, lo cual es muy valioso en entornos ruidosos, como fábricas con maquinaria electrónica pesada [52].
- 4) Se han desarrollado sensores ópticos para analitos químicos o parámetros físicos para los que no existen otro tipo de sensores. En la actualidad, existen nichos de mercado potenciales en los que el uso de sensores de fibra óptica puede ser una alternativa viable a los sensores electrónicos, como en la ingeniería civil (monitorización estructural de edificios [373]) o el análisis químico de gases. Gracias a que estos sensores no necesitan señales de polarización, son idóneos para trabajar con gases o vapores orgánicos altamente inflamables o con riesgo de explosión. Concretamente, la detección de compuestos orgánicos volátiles (COVs) [52] presenta muchos campos de aplicación, que van desde la industria química (seguridad laboral, seguridad ambiental, detección de fugas, etc.) hasta la alimentaria: se pueden monitorizar procesos de fermentación o maduración, así como comprobar el estado de los alimentos a partir del olor que desprenden (al estar formados por COVs) [374, 375].
- 5) La mayor parte de los sensores ópticos permiten realizar análisis no destructivos (sin un consumo significativo del analito), por lo que la muestra queda inalterada tras la medida. Este hecho es sumamente ventajoso a la hora de trabajar con muestras de pequeño volumen o cuando sea crítica la destrucción o degradación de la muestra (caso típico de las aplicaciones biotecnológicas y médicas [22]).
- 6) Las fibras ópticas son capaces de transmitir una mayor densidad de información que los cables eléctricos debido a que poseen un ancho de banda más grande. Esto se debe a que las señales ópticas pueden diferir en cuanto a su longitud de onda, fase, modulación de intensidad o polarización. Como resultado, una única fibra óptica puede, en principio,

transmitir simultáneamente varias señales, permitiendo de este modo el análisis de varios analitos al mismo tiempo. Así pues, esta propiedad permite transmitir la información de varios sensores por una única fibra, o lo que es lo mismo, la multiplexación de sensores. En determinadas ocasiones, la utilización de discriminadores adecuados posibilita el acoplamiento de diferentes sensores a un único sistema de transducción, disminuyendo de este modo el coste del sistema y posibilitando el despliegue de grandes redes de sensores. Un ejemplo de aplicación donde podría resultar útil un despliegue de esta naturaleza es el de la fermentación del vino: en este caso, podrían integrarse en una misma red sensores de fibra óptica que midieran variables tales como la temperatura, la humedad, la concentración de oxígeno, dióxido de carbono u óxidos de nitrógeno [52].

- 7) La fase sensora no necesita estar en contacto directo con el sistema óptico de medida. Esto simplifica extraordinariamente el diseño y desarrollo de sensores ópticos en los que la fase sensora necesite ser reemplazada tras un cierto uso, lo cual resulta inevitable cuando se desarrollan fases sensoras basadas en reactivos con una vida limitada o de un único uso (desechables). Una amplia variedad de sensores ópticos presentan un diseño muy sencillo que hace fácil tanto su utilización por parte de usuarios no expertos como la sustitución de cualquiera de sus componentes.
- 8) Los pequeños diámetros de las fibras ópticas (con valores típicos comprendidos entre 50 y 200 μm) y la disponibilidad de componentes ópticos de pequeño tamaño permiten la miniaturización de estos dispositivos. Asimismo, la biocompatibilidad de las fibras ópticas y la flexibilidad de conexión entre el receptor y la zona de medida posibilitan su uso para la detección, la medida y/o incluso la actuación de/sobre variables biomédicas [22, 23, 98]. En el ámbito biomédico, por ejemplo, esto también implica que se puedan hacer medidas no invasivas o mínimamente invasivas [22].
- 9) Los sensores ópticos ofrecen la posibilidad de obtener resoluciones analíticas a múltiples longitudes de onda e información temporal y espacial de la especie analizada, pudiéndose aplicar técnicas de tiempo resuelto [376, 377] y de fase resuelta [23, 51, 92, 99] para extraer una mayor información analítica.
- 10) Algunos sensores ópticos permiten trabajar en intervalos de temperatura extremos, lo que hace posible su esterilización a temperaturas elevadas y, por tanto, que puedan ser usados en el campo biomédico. Parte de los sensores ópticos pueden ser esterilizados usando rayos gamma, posibilitando también su uso en biotecnología [1].
- 11) Los sensores ópticos basados en la desactivación dinámica de la fotoluminiscencia [51, 73] se pueden emplear en un intervalo de concentraciones generalmente más amplio que los electroquímicos [1].

Por desgracia, los sensores ópticos (y en particular los optodos) también presentan una serie de inconvenientes tales como [1]:

- 1) La luz ambiental puede interferir en las medidas, lo que obliga a aislarlos adecuadamente o a modular la señal óptica para eliminar el ruido de fondo espectral.
- 2) La estabilidad temporal del sensor puede ser poco elevada debido a la fotodescomposición de los reactivos usados en la elaboración de la fase sensora. Este problema se puede compensar, en cierto modo, llevando a cabo la detección a diferentes longitudes de onda,

empleando sensores ópticos basados en tiempos de vida, o simplemente sustituyendo la fase sensora con una cierta periodicidad [98].

- 3) Los tiempos de respuesta pueden ser elevados, especialmente en aquellos casos en los que estén involucrados fenómenos de transferencia de masa, aunque este impedimento también lo presentan otro tipo de sensores como los electroquímicos. Este problema puede ser minimizado considerablemente usando fases sensoras delgadas y de pequeño tamaño [98].
- 4) En general, los sensores ópticos presentan intervalos dinámicos (de respuesta lineal a la concentración) menores que los electroquímicos [1].
- 5) La necesidad de indicadores más selectivos y procesos de inmovilización más reproducibles que permitan aumentar la selectividad y estabilidad a largo plazo de los optodos.
- 6) Desarrollo de materiales y/o técnicas de deposición que se puedan adaptar fácilmente a las diversas configuraciones morfológicas del sensor [22], sin que ello implique una pérdida de control sobre las propiedades fisicoquímicas de la fase sensora [99, 205].
- 7) Las fibras ópticas disponibles en la actualidad contienen impurezas de naturaleza espectral que pueden provocar absorción, fluorescencia o dispersión Raman de fondo. El material que constituye la fibra óptica determina el intervalo útil de longitudes de onda que puede transmitir a su través [52, 298]. Las fibras ópticas han sido perfeccionadas para ser utilizadas en aplicaciones de telecomunicaciones, es decir, para transmitir determinados intervalos de longitudes de onda (llamados *ventanas de telecomunicaciones*) donde el nivel de transparencia es máximo (esto es, donde existe una mínima atenuación y dispersión de la luz): la primera ventana está localizada alrededor de 850 nm, la segunda está centrada en 1300 nm y la tercera y última está localizada en 1550 nm. Actualmente, la gran mayoría de los sistemas de comunicaciones operan en la tercera ventana, debido a que las pérdidas por transmisión en este caso son del orden de 0.19 dB/Km. Sin embargo, una gran parte de los optodos desarrollados hasta la fecha operan en el intervalo VIS y el UV-vis. La transmisión de luz en estos intervalos no está tan explotada comercialmente, y pese a que hoy en día se dispone de fibras ópticas específicas para transmitir adecuadamente en dichas regiones (como las fibras solarizadas), su precio suele resultar relativamente elevado en la gran mayoría de los casos.
- 8) La creciente necesidad de accesorios ópticos comerciales es otro inconveniente. Se precisan fuentes luminosas estables, baratas y con largos tiempos de vida útil, así como mejores conectores y componentes ópticos. Aunque en la actualidad ya existen fuentes de luz para la región VIS (400-700 nm) a precios asequibles, su coste suele incrementarse considerablemente cuando nos desplazamos hacia la región del UV (muy especialmente en el caso de los LEDs). No obstante, en los últimos años se están logrando avances importantes en el desarrollo de LEDs UV [378].
- 9) El gran éxito de las comunicaciones ópticas hizo pensar que esta tecnología también se podría utilizar en otros campos, como por ejemplo, en el desarrollo de sensores ópticos. La fibra óptica tiene un tamaño reducido y está fabricada con un material inerte y muy abundante: el óxido de silicio. Pese a esto, en lo referido al campo de los sensores, la tecnología electrónica se encuentra mucho más avanzada y madura: la miniaturización permite la producción en masa y, por tanto, los sensores electrónicos tienen precios asequibles

[52]. Actualmente, la mayor parte del coste final de un sistema óptico de medida recae sobre los dispositivos fotónicos: multiplexores, circuladores, acopladores, filtros ópticos y sobre todo, las fuentes de luz y los detectores [51]. Así pues, los dispositivos fotónicos únicamente tienen un coste justificable en grandes redes o infraestructuras (como grandes instalaciones de almacenaje/transporte de productos químicos (barcos, cisternas, fábricas), centros de procesamiento de alimentos (bodegas, almacenes de curado), etc.), pero aún son menos competitivos que los sensores electrónicos en aplicaciones donde éstos ya se encuentran asentados [52]. No obstante, esta idea está lejos de ser pesimista, pues como hemos visto anteriormente, existen infinidad de aplicaciones en las que las propiedades intrínsecas de los sensores ópticos (y en particular de los optodos) satisfacen mejor sus necesidades técnicas que las de los sensores electrónicos [52].

Como puede apreciarse, los sensores ópticos (y en particular los optodos) parecen presentar, a priori, más ventajas que inconvenientes. Por otra parte, muchos de los inconvenientes mencionados para estos sensores están limitados a casos muy concretos y/o tienen una solución asequible. Todo esto hace que la investigación en el campo de los sensores ópticos haya experimentado un gran avance en los últimos años [50, 379].

AII.1 Clasificación de los optodos

Al igual que sucede con el resto de los sensores químicos, no existe una única clasificación general para los optodos. Sin embargo, una clasificación muy extendida consiste en agrupar los sensores de fibra óptica en función del lugar donde tiene lugar el reconocimiento del analito: dicha interacción puede producirse en la propia fibra óptica (*sensores intrínsecos*) o fuera de ella (*sensores extrínsecos*) (véase la Figura AII.1). A continuación mencionamos brevemente las características más importantes de estos dos grupos [15, 50, 52, 98, 198]:



Figura AII.1: Diferencias entre un sensor extrínseco e intrínseco [52].

Sensores extrínsecos: Están constituidos por un ‘*elemento sensor*’ externo a la propia fibra (p. ej., una fase sensora o la propia muestra conteniendo al analito), cuyas propiedades ópticas se modifican tras su interacción con el analito y las cuales pueden ser medidas por un instrumento de medida. En este caso, la fibra óptica actúa únicamente como una guía de luz, transmitiendo generalmente la radiación luminosa “hacia” o “desde” la zona de reconocimiento del analito: dicha interacción puede tener lugar en la propia muestra (*interacción directa*) o bien en una fase sensora inmovilizada sobre un soporte sólido (*interacción indirecta*) (véase la Figura AII.4) [52]. Así pues, en este tipo de sensores no es necesario que exista un contacto físico entre la muestra y la fibra, hecho que puede ser importante en el caso de

que las medidas se estén llevando a cabo en ambientes en los que el resto de elementos del sistema óptico podrían verse afectados (p. ej., en medidas de muestras de alta presión, donde el indicador se encuentra en la muestra y los cambios que se producen en dicho indicador pueden ser observados a través de una ventana) [1]. Los parámetros más significativos de la fibra óptica para este tipo de sensores son: la eficiencia de la transmisión de la luz (transmitancia), el ángulo de aceptación y el diámetro del núcleo de la fibra. Estos sensores pueden subdividirse a su vez en tres grandes grupos [50]:

- *Sensores de 1ª generación (optodos pasivos, no-modificados o directos)*: En ellos, la fibra óptica se utiliza exclusivamente como una guía de luz. Fueron los primeros sensores que se desarrollaron y consisten simplemente en una fibra óptica que transporta la radiación luminosa hacia/desde la muestra (p. ej., una disolución de una especie coloreada o luminiscente que absorbe parte de la luz y/o la emite a otra longitud de onda). La radiación transmitida, reflejada o emitida por la muestra es recogida por la misma fibra o por otra distinta, y conducida hacia un sistema óptico capaz de medir su intensidad y de relacionar dicha señal con la presencia del analito de interés. Este tipo de sensores se han utilizado tradicionalmente para realizar análisis espectrofotométricos a grandes distancias o para aquellas aplicaciones en las que no es posible un contacto físico con la muestra. Algunas de las ventajas destacables de este tipo de sensores son su robustez, simplicidad, estabilidad o durabilidad. Sin embargo, suelen ser poco selectivos y únicamente pueden ser empleados para un número limitado de analitos [98].
- *Sensores de 2ª generación*: La información analítica se genera a través de una reacción indicadora, ya que el analito no presenta ninguna propiedad óptica intrínseca que pueda ser medida de forma directa. En otras palabras, en un extremo de la fibra óptica se sitúa una fase sensora, la cual incorpora un indicador (transductor) cuyas propiedades ópticas se modifican en función de la concentración del analito presente en la muestra. Un subgrupo de estos sensores son los llamados “*sensores con depósito*”, en los cuales el reactivo se sitúa en un depósito alimentado de forma continua (favoreciendo así su reacción con el analito en el terminal sensible) [15, 98].
- *Sensores de 3ª generación*: Están constituidos por una biomolécula acoplada a un sensor de segunda generación (p. ej., un sensor de oxígeno o de pH). Tras reaccionar con la biomolécula, el analito a cuantificar es transformado/correlacionado con la especie monitorizada mediante el sensor de segunda generación [15, 98].

Los sensores extrínsecos de 2ª y 3ª generación también se denominan *optodos indirectos, modificados o activos*. Este tipo de sensores son los que poseen un mayor interés desde el punto de vista científico, dada su especificidad, sensibilidad y extenso campo de aplicación, ya que, en principio, podrían desarrollarse sensores específicos para cualquier especie de interés analítico. Las desventajas de estos sensores incluyen la posible lixiviación o fotodescomposición del indicador en contacto con la muestra, unos tiempos de respuesta elevados y una mayor complejidad de fabricación [15, 98].

Algunos autores también establecen una subclasificación de los sensores extrínsecos indirectos en función de su tipo de configuración (véase la Figura AII.2) [52]: por un lado, la luz incidente puede seguir un camino directo (atravesando al material sensible que contiene

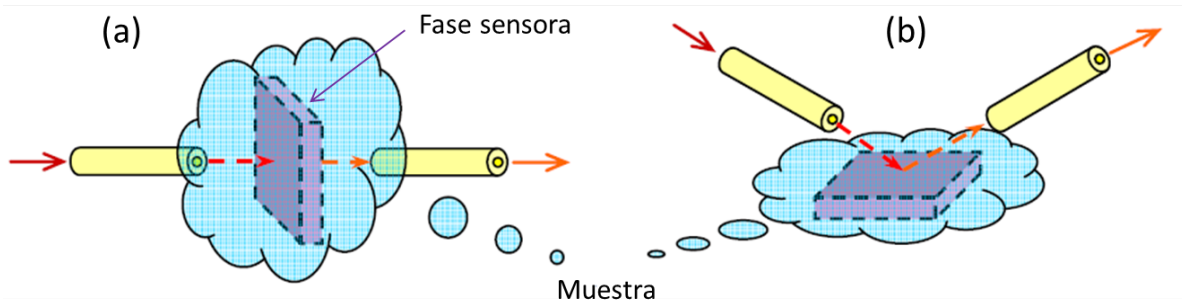


Figura AII.2: Diferentes configuraciones para los sensores extrínsecos indirectos: (a) la señal óptica pasa a través del material sensible registrándose de forma directa; (b) la luz incide con un cierto ángulo sobre el material sensible, registrándose indirectamente una parte de la señal óptica reflejada o emitida por la fase sensora [52].

el indicador) y finalmente ser recogida por otra fibra óptica (configuración en transmisión, (a)) [380]; por otro lado, la luz puede incidir con un cierto ángulo sobre el material sensible, recogiendo indirectamente una parte de la luz reflejada o emitida por la fase sensora con otra fibra óptica (configuración en reflexión, (b)). Esta última configuración también podría realizarse usando una única fibra (la misma fibra óptica llevaría la luz incidente hasta el material sensible y recogería la señal óptica reflejada o emitida) [381]. En algunos casos, cuando la distancia de separación entre la fuente de luz, la muestra y el detector es lo suficientemente pequeña, no se requiere el uso de fibras ópticas para el guiado de la luz: con un cierto ángulo de incidencia, la luz reflejada o emitida puede ser directamente acoplada al detector [382, 383].

En el caso de los sensores extrínsecos, existe una amplia variedad de posibilidades para situar la fase sensora en el extremo de la fibra óptica [15, 384–386], algunas de las cuales aparecen recogidas en la Figura AII.3. En la figura (a), el indicador se encuentra inmovilizado directamente sobre una membrana situada en el extremo de la fibra óptica. Ejemplos típicos de esta configuración incluyen indicadores inmovilizados covalentemente sobre membranas de celulosa, o unidos electrostáticamente a membranas de intercambio iónico. Alternativamente, el indicador puede presentarse en forma de sólido, fijado mecánicamente a una membrana situada en el extremo de la fibra óptica, como se muestra en la figura (b). La figura (c) representa otro tipo de configuración en la que una disolución homogénea del indicador es retenida por medio de una membrana que envuelve al extremo de la fibra óptica. En este caso, la membrana también puede servir para otros propósitos, como puede ser la exclusión de sustancias interferentes o el aislamiento óptico del indicador. En la figura (d), el reactivo indicador es encapsulado en el interior de una membrana tubular permeable al analito, o bien en el interior de un tubo capilar (cuando la fase sensora se prepara directamente por polimerización), el cual, a su vez, se sujeta al extremo de la fibra óptica (e). En algunos casos, también es posible fijar directamente el indicador sobre la propia fibra óptica, tras someterla a un tratamiento de silanización previo [15]. Sin embargo, la cantidad de reactivo inmovilizado por este procedimiento es relativamente baja y, además, suele ser menos reproducible que en el caso de que se inmovilice sobre un soporte sólido.

Sensores intrínsecos: Son aquellos en los que la propia fibra óptica actúa como un elemento sensor cuando algunas de sus propiedades ópticas son modificadas por el analito a cuantificar.

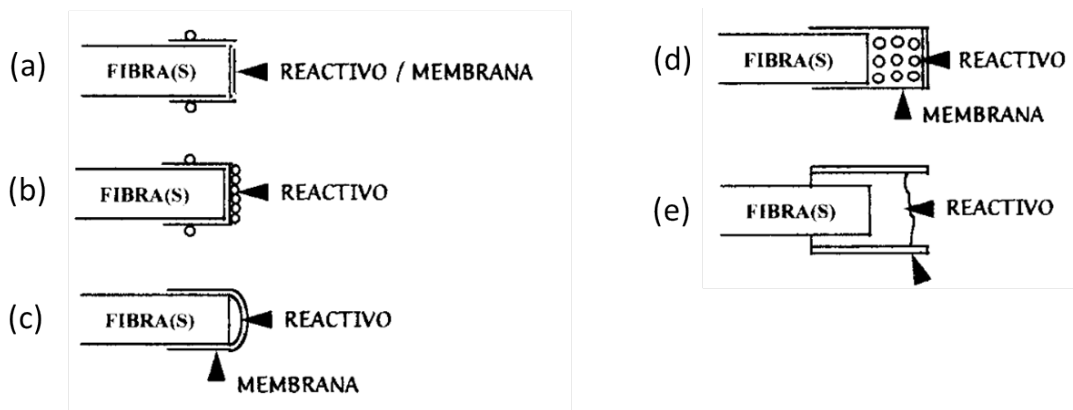


Figura AII.3: Distintas configuraciones de inmovilización de la fase sensora en los sensores de fibra óptica extrínsecos [15].

Así pues, en este caso, a diferencia de los sensores extrínsecos, no se mide una propiedad óptica del analito o de la fase sensora, sino el cambio en las propiedades ópticas de la fibra producido por la interacción con el analito, interacción que puede tener lugar tanto en el núcleo como en el revestimiento de la fibra óptica [15, 98]. Una característica muy importante de estos sensores es su posible utilización como sensores distribuidos, es decir, aquellos en los que la medida puede realizarse en cualquier punto de la fibra óptica, determinándose tanto su magnitud como su posición dentro de la misma [52, 98]. Dentro de los sensores intrínsecos se han descrito varias posibilidades: (a) sensores interferométricos, basados en los cambios de la fase de la luz transmitida a través de una fibra monomodo. Estos sensores son muy sensibles pero también costosos, ya que requieren el uso de fuentes de luz coherentes y dispositivos complejos para el control de la polarización de la luz. Estos sensores se emplean fundamentalmente en la medida de parámetros físicos tales como fluctuaciones en la presión, la temperatura o cambios en el campo magnético [387]; (b) sensores intrínsecos en los que una porción del revestimiento de la fibra óptica se sustituye por el reactivo indicador sensible al analito. Las propiedades ópticas del revestimiento de la fibra varían en función de la concentración del analito, modificándose de este modo su interacción con la onda evanescente. Dentro de este grupo se incluirían todos aquellos optodos en los que se inmovilizan covalentemente a la fibra óptica compuestos tales como fluoróforos, ionóforos o incluso anticuerpos [15]. El primer sensor de este tipo fue propuesto por Hardy *et al.* [388] en 1975; (c) sensores intrínsecos en los que el propio reactivo indicador actúa como núcleo transmisor de la luz a través de la fibra óptica [1, 98]. Otras posibles configuraciones para los sensores de fibra óptica intrínsecos son mostradas en la Figura ?? [52].

Por otro lado, la conexión de los optodos a los instrumentos de medida puede ser realizada adoptando distintas configuraciones, de las cuales, algunas de las más comunes aparecen recogidas en la Figura AII.5. De esta forma, el sensor puede estar constituido por un haz de fibras bifurcado: por uno de sus extremos se lleva la luz desde la fuente de excitación hacia la “zona activa” (fase sensora), recogiendo la luz reflejada o emitida por la fase sensora y llevándola hacia el sistema de detección a través de la otra rama del haz de fibras bifurcado (Figura AII.5(a)). Así pues, gran parte de la luz que llega al detector procede únicamente de la fase sensora, que se encuentra ubicada en la intersección de los conos de iluminación de las fibras utilizadas para la excitación y el cono de recepción de la rama del haz de fibras que lleva la luz al detector [99, 300, 389]. Otra posibilidad consiste en emplear una monofibra

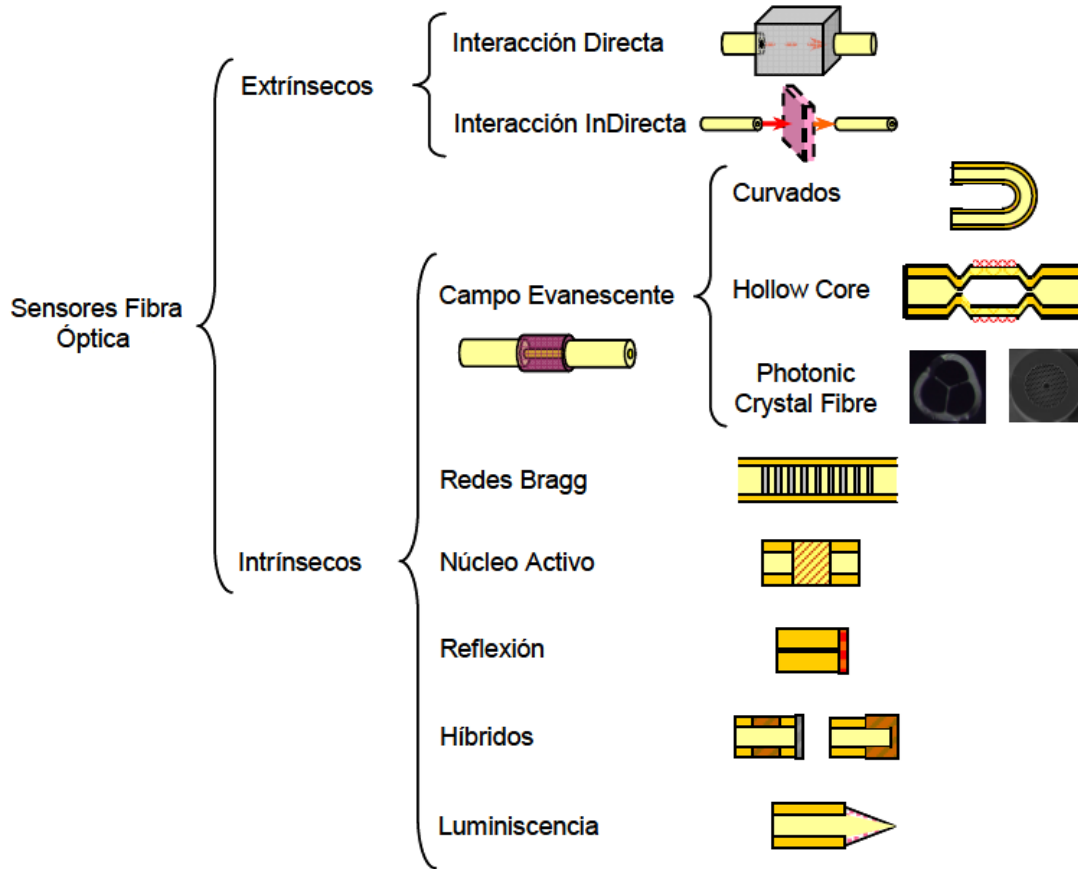


Figura AII.4: Clasificación de las distintas arquitecturas de fabricación de los sensores de fibra óptica [52].

para llevar la luz desde la fuente de excitación a la fase sensora y desde ésta al sistema de detección. En este caso, el sistema es algo más complicado, ya que se requiere del empleo de un divisor de haz para separar la luz reflejada procedente de la fuente de excitación de la luz que surge como resultado de la interacción con la fase sensora y que es conducida al detector (Figura AII.5(b)) [1]. Finalmente, existe otro tipo de sensores ópticos en los que se sustituye una porción del revestimiento de la fibra óptica por una fina capa de material sensible (fase sensora), modificando así sus propiedades de transmisión (Figura AII.5(c)). De este modo, cualquier interacción (de dicha fase) con el analito se traduce en un cambio en las propiedades de transmisión de la luz por la fibra óptica. Ésta es la base de los denominados sensores de onda evanescente [50, 52, 390].

Por último, cabe destacar que las áreas donde se han encontrado mayores aplicaciones para los sensores de fibra óptica son, entre otras: el diagnóstico clínico [101], la biomedicina y la biotecnología [272, 371, 391, 392], el medioambiente [27, 28, 393], el control de procesos industriales [374, 394, 395], el análisis agrícola [396, 397] y la seguridad [373, 398].

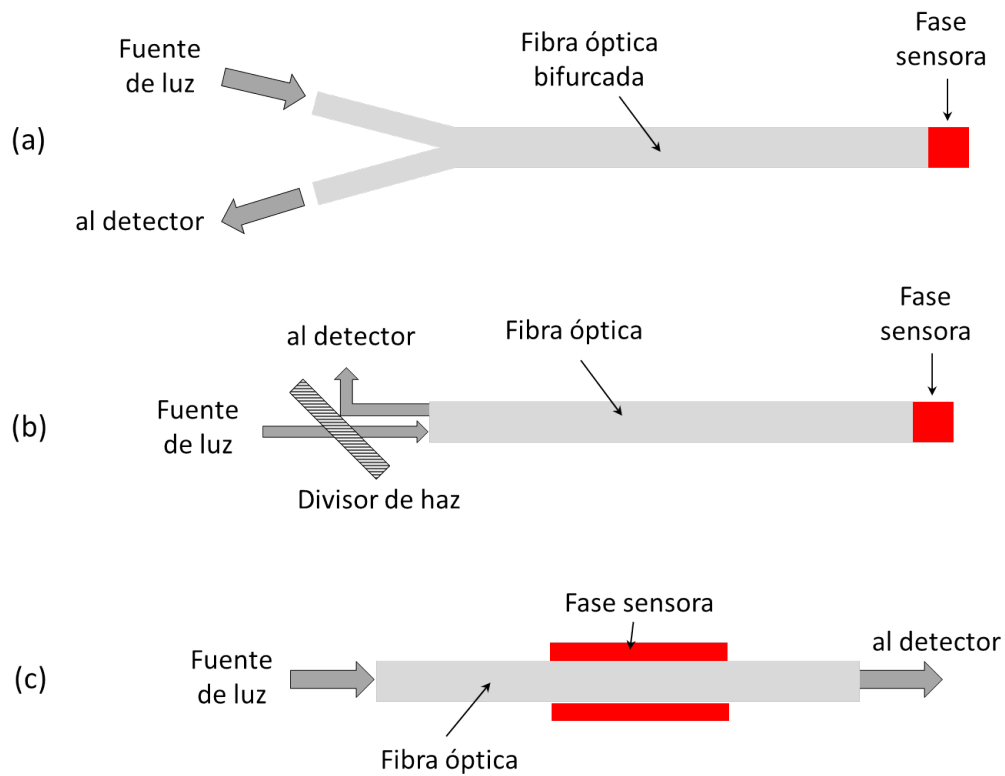


Figura AII.5: Tipos de conexión más comunes en los sensores de fibra óptica. (a) fibra bifurcada: la luz viaja por una rama hacia la fase sensora y por otra hacia el detector, (b) monofibra con la fase sensora en un extremo: se utiliza un divisor de haz para separar la luz de excitación y emisión, (c) monofibra con la fase sensora recubriendo una parte del núcleo/revestimiento de la fibra óptica [1].

Apéndice III:

Sensores ópticos luminiscentes para el control de oxígeno

AIII.1 Componentes de un sensor óptico de oxígeno

Los sensores ópticos de oxígeno se basan en el uso de fases sensoras químicamente activas que se implementan en dispositivos de medida. Las partes en las que se divide un sensor óptico para la determinación de oxígeno aparecen esquematizadas en la Figura AIII.1, y se describen a continuación [14]:

- 1) En primer lugar, podemos diferenciar la *fase sensora* o *zona de reconocimiento* del sensor, que es donde se produce la interacción selectiva entre el analito de interés (oxígeno) y el indicador luminiscente. Esta interacción produce un cambio en alguna propiedad óptica del sistema cuya magnitud será proporcional a la concentración de oxígeno, lo que constituye la primera etapa del proceso de transducción. En la mayoría de los sensores ópticos luminiscentes, esta transducción es de carácter físico (un cambio en las propiedades espectroscópicas de la fase sensora, como por ejemplo, la desactivación de la luminiscencia molecular del indicador luminiscente sensible al oxígeno), si bien en algunos casos este cambio también puede estar asociado a una reacción química (como ocurre en los biosensores enzimáticos con transducción de oxígeno) [14].

La fase sensora de un sensor óptico de oxígeno consta generalmente de dos partes: un indicador luminiscente y un soporte físico, que además puede aportar propiedades de selectividad al oxígeno. En ocasiones, es posible usar un indicador sensible a oxígeno (o estructuras supramoleculares derivadas de éste) directamente sobre la muestra a analizar [399, 400], sin embargo, el uso de una matriz soporte que aisle al indicador del medio mejorará generalmente las propiedades de sensibilidad y estabilidad de la fase sensora, y en aplicaciones biológicas evitará la citotoxicidad asociada a este tipo de compuestos [92].

- 2) A continuación podemos identificar un elemento *transductor*, encargado de transformar las propiedades de la fase sensora en una señal analítica útil (normalmente de naturaleza eléctrica). En los sensores ópticos de oxígeno, el elemento transductor suele ser un detector óptico (espectrofotómetro, fotodiodo, PMT, CCD, etc.), el cual transforma la señal óptica procedente de la fase sensora en una señal de naturaleza eléctrica.
- 3) Por último, la señal eléctrica del detector pasa a un *elemento electrónico*, donde se lleva a cabo una primera etapa de acondicionamiento de la señal (generalmente consiste en una

etapa de amplificación y filtrado de la señal eléctrica), seguida de un proceso de conversión analógico/digital y, finalmente, el procesamiento digital de la señal y la presentación de los resultados. En el caso de los sensores ópticos de oxígeno, este elemento es el encargado de proporcionar un valor de intensidad luminiscente, desfase, factor de modulación o tiempo de vida (dependiendo de la naturaleza de la señal óptica registrada y de la técnica de medida empleada) [51, 92]. En la mayoría de los dispositivos comerciales este elemento electrónico suele estar integrado en el sensor, de manera que la magnitud de la señal física medida se puede relacionar directamente con la concentración de oxígeno a partir de un calibrado previo [14].

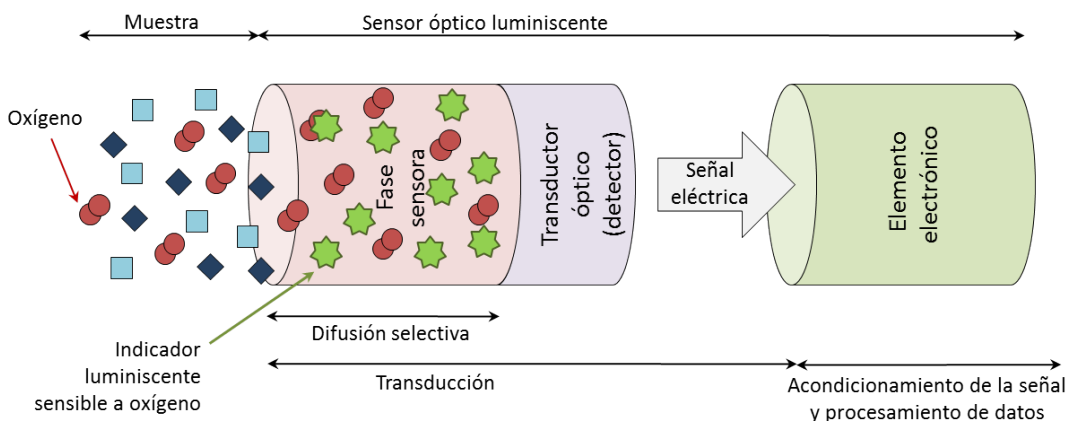


Figura AIII.1: Esquema general de un sensor óptico luminiscente para la determinación de oxígeno [14].

AIII.2 Componentes de una fase sensora óptica para oxígeno

Una fase sensora sensible a oxígeno consta generalmente de dos partes: (1) una molécula indicadora cuyas propiedades luminiscentes cambian en función de la concentración de oxígeno en el medio, y (2) un material o matriz de soporte donde dicho indicador es inmovilizado, de forma que quede aislado de posibles interferentes [14].

AIII.2.1 Indicadores sensibles al oxígeno

Diversos compuestos como los hidrocarburos aromáticos policíclicos (PAHs, del inglés *Polycyclic Aromatic Hydrocarbons*), el ácido 1-pirenobutírico (PBA) [401] o el decaciclono (DCY) [210], han sido usados como indicadores sensibles a oxígeno. Otro tipo de materiales como el fullereno C70 [402], las ftalocianinas [403] o los quelatos de aluminio [389], también han demostrado su utilidad en el desarrollo de fases sensoras ópticas sensibles a oxígeno [14].

Sin embargo, las excelentes propiedades luminiscentes de los complejos organometálicos (*organometallic compounds*, OMCs) de metales de transición y la atenuación de su luminiscencia por el O_2 , han hecho que este grupo constituya, hoy en día, la principal fuente de indicadores luminiscentes sensibles a oxígeno [404], siendo Ru(II) e Ir(III) [14], aunque también Re(I) [405], Os(III) [406, 407], Eu(III) [78, 408] y Pt(II) los metales más utilizados en

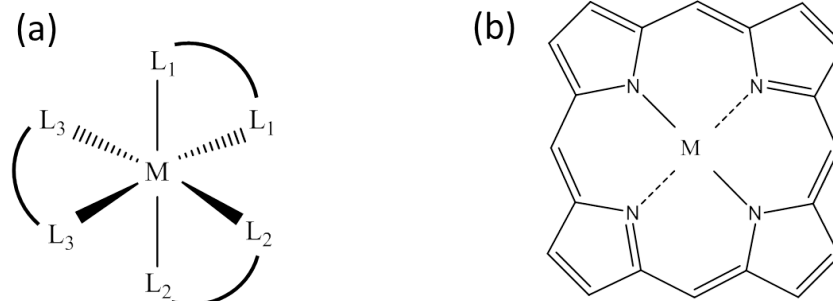


Figura AIII.2: Estructura química básica de: (a) un complejo organometálico octaédrico, donde L_1 , L_2 y L_3 pueden ser ligandos de diferente naturaleza; (b) un anillo tetrapirrólico de la porfirina. M representa a cualquiera de los metales de transición [14].

OMCs para la detección luminiscente de oxígeno [409]. Otro tipo de indicadores luminiscentes ampliamente utilizados en el desarrollo de fases sensoras ópticas para oxígeno son las metaloporfirinas (sobre todo de Pd(II) y Pt(II)), compuestas por un anillo tetrapirrólico con diferentes sustituyentes [14]. Otra clase de indicadores basados en complejos de Pt o Pd son las azotetrazobenzoporfirinas, las cuales ocupan una posición intermedia entre las porfirinas y la ftalocianinas [233]. La Figura AIII.2 muestra la estructura química básica de los complejos organometálicos y las metaloporfirinas [14].

Por su importancia, en la Tabla AIII.1 se recogen algunos de los indicadores luminiscentes (complejos metálicos de Ru(II) e Ir(III) y porfirinas de Pt(II) y Pd(II)) y soportes sólidos más utilizados en el desarrollo de fases sensoras ópticas sensibles a oxígeno. La mayor parte de los complejos y soportes recogidos en esta tabla se encuentran disponibles comercialmente.

Tabla AIII.1: Indicadores luminiscentes (complejos organometálicos de Ru(II) e Ir(III) y porfirinas de Pt(II) y Pd(II)) y soportes más utilizados en el desarrollo de fases sensoras ópticas sensibles a oxígeno [14, 92].

Complejo	Soporte	λ_{abs} (nm)	λ_{em} (nm)	τ (μ s) ^a	τ (μ s) ^b	Referencia(s)
Ru(bpy) ₃ ²⁺	PMMA/CAB/Si	460	610	0.90–1.53	0.62	[410, 411]
Ru(dpp) ₃ ²⁺	PS/Ormosil/Si	450	615	4.2–7.5	–	[386, 411, 412]
Ru(Phen) ₃ ²⁺	PS	450	590	3	–	[411]
Ir(ppy) ₃	PS	376	512	–	<2.0	[413]
Ir(ppy) ₂ (dptNH ₂) ⁺	pPEGMA	380	500/550	1.3	–	[414]
Ir(ppy) ₂ (mp-bpy) ⁺	PS	318, 494	665	112	<12	[415]
PtOEP	PS/pPEGMA	384, 505, 535	646	84–90	17	[412, 416, 417]
PtTFPP	PS/Si	398, 508, 540	650	56–71	–	[234, 411, 418]
PtOEPK	PS/PVC	398, 592	759	62	–	[419, 420]
PdOEP	PS/pPEGMA/Si	393, 512, 546	663	770–1000	20	[411, 417]
PdOEPK	PS/PVC	410, 602	792	440–480	–	[419, 420]
PdTFPP	PS	405, 525, 565	670	930	–	[418]

^aTiempo de vida del indicador inmovilizado en soporte y en ausencia de oxígeno. ^bTiempo de vida del indicador inmovilizado en disolución y en ausencia de oxígeno.

PMMA: poli(metilmacrilato); CAB: butirato acetato de celulosa; Si: sílice; Ormosil: silicatos modificados orgánicamente; S: sílica; PS: poliestireno; pPEGMA: poli(etilenglicol)etiléter metacrilato; dptNH₂: 4-amino-3,5-di-2-piridil-H4-1,2,4-triazol; mp-bpy: 2(4,4'-bis(2-(4-N,N-metilhexilaminofenil)etenil)-2,2'-bipiridina); PtOEP: octaetilporfirina de Pt(II); PtTFPP: pentafluorofenil porfirina de Pt(II); PtOEPK: octaetilporfirina cetona de Pt(II); PVC: policloruro de vinilo; PdOEP: octaetilporfirina de Paladio (II), PdTFPP: pentafluorofenilporfirina de Pd(II); PdOEPK: octaetilporfirina cetona de Pd(II) (véase la Figura AIII.3).

La principal ventaja de los metales de transición es que poseen orbitales d parcialmente ocupados. La formación de complejos con diferentes tipos de ligandos (véase la Figura AIII.3) hace que este orbital d se divida en dos niveles de energía, lo cual posibilita la absorción de luz a determinadas frecuencias [14]. La diferencia de energía entre estos dos niveles, su ocupación y orden determinan sus propiedades de emisión, por lo que tanto el ligando, como el catión y la geometría del complejo formado influyen en las propiedades luminiscentes y de atenuación con el oxígeno [205].

Además, la modificación de los ligandos de estos complejos puede ser útil para cambiar el carácter lipofílico del complejo, permitiendo que éste pueda ser solubilizado en materiales de diferente naturaleza, especialmente en aquellos de carácter apolar (como las siliconas y los polímeros) [206]. Del mismo modo, la solubilidad del contraión de los complejos cargados también puede contribuir a mejorar esta solubilidad [421].

En general, el indicador seleccionado debe poseer ciertas propiedades que le permitan ser inmovilizado en una matriz rígida, sin que ello afecte a sus propiedades fisicoquímicas. En general, el efecto de las matrices donde se encuentra inmovilizado el luminóforo tiene una gran influencia sobre el espectro de absorción y emisión de los complejos. Cuando el indicador se encuentra en disolución, el disolvente puede ser capaz de disminuir la energía del estado excitado del complejo, lo cual influye en la longitud de onda de emisión y en el tiempo de vida, debido a que la relajación de las moléculas en un disolvente es rápida (debido a la alta movilidad que presentan en estado líquido) [14]. Sin embargo, en sistemas rígidos, las rotaciones intramoleculares son más difíciles, por lo que el tiempo de vida de una molécula será mayor cuando ésta se inmoviliza en un soporte rígido (comparado con el tiempo de vida en disolución) [71], tal y como puede observarse para algunos de los complejos mostrados en la Tabla AIII.1. Éste es el principal motivo por el cual, cuando el indicador es inmovilizado en una matriz rígida, aumenta su sensibilidad al oxígeno, ya que como se comentó, la constante k_{SV} es directamente proporcional al tiempo de vida τ_0 .

Otro factor importante a tener en cuenta en el desarrollo de fases sensoras ópticas es la concentración del indicador, ya que si se realizan medidas basadas en la intensidad de la luminiscencia, éstas se verán afectadas por la cantidad de indicador inmovilizado [14]. Asimismo, dicha concentración también será importante en medidas basadas en el tiempo de vida de luminiscencia, ya que una alta concentración de indicador puede dar lugar a fenómenos de precipitación y autoatenuación que disminuyan el tiempo de vida del complejo, y por tanto, la sensibilidad al oxígeno [386].

Una característica deseable en los indicadores de oxígeno es que éstos posean un brillo elevado, entendiendo como tal el producto del coeficiente de absorción molar y el rendimiento cuántico de luminiscencia, lo que se traduce en un aumento de luz absorbida y/o emitida [14]. Esta característica no afecta a la sensibilidad de la fase sensora, pero sí incrementa la cantidad de luz de emisión que recibe el fotodetector [235], facilitando su implementación en dispositivos ópticos sencillos y baratos [51].

Los complejos de Ru(II), ampliamente usados y estudiados [422, 423], poseen tiempos de vida que, aunque relativamente largos (del orden de unos pocos μs), proporcionan una sensibilidad menor comparada con la de otro tipo de complejos como las porfirinas, que presentan tiempos de vida cercanos a los 100 μs (véase la Tabla AIII.1). Además, los complejos

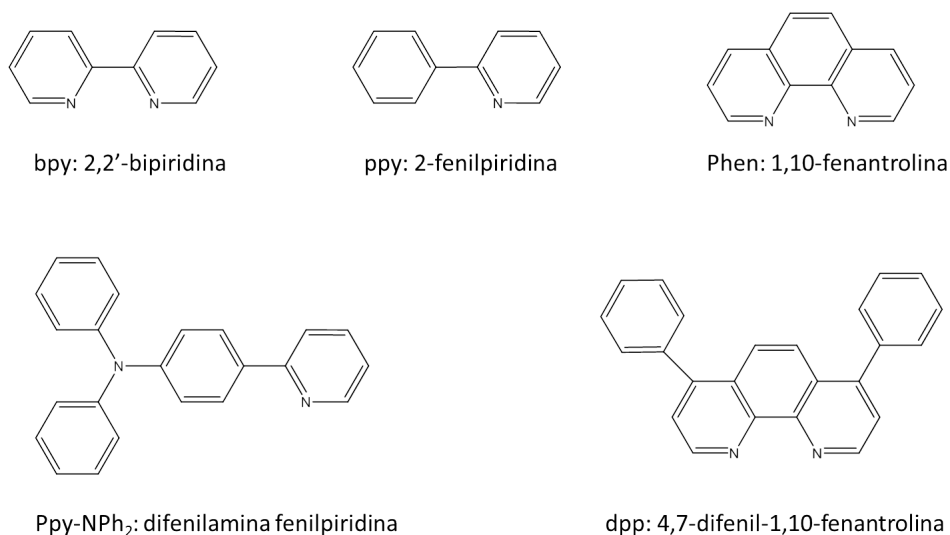


Figura AIII.3: Ligandos más comunes usados en los OMCs de metales de transición [14].

de rutenio suelen verse más afectados por la desactivación térmica, por lo que su sensibilidad al oxígeno puede variar notablemente con la temperatura [423]. Aun así, los complejos de Ru(II) suelen poseer una banda muy ancha de absorción en la región azul del espectro visible, lo que junto con un gran desplazamiento de Stokes, ha dado lugar a una gran variedad de aplicaciones [92, 206, 210, 424].

Menos sensibles a la temperatura que los complejos de Ru(II) son los complejos de Ir(III) [14]. Algunas modificaciones de los complejos de iridio mostrados en la Tabla AIII.1 han dado lugar a una gran variedad de estructuras [416, 425, 426]. También se pueden encontrar complejos de Ir(III) con ligandos coumarínicos [235] o incluso porfirinas de Ir [427]. En general, los complejos de Ir(III) han demostrado poseer una buena capacidad para modificar su espectro de emisión en toda la región UV [428, 429], aunque en la mayoría de los casos también poseen tiempos de vida del orden de los μs [14].

El uso de diferentes tipos de ligandos no solo permite modificar las propiedades espectroscópicas del complejo (longitud de onda de excitación y/o emisión, tiempo de vida, etc. (véase la Tabla AIII.1), sino que también influye sobre su fotoestabilidad [14]. La estabilidad fotoquímica del complejo es muy importante para su empleo en fases sensoras ópticas de oxígeno, debido a que la fotodescomposición del reactivo inmovilizado puede producirse por la exposición prolongada a la radiación electromagnética. Por tanto, la modificación de los indicadores también contribuye a mejorar la fotoestabilidad del luminóforo. Un ejemplo de esto lo encontramos en los complejos PtOEP y PdOEP. La modificación del anillo tetrapirrólico con un grupo cetónico, no solo produce un desplazamiento del espectro de emisión hacia el rojo, sino que además mejora la estabilidad química y la fotodegradación del complejo [419]. Del mismo modo, la introducción de sustituyentes fluorados incrementa aún más la estabilidad fotoquímica, como ocurre con el complejo PtTFPP [234], el cual es ampliamente usado como indicador de oxígeno [14].

AIII.2.2 Tipos de matrices o soportes

Según la morfología de la fase sensora donde se inmoviliza el indicador, podemos encontrar fases sensoras ópticas basadas principalmente en los siguientes tipos de formatos [14]:

- *Fases sensoras planas o membranas.* Históricamente, las membranas fueron los primeros soportes sólidos usados en el desarrollo de fases sensoras ópticas, debido a que ofrecen la posibilidad de formar películas sensoras delgadas (de espesor controlado) donde pueden ser inmovilizados una amplia variedad de reactivos [14].
- *Nanopartículas.* Combinan la flexibilidad de los indicadores disueltos con las ventajas de las membranas. Estas nanopartículas también se denominan a veces como PEB-BLEs (*probes encapsulated by biological localized embedding*) cuando la determinación de oxígeno (u otros analitos) es intracelular [14, 430].
- *Fibras ópticas.* Estos sensores consisten en un latiguillo de fibra óptica cortado por un extremo sobre el cual se fija un material sensible. Dicho material puede ser depositado sobre la fibra usando distintas técnicas de deposición [52, 78, 98].

El desarrollo de un sensor óptico requiere normalmente la deposición de la fase sensora en diferentes tipos de soportes donde llevar a cabo la medida óptica. La obtención de membranas lleva implícita la deposición de la fase sensora sobre un soporte sólido. Sin embargo, las nanopartículas pueden constituir en sí mismas el soporte de la fase sensora, al ser usadas directamente en el medio [74], o bien pueden ser depositadas sobre una superficie para obtener una membrana nanoparticulada [14, 99]. Tanto las membranas como las nanopartículas presentan diferentes ventajas e inconvenientes, y la selección del mejor formato para el soporte vendrá determinada por la aplicación concreta y por el material de fabricación [14].

Tabla AIII.2: Principales formatos y métodos de obtención de fases sensoras ópticas [14].

Formato	Método de fabricación / deposición	Referencia(s)
Membrana	Spin-coating	[73, 218, 425]
	Dip-coating	[14, 431]
	Knife-coating	[432]
Nanopartículas	Nano spray-drying	[433, 434]
	Precipitación	[102, 435]
	Miniemulsión	[436, 437]
Fibra óptica	Dip-coating	[52, 78, 438]
	Electrostatic Self Assembly method (ESAm)	[52, 439, 440]

La Tabla AIII.2 recoge los métodos de obtención de fases sensoras más comunes en el campo de los sensores ópticos de oxígeno. La elección final del formato y del método de fabricación dependerá del material de la fase sensora y de la configuración utilizada para realizar la medida (optosensor, optodo inalámbrico, microchip, etc.) [14].

En cualquiera de los formatos de matrices mencionados (membranas, nanopartículas o fibras ópticas), la inmovilización del indicador puede hacerse física o químicamente [14]:

Inmovilización física: el luminóforo sensible a oxígeno que se desea inmovilizar se puede añadir al cóctel de la membrana a depositar, cóctel que posteriormente será depositado sobre un soporte usando alguno de los métodos citados en la Tabla AIII.2. Si se lleva a cabo una polimerización durante la formación de la fase sensora, el indicador puede añadirse junto a los monómeros, quedando atrapado en el interior del material. También es posible llevar a cabo una inmovilización física del indicador en materiales porosos mediante la evaporación del disolvente [73, 100], o por impregnación o hinchamiento de la fase sensora [441, 442].

Inmovilización química: tiene lugar mediante la formación de enlaces covalentes entre el indicador y la matriz. La inmovilización química permite mejorar la estabilidad y evitar la migración de los complejos [443]. Esta inmovilización puede llevarse a cabo durante la síntesis del material, y luego ser depositado sobre un soporte, o bien llevarse a cabo dicha reacción de inmovilización cuando la fase sensora ya se ha depositado. En cualquier caso, la posibilidad de realizar una inmovilización química del indicador va a depender de los grupos funcionales de los que dispongan tanto la molécula indicadora como el material de la matriz, y de las condiciones de reactividad que éstos sean capaces de soportar [14].

El uso de soportes de diferente naturaleza, así como el de plastificantes, tienen una enorme influencia en la sensibilidad de la fase sensora [444]. En general, el uso de diferentes materiales influye sobre la difusión del oxígeno, que como ya mencionamos, está directamente relacionada con la sensibilidad k_{SV} . A continuación se detallan algunas de las matrices más utilizadas en el desarrollo de fases sensoras ópticas [73, 206, 210, 445], algunas de las cuales han sido utilizadas en el desarrollo de esta memoria.

AIII.2.2.1 Membranas poliméricas

Este tipo de membranas, normalmente de carácter hidrofóbico, suelen proteger al indicador del acceso de otros posibles atenuadores de la luminiscencia, como las especies iónicas [14]. Sin embargo, debido al carácter apolar de algunas de estas membranas poliméricas, pueden existir problemas de solubilidad del complejo, lo que produce la lixiviación de dicho complejo cuando la fase sensora entra en contacto con el agua, o problemas de agregación del mismo en la fase sensora, con la consiguiente pérdida de sensibilidad al analito [14].

Para comprender la influencia del material sobre la sensibilidad al oxígeno, se puede tener en cuenta el coeficiente de permeabilidad al oxígeno (P_{O_2}) del material, que se encuentra directamente relacionado con el coeficiente de difusión de oxígeno (D_{O_2}) y el coeficiente de solubilidad al oxígeno (S_{O_2}) del material [14], mediante la ecuación:

$$P_{O_2} = D_{O_2} S_{O_2}$$

El coeficiente de permeabilidad (P_{O_2}) suele ser expresado en las unidades ($\text{cm}^3(\text{STP}) \text{cm} \text{cm}^{-2} \text{s}^{-1} \text{Pa}^{-1}$), siendo éste el resultado del producto de los coeficientes (D_{O_2}) (en $\text{cm}^2 \text{s}^{-1}$) y (S_{O_2}) (en $\text{cm}^3(\text{STP}) \text{cm}^{-3} \text{Pa}^{-1}$). El coeficiente de difusión de oxígeno (D_{O_2}) representa el volumen de oxígeno (en cm^3), medido en condiciones estándar de presión y temperatura (STP, *standard temperature and pressure*), que pasa a través de 1 cm del material en 1 segundo. El coeficiente de solubilidad (S_{O_2}), es el volumen de oxígeno (en cm^3) que, a una presión parcial dada (en Pa), se disuelve en 1 cm^3 del material.

Según el trabajo de Mills [215], la influencia de la solubilidad sobre la permeabilidad es mucho menor que la de la difusión, por lo que en la mayoría de las fase sensoras, la solubilidad puede ser considerada como una constante, y se puede hablar de difusión y de permeabilidad indistintamente, aunque su significado físico no sea el mismo. Así, el coeficiente de permeabilidad puede tomarse como guía de la sensibilidad a oxígeno de una fase sensora. Diversos factores influyen de una forma u otra sobre la permeabilidad al oxígeno de un polímero, como por ejemplo, su polaridad, grado de entrecruzamiento, humedad, grosor de la película, etc., que además, no solo van a influir en la sensibilidad del material, sino también en otras propiedades como el tiempo de respuesta [14].

Además, como ya se comentó en la introducción (véase la ecuación (25)), otro parámetro a considerar en la inmovilización del indicador es la viscosidad (η) del disolvente, que afecta directamente al coeficiente de difusión de oxígeno (D_{O_2}) de la membrana, mejorando la sensibilidad de la fase sensora para valores de viscosidad más bajos [14]. En este sentido, la temperatura de transición vítrea (T_g) del material polimérico es un parámetro a considerar. Por debajo de la T_g , el polímero se vuelve duro y quebradizo, mientras que para temperaturas superiores a la T_g el polímero pasa a un estado dúctil [14]. Por tanto, un polímero con una T_g alta va a ser más rígido que otro con una T_g más baja. Así, polímeros con T_g más bajas van a tener una mayor movilidad de sus cadenas poliméricas, y por tanto, van a presentar una mejor difusión al oxígeno [14].

Una comparación entre soportes de diferente viscosidad demuestra que se obtienen mejores resultados para aquellos menos viscosos [417]. Sin embargo, aunque la difusión al oxígeno del material esté favorecida a bajas T_g , hay que tener en cuenta que la T_g también influye en las propiedades mecánicas del polímero, previene la migración del indicador y determina la posibilidad de realizar procesos de esterilización del material [14].

Además, el tamaño y distribución de las cadenas del polímero también juega un papel importante en la viscosidad del mismo [14], ya que polímeros con un peso molecular más alto poseen una viscosidad mayor que aquellos con un peso molecular más bajo [446].

Entre los diferentes materiales poliméricos empleados en la elaboración de fases sensoras ópticas para oxígeno, podemos encontrar siliconas, polímeros orgánicos y derivados de la celulosa [1, 14, 70]. La Tabla AIII.3 muestra algunos de los polímeros más usados en el desarrollo de fases sensoras ópticas [14] junto con sus correspondientes valores de temperatura de transición T_g y coeficientes de permeabilidad (P_{O_2}). De esta tabla, se puede deducir que la sensibilidad al oxígeno de los materiales mostrados sigue, en general, la siguiente tendencia: siliconas > celulosas > polímeros orgánicos. Sin embargo, pese a esto, los polímeros orgánicos suelen ser los más utilizados en la práctica, ya que cubren un amplio intervalo de permeabilidades y pueden ser fácilmente modificados para aumentar su difusión al oxígeno (la cual va a depender en gran medida de los grupos funcionales que posean en su estructura [14]). A continuación se mencionarán algunas características y ejemplos de cada tipo de material.

Siliconas: Las siliconas o polisiloxanos se consideran polímeros inorgánicos, ya que contienen átomos de silicio y de oxígeno en su cadena principal. Pertenecen al grupo de los elastómeros, por lo que la flexibilidad de su cadena principal es muy alta [14]. Así, debido a su alta permeabilidad al oxígeno y baja T_g comparada con la de otros polímeros (véase la Tabla AIII.3), las siliconas han sido ampliamente usadas en el desarrollo de fases sensoras ópticas de oxígeno [206, 210].

Tabla AIII.3: Tipos de (co)polímeros utilizados en el desarrollo de fases sensoras ópticas [14].

Tipo	(Co)polímero	Acrónimo	T_g ($^{\circ}C$) ^a	^{a,b} P_{O_2} ($\times 10^{-13}$) ($cm^3 cm cm^{-2} s^{-1} Pa^{-1}$)	Ejemplos
Siliconas	Siliconas (varias)	–	–	≈ 376 ([215])	[215, 447, 448]
	Poli(dimetilsiloxano)	PDMS	–123	695 (35 $^{\circ}C$)	[442, 449]
Polímeros orgánicos	Poli(1-trimetilsilil-1-propino)	PTMSP	–	5790 (30 $^{\circ}C$) ([450])	[232]
	Poliacrilamida	PAA	165	–	[451]
	Poliacetato de vinilo	PVAc	32	0.367	[452]
	Poliacrilonitrilo	PAN	125	0.00015	[432]
	Policloruro de vinilo	PVC	≈ 74	0.034	[420, 444, 452]
	Poli(metilmetacrilato)	PMMA	≈ 105	0.06–0.116 (35 $^{\circ}C$)	[452, 453]
	Poli(2-hidroxietil metacrilato)	HEMA	85	2.32–5.43 (35 $^{\circ}C$)	[451]
	Poli(decil metacrilato)	PDMA	–66	–	[454]
	Poli(trifluoroetil metacrilato)	PTFEM	69	–	[455]
	Poli(etilenglicol)etil eter metacrilato	PEGMA	–40 ([414])	–	[414, 417]
	Poliestireno (PS)	PS	100	2	[419, 456, 457]
	Poli(estireno-co-acrilonitrilo)	PScoPAN	–	0.0032–0.35	[458]
	Poli(pentafluoroestireno)	PFS	47	–	[443]
	Poli(estireno-co-divinilbenceno)	PScoDVB	–	–	[459]
Polisulfona	PSF	186	0.0711	[457, 460, 461]	
Celulosas	Acetato de celulosa	CA	200	0.585 (30 $^{\circ}C$)	[462]
	Acetato butirato de celulosa	CAB	–	3.56 (34 $^{\circ}C$)	[444, 452, 453]
	Etil celulosa	EC	43	11	[432, 444]

^aValores obtenidos de la referencia [446] (o especificado); ^bValores a 25 $^{\circ}C$ de temperatura (o especificado) y 1 atm de presión.

Las siliconas se pueden encontrar comercialmente como un líquido viscoso que solidifica durante la etapa de curación. Es posible distinguir entre siliconas de un solo componente o de dos componentes, en función del número de prepolímeros usados para su formación, lo cual influye notablemente en sus propiedades finales [14]. Las siliconas de un único componente, que se caracterizan por la especie química liberada durante su etapa de curación, han demostrado poseer mejores propiedades en términos de sensibilidad al oxígeno [211, 447, 448].

Sin embargo, algunas siliconas, aunque altamente permeables al oxígeno, carecen de propiedades mecánicas cuando son depositadas como membranas, precisamente debido a su baja temperatura de transición vítrea (T_g) [14]. Además, la permeabilidad al oxígeno debe ser analizada cuidadosamente, puesto que esto puede conllevar la permeabilidad a otros gases y vapores (interferentes) [463] que actúen como atenuadores de la luminiscencia.

Polímeros orgánicos: El reactivo utilizado en fases sensoras ópticas se inmoviliza, preferentemente, en polímeros rígidos y ópticamente transparentes. En este sentido, los polímeros cristalinos como el poliestireno o el poli(metilmetacrilato), los cuales presentan una $T_g \geq 100$ $^{\circ}C$ (véase la Tabla AIII.3), aunque poseen una menor permeabilidad al oxígeno que las siliconas, tienen una alta capacidad de adhesión a diferentes tipos de superficies [14]. Esto, junto a sus excelentes propiedades de selectividad (permeabilidad selectiva al oxígeno que evita que otros atenuadores entren en contacto directo con el luminóforo), ha hecho que los polímeros orgánicos sean ampliamente utilizados como soportes en el desarrollo de fases sensoras ópticas [14]. Además, el hecho de que posean una temperatura de transición vítrea elevada, permite someter a la fase sensora a determinados procesos de esterilización [14], como es el caso de la polisulfona, que presenta una elevada T_g (186 $^{\circ}C$) [457, 460].

El poliestireno está especialmente indicado para el desarrollo de fases sensoras ópticas [235, 416, 419, 420], y es usado normalmente como material de referencia [14, 73] debido a que ha demostrado una buena compatibilidad con un gran número de complejos. Además, su alta T_g previene la migración del complejo inmovilizado, y evita la agregación del mismo incluso tras largos periodos de tiempo [14, 70, 73].

El copolímero poli(estireno-co-acrilonitrilo) posee una permeabilidad intermedia entre el PAN y el PS ($0.00015 \cdot 10^{-13}$ y $2 \cdot 10^{-13}$ $\text{cm}^3 \text{cm cm}^{-2} \text{s}^{-1} \text{Pa}^{-1}$ respectivamente), en función del porcentaje de PAN presente en su composición [14]. De hecho, el PAN tiene muy mala difusión al oxígeno, por lo que a menudo se ha usado este material para evitar la sensibilidad cruzada con este gas en sensores de temperatura, o para aislar a complejos de referencia en medidas relativas [432].

La mejor permeabilidad al oxígeno la encontramos en el poli(1-trimetilsilil-1-propino) (PTMSP) [450]. Este polímero posee un grupo trimetilsilil que es el responsable de crear la rigidez en el polímero a la vez que de aumentar el espacio libre en su estructura [14]. Así, el PTMSP muestra un coeficiente de permeabilidad similar al de la silicona PDMS (véase la Tabla AIII.3), por lo que dicho polímero ha sido utilizado como matriz en fases sensoras ópticas sensibles a bajas concentraciones de oxígeno [232].

En general, la presencia de fluoruros en el material, al igual que en los complejos, aumenta la estabilidad y retrasa la degradación de la fase sensora [14]. La longitud del enlace C-F es menor que la del enlace C-H, por lo que su energía es mayor, lo que unido al carácter electronegativo del flúor, mejora el potencial redox del polímero a la vez que induce una mayor afinidad por el oxígeno [455].

En muchos casos, la formación de un copolímero permite adecuar las propiedades de difusión de las fases sensoras, por ejemplo, se puede añadir acrilamida para hacerlas permeables a otros iones de interés analítico [451]. En general, el uso de monómeros más polares permite disminuir la hidrofobicidad del polímero, lo cual puede dar lugar a la formación hidrogel, que presentan una mejor biocompatibilidad para el caso de sensores implantables [14, 464–468].

Derivados de la celulosa: La celulosa es un polímero natural formado por unidades repetidas del monómero glucosa, y entre sus derivados más importantes (ampliamente usados en el desarrollo de fases sensoras ópticas para oxígeno) se pueden encontrar el acetato de celulosa (CA), el butirato acetato de celulosa (CAB) o la etil celulosa (EC) [206, 210]. Estos polímeros difieren considerablemente en su coeficiente de permeabilidad (véase la Tabla AIII.3), que en general es alto. En el caso de la etil celulosa (EC), su permeabilidad puede variar en función de su contenido en etoxi [469].

Las celulosas presentan una mayor hidrofiliidad que las siliconas y los polímeros orgánicos, por lo que muchas veces se utilizan para la formación de hidrogel [206]. Estos hidrogel son insolubles en agua, pero suficientemente hidrofílicos para que sufran procesos de hinchamiento en medios acuosos, mejorando la biocompatibilidad de las fases sensoras [14].

Estrategias para mejorar la sensibilidad de las membranas poliméricas: Los problemas de linealidad y sensibilidad asociados con la compatibilidad matriz-indicador, pueden mejorar mediante el uso de copolímeros cuya polaridad optimice las propiedades del polímero para solubilizar al indicador [406].

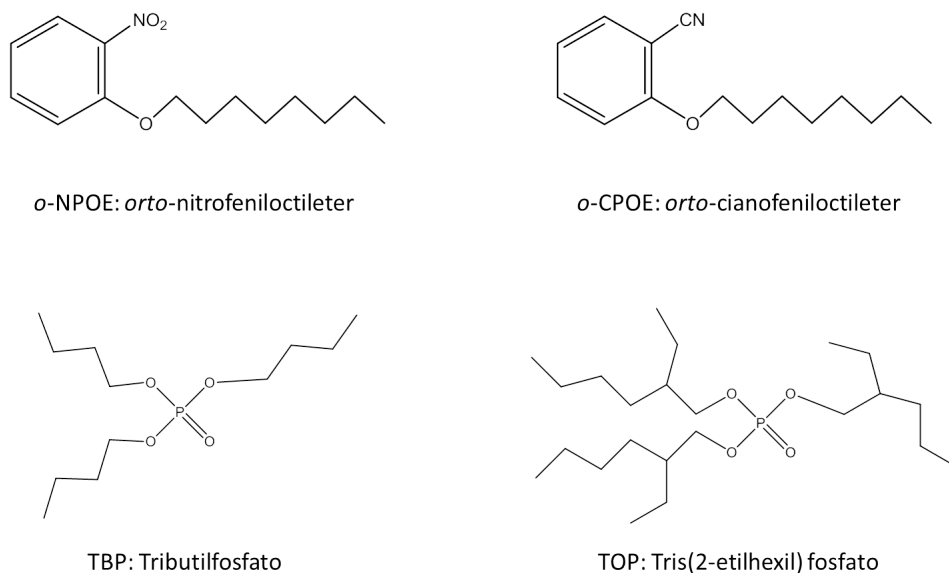


Figura AIII.4: Estructuras de los plastificantes más comúnmente usados en el desarrollo de fases sensoras ópticas para oxígeno [14].

Sin embargo, la estrategia más ampliamente utilizada para resolver estos problemas es el uso de plastificantes para aumentar el coeficiente de difusión de los polímeros, lo que puede ayudar a mejorar la compatibilidad entre la matriz y el indicador [14]. En la Figura AIII.4 se muestran las estructuras de los plastificantes más usados en el desarrollo de fases sensoras ópticas para oxígeno. Aun así, hay que tener en cuenta que los plastificantes también modifican la T_g , y por tanto, la viscosidad de la matriz [14], lo cual puede tener un efecto negativo [416, 470]. Por ejemplo, plastificantes como el *o*-CPOE o el *o*-NPOE pueden producir una disminución de la sensibilidad de la fase sensora en función del tipo de indicador, matriz y/o concentración de plastificante utilizados [14]. En muchos casos, se produce una disminución inicial de la sensibilidad para concentraciones de plastificante hasta el 10% [14], mientras que para concentraciones mayores la sensibilidad aumenta [416, 445]. Sin embargo, a pesar de esta mejora en la sensibilidad para concentraciones altas de plastificante, hay que tener en cuenta que las propiedades de adhesión del polímero pueden verse afectadas negativamente [14]. Del mismo modo, diversos tipos de plastificantes pueden afectar de diferente manera a la fotodegradación del complejo a lo largo del tiempo [14], o cuando éste es sometido a procesos de esterilización [425].

En otras ocasiones, para mejorar la solubilidad del complejo en la matriz polimérica, se hace uso de nanopartículas de óxidos metálicos donde el indicador es adsorbido o encapsulado. Estas nanopartículas se dispersan en la matriz polimérica mejorando su sensibilidad al oxígeno, mientras que su carácter polimérico permite su deposición en diferentes sustratos [209, 471, 472]. Estas nanopartículas sólidas también mejoran la señal de intensidad luminiscente emitida por el indicador, debido a su patrón de radiación de luz omnidireccional [461]. En muchos casos, también se añaden partículas de TiO₂ [209] o SiO₂ (sílice) [442].

AIII.2.2.2 Membranas sol-gel

El uso de procesos sol-gel para producir fases sensoras ópticas ha adquirido un gran interés en los últimos años, debido fundamentalmente a la flexibilidad de su diseño y facilidad de fabricación [434]. El material sol-gel se utiliza para crear soportes microporosos encargados de atrapar (con diferentes mecanismos) al indicador luminiscente, a la vez que permite la difusión del oxígeno dentro del material para que interactúe con el indicador inmovilizado [14].

Un sol-gel se produce por la hidrólisis y condensación de tetraalcoxilanos del tipo $\text{Si}(\text{OR})_4$, donde R es un grupo alquilo [206]. Los más utilizados son el tetrametoxisilano (TMOS), el metiltrimetoxisilano (MTMOS) o el tetraetoxisilano (TEOS) [14]. Estos organosilicatos producen una suspensión coloidal (*sol*), que, al condensar a temperatura ambiente, gelifica para producir un entramado de moléculas (*gel*). El secado posterior produce una densificación del gel que da lugar a una película porosa [14]. En la Figura AIII.5 se esquematizan las dos etapas del proceso sol-gel. De este modo, variando el tipo de catálisis, así como la temperatura y las concentraciones utilizadas, es posible modificar las propiedades del material nanoestructurado formado mediante este proceso [14].

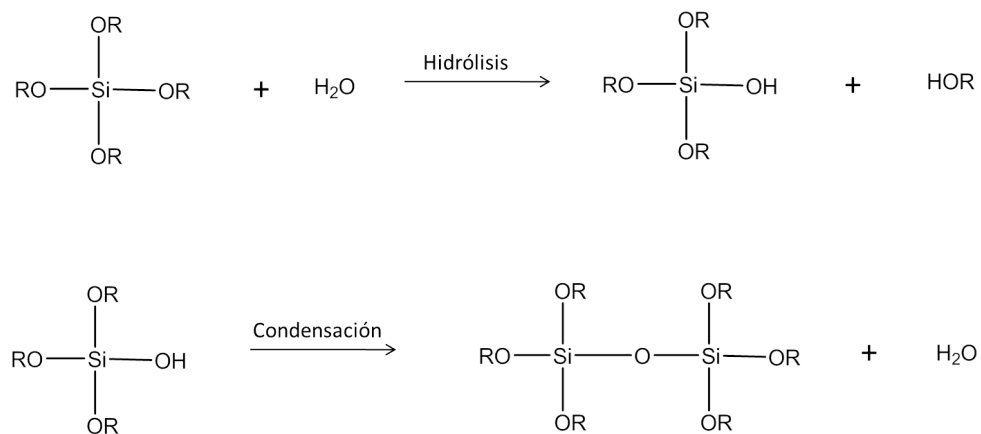


Figura AIII.5: Etapas de hidrólisis y condensación del proceso sol-gel [14].

Para sensores gaseosos, los silicatos modificados orgánicamente (*ORganically MOdified SILicates*, ORMOSIL) funcionan particularmente bien [14]. Estos organosilicatos se basan en el uso de algún precursor modificado orgánicamente, como el feniltrimetoxisilano, con cualquiera de los alcóxidos de silicio mencionados anteriormente [14]. La policondensación de estas moléculas ha producido materiales con propiedades de estabilidad y permeabilidad mejoradas [412, 473]. Añadiendo un indicador sensible a oxígeno durante la etapa *sol*, se pueden producir fases sensoras sobre una amplia variedad de sustratos [14], tanto fibras ópticas como superficies planas [218]. Además, muchos de ellos son solubles en disolventes, lo cual permite su deposición con diferentes métodos [434].

AIII.2.2.3 Óxidos metálicos nanoestructurados

Los óxidos nanoestructurados permiten crear membranas inorgánicas de tamaño, porosidad y transparencia perfectamente controlables [14]. Su obtención está ampliamente desarrollada debido al gran interés que despiertan estos materiales en campos tan relevantes como la microinformática, la robótica, los sensores electroquímicos, etc. Este tipo de material permite crear multitud de fases con características muy diferentes en función del óxido metálico usado, así como del proceso de síntesis [14]. Además, la reducción del tamaño de partícula en este tipo de fases, así como el control de la difusión del gas [14], ha hecho que estas fases nanoestructuradas presenten propiedades mejoradas para su uso como sensores de gas [73, 76].

Para el uso de este tipo de óxidos como fases sensoras de oxígeno, se pueden seguir dos estrategias: (1) la propia nanoestructura de óxido es el material sensible, de modo que cuando se expone a un gas, se produce un cambio en sus propiedades eléctricas [474] u ópticas [475]; (2) la nanoestructura se usa como soporte para inmovilizar una especie luminiscente (en este caso un indicador sensible a oxígeno), de modo que se mejora la interacción del indicador con el gas [73, 100].

Estos nuevos materiales nanoestructurados están basados en la dispersión de nanopartículas de óxidos metálicos sobre un soporte inerte (alcohol polivinílico, PVA) [70, 416], siendo los óxidos más utilizados los de aluminio, silicio, zirconio y titanio [14]. Su fabricación es muy simple y económica, pues se pueden conseguir hasta 200 m² de material por minuto mediante la técnica “*curtain coating*” (deposición en cortina o cascada), pudiéndose generar membranas de 1 a 30 mL/m² de volumen total de poros con diámetros que oscilan entre 1 y 50 nm [14].

Los óxidos metálicos de óxido hidróxido de aluminio (AlOOH) desarrollados por la empresa Ilford Imaging [476], han dado muy buenos resultados en el desarrollo de fases sensoras ópticas para detección de oxígeno [14, 73, 100]. Las membranas generadas con este tipo de óxidos son nanoporosas, pudiéndose controlar el tamaño, volumen y carga de los poros, lo cual permite incorporar indicadores luminiscentes u otros reactivos [100]. Las membranas desarrolladas con AlOOH han demostrado mejorar las propiedades de las fases sensoras cuando se inmovilizan indicadores sensibles al oxígeno [73, 100, 416]. En la Figura AIII.6 se muestran varias imágenes microscópicas de nanoestructuras AlOOH [14].

Las partículas de óxido de este material se aglomeran formando nanoporos en el interior, mientras que el espacio entre estos aglomerados da lugar a la existencia de macroporos [477]. Esta heterogeneidad da lugar a la formación de dos ambientes dentro de la fase sensora, con diferente accesibilidad al oxígeno en cada uno de ellos, lo que hace que la respuesta de la fase sensora tenga un comportamiento no lineal [14, 73]. Sin embargo, esta arquitectura de los poros también parece ser la responsable de que las fuerzas capilares conduzcan al oxígeno rápidamente hacia el interior de los poros, mejorando la sensibilidad al oxígeno de la fase sensora, que puede mejorar hasta 100 veces respecto al mismo indicador inmovilizado en una membrana clásica de poliestireno [14, 73].

Al mismo tiempo, la distribución del indicador en los nano- y macro- poros formados, proporcionan a la fase sensora una gran estabilidad frente a la fotodescomposición, debido a

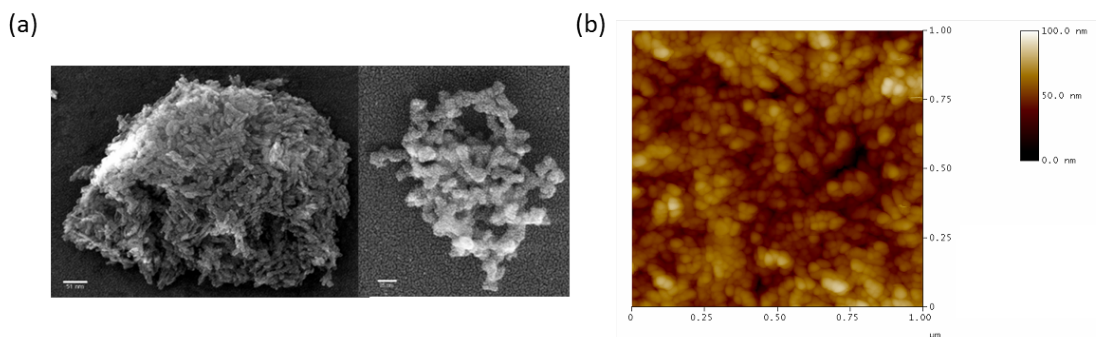


Figura AIII.6: (a) Fotografía de las partículas de AlOOH (tomada con un microscopio electrónico de barrido (SEM)). (b) Fotografía de estas partículas de AlOOH depositadas sobre PVC para formar la nanoestructura de óxido hidróxido de aluminio (tomada con un microscopio de fuerza atómica (AFM)) [14].

un mayor aislamiento de estos reactivos, lo que disminuye la probabilidad de formación de aglomerados y de precipitación de los mismos [477]. Esta característica también permite la incorporación de dos o más reactivos sin que se produzcan aglomerados, evitando procesos fisicoquímicos reversibles entre ellos, como los procesos de transferencia de energía (FRET) y de transferencia de protones [476], lo que abre nuevas posibilidades en el desarrollo de fases sensoras ópticas [14].

AIII.3 Diseño de los sensores ópticos de oxígeno

Conocidos los componentes de una fase sensora y sus características principales, nos centraremos en describir las relaciones de dependencia entre los distintos elementos y procesos que intervienen en el diseño y desarrollo de una fase sensora óptica, ya que éstos deberán cumplir ciertos requisitos de compatibilidad para hacer posible la integración de la fase sensora en un dispositivo óptico final capaz de resolver un problema analítico concreto [14].

La Figura AIII.7 muestra la interrelación entre los distintos aspectos a considerar en el diseño y desarrollo de un sensor óptico, donde las flechas indican la dependencia directa de un elemento sobre otro. Así, la definición del problema analítico va a influir en tres aspectos fundamentales: el formato de fase sensora (1), la elección de los materiales de la fase sensora (indicador luminiscente y matriz) (2), y la configuración del sensor (3). La composición de la fase sensora va a influir sobre las propiedades analíticas del sensor, mientras que el formato de la fase sensora y la configuración del sensor deben poder adaptarse a la situación real de medida que se pretende resolver, y de ahí que dependan directamente de la aplicación concreta que se le vaya a dar al sensor. Así, por ejemplo, si se quiere desarrollar un sensor enzimático con transducción óptica de oxígeno, es preciso elegir un material que posea determinados grupos funcionales para crear enlaces covalentes con la enzima, o bien elegir un formato de fase sensora que permita crear estructuras porosas donde inmovilizar la enzima físicamente [14].

Como hemos resaltado a lo largo de este capítulo, el tipo de matriz donde se inmoviliza el indicador influye sobre las propiedades de éste [14], por lo que dicha elección (matriz-indicador) debe hacerse de forma conjunta a la hora de resolver un problema analítico deter-

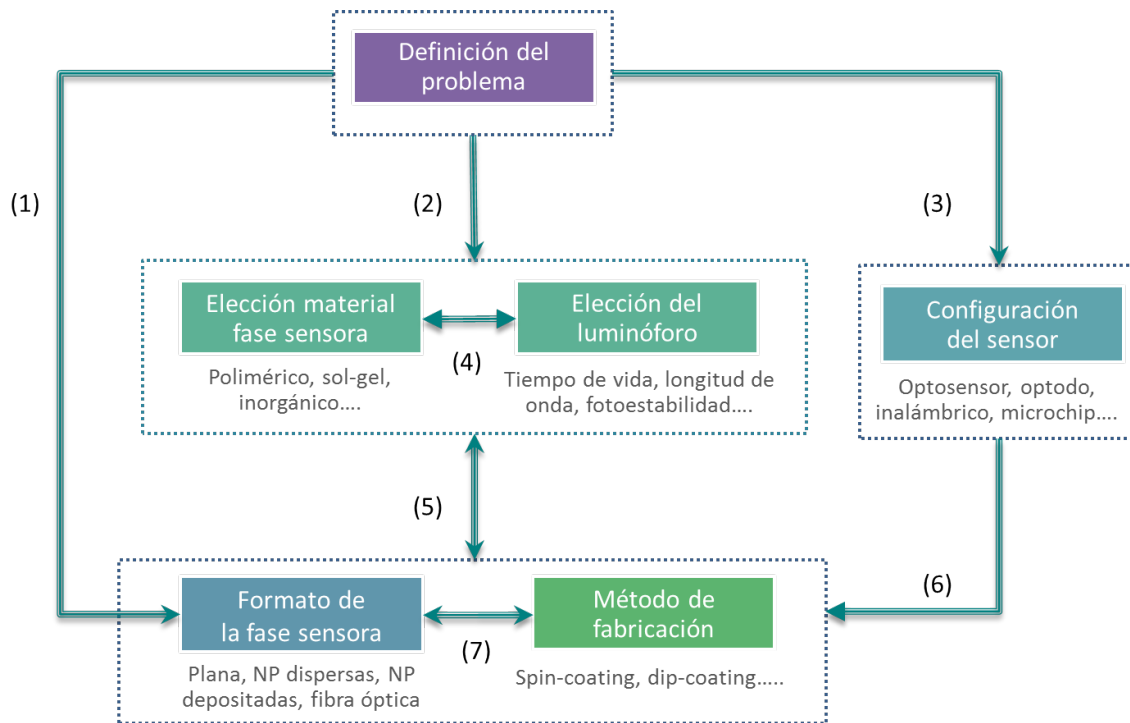


Figura AIII.7: Interrelación entre los diferentes elementos y procesos del diseño de un sensor óptico sensible a oxígeno [14].

minado (4). Asimismo, la elección de la fase sensora debe ser compatible con un determinado formato y método de fabricación (5). Por ejemplo, si se desea diseñar un material hidrofílico para mejorar la biocompatibilidad, deben tenerse en cuenta las propiedades de adhesión del mismo, así como su capacidad para formar membranas o nanopartículas (NP). Afortunadamente, el gran desarrollo experimentado por la Ciencia de los Materiales en los últimos años, ha permitido aumentar la versatilidad de estos materiales, haciendo posible su adaptación a casi cualquier tipo situación [14].

Por otro lado, la configuración del sensor también debe ser compatible con el formato de la fase sensora y, especialmente, con el método de fabricación de la misma. No obstante, en la práctica, es la configuración del sensor (determinada por el problema analítico concreto) la que influye sobre estos dos aspectos (6). Así, el método de fabricación de la fase sensora estará también determinado por estos dos aspectos: su relación con la configuración (6) y su compatibilidad con el formato (7) [14].

El proceso de diseño puede resultar complejo para ciertos problemas analíticos. Por ejemplo, si se desea desarrollar un sensor multiparamétrico, la compatibilidad entre indicadores es prioritaria y puede influir notablemente en la elección del formato de la fase sensora (en este caso, por ejemplo, sería recomendable usar NPs para evitar procesos de transferencia de carga), así como en el método de fabricación de la misma (el cual, a su vez, debe permitir la inmovilización de varios indicadores) [14]. Otros aspectos deseables a tener en cuenta en el proceso de diseño son: la sencillez y el bajo coste de los procesos de fabricación (especialmente importante para el caso de las aplicaciones comerciales).

Por tanto, podemos concluir que el diseño de una fase sensora óptica no puede hacerse de

forma secuencial, sino que debe hacerse teniendo en cuenta todos los aspectos mencionados, ya que en muchos casos habrá que renunciar a ciertos aspectos deseables en el sensor en favor de otros que resultan incompatibles con los primeros [14, 206].

Apéndice IV:

Lista de publicaciones y contribuciones a congresos

Revistas internacionales

- (1) P.K. Contreras-Gutiérrez, **S. Medina-Rodríguez**, A.L. Medina-Castillo, J.F. Fernández-Sánchez, and A. Fernández-Gutiérrez, “A new highly sensitive and versatile optical sensing film for controlling CO₂ in gaseous and aqueous media,” *Sensors and Actuators B: Chemical*, vol. 184, pp. 281-287, 2013.
- (2) **S. Medina-Rodríguez**, M. Marín-Suárez, J.F. Fernández-Sánchez, A. de la Torre-Vega, E. Baranoff, and A. Fernández-Gutiérrez, “High performance optical sensing nanocomposites for low and ultra-low oxygen concentrations using phase-shift measurements,” *Analyst*, vol. 138, pp. 4607-4617, 2013.
- (3) **S. Medina-Rodríguez**, A. de la Torre-Vega, J.F. Fernández-Sánchez, and A. Fernández-Gutiérrez, “An open and low-cost optical-fiber measurement system for the optical detection of oxygen using a multifrequency phase-resolved method,” *Sensors and Actuators B: Chemical*, vol. 176, pp. 1110-1120, 2013.
- (4) **S. Medina-Rodríguez**, A. de la Torre-Vega, J.F. Fernández-Sánchez, and A. Fernández-Gutiérrez, “Evaluation of a simple PC-based quadrature detection method at very low SNR for luminescence spectroscopy,” *Sensors and Actuators B: Chemical*, vol. 192, pp. 334-340, 2014.
- (5) **S. Medina-Rodríguez**, A. de la Torre-Vega, F.J. Sainz-Gonzalo, M. Marín-Suárez, C. Elosúa, F.J. Arregui, I.R. Matías, J.F. Fernández-Sánchez, and A. Fernández-Gutiérrez, “A novel multi-frequency phase-modulation method using rectangular-wave signals for improving the analytical sensitivity in luminescence spectroscopy” (Enviado a la revista *Analytical Chemistry*).
- (6) **S. Medina-Rodríguez**, A. de la Torre-Vega, J.F. Fernández-Sánchez, and A. Fernández-Gutiérrez, “On the calibration of chemical sensors based on photoluminescence: Selection of the appropriate model and criterion” (Enviado a la revista *Analyst*).
- (7) O. Ergeneman, G. Chatzipirpiridis, J. Pokki, M. Marín-Suárez, G.A. Sotiriou, **S. Medina-Rodríguez**, J. F. Fernández-Sánchez, A. Fernández-Gutiérrez, S. Pané, and B. J. Nelson, “In vitro oxygen sensing using intraocular microrobots,” *IEEE Transactions on Biomedical Engineering*, vol. 59, pp. 3104-3109, 2012.
- (8) M. Marín-Suárez, **S. Medina-Rodríguez**, O. Ergeneman, S. Pané, J.F. Fernández-Sánchez, B. J. Nelson, A. Fernández-Gutiérrez, “Electrophoretic deposition as a new approach to produce optical sensing films adaptable to microdevices,” *Nanoscale*, vol. 6, pp. 263-271, 2014.

Contribuciones a congresos nacionales e internacionales

- (1) **S. Medina-Rodríguez**, A. de la Torre-Vega, J.F. Fernández-Sánchez, and A. Fernández-Gutiérrez, “Desarrollo, implementación y evaluación de un sistema de medida para la caracterización de fases sensoras ópticas: determinación del tiempo de vida de luminiscencia mediante técnicas de fase resuelta,” *XII Reunión del Grupo Regional Andaluz de la Sociedad Española de Química Analítica (GRASEQA)*, Póster, Córdoba (España), 2010.
- (2) **S. Medina-Rodríguez**, M. Marín-Suárez, J.F. Fernández-Sánchez, A. de la Torre-Vega, E. Baranoff, and A. Fernández-Gutiérrez, “Fases sensoras ópticas para la detección de trazas de oxígeno usando medidas de desfase,” *XVIII Reunión de la Sociedad Española de Química Analítica (SEQA)*, Póster, Úbeda (Jaén, España), 2013.
- (3) **S. Medina-Rodríguez**, M. Marín-Suárez, A. de la Torre-Vega, J.F. Fernández-Sánchez, and A. Fernández-Gutiérrez, “Técnicas avanzadas de procesamiento de señal: nueva herramienta para medidas de tiempo de vida de fase resuelta a bajas condiciones de iluminación,” *XXXIV Reunión Bienal de la Real Sociedad Española de Química Analítica (SEQA)*, Póster y Oral, Santander (Cantabria, España), 2013.
- (4) M. Marín-Suárez, **S. Medina-Rodríguez**, O. Ergeneman, S. Pané, J.F. Fernández-Sánchez, B. J. Nelson, and A. Fernández-Gutiérrez, “Electrophoretic deposition to develop new optical sensing materials: application to a wireless oxygen sensing microrobot”, Póster y Oral, *Nano-Spain 2012 Conference*, Santander (Cantabria, España), 2012.
- (5) M. Marín-Suárez, **S. Medina-Rodríguez**, O. Ergeneman, S. Pané, J.F. Fernández-Sánchez, B. J. Nelson, and A. Fernández-Gutiérrez, “Deposición electroforética: herramienta para el desarrollo de fases sensoras ópticas adaptables a dispositivos nanométricos”, *XXXIV Reunión Bienal de la Real Sociedad Española de Química Analítica (SEQA)*, Oral, Santander (Cantabria, España), 2013.

Lista de Abreviaturas

- **A/D**: Analog-to-Digital
- **AFM**: Atomic Force Microscopy
- **AN**: Apertura Numérica
- **APPCC**: Análisis de Peligros y Puntos Críticos de Control
- **ASIC**: Application-Specific Integrated Circuit
- **ATP**: Adenosine TriPhosphate
- **CC**: Corriente Continua
- **CCD**: Charge-Coupled Device
- **CIC**: Centro de Instrumentación Científica de la Universidad de Granada
- **CID**: Charge-Injection Device
- **CITIC**: Centro de Investigación en Tecnologías de la Información y las Comunicaciones
- **CMRR**: Common-Mode Rejection Ratio
- **COVs**: Compuestos Orgánicos Volátiles
- **D/A**: Digital-to-Analog
- **DAQ**: Data Acquisition
- **DBO**: Demanda Biológica de Oxígeno
- **DFT**: Discrete Fourier Transform
- **DQ**: Dynamic Quenching
- **DQO**: Demanda Química de Oxígeno
- **DSP**: Digital Signal Processor
- **EPR**: Electron Paramagnetic Resonance

- **ESAm**: Electrostatic Self Assembly method
- **FD**: Frequency-Domain
- **FFT**: Fast Fourier Transform
- **FIA**: Flux Injection Analysis
- **FLIM**: Fluorescence Lifetime Imaging Microscopy
- **FOCS**: Fiber Optic Chemical Sensor
- **FRET**: Fluorescence Resonance Energy Transfer
- **GF**: Function Generator
- **IR**: Infra Red
- **ISFET**: Ion Sensitive Field Effect Transistor
- **IUPAC**: International Union of Pure and Applied Chemistry
- **LAN**: Local Area Network
- **LD**: Laser Diode
- **LED**: Light-Emitting Diode
- **LIA**: Lock-In Amplifier
- **LNA**: Low Noise Amplifier
- **LOD**: Limit Of Detection
- **LOQ**: Limit Of Quantification
- **LSM**: Least Squares Method
- **MAP**: Modified Atmosphere Package
- **MEMS**: Micro Electro-Mechanical Systems
- **MFCs**: Mass Flow Controllers
- **MIP**: Molecularly Imprinted Polymer
- **MIR**: Mid Infra Red
- **MMF**: Multi Mode Fibre
- **MRI**: Magnetic Resonance Imaging
- **NASA**: National Aeronautics and Space Administration
- **NIR**: Near Infra Red
- **NMR**: Nuclear Magnetic Resonance

- **OD:** Digital Oscilloscope
- **OER:** Oxygen Evolution Reaction
- **OF:** Optical Filter
- **OLED:** Organic Light-Emitting Diode
- **OMC:** Organometalic Compound
- **ORMOSIL:** ORganically MODified SILicates
- **OTR:** Oxygen Transfer Rate
- **PAHs:** Polycyclic Aromatic Hydrocarbons
- **PC:** Personal Computer
- **PCS:** Plastic Cladding
- **PDA:** Photodiode Array
- **PEBBLES:** Probes Encapsulated By Biological Localized Embedding
- **PMT:** PhotoMultiplier Tube
- **ppb:** Parts per billion
- **ppm:** Parts per million
- **PS:** Polystyrene
- **PSD:** Power Spectral Density
- **PSP:** Pressure-Sensitive Paints
- **PTFE:** Politetrafluoroetileno (teflón)
- **QY:** Quantum Yield
- **redox:** Reacción de reducción-oxidación
- **RLD:** Rapid Lifetime Determination Method
- **RMS:** Root Mean Square
- **RMSE:** Root-Mean-Square Error
- **ROM:** Read-Only Memory
- **ROS:** Reactive Oxygen Species
- **RPE:** Resonancia Paramagnética Electrónica
- **RRMSE:** Relative Root-Mean-Square Error
- **RS-232:** Recommended Standard 232

- **S**: Sample
- **SEM**: Scanning Electronic Microscope
- **SIT**: Silicon Intensifier Target
- **SMF**: Single Mode Fibre
- **SNR**: Signal-to-Noise Ratio
- **SQ**: Static Quenching
- **STP**: Standard Temperature and Pressure
- **TCSPC**: Time-Correlated Single-Photon Counting
- **TD**: Time-Domain
- **UGR**: Universidad de Granada
- **UV**: UltraViolet
- **UV-Vis**: UltraViolet-Visible
- **VIS**: Visible Spectrum

Lista de Figuras

1	Características analíticas básicas de un sensor químico	2
2	Componentes básicos de un sensor químico	4
3	Clasificación general de los sensores (bio)químicos atendiendo a diferentes criterios	5
4	Principales tipos de sistemas de transducción empleados en la fabricación de (bio)sensores químicos	7
5	Ejemplo típico de una curva de calibración de un sensor donde se muestra la relación entre la señal analítica y la concentración de analito. Principales parámetros descriptivos de los sensores ópticos	11
6	Clasificación de los sensores ópticos en función de la posición de la fase sensora respecto a la matriz medida (muestra) y el transductor	15
7	Diferentes tipos de guías de onda ópticas: de geometría cilíndrica (fibra óptica) y plana	16
8	Imágenes de un sensor de tipo microchip	16
9	Esquema de un electrodo de Clark	25
10	Proceso esquemático simplificado de la atenuación de la luminiscencia de un compuesto luminiscente ante la presencia de oxígeno	28
11	Diagrama de Jablonski	30
12	Representación de las reacciones implicadas en la excitación y emisión de un indicador. (i) Absorción de luz y excitación del luminóforo; (ii) Desactivación luminiscente; (iii) Desactivación por el oxígeno; (iv) Desactivación no radiativa	32
13	Espectros de emisión de un compuesto luminiscente a diferentes concentraciones de oxígeno entre 0% y 10%	39

14	Variación de la intensidad de luminiscencia en función de la concentración de oxígeno	40
15	Medidas de intensidad relativas donde se observan dos regiones espectrales: una de ellas no afectada por el oxígeno (asociada a la fluorescencia) y otra de ellas sí afectada por el oxígeno (asociada a la fosforescencia)	41
16	Medidas de tiempo de vida en el dominio del tiempo (o de luz pulsada)	44
17	Parámetros de un pulso de luz utilizado en medidas de tiempo de vida en el dominio del tiempo	45
18	Medidas de tiempo de vida en el dominio de la frecuencia (o de modulación de fase)	47
19	Componentes básicos de la instrumentación empleada para llevar a cabo medidas de luminiscencia	50
20	Lámparas convencionales: lámpara de arco de xenón y lámpara de mercurio de alta presión	51
21	Lámparas comerciales de pulsos	52
22	Diodos emisores de luz (LEDs) y un diodo láser	53
23	Espectros de emisión de diodos emisores de luz (LEDs)	54
24	Dependencia de la intensidad lumínica de un LED con la intensidad de corriente	54
25	Anchura de banda efectiva para dos tipos de filtros: de absorción y de interferencia	59
26	Imágenes de selectores de longitud de onda: filtros ópticos de colores (absorbancia), filtros ópticos de interferencia (reflectancia), imagen de un monocromador comercial, distribución interna de los componentes ópticos de un monocromador de Fastie-Ebert, diagrama de un monocromador de Czerny-Turner.	60
27	Concepto de atenuación en una fibra óptica. Curva de atenuación en función de la longitud de onda en una fibra óptica	63
28	Partes de una fibra óptica. Mecanismo de la propagación de rayos en una fibra óptica	63
29	Geometría de una fibra óptica y relación entre coordenadas cartesianas y cilíndricas	64
30	Perfiles de índice, secciones transversales y trayectorias típicas de propagación de rayos en diferentes tipos de fibras ópticas	65
31	Ilustración de la ley de Snell y del concepto de reflexión total interna	66
32	Guiado de rayos en una fibra óptica. Cono de aceptación de luz	67
33	Fototubo y su circuito complementario	69

34	Tubo fotomultiplicador (PMT). Detalle de funcionamiento de un tubo fotomultiplicador (PMT)	70
35	Fotografías de detectores multicanal: fotodiodo en serie (PDA), tubo vidicon (SIT), dispositivo de inyección de carga (CID) y cámara CCD	72
36	Equipos de luminiscencia comerciales aptos para llevar a cabo medidas de fosforescencia: espectrómetro de luminiscencia Aminco-Bowman Series 2, espectrómetro de luminiscencia Hitachi Instruments F-4500, espectrofotómetro de fluorescencia Varian Cary Eclipse, espectrofluorímetro Jobin-Ybon modelo Spex Fluoromax-3	73
37	Instrumentación empleada en fosforimetría de modulación de fase (dominio de la frecuencia): sensor comercial <i>NeoFox Sport</i> de Ocean Optics para la medida de oxígeno usando medidas de fase, osciloscopio digital, tarjeta de adquisición de datos AD/DA, detector de fase-fija (<i>lock-in amplifier</i> , LIA).	74
1.1	Diagrama esquemático de la arquitectura general del banco de pruebas desarrollado	119
1.2	Tarjeta de adquisición de datos AD/DA y accesorios. Tarjeta NI-DAQ PCIe-6363 National Instruments, bloque conector NI-BNC 2120 National Instruments, cable para la conexión tarjeta-bloque conector (NI-PCI Bus National Instruments)	120
1.3	Circuito electrónico diseñado para modular la corriente del LED (LED driver) en el sistema de medida propuesto. Diagrama esquemático. Fotografías desde distintos ángulos	121
1.4	Detalle de la excitación de una fase sensora con la fibra óptica bifurcada y la formación del “spot” luminiscente	122
1.5	Estructura y detalle de funcionamiento de la celda de flujo diseñada	123
1.6	Fotografía que muestra los distintos elementos que componen la estación de gases del sistema de medida propuesto. También se muestra una imagen del programa desarrollado en LabView para monitorizar y regular en tiempo real la cantidad de flujo de gas que circula por cada uno de los MFCs	124
1.7	Fotografía del módulo PMT usado como detector óptico en el sistema de medida propuesto	125
1.8	Fotografía del espectrómetro de fibra óptica comercial usado para la adquisición de las medidas de intensidad de luminiscencia en el sistema de medida propuesto. También se muestra una captura de pantalla del software usado para controlar dicho equipo	126
1.9	Fotografías del cuarto oscuro utilizado para alojar la celda de flujo y el módulo PMT en el sistema de medida propuesto	126

1.10	Acondicionamiento de señal en el sistema de medida propuesto: amplificador de voltaje de bajo ruido, filtro RC pasivo paso-baja de tres etapas	127
1.11	Equipos de adquisición de datos para la medida del desfase y/o del factor de modulación en el sistema de medida propuesto: un detector de fase-fija comercial (<i>lock-in amplifier</i> (LIA)) y un osciloscopio digital conectado a un ordenador personal para el posterior procesamiento de los datos usando MATLAB	127
1.12	Diagramas esquemáticos de los primeros circuitos desarrollados para el sistema de medida: circuitos diseñados para modular la corriente del LED y para la etapa de la detección óptica	130
1.13	Módulo APD comercial (Hamamatsu Photonics Japan, modelo C10508) usado como detector óptico en versiones anteriores del sistema de medida	131
1.14	Fotografía del banco de pruebas desarrollado en las primeras fases del diseño	132
1.15	Resumen gráfico de la evolución del diseño de la etapa de detección óptica en el sistema de medida propuesto	133
1.16	Evolución de la instrumentación empleada para la generación y la adquisición de las señales en el sistema de medida propuesto (versiones anteriores y actual)	133
1.17	Fotografía del banco de pruebas final presentado en esta memoria	134
2.1	Schemes of the devices developed for gas and aqueous determination of CO ₂	141
2.2	Recognition mechanism	142
2.3	Emission spectra of the proposed sensing layer in the absence of CO ₂ and in the presence of 100% CO ₂ in gas and aqueous phases	143
2.4	Variation of the relative fluorescence intensity (R.F.I.) of the proposed sensing film with the percentage of CO ₂ in gas and aqueous phases, and calibration curves in gas and aqueous phases	145
2.5	Emission spectra obtained with the fiber optic CCD spectrometer of the proposed sensing layer in the absence of CO ₂ and in the presence of 100% CO ₂ in gas phase. Variation of the relative fluorescence intensity (R.F.I.) observed with the optical fiber sensor with the percentage of CO ₂	148
3.1	Excitation and emission spectra of the dyes in the absence and in the presence of oxygen of PtTFPP and N969 immobilized into AP200/19	166
3.2	Variation of the phase shift of PtTFPP and N969 incorporated into AP200/19 with the oxygen concentration	169
3.3	Calibration curves of PtTFPP, N969, N1008 and EB146 incorporated into AP200/19 at 21 °C. Decay time and Stern-Volmer plots	171

3.4	Variation of the luminescence lifetime between 0 and 0.26% pO ₂ of PtTFPP, N969, N1008 and EB146 incorporated into AP200/19 at 21 °C, and the parameter $\Delta\tau_{0.05\%}$	173
3.5	Stability of the phase shift and amplitude of PtTFPP and N969 incorporated into AP200/19 at 21 °C	175
3.6	Effect of relative humidity (0% RH, 20% RH and 80% RH) on the phase shift of PtTFPP and N969 incorporated into AP200/19 at 21 °C	176
4.1	Schematic diagrams of the designed experimental setup for phase-shift measurements (based on I/Q method) and of the flow cell used	231
4.2	Phase-shift measurements <i>versus</i> oxygen concentration for 4 different modulation frequencies using the proposed system based on I/Q method at a single frequency, and the reference measurement system based on a commercial dual-phase lock-in amplifier	235
4.3	Temporal representation of a segment of the multifrequency excitation signal and the multifrequency emission signal registered simultaneously by the digital oscilloscope at a sampling rate of 5 MS/s and 0% O ₂	237
4.4	Normalized power spectrum of the multifrequency excitation signal and the multifrequency emission signal	237
4.5	Calibration curves of normalized phase-shift versus oxygen concentration (i.e., $\phi_{0,\omega}$ vs. O ₂ (%)) obtained from experimental data	238
4.6	Relative root mean-square error (RRMSE(%)) for the different proposed oxygen measurement strategies at 17 different oxygen concentrations	240
5.1	Schematic diagram of the experiment designed for measuring the phase-shifts using two different data acquisition devices: (1) a commercial dual-phase lock-in amplifier and (2) a digital oscilloscope connected to a personal computer for further data processing using the I/Q method	269
5.2	Calibration of the oxygen-sensitive film (PtTFPP/PS) using the proposed I/Q method and LIA. Phase-shift variation versus oxygen concentration. Stern-Volmer plots fitted according to the Demas model	272
5.3	Average RMSE values (expressed in units of % O ₂ (v/v)) obtained under different lighting conditions using I/Q method and LIA system	273
6.1	Waveform and amplitude spectrum of a sinusoidal wave, a square wave with a 50% duty cycle, and a rectangular wave with a 10% duty cycle with the same average current level	298

6.2	Effect of the modulation frequency on the apparent luminescent lifetimes estimated from phase shift and the modulation factor at 0, 0.5, 0.75, 1, 2, 3, 4, 5, 6, 7, 8, 9, 10, 12, 14, 16, 18 and 20 kPa O_2	300
6.3	RMSE in the determination of pO_2 between 0.5 and 20 kPa using the phase-based apparent lifetime with the conventional phase-modulation method and the proposed multifrequency phase-modulation method combining the n ($n = 1, 2, \dots, 5$) first harmonics	303

Lista de Tablas

1	Comparación entre los principales métodos de determinación de oxígeno . . .	26
2.1	Analytical properties of the proposed CO ₂ -sensing film in gas and aqueous phases	144
2.2	Analytical features of the proposed CO ₂ -sensing optical fiber sensor in gas phase	147
3.1	Maxima luminescence excitation and emission wavelengths ($\lambda_{exc/em}$) and luminescence lifetime in the absence of oxygen (τ_0) of the dyes incorporated into AP200/19	167
3.2	Oxygen sensitivity of dye-AP200/19 films between 0-1% and 0-10% O ₂	168
3.3	Measurement capability of the developed sensing films	172
3.4	Response times (t_{95}) of the dyes incorporated into AP200/19	172
4.1	Phase-shift measurements obtained at 16 different modulation frequencies and different oxygen concentrations (0%, 15% and 100% O ₂) using the multifrequency I/Q method	236
4.2	Parameters of the sensing film-calibration curves obtained by adjusting the experimental multifrequency phase-shift data to the Demas model	239
4.3	Relative root-mean-square error values (RRMSE) for the different oxygen measurement strategies at different oxygen measurement ranges (1-15% O ₂ and 0.25-50% O ₂ , respectively)	241
5.1	Statistical results of the validation of the IQ method using analog signals with different SNR levels	271

6.1	Accuracy for several combinations with the conventional phase-modulation method (sine-wave modulated excitation at $f_{sin} = 5145$ Hz) and the proposed multifrequency phase-modulation method ($f_1 = 1715$ Hz, $f_2 = 3430$, $f_3 = 5145$, $f_4 = 6860$, and $f_5 = 8575$ Hz) in the determination of pO_2 at four oxygen concentration levels	302
7.1	Summary of models included in this study. The parameters to be fitted and expressions for the response at null concentration Φ_0 and the sensitivity K are shown for each model	337
7.2	Calibration results of experiment 1 for each model and criteria	343
7.3	Root mean square error (RMSE) when the models are calibrated and evaluated with criterion (c): RMS relative error in pO_2 (expressed in %). Analytical signals: τ_ϕ (apparent lifetime estimated from phase-shift), τ_m (apparent lifetime estimated from modulation factor), I (luminescence intensity)	344
7.4	RMSE averaged for the 25 experiments, using different models and calibration criteria. RMSE evaluated from calibration (calib.) and test data	345
7.5	Relative degradation associated to over-fitting (D_{OF}) for different models and criteria when $RMSE_{test}$ is compared with $RMSE_{cal}$	346
7.6	RMSE averaged for the 25 experiments, for each model and criterion. For each model, the criteria used for calibration are in different columns; the criteria used for evaluation are in different rows. RMSE evaluated with calibration and test data	347